JOINT EUROPEAN TORUS JET

JET JOINT UNDERTAKING

PROGRESS REPORT 1988

Volume II

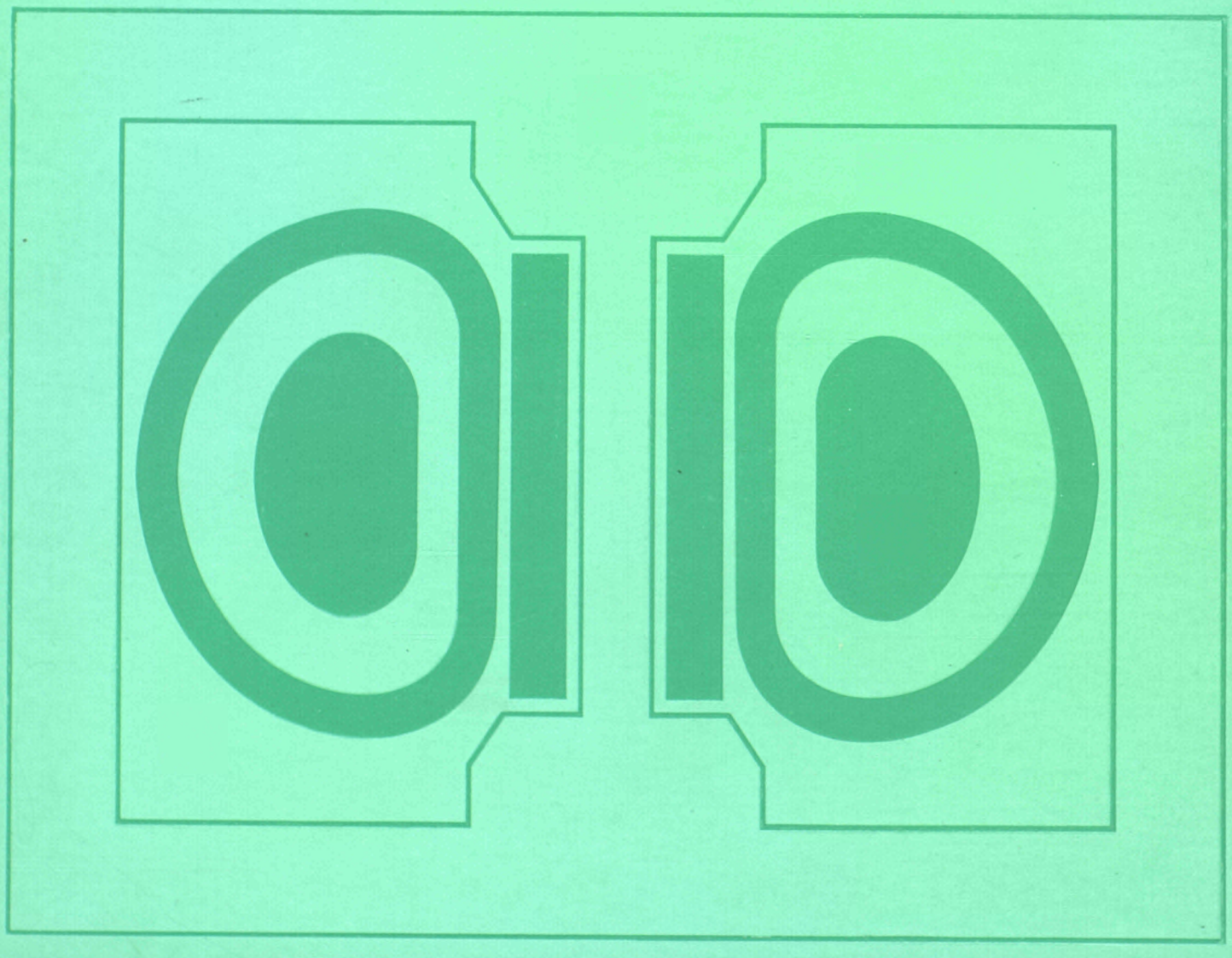

EUR 12323 EN
EUR-JET-PR6

JET JOINT UNDERTAKING

PROGRESS REPORT 1988

Volume II

JUNE 1989

This document is intended for information only
and should not be used as a technical reference.

EUR 12323 EN (EUR-JET-PR6) June 1989.
Editorial work on this report was carried out by B. E. Keen
The preparation for publication was undertaken by
the Documentation Service Unit, Culham Laboratory. UK.

Catalogue number: **CD-NA-12323-EN-C** *for the report* **EUR 12323-EN**

Printed in England

Contents

Volume I

Volume II

Appendix III

Reprints of JET Papers

(a) JET-P(88)15 JET Contributed Papers presented at the 15th European Conference on Controlled Fusion and Plasma Heating (Dubrovnik, Yugoslavia, 16th-20th May 1988) - Many Authors;

(b) JET-P(88)21 Experience with Wall Materials in JET and Implications for the Future - Invited paper presented at the 8th International Conference on Plasma Surface Interactions, Jülich, F.R.G., 2nd-6th May 1988) - P.H.Rebut, K.J. Dietz and P.P. Lallia

(c) JET-P(88)26 Plasma Performance in JET: Achievements and Projections - A. Gibson (for JET Team) - Invited Paper presented at 15th European Conference on Controlled Fusion and Plasma Heating (Dubrovnik, Yugoslavia, 16th-20th May 1988);

(d) JET-P(88)40 High Power Ion Cyclotron Resonance Heating in JET - J.Jacquinot (for JET Team) - Invited Paper presented at 15th European Conference on Controlled Fusion and Plasma Heating (Dubrovnik, Yugoslavia, 16th-20th May 1988);

(e) JET-P(88)44 The JET Plasma Boundary with Limiter and X-Point Discharges - P. Stott (for JET Team) - Invited Paper presented at 8th International Conference on Plasma Surface Interactions (PSI) (Jülich, FRG, 2nd-6th May 1988);

(f) JET-P(88)69 Contributed Papers to 15th Symposium on Fusion Technology, (SOFT), (Utrecht, The Netherlands, 19th-23rd September 1988) - Many Authors;

(g) JET-P(88)58 JET Results and the Prospects for Fusion - P.H.Rebut and P.P. Lallia - Invited Paper presented at 15th Symposium on Fusion Technology (SOFT), (Utrecht, The Netherlands, 19th-23rd September 1988);

(h) JET-P(88)61 Preparation for D-T Operation at JET - A.C. Bell et al - Invited Paper presented at 15th Symposium on Fusion Technology (SOFT), (Utrecht, The Netherlands, 19th-23rd September 1988);

(i) JET-P(88)63 Key Components of the JET Active Gas Handling System - Experimental Programme and Results - J.L. Hemmerich et al - Invited Paper presented at 15th Symposium on Fusion Technology (SOFT), (Utrecht, The Netherlands, 19th-23rd September 1988);

(j) JET-P(88)64 The JET Experience with Remote Handling Equipment and Future Prospects - T. Raimondi - Invited Paper presented at 15th Symposium on Fusion Technology (SOFT), (Utrecht, The Netherlands, 19th-23rd September 1988);

(k) JET-P(88)78 Contributed Papers Presented at 12th IAEA Conf. on Plasma Physics and Controlled Nuclear Fusion Research, (Nice, France, 12th-19th October 1988) - Many Authors;

(l) JET-P(88)43 JET Progress Towards D-T Operation - M. Huguet et al - Invited paper presented at 8th Topical Meeting on Technology of Fusion, (Salt Lake City, Utah, USA, 10th-14th October 1988).

Appendix III(a)
JET-P(88) 15

JET contributed papers to the 15th European Conference on Controlled Fusion and Plasma Heating (Dubrovnik, Yugoslavia, 16th-20th May 1988)

JET Authors

THE FINAL PHASE OF JET DISRUPTIONS

D.J. Ward, R.D. Gill, P.D. Morgan and J.A. Wesson

JET Joint Undertaking, Abingdon, Oxon. OX14 3EA, UK.

Abstract. It is widely believed that the loss of plasma energy in a disruption is due to the generation of a turbulent magnetic field. In studying fast disruptions in JET, it is found that the irreversible nature of the disruption is better understood in terms of radiation cooling.

Introduction. JET disruptions often end with a very fast decay of the plasma current. Fig.1 shows the plasma current for a 5MA discharge which terminated in a disruption. The current decay rate reaches $850MAs^{-1}$, compared with $0.5MAs^{-1}$ for a non-disruptive discharge. The dramatic difference in decay rate shows that a large change in plasma properties occurred in the disruption.

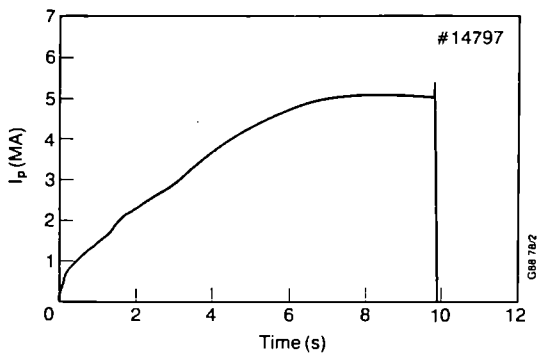

Fig.1 Plasma current for disrupting discharge.

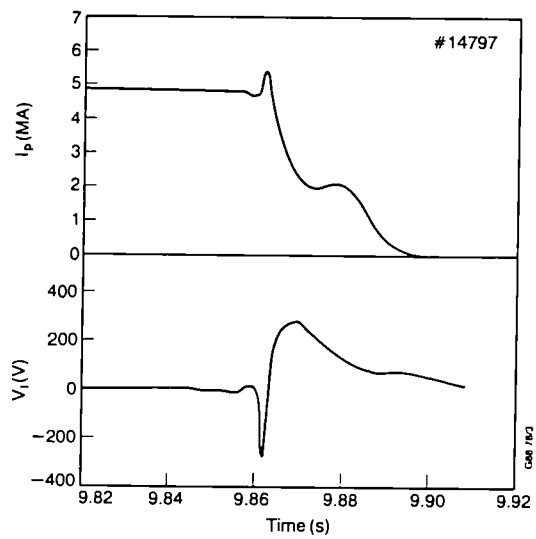

Fig.2 Expanded trace of plasma current and loop voltage.

Temperature Inferred from Resistance. The plasma resistance during the current decay is calculated by equating the ohmic dissipation to the known input power

$$I^2 R_p = \frac{d}{dt}\left(\frac{1}{2} L_i I^2\right) + I V_\ell \qquad (1)$$

where R_p is the plasma resistance, L_i the internal inductance and V_ℓ the toroidal loop voltage at the plasma surface. Fig.2 shows an expanded trace of the plasma current and voltage from one loop on the vacuum vessel for the same discharge as Fig.1. L_i was calculated to be $2\mu H$ before the disruption and the average loop voltage reaches 300V during disruption.

The calculated input power during the current decay reaches ≈ 10GW compared with ~ 10MW in a non-disruptive discharge. The resulting plasma resistance is ≈ 400μΩ. If the resistance is due to Spitzer resistivity then, taking $Z_{eff} = 3$, the implied electron temperature is

$$T_e \approx 5\text{eV}$$

Temperature Inferred from Runaway Electrons. The current plateau during the current decay shown in Fig.2 is a standard feature of fast disruptions on JET, and sometimes persists for 100's of ms. The plateau is due to a current carried by runaway electrons and the number of runaways generated can be used as an indication of the electron temperature.

Calculations of the rate of generation of runaway electrons [1,2,3] show that the important parameter is the ratio of the electric field to a critical value, the Dreicer field, E_D. If the electron temperature is suddenly reduced in the disruption, large electric fields are induced. For a current decay with time constant, τ, the fractional density of runaways generated is given approximately by [3]

$$\frac{n_r}{n_e} \approx \frac{\tau}{\tau_e}\left(\frac{E}{E_D}\right)^{3/8} \exp\left(-\frac{E_D}{4E} - \left(\frac{2E_D}{E}\right)^{1/2}\right) \qquad (2)$$

where τ_e is the electron collision time. For the observed runaway current of 2MA, approximately 10^{-4} of the electrons are runaways and for $\tau \approx 10$ms this implies

$$\frac{E_D}{E} = \frac{2.6\times10^{-17} n_e \ell n\Lambda (2\pi R) I}{T_e P_{in}} \approx 40 \qquad (3)$$

with T_e in eV. P_{in} is the ohmic dissipation and E_D is taken from [2]. With $n_e \approx 6\times10^{19}\text{m}^{-3}$, Eq.(3) gives

$$T_e \approx 4\text{eV}.$$

Temperature Achieved by Anomalous Conduction. The equilibrium temperature of a plasma confined in an ergodic magnetic field is estimated by writing tne effective conductivity as

$$\chi_\perp = \left|\frac{\tilde{B}}{B}\right|^2 v_{te}^2 \tau_e \qquad (4)$$

where $\tilde{B}/B$ is the level of magnetic field fluctuations, v_{te} the thermal velocity of electrons. Assuming a parabolic temperature profile and Spitzer resistivity, and balancing the Ohmic heating against the conducted power gives an expression for the central temperature

$$T_{eo} \approx 20\left(\frac{B_0 Z_{eff}}{\tilde{B}/B}\right)^{2/5} \text{eV} \qquad (5)$$

where $\ell n\Lambda = 10$ has been assumed. Fig.3 shows a plot of this function for $Z_{eff} = 3$ and $B = 3$T. Even with the perturbed field strength comparable to the poloidal field, the temperature is an order of magnitude larger than the experimental value inferred above. Measured values of $\tilde{B}/B_\theta$ are typically <10% [4].

It is seen, therefore, that the drop in electron temperature at the disruption is not due solely to enhanced transport across the minor radius. The alternative to thermal conduction is radiative cooling. For instance, an influx of impurity atoms at the disruption would cool the plasma while being ionised, then hold the temperature low by radiation.

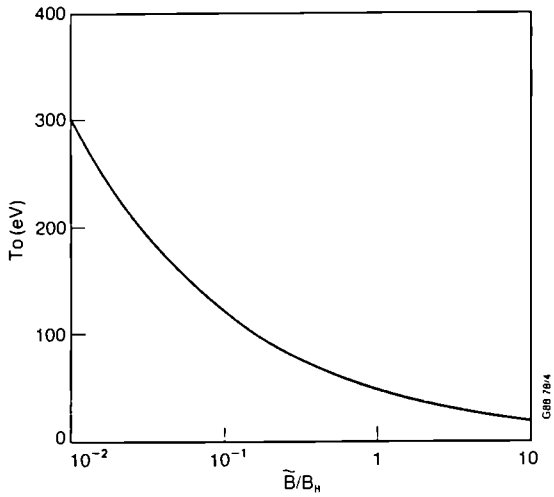

Fig.3 Predicted central temperature versus field fluctuation level.

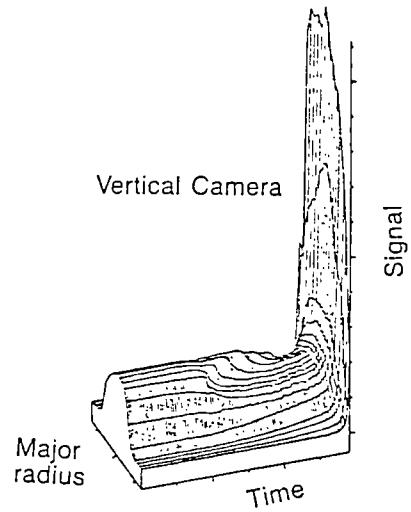

Fig.4 Soft X-ray emission for 3ms before disruption.

Soft X-ray Emission. The disruption observed in the soft X-ray emission proceeds in two stages, illustrated in Fig.4. First there is a broadening of the profile, taking ~2ms, followed by a spike in emission, lasting for ~200μs. Following the spike the plasma current increases momentarily and then decays away. Fig.5 shows this behaviour for one central soft X-ray chord with the plasma current also shown for reference.

The final spike in soft X-ray emission can be understood in terms of a rapid increase in impurity content. For low Z ions and for the X-ray filters used, the emission has the dependence

$$P_x \propto n_e n_z T_e. \qquad (6)$$

Incoming neutral atoms increase n_z but decrease T_e. Writing the impurity content as $n_z = n_o (1+\alpha t)$ gives

$$P_x = P_o (1+\alpha t)\left(1 - \frac{n_o E_i}{W_o} \alpha t\right) \qquad (7)$$

where P_o is the initial X-ray intensity, E_i is the ionisation energy of the incoming neutrals and W_o is the initial electron energy density.

For carbon or oxygen impurities at typically 4% concentration, Eq.(7) predicts an increase in soft X-ray emission by a factor of 5 to 10. This simple model shows how a large increase in soft X-ray emission can occur, but does not give a mechanism for the impurity influx.

Carbon III and Visible Bremsstrahlung. Fig.6 shows the intensity of a carbon III line (3p-3s transition at 465nm) and of visible bremsstrahlung (at 523.5nm) along lines of sight through the plasma centre. The disruption occurs at 10.522 seconds and there is an increase by a factor of 1,000 in the carbon III intensity, and a factor 200 in the visible

bremsstrahlung. Examination of several chords shows the carbon radiation comes from the plasma bulk rather than an edge shell.

Under these conditions, carbon III emission is a strong function of temperature, peaking around 7eV. The increase in intensity can be understood merely in terms of a drop in electron temperature from ≈ 500eV to ≈ 5eV. The visible bremsstrahlung emission requires a change in $Z_{eff}(\int n_e dl)^2$ by a factor of 10. For instance if Z_{eff} increases by ~50%, then $\int n_e dl$ must increase by a factor ≈ 3. The observed behaviour is consistent with an influx of neutral carbon atoms, such that the carbon density increases to a value comparable with the deuterium ion density, that is $n_C \approx n_D$.

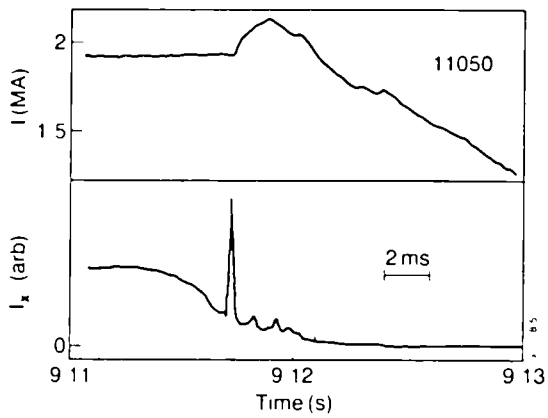

Fig.5 Plasma current and emission along one soft X-ray chord during disruption.

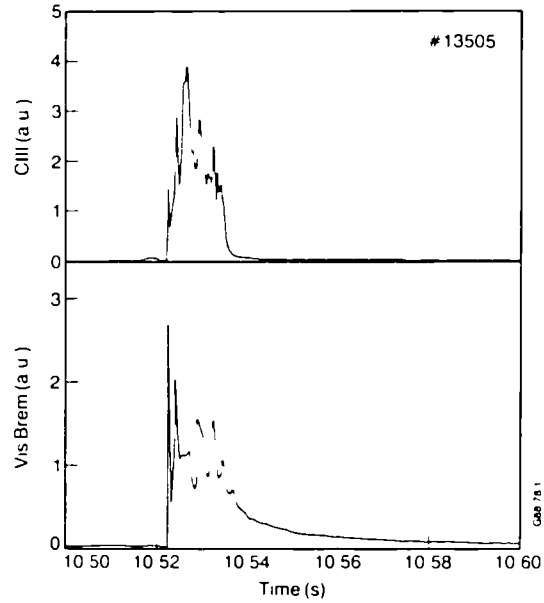

Fig.6 Carbon III line and visible bremsstrahlung emission during disruption.

Summary

1. The inferred electron temperature in JET during the current decay of a fast disruption is ≈5eV.
2. The lowest temperature which could be achieved by anomalous conduction is >50eV.
3. Radiation must play a role in the energy loss. A sudden increase in the plasma impurity content is required.
4. The soft X-ray spike at the disruption is consistent with a rapid influx of impurity atoms.
5. Carbon III and visible bremsstrahlung measurements are consistent with a temperature of ≈5eV and a factor ≈ 3 increase in electron density. This is again consistent with an influx of impurity atoms.

References

[1] H. Dreicer, Phys. Rev. 117 (1960) 329.
[2] A.V. Gurevich, Soviet Phys. JETP 12 (1961) 904.
[3] J.W. Connor, R.J. Hastie, Nucl. Fusion 15 (1975) 415.
[4] K.M. McGuire, D.C. Robinson, Phys. Rev. Letts. 44 (1980) 1666.

MEASUREMENTS OF 'SNAKES' FOLLOWING MULTIPLE PELLET FUELLING OF JET

A W Edwards, D Campbell, A Cheetham, R D Gill, C Gowers, K Hirsch[1], P Nielsen, J O'Rourke, H Salzmann[1] and D Zasche[2]

JET Joint Undertaking, Abingdon, Oxon, UK
Permanent addresses:
[1] Universität Stuttgart, 7000 Stuttgart 80, FRG
[2] Max-Plank-Institut für Plasmaphysik, 8046 Garching, FRG

INTRODUCTION

The extremely long lived density perturbation, or snake, first seen by the soft X-ray cameras following single pellet injection into JET[1], has now been observed following multiple pellet fuelling of JET discharges[2]. The snake is caused by a local density perturbation rotating at a rational q-surface, normally the q=1 surface. The snake can persist for longer than 2 seconds, suggesting that a magnetic island is formed at the rational q-surface, with ablated pellet particles being deposited inside this island. The long snake lifetime implies a change to a new non-axisymmetric equilibrium[1].

New diagnostics have contributed important new results on the study of snakes. Particularly an array of toroidal soft X-ray cameras and the LIDAR Thomson Scattering system[3], which makes simultaneous measurements of the electron temperature and density profiles possible. These will be presented in this paper, with particular emphasis on the creation of snakes and the subsequent snake profiles.

CERTAIN NECESSARY CONDITIONS FOR THE CREATION OF SNAKES

The soft X-ray signals for two time periods of 1 millisecond each recorded during the injection of successive D_2 pellets, the second of which created a snake, are shown in Fig.1. The upper signals are from the vertically mounted camera which views the incoming pellet trajectory. The bottom signal is that of a central detector in the horizontally mounted camera which views the injected pellet from behind and gives a measure of the pellet ablation rate. The two soft X-ray cameras[4] are located at the same toroidal position as the multiple D_2 pellet injector. Both pellet trajectories are clearly visible in Fig.1. In Fig.1a the maximum rate of pellet ablation is seen to occur around 60cms, which is outside the sawtooth inversion radius of 45cms, as determined from a tomographic analysis of the soft X-ray data[5]. Throughout this paper the sawtooth inversion radius is taken as being equivalent to the q=1 position. For the second pellet, shown in Fig.1b, the sawtooth inversion radius is determined to be at 42cms. This pellet is observed to penetrate well beyond this radius, with considerable pellet ablation occurring in the region of the q=1 surface. Around such a rational surface, the particles would not be expected to spread rapidly. A local drop in temperature could therefore occur, as only the electrons inside a narrow flux tube which intersects the pellet trajectory would interact with the pellet.

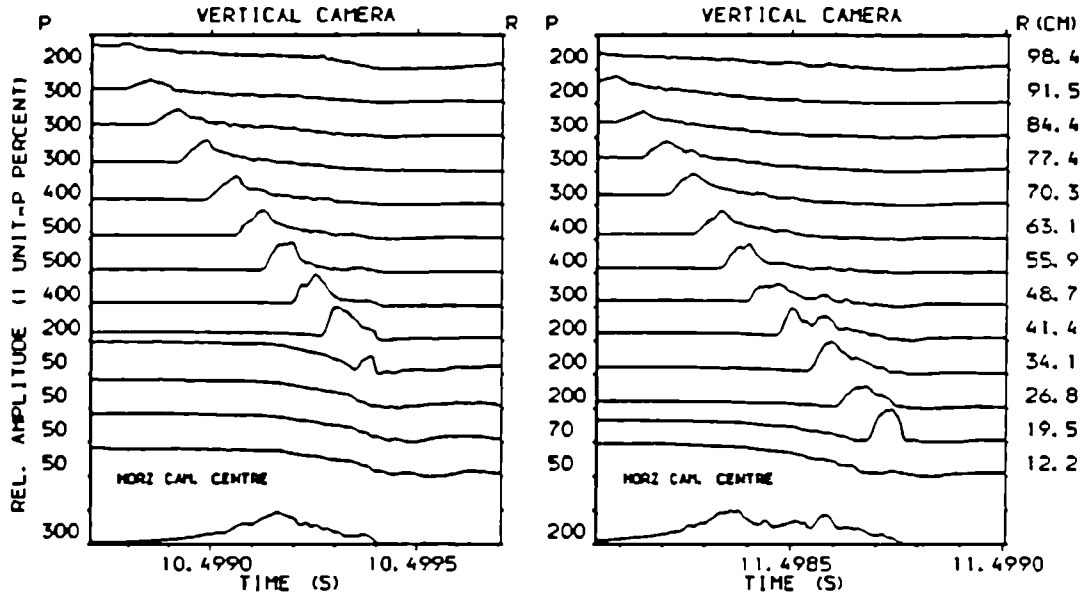

FIG.1: X-ray signals during the injection of two successive D_2 pellets, the second of which created a snake.

In Fig.2, LIDAR profiles of the electron temperature and density across the horizontal mid-plane of JET are shown, 19 milliseconds after the injection of a pellet which created a snake. At the sawtooth inversion radius, a clear local density enhancement and temperature depression are seen and it is this density perturbation which is labelled a snake. Local cooling is therefore observed at the q=1 surface, which can lead to a helical current perturbation and the formation of a magnetic island.

Certain necessary, although perhaps not sufficient, conditions for the creation of a snake are, therefore, firstly that a q=1 surface must exist within the plasma, secondly that the pellet must reach this q=1 surface and thirdly that sufficient pellet particles are ablated in the region of the q=1 surface so as to lead to the formation of a magnetic island.

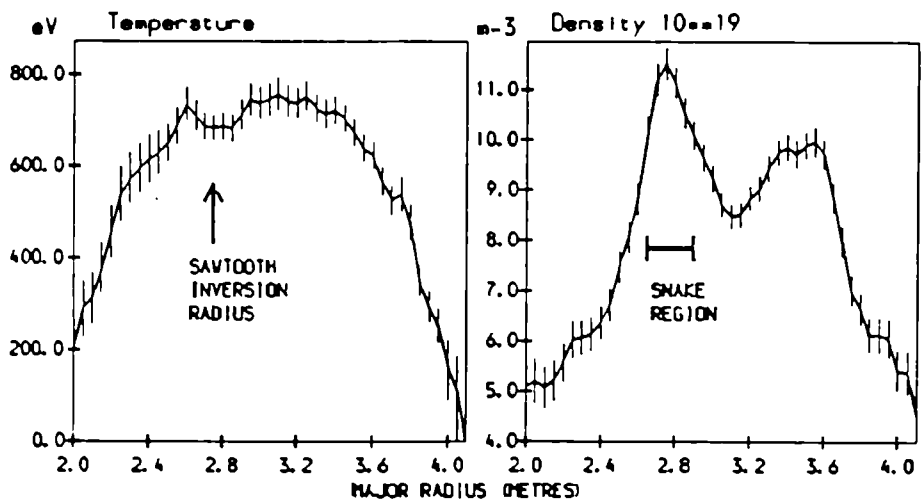

FIG.2:

Radial electron temperature and density profiles, 19 milliseconds after the injection of a pellet which created a snake.

SNAKE PROFILES AND THE SNAKE LIFETIME

From the soft X-ray cameras and toroidal detectors it is found that the snake has an m=1, n=1 structure, with typical dimensions (FWHM) of 25cm poloidally and 17cm radially, which is in good agreement with the radial dimension of the perturbation determined from the LIDAR profiles of Fig.2. From this knowledge of the mode structure, it can be determined from the soft X-ray data that the peak of the snake lies above the horizontal mid-plane at the toroidal location where the LIDAR profiles of Fig.2 are measured. The maximum density and temperature perturbation at this time is, therefore, considerably larger. Indeed, for this particular snake, the ECE grating polychromator experienced a periodic 2nd harmonic X-mode cutoff at the snake radius. From the maximum frequency at which the cutoff was observed, the density of the perturbation was determined to be 1.5×10^{20} m^{-3} ($\pm$ 10%) compared to the density measured by the LIDAR of 1.15×10^{20} m^{-3}. Further, this is not seen to change over a period of 350ms, at which time the plasma current was ramped down, implying an effective confinement time for the snake of the order of several seconds.

In Fig.3, the radial soft X-ray profile measured by the vertically mounted camera is shown. A pellet is injected at 8.5 seconds which creates a snake. This is seen to rotate for a period of 900ms before slowing down and stopping. This snake is observed to survive through many sawteeth, as is the case with all other snakes[1]. At 10 seconds, when LIDAR profiles were measured, the centre of the snake is determined from tomographic analysis of the soft X-ray data to be just above the horizontal mid-plane at the LIDAR port. These LIDAR electron density and temperature profiles are shown in Fig.4. The snake is clearly seen in the density profile, centred at 3.35m. The temperature profile over the corresponding region of this snake shows the temperature falling from about 1700 eV at 3.15m to 1450 eV at 3.5m. This does not show any equalization on either side of the snake, as might be expected if the density is confined within a magnetic island.

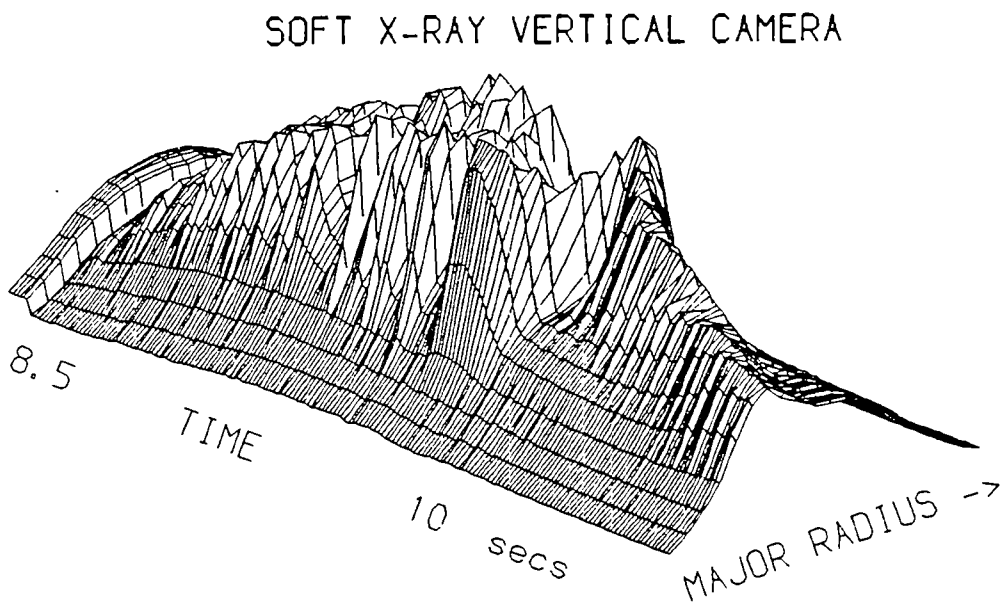

FIG.3: Soft X-ray flux around the time of pellet injection showing the 'snake' oscillation.

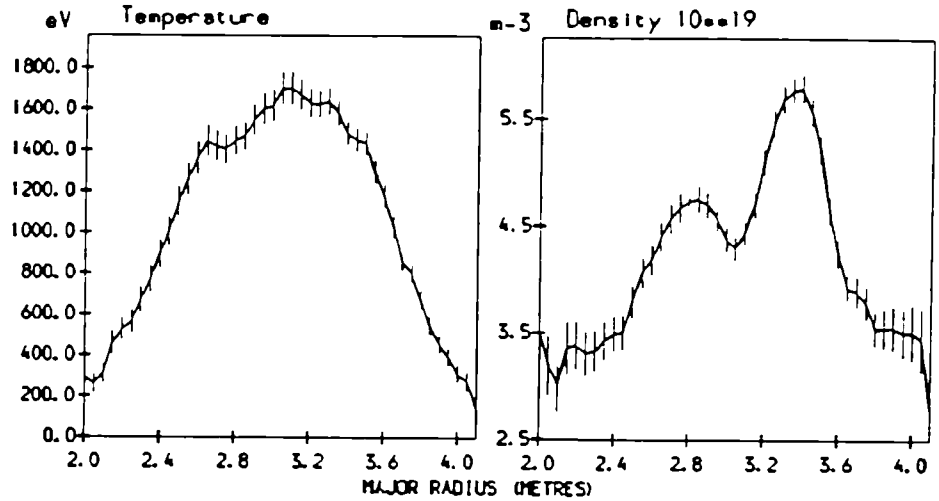

FIG.4:

Radial electron temperature and density profiles 1.5 seconds after the creation of a snake.

These LIDAR profiles are, however, taken at a time when the snake is 'locked' in one poloidal location. As the snake is an island deep within the plasma, if it is to 'lock', it must couple to a mode further out in the plasma which can interact with the vessel wall[6]. The magnetic signals show the presence of a large locked mode at this time. It might not, therefore, be expected that the temperature would be equalized at the extremes of the island at this time, as the snake has coupled to another mode. From Fig.3 it can be seen that, subsequent to these LIDAR profiles, the density perturbation decays away on a timescale of the order of 1 second. In other cases where the snake has been observed to couple to a 'locked' mode, then the density is seen to decay on a similar timescale. The application of on-axis ion cyclotron radio frequency heating (ICRH) is also observed to lead to the decay of the snake. The density is seen to decay on a timescale of the order of 100 milliseconds about 200 milliseconds after the ICRH is applied to the plasma.

SUMMARY

In conclusion, snakes have been observed during multiple pellet fuelling of JET. LIDAR Thomson scattering profiles of electron temperature and density provide clear measurements of the conditions necessary for the formation of a magnetic island at a rational q-surface in which a fraction of the ablated pellet particles can be trapped. ECE measurements in which a persistent periodic cutoff is seen at the snake radius implies a very long effective confinement time for the snake. The presence of 'locked' modes in the plasma, to which the snake can couple, or the application of on-axis ICRH leads to a gradual decay of the snake.

REFERENCES

[1] A Weller, et al., Phys.Rev.Lett. 59(20), 2303(1987).
[2] P Kupschus, G Schmidt, et al., Multi-Pellet Injection on JET, this conference.
[3] H Salzman, et al., Nucl.Fusion 27(11), 1925(1987).
[4] A W Edwards, et al., Rev.Sci.Instrum. 57(8), 2142(1986).
[5] R S Granetz, et al., Proc. 14th Europ.Conf. on Controlled Fusion and Plasma Heating, Madrid, 1987, part III, 1256.
[6] J A Snipes, et al., Effects of Large Amplitude MHD Activity on Confinement in JET, this conference.

SIMULATION OF SOFT X-RAY EMISSIVITY DURING PELLET-INJECTION AND H-MODE IN JET

D. Pasini , A. Edwards ,R. Gill , A. Weller[a] and D. Zasche[a]
JET Joint Undertaking, Abingdon, Oxon., OX14 3EA, United Kingdom
[a] *Permanent address : IPP, Garching, West Germany*

Introduction . Spatial profiles of soft X–ray intensity (E ≥1.75 keV) are measured on JET using one vertical and one horizontal X–ray diode array (100 detectors total). Using tomographic reconstruction techniques spatial distributions of local X–ray emissivity are then derived. Remarkable differences in the X–ray emissivity distributions have been observed depending on the type of plasma discharge. X–ray distributions measured during limiter discharges usually have a gaussian shape. In deep contrast, extremely peaked profiles of X–ray emissivity, with most of of the emission coming from a narrow central region, have been observed after pellet injection and flat or even hollow emissivity profiles have been observed during the H–mode of X–point discharges. In part 1 of this paper simulations which reproduce well both the shape and absolute emissivity of the measured profiles are presented. They show that peaked or hollow emissivity profiles reflect similar changes in the density distributions of the different species.

The vertical X–ray camera which directly views the trajectory of pellets injected into the plasma shows very intense bremsstrahlung emission from the interactions of plasma electrons with pellet particles. In part 2 of this paper a model which accounts for the main aspects of the observations will be discussed.

1. Simulation of emissivity profile .

Peaked profile – Fig. 1 shows the X–ray distribution before (t=4.44 s) and after (t=7.52 s) the injection of two D pellets (4 mm pellet at 4.5 s and 2.7 mm pellet at 5.5 s) into an ohmically heated plasma (# 13572,I=2.5 MA, B=2.8T). The first pellet, cooling the plasma, allows the second pellet to penetrate deep into the plasma, leading to a dramatic increase of the central emissivity and consequently to a strong peaking of the X–ray distribution. Very similar observations made on other experiments have already been reported [1,2].

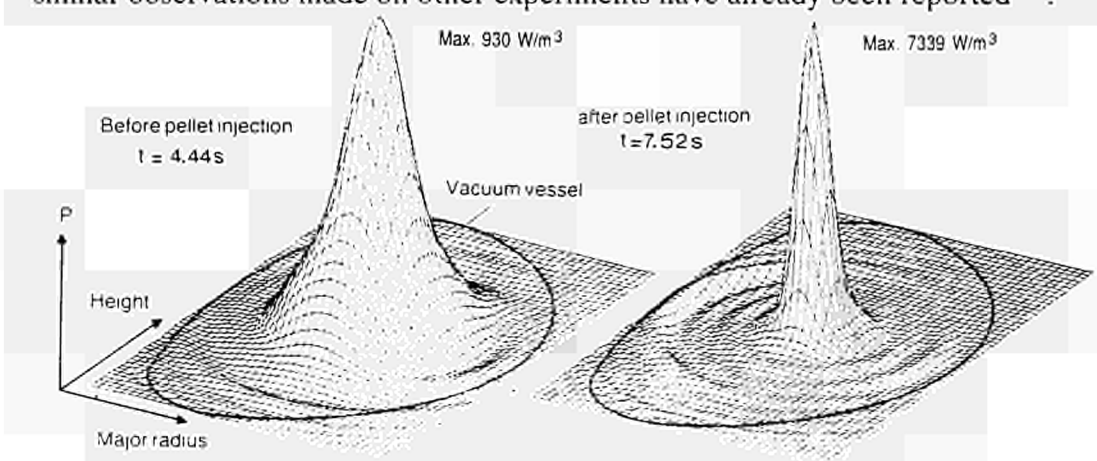

Fig. 1 – X–ray emissivity distribution before and after pellet injection.

Fig.2 shows the radial emissivity profile of the peaked distribution (t=7.52 s) together with two different simulations using the radiation code IONEQ[3]. Taking in account the transmission of the filter the code caculates for each radiating species a radial profile of emissivity and these are then summed up to yield a total profile. The radial charge state distribution for each species is calculated assuming coronal equilibrium and using the impurity concentrations derived from PHA spectra and the profiles of T_e and n_e measured with the LIDAR Thomson scattering diagnostic. The measured profile of n_e is also very peaked. In the first simulation (curve 1) which reproduces well the shape and absolute emissivity of the measured profile the density distributions of the different plasma species are assumed to be as n_e. The calculation shows that the observed emission is mainly due to free-free radiation from fully ionized C and O. In the second simulation (curve 2) the radial density distribution of D is taken as n_e but a much broader pre-pellet distribution is used for the C, O, Cl and Ni impurities. A peaked D density profile is to be expected as the second pellet deposits, in this case, a large part of its particles in the plasma center. The peaking of the impurities is more surprising and indicates an increase of the inward convection velocity. This result can be understood according to the neoclassical theory which predicts that the large density gradient of the D ions should drive the impurities inward. However since the neoclassical theory has not been adequate to describe the majority of experiments this interpretation should be looked at with caution and more work is needed to confirm it.

Hollow profile – Hollow X-ray profiles are observed in certain X-point discharges correlated with hollow electron density profiles. Fig. 3 shows such X-ray emissivity profile measured during an H-mode together with two simulations. The simulation which reproduces the measured profile well (curve 1) was obtained using the hollow electron density profile measured by interferometry and assuming for the other plasma species the same shape of density profile. A second simulation (curve 2), assuming flat density profiles over the central region, was run to verify that the hollowness in the X-ray profile was not due to line radiation from Ni or Cl but a rather a direct conseqence of the hollow densities.

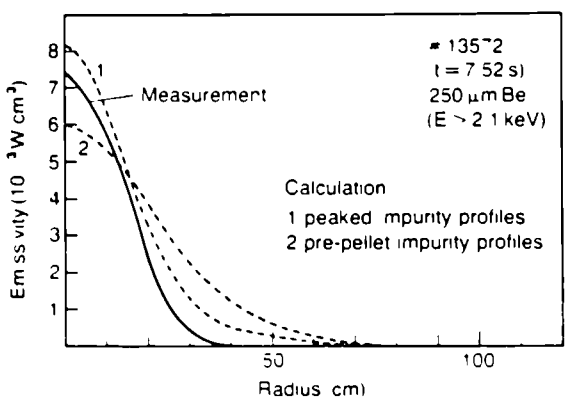

Fig. 2 – Profile of X-ray emissivity after pellet injection and two simulations assuming peaked or broad density profiles for the impurities.

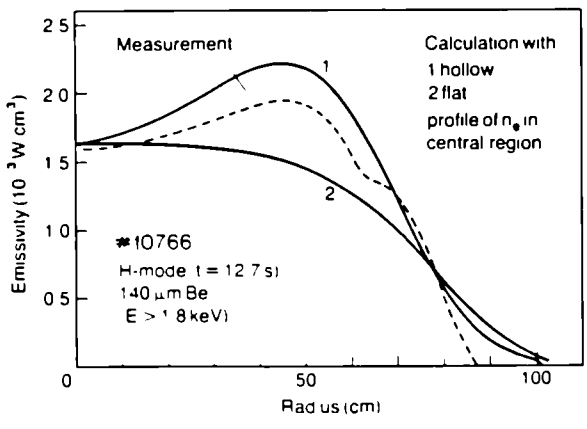

Fig. 3 – Measurement and simulation of hollow X-ray emissivity profile during an H-mode.

2. X–ray ablation emission . Detailed observations on D pellets injected into JET have been made with the vertical soft X–ray camera which directly views the pellet trajectory. Strong emission (Fig.4) is seen from the pellet-plasma interaction region due to bremsstrahlung radiation from collisions between the plasma electrons and the ablated pellet particles. The observations have been used extensively to determine the pellet velocity and depth of penetration. The time dependence of a single channel has shown that the emission originates from within a region with a diameter $2\ r_c = 7\ cm$ in the major radial direction and r_c is taken as the critical radius at which the ablatant flows along the magnetic field lines. The length of the hoze of ablatant along the field lines was determined from toroidally spaced X–ray detectors as much less than $2\ m$. Measurements with different Be filters showed that the effective temperature of the electrons in the region of the pellet was close to that of the plasma before pellet injection.

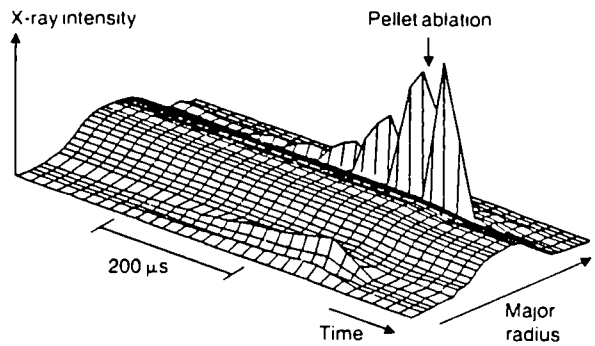

Fig. 4 – The ablation of a pellet as seen by the vertical X–ray camera.

The pellet ablation model of Parks and Turnbull[4] has been used to calculate the absolute intensity of the X–rays. For the shots considered here the model also gave an accurate prediction of the pellet range although a more complicated model[5] is generally required to predict the pellet range in JET. In this model the incident plasma electrons interact with the ablated particles which expand spherically with high density and low temperature near the pellet surface. In a later refinement to the theory[6], the ablated particles flow along the magnetic field lines at $r_c = 2.5\ r_p$, but we prefer to keep r_c as a free parameter as the measurements show a much larger (7×) value. Inside r_c we use the analytic asymptotic solution of PT but outside we have found the corresponding solution for cylindrical geometry. The temperature of the incident electrons differs significantly from T_e close to the pellet surface only. As the X–ray emission comes from much larger radii it is reasonable to use the plasma value of T_e everywhere. The ablatant density is

$$\rho = \rho_* \frac{1}{\alpha^{1/3}} \left(\frac{r_*}{r}\right)^{7/3} , \quad r < r_c \quad ; \quad \rho = \rho_* \frac{1}{\alpha^{1/3}} \frac{r_*^{7/3}}{r_c^2\ z^{1/3}} , \quad r > r_c \ .$$

where $\alpha^{1/3}$ is a constant near unity, r_* and ρ_* are the radius and the density at the sonic surface and z a variable along the field lines. As the velocity of the ablated particles is much less than the plasma electrons the X–ray emission may be calculated from the hydrogenic bremsstrahlung formula

$$P = 1.69 \times 10^{-32} \frac{\rho}{m} n_e \sqrt{T_e}\ e^{-E_c / T_e} \quad (\mathrm{W/cm^3})$$

where E_c is the energy cutoff. Integrating over the field of view (Fig.5) gives

$$P_x = 7.9 \times 10^{-38} \frac{\rho_*}{m} r_*^{7/3} \{(D/2)^{2/3} - r_p^{2/3}\} n_e \sqrt{T_e}\, e^{-E_c/T_e} \quad (W) \cdot$$

This expression (accurate to ~20%) depends only weakly on r_p confirming that there is little emission from the region near to the pellet. P_x has been compared with experiment (Fig.6) for the case of a 3.6 *mm* D pellet injected into a D plasma with $I = 3\ MA$, $B = 2.8\ T$, $n_e = 1.35 \times 10^{19}\ m^{-3}$ and $T_e = 4.8\ keV$. The calculated emission generally exceeds the observed value in the outer part of the plasma, but decreases to well below the observed value at the end of the pellet trajectory. The observation that P_x always increases sharply at the end of the trajectory is not adequately explained by this model.

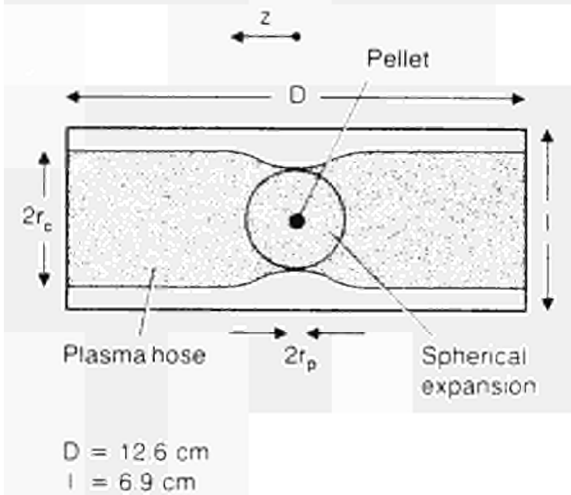

Fig. 5 – Schematic of the ablating plasma within the field of view of an X-ray detector ($D \times l$). For $r > r_c$ the particles flow along the field lines (z direction).

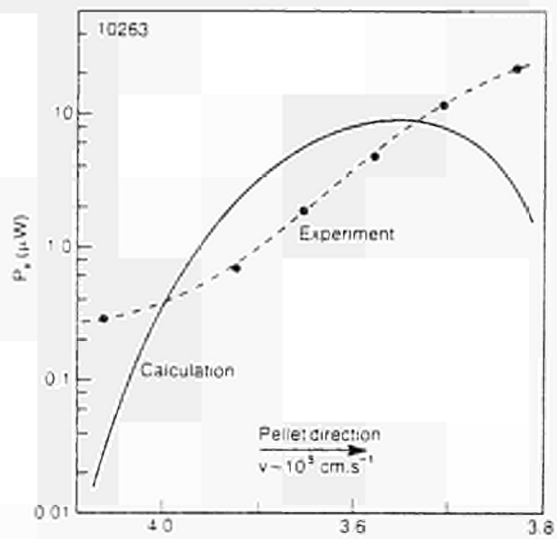

Fig. 6 – Comparison between measured (each data point corresponds to a particular detector) and calculated soft X-ray power versus radial position.

In conclusion : (1) the X-ray measurements support the concept of the formation of a plasma hose, but its radius is larger than predicted and it is quite short ($< 2m$), (2) the PT model provides an approximate estimate of the observed emission except towards the end of the pellet's range where the calculated value is much too small, (3) the X-ray energy spectrum is approximately as expected.

References

[1] R. Petrasso et al., Phys.Rev.Lett. 57(1986)1907.
[2] M. Greenwald et al., 11th Int. Conf. Plasma Phys. and Contr. Nucl. Fus. Res. Kyoto, 1986, IAEA-CN-47/A-III-1.
[3] A. Weller et al. JET internal report, JET-IR(87)10, 1987.
[4] P. B. Parks and R. J. Turnbull, Phys.Fluids 21(1978)1735.
[5] M. L. Watkins, EPS Conf.(Schliersee) vol. 10C (1986)156.
[6] P. B. Parks, Nuclear Fusion, 20(1980)311.

CURRENT TRANSPORT IN A CHAOTIC MAGNETIC FIELD AND SELF-SUSTAINMENT OF ISLANDS

Dr. P.H. Rebut

JET Joint Undertaking, Abingdon, Oxon, OX14 3EA, U.K.

Introduction

In previous work [1], it has been proposed that the anomalous transport observed in Tokamaks could be a consequence of the magnetic topology prevailing in such devices (i.e. the existence of small magnetic islands surrounded by regions where the field lines have an ergodic behaviour). The consequences for current transport and self-sustainment of the topology are considered in this paper. In particular, it is found that the diffusion of the current liberated at each sawtooth crash can sustain the topology between the inversion radius and the plasma boundary, thus extending the conclusion of Ref.[2] to most of the plasma volume.

Trajectories of Magnetic Field Lines in Cylindrical Coordinates (r, θ, Rφ)

We suppose that the magnetic field can be split in two terms: a dominant term $\bar{B}_o$ with cylindrical symmetry ($B_{or} = 0$) and a smaller term B_1, such that $B_1^2 \ll B_o^2$. B_1 is responsible for chaotic behaviour of the magnetic field lines.

- The following equations could be extended to any geometry by a suitable choice of coordinates.

We define
$$\psi = \int_o^r r' B_{o\phi}\, dr' \simeq \int_o^r r' B_\phi\, dr' \qquad (1)$$

ψ = const is the magnetic surface of the unperturbed field and L is the length along a magnetic field line: $d\phi = (B_\phi/BR)\, dL$

The trajectories of a field line are given by

$$dr = (RB_r/B_\phi)d\phi, \quad d\theta = (RB_\theta/rB_\phi)d\phi \qquad (2)$$

which defines a transformation $\bar{M}$ ($\bar{M}_o$, ϕ) (for $\phi = 0$; $\bar{M} = \bar{M}_o$). In particular: $\psi = \Psi(\psi_o, \theta_o, \phi)$ or inverting the previous expression $\theta_o = \Theta_{oi}(\psi_o, \psi, \phi)$; Θ could be a multivalue function (index i). In the same way, inverting initial and current positions along a magnetic line: $\theta = \Theta_i(\psi, \psi_o, -\phi)$

Flux conservation imposes: $d\psi\, d\theta = d\psi_o d\theta_o$, which can be written:

$$\frac{\partial \Theta_i}{\partial \psi_o} = \frac{\partial \Theta_{oi}}{\partial \psi} \quad (\geq 0) \qquad (3)$$

and
$$\int_o^\infty d\psi_o \left(\Sigma_i \frac{\partial \Theta_i}{\partial \psi_o}\right) = \int_o^\infty d\psi \left(\sum_I \frac{\partial \Theta_{oi}}{\partial \psi}\right) = 2\pi \qquad (4)$$

Let us define: $$F(\psi, \psi_o, \phi) = \frac{1}{2\pi} \Sigma_i \frac{\partial \Theta_{oi}}{\partial \psi} \qquad (5)$$

Invariance along a magnetic line:

A function f constant along a magnetic line satisfies the equation:

$$\vec{B}.\nabla f = 0 \qquad \text{which gives} \qquad \frac{\partial f}{\partial \phi} + rRB_r \frac{\partial f}{\partial \psi} + \left(\frac{RB_\theta}{rB_\psi}\right)\frac{\partial f}{\partial \theta} = 0 \qquad (6)$$

Θ_{oi} is invariant along a magnetic line: (initial condition)

$$\Sigma_i \frac{\partial}{\partial \psi}\left[\frac{\partial \Theta_{oi}}{\partial \phi} + r\,R\,B_r \frac{\partial \Theta_{oi}}{\partial \psi}\right] = 0 \quad \text{or} \quad \frac{\partial F}{\partial \phi} + \frac{\partial}{\partial \psi}\left(\Sigma_i rR\,B_r \frac{\partial \Theta_{oi}}{\partial \psi}\right) = 0 \qquad (7)$$

In a chaotic region, the number of value i increases equally over the whole region as ϕ increases and as a first term

$$\Sigma_i\, r\,R\,B_r \frac{\partial \Theta_{oi}}{\partial \psi} \longrightarrow -R\,K(\psi)\frac{\partial F}{\partial \psi} \qquad (8)$$

and $$\frac{\partial F}{\partial \phi} - \frac{\partial}{\partial \psi}\left(R\,K(\psi)\frac{\partial F}{\partial \psi}\right) = 0 \qquad (9)$$

F is the probability of finding a magnetic line starting at ψ_o in an interval $d\psi$ around ψ after a number of turns = $(\phi/2\pi)$.

Eq.(9) is a diffusion equation of magnetic lines to be compared with the similar equation in [1]

$$R\,K(\psi) = \frac{\Delta^2 R}{2L_o}\left(\frac{d\psi}{dr}\right)^2 \qquad (10)$$

where Δ is the distance between two chains of islands and L_o the mean length of magnetic line to cross one chain of islands. If m is the poloidal mode number and μm the bandwidth

$$\Delta = (3/2\mu m^2)\left(\frac{d\iota}{dr}\right)^{-1}, \quad L_o = 2\pi R\,(2\mu m/3)g(\gamma) \qquad (11)$$

with γ the overlapping coefficient: $\gamma = (\epsilon_1+\epsilon_2)/2\Delta$ and $g(\gamma) \sim 1$. For γ=1.2 ($g' < 0$) with these definitions, where ι=1/q is the rotational transform

$$\boxed{R\,K(\psi) \simeq [0.27/\mu^3 m^5 g(\gamma)]\cdot\left(\frac{d\iota}{d\psi}\right)^{-2}} \qquad (12)$$

Application to the current

The current flowing along the field line obeys in the first approximation

$$\vec{B}\ .\ \nabla J_{//} = 0 \qquad (13)$$

We shall suppose that this is true along N turns of the torus.
The diffusion of the magnetic field lines across the magnetic surfaces leads to a transport of current. We define a mean resistivity $\bar{\eta} = V/2\pi/RJ_\phi$

so that $$\bar{\eta}\,B_\phi\left(\frac{V}{2\pi R}\right) = \frac{V}{2\pi R}\int_{-\pi N}^{+\pi N} \eta(\psi)\frac{B\phi}{2\pi R}\frac{d\theta_\alpha}{2\pi}\,d\phi \qquad (14)$$

where V is the voltage per turn. Eq.(13) leads to $(J_{//}/B) = (J_\phi/B_\phi)$ is constant along a field line and follows Eq.(9):

$$\frac{\partial}{\partial\phi}\left(\frac{B_\phi}{J_\phi}\right) + \frac{\partial}{\partial\phi} RK(\psi) \frac{\partial}{\partial\psi}\left(\frac{B_\phi}{J_\phi}\right) = 0 \qquad (15)$$

which taking into account Eq.(14) gives

$$\boxed{2\pi N \frac{\partial}{\partial\psi} RK(\psi) \frac{\partial}{\partial\psi}\left(\frac{B_\phi}{J_\phi}\right) = \frac{B_\phi \eta V}{2\pi R} - \frac{B_\phi}{J_\phi}} \qquad (16)$$

where $(B_\phi\bar{\eta}/R)$ is a mean value over a magnetic surface ψ .

The conditions at the limits are that the flow of current is nul:

$$\frac{\partial}{\partial\psi}\frac{B_\phi}{J_\phi} = 0 \quad \text{for } \psi = 0 \text{ and } \psi = \psi_a \qquad (17)$$

where a is the radius of the plasma.

By integration, Eq.(16) gives $\boxed{\int_0^{\phi_a} \frac{B_\phi}{J_\phi} = \int_0^{\phi_a} \frac{\eta(\psi) B_\phi \, 2\pi R d\phi}{V}}$ (18)

Conclusions

Several conclusions can be deduced from these equations:

(a) When $(\pi NR\Delta^2/L_0 a_2)$ is large compared to 1 (small m numbers and larger islands), Eq.(16) becomes:

$$\frac{B}{J_{//}} = \text{const} = \frac{1}{V\,\phi_a} \int_0^{\phi_a} \eta(\phi)\, B_\phi\, 2\pi R\, d\phi \qquad (19)$$

which give the Taylor condition for reverse field pinch [3]. The next order term can be deduced from Eq.(16). Eq.(19) could also describe the state of the plasma after a disruption in a tokamak; nevertheless, the transport of current will take some time to allow the eddy current in the islands to die away. The effect on the heat transport should be much faster.

(b) When $(\pi NR\Delta^2/L_0 a^2)$ is small compared to 1 (the m number is large and the size of overlapping islands is small), we can define

$$\delta J_\phi = J_\phi - \frac{V}{2\pi R\eta} = 2\,\frac{\pi N}{B_\phi}\frac{\partial}{\partial\psi} RK \frac{\partial}{\partial\psi}\left(\frac{B\phi}{J_\phi}\right) \qquad (20)$$

which produces an extra current in the chaotic region if

$$\frac{\partial}{\partial\psi} RK \frac{\partial}{\partial\psi}\left(\frac{B_\phi}{J_\phi}\right) > 0 \qquad (21)$$

The critical profile in this case for large m numbers could be written with the hypothesis that B_ϕ and RK are constant:

$$\frac{\partial}{\partial r^2}(J_\phi) = -\alpha J_\phi^2$$

which could be integrated to give:

$$J_\phi = J_o/(\alpha r^2+1) \qquad (22)$$

The self consistency of the islands if m is lower but not too small (if not the tearing condition has to be taken into account [2,4]) is given in Ref.[1] (Ampères Law).

$$L_o \mu_o \delta J = B_\phi \qquad (23)$$

which linked to Eq.(23) leads to the self consistency condition; if the islands are sustained only by the transport of current, this imposes a curvature of the current greater than that given in Eq.(22). In Eq.(20) defining δJ, only current diffusion has been taken into consideration but other effects can play a dominant role such as a contribution of fast particles. Thermodynamic effects linked to a flow of plasma along the chaotic field lines may also sustain the islands. Local electric fields and non- ambipolar diffusion may be important. In this presentation, the estimation of N remains a problem.

(c) the current created between the two internal disruptions could be redistributed with this mechanism along the chaotic field line: at the edge of the q = 1 surface, an extra production of current δJ_s could be calculated:

$$2\pi\psi(\delta J_s/B_\phi) = \delta I_s = J_o^2 \int_0^{\psi_1}[(\eta(\psi_1) - \eta\psi)\, 4\pi^2 R]/V d\psi \qquad (24)$$

This current could assist in maintaining the chaotic region.

References

[1] P.H. Rebut, M. Brusati, M. Hugon and P.P. Lallia, Proc. of 11th Int. Conf. on Plasma Physics and Contr. Nucl. Fus., Vol.II, p.187 (1987);

[2] R.B. White and F. Romanelli, PPPL Report 2492 (1987);

[3] J.B. Taylor, Phys. Rev. Letters 33 (1974)19.

[4] P.H. Rebut and M. Hugon, Proc. of 10th Int. Conf. on Plasma Physics and Contr. Nucl. Fus. Vol.II, p197 (1985).

SIMULTANEOUS MEASUREMENTS OF ELECTRON THERMAL AND PARTICLE TRANSPORT IN JET

A Gondhalekar, D Campbell, A D Cheetham, A Edwards, J C M de Haas*, A Hubbard, P D Larsen, J O'Rourke and M L Watkins

JET Joint Undertaking, Abingdon, OX14 3EA, UK
*FOM Instituut voor Plasmafysica "Rijnhuizen", The Netherlands

1. INTRODUCTION

An important objective in tokamak research is to find suitable descriptions for the measured thermal and particle fluxes, and to identify the underlying mechanism of transport. Many detailed models for transport in tokamaks have been developed, which make specific predictions for correlations between thermal and particle transport coefficients. To exclude some of the contending models, accurate measurements of the correlations are required. Thermal and particle transport in JET have been described by expressions of the form [1,2]

$$Q = -\chi n \nabla T + Q_p \quad ; \quad \Gamma = -D\nabla n + \Gamma_p \qquad (1)$$

Q and Γ are the heat and particle fluxes, χ and D are the respective diffusivities, Q_p and Γ_p are convective (or pinch) fluxes. In order to reduce uncertainties arising from shot-to-shot and spatial variations it is necessary to determine the coefficients simultaneously at the same spatial point. In this paper we describe evaluation of thermal and particle transport coefficients by three different methods satisfying the above requirements: (a) From the velocity and damping of heat and density pulses propagating outwards following a sawtooth collapse. (b) Measurement of inward propagation of electron density and temperature perturbations produced when a small pellet is injected into the plasma. (c) The method of 'flux gradient' analysis applied to transient conditions. In the following we present determinations of χ and D for Ohmically heated discharges in deuterium, limited by the outer belt limiters, with I_ϕ = 3MA, $2.8 \leq B_\phi\,(T) \leq 3.4$, and $1.5 \leq \bar{n}_e(10^{19}\ m^{-3}) \leq 2.7$.

2. DETERMINATION OF χ_e AND D_e FROM SAWTOOTH PROPAGATION

The local electron thermal diffusivity χ_e is determined by analysis of propagation of electron temperature perturbations in the region outside the mixing radius after a sawtooth collapse [3]. $T_e(r,t)$ is determined from measurements of electron cyclotron emission, analyzed with a grating polychromator (KK2). Two parameters are derived, a heat pulse velocity and a damping rate of the pulse amplitude. χ_e is determined by comparison with simulations of these using a diffusive model including sources. Fig.1 shows representative parameters of the heat pulse propagation. Measurements are made in steady state, in a region bounded by the normalized minor radius $0.6 \leq r/a \leq 0.8$, and averaged over a period of ≈ 1s. From analysis of a number of discharges a value of $\chi_e = 2.9 \pm 0.4\ m^2/s$ is deduced.

The electron particle diffusivity D_e is determined in an analogous manner by measuring the propagation of a density pulse following a sawtooth collapse [4]. The density perturbation $\delta n_e(r,t)$ is observed using a multichannel reflectometer [5]. The diffusing perturbation is clearly seen at all positions outside the mixing radius r_m. The measured pulse delay time is compared with predictions of a diffusive model in which an equilibrium electron density profile is periodically flattened inside r_m. An edge recycling coefficient R=1, and a pinch flux $\Gamma_p = -Dnr/a^2$ are assumed. Fig.2 shows a comparison of the modelled and measured density pulse propagation. D_e has been varied to match the measured delay in the region, $r_m<r<0.85a$. Analysis of several discharges gives $D_e \sim 0.4$ m²/s with an estimated error of 30%. The above determinations of D_e and χ_e have been performed in the same discharges, covering the same spatial and temporal region, and yield $\chi_e/D_e = 7$.

3. DETERMINATION OF χ_e BY PELLET INJECTION

Here, the local thermal diffusivity is determined by analysis of the propagation of a 'cold front' into the region $r < r_p$, where $r_p = 0.6a$ is the pellet penetration radius. $T_e(r,t)$ at $r_p<r<a$ is measured using the KK2 instrument. In a previous investigation we have shown that the assumption of diffusive propagation of the 'cold front' into the region $r>r_m$ may be justified [6]. χ_e is determined by comparison with simulations using a diffusive model including sources. The initial condition, the temperature and density profiles immediately after pellet injection, is accurately determined from measurements of $T_e(r)$, $n_e(r)$, pellet mass, ablation rate and penetration depth. During evolution of $T_e(r,t)$ in the spatial region of interest, $\Delta t \leq 60$ ms, the perturbed density profile is assumed to be unchanged; the evolution of n_e is much slower than that of T_e, justifying this assumption. The model $T_e(r,t)$ evolution is most sensitive only to the local value of χ_e, enabling an accurate determination. Fig.3 shows a comparison of the measured and modelled $T_e(r,t)$ at radii $r<r_p$. A value of $\chi_e = 1.6 \pm 0.3$ m²/s is deduced at $0.45 \leq r/a \leq 0.55$. This value is close to that determined, under similar conditions immediately after pellet injection, using the heat pulse propagation method [7]. A heat pinch term Q_p is not included in the modelling employed here. However, preliminary indications are that a credible global power balance for electrons can not be constructed without such a flux. An exactly analogous determination of D_e is in preparation, but has not been completed yet.

4. DETERMINATION OF χ_e AND D_e USING THE 'FLUX GRADIENT' ANALYSIS

From eq.1 we have that a plot of Q vs $-n\nabla T$ has slope χ and an intercept Q_p. Similarly for D and Γ_p. Such plots were analyzed for steady-state heat flux for plasmas under various conditions [1]. This technique can be extended to transient conditions by plotting successive time points, yielding the transport coefficients in a single pulse. Transients in density can be induced by injection of a small (2.7mm) pellet or application of ICRF power. Analysis of these gives $D_e = 0.5 \pm 0.1$ m²/s. The corresponding thermal diffusivity is deduced to be $\chi_e = 2\text{-}3$ m²/s. The discharges analyzed have plasma parameters very close to those in section 2. Analysis of a number of discharges using this method yields $3 \leq \chi_e/D_e \leq 8$. Moreover, both these coefficients show an inverse dependence on the plasma current I_ϕ, fig.4 and ref[1].

Table I summarizes all the measurements described in sections 2-4.

5. DISCUSSION

The consistent behaviour of the measured χ and D suggests that these are linked, and that Q_p and Γ_p may be manifestations of the same transport mechanism [8]. Employing expressions derived in [8], we deduce that $2T\Gamma_p \partial ln n/\partial ln T = Q_p$. The measured values of Q_p [1] and Γ_p are in rough agreement with this expression. The derivations of [8] imply that $\Gamma_p \propto (-\nabla T/T)$ and that $Q_p \propto (-\nabla n/n)$. The dependence of Γ_p on the T_e scale-length can be inferred from analysis of the n_e profile evolution during transients in which the T_e profile undergoes a significant change. Peaking of the n_e profile after sawtooth collapse and during current ramp-down are two such instances. Fig.5 shows the measured and modelled evolution of the line-integrated density in a sawtoothing discharge; if $\Gamma_p \propto (-\nabla T/T)$, then the 30ms hesitation observed in the density rise following a sawtooth collapse is reproduced. Fig.6 shows a plot of Γ_p/nD against $-\nabla T/T$ during contraction of the plasma column in current ramp-down. Γ_p is calculated as $\Gamma_p(r) = 2\pi/r \int [S(r') - dn(r')/dt]r'dr' + D(r)\nabla n(r)$. Fig.6 demonstrates the close correlation between these two parameters.

TABLE I

χ_e $m^2 \cdot s^{-1}$	D_e $m^2 \cdot s^{-1}$	$-Q_p$ $kW \cdot m^{-2}$	$-\Gamma_p$ $10^{19}\ m^{-2} \cdot s^{-1}$	Method
2.9 ± 0.4	0.4 ± 0.12	-	-	(a) sec.2, r/a ~0.7
1.6 ± 0.3	-	-	-	(b) sec.3, r/a ~0.5
2 - 3	0.5 ± 0.1	4.3 ± 0.6 [1]	1.5 ± 0.2	(c) sec.4, r/a ~0.7

6. REFERENCES

[1] J Callen, et al., Nuclear Fusion 27(1987)1857.
[2] A Gondhalekar, et al., Bull. Am. Phys. Soc. 30(1985)1525 and JET Report JET-P(85)31.
[3] B J D Tubbing, et al., Nuclear Fusion 27(1987)1843.
[4] A Hubbard, et al., 13th Euro. Conf. on Contr. Fusion and Plasma Physics, 1986. Europhys. Conf. Abstracts, vol.10C, part I, p.232.
[5] R Prentice, et al., this conference.
[6] A D Cheetham, et al., 14th Euro. Conf. on Contr. Fusion and Plasma Physics, 1987. Europhys. Conf. Abstracts, vol.11D, part I, p.205.
[7] N J Lopes Cardozo, et al., 14th Euro.Conf. on Contr. Fusion and Plasma Physics, 1987. Europhys. Conf. Abstracts, vol.11D, part I, p.281.
[8] J O'Rourke, Nuclear Fusion 27(1987)2075.

ACKNOWLEDGEMENT

Part of the work discussed in this paper makes use of data obtained during pellet injection experiments performed under a collaboration agreement between the JET Joint Undertaking and the U.S. Department of Energy.

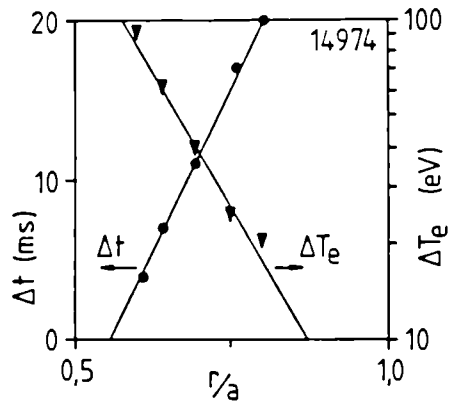

FIG.1 The peak amplitude of the heat pulse, ΔT_e, and the delay in the arrival time of the peak, Δt, vs r/a. Fitted lines give average speed and damping of the heat pulse.

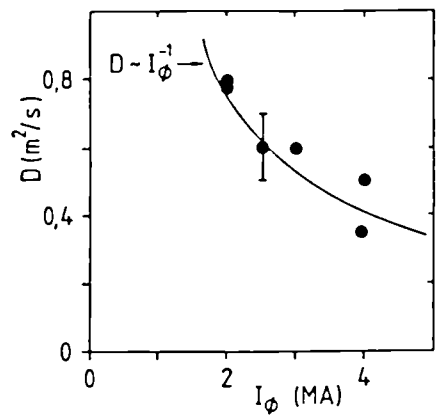

FIG.4 Average Diffusion coefficient $D(r/a \gtrsim 0.5)$ vs plasma current I_ϕ.

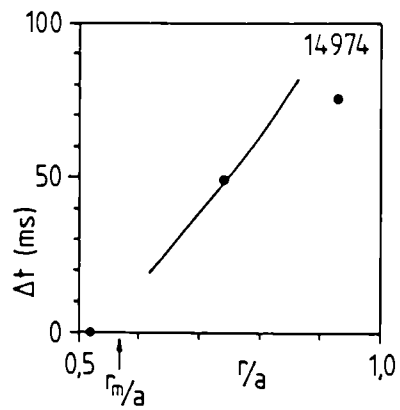

FIG.2 Delay Δt between sawtooth collapse and arrival of density pulse. Line is the prediction with $D_e = 0.39 m^2 s^{-1}$

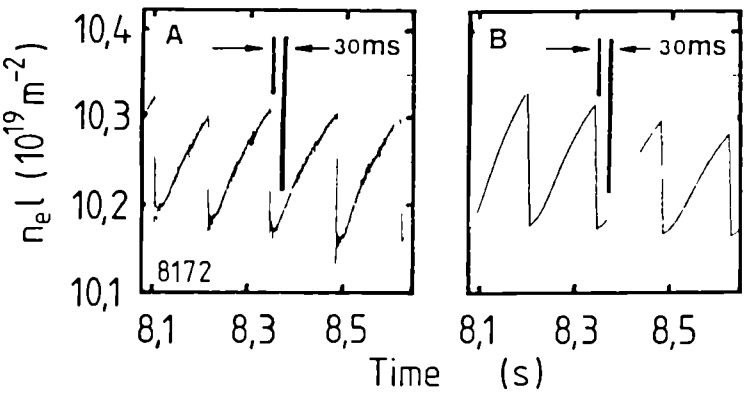

FIG.5 Fluctuations of line-integrated density, $n_e l$, during sawtooth activity: (A) measured, (B) modelled with a particle pinch proportional to the electron temperature scale-length.

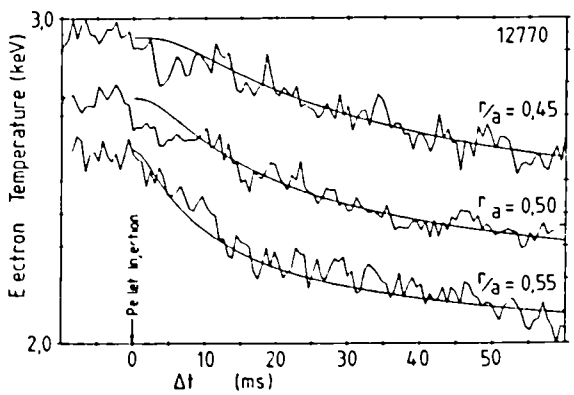

FIG.3 Evolution of T_e at different radii r a after injection of a pellet. The smooth lines are the modelled T_e evolution at the measurement radii.

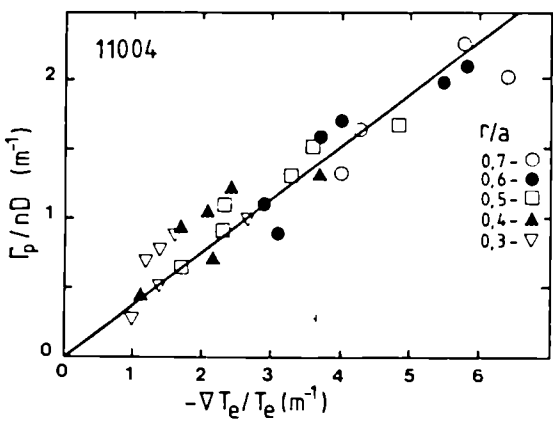

FIG.6 Evolution of Γ_p/nD with electron temperature scale-length ∇T T during decay of I_ϕ in discharge termination.

IMPURITY TRANSPORT IN JET DURING H-MODE, MONSTER SAWTEETH, AND AFTER PELLET INJECTION

K Behringer, B Denne, A Edwards, N Gottardi, M von Hellermann, E Källne, P D Morgan

JET Joint Undertaking, Abingdon, Oxon, U.K.

INTRODUCTION

The main impurities in JET plasmas are carbon, oxygen and nickel, with some chlorine occasionally. The nickel concentration $c_{Ni} = n_{Ni}/n_e$ depends critically on previous history of ion cyclotron heating (ICRH) and is usually $\leq 10^{-5}$ in ohmic heating campaigns. During ICRH, nickel is released from the antenna screens and subsequently deposited on limiters and protection tiles. After high power ICRH pulses, $c_{Ni} \approx 10^{-3}$ has been measured during ohmic phases and several $x10^{-3}$ during ICRH. Oxygen concentrations ($c_O = n_O/n_e$) have recently been 0.5-1% in deuterium (D) plasmas. In helium plasmas, c_O was about a factor 10 lower due to smaller oxygen influxes from walls and limiters. This lower oxygen production by helium (He) clearly indicates a chemical production mechanism. Carbon appears to be produced by physical sputtering and was several % in both D and He discharges with a tendency to increase during additional heating.

Impurity transport in JET has been studied from accidental metal injections and from the radial impurity ion profiles. Confinement times and profiles could usually be described by an anomalous diffusion coefficient $D \approx 1\ m^2/s$ and by an inward drift ($\propto r$) with $v_D(a) \approx 2$ m/s. Under some recent plasma conditions, impurity accumulation was expected, as reported in other experiments in sawtooth-free plasmas, H-mode plasmas and discharges with peaked electron density profiles after pellet injection. Long sawtooth-free periods have been observed in JET during ICRH ("monster sawteeth"). Respective changes of the total ion profiles of nickel, which is most likely to accumulate on axis, have been studied by means of line radiation from different ionization stages originating from various radial locations. These have been chosen according to the electron temperature, $T_e(0)$ ranging from 1 keV after pellet injection to 10 keV during monster sawteeth. The light impurity behaviour has been investigated by means of Z_{eff} profiles, charge-exchange recombination spectroscopy and from soft X-ray radiation which is often dominated by light impurity bremsstrahlung.

MONSTER SAWTEETH

Monster sawteeth were observed in both D and He plasmas with RF powers of 2-15 MW. Respective nickel concentrations in these plasmas ranged from a few 10^{-4} to several 10^{-3}. Because of deposition and subsequent erosion of nickel, c_{Ni} usually continued to increase during ICRH in discharges with and without sawteeth. Compared to normal sawtoothing discharges, some 20% increase in c_{Ni} was observed during monster phases, probably due to a slight increase in global impurity confinement. After the monster crash, impurity confinement often dropped significantly leading to substantial

loss of nickel even with ICRH continuing at the same power level.

Fig.1 shows c_{Ni} derived from Ni XXVII in the plasma centre and Ni XXV close to the edge during ICRH ($T_e(0)$ = 6 - 10 keV). Both ICRH phases of the pulse lead to higher nickel concentration. During the sawtooth-free period (6.2 - 8.7s), c_{Ni} continues to increase but in the same way at different radial locations. This means that the nickel ion profile does not change, ie., no nickel accumulation in the centre. Detailed investigations of sawtooth-free periods up to 3s have not shown any change of impurity transport. It is concluded that the absence of sawteeth, at least during ICRH, does not lead to accumulation of medium-Z impurities in the JET plasma.

PELLET INJECTION

Single pellets and sequences of D pellets of different size have been injected into JET discharges (the multi-pellet injector was provided by ORNL under a JET-USDoE Agreement). ICRH and neutral beam heating (NBI) have been applied to the resulting plasmas. Pellet injection usually led to electron density profiles which, after some initial rearrangement, were not significantly different from those produced by gas fuelling. In some cases when pellets penetrated to the plasma centre, strongly peaked n_e profiles were observed lasting up to 3s. Fig.2 shows an example of profiles peaked for about 3s after the second pellet. $T_e(0)$ drops to about 0.8 keV and slowly recovers to its pre-pellet value. Two nickel line intensities demonstrate the behaviour of the nickel ions: Ni XXVI, most abundant in the plasma centre below 2.5 keV, and Ni XI from the periphery under all conditions mentioned. While the Ni XI radiation reflects changes in edge density and some reduction in edge nickel content, a substantial increase in line radiation from the plasma centre is observed. Comparison with earlier phases of the pulse, taking into account changes in $n_e(0)$, shows that the axial nickel density increases by a factor >10. This behaviour has been observed on other tokamaks before [1] and has been interpreted as neoclassical-type accumulation. In the present example, accumulation disappears after about 3s when the n_e profiles revert to normal. Accumulation has been observed to survive low power NBI, but disappeared immediately after the onset of ICRF heating.

Even under these conditions, the nickel concentration remains very low. Z_{eff} and soft X-ray profiles are still dominated by light impurities and suggest that light impurity profiles are peaked, too [2]. For a short period after the second pellet in Fig.2, light impurity concentrations are quite low ($Z_{eff} \approx 1.5$). Therefore, the nickel behaviour expected from neoclassical theory [3] can be predicted without knowledge of the actual concentrations. Calculations demonstrate that the nickel density increase on axis and the observed time scale can be explained by a rearrangement of the nickel content due to the neoclassical inward drift, provided that the anomalous diffusion coefficient is reduced to $\approx 0.01\ m^2/s$.

H-MODE PLASMAS

H-mode phases lasting up to about 2s had already been observed in 1986 [4]. These were characterised by a continuous increase in electron density and radiation losses. Radiation profiles were hollow in the centre but showed unusually wide edge shells. Spectroscopic analysis showed radiation losses mainly due to oxygen and, to a lesser extent, to carbon. Nickel may have contributed about 10% in some cases. Detailed investigations showed that the radiation profiles, the unusual behaviour of line intensities from

different nickel ionisation stages and longer particle confinement times could be explained by a high inward drift velocity in a narrow region near the plasma edge and hollow profiles in the centre, a consequence of the non-stationary nature of these discharges. For the latter explanation, the interior diffusion coefficient had to be $\approx 0.2\ m^2/s$.

Already in 1986, a few H-mode pulses had short periods of edge localised activity (ELMs) most obvious from spikes in H_α radiation [4]. With NBI heating extended to 6s in 1987, up to 5 H-mode phases were observed with ELM periods in between. During the first quiet H-mode, lasting again 2s, the 1987 and 1986 results were virtually identical. Z_{eff} profiles, now available [5], were hollow as expected. The nickel behaviour during the subsequent phases is described in Fig.3.

During each ELM phase, particles are lost from the plasma periphery stabilising the density increase, on average. Global radiation losses (not shown) also stabilise, but are modulated according to the electron density behaviour. $T_e(0)$ decreases slowly after the initial H-mode phase. After some initial increase, nickel line radiation from the plasma edge (Ni XVII, Ni XVIII) drops during each ELM phase and generally decays to a small value. In contrast, Ni XXVI from the plasma centre continues to increase and a peaked nickel ion profile develops. Simultaneously, radiation profiles fill in (reaching $\approx 40\ kW/m^3$ on axis) and soft X-ray radiation increases. All these observations are an indication of impurity accumulation. However, n_e profiles are flat or even slightly hollow. Global impurity confinement is clearly higher than usual by about a factor 5.

A closer investigation of Z_{eff} profiles and soft X-ray profiles shows that nickel does not really develop a profile peaked on axis. The nickel density increases within the inner third of the minor radius, but the profile is actually hollow in the centre. Light impurity profiles remain hollow throughout all these phases and their concentration hardly changes. The plasma edge radiation is mainly due to oxygen, while the radiation increase in the interior is due to nickel. During the final H-mode phase in Fig.3, $c_{Ni} \approx 0.1\%$ results from a spectroscopic analysis in agreement with the local soft X-ray emission. The total nickel line radiation accounts for about half the local radiated power as measured by the bolometer. There is some contribution from chlorine, which tends to increase during the later phases ($c_{Cl} \approx 10^{-4}$). The remaining radiation fraction is due to light impurity radiation, ie. mainly bremsstrahlung.

The observed rearrangement of impurity ions is not readily interpreted in terms of neoclassical transport. Certainly, the non-stationary nature of the edge densities must be considered and several impurity species taken into account.

CONCLUSIONS

Long sawtooth-free periods, observed during ICRH in JET, did not lead to any obvious change in impurity transport. In some cases after pellet injection, when strongly peaked electron density profiles were observed, medium (and low) -Z impurities showed behaviour expected for neoclassical accumulation. ICRH appeared to destroy the accumulation process. During long periods of alternating H-mode and ELM phases, medium-Z impurities developed a generally peaked profile, but with a dip in the centre. Light impurity profiles were generally hollow. This rearrangement of impurity content was much slower than in pellet cases and there is no obvious explanation for this change.

FIG.1: Nickel concentrations from Ni XXVII in the plasma centre and Ni XXV near the boundary. ICRH power and $T_e(0)$ are also shown. The nickel ion density profile does not change during the monster sawtooth.

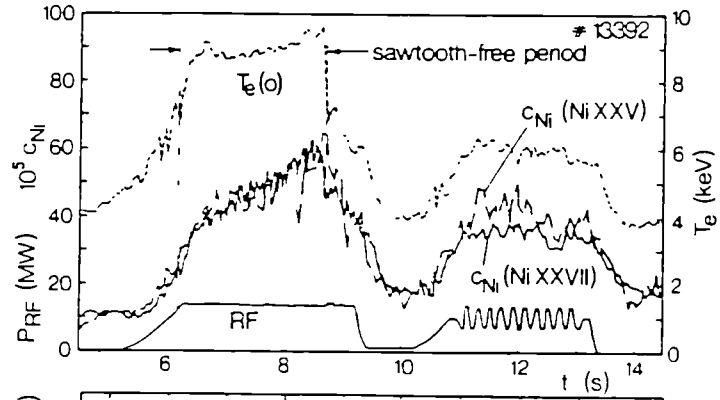

FIG.2: Densities, $T_e(0)$ and nickel line radiation after pellet injection. The increase in Ni XXVI radiation demonstrates a change in particle transport and neo-classical-type accumulation.

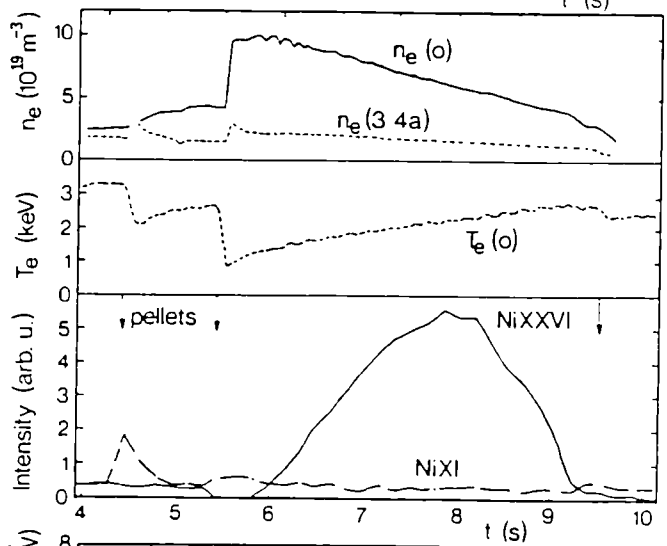

FIG.3: Radiation from different nickel ionisation stages during alternating H-mode and ELM phases. A peaked nickel ion profile develops resembling neoclassical-type accumulation.

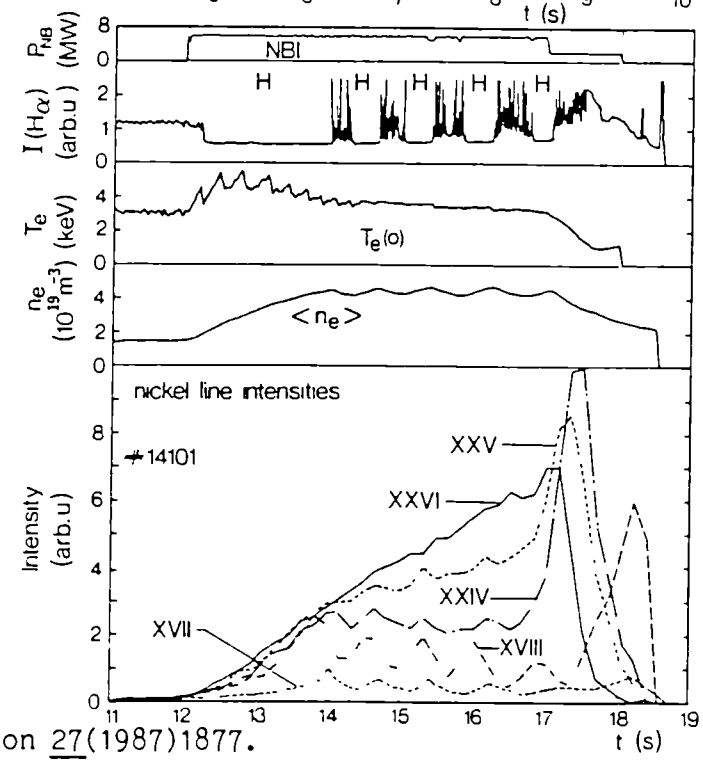

REFERENCES

[1] R Petrasso et al., Phys. Rev.Lett. 57(1986)707.

[2] D Pasini et al, this conference.

[3] P H Rutherford et al., Proc. of the Int. Symposium on Plasma-Wall Interaction, Jülich, FRG, 1976.

[4] A Tanga et al., Nucl.Fusion 27(1987)1877.

[5] P D Morgan, this conference.

RESULTS ON JET PLASMA AND IMPURITY BEHAVIOUR BASED ON MEASUREMENTS OF RADIAL PROFILES IN THE SOFT X-RAY REGION

H.W.Morsi, K.Behringer, B.Denne, E.Källne[a], G.Rupprecht[b], U.Schumacher[c]

JET Joint Undertaking, Abingdon, Oxon, U.K.
[a] Physics I, Royal Inst. of Technology, Stockholm, Sweden
[b] Now at European Southern Observatory (ESO), Garching, FRG
[c] MPI für Plasmaphysik, Association EURATOM-IPP, Garching, FRG

Abstract

First measurements of spatial profiles of the emission lines of different nickel ionisation stages were carried out at JET by means of the spatial scan double crystal monochromator. These profiles are compared with results of transport simulations, by which the calculated ionisation balance is verified. The measurements, furthermore, give the emission shells presently used for ion temperature measurements using X-ray line profiles.

1. Introduction

The measurements of the spatial and temporal distributions of impurities in magnetically confined high temperature plasmas are important for the investigations of impurity behaviour and radiation power losses. For electron temperatures of several keV the line radiation is emitted predominantly in the soft X-ray region. Therefore X-ray spectroscopy over a wide wavelength range (from about 0.1 nm to 2.5 nm) with continuous spatial scanning across the minor plasma radius is important both for studying the emission shells to understand the ionisation equilibrium and the impurity transport and for emission layer measurements in diagnostics like ion temperature measurements from X-ray line Doppler profiles.

For this purpose a double crystal monochromator [1], capable of continuous spatial scanning of X-ray spectral lines across the plasma minor radius, has recently come into operation at JET. The double crystal system allows effective shielding against neutrons and hard X-rays from the plasma.

2. The spatially scanning double crystal monochromator

A scheme (not to scale) of this double crystal monochromator is shown in Fig. 1. The two plane crystals simultaneously have to fulfill the Bragg condition $n\lambda = 2d \cdot sin\,\Theta$ (with λ the wavelength, 2d the lattice constant, Θ the Bragg angle and n an integer) within a relatively small angular margin. The crystal reflectivity has to be high and constant across the crystal surface to obtain high photon throughput of the monochromator [2]. The spectral resolution of the device is determined by the angular acceptance of the X-ray collimator and the rocking curve width of crystal 2.

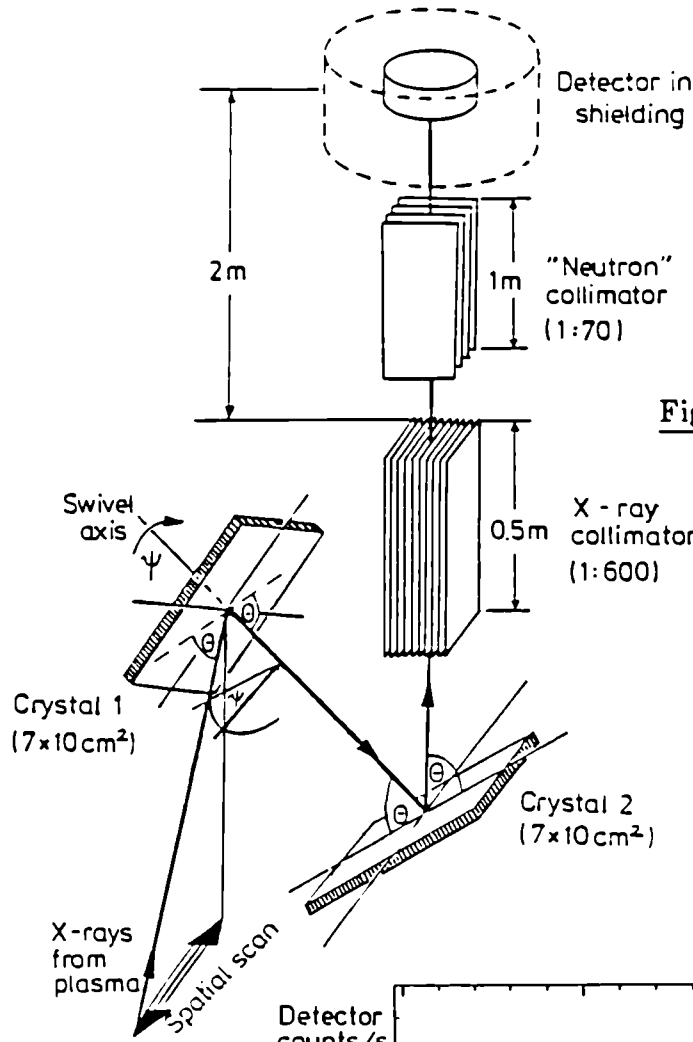

Fig. 1 Schematic of the spatial scan double crystal monochromator

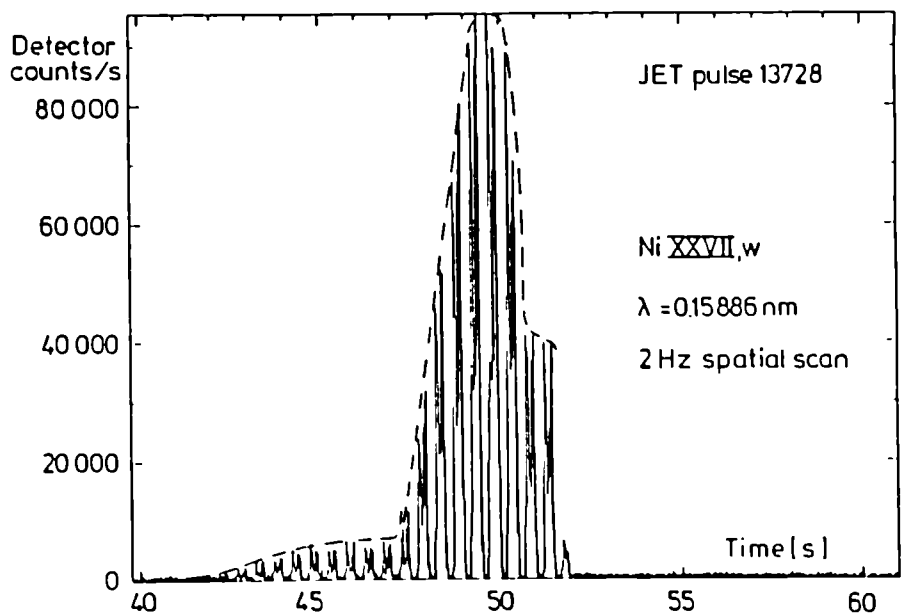

Fig. 2 Example of the count rate versus time for the helium-like resonance line of nickel spatially scanned with 2 Hz

The swivelling of crystal 1 by an angle ψ around the optical axis between the two crystals enables a continuous spatial scanning of the plasma. The detector is a large-area multiwire proportional counter [3]in a shielding block on top of the instrument. A "neutron" collimator is used for the reduction of the neutron and hard X-ray flux from the plasma for background count rate limitation. The neutron collimator, moreover, has to limit the acceptance angle in the non-dispersive direction for crystal 2, in order to obtain a smooth photon throughput as function of swivel angle as well as to define the spatial resolution of the instrument. Details of the properties and the tests of the monochromator as well as the measurements of the relative sensitivity of the instrument using a calibrated large-area X-ray source are described in [4].

For the first measurements LiF(220) crystals (2d = 0.2848 nm) were used allowing the wavelength range from 0.113 nm to about 0.203 nm to be covered with most of the hydrogen- and helium-like transitions of medium-Z impurities (like Ni). For the longer wavelengths of the oxygen lines KAP(001) crystals (2d = 2.6579 nm) will be used.

3. First results of spatially resolved X-ray line emission from JET

First measurements of the emission shells of several nickel ionisation stages were performed at JET by means of the spatial scan double crystal monochromator. The radial profiles are quite different for lines of different ionisation stages: The profiles of the lower stages are nearly flat, while those of the hydrogen- and helium-like transitions are peaked around the plasma center.

An example of the detector count rate for the helium-like resonance line (w) of nickel $1s^2\ ^1S_o - 1s2p\ ^1P_1$ taken at 2 Hz scan frequency is plotted in Fig. 2. The peaks just follow the time dependence of the line intensity (as obtained from the high-resolution X-ray spectrometer KX1 at JET, dotted line). Examples of the relative intensity distributions of the hydrogen-like nickel line Ly α_2 ($1s^2S_{1/2}$-$2p^2P_{1/2}$) and the helium-like w line are given in Fig. 3 versus radius R in the JET midplane. Abel inversion of these profiles gives the relative emission coefficients of these lines versus the distance (R - R_o) from the plasma center R_o, plotted in Fig. 4 (solid lines).

The radial profiles of these two nickel lines were also simulated using the impurity transport code [5]with the actual radial distributions of electron temperature T_e and density n_e as well as the atomic physics and transport data input. These simulated emission coefficient radial distributions are added into Fig. 4 as dotted lines. The agreement of measured and simulated profiles is satisfactory within the error bars of the plasma parameters and the assumptions underlying the analysis.

Acknowledgements

The authors are grateful to Drs. C. Andelfinger, W. Engelhardt and H. Röhr for many fruitful discussions and to J. Fink, R. Lobel, H. Schäfer, H.-B. Schilling, G. Schmitt, G. Snelling and B. Viaccoz for continuous support.

References

[1] W.Engelhardt, J.Fink, G.Fußmann, H.Krause, H.-B. Schilling, U. Schumacher, MPI für Plasmaphysik, Report IPP 1/212, IPP III/81, Garching 1982; C.Andelfinger, J.Fink, G.Fußmann, H.Krause, H.Röhr, H.-B. Schilling, U.Schumacher, P.Becker, H.Siegert, H. Belzig, A.Berghausen, R.Veigel, H.Zech, Report IPP 1/226, Garching, 1984

[2] U.Schumacher, Nucl.Instr.and Meth. A251, 564 (1986) and A259, 538 (1987)

[3] G.Rupprecht, JET-Report, to be published

[4] J.Fink, H.W.Morsi, H.Röhr, U.Schumacher, Report IPP 1/240 (1987); H.W.Morsi, H.Röhr,U.Schumacher, Z.Naturforsch. 42a, 1051 (1987); and to be published

[5] K.Behringer, JET-Report JET-R(87)08 (1987)

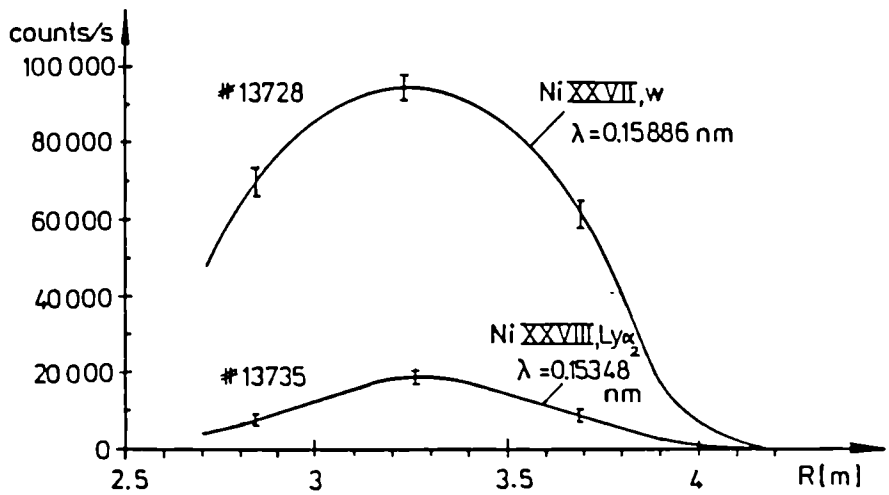

Fig. 3 Relative intensity distributions of nickel hydrogen-like Lyα_2 and helium-like resonance line w versus radius R in the JET midplane

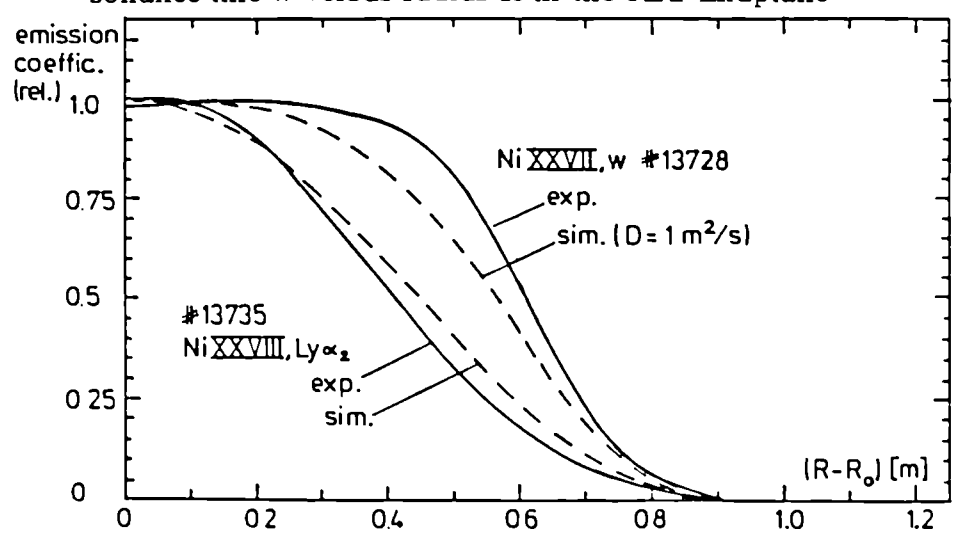

Fig. 4 The radial distribution of the emission coefficients of the nickel lines of Fig.3.

POLARIMETRIC MEASUREMENTS OF THE q-PROFILE

J O'Rourke, J Blum*, J G Cordey, A Edwards, N Gottardi, B Keegan, E Lazzaro, G Magyar, Y Stephan+, P Stubberfield, D Véron++, D Zasche**

JET Joint Undertaking, Abingdon, Oxon, OX14 3EA, UK
*Univ. de Grenoble, France/+CEN-Cadarache, France/++CEA-Limeil, France
**Permanent address: IPP-Garching, FRG

ABSTRACT

First polarimetric measurements of the poloidal field distribution on JET are presented. q_o appears to be significantly below 1 in sawtoothing discharges. ICRF stabilization of sawteeth leads to even lower q_o's.

1. DESCRIPTION OF THE DIAGNOSTIC

The six vertical channels of the JET far-infrared multichannel interferometer have been modified to also make polarimetric measurements (Faraday rotation). The configuration is essentially as described in reference 1, and consists of a simultaneous measurement of the probing beam intensity along two orthogonal directions of polarization.

In JET, however, the half-wave plates which are used for calibrating the system are located before the input of the beams into the torus (rather than at the exits). Also, the recombination of the probing and reference beams and the separation of the unrotated and rotated components is done in 2 stages, using a polarization-independent beam splitter for the former and a tungsten wire grid for the latter. (See figure 1).

The "interferometer" signal amplitude is proportional to cos Θ, where Θ is the angle of Faraday rotation, while the "polarimeter" signal is proportional to sin Θ. The first of these is squared to produce a DC signal proportional to $\cos^2 \Theta$, the second is multiplied by the first in a phase-sensitive detector to produce a DC signal proportional to sin Θ cos Θ. The two DC signals are digitized, and their ratio used to determine tan Θ. This method of measurement requires a calibration, which is performed by rotating quartz half-wave plates (located at the point of entry of the beams into the torus) to produce a rotation of the beam polarization in steps of 0.4°. The measurement of the Faraday rotation angle is made with an error < 5%, and a sensitivity of ~ 1%. The time resolution is 1-10 msec., determined by the integration time of the electronics. The lower limit on the time resolution is set by the 100 kHz modulation frequency of the polari-interferometer.

2. ANALYSIS

The Faraday rotation angle is proportional to $\int n_e B_{||} d\ell$, where n_e is the electronic density and $B_{||}$ is the magnetic field along the probing chord. This implies that polarimetric measurements must be used in conjunction with other diagnostics to infer the poloidal field distribution. In particular, the non-circularity of JET cross-sections means that the poloidal field enters into the Abel inversion of the chord- integrated data both as a parameter (determining the shape of the flux surfaces) and

as the unknown to be determined. The results presented here are derived using two approaches. In the first, the flux geometry is determined from magnetic measurements at the plasma boundary via an equilibrium identification code, IDENTC [2]. The poloidal field distribution is then determined by a generalized Abel inversion in this geometry. The electron density profiles are obtained from the interferometric data, or from the LIDAR diagnostic [3]. The agreement between these is generally very good (< 10%). The Abel Inversion is made in 2 steps. The discharge cross-section is divided into six nested elements, determined by the flux surfaces of tangency of the six polarimeter chords. A first calculation of the poloidal field distribution is made in this geometry, and used to calculate the expected angle of Faraday rotation on six vertical "virtual" chords, tangent to the same flux surfaces, but on the opposite side of the magnetic axis to the corresponding real chords. A Chebyshev polynomial is fitted to the complete set of Faraday rotation angles (real, virtual + zero points at the plasma boundary) and the second Abel inversion is performed on this smoothed data. This method ensures that the smoothed data conforms both to the data and to the transformation properties implied by the flux geometry. (See Fig.2.)

The major radius of the magnetic axis, R_o, and the elongation of the flux surfaces near the axis, κ_o, are directly related to the value of q_o which is inferred by Abel inversion in a given flux geometry. In fact, for a set of vertical probing chords, since the density profile is flat near the axis, the inferred value of the vertical field, $B_{||}$, is inversely proportional to the assumed κ_o. The inferred toroidal field at the axis, B_{TO}, is inversely proportional to the assumed R_o, and

$$q_o = \kappa_o \frac{r}{R_o} \frac{B_{TO}}{B_{||}} \sim \frac{\kappa_o^2}{R_o^2}$$

The position of the magnetic axis determined by the equilibrium reconstruction code is in good agreement with that determined by soft X-ray tomography [4]. However, the elongation of the central flux surface in the equilibrium reconstruction is systematicaly greater (5-10%) than the elongation of the SXR iso-emissivity surfaces. If the latter are taken to represent the true elongation of the flux surfaces, a lower value of q_o is deduced. (See Section 3).

Uncertainties in the absolute calibration, the electron density profile, and the flux geometry, as well as the intrinsic sparseness of the data, lead to an error in q_o of ± 15%. Nevertheless, as discussed above, much of this error is systematic and changes in the q-profile can be measured with considerably better accuracy. Initial experiments using a horizontal displacement of the plasma column across the lines of sight to reduce the sparseness of the data have not yielded significant changes in the value of q_o which is determined, suggesting that sparseness does not introduce large errors in this parameter (although this may not hold for the q-profile as a whole).

The second method of analysis is an integrated one, in which a solution to the Grad-Shafranov equation is found with the source term optimised to best fit both the polarimetric and magnetic measurements. Accordingly an objective function is built as the sum of the squares of the differences between calculated and measured quantities. Its minimum is found by expressing its gradient with respect to the free parameters, in terms of a set of generalized Lagrange multipliers, which are solutions of

the so called adjoint problem. The techniques used are Finite Elements for the partial differential equations and Conjugate Gradients for the minimisation. This approach is still being developed, in particular with respect to the treatment of the electron density profile. Preliminary results show that the Faraday rotation information improves the knowledge of the innermost region of the plasma, and stabilizes the solution against measurement errors. A case of consistent reconstruction is shown in Fig.3.

3. RESULTS

Figure 4 shows the evolution of q_o during a 4 MA, 2.8 T, ohmic discharge. The elongation of the inner flux surfaces has been taken to be that given by the tomographic reconstruction of the soft X-ray emmisivity. q_o decreases rapidly during the ramp-up of the plasma current, and reaches a value of 1 at 5.5 seconds, nearly simultaneously with the onset of sawtoothing, as evidenced by the soft X-ray emission. q_o then continues to decrease, ultimately saturating at a value of ~ 0.7. The steady-state value of q_o does not appear to depend on the flat-top plasma current or the safety factor at the plasma boundary. During a sawtooth, q_o changes little (< 5%). In fact, the change in q_o is at present confused by uncertainties related to the simultaneous redistribution of the density profile.

Figure 5 shows the evolution of q_o during a 2 MA, 2.1 T, radio frequency heated discharge. The interval from 7.5 to 9.2 seconds corresponds to a period of sawtooth stabilization, known as a "monster sawtooth" [5]. At the start of the RF pulse the Faraday rotation angles increase, largely due to the RF-induced density rise and, in the case of chords inboard of the magnetic axis, to the displacement of the magnetic axis with increasing β_p. During the monster sawtooth, q_o decrease by ~ 15%. A similar decrease is also inferred by IDENTC from magnetic data alone. These results are in good agreement with a field diffusion calculation performed using the TRANSP code [6], assuming neo-classical resistivity. (Note that the initial value of q_o in the TRANSP calculation is prescribed by the sawtoothing model that was adopted, which resets q_o to 1 after each sawtooth).

At the collapse of the monster sawtooth, the density profile is markedly perturbed, and this makes analysis of the q-profile more uncertain. Nevertheless it appears that when sawtoothing is re-established, q_o returns to approximately its pre-monster value.

Taken together, the above results suggest that ordinarily the steady-state value of q_o is determined by the sawtooth mechanism, perhaps indirectly via the temperature profile. When sawteeth are suppressed, q_o can evolve to lower values by field-diffusion.

REFERENCES

[1] Soltwisch H and Equipe T F R, Infrared Physics 21(1981)287.
[2] Lazzaro E, Mantica P, JET-P(87)58.
[3] Bartlett D V, et al., this conference.
[4] Granetz R S, Smeulders P, X-ray Tomography on JET, to be published in Nuclear Fusion.
[5] Campbell D J, et al., this conference.
[6] Goldston R J, et al., Journal of Computational Physics 43(1981)61.

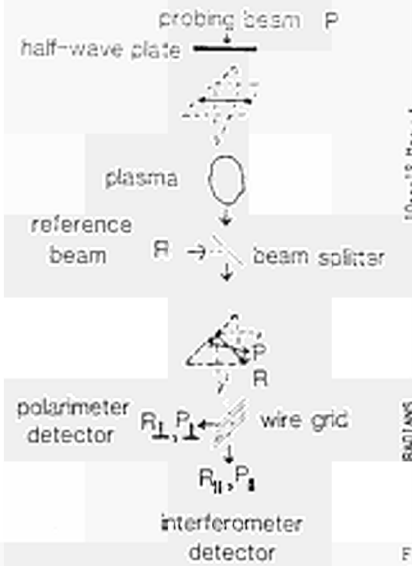

FIG.1: Schematic of the Faraday rotation measurement.

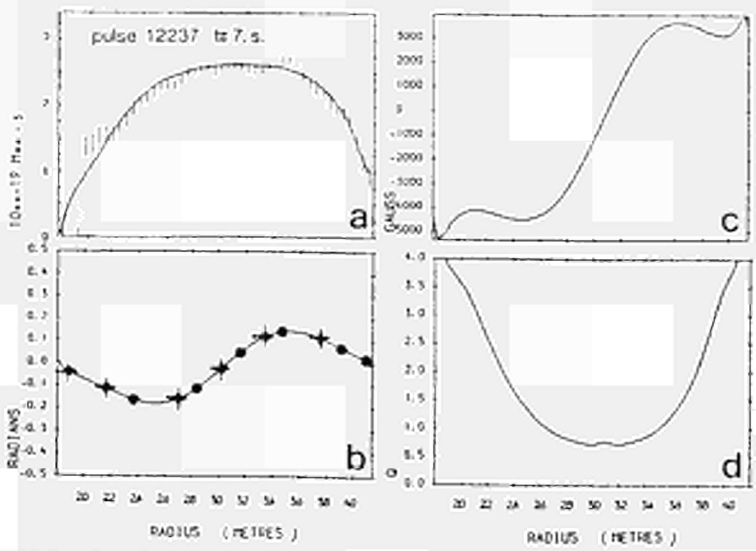

FIG.2: Example of data analysis:
a) Electron density profile.
Solid line: Abel inversion
dashed line: LIDAR data.
b) Crosses: Measured Faraday angles
solid circles: mirrored angles
solid line: polynominal fit.
c) Poloidal magnetic field.
d) q-profile.

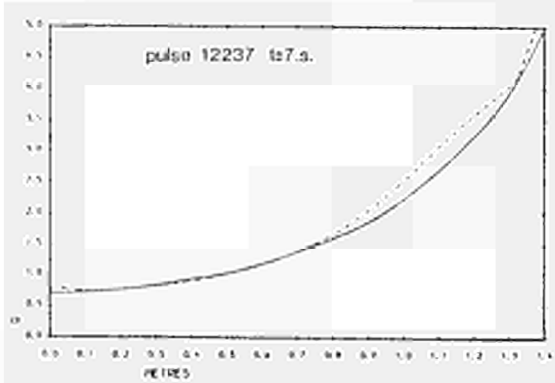

FIG.3: Solid line: q-profile from a consistent reconstruction
dashed line: q-profile from Abel inversion.

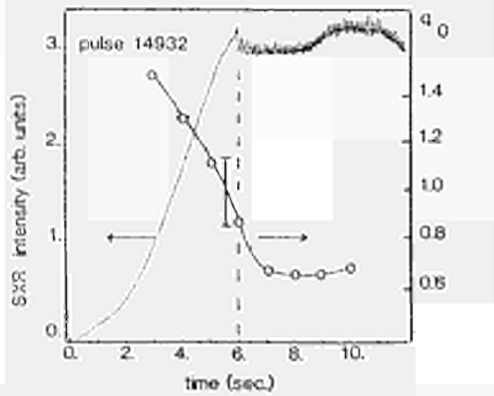

FIG.4: Evolution of q_0 (circles) and SXR intensity in an ohmic discharge.

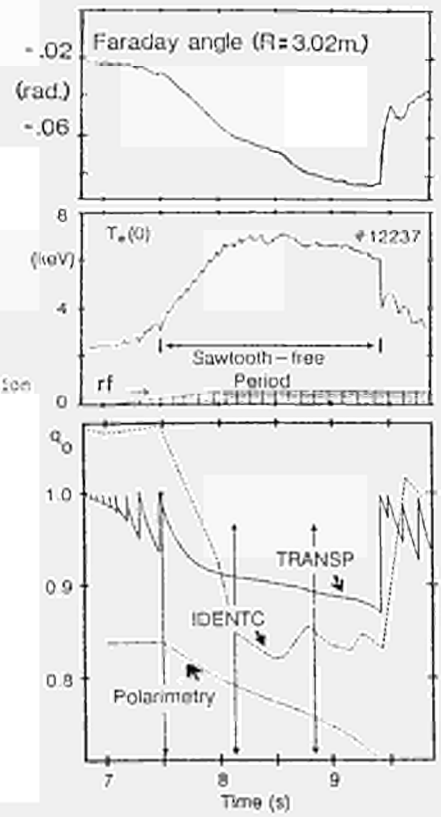

FIG.5: Evolution of the Faraday angle on a central chord, of the electron temperature and of q_0 (measured and modelled) during an ICRH pulse with sawtooth stabilization.

PROFILE BEHAVIOUR DURING L AND H PHASES OF JET DISCHARGES

C Gowers D Bartlett A Boileau+ S Corti A Edwards
N Gottardi K Hirsch[1] M Keilhacker E Lazzaro P Morgan P Nielsen
J O'Rourke H Salzmann[1] P Smeulders A Tanga M von Hellermann

JET Joint Undertaking, Abingdon, Oxon, OX14 3EA, England
+INRS, 1650 Montee Sainte-Julie, Varennes, Quebec JOL 2PO, CAN
[1] Institut für Plasmaforschung, Universität Stuttgart, FRG

INTRODUCTION H-mode operation of the JET tokamak was established in 1986[1]. Since then the phenomenon has been studied for a range of powers and particle energies of the Neutal Beam heating system. The operational regime has also been extended to higher plasma current[2]. The transition from L to H-mode after the initiation of NB injection, and the subsequent evolution of the profiles of the plasma parameters, have been investigated using a range of the existing diagnostics including bolometry, interferometry, soft x-ray tomography, charge-exchange and D_α visible spectroscopy, ECE and neutral particle analysis, and the new JET LIDAR-Thomson scattering[3] and FIR polarimetry systems[4]. The results of this study and of a preliminary analysis of the ballooning mode stability of the measured pressure profiles are reported and discussed below.

PROFILE EVOLUTION MEASUREMENTS Figure 1 shows the typical evolution of the main plasma parameters and H-mode signatures during the development of the discharge from an ohmic X-point to L-mode, to H-mode (with Sawtooth oscillations) and back to an ohmic X-point discharge. In this series of discharges the transition from L to H-mode is characterised by a significant fall in the D_α signal (vertical chord) after a series of "spikes". The spikes have been correlated with mhd modes near the plasma edge (Edge Localised Modes or ELMs). In about half the cases in the series the L to H transition and the termination of ELMs appear to coincide with a sawtooth crash.

The central region of the electron temperature profile, which can be slightly hollow during the ohmic X-point phase, figure 2a, quickly fills in and rises to close to 4 kev just after the transition phase. It remains around this value until the NB heating is terminated when it falls back again to the 2 kev range in about 100ms, a time comparable to the slowing down time of the fast ions. It is clear from the outer region of the T_e profiles that during this series of discharges a pedestal of about 400ev forms at R~4.0m during the L to H transition and this remains throughout the H-mode period.

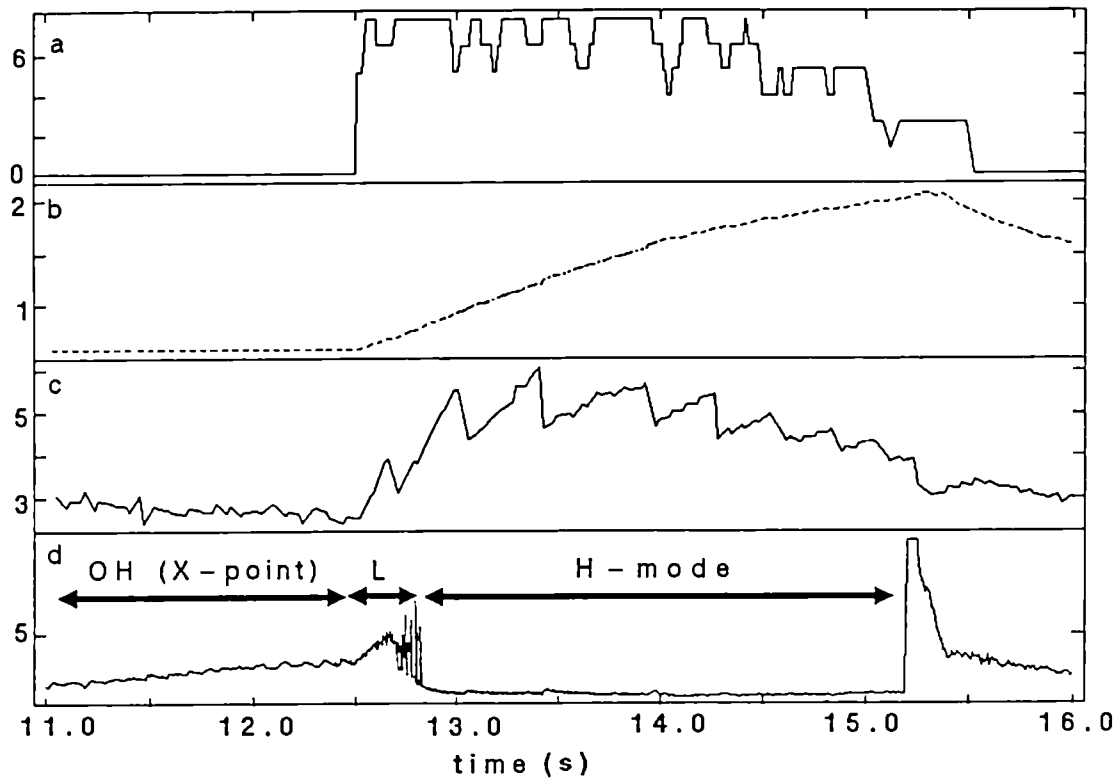

Fig.1 The different phases of development of a normal 3MA, 2.1T H-mode: a) total beam power (MW) b) line density ($x10^{20}$ m^{-2}) c) central ECE signal showing sawteeth (kev) d) D_α signal (arb. units)

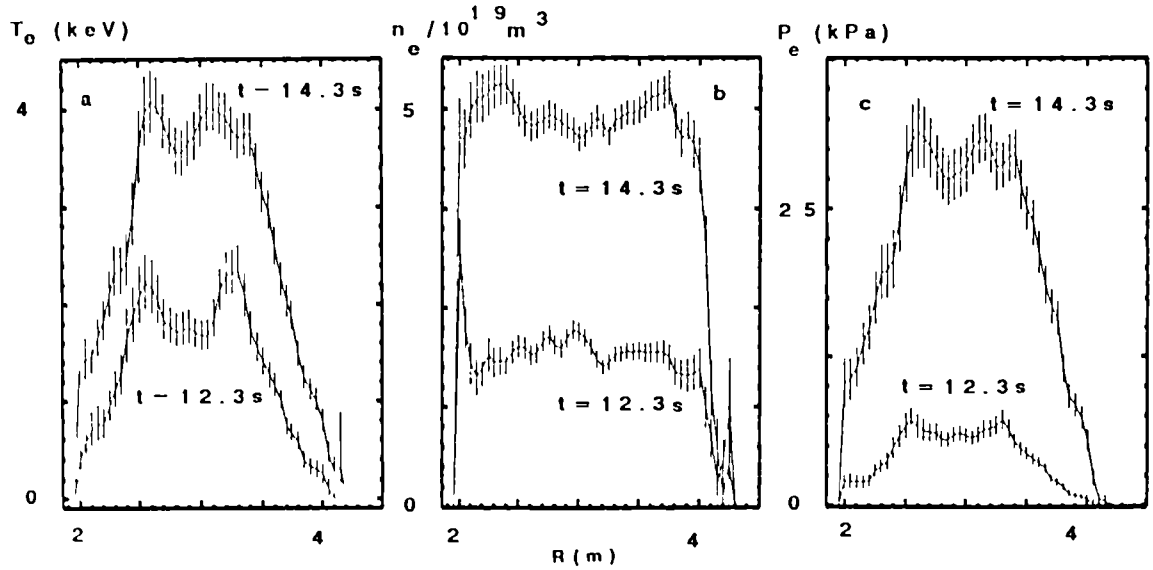

Fig.2 LIDAR electron a) temperature b) density and c) pressure profiles during ohmic X-point (12.3s) and H-mode (14.3s) periods of #14830. (bars denote measurement errors)

A more dramatic change is observed in the density profiles, figure 2b. During the transition the central peak flattens as the density rises and a steep edge gradient is formed. The overall level rises throughout the H-Mode period due to the fuelling effect of the beams giving gradients in the edge region up to $2x10^{20}$ m^{-4}. During the sawtooth rise phase the profile becomes slightly hollow and then flattens again immediately after the crash.

The LIDAR density profiles have been used in the analysis of the polarimetry results and these indicate that the q-profile broadens during the H-mode period.

$T_i(R)$ from multi-channel CXRS during the H-mode is similar in shape to $T_e(R)$ with central values in the range 4-6kev. When the ion component is included with the electron pressure profiles derived from the LIDAR T_e and n_e data, figure 2c, near the end of the H-mode, the central and global values for β are ~2.8% and 2% respectively, close to the highest values yet recorded on JET. The pressure profile has been found to be ballooning mode stable when examined using the analysis of reference [7], with the central region close to the stability limit.

The signals from the bolometer camera during the X-point phase are generally very asymmetric with much higher intensity on the lines of sight nearest the inner torus wall. In general this prevents Abel inversion for the X-point period. However, once the transition to H-mode has taken place, symmetry is restored (ie the total radiation is constant on a flux surface) and the generalised Abel inversion[5] can be carried out. The evolution of the total radiation profile is shown in figure 3. Again the profile exhibits a central depression throughout the H-mode, although it does tend to fill in somewhat as it evolves. The profile shape and the modest increase in the overall radiated power level indicate that significant impurity build up in the plasma centre is not occurring. This is supported for the light impurities by Z_{eff} profile results.

The hollowness during sawtoothing is also a feature of the soft X-ray profiles figure 4, and again in contrast to results on other machines, the increase in signal intensity is consistent with the density rise due to fuelling by the beams and not indicative of any significant increase in impurity radiation.

IMPURITY ACCUMULATION In the majority of the observed H-modes, which last for ~2s, no significant impurity accumulation in the centre of the discharge has been seen. This may be related to the presence of a large q=1 region in these sawteething H-modes and also to the long timescales that can be expected for the accumulation process on a large tokamak. This result is in contrast to ASDEX where in sawtooth and ELM-free H-modes, accumulation of iron was observed when the H-mode duration was sufficiently long (>150ms)[6].

SUMMARY The development of hollow n_e, soft x-ray emission and total radiation profiles is characteristic of JET H-modes. Impurity accumulation is generally not observed in the normal sawtoothing, ELM free discharges. A high central β is achieved and a preliminary analysis of the stability against ballooning modes indicates that, near the centre,the pressure profile is close to the limit but within the normal stability region.

References

[1] A Tanga et al 11th IAEA Conf. Kyoto 1986 IAEA-CN-47/K-I-1
[2] M Keilhacker et al, this conference.
[3] H Salzmann et al, Nuclear Fusion Vol.27 no 11 (1987) p1925
[4] J O'Rourke et al, this conference.
[5] N Gottardi et al, 12th EPS Budapest 1985
[6] M Keilhacker et al, 10th IAEA Conf. London 1984
[7] E Lazzaro et al, this conference.

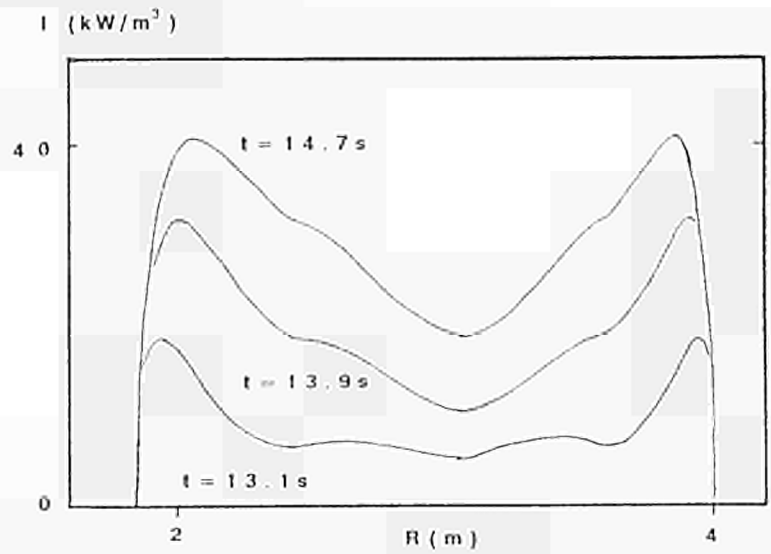

Fig.3 Total radiation profile evolution (#14830).

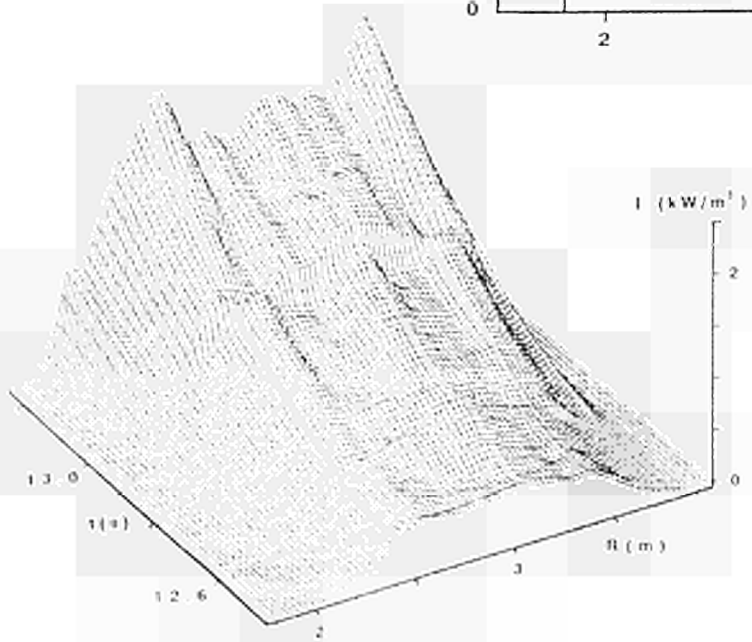

Fig.4 Soft x-ray intensity profile evolution (#14830).

IGNITION TOKAMAKS

R J Bickerton, G Apruzzese, A Tanga, P Thomas, J Wesson

JET Joint Undertaking, Abingdon, Oxon, OX14 3EA, U.K.

Ignition Conditions

For a D-T plasma the condition for thermonuclear ignition with $T_e = T_i$ is

$$\hat{n}_D \hat{T}_i \tau_\varepsilon = 5 \times 10^{21} \text{ m}^{-3} \text{ keVs} \quad (1)$$

This is valid for the range $7<\bar{T}_i<20$keV in which the $\overline{\sigma v}$ product for thermonuclear reactions is proportional to T_i^2. Condition (1) is insensitive to the pressure profile.

Applying energy balance arguments the condition (1) can be rewritten as,

$$\frac{P \tau_\varepsilon^2 f \gamma_p}{V} = 2.4 \quad (2)$$

where P(MW) is the total input power to the plasma, τ_ε(s) the global energy confinement time, V(m³) the plasma volume, f the correction due to depletion by impurities and γ_p the ratio of central to volume average plasma pressure.

Confinement Time

The JET data for limiter-bounded discharges is well described by the L-mode scaling law [1], namely

$$\tau_\varepsilon = 3.7 \times 10^{-2} I_p P^{-\frac{1}{2}} R^{1.38} (R/a)^{0.37} K^{\frac{1}{2}} \quad (3)$$

where I_p(MA) is the plasma current, K the plasma elongation, R(m) and a(m) the major and minor plasma radii. A study of JET and other data shows that the scaling with I_p, P and R is well established while the scaling with R/a and K is doubtful.

For H-mode data in JET the simplest representation is that τ_ε is twice the L-mode value.(JET Team, 1987)

Depletion Factor

Assuming that the impurities in the central plasma are fully ionised and serve only to deplete the reactive fuel density, then

$$f = \left(\frac{Z_i - Z_{eff}}{Z_i - 1}\right)^2 \left(\frac{2Z_i}{(2Z_i + 1 - Z_{eff})}\right)^2 \quad (4)$$

where Z_i is the average charge of the impurities and Z_{eff} the effective

charge. For JET the dominant impurities in the centre are carbon and oxygen, so if we take a mean $Z_i=7$ then for a plausible $Z_{eff}=2$, we have $f=0.8$. In JET the strongest dependence of Z_{eff} is on density [2]. An ignition experiment must operate with $Z_f<2$, which from JET data requires a plasma density greater than $5\times10^{19}m^{-3}$.

Pressure Ratio

The pressure ratio γ_p versus the safety factor q for JET limiter discharges varies linearly from 2.5 at q=2, to 4.3 for q=4. It then flattens out and $\gamma_p=4.5$ at q=11. There is ±25% scatter on γ_p due to sawtooth relaxations. The so-called "monster" sawtooth discharges are at the top of the observed band whilst H-modes are at the bottom. From (2) and (3) it is clear that to maximise the performance the ratio (γ_p/q^2) that should be maximised. This occurs at the lowest q at which the discharge can operate, the gain from higher current overwhelming the lower value of γ_p.

Plasma Parameters

Substituting from (3) into (2) the condition for ignition is

$$f\,\gamma_p\,\gamma_g^{\,2}\,I^2\,R^{2.5}\,a^{-2.74} = 3.46\times10^4 \qquad (5)$$

where γ_g is the ratio of the confinement time to the L-mode value.

The current I is related to the machine parameters by the expression,

$$I = \frac{5a^2B}{R\,q_\psi}\left(\frac{1+K^2}{2}\right)\left(1-\frac{a^2}{R^2}\right)^{-2} \qquad (6)$$

where q_ψ is the Shafranov q.

Enhanced Tokamak

We now estimate the parameters of a JET-like device upgraded to reach ignition conditions based on the JET experimental results as described above. Such an apparatus would permit the early study of a wide range of physics questions related to the achievement and the behaviour of an ignited plasma. In contrast to CIT this Enhanced Tokamak would be on the direct path to an eventual tokamak reactor, ie having moderate magnetic field strength and large physical size.

No significant engineering design work has yet been done on this device but a representative set of parameters is

$B = 5T$, $R = 4m$, $a = 1.4m$, $K = 2$, $\gamma_p = 3$, $f = 0.8$, $q_\psi = 2.5$ giving $I_p=15.9MA$ and for ignition $\gamma_g=2.2$. These are a plausible set of parameters in the light of the JET experimental results.

The values of the α-power and the energy confinement time at ignition are determined by the density. Combining the L-mode scaling with $\bar{T} \sim 10keV$ leads to the formula for the α-power [3].

$$P_\alpha = \frac{30\,M^2\,a^{0.74}q_{CYL}^2}{\gamma_g^{\,2}\,R^{1.5}\,K} \qquad (7)$$

where $q_{CYL} = \frac{5\ a^2\ BK}{R\ I}$ and $M = \frac{\bar{n}.R}{B} \times 10^{-19}$

from the JET experience a realistic value for M when operating with high input power at low q is $\sim$ 6. With the parameters given earlier, $\bar{n}=7.5\times10^{19-3}$ and P_α=42MW while from (3), τ_ε=2.7s. With these parameters $\bar{\beta}$=2.4% compared with the Troyon limiting value β_c=6.4% (β_c=2.8I/Ba%).

Comparison with other Devices

The table shows the main parameters of JET, Enhanced Tokamak, CIT and extended NET.

Apparatus	R (m)	a (m)	K	B (T)	I (MA)	q_{CYL}	q_Ψ	Y_g for ignition
JET	3	1.2	1.6	3.5	7	1.9	3	5.2
Enhanced Tokamak	4	1.4	2.0	5.0	16	1.5	2.5	1.9
CIT	1.8	0.5	2.0	10.0	9.0	1.5	2.4	2.3
NET-E	5.4	1.7	2.2	4.8	14.8	1.8	3	1.8

The figures are given for Z_{eff}=1 for the sake of comparison. Evidently Enhanced Tokamak is superior to CIT and similar to NET-E in performance.

Zero-Dimensional Code

So far we have used very simple arguments which lead to ignition independent of the plasma density provided only that the ion temperature lies in the range of 10-20keV. The density was fixed by appealing to the experimental experience of the Murakami parameter.

Steady state and dynamic calculations have been carried out using a more complex model in which,

(1) The proper variation of reaction rate with temperature is included over the entire ion temperature range.

(2) The confinement time is determined by the combination of the ohmic (neo-Alcator) value $\tau_{\varepsilon\Omega}$ and the L-mode $\tau_{\varepsilon L}$ so that

$$\tau_\varepsilon = \left(\frac{1}{\tau_{\varepsilon\Omega}^2} + \frac{1}{\tau_{\varepsilon L}^2}\right)^{-0.5} \qquad (8)$$

This has the effect of reducing the confinement time at low density.

(3) The density and temperature are assumed to have parabolic profiles giving Y_p=3.

(4) The full energy balance equation is used, ie $P_\Omega+P_\alpha+P_{AUX}=P_{COND}+P_{br}$ where P_Ω is the ohmic power input, P_{AUX} the auxiliary heating, P_{COND} the conduction loss and P_{br} the Bremsstrahlung loss. This code has been run for the parameters considered earlier (including Y_g=2.2). The ignition curves in the $\bar{n}$ vs $\bar{T}$ plane for P_{AUX}=0 are shown in figure 1. The ignition domain, shaded in the figure is bounded by upper and lower temperatures and by a minimum density determined by the density dependence of the ohmic confinement time. If a weaker dependence is chosen, as for example derived from JET ohmic data [4] then this minimum density would be much lower. Analysis of the results with finite P_{AUX} shows that a heating power of order 30MW would be sufficient to take the plasma to ignition.

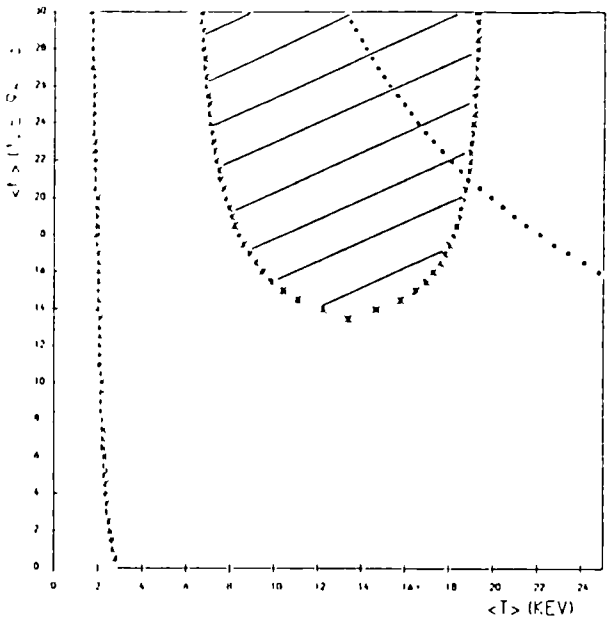

Fig. 1

Plot of ignition curve over <n>-<T> space for Enhanced Tokamak, with Z_{eff}=1.5, parabolic density and temperature profiles. Dotted line Troyon $\bar{\beta}$ limit, shaded region is the ignition domain. Left-hand line with <T>∿2keV describes the ohmic equilibrium.

Machine Parameters

The outline of the machine design can be discussed in terms of the parameters

R_o = geometric major radius of torus
ε_3 = clearance between plasma boundary and toroidal field coil
ε_2 = thickness of toroidal field coil
ε_1 = thickness of primary winding

Then the maximum toroidal field in the system B_{MAX} is $B_{MAX} = \frac{B_o R_o}{(R_o - a - \varepsilon_3)}$

taking B_o=5T, R_o=4m, a=1.4m and ε_3=0.2m gives B_{MAX}=8.3T (cf 7T in present JET). With ε_2=0.5m, ε_1=0.5m and the same B_{MAX} in the primary winding we find

Volt seconds = $2\pi(R_o-(a+\varepsilon_3+\varepsilon_2+\frac{1}{2}\varepsilon_1))^2 B_{MAX}$ = 142

This is an adequate number of volt seconds.

The current required in the toroidal field coils to produce 5T at 4m radius is 100MA. The cross-sectional area of the coils in the mid-plane is 6.75m² giving a mean current density of 1.5kA/cm². Scaling from JET the resistive power dissipation would be 600MW. The flat-top pulse length would be similar to that of JET, namely 20s.

References

[1] Goldston, R (1984) Plasma Physics & Controlled Nuc Fus, 26, 87
[2] Behringer K et al (1986) Plas Phys and Contr Nuc Fus, Vol 1, 197
[3] JET Team (1987) Plasma Physics and Controlled Nuc Fus, 29, 1219
[4] Cordey, J G et al (1985) Plas Phys & Contr Nuc Fus, 9F, Part 1, 26

EFFECTS OF LARGE AMPLITUDE MHD ACTIVITY ON CONFINEMENT IN JET

J A Snipes, D J Campbell, M Hugon, P Morgan,
D Stork, D Summers, K Thomsen,
B Tubbing

JET Joint Undertaking, Abingdon, Oxon, OX14 3EA, UK

Introduction Under many operating conditions in JET, particularly during long periods of additional heating, low m, n MHD activity (usually m=2, n=1 or m=3, n=2) persists with large amplitude ($\tilde{b}_r/B_\theta$(wall) $\gtrsim$ 0.1%) for many seconds. This allows the effects of such large MHD activity on confinement parameters to be assessed. While other loss mechanisms are also important in determining general confinement scalings, these results indicate that large MHD activity can lead to substantial losses of particles, momentum, and energy from the plasma. Other effects such as changes in wall pumping, the plasma boundary, radiative losses, and input power must be carefully excluded from the analysis as they can also alter plasma confinement. For most of this analysis, discharges were chosen that exhibited large amplitude MHD activity arising after a large sawtooth collapse following a period of sawtooth stabilization. The confinement parameters were determined before the sawtooth collapse and again after more than one confinement time following the collapse, when they had reached a new equilibrium value with the same input power in the presence of an MHD mode.

In addition to this analysis, correlations have been made between slowly rotating ($\sim$ 3 - 5 Hz) low m, n (usually m=2, n=1) magnetic activity, called quasi-stationary modes (QSM's), and central m=1, n=1 activity observed on the electron temperature profile. QSM oscillations are observed on the H_α/D_α signals, the infrared limiter viewing camera, and on ECE signals from the edge right up to the center of the plasma. This strong mode coupling [1] from the center to the edge indicates how such large amplitude MHD activity can affect global confinement properties.

MHD Effects on Particle Confinement Edge influxes as measured by H_α/D_α and CIII emission signals are modulated up to 50% by slowly rotating QSM's. Similar modulation is also observed on an infrared limiter viewing camera, with good phase correlation with the mode indicating that the bright emission corresponds to the X point of the MHD mode.

Particle pumpout rates tend to increase with the amplitude of the QSM reaching rates two to three times as fast as without the mode under some conditions. Wall pumping and boundary effects, however, can alter the pumpout rates and mask the MHD effects [2]. Figure 1 shows a comparison of two similar X point configuration shots, the first with a QSM after the large sawtooth collapse at 12 sec and the second without a QSM. The fourth trace from the top shows that the number of particles drops by more than 12% in the first shot, but by less than 5% in the second shot, indicating that about 7% of the total number of particles were lost due to enhanced particle flux by the QSM. In the first shot, $\tilde{b}_r/B_\theta$(wall) $\cong$ 0.23%. Similar enhanced pumpout rates are observed with QSM's after pellet injection, but the lack of similar shots with and without a QSM makes a quantitative comparison difficult.

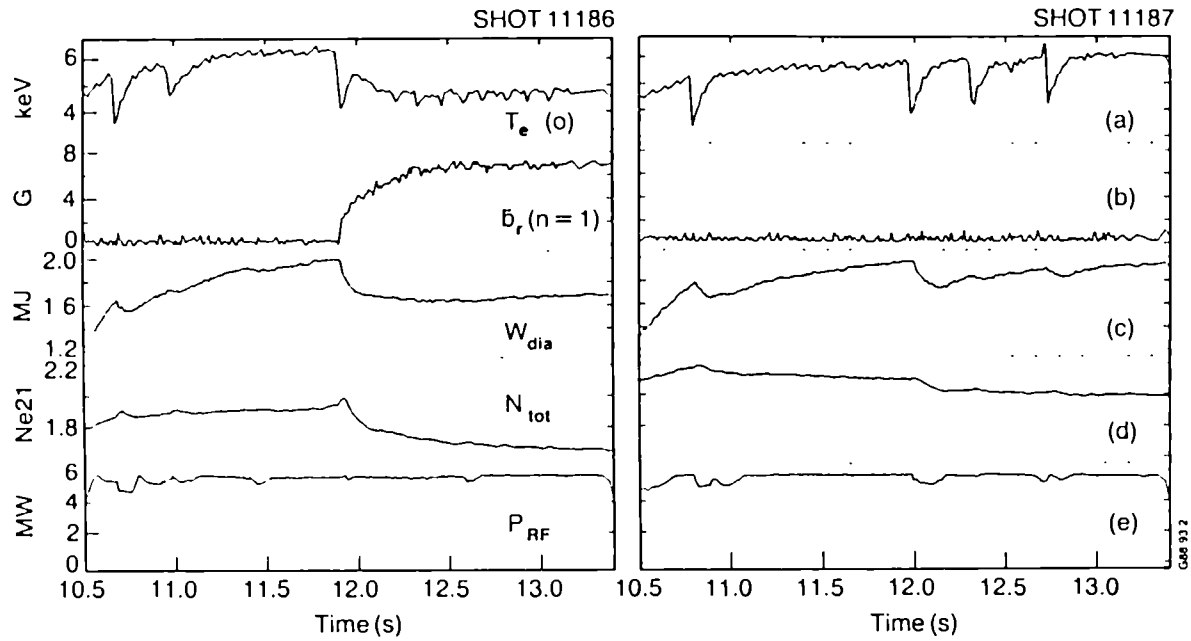

Figure 1. Comparison of two similar shots with and without a QSM. a) $T_e(0)$, b) QSM amplitude, c) diamagnetic stored energy, d) total number of particles, e) ICRH power. The degradation of particle and energy content is evident during the QSM.

MHD Effects on Momentum Confinement Neutral beam injection in the direction of the plasma current generally enhances the toroidal momentum of the plasma, but this extra input momentum can be reduced by the onset of low m, n MHD activity. Unlike the effect on particle and energy confinement, the plasma momentum appears to be affected by any observable amplitude of coherent MHD activity, in that there is almost always a good linear correlation between the MHD frequency of oscillation and the central ion toroidal rotation velocity [3]. This is particularly evident when mode locking occurs and the rotation ceases on the MHD signals as well as on the central ion toroidal rotation velocity, within the error of the measurement. Even in cases when the MHD activity is oscillating rapidly at amplitudes of only $\tilde{b}_r/B_0$(wall) ~ 0.01% (with m=3, n=2), there can be a loss of central plasma momentum by more than 50%. Such cases clearly demonstrate that strong toroidal mode coupling is responsible for the degradation in the central momentum, perhaps being lost to the vacuum vessel walls through induced eddy currents.

MHD Effects on Energy Confinement Large amplitude MHD activity can also significantly degrade the plasma stored energy. Figure 2 shows that the amount of enhanced degradation in the stored energy, $\Delta W/W$, depends almost linearly on the relative amplitude of the MHD mode, $\Delta b_r(n=1)/B_\theta$(wall). This data contains combined NBI, ICRH, and ICRH alone, fast oscillating m-3, n=2 modes, and slowly rotating or locked m=2, n=1 modes that arise after a large sawtooth collapse. The contribution to the drop in stored

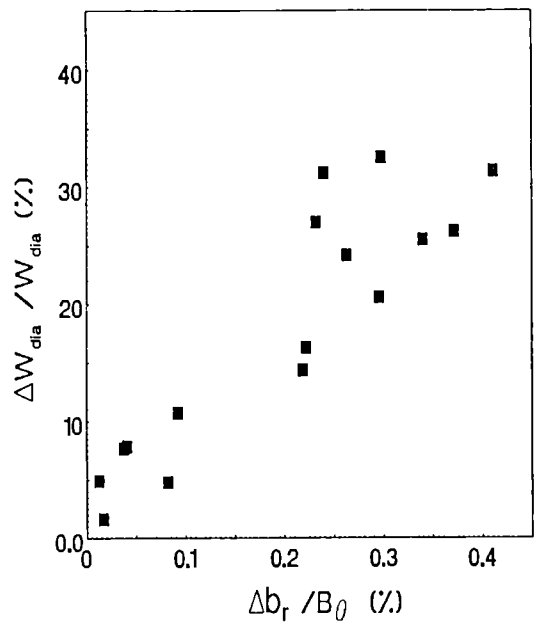

Figure 2. Relative change in plasma stored energy before and during a QSM versus the relative QSM amplitude.

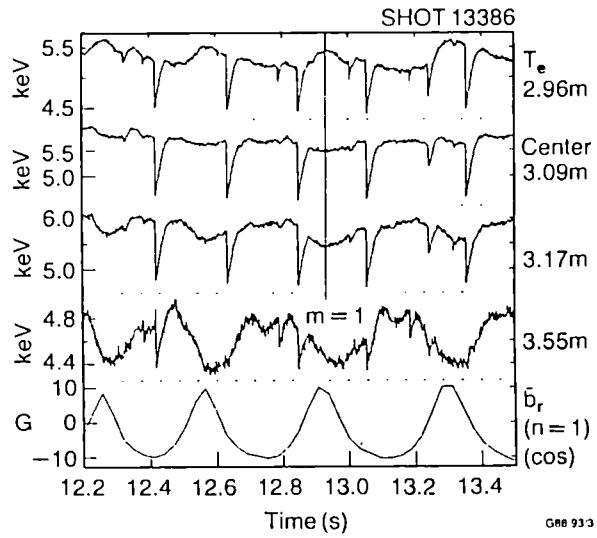

Figure 3. Effects of QSM on T_e at different radii showing strong mode coupling between m=1 and m=2.

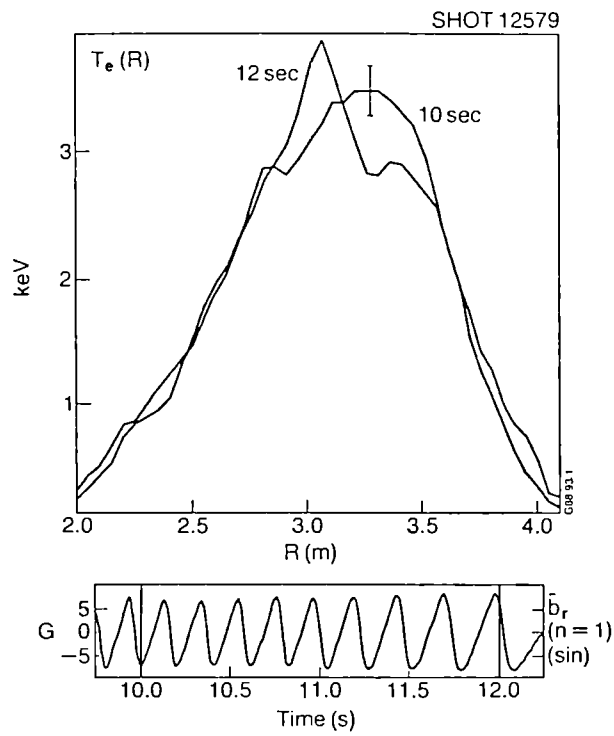

Figure 4. Thomson scattering electron temperature profiles at nearly opposite phases of the m=2, n=1 QSM oscillations showing a strongly coupled m=1 mode in the plasma center. A typical error bar shows the accuracy of the measurements. The phase of the oscillations on the QSM signal at the times of the two temperature profiles are indicated in the lower figure.

energy due to the sawtooth collapse itself is minimized by taking the measurement during the MHD activity only after more than one confinement time following the sawtooth collapse to allow the plasma to reheat.

The time evolution of this enhanced degradation is shown in Figure 1. The central electron temperature and stored energy remain low during the QSM on the first shot, but increase again with continued heating on the second shot without a QSM. The first shot had about a 17% drop in stored energy while the second shot without a QSM had an initial drop of 10% at the sawtooth collapse that subsequently returned to near the peak value of the stored energy before the ICRH was turned off. Since the drop in the electron temperature in both shots was about the same, the difference in the change in stored energy between the two shots must be due to the QSM. Note that locked modes arising before density limit disruptions also show a similar degradation in confinement [4].

Such evident MHD effects on global confinement parameters also manifest themselves directly in changes in the electron temperature from the edge right up to the center of the plasma. Figure 3 shows the strong toroidal mode coupling of the QSM oscillations near the plasma edge, analyzed with magnetic pick-up coils to be m=2, n=1, with oscillations on the ECE across much of the plasma. The m=1 character of the ECE oscillations is evident by the phase inversion across the plasma center. Note that the sawteeth persist despite this large m=1 mode. Further evidence of the effects of the QSM oscillations on the center of the plasma are shown in Figure 4. The LIDAR Thomson scattering system [5] acquired electron temperature profiles at nearly opposite phases of the QSM oscillations. The difference in the profiles indicates an m=1 structure across the plasma center with an amplitude of $\pm$ 600 eV. Such a large change in temperature is well outside the errors in the measurements.

Conclusion The strong coupling between MHD modes observed from the limiter right up to the plasma center demonstrates that these modes can affect most of the plasma. This strong mode coupling must then be at least partly responsible for the observed degradation in particle, momentum, and energy confinement during large amplitude MHD activity. The correlation of the X point of the magnetic island with locally enhanced radiation suggests that particle and energy transport may be increased locally around the X point of the mode. The observed degradation in particle and energy confinement depends on the mode amplitude rather than on whether or not the mode is rapidly oscillating or locked, while the loss of momentum depends on the frequency of oscillation of the mode more than on the mode amplitude.

References

[1] Snipes, J A, et al, 13th EPS Conf on Plasma Phys and Cont Fusion, Schliersee, Vol I, (1986) 152.
[2] Ehrenberg, J, et al, 7th Int Conf on Plasma Surface Interactions, Julich, 1988, to be published in Journal of Nuclear Materials.
[3] Stork, D, et al, 14th EPS Conf on Plasma Phys and Cont Fusion, Madrid, Vol I, (1987) 306.
[4] Snipes, J A, et al, "Large Amplitude Quasi-Stationary Modes in JET", JET preprint JET-P(88)01, submitted to Nuclear Fusion.
[5] Gowers, C W, et al, 14th EPS Conf on Plasma Phys and Cont Fusion, Madrid, Vol III, (1987) 1236.

LOCAL HEAT TRANSPORT IN JET PLASMAS

J.P.Christiansen, J.W.Connor*, J.G.Cordey, L.Lauro–Taroni,
D.Muir, H.C.Sack, A.Taroni, P.R.Thomas, F.Tibone, M.F.Turner*

JET Joint Undertaking, Abingdon, Oxon, OX14 3EA, UK.
**UKAEA Culham Laboratory, Abingdon, Oxon, OX14 3DB, UK*

INTRODUCTION

Two complementary approaches to the study of heat transport in JET plasmas are described in this paper. In the first approach, 1–D simulations have been performed using two different forms for the heat fluxes which are based on global scaling laws, have the scale invariance of theoretical models and represent the two generic models for the heat fluxes[1] capable of reproducing the main features of the plasma response to additional heating. Even though the mechanisms for confinement degradation are different, both forms can reproduce a wide range of data from JET and other machines. It is found with both models that the data can only be matched if the electron and ion transport coefficients have the same form and approximately the same magnitude.

In the other approach which will be described here the parametric dependence of the heat flux on local quantities has been obtained by fitting the data with a form with the scale invariance of the non–linear gyrokinetic equation of Frieman and Chen[2]. A good fit is obtained to a set of data obtained from neutral beam heated discharges with I_p=1–5 MA.

SIMULATIONS USING DIFFUSIVITIES WITH MODEL SCALE INVARIANCE

An extensive programme of simulation of JET discharges has confirmed the result[3] that models of the electron heat loss based on the dissipative trapped electron mode fail to reproduce T_e profiles. A similar conclusion has been reached concerning the Pogutse/Parail[4] and η_e models[5] by a direct comparison of the electron conductivity with the experimental values.

Two local transport models have been proposed at JET which provide the degree of profile resilience and confinement degradation required by the experimental data, are related to scaling laws for τ_E that fit the results from several devices and are sufficiently complete to be used in transport codes.

The first of these models[6] produces confinement degradation through a transport threshold at a critical value of temperature gradient. For simulations we have used

electron and ion heat fluxes

$$q_{eRL} = -n_e\chi_{eRL}(\nabla T_e - \nabla_c T_e) - n_e\chi_{e1R}\nabla T_e \quad \text{for } \nabla T_e \geq \nabla_c T_e$$
$$= -n_e\chi_{e1R}\nabla T_e \quad \text{otherwise}$$
$$q_{iRL} = K_{iRL}q_{eRL}(n_i\nabla T_i/n_e\nabla T_e)(T_i/T_e)^{1/2}$$

where $\chi_{eRL} = \chi_{e0R}(T_e q/B_T R^{1/2}T_i)(1+2d\ln(n_e)/d\ln(T_e))(C_1+R|\nabla q|/q)^{-1}$

and $\nabla_c T_e = \alpha(E_\parallel B_T/n_e\sqrt{T_e})^{1/2}B_T/q$

If SI units are used with keV for temperatures, then $\alpha\approx 6$, $C_1=2$, $\chi_{e0R}\approx 20$ and $\chi_{e1R}=0.1$ give a good match to the data. In order to reproduce T_{i0}, the total energy content and the NPA ion temperature profile, where available, it is found that $K_{iRL}\approx 1$ is required.

The second model is based on a resistive MHD scaling law for τ_E[7] and the confinement degradation occurs because of the nonlinear dependence of the heat flux on the pressure gradient. We have used

$$q_{ePT} = -n_e\chi_{PT}\nabla T_e$$
$$q_{iPT} = -n_i\chi_{PT}\nabla T_i$$
$$\chi_{PT} = C_{PT}/\mu_0\sigma(\mu_0 r^2\sigma v_A/qR)^{1/2}(\nabla p/\nabla_c p)$$

where σ is the Spitzer electrical conductivity, v_A the Alfven speed and $\nabla_c p$ the threshold pressure gradient for ideal ballooning instability. $C_{PT}\approx 0.035$ has been found to reproduce a wide range of data.

Both the above models have been used in a simple 1–D time independent code which is used for parameter scans. This code solves the ion and electron temperature equations and models the ICH and NBH fast ions. The heating deposition, electron, ion and current density profiles are represented by analytic forms. For the dynamics of particular discharges a full time dependent $1\frac{1}{2}$D transport/ equilibrium code JETTO is used. JET data is used for some quantities such as the density and radiation profiles.

Some uncertainty remains in the values of χ_{e0R} and C_{PT}. This largely because of the insensitivity of the calculated quantities such as temperature and density to these parameters due to non–linear effects and because of experimental errors. For some conditions the transport inside q=1 must be modified. The results of the simulation of a range of JET discharges such as the hot electron, hot ion and off–axis heating will be presented. Figures 1 and 2 show the model electron temperature profiles with the ECE data for 2MA/2.5T on– and off–axis ICH discharges.

EVALUATION OF THE THERMAL DIFFUSIVITY FROM HEAT FLUX DATA

The local heat flux in JET NBH discharges has been studied with the aim of determining values of local heat diffusivity[8]. No attempt is made to separate the total flux into an ion and electron heat flux since no ion temperature data is available. Similarly no allowance is made for the radiation loss channel; the latter can for some JET pulses be shown to be small compared with the total flux at plasma radii less than

0.85–0.95a. Thus the total flux q_{th} includes the Ohmic and NBH power inputs.

The data on q_{th} from 350 observations is analysed in terms of models q_f and it has been shown that[7,8]

$$q_f = -en\chi\nabla T_e - \Pi$$

represents the best fit to the data. The temperature gradient ∇T_e is determined from ECE and the density is measured by interferometer; the heat pinch is Π. Depending on how the data is selected various estimates of the heat diffusivity χ can be arrived at. One definite pattern emerges from the data: χ shows a pronounced dependence upon the current $I_p(x)$ enclosed within a surface x.; $\chi \approx 1/I_p(x)$.

By applying the similarity techniques of Connor and Taylor[9] to the gyrokinetic equation of Frieman and Chen[2], assuming that small space and short time scale turbulence is responsible for local transport, the diffusivity is constrained to the form

$$\chi = (v\rho^2/L)\, F(\nu L/v, \beta)$$

where ρ is the Larmor radius, L is some scale length, ν a collision frequency, v a thermal velocity and β the plasma beta. The function F can be arbitrary. In practice we have employed

$$\chi = C\, T_e^{3/2}/I_p^2 L\, (nL/T_e^2)^{\alpha}\, (nT/I_p^2)^{\gamma}$$

and apply non–linear regression techniques to the data on q, n, T etc.. It is found that C=10±0.4, α=0.4±0.02, γ=–0.42±0.02 and Π=2.6±0.5 represent the optimum values. This essentially implies that $\chi \approx 1/I_p(x)$. It should be stressed that there is a 32% scatter in the fit of q_f to the data q_{th}. A plot of the best fit against the data is shown in figure 3 and the scatter is evident.

Many approximations are made and the data contains scatter not only from the measurements but also from sawtooth oscillations. To improve on the latter we are repeating the above study for 150 JET ICH discharges. These discharges have been selected as they do not have sawtooth oscillations("monster sawteeth"). The results from the analysis will be discussed.

REFERENCES

[1] J.D.Callen et al, Nuclear Fusion 27 (1987) p1857
[2] F.A.Frieman and Chen Liu, Physics of Fluids 25 (1982) p502
[3] D.Düchs et al., Proc. 11th IAEA Conf., Kyoto 1986,1 (1987) p325
[4] V.V.Parail and O.P.Pogutse, JETP Letters 32 (1980) p384
[5] P.N.Guzdar et al., Physical Review Letters, 57 (1986) p2818
[6] P.H.Rebut, 1987 European Tokamak Programme Workshop (to be published)
[7] P.R.Thomas, JET Preprint JET–P(87)17 (to be published)
[8] J.P.Christiansen et al., JET Preprint JET–P(87)48 (to be published)
[9] J.W.Connor and J.B.Taylor, Nuclear Fusion 17 (1977) p1047

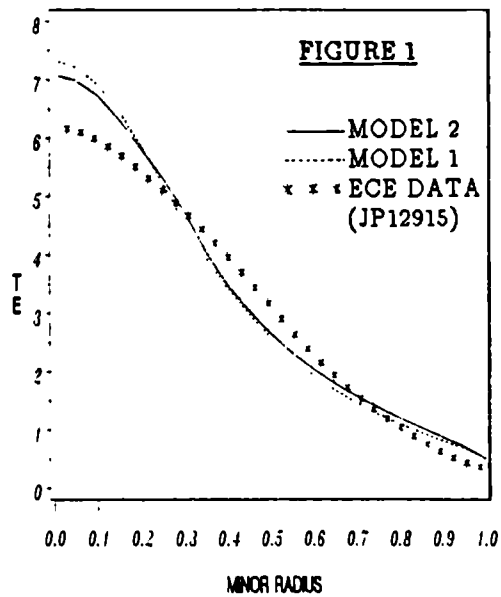

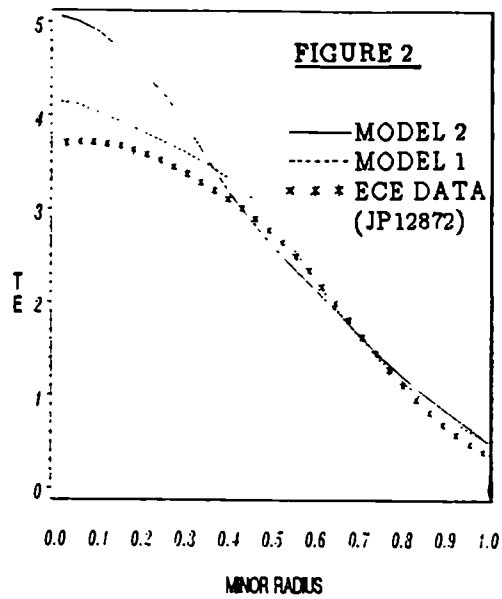

FIGURES 1 AND 2: The T_e and T_i profiles obtained using the two transport models compared with the experimental T_e data from ECE. Both discharges were at 2MA/2.5T with 7MW of ICH power. Figure 1 shows the result of heating on–axis whilst figure 2 corresponds to the ICH being absorbed at the half minor radius.

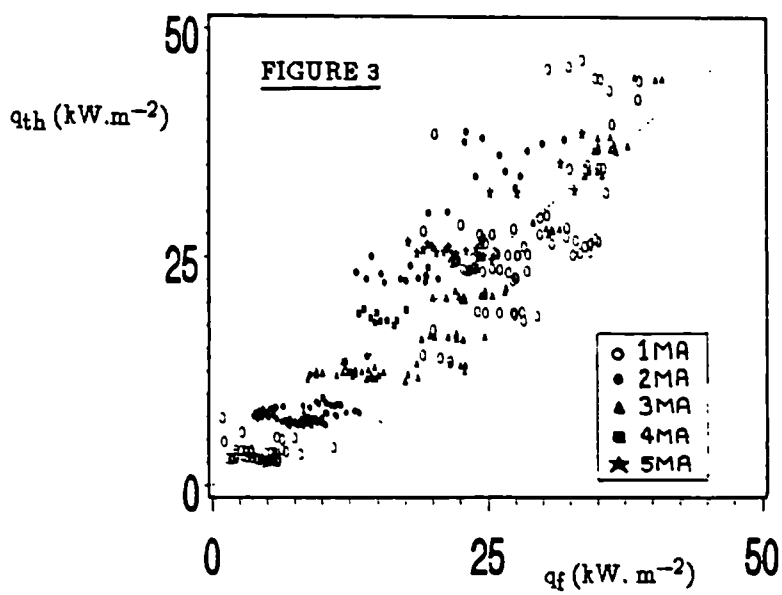

FIGURE 3: The experimental value of the heat flux q_{th} versus the fitted value $q_f = -\chi n \nabla T_e - \Pi$ where χ is constrained to a form compatible with the scale invariance of the non–linear gyrokinetic equation.

GLOBAL CONFINEMENT CHARACTERISTICS OF JET LIMITER PLASMAS

D J Campbell, J P Christiansen, J G Cordey, P R Thomas, K Thomsen

JET Joint Undertaking, Abingdon, Oxon, UK, OX14 3EA

Abstract

Data from a wide variety of plasma pulses on JET (aux. heating, current, field, minority species, plasma shape, etc) are analysed in order to assess the characteristics of global confinement. The scaling of confinement in ohmically and auxiliary heated discharges is examined. The ohmic confinement in the present new JET configuration (Belt Limiter) is essentially the same as previously. Confinement in auxiliary heated discharges shows presently a slight improvement since 1986. Both ohmic and non-ohmic data is used in a set of confinement time regression analyses and certain constraints derived from theory are imposed.

1. Ohmic Heating in JET

Previous work [1] on confinement in JET ohmic discharges was found to be best described by an empirical scaling law

$$\langle T_e \rangle \sim B_\phi^{\,a} \langle n \rangle^b \, q^c \, K^d \qquad (1)$$

T_e is electron temperature, B_ϕ toroidal field, n is electron density, while q is safety factor of a plasma configuration with elongation K; the brackets <> denote a volume average. The scaling parameters a, b, c, d were for 1984-85 data 1.8, -0.6, -1.0, 0.8 respectively. Eq.(1) is a consequence of Ohm's Law and similar expressions can be found for Z_{eff} and τ_E, the global energy confinement time. The ohmic data obtained from experiments on JET in 1986, 87 and 88 is still described by scaling laws of the type (1). Figure 1 shows a plot of $\langle T_e \rangle$ measured by ECE versus the expression (1). The fitting parameters a, b, c, d are now found to be 1.3, -0.55, -1.08, 0.68 respectively; the change in the exponent a is caused by a greater variety of B_ϕ values during 1986-88; in 1985 B_ϕ was mostly 3.4T. The data in Figure 1 includes 1984-85-86 data with toroidal limiters and 1987-88 data with belt limiters. The introduction of belt limiters have resulted in generally higher values of elongation K. The full data set (1984-88) is now more evenly balanced as regards variations in K and B_ϕ and this increases the level of confidence in the scaling law (1).

2. Decoupling of Ions from Electrons

The auxiliary heating systems (NBI and ICRH) on JET give access to 2 regimes in which the ion and electron temperatures are decoupled for periods longer than the global energy confinement time τ_E. Neutral beam

heated discharges following extensive helium discharge cleaning in 1986 yielded low densities (inner wall pumping) and subsequent hot ion modes [2] for which $T_i \sim 2T_e$. During 1987-88 ICRH discharges with hydrogen minority and up to 16MW of power have produced $T_e \sim 2T_i$. Figure 2 shows that substantial temperature differences $T_i - T_e$ occur only when the ratio τ_{eq}/τ_E exceeds 1; this result demonstrates that energy equipartition in JET is classical and is characterised by the time constant τ_{eq}. It is worth noting that the confinement time τ_E for the data in Figure 2 is largely independent of the sign of $T_i - T_e$ (but not the magnitude). Since $T_i - T_e \approx T_i$ or T_e the independence of τ_E upon the sign of $T_i - T_e$ provides some constraints on future Tokamak confinement theories: neither of the heat diffusivities χ_e or χ_i can have a strong temperature dependence.

3. Fast Ions from ICRH

It is possible to establish trends in JET data from power-density scans in ICRH heated discharges with fixed current-field (2MA, 2.2T). The energy content W_{dia} measured by the diamagnetic loop estimates the total energy $W_\perp$ (thermal and non-thermal).

At constant ICRH power W_{dia} decreases as n increases, while the energy content W_{kin} does not decrease with n. W_{kin} estimates the total thermal energy from ECE, interferometer and X-ray crystal spectrometer data. Because of this density dependence we can test the data on W_{dia}, W_{kin} against the fast energy content predicted by theory, ie,

$$W_f = \tfrac{2}{3}(W_{dia} - W_{kin}) \approx P_{RF}\,\tau_s/2 \quad , \qquad (2)$$

where τ_s denotes the classical slowing down time $\tau_s = 0.075T_e^{3/2}/n$ (for He^3 minority). The data values in Figure 3 of $\frac{2}{3}(W_{dia} - W_{kin})$ do exhibit the dependence (2) upon P_{RF} and τ_s (T_e, n). The scatter arises from taking differences between measurements which include both random and systematic errors. Indeed to achieve the level of agreement depicted in Figure 3 it has been necessary to reduce the ECE measurements systematically by 20%; this reduction brings together the ECE and LIDAR measurements of electron temperature. The value of τ_s is based on an average over a fraction of the plasma volume.

4. On-Off Axis ICRH Heating

In a sequence of 10 ICRH pulses the resonance positions for each of the 8 JET antennae has been moved from on-axis ($R \approx 3$m) to off-axis ($R \approx 3.5$m). The confinement properties of plasmas with different ICRH power deposition profiles can be described by an offset-linear law

$$W = W(0) + (\tau P)_{on\text{-}axis} + (\tau P)_{off\text{-}axis} \quad . \qquad (3)$$

The incremental confinement time τ and power level P associated with on-off axis heating allow for a range of increments. Figure 4 shows measurements of W plotted against the values predicted by (3). Eq.(3) gives a very good

description of the data from the 10 ICRH pulses which feature 100% off-axis as well as 100% on-axis heating; it is based on the transport models of [3]. The $\tau_{on\text{-}axis} = 0.21s$ and $\tau_{off\text{-}axis} = 0.15s$ showing that the confinement depends on the location of the heating power as shown in [3].

5. Confinement Scaling

Data obtained from JET experiments during 1984-1988 (approximately 3000 pulses) is employed in regression analyses as described earlier [1,2]. An empirical expression for the confinement time τ_E like

$$\tau_E = 0.3\ I_\phi^{1.1}\ n^{0.2}\ P^{-0.5} \qquad (4)$$

emerges as the best fit to the entire data. In Eq.(4) the units are I(MA), $n(10^{19}m^{-3})$ and power P in MW. The constraints imposed by applying the Connor-Taylor scale invariance techniques to the gyro-kinetic equation derived in [4] result in the scaling law

$$\tau_E \sim \rho^2\ v/L\ F(\nu L/v,\ \beta) \qquad . \qquad (5)$$

ρ is Larmor radius, v is thermal velocity, L is a length scale, ν is a collision frequency and F is an arbitrary function. If the latter is represented by a power law expression such that

$$\tau_E \sim \rho^2\ v/L(\nu L/v)^\alpha\ \beta^\gamma \qquad , \qquad (6)$$

then a wide range of scaling laws are possible depending upon the choice of ρ, v, L, ν, β; eg, ρ_e or ρ_i, v_e or v_i, L=a or $\nabla n/n$, $\nu = \nu_{ei}$ etc. Eq.(6) provides for a good test against JET data since $\nu L/v$ chosen as naZ_{eff}/T_e^2 varies by a factor 20 while β chosen as nT_e/I_ϕ^2 varies by a factor 10. An a priori choice of α and γ establishes a set of scaling laws: $\alpha = \frac{1}{2}$, $\gamma = -\frac{1}{2}$ yields the offset linear law of [2] and gives a good fit; so too do electrostatic models with $\gamma = 0$; $\alpha = 0$, $\gamma = -1$ (T-11 scaling) and $\alpha = 1$, $\gamma = -1$ (resistive fluid turbulence) do not fit the data. Applying regression analysis one finds; $\alpha = 0.3$, $\gamma = 0.1$ from the best fit correspond to

$$\tau_E = 0.22\ I_\phi^{1.05}\ n^{0.3}\ P^{-0.5}\ B_\phi^{0.15} \qquad (7)$$

We notice that (7) is essentially the empirical fit (4).

Acknowledgement

The authors gratefully acknowledge the skill and assistance provided by the ICRH and diagnostic teams on JET.

References

[1] Bartlett, D.V. et al. Nucl. Fusion 28(1988)73.
[2] Cordey, J.G. et al. Plasma Physics and Cont. Fusion, Kyoto (1986).
[3] Callen, J.D. et al. Nucl. Fusion 27(1987)1857.
[4] Frieman, E.A. and Chen, L. Phys. Fluids 25(1982)502.

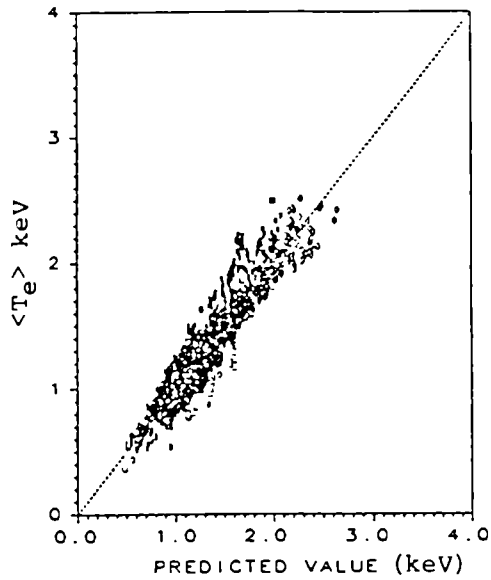

Fig. 1 $\langle T_e \rangle$ vs values predicted by eq (1)

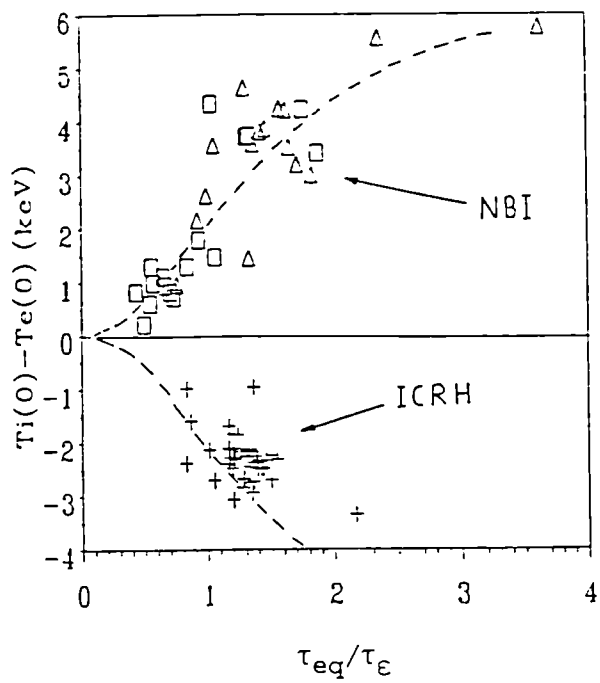

Fig. 2 Temperature differences in decoupled plasma regimes

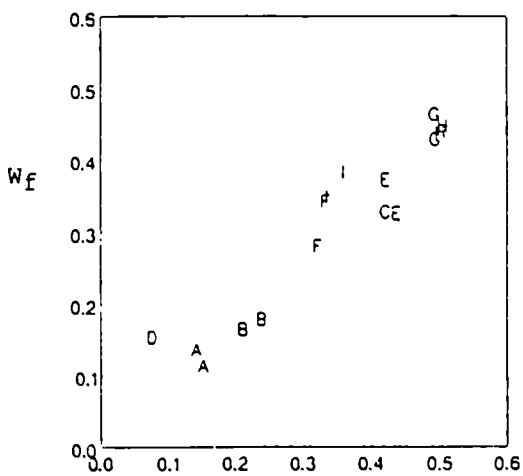

Fig. 3 Fast ion energy vs Power Tause 2 in ICRH discharges

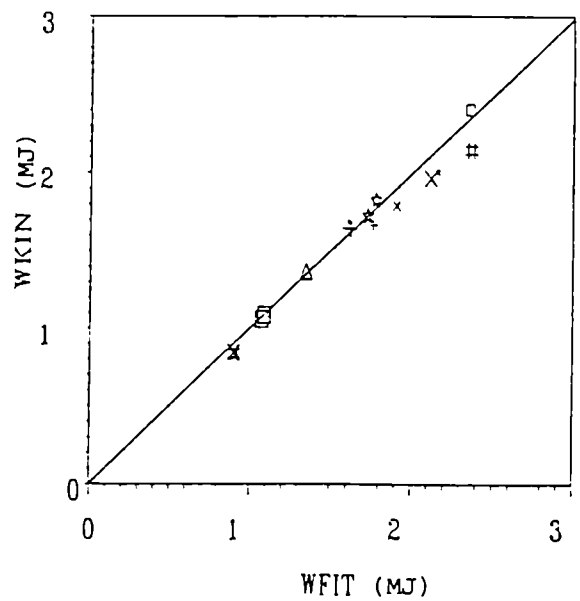

Fig. 4 Total energy vs the scaling law (3)

HIGH CURRENT OPERATION IN JET

P. Lomas, V. Bhatnagar, D. Campbell, J.P. Christiansen, P. Chuilon, S. Corti, B.J. Green, P. Harbour, J. How, J. Jacquinot, M. Keilhacker, T.T.C. Jones, L. de Kock, J. Last, E. Lazzaro, C. Lowry, G. Magyar, M. Malacarne, P.L. Mondino, P. Morgan, P. Noll, J. O'Rourke, A. Santagiustina, F.C. Schueller*, J. Snipes, D. Summers, A. Tanga, P.R. Thomas, K. Thomsen, B. Tubbing

JET Joint Undertaking, Abingdon, Oxon., OX14 3EA, UK.
*FOM Instituut voor Plasmafysica, 3430 BE Nieuwegein, The Netherlands.

ABSTRACT. Plasma currents of 6MA have been obtained in JET with a limiter configuration and 4.0MA have been obtained with a magnetic separatrix which was well separated from the limiters. A 4.5MA X-point discharge has been produced, but the separatrix was close to the belt limiter. These have been made possible by improvements to the primary configuration which reduce the stray field at breakdown, increase the volts-second capability and enhance the shaping effect due to the primary.

Scenarios have been tested which demonstrate the feasibility of 7MA limiter operation and 5MA X-point operation.

The physics issues to be discussed are magnetic configuration, breakdown, current penetration, stability and volts-seconds consumption. The confinement properties of limiter and X-points will be compared.

1. HIGH CURRENT LIMITER OPERATION

1.1 Breakdown. Reliable breakdown can be achieved with V_ℓ~10-30 Volts. At maximum premagnetisation, where the stray field is ~2E-2 Tesla, prompt breakdown is obtained provided the fields are tuned to give an hexapolar null in the centre of the chamber. In this case the volts seconds loss at breakdown is less than 1 volt-sec. Careful preprogramming of the vertical field is required until the plasma fields dominate the stray fields.

1.2 Current Penetration and Stability. The empirical stability diagram for JET [1] is shown in Fig.1 with the trajectory of a 6MA discharge superimposed. It is necessary to programme the current ramp rate, elongation, minor radius, gas feed and toroidal field so as to avoid the lower boundary where the rotating MHD which arises at rational q_ψ reaches sufficient amplitude to lock. These locked modes are particularly dangerous because they often persist from early times in the discharge and later grow to cause disruptions at high current. In the example of Fig.1 a current ramp as slow as 0.25MA/sec was necessary to allow the current to penetrate and thereby reach 6MA at $q_\psi<3$. Although the rotating modes are clearly visible these do not lock. At constant q_ψ larger current ramps are possible. Thus by simultaneous ramp of plasma current and toroidal field the discharge shown could safely be extended from 6MA/2.8Tesla to 7MA/3.4Tesla.

1.3 Volts-Seconds Consumption. Fig.2 shows the total flux swing at the plasma boundary together with the inductive flux and resistive flux on axis

as functions of plasma current for the same 6MA discharge illustrated in Fig.1. The maximum volt-sec available is also shown for maximum premagnetisation for the two cases (a) maximum uniform reverse current in primary stack and (b) maximum reverse current in central pancakes and maximum reverse current in top/bottom pancakes. For the first 5 seconds the resistive consumption is negligible but rises as q_ψ reaches 3 at 4.5MA. In this discharge the current ramp is only 0.25MA/sec and a total of 6 volt-sec is consumed resistively by the start of the flat top. Clearly at this rate there are insufficient volt-sec to reach 7MA at low q_ψ. However a current ramp of 0.5MA/sec with simultaneous toroidal field ramp has been demonstrated at low q_ψ up to 6MA. This scenario has sufficient volt-sec left to reach 7MA. For $q_\psi>3$ the resistive volt-sec is negligible during the current rise and at 5MA a flat top of 9 sec has been demonstrated.

1.4 Heating During the Current Rise. RF heating has been applied during the current rise before the onset of sawteeth. Very high electron temperatures result, and a saving of about 1 volt-sec resistive loss is found. Although the change in ℓ_i is small the onset of sawteeth is delayed by several seconds indicating either a change in the current profile near the magnetic axis or a stabilisation mechanism similar to the monster sawtooth [2].

2. HIGH CURRENT X-POINT PLASMAS. The formation of a magnetic separatrix is possible in JET at plasma currents 3-4MA by the combined effect of leakage fields from the primary and shaping coils, resulting in elongation <2. Higher currents can be achieved in the single null configuration by displacing the plasma axis away from the mid-plane and unbalancing the main vertical field coils. Fig.3 shows a 3.8MA X-point obtained in this way. This discharge entered the H-mode with neutral beam heating. An X-point has been produced at 4.5MA but in this case the separatrix was close to the lower belt limiter. A 5MA X-point should be possible with larger imbalance in the vertical field coils.

The X-point plasmas are no more vertically unstable than limiter plasmas with the same current and elongation. However, in the asymmetric configuration, the vertical motion is usually towards the X-point and the velocity is larger. Values of I_p/aB_t=2.5MA/(M-Tesla) have been achieved for X-points compared with 2.1 for limiter plasmas.

3. COMPARISON OF LIMITER AND X-POINT CONFINEMENT. Heating experiments are currently underway for high plasma currents in both limiter and X-point configurations. Values of $n_d(0)T_i(0)\tau$~1.8E20m^{-3}keV-sec have been achieved in recent 5MA limiter experiments which is similar to 3MA H-mode data. At 3.8MA $n_d(0)T_i(0)\tau$~3E20 has been achieved in the H-mode. In both 5MA limiter and 3.8MA H-mode the plasma energy content reaches ~7MJ. However, whereas the limiter case requires a power input of 15MW, the 3.8MA X-point requires only 8MW to reach this stored energy.

References

[1] J.A. Snipes et al. JET-P(88)01 Submitted to Nuclear Fusion.
[2] D. Campbell et al. JET-P(87)20 Submitted to Physical Review Letters.

Fig. 1
Empirical stability diagram showing:

- Stability boundaries in ℓ_i-q_ψ plane
- Trajectory in ℓ_i-q_ψ plane of 6MA pulse 13944
- Amplitude of $\dot{B}_\vartheta$ versus q_ψ
- quasi stationary mode amplitude versus q_ψ
- 1 sec after breakdown
- 1 sec intervals
- start of current flat top

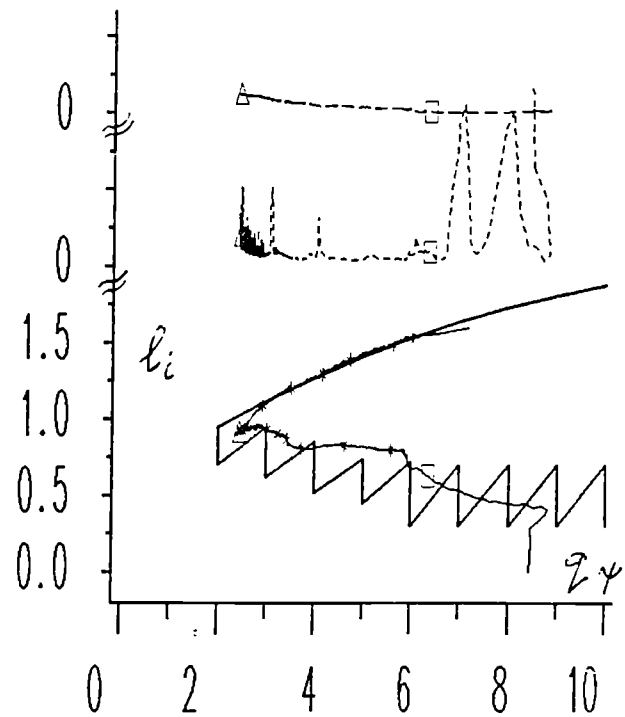

Fig. 2
Flux at plasma boundary versus plasma current (MA) for shot 13944

- Total flux change
- Plasma inductive flux change
- Plasma resistive flux change
- Volt-sec limit (a) see text
- Volt-sec limit (b) see text
- 1 sec after breakdown
- 1 sec intervals
- start of current flat top

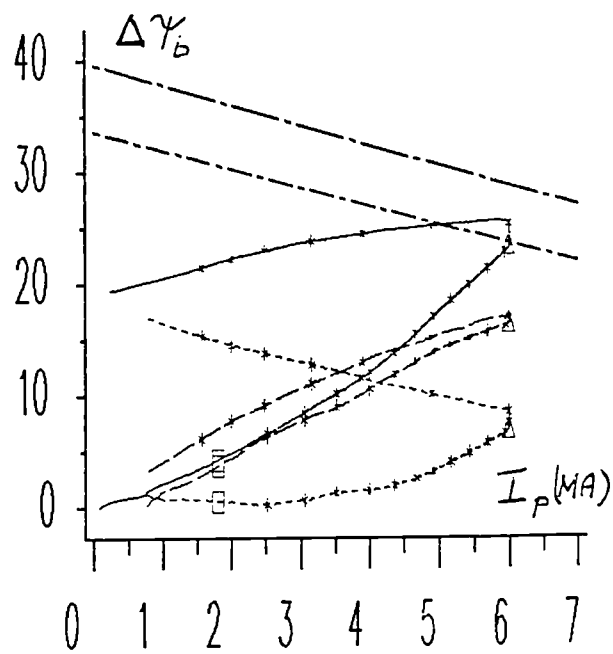

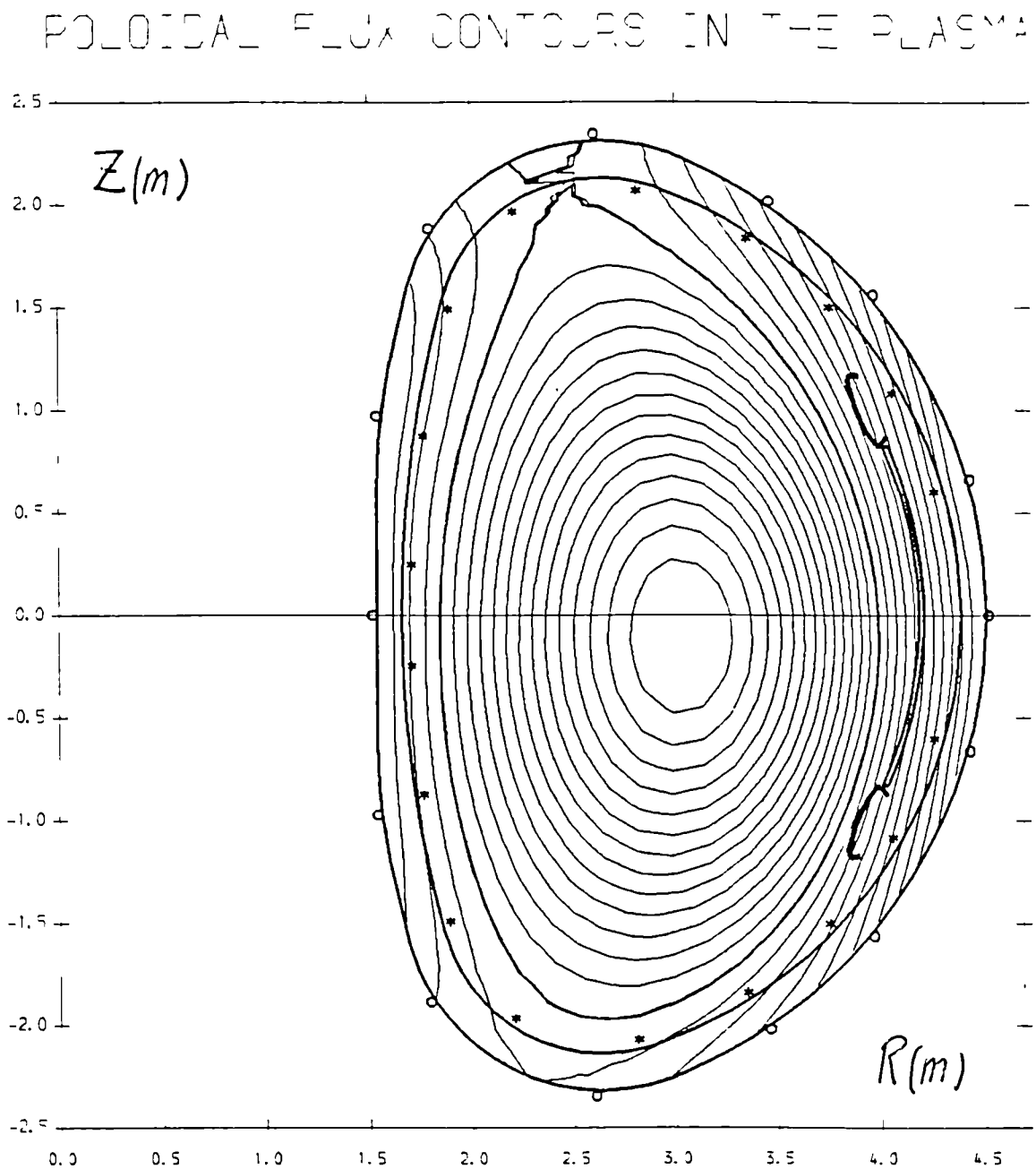

Fig. 3
Magnetic surfaces for H-mode shot 14883. I_p= 3.3MA, B_T=2.1 Tesla.
Note the single x-point at the top.

ION TEMPERATURE PROFILES AND ION ENERGY TRANSPORT IN JET DURING ADDITIONAL HEATING AND H-MODES

S Corti, A Boileau*, G Bracco+, M Forrest°, M von Hellermann, L Horton**, P Larsen, C Sack, H P Summers, A Taroni, F Tibone

JET Joint Undertaking, Abingdon, Oxon OX14 3EA, UK
*INRS Energie, Montreal, Canada/ °UKAEA Culham Laboratory, Abingdon,UK
**ORNL, Oak Ridge, USA

EXPERIMENTAL T_i PROFILES

The ion temperature is deduced in JET using various diagnostic systems in order to cover all possible plasma scenarios.

Ion temperature profiles have been in the past deduced from a model dependent analysis of the data obtained with an array of four passive Neutral Particle Analysers (NPA) only during ohmic and ICRH heated discharges [1].

In this paper we report on initial T_i profile measurements during Neutral Beam Injection. These have been obtained from both the multichord line-of-sight system of the visible charge exchange (CX) spectroscopy diagnostic which uses the JET Neutral Beams as diagnostic beams [2,3], and the upgraded version of the analysis of the NPA data.

With the CX spectroscopy system, radial profiles of ion temperature and toroidal velocity [4] are deduced from the Doppler broadened recombination spectra of fully stripped plasma ions such as deuterium, helium, carbon and oxygen. A multichord array in the near equatorial plane intersects the neutral beams at 8 positions between R=2.3m and R=4.1m with a spatial resolution of ± 10cm. An additional single vertical line intersecting the neutral beams in the plasma centre enables to compare the temperature of different ions and to investigate possible anisotropic velocity distribution functions.

In the first period of operation, ion temperature profiles were measured during H-mode phases of X-point discharges [5] and during combined RF and NB heating. Representative peaking factors of parabolic ion temperature profiles are between 1 and 2, the profiles becoming flatter during H-modes. Fig.1 gives an example of the time evolution of the ion temperature profile (based on O^{8+} (10 to 9)), while in Fig.2 profiles at different times are compared. Hollow ion temperature profiles can sometimes be observed. A more detailed investigation will be possible when a new system using a finer mesh of lines-of-sight employing 15 chords becomes operational.

In Fig.3 profiles obtained from the NPA data in different NBI scenarios are shown. They are obtained taking advantage of the fact that the JET NPA system can simultaneously measure hydrogen and deuterium particles. While the deuterium spectra are simulated taking into account a Fokker-Planck description of the slowing down of the beam particles [6], the hydrogen spectra remain Maxwellian and help in the reconstruction of the profile. In this way profiles during a hot ion mode discharge

(Fig.3a), during NBI into a limiter discharge (Fig.3b) and during NBI into X-point discharges both in L-mode phase (Fig.3c) and in H-mode phase (Fig.3d) have been obtained.

A broadening of the profile is observed at the transition from L to H mode, consistent with the CX spectroscopy.

TRANSPORT ANALYSIS

Initial results of ion transport analysis based on T_i-profiles measured by NPA were presented in [7]. The availability of an extended data base for ohmic and RF-heated plasmas allows us now to establish those conclusions more firmly. Furthermore, we are in a position to discuss preliminary results on local ion transport during NBI.

The predictive transport code JETTO connected to JET data banks has been used, adopting the same modelling techniques described in [7], unless otherwise specified. The main conclusion in [7], ie. the evidence for anomalous ion transport, has been confirmed by further analysis of ohmic and RF-heated discharges. It remains true even when the LIDAR electron temperature profile is taken as experimental reference instead of the ECE measurement (the former can be as much as 25% lower than the latter in some of the considered cases).

Figure 4 shows a representative example of our results, corresponding to the flat-top phase of a "monster sawtooth" for a deuterium plasma with 7.5 MW on-axis RF heating (H minority) and peak electron temperature T_{eo} = 7 keV (from LIDAR). Electron energy transport has been modelled here using a non-linear heat flux model ($\chi_e \propto \nabla p$ [8]), that yields T_e-profiles in agreement with the experimental data, and virtually insensitive to the variations in $T_i(\rho)$ shown in Fig.4. The three computed T_i-profiles in Fig.4 have been obtained assuming: a) $\chi_i = \chi_e$; b) $\chi_i = \chi_i(n_i) + \chi_{i,neo}$, where $\chi_i(n_i)$ is the anomalous conductivity due to the excitation of ion temperature gradient driven modes [7], while $\chi_{i,neo}$ is the Chang-Hinton neoclassical coefficient [9]; c) $\chi_i = 15\ \chi_{i,neo}$.

It is apparent that a strong ion thermal conductivity in the outer half of the plasma is necessary to reproduce the measured $T_i(\rho)$: $\chi_i = \chi_e$ appears to be the best available prescription.

The same prescription, when used in the simulation of an X-point discharge with NB heating, proves successful in reproducing $T_i(\rho)$ from NPA during the L- as well as during the H-phase.

We should stress the preliminary nature of these calculations, and the fact that we are simulating the behaviour of a plasma undergoing transients (Fig.5).

In the transport code simulation, the time evolution of the electron temperature is satisfactorily reproduced by using an empirical electron thermal conductivity model based on the "profile consistency" constraint [10], combined with Bohm-like transport in the region where $q<1$, to simulate the average effect of sawteeth.

Figure 6 compares the experimental NPA profiles during L and H mode with those computed using $\chi_i = \chi_e$.

During the early stage of the H-mode, to which the profile in Fig.6 refers, the thermal conductivity throughout the plasma is found to be comparable to its ohmic value. At the earlier L-mode time in Fig.6, χ is somewhat larger, but it evolves in time and no discontinuity is observed in transport at the transition to the H-mode.

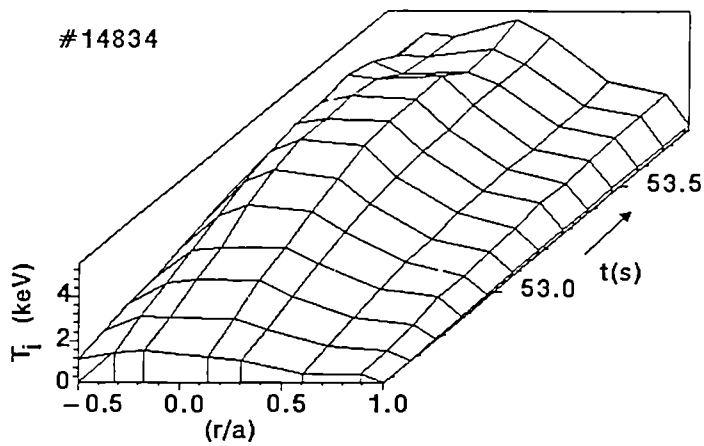

FIGURE 1

Time behaviour of T_i profiles from CX spectroscopy

FIGURE 2

T_i profiles from CX spectroscopy:
a) L – mode
b) H – mode, end of monster sawtooth
c) after sawtooth crash

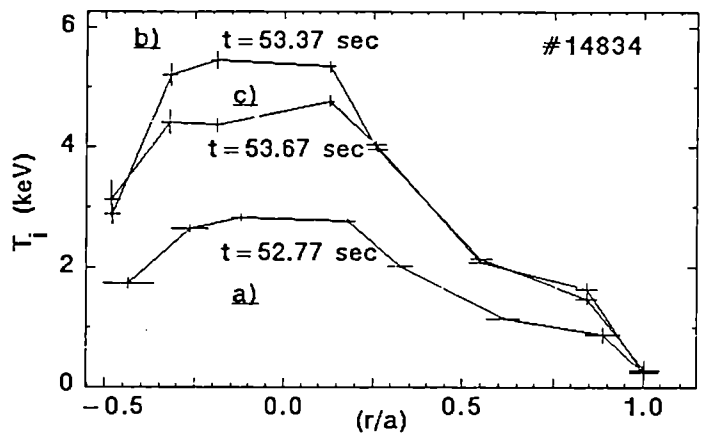

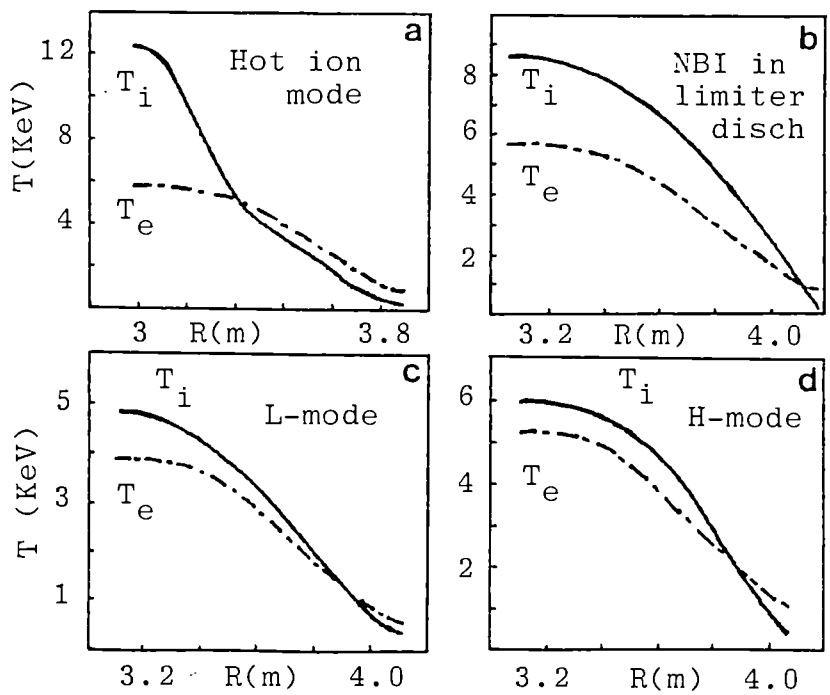

FIGURE 3

T_i profiles from NPA analysis in different NBI scenarios.
Also shown are T_e profiles from ECE (dashed lines).
a - # 10169
b - # 10981
c and d - # 10755

FIGURE 4

Experimental T_i profiles compared with those computed with:

a - $\chi_i = \chi_e$,

b - $\chi_i = \chi_i(\eta_i) + \chi_{i,neo}$

c - $\chi_i = 15\ \chi_{i,neo}$

for a 'monster sawtooth' with B_t=2.7 T, I_p=3MA, $\bar{n}_e = 3\ 10^{19}\ m^{-3}$, P_{RF}= 7 MW.

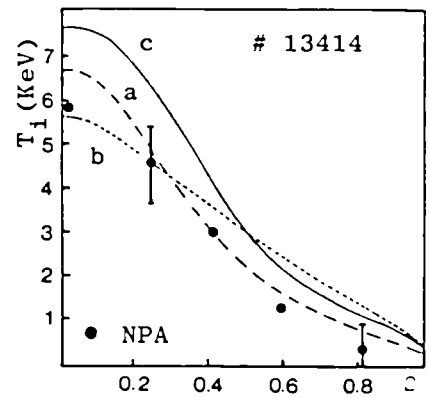

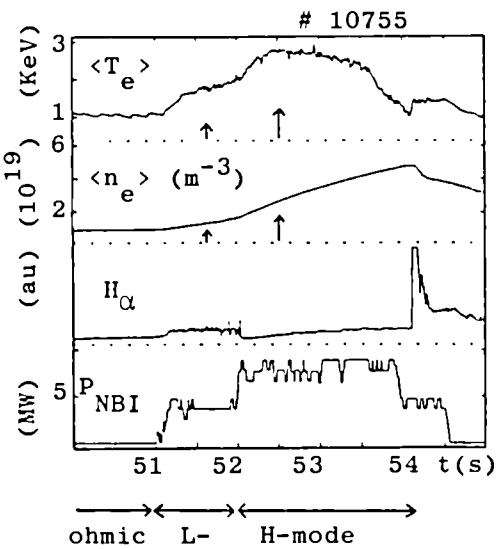

FIGURE 5 - Time evolution of volume average electron temperature and density, H_α radiation and auxiliary power. Arrows indicate the times for which T_i profiles are shown in fig. 3c,d. At these times NBI deposition profiles are centrally peaked and broad, with 60-70% of power being absorbed by plasma ions.

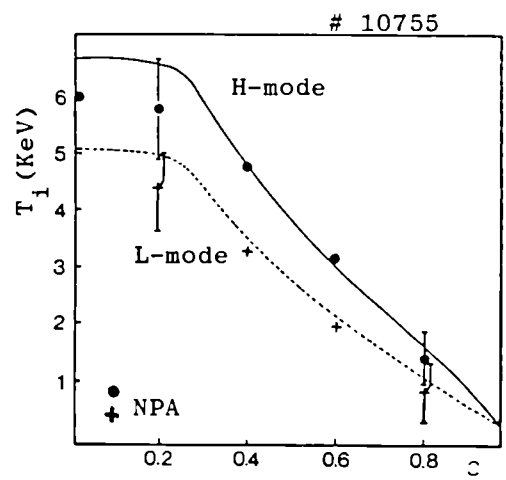

FIGURE 6

Experimental and computed T_i profiles during L- and H-mode for the same discharge as in fig. 5.
B_t=2T , I_p=2MA, 75 KeV D° injection into D plasma.
Simulation uses the model with $\chi_i = \chi_e$.

REFERENCES

[1] S Corti, et al., 13th EPS, Schliersee, 1986, vol.1, p.109.
[2] M von Hellermann, et al., 14th EPS, Madrid, vol.3, p.1260.
[3] A Boileau, et al., JET Report (87)44.
[4] N Hawkes, et al., this conference.
[5] D Bartlett, et al., this conference.
[6] S Corti, et al., 14th EPS, Madrid 1987, vol.3, p.1030.
[7] A Taroni, et al., 14th EPS, Madrid 1987, vol.1, p.173.
[8] P Thomas, et al., this conference.
[9] C S Chang, F L Hinton, Phys. Fluids 25(1986)1515.
[10] A Taroni, F Tibone, 14th EPS, Madrid 1987, vol.1, p.97.

PROFILES OF TOROIDAL PLASMA ROTATION

N C Hawkes[1], M von Hellermann, A Boileau[2], L Horton[3], E Källne[4], N J Peacock[1], J Ramette[5], and D Stork.

JET Joint Undertaking, Abingdon, Oxon, UK. [1] Culham Laboratory, Abingdon, Oxon, UK. [2] NRS-ENERGIE, CP1020, Varennes, Quebec, Canada J0l 2P0. [3] Fusion Energy Division, ORNL, Oak Ridge, Tennessee, USA. [4] Royal Institute of Technology, S10044 Stockholm, Sweden. [5] CEA Saclay, France.

INTRODUCTION

Strong toroidal rotation ($\omega_\phi \leq 10^5$ rads sec^{-1}) in Neutral Beam Heated (NBH) discharges in JET has been previously reported [1]. Recently the multi-chordal visible charge exchange recombination spectroscopy (CXRS) diagnostic has produced radial profiles of the toroidal velocities of dominant light impurities (carbon and oxygen). These are compared with X-ray spectroscopy and an estimate of plasma viscosity obtained.

INSTRUMENTATION

The spectroscopic sight-lines which will eventually be applicable to rotation measurements on JET are shown schematically in figure 1. An X-ray crystal spectrometer [2] viewed radiation from a NiXXVII resonance line, determining the central (major radius - 2.7-3.5 m) toroidal angular velocity via Doppler shift determination. The CXRS diagnostic [3] measures the Doppler shifted light from excited C^{6+} and O^{8+} ions resulting from charge-exchange collisions of the Neutral Beams with the fully-stripped impurity ions in the plasma. This diagnostic has 8 lines of sight across the plasma giving a toroidal rotation profile at points defined by the intersection of the chords and the neutral beams. In addition an XUV diagnostic [4] was occasionally used to make measurements on the lower ionisation states of nickel.

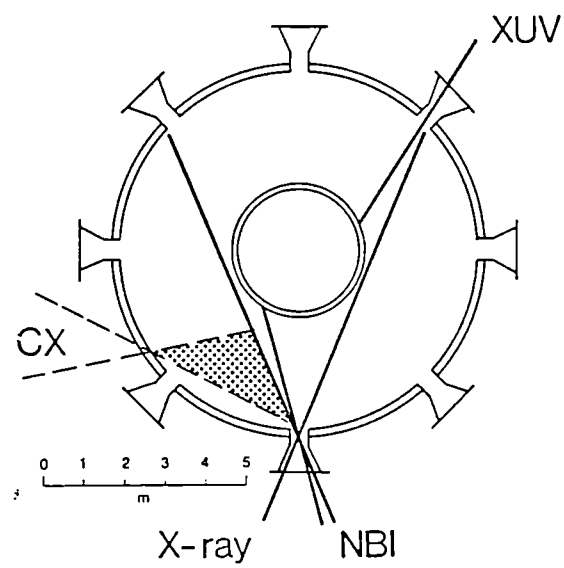

Fig.1: Schematic showing instruments on JET. NBI denotes the two banks of neutral beams, CX the 8 lines-of-sight of the charge exchange diagnostic, X-ray and XUV denote the sight lines of these two spectrometers.

RESULTS

Figure 2 shows an example of the time history of the rotation velocities derived from Doppler-shift measurements on the rotating C^{5+*} ions at different major radii. The discharge shown is one in which the H-mode was achieved during NBH in a single-null X-point discharge and the start of the H-mode is indicated by the drop in the edge H_α recycling. The rotation profile shapes show little change in time indicating that the velocity profile is established across the whole plasma radius rapidly (< 500 ms) after the start of injection. This is a similar timescale to the acceleration of the plasma to equilibrium speed.

The contrast to the plasma behaviour observed with ICRF heating is shown in figure 3. The CXRS diagnostic is not available when NBH is not applied to the discharge but rotation of the nickel lines measured by the X-ray and XUV diagnostics is shown. It is not possible to determine the unshifted (stationary plasma) position of any line with sufficient provision to ascribe absolute rotation velocities to the shifts observed. Previous measurements of rotating MHD modes on JET [1] and their correlation with the central NiXXVII Doppler-shift have shown that Ohmic plasmas prior to NBH are normally rotating slowly (~ 0.6 - 0.8 10^4 rads sec^{-1}) in the direction counter to the plasma current. ICRF can be seen to increase the counter rotation. This is consistent with previous observations [1] that ICRF slows down the NBH-induced plasma rotation during combined heating discharges.

Figure 4(a) shows an example from a shot similar to that of figure 2, of a rotation profile time history obtained from the CXRS diagnostic. The central measurement of rotation from the NiXXVII line agrees within errors with that of the CXRS for the near-axis rotation. The data in figure 4(b) show how the rotational profile develops through the period of the 'monster sawtooth' (figure 4(c)) developed in a JET H-mode discharge. A sawtoothing action of the central rotational velocity is evident which is similar to previous observations on the NiXXVII line [1] in L-mode discharges. The rotational profile appears to broaden during the JET H-mode. If a parabolic function is fitted through these rotational profiles a γ_2 value from 1 to 2 is normally obtained although the function is not a particularly good fit. At present the position of peak rotation appears to be shifted by ~ 10-15 cm with respect to the electron temperature maximum determined by the JET LIDAR Thompson scattering diagnostic [5]. The origin of the shift is under investigation but does not affect relative profile shapes.

VISCOSITY

A calculation has been made of the viscosity profile using the CXRS data and assuming that the momentum loss is governed by a diffusion type equation

$$\frac{\delta p}{\delta t} = - \text{div } \Gamma_p + S(r) = 0 \text{ (steady state)} \qquad (1)$$

$$\text{with} \qquad \Gamma_p = - \chi \text{ grad } p \qquad (2)$$

where $p(r)$ = $mv(r)$ is the plasma momentum
χ = diffusivity of momentum (viscosity)
$S(r)$ = field line averaged momentum source rate from the beams

For simplicity linear momentum in the outer semi-minor radius (not affected by the sawtooth) is considered and the rotational velocity of all ion species is assumed equal. This is valid to within a few per cent at the electron temperatures under consideration. $S(r)$ is available for JET from a neutral particle deposition code PENCIL [6], which also calculated the number of fast ions in trapped orbits and hence not contributing to the force balance. In solving (1) and (2) the momentum and source profiles have been approximated by low order polynomials. The calculated viscosity profile ($\chi(r)$) is shown in figure 5. Also shown as a sensitivity analysis is the difference which a shift of ~ 10-15 cm in the velocity profile would bring to the $\chi(r)$ calculation. $\chi(r)$ decreases monotonically with radius due to the momentum deposition profile being peaked near the axis and a near linear fall of momentum with minor radius. The viscosity derived is comparable to the diffusion coefficient of 1 m^{-2} s^{-1} assumed for impurities on JET. A global momentum time of ~ 0.66 secs is derived from integration of the stored momentum. This compares with an energy confinement time in this H-mode ~ 0.9 secs.

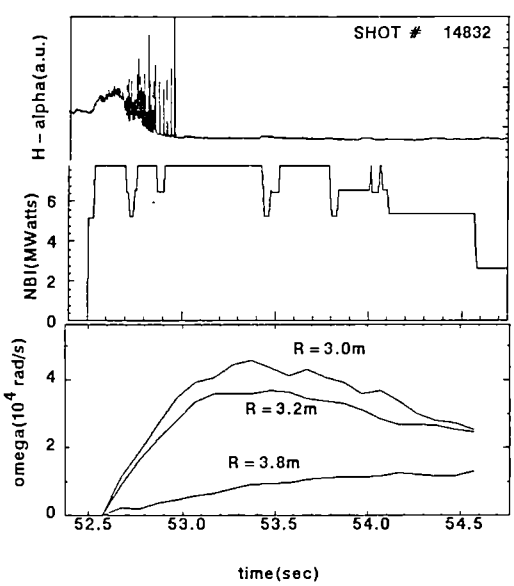

Fig.2: Time histories of the rotational velocities at 3 different radii in response to NB heating at the start of an H-mode discharge.

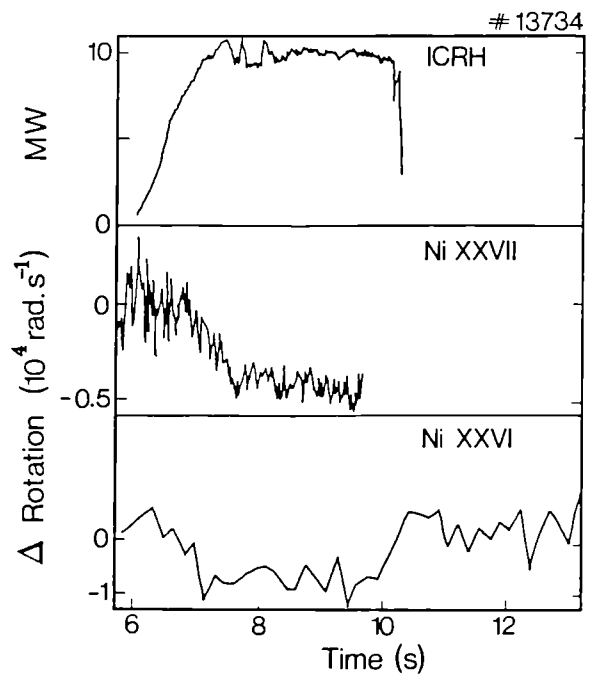

Fig.3: Rotation seen with the X-ray (NiXXVII) and XUV (NiXXVI) instruments during RF heating.

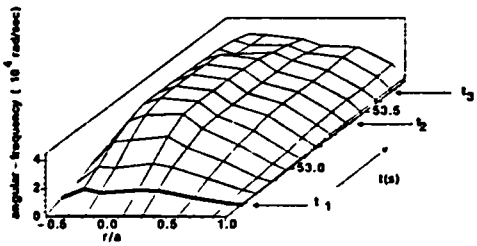

(a)

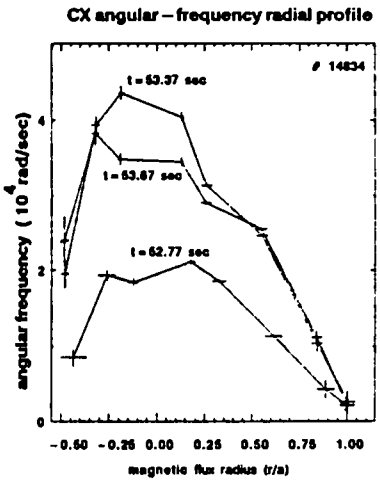

(b)

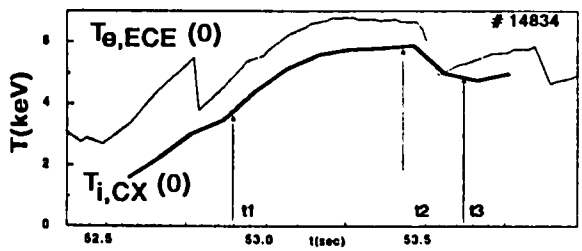

Fig.4: Rotational profile time development (a),(b) during an H-mode discharge showing the effect of the monster sawtooth as seen by the electron temperature diagnostic (c).

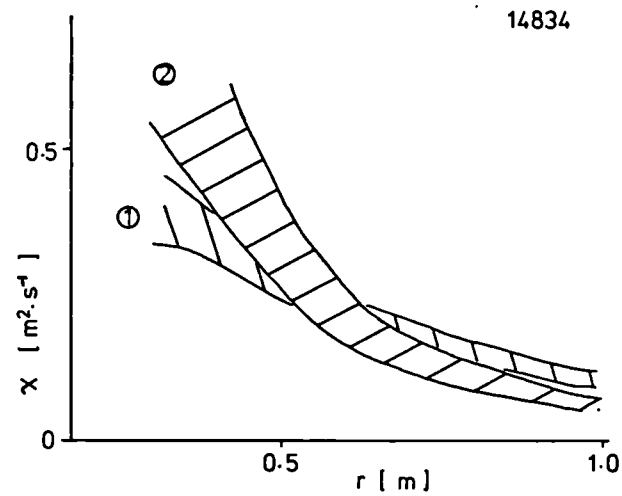

Fig.5: Derived viscosity profile at 2 times within an H-mode period (1) at the sawtooth peak (2) at the sawtooth crash. Hatched areas indicate the effect of the ± 8 cm error in radial measurement from the CXRS diagnostic.

CONCLUSIONS

Rotation profiles of light elements from the CXRS diagnostic can now be produced during NBH. Agreement exists between the central values and those obtained from the X-ray lines of nickel. The X-ray and XUV diagnostics are capable of detecting differences in toroidal rotation between ohmic and ICRF heating phases.

Using data from the CXRS diagnostic a viscosity profile has been derived.

References

[1] Stork D. et al, 14th Euro. Conf. on Cont. Fus. and Plasma Phys., Madrid (1987). Europhys. Conf. Abstracts 11D,I,306.

[2] Bartiromo R. et al, submitted to Rev Sci Instrum.

[3] Boileau A. et al, JET report JET-P(87)44.

[4] Schwob J.L., Wouters A.W. and Suckewer S., Rev Sci Instrum 59 (1987) 1601.

[5] Gowers C. et al, 14th Euro. Conf. on Cont. Fus. and Plasma Phys., Madrid (1987), ref [1], 1236.

[6] Stubberfield P.M. and Watkins M.L., JET Internal Report DPA(06)/87.

DIAGNOSING RF DRIVEN HIGH ENERGY MINORITY TAILS WITH γ-RAY AND NEUTRON SPECTROSCOPY

G Sadler, O N Jarvis, P van Belle
and J M Adams*

JET Joint Undertaking, Abingdon, Oxfordshire, OX14 3EA, England
* AERE Harwell, Didcot, Oxfordshire, OX11 ORA, England

INTRODUCTION

The emission of γ-rays from excited reaction products in JET plasmas has been monitored systematically since the first successful observations in 1987 [1]. Fusion γ-rays, ie. γ-rays emitted by fusion products from fuel ions, are routinely recorded for monitoring the fusion yield from D-^{3}He plasmas, as reported in a separate contribution to this conference [2]. Here we concentrate on γ-rays emitted by reaction products from interactions of RF driven minority ions with plasma impurities (mainly carbon and oxygen).

The experimental set-up is essentially the same as the one used in 1987 [1]. Two detectors, a 125 mm diameter by 125 mm long NaI (Tl) and a 75 mm by 75 mm BGO scintillator, are located in well shielded positions in the roof laboratory and view the plasma vertically along similar lines of sight. The results from both detectors are in reasonable agreement.

H MINORITY HEATING

A typical spectrum obtained during H minority heating is shown in figure 1. The most readily understood lines are those generated by RF accelerated H ions inelastically scattered from carbon and oxygen impurities in the plasma. For the excitation process to be energetically possible these ions have to exceed threshold energies of 4.8 MeV and 7.5 MeV for carbon and oxygen, respectively.

The most prominent lines, however, are caused by second harmonic driven deuterons reacting with ^{12}C to yield ^{13}C in an excited state. The intensity of the 3 MeV line as monitored with a single channel analyzer follows closely the sawtooth behaviour of the neutron yield (figure 2) and only emerges from the background when RF heating is applied, thus proving the correlation between RF heating and γ emission. The observation of the 3.8 MeV γ-line requires a certain fraction of the deuterons to exceed a threshold energy of 1.3 MeV; further analysis is hampered by the apparently erratic behaviour of the underlying cross section as well as the relative uncertainty in the density of the carbon ions. However, a simple model based on the ratio of the intensities of the 3.6, 3.8 MeV doublet to the 3 MeV line and the knowledge that the cross section leading to the doublet is approximately equal to the cross section leading to the 3 MeV state, yields deuteron tail temperatures between 300 and 500 keV for RF power levels between 9 and 15 MW. The tail temperature has been defined here as the e-folding energy of an assumed exponentially decaying energy distribution function.

The fact that the magnitude of the $^{12}C(d,n)^{13}N$ cross section for deuteron energies in the range of interest is comparable to the $^{11}C(d,p)^{13}C+\gamma$ cross section, coupled with the observation of 3 MeV γ yields in excess of 10^{13} γ's/sec, leads to the conclusion that, at present power levels (9-15 MW) and impurity concentrations ($\lesssim$ 10% C), about 10% of the observed neutrons originate from interactions with carbon. Moreover (d,d) neutrons created by the interaction of the deuteron tail with thermal deuterons from the bulk of the plasma contribute significantly to the total neutron yield. Unfortunately the energy spectrum of these neutrons is very broad, extending from $\sim$ 1.5 MeV to 3.5 MeV, which makes observations with our high resolution neutron spectrometers difficult. Nevertheless, comparing the intensity of the 2.5 MeV neutron peak to the total intensity of fast neutrons shows that up to 50% of the observed neutrons are of non-thermal origin under conditions of intensive H minority heating.

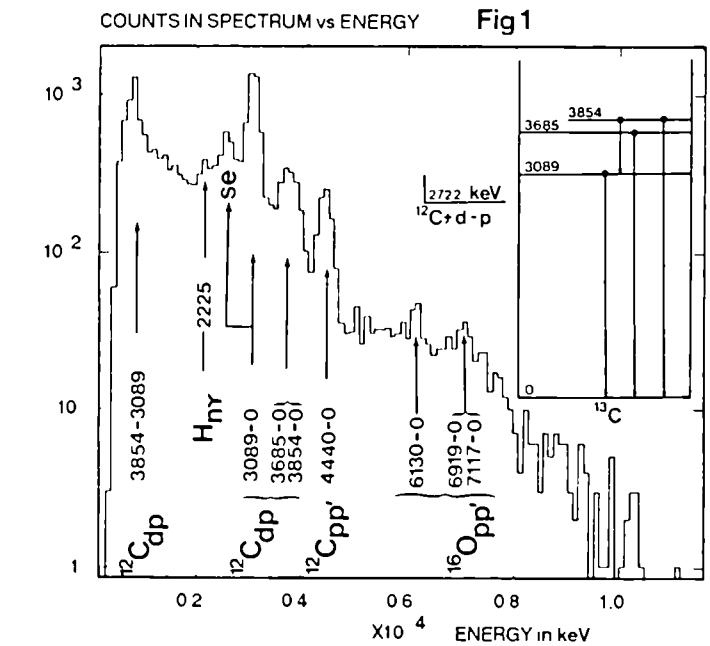

Fig. 1: Gamma spectrum recorded during H minority ICRF heating (I_p = 3 MA, B_T= 2.8 T and P_{rf} = 15 MW). The energy level scheme for ^{13}C has been taken from reference 4.

Fig. 2: The 3 MeV gamma radiation exhibits sawtooth oscillations and appears only when ICRF heating is applied (at 9 sec into the discharge).

Fig. 3: Vertical neutron and γ profiles obtained during NB heating (4 MW) (figs. a and b) and later in the same discharge during NB plus ICRH (H minority) heating (4 MW and 13 MW) (figs. a´ and b´).

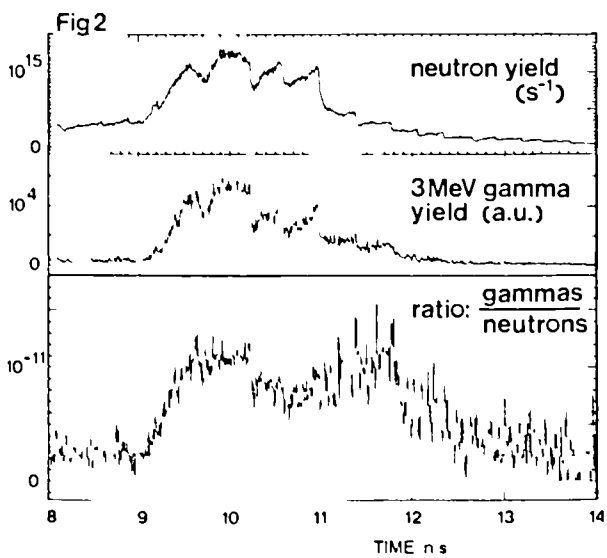

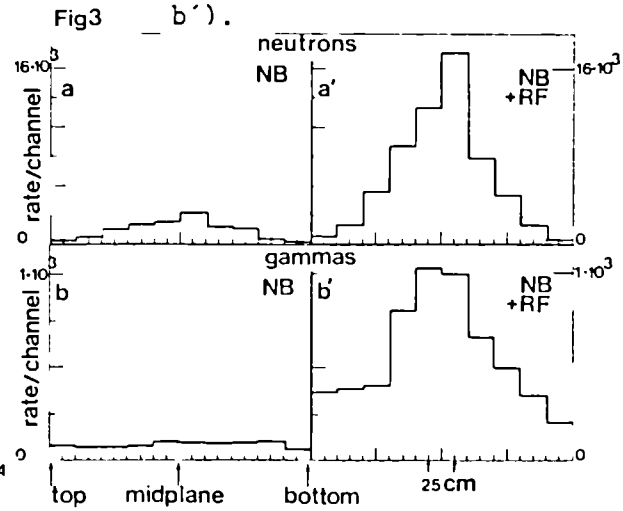

Finally, on one occasion the JET neutron profile monitor [3], which also monitors γ-rays on a regular basis, had been tuned to the 3 MeV γ-line and the resulting profile (figure 3b) demonstrates the central power deposition of RF energy. Assuming that the carbon impurity profile is flat then a power deposition volume of 8 m^3 can be deduced in reasonable agreement with other observations and calculations [5].

^{3}He MINORITY HEATING

Spectra obtained during ^{3}He minority heating are much richer in lines as can be seen from figure 4. All prominent γ-lines can be identified as emanating from the $^{12}C(^3He,p)^{14}N+\gamma$ reaction and transitions from 8 of the 9 first excited states in ^{14}N were observed. The highest γ energy observed so far is 7,028 keV; in order to populate the corresponding level the energy of the ^{3}He ions has to exceed a threshold of 2.81 MeV. This is the first direct evidence for ^{3}He ions reaching such high energies during RF heating. For this line to be seen, the RF power has to exceed 8 MW.

From the relative intensities of the various lines and knowledge of the cross-sections, the full distribution function of the fast ^{3}He ions could be reconstructed. This however, is a major task which has only been started recently. In the mean-while, a crude model based upon the comparison of the 6.4 MeV and 5.1 MeV line intensities and energy averaged cross sections has been applied to a 2 MA discharge with 10 MW RF power (# 14618). For this particular discharge we deduce a tail temperature of around 1.5 MeV.

The quite common observation of inverted sawteeth on the outer γ channels of the neutron profile monitor (figure 5) yields a further proof that these γ-rays are emitted by the plasma. It also shows that energetic ^{3}He ions are expelled from the middle of the plasma at the sawtooth crash. This effect is particularly prominent with monster sawteeth.

CONCLUSION

The reactions of energetic, RF-heated, H, D and ^{3}H minority ions with carbon and oxygen impurity ions have been monitored by observing γ-radiation from their excited reaction products. The importance of carbon as the major impurity in JET plasmas is amply confirmed. An indication of the energy of the minority ions is obtained from a study of reaction thresholds; for ICRF powers in excess of 8 MW, minority ions are accelerated beyond 7.5 MeV for protons (H minority, fundamental), 1.3 MeV for deuterons (H-minority, 2nd harmonic) and 2.8 MeV for ^{3}He (^{3}He-minority, fundamental). Equivalent tail temperatures in the MeV range have been observed for the minority ions.

Sawtoothing of individual gamma-ray lines shows the expulsion of fast ions from the middle of the plasma. Inverted sawteeth in the gamma-emission from the outer regions of the plasma provide conclusive evidence that these γ-rays were emitted from the plasma.

Finally, comparison of the 2.5 MeV neutron peak recorded with a neutron spectrometer with the total neutron yield shows that, under conditions of intense RF heating, a significant fraction of the emitted neutrons (50% or more) are of non-thermal origin.

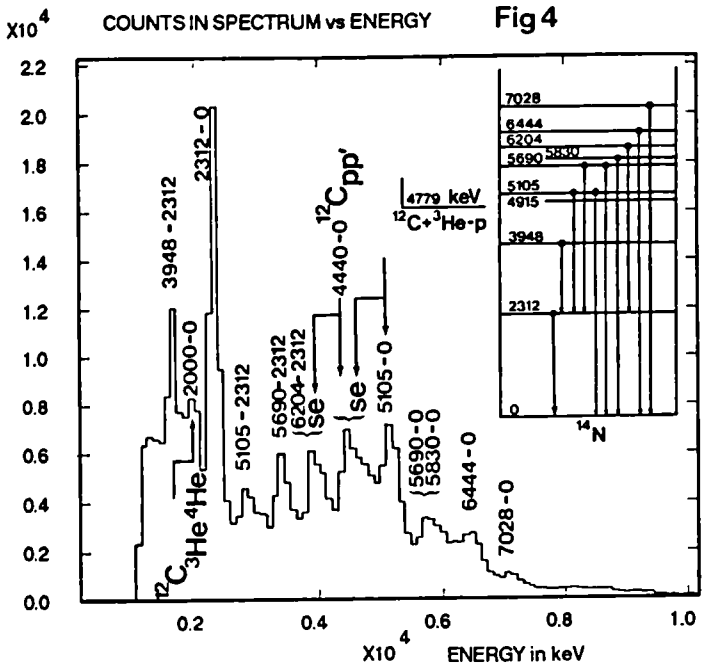

Fig. 4: Gamma spectrum recorded during ^{3}H minority ICRF heating (I_p= 2 MA, B_T= 3.4 T and P_{rf} = 10 MW). The energy level scheme for ^{14}N has been taken from reference 4.

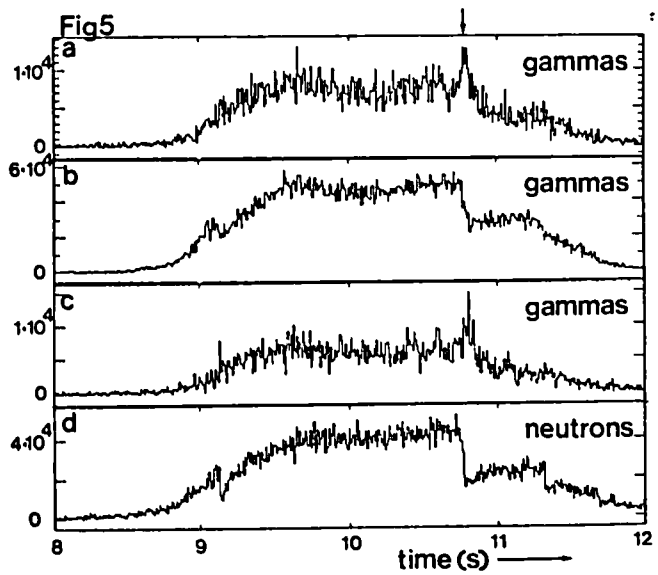

Fig. 5: Gamma-rays recorded with the neutron profile monitor. The inner channels eg. b and d, show normal sawtooth behaviour whereas the outer channels, eg. a and c, display inverted sawteeth.

REFERENCES

[1] Sadler G., Jarvis O.N., van Belle P., Hawkes N., and Syme B., Europhysics Conference Abstracts. 14th European Conference on Controlled Fusion and Plasma Physics, Madrid 22-26 June 1987, p1232.

[2] Cottrell G.A., Sadler G., van Belle P., Cordey J.G., Core W., Hellsten T., Jacquinot J., Start D.T.H., Thomas P.R. and Wesson J. (this conference).

[3] Adams J.M. et al, 14th European Conference on Controlled Fusion and Plasma Physics, Madrid 22-26 June 1987, p1224.

[4] Ajzenberg-Selove F., Nucl. Phys. A360 (1981) No 1.

[5] Evrard M. et al (this conference).

EDGE FLUCTUATION MEASUREMENTS DURING X-POINT PLASMAS IN JET

A Hubbard, D Bartlett, P Cripwell*, R Gill, P J Harbour, M Malacarne, P D Morgan, N Salmon and J Snipes

JET Joint Undertaking, Abingdon, Oxfordshire, OX14 3EA, UK
* Imperial College of Science and Technology, London SW7, UK

1. INTRODUCTION

Strong edge fluctuations are a characteristic feature which distinguish the L-mode phase of JET X-point plasmas from the relatively quiescent, high confinement (H) phase. Periodic spikes, seen by several diagnostics viewing the outer region of the plasma, usually appear with the application of ICRH or NBI, initially at a repetition frequency of $\sim$ 1-2 kHz. If sufficient power is applied, the spikes slow to a frequency of $\sim$ 100 Hz before disappearing at the L-H transition. Under some conditions, the H-phase is followed by a further period of similar spikes, during which a reduction in the global particle and energy content occurs. This sequence of L and H phases can be repeated several times during a discharge (see Figure 1).

Previous studies of the coherent edge spikes have relied mainly on data from magnetic pick-up coils and soft X-ray diodes /1,2/. Detailed measurements, described below, have recently been made with a number of new diagnostics. These include Langmuir probes and pick-up coils near the X-point position, a poloidal D_α array and a multichannel reflectometer and an ECE heterodyne radiometer viewing near the midplane. Comparison of the observed local perturbations with global changes, presented in Section 3, leads us to conclude that convection of particles from the outer region of the plasma during the spikes could be responsible for much of the observed reduction in plasma energy.

2. LOCAL MEASUREMENTS OF EDGE FLUCTUATIONS

A typical series of spikes leading up to an L $\rightarrow$ H transition is shown in Figure 2. The magnetic coil nearest to the X-point shows a field change of up to 9 T/S. The rise time of the initial spike is 50 μs, while the burst of activity lasts for $\sim$ 300 μs. A simultaneous spike of similar shape occurs on the current of all of the Langmuir probes in the X-point tiles. Previous analysis using a poloidal array of coils has shown simultaneous changes in $\dot{B}$ at all locations, with a magnitude largest at the top and bottom of the plasma and weakest at the outer midplane. The field perturbation which would be produced by a current flowing in the scrape-off layer has been calculated using Langmuir probe data for a similar discharge (Figure 3), and is consistent with these measurements.

Reflectometry and D_α measurements show well correlated but slightly slower changes. The coherent detector signal of the 18.6 GHz channel of the reflectometer, which corresponds to a critical density of 4.3 x 10^{18} m^{-3} (r_c/a = 0.92), shows a phase change of $\sim \pi$. Taking the density gradient from FIR interferometer measurements, a local density change of $\sim$ 1.1 x 10^{18} m^{-3} (25%) is calculated. The effect on a second channel with n_c= 1.9 x 10^{19} m^{-3} (r_c/a = 0.83) is much smaller, indicating a perturbation localized outside this radius. More complete analysis of $\delta n_e(r)$ should be possible when the full 12 channel system is operational /3/. During the same period, a 75% increase in D_α emission is seen along the chord viewing the X-point, indicating substantial recycling of particles at the divertor.

On a discharge with a lower field of 1.7 T, the electron temperature at r_c/a = 0.93 was measured using a heterodyne radiometer. Sharp dips of 20-30 eV are seen, correlated with the fluctuations on other diagnostics. At the end of the L-phase the edge T_e is 450 eV, 200 eV above the ohmic level. During the L → H transition it increases by 100 eV in $\sim$ 10 ms, apparently due to a sawtooth heat pulse. This jump does not occur on all discharges.

Soft X-ray measurements made on 2 MA X-point discharges in 1986 give further information on the topology of the perturbations. The outermost channels of the vertical poloidal array show an increase in $\sim$ 80 μs, while the effect on inner channels is reversed and on a slower time scale of $\sim$ 800 μs. This indicates a disruptive-like instability originating near the edge, with an inversion radius of $r/a \geq 0.9$. The relative amplitude of the perturbation on different chords shows a strong localization to $r/a \geq 0.7$ (Figure 4). The inversion radius is no longer visible with this diagnostic due to the loss of its outer channels.

3. EFFECT ON GLOBAL PARTICLE AND ENERGY CONTENT

Near the start of NBI, the plasma density and energy are rapidly increasing and there is often no abrupt change in $\dot{N}$ or $\dot{W}$ at the initial L → H transition. The global effect of the edge spikes is more clearly seen during the short L-phases later in the discharge. For example, during the first such phase of Pulse 13806 (Figure 1), the volume integrated particle content N_{tot}, obtained from the FIR interferometer, shows a mean net loss of 1.5 x 10^{19} particles (0.4%) for each of 17 spikes. For comparison, this would correspond to a local decrease of 10^{18} m^{-3} extending over $\sim$ 8 cm and is consistent with reflectometer and soft X-ray measurements. Calculations based on the typical enhancement of I_{sat} ($\sim$ 85%) give 4 x 10^{19} additional particles reaching the X-point tiles during a spike /4/. D_α measurements show that in this L-phase an average of $\geq$ 5 x 10^{18} particles/spike are recycled from the divertor region. While these values have absolute uncertainties of $\sim$ 50%, they indicate that a rapid outward convection of particles associated with edge spikes could cause the observed global loss.

The plasma energy W, as measured by the diamagnetic loop, shows similar time behaviour to N_{tot} but has a smaller relative change during the L-phase. In the above case, there is a mean decrease of 7.6 kJ (0.2%) per D_α spike, which could be accounted for by convective losses if the

particles ejected have a mean energy of ≤ 1.56 keV. This is only half the average plasma energy and is equal to the electron temperature at r/a = 0.8, inside the inversion radius for the edge instability inferred from soft X-ray data. The conclusion that increased losses during the L-phase are associated mainly with convection from the outer region is supported by specroscopic observations of Ni radiation, which continues to increase steadily in the centre while decreasing near the edge /5/.

While the initial transition from L to H-mode is necessary to attain improved confinement, the subsequent appearance of short L-phases may have operational advantages. Since the fluctuations appear to eject relatively cool particles, high plasma energies are achievable at lower densities than would be present in a continuous H-mode. This may be a useful means of controlling plasma density and avoiding disruptions, which will be increasingly important at higher currents and heating powers. The regime at which L-phases reappear has not yet been fully explored. They tend to occur earlier, and be of shorter duration, in discharges with a small separation from the outer limiter.

4. DISCUSSION AND CONCLUSIONS

Experimental data on JET indicate that fluctuations localized in the outer region of the plasma (r/a ∿ 0.9) are important to the physics of the L → H transition and to corresponding changes in N_{tot} and W. The gradual decrease in their frequency and the fact that parameters between spikes (eg. D_α, I_{sat}) are very close to those in the H-mode suggest that the plasma passes through a region of marginal stability before reaching a quiescent H-mode. Understanding the nature of the instability should help to assess the conditions necessary for the improved confinement.

Recent measurements and analysis of pressure and shear profiles in the outer region of the JET plasma /6,7/, show that conditions are stable to ballooning modes during the L-phase. They only marginally approach the second stability region at the L-H transition, although the measured T_e of 450 eV should be sufficiently high to attain this /8/. There is also evidence of currents flowing in the scrape off layer during the disruptive spikes /9/, though it is not clear whether they are a cause or effect of magnetic perturbations. Parameters in the divertor region are being assessed to see whether they support the presence of a thermal barrier.

REFERENCES

[1] M. Malacarne et al, Plasma Physics and Controlled Fusion 29 (12) (1987) 1675-1686.
[2] A. Tanga et al, Nuclear Fusion 27 (1987) 1877.
[3] R. Prentice et al, this conference.
[4] L de Kock et al, this conference.
[5] K. Behringer, B. Denne et al, this conference.
[6] E. Lazzaro et al, this conference.
[7] C. Gowers et al, this conference.
[8] C. Bishop, Nuclear Fusion 27 (1987) 1765.
[9] P.J. Harbour, Int. Workshop on Plasma Edge Theory in Fusion Devices, Augustusburg, DDR (April 1988).

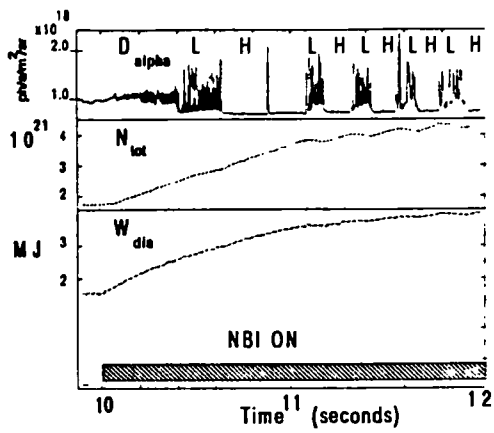

Fig. 1 Series of 5 L and H phases, showing effect on particle and energy content, (Pulse 13806, I_p = 3 MA, B_T = 2.1 T, P_{NBI} = 5.5 MW).

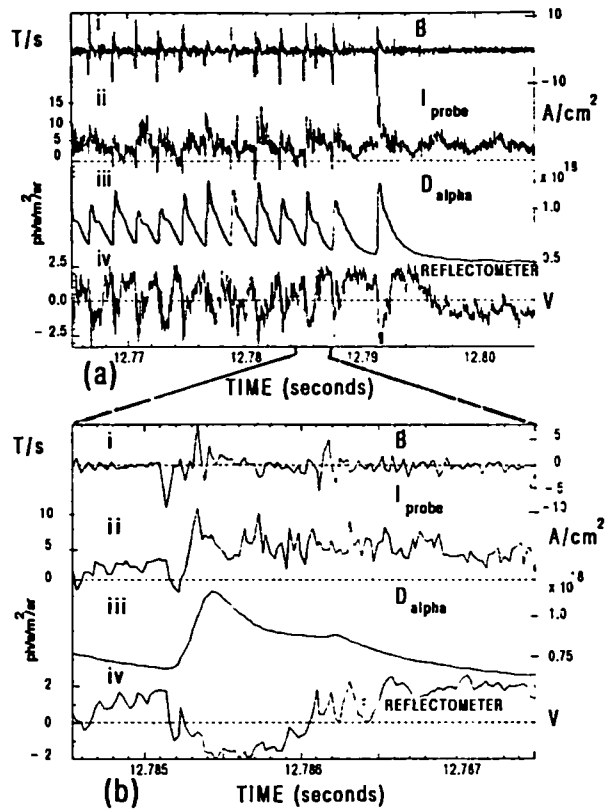

Fig. 2a) Edge fluctuations prior to an L → H transition, Pulse 14384 (I_p = 3.0 MA, B_T = 2.1 T, P_{NBI} = 7.5 MW), on
i) magnetic coil XP04,
ii) Langmuir probe (200 Hz oscillation is due to changing voltage),
iii) D_α channel viewing X-point
iv) Reflectometer channel with $n_c = 4.3 \times 10^{18}$ m^{-3}.

b) Expansion of a single spike.

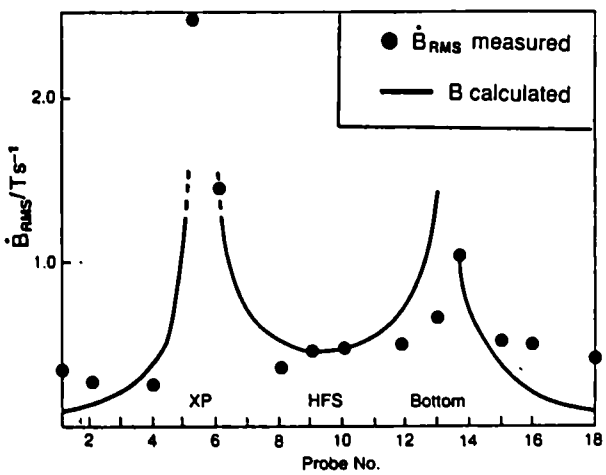

Fig. 3 Comparison of measured poloidal variation of $\dot{B}$ (Pulse with the field calculated from current typically measured in s.o.l. (normalized units). Absolute levels of B agree to within the scatter of present

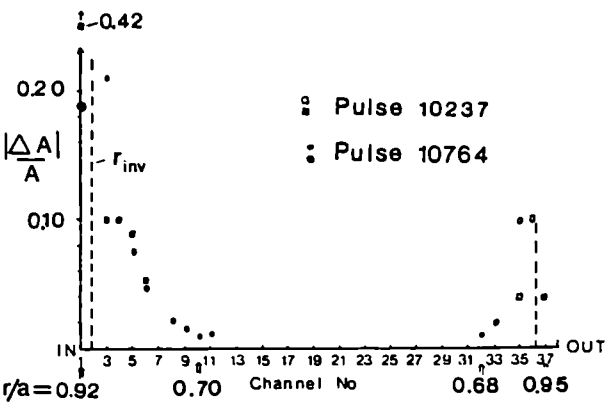

Fig. 4 Relative change in the soft X-ray emission during edge fluctuations (I_p = 2 MA, B_T = 2.2 T). Open and closed symbols indicate negative and positive changes. Minor radii of the outer flux surfaces crossed by the chords are shown.

THE ROLE OF THE SCRAPE-OFF LAYER IN X-POINT DISCHARGES IN JET

P J Harbour, L de Kock, S Clement, S K Erents, N Gottardi,
A E Hubbard, M Keilhacker, E Lazzaro, P D Morgan, D Stork,
D D R Summers, J A Tagle and A Tanga

JET Joint Undertaking, Abingdon, Oxfordshire, OX14 3EA, UK

INTRODUCTION

The plasma parameters in the X-point divertor in JET have been measured using an array of Langmuir probes in the divertor target tiles and supported by measurements of D_α radiation (2D with CCD camera viewing the target tiles; 1D using a poloidal array of telescopes) and bolometry. The Langmuir probe measurements show that the saturated flux of ions, I_{SAT}, parallel to the magnetic field is about 10 A cm^{-2} at the divertor separatrix in ohmic discharges. In L-mode with NBI it increases by a factor < 2, depending on power level (P_{NBI} < 7.5 MW) and then decreases when H-mode is established. The scrape-off thickness, λ_{ISAT}, is the same in ohmic and L-mode but decreases when H-mode is established. The corresponding values of electron temperature at the divertor target are $T_{e,t}$ ∿ 30 eV (OH) and ∿ 50-60 eV (H-mode). L-mode temperatures are not reported here because of rapid fluctuations in parameters. During ICRH the values of I_{SAT} increase by a factor ≤ 5 and T_e also appears to increase.

There are 40 poloidal bands of graphite tiles in JET (1987/8), shaped to collect the diverted plasma. The plasma impinges on two separate patches on each poloidal band (figure 1a). Eight Langmuir probes are flush-mounted in the target tiles, being designed to receive the inner

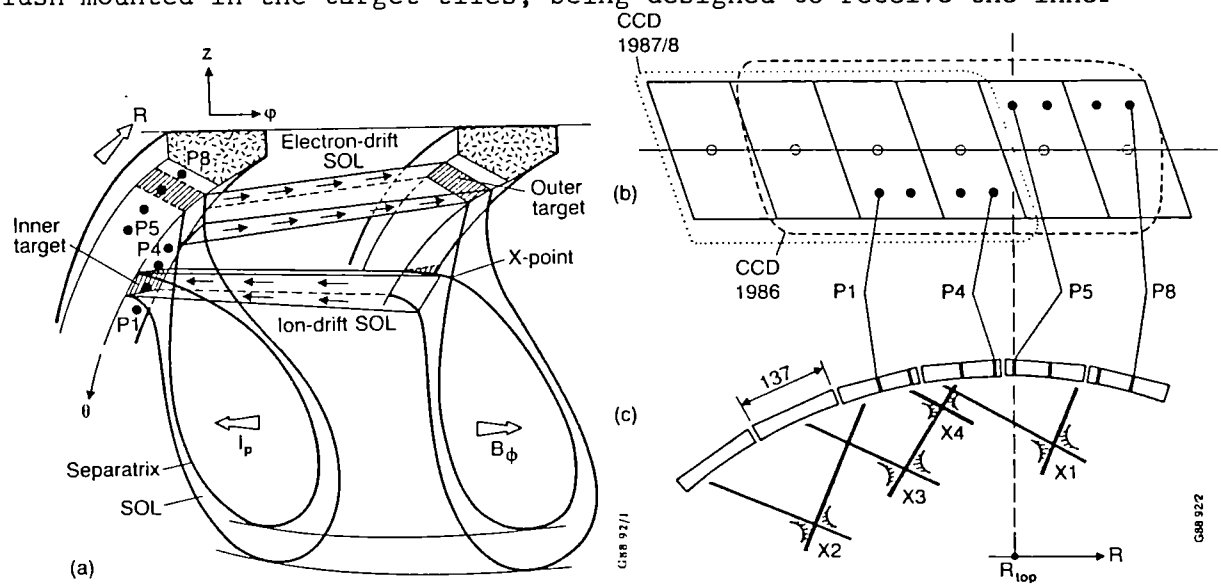

Fig. 1 Geometry of the X-point divertor in JET. (a) Shows two bands of graphite target tiles with scrape-off layer impinging on Langmuir probes P1-4 and P5-8. (b) Shows the tiles and probes and the view of the CCD camera. (c) Is a poloidal section through the tiles with X-point positions, estimated from our data, X1 (# 10722), X2 (# 14083), X3 (# 14820-34) and X4 (# 14883). (R_{top} = 2.630 m).

(high field side) and outer (low field side) diverted scrape-off layers. Fig. 1(b), (c) shows more detail of the experimental arrangement, including the view of the CCD camera, which actually covers 3 bands of tiles, whereas the D_α telescope array views a sector midway between two bands of tiles. The position of the X-point and hence of the inner and outer separatrices in the divertor may be varied: examples for several discharges are shown in Fig. 1(c). The Langmuir probes and D_α telescope are in Octant 8 and the CCD camera is in Octant 6, viewing tiles in Octant 5 and Octant joint 5/6.

EXPERIMENTAL RESULTS

Figure 2 shows the variation of parameters in a typical beam-heated discharge. The flux of ions towards the target measured by one of the probes, I_{SAT}, varies in a very similar way to the D_α (CCD) intensity at the same location on the tiles, but there are some differences between these signals and the intensity of D_α measured between the tiles, D_α (POL). During the ohmic phase of the discharge ($t \leq 12$ s), D_α and I_{SAT} are fairly constant but with small inverse sawteeth. With NBI they increase and fluctuate rapidly. The fluctuations (ELMs) [1] are best shown by the I_{SAT} trace because its sampling rate was faster for 12.1 s < t < 13.1 s. The fluctuation rate decreases in the late L mode and at 12.5 s the H mode is established with much more quiescent signals, again with inverse sawteeth, more prominent than before. There is an H → L transition at 14 s and a series of L-H-L transitions thereafter. Each group of ELMs, especially the first group, shows maximum and minimum values of I_{SAT} which are typical of L and H modes respectively. The power radiated from the X-point region (not shown) varies in a similar way to I_{SAT} and D_α, increasing from ∿ 0.9 MW (OH) to ∿ 1.2 MW (L), then decreasing to 0.8 MW (H1) and rising slowly during the H-phase to ∿ 1.2 MW (H2) with bursts of up to 1.8 MW in later L phases. The total electron content, N, is also shown in figure 2 and increases rapidly during L and H mode, decreasing at each subsequent L phase.

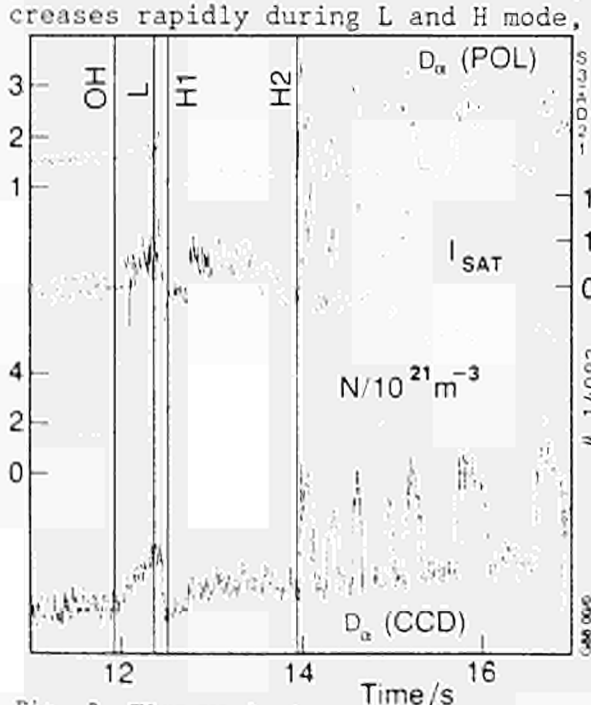

Fig. 2 Time variation of scrape-off parameters in a 2.0 MA, 2.1 T pulse.

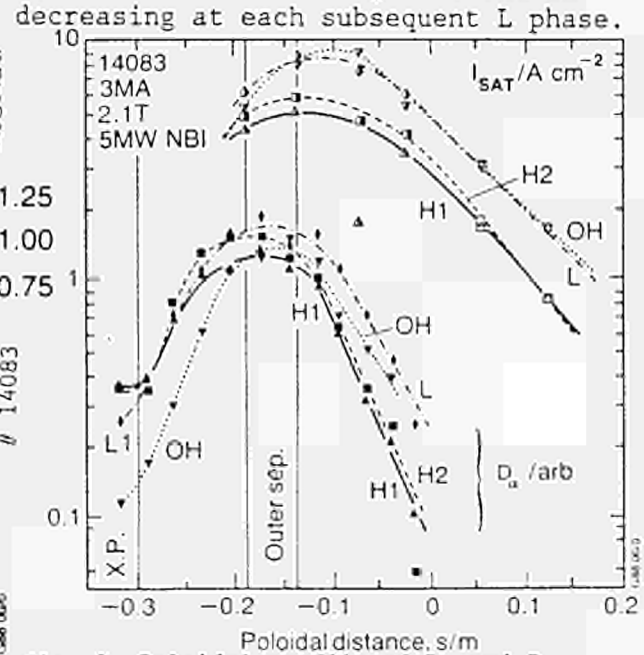

Fig. 3 Poloidal profile of D_α and I_{SAT} on the divertor tiles for the pulse shown in Fig. 2. Distance s is measured along the tiles from R_{top} (Fig. 1c).

Poloidal profiles of D_α and I_{SAT}, taken at the times indicated in figure 2, are shown in figure 3. The profiles are measured in terms of the poloidal distance, s, from the target tiles at the top of the torus, R_{top} = 2.630 m (figure 1 b,c). As is evident from figure 1 (c), only the X-point (X2) and outer scrape-off layer are visible for this discharge (# 14083). Probes 1-4 are not facing the plasma directly but are shadowed by the apex of the tile and corrected as described elsewhere [2]. The profiles of both D_α and I_{SAT} agree in showing a well defined maximum at the outer separatrix which appears to move to smaller radius during the H-phase. The profiles of I_{SAT} are flatter than for D_α, but both show no change between ohmic and L mode. Outside the separatrix the profiles are exponential with λ_{ISAT} = 133 mm (OH), 122 mm (L). Profiles in H-mode are steeper with λ_{ISAT} = 102 mm (H1), 92 mm (H2). The values of λ_{ISAT} quoted here are measured in the s-direction and will be modified later to equivalent midplane values. The similarity between scrape-off thickness in OH and L phases suggests, that, as with limiter discharges, there is no change in $D_\perp$ with NBI. The decrease in λ_{ISAT} by $\sim$ 25% in H mode suggests a strong decrease in $D_\perp$ to $D_\perp(H) \sim 60\% D_\perp(L)$ and even larger decreases have been observed.

The H-mode was studied in detail in a series of 3 MA, 2.1 T discharges with 7.5 MW NBI (# 14820-34). Figure 4 shows the average values during the H-phase of T_e, I_{SAT} and D_α. The profile of D_α on the electron drift side shows a maximum at s = -8 cm and that for I_{SAT} shows a maximum at s = -6 cm. Taking the outer separatrix at s = -7 ± 1 cm the data suggest that the maximum in T_e is not on the separatrix but further out into the scrape-off layer. The reduction in T_e at the separatrix is believed to be related to local recycling and finite thermal conductivity. The D_α profile on the ion drift side of the target tile shows the location of the inner separatrix. Extrapolating the I_{SAT} and T_e profiles to the inner separatrix suggests that I_{SAT} is larger and T_e smaller than at the outer separatrix and this is supported by other data (eg. # 14338 ohmic phase). The different T_e values at opposite ends of the same flux tube in the scrape-off layer lead to differing sheath potentials, causing electric current to flow around the scrape-off layer [3]. Currents of up to 10 A cm^{-2} have been measured, especially during the ELM phase [1].

The measured parameters from figure 4 have been used to calculate the density in the divertor ($n_d = 2\ I_{SAT}\ c_s/e$) and the heat flux parallel to the field at the target ($P_{\parallel,t} = 8\ I_{SAT}\ T_e$) and these are shown in figure 5(a) which also shows values of parameters at the midplane (n_m, $T_{e,m}$) derived using Spitzer conductivity and the sheath convection as described in [4]. The power flux to the target in these 7.5 MW discharges can be compared to that in a 9 MW discharge, # 10755 in 1986 [5] in which P_t^{outer} was determined by infrared thermography to be 10 MW m^{-2} onto the target tiles . The maximum H-mode value of $P_{\parallel,t}$ for this discharge was 60 MW m^{-2}, agreeing well with the 57 MW m^{-2} deduced here with Langmuir probes, even allowing for the difference in power. The profile of $T_{e,m}$ is monotonic despite the dip in the separatrix values of T_e in the divertor. Both $T_{e,m}$ and n_m are consistent with LIDAR and ECE profiles [1].

Figure 5(b) shows profiles of mean free paths in the outer divertor. The Coulomb mean free path (1 m $< \lambda_{ee,d} <$ 8 m) is always smaller than the connection-length, hence allowing a temperature difference to develop between midplane and divertor as is shown in figure 4 and 5a. The mean free path for deuterium atoms, $\lambda_D^{(0)}$ is also shown. This has been

evaluated using $\lambda_D^{(0)} = v^{(0)}/[n_d\langle\sigma v\rangle]$ with $\langle\sigma v\rangle = \langle\sigma v\rangle(T_e)$ and with $v^{(0)}$ taken at 1 eV or at T_e. The mean free path for D atoms with energy ≤ 1 eV is always smaller than λ_n in the divertor (= 110 mm, see figure 5a) and so slow D atoms (and D_2 molecules) are almost always ionised in the divertor in their first transit of the scrape-off layer. Faster charge exchange atoms have $\lambda^{(0)} > \lambda_n$ except at the outer separatrix. This may be critical and will be studied in more detail.

CONCLUSIONS

The plasma parameters measured in the divertor suggest that $D_\perp(H) \leq 0.6\ D_\perp(L)$. The power flow deduced agrees with that from 1986 discharges. The power and particle flow will be discussed in [2]. All atoms and molecules recycling from the divertor near the separatrix may be ionised locally but further out in the divertor scrape-off layer (larger s) the fast recycling atoms will escape from the divertor.

REFERENCES

[1] A. Hubbard et al, Edge Fluct. Measts. During X-Pt. Plasmas in JET. This Conf.
[2] P.J. Harbour et al, 8th Int PSI Conference, Jülich, May 1988.
[3] P.J. Harbour, paper presented at Int. Workshop on Plasma Edge Theory in Fusion Devices, Augustusburg, DDR, April 1988.
[4] P.J. Harbour, Nuclear Fusion 24 No 9 (1984) 1211.
[5] H.J. Jaeckel, P.J. Harbour, N. Gottardi et al, (EPS, Madrid), 1987.

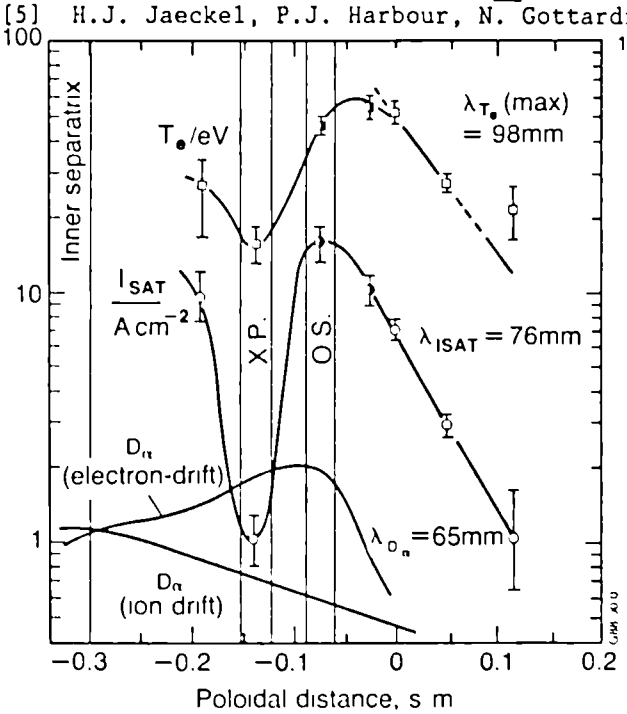

Fig. 4 Poloidal profiles of D_α, I_{SAT} and T_e in the divertor in a 3 MA H mode discharge (# 14820-34) (above).

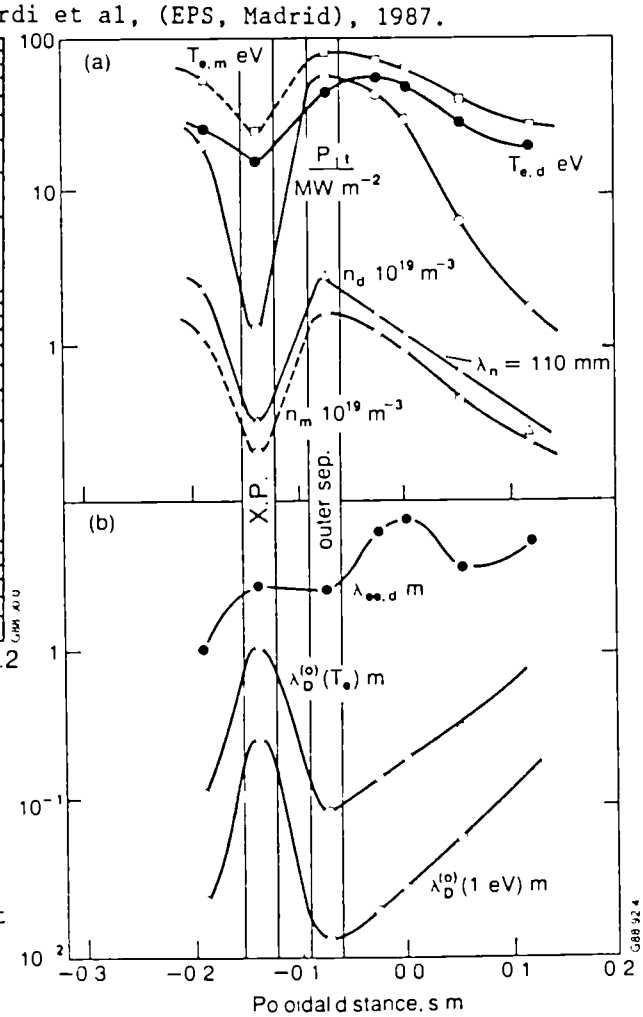

Fig. 5 Poloidal profiles of (a) power flux, $P_{\parallel,t}$, and density and temperature in the divertor, n_d, $T_{e,d}$ with equivalent midplane parameters n_m, $T_{e,m}$, (b) profiles of mean free path in the divertor (right).

STUDY OF PHOTONEUTRON PRODUCTION ACCOMPANYING PLASMA DISRUPTIONS IN JET

O N Jarvis, G Sadler and J L Thompson*

JET Joint Undertaking, Abingdon, Oxfordshire, OX14 3EA, UK
* Huddersfield Polytechnic, Huddersfield, W Yorkshire, HD1 3DH, UK

Abstract

The observed photoneutron yields due to major plasma disruptions in JET fall in the range from 10^{10} to 10^{15} neutrons, with instantaneous intensities reaching 5.10^{17} neutrons/sec. The runaway electron energies can exceed 60 MeV and the currents of high energy electrons can reach 1 MA. On average, the fraction of the available poloidal magnetic field energy that is transferred to high energy runaway electrons is $f \approx 3 \times 10^{-2}\ I_p^{0.6}$, with plasma current I_p in MA.

1. INTRODUCTION

Major plasma disruptions in JET are frequently accompanied by the acceleration of a strong current of high-energy runaway electrons, which produce photoneutrons when they eventually strike the vacuum vessel wall protection tiles or one of the plasma limiters. Measurement of the photoneutron yield constitutes a simple and non-invasive method of estimating the amount of energy carried by the runaway electrons.

The detailed theory of electron runaway in tokamaks has been given by Knoepfel and Spong [1], who concentrate on the birth process under non-disruptive conditions of relatively low loop voltage. Our present interest is with strong disruptions for which the magnitude of the measured loop voltage may exceed 500 V for periods of 5 ms or more. This implies that the maximum energy to which the runaway electrons may be accelerated easily exceeds 60 MeV. As we have no means of measuring the energy distribution of the runaway electrons, we assume an average energy of 60 MeV. Those electrons which produce photoneutrons must have energies well in excess of 7 MeV, the photoneutron reaction threshold for the elements contained in inconel (the material from which the vacuum vessel is constructed). Also, studies of induced activation in the vessel reveals the existence of radionuclides, such as ^{7}Be in the ^{12}C limiters, for which the reaction thresholds were over 26 MeV. As we have seen, energies calculated from the measured loop voltages are very much higher.

2. OBSERVATIONS

The time-resolved neutron emission was measured with three pairs of ^{235}U and ^{238}U fission chambers disposed around the tokamak. The source of

photoneutrons could well be highly localized, eg. a limiter. For such a source, the response from a single fission chamber could vary by a factor of 20, depending on the relative positions of source and chamber. In practice, the chambers usually give similar responses (to within a factor of 2) and only rarely show a factor of 10 variation from chamber to chamber. A single strike is therefore unusual. In any case, averaging the results of all three sets of chambers reduces the positional dependence to a factor of 1.5. The calibration to be associated with the chambers is that measured for a deuterium plasma discharge [2] and is known to ± 10% accuracy. The fission chambers are operated in both pulse-counting and current sampling modes and operate over an intensity range from 10^6 to 10^{22} neutrons/sec.

A typical example of the strong neutron emission which arises when a high plasma current discharge is terminated by a sudden disruption is shown in figure 1. The plot shows how the plasma current falls from - 2.5 MA to - 0.2 MA in a time interval of only 40 ms. There is a distinct hesitation midway down the plasma current collapse. The plot also shows the strength of the neutron production on a logarithmic scale covering six decades. The duration of the neutron pulse coincides with the hesitation in the plasma current decay. The obvious implication is that a runaway electron current of 1.5 MA has been generated. This hesitation in current decay is less pronounced for disruptions producing fewer neutrons, and imperceptible for those with weak emissions.

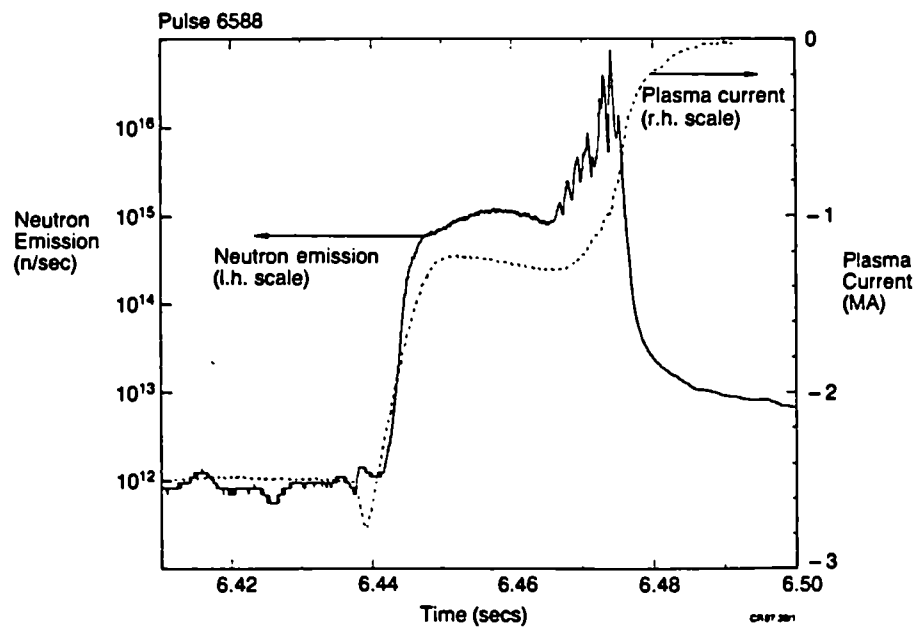

Figure 1:

Illustrating the relationship between the rapid decay of the plasma current during a disruption and the strength of the photoneutron emission. The total neutron emission is 5 x 10^{13} neutrons.

A total of 201 disruptions have been studied, covering the period between the startup of the tokamak and December 1986. These disruptions included all those producing at least 10^{11} photoneutrons; during this period there were nearly 10,000 discharges.

The variation in photoneutron yield for a particular set of plasma conditions is very considerable and it is difficult to discern how the photoneutron yield is to be predicted. The clearest correlation is obtained by plotting the average yield against plasma current at the instant of disruption, as shown in figure 2.

The yield is found to be fitted reasonably well with the variation $N = 7 \times 10^{12} I^{2.6}$ observed neutrons/disruption (I in MA). The photoneutrons are mostly produced several centimeters deep in the structure surrounding the plasma; it is estimated that only 1/3 of these enter the plasma region and so become available for detection. The true yield of produced neutrons

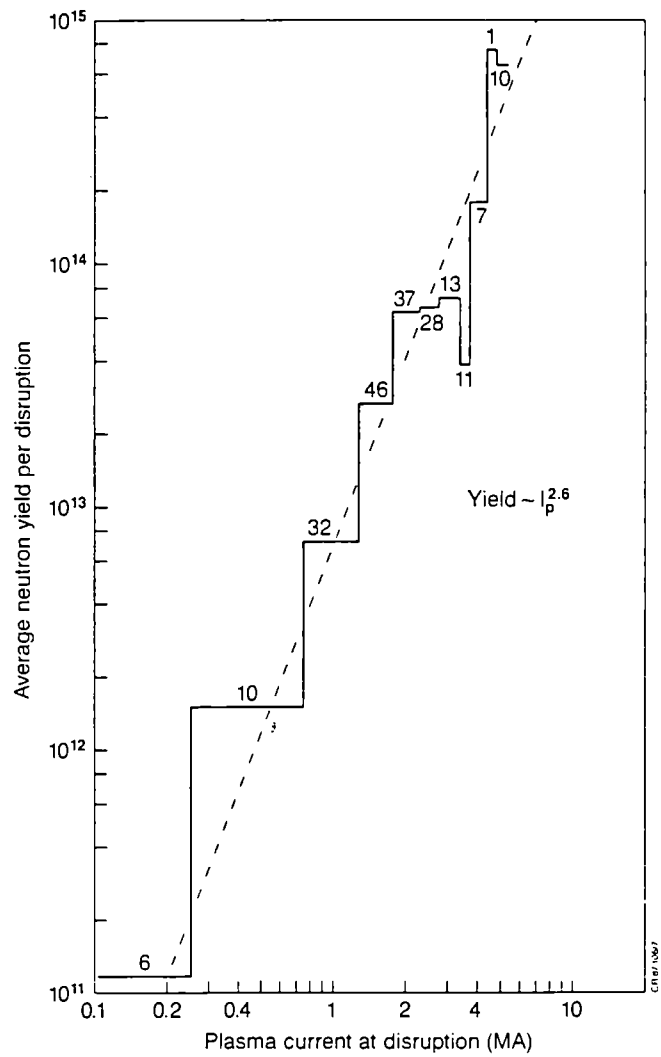

Figure 2:

A histogram showing the average number of photoneutrons produced per disruption as a function of plasma current at the instant of the disruption. For each plasma current interval (0.5 MA), the number of disruptions in the class is indicated.

per disruption is therefore $N = 2 \times 10^{13}\ I^{2\cdot6}$ (I in MA). The yield per runaway electron can be calculated [3]; for example, for electrons of energy E_0 (MeV) and a carbon tiled torus with inconel surrounding structures, this calculated yield is

$$Y = 4.8 \times 10^{-5}\ E_0 \text{ neutrons/electron}$$

Thus, the number of electrons per disruption is

$$N/Y = 4.2 \times 10^{17}\ I^{2\cdot6}\ E_0^{-1} \text{ electrons/disruption .}$$

These are relativistic electrons, making 1.6×10^7 revolutions of the torus per second. They give rise to a current of $1.1 \times 10^3\ I^{2\cdot6}\ E_0^{-1}$ kamps. Clearly, runaway electron currents of up to 1 MA are possible.

The total kinetic energy carried by these electrons is $NE_0/Y = 0.07\ I^{2\cdot6}$ (MJ). This is very high, 5 MJ for 5 MA disruptions. The total energy available for accelerating electrons is that associated with the poloidal magnetic field

$$W_M = \tfrac{1}{2}\ L\ I^2 = 2.4\ I^2 \text{ (MJ) with } L = 4.8\ \mu H$$

On average, the fraction converted to runaway electrons is $f = 2.9 \times 10^{-2}\ I^{0\cdot6}$. This fraction is relatively insensitive to the energy assumed for the runaway electrons, provided it is higher than 25 MeV. This estimate should not be relied upon to better than a factor of 3.

3. CONCLUSIONS

The essential conclusions from this study are

(i) Runaway electron energies are high (over 60 MeV) due to the measured loop voltage in a disruption exceeding 500 V for periods of 5 ms or more.

(ii) The neutron emission scales with plasma current as $I^{2\cdot6}$, so that a fraction $3 \times 10^{-2}\ I^{0\cdot6}$ (I in MA) of the poloidal magnetic energy is converted to runaway electron production. (It should be noted that the neutron yield from individual disruptions fluctuate considerably about the average yield for a particular plasma current).

(ii) The energy carried by the runway electrons is considerable (5 MJ for a 5 MA plasma). This energy is normally dissipated at a small number of locations around the vacuum vessel.

REFERENCES

1. H Knoepfel and D A Spong, Nuclear Fusion 19 (1979) 785.
2. O N Jarvis et al, "Further Calibration of the Time-Resolved Neutron Yield Monitor (KN1)", JET-IR(85)06.
3. O N Jarvis, G Sadler, J L Thompson, "Photoneutron Production Accompanying Plasma Disruptions in JET", JET-P(87)50.

REFLECTOMETRY ON JET

R Prentice, P Cripwell*, A E Costley, J A Fessey, J C M de Haas+, A E Hubbard, C A J Hugenholtz+, T Oyevaar, M Paume°, A J Putter+, A C C Sips+ and K Slavin

JET Joint Undertaking, Abingdon, Oxfordshire, OX14 3EA, UK
* On attachment from Imperial College of Science and Technology, London
+ FOM Instituut voor Plasmafysica, Rijnhuizen, Nieuwegein, Netherlands
° CEA Cadarache, St Paul lez Durance, France

INTRODUCTION

The reflectometry work on JET has two components. One is the development of a multichannel instrument to probe the plasma along a major radius with radiation propagating in the ordinary (o) mode (E ∥ B) [1]. This system is currently being installed and commissioned and preliminary results have been obtained with four of the probing channels. In addition, exploratory experimental work with radiation propagating in the extra ordinary (e) mode (E ⊥ B) is in progress. We report on both aspects of the work in this paper.

THE MULTICHANNEL O-MODE REFLECTOMETER

The o-mode instrument, shown in Fig. 1, has 12 discrete frequencies distributed over the 18-80 GHz band, enabling electron densities in the range 0.4-8 x 10^{19} m^{-3} to be probed. This instrument employs specially developed combiner and separator systems [2], antennas [3] and sensitive phased locked heterodyne detection systems [4]. The antennas are mounted within a port on the JET vacuum vessel and a special, oversized waveguide run, employing reduced height E-plane bends, transmits the radiation from the sources and returns the signals to the detectors sited outside the biological shield in the diagnostic hall.

The instrument has two modes of operation: narrow band swept and fixed frequency. When the frequency of each source is swept, at rates up to 5 kHz, the radial positions of the different critical density layers, ie. the density profile, can be determined. When the frequencies are held constant, the magnitude and direction of movement of the critical density layers can be determined with a spatial resolution of a few mm. This mode of operation should be well suited to studies of fluctuations and density changes. The two modes of operation can be interleaved during a plasma pulse.

Signals from three different detection systems are available from each channel [4]: a period detector which measures the difference in group delay between the arms of the reflectometer, a fringe counter which measures phase changes and a coherent detector which includes amplitude variations as well as phase changes, this being equivalent to homodyne detection.

The instrument is currently in the final stages of installation and commissioning but preliminary results have been obtained using the 18, 24,

34 and 39 GHz channels. Fig. 2 shows four coherent detector signals (bandwidth 0-250 Hz) from the reflectometer together with the line integrated density from a transmission interferometer operating at 2 mm wavelength. The effects of plasma sawteeth on the signals are clearly visible. The positions of the critical density layers for the four frequencies have been obtained using density profiles from the FIR interferometer. The general delay observed between the 34 and 24 GHz channels can be used to deduce a particle diffusion coefficient [6,7], the value of which is typically $\sim 0.4\ m^2s^{-1}$. On the time scale displayed no general delay can be resolved between the 24 and 18 GHz channels since the critical density layers are close together. The 39 GHz signal has a different appearance because its critical density lies inside the mixing radius for the sawtooth collapse.

The effect which an 'H' mode plasma has on the coherent detector and fringe counter signals can be seen in Fig. 3, where the H-alpha signal is also displayed. It will be noted that both the H-alpha and coherent detector signals show a marked reduction in the level of fluctuations during the 'H' mode period. Close examination also shows that small, periodic spikes on the H-alpha signal are correlated with sharp transitions in the reflectometer signals. Over the duration of the 'H' mode, both fringe counter traces show a total movement of about 20 mm. Results from the SXR diagnostic indicate that this movement is likely to be due to a general broadening of the density profile.

These preliminary results show that the basic microwave operation of the system is satisfactory and give encouragement for full system operation.

E-MODE REFLECTOMETRY

Reflectometry using radiation propagating in the extraordinary mode reflecting at the upper cut-off layer F_{uc}, has advantages for some applications over reflectometry using the ordinary mode. The profiles of $F_{uc}(R)$ mean that the inner half of the density profile is often accessible. The wavelength of the probing radiation is smaller and the spatial resolution, a function of the wavelength, is improved. Further, simultaneous measurements in both polarisations can give information on the magnetic field. To exploit these possibilities, a provisional e-mode instrument has recently been constructed on JET.

The reflectometer is set up in a Michelson configuration and can cover either the range 50-75 GHz or 75-110 GHz. The source is a remotely controllable Backward Wave Oscillator. The output frequency can be varied in discrete steps so that a number of different radial positions may be investigated during a single plasma pulse.

The e-mode instrument has measured sawtooth density pulses (Fig. 4) which have also been measured simultaneously by the o-mode system. By comparing the timing of the pulse peaks on the two reflectometers, the total magnetic field at the reflecting radius of the e-mode wave can be determined. The accuracy of the derived value is limited chiefly by the uncertainty of $n_e(R)$. While the present uncertainty in the determination of B_p is large (±50%), it is anticipated that it can be significantly when density profiles from the multichannel o-mode instrument become available.

Frequency spectra of the signals due to density fluctuations up to 40

kHz have also been obtained with the e-mode instrument, with critical radii varied from pulse to pulse. The system is being upgraded, as shown in Fig. 5, to include a second, fixed-frequency source. Waves at the two frequencies will be separated using a dual band-pass filter. It will then be possible for the first time to correlate signals with closely spaced input frequencies ($\Delta F \geq 1$ GHz), in order to study the radial localization of the reflectometer measurements, as well as the radial correlation length of density fluctuations.

REFERENCES

[1] R. Prentice, A.E. Costley, J.A. Fessey and A.E. Hubbard. Course and Workshop on Basic and Advanced Diagnostic Techniques for Fusion Plasmas. Varenna, Italy, September 1986. EU 19797, Vol 2, p451.

[2] F. Mederios and N. Williams. 12th International Conference on Infrared and Millimeter Waves. Orlando, Florida, USA, December 1987.

[3] F. Mederios and N. Williams. 17th European Microwave Conference. Rome, Italy, September 1987, p201.

[4] C.A.J. Hugenholtz and A.J. Putter. Rijnhuizen Report 86-170. FOM-Instituut voor Plasmafysica, Nieuwegein, Netherlands.

[5] A.E. Hubbard, A.E. Costley and C.W. Gowers. J. Phys. E:Sci. Instrum. 20, 423 (1986).

[6] A.E. Hubbard, D. Ward and T.E. Stringer. 13th European Conference on Controlled Fusion and Plasma Heating. Schliersee, April 1986. Vol 10C, Part 1, p232.

[7] A. Gondhalekar, D. Campbell, A. Cheetham, A. Edwards, J. de Haas, A.E. Hubbard, J. O'Rourke, P. Thomas and M. Watkins. This conference.

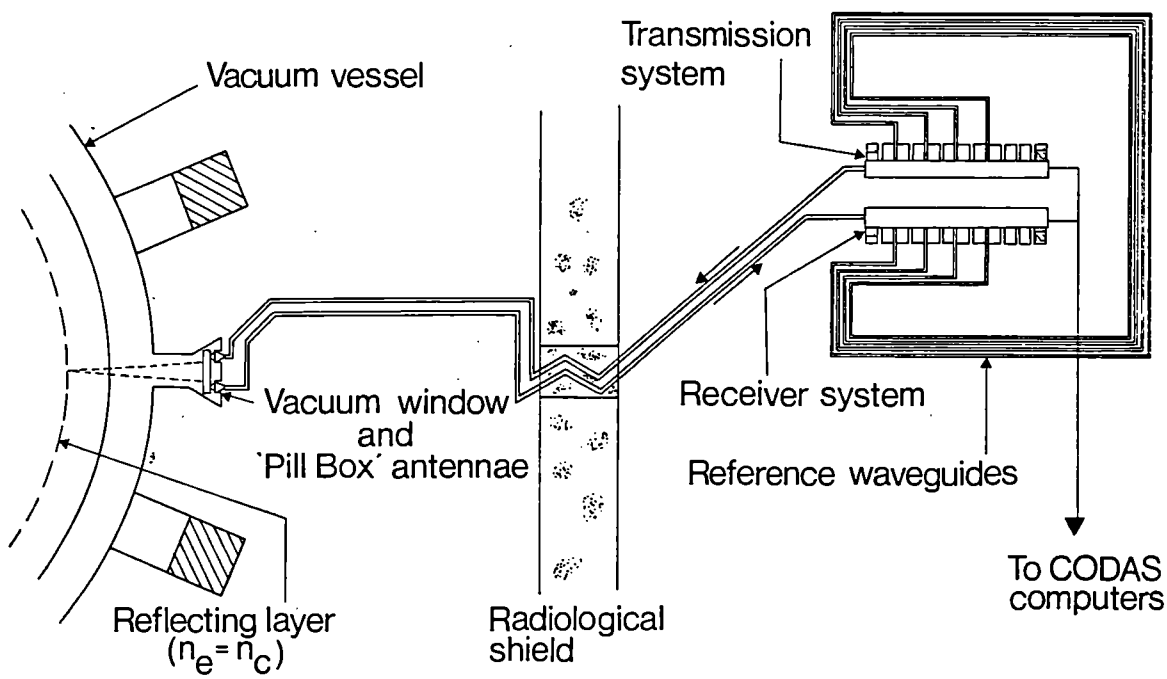

Fig. 1 Schematic of the JET mulitchannel reflectometer system

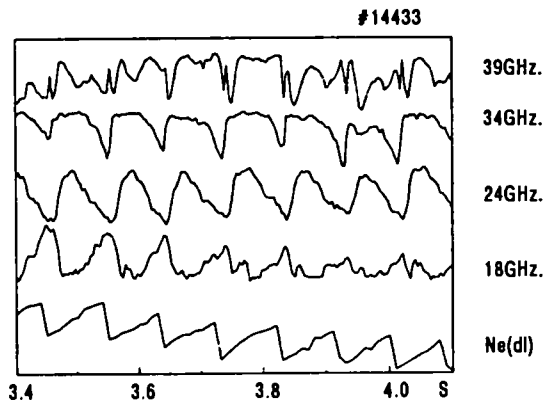

Fig. 2: Sawtooth activity monitored by the coherent detectors and the 2 mm interferometer.

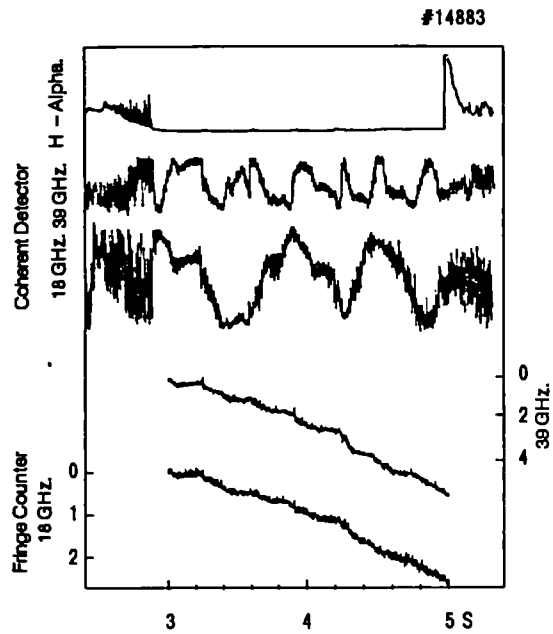

Fig. 3: Coherent detectors, fringe counters and H-alpha signals during an 'H' mode plasma.

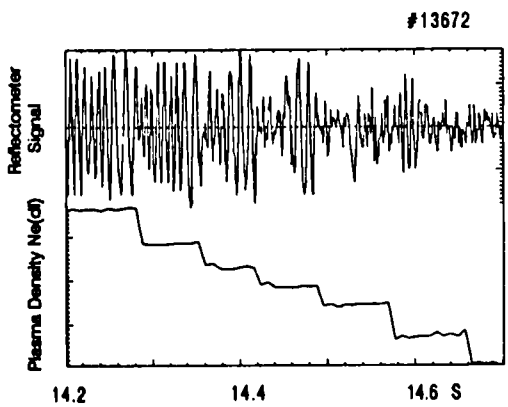

Fig. 4: Sawteeth monitored by the e-mode system working at 40 GHz. Absorption by the second harmonic of the electron cyclotron resonance occurs at 14.64 s.

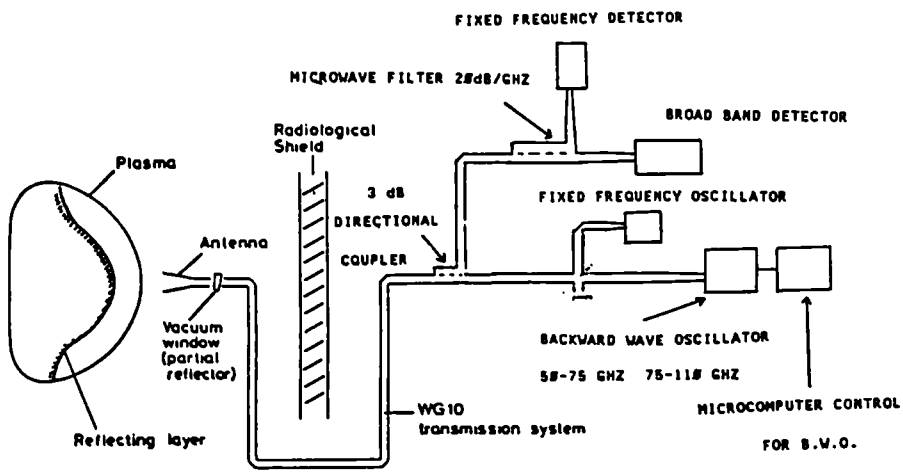

Fig. 5: Schematic of instrument for studies of density fluctuations.

PLASMA EDGE EFFECTS DURING ADDITIONAL HEATING IN JET WITH BELT.LIMITER CONFIGURATION

H Brinkschulte, S Clement[+], J P Coad, L de Kock, S K Erents*, G Neill, J Partridge*, J C B Simpson[°] and J A Tagle

JET Joint Undertaking, Abingdon, Oxfordshire, OX14 3EA, England
* Culham Laboratory, Abingdon, Oxfordshire, OX14 3EA, England
[+] Association CLEMAT/EURATOM, Madrid, Spain
[°] Surface Analysis Technology PLC, Ascot, Berkshire, SL5 7PW, England

Introduction

The efficiency of ICRH heating and current drive with Lower Hybrid waves is influenced by the properties of the plasma boundary. In addition, ICRH heating has a strong effect on the edge plasma: the plasma parameters density, temperature and particle flux increase. A knowledge of all these effects is essential in understanding the influence of the edge plasma on the behaviour of the confined main plasma during additional heating (impurity generation and transport, transition from L-regime to H-regime in discharges with magnetic separatrix, particle confinement during neutral beam fuelled discharges, etc).

Since the summer of 1987, the original arrangement of 8 discrete limiters in JET has been replaced by belt limiters (to allow heating powers up to 50 MW). Two toroidal rings of narrowly spaced carbon tiles were mounted close to the outer wall of the vacuum vessel, both rings separated by ≈ 1 m above and below the equatorial plane. Although the plasma boundary showed generally the same behaviour as for the discrete limiter configuration [1 - 3], new features were found with the new full toroidal belt limiter configuration with a total input power up to 22 MW.

Experiment

During the last upgrading of JET a large number of diagnostics for the scrape-off layer (SOL) were installed as shown in Fig 1.

- 20 fixed Langmuir probes in the belt limiter tiles at 4 different toroidal and poloidal positions.
- 2 fixed Langmuir probes in each of the ICRH antennae side protection tiles in octants 1D and 5D, at different radial positions.
- An array of 6 Langmuir probes (3 facing the electron drift direction and 3 the ion drift direction). These can be positioned at any radial position from the wall through the intermediate top vertical port in octant 5D.
- A fast transfer system (FTS) containing a collector probe (rotatable during the pulse or between pulses) and fixed Langmuir probes, entering the torus ≈ 40 cm above the equatorial plane in octant 7D.

Toroidal and Poloidal Symmetries and SOL Thickness

Measurements with the 20 belt limiter probes biased at -100V

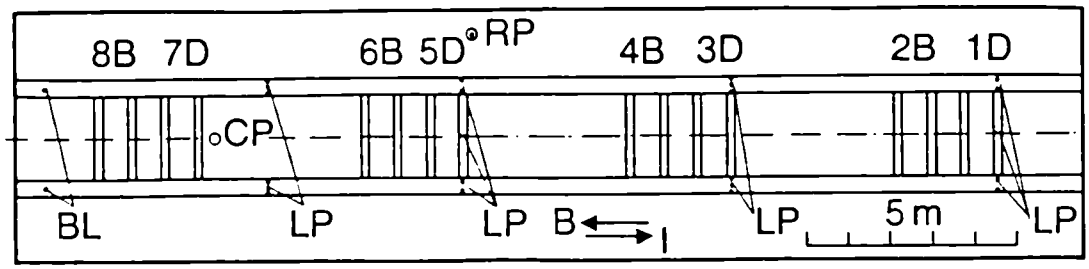

Fig 1: Unfolded view of the torus wall as seen from inside with 2 belt limiters BL), 8 ICRH antennae (1D to 8B), 24 Langmuir probes (LP), reciprocating probe (RP) and collector probes (CP) on FTS.

revealed all particle fluxes to be identical to within ± 10 % indicating that the plasma is toroidally symmetric to be better than 2 mm and consequently that the power is deposited uniformly on the 2 belt limiter rings. This simplifies the investigation of the plasma properties in the poloidal direction which can be done at any convenient toroidal location.

The 2 belt limiters define 2 different areas for the SOL: an inside or high field area (< 1 m above and below outer mid plane) and an outside or low field area (> ± 1 m away from the outer mid plane). Both areas - which are analysed by the corresponding probes - are separated by the plasma tangent lines on the belt limiters, (last closed flux surface LCFS) the exact location of which is unfortunately not known in JET with a precision better than 1 - 2 cm from the magnetic flux surface calculations.

Fig 2 gives the particle flux e-folding length as a function of total ICRH heating power for 3 different cases: a) and b) the 1986 discrete limiter configuration, b) after conditioning of the machine by heavy carbonisation, and c)-d) the 1987-88 belt limiter configuration for the inside area. For all plasma currents, the flattening of the profiles due to RF heating is always less pronounced for the belt limiter discharges than for the discrete limiter configuration. The boundary behaves differently when the plasma is heated by neutral beams (NB) where the SOL thickness does not change with total input power. Fig 3 shows almost constant particle flux (λ_I) and deposited power (λ_p) e-folding lengths for 5 MW NB heated discharges whereas λ_I and λ_p increase by a factor of 2 for the same RF power.

The latter has been attributed to direct deposition of RF power in the boundary causing an increase in the diffusion in the edge ($D_\perp$) or an ionisation in the boundary layer [3]. However, machine conditions and density behaviour (Figs 2 and 3) clearly show that flattening is associated with these effects as well as different phasing of the ICRH antenna [4].

The behaviour of the SOL inside and outside the belt limiters is presented in Fig 4, and was investigated for discharges with ohmic heating up to 3.5 MW and RF heated discharges up to 10 MW. For all cases, the SOL thickness is less outside (λ_{ne} = 6 mm, after correction by a factor of two for field line compression factor for 4 MA discharges) than inside ($\lambda_{ne} \approx$ 10 mm). During RF heating profiles flatten outside (λ_{ne} ~ 13 to 24 mm for 4 MA discharges) but do not change inside. The

edge parameters also increase during additional heating outside the belt limiters ($n_e(o) \approx 0.8 \times 10^{18}$ to 1.3×10^{19}, Fig 4) remaining almost constant inside the belt limiters.

Particle and Impurity Fluxes during Additional Heating

The total particle fluxes to the belt limiter from the outside and inside areas were determined from the appropriate probes in the belt limiters. During ICRF on JET the main species neutral influxes always increase with a magnitude which is proportional to the ICRH power, as is shown in Fig 5 for the fluxes measured by a probe located 24 mm from the LCFS in the area between the belt limiters. These fluxes are generally higher in Helium discharges than in Deuterium discharges for the same amount of total input power.

The impurity influxes also increase during RF heating in JET. The behaviour of Ni and C impurities in the SOL during high power combined heating discharges (ICRH and NBI) was investigated with the collector probe mounted in the fast transfer system. The probe was rotated from pulse to pulse yielding the radial distribution of the integrated deposition from each pulse. Ten consecutive high power discharges were recorded with up to 20 MW total input power. Fig 6 shows the Ni deposition increasing as a function of total RF input power. The impurity production is less when the power is applied in stages and/or the RF antennae are powered in dipole configuration. This Ni deposition is found to depend linearly with the total integrated He flux measured with the Langmuir probes located at the same position of the collector probes, on the FTS. This correlation is shown in Fig 7 and is remarkably good for the data gathered with these two independent diagnostics [5].

Conclusions

- For the belt limiter configuration, the general behaviour of the plasma boundary upon application of different types of heating does not change significantly compared with discrete limiter operation.
- The generally observed flattening of SOL profiles during RF heated discharges is dependent not only on RF power level but also on the density rise during heating and machine configuration and wall conditioning.
- It is found that SOL profiles outside the belt limiters are steeper than inside, when field line compression is taken into account. This is surprising in view of the shorter connection lengths between belts.
- A very good correlation has been obtained for helium fluxes and impurity fluxes measured by collector probes and Langmuir probes. Ni fluxs increases with additional input power, and is less during RF heated discharges with the antennae in dipole phasing than in monopole phasing.

References

[1] H Brinkschulte, et al... Proc. 13th EPS, Schliersee, April 1986 p.403
[2] J A Tagle, et al... Proc. 14th EPS, Madrid, June 1987, p. 662
[3] S K Erents, et al... J Nucl.Materials
[4] M Bures, et al... to appear in Plasma Physics and Controlled Fusion
[5] J P Coad, et al... 8th Internation. Conference Plasma Surface Interactions, Julich, May 1988

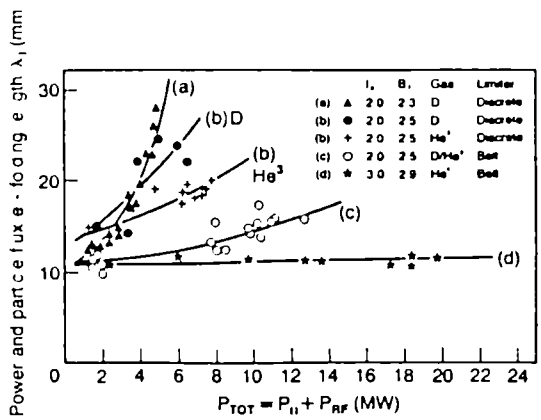

Fig 2: λ vs total RF power. For (b) carbonisation of wall.

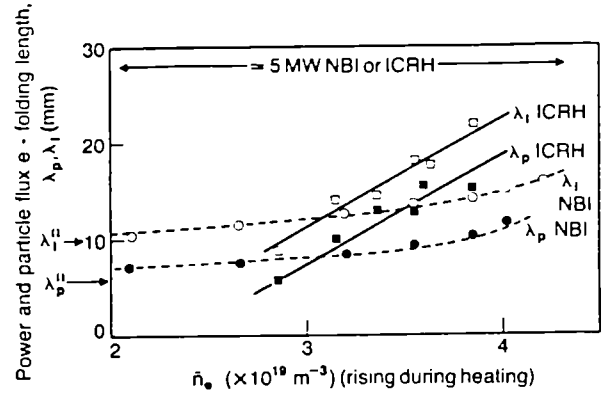

Fig 3: Effect of density rise on particle flux and deposited power for ICRH and NB heated discharges.

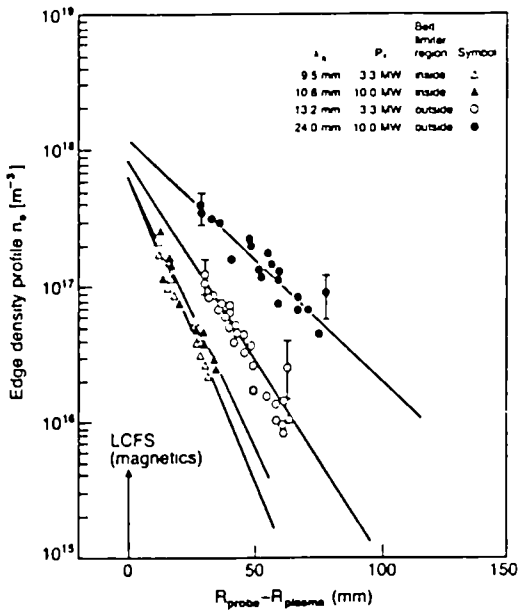

Fig 4: SOL profiles outside and inside belt limiters for ohmic and RF discharges.

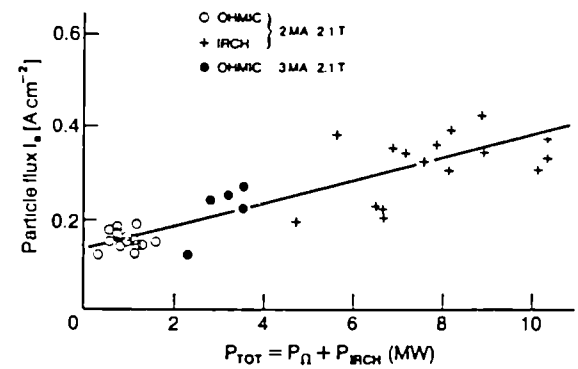

Fig 5: Particle fluxes 24 mm from separatrix vs RF power.

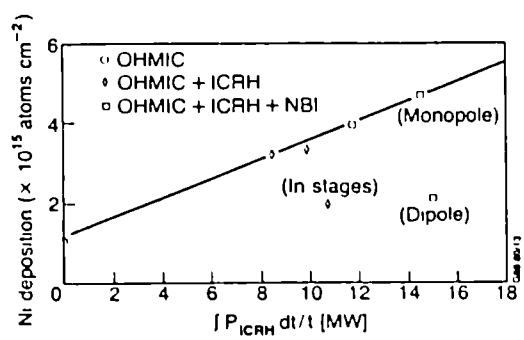

Fig 6: Ni deposition vs integral RF input power.

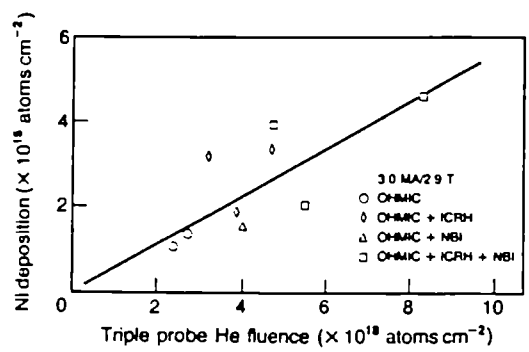

Fig 7: Ni deposition vs total He fluence.

ANALYSIS OF SAWTOOTH STABILIZATION IN JET

D J Campbell, L Baylor[1], V P Bhatnagar, M Bures, A Cheetham, J G Cordey, G A Cottrell, J de Haas[2], A W Edwards, L G Eriksson[3], A Gondhalekar, N Gottardi, R J Hastie[4], T Hellsten, J Jacquinot, E Lazzaro, L McCarthy, P D Morgan J O'Rourke, D Pearson[5], F Pegoraro, F Porcelli, G L Schmidt[6], J A Snipes, D F H Start, P Stubberfield, P R Thomas, K Thomsen, B J D Tubbing, J A Wesson

JET Joint Undertaking, Abingdon, Oxon, OX14 3EA, U K
[1] *Oak Ridge National Laboratory, Oak Ridge, U S A*
[2] *FOM Instituut voor Plasmafysica, Rijnhuizen, The Netherlands*
[3] *Chalmers University of Technology, Gothenburg, Sweden*
[4] *UKAEA Culham Laboratory, Abingdon, Oxon, OX14 3DB, U K*
[5] *Imperial College of Science and Technology, University of London, U K*
[6] *PPPL, Princeton University, Princeton, U S A*

Introduction — During experiments with high power additional heating in JET, it is found that the sawteeth may be spontaneously stabilized for periods of up to 3 s[1,2]. This offers an opportunity to study the behaviour of tokamak plasmas in the absence of mixing due to sawtooth collapses, which normally confuses transport and confinement analysis. In addition, recent measurements of the current density profile in JET have shown that during these periods the central safety factor q_0 reaches values of ~ 0.8, a result which raises fundamental questions about the nature and cause of the sawtooth instability in tokamaks. We propose that the stabilization may be due to the presence of a non–thermal ion energy distribution in the plasma.

Observations — Spontaneous stabilization of sawteeth has been observed over a wide range of conditions in JET (Table 1), the principal constraint being the requirement for a minimum level of auxiliary heating power ($P_{aux} \geq 3$ MW). This power threshold depends, however, on many parameters, among them: majority and minority gases, RF antenna configuration, density, heating profile and radiated power fraction. Nevertheless, certain heating schemes produce stabilization with high reliability for input powers above the threshold (eg ICRH monopole heating on–axis in D(He^3) with $I_p \leq 3.5$ MA).

Table 1 : Conditions for sawtooth stabilization

Combined heating (ICRH + NBI):
- o ICRH on–axis, NBI co–injection.
- o $I_p = 2 - 5$ MA ($q_\psi = 6 - 3.4$).
- o $P_{aux} > 7.5$ MW ($\langle n_e \rangle < 4 \times 10^{19}$ m^{-3}).

ICRF heating alone:
- o ICRH on–axis.
- o $I_p = 1.5 - 4$ MA ($q_\psi = 4.6 - 9$).
- o $P_{aux} > 3$ MW ($\langle n_e \rangle < 3 \times 10^{19}$ m^{-3}).
- o H, He^3 minorities, mono/dipole antenna

NBI heating alone (2 cases in SNX–point):
- o $I_p = 2$ MA, $P_{aux} = 7$ MW, $\langle n_e \rangle = 2 \times 10^{19}$ m^{-3}.
- o $I_p = 3$ MA, $P_{aux} = 7$ MW, $\langle n_e \rangle = 3.5 \times 10^{19}$ m^{-3}.

Evolution of the principal discharge parameters for one of the longest sawtooth–free periods obtained is shown in figure 1. As indicated in the figure, the plasma current was ramped

during this period, since there is evidence that this may prolong the stable period. The central electron temperature is usually found to saturate on a timescale of the order of the energy confinement time. However, the density, ion temperature and stored plasma energy can continue to rise throughout the stable period, depending on the heating scheme employed.

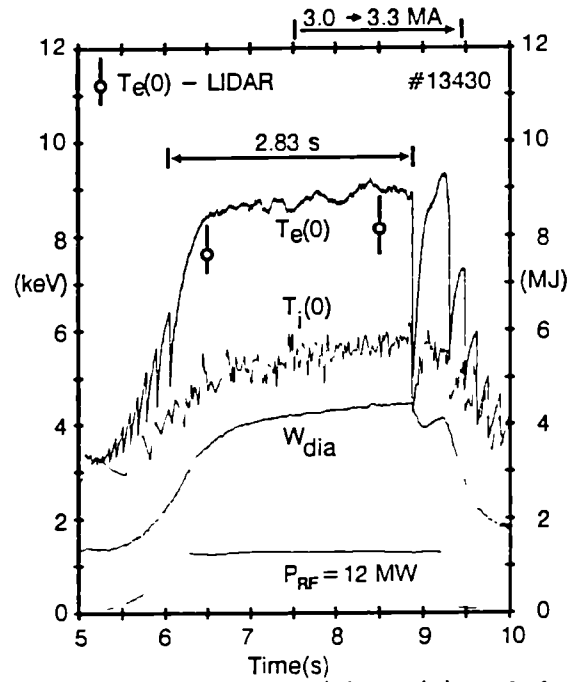

Fig 1 : Evolution of $T_e(0)$, $T_i(0)$ and the diamagnetic energy content W_{dia} during one of the longest sawtooth–free periods: I_p= 3 MA, q_ψ= 4.5, $<n_e>$ = 2.5 10^{19} m^{-3}

Transport and Confinement – It has previously been reported that electron thermal transport in this regime is well represented by a model in which profile[3] or temperature gradient[4] constraints are invoked. Recent analysis[5] of energy confinement during stable periods has confirmed that electron energy confinement is L–mode like (with the exception of stable periods achieved in H–modes), but that total energy confinement is 15–20% higher than in equivalent sawtoothing discharges, in part as a result of the central accumulation of fast ions which are normally depleted at sawtooth collapses. This suggests that sawtooth stabilization may be important in the confinement of α–particles in the near–ignition regime.

The absence of sawteeth also permits the determination of particle transport coefficients within the q=1 surface from the analysis of density profile evolution. It is found that the diffusion coefficient at r/a ~ 0.35 is 0.75 m^2s^{-1}, which is of the same order as that outside the q=1 surface in equivalent sawtoothing discharges. These results indicate that the principal advantage deriving from the stabilization of sawteeth will not be due to improved confinement inside the q=1 surface, but rather to increased fusion reactivity, due to the peaked profiles obtained, which may be further enhanced if non–thermal fusion scenarios are exploited.

Analysis – As reported previously[1,2], the sawtooth collapse terminating these periods follows the usual JET behaviour, which led originally to the conjecture that the stabilization occurred due to non–inductively driven or pressure driven current. However, recent analysis of the current profile evolution in this regime[6] has shown that the central safety factor q_0 attains a value well below unity before the final sawtooth collapse. Figure 2 shows the evolution of q_0 during a sawtooth–free period as determined by FIR Faraday rotation measurements (polarimetry), calculation of resistive diffusion (TRANSP[7]) – which at present excludes bootstrap current – and magnetic equilibrium analysis (IDENTC). The three measurements agree within systematic errors (± 20%), and show a monotonic decrease of q(0) during the stable period to values ~ 0.7–0.9. Since the sawtooth instability in JET strongly resembles an ideal mhd mode[8], this represents a considerable theoretical problem.

Discharges in which sawtooth–free periods occur are characterized by a population of energetic ions, principally RF–accelerated minority ions, with energies in the range of several hundred keV. The non–thermal β_p may be significant therefore, ~ 0.1, and it is thought that these ions may play a significant role in the stabilization mechanism. Figure 3 illustrates an experiment designed to investigate the role of additional heating. By lengthening the RF pulse it was possible to extend the stable period, up to a maximum of 3 s. When the ICRH was switched off during the stable period, the delay until a sawtooth collapse was a small fraction (~ 2%) of the central resistive skin–time, but was of the order of the central fast ion slowing–down time[9], τ_{FS}, where,

$$\tau_{FS}\,(s) = \frac{0.06\ T_e^{3/2}\ (keV)}{n_e\ (10^{19}\ m^{-3})}\ , \quad (1)$$

which was ~ 0.5 s for these conditions. Although the energy confinement time was also of this order, the decrease in β_p accompanying the switch–off was predicted to be stabilizing. This suggests, therefore, that the loss of fast ions was the dominant destabilizing effect.

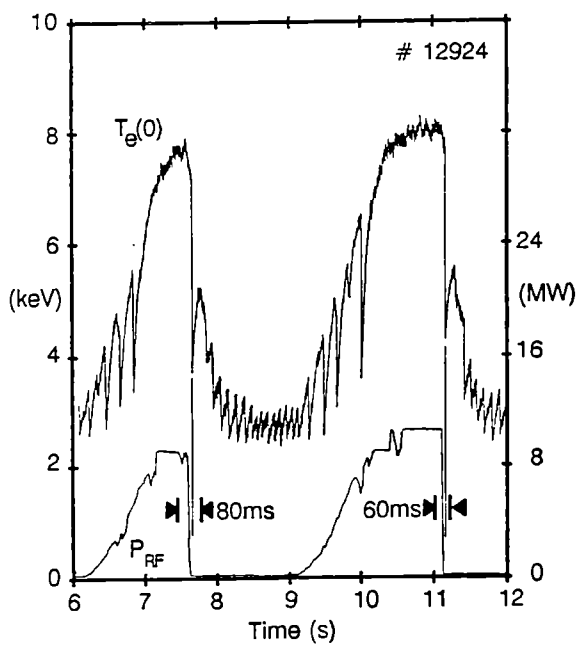

Fig 3 : Delay between switch–off of the RF power and end of a sawtooth–free period: I_p= 2.5 MA, q_ψ= 5, $\langle n_e \rangle$ = 2.0 10^{19} m^{-3}

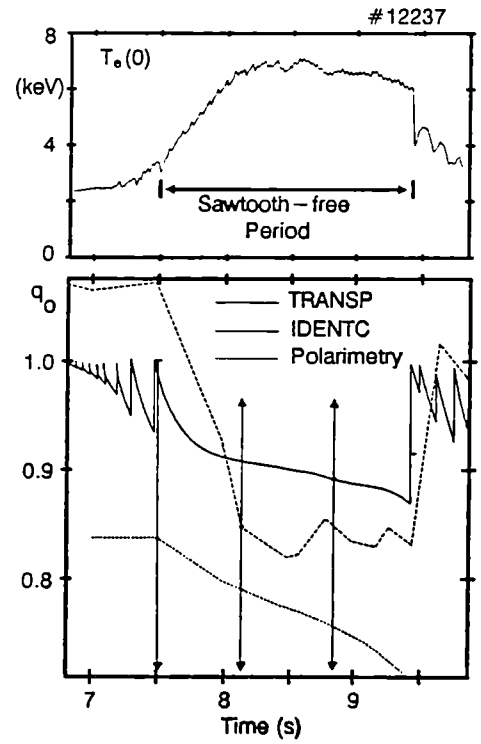

Fig 2 : Evolution of q_0 during a long sawtooth–free period, as determined by three independent techniques (see text): I_p= 2 MA, q_ψ= 5.8, $\langle n_e \rangle$ = 2.2 10^{19} m^{-3}

Theory – The influence of an energetic ion distribution on the stability of the resistive and ideal m=1 modes has been investigated using the experimental observations that $q_0 < 1$ and $\beta_p \geq 0.3$ during sawtooth–free periods. It is found that trapped hot ions introduce a new threshold for the m=1 instability[10]. Stabilization arises from the fact that the magnetic drift motion of the hot ions exceeds the phase velocity of the m=1 mode, with the result that additional energy is required to perturb this population. Under these conditions the dispersion relation for the mode is

$$[-\omega(\omega - \omega_i^*)]^{1/2} = \omega_A[\lambda_H + \lambda_K(\omega)]^{1/2}\,\frac{Q^{3/2}}{8}\,\frac{\Gamma[(Q-1)/4]}{\Gamma[(Q+5)/4]}\ , \quad (2)$$

where $$Q^2 = i\omega(\omega - \omega_i^*)(\omega - \omega_e^*)/\epsilon_\eta \omega_A^3 , \qquad (3)$$
with ω_e^* and ω_i^* the electron and ion diamagnetic frequencies , $\epsilon_\eta = \eta c^2/(4\pi r_0^2 \omega_A)$ the inverse magnetic Reynold's number, η the resistivity, $\omega_A = \hat{s} v_A/\sqrt{3} R_0$ with v_A the Alfvén velocity, $\hat{s} = r_0 q'(r_0)$ and $q(r_0) = 1$. The parameter λ_H (see ref [11]) is proportional to the mhd energy functional δW ($\lambda_H > 0$ for ideal mhd instability). Finally, the parameter $\lambda_K(\omega)$, which represents the hot ion effects, is defined by

$$\lambda_K(\omega) = \frac{4\pi^2 i}{(B_p \hat{s})_0^2 \ \xi_0} \int_0^{r_0} dr\, r^2 \int_{-\pi}^{\pi} \frac{d\theta}{2\pi} \vec{e}_{\|} \times \vec{\kappa} \bullet \vec{\nabla} \tilde{p}_{\perp h}(\omega) , \qquad (4)$$

where ξ_0 is the radial displacement , $\vec{e}_{\|} = \vec{B}/B$, $\vec{\kappa}$ is the curvature vector and $\tilde{p}_{\perp h}(\omega)$ is the perturbed transverse hot ion pressure. When the bounce averaged magnetic drift frequency $\omega_{D,h}$ of the hot ions is larger than the mode frequency ω, but $(1 - q_0) < \omega/\omega_{D,h}$, λ_K can be approximated as

$$\lambda_K(\omega) \simeq -(\pi/3\hat{s}^2)\,(r_0/R_0)\,\beta_{p,h}\,\omega/\omega_{D,h} , \qquad (5)$$

where,

$$\beta_{p,h} = -[8\pi/B_p^2(r_0)] \int_0^{r_0} dr\,(r/r_0)^{3/2} \frac{d}{dr}[(r/r_0)^{1/2}\, p_{\perp h}] . \qquad (6)$$

Resistive internal modes are unstable with a growth rate $\gamma/\omega_A \sim \epsilon_\eta^{1/3}$ in the limit where $|\lambda_H + \lambda_K| < \epsilon_\eta^{1/3}$ (and $\omega_i^* \sim \omega_e^*$, $\omega_i^*/\omega_A \leq \epsilon_\eta^{1/3}$). However, if $\beta_{p,h}$ is sufficiently large, the relevant regime satisfies $|\lambda_H + \lambda_K| > \epsilon_\eta^{1/3}$. If $(\lambda_H + Re\,\lambda_K) < 0$, the m=1 tearing mode should be stable because of a combination of toroidal and high temperature effects. In the remaining case, $(\lambda_H + Re\,\lambda_K) > 0$, the dispersion relation reduces to

$$\omega(\omega - \omega_i^*) = -\omega_A^2\,[\lambda_H + \lambda_K(\omega)]^2 . \qquad (7)$$

If also ω_i^* and $\lambda_K \to 0$, the ideal mhd dispersion relation is recovered. Using the approximate expression (5), it is found that the ideal internal kink mode is stabilized by the hot ions when

$$\beta_{p,h} > \alpha\,(r_0/R_0)\,\beta_p^2\,\omega_{D,h}/\omega_i^* , \qquad (8)$$

where α is a numerical factor, of order unity, primarily determined by the q–profile. For reasonable estimates of the hot ion distribution, this condition is consistent with experimental values of the relevant parameters. This result also reflects the fact that it is difficult to produce sawtooth stabilization when the RF deposition profile is centred significantly off–axis, since this would produce insufficient peaking in the profile of $p_{\perp h}$ within the region where $q < 1$ to yield a positive $\beta_{p,h}$. More detailed information on the energy and phase space distribution of the hot ions is required, however, to enable a more detailed comparison with the experimental results to be undertaken.

We wish to acknowledge R Goldston and D McCune of PPPL for the use of TRANSP, and C Best for supervising its installation at JET.

References

[1] D J Campbell et al, Proc 14th EPS Conf, Madrid, 1 21 (1987).
[2] D J Campbell et al, JET Preprint JET–P(87)20 (to be published).
[3] A Taroni and F Tibone, Proc 14th EPS Conf, Madrid, 1 97 (1987).
[4] M Brusati et al, Proc 14th EPS Conf, Madrid, 1 177 (1987).
[5] V P Bhatnagar et al, this conference.
[6] J O'Rourke et al, this conference.
[7] R J Goldston et al, J Comput Phys **43** 61 (1981).
[8] J A Wesson et al, Proc 11th IAEA Conf, Kyoto 1986, **2** 3 (1987).
[9] T H Stix, Nucl Fus 15 737 (1975).
[10] F Porcelli and F Pegoraro, Proc 2nd Euro Fus Theory Meeting, Varenna (1987).
[11] B Coppi et al, Proc 11th IAEA Conf, Kyoto 1986, **3** 397 (1987).

EFFECT OF SAWTEETH AND SAFETY FACTOR q ON CONFINEMENT DURING ICRF HEATING OF JET

V P Bhatnagar, D Campbell, J P Christiansen, J G Cordey, J Jacquinot, D F H Start, P Thomas, K Thomsen

JET Joint Undertaking, Abingdon, Oxfordshire, OX14 3EA, England

1. Introduction: The ion-cyclotron resonance heating (ICRH) experiments on JET have been carried out in a variety of conditions: Limiter and X-point configuration with H or He^3-minority heating schemes in D, He^3 or He^4-plasmas. Moreover, second-harmonic heating experiments in H-plasmas and combined ICRH and neutral-beam injection heating experiments have also been carried out. RF power exceeding 16 MW for several seconds have been coupled to a 3.3 MA JET plasma (f = 42 MHz) with 8 antennas operating in the dipole configuration [1]. The stored energy reached 6 MJ with T_{eo} = 8 keV, T_{io} = 6 keV and $n_{eo} = 6 \times 10^{19}$ m^{-3}. The radiated power was less than 42 % of the total input power. A significant fraction of the energy is carried by the heated fast ions which are well confined in JET.

In this paper, our efforts are directed to confinement scaling studies with plasma current I_p and safety factor q for the above mentioned heating scenarios and discharges. With the production of "Monster" or ultralong sawteeth (period greater than the energy confinement time) in JET, we are also able to assess the effect of sawteeth on confinement. The confinement data in JET fits well with an off-set linear law. Therefore, in the following, we present our results in terms of incremental confinement time (τ_{inc}) and demonstrate that τ_{inc} improves with I_p at lower currents (1 - 2 MA), saturates and subsequently degrades at higher currents (4 - 5 MA). These results are compared with a model which assumes that $\bar{\chi}$ (where $\bar{\chi} \propto 1/\tau_{inc}$; see below) depends on two competing mechanisms, that is, it decreases with I_p but increases as the size of the q = 1 surface is increased at higher I_p/B_ϕ or low q_a.

2. Results: For the results presented below, we include the JET ICRH data obtained in 1987 both for limiter and X-point discharges. The plasma parameters under ICRF heating are in the following ranges:

$0 \leq P_{RF}$ (MW) ≤ 16 ; $32 < f$ (MHz) ≤ 43 ; $2 \leq B_\phi$ (T) ≤ 3.5 ;
$1 \leq I_p$ (MA) ≤ 5 ; $0.7 \leq P_{OH}$ (MW) ≤ 4.5 ; $2 \leq \bar{n}_e \times 10^{-19}$ (m^{-3}) ≤ 5
$3 \leq T_e$ (keV) ≤ 10 ; $2 \leq T_{io}$ (keV) ≤ 7.5 ; $0.2 \leq P_{rad}/P_{TOT} \leq 0.8$
$2 \leq Z_{eff} \leq 5$

A plot of stored energy (from diamagnetic loop measurements) W_D vs ($P_T - W_D$) is illustrated in Fig.1 for different I_p as indicated where P_T is the total input power and the dot refers to the time derivative.

Similar data that exists for I_p = 1.5, 3, 3.5 and 4 MA is not shown on the figure for clarity. W_D also includes the significant perpendicular energy that is carried by the fast ions created during the minority heating and is estimated to be less than 1 MJ. It is clearly seen that the W_D follows an off-set linear law [2,3]. The τ_{inc} is determined by the slope of a line which is least square fitted to the data points for the power scan at a given I_p. Since there is little difference in the energy confinement for the various minority species heating scenarios [4] we do not identify them specifically in the data presented below. Except in some specific cases, generally monopole and dipole antennas give similar confinement results, we therefore do not separate the monopole and dipole data.

In order to reduce the scatter of the data, we have subdivided large data sets at a given I_p into smaller subsets generally regrouping them by a day or consecutive days of operation. We also exclude the data with $P_{rad}/P_{TOT} > 0.6$. The radiation can be systematically taken into account but has not yet been done for the data presented here. The off-axis heating data is also excluded and the minority ion-cyclotron layer lies within 20 cm of the magnetic axis. The data at a given I_p is further identified with respect to q, ie operation at 2 different B_ϕ with the higher B_ϕ pertaining to He^3-minority operation.

From Fig.1, we note that $\tau_{inc}(D)$ increases with I_p up to 3 MA but it is considerably lower at 5 MA. The τ_{inc} values both from W_D and W_e (electron kinetic energy) obtained from such scans at these and other currents are plotted in Fig.2 as a function of I_p. The W_e is calculated from n_{eo}, T_{eo} and integration over the profiles. It is seen that $\tau_{inc}(e)$ increases with I_p, saturates then decreases. The two low points at 3 and 4 MA correspond to large I_p/B_ϕ or low q_{cyl}-values. These points merge well into the crowd when the data is plotted as a function of I_p/B_ϕ or q_{cyl} (see below). Similar remarks apply for $\tau_{inc}(D)$ data. For the $\tau_{inc}(D)$ data, we have further identified exclusively non-monster scans which roughly follow the $\tau_{inc}(e)$ behaviour except that of a point at 3.3 MA. This corresponds to an exceptionally good series in which dipole phasing was used with pellet injection in some shots. The other $\tau_{inc}(D)$ data which feature monster sawteeth show a marked improvement over the non monster data and is related to the added contribution of perpendicular energy of the fast ions. Although occasional monster sawteeth have been obtained at 4 and 5 MA, there are no scans under such conditions to deduce τ_{inc} at these currents. Note that the present X point and limiter ICRH discharges give about the same τ_{inc} values. Also, the 2 ω_{CH} data point compares well with the other data.

The τ_{inc} data shown in Fig 2 is now plotted in Fig.3 as a function of $I_p B_\phi$ where this quantity is inversely proportional to q_{cyl} if the plasma cross sectional area is held constant (the experimental data fits a relation $q_{cyl} \sim 3.3 \times (I_p B_\phi)^{-0.8}$). It is seen that maximum τ_{inc} is found when $I_p B_\phi \sim 1$ or $q_{cyl} \sim 3.3$.

We now compare the τ_{inc} deduced from certain scans where we sort the data with and without monster sawteeth. The τ_{inc} values thus obtained

are plotted in Fig.4 as a function of I_p and the data points are identified as shown. It is found that on average, there is about 15 % improvement in $\tau_{inc}(D)$ with monster over the non-monster case whereas there is no improvement in $\tau_{inc}(e)$ on a similar comparison. This relates to the fact that fast ions in JET are well confined during a monster sawteeth and result in improvement of stored energy whereas frequent sawteeth may eject them periodically losing their contribution to stored energy. The monster sawteeth thus show their importance in reactor environment in preventing the ejection of α-particles due to frequent sawteeth crashes.

3. Modelling: We follow the local transport model such as given in Ref 2 to predict the variation of τ_{inc} with I_p and I_p/B_ϕ. In Ref.2, τ_{inc} is written as $\tau_{inc} = \tau_\chi . \eta$ where η is the heating effectiveness and it is equal to unity for central highly peaked power deposition profiles. τ_χ is defined as $\tau_\chi = 3\ ab/4\ \bar{\chi}$ where $\bar{\chi}$ is a spatially averaged heat diffusivity [2]. If $\chi = \infty$ inside the mixing radius r_m and $\chi(r) = \chi_o/\left(1 - \alpha\ (r/a)^2\right)$ outside r_m, we can write as follows:

$$\tau_\chi = (3\ ab/8\chi_o).(1 - r^2_m/a^2).\left(1 - (\alpha/2)(1 + r^2_m/a^2)\right).$$

For simplicity, we take $\alpha = 1$ and $\chi_o \ \alpha \ I_p^{-\beta}$ to get:

$$\tau_\chi(s) = \tau_{\chi_o}(s).I_p^{\beta}\ [MA]\ .\ \left(1 - (r_m/a)^2\right)^2$$

where τ_{χ_o} and β can be adjusted to fit the data. The experimental data fits a relation $r_m \cong 1.35/q_{cyl}$. Since τ_χ is a function of I_p and q_{cyl}, a single curve cannot be fitted to the data. Instead, a point by point comparison has to be made. For clarity, we show fitted points (diamonds) for $T_{inc}(e)$ only in Figs.2 and 3 which should be compared with triangles and are found to be in fairly good agreement assuming $\beta = 0.5$ and $\tau_{\chi o} = 0.14$ s. This fit can be further improved by adjusting the parameter α.

4. Discussion and Conclusions: The behaviour of experimentally obtained τ_{inc} of centrally heated ICRF discharges as shown in Figs 2 and 3 is understood in terms of a local heat transport model where $\chi_o \ \alpha \ I_p^{-\beta}$ and that $\bar{\chi}$ increases as the size of the $q = 1$ surface is increased at higher I_p/B_ϕ or low q_a. The actual value of β could be further improved if power scans are made at constant n_e. The effect of off-axis heating profiles on τ_{inc} has previously been discussed in [2,4]. The loss of fast particles by sawteeth is a significant energy loss which is avoided in a monster sawtooth discharge.

Acknowledgement: We wish to thank our colleagues in the JET team, especially the tokamak operation teams and those operating the diagnostics used in the experiments reported in this paper.

References

[1] J. Jacquinot et al, Invited Paper, this conference.
[2] J.D. Callen et al, Nucl. Fusion 27 (1987) 1857.
[3] P.H. Rebut et al, 11th IAEA Conf., Kyoto, Japan (1986), paper E/3/4
[4] V.P. Bhatnagar et al, 14th EPS Conf., Madrid, Spain, Europhysics Conf. Abstracts, 11 D, Part III, (1987) 805.

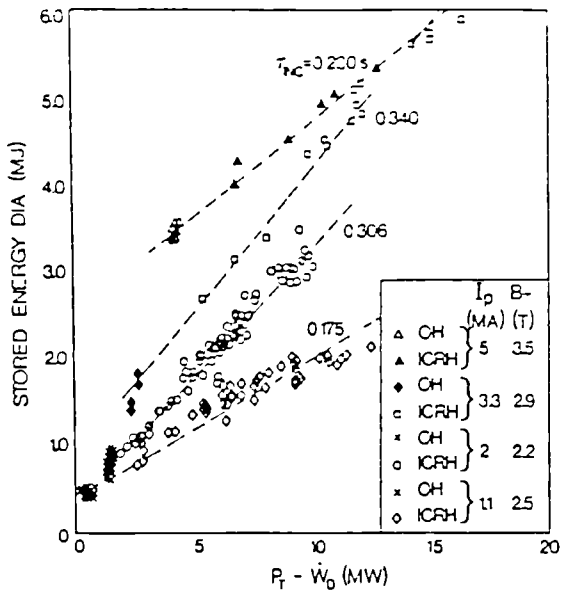

Fig.1

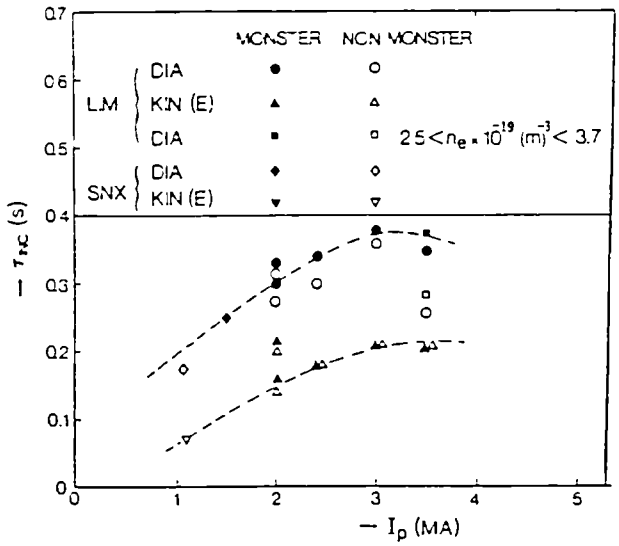

Fig.4: Plot of τ_{inc}(D) and τ_{inc}(e) vs I_p for monster and non-monster sawteeth data.

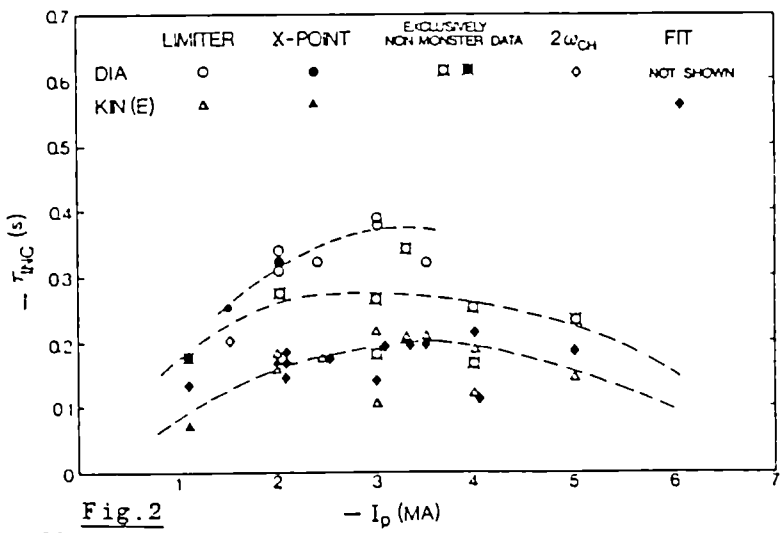

Fig.2

Fig.1: Plot of W_D vs $P_T - \dot{W}_D$ at different I_p. The scan at 1.1 MA refers to X-point.

Fig.2: Plot of τ_{inc}(D) and τ_{inc}(e) vs I_p. A fit of τ_{inc}(e) only is shown with $\beta = 0.5$ and $\tau_{xo} = 0.14$ s.

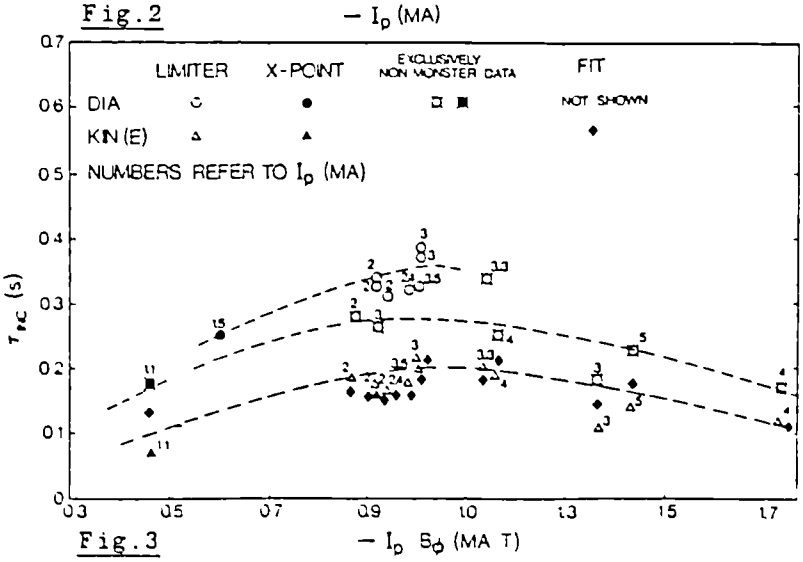

Fig.3

Fig.3: Plot of τ_{inc}(D) and τ_{inc}(e) vs I_p/B For fit, see caption of Fig.2.

HIGH ELECTRON AND ION TEMPERATURES PRODUCED IN JET BY ICRH AND NEUTRAL BEAM HEATING

D F H Start, V Bhatnagar, M Bures, D J Campbell, C Challis, G A Cottrell, L G Eriksson[1], T Hellsten, J Jacquinot, T T C Jones, A L McCarthy[2], D Stork, P R Thomas, E Thompson and K Thomsen

JET Joint Undertaking, Abingdon, Oxfordshire, OX14 3EA, England
[1] Chalmers University, Gothenberg, Sweden
[2] Flinders university, Bedford Park, South Australia

Introduction

The installation of 8 ICRF antennae on JET has enabled 16 MW of power to be coupled in both monopole and toroidal dipole configurations. With on-axis hydrogen minority heating such power levels have produced electron temperatures in the vicinity of 10 keV in the centre of the discharge. The highest temperatures often occur during sawtooth-free periods, or 'Monster' sawteeth which can persist for over 3 sec and during which the global energy confinement time is about 20 % greater than that in plasmas disrupted by sawteeth[2]. Recent experiments have been aimed at achieving both high electron and ion temperatures simultaneously. In this paper we describe the results of two such series of experiments. The first study used ICRF with ^{3}He minority ions in ^{4}He and deuterium plasmas and investigated the effect of minority concentration on bulk ion heating. The second series combined hydrogen minority ICRH in deuterium plasmas with up to 6 MW D° neutral beam power injected at an energy of 40 keV/nucleon to provide additional ion heating. We also report measurements of the electron heating rates for the RF-only experiments obtained from the initial rate of increase of the electron temperature during sawteeth. These results indicate an increase in the proportion of direct heating as the minority density is increased.

ICRF Heating with He^3 Minority Ions

The He^3 minority ICRF experiments were carried out using a plasma current I_p of 3.5 MA and an elongation ratio of 1.5. The toroidal field, B_T, was 3.4 T in order to make the ratio I_p/B_T(MA/T) close to unity to provide optimum confinement[3]. The RF frequency was 34 MHz to give on-axis heating. Deuterium and He^4 plasmas were used, (but with no discernible difference in results) with central electron densities, $n_e(o)$, in the range $3.8 \times 10^{-5} < n_e(o) < 4.8 \times 10^{19}$ m^{-3}. ICRF power levels of up to 12 MW were coupled using both monopole and toroidal dipole antennae configurations. The plasma Z_{eff} was typically 4.5 (visible bremsstrahlung) and the total radiated power was about 50 % of the input power. An example of the time evolution of the central electron and ion temperatures $T_e(o)$ and $T_i(o)$, during heating is shown in Fig 1 for a ^{3}He concentration $n_{He^3}/n_e(o) = 0.11$. The values of $T_e(o)$

and $T_i(o)$ were obtained, respectively, from ECE data and Doppler broadening measurements of X-rays from He-like nickel ions. Note that at 3.4 T the ECE diagnostic calibration gives a value of $T_e(o)$ which is about 20 % higher than Thomson scattering results. Neutral particle energy spectra confirmed the above $T_i(o)$ values. As the RF power is ramped up the sawteeth amplitude and period increase until at 47.8 sec, a 'Monster' sawtooth is formed. During the Monster sawtooth, $T_e(o)$ rises to 9.1 keV (ECE) and $T_i(o)$ = 7.8 keV. At t = 49.4 sec one of the RF generators tripped, causing a reduction in the power which, in turn, precipitated the sawtooth crash 0.3 sec later. This delay is routinely observed and has given rise to speculation that the fast minority ions stabilise the sawteeth. No further sawtooth stabilisation occurs beyond t 49.4 sec showing the existence of an RF power threshold between 7 MW and 9 MW for this operating scenario.

The values of $T_i(o)$ obtained with dipole phasing are shown in Fig 2 as a function of the RF power, P_{RF}, divided by $n_e(o)$ for a range of ^{3}He concentrations. There is clear tendency for the highest values of $T_i(o)$ to be achieved with the highest minority concentrations as expected since the minority ion tail energy will be least under these conditions. Conversely, stronger minority heating of the electrons is be expected at low ^{3}He density and there is a tendency in this direction in the values of $T_e(o)$ shown in Fig 3. The effect is less pronounced than in the case of $T_i(o)$, possibly because of increased direct electron heating through mode conversion or transit-time magnetic pumping (TTMP) at the higher He^3 densities. The monopole antennae phasing gave similar results.

Electron Heating Rates

An analysis[4] of the rate of rise of T_e following each sawtooth crash both during the RF ramp phase and following the Monster sawteeth, (see Fig 1) has enabled electron heating rates to be obtained. Results are shown in Fig 4 where the central power density, P_e, flowing to the electrons is plotted against P_{RF} for low and 'hign' ^{3}He densities. In the low density case, P_e shows the non-linear behaviour expected of minority species heating. Note the hysteresis effect, which could be due to the finite minority ion slowing down time, as P_{RF} is reduced from 11 MW to 8 MW. At the higher ^{3}He density the linear increase of P_e with P_{RF} implies an increasing proportion of direct electron heating through TTMP, Landau damping, or mode conversion of the fast magnetosonic wave. It sh uld be stressed however that this analysis does not give unambiguously the RF heating of the electron since it does not account for expulsion of the minority ions following the sawtooth crash or changes in the radiated and ohmic power.

Combined (H)D ICRF and D° Neutral Beam Injection

These experiments were carried out in deuterium limiter discharges with I_p 3 MA, and B_T = 2.8 T. The RF frequency was 43 MHz so that the $\omega \approx \omega_{CH}$ resonance intersected the magnetic axis. The central electron density was typically ~ 6 x 10^{19} m^{-3}. Power levels up to 15 MW of ICRF (dipole phasing) and 6 MW of NBI (E_{beam} = 80 keV) were used to give a maximum energy content of 6 MJ and a D-D reaction rate of 3.5 x 10^{15} s^{-1}.

The results are shown in Fig 5 where the values $T_i(o)$ = 7.7 keV and $T_e(o)$ = 10 keV were achieved at the highest power levels. These temperatures are similar to those achieved with the ^{3}He minority ICRF experiments but required approximately twice the value of $P_A/n_e(o)$. The precise explanation for this awaits further analysis but is probably due to a combination of factors such as the poorer confinement at the lower plasma current, the broader power deposition of the beam heating and increased radiated power.

Summary

Central electron and ion temperatures in the vicinity of 8 keV have been achieved simultaneously at moderate densities in JET both by He^3 minority ICRH and combined ICRH and NBI with total powers up to 22 MW. The ICRF ion heating appears to be optimum for 5 % < n_{He^3}/n_e < 10 %. Detailed analyses of sawteeth indicate an increase in the ratio of direct to minority ion heating of the electrons as the He^3 density increases.

Acknowledgement

We wish to acknowledge with pleasure the assistance of all our colleagues in the JET team. Particular thanks go to the tokamak operating team and to the members of all the diagnostic groups involved in the measurements reported here.

References

[1] P.R. Thomas et al, Proceedings of 6th European Tokamak Workshop Varenna, Italy 1987 to be published.
[2] D.H.F. Start et al, Proc of 7th Topical conf. on Applications of RF Power to Plasmas, Kissimee, 1987 p.286
[3] V.P. Bhatnagar et al, this conference.
[4] T Hellsten and W G Core, this conference.

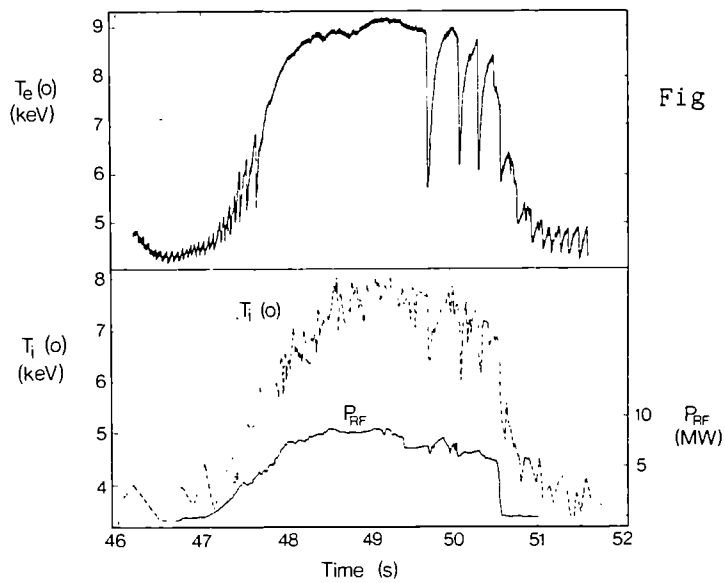

Fig 1: $T_e(o)$ and $T_i(o)$ during RF Heating. I_p = 3.5 MA, $n_e(o)$ = 4.7 x 10^{19} m^{-3}, $n_{He^3}/n_e(o)$ = 11 %.

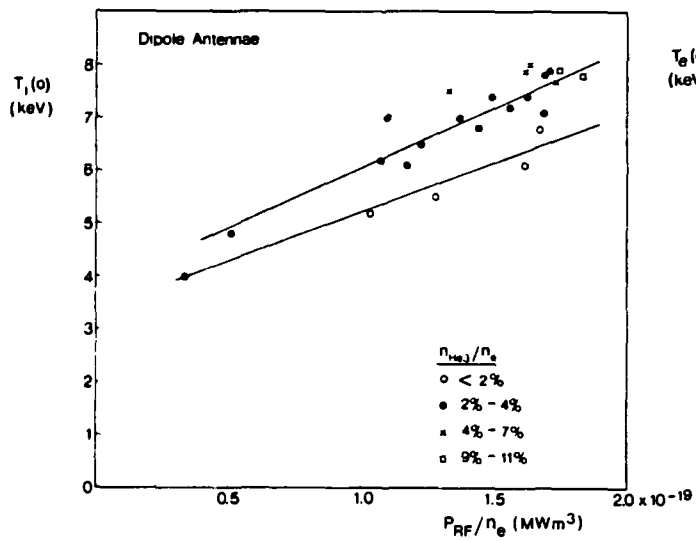

Fig 2: $T_i(o)$ vs $P_{RF}/n_e(o)$. The lines are least squares fits for He^3 densities < 2 % and 2 % - 4 %.

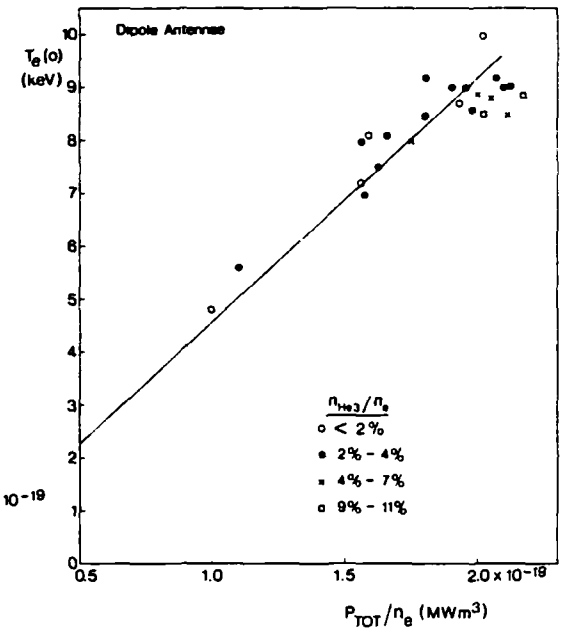

Fig 3: $T_e(o)$ vs P_{TOT}/n_e. The solid line is the best linear fit which passes through the origin.

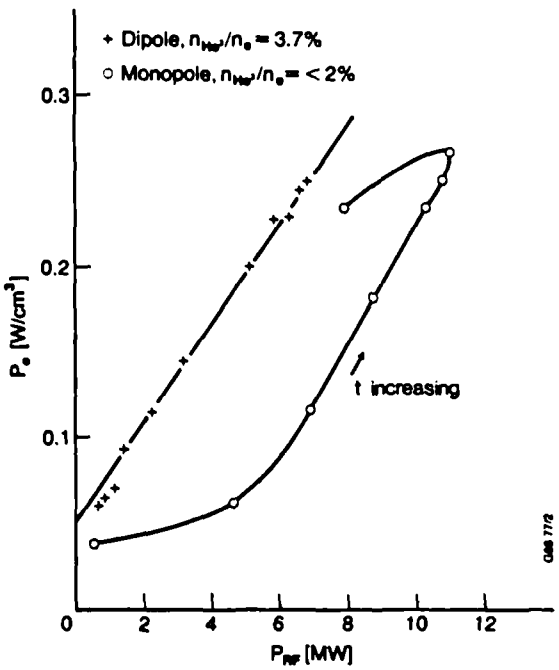

Fig 4: P_e vs P_{RF} showing minority heating (circles) and direct heating (crosses).

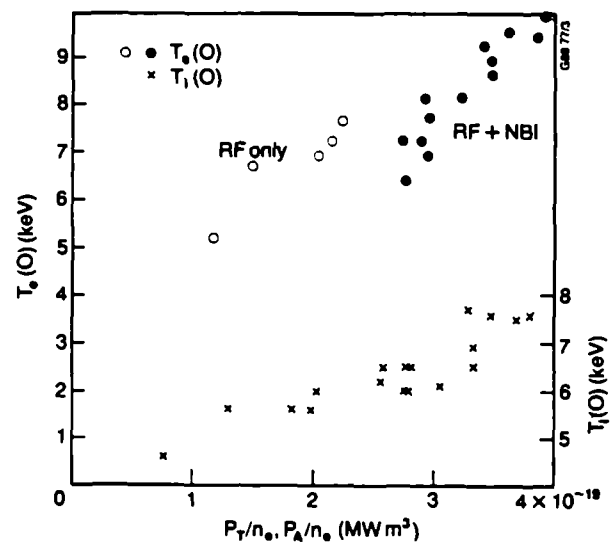

Fig 5: $T_e(o)$ and $T_i(o)$ vs total power and additional power P_A, respectively, divided by central density.

THE SAWTOOTH IN JET

R.D. Gill, D.J. Campbell, P.A. Duperrex, A.W. Edwards, W. Han, J. O'Rourke, F. Pegoraro, F. Porcelli, A. Taroni and F. Tibone

JET Joint Undertaking, Abingdon, Oxon., OX14 3EA, UK.

INTRODUCTION Detailed experimental studies [1] of the sawtooth collapse in JET have shown that it occurs very rapidly (~ 100μs) and X-ray tomography [2] has shown a strong m=1 component, with a spatial dependence in agreement with the predictions of an ideal mhd instability model [3]. However, there are still many remaining problems in our understanding of the sawtooth oscillation and some of these will be discussed below.

INSTABILITY GROWTH RATE The growth rate of the sawtooth instability has been determined by finding the radial centroid, $\bar{r}$, of the X-ray emission function calculated by tomographic inversion of the data collected with the two orthogonally mounted JET X-ray cameras. This quantity is a sensitive measure of the displacement of the plasma central region and is independent of the relative phase of the m=1 instability present during the sawtooth crash. Fig.1 shows a rather slow movement of $\bar{r}$ before the sawtooth collapse and the onset of a sudden growth in $\bar{r}$ during the collapse. The time behaviour of $\bar{r}$ is in good agreement with the perturbed magnetic field measurements made at the plasma edge [4]. Although the growth rate corresponds to the growth rate of an ideal mhd mode, there is no satisfactory explanation of the sudden increase in the growth rate of the instability or of its trigger mechanism.

The centroid is also a very sensitive monitor of plasma movements between sawtooth collapses and mhd activity and other effects are observed which are too small to be seen by individual X-ray detectors.

MONSTER SAWTOOTH During additional heating experiments it has been observed that there are long sawtooth free periods (≳3s), terminated by a large sawtooth called the "monster". Tomographic analysis of these (Fig.2) shows great similarities with normal sawteeth. The core of the initial symmetric state (1) is rapidly (in ≲ 100 μs) displaced radially (2) until it reaches the inversion radius (shown as a dotted line in the Fig.2) where it spreads poloidally (3). The displaced core then collapses with a rapid loss of energy (4) followed by a gradual return to a symmetric but much flattened state (5). The topology of the monster collapse is identical with the normal sawtooth but the inversion radius is considerably larger (by up to 50%). The n=1 nature of the collapse is clearly shown by the X-ray measurements taken with a set of toroidally spaced detectors (Fig.3) and from ECE measurements. This is also confirmed by the magnetic measurements which show a dominant n=1 component with a small n=2 component, similar to normal sawteeth. Although the early stages of the

collapse can probably be explained in terms of the growth of an mhd instability the subsequent rapid loss of energy from the displaced core requires alternative explanations such as enhanced transport for both monster and normal sawteeth.

PARTIAL SAWTEETH Partial sawteeth with a very small collapse amplitude are frequently observed, nearly always accompanied by m=1 mhd activity. The fast part of the collapse has not yet been observed in detail but it seems to involve processes leading to a flattening of the profiles around the q=1 surface with the central parameters remaining relatively unaltered. A slower process has also been observed which leads to an even smaller redistribution of energy at the q=1 surface. The reasons for the different behaviour of the partial sawteeth are unclear.

q-PROFILE It is well known that the q-profile plays a strong role in the sawtooth instability and the sawtooth inversion radius is generally taken to correspond to q=1. This conclusion has been further confirmed on JET by the existence of the m=n=1 "snake" oscillation [5] which also exists at this radius. The identification of normal sawteeth with an interchange instability led to the conclusion that $q(0) \approx 1$ and that the change in q(0) in the sawtooth crash was ~ 1-2%. This conclusion was supported by analysis of the movement of the snake during the crash.

However, the monster sawteeth show quite a different picture and raise new problems in understanding the sawtooth. Faraday rotation measurements [6], resistive diffusion calculation and magnetic equilibrium calculations all show that $q(0) \approx 0.8$ before both normal and monster sawtooth crashes and δq in the monster crash is ~ 20%. These observations are not in agreement with the earlier understanding of the sawtooth crash and an alternative theoretical approach has therefore been investigated.

THEORY We have taken the point of view that, for normal sawteeth as well as for monsters, q(0) is significantly below one, and that the onset of the collapse is determined by the stability threshold of resistive m=1 modes. The stability plane (Fig.4) is determined by the parameters [7,8,9] $\hat{\lambda}_H = -(r_o/R_o)^2 \delta W/\varepsilon_\eta^{1/3}$ and $\hat{\lambda}_* = \omega_{*e}/(\omega_A \varepsilon_\eta^{1/3})$, evaluated at the flux coordinate $r=r_o$ where $q(r_o)=1$. Here, δW is the normalised MHD energy functional, which includes the effects of toroidicity [10] and plasma shaping [11]. The numerical evaluation of δW shows that triangular shaping in JET gives a negligible contribution; the elliptical contribution is destabilising, although typically 10% of δW. The other parameters are as follows: $\varepsilon_\eta = \eta c^2/(4\pi r_o^2 \omega_A)$, η is the resistivity, $\omega_A = s_o v_A/\sqrt{3} R_o$ is the Alfvén frequency, $s_o = r_o q'(r_o)$ is the magnetic shear, ω_{*e} and ω_{*i} are the electron and ion diamagnetic frequencies respectively ($\omega_{*e} = Z\omega_{*i}$).

Although uncertainties remain in the exact location of the marginal stability curve, this is expected [7] to lie close to the curve shown in Fig.4. Layer effects near the q=1 surface, including electron thermal conductivity, ion viscosity, and tight aspect ratio, lead to stability on the left of this curve. Ideal MHD internal kink modes correspond to the regime where $\hat{\lambda}_H > 1$.

In our present approach, the nonlinear evolution of the m=1 mode must leave q(0) below one, in contrast with Kadomtsev's relaxation model, as no significant drop of q(0) can be expected during the ramp of normal sawteeth. The important point here is that stable q profiles with q(0)<1 are found if $\hat{\lambda}_H$ is negative and sufficiently large. This requirement can be satisfied, for instance, if the local magnetic shear parameter s_o is

small. In fact $\hat{\lambda}_H$ is negative and scales mainly with $s_o^{-5/3}$ during a sawtootn ramp in the ohmic phase, since the poloidal beta is small and the global equilibrium parameters cannot evolve significantly. Thus we propose an alternative prescription for the q profile in the relaxed state. We assume that the most significant changes in the q profile after the collapse are localised near the q=1 surface, where the magnetic shear is reduced over a radial interval of width $\Delta<r_o$. Outside this interval the q profile is only slightly modified, with q(0) being reset to a prescribed value below unity, while r_o is chosen to be near the observed inversion radius. This prescription is suggested by measurements of the q profile in Textor [12] and is compatible with initial measurements of q(0) in JET [6]. It can be justified in terms of the growth of a magnetic island which triggers the faster late stage of the collapse as a critical width of order Δ is attained. The pressure profile after the sawtooth crash is taken to be flat in the region where $q \leq 1$.

Using this prescription, the time evolution of $\hat{\lambda}_H$ and $\hat{\lambda}_*$ has been monitored with an equilibrium transport code which assumes neoclassical resistivity. JET plasmas with $q_\psi \approx 4.5 \div 5.5$ have been considered so far. The trend in the ohmic phase is shown by the solid-line trajectories in the stability plane of Fig.4. The trajectories start well in the stable region at the beginning of the sawtooth ramp and approach the marginal stability curve after about 90ms, at the end of the ramp. The first part of these trajectories is affected by the prescribed q profile after the collapse and should be considered with caution. However, for the same ohmic sawtooth simulated with two different initial values of s_o, the trajectories become close to each other on a time scale of the order of tens of milliseconds (Fig.4). A similar sensitivity has been observed with different choices of the initial q(0) ranging from 0.7 to 0.9, and even less to Δ ranging from $r_o/4$ to $r_o/2$. This is consistent with the requirement that the values of the stability parameters at the onset of the collapse should not depend on fine variations of the prescribed q profile.

The dotted lines in Fig.4 correspond to the evolution of the stability parameters during the ramp of a typical monster sawtooth for two initial values of s_o. For the case shown, the parameter $\hat{\lambda}_H$ becomes positive for $\beta_p \geq 0.15$ (β_p defined in Ref.[10]) after about 300ms. To account for the observed stability, it has been proposed that the resistive instability threshold is modified by the presence of non-thermal energetic ions [13].

REFERENCES [1] D.J. Campbell et al, Nucl. Fus. 26 (1986) 1085.
[2] A.W. Edwards et al, Phys. Rev. Lett. 57 (1986) 210.
[3] J.A. Wesson et al, IAEA Conf. (Kyoto) 2 (1986) 3.
[4] P.A. Duperrex et al, this conf.
[5] A. Weller et al, Phys. Rev. Lett. 59 (1987) 2303.
[6] J. O'Rourke, this conf.
[7] B. Coppi et al, IAEA Conf. (Kyoto), 3 (1986) 397.
[8] G. Ara et al., Ann. Phys. 112 (1978) 443.
[9] M.N. Bussac et al., IAEA Conf. (Berchtesgaden), 1 (1976) 607.
[10] M.N. Bussac et al., Phys. Rev. Lett. 35 (1975) 1638.
[11] J.W. Connor and R.J. Hastie, Culham Lab. Report CLM-M106 (1985).
[12] H. Soltwisch et al., IAEA Conf. (Kyoto), 1 (1986) 263.
[13] F. Porcelli and F. Pegoraro, II Euro. Fus. Th. Mth. (Varenna, 1987).

Fig.1 (right) Plasma centroid movement during sawtooth crash.

Fig.2 (below) Tomographic analysis of monster sawtooth crash.

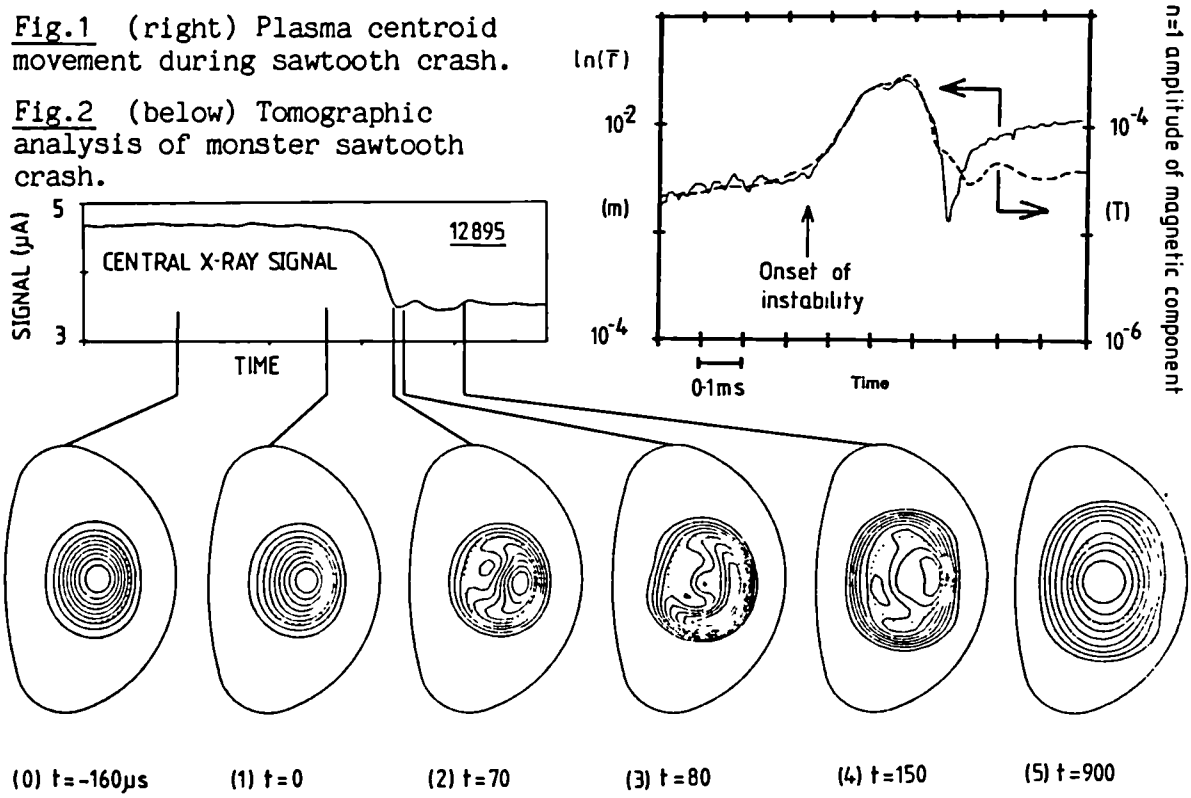

Fig.3 (right) Contour plot of toroidal X-ray emission during crash. (Chord radius = 38cm). n=1 is determined as there is only one point of maximum emission, at 110°.

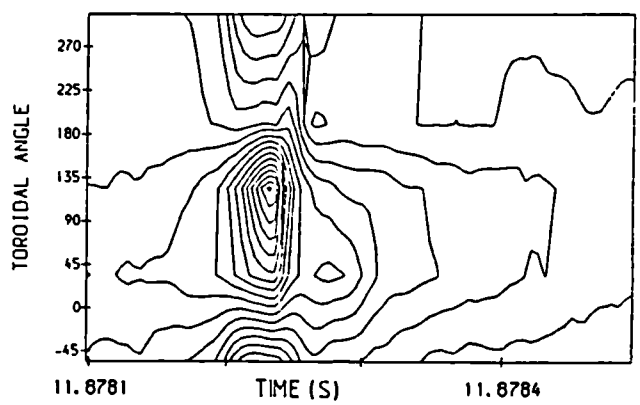

Fig. 4 Trajectories in the stability plane. Solid curves: ohmic sawtooth (period ~ 90ms); dotted curves: monster sawtooth (duration ~ 2s). The starting point in the stable region corresponds to the beginning of the sawtooth ramp. Initial values of the local shear: s_0=0.1 (upper solid and upper dotted curves); s_0=0.2 (remaining curves). Other initial values for all curves: q_0=0.8; r_0=40cm; Δ=r_0/2. The local shear increases along the trajectories: s_0=0.1(*); 0.2(x); 0.25(o); 0.3(Δ); 0.5(□); 0.7(◇).

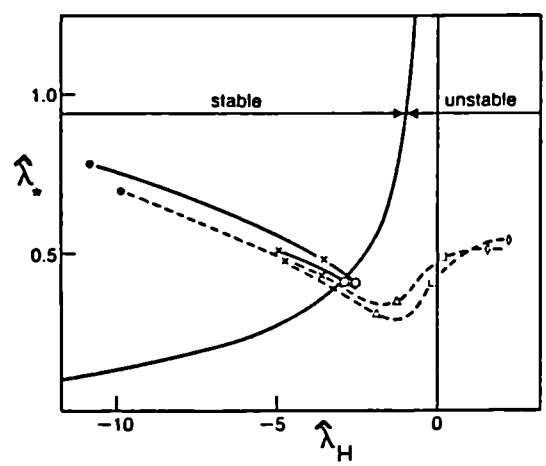

PREDICTIONS FOR ICRF POWER DEPOSITION IN JET AND MODULATION EXPERIMENTS DURING SAWTOOTH-FREE PERIODS

F. Tibone, M.P. Evrard[1], V. Bhatnagar, D.J. Campbell, J.G. Cordey, W. Core, L-G. Eriksson[2], J.C.M. de Haas[3], H. Hamnén[2], T. Hellsten, J. Jacquinot, S. Knowlton, R. Koch[1], H. Lean[4], F. Rimini, D. Roberts[5], D.F.H. Start, P.R. Thomas, K. Thomsen, D. Van Eester[1]

JET Joint Undertaking, Abingdon, Oxon., OX14 3EA, UK.
[1]LPP-ERM/KMS, Brussels, Belgium.
[2]Chalmers University of Technology, Göteborg, Sweden.
[3]FOM, "Rijnhuizen", Netherlands.
[4]Culham Laboratory, Abingdon, Oxon. OX14 3DB, UK.
[5]Princeton Plasma Physics Laboratory, New Jersey, USA.

Theoretical Predictions. Various computational tools are available at JET for prediction of ICRF power deposition profiles: these include the global wave codes LION and ALCYON [1,2], a ray-tracing code [3] and a simplified model [4] based on a parametrization of full wave code results. These codes can properly describe fundamental minority and 2nd harmonic majority heating, and direct electron heating due to transit time damping; the redistribution of power from the minority energetic ions to the background plasma is computed by solving the relevant Fokker-Planck equation. No satisfactory model is available for local electron heating due to mode conversion (experimentally observed in some of JET scenarios, see below).

Fig.1 shows a representative example of comparison between results from full wave and ray-tracing codes. They refer to on-axis minority heating of H in a D plasma, with strong single pass absorption. There is good agreement on the fractional power absorbed by the various species, and both codes predict strongly peaked deposition profiles. The local power density in the center is typically twice as high for the ray-tracing as for the global wave code; however, this figure is sensitive to the local geometry assumptions (volume effects) and to small uncertainties in the exact cyclotron resonance location related to magnetic field corrections. While this implies that we cannot rely on predictions in the vicinity of the magnetic axis, the integrated power absorbed within $r \sim (0.3\text{-}0.4)a$, i.e. the sawtooth region, is nearly the same for the two codes and is consistent with the experiment. The power deposition for cyclotron absorption predicted by the two codes differs more for heating scenarios with weak absorption, for which full wave calculations yield less peaked profiles.

Narrow deposition profiles are also predicted by all codes for JET off-axis heating, with the resonance position as far out as $r \sim 0.6a$.

The assumption on the minority spatial distribution in the plasma is a major source of uncertainty for all predictions. Only sparse evidence is available on the total number of minority ions in each experiment, and it

is even difficult to assess the uncertainty of this datum. The minority radial density profile is arbitrarily assumed to be either uniform, or of the same shape as the measured electron density profile. 50% variations in the assumed minority concentration near the cyclotron resonance can yield changes of tne same order in tne computed local deposition. A similar variation in the overall minority concentration can also affect significantly (20-30%) the power distribution to the different species.

Modulation Experiments During Monster Sawteeth. Since the upgrade of the JET ICRF power system to 8 generators/24MW, it has been possible to launch into the plasma very highly modulated RF pulses with ΔP up to ± 2.5MW, superimposed on an average power in the range 5-10MW. The simultaneous disappearance of sawteeth at these levels of RF power has allowed us to obtain much clearer experimental data than in previous experiments [5].

Figure 2 refers to one of the most recent results: a square wave modulated RF power of 7.2±1.6MW at 4Hz was launched into a deuterium plasma with ^{3}He minority, yielding a ΔT_{eo} of more than ±200eV, in phase with the RF power.

A fast-Fourier-transform-based analysis [5] shows that the T_e-response is still visible at 12Hz, the first harmonic present in a square wave. This supports the idea that direct electron heating is the largest contributor to the observed T_e modulation. Indeed, the transmission of power through the minority acts as a supplementary integrator, decreasing the amplitude of the response by a factor $\omega\tau_s$ - 4.5 in the 4Hz case (ω = modulation frequency; τ_s = fast ion slowing-down time). Thus, even if only 30% of the total power was directly absorbed by electrons, this effect would dominate the picture.

Information on the ratio between direct and indirect bulk plasma heating can be obtained by analyzing the effect of modulation on the plasma energy content W. This effect is clearly visible on both magnetic measurements available at JET, W_{dia} from diamagnetic loop (W_{dia}= 3/2 $W_\perp$, including the non-thermal component) and W_{mhd} from mhd equilibrium calcul- ations (W_{mhd}= 3/2 $W_\parallel$+3/4 $W_\perp$). Fourier analysis yields for this case ΔW_{mhd}= 42kJ and ΔW_{dia}= 56kJ, corresponding to $\Delta W_\perp$ = 38kJ, $\Delta W_\parallel$ = 9kJ and ΔW(anisotropic) = 20kJ. Thus we estimate that only 40% of the RF power results in the creation of an anisotropy in the velocity distribution of the minority. However, it should be stressed that this deduction is particularly sensitive to uncertainties in W_{dia} and W_{mhd}, and requires further confirmation.

In order to compare the modulation experiments with theory, we turn now to a case of H minority heating in ^{3}He, where the effect of direct electron heating is expected to be low. Fig.3 presents both amplitude and phase of $\Delta T_e(r)$ resulting from Fourier analysis, corrected for the modulation of the. magnetic axis shift, responsible for up to 40eV in ΔT_e in the gradient zone

Of the total modulated RF power (ΔP = 1.7MW), 80% is seen in the modulation of the energy content. Plasma energy modulation amounts to ΔW_{mhd} 34kJ and ΔW_{dia} = 62kJ, corresponding to $\Delta W_\perp$ = 41kJ, $\Delta W_\parallel$ = 2kJ and ΔW (anisotropic) = 37kJ. This means that 85% of the power goes to produce an anisotropic minority population. Considering that part of the remaining power will be absorbed by bulk minority ions, we conclude that direct electron heating is indeed a minor effect in this experiment.

The T_e-response has been simulated using a diffusion equation for the electron energy in cylindrical geometry, with radially constant heat

diffusivity. The assumed power deposition profile on the minority (a Gaussian with width 20cm) closely resembles those predicted by the various codes. The modulated component of the Ohmic power input has been found to be negligible, and non diffusive energy losses have been neglected. The model also allows for a small component of direct heating to be taken into account. A good agreement is found (see Fig.3a and 3b) assuming $\chi_e(0)$ = 2-4m²/s and a small amount of direct electron heating (5-10%). This value of χ_e near the plasma center is consistent with the local power balance, and is as large as that previously measured in the outer plasma using the heat pulse propagation technique [6].

Conclusions. Predictive calculations of ICRF power deposition profiles in JET using various numerical tools yield a consistent picture, in qualitative agreement with experimental evidence. Quantitatively the agreement is satisfactory, but the codes tend to overestimate the power density near the plasma center, and cannot describe situations where direct electron heating via mode conversion is important. Poor knowledge of the minority distribution in the plasma can cause a significant uncertainty in the predicted deposition profiles.

RF power modulation experiments have been successfully attempted during "monster sawteeth", without destabilizing the sawtooth-free discharge. We have presented a D(^{3}He) case where significant direct electron heating has been observed, and the measured T_e-response profile is dominated by this effect. Such a scenario is outside the boundaries of applicability of our theoretical models.

We have also shown results for a ^{3}He(H) plasma, where minority heating is clearly dominant. Theoretical predictions for power deposition can reproduce the observed amplitude and phase of $\Delta T_e(r)$ if an electron thermal conductivity χ_e = (2-4)m²/s is assumed in the central plasma region.

References

[1] L. Villard et al., Comp. Phys. Reports 4 (1986) 95.
[2] D.J. Gambier, A. Samain, Nucl. Fus. 25 (1985) 283.
[3] V.P. Bhatnagar, R. Koch et al., Nucl. Fus. 24 91984) 955.
[4] T. Hellsten, L. Villard, Proc. 14th European Conf. on Contr. Fusion and Plasma Heating, Madrid (1987), Vol.11D, Part III, p.1000.
[5] V.P. Bhatnagar et al., Proc. 12th European Conf. on Contr. Fusion and Plasma Heating, Schliersee (1986), Vol.10C, Part II, P.193.
[6] B.J. Tubbing, N.J. Lopes Cardozo, M.J. Van der Wiel, Nucl. Fus. 27 (1987) 1843.

Fig.1 Predictions from ray-tracing (solid) and global wave code LION (dashed lines) for H minority heating in a deuterium JET plasma. Due to the high temperature and toroidal mode number, mode conversion is negligible for this scenario.

Fig.2 Electron temperature traces at different radii (from the ECE polychromator) for a modulation experiment in a deuterium plasma with ^{3}He minority. RF power modulation at 4Hz; $\langle P_{RF}\rangle$=7.2MW, ΔP=±1.6MW. I_p=2MA, B_T=3.4T, n_{e0}=4.3×10^{19}m^{-3}, T_{e0}≈7keV. ρ is a normalized flux coordinate.

Fig.3 Amplitude (a) and phase (b) of the T_e response versus major radius, corrected for the modulation of the magnetic axis shift. ^{3}He(H) plasma with I_p=2MA, B_T=2.1T, modulation at 5Hz, $\langle P_{RF}\rangle$=5MW, ΔP=±1.7MW. The solid lines are the result of the model as defined in the text.

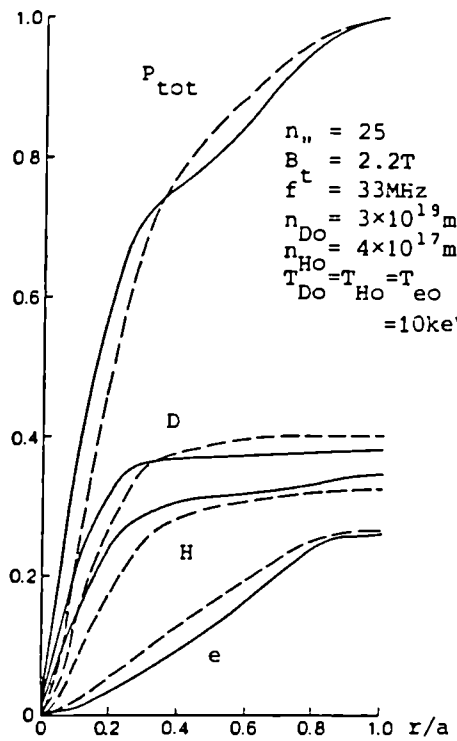

Fig. 1

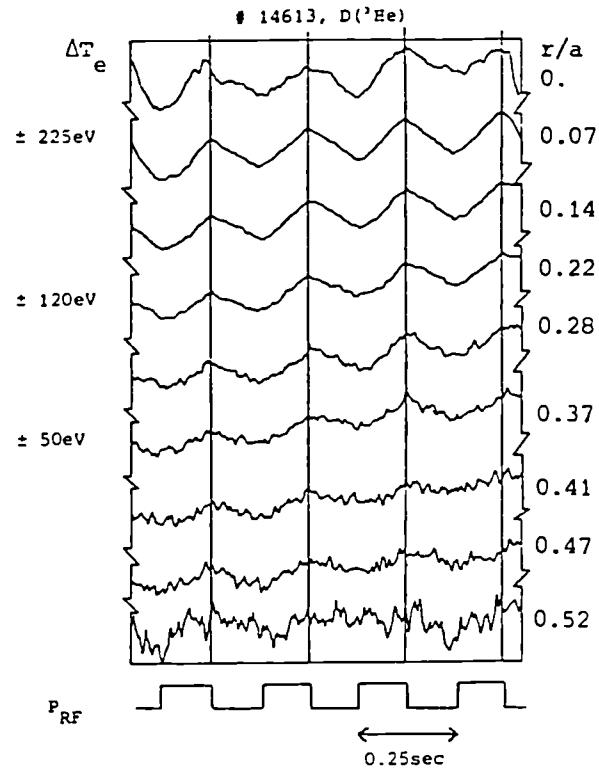

Fig. 2

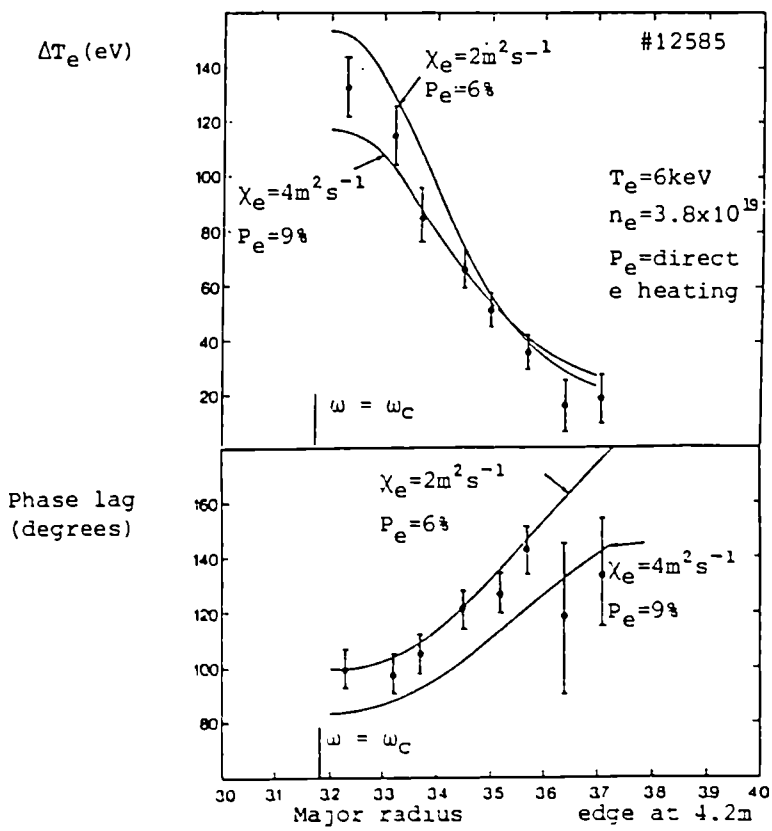

Fig. 3a

Fig. 3b

ANALYSIS OF CURRENT AND PRESSURE PROFILES IN JET H-MODE DISCHARGES

E. Lazzaro, K. Avinash, M. Brusati, N. Gottardi,
F. Rimini and P. Smeulders

JET Joint Undertaking, Abingdon, Oxon. OX14 3EA, UK.

INTRODUCTION.

High confinement discharges have been obtained in JET with a magnetic separatrix configuration with a single stagnation point [1] at currents up to 3 MA and intense neutral beam (NBI) heating. When the NBI power exceeds about 2.5 times the ohmic power a transition occurs from the low confinement (L) regime to the high energy confinement (H) mode.
The characteristic signatures of H-modes are, as observed previously in ASDEX [2] the sharp increase in density, the appearance of pedestals in the measured temperature profiles and a rather quiescent Mhd behaviour.
A significant difference between JET H-modes and those of ASDEX is the persistence in JET of sawtoothing conditions with $q(0)<1$ across the L-H transition. In ASDEX the disappearance of sawteeth was related to a flattening of the current indicated by reduction of the internal inductance.

An analysis of the X-ray emission signals, of the interferometric and LIDAR measurements of the density, of the ECE and LIDAR measurements of the electron temperature and pressure profiles consistent with the magnetic equilibrium, shows that JET H-modes may be characterised by a long non-steady state condition with unconventional density and pressure profiles which are flat or hollow within the $q=1$ surface, which expands after the L to H transition. Fig.1 shows the LIDAR, pressure and q profile for the 3 MA H-mode shot 14815, in the L and H phases.

The pressure and current profiles obtained in this class of H-modes allow sawtoothing, with $q(0)<1$ while keeping stability against localised or ballooning instabilities in the low shear plasma core according to Mercier criterion.

In the confinement region, outside the $q=1$ surface, there is evidence that the current and pressure profiles are related in a way similar to that of the theoretical model by B. Kadomtsev [4], in which the H-mode appears to be a branch of possible equilibria with minimal total plasma energy for a given total plasma current. The implications of the model are that only incoherent perturbations which leave the total current constant, are responsible for the relaxation to a minimum energy state, while low number modes can still be unstable. However this is not consistent with JET H-mode data as JET H-modes are sawtoothing because the core equilibrium still corresponds to an L-mode with degraded confinement which should hence be obtained by helicity constraint in the mixing region. Close to the Troyon limit finite aspect ratio and finite beta effects can be identified in the current density profile (Pfirsch-Schlüter current) not accounted for by the large aspect ratio model.

H-MODE EQUILIBRIUM AND MINIMUM ENERGY PRINCIPLE.

It has been shown that general variational principles lead to universal tokamak current and pressure profiles [3-5]. To describe JET H-modes we use a principle of minimisation for the plasma total energy:

$$W = \int dV \left\{ \left[F^2 + (\text{grad } \psi)^2 \right] / (2R^2) + P/(\gamma-1) \right\} \qquad (1)$$

with the following prescription chosen in accord with observations. In (1) $P(\psi)$ is the plasma pressure and $F/R=B_z$ the toroidal field. Specifically we consider that: a) sawtoothing inside the mixing radius $r=r_s$ is related to a unique helicity $K = \int A \cdot B dV$ for $0<r<r_s$. The plasma energy W should be minimised with constant K (L-mode). b) in the confinement region $r>r_s$ we use Kadomtsev minimisation of the total plasma energy W keeping the current in this confinement region constant (H-mode). In fact the constraints a) and b) are equivalent to that of keeping constant the total plasma current:

$$I = \int dV \left\{ RdP/d\psi + (F/R)dF/d\psi \right\} \qquad (2)$$

c) the equilibrium must be matched across $r=r_s$. The equilibrium for $r<r_s$ obtained from a) using a Lagrange multiplier ν, and choosing $A_z(r_s)=0$, implies:

$$J_z = \nu B_z = J_o; \; P = P_o \qquad (3)$$

both constant. In the confinement region $r_s<r<a$, for large aspect ratio, and $\beta_p \sim 1$ the minimisation scheme b) leads to a Grad-Schlüter-Shafranov equation of the Liouville type:

$$\text{div } (\text{grad } \psi/\lambda) = - Q \exp \{\psi/\lambda\} \qquad (4)$$

In azimuthal symmetry the solution of (4) with $\lambda = \beta_p \langle\psi\rangle/8\pi$ leads to the profiles [3,4] which have the remarkable consistency property:

$$q = q_o + H(r-r_s)(r^2-r_s^2)/a^{*2}; \quad J = J_o q_o^2/q^2; \qquad P = P_o q_o^2/q^2 \qquad (5)$$

with $a^{*2} q_o = I_p/\pi J_o - r_s^2$; $(a/a^*)^2 \sim q_a - q_o$. The equilibrium profiles of pressure or current are characterised by the scale length a* or the peakage parameter which is, for $r_s/a_* \ll 1$:

$$\langle P \rangle / P_o \sim q_o/q_a \qquad (6)$$

For a given value of the parameter $Q = (B^2_p(a)/2\mu_o)/P_o$ there are two possible solutions since:

$$(\langle P \rangle/P_o)^2 - \langle P \rangle/P_o + Q/8 = 0 \qquad (7)$$

and the solution with larger scale length (larger $\langle P \rangle/P_o$) could be interpreted as an ASDEX type H--mode which is sawtooth free with $q_o \geq 1$. In JET discharges however, q_a/q_o has remained constant ~4 through the L-H transition selecting a branch of equilibria which within the mixing region relaxes to profiles with constant helicity.

EXPERIMENTAL DATA.

Fig.2 and Fig.4 show the actual current and pressure profiles for the L-H transition in shot 10766, plotted against the theoretical model of Eqs.(5). It appears that over most of the plasma cross section the experimental H mode profiles fulfil the consistency relations (5) even if the space dependence is different from that of the theoretical models. This behaviour is quite general in the H phase but it can also occur during the L phase. Fig.4 shows the experimental temperature peakage $\langle T_e \rangle / T_o$ plotted versus q_o/q_a for a large number of JET-H mode discharges. The experimental points appear to be bracketed between the limits (a) of the ohmic profile consistency principle $\langle T_e \rangle / T_o \sim 3q_o/2q_a$ and (b) the limit (6) for $\langle P \rangle / P_o$. This might be an indication of the equivalence of the two principles. Finally, we consider whether data agree with the model [6] of the H-mode as a transition of the outer plasma layers into the second stability region for ballooning modes.

A ballooning stability diagram in the plane $[Jr/B_p, -2(R^2/B_p)\, q^2\, (dp/dr)]$ is shown in Fig.5 for shot 10767 for a surface close to the separatrix. Fig.6 shows the J profile consistency of shot 10767.

The L phase of the trajectory is all in the first stability region, and the L-H transition is only marginally approaching the second stability.

CONCLUSIONS.

The "diagnostic" integrals of motion I and K have been used to describe JET H-modes as states of constrained minimum energy. They appear to be one of two possible branches of stable finite β_p equilibria, the other being sawtooth free as in ASDEX.

REFERENCES

[1] Tanga, A, Denne, B., Harbour, P., Lazzaro, E., Noll, P. et al. Nucl. Fus. 27 (1987) 1877.
[2] Wagner, F. et al. Proc. of Tor. Plas. Varenna (1985).
[3] Montgomery, et al. Plasma Phys. 21 (1979) 239.
[4] Kadomtsev, B.B. J. Sov. Plas. Phys. 13 (1987) 7 (in Russian).
[5] Hsu, J.Y., Chu, M.S. Phys. Fluids 30 (1987) 1221.
[6] Bishop, C. Nucl. Fus. 27 (1987) 1765.

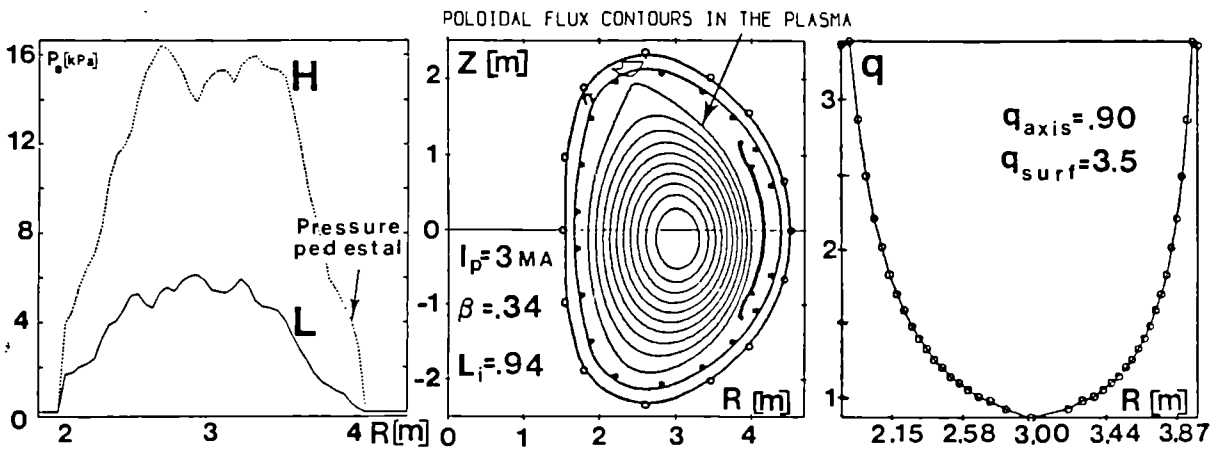

Fig. 1 Pressure and q profiles for shot number 14815 at t = 14sec.

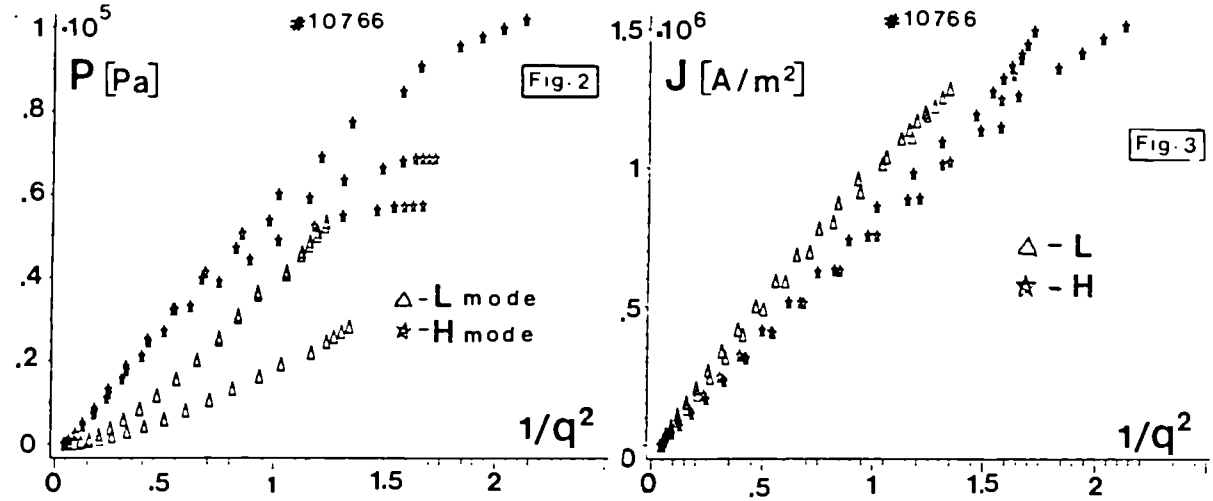
#10766
P [Pa]
Fig. 2
△ - L mode
☆ - H mode
1/q²

#10766
J [A/m²]
Fig. 3
△ - L
☆ - H
1/q²

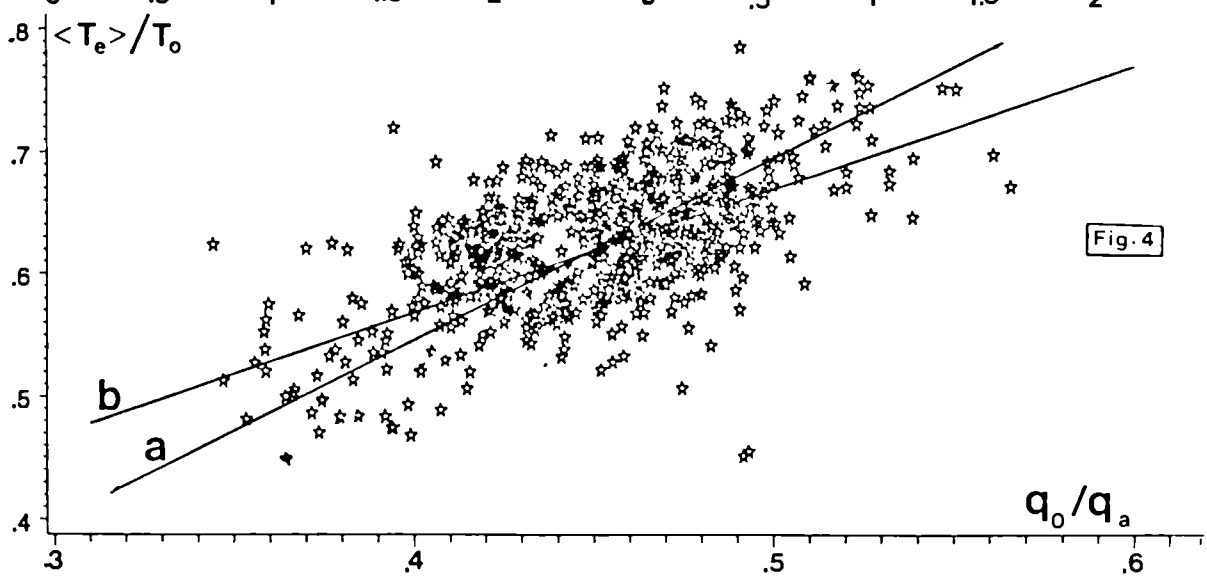
<Te>/To
Fig. 4
b
a
q0/qa

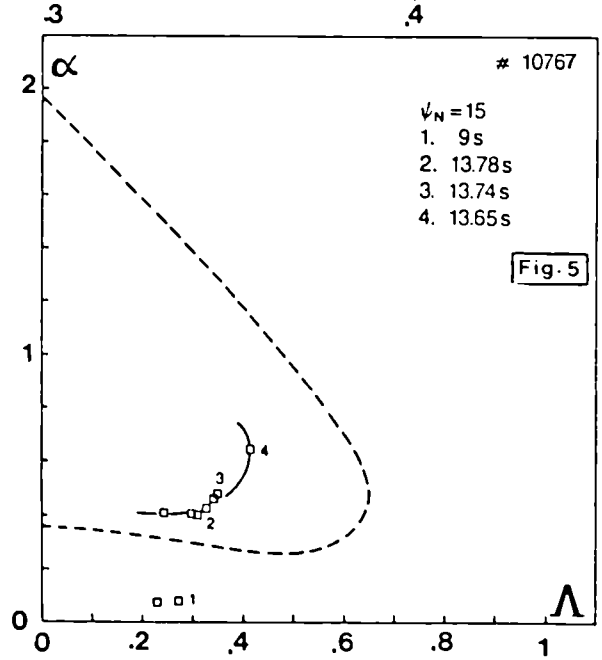
α
10767
ψN = 15
1. 9s
2. 13.78s
3. 13.74s
4. 13.65s
Fig. 5
Λ

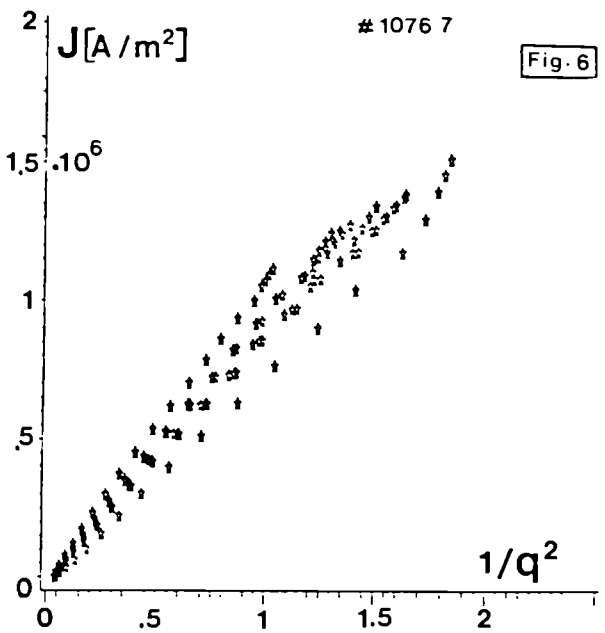
J[A/m²]
#1076 7
Fig. 6
1/q²

LOWER HYBRID WAVE STOCHASTICITY IN TOKAMAKS: A UNIVERSAL MECHANISM FOR BRIDGING THE $n_{\|}$ SPECTRAL GAP

D Moreau*, J M Rax*, A Samain*

JET Joint Undertaking, Abingdon, Oxfordshire, OX14 3EA, England
* From EUR-CEA Assoc, CEN Cadarache, 13108 St Paul lez Durance, France

Abstract

A global approach to the problem of LHCD is being attempted. For typical tokamak aspect ratios the propagation over long trajectories is stochastic and we describe the dynamics of the wave in the random phase approximation (RPA).

Motivation for a Global Approach to LHCD

Up to now, combined ray-tracing and Fokker-Planck codes have provided a fairly good description of LHCD if the waves are followed after one or a few reflections at the plasma edge and if the suprathermal electrons are allowed to diffuse towards the plasma core before slowing down[1]. In fact, because the absorption is based on the resonant interaction between the waves and the fast electrons the plasma is generally transparent to the highest phase velocity waves which are launched. This is usually referred to as the problem of the LH spectral gap.

If the wave is decomposed on the usual $\exp(-j\omega t + jn\phi + jm\theta)$ harmonic cylindrical basis, the local wave vector is given by:

$$k_{\|}(r) = (n + \frac{m}{q(r)})/R \qquad (1)$$

where $q(r)$ is the cylindrical safety factor. Under the condition $n\varepsilon >> 1$, where ε is the inverse aspect ratio of the tokamak, ray-tracing predicts a large increase in the poloidal mode number m which entails a significant upshift of the wave vector $k_{\|}$. However there are some drawbacks in using the geometrical optics for waves which are propagating over multiple passes through the plasma column. Such an approach is unable to take into account the spreading of wavepackets and therefore applies only during a characteristic correlation time of the wave. In our work we show how, due to toroidal effects, a stochastic instability appears[2], which leads to an exponential divergence of the rays and to the destruction of the correlations. The long time dynamics of the wave energy U(m) will be described as a random walk in m space[3]. Then the solution of the associated master equation can predict the steady state distribution U(m) and, via (1), the local and spectral power and current deposition, which are the crucial parameters for profile control experiments.

Resonant Toroidal Couplings

Our starting point is a modal analysis of the electric field $\bar{E}$ on a cylindrical basis:

$$\bar{E}(\bar{r},\omega) = \sum_{l,m,n} a_{lmn}(\omega)\ \bar{E}_{lmn}(\bar{r}) \qquad (2)$$

where l,m,n are the radial, poloidal and toroidal mode numbers related by the unperturbed cylindrical dispersion relation $D(\omega,l,m,n) = 0$. Fig 1 shows such a dispersion curve (f = 3.7 GHz, n = const) for the electrostatic branch and typical JET parameters. Toroidal effects induce couplings between the (l,m,n) modes and Maxwell equations can be written:

$$\frac{d}{dt}\, a_{lmn}(t) = - j\omega_{lmn}\, a_{lmn}(t) - j \sum_{l',m',n} V_{lmn}^{l'm'n'}\ a_{l'm'n'}(t) \qquad (3)$$

where $V_{lmn}^{l'm'n'}$'s are matrix elements of the toroidal perturbation, ie proportional to $\varepsilon^{|m-m'|}$. We are thus led to consider a system of coupled oscillators.

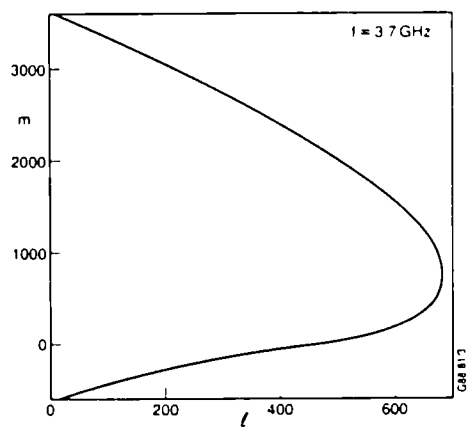

Fig 1: Dispersion Curve

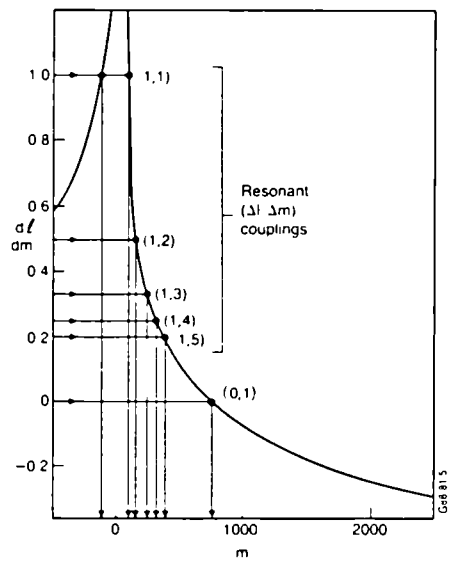

Fig 2: Resonant Couplings

Because the perturbation is stationary, toroidal couplings will be resonant when they couple modes which lie on the unperturbed dispersion curve, ie which correspond to the same eigenfrequency ($\omega_{l'm'n'} = \omega_{lmn}$). This will occur when the vector ($\Delta l = l-l'$, $\Delta m = m-m'$) is tangent to the dispersion curve, ie when the slope of the curve is rational:

$$\left(\frac{\partial l}{\partial m}\right)_{\omega} = \frac{\Delta l}{\Delta m} = \text{rational number} \qquad (4)$$

Fig 2 displays this set of resonances. We expect the dynamics of system (3) to be dominated by the resonant couplings and we are therefore tempted to apply the random phase approximation and to write a master equation for the wave energy $U(m) \alpha a_{lmn} \cdot a^{*}_{lmn}$ with n = const and $l = l(\omega,n,m)$:

$$\frac{dU(m)}{dt} = \sum_{m'} P(m' \to m)\, U(m') - \sum_{m'} P(m \to m')\, U(m) \qquad (5)$$

If the transitions took place in a continuum of states, the transition probabilities $P(m \overset{+}{\div} m')$ would be proportional to $\left|V^{lmn}_{l'm'n'}\right|^2$. So we must find out how to compute the resonant matrix elements. A second conceptual question also arises: under which conditions is the random phase approximation justified and what is the connection between $P(m \overset{+}{\div} m')$ and $V^{lmn}_{l'm'n'}$ in the actual problem?

Wave Stochasticity and Criterion for Random Phase Approximation (RPA)

To make progress concerning these questions, we go back to the standard ray-tracing and express it in terms of canonical action-angle variables of the cylindrical geometry, using the hamiltonian character of ray equations. Poincaré surface of section plots in the (θ,m) plane are shown in Figs 3, 4 and 5 for various increasing inverse aspect ratios.

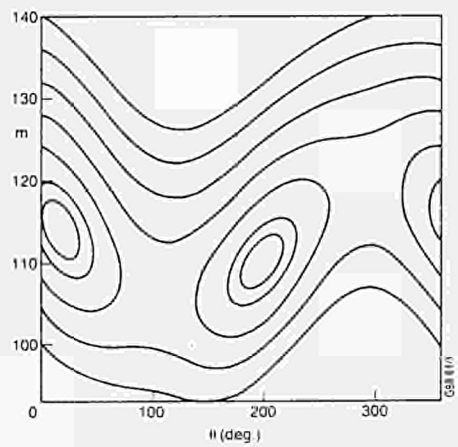

Fig 3: $r = r_o$ surface of section ($\varepsilon = 0.015$)

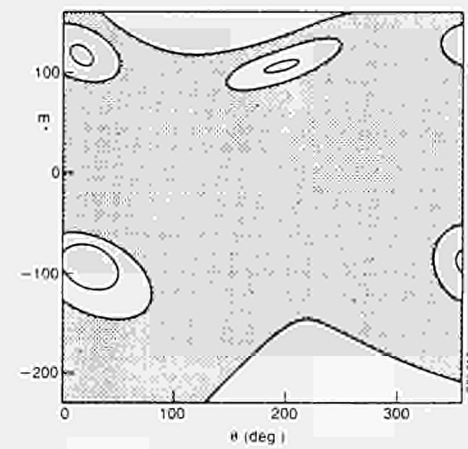

Fig 4: $r = r_o$ surface of section ($\varepsilon = 0.05$)

In Fig 3, ε is chosen sufficiently small (1.5×10^{-2}) to exhibit the island structure of phase space. The link between the ray and wave approaches yields the following relationship between the island width and the corresponding resonant matrix element:

$$\Delta m_{island} = 4\,\Delta m_{coupling} \cdot \left[\frac{2\left|V^{lmn}_{l'm'n'}\right|}{\omega''_{res}}\right]^{1/2} \qquad (6)$$

where ω''_{res} contains second derivatives of the dispersion relation. A successful check of this relation is shown in Fig 6 where we plotted the island width vs ε for various resonances and thus verified that $V^{lmn}_{l'm'n'}$ is proportional to $\varepsilon^{|m-m'|}$. For large values of ε, island overlapping leads to global stochasticity as shown in Fig 4 ($\varepsilon = 5 \times 10^{-2}$) and in Fig 5 ($\varepsilon = 0.3$). In the stochastic regime, it can be argued that the correlations are sufficiently weak to justify the use of the RPA in system(3), thus leading to (5). $P(m \overset{+}{\div} m')$ may then be deduced from quasi-linear theory $\left(P(m \overset{+}{\div} m') \cdot \Delta m^2_{coupling} = \omega_{bounce} \cdot \Delta m^2_{island}\right)$, which means that the diffusion of m scales as:

$$P(m \overset{+}{\div} m') \approx \left|V^{lmn}_{l'm'n'}\right| \cdot \frac{\Delta m_{island}}{\Delta m_{coupling}} \qquad (7)$$

To which extent the onset of global stochasticity is sufficient for applying the RPA on the "quantum" description of the mode couplings(3) is a fundamental question which will be the subject of future work.

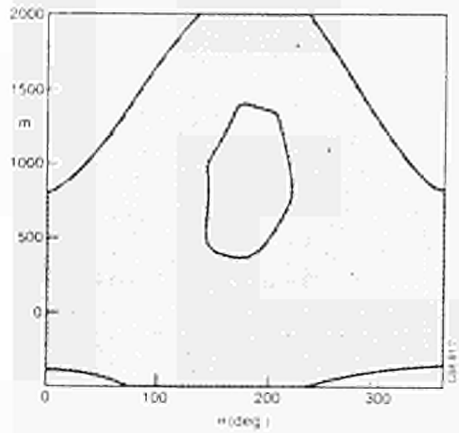

Fig 5: $r = r_o$ surface of section ($\varepsilon = 0.3$)

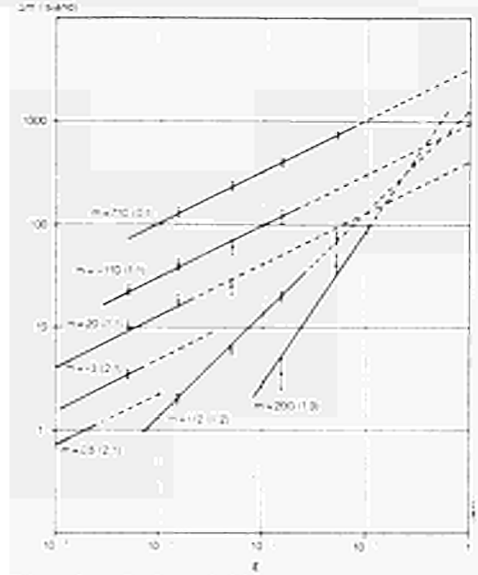

Fig 6: Island Width Versus ε

Conclusion

We propose a global stochastic description of lower hybrid wave propagation and power deposition in tokamaks. When the absorption rate $\gamma(m)$ of each unperturbed mode is included as a sink in system(5) a steady state solution can be found in the presence of a source at m - 0. Fig 7 shows that the absorbed power spectrum can be much broader and even very distinct from the launched spectrum when the so-called "spectral gap" has to be bridged by means of the stochastic diffusion. Finally, each $\gamma(m)$ has a radial distribution from which the total power deposition and driven current profiles are calculated.

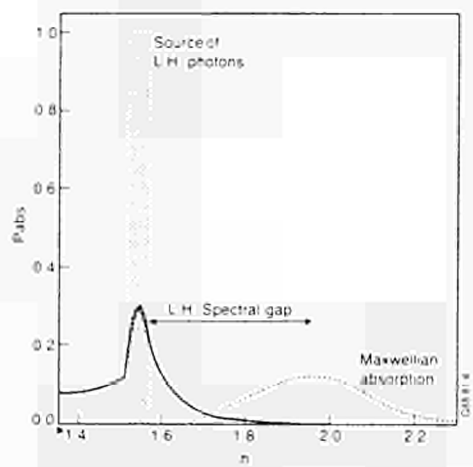

Fig 7: Thermal (...) and Non-thermal (—) absorption

References

1) P.Bonoli, 7th Topical conf. on Appl. of RF Power to Plasmas, Kissimmee p.85 (1987)
2) J.M.Wersinger, E.Ott and J.M.Finn, Phys. Fluids 21 (1978) 2263
3) S.V.Neudachin, V.V.Parail, G.V. Pereverzev, R.V.Shurygin, 12th Eur. conf. on Cont. Fus. and Plasma Phys., Budapest, Part II p.212 (1985)

ROLE OF ANTENNA SCREEN ANGLE DURING ICRF HEATING EXPERIMENTS IN JET

M Bures, V Bhatnagar, S Corti, G Devillers[1], B Denne, M Forest[2], T Hellsten, J Jacquinot, D Start

JET Joint Undertaking, Abingdon, Oxfordshire, OX14 3EA, England

[1] Attached from University of Grenoble, France
[2] EURATOM/UKAEA Association, Culham Laboratory

Introduction

To eliminate the excitation of the $\tilde{E}_{\parallel}$ component of RF field, the screen elements of JET antennae were installed at an angle of 15° with respect to the toroidal field. This implies that the elements are aligned with the magnetic field during the discharges with B_ϕ = 3.4 T and I_p = 5 MA for which the design was optimised. To test the effects of the magnetic field line direction at the plasma edge with respect to the antenna screen elements, some RF heating experiments were carried out with a reversed direction of toroidal field. Experiments were performed with the same target plasma conditions B_ϕ = 2.1 T, I_p = 2 MA, ^{3}He(H) heating scenario and density $\langle n \rangle = 1.7 - 1.8 \times 10^{19}$ m^{-3}. The antennae were phased as monopoles with $K_{\parallel}$ spectrum peaked at $K_{\parallel} = 0$ m^{-1}. A few discharges in the reversed field condition were run at somewhat higher field B_ϕ = 2.25 T.

Coupling Resistance and the Plasma Edge Parameters

In the reversed field case the coupling resistance R_c is typically 30 % lower as plotted in Fig 1. Also the time evolution is different. In the normal case, the coupling resistance is strongly modulated by the radial eigenmodes of the magneto-acoustic (MA) wave. Eigenmodes result from the density increase caused by the RF enhanced neutral gas and impurity influx. In the reversed field case, the eigenmode activity is less evident, despite the density increase as a function of power being the same. The plasma edge density and temperature were measured by the Langmuir probes placed in the protection tile of the RF antenna. There is evidence that the average value (integrated over the RF pulse) of density in front of the antenna screen increases from 2 x 10^{18} m^{-3} to 4 x 10^{18} m-3 in both cases. Also temperature increases from 15 eV to 50 eV in the normal case. The measurements suggest that in the reversed field case, the temperature profile flattens and the increase of temperature in front of screen is lower.

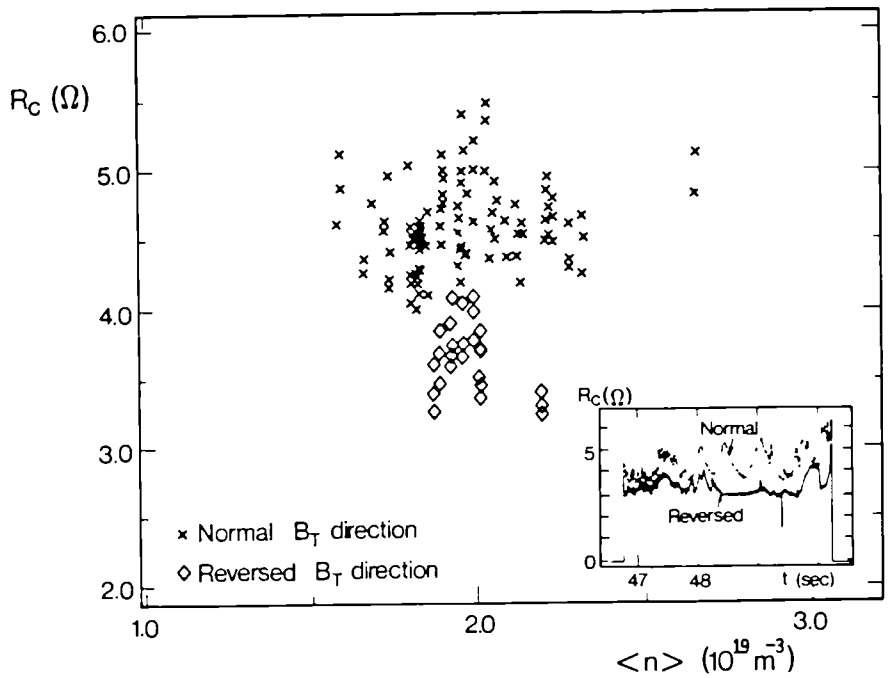

Fig 1: The coupling resistance as a function of average density. In the inset is plotted its time evolution.

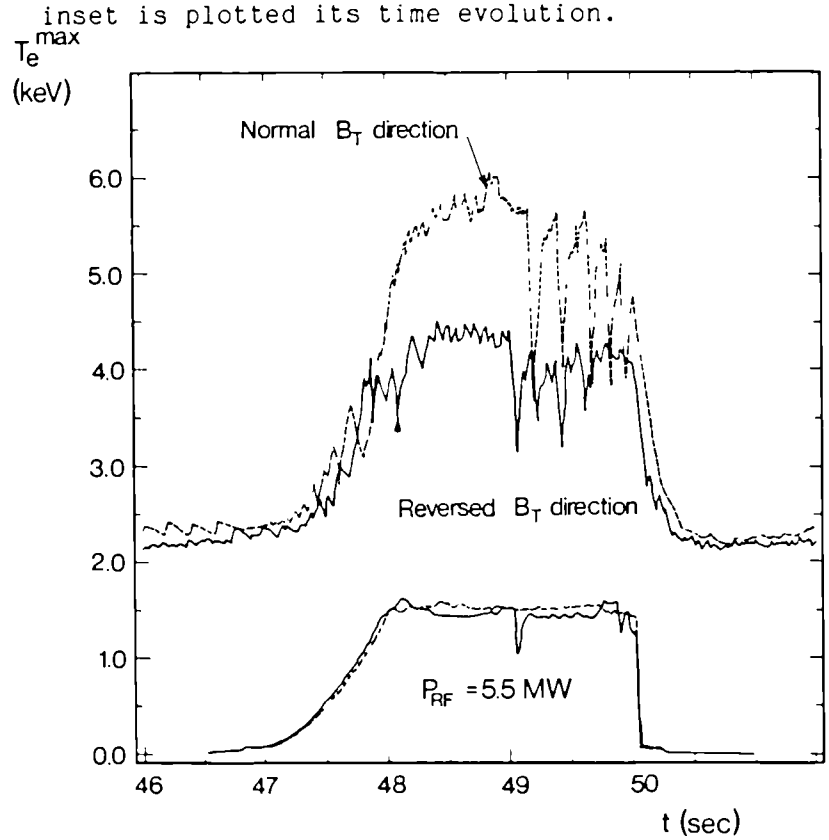

Fig 2: The time evolution of central electron temperature together with the trace of total RF power.

Heating Efficiency

In both cases the minority cyclotron layer was placed in the centre of the plasma. A number of significant differences in heating efficiency was observed. In the reversed field case:

a) The rate of increase of $T_e(0)$ and $< T_e >$ with $P_{RF}/< n >$ was 30 % lower. The example of $T_e(0)$ time evolution is plotted in Fig 2. "Monster" sawtooth phenomenon should be noticed.

b) The energy increase as a function of applied power can be characterised by the incremental confinement time $\tau_{INC} = \Delta W/(P_{RF} - \Delta P\Omega) = 0.16$ sec which is lower by 30 % than in the normal case (Fig 3). The plasma stored energy is derived from the electron temperature profile, ion temperature of plasma centre, density profile and Zeff. The same difference of 30 % is obtained from magnetic measurement.

c) The ion temperature increase measured by x-ray spectroscopy indicates no substantial difference in ion heating. Electron temperature profile does not show any particular feature in either case. Also the neutral hydrogen spectrum does not indicate any substantial difference in formation of an energetic hydrogen minority tail. The deuterium fast tail is starting to form due to the second harmonic minority heating in both cases.

Neutral and Impurtiy Influxes

When the RF power is applied, the density increases. The radiation power increases roughly linearly with density but somewhat faster in the reversed field case. The ratio P_{rad}/P_{TOT} versus P_{TOT} is plotted in Fig 4. The higher radiated fraction can be correlated to the enhanced

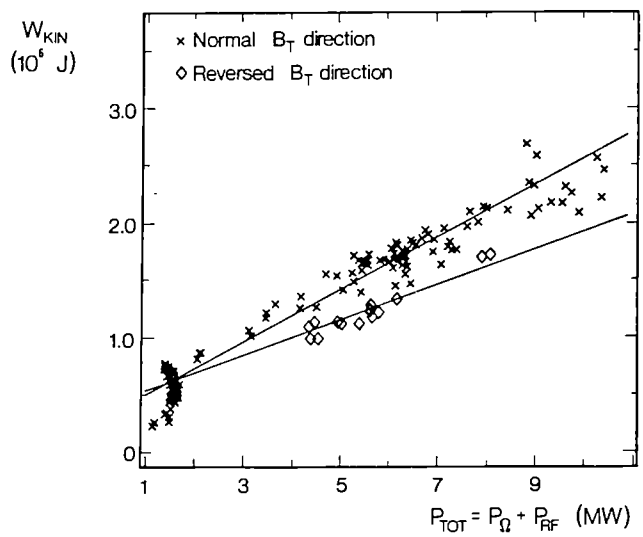

Fig 3: Plasma stored energy as a function of total power input

influx of metals, mainly the nickel. In Fig 5 the intensity of NiXXV line normalised to density is plotted versus the power input. It represents the number of nickel ions along the line of sight. Also the intensities of oxygen OV and carbon CIV lines differ in the 2 cases. Intensity of the oxygen line is higher roughly by factor 2 in the reversed field case, while the CIV intensity is lower. This might be correlated to lower deuterium influxes as measured by D_α emission recorded along the line of sight intercepting the limiters. No difference is observed monitoring the HeI line.

Conclusions

A clear difference in the impurity influxes as well as the heating efficiency was observed between the discharges with normal and reversed direction of the toroidal field. Also, the coupling resistance differs substantially. The results indicate that the coupling to MA wave respectively to slow wave is different in the 2 cases. The parallel component of the RF electric field is minimised when the screen elements are aligned along the magnetic field.

Acknowledgements

We wish to thank our colleagues in the JET team, especially the tokamak operating teams and those operating the diagnostics used in the experiments reported in this paper.

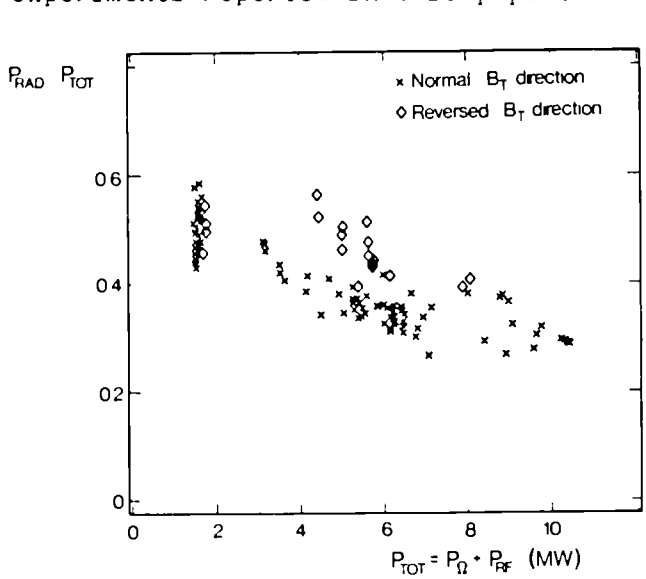

Fig 4: Fraction of radiated power as a function of total power input

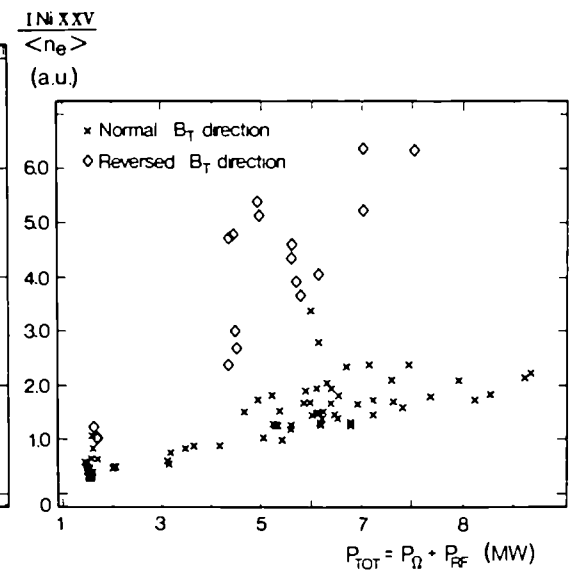

Fig 5: Measure of nickel ion density as a function of total power

IDENTIFICATION OF RADIAL AND TOROIDAL EIGENMODES IN THE COUPLING OF THE WELL DEFINED $k_{\|}$ SPECTRUM OF THE NEW JET ICRH ANTENNAS

A L McCarthy[1], V P Bhatnagar, M Bures, P L Colestock[2], M P Evrard[3], J M Gahl[4], T Hellsten, J Jacquinot, S Knowlton[5], D F H Start

JET Joint Undertaking, Abingdon, Oxfordshire, OX14 3EA, England

[1] Flinders University, Bedford Park 5042, South Australia
[2] Princeton Plasma Physics Laboratory, New Jersey, USA
[3] LPP-ERM/KMS; EUR-EB Association, 1040 Brussels, Belgium
[4] Texas Technical University, Lubbock, Texas 79409, USA
[5] Massachusetts Institute of Technology, Cambridge, Mass 02139, USA

Introduction

JET discharges heated with the new, wider antennas whose currents have a particularly well defined Fourier transform in $k_{\|}$, show a series of peaks in the coupling resistance when the monopole phasing is used. These peaks which we shall see to be characteristic of the excitation of eigenmodes [1,2] are particularly clearly seen in Fig 1a for which the magnetic field was ramped, and in Fig 2 in which the plasma density evolved linearly. In the monopole phasing the excited spectrum is peaked at $k_{\|} = 0\,m^{-1}$ and has half width $4\ m^{-1}$. For the dipole phasing, the maximum power is radiated at $k_{\|} = 7\ m^{-1}$ and the strength is zero at $k_{\|} = 0\ m^{-1}$. In the dipole configuration, variations of the coupling resistance are very much reduced, see Fig 1b.

By comparing predictions of a slab model with the analysis of the data for the spacings of the onset of these peaks, we make the first detailed and unambiguous identification of radial eigenmodes which are excited when low toroidal mode number fast waves are resonantly reflected between the ion-ion-hybrid cut-off layer and the antenna. We have developed an understanding of the asymmetry of the peaks in coupling resistance; we have modelled the peak-to-valley ratios for the coupling resistance; and we have shown why the variations of coupling resistance are very much reduced when the dipole phasing is used. Further, we have examined the data to gauge the effects of eigenmode excitation during high power ICRH heating.

The Slab Model

The plasma is treated as a slab between the antenna and the ion-ion-hybrid cut-off layer, having thickness d. In JET the poloidal length of the antenna is large compared to the width L_o, and we assume $k_y = 0$. All poloidal variations (y) are neglected.

The fast wave dispersion relation: $k_x^2 = k_o^2 S - k_z^2 - \dfrac{k_o^4 D^2}{k_o^2 S - k_z^2}$ applied to the slab can be considered in a manner analogous to that used by Stix [3] to identify and track the eigenmodes of the system; k_x, k_z and k_o refer to radial, toroidal and free space propagation. S and D are the usual sum and difference terms of the dielectric tensor.

The electric field at the antenna placed just outside the fast wave cut off layer is the sum of the incident wave E_y from the antenna, plus the multiply reflected waves, attenuated by α and phase shifted by β each transit around and across the toroidal slab to give:

$$E_{y\ \text{antenna}} = E_y \frac{1 + e^{-\alpha + i\beta}}{1 - e^{-\alpha + i\beta}}$$

In the full computation the attentuation α is determined by a mode conversion algorithm (Colestock and Kashuba [4]) dependent on the minority concentration and temperature.

The power P, delivered by the antenna may be written in terms of the antenna current I_o and this E field. Using , the antenna Fourier spectrum and $\tilde{E}_y$ the Fourier transform of E_y, the coupling resistance R_c is then written:

$$R_c = \frac{2P}{I_o^2} = \frac{1}{I_o^2}\ R_e \left\{ \frac{I_o^*}{2\pi L_o} \int_{-\infty}^{\infty} dk_z\ \varphi\ \tilde{E}_y\ \frac{1 + e^{-\alpha + i\beta}}{1 - e^{-\alpha + i\beta}} \right\}$$

For $\alpha << 1$, as expected near $k_z = o$, and nearly radial propagation, $\beta \sim 2\ k_x d$. When $k_x d = n\pi$, the last factor of the integrand is $\frac{2}{\alpha}$ giving an enhanced real contribution. When $k_x d \neq n\pi$, the last factor is $i\cot \beta/2$ and the contribution is imaginary.

For α large, as expected for large k_z, the integral is unchanged from the single pass model.

These resonant contributions with $k_x d = n\pi$ will be referred to as "poles" and they define the radial eigenmodes.

Contributions occurring for values of k_x having corresponding values of k_z with large values of the Fourier transform of the antenna current can make dominating resonant contributions to the coupling resistance.

Because the k_z value associated with these strong resonant contributions changes as the plasma parameters evolve in time, the power absorption spectrum in k_z varies in time and does not have the same shape as the Fourier transform of the antenna current. For monopole phasing, as k_z approaches zero, the antenna output increases (because of the Fourier transform of the antenna current and reduced attenuation while tunnelling from the antenna to the plasma), and reflectivity increases. Thus, we get the highest contributions to R_c, ie eigenmode onsets when the density and magnetic field are set to values which access a radial eigenmode with toroidal mode number $n_\varphi = 0$.

If now the plasma parameters are changed so that, eg the Alfvén velocity is reduced, the dispersion relation between k_x and k_z ensures that eigenmodes with successively higher toroidal mode numbers are accessed in order. Each of these higher k_z modes has decreasing reflectivity, and the antenna output in the monopole phasing decreases with n_φ so we obtain a decreasing coupling resistance giving the asymmetry typical of the peaks in the data presented in Figs 1a and 2a.

For the dipole phasing there is a zero antenna output with $n_\varphi = 0$ so that poles at small n_φ cannot contribute significantly to the coupling resistance. For larger values of n_φ, changes of the antenna output are small and no variations of the the mean coupling resistance are expected. Only small variations of the coupling resistance are seen because of the stronger absorption.

Results and Discussion:

The Alfvén speed varies with both magnetic field $\underline{B}$ and density. When $\underline{B}$ changes the position of the ion-ion-hybrid, cut-off layer changes, effectively changing the slab thickness. In addition, in high power ICRH heating pulses, changes in Z-effective change the mass density. These points are all taken into account, where appropriate in calculating changes to the optical path length. The spacings of the onsets of the eigenmodes seen in the data of Figs 1a and 2a are then found to correspond very well to changes of the optical path length by λ. In Fig 2d the slope of $\frac{k_x\ d}{\pi}$ against radial mode number is close to one.

To fit the peak-to-valley ratios and shapes of the peaks in the coupling resistance data, the minority concentration is varied at known temperature in the mode conversion algorithm. For the data of Fig 1a, the best fit (Fig 1d) was obtained with 20 % hydrogen minority ion concentration, a value close to that measured via charge exchange.

In Fig 5 an individual eigenmode was tracked. The electron temperature was among the highest with the level of RF power used (10 MW), even though during the peak temperature, the high coupling resistance is evidence of a high reflection coefficient and thus low absorption of energy per pass. The electron temperature profile conformed to those normally observed both in the valley at 51.4 s and near the peak, eg at 51.83 s. Stored energy and C III impurity radiation intensity are not dependent on the excitation of eigenmodes.

In a pulse not shown, 12 MW of RF power produces T_e = 9.5 keV and T_i = 8.0 keV at times when there is eigenmode excitation. But the peak-to-valley ratio is very small at these high temperatures so throughout almost the whole range of k_z there must be high absorption per pass.

In dipole phasing the variations of coupling resistance are much reduced compared with monopole phasing particularly when using hydrogen minority species heating, even when dramatic changes of density and temperature occur, eg during pellet injection.

Sawtooth-free periods are achieved both with monopole phasing in which eigenmode excitation is observed and also with dipole phasing, so that no special effects are attributable to eigenmodes in this regard.

Conclusions

Though there are in some cases large excursions of the coupling resistance, the excellent ICRH heating results obtained with the new antennas installed in 1987 are important evidence that the existence of eigenmodes does not cause problems in the physics of ICRH heating at these high temperatures, and that technical problems which eigenmodes might cause through large variations of the coupling resistance are reduced at high temperatures. The data presented is all for hydrogen minority species heating; He^3 minority species heating gives a more complicated set of coupling resistance peaks which we have not modelled.

We acknowledge with pleasure the contributions of the JET RF Division technical teams and the JET operating teams.

References

[1] Lapierre, Y., J, Plasma Phys 29 223(1983)
[2] Hellsten, T., and Appert, K., 13th EPS Conf. Schliersee V2 129(1986)
[3] Stix, T.H., Nucl. Fusion 15 737 (1975)
[4] Colestock, P.L., and Kashuba, R.J., Nucl. Fusion 23 763(1983)

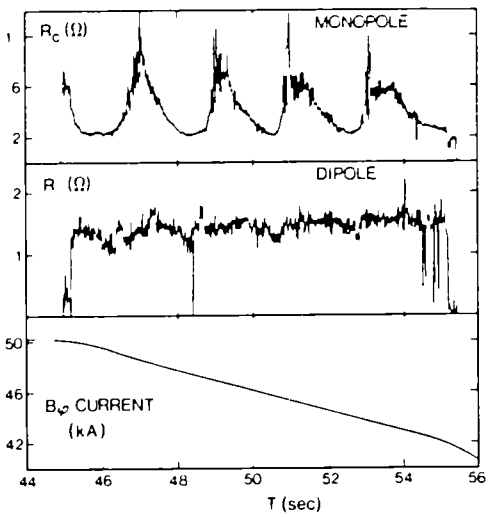

Fig 1: Eigenmodes: B_φ ramp
(a) Monopole, (b) Dipole
(c) B_φ Current
(d) Detailed Fitting

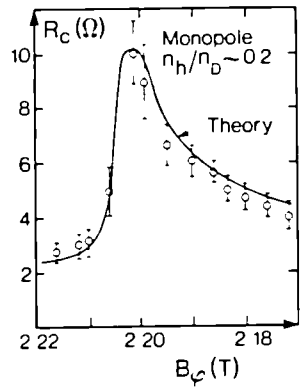

(d)

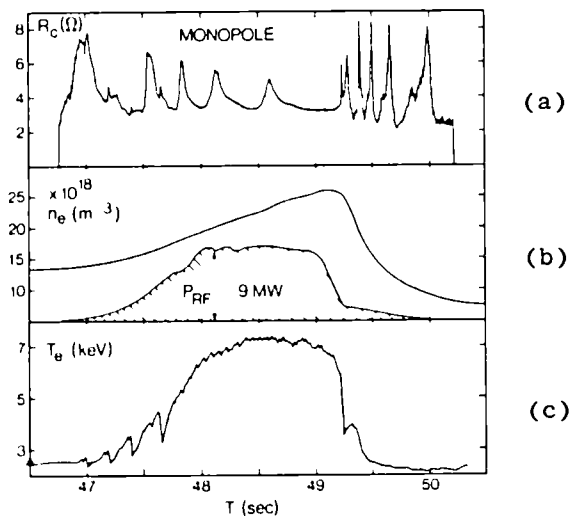

Fig 2: Eigenmodes: n_e ramp
(a) Monopole (b) n_e
(c) T_e
(d) Spacing of onsets

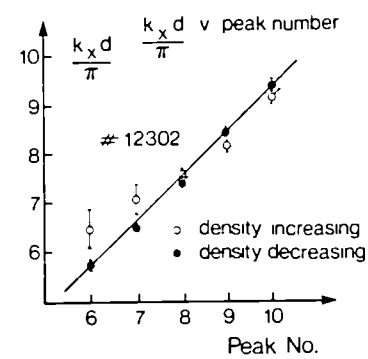

(d)

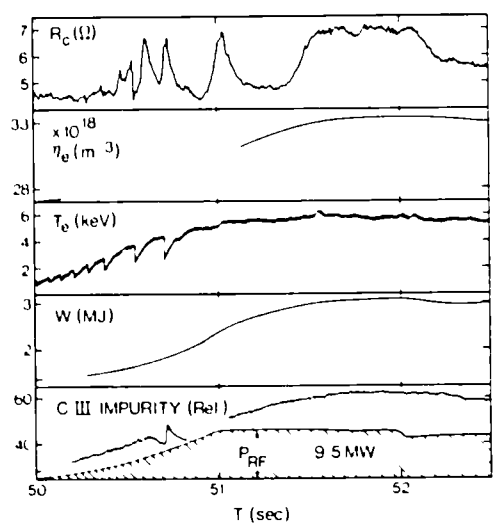

Fig 3: Eigenmodes during high power heating
T_e, Energy, Impurity, Profiles

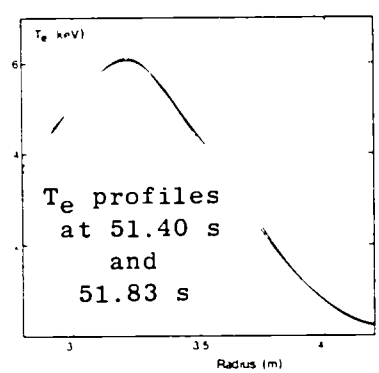

STUDY OF ICRF DRIVEN FUSION REACTIVITY

G.A.Cottrell, G.Sadler, P.van Belle, D.J.Campbell, J.G.Cordey, W.Core, T.Hellsten, J.Jacquinot, S.Kissel, D.F.H.Start, P.R.Thomas and J.Wesson
JET Joint Undertaking
Abingdon, Oxfordshire, OX14 3EA, England

1. INTRODUCTION AND EXPERIMENTS

A series of experiments is currently in progress on JET to study and optimise ICRF–driven fusion reactions between the highly energetic ^{3}He minority ions and the thermal deuterons during central high power RF heating at $\omega=\omega_c(^3\mathrm{He})$. The reaction rate in the tail was monitored by measuring the flux of 16.6 MeV γ–ray photons from the D[^{3}He,γ] ^{5}Li reaction[3,7]. With a coupled RF power to the plasma of 11.5 MW, the fusion yield so far achieved (in charged particle fusion products) is P_{fus}= 50 kW, giving a Q–value of $\simeq$ 0.5%, the highest achieved so far in a tokamak. Because of the strong non–linear variation of reactivity with RF power density, it has been possible to derive the effective RF power deposition radius in the plasma by data fitting. The value derived, r_d = 0.3 m, is close to that obtained from RF modulation experiments[1] as well as predictions by a full wave code.

Up to 11.5 MW of ICRH power was coupled to the plasma in the (^{3}He)D regime with plasma current: I_p= 2 MA–5 MA, toroidal field: B_φ=3.4 T, electron density: $\bar{n}_e$=(2–4) × 10^{19}m^{-3}, minority concentration: (1.6% $\leq \eta \{\equiv n(^3He)/n_e\} \leq$ 8.0%), and f_{rf} = (32–35) MHz giving central heating with the resonance located within 0.1 m of the magnetic axis. The ^{3}He was injected into the target D discharge at t = 1 sec before the application of the 3–5 second RF heating pulse. In discharges with $P_{rf} \geq$ 5 MW, long duration sawtooth–free periods ($\tau_{st} \leq$ 3 s) were routinely obtained[2]. In other cases, normal sawtoothing behaviour was observed. The D[^{3}He,γ] ^{5}Li (16.6 MeV) reaction cross–section is $\simeq 10^{-5}$ of that of the charged particle fusion

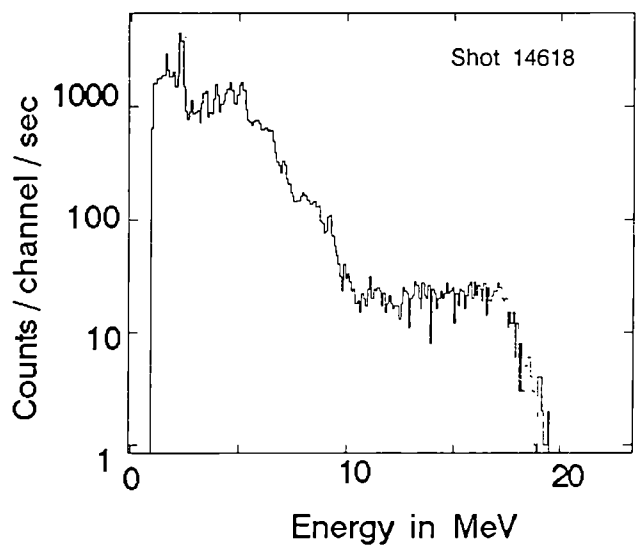

Figure 1.
Typical γ–ray energy spectrum observed during ICRH heating in the (^{3}He)D regime. Plasma parameters: I_p= 2 MA, B_ϕ = 3.4 T, $\bar{n}_e$=2.5 × 10^{19} m^{-3}, P_{rf}=9.8 MW, η=2%, Z_{eff}=2. The 16.6 MeV γ–yield is equivalent to 30 kW of fusion power in this case.

cross–section in the range 0–1 MeV. The 16.6 MeV γ–flux was measured using calibrated NaI and BGO scintillation detectors[3]. A typical γ–ray energy spectrum with RF heating is shown in Figure 1. The shape of the spectrum at $E_\gamma \geq 10$ MeV is caused by the natural line width (1.5 MeV), the instrumental resolution, and the existence of a second line at $E_\gamma = 13.5$ MeV[3]. Below 10 MeV, the γ–ray emission originates from $^3He \rightarrow C$ reactions[7]. The variation of γ–ray count rate with RF power is shown in Figure 2 for a number of discharges. Within the present range of JET parameters, the γ–yield varies as $N_\gamma \alpha P_{rf}^{5/3}$, implying that $Q_{rf} \alpha P_{rf}^{2/3}$.

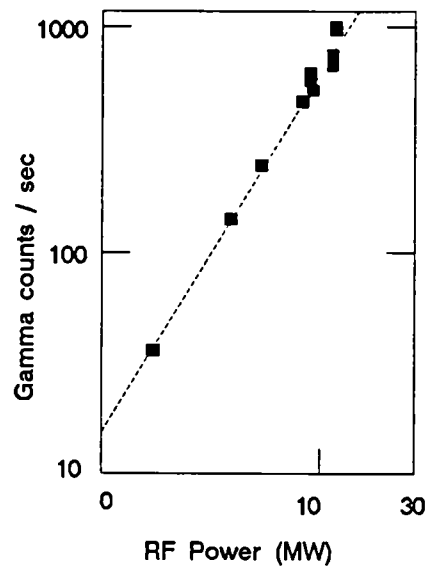

Figure 2.

Variation of γ–ray count rate from $D \rightarrow {}^3He$ reactions in the energy range (12–20) MeV with RF power for a number of discharges. Plasma parameters: I_p=(2–4) MA, B_ϕ=(3.2–3.4) T, η=(2–4)%. The highest count rate observed corresponds to 50 kW of fusion power.

2. THE MODEL AND METHOD OF ANALYSIS

The ICRH–driven minority tail was simulated using the steady–state, isotropic Stix formulation[4]. The minority velocity distribution function, $f(v)$, was calculated up to a maximum energy of 10 MeV ($\equiv mv_m^2/2$), beyond which orbit losses are expected to be important for the present range of plasma current in in JET and contributions to the reaction rate are in any case small. The local ^3He–D reaction rate was then calculated;

$$R(^3He\text{–}D) = 4\pi n_d \int_0^{v_m} v^2 dv\, f(v)\, \sigma(v)$$

where $\sigma(v)$ was taken as the Asher–Peres nuclear cross–section[5], and n_d is the deuterium density. The plasma model contained an admixture of three ionic species, D, ^3He, and an impurity assumed to be carbon with concentrations of the ion species adjusted initially to equate the model Z_{eff} with the experimental value (derived from measurements of the visible bremmstrahlung).

In applying the model to the experimental data, there were two main uncertainties. Firstly, there was no direct measurement of the absolute density of the minority ions. Therefore, in the present analysis, it was assumed that the the helium inventory (measured using the observed density increase at the time that helium was

injected into the discharge) was subsequently conserved and, moreover, was everywhere proportional to the plasma electron density. Secondly, there was no direct measurement of the RF power density. However it was possible to use the present γ–ray data to obtain an independent estimate of this quantity. The model was calibrated by assuming that a fraction, μ, of the total RF power coupled to the plasma was coupled to the minority ions within some plasma deposition volume, V_d. The remaining fraction $(1-\mu)$ was attributed to possible mode conversion, ion cyclotron and Landau damping and transit–time magnetic pumping. Analysis of the results of RF modulation[1], fast ion energy content with ICRF heating[6] as well as the results of full wave ICRF predictions, suggest that $\mu \cong 0.75$, a value which we use. The effective volume averaged electron temperature used in the model was 0.67 of the central value, a factor needed to bring measurements and predictions of the of the fast ion energy content in ICRF heated discharges into agreement[6].

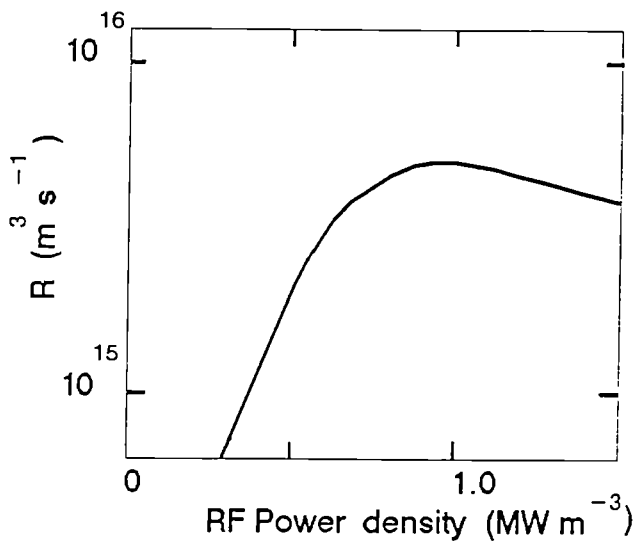

Figure 3.
Calculated ICRF–driven fusion reactivity shown as a function of RF power density for the typical JET parameters: $\overline{n}_e = 3 \times 10^{19} m^{-3}$, *volume–averaged temperatures* $\langle Te \rangle = \langle Ti \rangle = 4.5$ *keV,* $\eta = 4\%$ *and* $Z_{eff} = 2$.

A plot of the calculated local fusion reactivity as a function of RF power density is shown in Figure 3 for a typical set of JET parameters. The curve shows a characteristically steep rise in reactivity for RF power densities up to a threshold of approximately 1 MW m^{-3}, and thereafter a saturation. This behaviour is a consequence of the quasi–Maxwellian tail folded with the fusion cross–section which increases strongly with energy up to a maximum (at $E \cong 0.5$ MeV) and thereafter decreases. The integrated reactivity can also be seen to decrease at the highest RF power densities where too large a fraction of ^{3}He ions now appears in the far tail ($E \geq 0.5$ MeV). Because the JET γ–ray data spans a considerable range in RF power density, it was possible to calibrate the model (assuming V_d to be independent of RF power) using the measured relative fusion reactivities for a number of discharges with different RF powers. This makes use, in effect, of the strong variation and saturation shown in Figure 3. By minimising χ^2 with respect to the unknown deposition volume, a value $V_d = 6$ m^3 was obtained, equivalent to an effective deposition radius of $r_d = 0.3$ m.

This value is consistent with the <Te> taken in the fast ion energy analysis and is close to that obtained from analyses of RF modulation experiments. It was adopted in the model to compare measured and predicted values of the fusion power shown in Figure 4, where the code was run for the individual plasma parameters relevant to each discharge. It can be seen that reasonably good agreement was obtained between the experiments and the modelled fusion yields.

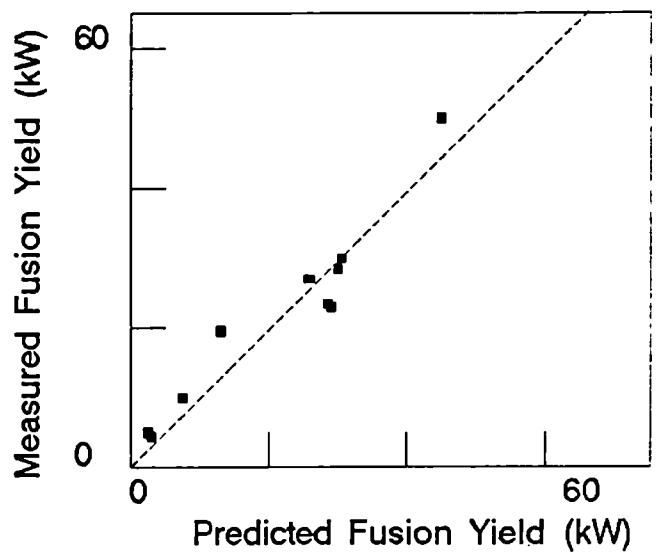

Figure 4.
Comparison of measured and calculated ICRF–driven fusion yields from (^{3}He)D nuclear reactions. The calculated yields are based on the isotropic Stix model as described in the text with plasma parameters relevant to each separate discharge in the diagram.

3. CONCLUSIONS

In experiments currently under way on JET to study the ^{3}He→ D ICRF–driven fusion reactivity, an effective $Q_{rf} \cong 0.5\%$ has been achieved with the application of 11.5 MW of ICRH heating power to the plasma. The variation of Q_{rf} during systematic scans of plasma parameters has enabled the calibration of a simple Stix model and will be useful in the future to validate more comprehensive codes in the prediction of non–thermal fusion yields based, for example, on fundamental heating of deuterium in tritium.

REFERENCES

1. Evrard, M. et al (this conference)
2. Campbell, D. et al (this conference)
3. Sadler, G., Jarvis, O.N., van Belle, P. Proc. 14th EPS Conference on Controlled Fusion and Plasma Physics, Madrid, Spain. 11D(III), 1232–1235, (1987)
4. Stix, T.H., Nuclear Fusion, 15, 737–754, (1975)
5. Asher–Peres, J.Appl.Phys., 50(9), 5569–5571, (1979).
6. Cordey, J.G., (private communication)
7. Sadler, G.,Jarvis, O.N.,van Belle, P., Adams, M. (this conference)

RESONANT ION DIFFUSION IN ICRF HEATED TOKAMAK PLASMAS

T. Hellsten and W. Core

JET Joint Undertaking, Abingdon, Oxon. OX14 3EA, UK.

1. Introduction. Wave induced particle transport occurs during ICRH of the resonating ion species due to absorption of the waves toroidal angular momentum [1,2]. For an asymmetric toroidal wave spectrum in which there is a direct input of wave toroidal angular momentum to the plasma, the resonating ions will undergo a radial drift across the magnetic flux surfaces. The direction of the radial drift will depend on the toroidal direction of the wave. For a symmetric spectrum the drift vanishes and only a diffusion term remains.

The diffusion increases with energy. In large tokamak plasmas with intense ICRF heating ions are heated up to the MeV range for which RF-diffusion becomes important.

The simultaneous diffusion in real and velocity space caused by the RF-field can lead to a pump out of particles from regions with high power densities, flattening of the heating profile and reduction of the average energy of the resonating ions. Further, space charges set up by the radial diffusion leads to a toroidal rotation of the plasma.

The diffusion problem has been studied by reducing it to a 2-D, time dependent diffusion equation, 1-D in velocity and 1-D in real space, which is solved by a modified version of the BACCHUS code [3].

2. The Reduced Diffusion Equation. As an ion resonates with the wave at the cyclotron resonance it will change its perpendicular and parallel velocity. An increase in the perpendicular velocity can lead to a transition from a passing orbit to a trapped orbit. For trapped particles the orbit width is increased. When the parallel velocity is changed for a trapped particle this leads to a radial displacement of the turning point in a direction depending on the sign of the parallel wave number [2]. To measure the particle transport in real space we represent the trapped particles by the minor radius of their turning points and passing particles by the minor radius where their drift orbit intersects the cyclotron resonance. We assume the wave spectrum to be symmetric so that the drift term vanishes. A diffusion equation in real and velocity space can then be obtained by adding the corresponding diffusion term in the quasi-linear RF-diffusion equation [4] yielding

$$\frac{\partial f}{\partial t} = C(f) + Q(f) + D(f) \qquad (1)$$

$$D = \frac{1}{r}\frac{\partial}{\partial r}\left(D_{RF}\, r \frac{\partial f}{\partial r}\right)$$

$$D_{RF}=\begin{cases}\dfrac{v_\perp^2}{\omega\,\omega_{ci}}\left(\dfrac{n_\varphi+\dfrac{m}{q}}{R_o}\right)^2\dfrac{\langle(\delta v_\perp)^2\rangle}{\tau_b} & \text{for trapped particles}\\ 0 & \text{for passing particles}\end{cases}$$

where C and Q are the quasilinear diffusion operators describing thermalisation due to Coulomb collisions and ion cyclotron heating, respectively. The perpendicular velocity at the cyclotron resonance is denoted by $v_\perp$, n_φ is the toroidal mode number, m the poloidal mode number, q the safety factor, R the major radius, r the minor radius, ω the wave frequency, ω_{ci} the cyclotron frequency, τ_b the bounce time for trapped particles and $\delta v_\perp$ the averaged increase in $v_\perp$ as the ion passes the cyclotron resonance. To obtain Eq.(1) we have assumed the cyclotron resonance to pass through the magnetic axis and that the poloidal cross-section of the magnetic surfaces are concentric circles. This time dependent, 3-D diffusion problem is rather difficult to solve. We wish therefore to reduce it further by integrating it over the pitch angle in the velocity space. To do so, we have to make an assumption of the anisotropy of the velocity distribution. By using various assumptions for the distribution function we can get upper and lower limits for the diffusion. A lower limit is obtained by assuming the distribution to be isotropic yielding a pitch angle averaged diffusion coefficient

$$D_1 = \left(\frac{\kappa m_i v}{B_o}\right)^2 \eta\,\frac{2P_M}{m_i n_i}\left[J_{n-1}^2\left(\frac{v\zeta k_\perp}{\omega_{ci}}\right)+\left|\frac{E_-}{E_+}\right|^2 J_{n+1}\left(\frac{v\zeta k_\perp}{\omega_{ci}}\right)\right]$$

$$\kappa = c(n_\varphi + m/q)/Ze\omega R \qquad (2)$$

where η is the ratio of the trapped particle intersecting the cyclotron resonance to the total number of particles, ζ is a characteristic pitch angle for trapped particles intersecting the cyclotron resonance, $k_\perp$ the perpendicular wave number, P_M the local power density for a Maxwellian velocity distribution in the absence of higher order finite gyroradius correction.

For intense ICRH the particles tend to become more trapped and the isotropic model will underestimate the number of trapped particles. An upper estimate of the diffusion can be obtained by assuming all particles to be trapped having orbits intersecting the cyclotron resonance which yields

$$D_2 = \left(\frac{\kappa m_i v}{B_o}\right)^2 \frac{2P_M}{m_i n_i}\left[J_{n-1}^2\left(\frac{vk_\perp}{\omega_{ci}}\right)+\left|\frac{E_-}{E_+}\right|^2 J_{n+1}^2\left(\frac{vk_\perp}{\omega_{ci}}\right)\right] \qquad (3)$$

A third more realistic model can be obtained by assuming the low energy ions to be isotropic and the high energy ions to be trapped ions. We assume the transition between these models to take place at the velocity V_γ [4,5] above which the pitch angle scattering becomes negligible. The following model for the diffusion coefficient can then be constructed

$$D_3 = g(v)\,D_2 \qquad (4)$$

$$g(v) = (1 - 3\bar{v}^2)(1 - a) + a$$

$$\bar{v}^2 = \frac{1 + (v/v^*)^2}{3(1 + (v/v^*)^2 + (v/v^*)^4)}$$

$$v^{*2} = 0.25\ V_\gamma^2$$

The form of $\bar{v}^2$ has been chosen such that $\langle v_{\parallel}^2 \rangle \approx \langle \bar{v}^2 v^2 \rangle$ where $\langle v_{\parallel}^2 \rangle$ is the averaged parallel velocity squared calculated with the BAFIC code [6].

3. Numerical Results. The effect of RF-induced diffusion on the velocity distribution models were calculated for the following scenario with these models: minority heating of H in a D-plasma at the fundamental cyclotron resonance $n_H(0)=3.5\times10^{11}cm^{-3}$, $n_D=3.5\times10^{13}cm^{-3}$, $n_i(r)=n(0)\ \exp(-0.5\ r^2)$, $T(r)=T_o\ \exp(-1.75\ r)$, $T_o=10$ keV, f=33 MHz and q(r)=const=1. The wave field is determined such that a Maxwellian velocity distribution should have in the zero gyroradius limit given rise to a flux surface averaged power density profile $P(r) = P_o \exp(-20\ r^2)$. For a large central power density and a long slowing down time the ions will near the centre diffuse to high energies. The high energy ions will then diffuse away from the centre to regions with lower wave fields and cool down there. They will then diffuse back again but now with a lower rate since their energy is reduced. This leads to a pump out of resonating ions from the central region. Fig.1 shows the evolution of the resonating ions on the magnetic axis for the various models. Fig.2 shows how the density profile evolves in time as calculated with model 3. Fig.3 shows the density profile at t = 1.5s for the various models. In the absence of neoclassical diffusion the density profile does not reach a steady state. On the long time scale the neoclassic diffusion have to be included which will reduce the density depletion. However, the velocity distribution normalized locally in space reach a steady state after about a slowing down time (1s). Fig.4 shows the averaged velocity squared for the various models compared to that in the absence of spatial diffusion, normalized to the velocity at r=0 before heating.

Acknowledgement. The authors are grateful to Drs. K. Appert, S. Succi and J. Vaclavik for providing the BACCHUS code which has been modified to solve the diffusion equations.

References

[1] Riyopoulos, S., Tajima, T., Hatori, T. and Pfirsch, D. Nucl. Fusion 26 (1986) 627.
[2] Chen, L., Vaclavik, J. and Hammett, G. PPPL-2441, Princeton University.
[3] Appert, K. et al., J. Proc. 11th European Conf. on Contr. Fusion and Plasma Physics, Aachen (1983) paper B29.
[4] Stix, T.H. Nucl. Fusion 15 (1975) 737.
[5] Anderson, D., Eriksson, L-G. and Lisak, M. Plasma Physics and Controlled Fusion 29 (1987) 891.
[6] Hellsten, T. et al., Proc. of 12th European Conf. on Contr. Fusion and Plasma Physics, Budapest (1985) Vol.II, p.124.

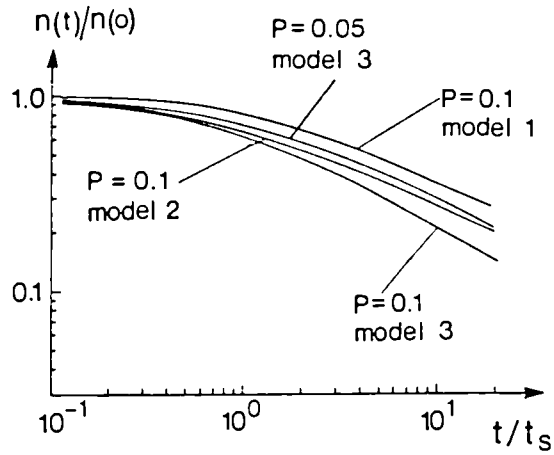

Fig. 1 Density on magnetic axis versus time. The slowing down time t_s = 1s.

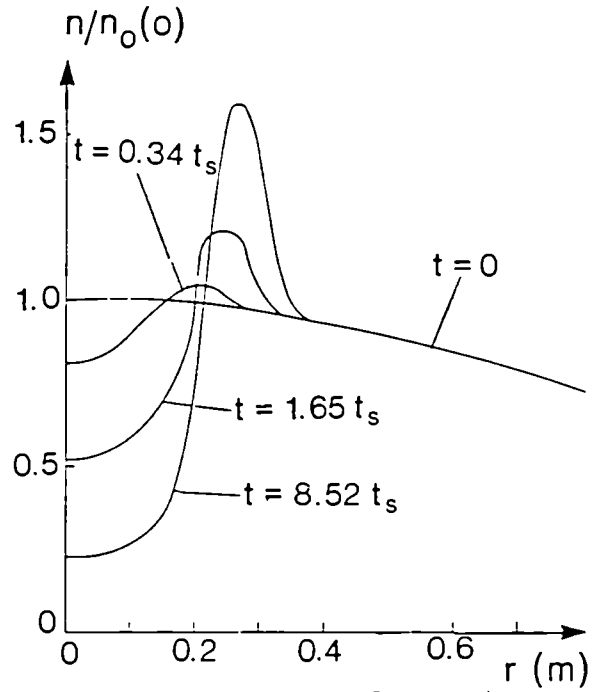

Fig. 2 Density profiles for various times as calculated with model 3 and p(0) = 0.1.

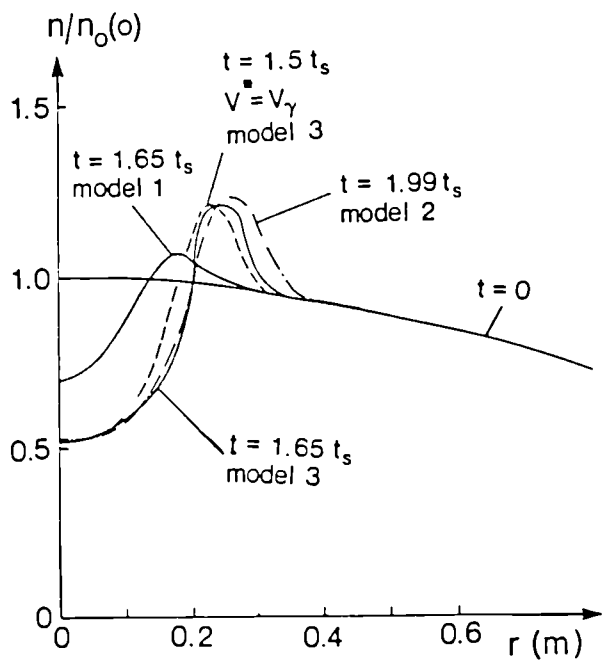

Fig. 3 Comparison of the density profiles with the different models at $t \approx 1.5 t_s$.

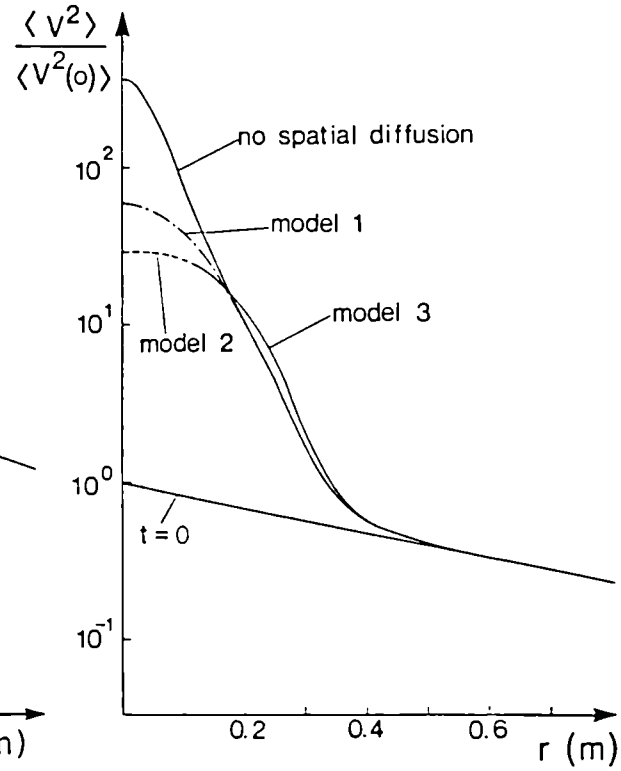

Fig. 4 Stationary profiles of the velocity squared for the various models.

INTEGRATED ELECTRON TEMPERATURE AND DENSITY MEASUREMENTS ON JET

D V Bartlett, D J Campbell, A E Costley, N Gottardi, C W Gowers, K Hirsch[1], S E Kissel, P Nielsen, S Nowak, J O'Rourke, H Salzmann[1]

JET Joint Undertaking, Abingdon, Oxon, OX14 3EA, U K
[1] Universität Stuttgart, 7000 Stuttgart 80, F R G

INTRODUCTION

The plasma electron parameters on JET are measured by three independent diagnostics: LIDAR–Thomson scattering (T_e and n_e), electron cyclotron emission (T_e) and FIR interferometry (n_e). Up to the present, data from these three diagnostics have in the main been treated independently. However, by combining the measurements in a systematic way, it is possible to obtain $n_e(R)$ and $T_e(R)$ with improved precision and reliability. In addition, some new diagnostic possibilities arise.

In this paper, the results of a systematic comparison of the diagnostics over an approximately six month period are presented. The benefits of this comparison are discussed.

MEASUREMENT SYSTEMS

The combination of LIDAR (Light Detection and Ranging) and Thomson scattering techniques yields a new method for obtaining T_e and n_e spatial profiles on large plasma devices, and has been applied for the first time at JET [1]. The system time resolves the spectrum backscattered from a short (300 ps) ruby laser pulse which is directed across the equatorial diameter of the plasma. By using the time of flight principle, it measures the profiles with a resolution of $\approx$ 12 cm (fixed by the pulse duration and the detection bandwidth, 700 MHz) at 2 s intervals throughout the lifetime of the discharge. The uncertainty in the LIDAR measurements is predominantly statistical and results in an uncertainty in T_e of $\approx$ 5%. The shape of the density profile measured with the LIDAR system is known to an accuracy of $\approx$ 5%, whereas the absolute level of the density is subject to a systematic calibration uncertainty of $\approx$ 30%.

The principles by which electron temperature is determined from electron cyclotron emission (ECE) measurements are well known [2]. The electron temperature is measured as a function of radiation frequency, and a frequency to space transformation is carried out using the measured toroidal magnetic field with a correction applied for the internal fields. The principal ECE system on JET is a Michelson interferometer which views the plasma along a sightline parallel to the major radius, 0.13 m below the plasma mid–plane. This instrument has a spatial resolution (both along and perpendicular to the line of sight) of 0.15 m and a temporal resolution of 15 ms. Other ECE instruments provide T_e measurements with space and time resolutions of 0.02 m and 10 μs respectively. Systematic errors dominate the ECE measurements and lead to $\approx$ 10% absolute uncertainty in T_e.

The JET far–infrared interferometer [3] measures the line–integrated electron density along a number of chords through the plasma using the 195 μm radiation from a DCN laser. In the measurements reported here, data from the six vertical chords has been used. The time resolution of the instrument, $\approx$ 100 μs, is determined by the fringe modulation frequency (100 kHz) and the line–integrated density resolution, $\approx 5 \times 10^{17}$ m^{-2}, is set by the minimum detectable phase shift ($\approx$ .05 fringe). The density distribution must be inferred by a generalized Abel inversion of the chordal data, and this can lead to uncertainties in local values of density of up to $\approx$ 10%.

Figure 1 shows the poloidal cross–section of JET, with the viewing directions of the three diagnostics.

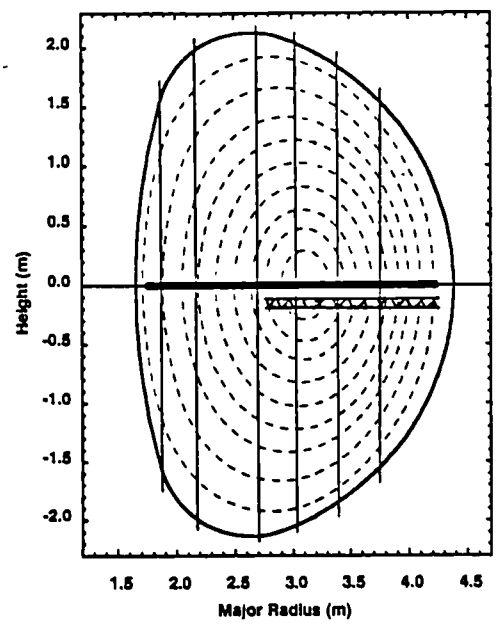

Figure 1: Schematic showing the viewing directions of the three diagnostics in the JET poloidal cross–section. The fine lines are the six vertical interferometer channels, the thick line is the LIDAR sightline, and the hatched zone the region of ECE measurements.

DENSITY COMPARISONS

Direct comparisons of individual measurements have been carried out for a wide range of plasma conditions. Figure 2 shows interferometer and LIDAR results for widely varying profile shapes.

The LIDAR measurement of $n_e(R)$ is essentially localized. On the other hand, the Abel inversion of the interferometer data must assume that the density is constant on the magnetic flux surfaces. The good agreement obtained confirms the validity of the assumptions in the Abel inversion, notably that the flux surfaces correspond to contours of constant density. Moreover, the detail observed when higher order polynomials are used in the inversion routine is shown by these comparisons to be real.

The shape of the density profile measured with the LIDAR is known to an accuracy $\approx$ 5% whereas the absolute level is subject to systematic calibration uncertainty $\approx$ 30%. By normalizing the line integral calculated from the LIDAR profile to that measured directly by the interferometer, it is possible to improve significantly the absolute level of LIDAR density profiles. A systematic comparison of the ratios of the line integrals (without normalization of the LIDAR) over a period of $\approx$ 6 months, figure 3, shows a small decrease in the LIDAR values compared to the interferometer. This may be due to a carbon deposit on the vacuum windows.

Events which produce rapid density changes, such as pellet injection, can cause errors in the interferometer's fringe counters. With multiple pellet injection, it is not possible to reconstruct the density evolution using only the interferometer data and working back from the decay at the end of the discharge. However, recovery of the full time evolution is frequently possible by comparing the interferometer and LIDAR data.

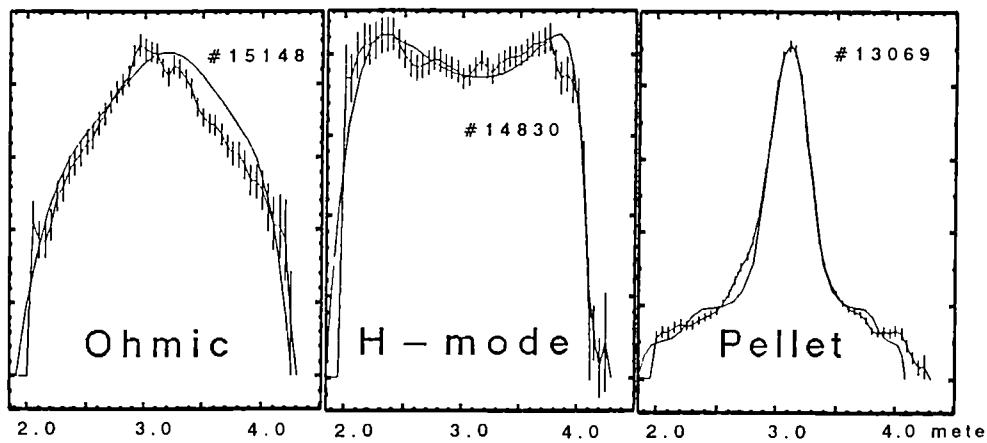

Figure 2: Density profiles of widely varying shapes measured by the interferometer and LIDAR. The LIDAR profile has been normalized to the interferometer data independently for each case.

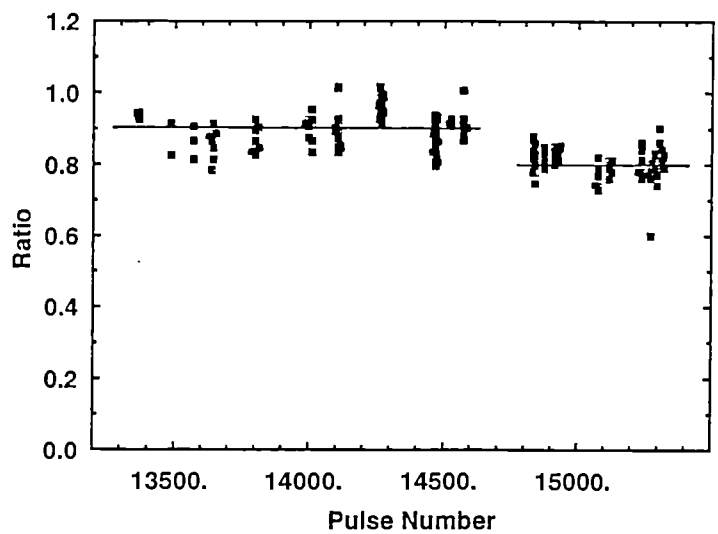

Figure 3: Ratio of the line integral density calculated from LIDAR profiles to the measured interferometer value for plasma pulses spread over a 6 month period. The ratio was initially constant at ≈ 0.9, but decreases to ≈ 0.8 in the last 2 month period.

TEMPERATURE COMPARISONS

Both the ECE and LIDAR provide localized temperature measurements, with similar spatial resolution. However, since the nature of the errors is quite different for the two diagnostics, a detailed comparison of data averaged over many JET pulses should allow the systematic uncertainties in the ECE temperatures to be evaluated, and the full time resolution of the ECE instruments to be exploited. Comparison of the measurements made by the two systems over a wide temperature range (for example, figure 4) show generally good linearity, but with a consistent difference in absolute

level of 10 to 20%. The source of this difference is being investigated. If it is a systematic error in the ECE spectral calibration, this can be removed by normalization against the LIDAR. The apparent shift between the two high temperature profiles of figure 5 suggests an error in the calculation of the plasma internal magnetic fields under these conditions. A systematic study is in progress to see if the ECE/LIDAR comparisons can be used to derive the local magnetic field in the plasma.

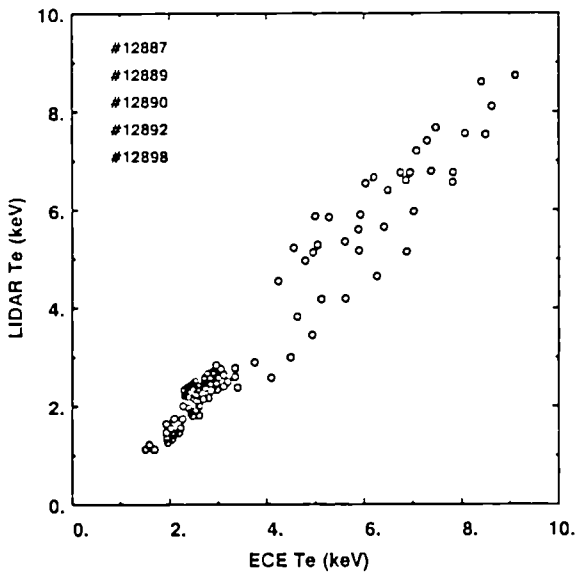

Figure 4: Comparison of T_e measured by LIDAR and ECE on a series of pulses with strong additional heating. The ECE values are ≈ 0.9 those of the LIDAR.

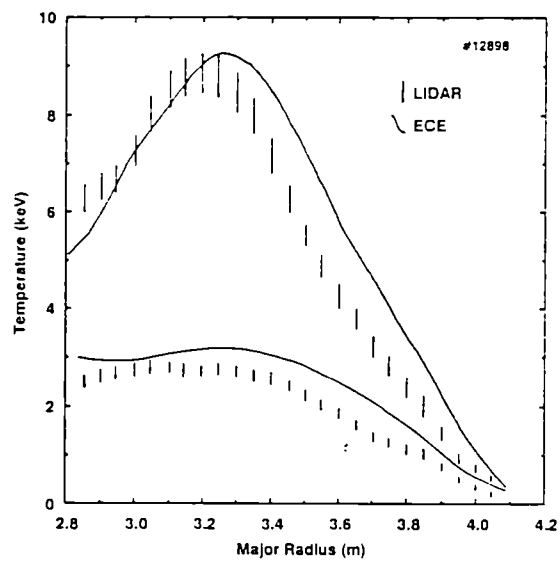

Figure 5: Comparison of LIDAR and ECE profiles at low T_e and high T_e (additional heating) on the same plasma pulse.

SUMMARY

The comparisons which have been made show that considerable benefit can be expected from integration of data from the three diagnostic systems. These benefits fall into three categories:

(i) Reduction of systematic errors. In each comparison, one diagnostic suffers more from systematic errors than the other (LIDAR measurements of n_e, ECE T_e measurements). (ii) Detection (and possibly correction) of measurements perturbed by adverse plasma conditions. (iii) New measurement possibilities. Comparisons between ECE and LIDAR may provide information about the accuracy of calculations of the plasma internal magnetic fields.

The pellet shot reported in this paper was obtained using a multi–pellet injector provided by ORNL under a JET–USDOE Agreement.

[1] H Salzmann et al, Nuclear Fusion, 27, 1925 (1987)
[2] A E Costley et al, Proc. of EC–4 The 4th Intl. Workshop on ECE and ECRH (Rome, March 1984)
[3] D Veron, in Workshop on Diagnostics for Fusion Reactor Conditions Varenna 1982, EUR 8351–II EN, Page 283 (Permagon, 1983).

Ion Cyclotron Emission Measurements On JET

P. Schild[a] and G.A. Cottrell

JET Joint Undertaking, Abingdon, Oxon OX14 3EA, United Kingdom

[a] *Permanent address : Lab. Phys. des Plasmas , Grenoble University, France*

Introduction

A JET ICRH antenna has been used in reception mode to monitor the time and frequency-resolved ion cyclotron emission (ICE) from deuterium 6 MA ohmically heated plasmas with antenna configuration in dipole phasing. The ICE spectrum is compared with a computed thermal spectrum for harmonics from 1 to 5 . It shows the characteristic harmonically related superthermal peaks[1,2]. These observations reveal that the superthermal emission is modulated in time and is correlated with inverted sawteeth and with the H–α signal located near the plasma edge.

ICE Spectrum

The antenna was used to monitor the ICE from 10 MHz to 100 MHz. The signal is detected using a spectrum analyser, which provides about six spectra per pulse. Previous experiments[2,4], made with the same equipement, suggest that the ion temperature could possibly be measured by analogy with the technique of electron cyclotron emission (ECE). However, the superthermal emission for deuterium ohmic cases masks the thermal emission, and is influenced by the fusion products of the D-D reactions [3].

To study the effects of these superthermal ions on the spectrum, we need to calculate the thermal level. To compute this, we have used a code based on Black Body radiation[5]. In this frequency range and ion temperature level (typically $T_i \approx 2$ *KeV* for ohmic pulses), we have $h\nu/kT \ll 1$, and can take the Rayleigh–Jeans law to get the thermal intensity. To take into account that the waves, before being received by the antenna, may make many reflections within the vacuum vessel, (in the optically thin limit), we include a slab model for these in the code. We use the formula :

$$I(\omega,T_i) = \frac{N^2\omega^2}{8\pi^3 c^2} kT_i \cdot (1 - e^{-\tau}) \qquad (1)$$

where N is the refractive index of the medium, defined by $N \sim \omega_{pi}/\omega_{ci}$, and the subscript i stands for the ion majority species, and τ is the total optical depth for the plasma at frequency $\omega/2\pi$. We calculate τ from the dielectric tensor for a cold plasma , including a small perturbation to take into account that the plasma is warm[8]. We also include the effects of finite larmor radius and non relativistics particles. Having solved the dispersion relation, we may use previous results[6,7] from ECE theory and calculate the optical depth. We also assume the ion temperature profile and the ion density profile to be parabolic. We then compute the thermal emission from the first to the fifth ion cyclotron harmonic for the ion majority species. We do not compute for harmonics greater than five, because these fall outside of our frequency range.

We calibrate the ICE signal by taking into account the coupling resistance of the antenna over our frequency range. This gives us a function with which we obtain the ICE power in front of the antenna

TOPIC: H Diagnostics
RESPONSIBLE AUTHOR: P. Schild
ADDRESS: JET Joint Undertaking, Abingdon, Oxon, OX14 3EA, U.K.

We now compare this calculated Black Body emission with a ICE spectrum from a 6 MA discharge with deuterium majority (figure 1).

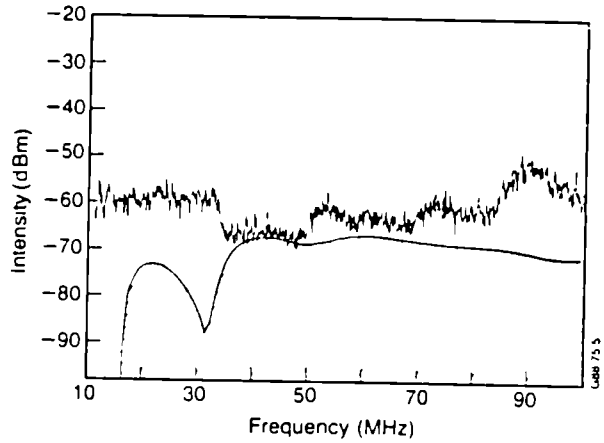

Fig. 1 : Comparison between the ICE spectrum and the computed thermal emission (B_0 = 2.18 T). The hached region represents the thermal emission.

It can be seen that the computed spectrum explains some of the underlying features of the experimental spectrum. However, below a frequency around 40 MHz, the thermal emission is not the main source of the emission. This is due to the weak absorption of the fundamental of deuterium $\omega = \omega_{cD}$ below 21 MHz. It can also be seen that our computation reproduces the ICE spectrum in the range 40–50 MHz, suggesting that the thermal spectrum of the bulk ions is visible in this interval.

We know that the observed peaks are linked with the presence of fusion products of D-D reactions[2]; T, ^{3}He, H^+ . The peaks A to F on figure 2 can be related to the cyclotron harmonics

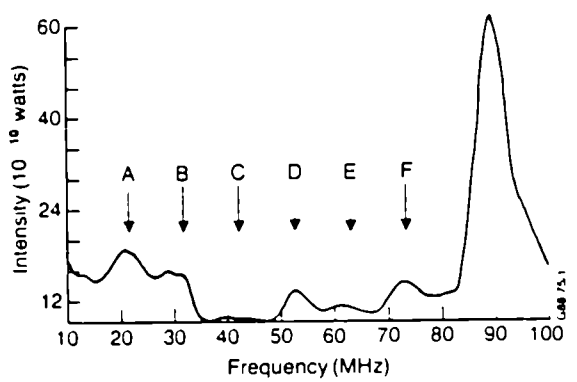

Fig. 2 : The peaks A to F are harmonics of T,^{3}He,H^+ for a magnetic field of 2.1 Tesla. The ICE spectrum is smoothed by a gaussian to improve the signal-to-noise ratio.

of the three particles. These are linked respectively by the following relations: peaks A to F are the cyclotron harmonics 2 to 7 of T; peaks A, C, E are the cyclotron harmonics 1 to 3 of ^{3}He; peaks B and E are the cyclotron harmonics 1 and 2 of H^+. In order to obtain the correspondence between them, we take the value 2.1 Tesla for the magnetic field. This means that the emission which produces the peaks is near the plasma edge. The last observation provides support to the interpretation[2] that the superthermal ICE is generated by fusion products near the pickup antenna.

Time Resolved Measurements.

We have observed the time-resolved emission of peak D with a sampling rate of 1 kHz. When the 6 MA current flat top is reached, inverted sawteeth are observed on the ICE emission. Comparison with a soft X-Ray signal from the plasma edge (figure 3) shows a good correlation between the two, which indicates it originates near the edge. We also compare the ICE signal with an H–α signal. It is also well correlated (figure 4). The ICE signal can be to delayed with respect to the soft X-Ray signal. The $q = 1$ surface is at radius $R \approx 3.7\ m$. So the ICE signal originates outside this surface. As the H–α emission originates from a region close to the limiter, the correlation with the ICE signal indicates further that the ICE emission is coming from the plasma edge. This localisation of the emission clearly must be taken into account in future models of the ICE spectrum.

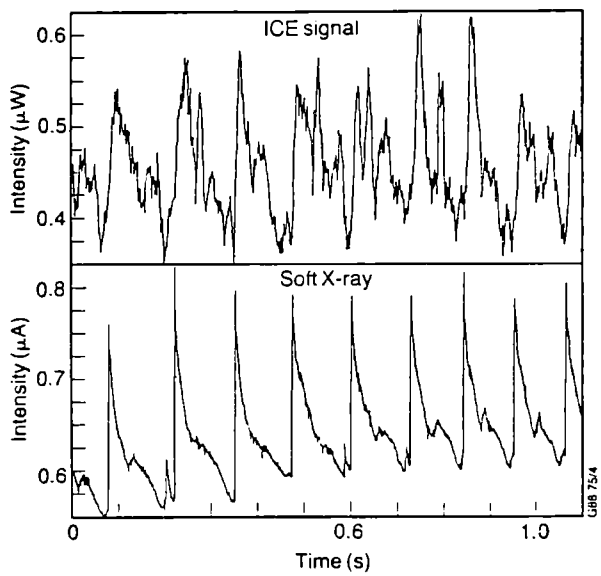

Fig. 3 : Time-resolved soft X-Ray ($R \approx 3.7\ m$) and ICE signals are compared, during the current flat top.

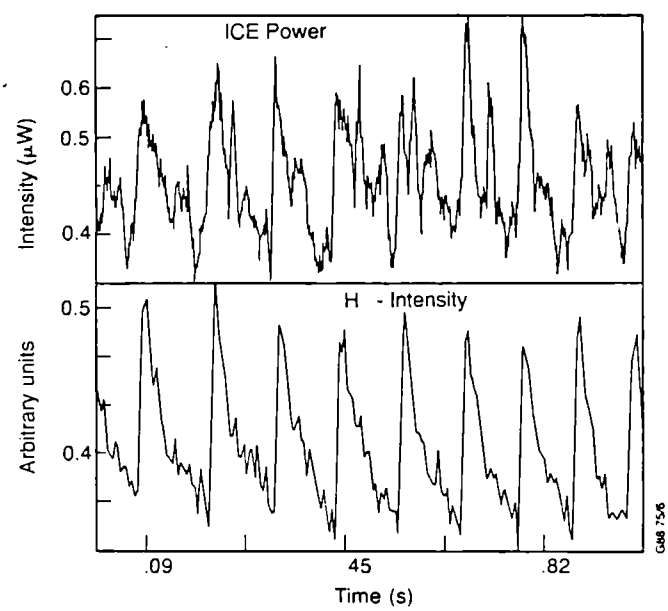

Fig. 4 : Time-resolved H_α signal are compared with ICE, during the current flat top.

Discussion and Conclusion.

Comparison between the ICE and the computed thermal emission spectrum reveals where the superthermal component of the emission is dominant. The nonthermal emission peaks can be interpretated in terms of the ion cyclotron harmonics of fusion products of the D-D reaction. It is possible to match the observed and calculated ICE harmonics peaks if the field is taken to be that value near the boundary (R = 4.2 m) of the plasma, suggesting that the origin of the emission is near the plasma edge. Taking the time-resolved emission of one of these peaks, we find the ICE signal shows inverted sawteeth. These two observations give support to the interpretation that the superthermal emission originates from the plasma edge, near the pickup antenna.

The coincidence of the inverted sawteeth of ICE and H-α signals in time gives strong support to the interpretation of the ICE as originating from the outside part of the plasma, in the near field region of the ICRH antenna. It is possible that deeply trapped fusion products, born in the central part of the discharge, can make large orbit excursion in the outer part of the plasma. These particles may suffer collective velocity-space instabilities which can drive unstable waves in this region.

Acknowledgement.

It is a pleasure to thank Dr A Edwards for the help to use the Soft X-Ray data and M. Brandon for experimental assistance.

References

[1] G.A. Cottrell et al, Proc. 13th Europ. Conf. on Controlled Fusion and Plasma Physics,Schliersee, W. Germany, Vol. II,37(1986)

[2] G.A. Cottrell, R. O. Dendy, Phys. Rev. Lett. **60** ,33(1988)

[3] W.H.M. Clark ,Proc 4th Inter. Symp. on Heating in Toroidal Plasma, Rome, Italy, Vol. I, 385-391(1984)

[4] G.A. Cottrell, Proc. Workshop on Application of RF Waves to Tokamak Plasma, Varenna, Vol. II,710-716(1985)

[5] Bekefi, Radiation Process in Plasma (1966)

[6] Bornatici et al, Plasma Physics, **23** ,1127(1981)

[7] Engelman et al, Nucl. Fus., **13** , 497(1973)

[8] Shkarofski , Physics of Fluids, **9** , 561(1966)

INVESTIGATION OF SLOWING-DOWN AND THERMALIZED ALPHA PARTICLES BY CHARGE EXCHANGE RECOMBINATION SPECTROSCOPY - A FEASIBILITY STUDY

Manfred von Hellermann, Hugh Summers, Alain Boileau *)

JET Joint Undertaking, Abingdon UK
*)INRS Energie, Varennes, Canada

Motivated by the expectation of achieving significant alpha particle production in the approaching fusion conditions of JET, JT60 and TFTR tokamaks, a range of alpha particle diagnostics have been under study in recent years [1]. One class is based on exploiting the charge exchange reaction through use of appropriate diagnostic or heating neutral beams. Single charge transfer with the associated excitation of recombination radiation can be used as a spectroscopic method for the measurement of alpha particle density and velocity distribution function. The charge capture and subsequent cascading and redistribution gives emission in the HeII n=4-3 (4686 A) line which can be transferred either by quartz fibres or by a mirror relay system to remote spectroscopic equipment beyond the biological shield.

For significant charge exchange the relative velocity of alpha particle and of injected neutral (hydrogen or deuterium) must be within a band of approximately 100 keV/amu which is defined by the fall of the effective charge exchange rate at higher relative velocities.

Visible charge exchange recombination spectroscopy of **thermal** ionized plasma particles, including helium, using the neutral heating beams is well established on JET [2]. The study presented here investigates the scope of information which may be achieved using the existing heating beam capability with upgrading to E_{beam}=140 keV at 0.7MWatt per beam on **slowing-down alpha particles** with energies $kT_i < E_{alpha} < 3.5$ MeV. Clearly the study must also be concerned with the CXRS spectral features associated with the background thermal helium at relatively higher ion temperatures than achieved at present and the merging of the cooling and thermal helium velocity distribution function.

For future JET operation with input powers up to 40 Mwatts of Ohmic and auxiliary heating it is expected to achieve, in particular during hot-ion modes [3] with low to moderate electron densities , alpha particle power levels of approximately 5 MWatts. For slowing down times in the order of 1 to 2 sec and an assumed main alpha particle production within a volume of roughly 50 m^3, we may expect alpha particle densities in the plasma centre between 10^{17} m^{-3} and 10^{18} m^{-3}.

For the geometry of the JET heating beams and the CXRS multichord viewing line system (cf. [4]) we can calculate from a known energy dependence of the effective excitation rate (Fig.1) and a slowing-down velocity distribution function (Fig.2) the expected recombination

spectra. An example of a theoretical spectrum consisting of the superposition of the contributions of thermalized and slowing-down alpha particles as well as the continuum background radiation is shown in Fig.3. The absolute photon fluxes are based on the extrapolated neutral beam data and an attenuation code used for the present low-Z impurity density calculations [2]. The spectrum representing the slowing-down alphas covers a spectral width in the order of 150A. The shape and Doppler shift depend on slowing-down parameters as well as the observation geometry and neutral beam energy.

The detection limit of the highest alpha particle energies contributing to the observed spectrum is demonstrated in a semilogarithmic plot (Fig.3b) where the continuum level and its associated noise level correspond to the actual observed levels of the current CXRS system. In order to discriminate the broad low-level slowing-down spectrum from the background continuum level two alternatives are being considered. One is active beam modulation and the other is the use of an additional passive viewing line which does not intersect the beams. The latter provides a simultaneously measured background spectrum.
Fig.4 shows an example of 2 actual JET spectra gained during NB injection in a deuterium plasma with a ^{3}He minority (2 to 5% of the electron density) typical for RF plasma heating. In this example the NB pulse was applied 2 sec after the RF pulse. Both viewing lines are fed into the multi-chord CXRS system enabling a subtraction of two spectra using one spectrometer and one 2-dim detection system. The residual of the subtraction is the CX Doppler broadened spectrum (representing in this example the plasma centre ion temperature of 4.3 keV) and the rms noise level of the continuum. A remaining small cold constituent, presenting approximately 10% of the total intensity, is supposed to be due to a non perfect toroidal symmetry in plasma boundary emmission.

Conclusion

A measurement of an alpha particle density radial profile in the quoted density range appears to be feasible. The reconstruction of a velocity distribution function in the energy range below 0.5 MeV in the plasma centre should be possible using either a passive viewing line for a simulataneous background subtraction or alternatively an active beam modulation technique. In the forthcoming JET operation period with combined NB and ICRH heating the high energy tails of helium minority velocity distribution function will be investigated.

[1] Workshop on Alpha Particle Diagostics, JET 1986, TFTR 1987
[2] A.Boileau et al. ,JET Report JET-P(87)44
[3] G.F. Cordey et al. ,JET Report JET-P(86)38
[4] see S.Corti et al, this conference

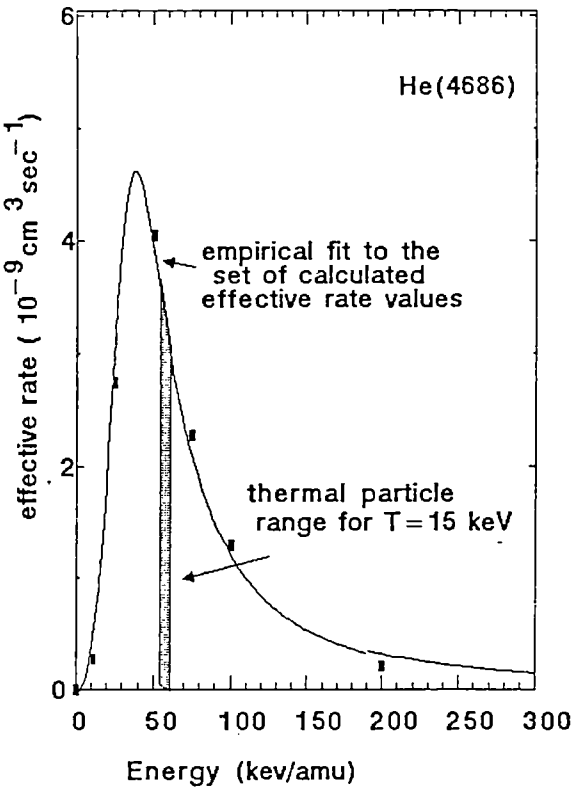

Fig.1 Effective excitation rate

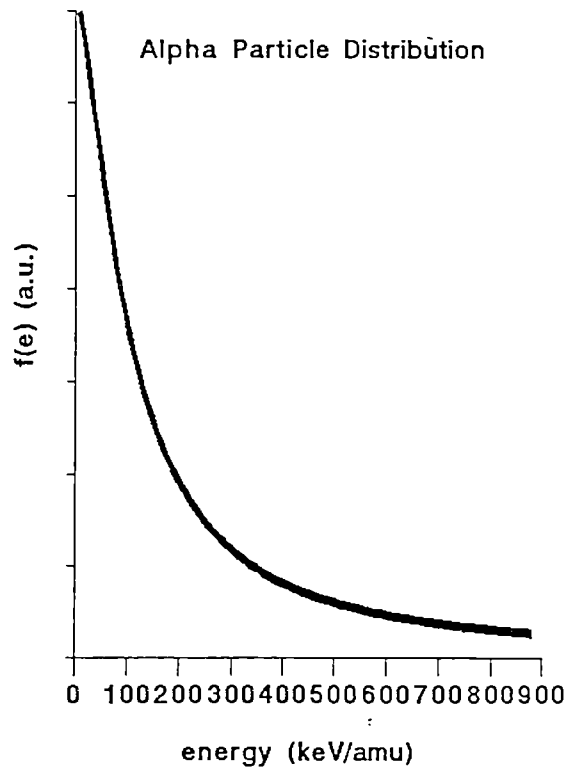

Fig.2 Alpha particle distribution function

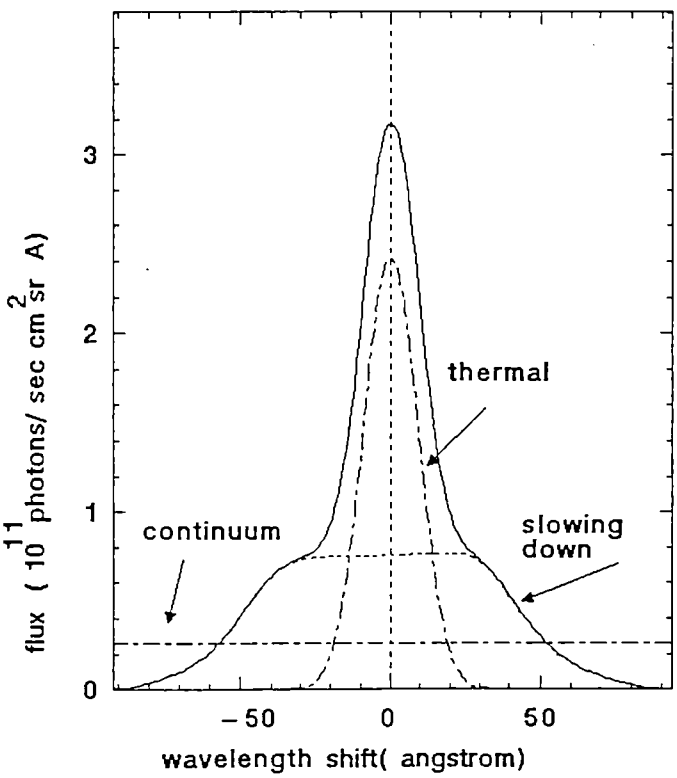

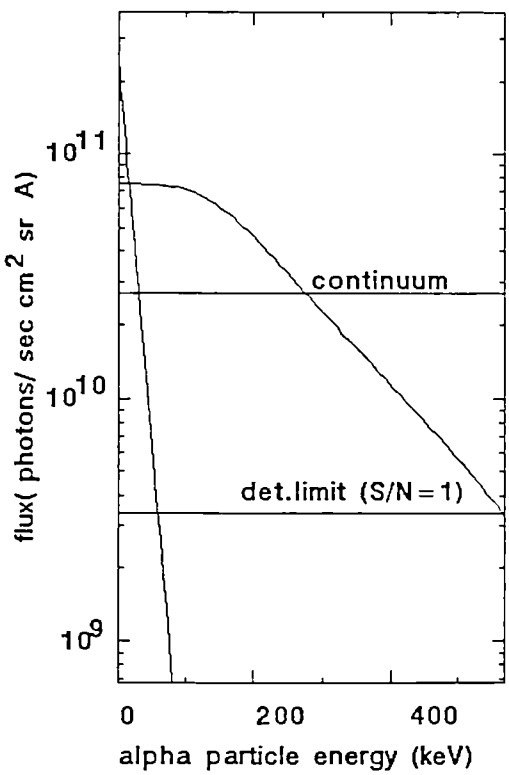

Fig.3 Thermal and slowing down spectrum for E=60keV/amu, P=5MWatt
n(alpha)=10**18 m**−3, n(electron)=5*10**19 m**−3

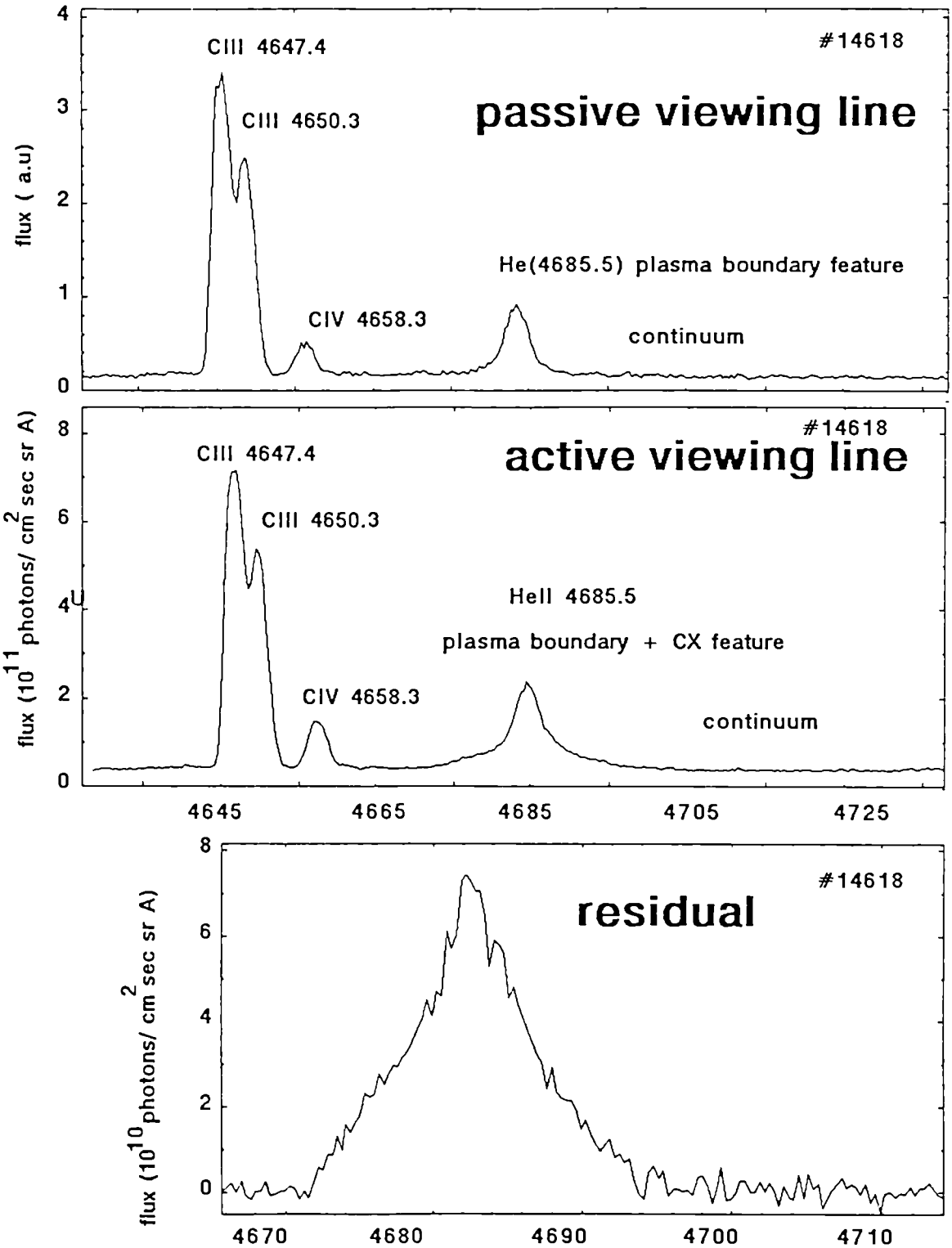

Fig.4 Background subtraction using a passive viewing line. The helium minority density is approximately 5*10**17 m** – 3. The background noise level is less than 5*10**9 photons/cm**2 sec sr A. The residual contains a CX component of 4.3keV and a cold boundary feature of 0.18 keV.

STUDIES OF ENERGY TRANSPORT IN JET H-MODES

M Keilhacker, B Balet, J Cordey, N Gottardi, D Muir, K Thomsen, M Watkins

JET Joint Undertaking, Abingdon, Oxon, UK, OX14 3EA

1. INTRODUCTION

The H-mode discharges in JET separatrix configurations with a single null X-point have the best confinement properties [1,2]. However, even these discharges exhibit a decrease of the global confinement time with increasing neutral beam injection power. Part of this degradation with power can be attributed to increased impurity radiation and poor beam penetration at the higher densities concomitant with improved particle confinement and the higher power levels. In addition, these discharges are not in steady-state, since the density increases steadily with time until impurity radiation precipitates a transition back to an L-mode.

In the present paper, the local heat transport properties in the interior of ohmic, L- and H-phases of 2MA discharges are determined (Section 2) using both the time-dependent energy balance code, TRANSP [3], and the timeslice code, QFLUX [2]. In addition, the global confinement properties of higher current discharges ($\lesssim$3.8MA) are analysed in Section 3.

2. LOCAL TRANSPORT ANALYSES

The input data to TRANSP and QFLUX comprises the magnetic flux surface geometry, temporal variation of the electron density profile (FIR interferometer), electron temperature profile (ECE), central ion temperature (X-ray crystal spectrometer measurement of Ni^{27+}, neutron yield and NPA data), radiated power profile (bolometer), the plasma current, loop voltage, Z_{eff} (visible bremsstrahlung) and edge particle confinement time (H_α monitors). Neutral beam heating is calculated by Monte Carlo methods in TRANSP and using the PENCIL code in QFLUX.

The ion temperature profile is not available routinely. It is calculated in TRANSP by assuming an ion thermal diffusivity either (a) of the neo-classical form enhanced by a factor adjusted continuously in time so as to regulate the central ion temperature at the measured value, or (b) proportional to the electron thermal diffusivity. Both prescriptions give good agreement with the measured diamagnetic stored total energy and reasonable agreement with the neutron yield; the ion temperature profiles using (b) are nearer to the NPA profile data. The ion temperature in QFLUX is assumed to have the same profile as the electron temperature, but normalised to the measured central ion temperature. Electron and ion contributions to the heat flow (which depend on the ion temperature profile through energy equipartition) are not separated and results are presented for the total heat flux, Q, across a flux surface of area, S, in terms of $n_e \nabla k T_e S$. An effective total heat diffusivity, $\chi = Q/n_e \nabla k T_e S$, is defined.

TRANSP Results: For JET pulse #10755 (2MA, 2.1T, $P_{NBI} \leq$ 9MW) the temporal variation of Q with $n_e \nabla k T_e S$ at three radial positions in the plasma interior (normalised radius, ρ = 0.5, 0.75, 0.9) is shown in Figure 1 (at times avoiding the collapse of a sawtooth) through the ohmic, L- and H-phases. The temporal variation of χ (at all times) at the three radial positions is shown in Figure 2(a). At the start of the L-mode χ is well above its ohmic value but decreases subsequently to a level close to its ohmic value prior to the transition to the H-mode. χ is maintained close to this level during the H-phase. The spatial profiles of χ at selected times throughout the discharge are shown in Fig 2(b).

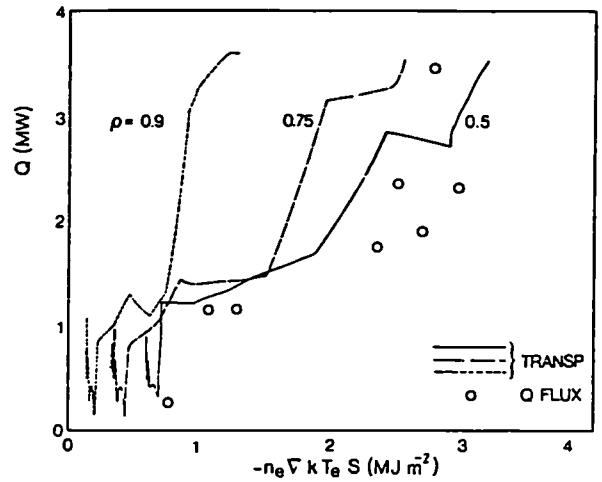

Fig 1:TRANSP and QFLUX results for the temporal variation of Q with $n_e \nabla k T_e S$ at various radii in JET pulse #10755.

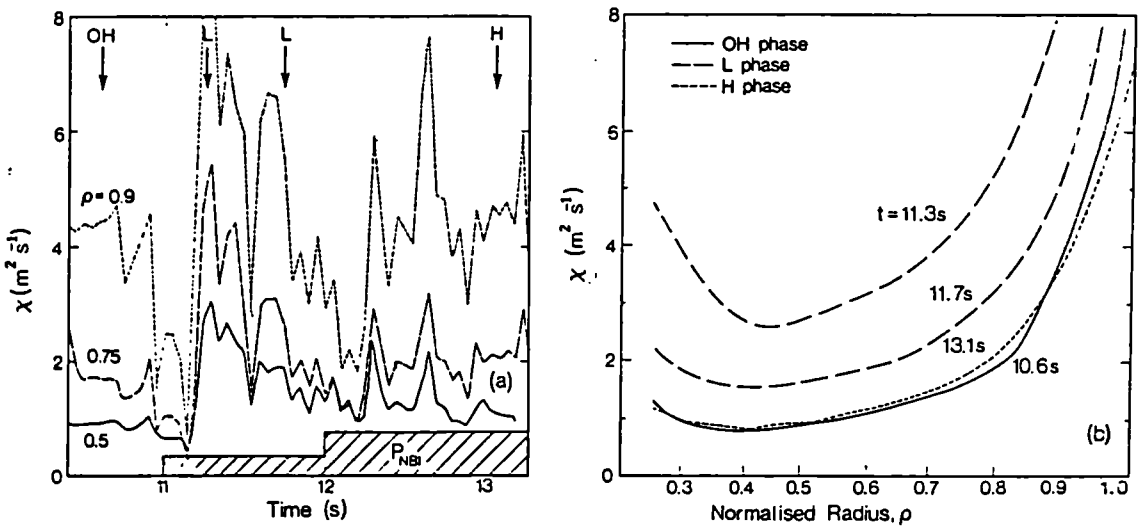

Fig 2:TRANSP results for (a) the temporal variation and (b) the spatial profiles of the total heat diffusivity, χ, for JET pulse #10755. Arrows in (a) indicate the times of the spatial profiles in (b).

QFLUX Results: For the same JET pulse, QFLUX results at a normalised radius, ρ = 0.5, and a limited number of time points show reasonable agreement with the results of TRANSP (Figure 1). Figure 3 shows an accumulation of data from a number of discharges at 2MA and 2.1T at the normalised radius, ρ = 0.5. In Figure 3(a), the data is distinguished according to the phase of the discharge, with χ decreasing continuously from the L- to H-phase. In Figure 3(b) the results are distinguished with respect to density and indicate that the transition from the L- to H-phase is concomitant with the increase in density that is observed. At constant density, χ increases with power, while at constant power, χ is reduced with increasing density. This result substantiates earlier indications [2].

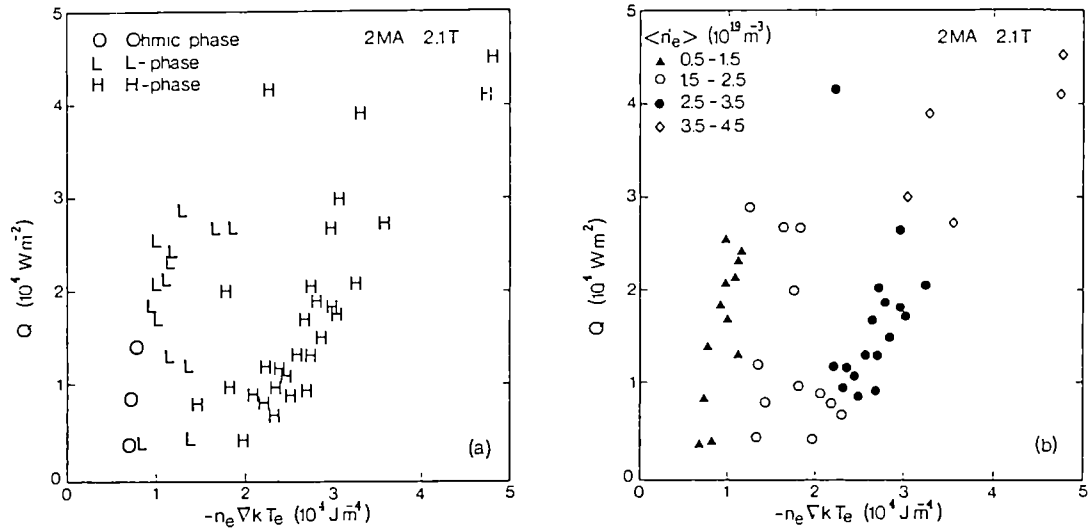

Fig 3:QFLUX results for data accumulated at several times during a number of pulses distinguished according to (a) discharge phase and (b) density.

3. GLOBAL ENERGY CONFINEMENT

The local transport analyses discussed in Section 2 were carried out for 2MA H-mode discharges since most of the H-modes obtained in 1986 were at this current. Since then a larger number of H-mode discharges with currents in the range 3 to 4MA have been obtained.

Figure 4 shows the global energy confinement time $\tau_E = W/(P_{tot}-\dot{W})$ as a function of the total net input power $(P_{tot}-\dot{W})$ for H-mode discharges with currents of 3MA and above. W is the diamagnetic measurement of the stored energy. Most of the data arise from one specific day of operation in February 1988 on which the neutral beam power, $P_{NBI} \leq 7.5$MW. These data are supplemented by the 3MA data obtained in November 1986 ($P_{NBI} \leq$ 10MW) [2]. Since in all these discharges the plasma density was increasing steadily with time the data set has been restricted to $\dot{W} \leq 0.2\ P_{tot}$, relatively close to steady-state conditions. Two density ranges (3-4 and 4-5 x $10^{19}m^{-3}$) are distinguished. At low powers the data seem to split into two branches with data at higher density corresponding to higher confinement times. At higher powers such a density dependence is less apparent.

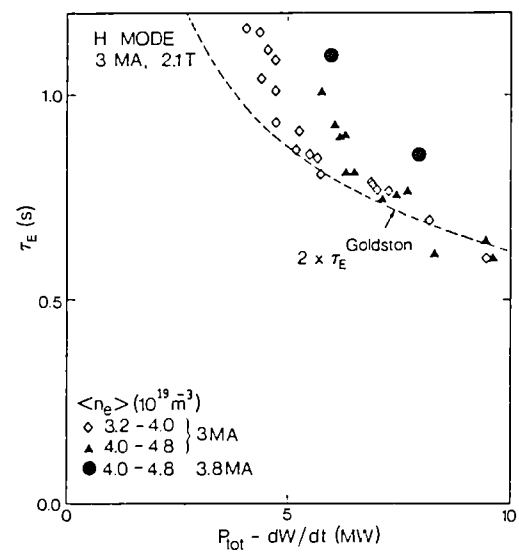

Fig 4:Global energy confinement time versus total net input power for H-mode data at currents of 3MA and 3.8MA.

Figure 4 also shows the first H-mode data obtained at a plasma current of 3.8MA. At a total heating power P_{tot} = 8MW this discharge resulted in record values of plasma energy (7MJ), energy confinement time with appreciable additional heating (0.9s) and fusion product $(n_i(0)\tau_E T_i(0)$ = 2.4 x $10^{20}m^{-3}$.s.keV).

4. CONCLUSIONS

Local transport analyses with both the TRANSP and QFLUX codes indicate that during the L-phase of JET single null X-point discharges the total heat transport coefficient in the plasma interior decreases from its initially high value to a level close to the ohmic value. This level does not change significantly during the transition to the H-phase, implying that the higher stored energy associated with the H-phase results from improved confinement at the very edge of the plasma. On the basis of a larger data set obtained at different times during different discharges, the underlying trend towards reduced confinement in the plasma interior with increasing input power is ameliorated, in part, by improved confinement at higher density.

The global analysis indicates that confinement during the H-phase continues to improve with current (up to 3.8MA), but still degrades with increasing neutral beam power.

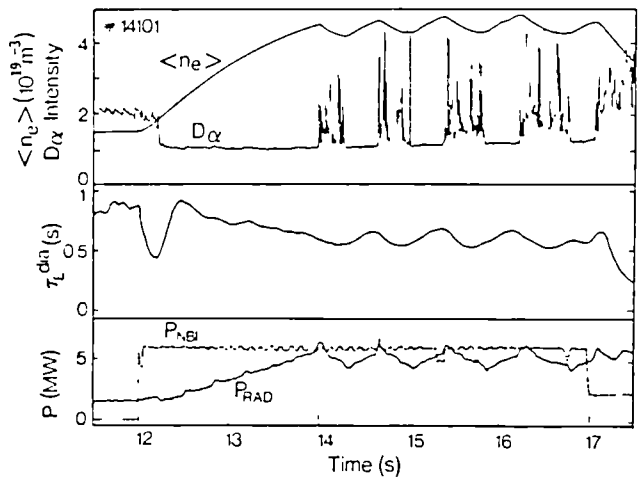

Fig 5:Characteristics of a JET discharge in which ELM-phases separate a train of shorter H-phases.

It is worth noting that conditions closer to steady-state have been achieved in discharges that exhibit ELMs separating a train of shorter H-phases. The duration of these ELM-phases can be affected by varying the radial distance between the separatrix and the belt limiters. As shown in Figure 5, for a certain optimum distance between separatrix and limiters, this procedure allows the plasma density and radiation to be kept closer to steady-state without too large an adverse effect on the global energy confinement time.

ACKNOWLEDGEMENTS

The authors would like to acknowledge R J Goldston and D C McCune of the Princeton Plasma Physics Laboratory for the use of the TRANSP code and C H Best for supervising the installation of TRANSP at JET.

REFERENCES

[1] Tanga, A., et al., Nucl. Fusion 27 (1987) 1877.
[2] Keilhacker, M., et al., Proc. 14th Eur. Conf. on Cont. Fusion and Plasma Physics, Madrid, 1987, 11D (III), EPS (1987) 1339.
[3] Goldston, R.J., et al., J. Comp. Phys. 43 (1981) 61.

THE JET H MODE

A Tanga, D Bartlett, M Bures, A Gibson, N Gottardi, C Gowers, P J Harbour, A Hubbard, M Keilhacker, E Lazzaro, P D Morgan, P Noll, P H Rebut, N Salmon, D Stork, D R Summers, A J Tagle, P R Thomas, K Thomsen, M von Hellermann, M L Watkins

JET Joint Undertaking, Abingdon, Oxon. OX14 3EA, England

Magnetic configuration

H mode has been obtained in JET with single null configuration and neutral beam heating. The single null magnetic configuration was obtained by using the multipolar field produced by shaping windings and primary coil stray fields[1]. The plasma equilibrium flux plot of a discharge with plasma current of 4 MA is shown in Fig. 1. Developments of higher current scenarios with single null configuration are based on differential currents in the main equilibrium coils and have been described[2]. Ranges of parameters of single null discharges are summarised in Table I. The elongation of single null discharges is larger than limiter discharges because of the need to keep the plasma detached from the bottom belt limiter. The magnetic axis of the plasma is displaced by 0.1 ÷ 0.2 m below the midplane; consequently plasma-antenna distance for single null configuration at high plasma current is larger than 0.1 m, causing values coupling resistance of the order of 1Ω or less. With single null configuration the operational space was confined by a low q limit of $q^* = \frac{5a^2}{Ip}\frac{B_T}{R}\left(\frac{1+k^2}{2}\right) > 2$; for values of q^* 2 to 3 there was still a low density disruptive limit of $\bar{n}_e(m^{-3}) = 0.35 \cdot 10^{19} Ip(MA)$. In the single null configuration JET has been operated with the ion (∇B) drift direction towards the X-point.

Features of the H-mode

Scans of neutral beam power, plasma current, toroidal field and X-point position have shown that threshold power for the H-mode transition depends strongly on toroidal field, with an empirical fit of the neutral beam power $P_{th}(MW) = 0.6(B_T(T))^{2.5\pm0.5}$. The minimum power threshold was 3 MW with a toroidal field of 1.8 T. There was no clear dependence on plasma current, within the power resolution of one neutral beam source of ±1 MW. The transition to the H-mode was achieved for X-point to the dump plates distances <5 cm. Within the limited neutral beam power available of 7 MW it was not possible to achieve H-mode with He^4 target plasma, suggesting a higher threshold for helium plasma, similar to D-III-D[3]. In deuterium, the H-mode transition was achieved with a minimum target plasma density of $\bar{n}_e(m^{-3}) = 0.5 \times 10^{19} Ip(MA)$.

The short (0.1-0.45 s) L phase is followed by a quiescent H phase, lasting up to 2.5 s. The collapse of the H-phase is caused by the build-up

of radiation losses, in the bulk plasma, which increase with plasma density until the total input power less radiation losses is equal to the power threshold. The duration of the quiescent H phase increases with (a) neutral beam power, (b) clean machine conditions and (c) He conditioned vessel surfaces leading to lower plasma recycling. Termination of the H phase is followed by either a full plasma disruption or reverting to an L phase. For plasma-limiter distances less than 5 cm a series of short (0.5 s) H and L phases is observed, with distances of the order of 10 cm within a Neutral Beam pulse of 5 s usually there are two or three H and L phases lasting 1 ÷ 2 s; finally for distances larger than 10 cm there is just one long H phase ending with plasma disruption.

At the lowest toroidal field of 1.8 T, the L phase lasts for just the slowing down time of the injected particles, while at 2.8 it lasts 0.6 s, (NB power 7÷8 MW). The L phase is characterized by edge relaxations which increase in amplitude and decrease in frequency until, at a sawtooth crash, the L to H transition occurs (as detailed elsewhere[4]). The edge relaxations are localized at r/a ∿ 0.90, according to the soft x-ray array. Each relaxation produces the loss of approximately 0.4% of the total plasma particles and 0.2% of total energy. The L to H transition is marked by a 20% increase of the electron temperature, confined to the separatrix, taking place in a time of the order of 10 ms.

The time evolution of electron temperature and plasma density are shown in Fig. 2. This figure is made up of a series of LIDAR profiles[5] taken on a sequence of subsequent reproducible plasma pulses, resulting a profile every 0.1 s. NB heating starts at 12.5 seconds, during the flat top of a discharge of 3 MA plasma current and with a toroidal field of 2.1 T. At the L → H transition, at 12.8 s the plasma density profile, already flat in the ohmic phase, exhibits the build-up of a steep edge gradient.

The density increase, throughout the H phase, occurs with a profile little altered in shape. It should be noted that flat density profiles are a common feature of both limiter and x-point JET discharges at low values of q_{cyl}. The sequence of electron temperature profiles shows the increased edge temperature and the perturbations caused by sawteeth activity. Electron temperature profiles in H-mode discharges are broad. For example, the values of the ratio of peak-to-average temperature is 1.7, virtually independent of q_{cyl}; in contrast to limiter discharges where, during the flat-top, the ratio of peak to average electron temperature varies as $T_e/\langle T_e\rangle \sim \frac{1}{3} q_{cyl} + 1$[6]. H-modes usually have sawteeth activity. However temporary stabilisation has been observed in a similar way than monster sawteeth observed in limiter discharges, with neutral beam power of 7 MW. Temporary stabilisation produced an increase in the peaking of the temperature profile.

Confinement time

The global confinement time (τ_e) increases in the H-mode, and is roughly a factor of two larger than in limiter discharges at the same plasma current and 50% larger than during the L phase[1]. In the current range 1.0 to 3.8.MA confinement times scale proportionally to plasma current and are not sensitive to toroidal field. The gain in confinement of the H mode, compared to th L mode, is mainly due to higher average

densities and partially to higher electron temperatures . The ion central temperature, measured by x-ray crystal and c-x spectroscopy, exceeded the electron temperature in the early part of the H-mode, at lower densities, while approaching the central electron temperature later at higher densities. In the early phase of the JET H-mode, after the L to H transition, the confinement time includes a strong contribution due to the large value of the derivative of total stored energy, of the order of 50% of the total input power. In this phase the power deposition profile of beams is centrally peaked. Gradually, the rate of increase of stored energy decreases and, at the same time, the beam power deposition profile becomes quite peripheral. A possible density dependence of energy confinement time is hidden in the non stationary nature of the discharge. Cleaner discharges tend to have lower radiation losses, with longer H-phases, and larger values of global confinement times. Local transport studies (7) indicate that the total energy diffusivity in the plasma interior returns to ohmic level already during the evolution of the L phase. Abel inverted bolometer radiation profiles typically show a steady increase of radiation during the H phase at the periphery of the plasma[8].

During long pulses, where a succession of H and L phases is observed, a gradual increase in the central radiation is also observed, suggesting a gradual drift toward the centre of metal impurities[8]. When a monster sawtooth during H-mode is present, the radiation profiles show a slight reduction of radiation losses across the radius.

Conclusions

In JET H mode the improvement in confinement is of the order of a factor of two compared to limiter discharges at the same level of plasma current. The threshold power scales greater then B_T^2. Global confinement time scales with input power and plasma current, roughly twice the Goldston scaling, but this should be offset against the increasingly off-axis heating due to bad beam deposition profiles at high neutral beam power. The values of q_{cyl} for H-mode discharges range between 1.8 and 4.5, compared with a range of 2 and 10 for limiter discharges. Sawtooth reconnection radii are in the range of $r/a = 0.5 \div 0.7$. It is possible that sawtooth activity has an effect on plasma confinement and on density and temperature profiles. So far ICRH have been unsuccessful in producing or sustaining an H-mode because of a) low coupling resistance due to large plasma-antennae separation and b) deleterious effect of increased impurity influx caused by the antennae. Future experiments will be carried out at larger plasma current and higher neutral beam power. The range of H mode discharges to will also be extended higher values of toroidal field .

References

(1) A Tanga et al. Nucl. Fus. 27 (1987) 1877.
(2) P Lomas et al. This conference.
(3) K H Burrell, presentation of the Workshop on H-mode in Tokamaks. San Diego, USA (Nov 1987).
(4) A Hubbard et al. This conference.
(5) C Gowers et al. This conference.
(6) D V Bartlett et al. in Proc. of 13th European Conference on Controlled Fusion and Plasma Heating, Schliersee, April 14-18, 1986.

References (continued) (7) M Keilhacker et al. This conference.
(8) K H Behringer et al. This conference.

Table I

Plasma current range in single null configuration	1-4 MA
Plasma current range with H mode	1-3.8 MA
Toroidal field range	1.7-2.8 T
Neutral Beam power range for H-mode	3-9 MW
Neutral Beam energy range	70-80 keV
Target discharge gas	Deuterium
Neutral Beams	D^+
Maximum line average density with H mode	$6 \times 10^{19} m^{-3}$

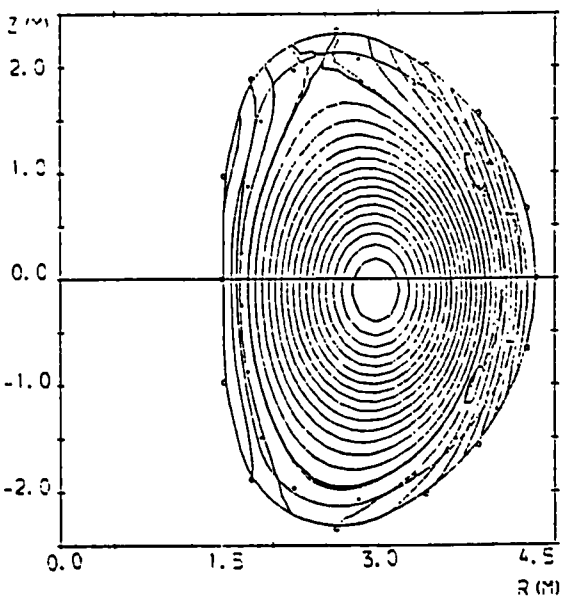

Fig. 1
Flux plot for pulse No: 14328
Plasma current 4 MA
Toroidal field 2.4 T
Plasma density $2.10^{19} m^{-3}$

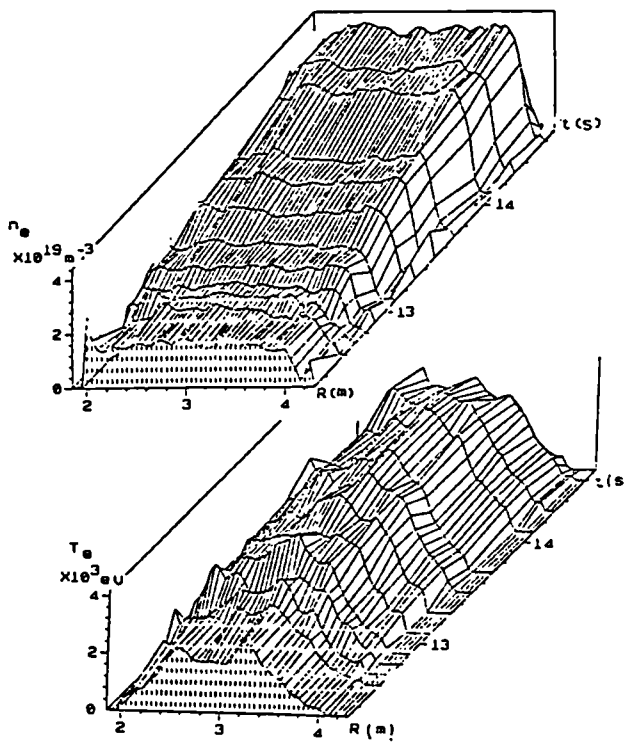

Fig. 2
a) Time evolution of the plasma electron density profile
b) Time evolution of the plasma electron temperature profiles
LIDAR profiles obtained from a series of reproducible discharges. Plasma current = 3.0 MA, Toroidal field = 2.1 T. NB power 7 MW, NB pulse starts at 12.5 s, L-H transition at 12.8 s.

THE EVOLUTION OF $Z_{eff}(r)$ PROFILES IN JET PLASMAS

P D Morgan

JET Joint Undertaking, Abingdon, Oxon OX14 3EA, UK

1. INTRODUCTION

The understanding and control of impurity production in JET plasmas remains a fundamental aim of the experiment. To this end, the global impurity content in the device is routinely monitored throughout each discharge by making measurements of the average ion charge $\bar{Z}_{eff}$, using visible continuum emission collected along two discrete lines of sight.

The use of a 15-telescope array aligned in a common poloidal cross-section has permitted the temporal evolution of $Z_{eff}(r)$ to be studied, under a variety of plasma conditions. In this paper, results are reported pertaining to a study of plasmas fuelled by gas or pellet injection and heated ohmically, by the application of ICRF or by NBI.

2. APPARATUS & ANALYSIS

The apparatus and method of analysis have been described in detail previously [1], albeit for a 13-channel version. The present system covers the same field of view, with two extra channels aligned on the zone where the magnetic separatrix is formed during X-point operation.

Each channel in the array measures the brightness $B = \frac{1}{4\pi} \int \varepsilon(\ell) d\ell$, at 523.5nm, along a chord through the plasma. Using the technique of Abel inversion, the brightnesses are transformed into the radial profile of continuum emissivity, $\varepsilon(r)$. Since $\varepsilon(r) \propto Z_{eff}(r)\, n_e^2(r)/T_e^{1/2}(r)$, knowledge of $n_e(r)$ and $T_e(r)$ permits the radial profile of Z_{eff} to be determined and its temporal evolution to be followed.

3. RESULTS AND DISCUSSION

(i) Ohmic Discharges with Gas Fuelling The precise value of $\bar{Z}_{eff}$ determined at any time during a discharge, for any given setting of machine parameters, is sensitive to the history of previous machine operation and cleaning procedures. This is also the case when additional heating is applied or D_2 pellets injected.

During the ohmic phase of a discharge, and following the establishment of a stationary density profile, $Z_{eff}(r)$ is usually peaked on axis with $Z_{eff}(o)/\bar{Z}_{eff} \leq 1.4$ and $Z_{eff}(o)/Z_{eff}(a) \leq 2.5$. Traces (a) of Figures 1, 2, 3 and 4 are representative examples of such profiles. For stationary discharge conditions, $\bar{Z}_{eff}$ decreases with increasing $\bar{n}_e$ and increases with I_p. Provided the vessel is well conditioned the data are represented by the relationship $\bar{Z}_{eff} \propto 1/(\bar{n}_e/J)$, where J is the plasma current density.

(ii) Discharges Heated by NBI

a) Limiter Discharges The injection of a beam of D atoms causes a

reduction of $\bar{Z}_{eff}$, the amount depending on the power of the injected beam, ie. on the flux of injected neutrals. Figure 1 shows two $Z_{eff}(r)$ profiles: (a) is prior to NBI while (b) was obtained after 5s of injection of a 5.5 MW beam of 80 keV D atoms. The relative shape of the $Z_{eff}(r)$ profile is little changed by the beam, but there is a reduction in the absolute values, $\bar{Z}_{eff}$ decreasing from ~ 2.6 to 2.3.

Despite a beam fuelling rate of 6×10^{20} s^{-1}, which increases the neutral source in the plasma centre by two orders of magnitude or more [2], recycling at the edge dominates the global particle balance. Recycling produces an electron influx that is ~ 4 × larger than the beam fuelling rate. The injected D atoms dilute the impurities, thereby reducing $\bar{Z}_{eff}$.

b) X-point Discharges When the plasma is limited by a magnetic separatrix (X-point discharge) and the H-mode of confinement is achieved following the start of NBI, a different form of evolution of $Z_{eff}(r)$ is observed from that reported in (ii)a. Figure 2 shows 3 profiles obtained during a discharge in which 7.5 MW of NBI were applied at 12.5s.

Profile (a) pertains to the ohmic phase of a discharge in contact with the belt limiters. Profiles (b) and (c) were obtained during the H-mode phase - (b) was evaluated 0.05s after the L to H transition while (c) occurs 1.1s later. During the H-mode, the profile of $Z_{eff}(r)$ steepens while the absolute values increase steadily - $\bar{Z}_{eff}$ increases from ~ 2.8 at 13.1s to ~ 3.7 at 14.2s. The profile is slightly hollow, as confirmed by soft X-ray [3] and spectroscopic [4] measurements. An improved global particle confinement time by a factor of 3-5 has been deduced from D_α measurements [1] and from impurity transport analysis [4].

(iii) Discharges Heated by ICRF The application of ICRF results in increased hydrogenic and impurity influxes. At power levels $\leq$ 4 MW both types of influx increase in proportion to the applied power and $\bar{Z}_{eff}$ is unchanged in value. However, at higher power levels $\bar{Z}_{eff}$ increases during the RF pulse and $Z_{eff}(r)$ evolves.

Figure 3 shows two $Z_{eff}(r)$ profiles: (a) pertains to the ohmic phase while (b) was evaluated after 4s of heating at a power of 11 MW. The increased impurity production at the plasma edge leads to an increase of $\bar{Z}_{eff}$ from ~ 3.4 to 4.8. $Z_{eff}(r)$ increases significantly in the outer region and its overall shape flattens with a slightly-hollow centre. Following switch-off of the RF source $\bar{Z}_{eff}$ decreases as the density rapidly decays, both to stabilise close to their ohmic values.

(iv) Discharges Fuelled by Pellet Injection Pellet injection has a dramatic effect on the temporal evolution of $Z_{eff}(r)$, due to the abrupt deposition of D atoms in numbers comparable to the plasma electron content, on a sub-millisecond time scale.

Multi-pellet fuelling has achieved values of $Z_{eff}(o)$ of 1.3 - 1.5, with $n_e(o) \geq 9 \times 10^{19}$ m^{-3}, following the injection at 0.5s intervals of 5 pellets during current ramp-up in a 3 MA limiter discharge [5]. Each pellet had an average electron content of 7×20^{20} - the initial plasma electron content was ~ 10^{21}. A single large pellet yields similar results, as reported in [1]; wherein the injection of ~ 4.5×10^{21} D atoms into a plasma of electron content ~ 1.3×10^{21} reduced $Z_{eff}(o)$ by > 3.

The effect of a single small pellet is less pronounced, but it well illustrates the plasma response to injection. In Figure 4, a time sequence of 4 $Z_{eff}(r)$ profiles is shown for a plasma of initial electron content

~ 1.4 x 10^{21} into which a D_2 pellet containing ~ 2.2×10^{21} atoms was injected. Profile (a) was obtained before injection. Profile (b) pertains to 0.1s after injection, which reduces $Z_{eff}(o)$, by ~ 40%, and also Z_{eff} at the plasma edge. However, at R ~ 3.6m, corresponding to the location of the q=1 surface, $Z_{eff}(r)$ has barely changed. The prompt reduction in $\bar{Z}_{eff}$ is consistent with a fixed plasma impurity content being further diluted by the injected D ions. Following injection, $Z_{eff}(r)$ fills in, traces (c) and (d). $\bar{Z}_{eff}$ increases until after 3-4s it is similar to that for a gas-fuelled discharge at the new, higher density.

4. CONCLUSIONS

The temporal evolution of $Z_{eff}(r)$ in JET plasmas has been studied using a 15-channel poloidal array to measure the visible bremsstrahlung emission. This has given an insight into the global impurity behaviour during ohmic, NBI and ICRF heating, and in the case of pellet injection.

The imprecisions in calibrating the array lead to systematic errors in the measured signals. The resulting absolute errors in the $Z_{eff}(r)$ profiles are estimated to be up to 25% on axis. At the plasma edge $n_e(r)$ is not well determined, leading to further uncertainties in $Z_{eff}(r)$, which is not usually evaluated for the outermost 0.3m. The relative errors in $Z_{eff}(r)$ are assessed to be about half the absolute errors, permitting changes in profile shape to be followed with reasonable confidence over most of the minor radius.

Under all conditions, recycling at the plasma edge plays an important role. During NBI in limiter discharges, $\bar{Z}_{eff}$ decreases but its profile shape is unchanged due to recycling being dominant over the central neutral source, in the global particle balance. In plasmas in which an H-mode is established $\bar{Z}_{eff}$ rises steadily and $Z_{eff}(r)$ becomes steeper, although with a hollow centre. At powers $\geq$ 4 MW, ICRH leads to a gradual increase in $\bar{Z}_{eff}$ with a flattening of $Z_{eff}(r)$, through increased impurity production at the plasma edge. Pellet injection, where deep penetration is achieved, causes a large abrupt decrease in $Z_{eff}(o)$, through dilution of the core impurities. However, on a time scale of 3-4s recycling establishes a higher $\bar{Z}_{eff}$ which is consistent with edge fuelling.

None of the scenarios above yield $Z_{eff}(r)$ profiles which indicate neoclassical accumulation of the light impurity species, such as C and O, in the plasma centre. However, metallic impurities such as Ni could accumulate significantly without being discernible on the $Z_{eff}(r)$ profiles, since their initial concentrations are low [4].

ACKNOWLEDGEMENTS The author is grateful to members of ED1 and ED2 who freely made available the results of their magnetic, electron temperature and density measurements.

REFERENCES

[1] P D Morgan and J J O'Rourke, Proc. 14th Europ. Conf. on Controlled Fusion and Plasma Physics 11D, (pt.3), p.1240 (1987).
[2] A Cheetham, et al., Proc. 13th Europ. Conf. on Controlled Fusion and Plasma Physics 10C, (pt.1), p.240 (1986).
[3] D Pasini, et al., this conference (1988).
[4] K H Behringer, et al., ibid.
[5] P Kupschus, et al., ibid.

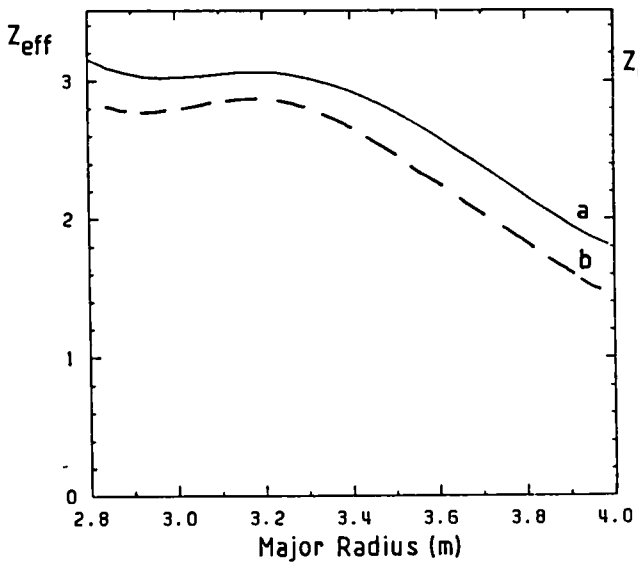

FIG.1: $Z_{eff}(r)$ profiles for pulse #10499. (a) t=6s, during the ohmic phase of the limiter discharge. (b) t=12s, during NBI. P_{NBI} = 5.5MW. I_p = 4MA.

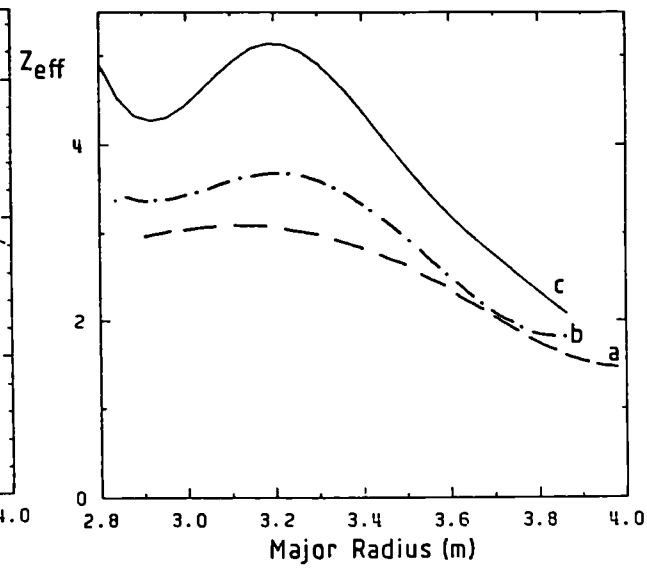

FIG.2: Radial profiles of Z_{eff} for pulse #14822. (a) t=5.1s, ohmic phase with plasma on limiters. (b) t=13.1s, 0.05s after start of H-mode. (c) H-mode, t = 14.2s. P_{NBI} = 7.5MW. I_p = 3MA.

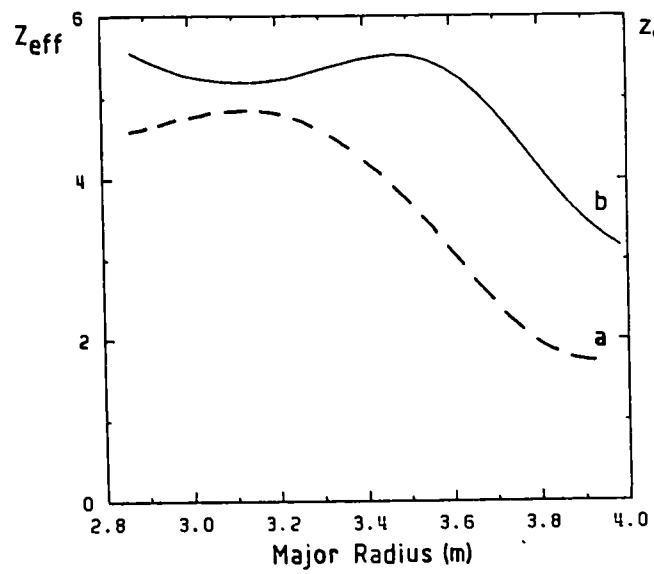

FIG.3: $Z_{eff}(r)$ profiles for pulse #13543. (a) t=10s, ohmic phase of limiter discharge. (b) t=14s, after 3s of 11MW of ICRH. 8 antennae in dipole configuration. I_p = 3.0-3.5MA.

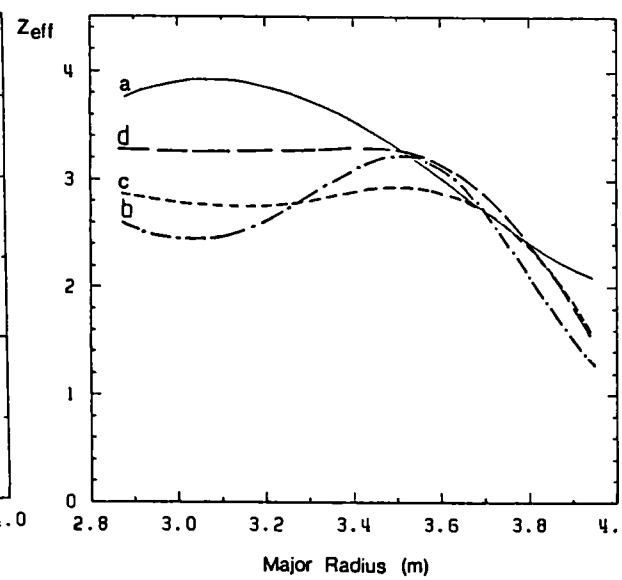

FIG.4: Radial profiles of Z_{eff} for pulse #9522. (a) t=6s (pellet injection at 7s). (b) t=7.1s. (c) t=8s. (d) t=12s. Profile evolves rapidly and $\bar{Z}_{eff}$ increases. I_p = 3MA.

MULTI-PELLET INJECTION ON JET*

P. Kupschus, A. Cheetham, B. Denne, M. Gadeberg, C. Gowers, A. Gondhalekar, B. Tubbing.

JET Joint Undertaking, Abingdon, OX14 3EA, England

and
G.L. Schmidt[a], S.L. Milora[b], L.R. Baylor[b], P. Colestock [a], S.K. Combs[b], G. Hammett[a], W.A. Houlberg[b], T.C. Jernigan[b], D. Schissel[c], M. Zarnstorff[a], US DOE (a: PPPL, b: ORNL, c: GA Technologies)

Introduction

JET and the US Department of Energy have jointly installed and are jointly operating a Multi-Pellet Injector for fuelling experiments on JET under the umbrella of the Bilateral Agreement on Fusion Research. The actual pellet launcher (built by Oak Ridge National Laboratory) can deliver multiple pellets of frozen fuel, from three different barrels in parallel in the sizes 2.7, 4 and 6 mm diameter (length equals diameter approximately) at a maximum frequency of several per second with nominal speed of up to 1500 ms^{-1}, which are injected horizontally into the midplane of the tokamak. More information can be found in [1] which also deals with the fuelling aspects of the pellet experiments described in the following. The JET Multi-Pellet Injector was brought into operation in last summer and systematic investigations with pellet injection have started later in the year with the aim to increase the central plasma in a more controlled way and to purify the plasma.

Since it is known that for large hot plasmas pellet penetration depths are likely to be insufficient to reach the centre of the discharge the overall strategy in the initial experiments has been to set up a high density target plasma in an ohmic discharge with central density peaking and to heat this subsequently in hope that the density profile will be maintained for a reasonable length of time. Mainly 2.7 and 4 mm deuterium pellets have so far been injected into the current flat top and into the current ramp, for plasma currents in the range of 3 to 5 MA in limiter discharges with toroidal fields of 2.1 to 3.4 T.

Review of initial experiments

Following the above mentioned strategy a large number (>100) tokamak discharges have been performed the evaluation of which is now being done but is hampered by the existence of particular problems with diagnostics to cope with rapid, multiple changes induced by the pellet events. It is therefore a tedious and time-consuming procedure to derive from the raw signals the time evolution of radial profiles needed for more detailed and subtle evaluation.

---

*This work has been performed under a collaboration agreement between the JET Joint Undertaking and the U.S. Department of Energy.

Peaked density profiles with high central density were established in the first example: Fig. 1 shows the time evolution of the electron density versus the major radius of a 2.5 MA/3T discharge (shot 13572) without auxilliary heating (as constructed from FIR laser interferometry and optical Bremsstrahlung measurement). One 4 mm pellet is injected into the early current flat top at 4.5 s and a combination of 2.7 and 4 mm pellets following each other in 10^{-3}s distance at 5.5s create a very peaked profile with a density on axis of more than $1.2.10^{20}m^{-3}$ (average $4.10^{19}m^{-3}$) decaying over 2s to $8.10^{19}m^{-3}$ still with a peaking factor $n_{e(o)}/ne$ of 3 (as supported by the LIDAR Thomson scattering profiles; the hollow profile at 4.5s may be a feature due to the limited number of signal traces available). The electron temperature on axis (being about twice the volume average one) drops with the first pellet from 3 to 2 keV and with the subsequent combined pellets to 1 keV but recovers in about 2s leading at 7.5s to a central electron pressure peak of 0.25 bar; tentative estimates give values around 2 during this time for Zeff (lower still for the pellet event itself) and around .6 sec for the energy confinement time, virtually constant over the density decay time.

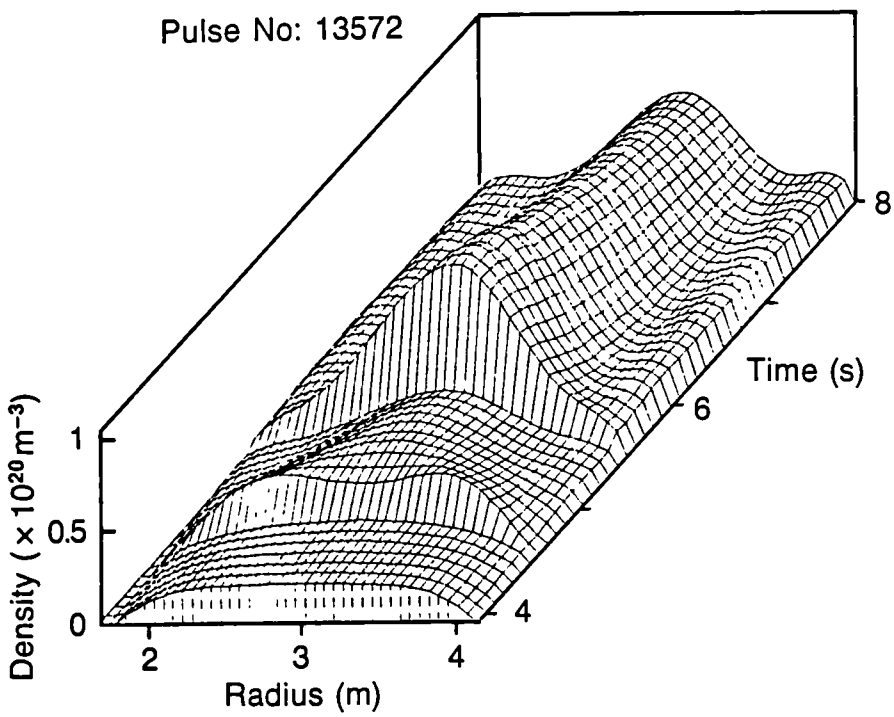

Fig. 1: Electron Density Profile over major radius R and time t for shot No. 13572

If the pellets do not penetrate sufficiently into the plasma to peak the central density strongly they nevertheless increase the average density on a faster time scale than gas feeding and to or even above the density limit. An example for this is shot 13544, a 3.3 MA, 2.8T discharge with three 4 mm pellets, fig. 2, followed up by on-axis RF heating of 16 MW at 42 MHz, H-minority ICRH. This drives the plasma stored kinetic energy up

to about 6 MJ with a radially very flat central density of 6.10^{19} m^{-3}. This profile holds on in time during the RF pulse - conditions are maintained for about two seconds - at a level which can also in the end be reached by gas puffing; however, the high D-D reaction rate of $1.4.10^{15}s^{-1}$ (no neutral beam heating) suggests a relatively clean plasma with a high deuteron content. The central electron pressure is exceeding .75 bar at a central electron temperature of 8 keV.

When pellets are too closely spaced in time locked modes - MHD activities with formation of almost stationary magnetic islands associated in this case with high-density operation - lead to rapid density pump-out and usually deterioration of peakedness [2].

Good profile peaking of density can be obtained by fuelling the tokamak discharge very early in the current ramp. Shot 14550 - the 3-dimensional density evolution can be found in [1] - shows a build-up to $9.10^{19}m^{-3}$ by injection of 7 2.7 mm pellets for a 3 MA/3T discharge, fig. 3. The central temperature is kept by the cooling of the pellets to about 1 keV before it takes off to 8 keV with RF (8MW) and NB (5MW) being applied at 3.5s; immediately the central density decay sets in and the peaking disappears with the total particle contents roughly maintained. The interesting part is the high electron pressure of .65 bar max and the high D-D reaction rate approaching $4.10^{15}s^{-1}$. The plasma energy is 4MJ but decaying in line with the temperature decay after 4.5s; with this collapse the central pressure as well as the D-D reaction rate are declining while the 13 MW are still maintained. A similar

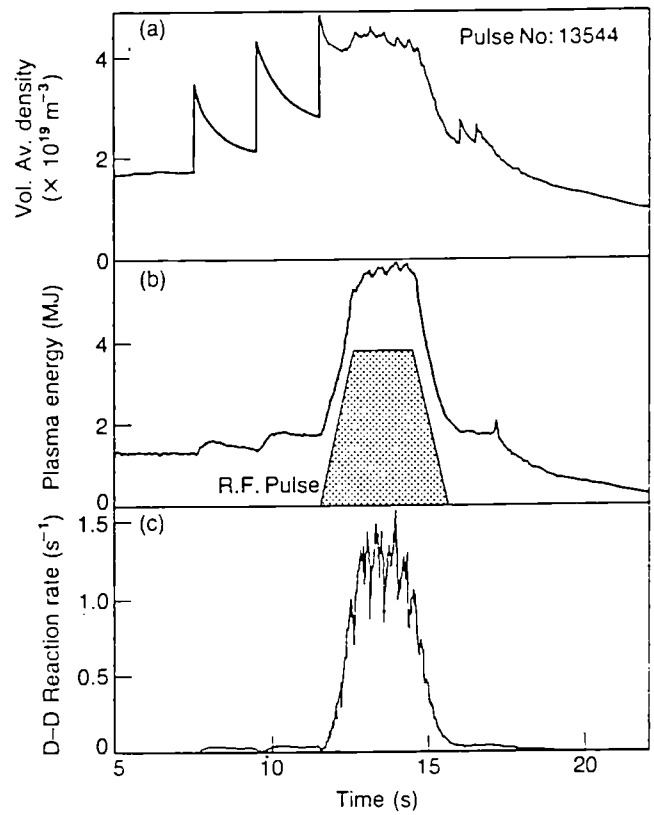

Fig. 2:

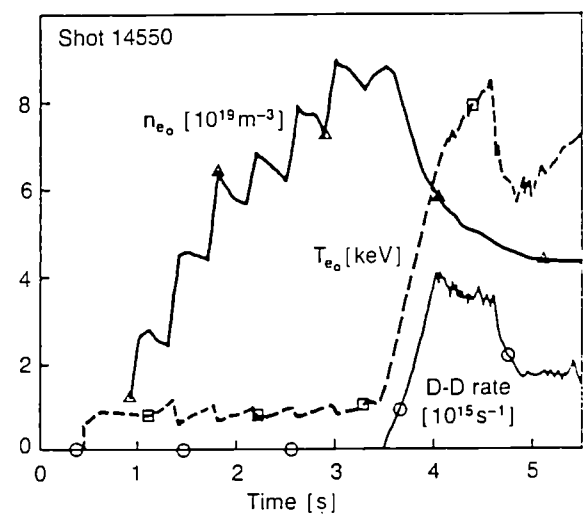

Fig. 3: Time trace of central electron density n_{e_o}, temperature T_{e_o} and D-D reaction rate

discharge - shot 14555 - exhibits very similar features: its D-D rate peaks at $4.3.10^{15}s^{-1}$ when the central electron temperature reaches 7.5 keV with combined auxilliary heating of 10MW ICRH and 5MW NB, it does however decay before the first temperature collapse .8s later and seems more to decline in parallel with the central density in this case. The D-D rate is still about $2.10^{15}s^{-1}$ 1.5s later when the LIDAR measures the radial electron pressure profile - fig. 4 - with about 0.5 bar peak and the highest pressure gradient, i.e. 2.2 bar m^{-1}, we have seen so far. Both shots exhibits global pressure values - as inferred from diamagnetic loop measurements - in excess of 35% of the Troyon limit.

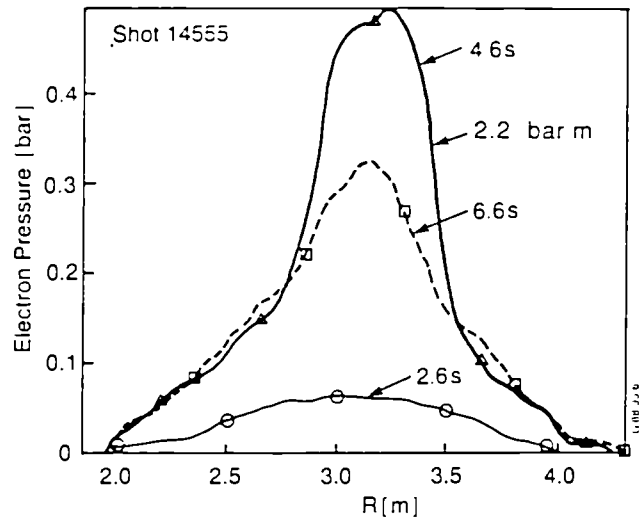

Fig. 4: LIDAR electron pressure measurement versus plasma diameter for 3 time slices in 2s intervals

Conclusions

The first series of multi-pellet injection experiments on JET have so far shown that with central deposition (usually to within one third of the minor radius) peaked density profiles with central values exceeding 10^{20} m^{-3} can be reached. These peaked profiles can persist for times in the order of seconds in the pure ohmic case. Auxilliary heating - on-axis radio frequency and combined RF and neutral beam heating (up to levels of 16MW) - seems to accelerate the slow central density decay considerably but generates for short times (some fraction of a second) high central electron pressure values (up to .75 bar) in a core with a high D-D reaction rate (up to $4.10^{15}s^{-1}$ at about 8keV electron temperature) presumably because of the high deuteron contents brought about by the injection of clean pellets. The next steps in the programme will be - apart from generally widening the operational range of injection application - to attempt to hold on to the peaked profiles by varying the heating and fuelling profiles and to understand the physics underlying the formation and the decay of this interesting core.

[1] S. Milora, this conference.

[2] J. Snipes, B. Tubbing, this conference.

SPONTANEOUS TRANSITIONS IN THE TEMPERATURE OF A TOKAMAK PLASMA WITH SEPARATRIX

P H Rebut, M L Watkins and P P Lallia

JET Joint Undertaking, Abingdon, Oxon, UK, OX14 3EA

1. INTRODUCTION

Tokamak experiments with a magnetic separatrix often exhibit spontaneous transitions in the edge electron temperature at the onset of an H-mode [1-3]. Such a transition might result, for example, from reduced edge losses due to the reduced recycling associated with the H-mode [4] or as a result of the edge plasma becoming stable again to ballooning modes in the second stable regime [5-6]. In the present paper, a two species plasma model is developed which exhibits a spontaneous transition in the edge electron temperature. The basis for the model is the critical electron temperature model [7] in which the anomalous transport disappears in the region of very high shear near a separatrix. The model has been shown to provide an acceptable interpretation of JET experimental data in terms of the global scaling of the stored electron energy and detailed profile analysis using transport code simulations [8,9]. In particular, a single formulation accounts for both the anomalous behaviour in ohmic plasmas and the degradation of confinement with additional heating (L-regime). The present work extends this formulation to the simulation of the electron temperature profiles and the improved energy confinement observed in H-mode plasmas in JET separatrix configurations.

2. TWO SPECIES PLASMA MODEL

Ion power balance

The ion power balance inside the separatrix may be written:

$$P_i + \int_V n\nu_{ei}k(T_e-T_i)dV = Q_i \qquad (1)$$

where P_i is the power directly heating the ions, n is the plasma density, T_e and T_i are the electron and ion temperatures and ν_{ei} is the energy equipartition frequency. The ion heat flux, Q_i, across the separatrix of surface area, S is:

$$Q_i = -\int_S n\chi_i \nabla k T_i dS = n\chi_i k(T_{ix}-T_{ia})S/\lambda$$

where χ_i is the ion heat diffusivity, and $T_{ix}-T_{ia}$ is the ion temperature difference over a distance λ in the vicinity of the separatrix.

To determine fully the energy equipartition term in equation (1) requires a full transport calculation of the temperature profiles. In the present analysis, this term is approximated by $n\nu_{ei}\, k(T_{ex}-T_{ix})V$, where it is assumed that the integral is dominated by a contribution over a volume V near the separatrix. The ion power balance can then be written in terms of T_{ex} and T_{ix}:

$$P_i + n\nu_{ei}k(T_{ex}-T_{ix})V = n\chi_i k(T_{ix}-T_{ia})S/\lambda$$

and the ion heat flux is given by:

$$Q_i = P_i + \frac{n\nu_{ei}kT_{ex}V + n\chi_i kT_{ia}S/\lambda}{1 + \nu_{ei}\, V\lambda/\chi_i S} - n\chi_i kT_{ia}S/\lambda \qquad (2)$$

Electron power balance

The electron power balance at the separatrix may be written:

$$Q_e = -\int_S n\chi_e \nabla kT_e dS = n\chi_e k(T_{ex}-T_{ea})S/\lambda \qquad (3)$$

where χ_e is the electron heat diffusivity and $T_{ex}-T_{ea}$ is the electron temperature difference over the distance λ.

Total power balance

The total power balance at the separatrix can be expressed in terms of Q_e alone by eliminating T_{ex} from equations (2) and (3):

$$P = Q_e + Q_i = Q_e + P_i + \frac{n\nu_{ei}eV(T_{ea}+\lambda Q_e/Sne\chi_e)+n\chi_i eT_{ia}S/\lambda}{1 + \nu_{ei}\, V\lambda/\chi_i S} - \frac{n\chi_i eT_{ia}S}{\lambda} \qquad (4)$$

With the simplifying assumptions that the edge temperatures (T_{ea} and T_{ia}) and power to the ions (P_i) are zero and with $\nu_{ei} = n\nu_o/T_{ex}^{3/2}$, equation (4) may be written in the form:

$$\bar{P} = \bar{Q}_e + \frac{\bar{Q}_e}{\bar{Q}_e^{3/2} + q} \qquad (5)$$

where $\bar{P} = P/p$, $\bar{Q}_e = Q_e/p$, with the power normalisation, p, and the parameter, q, defined as:

$$p = \left(n^2\nu_o eV(neS\chi_e/\lambda)^{1/2}\right)^{2/3} \qquad q = \chi_e/\chi_i$$

3. INTERPRETATION OF THE RESULTS

Given the electron and ion heat diffusivities the model determines the electron power flow, $\bar{Q}_e$, and hence the edge electron temperature (equation (3)) for a given power flow, $\bar{P}$, across the separatrix. The general solution of equation (5) is shown in Fig.1 for q in the range $0.0001 \leq q \leq 1.0$. For $\chi_e \sim \chi_i$, $\bar{Q}_e$ and the edge electron temperature increase monotonically with $\bar{P}$ (q = 1.0 curve in Fig.1). With decreasing χ_e/χ_i,

the rate of increase of $\tilde{Q}_e$ with $\tilde{P}$ is reduced at low $\tilde{Q}_e$ and the ions transport a larger fraction of the total input power (q = 0.1 curve). For $\chi_i >> \chi_e$ the ions transport a substantial fraction of the total input power (q = 0.0001 curve).

Of course the ion power flow is itself dependent on the electron temperature (through energy equipartition). As a result, for certain input powers, three solutions can exist (eg, q = 0.01 curve), two of which are stable (S_1 & S_2) and one unstable (U) to perturbations in the edge temperature. Under these conditions a transition between the two stable solutions will manifest itself in a spontaneous change in the electron temperature and the electron power flow across the separatrix becomes significant. These solutions occur above a certain power threshold.

4. RELEVANCE TO THE JET H-MODE

The transport models of [8,9] lead to temperature profiles in fair agreement with experiment. Inside the separatrix the electron temperature profile is determined largely by the critical temperature gradient and $\chi_i \sim \chi_e$. Under these conditions q ~ 1 and p ~ 9MW, typically. For an input power of 5MW, Q_e ~ 2.7MW and the edge temperature ~40eV.

Near the separatrix, however, the heat diffusivities will be reduced due to the local magnetic shear, ultimately being limited by neoclassical transport. χ_i will change less than χ_e. For typical JET conditions (q~0.03 in Fig.1 and p~3MW) a power in excess of 5.4MW is needed to make the transition from a low edge temperature (~250eV) with ion transport dominating the power flow to a high edge temperature (~1keV) with electron transport becoming more important. Such a spontaneous change in the electron temperature is identified with the pedestal observed to develop within ~0.05-0.1m of the JET separatrix when a transition is made from the L-H regime at an input power, P~5MW.

The simplified 1-D electron energy transport code [8,9] has been used to simulate the electron temperature profiles of JET Pulse #10755. The electron transport model presented at the Varenna Theory Conference (but with the anomalous diffusivity multiplied by the shape parameter $(R/r)(R\nabla T_e/T_e)(T_i/T_e)^{1/2}$ [9]) has been used in conjunction with the boundary condition given above for the edge electron temperature. The density, auxiliary heating and radiated power profiles are represented by analytical functions based on experimental data. Neoclassical corrections to the Spitzer resistivity are accounted for by a radial dependence in Z_{eff}. The electron temperature, the resistivity and the current density are assumed to be constant within the q=1 surface. The computed and experimental profiles show satisfactory agreement (Fig.2) in the ohmic, L- and H-phases. It should be noted that the same transport equations are used to simulate all phases of the discharge.

5. SUMMARY

The two species plasma model developed exhibits a spontaneous transition in the electron temperature in the high shear region in the edge of a tokamak plasma with separatrix where the transport is ultimately neoclassical. The transition occurs above a certain power threshold,

predicted to be about 5MW for JET, in accord with the power threshold for transition to the H-mode. Furthermore, the electron temperature profiles and energy confinement in ohmic, L- and H-phases of discharges in JET separatrix configurations are well simulated by the critical electron temperature gradient model, which contains intrinsically a degradation of confinement with additional heating.

References

[1] Tanga, A., et al., Nucl. Fusion 27(1987)1877.
[2] Keilhacker, M., et al., Plasma Physics and Controlled Fusion, 26(1984)49.
[3] Kaye, S., et al., J. Nucl. Mater. 121(1984)115.
[4] Cohen, S.A., et al., Plasma Physics and Controlled Fusion, 29(1987)1205.
[5] Keilhacker, M., et al., Proc. 14th Eur. Conf. on Cont. Fusion and Plasma Physics, Madrid, 1987, 11D(III), EPS(1987)1339.
[6] Bishop, C.M., Nucl. Fusion 27(1987)1765.
[7] Rebut, P.H., et al., in Plasma Physics and Controlled Nuclear Fusion Research (Proc. 11th Int. Conf., Kyoto, 1986), 2(1987)187.
[8] Rebut, P.H., et al., Proc. 14th Eur. Conf. on Cont. Fusion and Plasma Physics, Madrid, 1987, 11D(I), EPS(1987)172.
[9] Lallia, P.P., et al., 2nd Eur. Fusion Theory Meeting, Varenna (1987) and JET Preprint JET P(88)05.

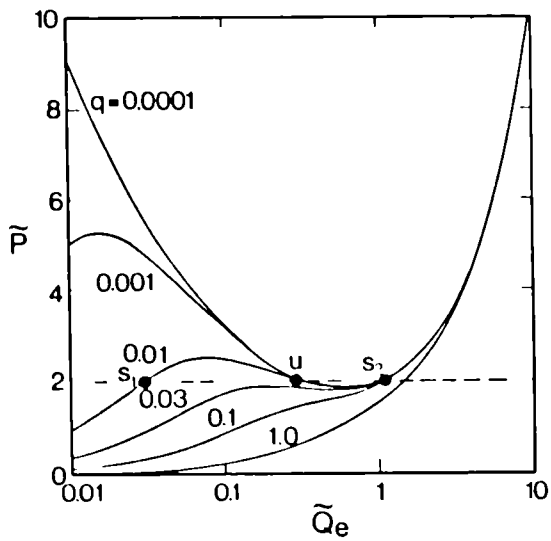

Fig 1: Solution to equation (5) for various values of the parameter q.

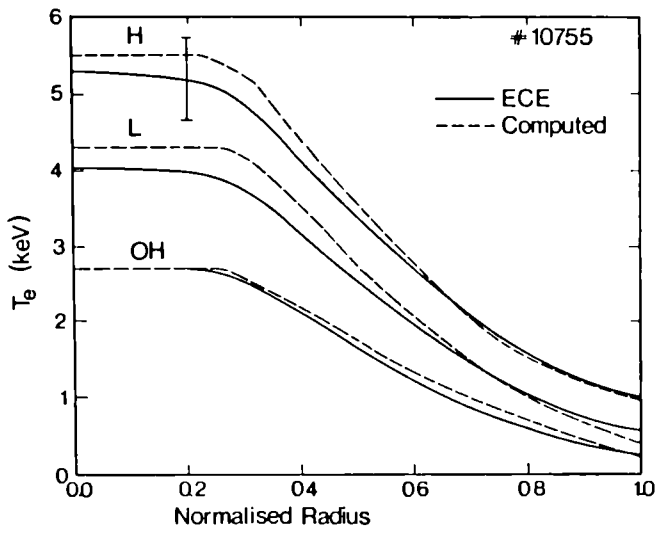

Fig.2: Experimental (—) and computed (---) electron temperature profiles at times 10.5s (OH), 11.7s (L-phase, P~4MW) and 12.7s (H-phase, P~8MW) during JET pulse #10755.

MEASUREMENT AND INTERPRETATION OF TRITON BURNUP IN JET DEUTERIUM PLASMAS

P Batistoni[1], J Argyle[2], S Conroy[4], G Gorini[3], G Huxtable[2], O N Jarvis, J Källne, M Martone[1], M Pillon[1], S Podda[1], M Rapisarda[2], G Sadler, D B Syme[2], P van Belle and K Verschuur[5]

JET Joint Undertaking, Abingdon, Oxfordshire, OX14 3EA, UK
[1] Associazione EURATOM-ENEA, CRE Frascati, Italy
[2] AERE, Harwell, Oxon, UK
[3] Scuola Normale Superiore, Pisa, Italy
[4] Imperial College of Science and Technology, London
[5] ECN Petten, The Netherlands

The confinement and slowing down of fast tritons has been investigated by measuring the ratio of 14 MeV and 2.5 MeV neutron production rates. Tritons of 1.0 MeV are produced in the d + d → t + p reaction at the same rate as the 2.5 MeV neutrons from the d + d → ^{3}He + n reaction. The majority of these tritons will remain confined in the plasma and slow down to thermal energies through Coulomb collisions with electrons and ions; a fraction will undergo fusion reactions t + d → ^{4}He + n, in which the 14 MeV neutrons are emitted. The fraction of the tritons which burn-up is essentially equal to the ratio of 14 MeV to 2.5 MeV neutron production.

The 2.5 MeV neutron emission is obtained from a set of fission chambers for which the calibration uncertainty is about ±10%. The 14 MeV neutron production is measured by means of the activation of Copper samples placed close to the plasma using a pneumatic transport system which returns them, after each discharge, to a counting room for the measurement of the induced γ-activity. The reaction ^{63}Cu(n,2n)^{62}Cu is employed; it has a threshold energy of 10.9 MeV and a fairly high cross section (0.44 b at 14 MeV). The experimental set-up and the first measurements, performed in 1986, are reported in /1/.

The absolute calibration of the activation technique has to be calculated in order to relate the total neutron emission to the local neutron flux at the irriadition position. The 1986 triton burn-up measurements, presented in /1/, made use of response coefficients calculated with FURNACE /2/, a code based on ray tracing and the discrete ordinates method. The absolute calibration has been revised recently using the neutron transport Monte Carlo code MCNP /3/ to provide a more detailed description of the vessel wall and the holes through the surrounding structure, through which the irradiation ends are inserted. Neutron activation response coefficients were calculated for three different samples (Indium, Zinc and Copper) for deuterium plasmas producing 2.5 and 14 MeV neutrons. The accuracy of the calibration was tested by comparing the results for the 2.5 MeV neutron yields with those obtained with the fission chambers; an overall agreement at the ±15% level was demonstrated

/3/. For the 14 MeV neutrons, the response coefficient calculated with MCNP for Copper was 1.6 times lower than that calculated with FURNACE. This reduction is in part due to use of more accurate activation cross sections ($\sim$ 20%) and to the inclusion of effects due to local inhomogeneities at the irradiation ends (10%). A small unexplained discrepancy remains. For the present work, we adopt the more recent MCNP results. The overall accuracy for the Copper response coefficients, including modelling, calculation statistics, and cross section uncertainties, is estimated to be about ±10%.

Further measurements have been obtained in 1987; ohmically-heated plasmas (with plasma currents up to 6 MA) and combinations of NBI and ICRH with up to 21 MW of additional heating power have been studied. All 1986 (corrected) and 1987 data are shown in figure 1 vs. the plasma current. Only measurements with statistical errors below 20% have been retained, these errors being actually less than 10% for most data points. The triton burn-up ratios fall in the range 0.5 to 1.5% depending upon plasma conditions. These conditions varied in the ranges: $1.8 \leq B_t \leq 3.4$ T, $1 \leq I_p \leq 6$ MA, $3.7 \leq T_e \leq 7$ keV, $1 \leq n_e \leq 7 \times 10^{19}$ m^{-3}, $1.6 \leq Z_{eff} \leq 8$, the main impurities being Carbon and Oxygen. Finally the neutron yield for these discharges varied between 10^{13} and 4×10^{15}.

The triton burn-up ratio, ρ, is proportional to the product of the triton confinement fraction f_c, the deuterium density n_D and the d + t fusion probability (which depends on the triton slowing down rate). The d+t fusion cross section has a maximum around $E_T \approx 170$ keV, well below the triton initial energy, so that the burn-up is sensitive to the slowing down mechanism for fast tritons. The main motivation for studying triton burn-up is to test the validity of the classical slowing down model for MeV ions without invoking anomalous losses or displacements of ions from their classical drift orbits. For this purpose, the burn-up measurements have been compared with model calculations based on classical triton confinement and slowing down in the plasma. Two codes have been used, each tending to stress different aspects of the problem. The first is a time-independent code, SOCRATE /4/, which takes into account the prompt-loss fraction of the tritons and the excursions from the flux surfaces on which they are born. The slowing down rate and the d + t fusion probability is calculated for each confined triton moving on the guiding centre drift orbit corresponding to the initial energy. The second is a time-dependent code, TRAP-T /5/, which assumes that the tritons stay on the flux surface on which they are born. Since the slowing down for tritons can be as long as 1 sec in JET, the time variation of plasma parameters has to be considered, especially for discharges with strong additional heating. Both codes calculate slowing down as due to electron and ion Couloumb drag, other collisional effects such as pitch angle scattering and energy diffusion being neglected. Both use the magnetic equilibrium flux surfaces and the plasma parameters $T_e(r)$, $n_e(r)$ and Z_{eff}, provided by other diagnostics, as input data. The triton source distribution is deduced on the assumption that $T_i(r) = T_e(r)T_i(o)/T_e(o)$. This approximation may be rather crude in the case of NBI heating where many of the tritons are produced by beam-plasma interactions. However, the 2.5 MeV neutron emission profiles are measured on JET /6/ and no important

differences in the profiles are observed between ohmic and NBI heated discharges. The ratio n_D/n_e is deduced from visible bremsstrahlung measurements of Z_{eff} and from the concentration of impurity species from UV spectroscopic measurements. Uncertainties in Z_{eff} propagate increasingly larger errors in the ratio n_D/n_e for higher Z_{eff} values; therefore, a restricted set of the 1987 discharges has been selected for which $2 \leq Z_{eff} \leq 3$ so that n_D/n_e varied between 0.83 (±7%) and 0.65 (±15%). For the discharges so selected, the total plasma current was 3 or 4 MA and the calculated prompt loss fraction was always less than 3%. Both ohmic and NBI and/or RF heated discharges with up to 15 MW additional power were included. Predictions for the triton burn-up were obtained for these discharges from the two codes; they are in remarkably good agreement (within a few per cent) in all cases, provided that the time independent code is run for several times representative of the discharge temporal evolution. This agreement indicates that the neglect of orbit drifts is a good approximation for JET plasma with $I_p \geq 3$ MA.

The comparison between experimental and theoretical burn-up ratios for the 1987 data is shown in figure 2. The error bars for the experimental values retain only the statistical errors; the systematic error is about ±15%. The error bars for the calculated burn-up values take into account the uncertainties in the input data for Z_{eff} and T_e. The electron temperature used is that measured by the LIDAR diagnostic which has recently become available /7/. It is based on Thomson scattering and does not suffer, unlike ECE, from problems associated with a magnetic field dependent calibration. The uncertainties in T_e, which propagate almost linearly in the burn-up ratio through the thermalization time of the tritons, is ±10%. Errors arising from approximations in the classical models adopted in the codes are difficult to assess. Both codes neglect losses due to pitch angle scattering but, since the loss cone is small, their effect is expected to be negligible.

It can be seen from Fig. 2 that agreement has been found between the experimental measurements and the theoretical calculations within the overall uncertainty of ±20% for both values. No particular trend has been found for additionally heated as compared to ohmic discharges. The present results, using the 1987 data, correlate rather better with the line for $\rho_{exp} = \rho_{th}$ than did the 1986 data reported in ref. [8]. The two sets of data are not inconsistent with each other but nevertheless there is an apparent improvement which can be attributed mainly to the use of LIDAR instead of ECE temperature data, and also to the selection of more reliable burn-up data (ie. ρ_{exp} for $Z_{eff} \leq 3$). Since the major source of uncertainty for high Z_{eff} discharges (ie. $Z_{eff} > 3$) lies in the ratio n_D/n_e, confirmation of the classical nature of the triton burn-up process now permits us to invert the problem and to consider the burn-up measurements as contributing to the evaluation of n_D/n_e.

REFERENCES

[1] P. Batistoni et al, Proc. 14th European Conference on Controlled Fusion and Plasma Physics, Madrid 1987, Vol III (1987) 1228.

[2] K.A. Verschuur, "Neutron Transport Calculations in Support of Neutron Diagnostics at JET", ECN-86-097.

[3] M. Pillon et al, "Calibration of Neutron Yield Activation Measurements at JET", JET-P(88)10.
[4] G. Gorini et al, "Calculation of the Classical Triton Burn-Up in JET Deuterium Plasmas", JET-P(87)35.
[5] O.N. Jarvis et al, "Time-Resolved Measurements of Triton Burn-Up in Beam-Heated Deuterium Plasmas", Bull. Am. Phys. Soc. 32 (1987) 1838.
[6] J.M. Adams et al, Proc. 14th European Conference on Controlled Fusion and Plasma Physics, Madrid, 1987, Vol III (1987) 1224.
[7] C. Gowers and H. Salzmann, "First Results from the LIDAR-Thomson Scattering System on JET", JET-P(87)16.
[8] J. Källne et al, "Triton Burn-Up Measurements in JET Using Neutron Activation Techniques", JET-P(88)9.

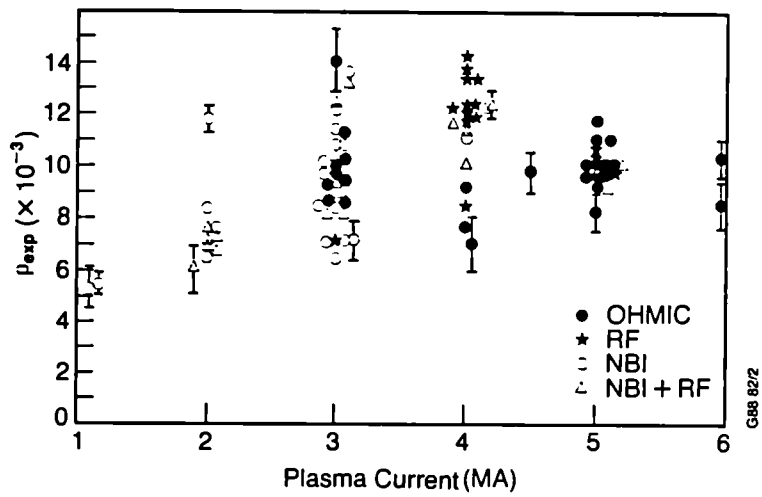

Figure 1:

Illustrating the range of conditions over which measurements of the triton burn-up fraction have been obtained.

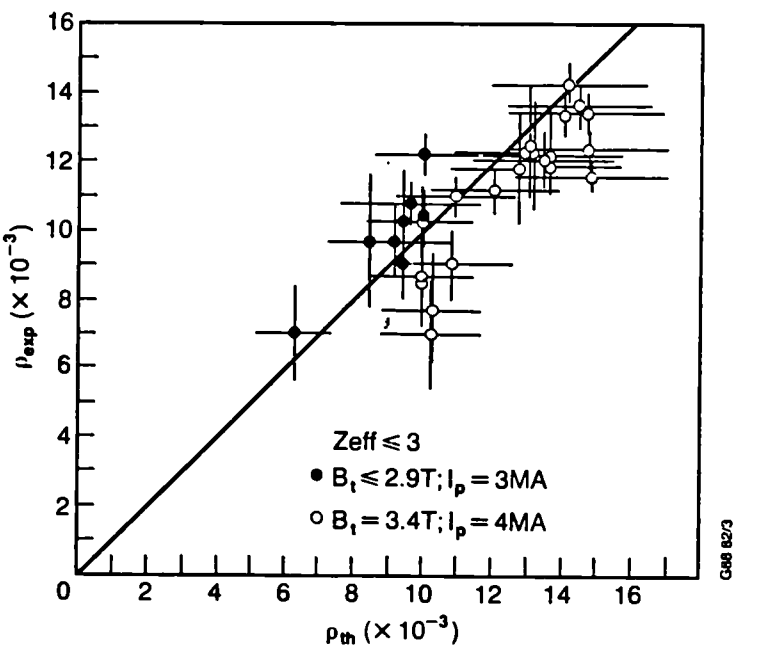

Figure 2:

Comparison of experimental with calculated triton burn-up fractions for the subset of measurements with $Z_{eff} \leq 3$. The solid line for $\rho_{exp} = \rho_{th}$ is provided as a guide to the eye.

THE JET MULTIPELLET LAUNCHER AND FUELING OF JET PLASMAS BY MULTIPELLET INJECTION*

S.L. Milora, G.L. Schmidt[a], T.C. Jernigan, L.R. Baylor, S.K. Combs, W.A. Houlberg, D. Schissel[b], P.Colestock[a], G.Hammett[a], M.Zarnstorff[a]

Oak Ridge National Laboratory, Oak Ridge,Tennessee 37831, U.S.A.

P. Kupschus, A. Cheetham, B. Denne, M. Gadeberg, C. Gowers, A. Gondhalekar, B. Tubbing

JET Joint Undertaking, Abingdon, Oxon OX14 3EA, U.K.

Pellet Injector System Description and Performance

A three-barrel repeating pneumatic pellet launcher developed at ORNL is the principal component of a new plasma fueling system for the Joint European Torus (JET) [1,2]. This versatile device consists of three independent machine-gun-like mechanisms equipped with high-speed extruders to provide solid deuterium to each gun assembly. The injector features nominal pellet sizes of 2.7 mm, 4.0 mm, and 6.0 mm, giving ideal volume-average plasma density increments of 0.82×10^{19} m^{-3}, 2.66×10^{19} m^{-3}, and 8.9×10^{19} m^{-3}, respectively, and has been qualified at repetition rates of 5 Hz, 2.5 Hz, and 1 Hz, respectively. Each gun can operate (individually or simultaneously) at the design repetition rate for 15-s pulses. Pellet speeds in the repeating mode average 1300 m/s; in the single-shot mode, the performance is close to 1500 m/s. Additional components of the ORNL pellet launcher system include: (1) an instrumented propellant and fuel gas feed system; (2) injector diagnostics, including a fiber-optic pellet detection system and optical systems for remote monitoring of solid hydrogen extrusions and high-speed flash photography of pellets; and (3) a data acquisition and remote control system consisting of a programmable logic controller (PLC) and a computer/CAMAC-based operator interface and data acquisition system.

The balance of the installation at JET consists of the following JET-supplied subsystems [3]: (1) a launcher-torus vacuum interface for differential pumping of propellant gas and extrudate fuel featuring a 50-m^3 vacuum chamber equipped with an 8×10^6 L/s cryocondensation pump; (2) a liquid helium delivery, storage, and recovery system and fuel and propellant gas distribution systems; (3) a fire control sequencer that provides timed trigger pulses for initiation of the extrusion process and programmable firing of pellets; (4) a microwave cavity-based pellet mass measurement system and an instrumented target array to facilitate aiming of all three guns; and (5) a PLC-based control system and computer operator interface for these subsystems.

*This work has been performed under a collaboration agreement between the JET Joint Undertaking and the U.S. Department of Energy.

[a]Princeton Plasma Physics Laboratory, Princeton, New Jersey, U.S.A.

[b]GA Technologies, Inc., San Diego, California, U.S.A.

The fueling system became operational on JET in October 1987. To date, plasma fueling experiments have been performed with the 2.7- and 4.0-mm guns operating in the multipellet mode.

Pellet Penetration and Particle Deposition Profiles

Penetration of the 2.7- and 4.0-mm pellets for ohmic plasmas without significant populations of suprathermal electrons agrees with the neutral and plasma shielding model [4], as shown in Fig. 1. Measured penetration is determined from vertical soft x-ray data in all cases. The calculated penetration uses T_e profiles from second harmonic ECE data and n_e profiles from six vertical chords of an FIR interferometer. The 2.7-mm pellets have a pellet-by-pellet mass correction in the calculated penetration using the signal from the microwave cavity. The larger scatter in the 4-mm data may be due to pellet mass variation in the experiment; the calculated penetration is based on an average mass. Earlier JET data from 3.6- and 4.6-mm pellet experiments using the IPP Garching single-pellet injector show similar agreement with the model [5].

The gross particle deposition has been determined by volume integration of the density profiles after pellet injection. This gives, on average, 6.6×10^{20} and 2.3×10^{21} particles for the 2.7- and 4-mm pellets, respectively, which corresponds to ≈70–75% of the pellet inventory as determined by the ideal pellet dimensions. The discrepancy results from a loss of pellet mass by erosion of the pellet diameter in the gun barrels.

Details of the particle deposition in ohmic plasmas are illustrated in Fig. 2 by LIDAR Thomson scattering profiles taken within 20 ms of pellet injection. Figure 2a shows the plasma density profiles after the first and third pellets in a sequence of three 4-mm pellets injected into a 3-MA ohmic discharge at 1 Hz. The profile is strongly inverted after the first pellet (which penetrates to $R \approx 3.4$ m) but more centrally peaked after the third pellet, which penetrates to the magnetic axis. Central penetration is accomplished as the central electron temperature decreases from 4 keV to 2.5 keV during the fueling pulse. As shown in Fig. 2b, a deeper deposition profile can be achieved by injecting a 2.7-mm pellet a few milliseconds after the 4-mm pellet. This technique was used to produce the highly peaked density profile shown in Fig. 2c. The subsequent evolution of the density profiles in ohmic and auxiliary heated discharges is discussed by Kupschus et al. [6].

Plasma Fueling Experiments

One of the primary objectives of the experimental program on JET is to produce clean, centrally peaked, high-density target plasmas for central and off-axis heating (ICRF and NBI) experiments. To date, the 2.7-mm and 4-mm injectors have been used for this purpose in X-point and limiter plasmas at up to 5 MA of plasma current. Plasma density buildup has been demonstrated in the startup and flattop phases of ohmic limiter and X-point discharges using 2.7-mm pellets for pulse lengths exceeding 2.5 s. Figure 3 illustrates the plasma density evolution from FIR data in response to injection of 2.7-mm pellets at 2.5 Hz starting 1 s into the discharge (at $I_p = 1.5$ MA) and continuing until the start of the current flattop phase of a 3-MA limiter plasma. In this discharge, a centrally peaked density profile is maintained in time as the second and subsequent pellets penetrate to and somewhat beyond the magnetic axis. This was accomplished by adjusting the fueling rate so that the central electron temperature was maintained in the range of 1.2–1.3 keV throughout the fueling pulse. The volume-average density increases linearly during pellet fueling, and 75% of the particle input rate is accounted for in the rate of rise of the plasma particle inventory. Peak to volume-average density ratios in the range of 2–2.5 are maintained during the fueling pulse, compared with 1.3 for gas puffing cases. The

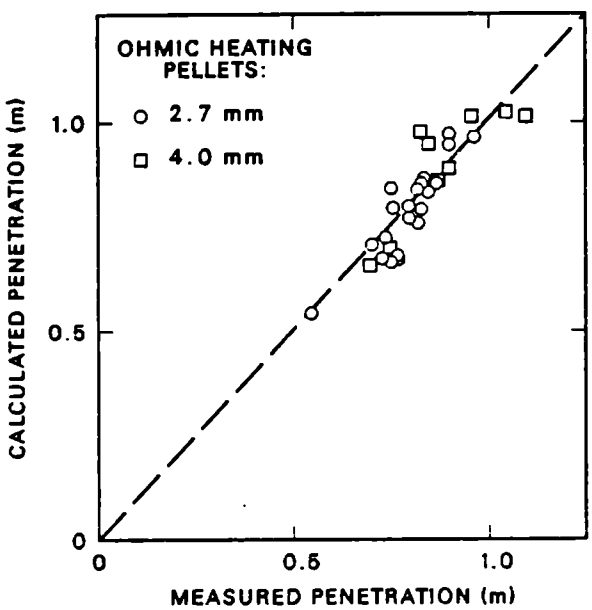

Fig. 1. Measured and calculated penetration for 2.7- and 4.0-mm pellets.

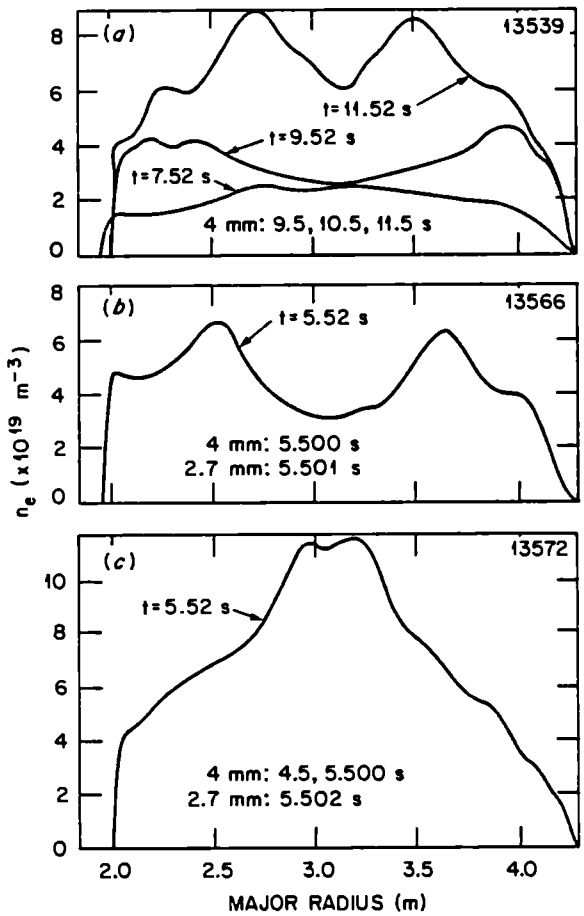

Fig. 2. Density profile shapes after 4-mm and combined 4-mm and 2.7-mm pellets in 3-MA ohmic discharges.

peaking factor is sensitive to pellet penetration, as demonstrated by comparing Fig. 3 (shot 14550) and Fig. 4 (shot 14545). The conditions of Fig. 4 differ from those of Fig. 3 in that the central electron temperature is higher (2–2.2 keV) during the fueling pulse, resulting in reduced pellet penetration (to R = 3.25–3.35 m). The density profiles are consequently broader, giving peaking factors of 1.75 and central densities 50% smaller than the values on shot 14550. While the volume-average density increments during pellet injection for these two cases are similar, the density decay after pellet injection is somewhat more pronounced on shot 14545, giving a 15% smaller volume-average density at the end of the pellet fueling pulse. The response of these profiles to auxiliary heating, which starts at 3.5 s, is discussed by Kupschus et al. [6] at this conference.

Long-pulse plasma fueling has also been performed in the flattop phases of ohmic discharges using primarily the 2.7-mm gun. In limiter plasmas, the volume-average density can be maintained at 3.5×10^{19} m^{-3} at an injection frequency of only 1 Hz. Preliminary experiments in ohmic X-point discharges indicate that pellet fueling provides better control over the density level than gas puffing but that the fueling efficiency is lower (i.e., the plasma pumpout is faster) than in the high-recycle limiter plasmas. For 2.7-mm pellets that penetrate to R = 3.5–3.6 m (i.e., about halfway to the axis), injection

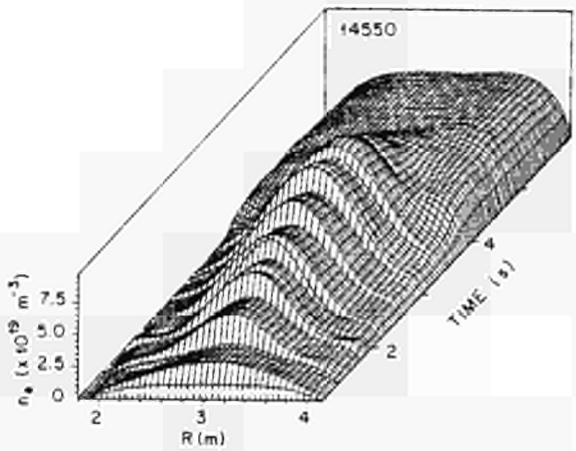

Fig. 3. Plasma startup with centrally penetrating 2.7-mm pellets at 2.5 Hz. Auxiliary heating starts at 3.5 s.

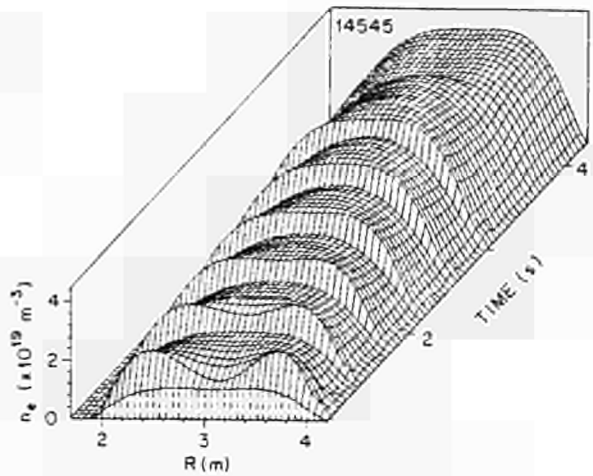

Fig. 4. Plasma startup with noncentral penetration. Auxiliary heating starts at 3.5 s.

frequencies of 2 Hz are required to maintain the volume-average density in the range of 2×10^{19} m^{-3}. A more pronounced effect has been been obtained by injecting a 4-mm pellet (which penetrates to $R = 3.15$ m) followed by 2.7-mm pellets at 5 Hz. In this case, a central density of 5×10^{19} m^{-3} was sustained with a profile shape similar to that of Fig. 4. For conditions typical of the flattop phases of JET discharges, deep pellet penetration is not achieved with 2.7-mm pellets alone, and to date we have not observed density profile peaking as strong as that observed on ASDEX [7] with partial penetration.

Summary

A new multipellet long-pulse plasma fueling system is in operation on JET. In the initial experimental phase, a variety of plasma density profile shapes have been produced with peak to average values ranging up to 2.5 and peak plasma density up to 1.2×10^{20} m^{-3}.

References

[1] S.L. Milora et al., in *Proc. 12th Symp. on Fusion Engineering (Monterey 1987)*, IEEE, Vol. 2, pp. 784–86 (1987).
[2] S.K. Combs et al., "A Three Barrel Repeating Pneumatic Pellet Injector for Plasma Fueling of the Joint European Torus", to be published in J. Vac. Sci. Technol.
[3] P. Kupschus et al., in *Proc. 12th Symp. on Fusion Engineering (Monterey 1987)*, IEEE, Vol. 2, pp. 781–83 (1987).
[4] W.A. Houlberg, S.L. Milora, S.E. Attenberger, "Neutral and Plasma Shielding Model for Pellet Ablation", to be published in Nucl. Fusion.
[5] M.L.Watkins et al., in *Proc. 14th European Conf. on Controlled Fusion and Plasma Heating (Madrid, 1987)*, Vol. 1, pp. 201–4 (1987).
[6] P. Kupschus et al., these proceedings.
[7] M. Kaufmann et al., "Pellet Injection with Improved Confinement on ASDEX," to be published in Nucl. Fusion.

(Invited paper presented at the 8th International Conference on Plasma Surface Interactions, Jülich, FRG, 2nd-6th May 1988)

Experience with Wall Materials in JET and Implications for the Future

P H Rebut, K J Diëtz, P P Lallia

Abstract

A variety of materials have been used in JET for wall protection and high heat flux components. The machine initially operated with metallic walls, but the inner surface of the vessel (~200m²) is now covered to more than 50% with fine grain and carbon fibre reinforced graphite tiles. The remaining wall area is carbonized. This paper presents the materials behaviour in the presence of plasma; their influence on plasma properties; the conditioning methods employed; a discussion of future enhancements of inner wall components and the planned use of beryllium as an alternative to the present concept of an all-graphite machine. It is essential for the further development of fusion that the experience gained in JET is transferred to the next machine, which should produce a burning plasma on a scale comparable to a reactor. Such a proposed machine is a single null divertor tokamak with the following parameters: 3m plasma minor radius, 7.5m major radius, elongation ~2, aspect ratio ~2.5, toroidal field 4.5T, pulse duration 2000s and fusion power up to 5GW. The underlying physics for the choice of these parameters and the basic design is presented. Based on this concept and the experience with materials in JET, the lay-out of inner wall components, as well as possibilities for plasma exhaust and refuelling are discussed. As a consequence of this assessment, open questions with respect to the physics of the plasma edge and materials properties are highlighted.

Introduction

The study of plasma facing components requires a reference design with data on machine configuration, operation modes, plasma edge parameters in normal and abnormal operating conditions, materials data and power levels.

Tokamaks may employ limiters and/or divertors in a variety of configurations and the plasma facing components must be designed within boundary conditions imposed by the envisaged machine configuration. Compromises will be required to take into account access restrictions for installation, required compatibility with remote maintenance, possible interference with diagnostics, and the need to install sufficiently large surface areas to reduce thermal loads to acceptable levels.

Requirements concerning power handling capabilities and resistance against eddy current forces result not only from the different plasma configurations (X-point, limiter, inner wall discharges) but also from the various operation modes. For example, JET employs a variety of plasma currents, toroidal fields, elongations and heating powers. The inner wall components must cope with all of these. Knowledge of edge parameters is essential for the design of elements in direct contact with the plasma. For a maximum tolerable heat load on inner wall components, the scrape-off thickness and the power flux define the shape of the surface intercepting the plasma. Particle fluxes and energies at the edge influence impurity release rates and determine the lifetime of high-heat-flux components.

A variety of materials have so far been used for plasma facing components in JET. They range from nickel based alloys for the wall protection used initially [1], to carbon fibre composites (CFC) [2] for areas of the vessel which are exposed to shine-through from the neutral beams. In future, it is planned to employ annealed pyrolytic graphite for the leading edge of a pump limiter [3] and the use of beryllium [4] has been proposed as an alternative to graphite for limiters and wall protection.

Wall Components

In contrast to beam line components of the JET Neutral Injectors [5], which are actively cooled, all wall components in JET are inertially cooled during discharges. Consequently, the possible pulse duration is limited by the surface temperature, which is determined by the thermal diffusivity of the plasma facing material. Material in contact with the plasma (so far, graphite) is cooled by radiation in the 10 to 20 minute intervals between discharges. This limits the possible duration of the interaction with the plasma to times of about 10s at full power.

From the start of JET operation, fine grain high-purity graphite has been employed for the limiters. Based on good experience with graphite 5890 PT in TFR [6], this material was chosen initially. However, difficulties were experienced with the availability of the required six tonnes of graphite. Therefore, a study was initiated [7] and EK 986 was identified as an alternative. Data for the various materials used, and for others of possible future interest have been published previously [8]. During the ohmic phase, four discrete limiters [9] were employed, and later, eight were installed when additional heating reached levels exceeding 10MW. Extensive operational experience exists [10], and no failures occurred. Macroscopic surface damage was observed once only over an operating period of four years [11].

Belt limiters [12] are now in use, whose power handling capabilities exceed 40 MW for ten seconds. Again, fine grain graphite was selected as limiter material. Operational experience is good, but so far the belt limiters have received only ~25% of the designed heat load.

For the walls and wall protection [1], Nicrofer 7216 (equivalent to Inconel 600) was used initially. After a short operational period, melting of the surface of the inboard wall resulted from the interaction with runaway electrons which were created during disruptions [13]. This was avoided by changing to graphite as a low density low-Z material for wall protection. The energy deposition which was localized near the surface of the high-Z material, is now distributed over a larger volume. For typical runaway energies of 20-40MeV, the electron penetration depth is now about 15cm.

Damage was observed again when the wall protection was used as a limiter. The protection does not form a perfectly smooth boundary and the octant-joints [2], especially, protrude a few mm. Overloading occurred in these areas at the midplane of the inboard wall, and as a consequence, the tile material was changed to a carbon fibre composite (DMS 678). Operational experience is good, so far; in cases of runaway impact, the graphite is eroded but remains structurally intact. In addition, carbon fibre reinforced graphite is used in areas where the shine-through from neutral beams is intercepted by the inner wall. Power loads in excess of $30MWm^{-2}$ can be sustained for a few seconds. Fine grain graphite would fail in fracture, under these conditions.

In addition, damage to the top and bottom of the vacuum vessel was observed due to vertical instabilities. Eight poloidal rings (consisting of graphite) were installed to protect the vessel. These initially covered the octant-joints [14] and were used as well as energy dumps for X-point operation. The available surface area was not large enough and therefore 40 poloidal rings are now installed. These cover the octant-joints and bellows protection plates [1]. The power handling capability is still limited to ~40MJ in 2s. Improved water cooled dump plates, covering the top and bottom of the vessel, will be available for X-point operation in 1989. Fig.1 shows the inside of the JET vessel in its present state.

Wall Conditioning Techniques and Impurity Behaviour

Typical procedures, following opening the vessel to air and prolonged personnel access, are to rinse the inside of the vessel with demineralized water followed by a twenty-four hours bake-out under vacuum at a temperature of 300°C. Then, R.F. assisted glow discharge [15] in hydrogen (deuterium) is carried out for about seventy hours. This operates typically at current densities of $1\mu Acm^{-2}$ at a cathode fall of 300V, vessel temperatures of 300°C, neutral pressures in the lower 10^{-3} mbar range, and with pumping speeds of $6200ls^{-1}$ for hydrogen.

To reduce the metal contamination, plasma activated deposition of carbon from a deuterium-methane mixture was used (carbonization) and the vessel was covered by carbon films [16,17] of thicknesses up to ~1μm.

With increasing amounts of solid graphite in the vessel, it became apparent that the glow discharge conditioning with hydrogen (deuterium) became less effective and the oxygen concentration in the plasma increased to values of 1-2%. Residual gas analysis during conditioning showed that neither water nor carbon oxides were significant components in reaction products removed. Thes consisted mainly of hydrocarbons (acethylene ~50%, methane 30%, ethylene balance).

Conditioning the vessel with tokamak discharges in helium resulted in decreased oxygen levels, and therefore, following a recommendation [18] of TEXTOR, glow discharge cleaning in helium was introduced. With this method, oxygen is removed in the form of carbon-oxides and average removal rates of up to 10mbarl were observed for glow discharge times of ten hours. There are indications that improved plasma performance can be achieved using this method.

Carbonisation was frequently carried out to reduce the concentration of high-Z impurities at the plasma centre. During a transient phase (20-200 discharges), depending on the thickness of the deposited layer [19], metals are suppressed to concentrations below 10^{-4} and oxygen and carbon become the dominant impurities even at low densities [20].

For initial operations of JET, when there was only a negligible amount of graphite in the vessel, typical impurity concentrations in the plasma were 2-3% carbon, 1-2% oxygen and ~0.2% metals. With increasing amounts of graphite inside the vessel, following helium conditioning and carbonisation, typical concentrations of metals (10^{-6} - 10^{-4}) and oxygen (~0.5%) decreased whereas carbon increased (typically 5%).

The presence of carbon in the plasma was expected and cannot be avoided, whereas the source of oxygen contamination could not be identified unambiguously. However, it appeared to be related to the amount of graphite in the vessel and was therefore attributed to the absorption of water in the graphite and its release during discharges.

The values of the effective charge, Z_{eff}, are close to two at the density limit, which indicate a dilution of about 20% in the core of the plasma [21]. This situation can be improved by pellet injection, in which Z_{eff} values close to unity can be obtained [22], where the mechanism is dilution of impurities by increasing the hydrogen (deuterium) concentration. With helium glow discharge conditioning, Z_{eff} values less than two appear to be possible even in 5 MA discharges with additional heating.

The density limit of ohmic discharges was increased during neutral beam injection by about a factor of two, but initially it was not possible to achieve a similar increase with RF-heating. Following heavy carbonisation this behaviour changed and it is now possible, with a reduction of high-Z impurities, to run RF-discharges at densities close to those possible with neutral injection. The main source of high-Z impurities are the antenna screens which release nickel into the plasma. Carbonisation suppresses this metal source temporarily, but it has draw-backs in problems with density control and recovery from disruptions. Therefore, it is proposed to replace the nickel screens with beryllium, and due to their higher electrical and thermal conductivity, active screen cooling is no longer required.

Abnormal Operation Conditions

It is generally observed in limiter tokamaks that during a disruption the

plasma thermal energy is dumped on the limiter and about 50% of the magnetic energy of the plasma current are dissipated in the vessel walls. The time-scale ranges from hundreds of microseconds for the thermal dump to tens of milliseconds for the deposition of the magnetic energy. In addition, runaway electrons are produced in the decaying plasma by the voltage spike accompanying the current decay. The power loading of inner wall components is rather localised during such an event and can only be accommodated by sacrificing parts of the surface which evaporate. In JET, a deposition of up to 500 MJm^{-2} was observed [7]. The main reasons for disruptions are: due to exceeding the density limit (power radiated outside the q = 2 surface not balanced by power input) creating locked modes (m = 2, n = 1); or by objects falling through or being injected into the plasma. The latter can be parts of the wall protection tiles, flakes of redeposited material, plasma probes, or molybdenum during neutral beam injection originating from flaking molybdenum coatings on beam dumps. During high current radial disruptions (normal disruption) (up to 7MA) or vertical instabilities, the forces acting or the vacuum vessel are calculated to reach values of 900-1200 tonnes. Without additional stiffening of the vessel by internal rings and outer supports, the material of the vacuum vessel (Nicrofer 7216 LC) can yield. In this case, the vessel lifetime would be reduced by low cycle fatigue to about 1000 disruptions at full current. There are several possibilities to minimize the occurrence of disruptions (e.g. not to operate close to the density limit, to stabilize the m = 2, n = 1 modes before they lock and to have strict quality control for all in-vessel components).

Wall Pumping

With the introduction of graphite as wall protection, density pump-out occurred during discharges when the wall protection was used as a limiter [14,21]. This phenomenon could be used to terminate beam-heated discharges with densities above the ohmic density limit. Furthermore, helium conditioning of the inner wall [23] increased the pumping capability and made it possible to operate at low densities and high heating power in the hot ion mode. Wall pumping was not only observed with discharges at the inner wall. For divertor discharges in JET, when the bellows protection was used as plasma facing component, strong density pump-out was also found.

Mechanisms governing wall pumping are not yet fully understood. A variety of models exist ranging from assuming transient effects [24,25] similar to hydrogen pumping by metal walls [25,26], to the co-deposition of hydrogen and carbon in form of saturated H-C films [24,27]. To date, it is not clear what is the dominant process. Experimental evidence exists from JET, derived from gas balance measurements in ohmic discharges, which supports the co-deposition model. Only 30-40% of gas input during discharges can be found in the exhaust gas even after waiting for times up to 24 hours. To date, it is concluded that most of the deuterium introduced into the JET vessel remains in the form of a deposited layer of hydrocarbons.

Experiments on particle balance of heated and pellet fuelled discharges are being carried out. First results indicate a higher retention, as in ohmic discharges. If this can be further corroborated by experiments, there will be serious implications for the tritium inventory of machines with graphite walls.

Future Developments

During the 1988/89 shutdown starting at the end of 1988, major new components will be installed in the vessel. To stabilize the m=2, n=1 intstability mode, eight saddle coils will be installed each with an area of $\sim 6m^2$ covering one and a half octants. The coils each have three windings and will be driven with voltages up to 5kV, currents up to 5kA and frequencies from DC to 10kHz. They are bakeable to 773K and will be protected from the plasma by graphite. X-point dump plates will be installed at the top and the bottom of the machine, whose surface in contact with the plasma will be $\sim 26m^2$. These consist of a water-cooled support structure (Nicrofer 7612) covered with 25mm thick CFC graphite tiles. These tiles are pressure contacted to the backplate, and will be inertially cooled.

Existing wall protection will be modified to blend with the saddle coils and the dump plates. To prevent runaway damage and to allow for higher power loads during normal operation, more CFC graphite will be used and protruding edges will be removed from the inboard wall.

In early 1990, two pump limiters will be installed. For the leading edges, inertia cooled annealed pyrolytic graphite will be used to sustain the expected power loads of 30 to $50MWm^{-2}$ for times of 3-10s. The surface temperature will not exceed 2200K in these conditions. Bonding of the pyrolytic graphite to the watercooled support structure is a problem still to be solved. Fatigue lifetime and degeneration of the material under high loads needs to be tested. The pump limiters will operate as stand alone limiters for a few seconds with a particle removal rate of 9-12% of the particles reaching them, in load sharing with the inner wall with removal rates of 4-6%, together with the belt limiter at a removal rate of 1-3% and with L-mode plasmas. Removal rates of $\sim$1% are sufficient to balance the density rise due to neutral injection (20MW at 140keV).

The Use of Beryllium

Preparations have been made to use beryllium as an alternative to graphite, in case major difficulties are experienced with graphite under high power loads in discharges of long duration. Problems might arise from impurity production, dilution, density limits, density control and tritium inventory, which could be less severe with the use of beryllium. High power long pulse operation in JET has not yet started and it is too early to arrive at firm conclusions about the future use of graphite.

The antenna screens which have provided a continuous source of high-Z impurities may be exchanged for beryllium which then will alleviate the need for carbonisation of thicknesses up to 1.5μm. This process is unsatisfactory as the density and isotope control become extremely difficult and, in addition, is detrimental to the operation of neutral beam injection. The carbon deposited on the copper duct scrapers must be removed manually after each carbonisation, otherwise it is transported by the beams into the plasma and leads to disruptions.

Beryllium could be used at any time from the beginning of 1988 onwards. The graphite belt limiter and antenna tiles would be exchanged for beryllium and all other areas of the vessel in contact with the plasma could be covered by a beryllium layer of $\sim$10μm thickness. Alternatively, only evaporation could be used. Four evaporators capable of evaporating 1 kg beryllium each are being tested and will be available for that purpose. For a few tens of discharges, the vacuum vessel would have a surface consisting mainly of beryllium. Details of the planned beryllium operation have been reported previously [4]. The use of beryllium as a getter material has been strongly supported by gettering experiments with boron in TEXTOR [18], where the supression of oxygen impurity has proven to be beneficial for the plasma.

Extrapolation into the Future

Experience gained in JET can only be projected into the future if the results obtained are relevant to the requirements of a next generation machine. It is clear that the problems already encountered in JET, will further increase when the plasma and wall parameters of a fusion reactor are encountered. The next step tokamak will have to tackle fully those problems, since it should be relevent in size to a reactor and provide an ignited plasma for a duration of at least days in semi-continuous operation. The scientific and technical aims of such a machine should be to study a burning plasma, to

test wall technology, to provide a test-bed for breeding blankets and above all to demonstrate the viability of fusion and its potential as an energy source.

The physics results obtained so far in JET have shown or confirmed several features of tokamaks, specially relating to heat and particle transport:

- With ohmic heating only, electron energy transport is anomalously high in comparison with expectations of neoclassical theory and shows a different scaling with plasma parameters. The ion energy and particle transport are also anomalous in JET;
- The confinement properties degrade further when additional heating power is applied (so far almost independently of heating method). With ICRF heating, plasma heating occurs mostly through very energetic ions, which exceed 1 MeV in energy at high power input, and which supports the idea that confinement degradation will also result from α-particle heating;
- The electron temperature profile is resilient to changes in the input power, while the density profile can be changed more readily;
- The improved confinement observed in JET H-mode plasmas exhibit the same degradation with increasing additional heating power as L-modes. The consequences are that an H-mode may help to go through the "ignition pass", if the required additional power is moderate, but also that the benefit of the H-mode would vanish when the reactor delivers its full output power;
- Global confinement in JET seems better described by an offset linear dependence between the energy and the power [28]. The linear energy increment is proportional to the current as long as the volume in which internal disruptions occur is not too large (i.e. when $q_{cyl} \geq 3$);
- The maximum density without disruption depends on the cleanliness of the plasma. This can be increased by pellet injection and by increasing the input power. The prospects of increasing the density above the normal Murakami limit in the presence of powerful α-particle heating looks reasonably good.

An interpretation of JET confinement results, based on the existence of chaos in the plasma, has led to local transport laws which can describe JET results rather well [29,30]. Expressed in terms of global scaling laws, the agreement is also reasonable as the fit found with the JET data points applies also to other Tokamaks.

The relationship between confinement laws and the plasma beta (ratio of kinetic to magnetic energy) is difficult to identify, especially in the heat diffusivity coefficient. When the power input is very large compared to the ohmic case (i.e. the relevant case for a power reactor), the confinement time according to this interpretation should scale as:

$$\tau_E \propto \beta^{-\alpha} I a R^{1/2}$$

where I is the plasma current, and R and a the major and minor radius, respectively. The exponent α was taken to be zero in the JET simulations and values above unity can be reasonably excluded. At the Troyon β limit, $\beta = g \frac{I}{aB}$ [31], the ignition product becomes:

$$nT\,\tau_E \propto g^{(1-\alpha)} \left(q\frac{R}{a}\right)^{\alpha} I^{\alpha} B R^{1/2}$$

where q is the safety factor and g is a constant.

As the product $nT\tau_E$ is a good measure of the power amplification of a thermonuclear D-T plasma (as long as the temperature is larger than 7keV), this expression shows the importance of the current capability of the machine.

Based on this analysis of results obtained in JET, it should be difficult to achieve ignition in most of the tokamaks so far being discussed or designed. To demonstrate the viability of thermonuclear fusion and its potential as an energy source, a tokamak is proposed 2-3 times larger than JET in linear dimensions, at a magnetic field of ~4.5T, with a current capability reaching 30MA. A single null divertor configuration should be used to ensure helium exhaust and to possibly benefit from an H-mode in enlarging the ignition domain. Confinement degradation for α-particle heating and L-mode behaviour is taken into account in the design. The additional heating power requirements are relatively low (≤ 50MW). The maximum thermal output of such a machine depends on the maximum density which can be achieved and on the ability to limit dilution of the plasma by helium and impurities. With $Z_{eff} < 2$ and a Murakami parameter $M = \bar{n}\frac{R}{B} = 15$, the maximum fusion power should be around 4GW, with still a safety margin on the limit in β.

The proposed machine is a true "Thermonuclear Furnace" because it has all the elements in contact with the burning plasma inside the vacuum vessel which will be required for a reactor. On the basis of the proposed design, problem areas related to wall components can be assessed and, based on JET experience, possible solutions can be discussed.

The Thermonuclear Furnace

The design should present only minimal technical risks. It uses conventional or proven technology as far as possible. The tokamak cross-section is shown in Fig. 2. The machine consists of twenty identical sectors, of which each one incorporates a toroidal field coil, the mechanical structure, part of the vacuum vessel and one integrated unit. Due to the box-like shape, the sectors are strong enough to withstand forces during a disruption at full current. The sectors would be joined by welding lips and so form the vacuum enclosure. The material of the wall would be stainless steel (AINSI SS 316 or equivalent) of about 3 mm thickness. The wall would be watercooled, and at the same time, the water forms the blanket of thickness 40-60 cm.

The plasma is in a single null divertor configuration. The divertor plates are exchangeable and it is possible to incorporate blanket test modules into the divertor supports. The plasma occupies about 50% of the toroidal field volume. Thus, a drastic relative reduction in costs could be achieved. In this proposal, copper coils are used to minimize the technical complexity and risk by reducing the number of concentric vessels and structures and by decreasing the neutron shielding requirements. Table I lists the main parameters of the furnace.

Wall Concept

The design of the proposed machine aims at a plasma size comparable to a reactor. This results in modest requirements for the power handling capabilities, so that there is no need to develop new techniques for high heat flux components. The wall concept is based on graphite components covered with a renewable thin beryllium layer in order to block the chemical reactivity of graphite. Radiation cooling for inner wall components is envisaged as in JET and active cooling for divertor components. Heating by neutrons (nuclear heating) will produce the main thermal load for the inner wall components and contribute significantly to the divertor loads.

The power output is rated at 0.5-4GW depending on the achievable central density. For further evaluation, a power production of 2.5GW is assumed. 2GW is emitted as neutrons, and the rest as α-particles. Power losses from the plasma are by radiation and conduction; convection and charge exchange neutrals are neglected. The radiation from the plasma volume is mainly due to bremsstrahlung and it contributes ~20% to the power balance. It is assumed that low-Z radiation from the plasma edge contributes another 20% and a further 20% would be radiated from the X-point during L-mode operation. Half of the latter would be intercepted by the divertor plates which as well would receive 40% of the total power by conduction.

Table II sets out the basic data for loads on wall components. These are averaged assuming equal power distribution on the respective components. Following experience on JET, all wall and divertor components would be low-Z materials (i.e. carbon, beryllium, boron and lithium or combinations).

Wall Protection

Fig.3 shows a diagram of the inboard wall. The wall protection consist of graphite tiles, which is radiation cooled. Pressure contacts are not considered to be sufficiently reliable. There would be two types of protection. The first forms a poloidal ring of 300mm width, in each sector, in a configuration reminiscent of the belt limiter in JET. The tiles radiate to water cooled fins which form part of the blanket. The thickness of each graphite tile would be 30mm and the depth 50 to 100mm. The cooling fins are recessed by 20mm, and therefore, 20mm of graphite can act as a sacrificial layer during disruptions. The second purpose of the tiles is to shield the toroidal field coils which are partly situated behind a gap in the blanket. Tile temperatures are mainly determined by nuclear heating and should reach ∿1500K at the front surface. Situated between the rings is further protection over a height of 5m in the form of tiles similar to the wall protection in JET. These are wall radiation cooled and have a thickness of 20mm. Their front temperature will also be 1500K. The rest of the inside of the vessel would be carbonized. The material for the tiles would be carbon fibre reinforced graphite of a type similar to that presently used in JET. It is not anticipated that the inner wall protection presents any major problems during normal operation conditions. Fig.4 shows a three-dimensional view of the inboard wall.

Divertor

The divertor presents the main technical challenge in the design of inner wall components. This challenge is reduced to a level which can be handled if the region of high power deposition is expanded over a larger area. This can be achieved by moving the X-point vertically or horizontally using the existing coil set (or preferably sets of internal coils), with minimal effects on the overall plasma geometry. Alternatively, the movement can be achieved by oscillating the divertor components horizontally. The main advantages of this scheme are:

- no need for absolute positioning of the divertor components with an accuracy of millimetres as in JET. Feedback control could be used;
- in spite of high local thermal loads the average loads remain small;
- heat transfer to the cooling medium corresponds to the average loads;
- lifetime increases according to the ratio of peak load to average load.;
- to compensate for erosion, material (beryllium, hydrocarbons) can be injected which would be deposited in areas with low loads;
- deposited and redeposited layers are burnt off before they can flake and before large amounts of tritium could accumulate.

For the movement, the limiting factor is the sweep frequency which must be low enough so that additional coils are not required in the vacuum vessel, and must be high enough to minimize thermal stresses in the divertor material. As an alternative to this movement, use of liquid metals (lithium or beryllium) could be envisaged to act as a divertor target producing a high density ionized shield (plasma plugging, if possible). In this paper only the relative movement between plasma and divertor will be discussed.

Fig.5 shows a cross-section through the divertor region. The divertor plates extend above and below the X-point. In the down-stream region, additional wall protection is installed (cone between the divertor plates) to avoid direct line of sight between the plasma and the blanket and to protect the blanket against damage by loss of plasma control during a vertical instability. The divertor receives only a moderate average power level of 130 Wcm^{-2} from radiation and conduction. The X-point can be moved horizontally and vertically to distribute the power load evenly over the whole divertor surface. As H-mode operation is not envisaged, the outer and inner part of the divertor plates can be used to this purpose.

The material proposed for the divertor plates is carbon fibre graphite of 40mm thickness. It is brazed in blocks of 10 x $10mm^2$ surface area to water cooled copper plates of 10mm thickness. The average heat flux (conduction plus nuclear heating) is ∿$1.8MWm^{-2}$. This can be removed without having to resort to two-phase cooling. In the proposed design, the peak loads on the surface during the sweeping of the X-point should be about x5 higher than the average load (∿$10MWm^{-2}$). For the calculation of thermal response, the high thermal conductivity of the fibre graphite was not taken into account as it degrades at low neutron doses (∿$10^{20}cm^{-2}$) to that of fine grain graphite [32]. For a sweep frequency of 1Hz, the thermal stresses at the surface will be about 25MPa in compression (limit 100MPa) and the peak temperature will be ∿1400K. The material thickness is mainly limited by the average load and the resulting front temperatures. An alternative set of parameters would be: 60mm material thickness, sweep rate 3Hz, surface temperature 1600K and thermal stress 55MPa. More detailed calculations should take into account the annealing of radiation damage and a varying thermal conductivity inside the material.

It is proposed that the graphite divertor should be covered with a thin layer of beryllium to employ the good properties of both materials. A beryllium carbide layer would be formed [33] at temperatures above 700K. It is envisaged that such a scheme should be validated in JET.

The lifetime of the divertor plates is determined by the erosion due to particle impact. A detailed modelling of the plasma edge and the divertor region is required to assess the particle fluxes and energies, but is presently not available. Therefore, a worst case assessment is made. The energy (∿300eV) and the temperature (∿750K) of the maximum sputtering yield is taken for the sputtering of carbon by deuterium. For 300eV ions and an energy transmission factor of 17 [34], the particle outflow from the plasma is $7x10^{23}$ particles per second.

With a sputtering yield of 0.2 [35], this is equivalent to a removal of about 35 monolayers per second. Neglecting any increase in lifetime due to lower particle energy, possible supression of chemical activity and redeposition, the lifetime would be at least two months of continuous operation at a level of 2.5GW. It should be mentioned that H-mode operation might immediately halve the divertor lifetime, as the outer part might not be allowed in contact with the plasma and the loads would be doubled on the rest.

It appears that a fast movement (sweep frequency >10Hz) of the X-point is difficult to achieve and therefore peak loads up to a factor five higher than the average loads can be expected for times of at least 0.1s. These should be taken by the thermal inertia of the divertor components and then be transferred to the cooling water at the moderate heat transfer discussed above. Lifetimes will not be affected as average loads do not change. Experience in JET shows that graphite fibre material is well suited to operate in such a way.

For 2.5GW thermal output, the neutron flux density is $5.3x10^{13}cm^{-2}s^{-1}$. To reach a dose corresponding to one displacement per annum, the plasma should burn for 216 days continuously (1dpa = $10^{23}cm^{-2}$). This is in excess of the predicted lifetime of the divertor components in the above assessment. In the long term, it would be necessary to validate schemes like the high recycling divertor or to develop liquid or plasma or gaseous energy dumps to arrive at lifetimes of several years.

In this proposal, Beryllium as a metal cannot be used as wall protection because the temperatures required for radiation cooling would be too high. In addition, it can not be envisaged for the divertor plates. The stresses induced during sweeping of the X-point ($10Wm^{-2}$, 235MPa in compression after 0.03s) requires execution of a cycle in a fraction of this time to avoid plastic deformation. Sweep frequencies higher than 10Hz are not compatible with internal coils (300V/turn required at 10Hz) and, therefore, the use of massive beryllium is not proposed.

The design of the inner wall components and the divertor plates for the heat loads discussed above does not present major technical risks. However, the impact of the design on plasma behaviour was not assessed and the impurity behaviour in such a configuration must be studied.

Disruptions

Problems arise if longer burn times than 200-400 days are required or when abnormal operation conditions (disruptions) are taken into account. During a disruption, the thermal energy in the plasma is dumped onto areas in direct contact with the plasma and ~50% of the magnetic energy are deposited on the wall protection. The time-scales will be many x100 μs for the divertor plates and many x10 ms for the inner wall. The energies considered are ~1.8GJ for the inner wall and ~1GJ for the divertor. The deposition area may be rather localized. It is clear that for the times mentioned, there exists no material which can take the resulting loads without melting or in the case of graphite, without vapourizing. At the inner wall; 30kg of graphite will evaporate for each disruption. In the case that one ionization step is taken into account during the interaction (plasma shielding), the amount of material lost would be only ~10kg. The respective value for the divertor would be about 7kg. If such an interaction was not localized, several thousand disruptions could be sustained.

It will never be possible to avoid disruptions completely. Therefore, each machine must have the capability of withstanding hundreds of disruptions without being destroyed. Unfortunately, the interaction with wall components is not yet fully understood and effort is required to study in divertor machines the pattern of power deposition and deposition times during disruptions, to model the interaction of materials with extremely high heat loads and, if possible, outside a tokamak, to verify the models by experiments. In addition, disruptions, as the source of this problem, should be controlled, and, therefore, schemes should be devised and tested to minimize their occurrence.

Exhaust and Refuelling

Pumping of the proposed machine can be achieved with existing techniques. Here again, the physical size is beneficial because it allows installation of pumping ducts of sufficient cross-section. Each machine sector has two pumping ducts with an area of ~$0.8m^2$ each. The ducts with a length of 10m end outside the biological shielding. The conductance for deuterium is ~$3x10^4 ls^{-1}$. A cryopump of ~$1.5x10^5 ls^{-1}$ pumping speed would be installed at the end of each duct. The installed pumping speed at the divertor would therefore be ~$10^6 ls^{-1}$ for deuterium and by using charcoal at 4K a similar pumping speed for helium could be achieved. The vacuum time constant would be about 3s. If during a detailed study, these values turned out to be too low, thermomechanical pumps [36] could be installed which would increase the pumping speeds by x100.

Without a detailed study of particle transport for hydrogen and helium in the plasma, reliable predictions cannot be made for recycling fluxes and the pumped fraction. Models for α-particle transport cannot yet be verified experimentally. JET might contribute information as soon as a sufficient number of α-particles are produced.

Refuelling can either be implemented by gas or by pellet fuelling or a combination of both. From observations in JET [22], pellet fuelling can produce densities far above the Murakami limit, reduce the impurity concentration and increase energy confinement times. To obtain these favourable features, it seems necessary to inject the pellets at such speeds that they penetrate at least well beyond the $q = 2$ surface before ablation. For the proposed machine, speeds ≥$10kms^{-1}$ would be required with the necessary development of pellet injection.

Summary and Conclusions

Only low-Z materials can be employed inside the JET vessel. Carbon in a variety of forms is extensively used for plasma facing components either as fine grain graphite, carbon fibre reinforced graphite or as a carbon film. Operational experience is generally good. However, the following problem-areas have been identified:

- Wall conditioning, isotope and density control require wall temperatures above 250°C;
- Graphite seems to be the main source of oxygen;
- Frequent conditioning with helium is required;
- Carbon films on exposed areas have a limited lifetime;
- Carbon retains hydrogen introduced into the vessel in the form of hydrogen-rich carbon films deposited during discharges, which leads to difficulties in density control, recovery from disruptions and tritium inventory;
- graphite is the main impurity at typically 3%, and leads to increased Z_{eff} values and plasma dilution;
- Fine grain graphite, if overloaded thermally, is prone to fail in fracture. Carbon fibre reinforced graphite is extremely forgiving when thermally overloaded and should replace the fine grain graphite for plasma facing component, even if the thermal erosion may be higher.

Extrapolation of results from JET show that high plasma currents are needed for a reactor which would be of such a size that confinement will no longer be the dominant issue. The main problems would be impurity production and their control, fuelling and exhaust and resistance against disruptions.

Technical considerations such as stress levels in coils, wall loadings and economy suggest the design of a "Thermonuclear Furnace" with several GW thermal output. Its aims should be to study an ignited plasma with semi-continuous operation, to test wall technology and breeding blankets and to show the prospect of fusion as a reliable energy source. The most promising solution for the divertor is based on the movement of the X-point relative to the divertor plates, using graphite fibre material and to block the chemical activity by a beryllium layer. However, studies are required to validate this scheme.

The technology to build such a machine exists but there are still uncertainties due to unavailable data. JET can contribute in filling this gap by providing information on:

- Particle fluxes and energies in the divertor region; - α-particle transport;
- Stabilisation of disruptions;
- Behaviour of beryllium as an alternative low-Z material;
- Deep fuelling of the plasma with high speed pellets;
- Tritium retention.

Additional effort is required in the areas of:

- Erosion-deposition processes and their application to a reactor
- Interaction of solids with plasmas at GJ energies during periods of hundreds of microseconds;
- Properties of liquid/gaseous/plasma targets for the divertor;
- Plasma exhaust and refuelling.

Acknowledgements:

The authors wish to thank Dr. E. Deksnis for performing thermal and stress analysis and Dr. G. Sadler for calculating the nuclear heating in various components.

References

[1] G. Duesing and K.J. Dietz, J. Vac. Sci. Technol. A3 (1985) 1151.

[2] M. Pick et al., Proc. 12th SOFE, Monterey, USA, 1987.

[3] K. Sonnenberg, J. Nucl. Mat. this conference.

[4] P.H. Rebut et al., JET-R (85) 03.

[5] R. Haange, Proc. 9th Symp. Eng. Problems of Fusion Research IEEE, 1981, p.1352

[6] TFR Group, Proc. Int. Conf. Plasma Wall Interaction, Jülich 1976 (Pergamon Press 1977), p.3.

[7] W. Delle et al., Jül-Spez-401, May 1987.

[8] J. Dietz, J. Nucl. Mat., 154-156 (1987) in print.

[9] J. Dietz et al., J. Nucl. Mat., 128+129 (1984) 10.

[10] M. Huguet et al., Fusion Technology 11 (1987) 43.

[11] M. Huguet et al., Proc. 11th Symp. Fusion Eng., Austin, 1986 (IEE publication, 1986) p.1238.

[12] G. Celentano et al., Proc. 14th SOFT, Avignon, 1986 (Pergamon Press, 1986) p.581.

[13] K.J. Dietz et al., in: Tokamak Start-up, Ed. Heinz Knoepfel (Plenum Press, 1986) p.317.

[14] K. Sonnenberg et al., Proc. 14th SOFT, Avignon, 1986 (Pergamon Press, 1986) p.273.

[15] E. Usselmann et al., Proc. 13th Symp. Fusion Technol. (1984) 150.

[16] P. Coad et al., J. Nucl. Mat. 145-147 (1987) 747.

[17] J. Winter, J. Vac. Sci. Techn. A5(4) (1987) 2286.

[18] F. Waelbroeck and J. Winter, private communication.

[19] M. Stamp et al., Proc. 12th Europ. Conf. Contr. Fusion and Plasma Physics, Budapest, 1985 (European Physical Society, 1085) p.539.

[20] K. Behringer, JET Progress Report 1986, (EUR-JET-PR4, March 1987), p.41.

[21] L. de Kock et al., J. Nucl. Mat. 145-147 (1987).

[22] A. Gondhalekar et al., 11th Int. Conf. Plasma Phys. Contr. Nucl. Fusion Research, Kyoto, 1986, paper IAEA-CN-47/I-I-6.

[23] R.J. Bickerton, Plasma Physics and Contr. Fusion, Vol. 29-10A, p.1219 (1987)

[24] J. Winter, J. Vac. Sci. Techn. A (1987), in press.

[25] F. Waelbroeck et al., J. Nucl. Mat. 85+86 (1979) 345.

[26] M.A. Pick and K. Sonnenberg, J. Nucl. Mat. 131 (1985) 208.

[27] W.L. Hsu and R.A. Causey, J. Vac. Sci. Tech. A (1987), in press.

[28] J.G. Cordey et al., Proc. 11th IAEA Conference, Kyoto, Japan, 1986, Vol. I, pp. 99-110

[29] P.H. Rebut et al., Proc. 11th IAEA Conference, Kyoto, Japan, 1986, Vol. 2, pp. 187-196

[30] P.P. Lallia et al., 2nd Eur. Fusion Theory Meeting, Varenna (1987) and JET Preprint JET-P(88)05

[31] F. Troyon, Phil. Trans. R. Soc. London A322, 163-171 (1987)

[32] B.T. Kelly, Physics of Graphite, Applied Science Publishers, London and New Jersey, 1981

[33] T.G. Nich, etal., Scripta Metallurgica 20 (1986) 87

[34] P. Mioduszewski, J. Nucl. Mat. 145-147 (1987) 210

[35] J. Roth, J. Nucl. Mat. 145-147 (1987) 87

[36] H. Hemmerich, JET-P (87) 03

TABLE 1

Main Parameters of the Furnace

Plasma minor radius (horizontal)	(m)	3
Plasma minor radius (vertical)	(m)	6
Plasma major radius	(m)	7.5
Plasma aspect ratio		2 - 2.5
Flat top pulse length	(s)	600-2000
Toroidal field (plasma centre)	(T)	4.5
Plasma current	(MA)	30
Voltseconds	(Vs)	425
Additional heating	(MW)	50
Fusion power	(MW)	500-4000

TABLE 2

Loads on Wall Components

Surfaces		
Wall	(m^2)	1660
Divertor	(m^2)	190
Plasma	(m^3)	1310
Volumes		
Vessel	(m^2)	3260
Plasma	(m^2)	2410
Wall loads		
Nuclear heating (graphite)	(MWm^{-3})	12
Radiation	(MWm^{-2})	0.15
Divertor loads		
Radiation	(MWm^{-2})	0.3
Conduction (averaged)	(MWm^{-2})	0.89
Nuclear heating (graphite)	(MWm^{-3})	12

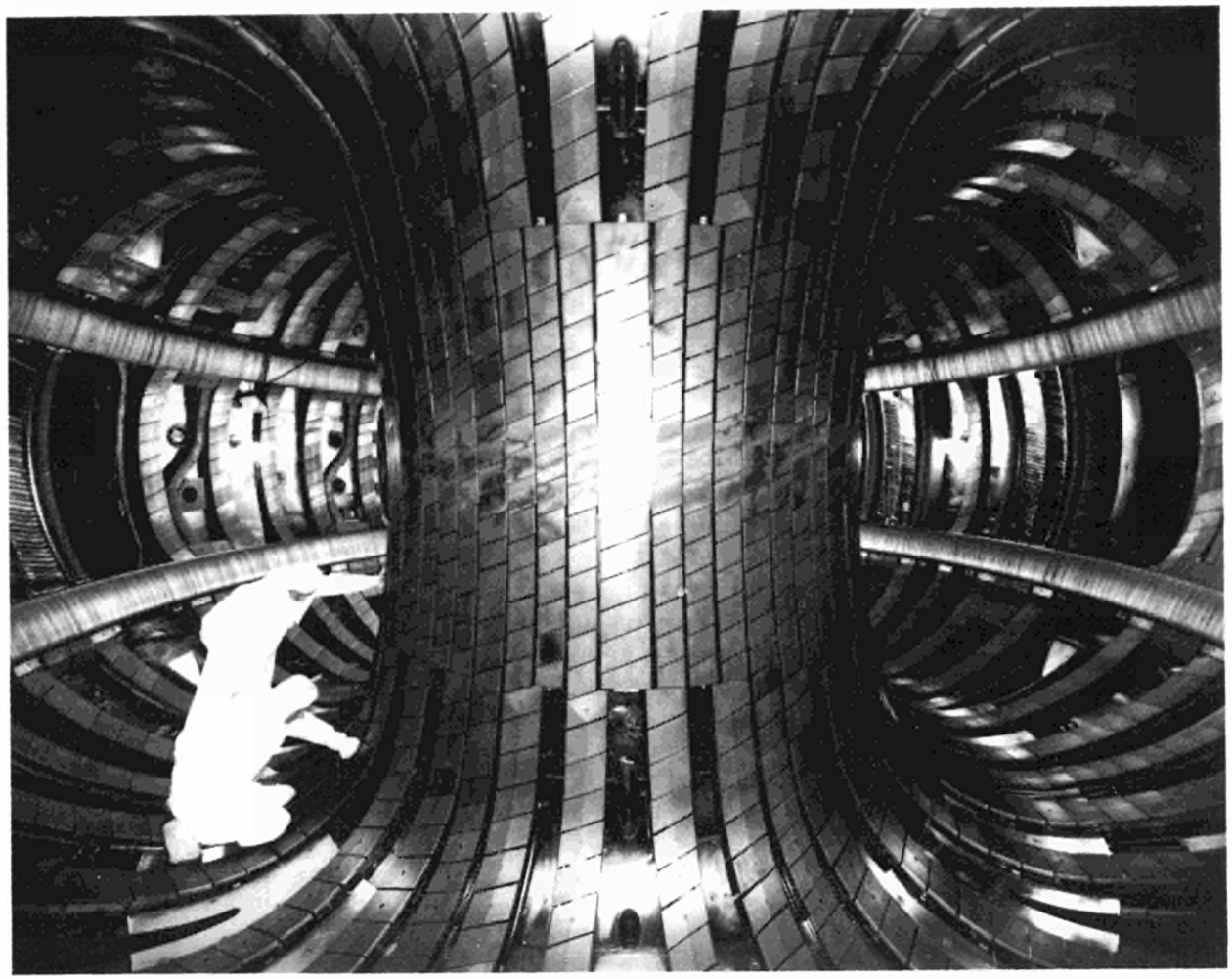

Fig. 1 The inside of the JET vacuum vessel in its present state showing belt limiter, octant-joint and bellows protection, inner wall protection and RF-antennae

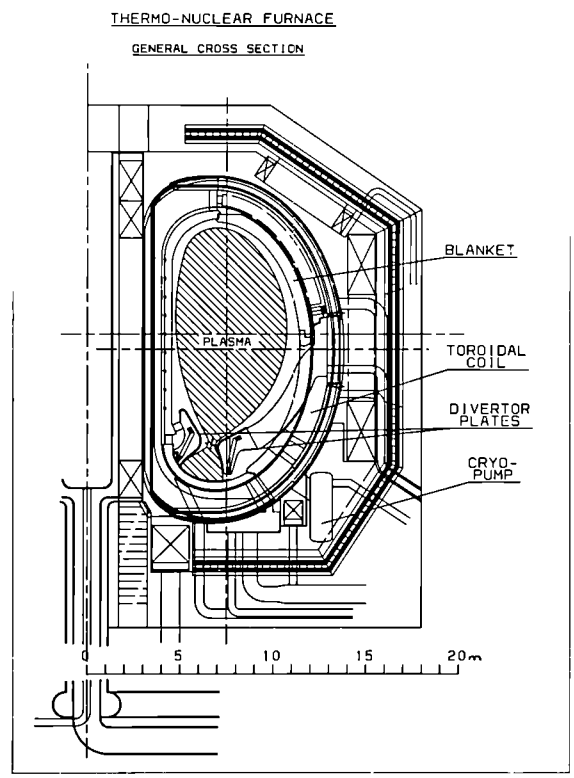

Fig. 2 Cross section of the thermonuclear furnace

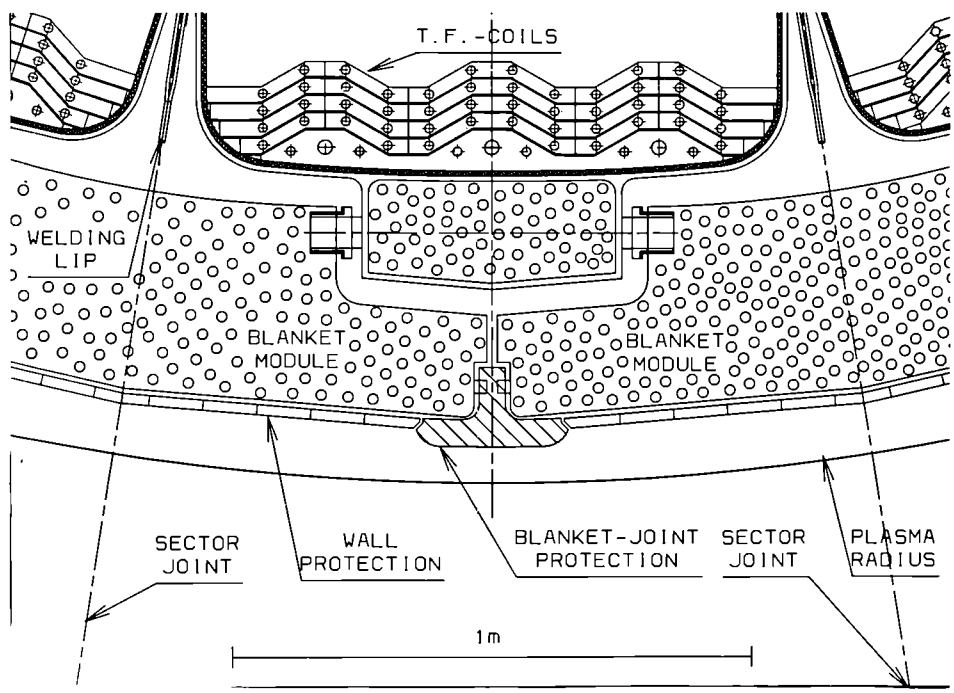

Fig. 3 Inner wall protection, plan view

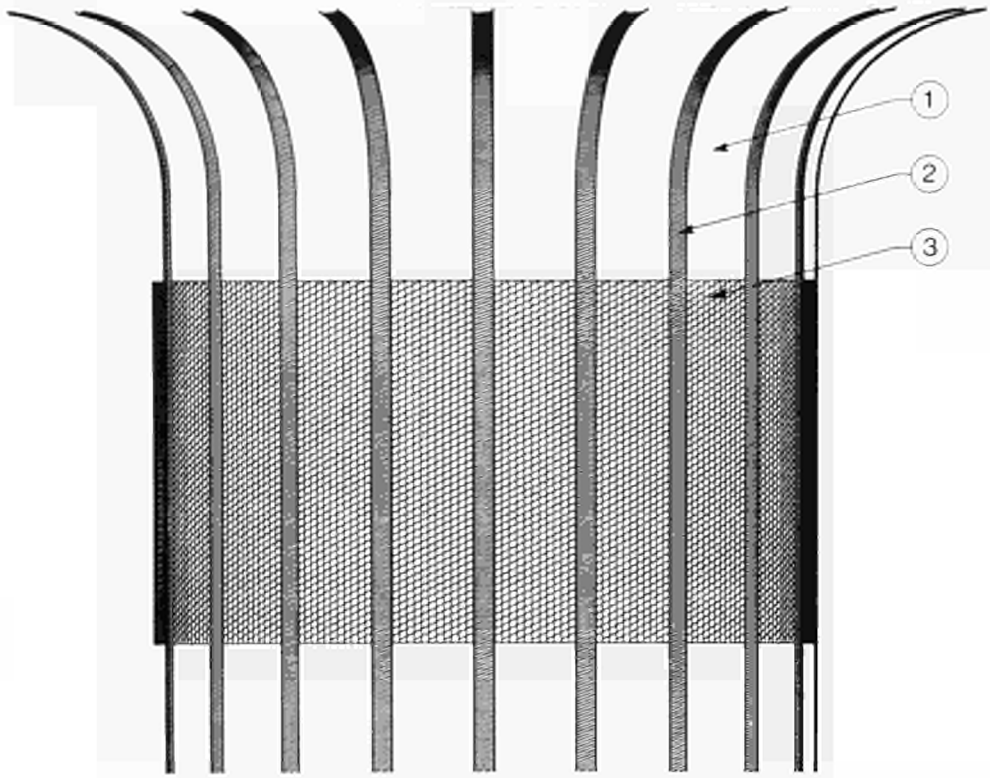

Fig. 4 Inner wall protection, three dimensional view. Carbonized area[1], poloidal graphite rings[2], wall tiles[3]

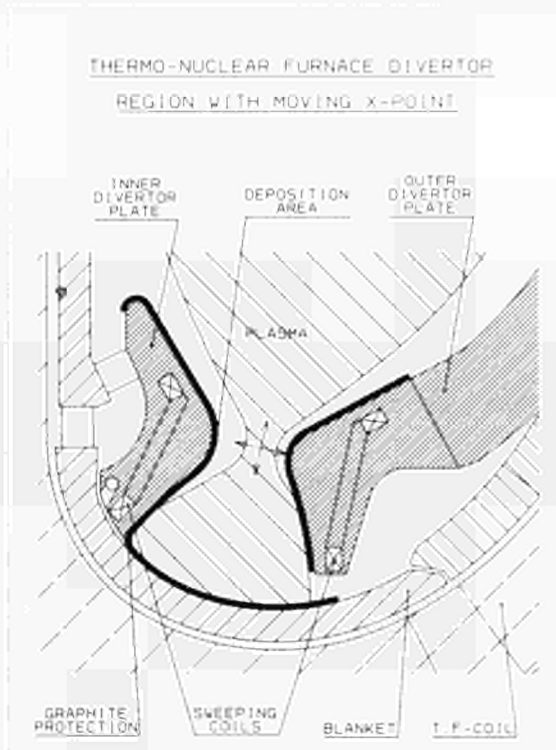

Fig. 5 Cross section through divertor area

Appendix III(c)
JET-P(88) 26

Plasma Performance in JET
Achievements and Projections

The JET Team*

(Presented by A. Gibson)

JET Joint Undertaking, Abingdon, Oxfordshire, OX14 3EA, UK

ABSTRACT

An account is given of recent experimental advances on JET, especially as they relate to fusion performance. Scaling relations are used to identify the critical parameters which need to be optimised to secure the best fusion performance. Finally the established best performance of JET is used as a base to project the performance to be expected in future D-T operation.

KEYWORDS

Fusion; Tokamak; Magnetic Confinement.

1. INTRODUCTION

The JET device has been described elsewhere (Bickerton et al 1987; Bertolini and Huguet et al., 1987). A number of major enhancements carried out in 1987 are listed in Table I. These new features have permitted the following new types of operation.

(a) Routine operation and heating with plasma current, I_p, up to 6MA.
(b) X-point operation up to $I_p = 5$MA.
(c) Routine X-point operation with H-mode up to $I_p = 4.5$MA.
(d) Long pulse high-power operation (plasma duration up to 20s and heating pulse duration > 6s).
(e) Total power to plasma up to 26MW with a delivered energy in excess of 60MJ (up to 17MW from Ion Cyclotron Resonance Heating (ICRH), and up to 13MW from Neutral Beam Injection (NBI)).
(f) Total plasma energy content greater than 10MJ.
(g) Operation with large additional heating and with small metallic impurity content ($\sim 10^{-4} n_e$) and $Z_{eff} = 2$ ($n_D/n_e \sim 0.8$).
(h) Production and heating of high peaked densities using pellets ($\hat{n}_e > 10^{20}$m^{-3}).†

Figs. 1 and 2 show typical magnetic configurations for high current limiter and X-point discharges. Fig. 3 shows an example of a peaked density profile produced by injection of 2.7 and 4mm pellets of solid deuterium into a 2.5MA, 3T ohmic discharge (see Kupschus et al., 1988), note that the peaked profile persists for more than 2s while the density decays from an initial 1.3×10^{20}m^{-3} to 0.6×10^{20}m^{-3}. Until recently attempts to apply ICRH heating to such discharges lead to a rapid flattening of the density profile typically in ~ 0.2s. However, by injecting the pellet during the current rise phase, before the onset of the sawtooth relaxation, it has now proved

CR8863

* See Appendix 1

† n_e is the electron density, n_D the deuterium ion density, Z_{eff} the effective charge number. $\hat{n}$ denotes a value on the magnetic axis, quantities without a hat are volume average values, also indicated by a bar.

Table I
Major enhancements to JET
carried out in 1987

Extensive improvements to the main poloidal circuit to give: improved X-point operation improved control of current rise phase increased volt-second capability	Second NBI box *(first injection, into JET May 1988)* Cryo pellet injection system *(single pellet using Garching gun; multiple pellet using ORNL gun, in collaboration with US–DOE)*
New dual belt limiter system *(carbon tiles on a water cooled base)* plus, carbon tiles on all exposed surfaces *(specially shaped at X-point target)*	Improved vessel mechanical restraints for disruption protection
Eight ICRF antennae between the belts *(water cooled carbidised nickel Faraday screens; carbon side tiles)*	Increased diagnostic capability, especially: Time of flight laser scatter system **(LIDAR)** to measure $T_e(r)$; $n_e(r)$ Faraday rotation polarimeter to measure $B_\theta(r)$

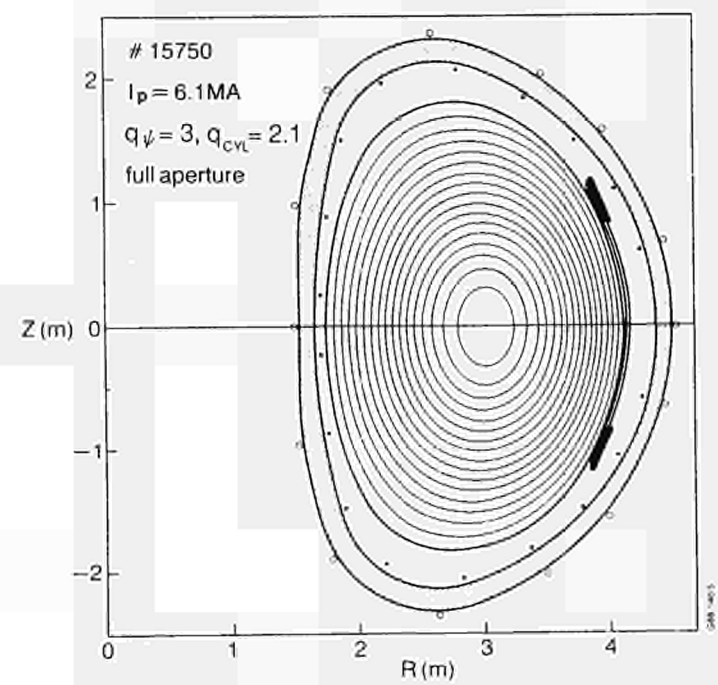

Fig. 1 Magnetic Flux Surfaces inferred from external magnetic measurement and an equilibrium identification code (IDENTC) for a limiter discharge with $I_p = 6.1$ MA in JET.

G88.140/5

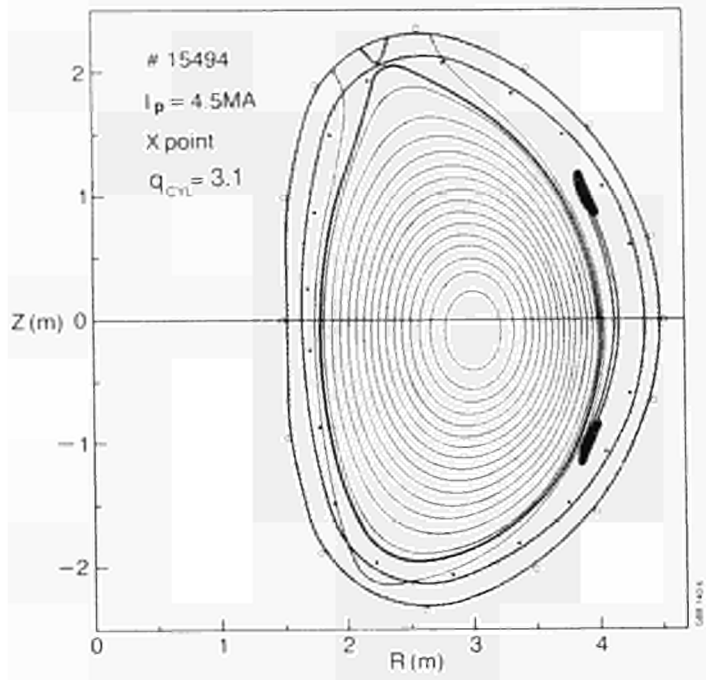

Fig. 2 JET magnetic flux surfaces for an X-point discharge with $I_p = 4.5\,MA$. G88.140/6

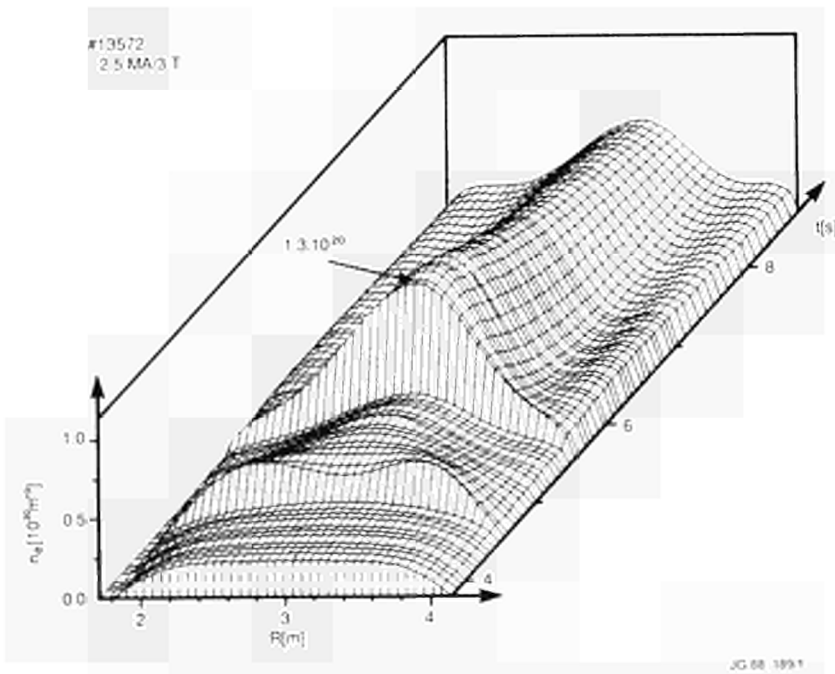

Fig. 3 Peaked density profile produced by pellet injection into an ohmic discharge. JG88.189/1

possible to sustain and heat the peaked density profile produced by pellet injection (Kupschus et al., 1988). An example is shown in Fig. 4 where the initial peaked profile with central density and electron temperature of $1.4\times10^{20}\mathrm{m}^{-3}$ and 0.4 keV is heated by 8 MW of ICRH over a 1.5 s period to a central electron temperature of 11 keV, ion temperature 8 keV, while the peaked density profile persists and the central density falls to $0.6\times10^{20}\mathrm{m}^{-3}$. At this time, $\hat{n}_e/n_e=2$ and $\hat{T}_e/T_e=4$. This type of discharge will form an interesting starting point for the production of high performance plasmas in the next JET campaign.

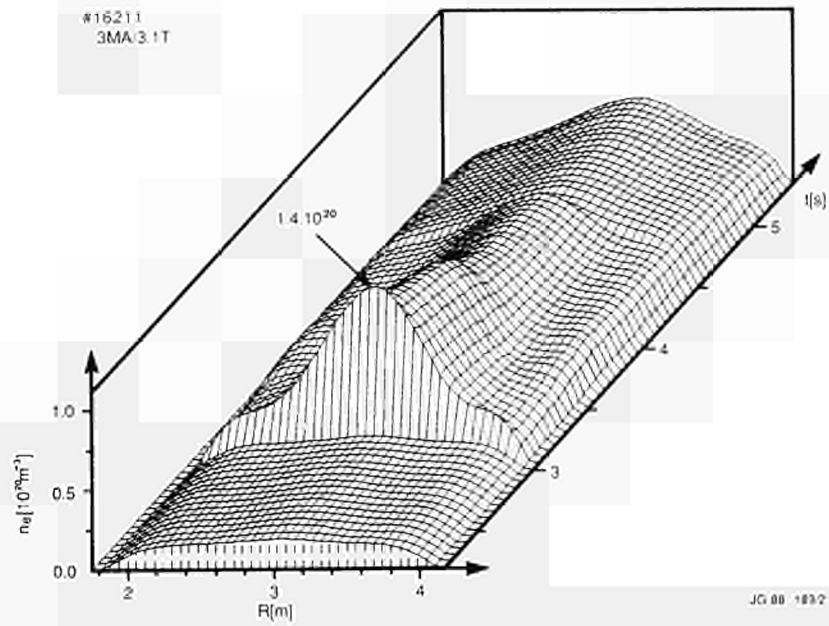

Fig. 4 ICRH heating of a peaked density profile produced during pellet injection in the current rise phase of a discharge. JG88.189/2

The rest of this paper is arranged as follows: Section 2 identifies the parameters which might limit fusion performance in JET and describes the values which have been obtained so far. Section 3 discusses the important question of the values which can be obtained in the core of the discharge and their relation to sawtooth behaviour. Section 4 discusses scaling relations. Section 5 describes the fusion parameters $\hat{n}\hat{T}\tau_E$ and Q already obtained in JET, while section 6 projects the values of these quantities which might be possible in D-T operation in JET in the future.

2. LIMITING PARAMETERS

Three quantities play a particularly important role in determining the extent to which any magnetic confinement system can approach the plasma conditions necessary for a fusion reactor. They are the operating density n, the β value (ratio of plasma to magnetic pressure) and the energy confinement time τ_E. The ion temperature too is clearly important, but a number of tokamaks, including JET, have now demonstrated that the necessary temperatures can be obtained.

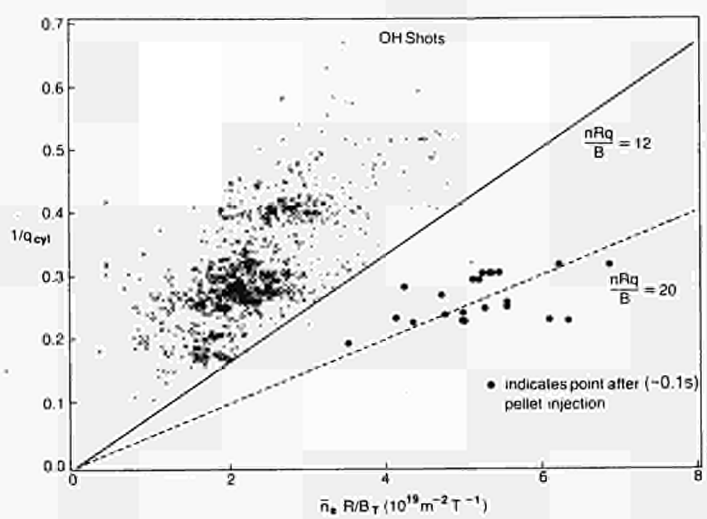

Fig. 5 Density limit diagram for JET ohmic heated discharges. G88.140/10

2.1 Operating Density

Fig. 5 shows the range of densities over which JET has already operated with ohmic heating alone. The graph is a plot of $1/q_{cyl}$ versus $n_e R/B_T$ where:

$q_{cyl}=5AB_T/\pi RI_p$

A = plasma cross-sectional area

B_T = toroidal magnetic field on magnetic axis

R = major radius of magnetic axis

I_p = plasma current

Units are m, T, MA

It will be seen that normal JET ohmic operation is restricted to densities such that $n_e Rq_{cyl}/B_T \leq 12\times10^{19}\mathrm{m}^{-2}\,\mathrm{T}^{-1}$, but that with

pellet injection this limit can be increased to $20\times10^{19}m^{-2}T^{-1}$. Fig. 6 shows a similar diagram for discharges in which substantial additional heating from ICRH, NBI or both is applied. Again densities up to the line $nRq_{cyl}/B_T \leq 20\times10^{19}m^{-2}T^{-1}$ are readily obtained. In the important JET operating range near $q_{cyl}=2.5$ operating densities up to $n_e \sim 8\times10^{19}m^{-3}$, corresponding to $nR/B_T=7\times10^{19}$ have been obtained.

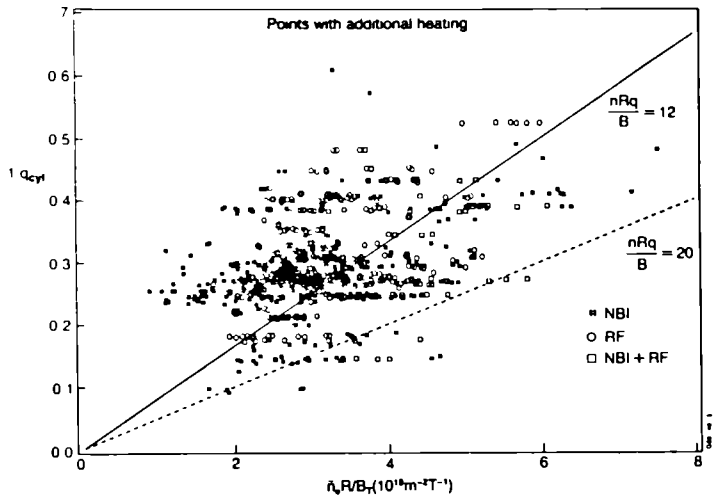

Fig. 6 Density limit diagram for JET discharges with additional heating. G88.140/15

2.2 β Value

Troyon (1984) used computational methods to establish a β limit in tokamaks for reasonable profiles, which is:

$$\beta_{Troyon}=2.8\times10^{-2}\, I_p/B_T a$$

where a = plasma horizontal minor radius (Units are m, T, MA).

Many tokamak experiments have shown that this limit can be obtained in practice. Fig. 7 shows the results of a series of experiments in JET at low toroidal magnetic field ($B_T=1.4$T) with ICRH heating, the series was limited to an ICRH power of 10MW, but the ratio β/β_{Troyon} reached 0.6 with no strong deterioration in

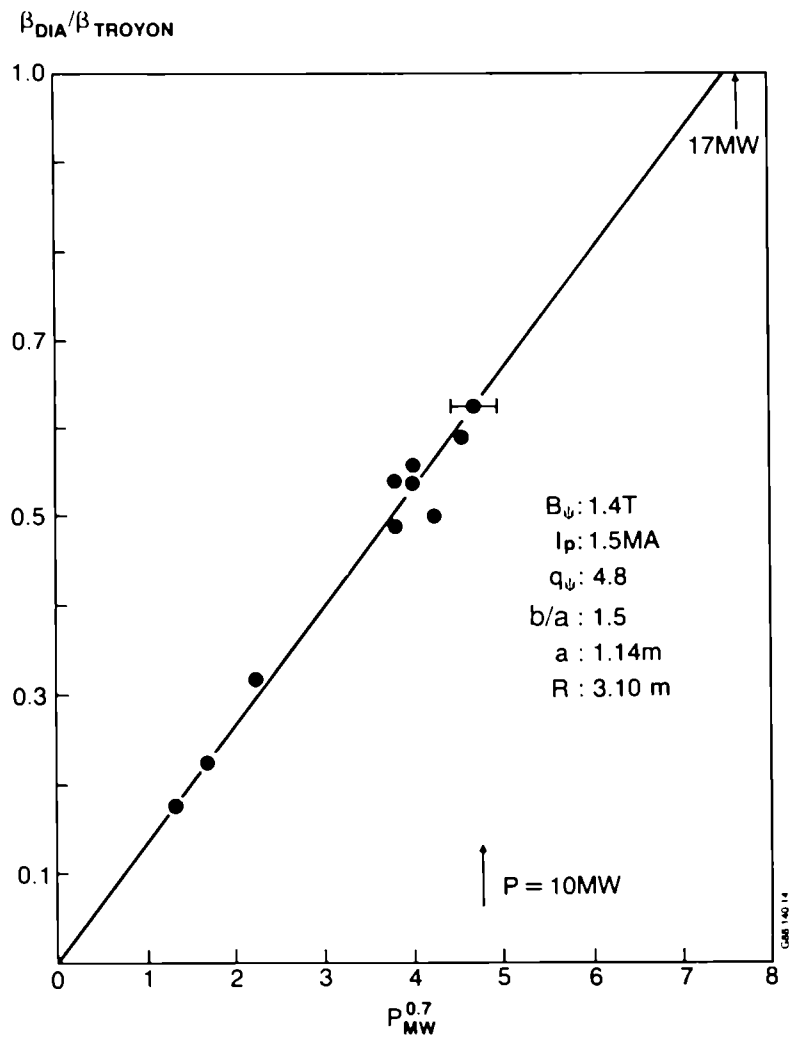

Fig. 7 Ratio of β to Troyon value as a function of increasing ICRH power for a series of JET discharges. G88.140 14

confinement properties. Experiments using larger heating powers are planned to establish the β limit behaviour in JET.

2.3 Energy Confinement Time

The energy confinement time in JET ohmic discharges reaches values in excess of 1.2s and has been discussed elsewhere (Gibson 1987). However, the temperatures reached in these discharges are too low for fusion, so the important confinement time behaviour is that in additionally heated discharges. Figs. 8 and 9 show the measured energy replacement time as a function of the total power flow through the plasma. This quantity is the total power input (P_T) (ohmic plus additional heating) less the rate of change of total plasma energy (dW/dt). The discharges have been chosen to be near steady state so that $P_T^{-1}(dW/dt)$ is less than 0.1. Fig. 8 shows results for a wide selection of JET limiter and L-mode X-point discharges at a variety of plasma currents (the confinement times shown come from diamagnetic measurements, which may over estimate by ~10% for the 6MA discharges). The confinement time scaling given by Goldston (1984) is shown for comparison. Fig. 9 shows similar data for H-mode discharges (see Tanga et al., (1987) for a description of JET L- and H-mode discharges). The Goldston scaling multiplied by two is shown for comparison. In both cases, a characteristic fall in confinement time occurs with increasing power flow. The best confinement time in H- mode discharges at low power is in excess of 1 s and comparable with the best ohmic discharges. At the highest powers, the best confinement times at present are about 0.6s, but the best H-mode discharges at power levels in excess of7 MW still have confinement times as long as 1s.

3. CENTRAL PARAMETERS AND SAWTOOTH BEHAVIOUR

It will be shown in section 6, that the peak values of n_D and T_i in the centre of the discharge play a particularly important role in determining the fusion relevant performance of an experiment such as JET. In the past, these central values in tokamaks have been severely limited by the occurrence of the internal relaxation or sawtooth oscillations, which cause repetitive collapses of the

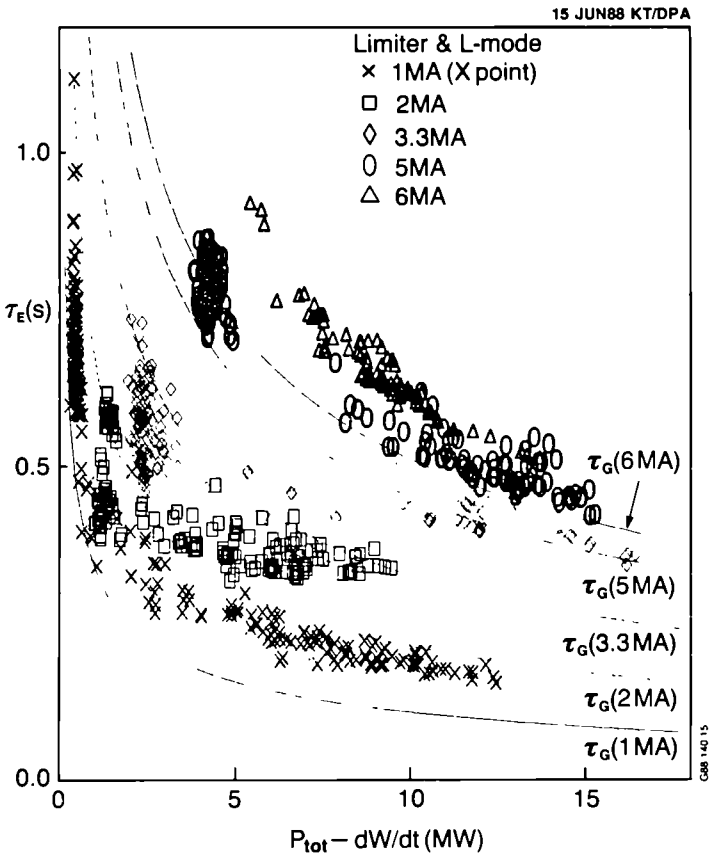

Fig. 8 Measured energy replacement time as a function of total power flow for JET limiter and L-mode discharges.

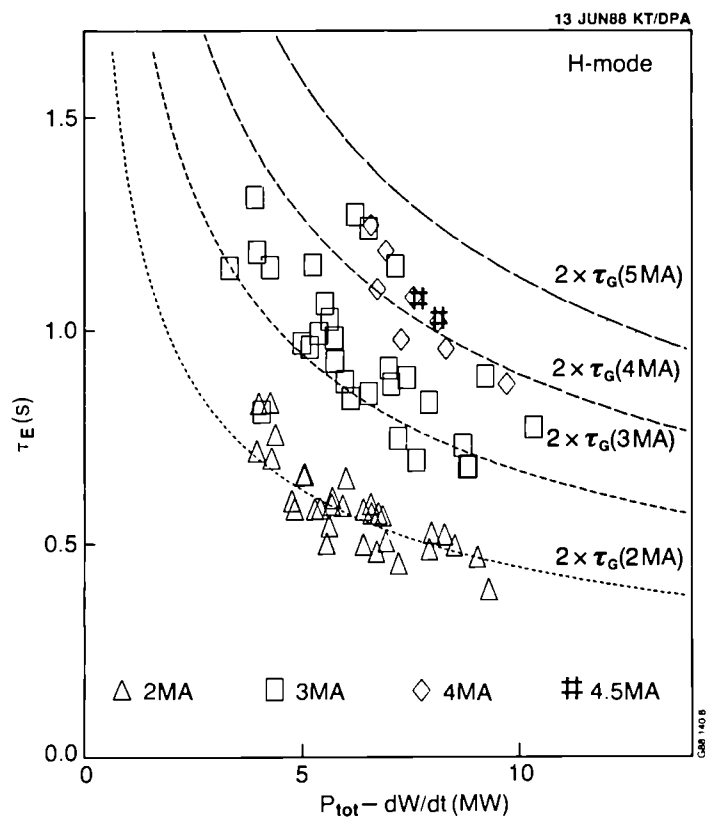

Fig. 9 Measured energy replacement time as a function of total power flow for JET H mode discharges.

central temperature and of the overall fusion neutron yield. It has been reported (Jacquinot, 1987), that in JET, spontaneous stabilization of this mode can occur, to produce a so called 'monster sawtooth'. This phenomenon has now been observed in many different additionally heated JET discharges: with ICRH; with NBI; with combined ICRH and NBI; in L-mode and in H-mode; and with and without pellet injection. Cases have been obtained where the monster sawtooth period (i.e. period without a sawtooth crash) lasts for more than 3 s, or about 6 energy replacement times. An important aspect of the phenomenon is that it allows peaked temperature profiles to develop and be maintained for long periods. An example is shown in Fig. 10. It will be seen that starting with a very flat central electron temperature profile at the crash of the previous sawtooth, a peaked profile is established after about 0.7 s, this peaked profile is then maintained until the end of the monster period when it crashes to give again a flat central distribution. Further information is given by in Campbell et al. (1988) and Bhatnagar et al. (1988).

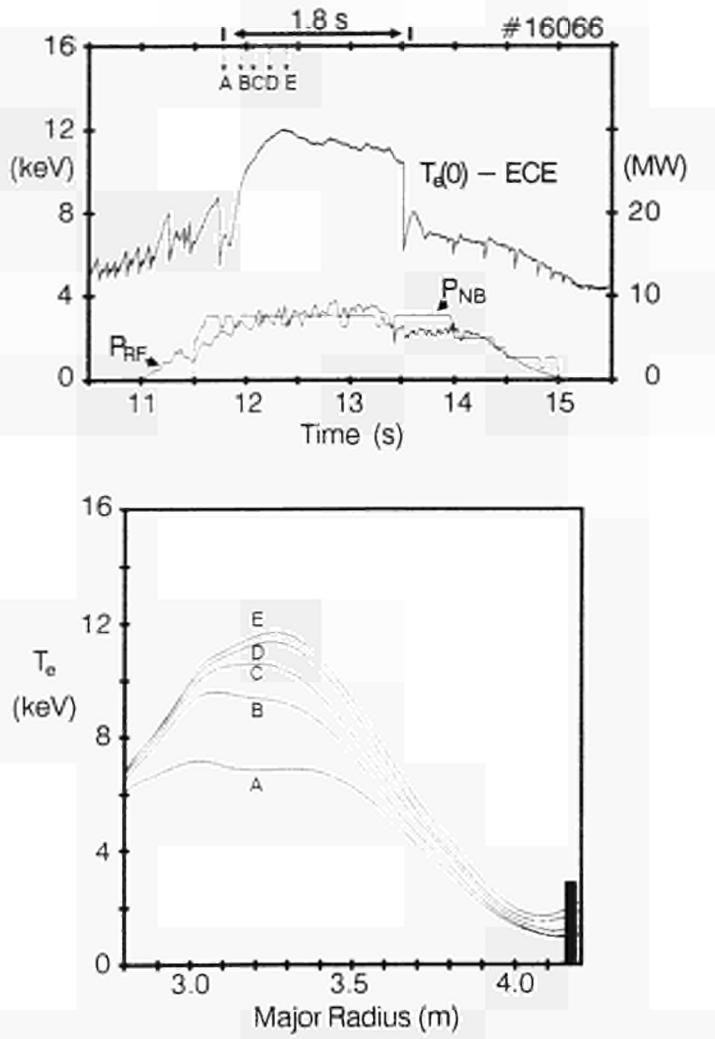

Fig. 10 The development and maintenance of peaked electron temperature profiles during a monster sawtooth period. This particular discharge is in double-null X-point configuration $I_p = 3MA$, $B_T = 3.2T$, $q_{cyl} = 5$ with H minority ICRH heating of a deuterium discharge with 80 keV D° NBI. The electron temperature and plasma energy increase for the first 0.7 s of the monster reaching 12 keV and 7 MJ, the mean density continues to increase for the first 1.2 s reaching $2.4 \times 10^{19} m^{-3}$, after this time the gross parameters remain constant. The monster ends in a crash with an associated burst of MHD activity after a total of 1.8 s, by this time the central ion temperature has fallen from its initial value of 14 keV to equal the final electron temperature of 11 keV.

It has long been speculated that the value of q_ψ (the number of times that a field line must encircle the major torus axis to complete one trip around the minor axis), near the magnetic axis of a tokamak, could not fall significantly below 1 and that the sawtooth relaxation operated to maintain this value. Measurements by Soltwisch on the Textor tokamak (Wolf et al., 1986) have convincingly demonstrated that this is not necessarily so. Measurements on JET show that during a monster sawtooth the value of q_ψ on axis drops well below 1, reaching values of 0.65 ± 0.1. (O'Rourke et al., 1988). An example is shown in Fig. 11. In addition to the polarimeter measurement, the figure shows, for comparison, two other estimates of q_ψ on axis. The first is from the TRANSP code which accurately calculates the current profile development from field diffusion, in this code $q(0)$ is arbitrarilly set to 1 at each sawtooth crash and so is necessarily equal to 1 at the start of the monster period. The second estimate is from the magnetic measurement using the equilibrium identification code IDENTC. In this case, this code shows a surprisingly large $q(0) = 1.7$ at the start of the monster. In view of these uncertainties in absolute value, the scales for the two code estimates have been shifted to agree with the polarimeter measurement in the diagram (the separate scales are shown so that the shift can be seen). It will be seen that all three estimates show a decrease in $q(0)$ during the monster by $\Delta q(0) \sim 0.15$. The TRANSP estimate and the polarimeter measurement agree well, the IDENTC estimate may show systematic differences but the values are within the experimental errors of the two methods.

This behaviour of $q(0)$ and hence the current density profile $j(r)$ during the monster period, provides

encouragement that in the future, control of $j(r)$ in JET, (for instance by Lower Hybrid Current Drive (LCHD)) should allow the sawtooth free period to be extended.

4. SCALING RELATIONS

Bickerton (1987) showed that a variety of scaling relations can give an adequate representation of JET global energy confinement time data. Here we consider just two relations, typical of the two main types. The first, typical of a power law dependence is that developed by Goldston (1983) from a study of many small tokamaks, which has proved remarkably successful in representing the confinement time behaviour in later large tokamaks. The second, typical of an 'offset linear law' is that derived by Rebut and Lallia (1988), based upon the concept of transport in a system where the magnetic surfaces, present in a true axisymmetric system are, due to helical distortions, breaking down into overlapping island chains and ergodic regions. The two relations are shown in Table II.

Figs. 12 and 13 show JET data with additional heating compared to the two scaling relations. Both relations fit the data well, the L-mode data is fitted with H=1, the H-mode confinement is substantially better with H=2. All the data lie within about

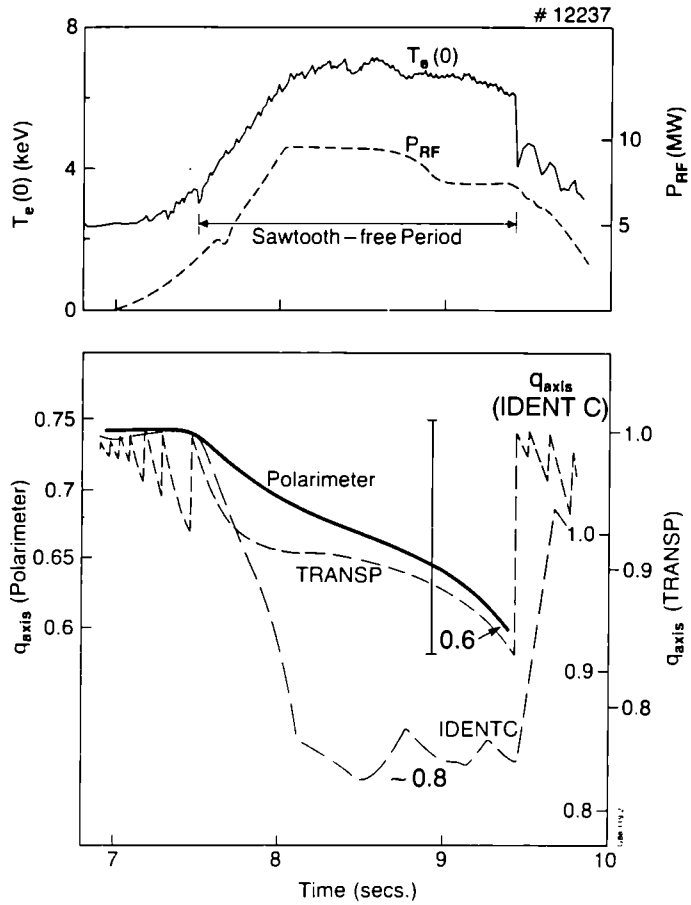

Fig. 11 The evolution of q_ψ on axis from polarimetry (using the inner flux surface elongation from X-ray tomography) during a monster sawtooth. 'TRANSP' and 'IDENTC' code estimates shown for comparison $I_p = 2MA$. G88.119/2

Table II
Scaling relations

Goldston

$$\tau_{EG} = C_G \; H \; I_p \; P_T^{-0.5} \; R^{1.75} \; a^{-0.37} \; (b/a)^{0.5}$$

i.e. $W(P_T) \propto P_T^{+0.5}$

$n T \tau_E \propto P_T \tau_E^2$; independent of P_T

$C_G = 3.7 \times 10^{-2}$ (from fit to small tokamaks)

Rebut-Lallia

$$\tau_{ERL} = H \; [\, C_R \; n^{0.75} \; Z_e^{0.25} \; B_T^{0.5} \; I_p^{0.5} \; L^{2.75} \; P_T^{-1} + C_L \; I_p \; L^{1.5} \; Z_e^{-0.5} \,]$$

i.e. $W(P_T) \propto k_1 + k_2 P_T$

$n T \tau_E \propto P_T \tau_E^2$; shows a minimum vers P_T

$C_R = 5.2 \times 10^{-2}$, $C_L = 2.4 \times 10^{-2}$ (from fit to JET data)

$L = [\, Rab \,]^{1/3}$

units: MA, MW, m, $10^{19} m^{-3}$, tesla.

In each case H is a multiplier ≈ 1 *for L mode data* ≈ 2 *for H mode data*

CR88602

a factor 1.4 of the fit, there is some tendency for the Goldston fit to require H slightly above the values quoted and the Rebut-Lallia fit to require slightly smaller values of H. Figs. 14 and 15 show the two relations compared with data from a wide range of tokamaks. Again, both relations show a tolerable fit (now on a log scale). Almost all of the data lies within a factor 2 of the fit and the better confinement of the H mode data (JET data only plotted) is apparent.

5. VALUES OF FUSION RELATED PARAMETERS OBTAINED IN JET

We define a fusion parameter

$$X = \hat{n}_i \hat{T}_i \tau_E \qquad (m^{-3}, keV, s) \ldots (5.1)$$

The importance of this parameter derives from the fact that in the important temperature range:

$$7\,keV < T_i < 25\,keV;$$

the D-T thermal fusion reaction rate coefficient $<\sigma v>_{DT}$ is proportional to T_i^2.

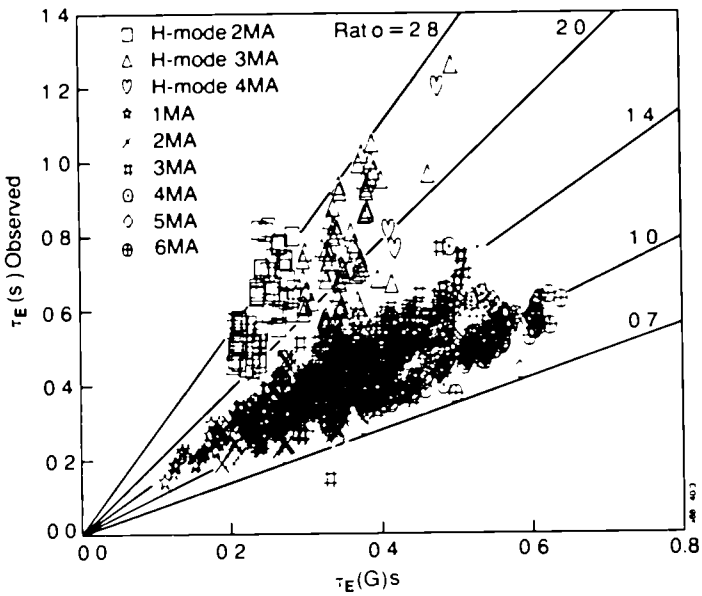

Fig. 12 Energy replacement time measured in JET compared with the Goldston scaling relation. G88.140 3

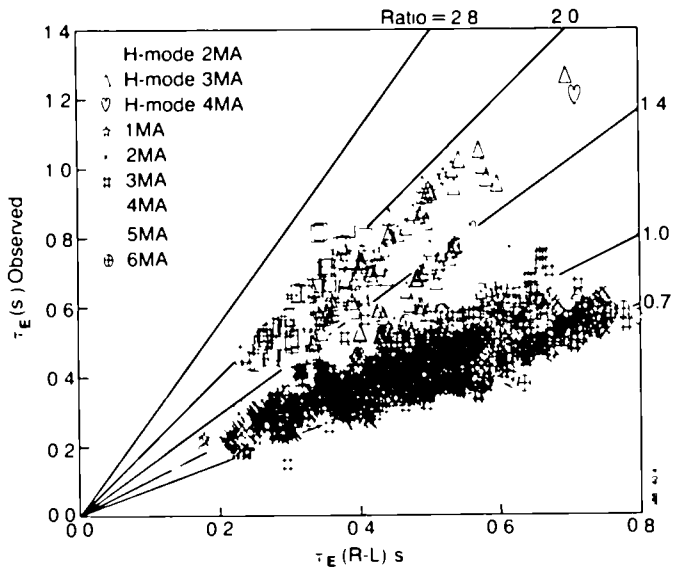

Fig. 13 Energy replacement time measured in JET compared with the Rebut-Lallia relation. G88.140 4

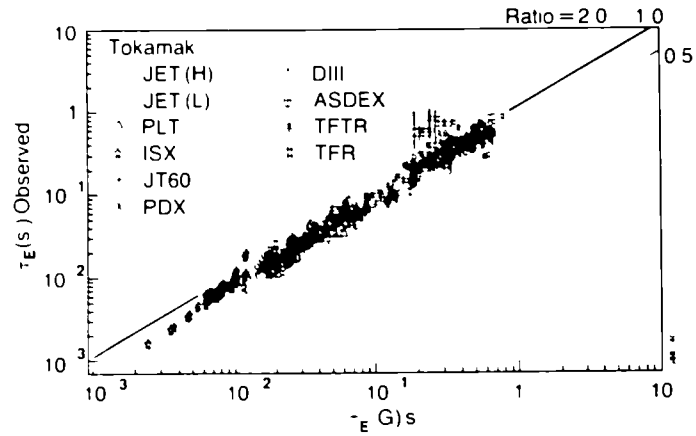

Fig. 14 Energy replacement time for a number of tokamaks compared with the Goldston relationship. G88 140 1

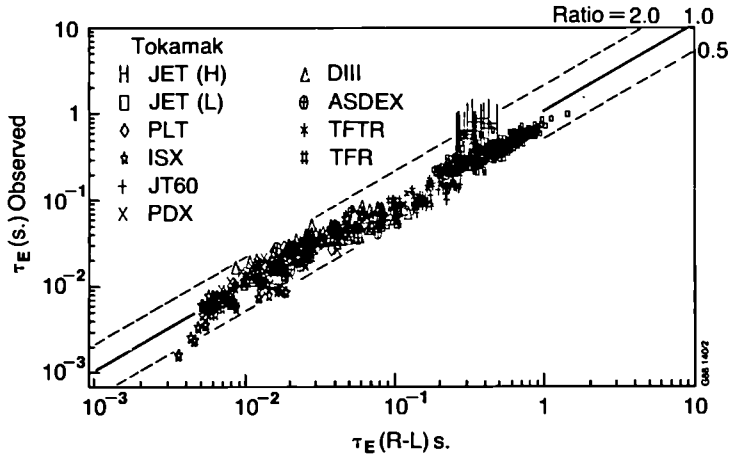

Fig. 15 Energy replacement time for a number of tokamaks compared with the Rebut-Lallia relationship. G88.140/2

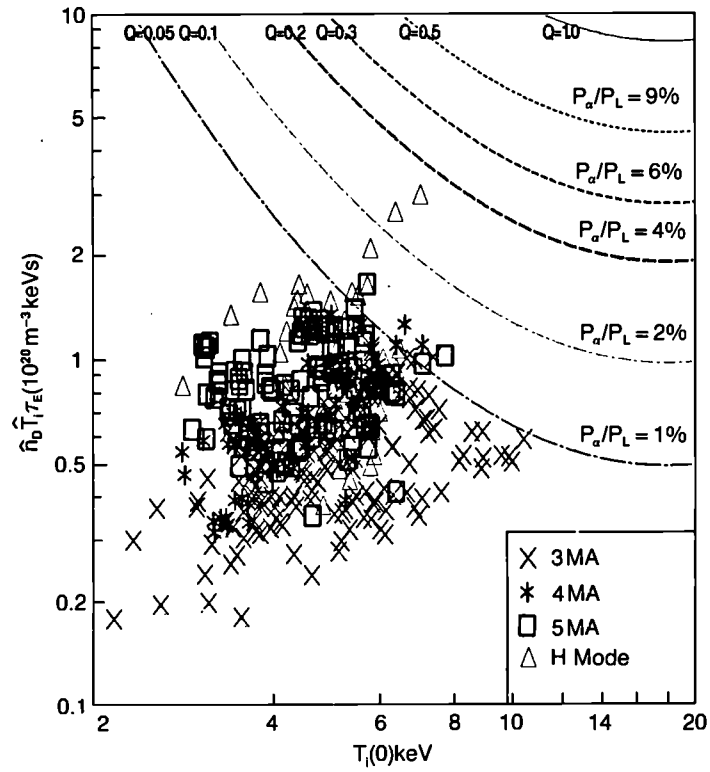

Fig. 16 Measured values of $\hat{n}_D\hat{T}_D\tau_E$ as a function of $\hat{T}_D$ in JET. The dashed curves are contours of $P_{\alpha(thermal)}/P_{Loss}$ or equivalently of $Q_{thermal}$ which would be obtained if n_D was replaced with 50% n_D and n_T.

It then follows that:

$$\frac{P_{\alpha(thermal)}}{P_{Loss}} \sim 2\times10^{-22}\ X \quad \ldots(5.2)$$

where the coefficient is correct for any reasonably peaked profile. That is for $n(\rho)/\hat{n}$ and $T(\rho)/\hat{T}$ $\propto(1+\rho^2)^{\alpha}$ where $\rho = r/a$, the variation is $\pm 10\%$ for $\alpha_n + \alpha_T = 1 \rightarrow 4$; for flat profiles the coefficient is 3.3×10^{-22}.

Fig. 16 shows measured values $\hat{n}_i\hat{T}_i\tau_E$ for a variety of discharges in JET. The best value of $\sim 3\times10^{20}\mathrm{m}^{-3}\mathrm{keV\,s}$ is obtained for an H-mode discharge with a central ion temperature of 7 keV. Also shown on Fig. 16 are curves of constant P_{α}/P_{Loss} or equivalently constant Q (the ratio of total fusion power released to total power input). These quantities are the values that would be realised, from thermal processes only, in discharges with the same values of $\hat{n}_i\hat{T}_i\tau_E$ and $\hat{T}_i$ as those shown, if the deuterium ions were replaced by an equal mixture of deuterium and tritium. In order to take account of the fact that for most points on the diagram much of the ion temperature profile is at temperatures too low for equation (5.2) to be valid, the Q curves have been calculated by integrating over profiles with $\alpha_n = 0.5$ and $\alpha_T = 1.5$. It will be seen that on this basis the best $\hat{n}_D\hat{T}_D\tau_E$ value of 3×10^{20} would correspond to

$$Q(\text{thermal}) = 0.1 \rightarrow 0.2 \text{ or } P_{\alpha}\ (\text{thermal})/P_{Loss} = 2\% \rightarrow 4\%.$$

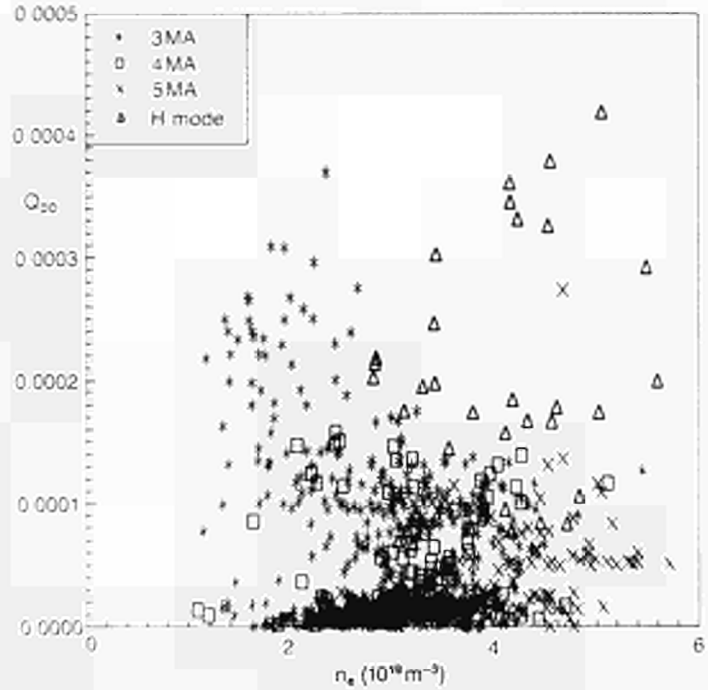

Fig. 17 Measured values of Q_{DD} in JET as a function of mean density.

Fig. 17 shows observed values of Q_{DD}, the ratio of total fusion power released in the D-D reaction in JET to power input. The values are obtained directly from the measured neutron yield, the largest observed value is $Q_{DD} \sim 4\times10^{-4}$. The ratio of the thermal component of Q for a 50% D-T plasma to that for a D-D plasma in the same condition is about 200 for a mean $T_i = 10$ keV. The ratio for the beam component is considerably higher especially if account is taken of the fact that in D-T, JET beams will operate at 140 keV instead of 70 keV at present. Consequently the best present value of $Q_{DD} = 4\times10^{-4}$ should correspond to a Q_{DT} well in excess of $Q_{DT} = 0.1$.

6. VALUES OF FUSION RELATED PARAMETERS PROJECTED FOR JET IN THE FUTURE

The expression $X = \hat{n}_D\,\hat{T}_i\,\tau_E = \gamma_n\,\gamma_T\,\bar{n}_D\,\bar{T}_i\tau_E$

can be written $X = 1.06\times10^{20}\,P_T\,\tau_E^2\,\gamma_n\gamma_T/Rab \quad \ldots(6.1)^*$

where $\gamma_n = \hat{n}/\bar{n}, \quad \gamma_T = \hat{T}/\bar{T} \quad \ldots(6.2)$

b is the vertical minor radius

and the units are MW, s, m, keV

---

* More formally the expression $\gamma_n\gamma_T$ in (6.1) should be replaced by γ_p where $\gamma_p = \hat{n}.\hat{T}/\overline{nT}$ where the bar now indicates the volume average of nT.

For nearly all JET discharges however the quantity $S = \bar{n}.\bar{T}/\overline{nT}$ is very close to one and we shall use the form with $\gamma_n\gamma_T$ because it gives better insight. However, it is worth noting that about 2% of JET limiter and L-mode discharges have $S > 1.5$ as do about 14% of JET H-mode discharges.

Substituting the Goldston form for τ_E from Table 2 gives:

$$X \propto H^2 \gamma_n \gamma_T I_p^2 \ (R/a)^{2.5} a^{-0.24} \quad \ldots(6.3)$$

Hence for a given device the maximum X is determined and is obtained by maximising:

$$H^2 \gamma_n \gamma_T I_p^2 \quad \ldots(6.4)$$

The value of the peaking factor $\gamma_n \gamma_T$ clearly plays an important part in optimising the value of the fusion parameter X which can be obtained. Fig. 18 shows the values of $\hat{n}_e/\bar{n}_e$ versus $\hat{n}_e$ for a large number of JET discharges, points are also shown after pellet injection. Typical values of $\hat{n}_e/\bar{n}_e$ without pellets are ~1.8 and after pellet injection ~3. Fig. 19 is a similar plot for $\hat{T}_e/\bar{T}_e$, a typical value for non-monster cases is ~2.2 and during a monster period ~2.6. Fig. 20 is a plot of $(\hat{T}_e/\bar{T}_e)\cdot(\hat{n}_e/\bar{n}_e)$ versus q_{cyl}, points for H-mode discharges are indicated. For limiter and L-mode discharges a typical value is 4, somewhat higher in monster periods. Even for q_{cyl} values as low as 2.5 values of $\gamma_n \gamma_T$ of 4 to 5 are obtained. However, in H-mode discharges the best values are about 3.

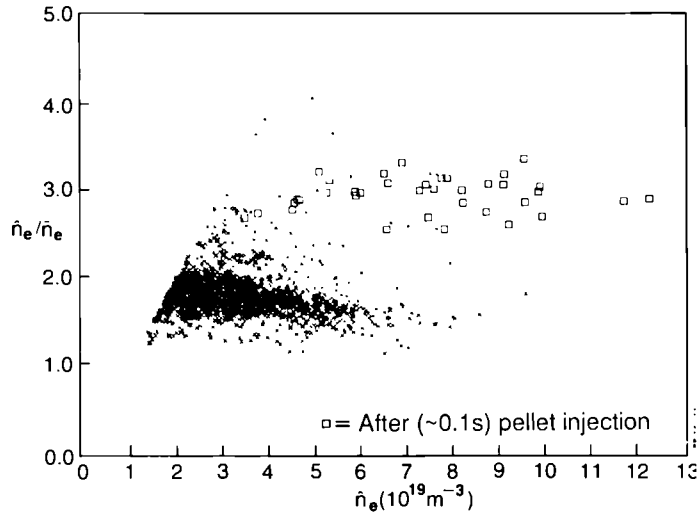

Fig. 18 $\hat{n}_e/\bar{n}$ versus $\hat{n}_e$ for JET discharges. Values after pellet injection are indicated. G88.140/11

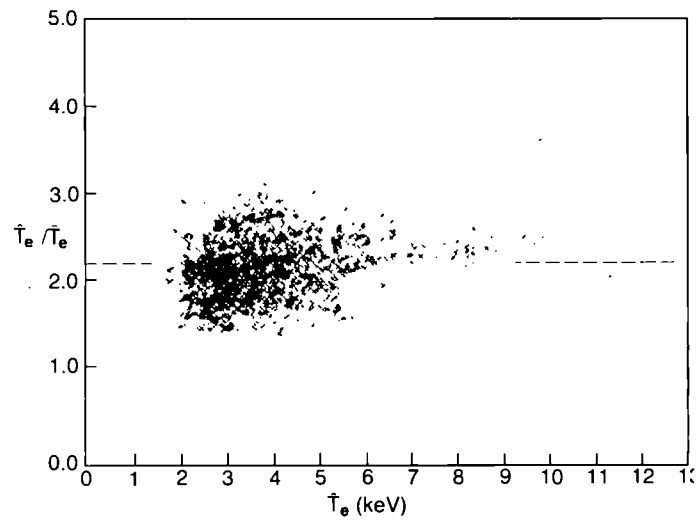

Fig. 19 $\hat{T}_e/\bar{T}_e$ versus $\hat{T}_e$. G88.140/12

We now calculate the quantities related to fusion performance which are listed in Table III and the quantities in Table IV which show the margin to the β limit and the operating density. We calculate these quantities for a projected L-mode discharge in JET in Table V and for a projected H-mode discharge in Table VI. In each, case the projection is made in two ways: (a) by using the Goldston and Rebut-Lallia coefficients given in Table II; (b) by adjusting the value of H to fit the confinement time observed in a particular (good) reference JET discharge. In each case, the values of the assumed plasma parameters are given at the head of the table and in brackets are given the values actually used or observed in the reference discharge. The machine parameters set for both L-mode and H-mode discharges (P_T, I_p etc) are expected to be possible with the equipment already installed on JET (the H-mode value assumed for P_T probably requires that a few MW of ICRH can be coupled in addition to the NBI power available at the assumed 150 keV). The important plasma parameter assumptions in Table V and Table VI are the values of Z_{eff}, q_{cyl} and $\gamma_n \gamma_T$. The Z_{eff} value is reasonable in view of present experience at high power levels and relevant densities. The values of q_{cyl} (1.8 for L-mode and 2.2 for H-mode) have been demonstrating in JET by operating at reduced toroidal field. However the large size of the $q=1$ region in these discharges generally leads to lower values of τ_E than would be given by the Goldston or Rebut-Lallia relations. Using these relations at these low q values implies that this problem can be overcome, for instance by using monster type discharges where $q(o)$ falls significantly below one or by controlling the current density profile with LHCD. The values assumed for $\gamma_n \gamma_T$ are based on Fig. 20 which uses $\hat{T}_e/\bar{T}_e$ for γ_T wheras the important quantity is $\hat{T}_i/\bar{T}$, for most of the range T_e and T_i are fairly well coupled so the difference should not be important. The value $\gamma_n \gamma_T = 4$ at $q_{cyl} = 1.8$

assumed in the L-mode case requires some improvement over the value of $\gamma_n\gamma_T = 3.5$ in Fig. 20. The value of $\gamma_n\gamma_T = 1.5$ at $q_{cyl} = 2.2$ assumed for the H-mode case corresponds to observed values in Fig. 20. The difference in assumed peaking factor leads to similar performance predictions for L-mode and H-mode projections and this difference in assumption is reasonable on the basis of present experience, where H-mode discharges generally have flatter profiles (see Fig. 20).

With these reservations we see from Tables V and VI that it is reasonable on the basis of present experience to expect that in D-T operation JET will achieve the following parameters.

$\hat{n}_i \hat{T}_i \tau_E$	$0.2 \rightarrow 0.5 \times 10^{21} \mathrm{m^{-3}\,keV\,s}$
$P_{\alpha(thermal)}/P_{Loss}$	$0.05 \rightarrow 0.1$
$P_{\alpha(total)}/P_{Loss}$	$0.1 \rightarrow 0.2$
P_α(MW)	$2.6 \rightarrow 4.7$
$Q_{thermal}$	$0.3 \rightarrow 0.6$
Q_{total}	$0.5 \rightarrow 1.4$

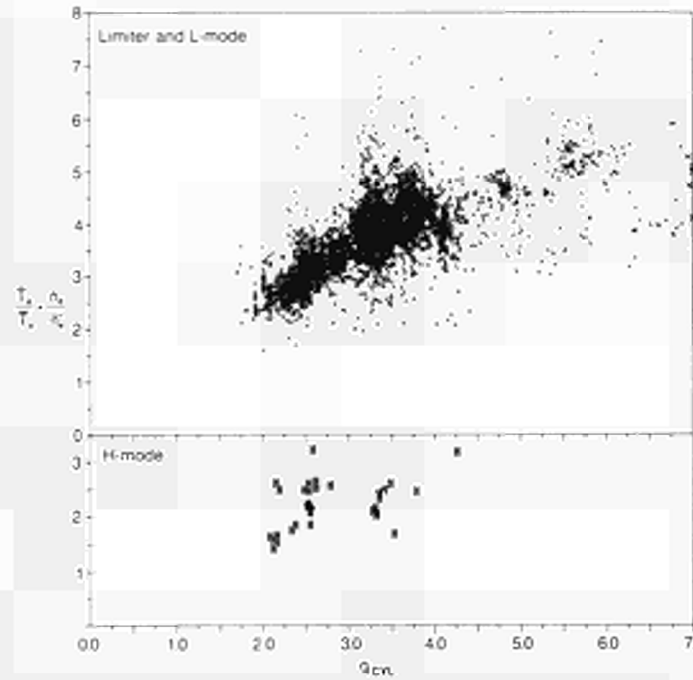

Fig. 20 $(\hat{n}_e/\bar{n}_e)\cdot(\hat{T}_e/\bar{T}_e)$ (representing $\gamma_n\gamma_T$) versus q_{cyl} H-mode points are indicated. G88.140

The projected $\beta/\beta_{Troyon} \lesssim 0.5$ and $nR/B_T \lesssim 4 \rightarrow 6 \times 10^{19} \mathrm{m^{-2}\,T^{-1}}$ should be possible and the assumed mean density of $\sim 5 \times 10^{19} \mathrm{m^{-3}}$ should lead to $T \gtrsim 5$ keV with the available heating power.

If it proves possible to obtain larger values of $\gamma_n\gamma_T$ in H-mode discharges (for instance by extending the combination of monster sawtooth behaviour and H-mode which has already been observed; or by using the LHCD system, which is in manufacture; or by using pellet densification and subsequent heating as demonstrated in the L-mode discharge of Fig. 4) then still higher values may be possible. Thus if $\gamma_n\gamma_T = 3$ could be obtained in H-mode the values given above would be increased by about a factor of 2.

Table **III**
Performance parameters to be calculated using the two scaling relations

τ_E

$$X = \hat{n}_i \hat{T}_i \tau_E = \frac{1.06 \times 10^{20} P_T \tau_E^2 \gamma_n \gamma_T f_i}{Rab}$$

$$f_i = \frac{2n_i}{n_i + n_e} \; ; \quad f_e = \frac{2n_e}{n_i + n_e}$$

$$\frac{P_{\alpha\,(thermal)}}{P_{LOSS}} = 2 \times 10^{-22} X$$

$\frac{P_{\alpha\,(total)}}{P_{LOSS}}$ is calculated using the approximate relation $\frac{P_{\alpha\,(beam)}}{P_{beam}} \sim 0.12\,\bar{T}_e(\mathrm{keV})/5$

for ~ 150 keV D^0 injected into 50 : 50 D–T plasma we shall take $P_{beam} = \frac{1}{2} P_T$ for L mode and $P_{beam} = P_T$ for H mode

Table **IV**
Quantities which define the margin in β and n

$$\frac{\beta}{\beta_{Troyon}} = \frac{3 P_T \tau_E}{R b I_p B_T}$$

$$\frac{\bar{n}_e R}{B_T} = \frac{1.06 \times 10^{20} f_e P_T \tau_E}{ab B_T \bar{T}}$$

or for $\bar{T} = 5$ keV

$$\left[\frac{\bar{n}_e R}{B_T}\right]_5 = \frac{2.12 \times 10^{19} f_e P \tau_E}{ab B_T}$$

(according to fig.6 this quantity must be less than about $7 \times 10^{19} \mathrm{m^{-2}\,T^{-1}}$ for $q_{cyl} \sim 3$).

or $$\bar{n}_{e5} = \frac{2.12 \times 10^{19} f_e P \tau_E}{abR}$$

(this quantity must be less than the assumed density in order that $\bar{T}_e$ can be > 5 keV so that the expression for $P\alpha/P_{loss}$ in table **III** is valid).

Table V
L Mode projected performance

Assumed parameters (values for # 14959 in brackets)

P_T = 30MW	(11.6)	$\gamma_n \gamma_T$ = 4	(4)
I_p = 7MA	(4)	Z_{eff} = 2	(2.5)
$\bar{n}_e$ = 5×10^{19}m^{-3}	(3.3)	R = 3m	(3)
B_T = 3.4tesla	(3.4)	q_{cyl} = 1.8	(3.2)
a = 1.2m	(1.14)	b = 1.9m	(1.8)

Quantity	Using fitted coefficients		Scaled from Pulse 14959 which had $\hat{n}_D \hat{T}_i \tau_E = 1\times10^{20}$	
	Goldston	Rebut-Lallia	Goldston	Rebut-Lallia
H	1	1	1.17 [H chosen to fit τ_E(obs)=0.4s]	1
τ_E (s)	0.38	0.51	0.45	0.51
$\hat{n}_i \hat{T}_i \tau_E$ (10^{20})	2.4	4.2	3.3	4.2
$P_{\alpha\,(thermal)} / P_{LOSS}$	0.05	0.09	0.07	0.09
$P_{\alpha\,(total)} / P_{LOSS}$	0.09	0.13	0.11	0.13
P_α (MW)$_{total}$	2.9	4.7	3.8	4.7
$Q_{thermal}$	0.25	0.46	0.35	0.46
Q_{total}	0.49	0.78	0.63	0.78
β / β_{Troyon}	0.25	0.34	0.3	0.34
$(\bar{n}_e R/B)_{T=5}$ (10^{19}m^{-2}T^{-1})	3.5	4.6	4.1	4.6
$\bar{n}_{eT=5}$(10^{19}m^{-3})	3.9	5.2	4.6	5.2

CR 88608

Table VI
H Mode projected performance

Assumed parameters (values for # 15894 in brackets)

P_T = 15MW	(7.4)	$\gamma_n \gamma_T$ = 1.5	(3.1)
I_p = 6MA	(3)	Z_{eff} = 2	(2)
$\bar{n}_e$ = 5×10^{19}m^{-3}	(4.8)	R = 3m	(3)
B_T = 3.4tesla	(3.2)	q_{cyl} = 2.2	(4.3)
a = 1.2m	(1.1)	b = 1.9m	(1.9)

Quantity	Using fitted coefficients		Scaled from Pulse 15894 which had $\hat{n}_D \hat{T}_i \tau_E = 1\times10^{20}$	
	Goldston	Rebut-Lallia	Goldston	Rebut-Lallia
H	2	2	2.8 [H chosen to fit τ_E(obs)=1s]	1.7
τ_E (s)	0.92	1.26	1.3	1.1
$\hat{n}_i \hat{T}_i \tau_E$ (10^{20})	2.6	4.9	5.2	3.6
$P_{\alpha\,(thermal)} / P_{LOSS}$	0.05	0.1	0.1	0.07
$P_{\alpha\,(total)} / P_{LOSS}$	0.15	0.2	0.2	0.17
P_α (MW)$_{total}$	2.6	4	4.2	3.2
$Q_{thermal}$	0.3	0.5	0.6	0.4
Q_{total}	0.9	1.3	1.4	1.1
β / β_{Troyon}	0.36	0.49	0.5	0.42
$(\bar{n}_e R/B)_{T=5}$ (10^{19}m^{-2}T^{-1})	4.2	5.7	5.9	4.9
$\bar{n}_{eT=5}$(10^{19}m^{-3})	4.7	6.5	6.7	5.6

CR 88607

7. CONCLUSIONS

7.1 JET has operated with up to 6MA of plasma current in a plasma with a volume of $120m^3$. Operation has taken place in full aperture limiter discharges and in X-point discharges. Over 10MJ of plasma energy has been produced.

7.2 The best operation has produced $\hat{n}_D \hat{T}_i \tau_E$ values of about $3 \times 10^{20} m^{-3}$ keV s, with $\hat{T}_i \sim 7$ keV. The observed Q_{DD} of 4×10^{-4} would correspond to Q_{DT} substantially greater than 0.1 for a D-T mixture with the same plasma conditions. Other operation has separately produced confinement times in excess of 1 s, ion temperature in excess of 15 keV and central electron density in excess of $1 \times 10^{20} m^{-3}$.

7.3 These parameters are already commensurate with those required in the plasma of a reactor.

7.4 The observed scaling behaviour, when applied to parameters already possible in the JET design, but not yet exploited (i.e. high power operation at high current, in L-mode and H-mode), suggests that in D-T operation JET should be able to obtain some 3 to 5MW of α particle power with:

$$\hat{n}_i \hat{T}_i \tau_E \sim 0.2 \rightarrow 0.5 \times 10^{21} m^{-3} \text{keV s and } Q_{total} \sim 0.5 \rightarrow 1.4 \ (Q_{thermal} \sim 0.3 \rightarrow 0.6)$$

7.5 If these conditions can be obtained, α particle heating of the plasma core will be evident and a secure base will have been established for the next generation of fusion devices.

7.6 The most important conditions to be met to obtain this type of operation are as follows:

a) The presently observed scaling behaviour must continue over the modest parameter extension that is required.

b) The peakedness obtained in many present discharges must continue to be possible at higher powers and higher currents (similar q_{cyl}). Any improvement in peakedness, for instance by extension of monster behaviour, pellet injection or LHCD would improve the projected performance.

c) The control of impurities, fuelling and wall pumping must continue to give central $Z_{eff} \sim 2$ and keep the average density down to about $5 \times 10^{19} m^{-3}$ in the face of increased heating power. In the future, it must be possible to maintain a D/T ratio around 0.5.

d) The ability to couple at least some RF power into H-mode discharges is very desirable but has not yet been possible.

8. ACKNOWLEDGEMENT

Pellet injection results were obtained during work performed under a collaboration agreement between the JET Joint Undertaking and the US. Department of Energy (USDOE)

REFERENCES

Bertolini, E., Huguet, M. et al. (1987). Proc. 12th Symp. Fus. Eng. (Monterey, U.S.A.) also JET Report P(87) 52.
Bhatnagar, V. et al. (1988). Europhysics Conference Abstracts **12B**, 358*.
Bickerton, R. J., et al. (1987). Plasma Physics and Controlled Fusion **10A**, 1219.
Campbell, D. J. et al. (1988). Europhysics Conference Abstracts **12B**, 377*.
Gibson, A. (1987). Phil. Trans. R. Soc. London **A322**, 67.
Goldston, R. (1984). Plasma Physics and Controlled Fusion **26**, 87.
Jacquinot, J. et al. (1987). Nuclear Fusion Supp. CN–47, I, 449.
Kupschus, P. et al. (1988). Europhysics Conference Abstracts **12B**, 143*.
O'Rourke, J. (1988). Europhysics Conference Abstracts **12B**, 155*.
Rebut, P-H., Lallia, P., Watkins, M. (1988). JET Report P(88) 05.
Tanga, A. et al. (1987). Nuclear Fusion **27**, 1877.
Troyon, F. et al. (1984). Plasma Physics and Controlled Fusion **26**, 209.
Wolf, G. H. et al. (1986). Plasma Physics and Controlled Fusion **28**, 1413.
*Contributed Papers Proceedings 15th European Conference on Controlled Fusion and Plasma Heating (Dubrovnik 1988).

APPENDIX. 1

THE JET TEAM

JET Joint Undertaking, Abingdon, Oxon, OX14 3EA, U.K.

J.M.Adams[1], F.Alladio[4], H.Altmann, R.J.Anderson, G.Appruzzese, K.Avinash[14], W.Bailey, B.Balet, D.V.Bartlett, L.R.Baylor[23], K.Behringer, A.C.Bell, P.Bertoldi, E.Bertolini, V.Bhatnagar, R.J.Bickerton, A.Boileau[3], T.Bonicelli, S.J.Booth, G.Bosia, M.Botman, D.Boyd[30], H.Brelen, H.Brinkschulte, M.Brusati, T.Budd, M.Bures, T.Businaro[4], H.Buttgereit, D.Cacaut, C.Caldwell-Nichols, D.J.Campbell, P.Card, J.Carwardine, G.Celentano, P.Chabert[26], C.D.Challis, A.Cheetham, J.Christiansen, C.Christodoulopoulos, P.Chuilon, R.Claesen, S.Clement[29], J.P.Coad, P.Colestock[6], S.Conroy[12], M.Cooke, S.Cooper, J.G.Cordey, W.Core, S.Corti, A.E.Costley, G.Cottrell, M.Cox[7], P.Cripwell[12], F.Crisanti[4], D.Cross, H.de Blank[15], J.de Haas[15], L.de Kock, E.Deksnis, G.B.Denne, G.Deschamps, G.Devillars, K.J.Dietz, J.Dobbing, S.E.Dorling, P.G.Doyle, D.F.Düchs, H.Duquenoy, A.Edwards, J.Ehrenberg[13], T.Elevant[11], W.Engelhardt, S.K.Erents[7], L.G.Eriksonn[5], M.Evrard[2], H.Falter, D.Flory, M.Forrest[7], C.Froger, K.Fullard, M.Gadeberg, A.Galetsas, R.Galvao[8], A.Gibson, R.D.Gill, A.Gondhalekar, C.Gordon, G.Gorini, C.Gormezano, N.A.Gottardi, C.Gowers, B.J.Green, F.S.Griph, M.Gryzinski[25], R.Haange, G.Hammett[6], W.Han[9], C.J.Hancock, P.J.Harbour, N.C.Hawkes[7], P.Haynes[7], T.Hellsten, J.L.Hemmerich, R.Hemsworth, R.F.Herzog, K.Hirsch[13], J.Hoekzema, W.A.Houlberg[23], J.How, M.Huart, A.Hubbard, T.P.Hughes[31], M.Hugon, M.Huguet, J.Jacquinot, O.N.Jarvis, T.C.Jernigan[23], E.Joffrin, E.M.Jones, L.P.D.F.Jones, T.T.C.Jones, J.Källne, A.Kaye, B.E.Keen, M.Keilhacker, G.J.Kelly, S.Knowlton, A.Konstantellos, M.Kovanen[20], P.Kupschus, P.Lallia, J.R.Last, L.Lauro-Taroni, M.Laux[32], K.Lawson[7], E.Lazzaro, M.Lennholm, X.Litaudon, P.Lomas, M.Lorentz-Gottardi[2], C.Lowry, G.Magyar, D.Maisonnier, M.Malacarne, V.Marchese, P.Massmann, L.McCarthy[27], G.McCracken[7], P.Mendonca, P.Meriguet, P.Micozzi[4], S.F.Mills, P.Millward, S.L.Milora[23], A.Moissonnier, P.L.Mondino, D.Moreau[16], P.Morgan, H.Morsi[13], G.Murphy, M.F.Nave, M.Newman, L.Nickesson, P.Nielsen, P.Noll, W.Obert, D.O'Brien, J.O'Rourke, M.G.Pacco-Düchs, M.Pain, S.Papastergiou, D.Pasini[19], M.Paume[26], N.Peacock[7], D.Pearson[12], F.Pegoraro, M.Pick, S.Pitcher[7], J.Plancoulaine, J-P.Poffé, F.Porcelli, R.Prentice, T.Raimondi, J.Ramette[16], J.M.Rax[26], C.Raymond, P-H.Rebut, J.Removille, F.Rimini, D.Robinson[7], A.Rolfe, R.T.Ross, L.Rossi, G.Rupprecht[13], R.Rushton, P.Rutter, H.C.Sack, G.Sadler, N.Salmon[12], H.Salzmann[13], A.Santagiustina, D.Schissel[24], P.H.Schild, M.Schmid, G.Schmidt[6], R.L.Shaw, A.Sibley, R.Simonini, J.Sips[15], P.Smeulders, J.Snipes, S.Sommers, L.Sonnerup, K.Sonnenberg, M.Stamp, P.Stangeby[18], D.Start, C.A.Steed, D.Stork, P.E.Stott, T.E.Stringer, D.Stubberfield, T.Sugie[17], D.Summers, H.Summers[19], J.Taboda-Duarte[21], J.Tagle[29], H.Tamnen, A.Tanga, A.Taroni, C.Tebaldi[22], A.Tesini, P.R.Thomas, E.Thompson, K.Thomsen, P.Trevalion, M.Tschudin, B.Tubbing, K.Uchino[28], E.Usselmann, H.van der Beken, M.von Hellermann, T.Wade, C.Walker, B.A.Wallander, M.Walravens, K.Walter, D.Ward, M.L.Watkins, J.Wesson, D.H.Wheeler, J.Wilks, U.Willen[11], D.Wilson, T.Winkel, C.Woodward, M.Wykes, I.D.Young, L.Zannelli, M.Zarnstorff[6], D.Zasche[13], J.W.Zwart.

PERMANENT ADDRESS

1. UKAEA, Harwell, Oxon. UK.
2. EUR-EB Association, LPP-ERM/KMS, B-1040 Brussels, Belgium.
3. Institute National de Récherches Scientifiques, Quebec, Canada.
4. ENEA-CENTRO Di Frascati, I-00044 Frascati, Roma, Italy.
5. Chalmers University of Technology, Göteborg, Sweden.
6. Princeton Plasma Physics Laboratory, New Jersey, USA.
7. UKAEA Culham Laboratory, Abingdon, Oxon. UK.
8. Plasma Physics Laboratory, Space Research Institute, São José dos Campos, Brazil.
9. Institute of Mathematics, University of Oxford, UK.
10. CRPP/EPFL, 21 Avenue des Bains, CH-1007 Lausanne, Switzerland.
11. Swedish Energy Research Commission, S-10072 Stockholm, Sweden.
12. Imperial College of Science and Technology, University of London, UK.
13. Max Planck Institut für Plasmaphysik, D-8046 Garching bei München, FRG.
14. Institute for Plasma Research, Gandhinagar Bhat Gujat, India.
15. FOM Instituut voor Plasmafysica, 3430 BE Nieuwegein, The Netherlands.
16. Commissariat à l'Energie Atomique, Cadarache, France.
17. JAERI, Tokai Research Establishment, Tokai-Mura, Naka-Gun, Japan.
18. Institute for Aerospace Studies, University of Toronto, Downsview, Ontario, Canada.
19. University of Strathclyde, Glasgow, G4 ONG, U.K.
20. Nuclear Engineering Laboratory, Lapeenranta University, Finland.
21. JNICT, Lisboa, Portugal.
22. Department of Mathematics, University of Bologna, Italy.
23. Oak Ridge National Laboratory, Oak Ridge, Tenn., USA.
24. G.A. Technologies, San Diego, California, USA.
25. Institute for Nuclear Studies, Swierk, Poland.
26. Commissariat à l'Energie Atomique, Cadarache, France.
27. School of Physical Sciences, Flinders University of South Australia, South Australia SO42.
28. Kyushi University, Kasagu Fukuoka, Japan.
29. Centro de Investigaciones Energeticas Medioambientales y Tecnologicas, Spain.
30. University of Maryland, College Park, Maryland, USA.
31. University of Essex, Colchester, UK.
32. Akademie der Wissenschaften, Berlin, DDR.

CR 88.49.1A (rev.25/7/88)

High Power Ion Cyclotron Resonance Heating in JET

The JET Team
(presented by Dr J Jacquinot)

ABSTRACT

Ion Cyclotron Resonance Heating (ICRH) powers of up to 17 MW have been coupled to JET limiter plasmas. The plasma stored energy has reached 7 MJ with 13 MW of RF in 5 MA discharges with $Z_{eff} \simeq 2$. When $I_p/B_\phi \simeq 1$ MA/T the stored energy can be 50 % greater than the Goldston L mode scaling. This is due to transient stabilisation of sawteeth (up to 3 s) and to a significant energy content in the minority particles accelerated by RF (up to 30 % of the total stored energy). Central temperatures of $T_e \sim 11$ keV and $T_i \simeq 8$ keV have been reached with RF alone. (He^3)D fusion experiments have given a 60 kW fusion yield (fusion rate of 2×10^{16} s^{-1} in the form of energetic fast particles (14.7 MeV(H), 3.6 MeV(He^4)) in agreement with modelling. When transposing the same calculation to a (D)T scenario, Q is predicted to be between 0.2 and 0.8 using plasma parameters already achieved. For the first time, a peaked density profile generated by pellet injection could be reheated and sustained by ICRF for 1.2 s. Electron heat transport in the central region is reduced by a factor 2 to 3. The fusion product $n_{io}\tau_E T_{io}$ reaches 2.2×10^{20} m^{-3}.s.kev in 3 MA discharges which is a factor of 2.3 times larger than with the normal density profile.

KEYWORDS

ICRH, Tokamak, Confinement, Scaling, Fusion Yield, Heating Scenarios, Fast Ions, Pellet, Peaked Density Profiles.

INTRODUCTION

Following closely a programme established in 1982, JET has completed the installation of 8 antenna generator units in July 1987. The power plant can deliver 24 MW for 20 s in a well matched load placed at the generator output. Taking into account the losses in the transmission line, in the antenna screen and reflection, the maximum effective wave power launched in the Torus was about 15 MW for usual plasmas conditions. It reached 17 MW in some cases. This new antenna system incorporates modifications to the internal structure in order to offer a choice of $k_\parallel$ spectra found useful in previous experiments (Jacquinot, 1987a, 1987b).

Since July 1987, the ICRF system has been mainly involved in 3 topics of the JET programme:

(i) High power heating of "limiter" discharges, ie with a boundary defined by the belt limiter or by the antenna side protection. The emphasis was placed on high current (up to 6 MA). A limited number of experiments were devoted to high β targets.

(ii) High fusion yield experiments using either the fundamental cyclotron acceleration of the He^3 minority ions to an energy close to the maximum of the (D-He^3) fusion cross section (0.4 MeV) or, in combination with D beam injection, the second harmonic acceleration of D ions to maximise the D-D fusion reaction.

---

[1] For list of authors, see A Gibson and others, these proceedings

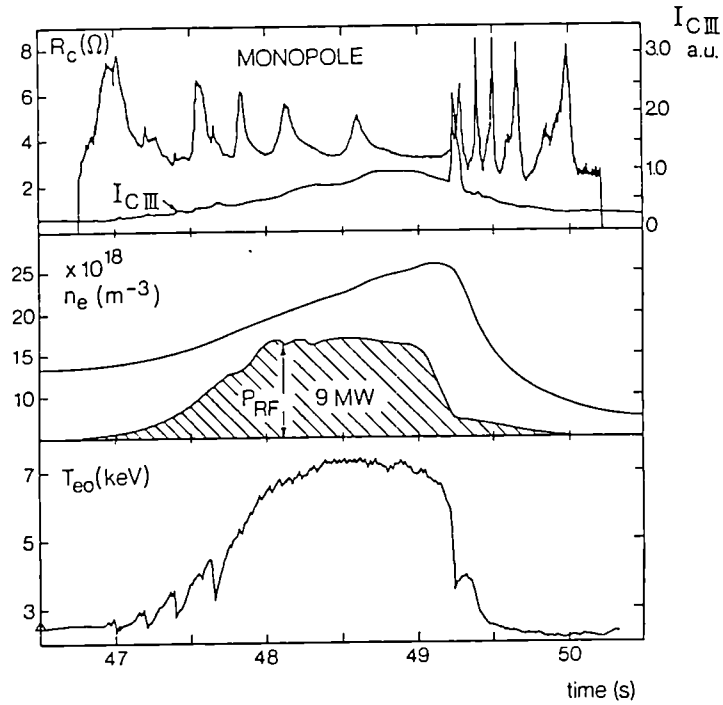

Fig. 1. Time evolution of the antenna loading resistance, intensity of CIII line radiation, volume average electron density and central electron temperature. Radial eigenmodes modify R_c but have no effect on T_{eo} and on the impurity radiation from the edge.

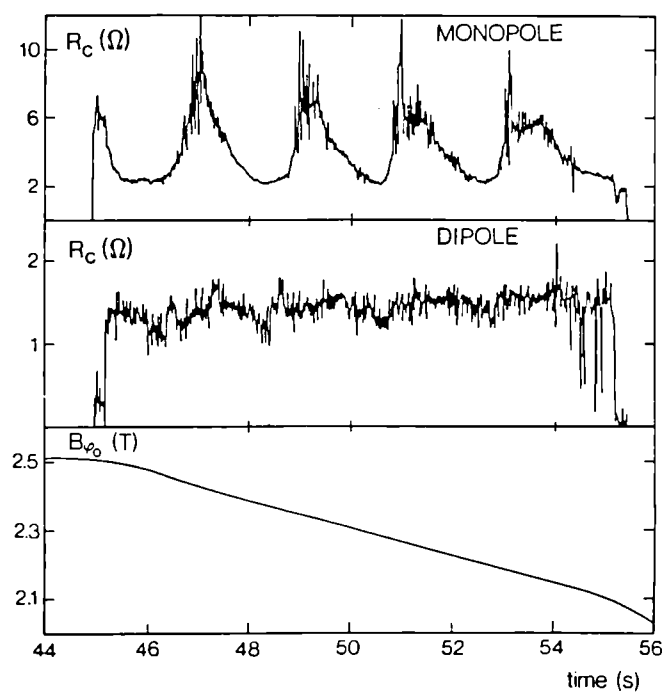

Fig. 2. Loading resistance with monopole and dipole phasing. Eigenmodes appear only for monopole phasing and are identified by their spacing during a toroidal field scan.

(iii) Heating pellet fuelled discharges with particular emphasis on a plasma target exhibiting a peaked density profile.

A very limited amount of time was devoted to coupling ICRH power into single null X point plasmas. The result was disappointing as no H-mode could be generated or sustained. Thereafter, the X point programme concentrated on using neutral beam injection.

This paper is organised as follows:

The first part describes briefly the ICRH system. The consequences of its unusual features are discussed, eg monopole versus dipole and the effect of the screen angle.

The power deposition profile and the energy stored in fast particles are discussed in a second part using power modulation during monster sawteeth to investigate the power balance with increased accuracy.

The third part examines the results of high fusion yield experiments and attempts to extrapolate the results to the most promising scenario which involves fundamental cyclotron acceleration of a large minority of deuterons in a tritium plasma.

The global performance in limiter plasmas is the subject of the next 2 parts. The emphasis is placed on the best operating regimes characterised by on axis ICRF heating producing long sawteeth and a large component of the fast ions. The recent improvement of central confinement obtained with combined operation of Pellets and ICRF are also presented.

The last part summarises the results and mentions the area of future development.

SPECIAL FEATURES

Homodyne Drive and Eigenmodes, Monopole versus Dipole, Screen Angle

The JET ICRF system has been described previously (Kaye, 1987; Wade, 1985) and it is summarised by the following table:

TABLE 1 JET ICRH System

Power	- 8 units of 3 MW (20 s) with 16 power tetrodes.
Frequency	- 23 to 57 MHz in 8 preset frequency bands.
Antennas	- 8 units, each with 2 inputs with either in phase drive (monopole) or out of phase drive (dipole). - water cooling of the screen (nickel). - screen angle: 15°. - location on the low field side between 2 belt limiters (carbon tiles).

Each unit can be driven either independently (heterodyne drive) or by a common oscillator (homodyne drive). The experiments analysed in this paper have all been obtained in the latter mode of operation which avoids problems of cross-talk and beat oscillations between adjacent frequencies. Homodyne drive imposes a phase relationship in the antenna array. All power units are driven at present with an identical input phase. However, the phase of the output of the amplifier units is not monitored. The phase control system, to be installed after June 1988, will allow to launch a partially travelling wave (directivity 20 to 25 %).

$k_{\|}$ Spectrum and Eigenmodes

The new antennae are equipped with central conductors having a wider toroidal extent (40 cm instead of 32 cm). This increased width and the precise phasing of the current flowing in the 4 conductors separated by a larger gap (20 instead of 10 cm) give a $k_{\|}$ spectrum far more accurately defined than in all previous ICRF experiments. In monopole operation, the spectrum at the antenna is centred on $k_{\|}$ 0 with a half width of $\pm$ 4.5 m^{-1}; in dipole operation the peak of the spectrum is at $k_{\|}$ - [illegible] m^{-1} and the half width is $\pm$ 3.5 m^{-1}.

With such a narrow spectrum, the coupling resistance ($R_c = 2\ Z_o^2\ P/U_A^2$; Z_o characteristic impedance of the antenna, P net coupled power, U_A peak voltage of the antenna) exhibits a periodic resonance structure when either the toroidal field or the plasma density is scanned (Figs. 1 and 2). The resonance structure is more pronounced in monopole operation and when the plasma is cold. A detailed analysis (Stix, 1975) has identified the structure to be radial eigenmodes of waves reflecting back and forth between the low field side cut-off located close to the outside wall and the ion-ion hybrid cut-off normally placed close to the magnetic axis. Calculations (Colestock, 1988) taking into account the damping of the fast magnetosonic wave due to both mode conversion and direct cyclotron and electron absorption are in close agreement with the observed resonance structure.

It is important to note that these eigenmodes have no influence on the heating efficiency (Fig. 2) or on the impurity release. However they pose a technical challenge for the antenna matching system. The JET matching feedback loop based on the impedance transformation at the end of a long transmission line, produced by a small frequency change (~ 50 KHz), has been effective in following these large coupling changes.

Dipole versus Monopole

Operation with the dipole phasing when compared to the monopole phasing is characterised by the following aspects:

(a) The coupling resistance is lower (Fig. 2) and decreases faster with plasma-antenna distance.

(b) The radiated power and the nickel contamination is lower.

(c) The power threshold for the monster sawtooth is higher.

Point (b) is particularly relevant to the experiments with powers exceeding 15 MW as the amount of nickel released from the antenna screen may cause disruptions. In hydrogen minority heating, the nickel concentration is approximately of factor 2 lower in dipole operation. In helium 3 minority schemes, the reduction is more pronounced and a decrease by a factor of 4 has been observed.

Since the calculated damping per pass is larger in dipole phasing and with H minority heating one is tempted to suggest that edge absorption enhanced by multiple reflections is responsible for the impurity release. This explanation is contradicted, however, by the observation that we have not found any correlation of the nickel and carbon release with the eigenmode structure which is a direct measure of multiple reflections. The experiments with reverse toroidal field (see below) suggest instead that direct slow wave coupling by the antenna is responsible for the edge effects induced by ICRF.

Screen Angle

The screen elements of the antenna screens are inclined by an angle of 15° with respect to the horizontal plane. The elements are designed to be aligned with the Tokamak magnetic field in full bore 5 MA discharges. This design was chosen to optimise coupling to the fast magnetosonic wave and to minimise the excitation of slow waves which require a finite value of $E_\parallel$, the wave electric field parallel to the static magnetic field.

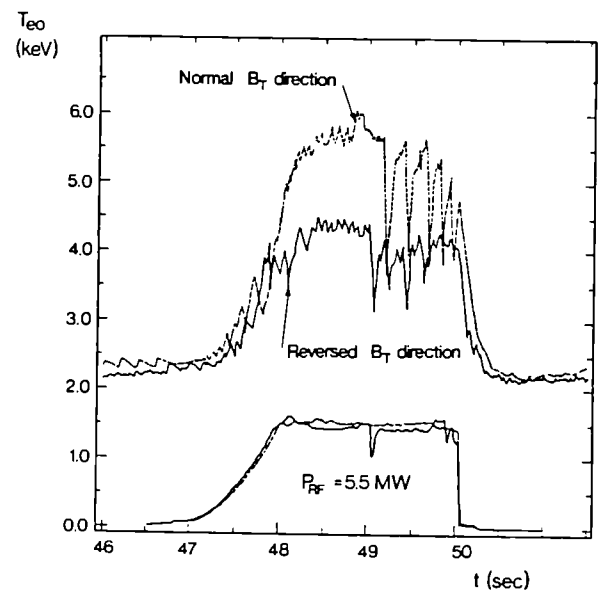

Fig. 3. Evolution of the central electron temperature T_{eo} for 2 values of the angle Θ_A between the screen bars and the local magnetic field: Θ_A = 5° for the "normal" case and 20° for the "reverse" case.

A series of experiments (Bures, 1988) have been performed with 2 MA discharges (H minority, 2.1 T) differing only by the direction of the static toroidal magnetic field. With the "normal" direction, the angle between the field and the elements was 5°, with the reverse direction, the angle became 25°. The overall heating characteristics are far better in the "normal" case. In particular:

(a) The heating efficiency (ΔT_e, ΔW) is 30 % higher. Figure 3 illustrates the difference in evolution of T_{eo}. Both discharges switch to a monster sawtooth, but the duration is longer with the normal field direction.

(b) The release of nickel, carbon, oxygen during the heating is about a factor of 3 (Ni) and 2 for (C and O) lower in the normal case. The total radiated power is 40 % of the input power in the reverse case compared to 30 % in the normal configuration.

(c) R_c is lower in the reverse field case (typically 4.5 ohms in the "normal", 3 ohms in the reverse case). The eigenmode structure is less apparent in the reverse case.

(d) The perturbation of the scrape off layer is lower in the normal case (less flattening of the density and temperature profile).

These results suggest that an ICRF antenna can couple a considerable amount of slow wave if the screen elements have an angle with the static magnetic field. This slow wave does not contribute to bulk heating and may generate impurity release by edge interaction. It is likely that, even in the normal case, a significant amount of slow wave power is being coupled and is responsible for some deleterious edge effects. This intepretation is also compatible with the insensitivity of impurity release by the eigenmodes of the fast wave.

DEPOSITION PROFILE, ENERGY STORED IN THE FAST MINORITY IONS

In some conditions, called "Monster Sawteeth" the plasma is very quiescent during a period of up to 3 s. Modulation of the ICRF power during this period gives accurate insight in the energy balance and in the power deposition profile (Tibone, 1988). So far, results have only been obtained in the He^3 and H minority case with monopole phasing.

The response to this modulation of the diamagnetic loop (W_{dia}) and MHD signals (W_{MHD}) shows that about 75 ± 10 % of the input power appears in the total stored energy (presumably the rest is deposited in outer layers and is not measured due to finite time response of the diagnostics). The same measurements used to derive the quantity $4(W_{dia} - W_{MHD})/3$ show that most of the RF power (up to 70 %) first appears in the form of plasma energy with strong perpendicular anisotropic tail which subsequently relaxes on the electrons.

Direct electron heating is apparent in the He^3 minority case with an instantaneous response of local ECE measurements at the onset of each step of the square wave modulation. Direct electron heating amounts to about 5 to 10 % in the H minority case and 10 to 30 % in He^3 minority heating case.

The power deposition profile appears highly localised in the vicinity of the minority cyclotron resonance as already mentioned in a previous paper (Jacquinot, 1987). It is well described by a gaussian profile with a 20 cm e-folding length in agreement with full wave or ray-tracing calculations (Tibone, 1988).

In the quasi-stationary state, the plasma contains a significant amount of energy stored in fast ions (W_f). Figure 4 compares $W_{f\ exp}$ to a calculated

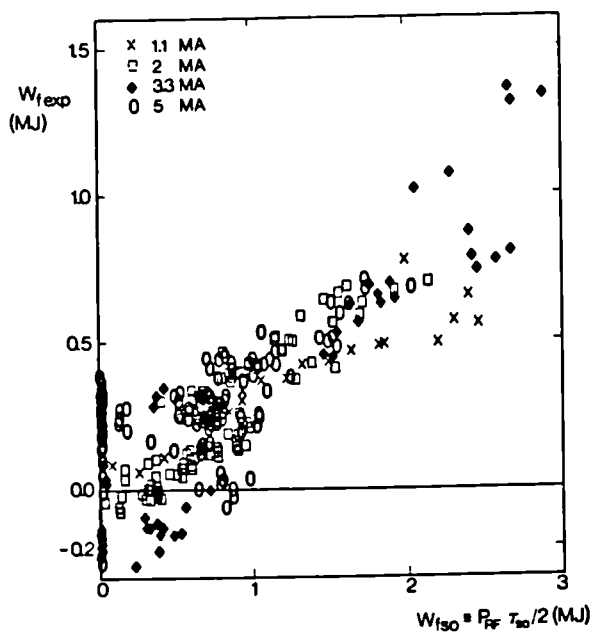

Fig. 4. Energy stored in fast particles (fundamental resonance of minority species) versus $P_{RF}\ \tau_{So}/2$ where τ_{So} is the classical Spitzer slowing down time calculated for the parameters of the plasma centre.

value W_{fso} based on Stix's quasi linear treatment (Stix, 1975) of an energetic minority tail. $W_{f\ exp}$ is deduced from the difference between the diamagnetic energy and a thermal kinetic energy (volume integration of $n_eT_e + n_iT_i$). The offset in Fig. 4 is due to systematic errors. W_{fso} is equal to:

$$W_{fso} = P_{RF} < \tau_{so} > /2$$

where P_{RF} is the coupled power and $< \tau_{so} >$ is the classical Spitzer slowing down time by electron drag using the central value of n_e and T_e (from the ECE system). A good agreement is found between the scaling of the 2 quantities. The calculated value is a factor 2 too high. The difference results from the use in the calculation of central values of n_e and T_e. A full calculation (Eriksson, 1988) including profiles effects is in close agreement with the observation.

W_f amounts typically to 15 % of the stored energy in usual belt limiter discharges. It can reach 30 % (about 2 MJ) for the lowest density plasmas using a double null X point configuration. The entire data base for W_f scales, as expected, with $T_e^{3/2}/n_e$ suggesting that the fast particles have a classical slowing down time.

(He^3)-D AND (D)-T HIGH FUSION YIELD SCENARIOS

The fundamental cyclotron acceleration of He^3 minority ions gives the opportunity to study experimentally non thermal high fusion yield schemes and to simulate (D)T scenarios where deuterium would replace helium 3. The basic reactions are:

$$D + He^3 \rightarrow H(14.7\ MeV) + He^4(3.6\ MeV)$$
$$D + He^3 \rightarrow L_i^5 + \gamma(16.6\ MeV)$$

The second reaction occurs with a much smaller probability via the same resonance; it was used as a diagnostic (measurement of the 16 Mev γ production (Sadler, 1988)) to monitor the fusion yield.

Figure 5 summarises the experimental results (Cottrell, 1988). With 11.5 MW of ICRF in 3 MA plasmas, about 60 kW of fusion power has been generated in charged particles corresponding to

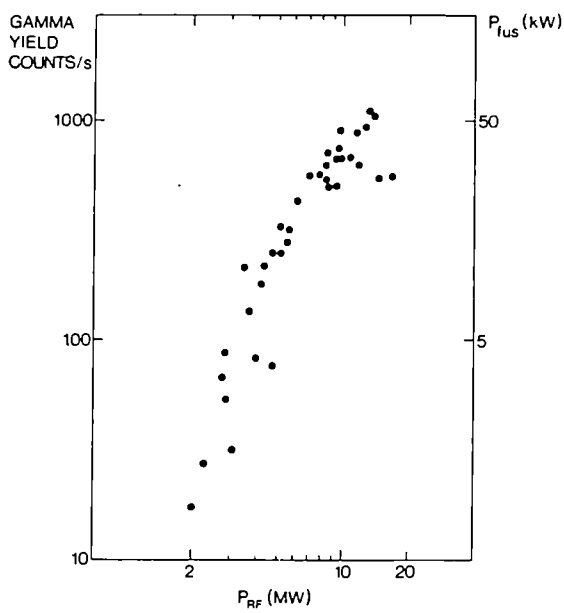

Fig. 5. Fusion power from D-He^3 reactions versus coupled RF power. He^3 minority heating in a deuterium plasma.

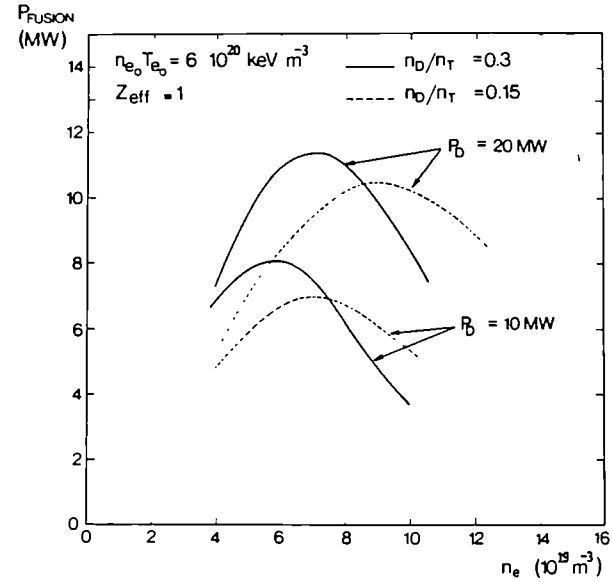

Fig. 6. Calculated fusion power for D minority heating in a tritium plasma. The calculation takes into account the profiles of the power deposition and of the plasma parameters. P_D is the RF power coupled to deuterons (~ 85 % of the coupled RF power).

an effective Q ~ 0.5 % and a fusion reaction rate of 2 x 10^{16} s^{-1}. This value is by a factor 3 less than the calculated optimum which is reached when the energy of the minority corresponds to the maximum of the fusion cross section. The measured fusion yield agrees well with simulations based on Fokker-Plank calculations and measured plasma parameters (Eriksson, 1988).

Carrying over these encouraging results to a (D)-T plasma requires a number of adjustments:

(a) The minority concentration n_D/n_T should be increased to about 30 % and the electron density should be raised to about 6 10^{19} m^{-3}. Both measures avoid that the energy of the minority exceeds the optimum of the fusion D-T cross section.

(b) The parameters quoted in (a) necessitates using a dipole phasing ($k_\parallel \approx 7\ m^{-1}$) in order to prevent mode conversion at the D-T hybrid resonance resulting in direct electron damping. TTMP and electron Landau interactions with the fast magnetosonic wave is estimated to damp ~ 15 % of the coupled wave power into electrons if $T_{eo} \approx 10$ keV.

(c) The damping per pass is expected to be large (90 % per pass). Interaction with the second harmonic resonance of tritium on the extreme low field side is prevented by locating the resonance either on axis or slightly shifted to the low field side.

Figure 6 gives the enhancement of fusion reactivity expected from the deuterium tail as a function of P_d, the RF power coupled to the deuterons. This calculation is a Fokker Planck treatment taking into account (Eriksson, 1988) the profiles of the power deposition and of the plasma parameters. The product $n_{eo}\ T_{eo}$ has been fixed to 6 10^{20} (m^{-3} keV), a value achieved with 10 MW of ICRF being the only additional heating source. $Q \geq 0.5$ can be achieved if Z_{eff} can be maintained close to unity. A self consistent set of parameters necessary to achieve Q = 1 is given in Table 2.

TABLE 2 Conditions for Q = 1 required in a (D)T Plasma with ICRH alone

Power to D tail	$\geq$ 20 MW
n_{eo}	$\approx$ 7 10^{19} m^{-3}
n_D/n_T	$\approx$ 0.2
τ_E	$\geq$ 0.6 s
Z_{eff}	$\leq$ 2

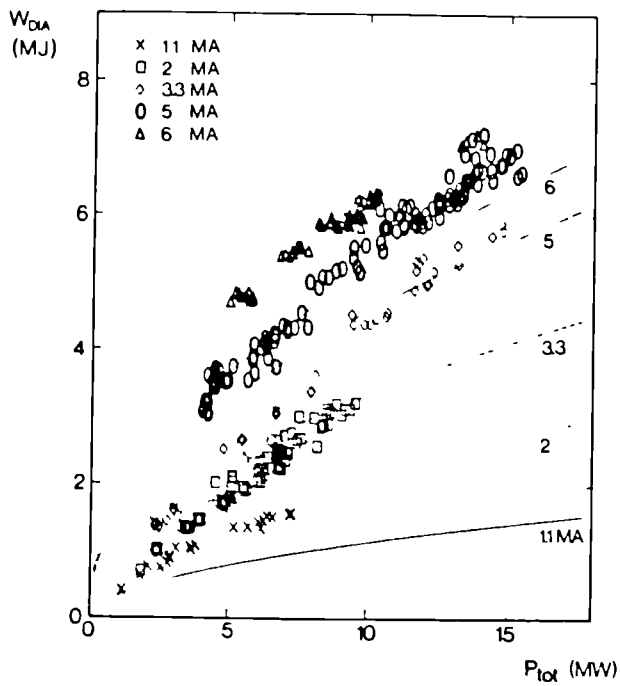

Fig. 7a. Stored energy (diamagnetic measurements) versus input power for H minority heating and comparison to the Goldston scaling.

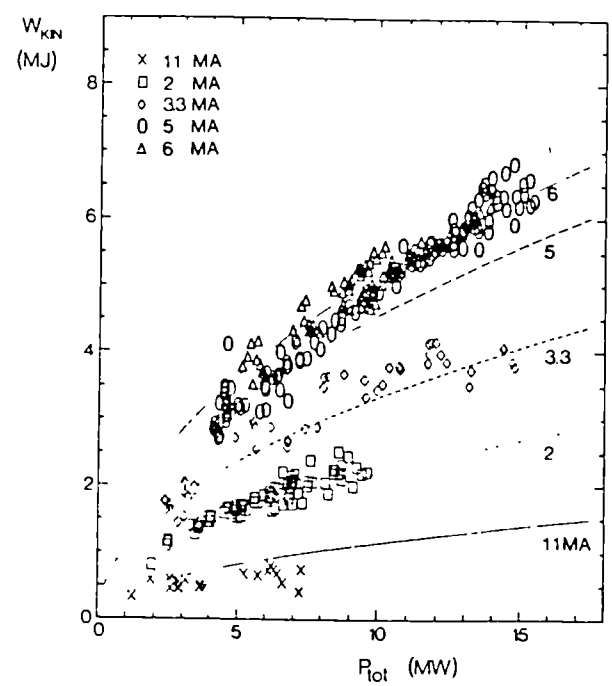

Fig. 7b. Kinetic stored energy (volume integration of $n_eT_e + n_iT_i$) for the same data set as Fig. 7a.

LIMITER PLASMAS, GLOBAL CONFINEMENT AND I_p SCALING

A new result obtained by ICRF heating of limiter plasmas is the attainment of regimes in which the total stored energy can be up to a factor 1.5 greater than predicted by the Goldston L mode scaling (Goldston, 1984) (Fig. 7a).

Contrary to the H-mode, there is little improvement in the kinetic energy content (Fig. 7b) and most of the improvement comes from the storage of fast particles and from the development of a stable peaked temperature profile. Table 3 summarises the conditions for obtaining this regime. The narrow power deposition of ICRF and its stabilising effect on the sawteeth play a major role.

TABLE 3 Conditions for Improved Stored Energy in Limiter Plasmas

Peaked deposition profile:	on axis ICRF heating (all minority scenarios)
Long sawteeth	: $\tau_{ST} \geq \tau_E$, ie monsters
Moderate densities	: $n_e \leq 4\ 10^{19}$ cm^{-3}; large W_f, ie $W_f/W \geq 0.15$
I_p/B_ϕ	: $\approx$ 1 MA/T, eg $q_{cyl} = 3.3$

In the best conditions, the incremental confinement time, τ_{inc}, reaches 340 ms in 3.3 MA, 2.8 T plasmas (Fig. 7c). τ_{inc} first increases with I_p, reaching an optimum (Bhatnagar, 1988) for I/B $\approx$ 1 MA/T then decreases to $\approx$ 220 ms in 6 MA plasmas. This behaviour is correlated with the period of the sawteeth which also reaches a maximum ("monster" of up to 3 s) when I/B ~ 1 MA/T.

At low or medium I_p values, no difference in stored energy is found between the 4 ICRF scenarios (H, He^3, monopole, dipole). At 5 MA with He^3 minority heating, large fishbone-like activities develop early in the sawtooth period and prevent the rise of T_e. Then τ_{inc} is

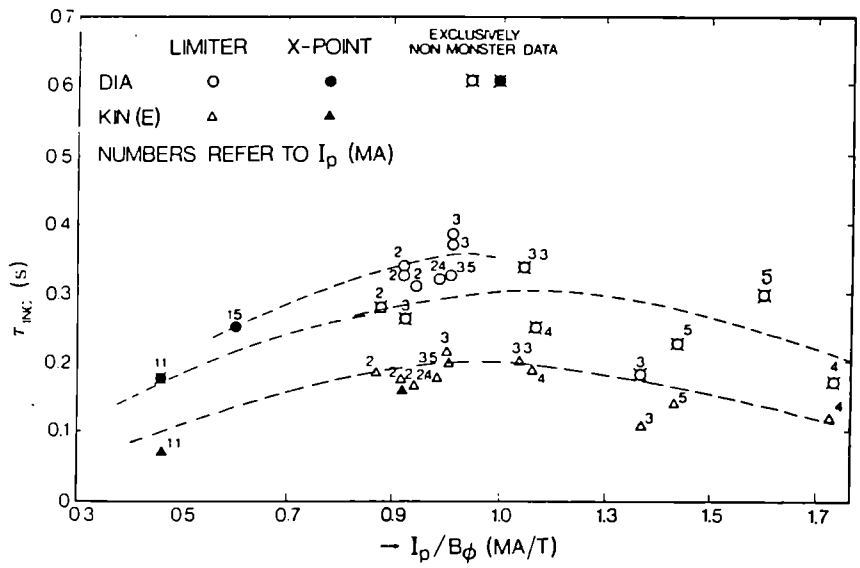

Fig. 7c. Incremental confinement time of the stored energy (diamagnetic; DIA) and the electron thermal energy content (KIN(E)) versus I_p/B_ϕ

only 250 ms in this regime. It is not clear why this phenomenon does not appear in the H minority case in 5 MA plasmas. In this case τ_{inc} is improved (300 ms) and 7 MJ has been obtained with a total input power of 15 MW.

In the series of experiments of Fig. 7a, the total radiated power was about 40 % of the input power. Since the radiated power is peaked at the plasma edge, it plays no role in the energy balance in the plasma core. Z_{eff} was about 2 in high current discharges and $\geq$ 3 below 3 MA.

The central electron and ion temperatures are presented in Figs. 8 and 9. Whilst T_{eo} follow a linear scaling with $P_{tot}/\langle n_e \rangle$, the ion temperature tends to saturate showing that the hydrogen minority becomes decoupled from the plasma ions at high power density. Higher ion temperatures (up to 8 keV) have been obtained either with He^3 minority heating (Start, 1988) at high He^3 concentration (11 %) and using dipole phasing or during the heating of a peaked

density profile produced by pellets in 3 MA plasmas. In the latter case, T_{eo} (ECE) = 11 keV, T_{io} = 7.8 keV, with P_{RF} = 7.4 MW. The $n_{io}\tau_E T_{io}$ values obtained with ICRF in limiter plasmas are summarised in Fig. 10.

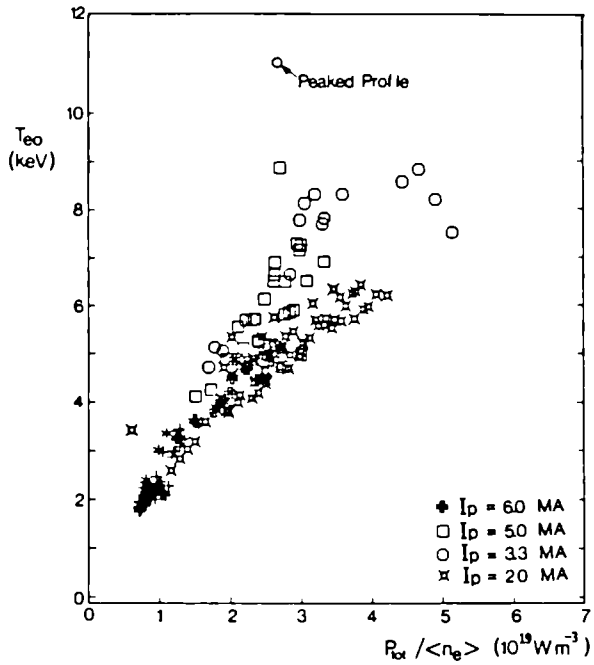

Fig. 8. Central electron temperature versus $P_{tot}/< n_e >$. The case denominated "peaked profile" was created by pellet injection.

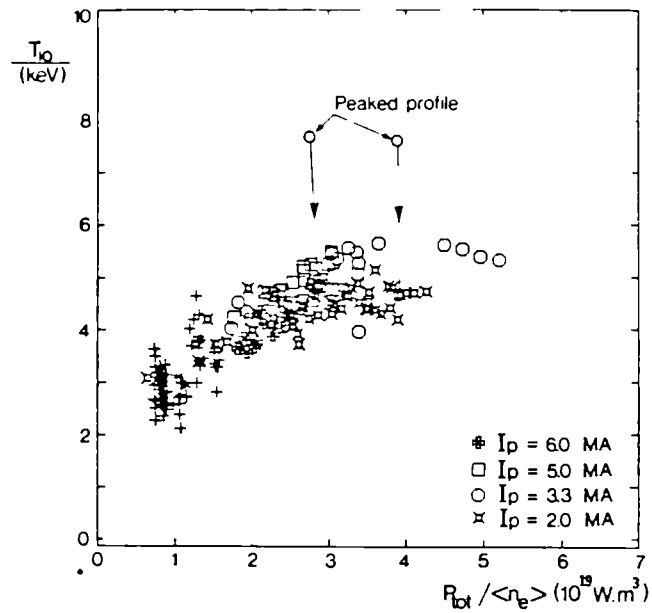

Fig. 9. Central ion temperature versus $P_{tot}/< n_e >$. T_{io} is deduced from Doppler broadening of a Ni line.

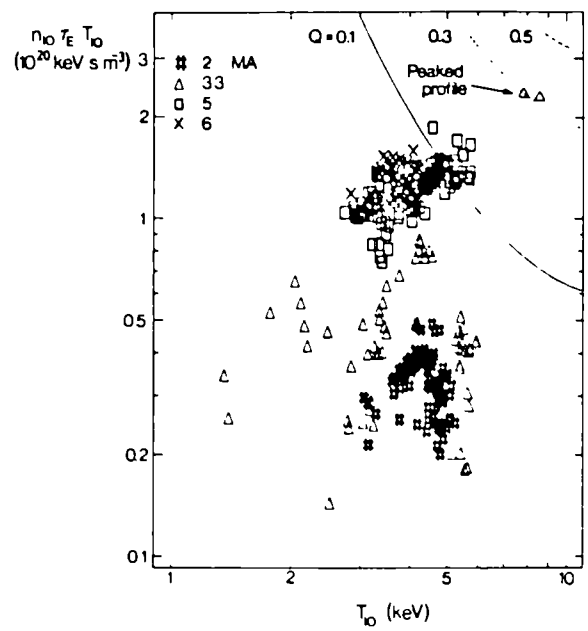

Fig. 10. Fusion parameter, $n_{io}\tau_E T_{io}$ versus the central ion temperature T_{io}.

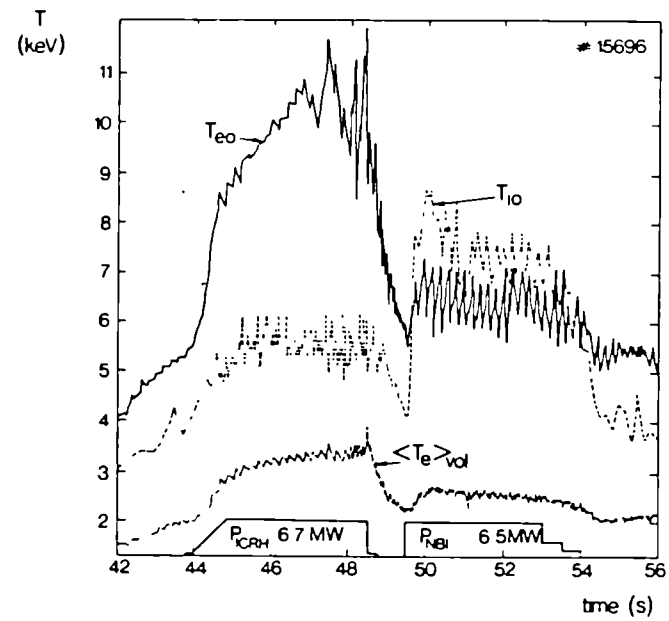

Fig. 11. Evolution of the central electron and ion temperature for ICRH or NBI during the same discharge (3 MA, 3.1 T, H minority in a helium plasma).

It is instructive to compare ICRF to neutral beam (NBI) heating in the same pulse with the same power in the conditions corresponding to the improved L mode scaling (3 MA, 3.15 T, H minority, dipole).

The behaviour of the ion and electron temperature is remarkably different (Fig. 11). With NBI, one always obtains $T_i > T_e$ while ICRF always yields $T_e > T_i$. Figure 12 shows that the radiated power with ICRF is generally larger than with NBI despite a somewhat lower density (- 10 %) in the ICRF case. However the stored energy is significantly higher with ICRF probably as a result of a more peaked deposition profile and longer sawtooth periods.

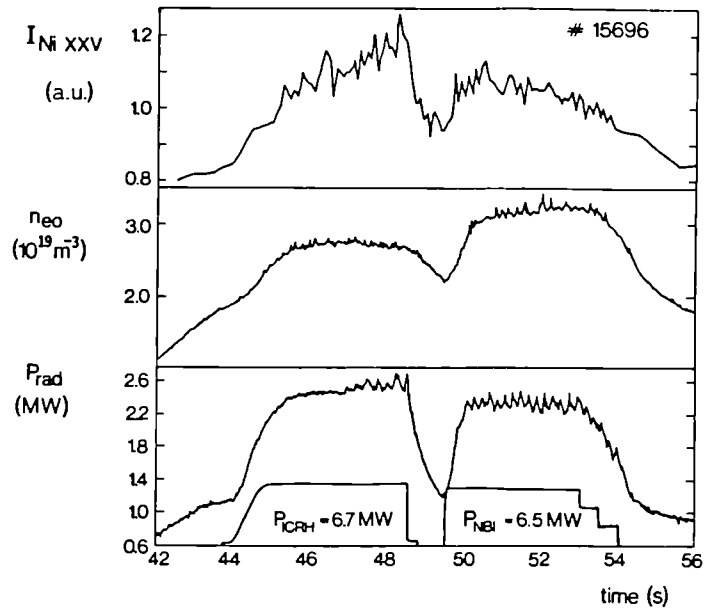

Fig. 12. Evolution of nickel contamination, central density and total radiated power for ICRH and NBI during the same discharge (same case as Fig. 11).

HEATING PEAKED DENSITY PROFILES

It has been suggested (Furth, 1986; Schmidt, 1987) that central heating of a peaked density profile generated by pellet injection (Kupschus, 1988) could lead to improved energy confinement as observed in TFTR supershots.

Recent experiments have demonstrated that this improvement indeed occurs. Figures 13a and 13b show that:

(a) A reheated peaked profile can be sustained for about 1.2 s in a 3 MA discharge with pellet injection at the end of the current rise. However, the peaked profile is subject to a sudden instability (cf Fig. 13a at 44.4 s) which relaxes the profile to the usual shape (a monser sawtooth Te profile).

(b) The central energy confinement in the peaked region is improved. For 8 MW of ICRF, T_{eo} rose to 11 keV (Fig. 13b) and T_{io} to 8 keV. The T_e profile steepens showing a decrease of the electron energy transport coefficient in the centre by a factor 2 to 3 compared to the relaxed state. The fusion product $n_{io}\tau_E T_{io}$ reaches 2.2 10^{20} m^{-3} s^{-1} keV, a value 2.3 times greater than in the normal limiter discharges.

CONCLUSIONS

High power ICRF heating with up to 17 MW has been particularly successful in heating plasmas resting on toroidal belt limiters. With RF heating alone central temperatures of T_e = 11 keV and T_i = 8 keV have been reached. H minority heating and moderate plasma current give the highest incremental confinement time (τ_{inc} = 340 ms). In these discharges monster sawteeth of up to 3 s have been obtained.

Peaked profiles created by pellet injection have been reheated by ICRF. In most cases the peaked profile disappeared in 0.5 s. During the peaked density phase, the energy confinement

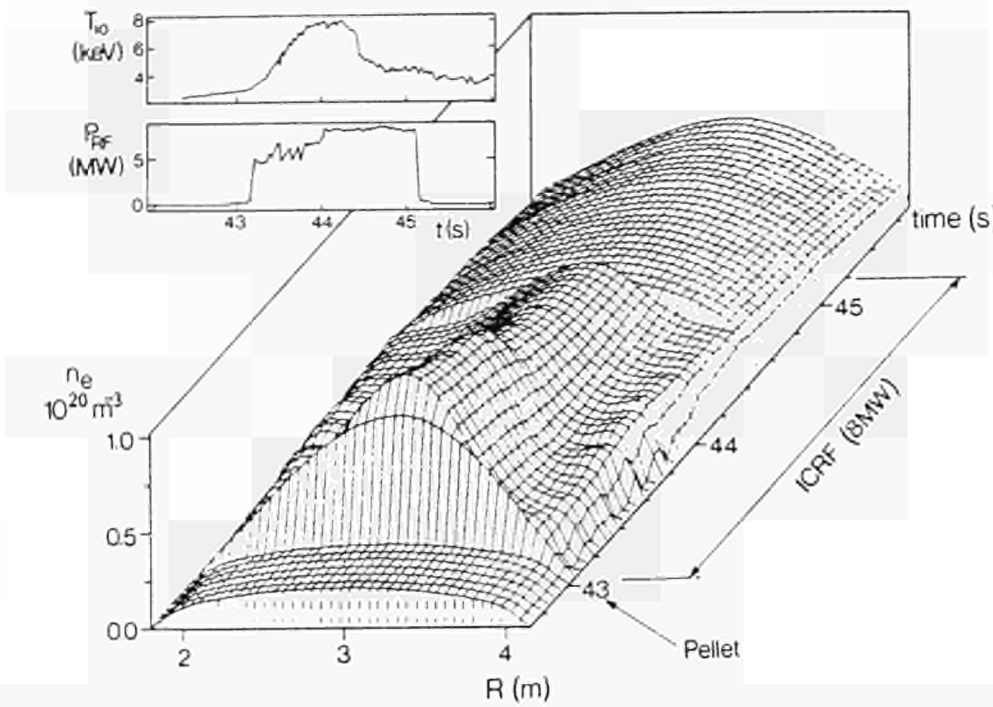

Fig. 13a. Evolution of the density profile. A peaked profile is created by a 4 mm pellet at 43 s. ICRF power is ramped up from 43.2 to 44 s and maintained constant at 8 MW until 45.2 s. Note the sudden relaxation of the profile at 44.5 s.

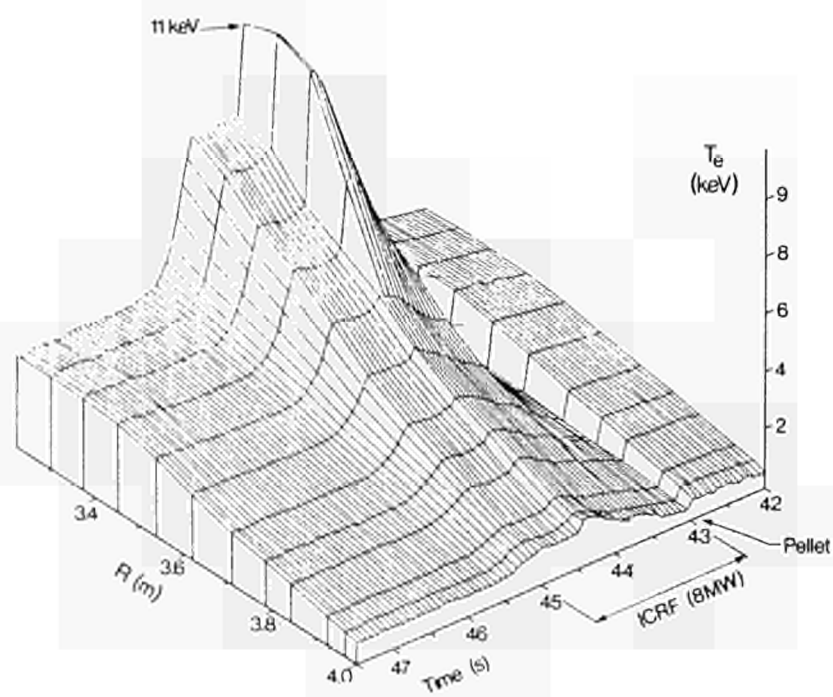

Fig. 13b. Evolution of the electron temperature profile. Note that the peaked T_e profile relaxes also at 44.5 s. The time axis has been reversed in order to show the shape of the T_e profile more clearly.

in the plasma centre ($r/a \leq 0.4$) is improved and a fusion product of $n_{io}\tau_E T_{io} = 2.2\ 10^{20}\ m^{-3}$ s keV, the highest value in JET limiter discharges is obtained.

Impurities are reduced when the elements of the antenna screen are parallel to the magnetic field and when the dipole configuration is used. High power ICRF heating have been performed in 5 MA plasmas with $Z_{eff} \sim 2$.

The heating and impurity release is unaffected by the eigenmodes of the fast waves. These observations suggest that, despite the filtering effect of the screen the antenna launches some slow wave component responsible for the impurity production.

RF driven high fusion yield scenarios have been tested using the fundamental cyclotron absorption of He^3 minority ions. A maximum yield of 60 kW has been obtained in the form of charged particles. The same discharge transposed to (D)T with D minority heating would give $Q = 0.2$. Transposition of the best peaked profile heating achieved today would give $Q = 0.8$ assuming $Z_{eff} = 1$.

The JET ICRF system will be modified to allow for phasing the 8 antennae. A travelling wave with an expected maximum directivity of 20 - 25 % is expected to modify significantly the gradient of the safety factor in the central region. Screens with bars made of Beryllium will replace the present Nickel in an attempt to remove the radiation problem in the H-mode plasmas and to improve the density control by avoiding carbonised structures.

ACKNOWLEDGEMENT

Pellet injection results were obtained under a collaboration agreement between the JET Joint Undertaking and the US Department of Energy.

REFERENCES

Bhatnagar, V. P. and others (1988). This conference.
Bures, M. and others(1988). This conference.
Colestock, P. (1988). Private communication.
Cottrell, G. A. and others. This conference.
Eriksson, L. G. and T. Hellsten (1988). Private communication.
Furth, H. P. (1986). Plasma Phys. Control Fusion 28, 1305.
Goldston, R. J. (1984). Plasma Phys. Control Fusion 26, 87.
Jacquinot, J. and JET Team (1987). Proc. 11th Int. Conf., Kyoto (1986), Vol. 1, IAEA, Vienna, 449.
Jacquinot, J. and others (1987). Proc. 7th Top. Conf. on Applications of Radio Frequency Power to Plasmas, Kissimee. AIP Conf. Proc. 159, 220.
Kaye, A. S., J. Jacquinot, P. Lallia and T. Wade (1987). Fusion Technology, Vol. 2, 203.
Kupschus, P. and others (1988). This conference.
McCarthy, A. L. and others (1988). This conference.
Sadler, G. and others (1988). This conference.
Schmidt, G. and others (1987). Proc. 11th Int. Conf., Kyoto 1986, Vol. 1, IAEA, Vienna 171.
Start, D. and others (1988). This conference.
Stix, T. H. (1975). Nuclear Fusion, 15, 737.
Tibone, F., M. P. Evrard and others (1988). This conference.
Wade, T. (1985). Proc. 11th Symp. Fusion Engineering, Austin, Texas.

The JET Plasma Boundary with Limiter and X-point Discharges

The JET Team
(presented by Dr P E Stott)

Abstract

The JET tokamak has been operated in various limiter and magnetic separatrix configurations with ohmic, neutral beam and ion cyclotron heating. Radial profiles of plasma density, temperature and particle flux in the scrape-off layer have been measured and scalings with core plasma parameters have been established for the limiter discharges. In the magnetic separatrix configuration, H modes with energy confinement times up to 1s have been obtained with neutral beam heating. There are large, localised fluctuations in the edge parameters which appear to be well correlated with the periodic global particle losses. The main impurities are oxygen and carbon. The only significant metallic impurity is nickel which originates from the ion cyclotron heating antennas.

1. Introduction

JET is a large tokamak [1] which can be operated with the plasma boundary defined by either material limiters or a magnetic separatrix. Several different limiter configurations have been tested. Until the end of 1985, JET had 4 discrete carbon limiters and 2 ion cyclotron antennas located in the mid plane on the outboard side of the discharge. In 1986 these were increased to 8 limiters and 3 antennas. The discrete limiters were replaced in mid 1987 by two continuous carbon belt limiters, (figure 1) also on the outboard side but 1 m above and below the midplane. Between the belt limiters there are now 8 ion cyclotron heating antennas with nickel surfaces facing the plasma and protected on either side by carbon tiles (figure 2). Since 1983 the inconel wall of the vacuum vessel has been progressively covered by protective carbon tiles so that now some 55% of the surfaces facing the discharge are carbon and in particular all of the prominent surfaces are protected. The carbon tiles protecting the inner wall of the vacuum vessel have also been used as an inboard limiter. The torus now contains approximately 6 tonnes of fine grain, high purity carbon [2].

In the discharges bounded by a magnetic separatrix, the main emphasis has been on the single null configuration with the X point at the top of the vacuum vessel (figure 3), but there have been some experiments also with double nulls [2,3]. Several different arrangements of carbon tiles protecting the vessel in the vicinity of the X points have been tested and the present set consists of 32 poloidal bands of carbon[4]. The JET vacuum vessel is constructed of inconel and is normally operated at temperatures in the range 300 - 350°C. The discrete limiters, the X point tiles and the protective tiles are all at or above the wall temperature, but the belt limiters and the ion cyclotron antennas (since 1987) are water cooled and thus may be at a lower temperature.

The plasma boundary is studied by an extensive range of diagnostics. Radial profiles of electron temperature, density and parallel particle fluxes are measured with Langmuir probes. An array of 6 probes (3 facing in the electron drift direction and 3 in the ion drift direction) can be inserted into the boundary layer using a probe drive system located at the top of the torus [5]. The probes are located at different radii and by moving the array between discharges a complete profile can be measured. Recently a reciprocating drive mechanism has been added allowing the probes to be inserted deeper into the plasma without overheating and providing a radial profile over 100 mm in ~ 400 ms. Moveable Langmuir probes can also be introduced close to the mid plane between the belt limiters. These moveable probes are supplemented by fixed probes in the belt limiters, antenna shields and X point protection tiles. For comparison between data measured with probes at different poloidal locations, corrections are applied for the volume between magnetic flux surfaces (usually referred to as flux surface compression). With these corrections the data are generally in good agreement.

Information on impurity erosion and deposition at the limiter and wall surfaces is obtained from long term samples which are removed when the vacuum vessel is opened and from surface collector probes which can be inserted into the boundary layer at two positions and exposed to

selected discharges. The probes provide spatial resolution and can be rotated behind collimating slits to provide time resolution[6]. This paper provides an overview of JET results. More detailed results will be found elsewhere in these proceedings.

2. Plasma Parameters in the Boundary Layer

a) Resumé of results with the discrete limiter configuration

Extensive measurements of the parallel ion flux $\Gamma_i(r)$ and electron temperature $T_e(r)$ in the boundary layer have been reported previously for the discrete limiter configuration using the moveable probes on the vertical drive system and the fixed antenna probes. These results will be briefly summarised here. Both $T_e(r)$ and $\Gamma_i(r)$ are well fitted by exponentials. The plasma electron density $n_e(r)$ can be deduced if it is assumed that $T_e = T_i$.

i) Ohmic discharges

The scaling of the edge parameters with the core plasma parameters has been studied extensively and reported previously [7]. As an example the dependence of the ion flux, electron temperature and density on the mean plasma density is plotted in Figure 4. The ion flux is seen to be relatively independent of the mean density but the edge electron temperature falls and the edge density rises as a function of the mean density. These data were all taken during a single discharge in which the mean density was steadily increasing with time during the current plateau, and thus the plasma may not have been in perfect equilibrium. However similar behaviour is seen also in steady state conditions when discharges at different densities are compared. Although the particle flux is independent of the mean density there is a strong dependence on the discharge current.

Detailed scalings of the scrape-off layer width (i.e. the e-folding lengths of the density, temperature etc) as a function of the global plasma parameters such as discharge current and mean density have been reported previously [7]. For example the density scale length gets shorter whilst the temperature scale length gets longer as the mean density is increased.

ii) Neutral Beam Heating

Measurements of the scrape-off layer parameters have been made with neutral beam heating at various discharge currents [8]. The mean density rises strongly throughout the injection period and so steady state conditions are not usually reached. The edge temperature, which before injection was falling due to the rising density in the ohmic plasma, rises immediately after injection, and then starts to fall again as the density rises due to beam fueling. The slow time scale (0.3 to 0.5s) of the change in the edge parameters when the beams are turned on indicates that the boundary layer is influenced by power and particles diffusing out from the central core rather than by direct deposition at the boundary.

(iii) Ion Cyclotron Heating

In contrast with neutral beam heating there are clear indications that ion cyclotron heating has a direct effect on the boundary [9,10]. The most serious effect is an influx of nickel from the antenna screens. The plasma edge density and temperature increase immediately when the ion cyclotron power is turned on (unlike neutral beam heating where there is a significant time delay) and the width of the scrape-off layer increases with power (whereas with beam heating the width is found to be independent of power). The edge parameters and nickel influx during ion cyclotron heating also depend on the phase of the antennas (i.e. dipole or monopole) and on the angle between the slots in the Faraday screens of the antennas and the tokamak magnetic field. This angle determines the efficiency of coupling between the antenna and the fast and slow magnetosonic waves. The results suggest that the coupling into the slow wave is responsible for the boundary effects observed with ion cyclotron heating [12].

Recent measurements have shown that there does not appear to be a localised increase in the H_α light at the antennas compared to other parts of the boundary.[13] Thus there may not be an increase in the local ionisation, despite the strong increase in the nickel influx from the antenna screens.

(iv) Combined Heating

As might be expected, the effect of combined heating is to superimpose the separate effects of the component heating methods. Thus the boundary parameters are changed by the NBI indirectly through the change in the core density and temperature whilst the boundary is modified directly by the localised ICRH effects. It is difficult to separate these effects in detailed studies, particularly since they depend on the ratio of ICRH to NBI power, and so the main emphasis has been to establish empirical scalings simply in terms of total power which can be used to extrapolate the boundary parameters up to the maximum heating powers planned for JET.

(b) The belt limiter configuration

Results with the new belt limiter configuration are qualitatively similar to those with the discrete limiters but there are some detailed differences. Langmuir probes have been installed in the limiter tiles at different toroidal locations and these confirm that the plasma-limiter interaction is toroidally symmetric to within a few mm [14]. Densities and temperatures in the boundary layer are lower with the belt limiter than for similar discharge conditions with the discrete limiters and this is qualitatively consistent with the larger area of the belt limiters. The boundary parameters scale with mean plasma density in a similar way to the scalings already reported for the discrete limiters. Thus the boundary temperature decreases and the boundary density increases as the mean density is increased. However, the boundary density for the belt limiters has a weaker dependence on the discharge current than was reported for the discrete limiter.

The belt limiters introduce a topological change in the scrape-off layer which is now divided into two poloidally separated regions as shown schematically in figure 5a; a region between the belts on the outboard (i.e. low toroidal field) side of the discharge which is characterised by relatively short connection lengths (typically $\sim$ 8 m) to the limiters, and a region on the inboard (i.e. high toroidal field) side which is characterised by long connection lengths (typically $\sim$ 60 m)[15]. The scrape off layer widths in these two regions are different. Examples of the edge density profiles are shown in figure 6. The scrape off layer is wider in the outboard region ($\lambda_n \sim$ 8.3mm) than in the inboard region ($\lambda_n \sim$ 6.1 mm). When the ratio of the connection lengths is taken into account, the effective diffusion coefficient in the outboard region is larger than in the inboard region.

Generally the broadening of the scrape-off layer during ICRH is less with the belt limiters than with the discrete limiters but this may be due to better conditioning. Typical changes are shown also in figure 6. The outboard scrape-off layer does not change significantly (the density e-folding length changes from 8.3mm to 9.1mm). However there is a substantial change in the inboard scrape-off layer (density e-folding length increases from 6.1mm to 9.8mm). This is surprising since the ICRH antennas are located in the outboard region, and is further evidence of the complexity of the interaction between the ICRH and the boundary plasma.

Continuous profiles in the boundary can be measured in a single discharge using the reciprocating drive, and it is possible to see finer structure in the profiles (figure 7). There is a clear indication of a change of slope in the density and temperature profiles and a maximum in the floating potential which is interpreted as indicating the position of the last closed flux surface. This is a few cms outside the position computed from magnetic measurements but the discrepancy is within the expected uncertainty of the magnetic measurements.

(c) X Point Configurations

H-modes lasting for $\sim$ 2s were first produced during 1986 in the single null X-point configuration with up to 10 MW NBI into 3 MA discharges [3]. During 1987-88 the pulse length of the NBI has been extended to 6s, and the discharge current increased to 4.5 MA. The global energy confinement time exceeds 1s but degrades with increasing neutral beam power.

Measurements of profiles in the scrape-off layer of X-point discharges have been difficult due to problems of positioning the probe correctly in these elongated discharges. Preliminary data show (figure 8) very steep gradients of density just inside the separatrix for the H mode, but the density in the scrape-off layer during the H mode is less than in Ohmic discharges. In contrast there is a much smaller change in the temperature which at the separatrix is possibly slightly lower in the H mode than in the ohmic phase.

The scrape-off layer intercepts the wall at the X-point on a set of special carbon tiles (figure 9). There are in fact two areas of intersection on each tile, corresponding to the direction in which the field lines are followed in the poloidal direction. (figure 10) The plasma parameters near to the X-point have been measured [16] using an array of probes mounted in the tile and by measurements of D_α radiation and bolometry. Typical data are shown in figure 11. The D_α intensity has been measured in two places (i) at the tile (with a CCD imaging camera) (ii) at a point mid-way between two tiles. The D_α signals and the ion flux to the tile all have the same general behaviour though there are some detailed differences. During the ohmic phase there are small inverse sawteeth, and there is a large increase in all the signals during the L mode when NBI is first applied. After the H mode is established there is a sharp reduction in the three signals. The ion flux parallel to the magnetic field is about 10 A cm^{-2} in ohmic discharges and increases by a factor $\gtrsim$ 2 in the L mode (the precise value depends on the neutral beam power), before decreasing again when the H mode is established. The corresponding values of electron temperature at the tile are $\sim$ 30 eV in the ohmic phase and 50 - 60 eV in the H mode. The profile of T_e across the tile is peaked slightly outside the separatrix and it is thought that this is due to the effects of local recycling. The density is larger and the temperature lower at the inner interaction region than in the outer region. For example in a 3MA, 2.1 T ohmic discharge, n_e and T_e are 9 x $10^{18} m^{-3}$ and 10eV at the inner region and 3 x $10^{18} m^{-3}$ and 30eV at the outer region. The different values of T_e at opposite ends of the same flux tube in the scrape-off layer leads to different sheath potentials and to a net flow of electric current. Currents in the expected direction from outer to inner regionor have been measured up to 10A cm^{-2} in the ohmic phase and up to 40A cm^{-2} during fluctuations associated with ELMs [20]. These high currents vary randomly from probe to probe in the target tile indicating that the boundary is turbulent during ELMs.

During the H mode there are large fluctuations (ELM's) in all the boundary parameters [17]. At $\sim$ 14 s there is an H $\rightarrow$ L transition followed by periodic changes between the two modes which persist until the end of the NBI. The power radiated from the X point region is not shown but varies in a similar way, increasing from $\sim$ 0.9 MW during the OH phase, to $\sim$ 1.2 MW in the L mode, decreasing to 0.8 MW at the onset of the H mode and then rising slowly to $\sim$ 1.2 MW with bursts up to 1.8 MW during the later L mode phases. The detailed analysis of poloidal profiles across the X point region has been discussed in more detail elsewhere [16,4].

Recent experimental data show that the fluctuations localised in the outer region of the discharge (r/a $\gtrsim$ 0.9) are important to the physics of the H mode. These strong edge fluctuations are characteristic of the low confinement (L mode) phase of X point discharges with NBI in contrast to the relatively quiescent, high confinement (H mode) phase. The fluctuations are characterised by periodic spikes seen on many diagnostics, initially at a repetition frequency of 1 - 2 kHz at low heating powers, which slows to $\sim$ 100 Hz before disappearing at the L $\rightarrow$ H transition. A typical series of ELMs is shown in figure 12. Spikes are seen in a magnetic pick-up coil located near to the X point, and these are correlated with spikes in the ion current to the X point tiles, the D_α emission from the X point region, and density in the scrape off layer measured with a reflectometer in the mid plane. The reflectometer measures fluctuations about the density layer $n_e \sim 4.3 \times 10^{18}$ m^{-3} which is located at r/a $\sim$ 0.92. The magnitude of the fluctuation is estimated to be $\sim$ 1.1 x 10^{18} m^{-3} i.e. a relative local fluctuation of $\sim$ 25%. A second reflectometer channel (not shown) at a smaller minor radius (r/a $\sim$ 0.83) shows a much smaller perturbation, indicating the localised nature of the perturbation. This local change in edge density is consistant with the change in the total number of electrons measured with a far infra red interferometer. On a different discharge with similar conditions, fluctuations of $T_e \sim$ 20 - 30 eV have been measured at r/a = 0.93 using an ECE technique. The D_α signal shows a 75% increase along the viewing chord indicating a substantial ($\gtrsim$ 5 x 10^{16} particles per spike) additional recycling at the X point tile. While all of these measurements have large relative uncertainties, they indicate that a rapid outward convection of particles from the plasma boundary is associated with the ELMs and could cause the observed global losses.

Impurities

The most important impurities in JET are nickel, oxygen and carbon [18, 19, 22]. The concentration of nickel relative to the electron density varies from less than 10^{-5} in ohmic discharges to more than 10^{-3} in discharges with ion cyclotron heating. The nickel originates from the nickel Faraday screens on the ion cyclotron antennas, and is released only from antennas to which r.f. power is applied. Thus the release is not due to general changes in the scrape off layer during ion cyclotron heating but must involve a very localised mechanism, possible the acceleration of particles by local electric fields. The nickel contaminates the carbon limiters, and thus nickel concentrations in the discharge build up progressively during a series of discharges with ICRH. The nickel is eroded and the limiters progressively cleaned up during a series of ohmic discharges. This is an interesting observation, showing that carbon limiters are self cleaning once the primary source of metals is removed.

Oxygen concentrations are typically 0.5 to 1% of the electron density in deuterium discharges but are much lower in helium discharges indicating thet the release mechanism is chemical. Carbon concentrations are typically a few percent of the electron density and the main influx comes from the carbon limiters or X point tiles. The influx due to physical sputtering has been calculated using measured values for the temperature and ion flux in the scrape-off layer, and assuming that all of the carbon returns to the limiter and self sputters. These calculated fluxes increase with plasma current and decrease with the mean plasma density (figure 13). Quantitative comparison between the calculated and measured fluxes is complicated by the contribution to sputtering of carbon by oxygen. Unfortunately the measured carbon influx for these discharges is not available for direct comparison with the calculated fluxes, but a similar dependence on current and density is observed for the carbon concentration in the plasma (figure 14). This is consistent with physical sputtering as the main release mechanism.

Conclusions

JET has operated with several different limiter and X point configurations. Detailed measurements of the scrape-off layer parameters have been made for a range of different core plasma parameters in discharges with ohmic, neutral beam and ion cyclotron heating.

In ohmically heated discharges, the ion flux along field lines in the scrape-off layer is independent of the mean density of the core plasma, but increases with the discharge current. However, the density of the scrape off layer increases whilst the temperature decreases as the core density is increased. In discharges with neutral beam heating the changes in the scrape off layer are dominated by the increase in the core density which results from the beam refueling. In discharges with ion cyclotron heating there are clear indications of localised heating effects in the plasma boundary - probably due to coupling of power at the antenna into the slow magnetosonic wave.

Since mid 1987 JET has operated with two belt limiters on the outboard side of the discharge approximately 1m above and below the midplane. The scaling of the scrape-off layer parameters with the core plasma parameters is qualitatively similar to the scalings which were observed for the earlier discrete limiter configuration, but there are some quantitative differences resulting from the different topology and increased surface area of the belt limiters. In particular the region of scrape-off layer between the two belts on the outboard (low field) side behaves differently to the region on the inboard (high field) side.

In discharges bounded by a magnetic separatrix rather than material limiters, JET has established an improved confinement (H-mode) regime with neutral beam heating. The boundary plasma parameters have been measured with moveable probes in the scrape-off layer and with fixed probes in the X point tiles. The densities and temperatures measured with the tile probes at opposite ends of the same magnetic field line are

different leading to a net flow of electric current along field lines in the divertor scrape-off layer. Fluctuations in the density, temperature and other edge parameters (ELM's) have been measured, during the low confinement (L mode) phase. These observations are consistent with an outflux of particles from the boundary comparable to the observed global particle losses.

The main impurities in JET are oxygen, carbon and nickel. The oxygen influx is much smaller in helium discharges than in deuterium indicating a chemical origin for the release mechanism. The carbon influx is mainly from the limiters and is consistent with physical sputtering being the dominant mechanism. The nickel originates from the Faraday screens on the ion cyclotron antennas from which it migrates to the limiter. Thus the nickel accumulates on the limiter surfaces and increases during a series of discharges with ion cyclotron heating. The limiters are progressively cleaned up by a subsequent series of ohmic discharges, as the nickel is eroded from the leading edges of the limiters and redeposited at larger radii away from the erosion zone.

Acknowledgements

The assistance of my colleagues in providing data for this paper is acknowleged. In particular I am grateful to Susanna Clement for her help in collating the data and writing the paper.

REFERENCES

[1] P.H. Rebut et al, Plasma Physics & Controlled Nuclar Fusion Research (1986) 1, 31.

[2] A. Tanga et al, Plasma Physics & Controlled Nuclear Fusion Research (1986) 1, 65.

[3] A. Tanga et al, Nuclear Fusion 27, 1877 (1987).

[4] P.J. Harbour et al, This Conference.

[5] S.K. Erents, J.A. Tagle, G.M. McCracken, P.C. Stangeby and L. de Kock, Nuclear Fusion 26 (1986) 1591.

[6] H. Bergsaker, J.P. Coad, L. de Kock, B. Emmoth, C.J. Hancock, A. Stevens and J. Vince. Proceedings of 14th Euro. Conf. on Controlled Fusion and Plasma Physics, Europhysics Conf. Abstracts, Vol IID (1987) 732.

[7] J.A Tagle, S.K. Erents, G. McCracken, R.A. Pitts, P.C. Stangeby, C. Lowy and M.F. Stamp. 14th Euro. Conf. on Controlled Fusion and Plasma Physics, Madrid (1987), Europhysics Conf. Abstracts, Vol IID (1987) 662.

[8] S.K. Erents, J.A. Tagle and G.M. McCracken. 14th Euro. Conf. on Controlled Fusion and Plasma Physics, Madrid (1987), Europhysics Conf. Abstracts, Vol IID (1987) 740.

[9] H. Brinkshulte, J.A. Tagle, M. Bures, S.K. Erents, P.J. Harbour, T. Huld, A.S. Kaye, C. Lowry and G.M. McCracken. 13th Euro Conf. on Controlled Fusion and Plasma Heating, Schliersee (1987), Europhysics Conf. Abstracts, Vol 10C Part I (1986) 403.

[10] S.K. Erents, J.A. Tagle, G.M. McCracken, et al. Journal of Nuclear Materials 145 - 147 (1987) 231.

[11] M. Bures, J. Jacquinot, A.S. Kaye, H. Brinkschulte, K.D. Lawson and J.A. Tagle. Plasma Physics and Controlled Fusion, Vol. 30 No.2 (1988) 149.

[12] J. Jacquniot et al, 15th Euro. Conf. on Plasma Physics & Controlled Fusion, Dubrovnik, (1988).

[13] D.D.R. Summers. Private Communication.

[14] S.K. Erents, J.A. Tagle, G.M. McCracken, G. Israel, H. Brinkschulte and L. de Kock. These Proceedings.

[15] J.A. Tagle, S.K. Erents, M. Bures, H. Brinkschulte, G.M. McCracken, L. de Kock, J.P. Coad and J. Simpson. These Proceedings.

[16] P.J. Harbour, L. de Kock, S. Clement, S.K. Erents, N. Gottardi, A.E. Hubbard, M. Keilhacker, E.Lazzaro, P.D. Morgan, D. Stork, D.D.R. Summers, J.A. Tagle and A. Tanga. 15th Euro. Conf. on Plasma Physics & Controlled Fusion, Dubrovnik (1988).

[17] A.E. Hubbard, D. Bartlett, P. Cripwell, R. Gill, P.J. Harbour, M. Malacarne, P. Morgan, N. Salmon and J. Snipes. 15th Euro. Conf. on Plasma Physics and Controlled Fusion, Dubrovnik (1988).

[18] K. Behringer et al, This Conference.

[19] M. Stamp et al, This Conference.

[20] P.J. Harbour, International Workshop on Plasma Edge Theory in Fusion Devices, Augustusburg, GDR (1988, to be published in Contributions to Plasma Physics.

[21] P.H. Rebut, K.J. Dietz, P.P. Lallia. This Conference (Paper I17).

[22] K.H. Behringer. J. Nucl. Mat. 145 - 147 (1988) 145-153.

Fig. 1 General view inside the JET vacuum vessel showing the belt limiters, ion cyclotron antennas and carbon protective tiles.

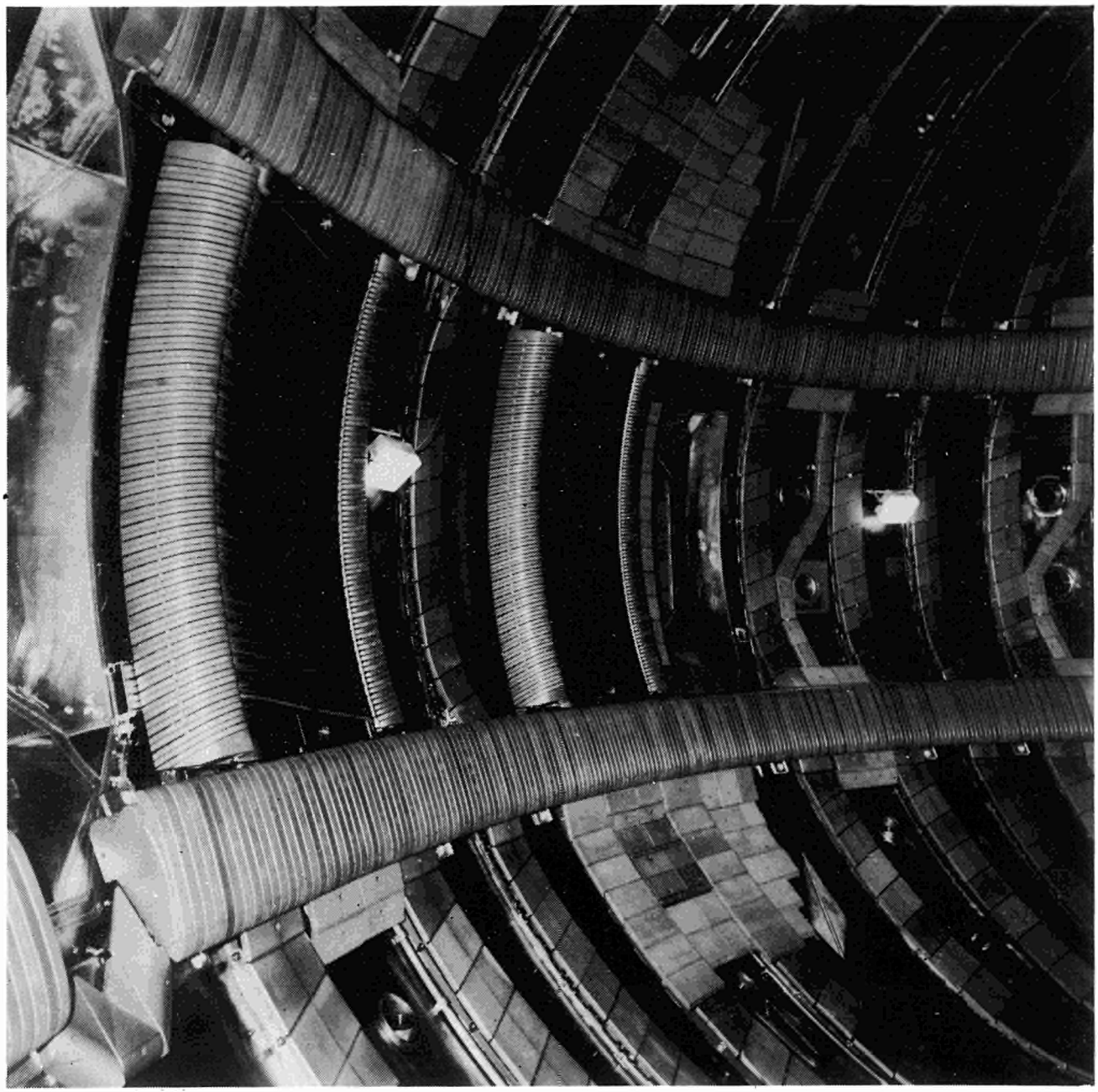

Fig. 2 Close up of the new belt limiters and ion cyclotron antennas which have a nickel Faraday screen protected on either side by carbon tiles.

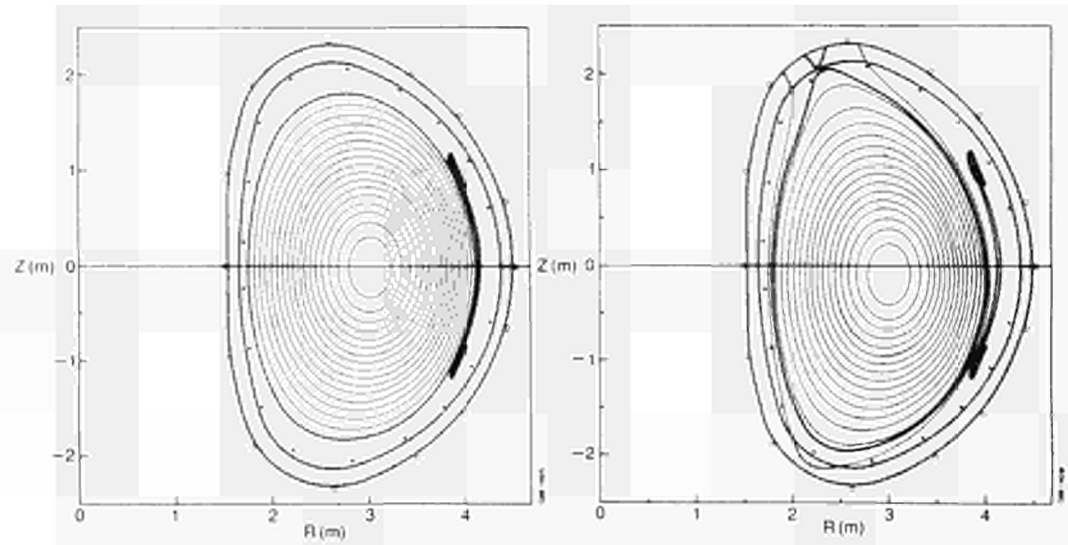

Fig. 3 Poloidal cross-sections of (i) a limiter discharge ($I_p = 6.1$ MA) (ii) an X point discharges ($I_p = 4.5$ MA).

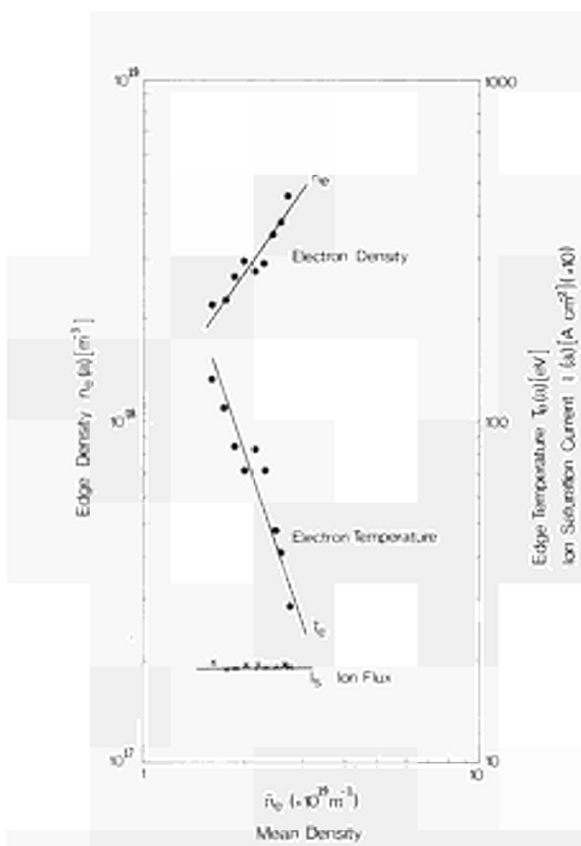

Fig. 4 Scaling of edge density, temperature and ion flux with mean density in an ohmic discharge in the discrete limiter configuration.

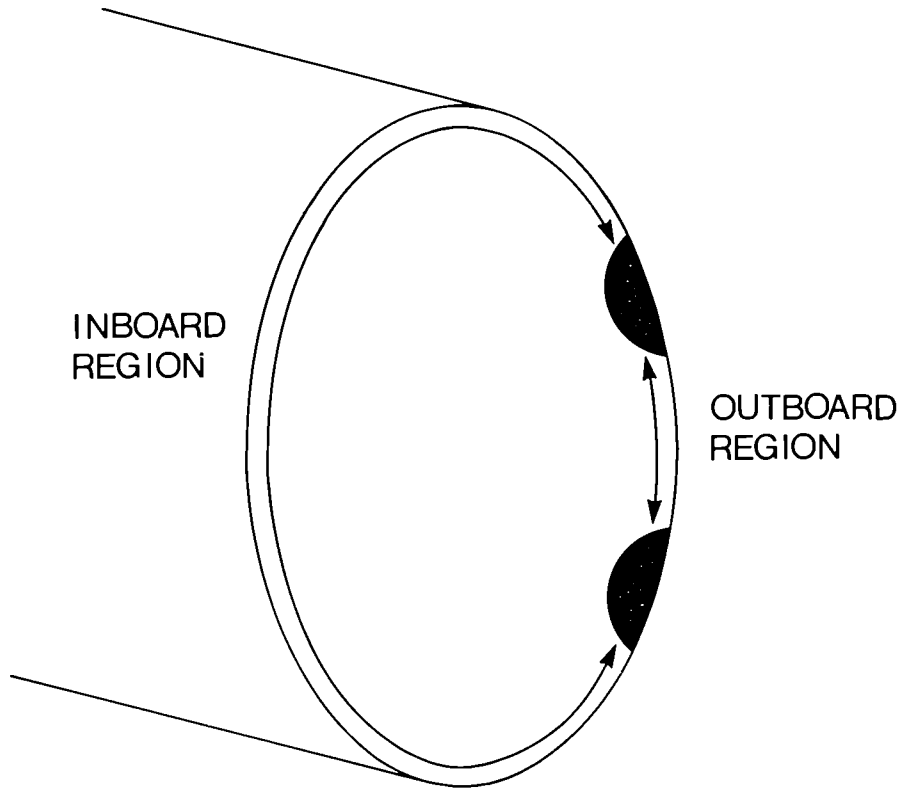

Fig. 5 Schematic of the two regions of the scrape off layer in the belt limiter configuration.

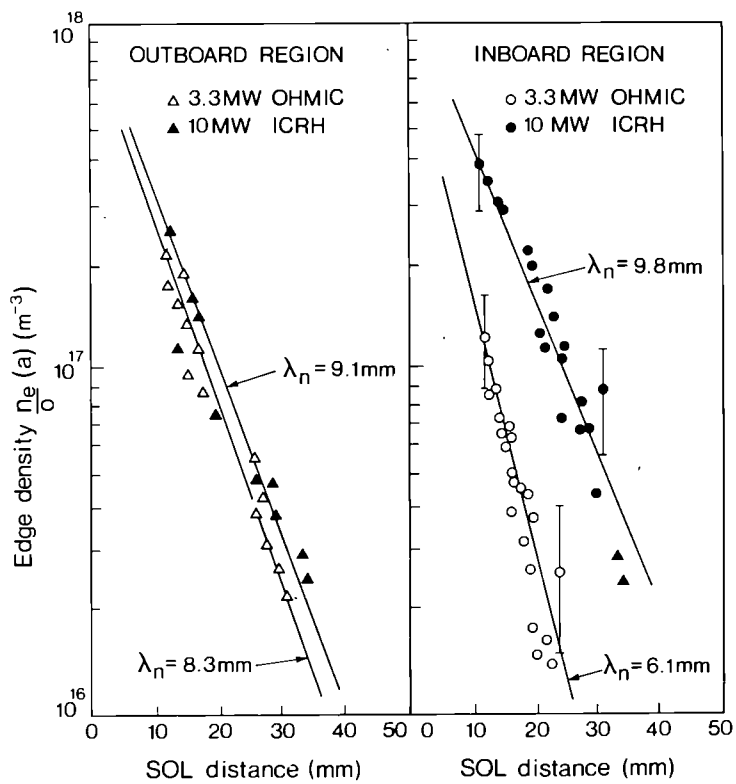

Fig. 6 Profiles of edge density in the two regions of the scrape off layer for ohmic and ICRH discharges. To allow comparison between the data, in figures 6, 7 and 8 the probe scans have been corrected for the flux surface compression and the ascissae are in the outboard mid plane.

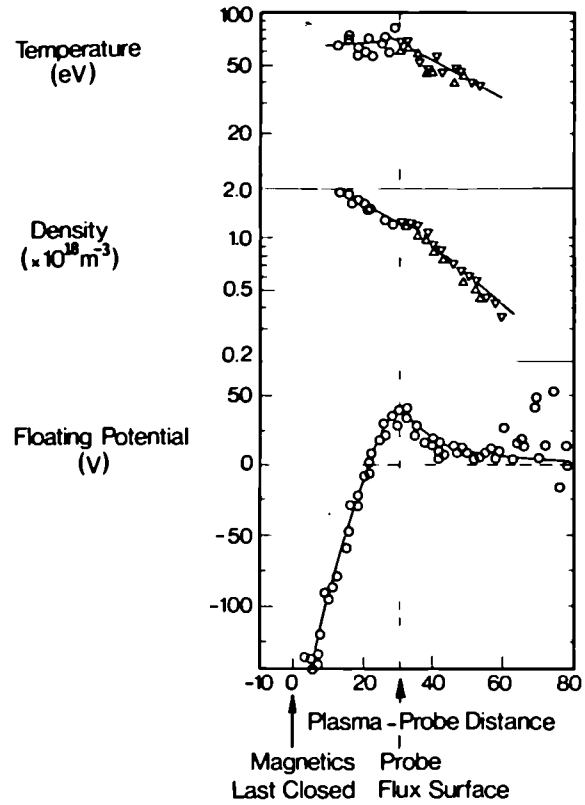

Fig. 7 Density, temperature and floating potential profiles measured with the reciprocating probe. The change in the slope in the temperature profile and maximum in the floating potential is interpreted as the true position of the last closed flux surface.

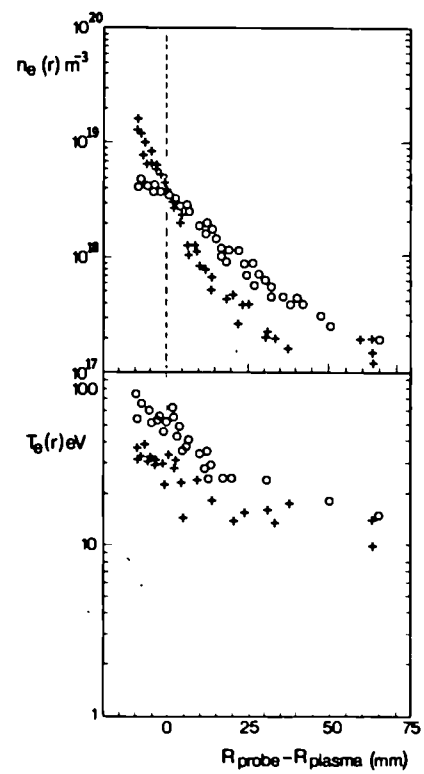

Fig. 8 Profiles of density and temperature in the scrape-off region in the X-point configuration.
0 Ohmic discharge (3 MA, 1.8 T_e) ndl = $4 \times 10^{19} m^{-2}$)
+ H mode discharge (7 MW, NBI)
ndl = $1.8 \times 10^{20} m^{-2}$)
showing the steeper density gradient in the H mode

Fig. 9 Close up of the vacuum vessel showing the carbon tiles in the X point region.

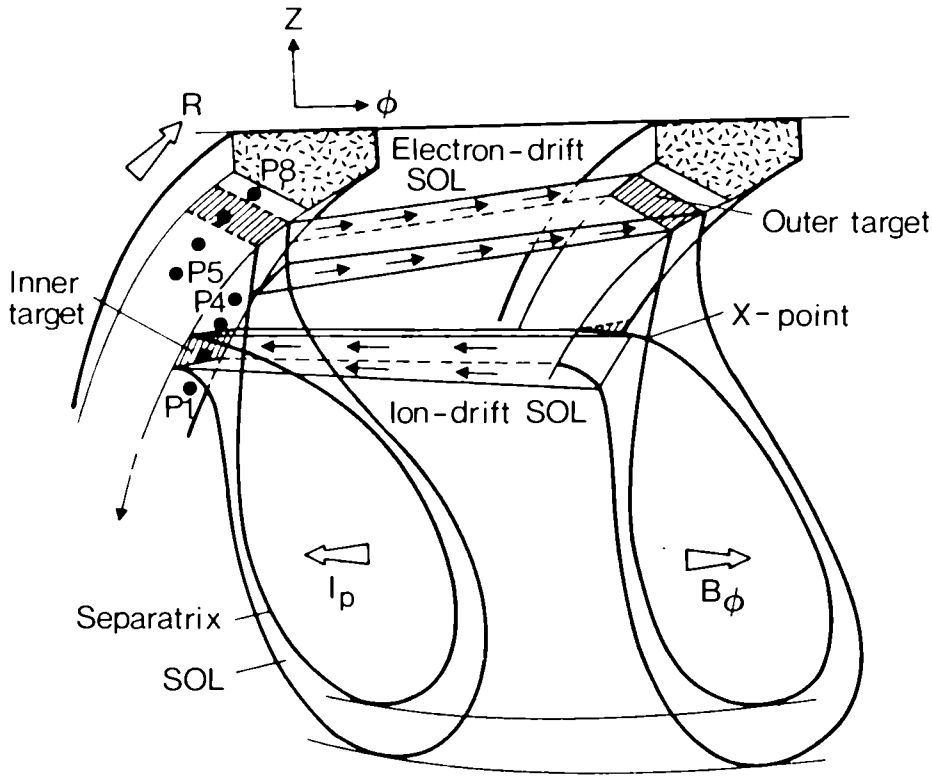

Fig. 10 Schematic of the intersection of the scrape off layer with the X point tiles.

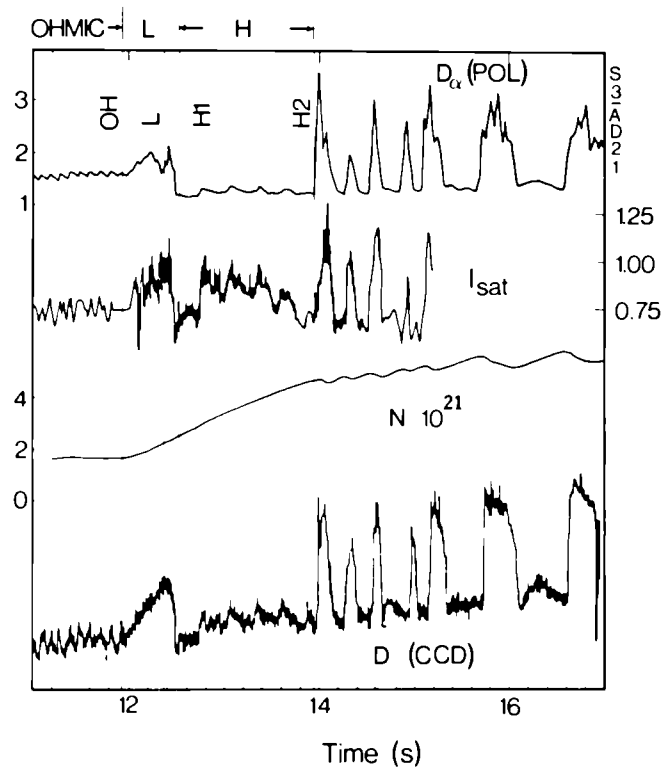

Fig. 11 Parameters during an X point discharge. Two traces of Dα light are shown: the lower trace (Dα(CCD)) is measured at the Xpoint tile; the upper trace (Dα(POL)) at a point mid way (toroidally) between two tiles. Both show strong increases in Dα emission during periods of reduced (L mode) confinement. The ion saturation current (I_{SAT}) is measured with a langmuir probe in the tile surface. The total plasma density is measured with a far infra red interferometer.

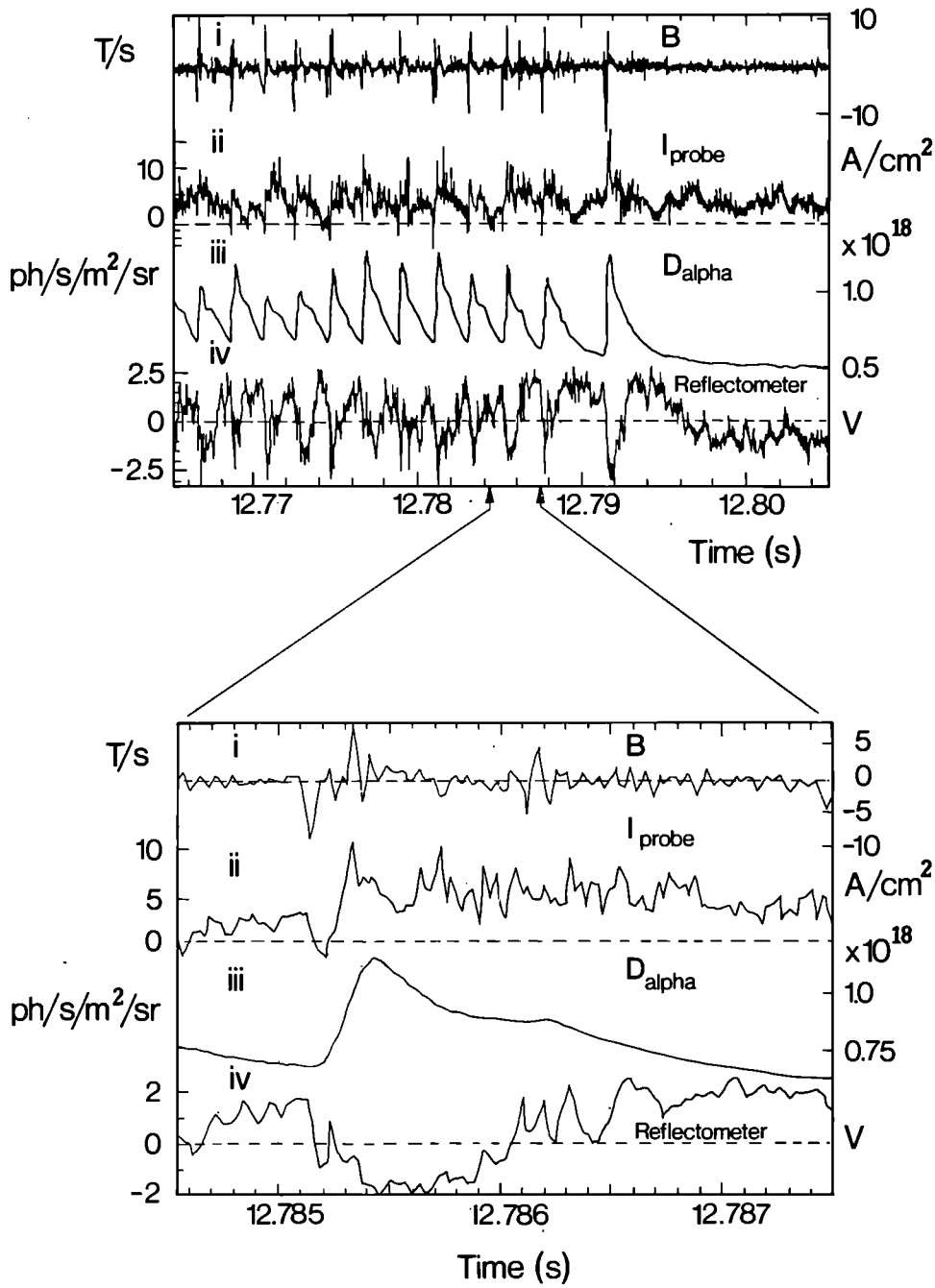

Fig. 12 Fluctuations in the boundary layer during the L-mode of an X point discharge.

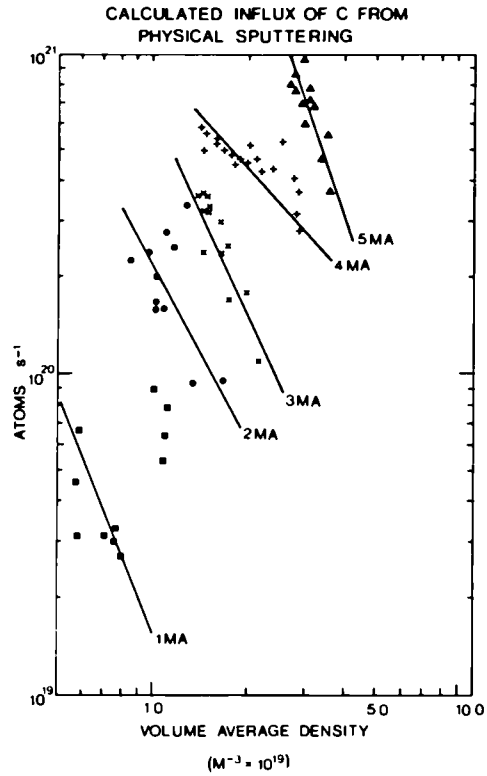

Fig. 13 Carbon influx from the limiter calculated for physical sputtering (D onto C plus C self sputtering) using measured profiles of deuteron temperature and ion flux.

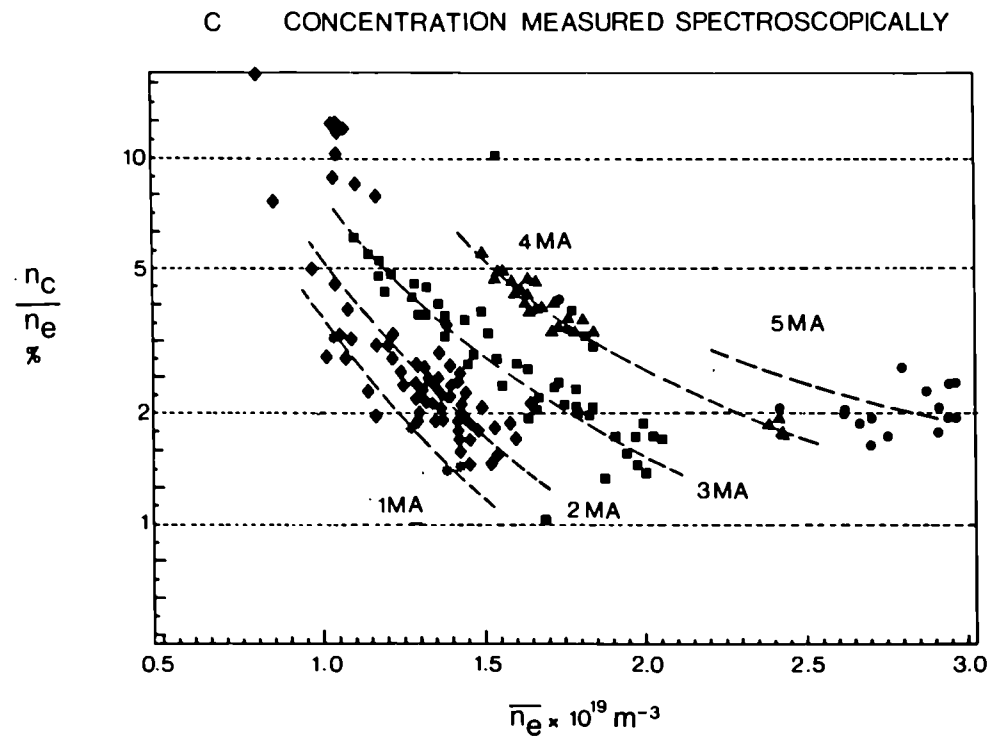

Fig. 14 Carbon concentrations measured spectroscopically.

JET contributed papers at the 17th Symposium on Fusion Technology (SOFT) (Utrecht, The Netherlands, 19th-23rd September 1988)

Many Authors

THE DESIGN OF THE JET LOWER HYBRID LAUNCHER

A S KAYE, H Brinkschulte, G Evans, C Gormezano, J Jacquinot, S Knowlton, X Litaudon[+], D Moreau[+], M Pain, J Plancoulaine, C Walker, G Wilson

JET Joint Undertaking, Abingdon, Oxfordshire, OX14 3EA, England
[+] Associated Staff from EUR-CEA, Cadarache, France

A large lower hybrid current drive launcher has been designed for coupling 12 MW of 3.7 GHz power to the JET plasma for 20 second pulses. The launcher utilises the multijunction technique to achieve 384 waveguides at the grill mouth in a single JET port, with a central $N_{\parallel}$ of 1.8. The design features of this launcher are described with details of the principal components and the results of high power RF tests of these components.

1. INTRODUCTION

The JET program was extended in 1986 to include the provision of a substantial Lower Hybrid Current Drive (LHCD) system. This system will drive forward currents in the outer regions of the plasma, providing a means of changing the radial current profile.

The LHCD program, the overall system and the anticipated influence on the plasma have been previously described[1,2]. A total of 24 klystrons producing up to 15 MW at 3.7 GHz will be coupled to a single launcher, giving a maximum of 12 MW coupled to the plasma. This is predicted to drive up to 3 MA current, depending on plasma conditions and the validity of the scaling relationships used.

It is planned to mount a test launcher (so-called $L\phi$) on JET in 1989, comprising one sixth of the final number of waveguides to JET design, and in addition, the same number of waveguides supplied by the TORE SUPRA team. Much of the equipment of $L\phi$ (vacuum vessel, side protection, position control ...) will be re-used in the final (L_1) launcher to be installed in 1990. The design of the $L\phi$ launcher is essentially complete and manufacture is well advanced. Prototypes of many of the components have been tested at high RF power under vacuum.

This paper gives an overview of the design of this launcher, describes in more detail key components of this launcher, and gives the results of RF testing of these components.

2. OVERVIEW OF LAUNCHER

The design of the LHCD system was severely constrained by the requirement to drive substantial currents using one main horizontal port (0.4 x 1 m). Scaling from results on other machines and theoretical models shows the power required to be in excess of 10 MW. Experimental data gives a close proportionality of maximum power density at the grill mouth and frequency. This defines a minimum frequency for the given port size. Increasing the frequency increases the losses, demands tighter manufacturing tolerances and increases the number of guides at the grill mouth. Taking into account also the availability of klystrons, a frequency of 3.7 GHz was adopted.

The selection of $N_{\parallel}$ is a trade-off between current drive efficiency and accessibility. A value of 1.8 has been chosen. The corresponding wavelength across the grill mouth is 44 mm, giving 8 wavelengths across the port. A maximum height of 80 mm is required for single mode waveguide at 3.7 GHz. A value of 72 mm conveniently allows 12 waveguides per column

within the port. Thus a configuration of 48 modules in 6 rows x 8 columns, each module one wavelength (44 mm) wide and 2 waveguides high was adopted. Each of 24 klystrons is arranged to drive 2 modules in one column, giving a degree of control of the $N_{\parallel}$ spectrum (± 0.3) by adjusting the klystron phase, whilst also enabling a convenient splitting network.

FIGURE 1
Mouth of the prototype multijunction module

In order to optimise the spectrum under both matched and mismatched conditions, each module is subdivided into 4 waveguides at 90° phase shift between adjacent guides in each row. The resulting module is shown in Figure 1. The waveguide dimensions at the grill mouth thus become 72 x 9 mm, with a 2 mm wall thickness, with 384 waveguides in total.

Placing the windows close to the plasma avoids problems with multipactor arcing, but requires many windows in very inaccessible positions. JET is required to operate on tritium, and these windows must be able to be remotely replaced. JET has therefore chosen to locate them away from the grill mouth accepting the consequential requirement to treat the waveguide surface to control multipactor arcs. In addition, JET have chosen to use splitting networks inside the vacuum system to minimise the number of windows. A total of 48 windows are used at 250 kW/window, which is within the capability of established klystron window technology.

The internal splitting is achieved using the 'multijunction' technique. The JET design (Figure 2) uses 6 E-plane junctions and one H-plane junction to divide each waveguide into 8 at the grill mouth. Integral phase shifters are used to give the desired phase distribution at the grill mouth. An external 3 dB sidewall coupler is used to split each klystron output to drive 2 modules. The multijunction design is compact and convenient for large arrays, and also reduces the power reflected to the klystron. A significant disadvantage is that the E-plane junction is a 3-port junction, the performance of which is sensitive to the amplitude and phase of the reflected power,

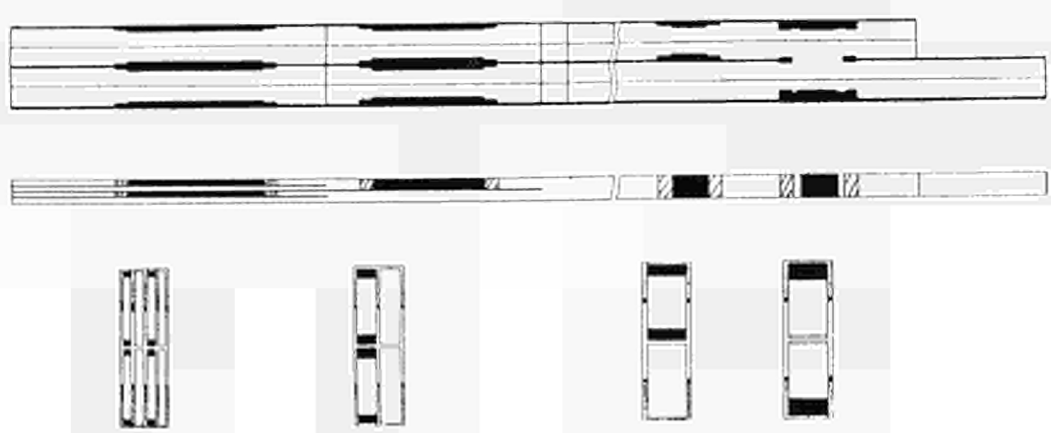

FIGURE 2
The multijunction module

which in turn depend on plasma conditions at the grill mouth which vary during operation. Thus, under conditions of high reflected power, both the amplitude and phase distribution at the grill mouth are dependent on the target plasma. The H-plane junction utilises a matched load on the fourth port to alleviate this effect.

The estimated loss in the launcher is 3 %. Under JET nominal duty cycle of 20 second pulses every 10 minutes, this would require active cooling of the launcher. However, a factor 3 reduction in duty cycle enables radiation cooling with an asymptotic temperature of c. 500°C. The launcher is therefore not actively cooled.

Disruption forces on the launcher are substantial due to the vertical flux threading the waveguide. The flux diffusion time is typically 0.1 sec for stainless steel guides, 3 secs for copper. For comparison, the worst case disruption is taken to be 7 MA in 7 msecs. The use of a low conductivity alloy such as stainless steel thus strongly reduces the disruption loads. The use of low conductivity alloys, however, demands the use also of high conductivity coatings to obtain acceptably low RF losses, which is both difficult and expensive. JET have opted to use coated stainless steel. The torque on the launcher is computed to be 4 Tonne.m. (primarily on the support structure).

Matching of the launcher depends on the plasma density at the grill mouth. As the JET plasma position is constrained by other requirements, the launcher has been designed to be movable during the pulse using hydraulic actuators; typical response is 20 mm in 0.15 seconds. This requires the use of a very rigid mechanical structure, and also the provision of a bearing inside the JET vessel. Whilst the design of this bearing is on-going, the basic unit is a 50 mm diameter ball running in a conforming track. The launcher movement also requires provision of a 1.5 m diameter double inconel 600 bellows with 300 mm stroke and a fatigue life in excess of 10^5 cycles.

The waveguide modules are fixed in the assembly at the grill mouth, where all modules are welded together. Thermal expansion of these waveguides is accommodated by individual bellows at the rear of the launcher. Operation of the external hybrid junction requires equality of electrical length of the 2 driven modules; this is obtained by external physical adjustments. Radiation transfer will limit the temperature difference between adjacent waveguide modules to less than 50°C, which is acceptable. A phase control system[3] is being developed to measure the phase distribution at the grill mouth. Temperature variations between modules not driven by the same klystron can be compensated at the klystron.

Passive waveguides are utilised either side of the launcher to improve matching at the sides. Graphite tiles surround the launcher to protect the grill mouth from the plasma. These are 5 mm forward of the magnetic surface through the grill mouth. Cooling of the tiles is by radiation to water cooled fins.

The launcher is shown in Figure 3.

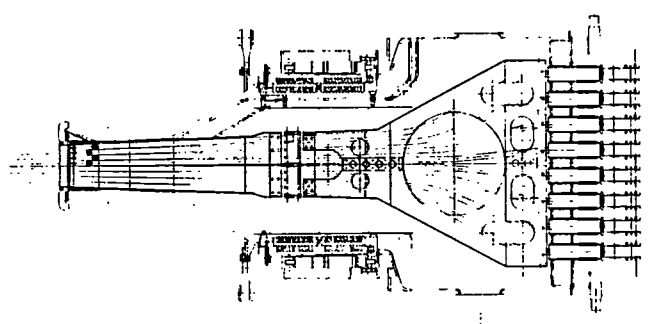

FIGURE 3
The LHCD launcher

3. DETAILED DESCRIPTION AND RF TESTING OF MAIN COMPONENTS

3.1. Multijunctions

The multijunction unit has been shown schematically in Figure 2. This unit is manufactured by machining from solid in 3 longitudinal sections with the V-joint at the centre line of the waveguide to avoid current flow across the joint (but at the risk of increased electric field). Manufacturing tolerances are ± 0.2 mm on waveguide internal dimensions and ± 0.05 mm on V-groom location. Each assembly is vacuum brazed to restrain thermal stresses in the reduced section. Each unit is internally electroplated with 15 microns of copper.

Sections of brazed and clamped waveguide have been tested under vacuum up to 200 kW, 20 second pulse with short-circuit termination. The prototype multijunction has also been tested up to 200 kW, 20 seconds with short circuit terminations on all ports, which gives a very non-uniform power distribution. A matched termination for the grill mouth is being manufactured for these high power tests.

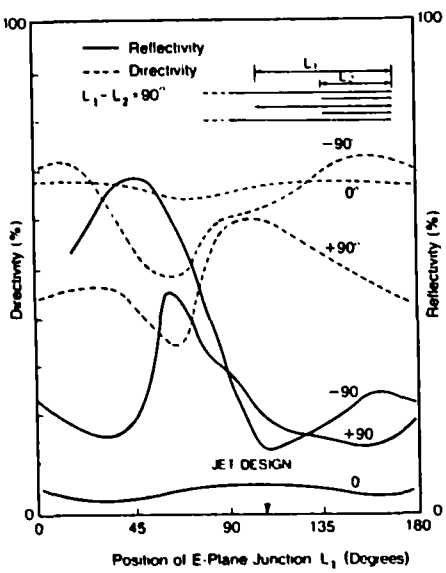

FIGURE 4
Effect of E-plane junction length on grill performance for zero and ± 90° phase between adjacent modules

The peak electric field in the waveguide reduced section is c. 4 kV/cm (at 20 % reflection). This value was consistently obtained at Petula and has been adopted as the design criterion for the multijunction phase shifters, assuming uniform power splitting. The optimum length of the E-phase junctions depends on the reflected phase at the mouth. This has been investigated numerically[4] using the SWAN code and the results are summarised in Figure 4. Based on this data, the lengths indicated on this figure have been chosen. The H-plane junction has been designed under contract and a prototype unit tested at low and high power. This unit has no matching features on the long faces in order to facilitate machining. The multijunction length has been increased such that the electron cyclotron resonance lies within the plain waveguide section of the multijunction.

The thermal diffusion time in stainless steel on a 36 mm half height of the waveguide is c. 300 seconds, and for copper c. 10 seconds. For the JET pulse length of 20 seconds, thermal conduction only marginally effects the temperature profiles within a pulse, even for copper. On the other hand, in the period between pulses, even stainless steel will approach uniformity. Thus, for an isolated pulse, the low thermal conductivity of stainless steel is not a disadvantage. The temperature rise per pulse is c. 25°C, being maximum close to the grill mouth where radiation cooling is least effective. Temperature increase in this region will be the limiting factor in the duty cycle.

3.2. Vacuum matched loads

The matched load on the multijunction unit uses silicon carbide as the absorbing medium in a weakly resonant configuration. It is rated at 20 kW for the JET duty cycle, 300 kW for 100 microsec, with a 3.7 ± 0.01 GHz bandwidth from 20 to 500°C. Cooling is by radiation only.

3.3. Vacuum waveguide

The waveguides are also stainless steel and are produced by drawing of 4 mm wall rectangular section, then bending to the developed profile and silver plating internally. Tolerances of ± 0.2 mm on internal dimensions are achieved in the straight tubes, increasing to ± 0.5 on the inside of the bends. Low power measurements show low VSWR and losses and electrical length to be close to theoretical. The connection of this waveguide to this multijunction is by a TIG welded butt joint. This joint has been tested with 200 kW, 20 second pulses under vacuum.

3.4. Windows

The windows are double windows with continuous ion pumping/monitoring of the interspace vacuum. The ceramics are BeO pill boxes, the design being based on an existing commercial design for klystron windows. There are 48 windows in close-packed array, each of which can be replaced remotely. The connection to the vacuum waveguide is a clamped joint which has been tested to the full duty required.

3.5. Coatings

Both silver and copper coated waveguides, 72 x 9 mm x 1 m long, have been tested under vacuum with short circuit termination. The losses were found to be within 20 % of theoretical. The limiting power was higher for silver (50 kW against 30 kW). With an added 660 gauss magnetic field (2 ω_{CE}), enhanced breakdown was also observed on the copper.

Various coatings for controlling multipactor arcs have been assessed. Samples of 'black gold'[5] were found to have excess losses at this frequency (typically 2 - 5 x copper). Carbonised copper was found to have losses close to theoretical, but much improved multipactor thresholds (c.80 kW in the above test) although with increased outgassing. No method of carbonising silver has been found.

JET propose to silver plate the vacuum waveguide and to use carbonised copper on the multijunction unit which spans the electron gyrofrequency resonance and its harmonics.

3.6. Position control system

This system utilises a total of 5 hydraulic cylinders. Three of these are used only to support the vacuum load of c. 17 tonnes, being driven by constant pressure accumulators. Two cylinders are used for position control. This configuration much reduces the capacity of the control valve, and enables the system to be designed with a higher probability that any failure will be in the withdrawn position. Fluid-mechanical interlocks are used to limit the acceleration and velocity to within safe limits. The working fluid is 5 % glycol in water, both for improved radiation resistance and reduced fire and contamination hazard. This system will be described in detail elsewhere.

4. CONCLUSION

A large lower hybrid phased array launcher has been designed for coupling 20 second pulses of 15 MW, 3.7 GHz power to the JET plasma for driving currents. Key components have been manufactured and tested. The test launcher will be installed on JET in 1989.

ACKNOWLEDGEMENT

The assistance of the TORE SUPRA team in provision and operation of the RF test bed and interpretation of the results is gratefully acknowledged.

REFERENCES

1. J. Jacquinot et al, Proc. 14th Symp. on Fus. Tech., Vol. 1, p. 287, (Avignon, 1986).
2. C. Gormezano et al, Proc. 12th Symp. on Fus. Eng., Vol. 1, p. 38, (Monterrey, 1987).
3. G. Bosia, Proc. 7th Top. Conf. on Appl. of RF Power to Plasmas, p. 139, (Kissimee, 1987).
4. D. Moreau et al, Ibid., p. 135.
5. H. Derfler et al, Proc. 4th Int. Symp. on Heating in Toroidal Plasmas, EUR 9341 EN, Vol. 2, p. 1261, (Rome, 1984).

CONCEPTUAL DESIGN OF PLASMA EXHAUST CRYOPUMPING IN NET

W. OBERT[1] and D. PERINIC[2]

[1]JET Joint Undertaking, Abingdon, Oxon, OX14 3EA, England
[2]Kernforschungszentrum Karlsruhe GmbH, Postfach 3640, D-7500 Karlsruhe 1, West Germany

The vacuum requirements for the Plasma Exhaust Pumping System (PEPS) of NET and the design requirements for NET-operation are described. Various possible solutions of cryopump arrangements are analyzed and discussed. A conceptual design is presented, which is based on four cryopumps, each with a pumping speed of 150.000 ℓ/s.

1. INTRODUCTION

Future fusion devices as NET require large pumping speeds in comparison to commercially available turbomolecular pumps (more than a factor of 10). In addition, the pump units have to be fully tritium compatible.

The required pumping speeds of NET are moderate for cryopumping standards and cryopumping can be regarded as tritium compatible (see below). However, large amounts of helium have to be pumped which is not possible by simple straightforward cryocondensation. Helium pumping requires more sophisticated technology such as cryotrapping or cryosorption which are well known techniques for UHV system but have never been built to the large scale which is required for NET.

For the cryosorption of helium a development programme has been started at KfK to study:

- sorbent materials and preparation techniques
- bonding techniques for the sorbents
- cryosorption pumping on an experimental test facility for a single stage and for a two stage compound cryopump
- theoretical pumping efficiency of various pump configurations and to optimize the geometry.

The design considerations and a conceptual design for a cryopumpsystem for NET are presented in the following, based on the available NET data[1]. For more details see[2].

2. CRYOPUMPING

The main advantages of cryopumping are:

- Provision of absolute oil and hydro-carbon free vacuum
- no corrosive process fluid or gas
- no moving parts inside the pump device, no bearing or electrical insulation
- accident proof, no problem with mechanical debris, no damage at sudden venting
- compatible with high magnetic fields
- compatible with corrosive gases
- no vibration
- high lifetime, no routine maintenance
- stable against power failures
- extremely versatile, easy to scale to very large systems, easy system integration, no installation or orientation limitations
- longterm experience available for very different and also very large systems
- high specific pumping speeds allow minimum valve sizes
- selective pumping of different gases.

These advantages have to be weighed against the inherent problems of cryopumping which are

- limited capacity requires regeneration and separation valves
- the batch operation may cause fluctuation in flow and pressures
- limited access time by cooldown (unless pump is cold in standby)
- accumulation of the cryopumped gas requires safety considerations regarding the systems inventory (H2/air mixture ignition, tritium radiological limit)
- for cryosorption pumps an additional restriction is the risk of contamination of the active pumping surfaces.

3. NET VACUUM REQUIREMENTS

3.1 The NET vacuum system

The NET vacuum is a toroidal volume with an internal surface of ≤ 1000 m² and with a volume of ≤ 1100 m³ which has 16 divertor outlets on the bottom of the Torus (see Figure 1).

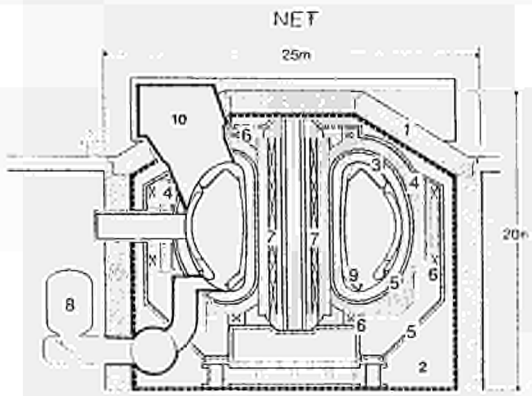

Fig. 1 The NET device

The divertor itself, its operation principle, design and boundary conditions are described in[3]. From the divertor which is mainly a horizontal duct with an entrance restriction on the Torus end yields a pumping duct (basically a circular tube of typically 1.5 diameter and a length in range of 10 m depending on the final design to the pumping station). The conductance of the pumping duct has been evaluated[2,3] to ∿ 65 m³s⁻¹.

3.2 Operation modes

Mainly four different operation modes of the NET Plasma Exhaust Pumping System have to be considered (see Table 1).

- The first pump down from atmosphere.
- The dwell period, the pumping between the burn periods in order to prepare the vessel background for the next burn period.
- The burn period which is the stationary operation mode of the plasma.
- The discharge cleaning. This mode has to be assessed separately.

Requirements for discharge cleaning are not defined yet and will probably not influence the following design considerations. For more detailed information see[1].

3.3 Symmetry conditions

No pumping symmetry is required at the torus because the gas flow pumped from a divertor is only a small fraction (< 0.5%) of the gas flow inside the torus. For this reason, simultaneous zero pumping is admissible at a defined number of divertors.

3.4 Required pumping speed and flow rates

The NET power output of 620 MW corresponds to a He mass flow of

$$m_{He} = 2.1 \times 10^{20} \text{ He atoms s}^{-1} = 8 \text{mbl s}^{-1}$$

From the concentration of 5 vol.% He in DT the DT mass flow is

$$m_{DT} = 40 \times 10^{2} \text{ DT} = 152 \text{ mbl s}^{-1}.$$

3.5 Required total pumping speed

As a basis for the pumping loop layout a value of

$$S_{total} = 250 \pm 50 \text{ m}^3\text{s}^{-1}$$

required at the divertor for He and DT exit has been taken (see Table 1) and for simplicity all calculations will be made for 250 m³s⁻¹.

3.6 Pressures/flow regime

The partial pressure at the divertor has been evaluated[2] to

$$P_{He} = 3 \times 10^{-5} \text{ mb} \quad P_{tot} = 6 \times 10^{-4} \text{ mb}$$

based on a concentration of 5% He and 95% DT.

The flow conditions have been found to be molecular up to the pump entrance. Inside the cryopump configuration the free mean path will be according to the lower temperature and the corresponding higher density shorter, the internal conductance of the cryopump will be reduced and the total pumping speed will be enhanced[4].

Mode of operation	Pressure at 300 K [mbar]	Req. pumping speed at 300 K [m^3 s]	Flow regime	Gas composition [mole %]
Pumpdown	$10^{3} - 10^{-8}$	200	Viscous intermediate molecular	90 H_2O, 10 air
Burn time 620 MW = 2.1 x 10^{20} He atoms s^{-1}	6.6 x 10^{-4}	250 ± 50	Molecular	90 DT, 5 He, 3 impurities, 2 H_2
Dwell time from 10^{19} atoms/m^3 to 10^{18} atoms/m^3 in 20 s	2.5 x 10^{-3} – 2.5 x 10^{-5}	250 ± 50	Intermediate molecular	84 DT, 10 C (H, D, T)$_4$ 2 H_2O, 2 air, 1 He, 1 H_2
Conditioning	~ 10^{-3}	To be defined	Intermediate	To be defined

Table1: Pumping requirements at the inlets of the pumping ducts for various modes of NET operation /1/

3.7 Size limitations

The radiological cryopumped inventory limit for NET is set to 150 g T2=550bl(STP) = 25 mol. With a T2 flow rate of ∿ 80 mbls^{-1} the operation period is limited to ∿ 2h.

This limit determines the required cryopump/ sorption capacity. For a single stage pump the required sorption area for both He and DT together (1100bl(STP)) has to be ∿ 50m^2 based on a specific sorption capacity of 2 mbl cm^{-2} for a good sorbens (in the case of a two stage pump 2.5 m^2 for He only). A total of 30 kg of activated charcoal (∿ 50 mbl g^{-1} spec. sorption capacity) can provide the necessary capacity.

The size of the vacuum housing is also given by a safety limit, by the 15 mb partial pressure ignition limit for hydrogen in air which calls for a volume of < 50 m^3.

4. PUMP ARRANGEMENTS

Various pump arrangements have been analysed, including individual pumping of each divertor, combinations of two, four and eight divertors for a single pump unit, and ring line pumping (see Fig. 2).

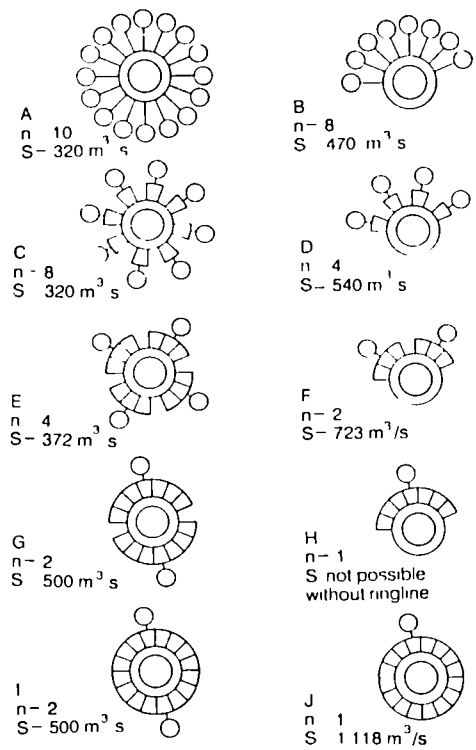

S – total pumping speed required at pump inlets
n – number of pump units

Fig. 2 Pump arrangements

The following conductances (300 K) have been assumed:

- Pumping duct (1.5 m Ø,10 m long) C = 65m^3/s.
- Ring line segment between two pumping ducts (2 m dia., 4 m long) C = 300 m^3/s.
- Each pump arrangement provides a total of 250 m^{3}s^{-1} at the divertor exits.

The smallest single cryopump and the lowest total pumping speed is required in arrangement A. The disadvantage of this layout is the large number of pumps.

Reducing the number of pumps simplifies the cryosupply and control arrangements and diminishes the costs. In arrangements C and D, the pumping ducts are connected in pairs.

The combination of pumping ducts or at the ultimate a ring line offers clear advantages in cutting down the number of cryopumps.

Combining four ducts as in cases E and F, or eight ducts as in G, allows the number of pumping units to be reduced to four or only two.

If a ring line is used, all pumping could be provided by only one pumping unit. The main obstacle to a ring line is the electrical short circuit it would represent for the main plasma current and an arrangement with bellows or electrical breaks is required. (Similar breaks are needed for the vacuum vessel).

Fewer cryopumps also mean valuable space saved around the torus. Arrangements B, D, F, H and J require 50% less space than arrangements A, C, E, G and I.

Because of regeneration and standby/spare requirements, more pumps will be installed than shown in Fig. 2.

5. CONCEPTUAL DESIGN

A conceptual cryopump design is shown in Figure 3. It is based on

- Single-stage 4 K condensation/sorption surface for simultaneous pumping of DT and He.
- High trapping efficiency.
- Scaling capability to other pumping needs.
- The size of the vacuum housing is defined mainly by inventory/safety considerations.

In order to demonstrate the possibility to create free space around the torus, arrangement D (4 cryopumps operational) was chosen as a reference case, with a total pumping speed required at the pump inlets of 540 m³/s (135 m³/s each), in operation. The main cryopump data are shown in Table 2.

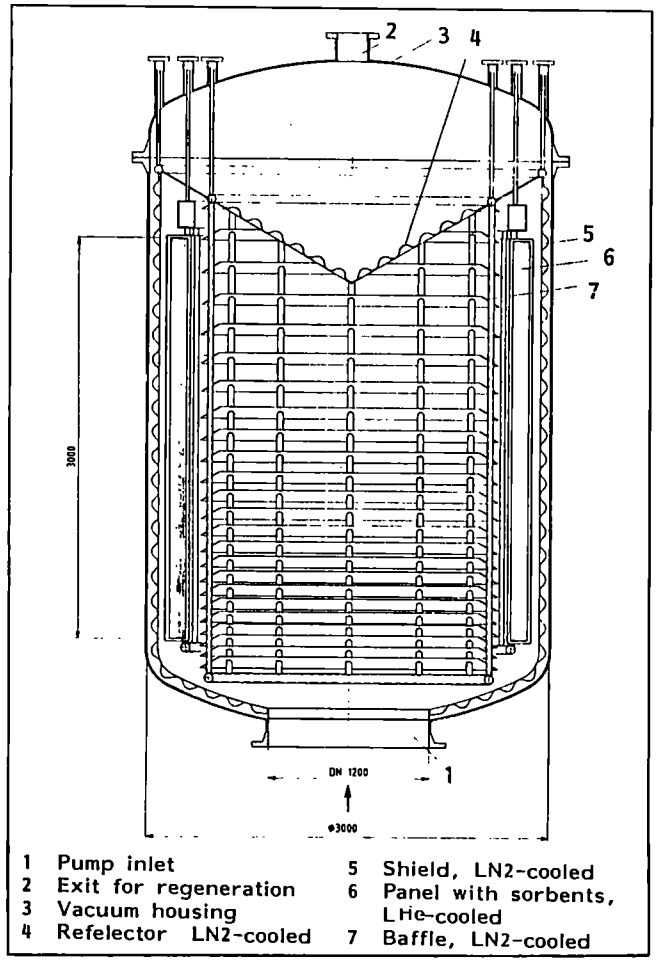

Fig.3 Conceptual layout of the cryopump

Table 2: Technical data of the proposed cryopump

Pumping speed for helium, DT	~ 150 m³/s
Entrance gate valve	ND 1200 mm
Vacuum housing volume enforced by the 15 mbar ignition limit for DT	> 20 m³
Active pumping surface at 4.2K for a sorption capacity of 2 mbarl/cm² and an inventory of 1000 barl for DT and He	> 50 m² circular panel made of extruded aluminium V-shape arrangements
Sorbent with a sorption capacity of 30 - 60 mbarl/g	Submicroporous material (activated carbon or molecular sieve) total mass: 17 - 35 kg
Bonding	Inorganic material (cement, braze)
Cooling power required at 4.2K	~ 60 W in normal operation, ~ 150 W during cooldown

5.1 Set up

The proposed cryopump is a cylindrically set up from outside to the inside: vacuum vessel (∿ 2.5 m diam.), LN2 radiation shield, LHe cooled < 5 K sorption/condensation surface, LN2 radiation baffle with high particle transmission and LN2 particle reflector opposite the pump inlet (opening < 1.2 m dia.). The height is ∿ 3 m. An overall trapping of 80% of the particles entering the pump is expected.

5.2. Orientation

The orientation of the cryopump is basically free but a vertical position with the pump inlet at the bottom is preferred in view of water accidents and dust.

5.3 Regeneration valve

The cryopumps have to be routinely regenerated (cycle 2.3h: ≤ 1h) to desorb to He and DT. Full regeneration, i.e. warming up to > 100 K is required to clean the pump from impurities (cycle depending on impurity level ∿ 150h (weekly: 20h).

The requirements for a regeneration valve have been assessed[2] and a 'regeneration flap' with a conductivity in the range of 10^{-1} $mbls^{-1}$ was found to be sufficient.

5.4 Two stage cryopump

A single stage cryopump has been proposed as the simplest approach and as tests[5] have proven that the He/DT mixtures can be pumped by a single stage sorption pump as long as the capacity for both He and DT is large enough.

To modify the design to a two stage pump would not be difficult.

The possible contamination effect from plasma exhaust impurities have been assessed in[2].

5.5 Thermal load

The thermal load has been calculated[3] with regard to the load from the support, from thermal radiation, thermal load from base pressure, gas condensation load and tritium decay. The neutron heating will depend on the final position and neutron flux but will be small if the pump is installed outside the biological shield (see Figure 1).

For all the NET plasma exhaust cryopumps a total power in the range 200 W - 300 W/< 5 K will be required for the basic heat load. In order to allow fast regeneration cycles and therefore quick cooldown the total power should be in the range of 500 W - 600 W.

The structural mass and the LN2 and LHe inventory of the cryopumps is minimised in order to have short access time for cooldown and regeneration and in order to minimise the heating effects due to neutron interaction if the pump is installed close to the Torus.

REFERENCES

1. P. Dinner et al., 'Next European Torus Exhaust and Fuel Processing System', Fusion Technol. 14, (1988) 178.
2. W. Obert and D. Perinic, 'Conceptual Design for the Plasma Exhaust Cryopumping of NET', Kfk Primaerbericht, Internal Report No: 03.07.01(02B, April 1987.
3. A. de Matteis, M.F.A. Harrison and E.S. Holston, 'A Sensitivity Analysis of the Effects of Pump-Duct and Down-Pipe Geometry on the pumping requirements of a NET-like Single-Null Divertor', EUR/FU-XII/ 80/88/81, January 1988.
4. W. Obert, "JET Cryopump System and its Cryolines for Neutral Injection,. SOFT 13, Varese, 1984.
5. D.W. Sedgley, A.G. Tobin, 'Development of Charcoal Sorbents for Helium Cryopumping, Grumman Aerospace Corporation, report ES-84-21.

CRYOPUMPING IN THE ACTIVE (D/T) PHASE OF JET

Wolfgang OBERT

JET Joint Undertaking, Abingdon, Oxon, OX14 3EA, England

The special problems related to the operation of the cryopumpsystems at JET during the active (D/T) phase are reviewed. The main aspects are the effects of neutrons - thermal load and activation of the cryogenic fluids and structure - the tritium inventory and safety, the radiation compatibility of cryostructure and instrumentation and the production of hazardous ozone under radiation conditions. Most of the results of the analysis can be applied to any other fusion cryosystem by appropriate scaling.

1. INTRODUCTION

Cryogenics is an indispensable technique for today's and future fusion devices. Its main use is for cryopumping and for superconducting magnets[1]. At JET three large scale cryopumpsystems each with 8 x 10^6 ℓs^{-1} pumping speed are installed for 2 Neutral Injectors and 1 Pellet Injector system.

2. THE JET CRYOPUMPSYSTEMS

The set up of the cryopumpsystem and its cryosupply is described in[2]. Each system (Fig. 1) comprises of two 'cryopumpassemblies' which cover completely the side wall of the Injector Box. Each 'assembly' has a size of 3 x 6 m and is 30 cm deep. The pump-configuration is a unique design and provides a trapping efficiency for the incoming particles of close to 50%. The cryopump system is modular built and each module consists of 9 aluminium extruded cryopanels with integrated cooling channels. The 6 m high system is cooled by the thermosyphon principle. The weight of the liquid helium (LHe) and liquid Nitrogen (LN2) structure and the LHe and LN2 content have been minimised in order to minimise the irradiation interaction (structure: LHe: 560 kg Al/340 kg St.St., LN2: 2800 kg Al/1300 kg St.St., content LHe 150ℓ, LN2 250ℓ).

3. THE NEUTRON LOAD

The neutrons from the fusion plasma will cause thermal load to the cryosystem, activation of the cryogenic fluids and cryostructure and can produce hazardous oxygen. Most of the following analysis for the JET cryosystem can be transferred to any other system by scaling the results with the fusion yield.

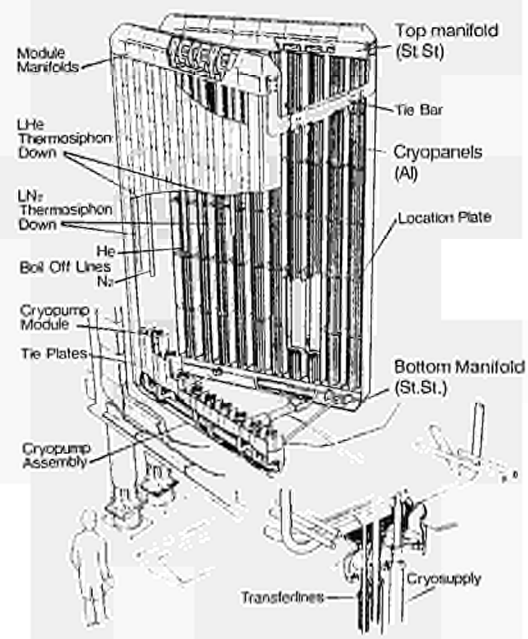

Fig. 1 - Cryopump system set up

3.1 Fusion yield

The maximum neutron output of JET is envisaged to be up to 10^{20} n/shot or 10^{19} n/s (compared with 2 x 10^{21} n/s for NET) with a neutron energy of 14 MeV. Over the lifetime of JET 10^{24} neutrons are expected (5000 shots/year).

An analysis[3] based on a detailed transport code gives a neutron flux direct from the plasma to the cryopump of $\sim$1.5 x 10^{11}n/cm^2•s for neutrons above 10 MeV. Taking into account the

shielded cryopump position (Figure 2), a flux of 4 x 10^9 n/cm^2•s has been calculated.

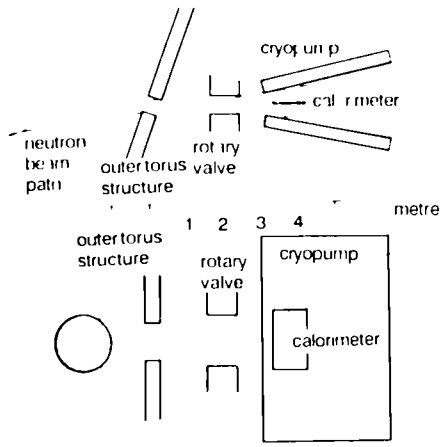

Fig.2 Neutron beam path and cryopump position

3.2 Dose rate

Based on the most pessimistic figures of 3.1 and a total of 10^{24} neutrons per JET lifetime a total dose rate for the cryopumpsystem of less ∿ 10^8 rad is expected.

3.2 Nuclear heating

The neutrons from the fusion reaction will heat the cryostructure, the bulk LHe and LN2 due to elastic scattering, inelastic scattering, neutron capture and γ-ray adsorption. The heat input to 1 cm^3 of different material and the total value for the LN2 and LHe loop, has been evaluated in Table 1. The range stated is due to the uncertainty in the γ-radiation adsorption. The data are conservative as the same neutron flux has also been used for the well-shielded part of the system; on the other hand, the low energy neutrons could have been underestimated.

	Energy release (mW cm^3)			heat load (W)	
	neutrons	γ ray	total	He loop	N2 loop
Al	0.15	0.03	0.18	37.82	185.411
StSt	0.16	0.16	0.32	13.30	52.118
Cu	0.16	0.2	0.36	8	
LHe			0.34	6	
LN2			0.18		25
Total				120 W	<5[illegible] W
duty cycle 1:60				< 2 W	< 9W
cryosupply rating for				1.0 W	10 kW

TABLE 1
Nuclear heating of cryopump (4x10^8 n/cm^3s)

- The heat load during the pulse for the He and N2 loop is < 120 W and < 550 W respectively and is close to, or lower than, the base load of the system (LHe ∿100 W, LN2 ∿10 KW). The averaged thermal load (duty cycle 1:60) is less than a few percent of the basic load.

The local heat load in the cryopanel fins is compatible with the admissible local peak loads[4] for the fin temperature gradients and the thermosyphon cooling flow (designed for ∿ 10 times the base load).

3.3 Activation

3.3.1 Cryostructure

The activation process of Al, St.St.and Cu, their reaction products and the resulting activities are listed in Table 2, together with dose rates after 10^4 full performance 10 sec plasma pulses over 2 years. The activated Al-panels will produce a dose rate of 37 mR/hr. After 9 days this value will have dropped by 10^4. For the St.St. manifolds on top and bottom ∿ 16 mR/hr are expected which takes many years to decay.

reaction	half life time	γ energy	dose rate after 10^4 pulses
Aluminium			
$Al^{27}(n,\alpha)Na^{24}$	15 h	2.76 MeV 1.38 MeV	38 mR/h
Stainless Steel			
$Fe^{54}(n,p)Mn^{54}$	314 d	0.83 MeV	5 mR/h
$Ni^{58}(n,p)Co^{58}$	71 d	0.81 MeV	11 mR/h
Copper			
$Cu^{63}(n,\alpha)Co^{60}$	5.3 y	1.3 MeV 1.2 MeV	10 mR/h
$Cu^{63}(n,\gamma)Cu^{64}$	12.8 h	0.04x	0.7 mR/h
$Cu^{63}(n,2n)Cu^{62}$	12.8 h	1.3 MeV	0.06 mR/h

TABLE 2 - Activation of cryopump structure

3.3.2 Liquid nitrogen

The reactions for N_2 and He are given in Table 3, the most relevant is the production of N^{13} (anihilation γ-ray, 0.5 MeV) with 9-min half-life time.

Table 3 shows also the calculated discharge

rates for the 250ℓ LN2 and 250 ℓ/h boil-off rate per cryopump. For 3 cryopumps the discharge will be still lower than the expected release of activated Torus Hall air of ∿ 5 x 10^{13} Bq/y. Therefore no measures are foreseen to handle the LN2 boil-off by a close loop with reliquefaction or by a retention system[5].

Note: With the half life of the N^{13} being 9 min, a retention of e.g. ∿ 1 hr would be sufficient to have the activity reduced by 10^3.

3.3.3 Liquid Helium

He^4 will not be activated by the neutron flux. However the production of tritium is possible by a He^3 (n,p) H^3 reaction which has a high cross-section for thermal neutrons. Assuming a concentration of He^3 in He^4 in the ppm range, a production rate of ∿ 2 Bq/gm y Tritium could be expected i.e. for the 150ℓ LHe cryopumpcontent 2 x 10^4 Bq/y.

Impurities have not been analysed as it is assumed that they will be frozen in the heat exchangers of the cryoplant and will not reach the cryopumps. Bulk impurities such as debris and swarf are retained by mechanical filters.

nuclear reaction	half life time	discharge
N^{14}(n,2n) N^{13} (β^+)* C^{13}	9.96 m	2.6 x 10^{12} Bq/y
N^{14}(n, p) C^{14} (β^-) N^{14}	5730 y	6.5 x 10^5 Bq/y
N^{15}(n, γ) N^{16}	7.4 s	4.1 x 10^7 Bq/y
He^4		
He^3(n,p) H^3 (β^-) He^3	12 y	2 x 10^4 Bq/y

*produces 0.5 MeV anihilation γ radiation

Table 3 Cryogenic boil-off activation

3.4 Radiation damage

The complete cryopumpsystems have been designed from the beginning to be compatible with the 10^8 rad dose rate, The materials were selected accordingly[6].

All control sensors are expected to remain fully operational under the expected radiation dose (10^8 rad), possibly with a slight performance change which may require recalibration. In addition, tests with 50 m long capillaries showed that the hydrostatic pressure capillaries can be extended into the radiation free cryogenic supply area and that this way the levels and pressures can be measured without radiation problems.

3.6 Remote Handling

The installation of the cryopumpsystem into the Injector Box has also already been designed in view of remote handling aspects:

- the cryopumpsystem does not need to be moved for access on any other Injector components and remains basically stationary inside the Injector Box.
- for the removal or installation of the cryopump, no pipe or cable needs to be cut or welded.
- the cryopumpsystem is sealed on the bottom of the Injector Box with a JET remote handling standard vacuum seal and the cryoline connection is a Johnson coupling also with a JET remote handling standard clamp (see Figure 3). Together with the flexible cryolines the disconnection of the cryolines and the removal at installation of the cryopump is fully compatible with remote handling.

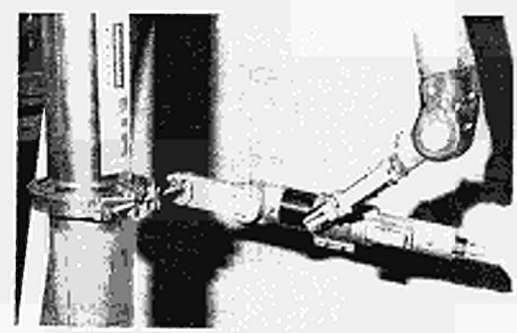

FIGURE 3 - Cryoline couplings

4. CRYOGENIC IRRADITION HAZARD

A series of serious explosions are known from literature which occurred when operating LN2 cryoloops under radiation conditions[7]. The reason for these explosions was traced to the

combination of irradiated LN2 or LO2 with organic materials or to the production of explosive ozone (ozone has a decomposition enthalpy of 708 cal/g compared to 1120 cal/g of TNT) from oxygen which either came from the residual oxygen content of the LN2 itself or direct from the atmosphere. (Note: the differences in boiling temperatures LN2:77K, LO2:90K causes enrichment of O2 in LN2 and also concentration of liquid O2 on LN2 cold surfaces). Therefore, access of oxygen to the cryoloops or insulation vacuum has to be eliminated and in some laboratories closed loops and tertiary containments are used in heavy radiation environments. The U.S. Atomic Energy Commission (AEC) defined ozone as a hazard and hence subject to a 25 mg limit.

At JET the following measures are taken in order to prevent the production of ozone:

- each liquid nitrogen delivery is controlled for oxygen content (specified < 5 ppm O2 content, typical sample 1-2 ppm). (Consumption of < 250 ℓ LN2/h gives < 80 g O2 for 1 week (150 h) operation.
- the injector vacuum is permanently monitored with a sensitivity of 10^{-7} mb for O2 partial pressure. The ∿ 10^{6} ℓs^{-1} pumping speed for O2 of the crypumps gives a sensitivity of 10^{-1} mbℓs^{-1} O2. Over a typical period of 10 h (daily regen.) < 5g of O2 would be condensed. The possible Ozone production under the above quoted conditions has been evaluated based on [8] and was found negligible. Further investigations are under way.

5. TRITIUM

5.1 Tritium Inventory, limits and flows

The cryopumped D/T is kept on the cryopumpsurface in a releasable form. The radiological safety limit at JET is set to 10 g Tritium.

There is also a limit of cryocondensed D/T due to the capacity of the JET Active Gas Handling System (AGHS) (rated for batches of 2000 bar l hydrogen isotope mixture).

The D2 load in the Neutral Injection System is typically 2.5 bar l for a 10 sec pulse. One day of operation accumulates with 40 pulses 100 bar l D2. The T2 flow from the Torus through the closed fast shutter has been evaluated to 1.2 mg and 4 mg per pulse with and without disruption respectively, which results in 40 and 160 mg respectively per day. The flow of D/T from the Torus with the fast shutter open would be ∿ 110 mbℓ per pulse(∿ 50% T2). The flow of T2 from the reprocessed D2 feed with 0.25% T2 content is ∿70 mg per day for one NI system (All data for 40 pulses/day).

The H2 load of the Pellet Injection could be as much as 5000 bar l H2 per day and will probably require one or more regeneration cycles per day due to the limited AGHS capacity.

A Neutral Beam Injector for Tritium would require T2 for the neutralizer gas and a total Tritium flow of 1.7 bar l (=450 mg) will be discharged to the cryopumps over a 10 s pulse. 20 pulses/day yields a total load of 9 g T.

5.2 Tritium release

The release of Tritium to the atmosphere via cryogenic relief valves or rupture discs is a potential hazard which could occur in case of a major leak in the LHe or LN2 loop inside the Injector box. A fast acting relief valve connecting the Injector to the JET EDS system[8] and a pressure control relief valve for the cryo boil-off with a higher set point is foreseen in order to avoid the release of Tritium via the cryogenic boil-off loop.

5.3 Tritiation of water

The liquid nitrogen cooled surfaces of the cryopumpstructure are able to pump/trap certain amounts of Tritium. A amount of < 30 mgT (300 G') could be trapped on the LN2 shields of a JET cryopump (all will be released at ambient temperature). Investigations have started to what extent this Tritium could - by isotope exchange with water residues on the LN2 panel surface - become transformed to tritiated water which may only be released by proper baking.

The implication of water leaks with regenerated tritium inside the Injectors are another item under investigation.

5.4 Thermal load from Tritium decay

The decay of the condensed Tritium will cause additional heat load to the LHe-loop. The decay rate of $6 \times 10^{-6}\ h^{-1}$ and 5.4 keV per decay gives a heat load of Q = 0,13 W per gramm T.

Even for a Tritium injector with ≤ 9 g T inventory on the cryopanels, the heat load will be < 2 W which is small compared with the 100 W cryogenic power allocated per cryopump system.

6. CONCLUSION

In the D/T phase of JET a neutron yield of up to 10^{20} n per 10 sec shot (10^{19} n/s) and total 10^{24} neutrons over the total period can be expected. The neutron flux at the cryopump has been evaluated to be less than 4×10^{9} n/cm²s. The cryopump systems have been designed for maximum weight and minimum LHe and LH2 content in order to minimise the effects of radiation. The nuclear heating of the cryopump structure and the bulk LHe and LN2 is acceptable. The activation of the structure will produce a dose rate of ∿ 50mR/h and calls for remote handling. The installation of the cryopumps is compatible with remote handling and the supply philosophy (control from central distribution, no valve or control in Torus Hall) minimises remote handling requirements. The activation of the LN2 boil-off is low enough that it can be discharged into the atmosphere.

The effects of Tritium on the cryopump require at least daily regeneration, the release of Tritium out of cryogenic safety devices in case of a cryogenic leakage has to be avoided and the tritiation of cryocondensed water on the LN2 cooled radiation shields is being assessed.

ACKNOWLEDGEMENT

The author's thanks to A. Avery (Winfrith AEA) for the provision of the activation and nuclear heating data and many helpful discussions.

REFERENCES

1. W. Obert, 'Cryogenics of the Joint European Torus (JET) and the Next European Torus (NET)', Proc. 12th Inter. Cryogenic Engin. Conf., ICEC 12, Southampton (1988).

2. W. Obert et al., 'The JET Cryopumpsystem and its Cryolines for Neutral Injection', Proc. 13th Symp. on Fusion Technol., SOFT 13, 1984.

3. A. Avery, Atomic Energy Establishment, Winfrith. (private information).

4. W. Obert 'Updated Peak Load Analysis for JET Cryosystem He Panels', Internal JET Report, CSNI C(83)1, PDN 17, Issue 2.

5. G. Pinter 'Cryogenic Retention System for the De-Activation of Nitrogen', Proc. IEEE 10th Symp. on Fusion Engineering, Philadelphia, Pa, 1983.

6. M.H. van der Voorde and C. Restat, 'Selection Guide to Organic Materials for Nuclear Engineering, CERN Report 72-1, 1972.

7. W. Obert 'Cryogenic Safety Problems due to Radiation Effects', Int.JET Report JDN/C(80)26.

8. J.D. Gault et al., 'Ozone Formation by the Radiolysis of Liquid Nitrogen: Calculation and Measurement', Nuclear Safety, Vol. 14, No. 5, Sept. - Oct. 1973.

9. M. Wykes, Torus Overpressure Protection in D-T, JET Internal Report, CM 406.

PROTOTYPE OF A HIGH SPEED PELLET LAUNCHER FOR JET

K. SONNENBERG, P. KUPSCHUS, J. HELM, D. FLORY and F. ZACCHIA

JET Joint Undertaking, Abingdon, Oxfordshire, OX14 3EA, UK.

JET is planning to build a high speed prototype pellet injector capable of delivering single D_2-ice pellets, one per plasma pulse, with a velocity of up to $5 kms^{-1}$. The prototype will be based on a 2-stage gun system which is presently being developed at JET using a test stand. One gun of the teststand will be transformed into the prototype used at the torus.

Earlier tests have shown that D_2-ice pellets can only sustain peak accelerations of $\approx 5.10^6 ms^{-2}$ without breaking and that they suffer from an erosion effect in the barrel limiting the pellet velocity to about $2.7 kms^{-1}$. Results are presented proving that these problems can be overcome by accelerating the ice in a protective sabot (cartridge). With this method velocities of up to $3.8 kms^{-1}$ have been obtained. The sabot technique, however, requires a separation of the sabot from the pellet before this is injected into the plasma. Three possible separation methods are described and experimental results of one of them are presented. Also improvements of the gun are discussed which allow to operate the gun by remote control.

1. INTRODUCTION

Present JET results employing a conventional pellet injector strongly suggest that deep fuelling does improve the plasma performance by generating peaked plasma profiles, by reducing the impurity content and by a better plasma confinement [1]. Deep fuelling, however, is only possible into relative cold plasmas. JET is therefore developing injectors which can accelerate pellets to much higher velocities than conventional guns. This will allow us to study deeper fuelling also for hotter plasmas. To overcome the basic problem of conventional pneumatic guns - namely the use of propellant gas at room temperature which limits the maximum speed to $\approx 2 kms^{-1}$ - JET will employ the 2-stage gun principle [2].

As a first step JET plans to build a high speed prototype injector capable of delivering one single pellet of about 5mm diameter with a velocity of up to $5 kms^{-1}$ into each plasma pulse. A major design goal is the reliability of the gun components to avoid their frequent replacement which is a typical drawback of conventional 2-stage gun systems. In order to solve these technical problems and to find the optimal gun parameters a teststand has been set up at JET, from which the prototype pellet injector will emerge.

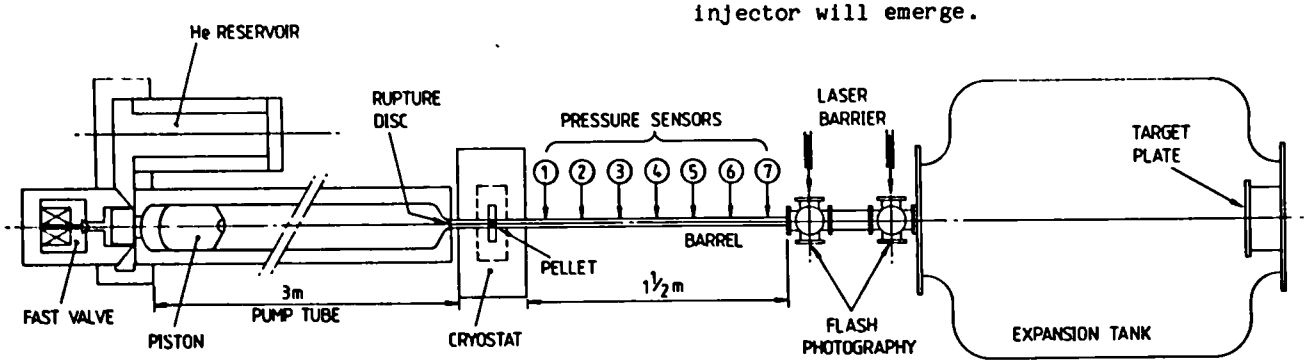

FIGURE 1: Schematic diagram of the teststand

2. TESTSTAND FOR THE JET-PROTOTYPE INJECTOR

The teststand consists out of:

- a 2-stage gun system
- a cryostat for pellet production and
- diagnostic systems to measure the velocity, acceleration, size, shape and flight path of the pellet.

For the 2-stage gun pump tubes of up to 3m length and inner bores of 50, 60 and 80mm diameters can be operated up to a peak pressure of 3500 bar. For the driving of the piston the pump-tube is connected to a high pressure (250 bar, 3.5l) Helium reservoir via a fast valve. For optimizing the acceleration of the pellet a rupture disc can be installed at the rear end of the barrel or a rupture collar on the sabot can be employed. The useful length of the barrel is limited by the pressure drop of the propellant gas in the barrel due to the gas expansion, friction in the gas and the heat losses to the barrel. Under the present conditions the maximum useful length of the barrel is 1.5m.

The design of the 2-stage gun is governed by the main goal of increasing the temperature of the propellant gas as far as possible. The restraining factors can be qualitatively described in the following way: The temperature increase is determined by the compression ratio of the propellant gas (ratio of peak and initial pressure). Unfortunately, the peak pressure on the one hand is being limited to a certain degree by the strength of the pellet and on the other hand the initial pressure cannot be reduced below a certain value which is determined by volume of the pump tube. This is due to the fact that sufficient propellant gas must be available to fill the barrel with a high pressure and in addition leaving enough gas in the pump tube so that the piston can safely be reflected on a gas cushion. It is therefore advantageous to increase the volume but preferentially by increasing the length of the pump tube, since a large cross-section creates problems for the gas flow from the pump tube into the barrel. Another reason for keeping the initial pressure reasonably high is to achieve a long pressure pulse (Δt longer than the acceleration time of the pellet) which is mandatory to keep the propellant pressure in the barrel as constant as possible. Fortunately the pressure pulse can also be lengthened by increasing the mass of the piston ($\Delta t \sim M^{0.5}$) and by using longer pumptubes ($\Delta p \sim L$). For practical reasons the length of the pump tube has been limited to 3m.

The main diagnostic systems are pressure sensors positioned along the barrel. From the sudden pressure rise the time can be determined when the pellet passes the sensors[4]. This allows to calculate the pellet velocity and acceleration as a function of time. It is interesting to note that the value of the sudden pressure rise appears to represent the driving pressure or acceleration, respectively for the pellet. This is only possible if the friction between the barrel and the pellet is negligible as compared to the propellant force. The size and shape of the pellet is determined by flash photography of the pellet. From the imprint the pellet leaves on the target plate at the rear flange of the expansion tank the reproducibility of the flight path of the pellet as well as the degree of separation of the pellet from the sabot can be found.

3. ACCELERATION OF D_2-ICE PELLETS BY 2-STAGE GUN

a) Two stage gun systems have proven their potential in the past to accelerate plastic pellets up to 10 kms^{-1}[2]. In order to achieve such velocities, very high acceleration values ($\approx 10^8 ms^{-2}$) have been employed. In comparison due to the much lower strength only about

$5.10^6 ms^{-2}$[4] can be applied to D_2-ice pellets without breaking them.

Another problem is that D_2-ice pellets suffer from a strong erosion effect when moving at high velocities through the barrel. As shown earlier[4] the erosion is due to friction between the barrel and the pellet stripping off and evaporizing outer layers of the pellet. Friction and erosion have two implications on the acceleration of D_2-ice:

- the ice is being softened and
- the barrel provides less guidance for an eroded pellet.

As a consequence the peak acceleration tolerable further into the barrel is much smaller ($\approx 2.10^6 ms^{-2}$) than during the initial phase of the acceleration.

D_2-ice pellets are also very prone to damage by shock waves which are generated by rupture discs, which therefore cannot be employed to optimize the pellet release pressure.

The maximum velocity which has been reached because of these difficulties for a D_2-ice pellet is $2.7 kms^{-1}$.

b) Sabot supported D_2-pellets

In order to overcome the problems caused by erosion, shock sensitivity and the limited strength of the D_2-ice plastic sabots as shown in Figure 2 have been employed. For the present cryostat it is, however not possible to use "closed" sabots (2a) because the heat transfer from the ice to the cryocell is insufficient leading to a poor quality of the ice. By improving the heat transfer through slots in the wall of the sabot ("cage type", 2b) good results have been achieved. It was possible:

- to improve the resistance against shock waves so that rupture discs can be used for optimizing the release pressure
- to increase the maximum acceleration which is tolerable without breaking the pellet to $8\text{-}9.10^6 ms^{-2}$. As a result a maximum velocity of $3.8 kms^{-1}$ has been reached.
- due to the slots in the sabot erosion cannot be avoided.

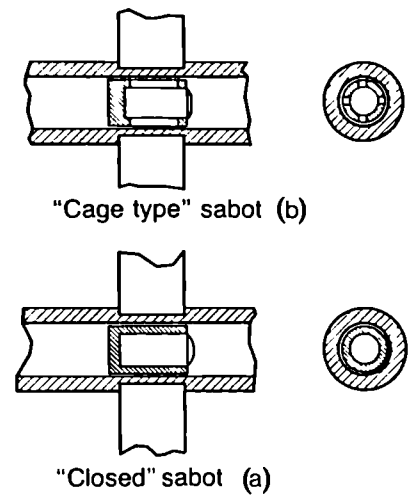

FIGURE 2
Sabot types

In order to obtain a better support for the D_2-ice pellet a new cryostat has been built in cooperation with the CEN in Grenoble. In this cryostat the ice can be produced outside the sabot and both pellet and sabot can be joined together afterwards. This will allow the use of "closed" sabots.

c) Sabot-Pellet separation

The principle method shown in Figure 3 is to use a split sabot both halves of which are radially separated by an internal pressure and caught by a conical anvil positioned in front of the entrance tube for the D_2-pellet.

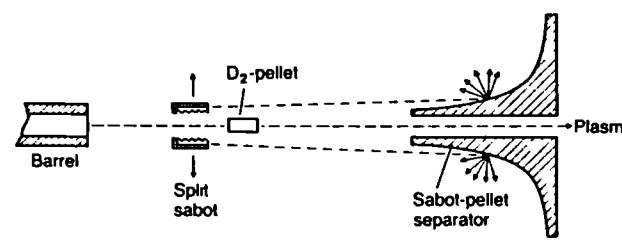

FIGURE 3
Sabot pellet separation

We are developing 3 methods for generating the internal pressure to separate the sabot halves radially

i) for the "cage type" sabot the pressure generated by the erosion effect could be sufficient.

ii) positioning an E.M. coil at the muzzle of the barrel an eddy current would be induced in a metal film deposited on the inner surface of the plastic sabot. The eddy current heating of the metal layer in turn will heat and evaporize a thin layer of the D_2-ice to generate the pressure for separation.

iii) by shaping the rear end of the sabot as shown in Figure 4 the propellant gas can be employed for splitting the sabot.

FIGURE 4
Different sabot shapes for the third method

In Figure 5 a result of the third method is shown for plastic pellets. The photo is taken about 50cm in front of the muzzle. A separation of about 1.5-2° has been achieved. The reproducibility of the pellet trajectory is about ±10'.

4. IMPROVEMENT OF GUN PERFORMANCE

a) There are two aspects for improving the gun performance.

i) to allow higher pellet velocities and

ii) to develop the 2-stage gun toward repetitive and remotely controlled operation.

i) The first aspect is associated with reducing the pressure drop along the barrel which is due to expansion,

FIGURE 5
Sabot-Pellet separation

internal friction and heat losses of the gas. The most effective way of reducing the pressure drop is to employ preheated gas, which would result in much higher gas temperatures and gas velocities after the adiabatic compression. The technical problems for preheating the gas are however difficult to overcome and it cannot be implemented for the prototype. Other measures, in particular to reduce the heat losses of the gas, are also being studied. For example the change to stainless steel as a barrel material with a much lower heat conductivity as compared to normal steel, has reduced the pressure drop in the barrel. Although this had no dramatic effect on the pellet velocity the pressure increase at the muzzle of the barrel was sufficient to improve the separation of the sabot.

ii) A precondition to build a repetitive gun is to avoid replacements of gun components after each shot. This is particularly important for rupture discs which are used to separate the pressure reservoir and the pellet from

the pump tube. The first has been substituted by a fast valve [5]. The rupture disc between the pump tube and the pellet which allows to optimize the release pressure of the pellet will be replaced by a sabot with a rupture collar.

Another problem is to avoid damage of the piston upon its impact onto the front face of the pump tube and due to friction between the wall of the pump tube and the piston. The first problem can be solved by selecting pressure parameters which allow to reflect the piston softly on a gas cushion at the front end of the pump tube. To keep this gas cushion effective at least as long as the piston is oscillating in the pump tube the propellant gas must be trapped in the barrel and cylinder until the piston comes to rest. For this purpose it is foreseen to employ a fast plug valve at the muzzle of the barrel which can be quickly closed after the pellet has left the barrel.

It appears that damage of the piston due to friction can be avoided by employing centering forces generated by the gas flow if the piston is properly shaped and the gap between the piston and the wall is optimized. Also low friction coatings of the piston and glide rings are used to increase the lifetime of the piston. Even without taking all these precautions pistons have survived up to 50 shots, almost sufficient for operating the prototype gun.

5. CONCLUSIONS

- D_2 ice pellets must be supported by sabots to allow higher acceleration values, to avoid erosion and to increase the shock resistance. So far only "cage type" sabots could be employed. Nevertheless it was possible to increase the peak acceleration by about a factor two and to improve the shock resistance. As a result pellet velocities of up to 3.8 kms^{-1} have been reached. Higher velocities can be expected if pellets in closed sabot can sustain higher acceleration still.
- several methods are being studied to separate the sabot from the pellet. One has already been tested successfully.
- progress has been made to improve the gun performance with regard to higher pellet velocities and towards a remotely controlled operation. Pistons have been developed which survive many shots and rupture discs have been substituted by fast valves.

REFERENCES

1. P. Kupschus, G. Schmidt, A. Gondhalekar, to be published.
2. A.E. Seigel, NATO Report, AGARDS$_1$.
3. J. Lafferanderie et.al., Proceedings of 14th SOFT, Avignon, France, 8-12 September, pp. 1367.
4. K. Sonnenberg et.al., Proceedings of 12th SOFE, Monterey, California, 13-16 October 1987, Vol. 2, pp. 1207.
5. K. Sonnenberg, to be published.

CONDITIONING OF THE JET NEUTRAL BEAM SOURCES

H D Falter, G H Deschamps, R S Hemsworth, P Massmann

JET Joint Undertaking, Abingdon, Oxon, OX14 3EA, England

The JET beam sources require several hundred beam pulses for conditioning up to 80 kV or 160 kV. Once conditioned, only some 30 pulses are required to recondition the sources after a shutdown of several weeks with the beam sources vented with atmospheric air. Conditioning with low currents by using argon beams results in a source which is also conditioned for deuterium beams.

1. INTRODUCTION

The beam sources for the JET Neutral Injectors operate at present at 80 kV 60 Amps with hydrogen beams and 80 kV 41 Amps with deuterium beams. In a second stage the sources will be modified to operate at 140 kV 30 Amps in deuterium using a three grid accelerator instead of the four grid system used at present for the 80 kV operation. Finally, during the active phase of JET, it is foreseen to operate one injector with tritium beams at 160 kV 30 Amps.

The beam sources must be conditioned before they can be operated successfully at full voltage and current. The JET beam sources were initially tested by Culham Laboratory [1] in the case of the 80 kV sources. The CEA in Fontenay aux Roses modified, tested, and conditioned one prototype source to 160 kV [2]. Most of the 80 kV sources for the second JET injector and all the production 140/160 kV sources have been or are being conditioned in the JET Neutral Beam Test Bed.

2. ACCELERATOR OF THE JET BEAM SOURCES

The 80 kV JET beam sources use multi-aperture grids with grid spacings of 3.5 mm between the plasma grid and the gradient grid and 7.5 mm between the gradient grid and the suppressor grid (Fig.1). The voltages of the grids are typically 80 kV for the plasma grid, 72 kV for the gradient grid and -2.5 kV for the suppressor grid, yielding electrical gradients of up to 10 kV/mm. The grids are made from electrodeposited copper with integrated cooling channels around the apertures. The surface areas of the grids are of the order of 0.1 m² each side. The grids are supported with alumina post insulators inside the vacuum.

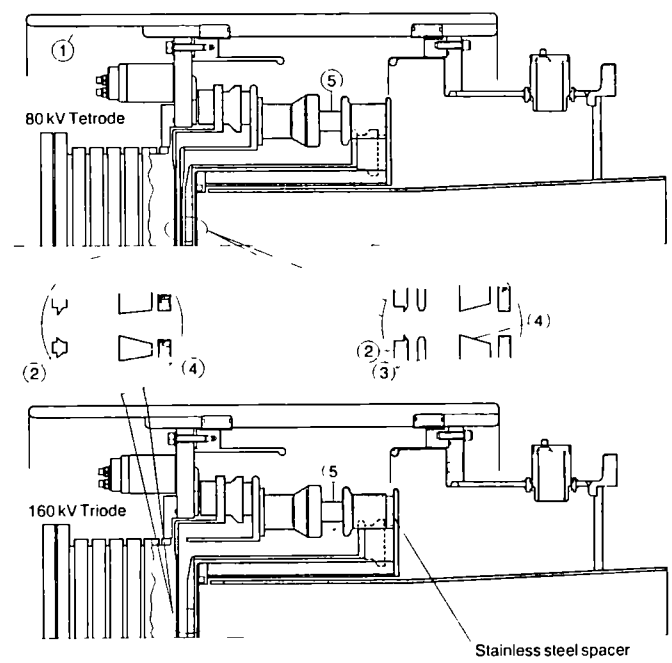

Fig.1: Cross section through the 80 kV and 160 kV grid assembly showing the main insulator (1), the plasma grid (2), the gradient grid (3), the suppressor grid (4), and the post insulators (5)

In the case of the 140/160 kV beam sources the gradient grid is omitted and the spacing between plasma grid and negative grid increased to 27.2 mm. This reduces the maximum electrical gradient to 5.88 kV/mm.

3. CONDITIONING OF THE JET BEAM SOURCES

3.1 Conditioning procedures

As for most neutral injection systems, the high voltage is supplied from a power supply with a tetrode switch at the output. If an over-current is detected, the high voltage is switched off for a predetermined time of typically 50 ms, as Fig.2 shows. At the beginning of the fast turn off and before the re-application of the extraction voltage the arc current of the plasma source is also turned off for typically 1 ms.

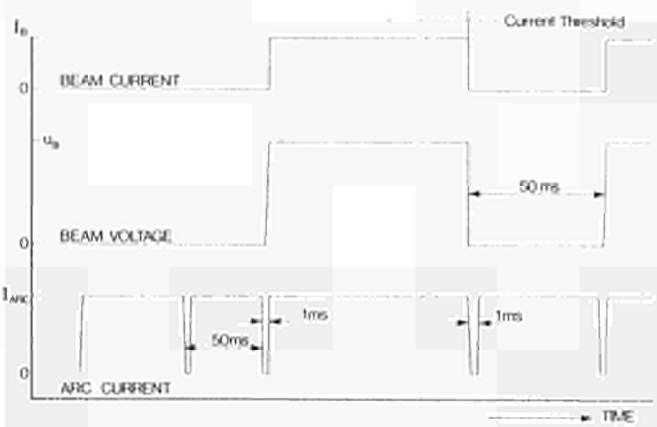

Fig.2: Schematic timing sequence of a beam pulse with a re-application of the extraction voltage.

Conditioning normally starts at a voltage of 30 kV in case of the 80 kV beam sources and 50-60 kV for the 140/160 kV beam sources. Initially the 80 kV beam sources are conditioned to approximately 60 kV, where the first characterisation of the source is carried out, defining the alignment and the perveance. This requires that the beam sources are running with a reasonable ratio between beam-on time and time lost from breakdown/re-application as the data are mainly derived from thermal diagnostics After the initial characterisation, the conditioning continues either up to the design parameters of the beam sources or to the limit set by the condition of the power supplies. At the end of the conditioning the sources are operated at the established voltage and current for typically 100 pulses with 90-95% of beam-on time per pulse. Fig.3 shows, how the voltage can be increased with an increasing number of beam pulses for two different sources. One of the beam sources was conditioned with the so-called "procedure II" in which the voltage is increased in steps of 2.5 kV if the beam is on for more than 80% of the attempted time in three out of five consecutive pulses. A more aggressive "procedure I", increasing the voltage by 5 kV if the beam-on time is above 50% of the attempted pulse length, was used for the other source.

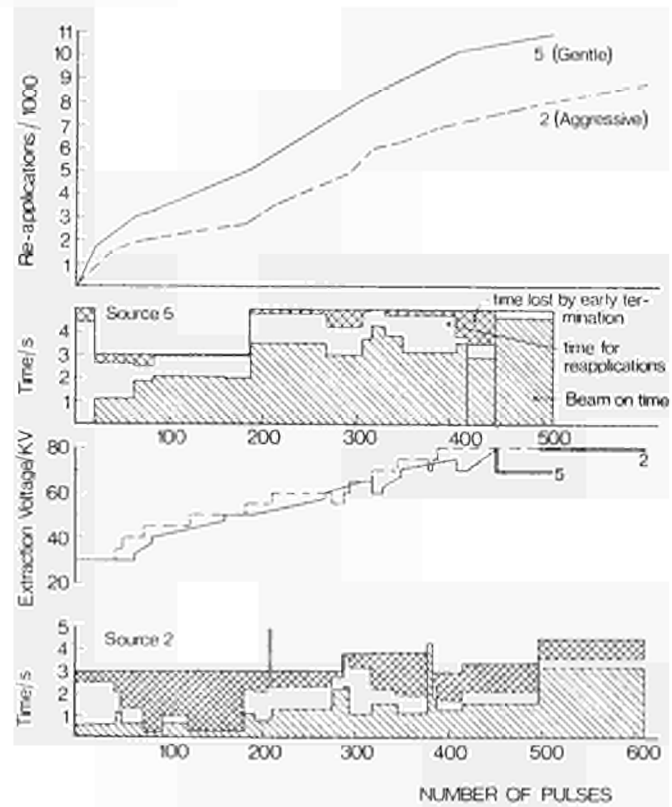

Fig.3: Voltage and number of re-applications as a function of the pulse number for two 80 kV sources with different conditioning procedures. Also shown are the average on time per pulse, time for re-applications, and time lost by early pulse termination.

3.2 Comparison of the conditioning procedures

The data shown in Fig.3 show that the gain in voltage with an increasing number of pulses is very much the same for both conditioning procedures. The gentle procedure II achieves a considerably higher beam-on time, but also a higher number of re-applications. The aggressive procedure I results in a high proportion of lost time due to early terminated pulses (power supply problem). So far it cannot be concluded whether this is compensated for by a more rapid conditioning with procedure I, or by a beam source which is easier to condition. Table 1 and Fig.4 give data from three more beam sources, confirming that the difference between the sources masks any difference in the success of the conditioning procedures. In both procedures the beam-on time improves considerably if the voltage is reduced by 5 kV, demonstrating the benefit of "overconditioning".

Table 1

Speed of conditioning for five 80 kV beam sources, with the number of re-applications required to get the first measurable beam at 30 kV, the number of re-applications, and the beam-on time required to establish good pulses at 60 kV.

BEAM SRC.	BEAM AT 30 kV	GOOD BEAM AT 60 kV			PROC
	re-app.	re-app.	on-time	pulses	
2	270	500	250	300	I
5	1700	7200	590	270	II
9	100	1200	130	80	I
15	0	700	140	65	II
A	366	3500	404	130	II

The history of the various beam sources prior to the conditioning is shown in Table 2.

All the beam sources conditioned with procedure II (5, 15 and A) had at least some new grids. The beam sources conditioned with the aggressive procedure I all had already conditioned grids, which had been flooded during water accidents and handled during refurbishing of the sources.

Beam source 15, which conditioned very easily, was completely new, showing that new grids need not be more difficult to condition than used ones.

Table 2

Status of the 80 kV beam sources prior to the conditioning.

BEAM SRC.	STATUS BEFORE CONDITIONING
2	Preconditioned beam source, flooded with water, grid hoses replaced, grids handled
5	New grids
9	Pre-conditioned, flooded with water, post insulators replaced, grids handled
15	New beam source
A	Old prototype, rebuilt with welded joints instead of bolted joints, one half of the plasma grid new

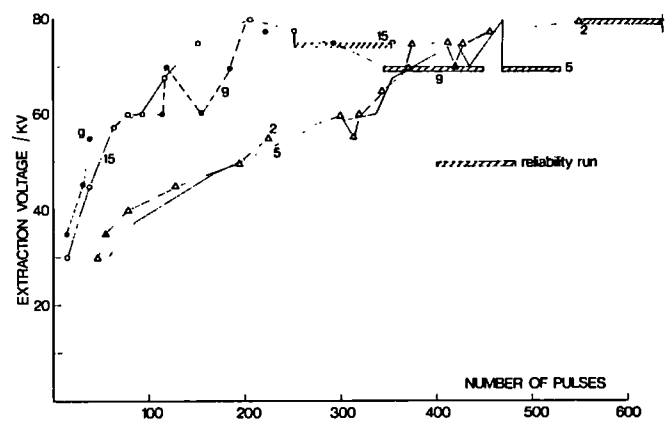

Fig.4: Conditioning of four 80 kV beam sources using procedure I (2 & 9) and procedure II (5 & 15).

3.3 Reconditioning after venting

Table 3 gives the time required for reconditioning the beam sources of one JET injector after a maintenance period of several weeks during which the beam sources were vented with atmospheric air. Typically 40 beam pulses of 0.75-1.0 s duration were required to bring the sources up to full performance. Only source N°5

Table 3

Source	Pulses	Voltage	On-time
8	30	80 kV	> 90%
11	20	80 kV	> 80%
5	60	80 kV	> 60%
6	40	80 kV	> 80%
7	40	80 kV	> 80%
2	50	80 kV	> 80%

The first column gives the number of the source, the second the number of pulses required on the injector to achieve the operating voltage and the beam-on time of the third and fourth column.

which was difficult to condition initially, needed longer. Hardly any reconditioning is necessary when the system is kept under vacuum over the weekend.

3.4 Conditioning with a heavy gas

The extracted current at perveance match is proportional to $1/\sqrt{M}$ with M being the mass of the extracted ions. Operating the sources with a heavy gas, for example argon, reduces the extracted current at perveance match considerably. This is of interest for operation at 160 kV with tritium beams. The same source as used for 140 kV deuterium operation will be used unchanged for 160 kV tritium operation. The conditioning from the operating level of 140 kV with deuterium to 160 kV could be done with argon beams thus avoiding the high power loadings on the ion dumps with deuterium beams and the gas (T_2) consumption with tritium beams.

Fig.5 shows the conditioning history of beam source A, which was conditioned up to 60 kV with hydrogen beams, between 60 and 80 kV with argon beams, and then operated at 80 kV with deuterium beams.

Initially 150 pulses with 4,000 re-applications were needed to condition the source to 60 kV with hydrogen beams. Changing to argon, a further 80 pulses without plasma in the plasma source (hence no extracted beam) and with increasing gas flows were required before the system could withstand 60 kV. From there conditioning with argon beams started. (The necessity for this 'gas conditioning' is unexplained.) The voltage could be increased to 80 kV within less than 200 pulses and less than 6,000 re-applications, but the actual beam-on time per pulse was only of the order of 3 seconds out of the attempted pulse length of 5 seconds. This improved after the gas flows through the plasma source and the neutraliser were changed to a lower flow through the source and a

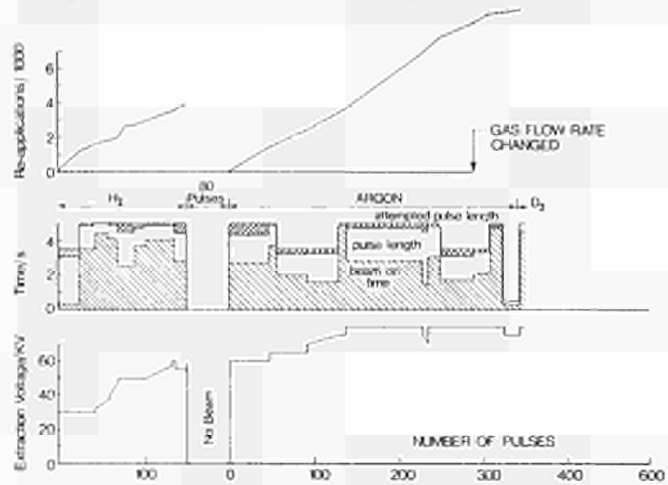

Fig.5: Conditioning history of a beam source conditioned with hydrogen beams to 60 kV, with argon beams from 60 to 80 kV and then with deuterium beams at 80 kV.

higher flow through the neutraliser. This indicates, that the pressure between the grids had been too high. A few pulses after the gas flows had been changed the beam-on time increased to some 90% of the attempted time.

Changing from argon beams to deuterium beams resulted straightaway in good pulses at 80 kV and beam currents up to 41.5 Amps, which corresponds to the beam current at perveance match. This demonstrates that conditioning in argon is successful. With more experience in running argon beams it is very likely that the conditioning would be faster than shown in Fig.5.

4. Conditioning of the 140/160 kV sources

For the 160 kV operation two of the 80 kV high voltage power supplies are connected in

series [3] feeding two beam sources of 30 Amps each. So far 5 140/160 kV sources have been installed in the Test Bed. Only one source has actually been conditioned to 160 kV. The conditioning of the 160 kV beam sources has been frequently interrupted by problems with the power supplies, and no complete conditioning history is yet available for the 140/160 kV sources.

Fig.6 shows the partial conditioning of two sources. We see again, as in the 80 kV cases, that the conditioning is quite fast at lower voltages, followed by a slower rate of rise above 100 kV of approximately 0.1-0.25 kV per pulse. This suggests, that another 100-200 pulses would be sufficient to condition the source to 140 kV. Within the even more limited data of the second source the same behaviour is seen.

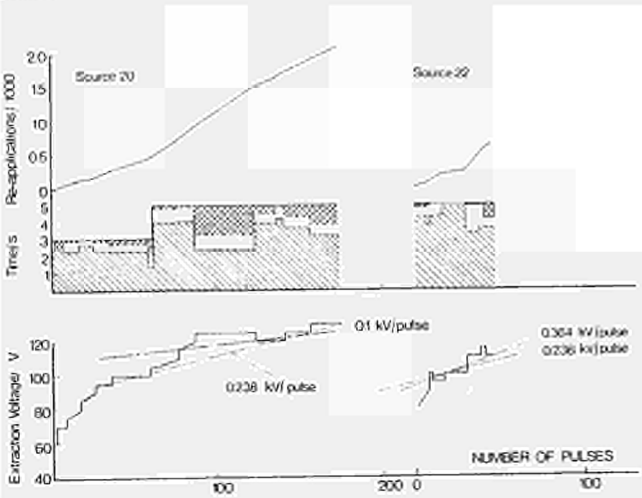

Fig.6: Partial conditioning history of two 160 kV beam sources.

In the case of the 140 kV sources we have again seen that the effective pulse length drops below the attempted pulse length if the conditioning is more aggressive. Within the limited data available there is no sign that more re-applications (breakdowns) speed up the conditioning process.

5. Discussion

The conditioning procedures used in this paper appear to be comparably successful. The aggressive procedure puts much more strain on to the power supplies. In our case this causes lost time due to an early termination of the pulse and might contribute to hardware failures, and the gentle procedure appears to be more attractive. In the case of the 160 kV beam sources we already have sufficient power supply problems with the gentle procedure and could not compare the two procedures. However the gentle procedure appears to give a reasonable rate of conditioning.

Argon beams have been used successfully for conditioning an 80 kV beam source. This is interesting for applications with tritium beams at 160 kV, when the beam sources will have been conditioned to 140 kV with deuterium beams. Using deuterium above 140 kV would overload the power supplies and the beam dumps, due to the mass dependence of the perveance match current.

ACKNOWLEDGEMENT

We thank Dr T T C Jones from the JET Neutral Beam Operations Group for providing the data for the reconditioning discussed in 3.3.

REFERENCES

1. T Green, Performance Data for the 80 keV Injectors for JET, Proc 13th SOFT, Sept 1984, Varese, Italy, pp 693-702.

2. M Fumelli et al, Operation of a 160 kV 30 A Deuterium Neutral Beam Injector, Proc 13th SOFT, Sept 1984, Varese, Italy, pp 617-621.

3. P L Mondino et al, Design, Commissioning and Early Operation of the Power Supply and Protection System for the Extraction Grid of the JET Neutral Injectors at 160 kV, Proc 14th SOFT, Sept 1986, Avignon, France, pp 933-939.

THE JET HIGH TEMPERATURE IN-VESSEL INSPECTION SYSTEM

T BUSINARO, R CUSACK, L GALBIATI, T RAIMONDI

JET Joint Undertaking, Abingdon, Oxfordshire, OX14 3EA England

The JET In-Vessel Inspection System (IVIS) has been enhanced for operation under the following nominal conditions: vacuum vessel at 350°C; vacuum vessel evacuated (~ 10^{-9} mbar); radiation dose during D-T phase 10^{8} rads. The target resolution of the pictures is 2 mm at 5 m distance and tests on radiation resistance of the IVIS system are being carried out. Since June 1988, the new system is installed in the JET machine and the first inspections of the entire vessel at 250°C have been satisfactorily done.

1. INTRODUCTION

Periodic inspections of the interior of the vacuum vessel have to be done to check for damage due to plasma disruptions. A system was developed to scan the vessel using four TV probes through small apertures in the top of the vessel without breaking the vacuum. A great effort of miniaturization was required to compress the optics and electronics into the small diameter available.

Another problem was to provide sufficient illumination, particularly since the vessel has been carbonized. The initial solution was to use high-energy flashlight and digital frame grabbers. The system was completely automatic, with microprocessor control. The vessel surface was divided into viewing areas and for each of these "named positions" the orientation, viewing and light parameters were optimized and stored on disc. The operator calls up the named positions using a keyboard or mimic diagram and the camera is pointed at the desired location with aperture, focus and flash intensity as previously chosen. In this way a series of photos are taken and can be stored on disc or tape for comparison with previous shots. Digital filters are used to enhance contrast and reduce flickering. However, even increasing the sensitivity by integrating successive flashes, the image obtained of the inner part of the vessel remained hazy because direct light impinging on the viewing glass is scattered inside it.

Recently considerable improvements have been made. Some more penetrations were made available to provide continuous lighting. Four vacuum-tight assemblies of silica light guides are illuminated by small powerful purpose designed projectors sited above the penetrations. A drawback of the original system was that the vessel had to be cooled down to below 50°C to do an inspection. After feasibility tests high temperature probes to be used at 350°C were designed and manufacture is now complete. The prototype was tested in a rig at 400°C. As with the previous model, space restrictions called for painstaking rearrangement of wiring and connectors to eliminate noise and faults. The zoom was eliminated to make room for the cooling jacket but with better lighting the system is expected to be quite satisfactory. The device is equipped with sensors to detect cooling water leaks.

If time and resources permit a study will be carried out on the feasibility of using prisms suspended in the vessel. This would obviate the optical problems connected with the cylindrical viewing glasses but would introduce others.

2. SYSTEM DESCRIPTION

1.1 Viewing probes

Each probe consists of a stainless tube terminating in a glass cylinder. The viewing probe, as shown in Fig.1, is lowered into the

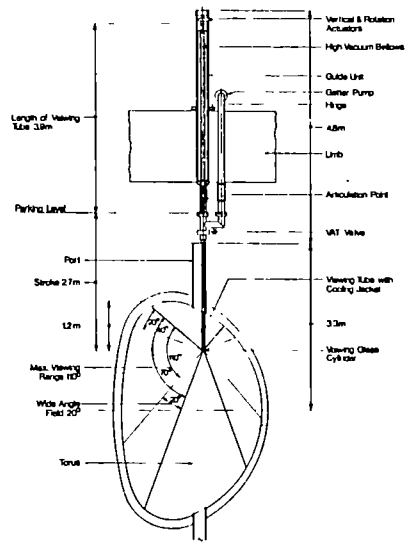

Fig. 1 Viewing Probe

vessel by a carriage driven along a guide unit which is suspended from the magnetic limb by means of a gimbal arrangement and centred with the top of the port using a hinge connection. This method of suspension allows the guide unit to comply with the thermal deformation of the vessel. The viewing probe itself is centred with the top of the port by flexible phosphor-bronze "fingers" to allow self alignment of the probe during insertion and reduce shocks due to vibrations of the port. Long vertical bellows, with 6:1 compression ratio, allow for the vertical stroke of the carriage while forming a vacuum barrier. A separation valve between guide unit and vacuum vessel is opened to insert the viewing probe after checking that the vacuum in the IVIS system matches that of the vessel.

Inside the long stainless tube a coaxial water cooled jacket has been provided to protect a high sensitivity black and white camera situated on the lower part of the probe, as well as its lenses and the motorised mechanisms for controlling iris, focus and prism tilt, from the heat radiated from the vessel wall (see Fig.2).

An external mechanism allows the cooling jacket with the camera to rotate inside the viewing cylinder. The resulting tilt and rotation of the prism allows a whole quadrant of the vessel

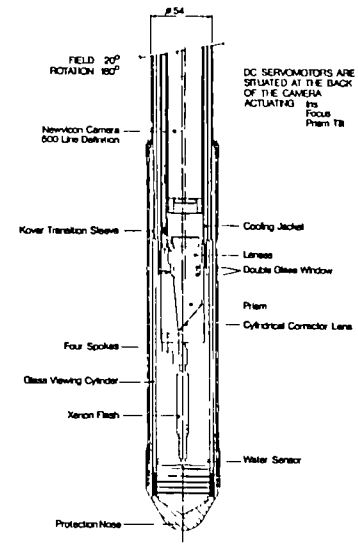

Fig. 2 Viewing Probe (Detail)

to be explored from any of the viewing positions. A flash tube, fitted at the end of each viewing probe, provides additional powerful sources of light for darker areas for single shot pictures.

A detailed description of the optics and mechanical structure of the viewing probes is reported in [1].

2.2 The cooling system

The new viewing probes are able to operate at high temperature (up to 350°C) having been isolated from the vessel thermal radiation by coaxial water cooled jackets.

The cooling jackets, shown in Fig.3, consist of two concentric cryogenic tubes 4 m long and 38.1 and 44.4 mm in diameter. In the gap between them there are 22 cryogenic tubes of 3 mm in diameter, spaced at regular intervals. The cooling water flows from the top to the bottom of the cooling jacket inside the 22 small tubes and returns to the top through the space

between them. The thermal shielding has been designed for heat flow up to 2.5 KW/m².

In agreement with the design, the experimental results show that the cooling jacket keeps the working camera at less than 35°C with the entire probe fully immersed in an evacuated 4 m long oven at the average temperature of 350°C with an 18°C cooling water flow rate of 6 ℓ/min (see Table 1). While with this flow the resulting drop of pressure across the inlet and outlet hoses is only about 100 mbar, the cooling jacket is able to operate at 7 bar.

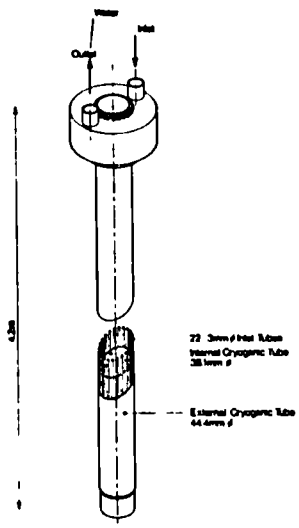

Fig. 3 Water Cooling Jacket

Furthermore, in order to reduce the heating of the camera lens due to thermal radiation coming from the front of the camera, a double glass window has been fitted between the prism and the lens and a cooling air flow (10 ℓ/min) is forced between the two glasses.

WATER FLOW RATE ℓ/min	PRESSURE DROP mbar	CAMERA TEMPERATURE °C		
		a)	b)	c)
6	100	30.5	32.5	34.5
9	250	27.5	29.0	32.0
12	500	26.0	27.0	30.0

Table 1

Camera Temperature vs Water Flow Rate at a = 12°C, b = 15°C, c = 18°C

2.3 Continuous lighting system

In addition to the flash fitted in each probe a new lighting system has been developed in order to provide a continuous high intensity light source during the in-vessel inspections. The design of this system had to consider requirements of maintenance (i.e, it should not require maintenance inside the vessel) and that the vessel wall geometry not be affected.

To solve those problems a retractable 25 mm diameter 1.6 m long fused silica light guide assembly has been used. It collects the light from a powerful compact mirror arc lamp (400 W) and diffuses it in the vessel when the system is inserted.

In this design, as shown in Fig.4, only the light guide assembly is permanently installed in the vessel, while the light source is mounted in the external accessible part of the tokamak. A

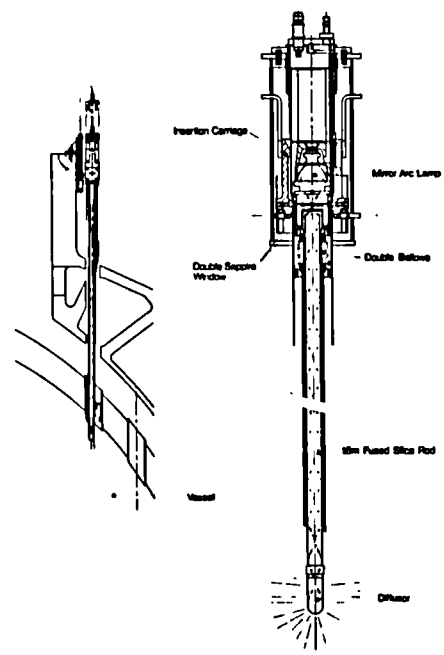

Fig. 4 In Vessel Lighting System

double bellows and double sapphire window system assures the vacuum seal of the vessel and the passage of the light into the silica rod. The penetration of the light guide in the vessel when needed, is done by a motorised trolley fitted on the top of the bellows that assures a

removable mechanical connection between the lamp unit and the light guide assembly.

The efficiency of this system depends mostly on the quality of the silica rods. Imperfections, scratches or bubbles in the light guide reduce the amount of light that reaches the bottom of the silica rod where a 65 mm length of very rough surface diffuses the light all around. Experimental measurements of illuminance at 1 m distance from the diffusor of the lighting system, using a 400 W arc lamp are shown in Fig.5. This lighting system is at present the subject of a patent application.

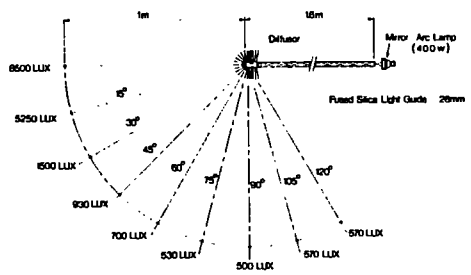

Fig. 5 Illuminance of Ivis Lighting System

3. GLASS VIEWING CYLINDER PROTECTIONS

In the present IVIS design the viewing cylinder is the most vulnerable part of the entire probe. Thermal stresses on the glass and undesirable mechanical shocks during inspections could cause the rupture of the viewing cylinder and consequently the failure of vessel vacuum seal and long delay to recover from it. Care was taken in the design in order to contain the thermal stresses in the glass particularly in the region of the welding with the metal tube. An intermediate Kovar collar whose thermal expansion characteristics are compatible with those of the borosilicate glass, had been used to join the viewing cylinder to the long stainless tube. Having assumed a linear thermal gradient from this welding of 100°C in 5 cm, a finite element calculation showed both compression and tension stresses on the glass of the order of 0.4 kg/mm^2, which compares to an allowable design tension stress for the borosilicate of 0.6 kg/mm^2, ten times less than the allowable compression stress. A metal nose pressed against the base of the glass cylinder by four spokes is used to protect the glass against rubbing on the vessel port. It also gives some benefit precompressing the glass, thus reducing the tensile stress.

Finally in order to prevent glass ruptures due to water leakages coming from the cooling jacket, a simple water sensor, based on measurements of electrical conductivity, has been installed at the bottom of the viewing cylinder.

4. RADIATION RESISTANT DESIGN

The new viewing probes (except the camera lenses) and the lighting system have been designed to be radiation resistant to withstand the above mentioned dose of 10^8 rads. To achieve that goal all components had been selected for that figure and tests on the entire system are being carried out.

Partial results of radiation test of the used TV cameras are reported on [2]. Temperature bleaching tests on the viewing cylinder show a recovery of 80% at 250°C after the glass was totally blackened by gamma exposure [3].

The fused silica rod light guides and sapphire windows of the lighting system are guaranteed by the manufacturers. The present camera lenses will be substituted with non-browning lenses during the D-T phase of the machine.

5. CONTROL ASPECTS AND OPERATION

The following movements are needed for each new probe: focus, iris, vertical stroke, prism tilt and rotation. Radiation resistant high quality miniature potentiometers have been used to provide a reference position. All movements are controlled by closed loop analogue circuits. Having continuous lighting, operations are much simpler then with the former system that had only flash light.

At present a provisional console with the aid

of PC graphics tools enables the operator to select the viewing points inside the vessel. Prism tilt and rotation are roughly shown on the PC monitor. The iris and focus are manually set in order to have the best pictures shown simultaneously on four black and white high quality monitors. If necessary a flash shot could be taken and the resulting picture grabbed for image analysis and enhancement.

6. PICTURE QUALITY AND OPTICS DRAWBACKS

In the present system good quality pictures could show a definition in the central region of up to 500 line which matches the target specification. Limitation in the quality is due to the aberrations introduced by the glass cylinder only partially corrected by an additional lens on the prism. Another drawback is glare in the glass which is particularly disturbing and strongly depends on the viewing angles.

As a result good pictures of the vessel floor and ceiling could be seen, as shown on Fig.6, taken at 250°C during the last inspection on 24.07.88, while the inner wall viewing remains partially affected by glare effects.

Fig. 6 Picture of Lower Part of JET Vessel Taken at 250°C

7. FUTURE ENHANCEMENTS

During the shutdown of the machine in July 1989 three new light units will be added to the present lighting system in order to improve the inner wall viewing. A rotating reflector will be also added on the silica rod diffusor to shadow the viewing probes from the direct light.

Feasibility tests will be carried out in order to substitute the viewing glass cylinder with a flat glass window. This solution, that requires fitting the prism in the vacuum, should solve all problem related to the glare and mechanical shocks to the glass cylinder, and will remove the optical aberrations with a strong improvement of picture quality. On the other hand problems such as the prism movements (tilt and rotation) in vacuum and at high temperature have to be solved.

A new man machine interface using advanced graphic work station will also be considered in order to facilitate the inspection.

ACKNOWLEDGEMENTS

Important contributions are acknowledged from:
Prof. W. Welford of Imperial College of London for the optics design; H. Watson and R. Govier of Culham Laboratory for the glass techniques; G. Dalle Carbonare (JET), for mechanical design of the lighting system.

REFERENCES

1. T. Raimondi, R. Cusack, L. Galbiati, "The JET In-vessel Inspection System", 14th Symposium on Fusion Technology, Avignon, France, 8-12th September 1986.

2. J. Quartly, "Television systems for inspection and maintenance in nuclear plant and the JET torus", American Nuclear Society winter meeting, Los Angeles, USA, 15-19th November 1987.

3. G. Viezzoli, "Optical behaviour of Kodial glass under irradiation and its recovery at high temperature", NET (TASK-RM3), doc. ENEA-TIB 7062(NET), Rome, 3rd June 1987.

OPERATIONAL EXPERIENCE OF JET SURFACE PHYSICS DIAGNOSTICS

C J Hancock, D Jakob[1], G F Neill, P Prior[2], C Nicholson,
A L Stevens and J Vince

JET Joint Undertaking, Abingdon, Oxon, OX14 3EA
[1]Arthur Pfeiffer Vakuumtechnik GmbH, Wetzlar, FRG
[2]GEC Energy Systems Ltd, Leicester, UK

1. INTRODUCTION

The JET Plasma Boundary diagnostics are an integrated facility for exposure of electrical and collector probes in the plasma scrape-off layer and subsequent surface analysis of the collector probes by means of ion beam techniques (RBS, NRA, PIXE) and Scanning Auger electron analysis.

Following a proposal (reference 1) in 1980, the equipment was designed and manufactured and then commissioned progressively at JET during 1984-1986. This article describes the facility and the operating experience gained on measurements performed during JET discharges with emphasis on the problems of precision mechanisms working in Ultra High Vacuum under automatic control.

2. SYSTEM DESCRIPTION

2.1 Probes

The probes which the system exposes to plasma are:

2.1.1 Electrical Probes

The electrical probes consists of an array of insulated carbon elements which are connected electrically through power supplies to the torus earth. By applying different voltages and measuring the current, information is obtained relating to plasma density, temperature and heat flux.

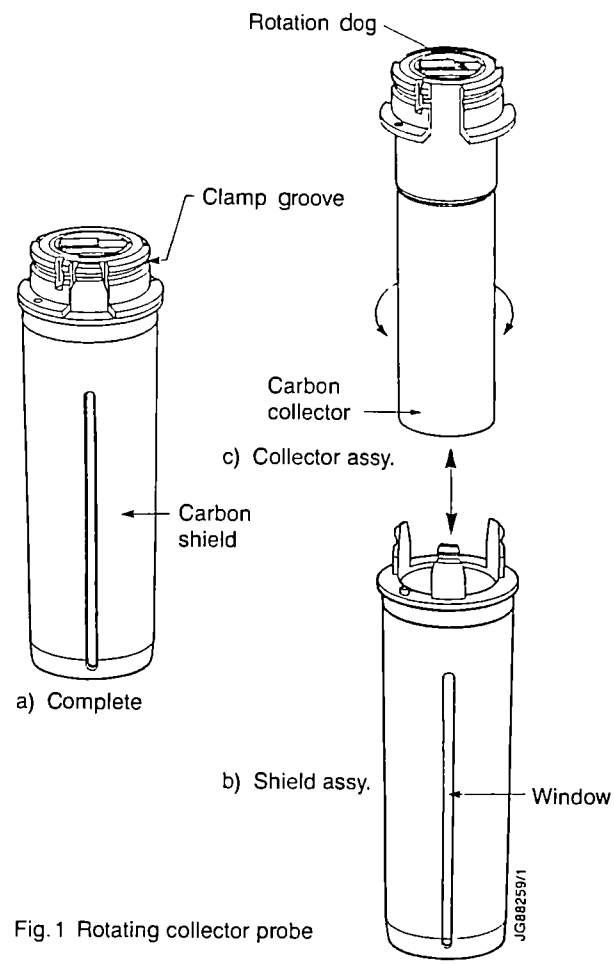

Fig.1 Rotating collector probe

2.1.2 Collector Probes

Collector probes (see figure 1) consist of an inner cylinder (collector) and an outer shield. The shield has a 3 mm wide slit and the cylinder is rotated during a pulse to collect a deposit of hydrogenic and impurity species.

The time and space (radial) dependent deposition is subsequently analysed to study impurity release and recycling of hydrogen and its isotopes.

2.2 Exposure and Transport

Probes are exposed at three positions in the vacuum vessel by separate systems. One of these is fitted to a horizontal port and is called the Surface Probe Fast Transfer System (reference 2) and the other two are fitted to vertical ports and called Plasma Boundary Probe Systems. This article refers only to the horizontal port system.

2.2.1 Surface Probe Fast Transfer System

This system makes a direct vacuum connection from a horizontal port, through the biological shield wall to the analysis station (see figure 2).

The 27 m long, 150 mm bore tube encloses a railway and the three metre long train carries up to two collector probes and two electrical probes.

The axial positions of the probes are set in the diagnostic hall, so that they will be in the correct radial position when the train is docked at the torus. A 300 mm steel radiation blocking shield is raised and the train driven towards the torus. The position information for the train drive is provided by a laser distance meter, reflecting the beam from a corner tube mirror on the rear of the train. It is accurately positioned at the torus by a pneumatic ram and a pneumatically driven electrical connector makes the probe circuits. The blocking shield is closed behind the train.

After exposure the process is reversed and the train is driven back to the diagnostic hall. Here the collector probes are transferred to the to the analysis station.

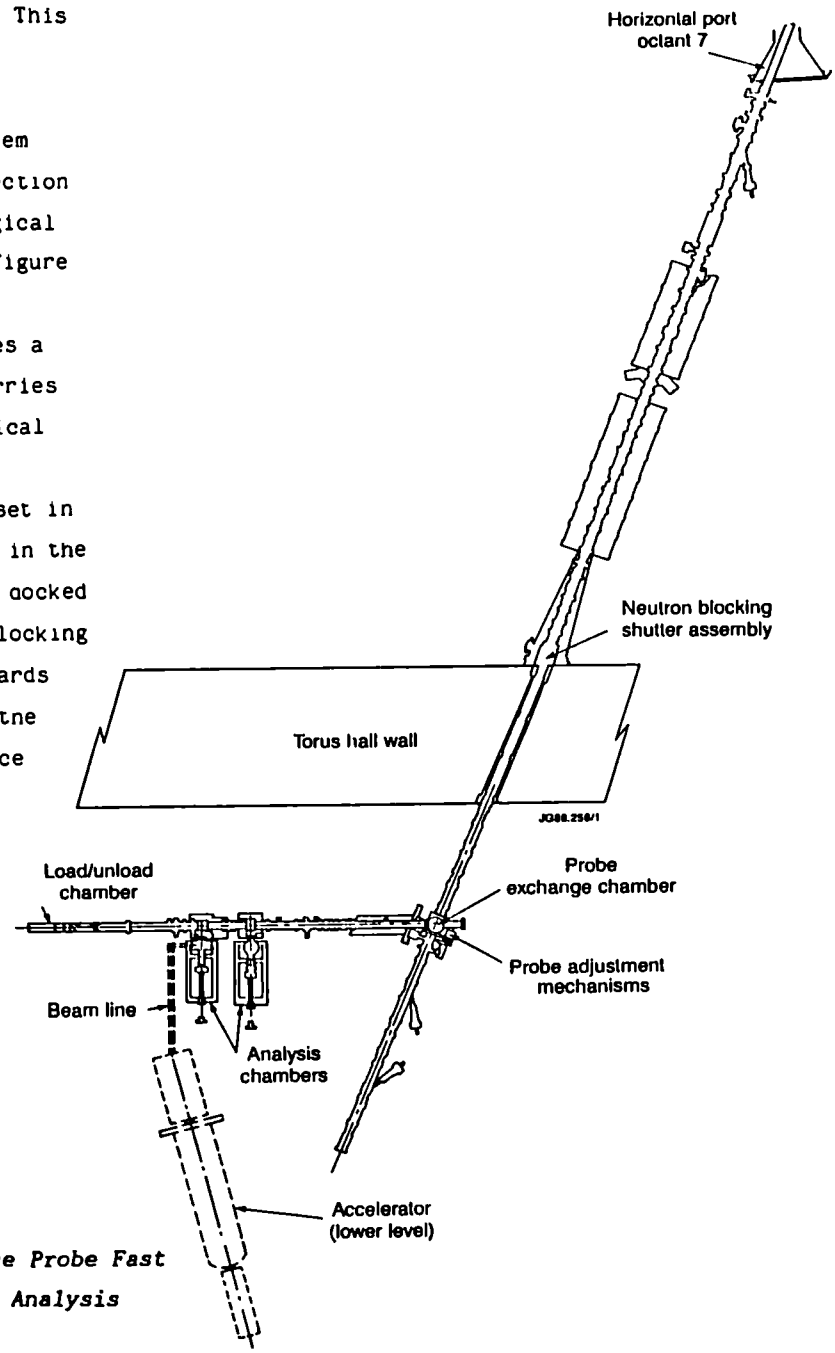

Fig 2: Plan view of the Surface Probe Fast Transfer System and the Surface Analysis Station.

The train drive system is novel in that it is a linear motor system with motors fixed externally to the tube and the aluminium reaction plate on the train. This is the complete opposite of conventional linear motor driven railways, which have the motors on the train, and has the advantage that there is no sliding friction on drive components inside the vacuum and no flanges in the vacuum envelope.

The motor for rotating the collector probes is also novel in that it has no magnetic circuit of its own and uses the torus magnetic field instead. Two coils oscillate through 6° as the direction of the current through them is switched and rotate the probes in one direction only by means of a ratchet.

The system was supplied by GEC Energy Systems Ltd under contract to Culham Laboratory.

2.3 Surface Analysis Station

The collector probes from the two exposure points are transferred to the Surface Analysis Station, where they are transported by a rack and pinion drive to one of the analysis stations.

The system was supplied by Pfeiffer under contract to IPP Garching.

The analysis methods are: Rutherford Backscattering, Thermal Desorption Spectroscopy, Nuclear Reaction Analysis, Elastic Recoil Detection, and Proton Induced X-Ray Spectroscopy in Chamber I (10^{-9} mbar), and Auger Electron Spectroscopy and X-Ray Photoelectron Spectroscopy in Chamber II (10^{-10} mbar).

3. OPERATION OF MECHANISMS IN UHV

3.1 Problems - General

From the engineering point of view this equipment is a mechanical handling system for probe transportation. The mechanisms are complex with over 3,000 individual components moving in in UHV and considerable effort has been necessary to develop them to function satisfactorily under automatic control.

The design restraints for the JET environment, with bakeout at 300°C, which have in general been taken into account by the designers of this equipment, include no organic materials or high vapour pressure metals, no friction between components of similar materials, no trapped volumes, no magnetic materials in the torus, no materials generating debris and only materials with high radiation resistance.

The vast majority of faults, that we have discovered and rectified that relate to UHV operation, have been very simple in nature and caused by a lack of attention to detail in design, manufacture and assembly. Small errors in, for example, component clearance and alignment, burrs etc which are so minor that they would be cured by bedding in with lubrication on mechanisms working in air and consequently never be discovered, will cause failures in mechanisms working in UHV.

The only mechanisms that have required redesign because of problems of working in UHV are those where there is a limiting friction condition, i.e. the mechanism works when the friction co-efficient is below the limiting value and fails when it is above the limiting value. One example of this is shown in the next section. Such mechanisms can work in air and in unbaked vacuum, but fail because of an increased friction coefficient after baking.

3.2 Collector Probe Clamp - Specific Problem

The probe is clamped by the mechanism shown in figure 3.

The clamping mechanism is moved to engage the probe and the three equi-spaced balls are positioned opposite the clamp groove in the probe (see also figure 1). The outer sleeve is then moved which presses the balls into the groove and locks the probe on the clamp. The

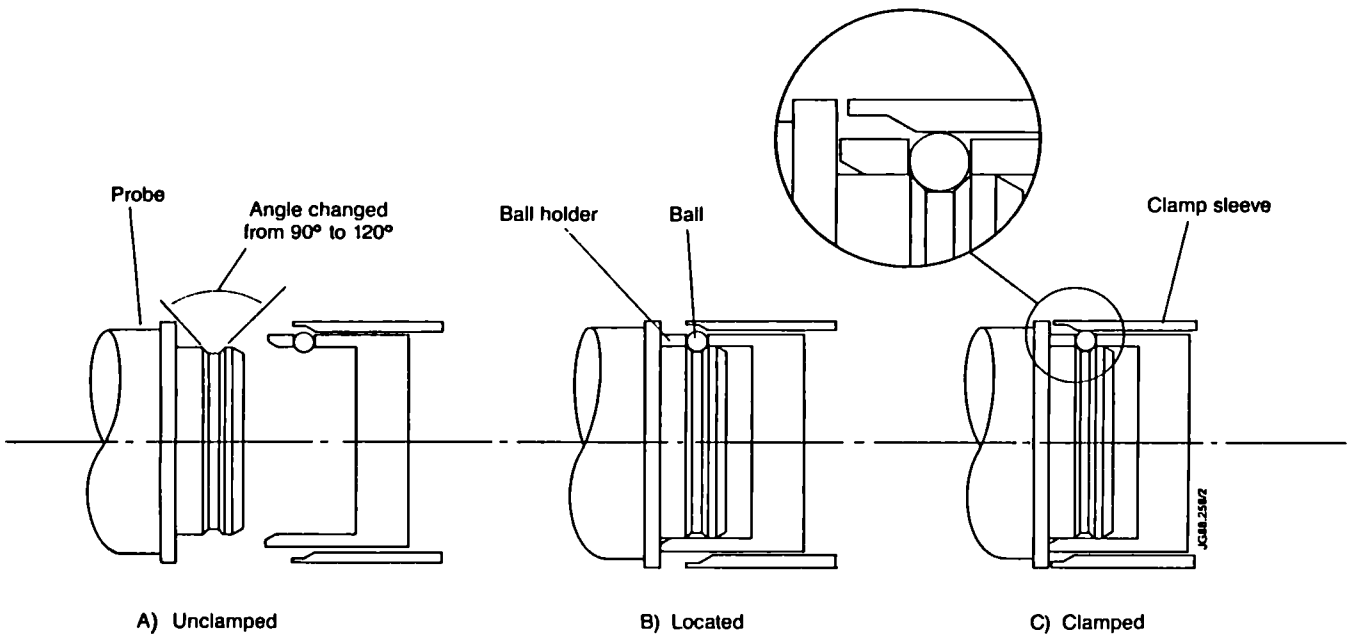

Fig.3 Probe clamping mechanism

mechanism is used in various places on the system with different actuation and locking methods.

The balls are made of tungsten carbide with 5% cobalt as a binder and the other parts of nimonic 80A, a hard non-magentic material.

The problem was that the clamp mechanism would not dis-engage from the probe in UHV. It worked satisfactorily in air and in unbaked vacuum, but repeatedly caused problems after baking.

The reason was that the ball that is shown in figure 3 in the uppermost position has to be driven vertically upwards when the probe is disengaged from the clamp mecnanism. It became trapped between the 45° angle of the groove in the probe and the vertical face of the hole in the ball holder. This corresponds to a friction coefficient of approximately 1. The solution was to change the included angle of the groove from 90° to 120° making it easier for the ball to be driven upwards.

3.3 Mechanism Elements Used Successfully

3.3.1 Ball Bearing

Silver coated ball bearings are used exclusively. They are proven on commerically available rotary feedthroughs and are avaiable in sizes up to 22 mm and 7/8 inch outside diameter. Over 200 are used and there have been few problems. High temperature bearings lubricated with MoS_2 powder were rejected because of creation of debris.

3.3.2 Gears (Rack and Pinion)

There are two rack and Pinion drives. One uses an aluminium bronze pinion driving a stainless steel rack and the other uses a pinion with six small ball bearings driving a stainless steel rack. This reduces friction and debris creation.

3.3.3 Flexible Cables

Flexible cables are required to make connections to the probes which are moved axially in UHV. Eight copper wires (0.5 mm dia) are each insulated by alumina beads (1 mm diameter) and together wound into a helical coil ~ 25 mm diameter. Provision has been made to trap any debris created from the alumina beads but in practice the amount collected has been small.

3.3.4 Potentiometer

In order to get a position decoder in UHV, we removed the track from a commercially available Cermet potentiometer, baked it in a vacuum oven, tested it and proved it satisfactory. It was built into the probe rotation drive using beryllium copper contacts.

3.3.5 Make and Break Electrical Contacts

Electrical contacts are made to the train by the electrical connector assembly Nickel pins on the connector are moved vertically upwards to make contact with silver coated buttons rivetted to beryllium copper leaf springs on the train. These contacts perform well for low level signals and currents up to 4A.

3.4 Experience

The following is a summary of experience gained on operation of this facility.

3.4.1 Clearances

There must be a positive clearance (minimum 0.1 mm) between sliding components. Precision location is possible, as long as there is definite clearance over the full travel. It is not good enough to rely on numbers on drawings and conventional component inspection. The final assembly must rattle when shaken!

3.4.2 Chamfers

When two components are located by a motion inside UHV then both components should be chamfered to a maximum angle of 30° and preferably 15°. Sharp edges are disastrous.

3.4.3 Choice of Materials

The choice of mating materials must be sensible eg. aluminium bronze and stainless steel for plain bearings. Many combinations have been proven successful on these systems. The main point seems to be to avoid friction between components made of the same material. Similarly there is no magic combination which will compensate for inadequate clearances, chamfers etc.

3.4.4 Thermal Expansion

Mechanisms must be able to cope with thermal expansion up to 300°C and those close to the plasma considerably hotter. Nimonic 90 disc springs have been used to clamp assemblies made of different materials. Extra differential expansion due to variations in heating and cooling rates of mating components has also given problems.

3.4.5 Screw Threads

The comments for clearance between sliding components and materials also apply to screw threads. We have specified different diameters for male and female parts on fine threads, ie. an M36.9x1 male in an M37x1 female, to ensure adequate clearance. The cold weld is broken when the screw is unlocked and the screw will turn without siezing.

3.4.6 Alignment

For mating parts to engage reliably, mechanisms must be designed for minimal movement with the differential pressure forces when vacuum is applied. In addition the mating parts (eg. probe and clamp (figure 3) must be held precisely but flexibly to allow for occasional errors in the position of the mating part. These conflicting conditions are not easy to achieve and we occasionally have problems despite accurate alignment.

3.5 Conclusions

From our experience, light mechanisms in UHV can function satisfactorily with sensible design and considerable attention to detail by all involved in design and manufacturing.

REFERENCES

1. D.H.J. Goodall et al - Proposed Plasma Edge Diagnostics for JET. Plasma Surface Interactions in Controlled Fusion Devices - Garmisch 1980.

2. R. Charles et al - The JET Fast Transfer Diagnostic System - Installation and Commissioning 14th SOFT Avignon pp 1499-1504.

FULL POWER OPERATION AT JET: CONSEQUENCES FOR IN-VESSEL COMPONENTS

M.A. PICK, G. CELENTANO, E. DEKSNIS, K.J. DIETZ, C. FROGER, M. HUGON, M. HUGUET, P.H. REBUT, R. SHAW, L. SONNERUP, P. STOTT

JET Joint Undertaking, Abingdon, Oxfordshire, OX14 3EA, UK.

Utilising to the fullest the enhanced capabilities of JET requires the installation of new in- vessel components. In this paper we discuss the requirements and describe the hardware solutions which are to be implemented and their effect on the future operation.

1. INTRODUCTION

As JET is approaching full power operation and is in many cases going beyond the design values it is worth noting the situation with the present in-vessel components before describing the new components ready for installation starting at the end of 1988.

The major component installed in the last major shutdown was the belt limiter[1]. This double ring, which has a diameter of approximately 800 cm, was installed to a precision of +1mm concentric with the plasma[2]. Experience has shown that it performs very well and is both mechanically strong and resilient. No problems such as leaks or broken tiles have occurred on this component whatsoever. It was designed for a load handling capability of 40 MW for 10 s which can certainly be reached and very likely surpassed. The other important change undertaken during the last shut-down and refined during the subsequent operational period was the installation of fibre reinforced graphite (CFC) tiles in the equatorial region of the inner wall. This also has proven to be a full success. The heat shock resistance[3] of the material has been of great benefit and has virtually eliminated the need to frequently replace damaged tiles on the inner wall as previously. Another area where power handling capabilities were required during the recent operational period were the X-point regions, both at the top and bottom of the machine. Several changes in the tiles, their design and their alignment were required during this operational period due to the unexpectedly successful operation in that mode which resulted in the occasional deposition of 50 MJ and more on the X-point tiles which had originally not been designed for that purpose. This region of the torus will greatly benefit from the planned new installation of separatrix energy dump plates. One of the major advances during the last year was the increase in the plasma current beyond its design value of 4.8MA to 6MA and recently even to 7MA. The new problems which arise when operating at these high currents are the high mechanical forces exerted on the vessel itself. It is for that reason that new restraint rings were designed which will be installed in the vessel during the next year.

2. THE NEW IN-VESSEL COMPONENTS

To handle the power deposited in the region of the X-point we will install in the coming year two complete rings of water cooled inconel plates, each covered by CFC tiles, at the top and the bottom of the vacuum vessel. Fig. 1 shows the X-point dump plates located inside the vacuum vessel as well as the saddle coils, described below.

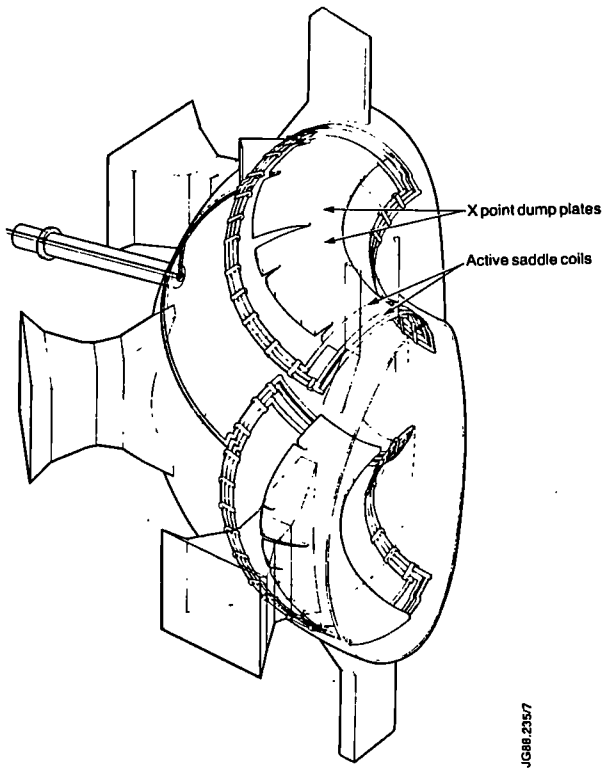

FIGURE 1
Three dimensional view of two octants showing the location of the X-point energy dump plates and the saddle coils. Indicated is a feed-through for powering the saddle coils as well as the clamps holding the coils to the vessel wall.

Major disruptions pose an increasingly serious problem for large tokamaks and therefore also for plasma operation. They cause very large stresses on the vessel and the mechanical structure. Unless remedial action is taken the "operating window", i.e. the parameter range allowed by plasma physics constraints as well as machine constraints, will become increasingly limited due to the requirements for safe operation. In particular additional limits on the plasma current and elongation would have to be imposed. Two new pieces of hardware will be installed in the vessel in the coming year with the aim to alleviate these problems. Firstly, restraint rings will be welded onto the inner wall of the torus above and below the mid-plane in order to strengthen the vessel, thereby avoiding excessive stresses. Secondly, to reduce the likelihood of disruptions occurring and consequently reducing the stresses on the vessel as well as possibly allowing for a higher density limit, a disruption feedback control system will be installed on JET. A cross-section of the torus, Fig. 2., shows how the in-vessel components including the saddle coils, the dump plates and the restraint rings are located around the vessel wall. Before describing the disruption control system it is necessary to outline briefly the behaviour of disruptions on JET.

2.1 Disruptions and the Disruption Control System on JET

Density limit disruptions are preceeded by a series of precursers. These appear between 100 ms (for low q_ψ discharges) to 1 s (for high q_ψ discharges) before the actual disruption When the radiated power has reached 100% of the

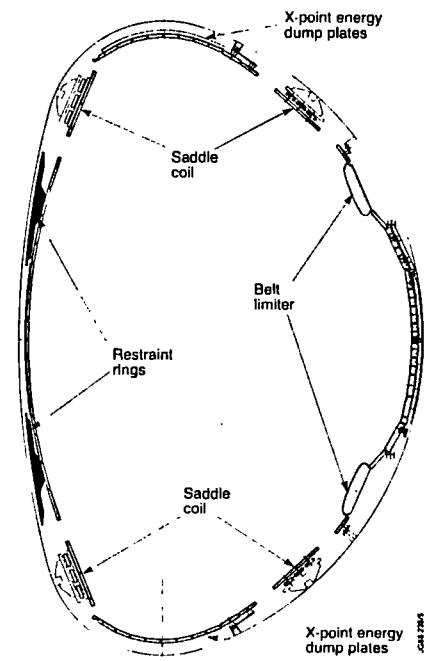

FIGURE 2
A poloidal cross-section through the torus showing the location of the in-vessel components and the graphite tile cladding.

total input power, the temperature and the current density profile start to contract. This contraction generally allows for the successive destabilisation of the m=3, n=1, and the m=2, n=1 tearing modes. These modes first rotate at the Mirnov frequency, which is typically between 1 kHz (for ohmically heated plasmas) and 10 kHz (for neutral beam heated plasmas). As a function of time these modes slow down and then lock in a fixed toroidal position. The position is given by some arbitrary inhomogeneities, either in the magnetic field or in the symmetry of the inner vessel. Locking generally occurs when the perturbed magnetic field amplitude is of the order of 10 Gauss. Subsequently, the plasma experiences several minor disruptions followed finally by the major disruption. The m=2, n=1 magnetic island plays a dominant role during the disruption process.

The principle of the disruption feedback control is to limit the growth of the m=2, n=1 tearing mode by counteracting its perturbed magnetic field. A magnetic field is created which has exactly the m=2, n=1 symmetry but with opposite polarity by passing a current through a set of four saddle coils on the upper and lower halves of the torus, Fig. 1. The saddle coils are fed by a set of amplifiers which are capable of delivering 3kA for frequencies from 0 to 1kHz and 3kA/f (where f is the frequency in kHz) from 1 to 10 kHz. The coils will produce a field having an amplitude of approximately 2 Gauss for the m=2, n=1 component at the q=2 surface (assuming 3kA is flowing in the coils and the wall is perfectly conducting). The feedback signal itself is derived from a set of pick-up coils located inside the vessel near the mid-plane of the outer wall. These pick-up coils should allow the detection of the m=2, n=1 mode in the plasma with a sensitivity of 0.1 Gauss. This high sensitivity is required for the pick-up coils in order to enable the system to operate as early as possible, while the mode is rotating and the amplitude is still small. An alternative method of detection, using the saddle coils themselves as the antenna, is also being investigated.

2.2 The Restraint Rings

Since operation of JET at high plasma currents of 6 and even 7MA represents a considerable extension of the original design parameters of the machine a complete assessment of the consequences of such high current operation was undertaken. In particular, the large centripetal forces which are generated on the vacuum vessel during a radial disruption, pose a threat to the vessel. Careful calculations were undertaken to better estimate the forces involved. For the stress analysis of the vacuum vessel, a large and complete finite element model was established. The results of these assessments (the details of which will be published separately as a JET report) show additional radial forces of 20,000 kN on the vessel during a typical disruption at 7 MA plasma current[4]. This is more than 3 times the radial force due to the atmospheric pressure (6000 kN). Such high levels of load produce large deflections, especially at the ends of the vertical ports (typically 5 to 10 mm) and along the inboard wall of the vessel (typically 15 to 20 mm). Since the forces rise to their maximum and decay in approximately 15 ms, they introduce dynamic effects wherever equipment with a significant mass is attached to the vessel. This in turn leads to high local stresses in fastenings and in the vessel wall itself.

The reason for the large deflections is to be found in the low stiffness of the inboard vessel wall in combination with large inwards forces due to the poloidal eddy currents at the thermal quench in a disruption. In order to remedy this situation, two inconel strengthening rings, above and below the mid-plane of the torus, will be welded onto the inboard wall, Fig. 2. They will resist the local radial forces in this area

by their hoop strength and stiffness, and reduce the displacements of the vessel wall and ports by an order of magnitude, down to less than 2 mm. They will also eliminate the risk of overloading the existing ring reinforcements along the outside of the vessel, which at present carry all the radial loads by their hoop strength. The new rings on the inboard wall will carry approximately 30% of the radial load in a radial disruption, i.e. up to 8000 KN.

2.3 The Separatrix Energy Dump Plates

The high power densities deposited in the region of the X-point during the previous operating period of JET required that the X-point tiles be modified. This was due to the fact that the X-point position, for operational reasons, varied widely. Therefore not only did the position of the separatrix move but also the angle of incidence of the field lines as well as the power density itself. During the 1988 operational period the power was deposited onto initially 40 poloidal rings of individual tiles; these were later replaced by 32 poloidal rings of larger and differently shaped tiles. It was found to be difficult to align the tiles in such a way as to equally distribute the power over all the tile rings. Variations occurred when the X-point was moved due to the magnetic field configuration in this operating mode. When the X-point is further from the tile surface then the angle of incidence of the field lines onto the tiles is increased and the power will tend to be deposited well down onto the tile edges. In this case the power density can reach very high values on the tile edge, which intercepts the field lines in an almost normal direction, and the tiles are consequently damaged due to thermal shock. As the X-point moves closer to the tile surface the angle of incidence is decreased but the absolute tile positions now become more critical, i.e. the X-point tiles begin more and more to act as "limiters". Under these conditions a tile which is slightly more proud than the adjacent tiles will shield the adjacent tiles and itself be burdened with a large fraction of the plasma power. This situation was again the cause of numerous damaged tiles. The precision required in order to ensure an equal loading of the tiles is on the order of ±1 mm. This is, naturally, similar to the precision required on both the belt limiter and the inner wall in the equatorial region.

A solution to the above dilemma is the design of the water cooled energy dump plates as will be installed in the coming year. This will provide for a complete toroidal ring of tiles sufficiently wide to cover the possible positions of the branches of the separatrix. The angle of incidence of the field lines is of secondary importance in this case because the sides of the tiles are not accessible to the plasma. The relative and the absolute vertical positions of the dump plates will be within ±1mm of one another thereby eliminating the possibility of the power being intercepted by only a very limited number of tiles even when the X-point is very close to the surface of the dump plates. The reason for the water cooling is to enable the CFC-tiles to be cooled to a lower temperature between discharges thereby eliminating the problem of the temperature ratcheting up to high values due to successive discharges. In the case of beryllium tiles the water cooling is essential in order to cool the tiles to approximately 100°C or less between discharges to ensure that the tiles remain well below the melting temperature during a full power discharge.

2.4 The Inner Wall Tile Protection

It was previously shown that the inner wall of JET is not perfectly circular. The deviations are, in large part, simply related to the fact that the JET vessel is made up of individual flat sections[5]. In the past this was the cause of high power deposition on selected

tiles, in particular to those at the octant joints. The subsequent exchange of the original fine grain graphite tiles by CFC-tiles as well as the elimination of protruding edges virtually eliminated the problem. In the next shut-down we will re-install and align the tiles in the equatorial region of the inner wall in such a way that they will all lie within ±1 mm of a circle concentric with that of the belt limiter which was shown to be almost ideally centered with respect to the plasma. At the present time a band of tiles only three tiles high at the centre is made of CFC-tiles. After the next shut-down this will be increased to a band nine tiles high. It was found that slight discrepancies in the exact positioning of the CFC-tiles are smoothed away by erosion due to the action of the plasma itself, without damaging the tiles.

SUMMARY

The installation of the new vessel restraint rings as well as the dump plates and saddle coils will allow JET to operate safely with plasma currents of 7MA and with >40MW additional heating in limiter, single and double null X-point configurations. It will thus allow to fully exploit the versatility of the JET machine.

REFERENCES

1. K. Sonnenberg et al., Proc. 14th SOFT, Avignon, 1986 (Pargamon Press, 1986) p.273.
2. S.J. Tagle et al., Proc. of the 8th Int. Conf. on Plasma Surface Interactions, 2-6 May 1988, Julich, Germany, J. of Nucl. Mat., in print.
3. P. Massmann et al., Fusion Technology 1 (1986) 545.
4. L Sonnerup (to be published), and M. Huguet and E. Bertolini and the JET Team, 8th Topical Meeting on Technology of Fusion Energy, October 9-13, 1988. Salt Lake City, Utah, (to be published).
5. M.A. Pick et al., Proc. of the 12th Sym. on Fusion Engineering, 12-16 October 1987, Monterey, Calif., IEEEC Cat. No. 87CH2507-2, Vol. 1, pp. 137-140.

INTEGRATED ENGINEERING DESIGN OF NEW IN-VESSEL COMPONENTS

M.A. PICK, G. CELENTANO, K.J. DIETZ, C. FROGER, L. ROSSI, R. SHAW, L. SONNERUP

JET Joint Undertaking, Abingdon, Oxfordshire OX14 3EA, UK.

Design details of the new in-vessel components are described with emphasis on those details which ensure: optimum operational as well as installation and remote handling capabilities, precise geometry and high reliability in severe environmental conditions in terms of heat load, forces and radiation.

1. INTRODUCTION

During the next operating period JET will run with maximum power of up to 40 MW for 10s and plasma currents up to 7 MA. The additional components which are to be installed in the vessel during the coming year include X-point energy dump plates, disruption control saddle coils and vessel restraint rings. An overview for the requirement of these components as well as figures showing their configuration inside the vessel is given in reference 1. The experience gained in operating JET for several years has led to certain principles for the design of the in-vessel components which have been strictly followed in the design of all the new equipment. The first important point is that in order to retain the versatility of the machine in terms of plasma configuration, which has proven so valuable in the past, the components should take up as little space as possible. A second point learnt during previous operating periods of JET is that the positional accuracy with respect to the magnetic field required of all those first wall components which may interact with the plasma, such as limiters; inner wall protection tiles; RF antennae; X-point protection tiles; etc., is in the order of ± 1 millimeter. This precision was achieved and demonstrated[2] with the belt limiter previously which will therefore be used as a reference in future installations. Larger deviations cause non-uniform power deposition with the result that selected areas will be overloaded and damaged.[3] Another important detail which has been taken into account is the consequence of several water leaks which have in the past occurred on JET and which were often associated with the failure of bellows. No in-vessel bellows have been included in the design of the new components. In order to fulfil the requirements of the new components as well as conforming with the above points the design of all the in-vessel components was viewed as a single design.

Figures 1 and 2 illustrate the complete integration of the new components into one coherent design. The components are covered in graphite or carbon fibre composite (CFC) tiles which provide an almost complete coverage of the inside of the vessel. Apart from the outboard side of the vessel this coverage is only interrupted in the areas immediately adjacent to the saddle coils where two bands of tiles have been omitted in order to facilitate the field penetration of the disruption control system. The following provides some information on details of the design of the various components emphasizing only the most important aspects which have been incorporated to fulfil the experimental requirements as well as those for installation.

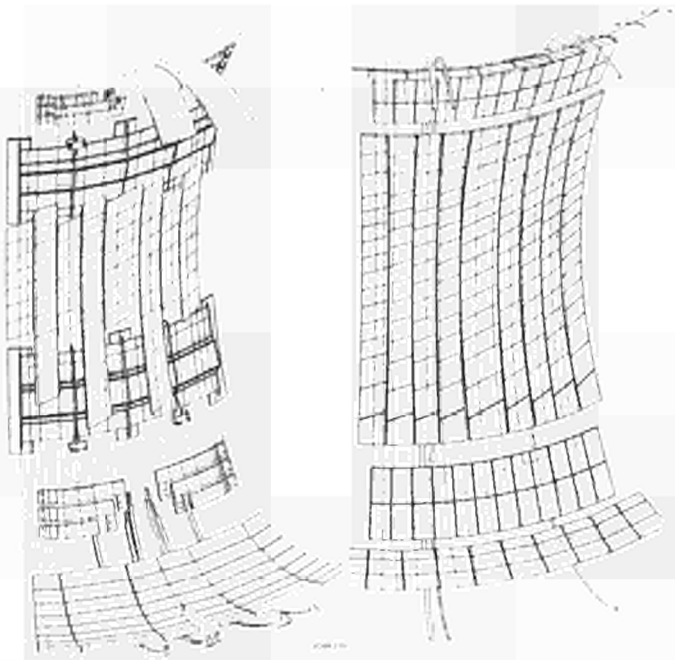

FIGURE 1 AND 2
The graphite tiles provide an almost complete coverage of the inner wall protecting the restraint rings, saddle coils and dump plates. The coverage is interrupted only in the areas immediately adjacent to the saddle coils in order to facilitate the field penetration of the disruption control system.

2. THE SADDLE COILS

The design of the saddle coils was required to take into account the severe conditions in which the coils must operate, namely up to 500°C in temperature, high radiation and forces on the coils of up to 40 kNm^{-1}.

Each of the eight coils spanning two octants consists of three windings and are designed to carry 5kA with a maximum voltage of 6kV to the vessel. The coils are of inconel bars (20 x 70mm) which are machined and bent to the exact theoretical shape prior to installation. An overview of how the coils are located in the vessel relative to the dump plates is shown in Fig. 3. Two features in the design of the saddle coils have been included to accommodate deviations of the actual dimensions from the theoretical ones. In the factory the coils are pre-assembled and installed into a dummy vessel which spans the lower section of two octants and which is machined to with ±1mm of the theoretical vessel dimensions. This is done in order to check all the overall dimensions. The pre-assembled sections of the coil are shipped as a whole and are installed and connected inside the JET vessel. The connectors themselves allow for 10mm leeway at the connectors, and in addition, at each 90° corner, where there is a crossing from the toroidal to the poloidal sections, there is a flexible connector made up of nickel laminates. These flexible connectors can accommodate the expansion of the perpendicular bars as well as the forces which occur during disruptions and vertical instabilities causing differential movements of individual vessel sectors.

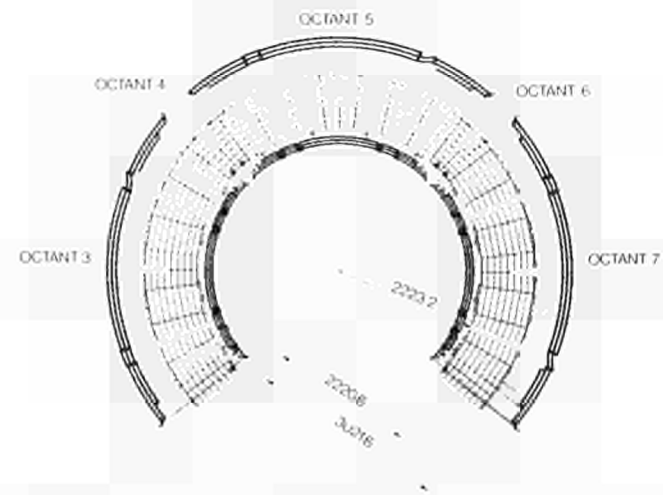

FIGURE 3
An overview of the location of the dump plates relative to the saddle coils and indicating representative dimensions.

An example of the clamps which hold the coils in place is shown in Fig. 4. Inside the clamp the three inconel bars are each held in place by eight insulating alumina balls. To facilitate the assembly, the balls are held in a short groove in the bar. The balls are held in place by a spherical seating in the screws which, after being set into position, are tack welded in place. These clamps, of which there are numerous, hold a total of approximately

10,000 alumina balls. The large number is required in order for the clamps to withstand the large forces due to the interaction of the alternating coil current and the magnetic field.

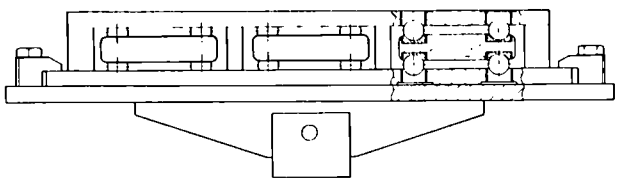

FIGURE 4
An example of one of the many clamps holding the three turns of the saddle coil to the wall of the vessel. Each inconel bar (20 x 70mm) is held in place by eight insulating alumina balls.

3. X-POINT DUMP PLATES AND PROTECTION TILES

In the X-point configuration particles will flow towards the vessel wall which must therefore be protected by an actively cooled energy dump plate system. Water cooled inconel plates which are covered by low Z material will be installed over 1m of poloidal arc at the top and bottom of the vacuum vessel. The low Z materials considered were fine-grain graphite, carbon fibre composites (CFC) and beryllium. Based on early observations[4] of the X-point configurations a peak flux density of $5MW/m^2$ for 10s must be sustained by the respective material with $T_{max} < 2000°C$ for graphite and $T_{max} < 1200°C$ for beryllium. This is readily achieved, as shown in Fig. 5. The pulse repetition rate is determined by the length of time it takes a tile to cool down to a predetermined acceptable temperature. For graphite tiles this initial temperature may be as high as 400°C whereupon the radiation cooling of the tile to the vessel as well as to the water cooled inconel plate is sufficient to allow one discharge every 30 minutes. If these tiles were to be of beryllium they would need to be cooled to <100°C before a discharge in order to avoid melting in a subsequent full power discharge. This implies that a good thermal contact must be maintained between the tiles and the inconel plates. The design of the tile attachment is shown in Fig. 6. The protection tiles have been chosen to be of CFC material since tests done at JET indicate that these materials are highly resistant to thermal shock[5]. The tiles, Fig. 6, are shaped in such a way as to eliminate the possibility that selected field lines penetrate the gaps between the tiles and impinge directly on the inconel plates.

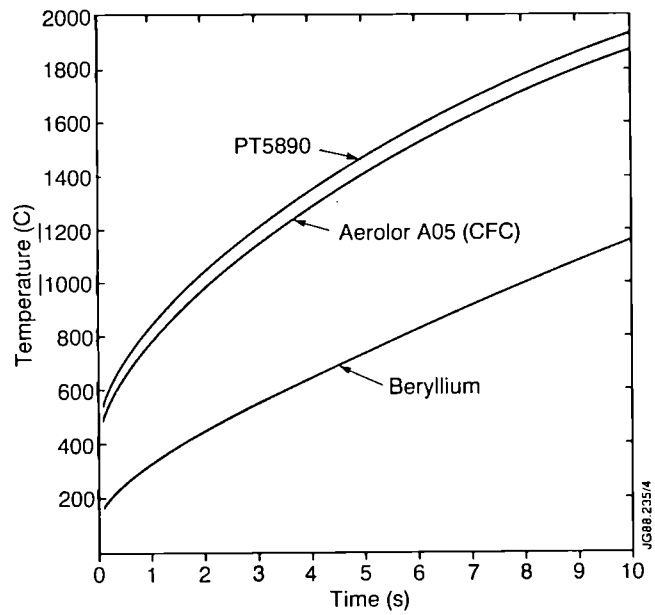

FIGURE 5
Surface temperature rise of X-point dump plate tiles exposed to a peak flux density of 5 MW/m^2. Graphite and Be should not exceed ~2000 and 1200°C respectively. The temperature rise for CFC and fine grained graphite is similar.

The dominant design criteria for the water-cooled inconel plates are: a) the efficiency of heat removal and b) susceptibility to eddy currents during disruptions.

The dump plates consist of 25mm thick inconel plates. The plates are shaped to conform with the vessel. The water cooling channels consist of transveral holes 11mm in

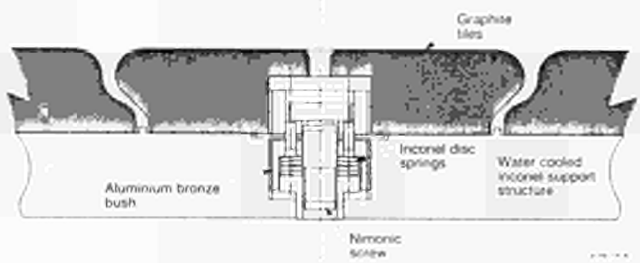

FIGURE 6
A rather complicated design was adopted for the tile attachment in order to ensure good thermal contact between the tile and the support structure as well as for remotely removing and attaching tiles. In addition precautions have been included in the design to remotely repair the attachment in case the system is fused.

diameter which have been drilled (using "deep drilling" techniques) into the plate. The transversal holes are joined on each side of the plate by a channel cut into the edge of the plate and then closed by welding a narrow plate over the top. Fig. 7 indicates how the water flows through one of the plates. The flow pattern is the result of detailed calculations and computer simulations with the object of uniformly cooling the plate whilst minimising the total flow. Analyses of the plates by the SPARK code[6] have shown that forces due to eddy currents directly induced in the plates are very small. However, the plates share eddy currents which are induced in the rigid sectors of the vacuum vessel. These forces are substantial, on the order of <8 KN/support, but are largely determined by the resistance of the supports of the plates themselves. The supports are shown in Fig. 8. A combination of slots, clearances and spring washers enables the supports to withstand the expected forces due to eddy currents, both induced and shared as well as to accommodate the expected displacements due to temperature differences between the plates and the vessel which will occur when operating with a hot vessel (usually 300-350°C) and cooled plates as well as when cooling the vessel after operating with uncooled dump plates when these will become substantially hotter than the vessel due to temperature lag.

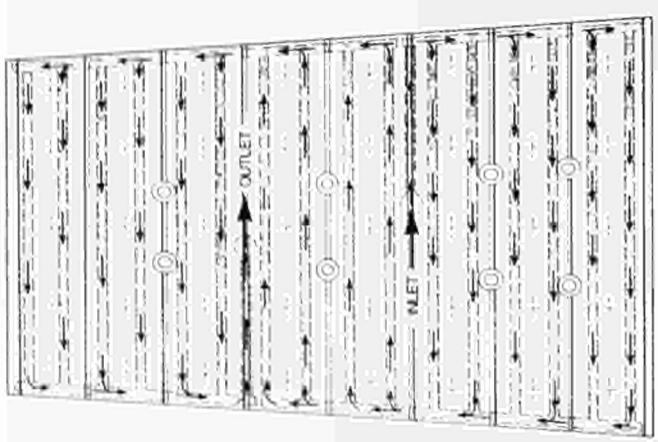

FIGURE 7
An example of the inconel X-point energy dump plate showing the cooling water holes and channels and the water flow pattern.

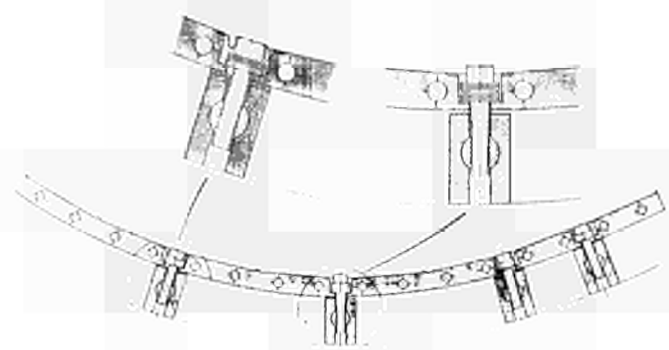

FIGURE 8
The supports for the dump plates have been designed to accommodate the large force (~8KN/support) as well as differential expansion of the dump plates versus the vessel wall. The screws are of inconel and the cyclindrical nuts are of aluminium bronze.

4. THE RESTRAINT RINGS

Each ring consists of inconel 600 ribs welded onto the rigid sectors of the inner wall and connected by 12mm thick inconel plates as shown in Figs. 1 and 9. During a disruption at 7 MA each ring must withstand a compressive hoop force of about 700 kN without buckling, as well

as a radial force on the order of 4000 kN, which, divided by the 32 ribs, means that each rib, including the rib weld onto the rigid sector as well as the rigid sector itself, must withstand about 125 kN without any plastic deformations.

The resulting compressive stress in each plate due to the hoop forces is 90 MPa which is about half the acceptable limit for the material used at the operating temperature. The shape of the plates is a result of considerations aimed at maximising the bending inertia of the ring whilst minimising the space required.

In order to distribute the radial force more evenly onto the widest of the rigid sectors, namely the one in the middle of each octant, and to thereby ensure that it does not bend excessively during a disruption, the ribs are first welded onto plates which are, in turn, welded onto the rigid sector along two lines closer to the sector edges (see Figs. 1 and 9). A similar design is required at the octant joints themselves.

A detailed study of the welding technique, the welding design and the welding sequence of the ring onto the vessel was undertaken to ensure that the method chosen would guarantee that the installation could be performed with high accuracy, minimal distortions, clean conditions, high speed (200 m of welds) and, of course, the required strength as well as readily available qualified welders and welding equipment. The technique chosen was automatic cold wire TIG. A welding design has been applied which includes a weld back plate. It should ensure that the quality of the weld will be maintained whilst locally allowing for a certain variation in the weld gap. As described in 1 the effect of the rings will be to decrease the displacements by an order of magnitude not only at the inner wall but also at the vertical ports. This will allow the safe operation of JET at 6 and 7 MA plasma current.

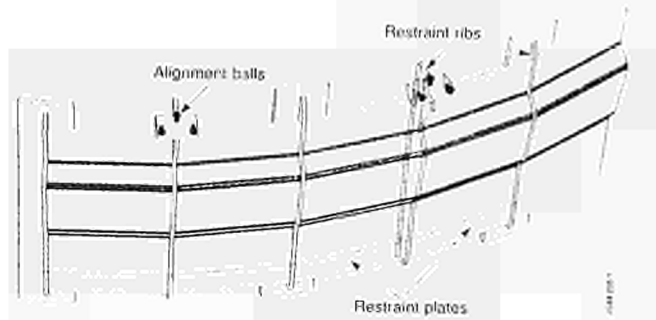

FIGURE 9
The inconel vessel restraint ring, consisting of ribs and plates shaped to maximise their inertia, is welded onto the inner wall of the vessel. The alignment balls, which form a permanent feature of the rings, are used to align the dump plates, saddle coils as well as the inner wall tiles.

5. CONCLUSIONS

The three major new components to be installed in the next year have been integrated into a single design so as to retain as much space as possible for plasma operation. Numerous design details have been incorporated to ensure that the expected forces and heat fluxes during operation as well as disruptions do not damage the machine thereby allowing experiments to fully investigate the plasma parameter space.

REFERENCES

1. M.A. Pick et al., ibid.

2. S.J. Tagle et al., Proc. of the 8th Int. Conf. on Plasma Surface Interactions, 2-6 May 1988, Julich, Germany, J. of Nucl. Mat., in print.

3. M.A. Pick et al., Proc. of the 12th Sym. on Fusion Engineering, 12-16 October 1987, Monterey, Calif., IEEEC Cat. No. 87CH2507-2, Vol. 1, pp. 137-140.

4. A. Tanga et al., Proc. of the 12th Eur. Conf. in Controlled Fusion and Plasma Physics, Vol. 9F, Part 1, pp. 70, 1985.

5. P. Massmann et al., Fusion Technology 1(1986)545.

6. D. Weissenberger, SPARK Version 1.1 user manual, PPPL-2494, January 1988.

THE PERFORMANCE OF JET PF SYSTEM FOR 7MA MATERIAL LIMITER AND 5MA MAGNETIC LIMITER OPERATION

A.SANTAGIUSTINA, E.BERTOLINI, T.BONICELLI, M.HUART, J.LAST, P.LOMAS, V.MARCHESE, P.L.MONDINO, P.NOLL, F.PETREE, C.RAYMOND, A.TANGA

JET Joint Undertaking, Abingdon, OXON OX14 3EA, UK

The JET PF Circuit enhancements have allowed operation with plasma currents up to 7MA with a material limiter configuration and up to 5MA with a magnetic separatrix. This paper summarises the latest major modifications of the PF Circuit and describes their commissioning and their performance in operation.

1. INTRODUCTION

Two major modifications of the Poloidal Field Circuit were carried out during the last JET operating phase: the Current Modulation Circuit (CMC) for the JET Magnetising Coils (P1) and the new Vertical Field Circuit for the control of the current imbalance in the JET Vertical Field Coils (P4).

The CMC causes the current flowing in the six central P1 subcoils (P1-1,2,3 upper and lower) to differ from that in the two top and bottom P1 subcoils (P1-4,5 upper and lower). This permits the current in the six central coils to be increased from 40kA to 60kA because, at full toroidal field, the outward force of these coils is balanced by the compression force of the toroidal coils. The P1 magnetomotive force is therefore increased. Moreover the leakage flux due to the current difference (ID) between P1-1,2,3 current and P1-4,5 current produces an hexapolar field that helps the generation of the magnetic separatrix configuration. The Current Modulation Circuit is shown in fig.1. The main new components are: the PFX Amplifier (2.1kV at 35kA) which generates the P1 current difference, the blocking diodes (BDXA, BDXB) that withstand the large reverse voltage (12+12kV) following interruption, the PFX filter (C_3=15mF, R_{13}=80mΩ) which protects PFX from overvoltages produced by the discharge of the Commutating Capacitors, the new P1 protection cubicle (P1-MPC) which protects the P1 coils from the many new fault situations, the new digital Plasma and P1 current control (PCC) which supervises the operation of the new System.

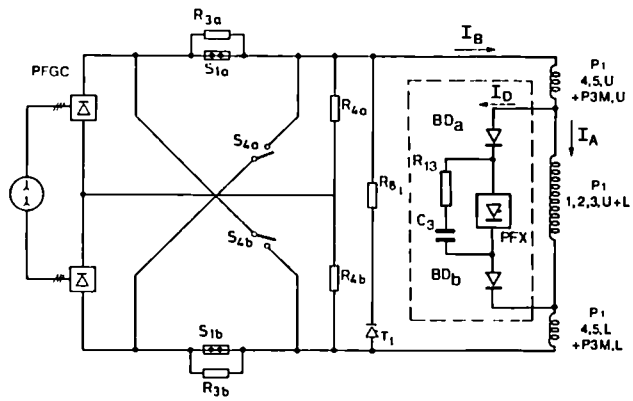

Fig 1: Configuration of the JET Magnetising Circuit with the Current Modulation Circuit for the P1 coils

The main design features of the CMC Circuit are described in detail elsewhere [1].

A new Vertical Field Circuit for the control of the P4 imbalance current permits a difference of current between P4 upper and P4 lower coil, thereby extending the operation with magnetic separatrix to plasma currents of 5MA and higher.

2. COMMISSIONING OF THE CURRENT MODULATION CIRCUIT

The commissioning of the CMC began in

November 1987 after a two-week shutdown to complete installation.

The main commissioning items of the CMC are listed in Table 1. This plan was performed successfully in about two and a half JET commissioning weeks. About one week was dedicated to the local commissioning (Table 1, item A). Each P1 Current Protection (24 in total) was tested by primary injection of current through its current transducers (Table 1-B). To avoid exceeding the nominal current of the P1 coils, these tests were performed with the main busbars disconnected from the coils and connected to a short circuit. The calibration tests have found large differences (up to 20%) in the measurements made on the various current transducers in the Circuit.

TABLE 1: CMC COMMISSIONING PLAN (NOV 87)

	NO OF PULSES
a) Local Units Tests	
1. PFX, OHC, BUSBARS High Voltage Tests	
2. PFX and FILTER Power Tests on Dummy Load (20kA)	
3. PCC Control microprocessor runs in open loop	
4. Injection of P1-MPC protections, CODAS end to end	
b) Current Tests with PFGC in Short Circuit	
1. Calibration of Shunts for P1 currents measurements	6
2. Primary injection of 24 P1-MPC protections	24
c) Tests with PFX on P1-1,2,3 with Power	
1. Power tests of PFX, FILTER and BDX (32kA)	6
2. P1-MPC Protection 5 (P1 current in opposite direction)	2
d) Integrated Tests of PFX, PFGC, P1, PCC	
1. Premagnetisation only 10, 20, 30, 40kA	4
2. ID Control and Stray Fields during Premagnetisation	4
3. Interruptions of 10, 20, 30, 40kA	5
4. PCC P1 current limiters: IBMAX, IBMIN, IAMAX	5
5. Protective actions: CISS ES, Soft-Stop, intertrips	5
6. Full performance (full PFX current and P1 swing)	2
e) Integrated Tests with Plasma	
1. PCC plasma feedback loop performance	2
2. PCC ID control loop performance	2
3. PCC plasma termination (DIP, IPMIN)	2
4. Coupling of Plasma Shape and Radial Position Control	2
5. Test of the P1 limiters and control sequences	8
6. Test of the plasma shapes produced by PFX current	2

The concept of active stray field compensation [2] has been tested to check that the field produced by a difference of current (ID) between P1-1,2,3 and P1-4,5 coils can eliminate the hexapolar stray field produced by P1 (fig.2).

The two extra P1 subcoils have already reduced the P1 stray field at the inner wall from 60mT to 10mT. With about 3kA of P1 current difference (ID) and with only 2 instead of 4 P3M turns, the stray field level can be reduced to a

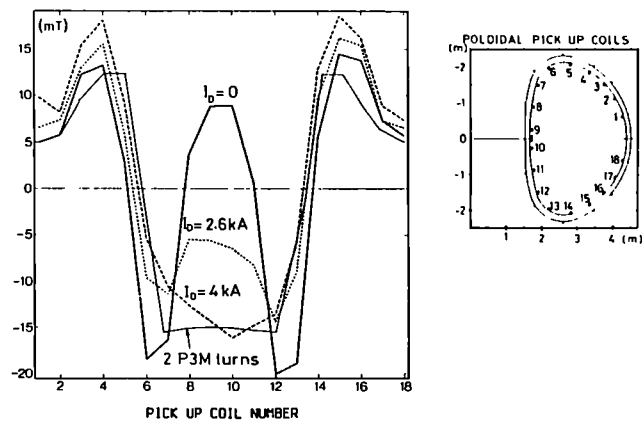

Fig 2: Stray Fields produced by P1 coils and 2+2 P3M coils, by different P1 coil current difference ID and 40kA Premagnetisation in P1-4,5. The fields produced by 2 P3M turns are also shown for reference.

negligible value inside the whole vacuum vessel.

The Interruptions Tests (Table 1-D3) have shown the correct operation of the blocking diodes stack (BDXA, BDXB) and the PFX filter. The waveforms of the busbar voltages produced by a 40kA interruption are shown in fig 3.

The overshoot of the P1-1,2,3 voltage is higher than predicted by the computer simulations. Also the current (400A) flowing through the BDX and PFX filter, due to the discharge of the Commutating Capacitors and the dI/dt of this current at BDX turn off (1A/μs),

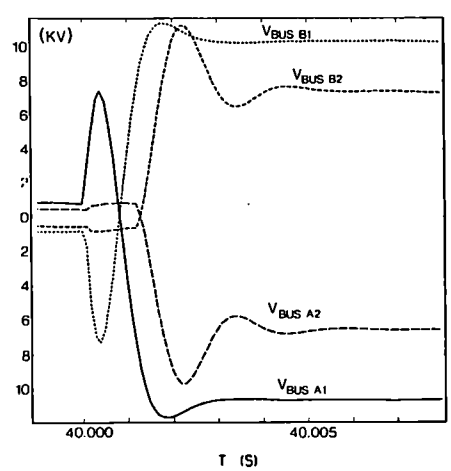

Fig 3: Voltage between Ohmic Heating Circuit busbars and earth produced during the interruption of a 40kA current.

are twice the expected value. The difference is probably due to a reduction of the P1-4,5 inductance, due to eddy currents in the vessel and in the central JET mechanical structures. Despite these difference the blocking diodes still operate within their design voltages.

The digital control of the plasma current (PCC) became operational in JET in 1986. In order to control the new complex JET Magnetising Circuit, a new series functions had to be provided. These are:

- the IB Premagnetisation Control
- the control of the ID P1 Coil Current Difference
- the IBMIN Minimum P1-4.5 coils current limiter
- the IBMAX Maximum P1-4,5 coils current limiter
- the IAMAX Maximum P1-1,2,3 coils current limiter, function of the Toroidal Field.

The new PCC limiter functions have added a new level of protection and have simplified greatly the operation at full performance near the machine limits. The intervention of the P1-MPC protections and the following drastic termination of the pulse due to changes of plasma resistivity can be avoided.

The sequence and logic of intervention of the PCC control algorithms [1] is summarised in fig.4.

The performances of the difference PCC functions after corrections and optimisations performed during commissioning are shown in Table 2.

After recalibration of the CMC current transducers and a modification of the P1 cooling system, allowing I^2T of $40 \cdot 10^9 A^2s$ in P1-1,2,3, the full P1 current swing pulses were repeated (Table 1, D6).

The measured total P1 flux swing (fig.5) is 42Wb at the inner wall and 39.8Wb at the outside. The flux swing linked with a standard plasma current is slightly more than 41Wb with an increase of around 7Wb from the JET design value (34Wb).

The measured vertical field on the JET midplane produced by 35kA of P1 coil current difference (ID) is shown in fig.6. The field,

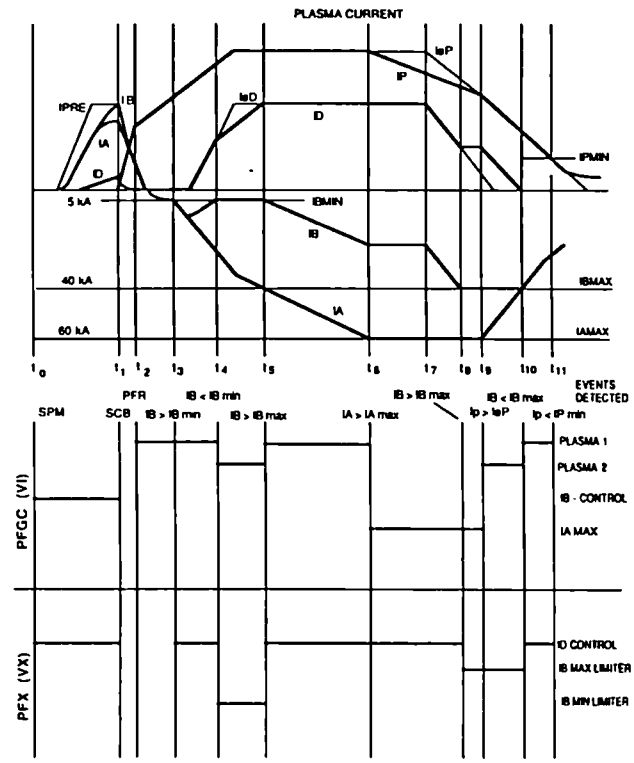

Fig 4: Changes of PCC algorithms during a JET pulse

TABLE 2: PERFORMANCE OF THE DIFFERENT FUNCTIONS OF THE PLASMA AND P1 CURRENT CONTROL

IP PLASMA CURRENT CONTROL
- Closed loop response time T_c = 0.15s
- Percentual plasma current error I_{PE} = 1-2%

IB PREMAGNETISATION CURRENT CONTROL
- Overshoot I_o = 0.6kA

ID CURRENT CONTROL
- Closed loop response time T_d = 25ms
- ID current error I_{DE} = 1-2kA

IB MAXIMUM CURRENT LIMITER

IB MINIMUM CURRENT LIMITER
- Closed loop response time T_e = 30ms
- IB current overshoot I_{BO} = 1-2kA

IA MAXIMUM CURRENT LIMITER
- IA current overshoot I_{ao} = 1kA

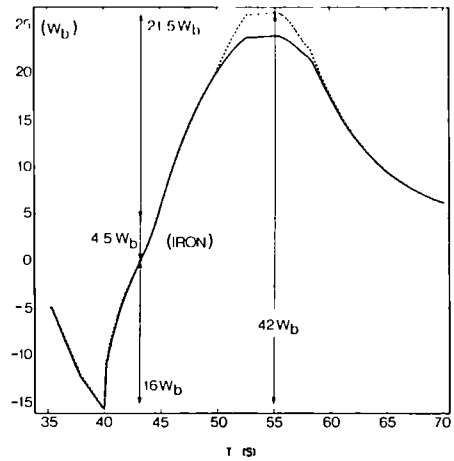

Fig 5: Complete P1 flux swing measured in a commissioning pulse at the vacuum vessel inner wall (dotted line) and at the outer wall (continuous line).

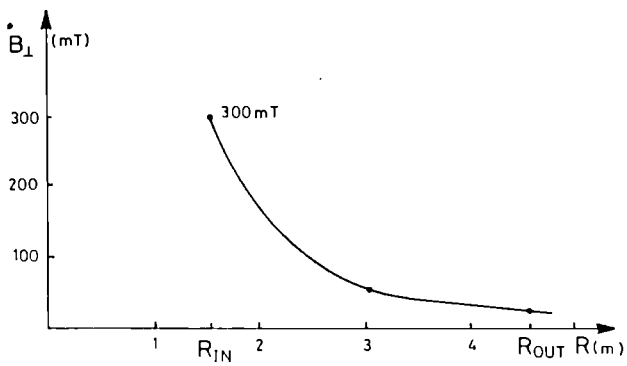

Fig 6: Midplane Vertical Field Produced by 35kA of P1 coil current difference ID.

mainly hexapolar, is particularly strong on the inside in front of the iron collars.

During these tests the coils and the power supplies were tested at their maximum performances. In Table 3 the main parameters of the JET Magnetising Circuit are listed together with their design values and the maximum values reached in these commissioning pulses and in operation.

3. THE NEW VERTICAL FIELD CIRCUIT FOR THE CONTROL OF P4 CURRENT IMBALANCE

With the extra quadrupolar and hexapolar fields produced by the CMC, magnetic separatrix operation at 4-4.5MA with single null and 3.5-4MA with double null has been obtained. To extend the single null configuration at 5MA and over, avoiding too high shear stresses in the collar tooth region of the TF coils [3], a new configuration has been proposed making use of an imbalance of current in the Vertical Field Coils. With a current imbalance of 500kA turns, more in the upper P4 coil than in the lower P4 coil, a single null 7MA configuration has been predicted by computer simulations.

TABLE 3: MAIN PARAMETERS OF THE JET PF SYSTEM: JET DESIGN VALUES, VALUES REACHED DURING COMMISSIONING AND DURING HIGH CURRENT OPERATION

		Design Value	Comm Value	Operation	
PLASMA CURRENT	(MA)	4.8		7	5X-P
FLAT TOP TIME	(s)			2	5
RISE TIME	(s)			9	10
LOOP VOLTAGE	(V)			1-1.3	1
P1-4,5 CURRENT	(kA)	40	40	40	30
P1-1,2,3 CURRENT	(kA)	40	60	60	47
P1 FLUX SWING	(Wb)	34	42	42	32
PFGC ENERGY	(GJ)	2.6	2.3	1.9	0.75
R4 ENERGY	(GJ)	0.48	0.2	0.2	0.08
R3 ENERGY	(GJ)	0.80	0.3	0.3	0.17
R8 ENERGY	(GJ)	0.81	0.6	0.6	0.32
PFX I**2*T	(GA²s)	16	9	0.7	9
PFGC I**2*T	(GA²s)	90	56	41	15
P1-4,5 I**2*T	(GA²s)	32	24	19	7
P1-1,2,3 I**2*T	(GA²s)	32	38	25	21
MAX PFGC CURRENT	(kA)	85	70	73	37
AT: PFGC VOLTAGE	(kV)	5	3	3	1
PFGC SPEED	(rpm)	225	150	165	110
MAX PFGC EXC CUR	(kA)	5.6	4	4.2	2
MAX PFX CURRENT	(kA)	35	35	20	32
MAX PFX VOLTAGE	(kV)	2.8	2.1	2.2	1.4
MAX PSFA CURRENT	(kA)	35		12	35
MAX PVFA CURRENT	(kA)	35		27	25

In May 1988, the Vertical Field Circuit was modified to control the imbalance of the P4 current. The new scheme is shown in fig.7. The blocking diode of PVFA 3-4 and the temporary Booster Amplifier are split between the upper and the lower half of the circuit. A new cable (10kA, 20s) connects the midpoint of P4 coils with the midpoint of the Vertical Amplifier.

Additional current transducers, new protections and a new control system have been provided. The new protections are the DC overcurrent and the I^2T protections of the new cable and two independent overcurrent protections for the Amplifier's Unit 3 and Unit 4. The new control functions comprise the feedback control of the P4 current imbalance, the limiter of the P4 current imbalance, the P4

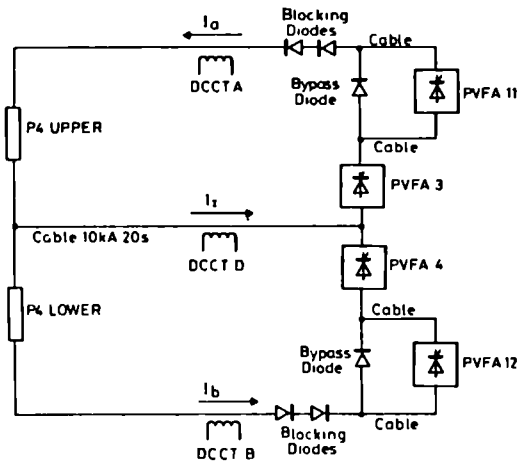

Fig 7: New Vertical Field Circuit for the control of P4 Current Imbalance I_I.

average current limiter and the limiter of the voltage imbalance.

4. OPERATION OF THE NEW POLOIDAL FIELD CIRCUIT

4.1. 7MA Limiter Operation

The reduction of stray fields obtained by the extra two P1 subcoils has allowed reliable breakdown at maximum premagnetisation current (40kA) with a flux loss of less than 1Wb ". The extended P1 flux swing has permitted routine

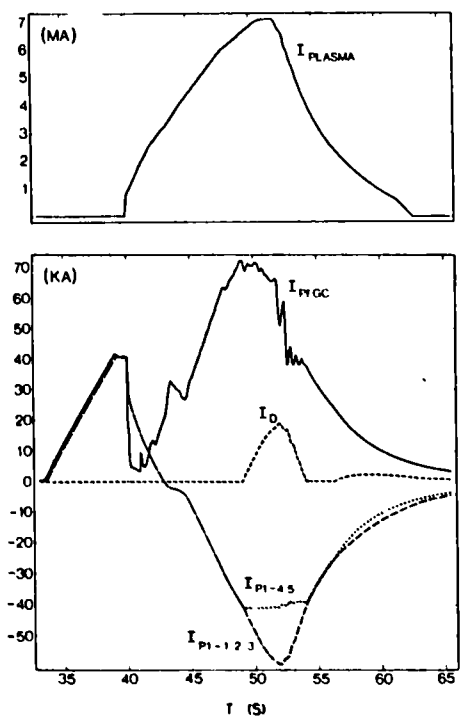

Fig 8: PF System Currents during a 7MA plasma pulse.

operation at 6MA for 7s and a few test pulses at 7MA. In the 7MA pulses, because $Q\psi$ is less than 3, to avoid disruptions during the rise phase, the rate of rise of the plasma current is limited to 0.6MA/s, using simultaneous Toroidal Field ramp up. The operation at $Q\psi<3$ also increases the plasma resistive losses. In fig.8 the main PF current waveforms are shown.

4.2. 5MA Magnetic Separatrix Operation

The new modifications allowed routine operation with magnetic separatrix in single null configuration, with plasma current up to 5MA. The simulated 7MA X-point configuration exceeds the actual operational limit imposed to the quadrupole field at high plasma current to prevent vertical disruptions from overstressing the vacuum vessel.

The magnetic configuration of a 5MA X-point discharge is show in fig.9. In fig.10 the relative Poloidal Field Circuit voltage and current waveforms are shown.

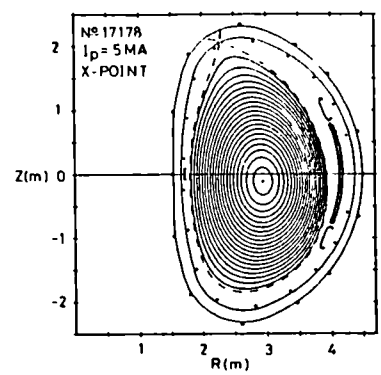

Fig 9: JET magnetic flux surfaces for an X-Point discharge with I_p = 5MA.

The up/down disymmetry of the plasma and PF coils configuration and the vertical displacement of the plasma current centre has coupled the Vertical Position Control System with the remaining part of the PF circuit. During sudden changes of plasma current profile, vertical instabilities have been experienced, generated by the fast rearrangement of the vertical equilibrium and the saturation of the Plasma Vertical Position Control System.

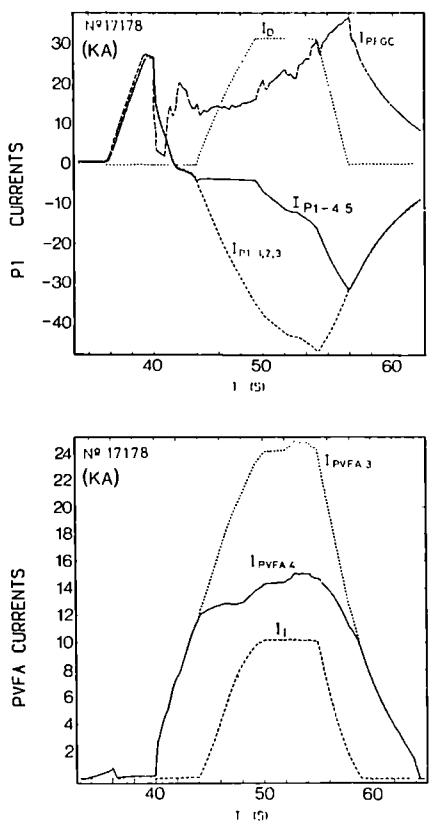

Fig 10: PF System Currents in a 5MA X-Point discharge.

5. FUTURE ENHANCEMENTS

5.1. Disruptions are still the major cause of concern in the operation of JET at high plasma currents and large elongation ratio. Many improvements of the Poloidal Field Power Supplies and Control Systems are necessary in order to reduce the number of shocks to the vessel during Tritium operation to a minimum.

To avoid disruptions due to the m=2, n=1 locked mode, two new high frequency amplifiers (0-10kHz, 3kA, 0.7kV) will be connected to eight saddle coils to try to stabilise m=2, n=1 mode by feedback.

To reduce the risk of vertical instabilities, new control schemes will be implemented in the next shutdown period [5]. A study to upgrade in voltage and speed the Radial Field Amplifier is in progress to overcome the problem of voltage saturation during single null operation and increase the stabilisation margin.

5.2. To improve the X-Point configuration at high plasma current the PF Circuit Amplifiers (PFX, PSFA, PVFA) will be upgraded from the actual rating of 35kA for 12.7s to 40kA for 15s, by changing the thyristors in the bridges.

5.3. The Poloidal Vertical Boost Amplifier will be operational after the next 88/89 JET shutdown period and will provide a better control of the Plasma Radial Position during the early phase of the discharge, allowing a more reliable plasma start up.

ACKNOWLEDGEMENTS

This paper contains experimental results that were produced by the dedication and efforts of all the JET team. The authors would like particularly to thank L.Zannelli and T.Eriksson who collaborated in the installation of the new equipment and A.Moissonnier for his great help in the trouble shooting.

REFERENCES

1. P.L.Mondino, T.Bonicelli, T.Eriksson, M.Huart, F.Petree, C.Raymond, A.Santagiustina and L.Zannelli; "The PF system enhancement in JET to produce plasma currents up to 7MA with material limiters and up to 4MA with magnetic separatrix, a report on the electrical study", Proceedings of the 12th Symposium on Fusion Engineering, Monterey, USA, October 1987.

2. E.Bertolini, J.R.Last, P.L.Mondino, P.Noll, A.Santagiustina; "The development of the JET electromagnetic system", Proceedings of the 14th Symposium of Fusion Technology, pp263-271, Avignon, France, September 1986.

3. J.R.Last, et al; "Upgrading the JET Magnet System for 7MA Plasma", To be presented at the 8th Topical Meeting on Technology of Fusion Energy, Salt Lake City, Utah, USA, October 1988.

4. P.J.Lomas et al; "High current operation in JET", 15th European Conference on Controlled Fusion and Plasma Heating", Dubrovnik, Yugoslavia, May 1988.

5. M.Garribba et al; "A dual system for the stabilisation of the vertical plasma position of the JET experiment", this volume.

THE DESIGN, CONSTRUCTION, INSTALLATION AND TESTING OF A BOOST AMPLIFIER FOR THE VERTICAL FIELD POWER SUPPLY OF JET

M.Huart, G.L.Basile*, D.Ciscato**, O.Buc, J.K.Goff

JET Joint Undertaking, Abingdon, Oxon, OX143EA, UK
* OCEM Spa, San Giorgio di Piano, Bologna, Italy
**Universita di Padova, Padova, Italy.

The Poloidal Vertical Field Boost Amplifier (PVFB) is designed solely to assist the plasma start-up phase in JET (1-2s)). Its rating of 11kV no load, 6.0kA DC is obtained from four identical modules each consisting of dry-type transformer and air-cooled thyristor rectifiers mounted in high voltage decks. The paper will review the system design of the power supply, the layout of control and protection, the firing generation and monitoring as well as the thyristor failure detection. Finally, the paper will review the factory tests performed on the equipment.

1. INTRODUCTION

The Vertical Field Circuit of JET is supplied from an amplifier (PVFA 3-4) rated 2.8kV no load, 35kA for 12.7 seconds. The need to provide a higher (boost) voltage during the plasma start-up is reviewed in [1], and stems from the new configuration of the Poloidal Field Circuit introduced in early 1985. To maintain the radial equilibrium of the plasma column during the early fast rise phase, the voltage applied to the vertical field coils should be approximately equal to half the voltage applied to the magnetising coils, typically 10kV-20kV, depending on the premagnetisation current.

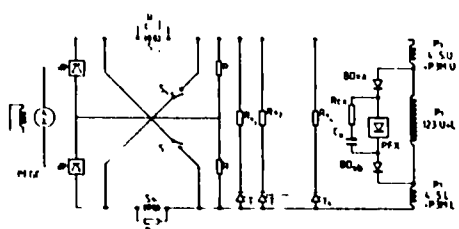

FIG 1 a ARRANGEMENT OF JET POLOIDAL MAGNETISING CIRCUIT

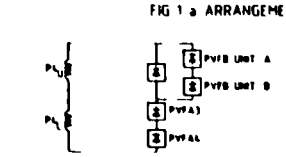

FIG 1b
ORIGINAL DESIGN OF VERTICAL FIELD CIRCUIT WITH BOOST AMPLIFIER

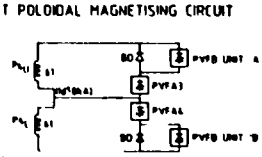

FIG 1 c
REVISED DESIGN OF VERTICAL FIELD CIRCUIT TO OBTAIN CURRENT INBALANCE IN COIL P4

With the limited capability of PVFA 3-4, the radial position control saturates for 150-300 milliseconds causing a radial position error and restricting the parameter range for breakdown.

2. REFERENCE DESIGN

The Design Study for the Poloidal Vertical Field Boost Amplifier started in late 1985.

The preparation of technical specifications was produced in early 1986 and the procurement contract was placed in October 1986 with the firm OCEM Spa after a Call for Tender.

The PVFA 3-4 was originally fitted with a series blocking diode rated 12.0kV, 35kA. The higher voltage required could be obtained by connecting in parallel to this "by-pass" diode a "boost" amplifier of low current rating (~6kA) (fig 1b). The reference design arrived at a configuration of four identical series connected modules, each rated 2.7kV, 6kA for 0.5s.

The design established the possibility to feed the modules of the boost amplifier directly from the output of the PVFA 3-4 33kV/1.05kV transformers.

The transformers of PVFB have therefore a ratio near unity (1050V/1015V) and therefore a

dry-type transformer for indoor use was an attractive solution as it would lead to a more compact design with the rectifier mounted above the transformers.

In addition, various other features were fixed, namely:

- the thyristor rectifiers are to be air-cooled in preference to water cooling in view of the higher reliability and lower maintenance,
- each module consists of two series connected thyristor bridges and thereby avoids series connected thyristor in bridge arms (fig.2),
- the rectifiers of each module are housed in H.V. decks. This reduces the insulation level of the rectifier components from 20kV rms to 5.5 rms test voltage. It led to a more compact design of the rectifier and it simplified the design as 6-12kV is the insulation level of currently available components (power capacitors, voltage/ current transducers, pulse transformers, fuse microswitches, etc).
- the rectifiers have no thyristor fuses. The failure of thyristors is detected by the reverse current and causes the full inversion in less than one cycle and the subsequent tripping of the circuit breaker. In fact, if fuses were fitted, the low value of the fault current with respect to the pulse current means that it would take several cycles before the fuse cleared the fault.
- the H.V. decks are fitted with autonomous fire detection and fire suppression equipment. The fire detection module causes both the 33kV circuit breaker and the 240V supply to the H.V. deck to be tripped and halon to be released within 5 seconds of a fire being jointly detected by two separate sensors.

3. POWER SYSTEM DESIGN - OVERCURRENT PROTECTION

The power system design is dominated by the large fluctuation in fault level due to the variation of the 33kV busbar voltage, the

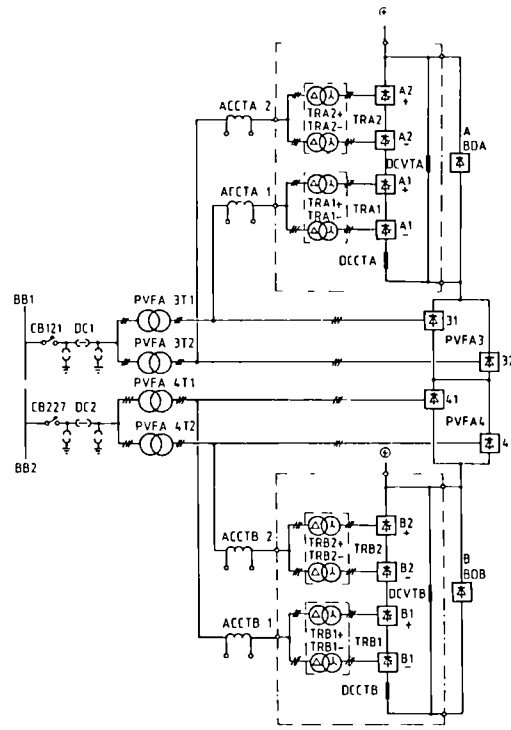

FIG. 2 ARRANGEMENT OF VERTICAL FIELD AMPLIFIER AND BOOST AMPLIFIER

voltage drop due to the commutation of the PVFA 3-4 bridges and the impedance of the PVFB transformers.

First, the impedance was chosen on consideration of the detection of the minimum fault current. This was defined as the short circuit, across one module only, that occurs when the PVFB is rectifying a current equal to the setting of the DC overcurrent trip (set at 130% rated current). The fault current was set at 160% rated current to allow for discrimination. In the same condition, the short circuit of one bridge only would lead to a fault current equal to 170% rated current.

This gave a maximum impedance of 5%. The impedance of the PVFB transformers was chosen as 4.5% ± 10%. The transformers are rated 1050V/1015V - 1015V, 3400kVA.

Despite this rather low impedance, the fault current level in PVFB when the PVFA is operating at its rated current of 35kA DC would be no more than 6.0kA, too low to be detected.

To overcome this difficulty, both the DC and

AC overcurrent protections have two levels. The lower level, corresponding to 1kA DC equivalent is selected whenever the DC or AC current signals from the PVFA rectifier rectifier exceed a level higher than 8kA DC equivalent (fig.3).

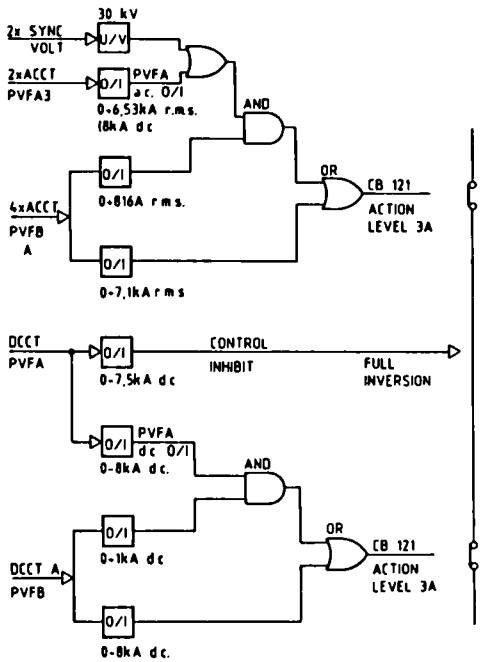

FIG.3 CONCEPT OF THE OVERCURRENT PROTECTION AND CONTROL INHIBIT (ONE UNIT ONLY)

4. RECTIFIER ASSEMBLY - HV DECK

The circuit diagram of the H.V. Deck is shown in fig.4. Each H.V. Deck contains two thyristor bridges series connected with the mid-point connected to the H.V. Deck frame. The insulation level of the rectifier within the H.V. Deck is 5.5kV rms. Wherever possible, an insulation level of 10kV rms has been used in the design of the assembly and in the selection of components.

Each thyristor bridge is rated 1370V DC no load and 6kA 0.5s every 10 minutes. The rectifiers use a single thyristor per arm, type DCR 1476, V_{RRM} = 3600 V, I_{AV} = 1360 A (single side cooling). The junction temperature for the rated duty is 50°C above the heatsink temperature estimated as 47°C in an external ambient of 35°C. The thyristors are clamped on aluminium extrusion forming the positive and negative terminals of each bridge. The air cooling of the heatsink is assisted by a fan capable of 230 m^3/hour at 6mm H_2O.

The AC input is supplied from bushings at the bottom of the H.V. Deck through individual Rogowski coils aimed at detecting thyristor failures. The DC outputs are connected at the top of the H.V. Deck.

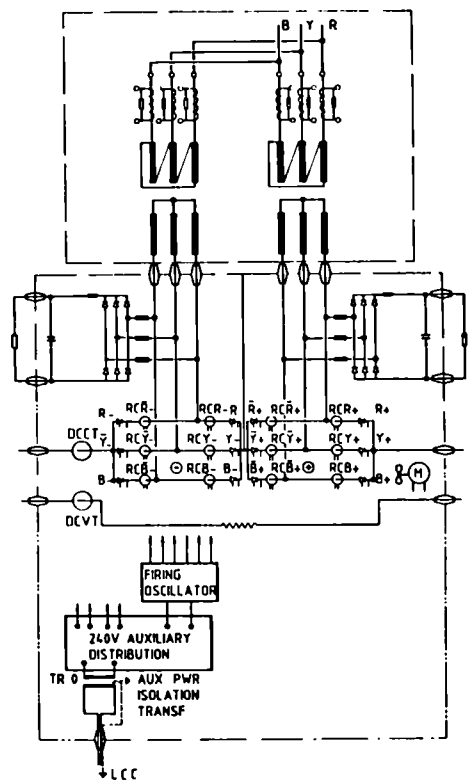

FIG.4 CIRCUIT DIAGRAM OF H.V. DECK.

5. LAYOUT OF THE CONTROL AND PROTECTION

The control, monitoring and protection (CMAP) functions related to the rectifiers are located at H.V. Deck potential, in a segregated compartment. All signals between the H.V. Deck CMAP system and the power circuit sensors are transmitted either optically or through a high voltage isolation interface (15kV DC).

All other CMAP functions related to the complete Boost Amplifier as well as the interfaces with PVFA, the Control and Data Acquisition System (CODAS), the Central Interlock and Safety System (CISS) are housed in a segregated Local Control Cubicle (LCC) situatated outside the HV area for accessibility during operation.

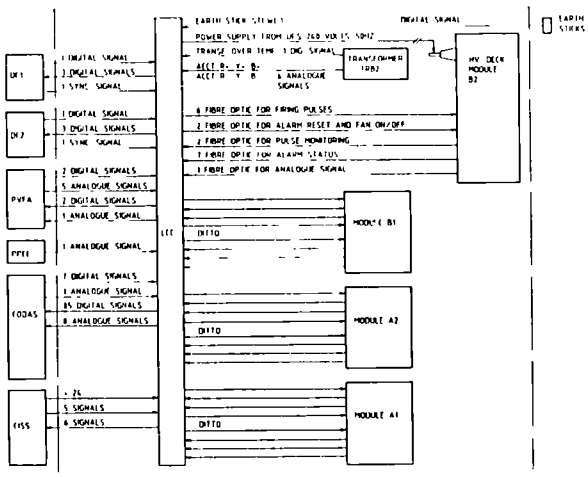

FIG. 5 LAYOUT OF CONTROL SIGNALS

The layout of signals is shown schematically in fig.5. Signal transmission between each H.V. Deck and the LCC is through Hewlett Packard plastic fibre optic cable type HFBR-3530. JET favoured the use of individual fibres rather than multiplexed serial links. The total number of fibre links installed is 72 with a further 12 available for spare status and four available for spare commands.

The CMAP functions are distributed in the LCC as follows: one "system" crate houses the control loops, two "modules" crates house the alarm status and protection of each module, one "unit" crate holds the firing pulse generation and alarms related to the units. Two crates handle the conditioning of all external signals (capacity for 187 including spares) with the exception of optical signals routed directly to the "unit"/"module" crates.

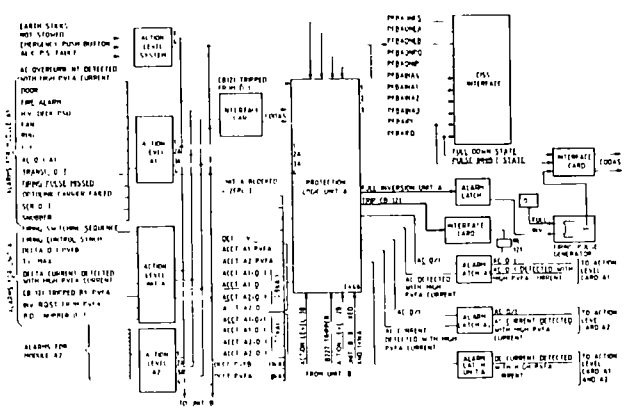

FIG 6 LAYOUT OF PROTECTION AND INTERLOCK

The layout of the protection logic is shown schematically in fig.6 where only one unit is represented. The layout has been simplified by the adoption of "action levels" which relates to the level of protection action resulting from fault conditions. Four levels have been identified, namely:

- action level 1 inhibits the next JET pulse through CISS;
- action level 2A/2B causes the immediate inversion of unit A/B to transfer the DC current to the freewheel diode followed by the blocking of firing pulses of unit A/B;
- action level 3A/3B causes in addition the tripping of the 33kV circuit breaker related to unit A/B;
- action level 4 causes the tripping of both circuit breakers.

The PVFB has a short time rating (nominal 0.5s). To ensure a proper thermal protection of the various components in all scenarios, the following protections have been implemented:

- thyristor junction temperature simulation (ΔT_{j-h}=65°C)
- heatsink overtemperature (T_h=60°C)
- primary cable temperature simulation (ΔT_c=50°C, τ=1600s)
- transformer cooling air temperature (T_a=150°C)

These define the current capability of the PVFB (fig.7).

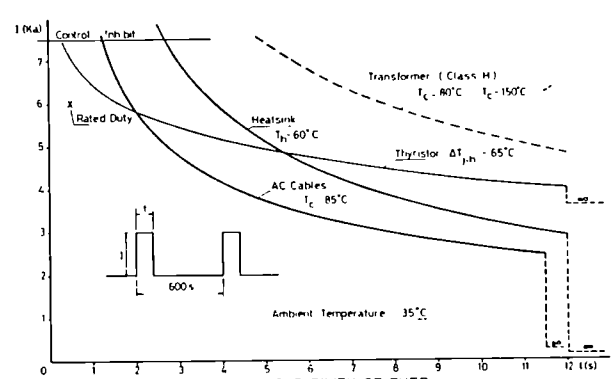

FIG 7 CURRENT CAPABILITY OF PVFB

6. THYRISTOR FIRING GENERATION, DISTRIBUTION AND MONITORING

The firing pulse generator of each PVFB unit is digital. A PLL provides the clock signal to a counter modulo 3072 and a 12 bit tracking ADC converting the analogue control signal from the voltage feedback amplifier. The output of the counter is a synchronised reference sawtooth with a bit resolution equivalent to 0.12 electrical degrees.

The output of the counter and the ADC are summated in a modulo 3072 adder to provide a sawtooth phase shifted with respect to the reference. It is then decoded to derive two sequences (30 degrees phase shifted) of pulses (spaced by 60 degrees) which are sent to each HV deck module.

The firing pulse generator is also provided with logic inputs for full inversion, blocking firing pulses and for reset. The decoder output is checked for correct sequencing.

The pulses to each module are transmitted through plastic fibre optic links to the H.V. Deck. They are split by the receiver between the firing pulse amplifiers of each bridge. Each firing pulse amplifier is used to gate the 20kHz pulses from a common power oscillator. Part of the initial peak of thyristor gate pulses is shunted through a fibre optic link (for isolation) to a receiver in the H.V. Deck control compartment where the signals are combined into a serial pulse train for transmission to the LCC. The parallel signals originally sent to the H.V. Deck are then compared with the serial signal using combinational logic to provide indication of any "missed" pulse in any particular thyristor (fig.8).

The original concept of this system indicated that large scale logic integration would be desirable. This led to the consideration of Application Specific Integrated Circuits (ASIC) which uses complementary metal oxide semiconductor (CMOS) Erasable technology to provide User Configurable Integrated Circuits (UCIC). The logic design entry is made through a "PC" using high level macrofunctions, state machine descriptions or Boolean equations.

Using these "programmable logic devices" (PLDs), minor design errors were then reprogrammed in a few hours.

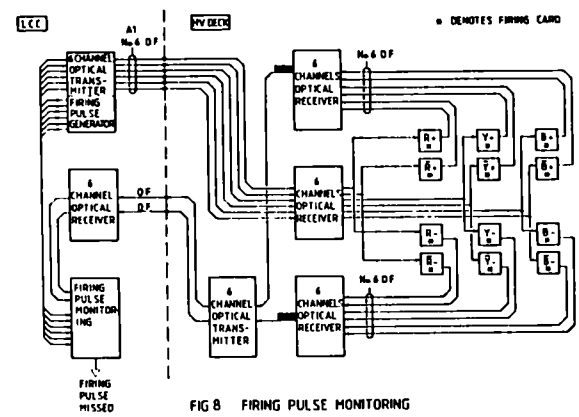

FIG 8 FIRING PULSE MONITORING

7. THYRISTOR FAULT CURRENTS. BREAKDOWN AND DETECTION.

7.1 Thyristor fault current.

The following faults have been simulated in conditions leading to the worst fault current (maximum voltage, minimum reactance) namely: short circuit across one bridge, across two bridges and across the load. The calculated waveforms of fault current were then sent to the device manufacturer to assess junction temperature and thyristor survival.

The worst case is the short circuit of one bridge only. The initial peak current is 32kA decaying to 24kA, values above the surge rating of the thryistors (respectively 29kA/10ms and 18.5kA/100ms). There is however no danger of explosion since the explosion rating lies between 5 and 10 times the surge rating.

With a short circuit across two bridges (one H.V. Deck), the fault currents (24kA, 17kA) are within the surge rating of the thyristors.

With a short circuit across the load, the fault current in PVFB is low due to the voltage drop in PVFA transformers.

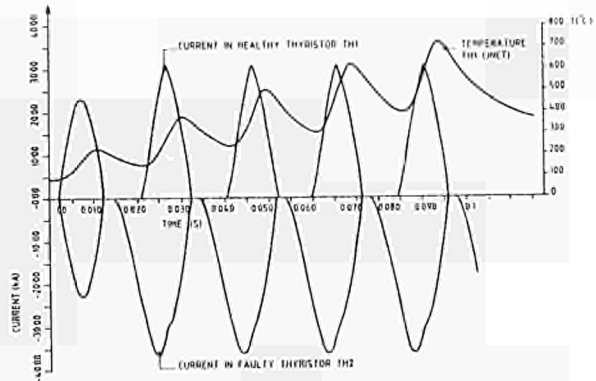

FIG.9 FAULT CURRENTS AND THYRISTOR JUNCTION TEMPERATURE

7.2 Thyristor breakdown.

The fault current resulting from a thyristor breakdown have been simulated in the worst conditions of voltage and impedance. The currents in the healthy and faulty thyristors are shown in fig 9. The surge rating for 0.1 second is exceeded. However, if the detection of the failure and the full inversion of the bridge occurs within a cycle, the surge rating will not be exceeded hence assuring survival of the healthy thyristors.

7.3 Detection of thyristor failure.

The detection of thyristor failures is achieved by the monitoring of the reverse current in the thyristors. The arms of the bridges are fitted with individual Rogowski coils (fig 4). The signals from the coils are routed to active integrators as shown in fig 10a. The diode clips the forward arm current. The output for a healthy thyristor is shown in fig 10b. The time constant of integration is clearly visible. At steady state, the output oscillates between -0.5 volt (diode) and +0.5 volt/2 + 1.5 times the initial voltage offset (120° conduction). This offset can be kept low by using a low time constant (low gain) since the reverse current to be detected is short lived (1 or 2 cycles). The parameters adopted were: gain of integrator = 100, time constant = 1s, maximum positive output voltage including offset = 0.475 V, tripping level of detection: 1 volt (≡ 1.7kA reverse current).

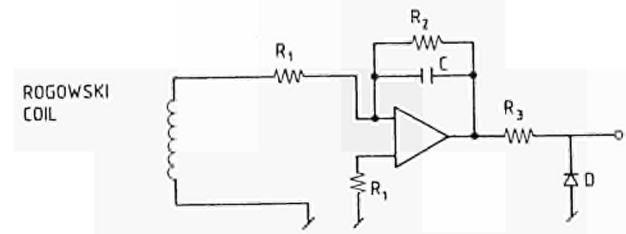

FIG. 10a. REVERSE CURRENT DETECTOR

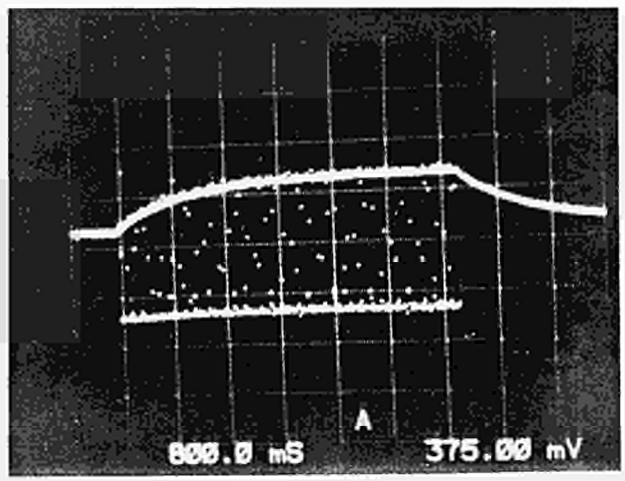

FIG. 10b. OUTPUT OF REVERSE CURRENT DETECTOR.

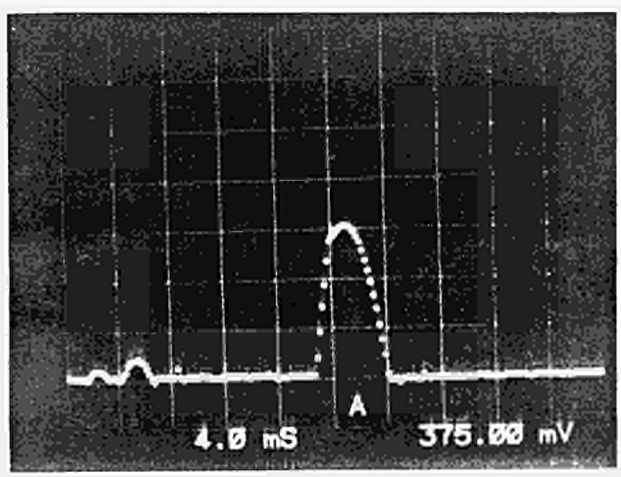

FIG. 10 c. OUTPUT OF REVERSE CURRENT DETECTOR.

8. FACTORY TESTS

The factory tests of the transformers included the routine tests and in addition a

short circuit withstand test to prove the mechanical design. Nine short circuits (0.5s long) were performed at the High Current Laboratory of CESI (Milan) on transformer 74066 which passed the test successfully.

The factory tests of the HV decks and LCC consisted of functional tests and power tests. The functional tests were aimed at checking the correct operation of all alarms, protections, commands, as well as checking the calibration of monitoring circuits.

On completion of these tests, the LCC was installed in a temperature controlled room and the temperature was set to 50°C ambient. The equipment was left energised overnight to detect spurious faults and the functional tests were repeated to check the correct operation at elevated temperatures. A similar test was performed on one H.V. Deck module.

The power test consisted of 1) load test to check the firing pulse synchronisation and the voltage loop, 2) high current test to check the calibration of DCCT against an external shunt and the correct operation of the reverse current detection. Due to supply limitation, the maximum current was limited to 3.7kA. The calibration of the DCCT was within 0.1% of full scale. To check the correct operation of the reverse current detection, the connection of one Rogowski coil was inverted. Fig 10c shows the output signal of the integrator. The first current pulse corresponds to a transient during the release of firing pulses. The second current pulse has a peak of approximately 2.0kA and is sufficient to trip the reverse current detection and to cause the full inversion before the subsequent cycle.

9. SITE INSTALLATION AND TESTING

The installation of the PVFB on the JET Site was completed in August 1988. The functional tests with CODAS, CISS, PVFA will take place in October 1988 and the power tests on dummy load will be performed in November and December 1988.

ACKNOWLEDGEMENT

The authors would like to acknowledge the contribution of A.Santagiustina toward the reference design, mainly through the extensive computer simulation of the poloidal field circuit.

REFERENCE

[1] P.L.Mondino et al "The Development of the JET Poloidal Field Power Supplies to Reach the Nominal Flux Swing Capability", Proceedings of the 14th Symposium on Fusion Technology, pp. 859-866, Avignon, France, September 1986.

ALIGNMENT OF THE JET HIGH POWER PARTICLE BEAMS

P Massmann, G H Deschamps, H D Falter, R S Hemsworth and A Meinberger*

JET Joint Undertaking, Abingdon, Oxon, OX14 3EA
*Fachhochschule Aachen, Juelich Branch, West Germany

The alignment procedure for the JET beams is described. Deviations up to 0.5^0 of the actual beam axis from the nominal geometric centre line have been found in the Test Bed. Vertical deviations can usually be corrected by a single source adjustment. Horizontal deviations are deduced to be caused simultaneouly by mechanical inaccuracies, power effects and by the vertical component of the Earth's magnetic field.

1. INTRODUCTION

The JET D^0 injectors deliver a power of about 10 MW with a peak power density of nearly 10 kW/cm^2 for pulse lengths of some 10 s. The lengths of the beam line is about 10 m, the beamlet divergence is around 0.7^0. To keep the component power loading at the beam edge below a dangerous level, and for optimum transmission through a tight geometry, precise knowledge of the beam profile along the beamline is essential. For safe operation of the JET beams the tolerable alignment accuracy is about 0.1^0.

The original procedure provided that the optimum alignment of each individual PINI (Positive Ion Neutral Injector) source, as defined by the Torus entrance port, was to be determined in the Neutral Injection Test Bed prior to installation on the injectors. The Torus magnetic stray field, the only important item which is not duplicated or simulated in the Test Bed, was to be screened by iron shielding around the injectors. Therefore the alignment diagnostics on the Torus lines has been limited, only allowing horizontal checks on the Calorimeters or the Box Scrapers.

Experience has shown that the alignment is

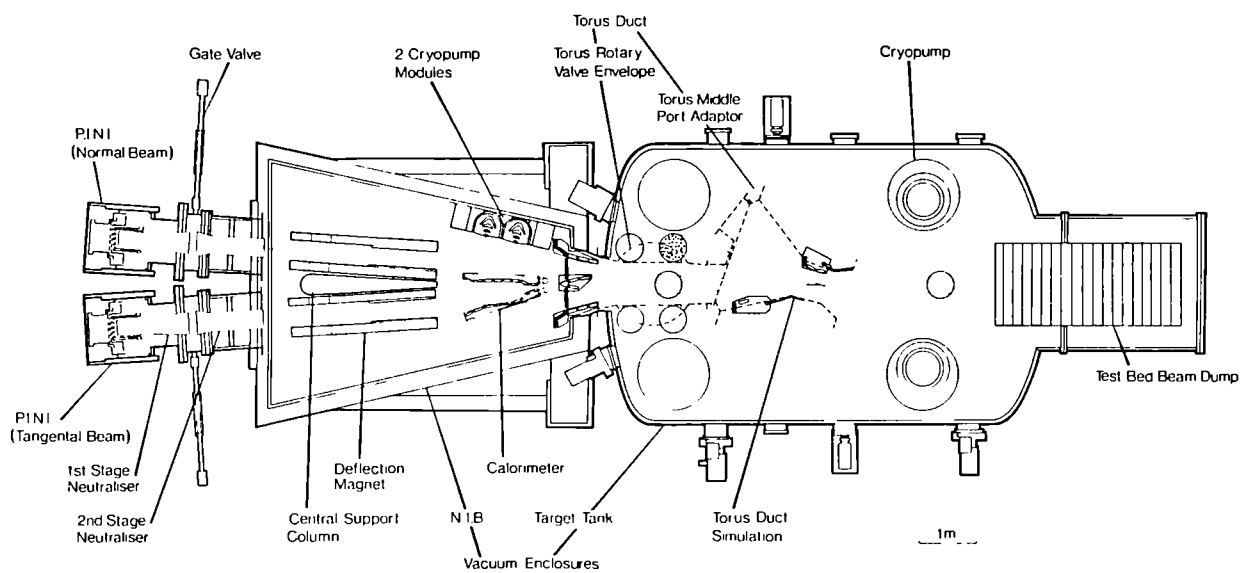

FIGURE 1: Plan View of the Test Bed

not transferable. One reason is the high stray field still present despite the shielding, which has led to the application of extra compensation coils. Moreover, the final alignment is of necessity determined in situ. To facilitate this, the manual Torus PINI steering will be replaced by a remote system.

The majority of the alignment measurements have been performed in the Test Bed, which remains irreplaceable to obtain indicative and special data.

2. EXPERIMENT

2.1 Test Bed

Fig. 1 shows a plan view of the Test Bed equipped for a dedicated injector test (Quadrant Test). The measurements were done with one PINI mounted at the left hand (position 4) or the right hand port (position 1) located side by side above the horizontal midplane of the Neutral Injector Box (NIB).

The sources can be steered remotely by means of pneumatically driven, adjustable flanges. The displacement of a steering flange is recorded by vertical and horizontal sensors. With the installation of a new source the steering flange is aligned to the geometric (beam) centre with a telescope. After pump down this is reset using a laser system. The horizontal and vertical sensor readings are then set to zero.

2.2 Diagnostics

Determination of the actual alignment occurs mainly by thermal diagnostics on actively cooled beam stopping panels by fast bare wire thermocouples (TCs) inserted in the metal 3 mm below the exposed surface. Stainless sheathed TCs in the cooling channels allow to measure the power on a panel or subcomponent by water calorimetry. Most of the measurements are done on the Test Bed Beam Dump (TBBD, Fig. 2) at nominally 12180 mm from the source. The TBBD panels are mounted horizontally to form a curved "Vee" in the vertical direction. The dashed lines show where the nominal vertical centre planes intersect the panels. The nominal beam centres land on element 18 (shaded). The crosses indicate fast TCs. Panel water TCs are marked by a "W".

Vertical beam profiles from the fast TCs are obtained by a Gauss fit through the maximum temperature points plotted against the distances to the nominal beam centres. Line power density profiles are derived from water calorimetry by applying the Gauss fit to a spatial plot of the integrated powers over the projected vertical panel heights. The two methods agree well. Profile variations along the dump are neglected.

Horizontal profiles are measured on element 18. In this direction the beam is effected by scrapers and the profiles have to be corrected by transport calculations. These use the divergence from a vertical profile. The correction is obtained by comparing the Gauss fit through the calculated points with the one through the measured points.

The JET injectors and the Test Bed are also equipped with optical beam scanners, which record line integrated H- alpha intensity profiles. The scanner zero alignment is determined with a fluorescent light tube suspended along the nominal beam centre. For this purpose the H-alpha filter is removed.

At present this method is not yet refined enough to be routinely available. The main problems arise from background and reflection effects causing non- zero baselines and asymmetric plateaus in the wings of the profiles. The presented data have been evaluated by hand fitting Gaussians through selected points of the profiles.

3. MEASUREMENTS

3.1 Alignment

The optimum alignment is determined on the TBBD from a horizontal scan after alignment of the perveance matched beam to the nominal vertical centre. The PINI is then moved horizon-

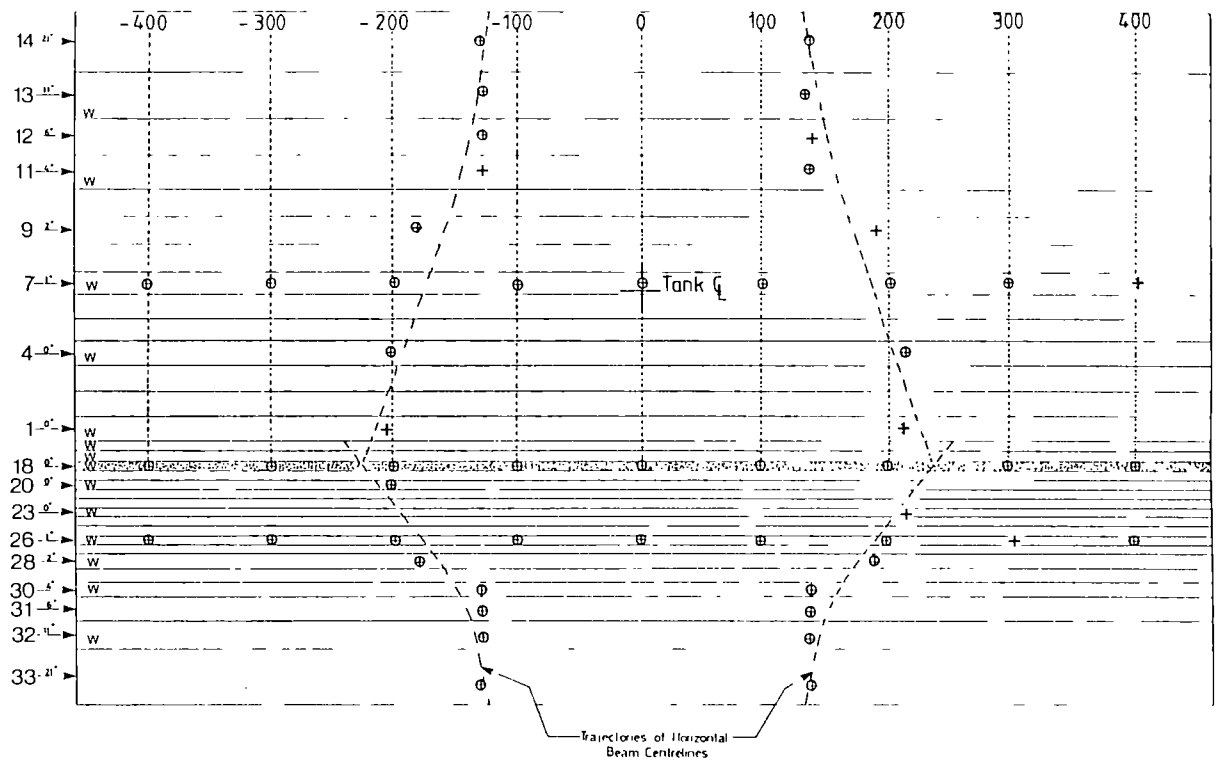

FIGURE 2: Projection of Test Bed Beam Dump onto a Plane Normal to the Target Tank Centre Line

tally by about 100 mm and the horizontal and the vertical positions are recorded. In a plot of the horizontal position versus the flange reading a straight line is fitted through the data parallel to the line expected from the movemment of the PINI flange. The offset between the two lines yields the deviation from the nominal centre. The vertical alignment is found from the vertical position together with the relation between the two readings. The vertical position is not derived from a scan because energy reflection in the TBBD leads to errors when the beam is moved away from the vertical centre.

Fig. 3 shows a horizontal scan comparing the TBBD data with values from Beam Scanner 2. The solid points would have been measured if the TBBD were at the scanner distance at 6970 mm from the source (shaded port Fig. 1). Both methods indicate about 0.45^0 offset to the right. This is, within the experimental errors, in agreement with calorimetric measurements on the Test Bed Box Scraper.

3.2 Beam Position Variation

First indications, that the beam position depends not only on mechanical alignment, have been found during the 1st injector test (Quadrant Test). Whereas the vertical position only showed small variations, larger deviations were found horizontally. Fig. 4 shows a temporal movement to the right during a pulse. The difference between an undeflected (a) and a neutral beam (b) is surprisingly small. The movement is less at lower source power (c). In H_2 for pulses of a few s the right hand deviation is even larger than in D_2 at comparable voltage.

Changes in the horizontal position have also been found during perveance scans. Curves b) in Fig. 5 show the right hand movement of a H_2 beam formed by a 4 grid accel stack of a PINI in position 4. The data were recorded after source alignment at 60 kV (Fig. 3). The deviation gets larger as the power is increased without yielding a direct dependence. A plot versus arc current results in a similar picture. Curve a) is

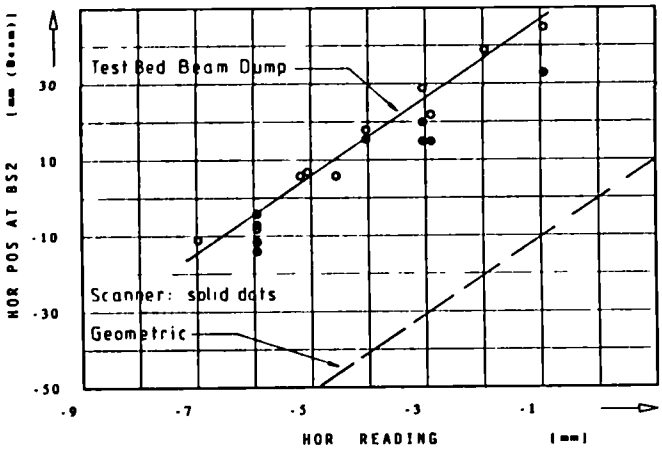

FIGURE 3: Comparative Horizontal Alignment Scan

obtained with a D_2 beam in position 1 from a 3 grid accel system after alignment at 140 kV. In this position the source is mounted upside down. Now the beam moves to the left with higher perveance.

Various experiments have been done in different gases with a particular 4 grid source, PINI A. The data were obtained on the TBBD with an undeflected beam in position 4. The results are summarised in Table 1. The data now confirm a source gas dependence. H_2 yields the largest deviation from the nominal centre, D_2 beams are less offset, whereas in Ar the actual centre agrees with the geometric alignment. Rotating the PINI by 180^0 about its centre line gives an offset to the left which is in disagreement with a pure source effect. Note that in this position the real beam axis agrees with the PINI centre line. The comparison between H_2 and D_2 at the same power yields a deviation to the right in H_2. This offset is again increased when the power is doubled. The last 3 measurements show the reproducibility of the gas effects. Changing back to H_2 yields nearly the same position and D_2 results in an offset to the left bringing the beam axis back to the PINI centre line.

The gas dependence of the vertical position is small. The only larger variation is obtained by rotation of the PINI. Like in the horizontal case the measured offset is not consistent with a deviation induced inside the PINI.

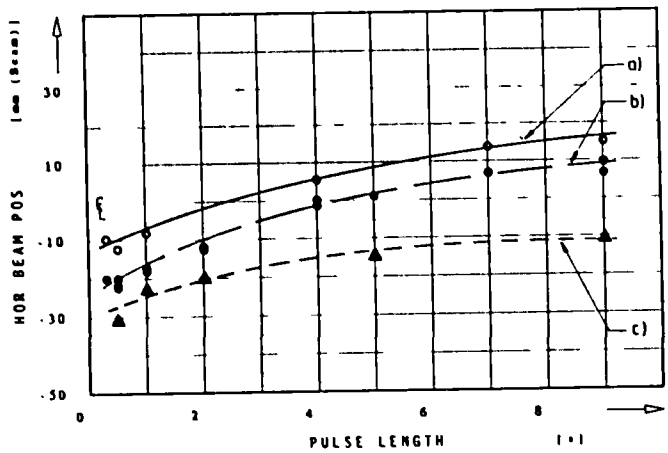

FIGURE 4: Beam Movement with Time
a) 80 kV undeflected, b) 80 kV deflected, c) 60 kV deflected. Measurements with Deuterium beams

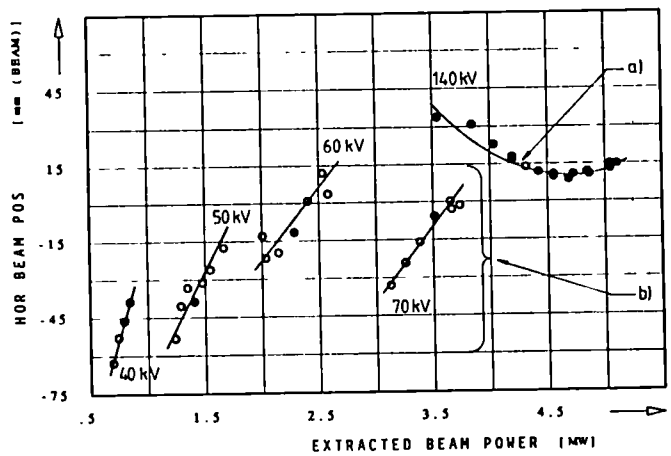

FIGURE 5: Beam Movement with Perveance
a) Deflected D_2, 3 grids, position 1; b) Undeflected H_2, 4 grids, position 4

4. DISCUSSION AND CONCLUSION

It is shown that actual beam positions can be determined on the TBBD with an absolute accuracy of 0.05^0. The consistency of the TBBD data is confirmed by calorimetric and optical measurements. As demonstrated, the scanner technique can yield reasonable results if changes in the sofware are introduced.

Considerable deviations of the actual beam axis from the nominal centre have been found. Vertical offsets can usually be corrected by a single source adjustment. Since the vertical alignment is less critical this is not further

TABLE 1
Summary of PINI A Alignment Data

SHOT NO	DEVIATION [deg] Horizontal	Vertical	SOURCE GAS	BEAM POWER [MW]	BEAM VOLTAGE [kV]	PINI STEERING STATUS
21406	0.33	0.41	Hydrogen	1.8	55	new source
21412	-0.04	0.03	Hydrogen	1.8	55	re- aligned
21743	-0.37	-0.02	Argon	0.8	80	unchanged
21927	-0.18	0.02	Deuterium	3.3	80	unchanged
22219	0.01	0.00	Deuterium	2.4	70	re- aligned
22257	-0.19	-0.24	Deuterium	2.3	70	upside down
22273	-0.03	0.00	Deuterium	2.3	70	re- aligned
22290	0.14	0.03	Hydrogen	2.3	60	unchanged
22297	0.00	0.03	Hydrogen	2.2	60	re- aligned
22308	0.13	0.04	Hydrogen	4.0	75	unchanged
22323	0.00	-0.04	Hydrogen	4.3	80	re-aligned
22340	-0.26	-0.07	Deuterium	2.3	70	unchanged
22425	0.02	0.08	Hydrogen	4.8	80	unchanged

discussed.

Horizontally the beam position depends on more than one parameter. One always expected effect is the vertical component of the Earth's magnetic field, which has been measured to be about 0.4 G. A single 80 kV H^+ ion travelling 12 m would be deflected about 70 mm to the right. The misalignments found with new sources in position 4 are all to the right and mostly of the same order (#21406, Table 1). Also the gas dependence (#22290) suggests a magnetic deflection.

This seems to be contradicted by the fact that the deflection increases with beam energy (Fig. 5). Table 1 shows however that there is an additional effect of power, i.e. thermal expansion (#22308). Fig. 6 then means that this process is also a function of time.

Consequently beams with the lowest power and the highest mass should show the smallest deflection, which is the case for Ar (#21743). Here the actual and the nominal centres agree. This suggests that the deviations could be caused by dynamic effects only. Also the H_2 data in Fig. 5 point in this direction. Extrapolation of the perveance matched points (inversed symbols) to zero would yield -0.4^0 deviation, which is close to the offset found in Fig. 3.

Unfortunately the deviations are not the same for all PINIs, i.e. there must be inaccuracies in the sources or in the PINI attachment to the injectors. The PINI rotation (#22257) seems to show that the attachment might be less reproducible than anticipated. Latest data from one of the injectors show that in single cases the steering can deviate as much as 0.3^0, after simply taking off and re- installing a PINI.

In conclusion it follows that for a quantitative understanding more unambiguous measurements are needed to unravel the superimposed effects. This is especially desirable for the variation with perveance which is not yet understood. The indication that already the Earth's magnetic field yields a substantial deflection and irreproducibilities in the PINI attachment need serious attention with a view to safe injection into the tokamak.

A NUMERICAL MODEL OF THE JET POLOIDAL CIRCUIT

P. RUTTER, T. BONICELLI, A. SANTAGIUSTINA, P.R. THOMAS and B. TUBBING

JET Joint Undertaking, Abingdon, Oxfordshire, OX14 3EA, England

The electrical circuit controlling the JET poloidal field system has been modelled numerically to enable modifications and enhancements to be analysed prior to installation. The model has been tested against a number of typical JET pulses with good agreement. A major enhancement of the system has been the current modulation circuit that causes different currents to flow in two parts of the JET primary magnetizing windings. The extra electromotive force obtained from this configuration allows plasma currents up to 7 MA to be sustained with material limiters. Magnetic separatrix limited plasmas with currents up to 5 MA are now also possible. The numerical model has been used to evaluate machine performance in these situations and to indicate where nominal thermal limits on coils would have been reached. A system to recover from a disruption using a series of fast rises has been analysed. It is intended that the model should become part of a larger system designed to help in the organisation of pulse schedules.

1. INTRODUCTION

The Poloidal Field (PF) power supplies of JET are described in detail elsewhere[1]. The configuration of the JET PF system which is modelled is shown in Figure. 1.

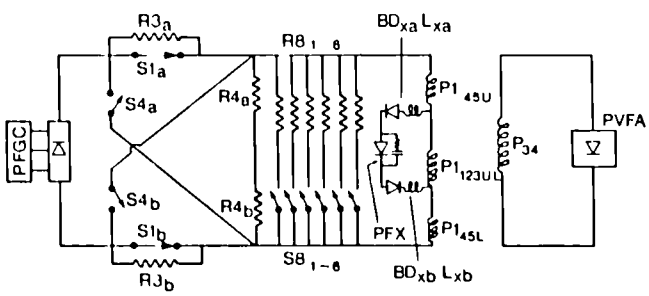

FIGURE 1
The circuit modelled

The Poloidal Flywheel Generator supplies, through two diode converters (PFGC), the ohmic heating circuit which modulates the flow of power from the generators to the magnetizing windings of JET.

These consist of the coil P1 which contains 6 central and 4 outer pancakes plus a few turns of the outer coils P3m. The vertical field coils P34, which provide for radial equilibrium are supplied by AC/DC thyristor converters. The current modulation circuit supplies the six central pancakes of P1, independently from the four end pancakes at the top and bottom, and is powered by the Poloidal X-point Field Amplifier (PFX).

The operation of the ohmic heating circuit can be divided into three phases; premagnetization (PRE $\leq$ t $<$ SCB), fast-rise (SCB $\leq$ t $<$ PFR) and slow-rise/flat top (PFR $\leq$ t). During the premagnetization phase with S1 closed and S4 open, the generator supplies power to the transformer coils and the kinetic energy is converted into magnetic energy. At the beginning of the fast-rise phase, the circuit breakers S1 interrupt simultaneously the current flowing through them. Due to its large inductance, the load acts as a current generator forcing current through the commutating resistors R3 and R4. This causes a high negative voltage across the transformer coils, which produces the gas breakdown and the plasma formation. During the fast-rise phase, the load current decays with a time constant that depends on the equivalent inductance/resistance (L/R) of the circuit and is not strongly influenced by the generator voltage due to the connection of the resistor R3. When the voltage across the transformer coil is equal in amplitude to the generator voltage, the revers-

ing make switches S4 are closed, allowing the reconnection of the generator to the transformer coils. This marks the beginning of the slow-rise phase. From this time onwards (the slow-rise and flat-top phase), the coil voltage is smaller than the premagnetization phase and so can be controlled with the excitation of the generator.

The model includes a description of the feedback systems so determining the voltages which control the amplifiers and the flywheel generator.

2. EQUATIONS GOVERNING THE SYSTEM

2.1 The voltages across the coils are given by

$$\dot{\psi}_i = V_i^a - R_i I_i$$

where ψ_i is the magnetizing flux in coil i, V_i^a is the applied voltage, $R_i I_i$ is the resistive voltage.

2.2 The plasma loop voltage V_L, is obtained using Spitzer resistivity, a zero dimensional power balance and a prescribed form for the breakdown losses.

2.3 The fluxes ψ_i are related to the currents I_j by

$$L_{ij} I_j = \psi_i - \psi_{\emptyset i} \tanh \left(\frac{\sum I}{I_\emptyset}\right)$$

L_{ij} is the incremental inductance matrix for the coils and plasma

$\psi_{\emptyset i}$ represents the magnetization flux due to the iron core

$I_\emptyset = 10^5$ ampere turns is empirically derived

$\sum I$ is the total ampere turns around the iron core.

2.4 The generator

The load characteristic is modelled by

$$\left(\frac{V_g}{K_1}\right)^\alpha + \left(\frac{I_g}{K_2}\right)^\alpha = I_f^\alpha$$

$\alpha = 1.31$ and $K_2 = 20$ are empirically derived constants

$K_1 = 2.7 \times 10^{-3}$ N

N is the generator speed in radians/sec

I_f is the generator field winding current.

The mechanical equation for the generator speed N, used to determine K_1 above, is solved using a simple representation of the coefficient of friction.

2.5 The switching network

The state of the switching network defines the phases of operation of the JET ohmic heating system.

2.5.1 Premagnetization: PRE $\leq$ t < SCB, has S1 closed and S4 open (see Figure. 1).

2.5.2 Fast Rise: SCB $\leq$ t < PFR, has S1 and S4 open.

2.5.3 Slow-Rise, Flat-Top, Decay: PFR $\leq$ t, has S1 open and S4 closed.

2.6 The feedback systems

2.6.1 The vertical field amplifier is connected to a feedback system which is a combination of position feedback and pre-programmed waveform. The position feedback utilizes a PID controller acting on the control flux thus

$$V_{PVFref} = g_R \left(\delta \dot{\psi}_R \tau_{DR} + \delta\psi_R + \int \delta\psi_R \, dt/\tau_{IR}\right)$$

The amplifier response is limited by a maximum negative slew-rate of 200kV/sec which simulates the response of the thyristor bridge. The control flux $\delta\psi_R$ is derived from the difference between the fluxes on the inboard and outboard sides of the vacuum vessel. $\delta\psi_R$ effectively measures the plasma position. This in its turn is obtained self-consistently by imposing the force balance equation when solving for the coil currents in terms of the fluxes.

2.6.2 The PFX (see Figure 1) feedback system is a combination of current feedback and preprogrammed waveform. The current feedback utilizes a proportional controller acting on the reference current and limits on the current in the outer P1 coils.

2.6.3 The PFGC feedback system is governed by the reference voltage V_{ref} which uses a combination of plasma current feedback and preprogrammed waveform. The current feedback uses a PID controller such that

$$V_{ref} \quad g_i \left(\delta I + \frac{d\,\delta I}{dt}\,\tau_{DI} + \int \delta I\, dt/\tau_{II}\right) + V\emptyset I$$

The current I used for control and the values of g_I, τ_{DI} and τ_{II}, vary depending on the phase in which the system is operating and various limits imposed on the system.

2.7 The plasma geometry is determined in the manner suggested by Zakharov[2].

2.8 Zero dimensional models are used to model the current penetration and the power balance.

3. COMPARISON OF MODEL AND MACHINE

The model has been tested against a range of JET shots to verify that it adequately mirrors operation of the machine. Each JET shot is controlled by a set of waveforms which determines the operating parameters for the various subsystems. Each waveform used for a particular shot is stored on the network of NORD minicomputers and these can be read into the model to perform a simulation. The two shots shown here are fairly typical examples of a 3MA and 6MA plasma.

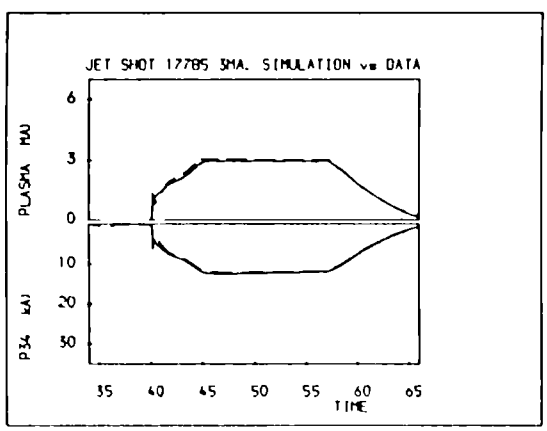

FIGURE 2
3MA simulation, plasma current and P34 current.
Simulation is the solid line.

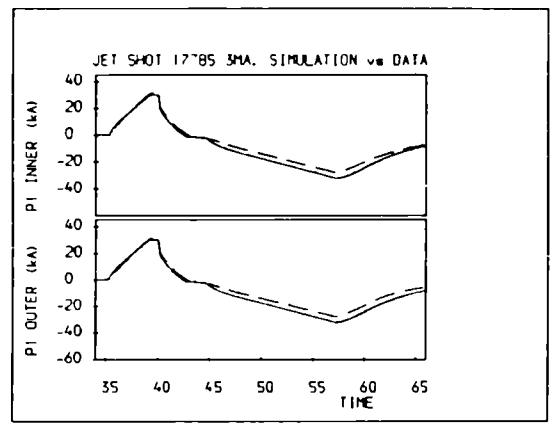

FIGURE 3
3MA Simulation, primary coil currents
Simulation is the solid line

The 3MA simulation is compared with actual machine performance in Figures 2, 3. This shows adequate agreement in all of the parameters shown except for the plasma elongation. The way this is modelled in the computer simulation is known to have deficiencies and attempts will be made at a later stage to try to improve on it. However, for the purposes to which the model has so far been put, this is not a serious shortcoming.

The 6MA example terminated early due to a hardware limit being reached and this accounts for the large deviation of the model from experimental results after 54 seconds. These results are shown in Figures 4, 5.

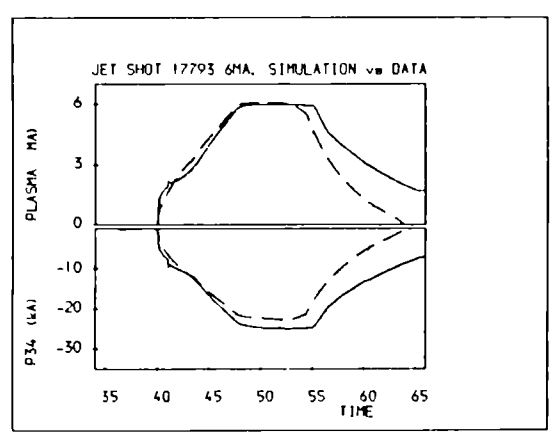

FIGURE 4
6MA simulation, plasma current and P34 current
Simulation is the solid line

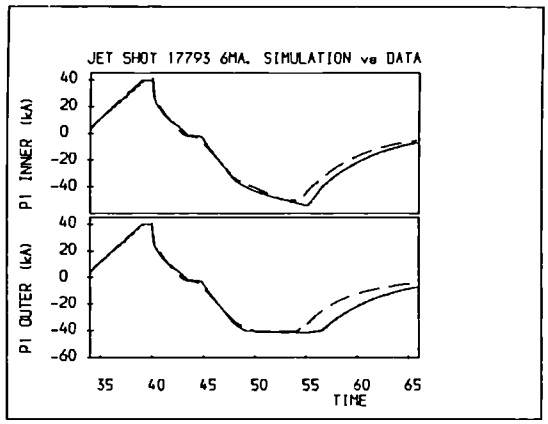

FIGURE 5
6MA simulation, plasma geometry
Simulation is the solid line

4. 7MA AND 4MA SEPARATRIX SCENARIOS

As mentioned previously the Current Modulation Circuit (PFX) was introduced to enable the flux variation to be increased from 34Wb to 40.6Wb and to control leakage flux, thus allowing plasmas to be sustained with currents up to 7MA[3] and helping the generation of the magnetic separatrix[4]. This scenario has been evaluated by the model with a view to optimizing performance and checking which coils and amplifiers will reach or exceed their nominal limits.

The optimization could then reduce the scope of modifications needed to allow successful 7MA operation. The calculations show that a 4s flat top will be available with a resistive loop voltage of 1V. A lower resistive loop voltage of 0.5V would allow a flat top of up to 10s to be achieved. The simulations indicate that in certain situations the thermal limits on the central P1 coils will be reached and/or the maximum current available from the PFGC will be exceeded. The former can be overcome when the thermal limitation to the central P1 coils will be increased from 32 to 46GA²s by a modification to its cooling system. The limitation coming from PFGC can be removed reducing the plasma current derivative during the last 1-2s of slow-rise.

The 4MA X-point scenario does not need all of the available flux swing and so the resistive loop voltage is not critical. The generator convertor controls the voltage increasing all P1 currents on demand from the plasma current controller to reach and maintain the required plasma current.

5. MULTIPLE FAST-RISE SCENARIOS

A significant amount of experimental time at JET has been lost in recovering from plasma disruptions. The He^4 glow discharge cleaning, while reasonably successful in cleaning the vessel, does take about 1½ hours to complete. It also involves operating the neutral beam rotary valves and all diagnostic valves; a tedious and potentially error prone business.

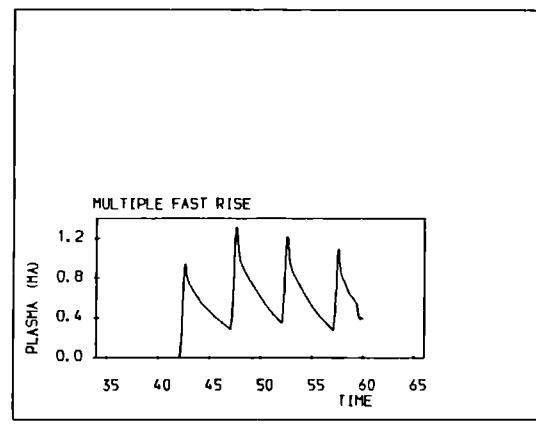

FIGURE 6
Multiple fast rise. Plasma current

Another option is to run a number of fast-rise pulses. This has been a success at times and, usually after 3 or 4 failed fast-rises, a good breakdown has been achieved. On a number of occasions however, the discharge which follows has been terminated by a high density disruption putting us back to square one.

The model described here has been used to assess the possibility of running a series of fast-rises in one JET discharge. Breakdown can be achieved using the poloidal flywheel generator without using the switching network. Excitation of the flywheel generator to 8kV will

produce a loop voltage of the order of 10V. Because the current in the primary is small (approximately 10kA), the stray fields are small, so facilitating breakdown. The repetition frequency of breakdowns is determined by the natural decay time of the plasmas, which with the resistors R8 out of circuit is of the order of a few seconds. Figures. 6 and 7 show plots of the plasma current, the primary coil currents and the inductive voltages across the primary windings. The simulations show that we can expect to run a breakdown approximately every 5 seconds.

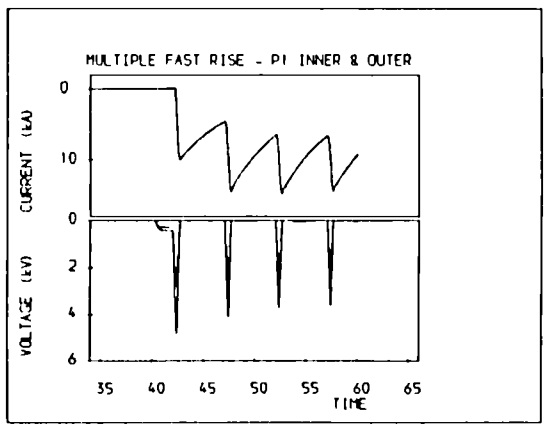

FIGURE 7
Multiple fast rise P1 currents and voltages
Solid inner coils, dashed - outer coils.

6. CONCLUSIONS

The model of the JET poloidal circuit described here has enabled a number of possible scenarios to be examined before implementation. Some modifications to the JET circuit which would allow these scenarios to go ahead have been indicated or alternative means of achieving the same end have been optimized. The model has been implemented in code on the JET IBM computer and a simple means of running the code has been provided. It is intended that the code should be made available on one of the network of NORD minicomputers which is used for the preparation of pulse schedules. A simulation of the JET pulse will be run from the waveforms in the proposed pulse schedule giving a good indication of the systems response. This promises the possibility of a large saving in actual machine time.

REFERENCES

1. E. Bertolini, P.L. Mondino and P. Noll, "The JET Magnet Power Supplies and Plasma Control Systems", Fusion Technology Journal, Vol. 11, N°1, pp.71-119, January 1987.

2. L.F. Zakharov, Zh. Tech. Fiz 41 (1971) 823.

3. "The Performance of JET PF System for 7MA Material Limiter and 5MA Magnetic Limiter Operation", A. Santagiustina et al, this conference.

4. P.L. Mondino et al, "The PF System Enhancement in JET to Produce Plasma Current up to 7MA with Material Limiters and up to 4MA with magnetic Separatrix: a Report on the Electrical Study", Proc. 12th Symposium on Fusion Engineering, Monterey, USA, October 1987, Vol 2, p819.

MACHINE UTILISATION AND OPERATION EXPERIENCE WITH JET FROM 1983

B.J. GREEN, P. CHUILON, B. NOBLE, R. SAUNDERS, D. WEBBERLEY

JET Joint Undertaking, Abingdon, Oxfordshire, OX14 3EA. UNITED KINGDOM.

The operation of JET commenced in June 1983 and is scheduled until the end of 1992. This seemingly long period is actually quite limited when compared with the time needed to implement and commission the planned machine enhancements, and pursue research and developments which result from the experiments. There is an ever-present urgency to make the best use of the machine. 1983-84 was a learning period and only in 1985 was it felt worthwhile to adopt double-shift day working. Data has been compiled and analysed for utilisation of the machine, delays in terms of time lost and systems involved, and number and frequency of machine pulses. This paper presents an overall picture of machine availability and utilisation. It describes the JET operational arrangements and the experience of system faults. Finally, it draws conclusions and identifies lessons learned which may be relevant to the next stage of fusion power development.

1. WHY IS THIS TOPIC IMPORTANT?

The cost of plant involved in the JET experiment is high and hence JET must be used as often and as successfully as possible to maximise the operation information (for both plasma and machine systems) in the limited life of the project.

JET is generating unique plasma information for the international fusion data base because of JET's ability to operate over a wide range of plasma conditions.

The machine systems information (capability, reliability) is required to assist in the design of future controlled fusion machines and in the assessment of reactor reliability, environmental impact and economics. Again JET's size and subsystem capabilities can make unique contributions. In particular, operation experience with JET will be important when considering realistic availability targets for the next step (e.g. NET, ITER etc).

2. WHAT IS A USEFUL MEASURE OF OPERATION PERFORMANCE?

In an experiment like JET, it is important to distinguish between operation performance and scientific programme performance. In this paper we will concentrate on operation performance. The chosen measure of this performance is the number of successful tokamak pulses (TS) achieved i.e. pulses for which all systems performed successfully. For a meaningful measure of performance these TS pulses must have been achieved in the implementation of an agreed scientific programme.

Each JET pulse is classified as follows:

TS =Successful tokamak pulse - all systems for the production of plasma were working, (account not taken of the quality of the discharge).

TF =Failed tokamak pulse - the specified plasma pulse was not achieved because of some system or operator fault.

CS =Successful commissioning pulse - typically dry run, single system power test. No attempt to produce a plasma.

CF =Failed commissioning pulse - the specified pulse was not achieved because of some system or operator fault.

The measure of scientific programme performance must be measured in some other way e.g. the achievement of specific goals in plasma parameters. For JET, the cumulative number of fusion neutrons and the $n_i \tau_L T_i$ value have been chosen.

3. IMPROVEMENT OF JET OPERATION PERFORMANCE

Since JET operation began on June 25 1983 there has been a continual review of performance and as the programme has progressed, certain measures have been taken for improvement. Basically there are two main ways to improve

machine performance:

i) maximise the available operation time,

ii) reduce the delays in operation.

Relevant JET experience will now be described.

3.1 Time available for operation

JET began in a basic configuration and the strategy was to continually add systems to bring it up to its extended performance state ("phased exploitation"). Further, JET is an experiment and subsystems will be altered in the light of operation experience. Installation and commissioning of new and modified equipment takes some time. Thus, since 1983, the operation of JET has been broken by significant periods of shutdown (Fig.1). The relative time devoted to machine operation in 1983/84/85 was not great but improved markedly in 1986. Once again in 1987 the relative time devoted to machine operation was reduced (Fig 2).

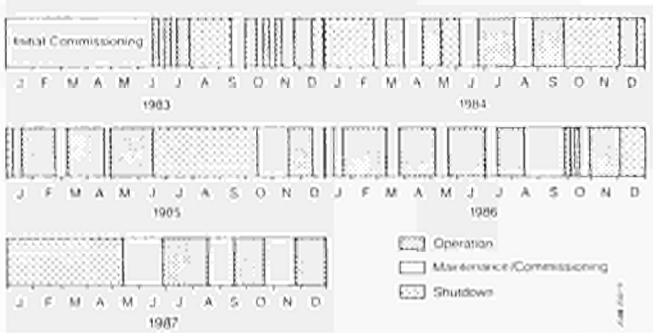

Fig.1 JET Operation Calendar 1983-1987

JET has sought to improve operation by having regular maintenance/recommissioning intervals between operation periods. The extent of plasma operation which is possible before a maintenance/recommissioning period is required has not been systematically studied, however the pattern of 6 to 7 weeks operation broken by a 1 to 2 week period has been successful.

Often the installation and commissioning of new equipment takes place in this period and usually determines its duration. Sometimes the commissioning of new equipment can spill over into plasma operation periods and this reduces the time available for the experimental programme. While all difficulties cannot be foreseen, the installation and commissioning of new equipment must be properly planned; and this certainly includes the timely preparation of commissioning procedures, implementation of an acceptable man/machine interface and proper operation documentation.

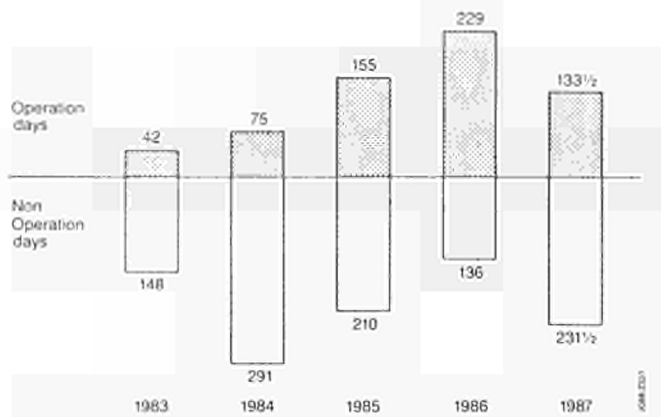

Fig.2 Numbers of Operation Days 1983-1987

JET has also increased the time for machine operation by introducing double-shift day and weekend working. In both cases the JET Project has been somewhat constrained by the limited manpower available for operations. The improvements made are shown below:-

1983/84 Some weekend operation. Single-shift days (10 to 12 hrs). Up to 60 hr/week.

1985 Monday commissioning: single-shift day. Tuesday to Friday: double-shift (16 hr) days. 74 hr/week. Single-shift days for maintenance and commissioning.

1986 Monday to Friday: double-shift days. (80 hr/week). Some weekend operation.

1987 Double-shift days attempted for maintenance and commissioning. Some weekend operation. Monday commissioning reduced.

A significant part of each day can be lost to operation because the power supply re-energisation and isolation procedures are complex and time-consuming. Although they have been improved, they still take up 1½ to 2 hours of tokamak operation time. Nevertheless the average number of hours available for pulsing in a 16 hour double-

shift day including 1 hour for meal breaks has been increased to nearly 13 hours (Fig. 3). This time is affected strongly by commissioning and recommissioning requirements following shutdowns.

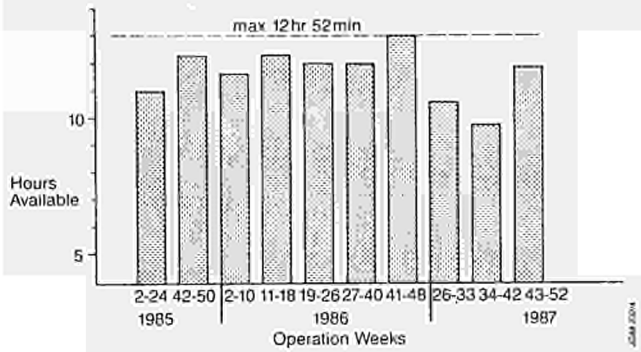

Fig.3 Average Daily Hours Available for Pulsing

3.2 Delays In Operation

• Faults which occur during operation days are recorded by the Engineer in Charge of operations (EiC) in a shift report. They are identified by subsystem, any associated delay to operation is noted and the action taken or required is outlined. Not all system faults cause actual operation delay and some faults are "hidden" by others. This fault recording is continually being reviewed for improvement. Other fault reporting systems (e.g. Power Supplies and CODAS) are used primarily to specify remedial and maintenance work. These fault recording systems are narrower in scope than the EiC system but provide more detail for the subsystem involved as they include faults not "seen" by operations. The EiC fault reporting provides data for the analysis of frequency and delays due to subsystem faults. In this way the major sources of lost operational time can be identified and appropriate action defined.

An analysis of faults indicates that the delay is typically 20% of the total time available for operation (Fig.4). The analysis of the subsystems responsible for delays (Fig.5) clearly shows that two subsystems dominate i.e. Power Supplies and CODAS. Other systems which have significant fault delays are: Vacuum Systems, Neutral Beam, Operator and Water/Air.

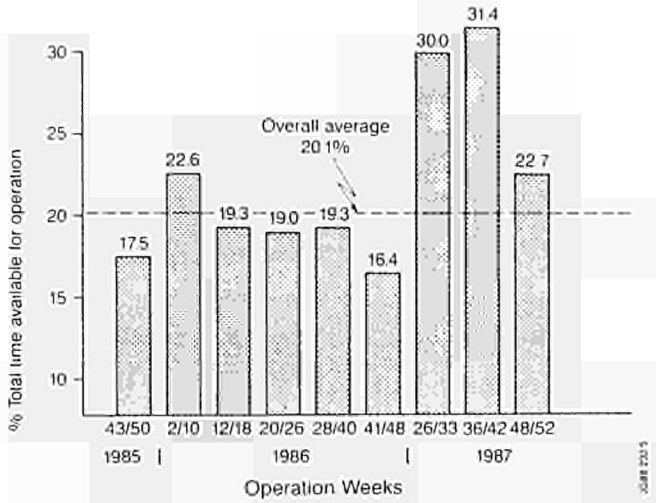

Fig. 4 Relative Time Lost due to All Faults

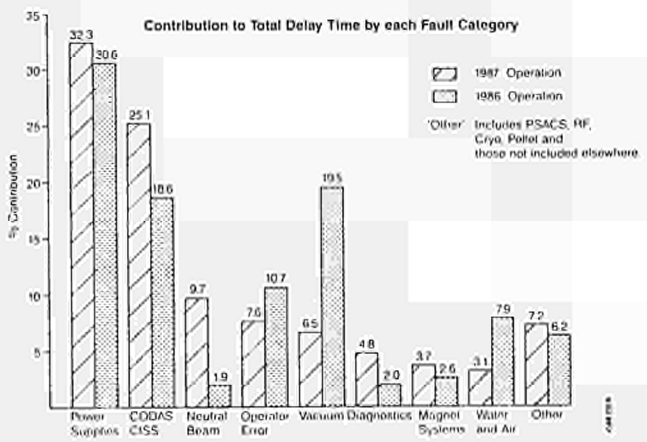

Fig.5 Relative Delays for Each Fault Category

An analysis of the number of faults for each subsystem (Fig.6) reveals a different picture in that CODAS and Operator categories dominate. This means that the average time per fault occurrence (Fig. 7) is quite small for the CODAS and Operator categories but is large for Power Supplies and for Vacuum Systems faults. This is because, in both of these categories, trouble-shooting requires electrical isolation before the fault-finding can commence. In many cases the remedial work involved is lengthy (e.g. welding to repair vacuum leaks, replacement of electrical switchgear) and almost always needs testing before operation can be restarted.

Some measures have been taken to reduce the time lost in identifying and rectifying systems faults:

i) trouble-shooting procedures have been improved,

ii) up-to-date documentation has been provided,

iii) written procedures have been prepared.

The availability of 'expert' staff is also important - the JET situation where design staff has been involved with the installation, commissioning and operation of equipment has shown clear advantages over the industrial practice of separating the design, installation, commissioning and operation phases with handovers between different staff teams before each new phase.

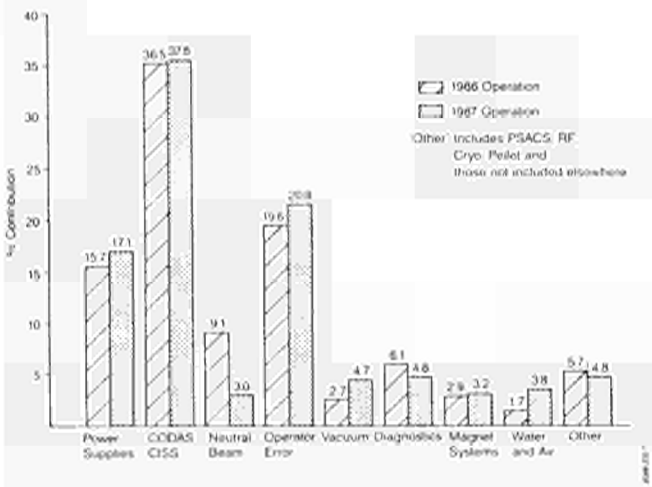

Fig.6 Relative Number of Faults per Category

It is difficult to quantify system operation reliability because of the continual changes and new modes of operation. However, an analysis of JET power supply subsystem faults (M. Huart et al SOFT 14) showed how regular maintenance has increased reliability. The reduction in frequency and severity of faults in some subsystems clearly demonstrates the benefits of:

a) simple system control and protection,

b) more automation of operator activities,

c) improved man/machine interface,

d) improved operator procedures,

e) stricter control of system interventions.

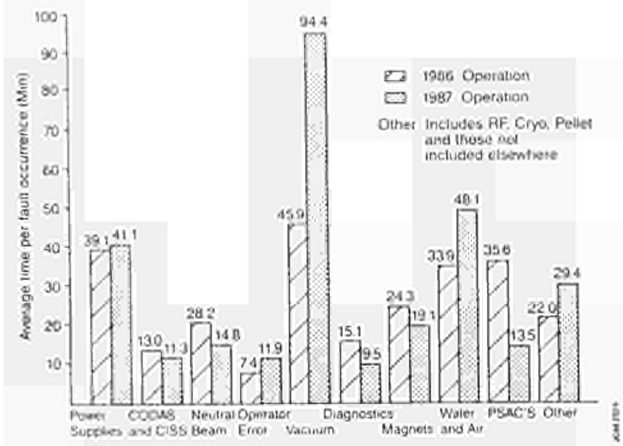

Fig.7 Average Time per Fault for Each Category

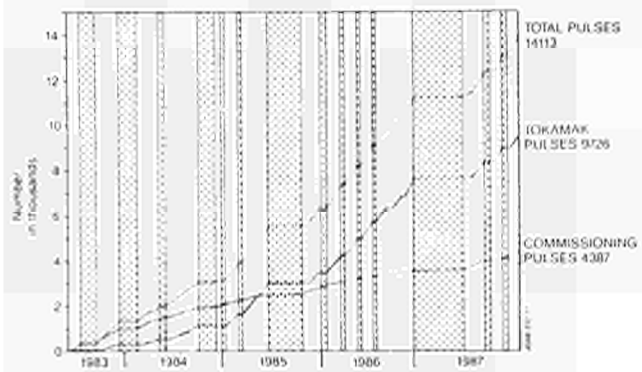

Fig.8 Cumulative Totals of JET Pulses

4. PULSE PERFORMANCE

The growth of the cumulative numbers of JET tokamak and commissioning pulses is shown in Fig.8. Overall, the relative amount of commissioning has decreased but the average number of pulses per year has not yet reached the design target of 5000. The improvement of machine operation discussed above can be seen in Fig.9. The number of tokamak pulses per week has increased and the weekly number of successful tokamak pulses is regularly between 100 and 150.

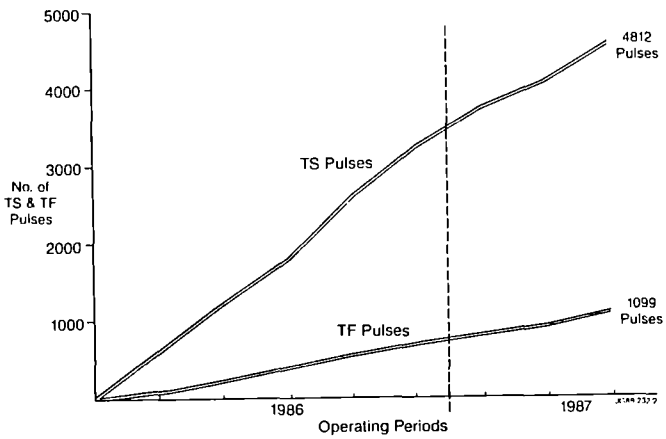

Fig.9 Tokamak Pulses for 1986/87

5. CONCLUSIONS

After a learning period (1983/84), routine double-shift day JET operation began in 1985. Operation performance has been continually improved by:

i) increasing the time devoted to operation e.g. double-shift days, weekend work, optimum preparatory and operation activities

ii) reducing the time lost due to system faults e.g by design simplification, control of interventions, regular maintenance, optimisation of trouble-shooting procedures, automation of many operation activities

iii) optimising the organisation and planning of operation (e.g. use of back-up programmes) and closer co-ordination of installation, commissioning and operation activities.

Further improvement could be made in all three of the above areas.

6. LESSONS FOR THE NEXT STEP

The Next Step (NET, ITER etc) will be an experiment like JET only more complex, with even greater demands on the "quality of operation performance". Certain experience gained in the operation of JET appears relevant:-

i) in the setting of availability targets, adequate time should be allowed for:
   a) upgrading systems (if, like JET the phased exploitation strategy is used)
   b) maintenance and repair (note the impact of radioactivity)
   c) regular recommissioning.

ii) adequate manpower is required; where possible design staff should be used for installation, commissioning and operation. Proper training of staff (and system documenation) are required.

iii) at the system design stage, proper thought should be given to commissioning and operation (in particular the man/machine interface e.g. machine protection interlocks, alarm handling, control software). Autonomous control is important as it allows commissioning in parallel.

iv) strict configuration control should be applied (to ensure access for remote handling and to facilitate trouble-shooting).

v) design attention should be given not only to new technology and novel items but also to "standard" things e.g. piping, cabling, cranes, shielding elements.

vi) particular design attention should be given to systems which appear likely to cause the greatest delay e.g. the control, monitoring and data acquisition system and the power supplies; also the location and repair of vacuum leaks.

vii) system operation should be automated as much as possible but controls kept simple

viii) operation should be organised so that responsibilities are clearly defined.

ix) planning must be thorough so that machine operation time is optimised.

x) interventions on machine systems should be strictly controlled.

DIAGNOSTICS FOR THE JET MULTI-PELLET INJECTOR

W. BAILEY, P. KUPSCHUS, M. GADEBERG, T. SZABO, D. CRACKNELL*, M.J. ADAMS*, B. MILLS*

JET Joint Undertaking, Abingdon, Oxon. OX14 3EA, England

Instruments to measure the mass, velocity, and timing and to visualise the integrity of Deuterium pellets injected into JET are described. The developments necessary to update the equipment for the later phases of JET are indicated.

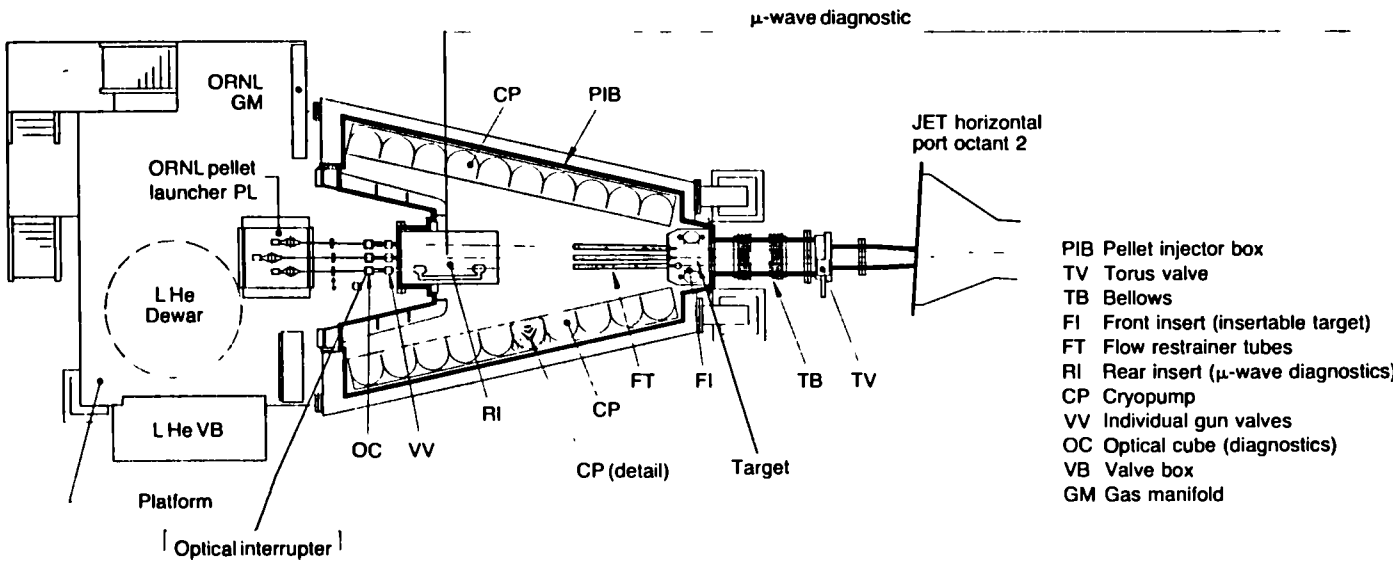

JET Multi-pellet injector

1. INTRODUCTION

A multi-pellet injector for fuelling and refuelling of the JET plasma has been jointly constructed under an agreement between the Joint European Torus, JET, and the United States Department of Energy, by JET and the Oak Ridge National Laboratory (ORNL)[1,2]. Pellets of deuterium ice of nominal length and diameter 2.7, 4.0 and 6.0 mm are injected with a velocity ≈ 1.4 Km s^{-1} and divergence ≈ ± 0.5° from the barrel. To prevent disturbance of the plasma by the propellant, a cryocondensation pump of capacity 8 x 10^6 ℓ(H_2)s^{-1} and ultimate pressure <10^{-5} mbar separates the injector from the torus. This contains the μ-wave diagnostic and the remotely indicating target. Instruments used in the active phase of JET will have to survive 10^8 rad and be remotely handleable.

Purpose of Diagnostics:

1.1 To set the injector to produce the required pellet trajectory.

1.2 To measure pellet mass, velocity and timing and to visualise integrity. To transfer a standard set of data to the JET Pulse File.

1.3 To assess pellet penetration and plume appearance.

The measurement sequence along the pellets' flight is, Optical Interrupter and Video Camera, Microwave Interferometer, Target and H_α measurements.

*GEC-Marconi Research Centre, Great Baddow, Chelmsford, Essex, England

2. OPTICAL INTERRUPTER AND VIDEO CAMERA

The first timing signal is generated by the interruption of a light beam (≈ 200 μwatts, λ = 850 nm) by the pellet just after it emerges from the barrel. The collimated 4 mm dia. light beam is formed by one 5 mm dia. glass sphere from the output of one optical fibre and coupled into the return fibre by another. The source and trigger electronics is remotely situated beyond the biological shield.

The signal generated primes a CCD camera and triggers a high speed spark, duration < 0.1μsec, to capture an image of the pellet in flight. The trigger is used with the first μ-wave signal (q.v. sect. 3):-

1) to calculate pellet velocity,

2) to generate timing signals,

a) to synchronise with the impact of the pellet on the target,

b) to synchronise with the passage of the pellet past the plasma limiter - the "Real Time Trigger" to initiate plasma diagnostics

c) to trigger the CCD camera capturing the image of the pellet plume. The video outputs of the CCD cameras are transferred to frame stores and permanently stored on optical discs.

3. MICROWAVE MEASUREMENTS

Birnbaum and Furneau[3] show that if the resonant frequency of a particular cavity, of volume V, is f_1, when a sample of volume v and dielectric constant $\epsilon=\epsilon'-i\epsilon''$ (Deuterium ice $\epsilon \approx 1.3$) is located at E_{max}, the resonant frequency of the cavity becomes f_2 where :

$$\frac{f_1 - f_2}{f_2} = 2(\epsilon'-1)\frac{v}{V}, \quad \frac{1}{Q_2} - \frac{1}{Q_1} = 4\epsilon''\frac{v}{V}$$

In each pellet trajectory two cavities are encountered, the first a short-circuited half-wave cavity (apertures 15 mm dia and Q ≈ 236) for mass measurement. In series with this and 416 mm down range, the second full wave cavity (apertures 20 mm and Q ≈ 165) is used primarily for alignment of the pellet trajectory to the design axis. The two cavities in one pellet path form one arm of a microwave bridge, two such arms are combined with a "Magic T" to form a complete bridge. The bridge is adjusted so that at the resonant frequency of the individual cavities, which is the fixed operating frequency, the output is a minimum (≈ 40 dB down on the input). The perturbation of any cavity by a pellet unbalances the bridge and causes an output. At the low levels used the detector output voltage is proportional to power input and the system output voltage is approximately proportional to (pellet mass)^2. For accurate mass measurements a "look-up" table must be used together with the measured drive signal. Figure 1 shows the form of this.

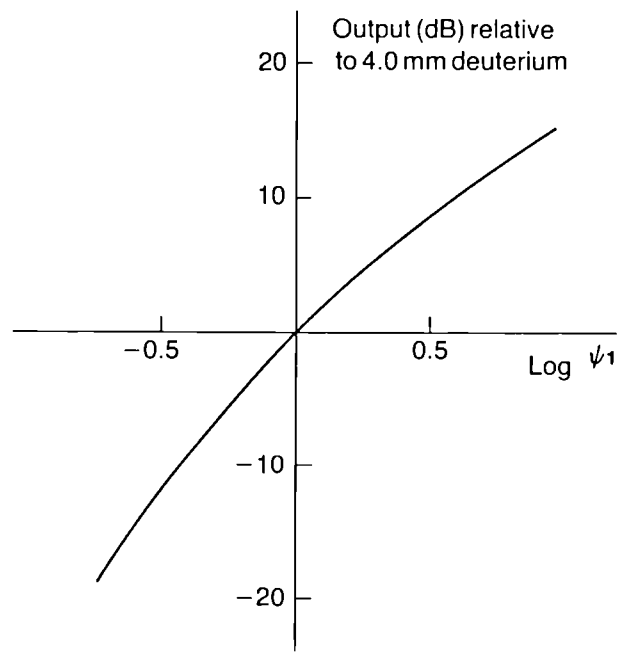

ψ_1 = mass relative to 4.0 mm deuterium.

Theoretical curve

FIGURE 1

The pellet divergence requires an aperture of 15 mm at the first cavity, and the operating frequency chosen, 4.5 GHz, together with apertures in the narrow wall of the waveguide WG12 and tubular extensions to the aperture ensures a maximum of 1% error for ± 3 mm trajectory displacement at the first cavity.

Compact design minimises the error caused by heat fluxes, but a temperature difference across the mass measurement cavities of ± 0.1°C causes a measurement error of 4.5%. The circulation of controlled temperature water, the provision of massive copper thermal shunts and aluminium foil radiation shielding from the cryopump substantially betters this. The predicted changes in cavity resonant frequency and the mass accuracy for a maximum deviation of the excitation frequency of ± 1 PPM (a crystal controlled oscillator is used) and ± 3 mm trajectory wander are given in the table.

Pellet size dia and length, mm	Shift of Resonant Frequency (for central pellet) MH_z	Mass Accuracy
6	7.993	± 2.1 %
4	2.337	± 2.62 %
2.7	0.478	± 3.33 %

4. REMOTE INDICATING TARGET

It is necessary to align the centre of the pellet dispersion circle within a few mm of the centre of the 60 mm dia tubes, which separate the pump from the torus and aid differential pumping. Stepping motors position a target at the exit of the flow retainers, with an error < 1 mm, and withdraw it at the completion of alignment. The operating principle of the target is to measure the relative times at which the sound wave emanating from the impact arrives at transducers in known positions on the target. A high sound velocity helps target survival, by removing energy from the impact area as fast as it arrives, and a small velocity dispersion preserves the wavefront shape as it propagates. IMI 318 titanium alloy was chosen for the target material and after months of intermittent use it is virtually undamaged. To detect the wavefront, Piezo-resistive sensors of graphite (12 μm x 1 mm section) mounted in Kevlar (Dynasen) were chosen for their radiation resistance, they are energised for a short time only (50 V for 200 μsec) to prevent their destruction. The 50 Ω sensors are connected by 50 Ω lines to a bridge balanced by similarly mounted sensors external to the vacuum. The sensors are compressed onto the outside of the target by massive blocks. To prevent confusion between the longitudinal wave (@ 6000 ms^{-1}) which propagates most strongly forward, and the transverse wave (@ 3000 ms^{-1}) which propagates laterally from the point of impact the sensors are positioned to intercept the former, i.e. some distance behind the impact plane on the sloping side of the conical target. The sensors are arranged in pairs on the x and y axes respectively. It can be shown that the distance of the impact from axes whose origin is at the centre,

$$x \atop (\text{or } y) = \frac{V^2(T_A - T_B)(T_A + T_B)}{4R},$$

where V is the velocity of sound, $T_{A,B}$ is the time for the sound wave to reach the A,B sensors on that axis, R is the radial distance of the sensors from the axis. For small displacements, $x = K(T_A - T_B)$ where K = 4.1 mm/μsec, taking $V = 6070\ ms^{-1}$ for our equipment.

An optical point of entry indicator is being developed to replace the equipment as higher pellet velocities are used. Optical interrupters in X and Y will transmit position and timing information through an optical fibre

using wavelength division multiplex working. Two fibres are required for each pellet path.

White light is dispersed into a spectrum across the aperture in X and Y directions and then focused into a return fibre. Beyond the biological shield the returning light is dispersed into a spectrum on a linear diode array. A pellet obscuring a part of the spectrum in the aperture results in a diminution in the signal of that part of the array. As the fastest pellets will only be in the aperture approximately 1 μsec, the diodes must have separate sample and hold amplifiers, operated from a common trigger, which can be read by a transient digitiser.

5. H_α PERISCOPE

The visible pellet plume has been viewed through a periscope inserted into the torus. The higher performance now achieved with JET brings enhanced disruption forces, necessitating the construction of a flexible link in the periscope. When re-commissioning is complete, shortly, we expect to see the pellet plume on its CCD camera and measure the H_α radiation in the integrating sphere. A temporary system is now used to provide H_α data by viewing the plasma along an unused pellet line underneath the 4 mm gun.

5.1 Microwave Emission

A signal from the microwave detector, similar in shape and timing to the H_α signal on pellet injection has been observed. We propose to investigate this signal at the earliest opportunity.

6. OUTLOOK FOR THE ACTIVE PHASE AND FASTER PELLETS

The replacement of a few parts by radiation resistant glass will permit the use of the interrupter.

Pellet photography will require the camera to be positioned beyond the biological shield and the image it views transferred by a periscope.

The source and detector for the μ-wave detector must be remotely sited.

Whilst the present target is radiation resistant it will be eventually damaged by faster pellets. The optical indicator now being developed will then replace the target.

7. CONCLUSIONS

Diagnostics are reliably recording mass, velocity, timing and integrity of all deuterium pellets injected into JET. The temporary arrangements for H_α measurements will shortly be replaced by more comprehensive instrumentation. Work is in hand for the systems to evolve into the forms necessary for higher pellet velocities and the active phase of JET.

ACKNOWLEDGEMENTS

It is a pleasure to acknowledge the contribution of our U.S. and JET colleagues in the Pellet Group and the rapid precise work of the JET and Culham Mechanical Workshops.

REFERENCES

1. P. Kupschus et al., Proceedings of IAEA 12th Symposium on Fusion Engineering, Monterey, October 12-16, 1987.

2. S Milora et al., ibid.

3. "Measurement of the Dielectric Constant and Loss of Solids and Liquids by a Cavity Perturbation Method". George Birnbaum and Jacques Franeau, J. Applied Physics 1949, Vol.20, pp.817-818.

NEW PIEZO DRIVEN GAS INLET VALVE FOR FUSION EXPERIMENTS

E. USSELMANN, J.L. HEMMERICH, J. HOW, D, HOLLAND, J. ORCHARD, T. WINKEL,
JET Joint Undertaking, Abingdon, OX14 3EA, UK;
L. GROBUSCH, KFA Jülich, W. Germany;
U. SCHARGITZ, Krauskopf Elektrotechnik, Giessen, W. Germany;
N. PÖCHEIM, VAT, Haag, Switzerland.

The gas inlet valves used at the JET experiment are described and their performances are discussed. A new gas-valve development suitable to replace the existing valves at JET and for future use in large fusion experiments is presented. The new valve is equipped with a piezo-electric translator and has a dosing range of 0-800 $mbarls^{-1}$ for D_2. The operating mode of the valve is fail-safe closed with a leak-rate of $\leq 10^{-9}$ $mbarls^{-1}$. The design, the test results and throughput values in dependence of filling pressure and control voltage are presented and experiences with the prototype valve as a new gas inlet valve for the JET operation are described.

1. DESCRIPTION OF EXISTING GAS INTRODUCTION AT JET

The introduction of the process gas into the JET tokamak is handled by a Gas Introduction Module (GIM) mounted close to the Torus[1]. In fact four GIM's are installed to have the possibility to use different gases or gas quantities during one plasma pulse.

Each module consists of an arrangement of four shut-off valves, one fast inlet valve, one dosing valve and two calibrated gas reservoirs (Figure 1). The shut-off valves are required to protect the tokamak against gas inlets through the dosing valve (which is not designed to be an absolute valve), and for filling or evacuating the gas reservoirs. As a consequence, the control of the GIM consists of a rather complex system including interlocks, timers, pressure set points, etc. The operational experience with the GIM's over the years has shown that some improvements in reliability, especially of the dosing valve, are desirable in view of the active phase of JET. This dosing valve is an all metal valve suitable for tritium environment which is driven by eddy currents in an aluminium disc connected to a conical needle moving in and out of a cylindrical orifice (Figure 2).

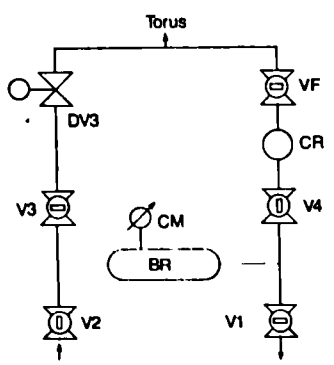

DV3 = Electrodynamic Dosing Valve
VF = Fast Inlet Valve
CR = Gas Reservoir 0.2ℓ
V3 = Shut-off Valve
V4 = Shut-off Valve
BR = Gas Reservoir 18.6ℓ
CM = Absolute Pressure Gauge 100 Torr
V2 = Filling Valve
V1 = Valve to Vacuum Line

Fig. 1 JET Gas Introduction Module (GIM) (Schematic)

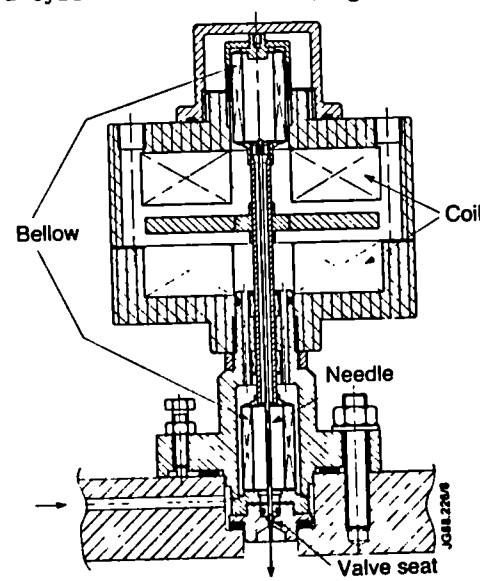

Fig. 2 Electrodynamic Dosing Valve (cross section)

Bellows arrangements on either side of the disc provide the vacuum seal to atmosphere and the compensation for the vacuum forces. These edge-welded bellows have had some fatigue problems in the past and we will need double bellows (secondary containment) with very much improved reliability for the tritium phase.

Furthermore, the limited dynamic range of the present dosing valve makes it necessary to adjust reservoir prefill pressures to obtain desired flow rates, which would add to the complexity of tritium gas handling systems.

2. NEW VALVE DEVELOPMENT

These experiences were the incentive to design an improved valve with reliable components, tritium compatible and with combined capability for gas puffing in the prefill phase of the pulse and for dosing in feed-back control during the pulse.

2.1 Valve Description

The new valve developed together with industry is based on a piezo-electric translator controllable by a driving voltage of 0 to -1000V giving an actuator stroke of 0-40 µm.
Figure 3 shows a cross section of the valve.

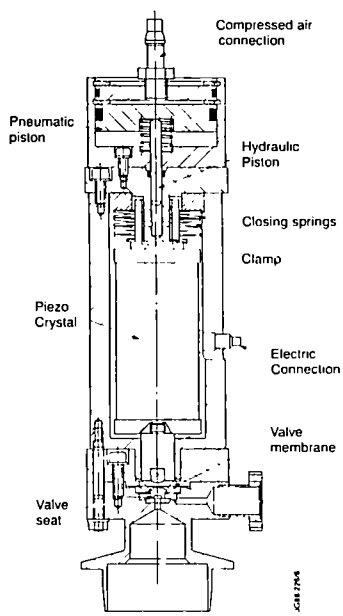

Fig.3 Piezo-electric Valve (cross section)

This valve is an all-metal valve designed to be fail-safe closed. The closing spring applies, via the piezo-translator, sufficient sealing force onto the valve seat to achieve a He leak-rate of $< 10^{-9}$ mbarls^{-1}. The process gas is only in contact with metal surfaces and the valve can be baked for conditioning purposes to 300°C after the removal of the drive assembly.

All non metal components used in the valve assembly are selected to withstand an accumulated radiation dose of at least 10^8 rad. The very short stroke of the piezo translator makes it necessary to compensate for the differential thermal expansion of the piezo crystal and the valve housing. Therefore an integral mechanical zero reset has been incorporated in the valve design providing always identical starting positions (fully closed) before operating the valve.

For the operation of the valve a driving voltage of -1000V is applied to the piezo assembly thus increasing its length against the closing springs by 40 µm. This movement still keeps the valve closed. In this fully extended mode a pneumatic/hydraulic clamp on the upper part of the valve "arms" the valve by keeping the closing springs in their compressed position. A reduction of the control voltage from -1000V to 0V opens the valve gradually, the stroke being linear with the voltage.

2.2 Throughput Measurement

In a test set-up consisting of a large vacuum chamber (2.84m^3) with a UHV pumping system the gas throughput for D_2 was measured in dependance of the feeding pressure in the gas reservoir, and of the control voltage of the piezo valve (bias voltage).

The gas throughput was derived from the time constant of the pressure drop in the gas reservoir measured with an absolute gauge (0 - 10000 Torr). Figure 4 shows the test set-up and

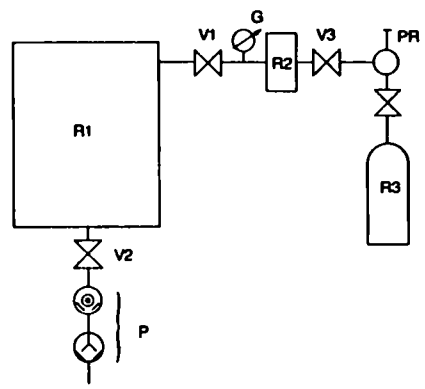

R1 = Test Vessel (2,84 m³)
R2 = Gas Resevoir (1ℓ)
R3 = D_2 gas bottle
V1 = Piezo valve
V2 = Pump set valve
V3 = Filling valve
P = Turbopump set
G = 10000 Torr absoloute gauge
PR = Pressure regulator

Fig.4 Test set-up for throughput measurments (Schematic)

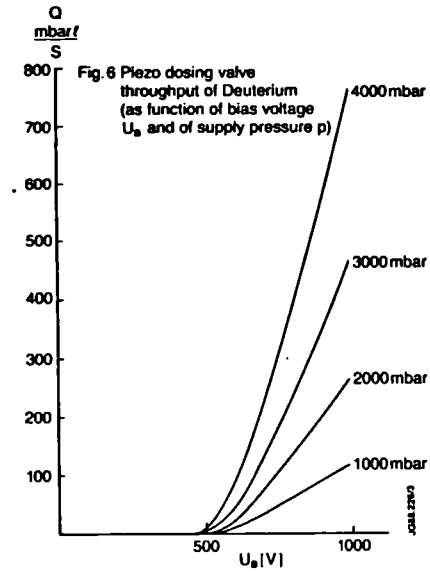

Figures 5 and 6 are throughput diagrams in dependence of upstream feeding pressure and of the control voltage of the piezo crystal.

After the throughput measurements reliability tests were performed with the valve being operated for more than 1000 operations to assess the reproducibility of throughput and to obtain experience about the lifetime of mechanical components. These tests resulted in some improvements in the design which were meanwhile incorporated by the manufacturer.

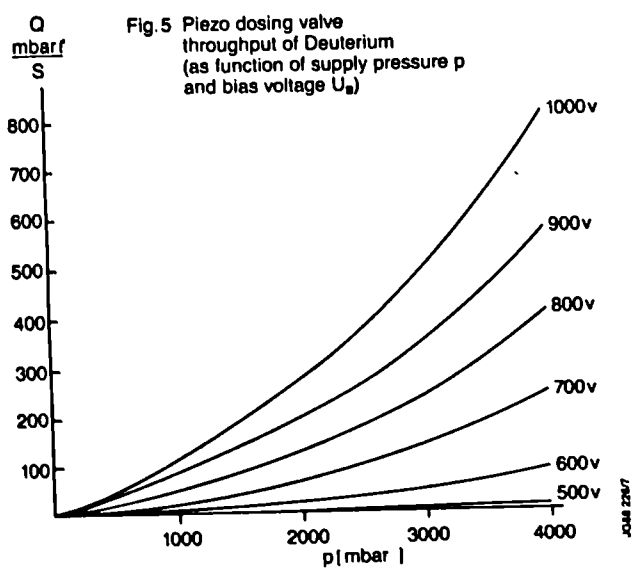

Depending on the upstream pressure of the gas reservoir feeding the valve we obtain a reproducible fully proportional control of the throughput from 10^{-9} mbarls^{-1} to - 800 mbarls^{-1} for D_2. An improvement to other piezo-driven dosing valves (e.g. Veeco valves) is the arrangement of the valve seat relative to upstream gas flow. In the other design the feeding gas tends to close the valve whereas in our valve the membrane carrying the valve seat is lifted by the upstream pressure of ≥1 bar absolute.

2.3 New Valve Operation

The control required to operate the valve consists of an inverting fast amplifier with a gain of 100 to provide 0 to -1000V from a 0 to 10V control voltage. The amplifier has a 100 kΩ output resistance, the piezo translator with a 1 µF capacity will therefore react with a time constant of ~ 100 ms.

To operate the pneumatic/hydraulic clamp a solenoid valve controller (with some timing sequences) controls the compressed air for the clamp and for the filling valve of a gas reservoir upstream to the gas introduction valve. This gas reservoir (0.76 l) is monitored

with an absolute vacuum gauge (0-1000 Torr) for inventory accounting and flow rate measurement during the pulse. The 0-10V output of this gauge represents a 0-1000 mbarl gas quantity.

For the prototype trials which have been going on for several months during JET operation, the gas to the reservoir is supplied from a Fe-Ti hydrid storage bottle directly mounted close to the gas introduction valve introducing ultra high purity D_2 gas through short pipes into the torus.

Figure 7 shows the set up of the prototype piezo gas inlet valve on the JET tokamak.

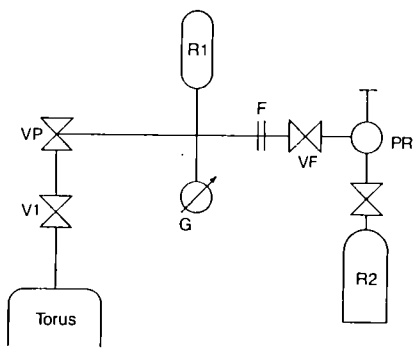

V1 = Manual Shut-off Valve
VP = Piezo Valve
R1 = Storage Tank 0,76ℓ
G = 1000 Torr Absolute Gauge
F = Dust Filter
VF = Refill Valve
PR = Pressure Regulator 1 to 6 bar
R2 = Ti-Fe Storage Bottle ~ 15bar

Fig.7 Piezo Valve Installation Arrangements at Torus (Schematic)

The control sequence for the valve is performed by the JET computer system (CODAS)[2] and is included in the countdown for the plasma pulse and consists of the following steps:

(a) At start of countdown ("arm")
- -1000V are applied to the piezo translator
- feeding valve to gas reservoir is closed
- pneumatic/hydraulic clamp is closed after expansion of piezo crystal

(b) During the pulse
- a voltage of 0-10V from the JET computer system initiates the opening of the valve
- for prefill a waveform on fixed voltage for a variable time
- for density feed-back a variable voltage in a given time window

(c) After pulse ("disarm")
- pneumatic/hydraulic clamp is opened to allow closing springs to move
- feeding valve of gas reservoir opened to refill with process gas from gas bottle

Typical prefill waveforms are shown in Figure 8.

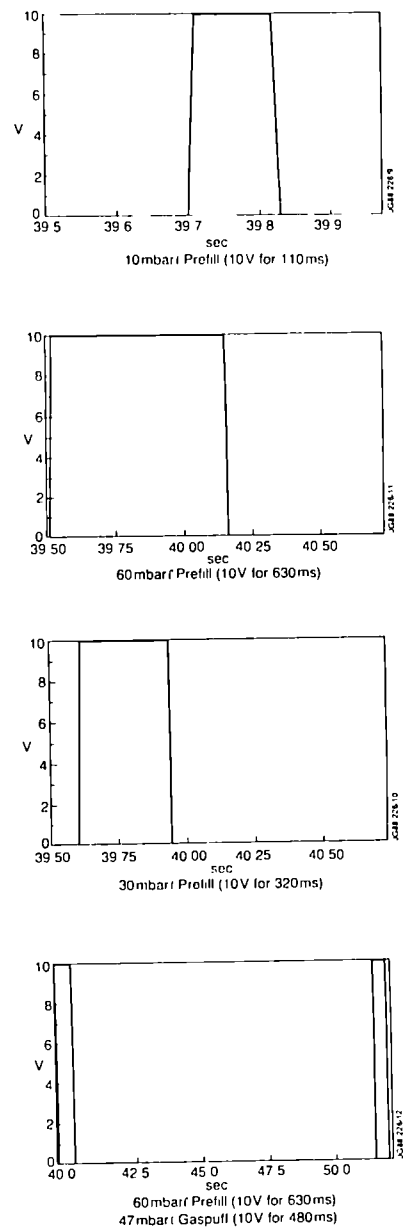

Fig 8 Piezo Valve Prefill Waveforms

Figure 9 shows plots from the JET pulse-file showing records of gas reservoir pressure and control voltage for prefill and density feed-back during a JET pulse (No. 17128). It can be seen, that both prefill and density feedback were carried out from the piezo valve system and - 200 mbarl of D_2 was injected.

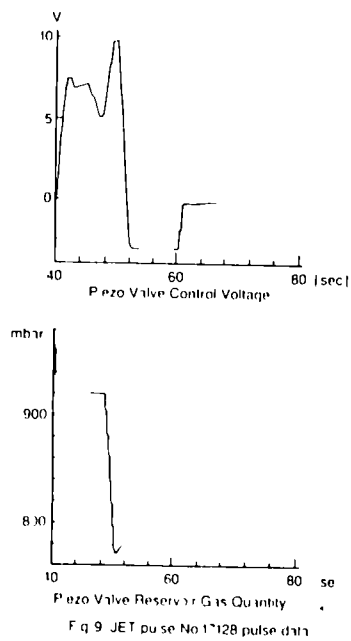

Fig 9 JET pulse No 17128 pulse data

3. CONCLUSION

After the test runs and subsequent improvements of the valve, the experience gained with the new valve at JET are very satisfactory. The new valve is used in parallel to the existing GIM's as required by the experimental program of JET. Further experience will show whether this valve is a reliable alternative to the existing Gas Introduction Modules for the active phase of JET.

REFERENCES

1. A. Boschi, K.J. Dietz, P.H. Rebut, The Gas Introduction System of JET, Proceedings 13th Soft 1984, Volume 1, 247.

2. H. van der Beken, C.H. Best, K. Fullard, R.F. Herzog, E.M. Jones, C.A. Steed, CODAS: The JET Control and Data Acquisition System, Fusion Technology, January 1987, p.120.

DESIGN OF A THOMSON SCATTERING DIAGNOSTIC SYSTEM TO MEASURE FAST ION- AND ALPHA-PARTICLE DISTRIBUTIONS IN JET

J.A. HOEKZEMA, A.E. COSTLEY, T.P. HUGHES, N.P. HAMMOND
JET Joint Undertaking, Abingdon, Oxon, OX14 3EA, UK

H.J. BARKLEY, W. KASPAREK, G.A. MÜLLER, L. REBUFFI, P.G. SCHÜLLER, M. THUMM
Institut für Plasmaforschung, Universität Stuttgart, Federal Republic of Germany

A diagnostic system to measure the velocity- and spatial distribution of fast ion populations in JET is being designed. The diagnostic is based on collective scattering of microwave radiation. A high power (up to 1MW), long pulse (up to CW) gyrotron is envisaged as the microwave power source at 140GHz, while the scattered radiation will be detected using a heterodyne system. The diagnostic is especially important for the measurement of the fast alpha particle distributions in the DT-phase of JET. This paper gives a short description of the diagnostic method, the expected performance for JET conditions and describes in some detail the technical design of the transmission line. In view of the frequency that was chosen and the high unit power, the design of the transmission line is highly relevant for possible next generation Electron Cyclotron Heating programmes.

1. DIAGNOSTIC METHOD

1.1. Collective scattering

If the parameter α, defined by $\alpha=1/k\lambda_D$ where k is the scattering wave vector and λ_D is the Debye length, exceeds unity, scattering of electromagnetic radiation is from fluctuations with scale length greater than λ_D. Shielding electrons, moving with each ion, now scatter collectively and the scattered spectrum is affected by the ion velocity distribution. The spectral function, S, may be written as the sum of contributions from electrons and from different ion populations. For measurements on minority populations, like α-particles, the value of α should typically be larger than 2 to ensure that the α-feature is dominant compared with the electron-feature ($S\alpha/Se$ scales approximately with $\alpha^4 n_\alpha/n_e$). As was shown in Ref 1, the unfolding of the spectrum to obtain the velocity distribution along the scattering vector is straightforward if a scattering vector oblique to the magnetic field direction is chosen (more than 10° off-normal). An example of a scattered spectrum is shown in Figure 1, for a typical expected set of JET-plasma parameters, including fast (not yet slowed down) α-particles as a minority species.

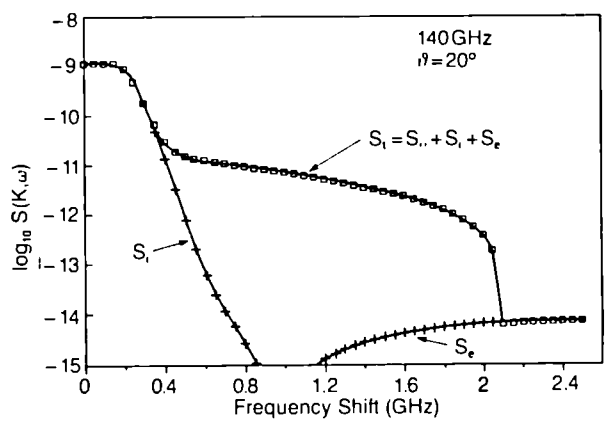

FIGURE 1
Predicted scattered radiation spectrum for JET with plasma conditions: $n_e(0) = 5\times10^{19}m^{-3}$, $n_\alpha(0) = 4\times10^{17}m^{-3}$, $T_e(0) = 10keV$ and $T_i(0) = 12keV$. S_i, S_e and S_α are the bulk ion, electron and α-particle contributions respectively and S_t is the total. Note that, for a scattering angle of 20°, the α-feature dominates in the range 0.5 to 2.0GHz.

1.2. Optimum frequency

At full field operation of JET (3.4T), the optimum frequency for which a sufficiently powerful source can be envisaged is around 140GHz. At this frequency the background

radiation, which is dominated by Electron Cyclotron Emission, shows a minimum because the fundamental resonance and the second harmonic resonance are situated in the low temperature edge regions of the plasma. The plasma is accessible to ordinary mode, injected vertically, up to a cut-off density $2.4 \times 10^{20} m^{-3}$. Collective scattering dominates and a sufficient contrast ratio S_α/S_e is guaranteed for the whole range of possible plasma parameters, provided the scattering angle does not exceed 60°. The optimum frequency is proportional to the magnetic field value and for operation at lower fields a lower frequency would be preferable. At very high plasma current (7MA) and full field, the high poloidal field value causes a wider separation of the electron cyclotron resonance layers, reducing the background radiation in the 150-155GHz region. Stepped tunability of the RF-source over a limited frequency range (120-160GHz), which is an intrinsic possibility of gyrotrons using a high order mode[2], would therefore be advantageous.

1.3. Geometry

The proposed geometry for the diagnostic is sketched in Figure 2. Since refraction effects can be important at higher densities, a symmetric injection-detection geometry is chosen in which injected and detected radiation are similarly affected by refraction. Nevertheless, precise control of injection as well as detection angles is necessary (between shots), which is accomplished by rotatable mirrors, which are also used to scan the plasma on a shot-to-shot basis, to measure spatial profiles.

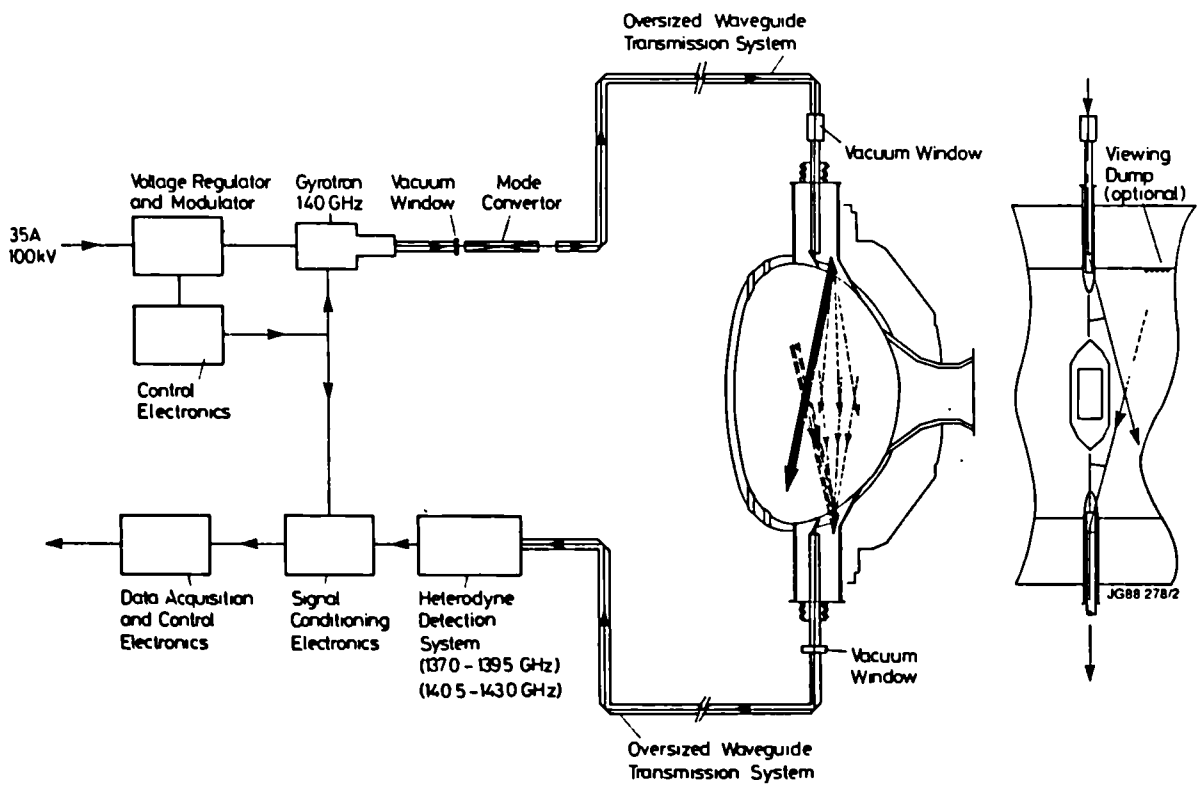

FIGURE 2

Schematic overview of the diagnostic system.

2. EXPECTED PERFORMANCE

2.1. Expected plasma parameters

The expected plasma parameters are a small (but essential) extrapolation of present JET results. It is expected that it will be possible to generate 5MW of α-particle power over a wide range of densities from 2×10^{19} m^{-3} (hot ion regime where the beam-plasma contribution is dominant) to $1.5\times10^{20}m^{-3}$ (H-mode, with dominant thermal contribution to fusion).

2.2. Signal to noise ratio

The main source of noise will be due to statistical fluctuations on the background ECE-radiation. The radiation temperature is T_b<500eV. Since the equivalent radiation temperature of the scattered radiation is ∿1eV, modulation of the injected radiation is necessary to discriminate the scattered radiation from the background. The expected signal to noise ratio is:

$$s/n=7\,\frac{(\frac{P_{inj}}{300kW})(\frac{n_\alpha}{10^{17}m^{-3}})(\frac{\tau}{200ms})^{1/2}}{(\frac{D}{0.06m})(\frac{f}{140GHz})^3(\frac{T_{eb}}{500eV})(\frac{N}{5})^{1/2}(\frac{|\sin\theta\sqrt{\sin\frac{\theta}{2}}|}{1/7})}$$

Here P_{inj} is the power modulation depth, τ the integration time (time resolution), D the beam waist and N the number of spectral channels. The different parameters are normalised to their expected values, except for n_α, where the minimum value is used. At low densities the α-particle density can reach the 5% level due to long slowing down times, and s/n can be up to 100. A s/n>5 is necessary for the measurement and it is clear that s/n can be traded in against better time- or spectral resolution.

3. TRANSMISSION SYSTEM

3.1. Requirements

The power source envisaged is a high power gyrotron, presently under development at Varian[3] emitting power in a rotating whispering gallery mode (probably $TE_{15,2}$). The gyrotron will be located outside the torus hall and the RF power will be transmitted over a distance up to 50m. Injection should be in a Gaussian beam or in the HE_{11} mode, with slightly elliptical polarization, to couple to the Ordinary mode in the plasma. The mode purity at injection should be maximized to limit direct illumination of the receiver. Special requirements are a high power capability (up to 1MW), wide band transmission (120-160GHz) and remote maintenance possibilities for the parts inside the torus hall. The most important elements of a transmission system that meets these requirements are described below.

3.2. Mode convertor

Since a whispering gallery mode cannot be conveniently transmitted with high efficiency (especially around bends), it is necessary to convert this mode close to the gyrotron. A quasi-optical mode transformer, which is basically an overmoded slot radiator combined with a cylindrical reflector of parabolic cross-section, is used to directly convert the radiation to a Gaussian beam. The conversion efficiency of such a conventional Vlasov convertor[4] is only 80%, but it may be possible to reduce the diffraction losses (this is a subject of further investigation). Step-tuning of the gyrotron frequency only needs replacement of the two matching mirrors R_1 and R_2 (see Figure 3), since the radiation angle is determined by the dimensions of the gyrotron cavity and therefore remains constant.

3.3. Polarizer

The linearly polarized radiation emitted from the convertor is changed to a controlled elliptical polarization by a corrugated surface reflector having fixed groove depth combined with a polarization rotator. The rotatable device consists of a smooth roof top mirror, facing a flat corrugated surface (see Figure

3,4). A corrugation period of 0.56λ is chosen (with equal groove and tooth width) and an electrical slot depth 0.2λ, where λ is 2.14mm, but the structure has wide band characteristics.

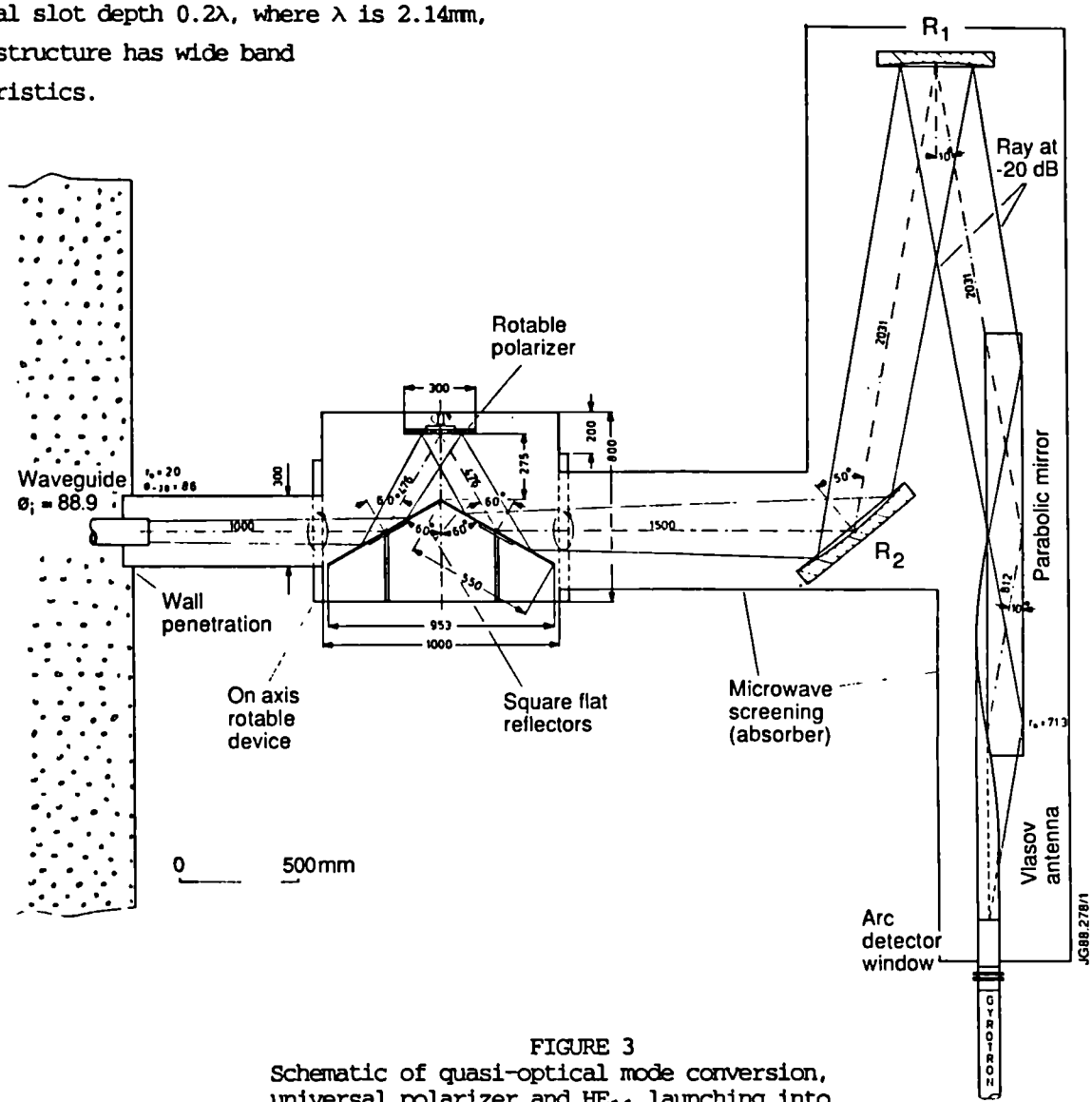

FIGURE 3
Schematic of quasi-optical mode conversion, universal polarizer and HE_{11} launching into corrugated waveguide.

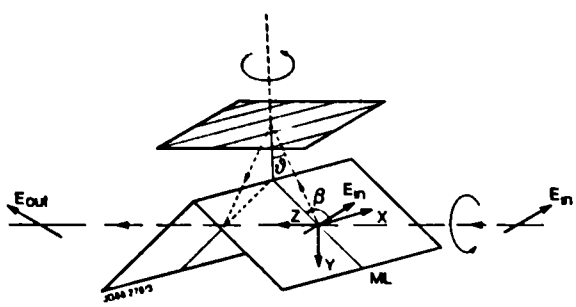

FIGURE 4
Schematic of the universal polarizer.

3.4. HE_{11} transmission

After conversion to a Gaussian beam with the required elliptical polarization, it is convenient to switch from quasi-optical transmission to waveguide transmission. The Gaussian beam couples well to an HE_{11} mode, which can be transmitted in a corrugated waveguide. In

comparison with a quasi-optical reflector beam waveguide, this has the advantage that it needs no remotely controlled alignment and adjustment and has inherent RF-shielding. Also, the HE_{11} waveguide has broadband characteristics. To limit the power density and the electric field strength (for optimum window transmission and prevention of arcing) and to facilitate bends in the waveguide, a relatively large diameter is chosen (88.9mm). By reducing the corrugation depth to $0.3\lambda/4$ and choosing a low conductivity material for the waveguide (eg, stainless steel), the waveguide acts as a mode filter for higher order spurious modes, while the attenuation of the HE_{11} mode remains negligible. Several possibilities to manufacture the corrugated waveguide are being investigated. A promising approach is plasma spraying of metal (or alternatively electroplating) on aluminium mandrels, which are subsequently chemically removed.

3.5. Bends

The highly oversized dimension of the waveguide makes it possible to use quasi-optical (mirror) bends. The main advantages of these HE_{11} mitre bends are the compactness and large bandwidth. The expected losses per bend are 0.4% and 0.55% for an H-plane and E-plane bend respectively. Theoretically the mode conversion losses (0.25% in both cases) can be reduced by using phase corrected (curved) mirrors. Correct alignment of the mirrors is very important and optical surfaces are used to allow alignment with a He-Ne-laser. Two mitre bends are switchable, to allow switching to a dummy load and switching to a different launcher system (to be used for other diagnostic purposes).

3.6. Launching system

Behind the vacuum window (which could be similar to the gyrotron window), the radiation is guided by a corrugated stainless steel waveguide and a mitre bend into the upper vertical port. A defocusing (70°) mitre bend followed by a conical waveguide launch the beam onto an ellipsoidal reflector, which focuses the beam in the centre of the plasma. A mechanical drive makes rotation of the last reflector possible to allow a radial scan of the plasma volume. The antenna system is supported outside the torus, decoupled from the vacuum vessel by bellows. The mirrors are inertially cooled by the waveguide. The receiver antenna is identical to the launcher and mounted symmetrically. The correct antenna pattern for reception is achieved by tapering down to a monomode waveguide.

4. STATUS

The scientific design of the system is essentially completed and the engineering design is currently in progress. It is intended to install the system on JET during the first half of 1990 for measurements during the final DD phase and throughout the DT phase of JET operation.

ACKNOWLEDGEMENT

The scientific feasibility of the transmission system was determined by the Stuttgart ECRH group under contract to JET.

REFERENCES

1. T. P. Hughes and S. R. P. Smith, JET-P (1987) 46(1987) to be published in Nuclear Fusion.

2. K. E. Kreischer and R. J. Temkin, Phys. Rev. Letters 59 (1987) 547.

3. K. Felch et al., Conf. Digest 12th Int. Conf. on Infrared and Millimeter Waves, Lake Buena Vista (Orlando), Florida (1987) 146.

4. S. N. Vlasov et al., Radio Eng. Electron. Phys. 20 (1975) 14.

AUTOMATIC WELDING AND CUTTING OF JET STANDARD JOINT CONFIGURATION

P. PRESLE, L. GALBIATI AND T. RAIMONDI

JET Joint Undertaking, Abingdon, Oxon, OX14 3EA, England

The automatic welding and cutting trolleys developed for the JET standard lip weld joint are driven electrically on roller bearings which clamp pneumatically the lip (2 x 2 mm) forming the standard JET edge weld configuration. Arc voltage control is used to follow irregularities on the lip edges and geometric changes when the welding trolley moves around corners. Pulse welding makes it possible to work in any attitude. On the cutting trolley the TIG torch is replaced by a nibbler which cuts the joints ready for rewelding, all material offcuts being captured by a vacuum system. It also allows flush trimming of two joint lips, thus allowing subsequent welding even with imprecise initial alignment. To date, 250 metres of lip joint have been trolley-welded, without detectable leak, and over 180 metres cut with the cutting trolley. Typical weld penetrations in the range of 1.7 to 2.5 mm have been achieved, depending on the lip material and the shielding gas.

1. INTRODUCTION

For high vacuum applications welding is considered, in these cases, as the most reliable joining method. In general, the joining and separating operation must be repeated a number of times and motorised carriages automatically guided are envisaged. This solution is often preferred even if personnel access is allowed as it gives reliable results and avoids human errors.

The following problems are encountered:

- Remote positioning of guiding rails.
- Space required by guiding rails and interference with the design requirements of the duct.
- Precise positioning of mating surfaces.
- Space required by the motorised carriage.
- Ability for cutting and rejoining a number of times without substantially altering the relative positions of the adjacent parts.
- Complete swarf removal during cutting operations.
- Initial remote positioning of the automatic carriages.
- Position control of the welding or cutting heads along the joint.
- Ability to continue welding by closing large gaps between lips.

It is the scope of the concept hereby described to give viable solutions to the above problems[1].

2. SYSTEM DESCRIPTION

The mating surfaces of the Octant U joint, large ducts and rectangular ports, consist of two lips 2 x 2 mm, which meet on a plane perpendicular to the axis of the duct to be connected or separated. A trolley, provided with either a torch or a cutting head, is positioned on the lips. Two motorised rollers squeeze the lips onto each other, and move the trolley along by friction. They are mounted in a toe-in angle, in order to keep the trolley pressed against the joint even in an upside down attitude.

The lip joint chosen offers the following advantageous features:

- Locate and guide the trolley, thus avoiding need of rails. Initial positioning of the trolley is straightforward and can be quickly done by means of a telemanipulator.
- Provide margin for repetition of joining and

cutting operations, without varying the relative positions of the adjacent parts.

- The lips can be thin enough, even for ducts with large cross-section, to permit cutting with nibbling machines.
- The joint is totally located at one side of the separating wall of the duct, allowing total removal of the chips, avoiding the danger of them falling through the separating walls.
- The welds are kept largely free of stresses due to the flexibility of the lips.
- The disadvantage is that it is not a structural joint so that external supports have to be provided in some cases. This limits accessibility of the joint.

3. DESCRIPTION OF THE WELDING TROLLEY

The basic design is shown in Figure 1. The trolley comprises a bogey unit, torch assembly and jack system which are mounted together on a common support frame.

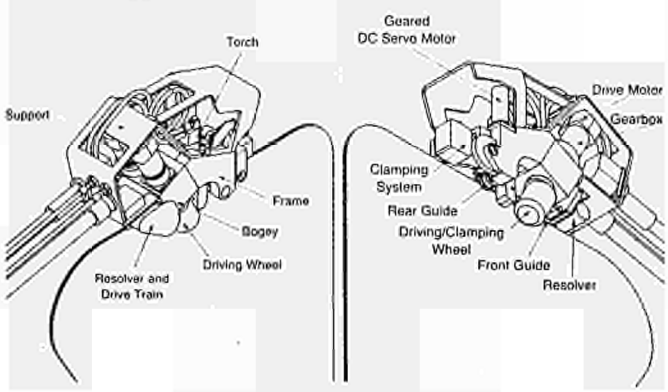

FIGURE 1
Welding trolley

The bogey is made up of two driving wheel sub-assemblies each of which consists of a wheel bearing, gearbox and electric motor all mounted eccentrically on a shaft which can be turned by a rack and pinion actuated by opposed air cylinders, pressurising of one of these cylinders will turn the shaft and bring the wheels either closer or further apart. The clamping force can exceed 1600 N for air pressure supply in excess of 6 bars. The bogey is pivoted so that the wheel axes are not perpendicular to the joint but are given a toe-in angle which makes them point inwards.

During motion of the trolley the driving wheels pull the support frame against the edge of the lips with a force equal to the inwards friction force produced between wheel and plate. Therefore the trolley will be able to ride upside down along the lips as long as the inwards friction force is superior to the trolley weight. The support frame carries two guide rollers disposed respectively at the forwards and rearwards ends of the carriage and bear on the edges of the lips. The driving wheels are mounted at a substantial toe-in angle so that they can negotiate bends of small radius while keeping the two rollers bearing hard against the lip edges.

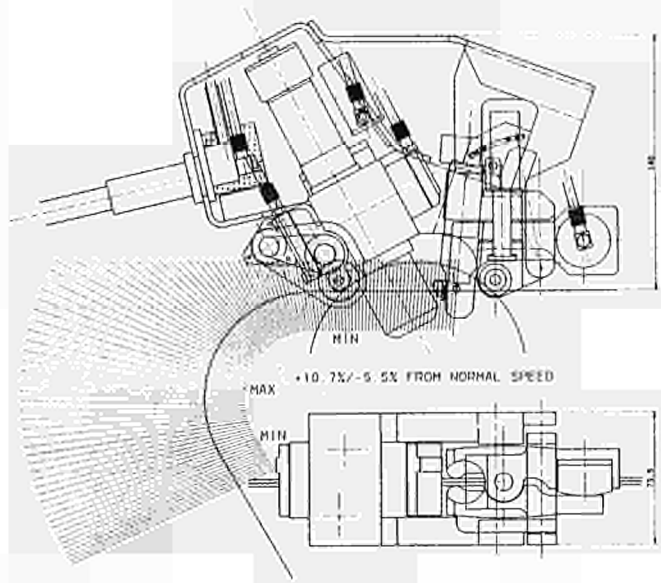

FIGURE 2
Velocity variations

Welding is done with a TIG torch mounted vertically on a pivoting arm, at the back of the

trolley. Seam tracking in the plane of the lips is achieved through AVC (Arc Voltage Control described later) by a geared DC servo. The motor can raise or lower the pivot arm in order to maintain a constant voltage between the torch tungsten and edge of the lips. The position and length of the pivot arm is such as to limit velocity variation of the tungsten tip relative to the edge of the lips during straight line and curved edge welding. Optimum figures on velocity variations is 10.7% to - 5.5% ref. figure 2.

The clamping of the trolley onto the lips is normally sufficient too close the gap between lips when the components are in tolerance. Excessive gaps may occur for the following reasons: lips out of flatness tolerance, weld deformation or unflush weld caps. The trolley has the capability of closing some of these gaps with an automatic clamping system, tack welding the joint at pre-programmed locations, prior to performing the continuous TIG weld. This clamping system is mounted as part of the torch assembly pivot arm in order to squeeze the lips consistently on the edge, in both straight line and curved positions.

Constant speed is achieved through a resolver geared wheel that rides on the lip edges and this gives a true feedback of the trolley speed.

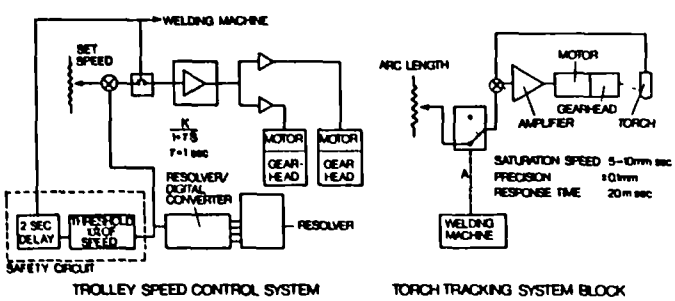

TROLLEY SPEED CONTROL SYSTEM

TORCH TRACKING SYSTEM BLOCK DIAGRAM

FIGURE 3
System control

4. DESCRIPTION OF THE CONTROL SYSTEM

The control of the welding trolley is incorporated in the Protig TIG welding machine[2] which is micro-processor based. The block diagram in Figure 3 shows the tracking system for the welding torch and the servo speed for the movement of the trolley.

The tracking system is an AVC synchronised with the pulsed current coming from the welding machine. The frequency of this pulse is 1.5 Hz and the duty cycle of the high current is 60% - that means 400 msec for high current and 266 msec for low current, figure 3. During the period of high current the system is switched to AVC mode using the arc voltage as a position feedback for the Servo. Instead during the low current time (266 msec) the torch is kept at the same position as at the end of the high current pulse. Using this system the weld nugget is independent of the gravitational effect.

4.1 Transporter speed control servo

Figure 3 shows also the block diagram of the velocity servo that moves the trolley at preset speed.

The resolver and the resolver to digital converter provide the position and speed signals that are processed by the welding control system which closes the velocity loop.

A safety circuit will stop the trolley when the travel speed deviates more than 10% from the set point for longer than 2 sec.

5. DESCRIPTION OF THE CUTTING TROLLEY

The basic design is shown in figure 4. The trolley comprises a bogey unit cutting head assembly and jack system on a common support.

A similar bogey design has been adopted for use on the cutting trolley. The function of the bogey assembly has been described previously in section 3.

5.1 Description of the Cutting Head

The cutting head is articulated on a support

block which is linked to the bogey body at the back of the trolley and is kept pressed against the lip edges by an air jack system.

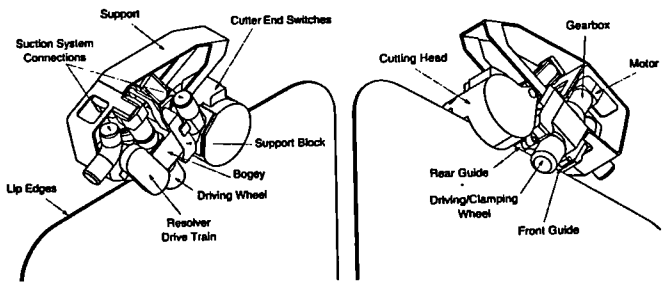

FIGURE 4
Cutting Trolley

The head is split in two, one half includes the hydraulically actuated punch, the other houses the mating die ring. Both halves are held together by a centralizing pin which also acts as a guide for the hydraulic piston, ref. fig. 5. The punch reciprocates nibbling crescent shaped chips off the welded lip as the bogey unit traverses the cutting trolley forward. After each cutting stroke, the punch is retracted by a small air cylinder incorporated opposite to the hydraulic cylinder.

The punch life is increased by partially rotating it during the return stroke. Index increments approximately of 0.5 degree are produced by the return motion of the punch in contact with the lip and linear step motion of the cutting trolley.

It is possible to index the die-ring in the housing four times to present a new cutting zone to the punch without disassembling the unit.

Cutting depth is controlled by the relationship of the punch and hub diameters and the step distance of the trolley. A maximum step equal to half the first crescent cut length will produce a minimum constant cutting depth (2 mm).

Typically lip welds can be removed by setting a 5 mm step distance which produces a constant cutting depth of 2.92 mm after 15/20 mm of trolley travel.

The punch stroke can be reduced by incorporating a spacer behind the hydraulic piston. This allows the puncher to constantly reference on top of one lip while flush trimming the other lip to the same level. Therefore subsequent welding even with imprecise initial alignment can be achieved.

During all the cutting and flush trimming sequences all material off-cuts are removed by a suction system.

5.2 Control System

The cutting tool controller is a stand alone unit based around standard Siemens micro-processor boards. The unit controls all the functions of the tool from operating pneumatic and hydraulic valves to closing the velocity loop.

The clamp and punch mechanism are operated simply by electrically driven valves with feedback derived from limit switches.

The position and velocity data are derived from a resolver as previously described. This information is used to move the trolley a known distance ready for the next cutting.

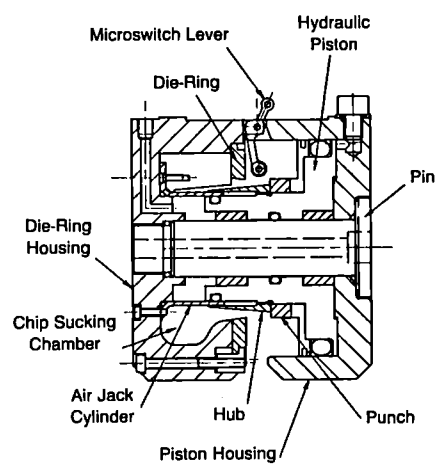

FIGURE 5
Cross-section of cutter head

6. MATERIALS

Both trolleys were handleable by the JET servo manipulator and will be made compatible with the JET remote welding system.

For reduced weight, the cutter head housing and torch welding clamping system are in titanium alloy, bogeys and frame are in aluminium alloy.

For high resistance to wear the material chosen for the cutting punch and die-ring is based on powder metallurgy sintered.

7. RESULTS

Welding - To date 250 metres of lip joints have been trolley-welded, without detectable leak. Typical weld penetrations in the range of 1.7 to 2.5 mm have been achieved, depending on the lip material and the shielding gas. Ref. fig. 6.

The welding parameters used were 60/15 amps, high/low current with 50% pulse width at 1.5 Hz, welding speed 1.7 mm/sec.

Cutting - Over 180 metres of lip welded joints have been cut during the JET machine shut-downs.

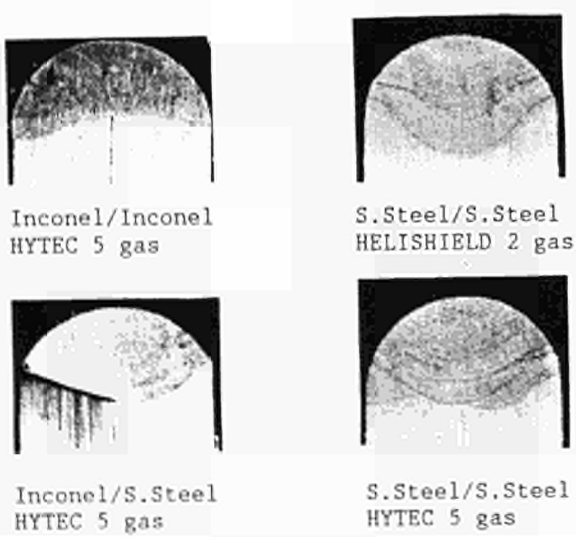

FIGURE 6

Weld nugget macrograph HYTEC 5 - 95% Ar, 5% H_2
HELISHIELD2-25% Ar,75% He

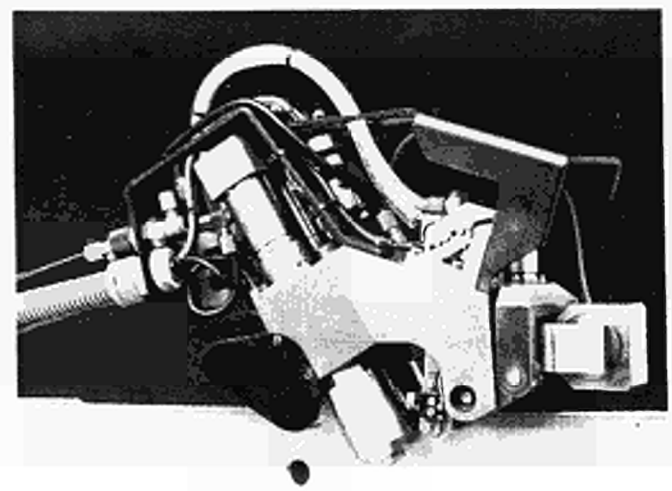

FIGURE 7
Welding trolley

FIGURE 8
Cutting trolley

ACKNOWLEDGEMENT

The authors are grateful to G. Dalle Carbonare for his mechanical design contribution.

REFERENCES

1. S. de Burbure et al., "Remote welding and cutting for the JET project". Proc. of the Eng. Problems of Fus. Research, Chicago, 1981.
2. A. Galetsas, "The JET remotely controlled welding system", Proc. this symposium.

A DUAL SYSTEM FOR THE STABILISATION OF THE VERTICAL PLASMA POSITION OF THE JET EXPERIMENT

M Garribba, D Ciscato*, M Browne, S Dorling, P Noll

JET Joint Undertaking, Abingdon, Oxon OX14 3EA, UK
*Universita' di Padova, Padova, Italy

The vertical position of the JET plasma is unstable without feedback stabilisation. The growth rate can reach $200s^{-1}$ for strongly elongated plasmas ($b/a \simeq 2$). A failure of the stabilisation at large plasma current (7MA) can cause damage to the vessel due to large vertical forces. A dual system which continues the stabilisation even in case of faults in the measurement system or in the conditioning electronics is needed for high reliability. A significant simplification in the control was also achieved by avoiding magnetic signals integration.

1. INTRODUCTION

The JET vertical position control system comprises a Poloidal Radial Field Amplifier (PRFA) and a radial field coil represented by series connetcted subsections of PF coils P2 and P3 (fig 1). For feedback stabilisation, the rate of radial flux change is measured between symmetric locations $Z \simeq \pm 1.7m$, $R \simeq 3m$ inside the vessel, using the flux propagation method [2]. A linear combination of magnetic signals from four internal pick-up coils and from to external differential loops (saddle coils) is used for this purpose. For control of the vertical position at a slower time scale, a PRFA current feedback loop is employed. Without feedback stabilisation the plasma position is unstable with a growth rate γ in the range 100 to $200\ s^{-1}$. It is governed by the decay time of eddy currents in the vacuum vessel $T_V \simeq 3ms$, and also to a minor extent by eddy currents in the mechanical shell. A short amplifier time constant $T_A < T_V$ is therefore essential.

The PRFA uses 50 Hz thyristor bridges, allowing 4 quadrant operation with voltage range ±4kV at full load current ±3kA. Two separately controlled units (range ±2kA) are connected in series with the radial field coil, employing 12 pulse operation corresponding to an average time lag of 1.67ms for small amplitude changes. The PRFA is configured as a voltage amplifier due to internal voltage feedback (fig 2). A rate limiter ensures safe operation with inductive load and at large positive or negative amplitude demands.

2. CONTROL SYSTEM

For the definition of suitable controller functions F_{CL}, F_{CI} (fig 3) the previous system analysis [1,3] on the basis of a simplified model, has been extended. The model comprises three circuit equations for currents in the radial field coil, the vessel and the mechanical shell and a vertical force balance equation for the plasma. Rigid vertical displacements δZ_p of a vertically elongated plasma with peaked current profile were assumed (no skin effect, no change of current). The amplifier transfer function is taken as $F_A \sim (1 + sT_A)^{-2}$, $T_A \simeq 2ms$.

The loop gain K_o for voltage signals V_L (fig 3) is the dominant parameter characterising

the stability region (fig 4). For a given degree of open loop instability (growth rate γ) a certain range of K_0 is possible. The upper limit gives a growing eigenmode at a frequency in the order of 100Hz, at the lower limit the frequency is in the order of 10Hz. The curve R_0 in fig 4 shows the maximum theoretical region, for pure voltage feedback in the stabilisation loop and absence of PRFA current feedback.

Previously, both non-integrated and integrated magnetic signals were used and proportional control was applied in the stabilisation loop, corresponding to a transfer function $F_{CL} = P_L(1 + 1/sT_L)$ in fig 3. The PRFA current was controlled by integral control $F_{CI} = 1/sT_I$, whereby the reference V_{0Z} is usually set to zero. A slightly reduced stabilisation range R_1 is obtained (fig 4).

The stabilisation system was simplified significantly by omission of all signal integrators (corresponding to $F_{CL} = P_L$). This required however the inclusion of some proportional feedback in the current loop ($F_{CI} = P_I + 1/sT_I$). The resulting stabilisation range R_2 (fig 4) is insignificantly different from R_1.

The stability region was tested experimentally at low plasma current, using a step of the current reference V_{0Z}. In pulse 14691 K_0 as increased 25% beyond the nominal value $K_0 = 1.0$. A damped oscillation ith $f \simeq$ 100Hz is visible (fig 5). In pulse 16972 K_0 was reduced to 0.8. The vertical position is almost unstable and a frequency $f \simeq 7$Hz is seen (fig 6).

3. DUAL SYSTEM

Fig 7 shows the block diagram of the dual system. At power level a duplication is already implemented: two indipendent PRFA units are connected in series. If one unit trips it is put into freewheeling mode and the other one takes over. For high reliability this concept is extended to the measurement and control part. Two opposite octants are equipped to route the magnetic signals to the controller. The feedback signals are first individually filtered with a passive first order filter, which also adds a test signal. An isolation amplifier stage provides the necessary galvanic insulation between the torus and the control electronics. The six signals are then summed with appropriate weights to obtain the feedback signal DVZ. The signal of the active channel is compared with one passed through a passive dummy channel. A comparator decides wether one active channel is faulty and operates a switching network so as to take the PRFA input signal from the healthy channel only. With this configuration a complete independendence of action between the PPCC fault detection system and the PRFA fault detection system is achieved.

4. TEST SIGNAL INJECTION

The test signal injection is performed by signal transformers, which avoid any common mode voltage injection between two different channels. The test signal is summed with opposite polarities in all channels as shown in fig 8. When one injected signal is missing the faulty state is detected according to fig 8. The adopted scheme allows the detection of a cable disconnection. In the case of an open circuit the test signal is however not completely lost, but a contribution of ~24% of the original value is expected, due to the capacitive current in the cable.

5. FAULT DETECTION SYSTEM

Fig 9 shows the block diagram of the fault detection. An input high pass filter prevents transient saturations of the next gain stage. The signal A_3 coming from the active channel can be split in two terms:

$$A_3(t) = A_{30}(t) + A_{31} \sin \omega t$$

$A_{30}(t)$ is the feedback signal from the magnetis measurements, A_{31} is the injected test signal. A_d is a pure sine wave because it comes from the dummy channel. It matches the active channel phase within a certain error $\delta\varphi$. After multiplying the two signals a dc component M_{dc} can be retrieved:

$$M_{dc} = \frac{1}{2} A_{31} A_d \cos \delta\varphi$$

A fault occurring anywhere in the signal conditioning changes the amplitude of M_{dc} in both directions. A normal operation indow is defined together with the filter time constant for retrieving M_{dc}. Two opposite constraints are taken into account: a) the filter must provide a clean dc component; b) the reaction in case of fault must be within few milliseconds. The resulting compromise is such that the worst fault considered (saturation of a summing amplifier) does not imply the loss of the control.

An analysis of the robustness of the fault detection against plasma oscillations in the 1kHz range is also carried out. This is based on amplitudes and frequencies of oscillations observed on a certain range of JET shots. The result is that a first order low pass filter with 20Hz bandwidth and two thresholds at ±40% of the normal level can reject the disturbances and contain the response time of the fault detection in the range of 1.6 - 4.8ms. Table II shows the actions in case of faults occurring.

6. CONCLUSIONS

Since high reliability is required for JET 7MA operation, a dual stabilisation system including a protection system against faults in the electronics and in the measurements is proposed here. The intermediate result of this design is that a substantial simplification in the control system is achieved by omitting the integrators in the stabilising loop. The implementation of the dual system will also reduce the pick up of helical plasma modes, because the plasma position is measured at two opposite points in the torus. These modes have occasionally lead to abnormal stabilisation behaviour prior to a disruption.

REFERENCES

1. E Bertolini, P L Mondino, P Noll, Fusion Technology Vol 11, January 1987, pp 71-119

2. F Scheider, Proceedings 10th SOFT, Padova, September 4-8, 1978, p 1013

3. P Noll et al, Proceedings of 11th Symposium of Fusion Engineering, Austin, Texas, November 18-22, 1985, Vol 1, p33

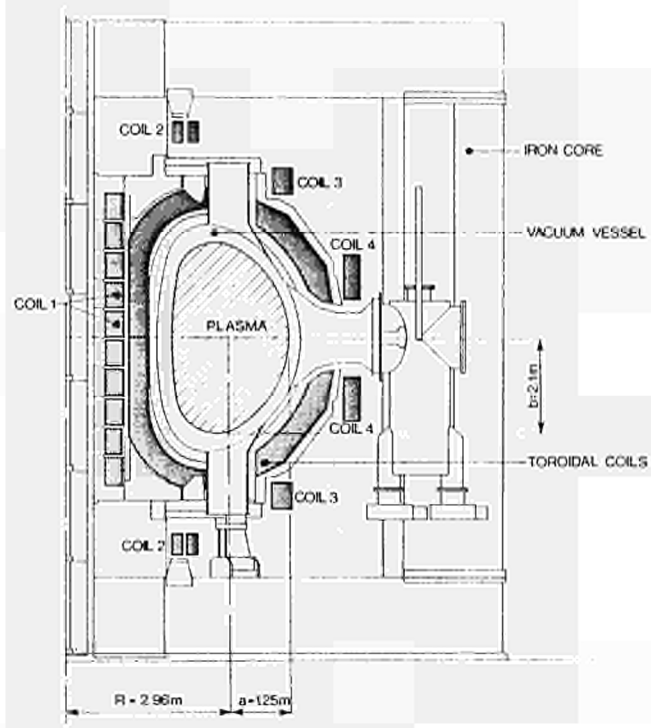

Fig 1: Layout of JET device

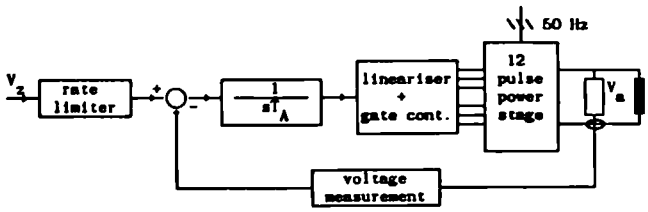

Fig 2: PRFA amplifier model

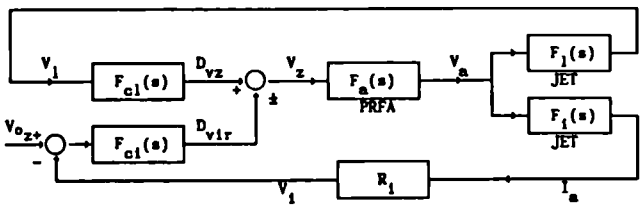

Fig 3: Block diagram of control system

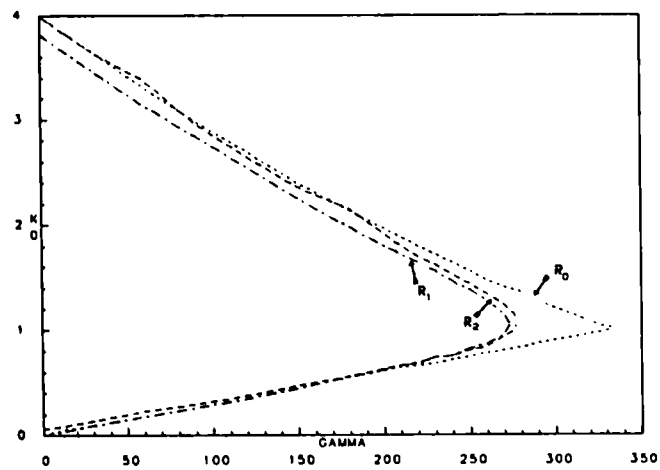

Fig 4: Stability region of the controller

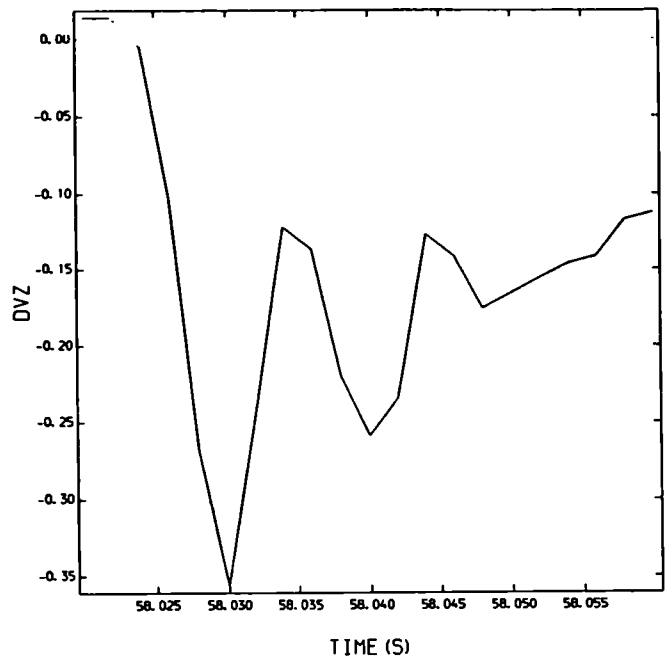

Fig 5: Shot # 14631, High frequency oscillations

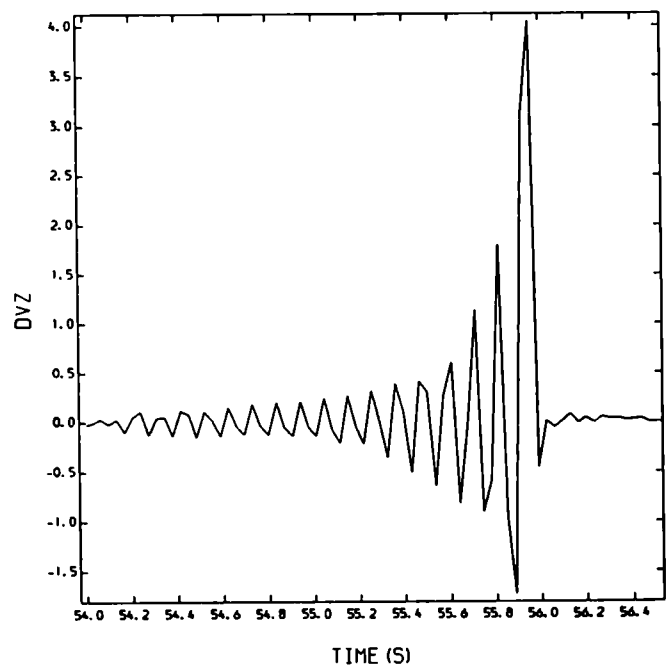

Fig 6: Shot # 16372, Low frequency oscillations

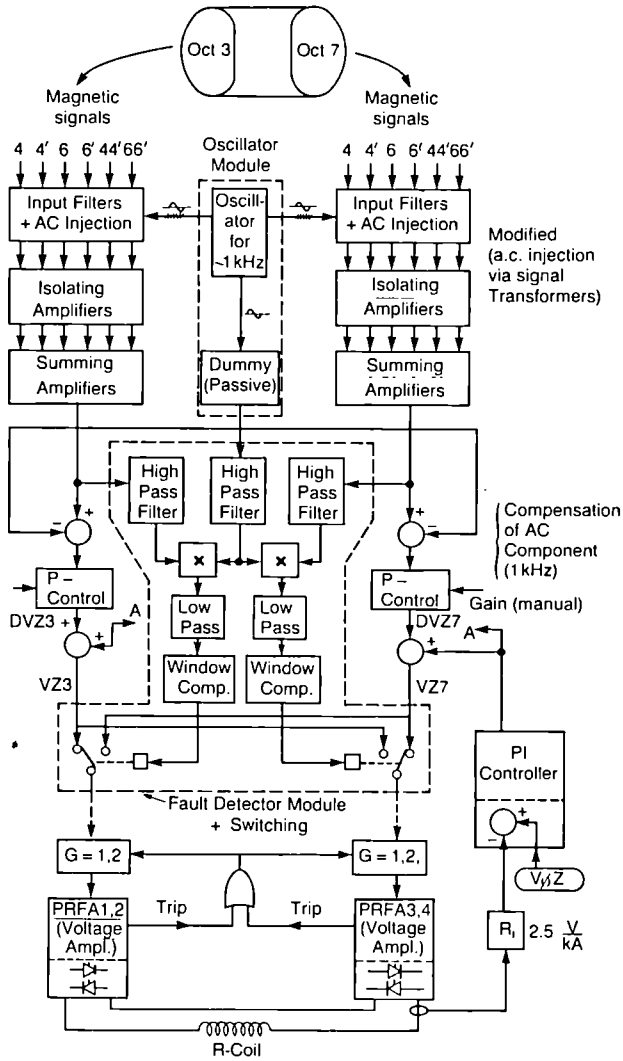

Fig 7: Block diagram of dual stabilisation system

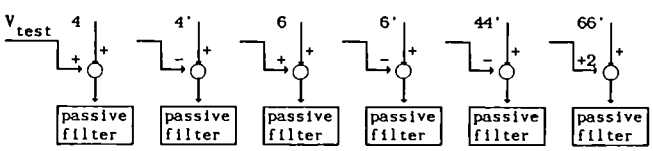

Channel	4	4'	6	6'	44'	66'	Net Signal (V)
Healthy	+1	-1	+1	-1	-1	+2	+1
Faulty	0	-1	+1	-1	-1	+2	0
Faulty	+1	0	+1	-1	-1	+2	+2
Faulty	+1	-1	0	-1	-1	+2	0
Faulty	+1	-1	+1	0	-1	+2	+2
Faulty	+1	-1	+1	-1	0	+2	+2
Faulty	+1	-1	+1	-1	-1	0	-1

Fig 8: Signal injection and working possible conditions

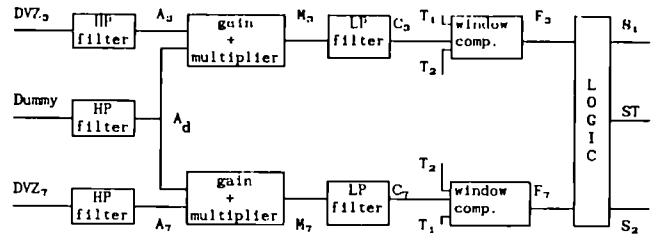

Fig 9: Block diagram of the fault detection

Table II: Actions in case of PPCC fault

ST = 0 Normal situation with V_{z_3} driving PRFA A,B and V_{z_7} PRFA C,D.

ST = 1 Channel 3 disconnected V_{z_7} is driving both PRFA units.

Possible faults:

a] disconnection of one magnetic signal.

b] saturation of any signal amplifier.

c] no power supply to signal amplifiers.

d] saturation of channel 3 of the fault detector.

ST = 2 Channel 7 disconnected V_{z_3} is driving both PRFA units.

Possible faults:

same as in the case ST = 1 but in channel 7

ST = 3 Abnormal functioning with V_{z_3} driving PRFA C,D and V_{z_7} driving PRFA A,B.

Possible faults:

e] no test signal from the oscillator.

f] channel 3 and 7 of the fault detector saturated.

JET NEUTRAL BEAM SPECIES MEASUREMENTS BY DOPPLER-SHIFT SPECTROSCOPY

G H Deschamps, H D Falter, R S Hemsworth, P Massmann

JET Joint Undertaking, Abingdon, Oxon, OX14 3EA, England

The species mix of the JET neutral injector ion sources is measured several times per pulse for 3 seconds by Doppler-shift spectroscopy. The full-energy ratio increases with beam current: 85% for 60 Amps in hydrogen and 44 Amps in deuterium, and the half and third energy neutrals represent 10 and 5% respectively. No variation greater than ± 2% is observed throughout the pulse.

1. INTRODUCTION

The neutral beams of the JET injectors are produced by extraction of hydrogen or deuterium positive ions from a magnetic multi-pole plasma generator at voltages between 40 and 160 kV. The ion current yield of 10 to 60 Amps is partially neutralised in a gas target of about 10^{16} mol/cm^2 and the positive molecular ions dissociate into full-, half-, and third-energy particles in various proportions depending on the energy. Fast excited atomic neutrals which emit Balmer-alpha light are created by collisions with the background gas. These can have the same energy as the extracted ions or one half or one third of that energy.

On the JET neutral injection test bed the Balmer-alpha light is collected and analysed by two grating monochromators viewing the beam at an angle of less than 50° relative to the beam axis. The three different energies of these fast neutrals result in three Doppler shifted lines which are readily resolved down to energies of 20 keV per nucleon. The analysis of the Doppler shifted spectrum may be used to determine the extracted or the neutral species mix [1,2,3,4,5]

In this paper we present the results of deuterium and hydrogen species measurements from the tests on the ion sources now in operation on JET. The time-averaged species mix is given as a function of the extracted beam current. Additionally the species ratios are plotted as a function of time during the first 3 seconds of a pulse.

2. EXPERIMENTAL SET-UP

2.1 Description of the apparatus

The Doppler shift spectroscopy measurements on the neutral injector test bed are carried out by two grating monochromators manufactured by Spex and Jarrell-Ash.

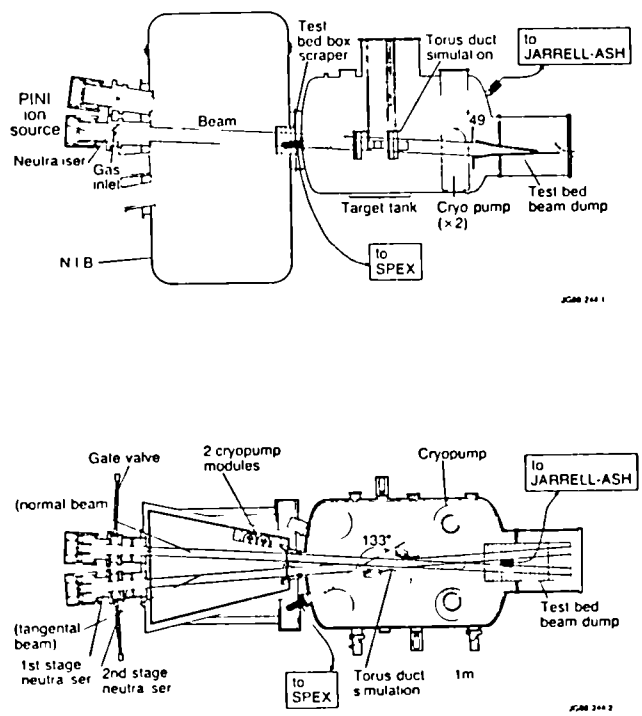

Fig 1 - SPEX and JARRELL ASH monochromators position and angle

The Spex is a modified 0.5 metre 1800 gr/mm Czerny-Turner spectrometer coupled to a 5 Hz vibrating mirror. The Jarrell-Ash is a 0.5 m Ebert monochromator with an 1800 gr/mm grating and a hexagonal mirror rotating at 50 to 100 rpm.

The light is collected at an angle to the beam of 133 degrees for the Spex and 49 degrees for the Jarrell-Ash (Fig.1) and focussed onto a low loss optical fibre of circular cross section 30 metres long. The other end is matched to the entrance slit of the monochromator for optimum transmission either through a fishtail (Jarrell-Ash) or by lens focussing (Spex).

2.2 Signal conditioning

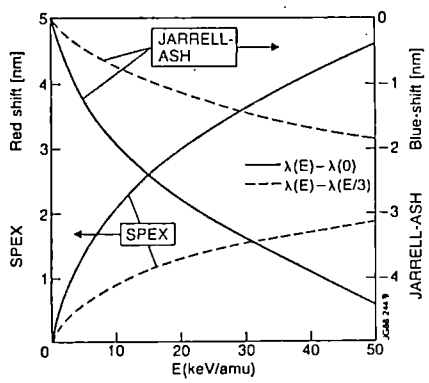

Fig. 2 - Doppler-shift vs. energy

$$\lambda(E)\ [nm] = 656 - 0.958 \cdot \cos\theta \cdot \sqrt{E} + 7 \cdot 10^{-3} \cdot E$$

The Balmer-alpha spectrum is resolved by the settable grating between typically 648 and 656 nm for the Jarrell-Ash and 656-664 for the Spex depending on the Doppler shift which is given as a function of energy in Fig.2. The dispersed light is time resolved by electronically driven mirrors either continuously (Jarrell-Ash) or periodically (Spex).

The signal is amplified by a low noise photomultiplier of constant gain over the spectral range. The total transmission of the monochromators has been calibrated with a constant H_α source as a function of the grating wavelength λ_G. The results are plotted on Fig.3. Both monochromators cover about 10 nm, full width at half maximum. The dotted curve on Fig.2 shows that the difference in wavelength between full and third energy do not exceed 2 nm up to 50 keV/nucleon which means that the Spex transmission can be kept constant for the full Doppler shifted spectrum providing the grating setting is equal to the third-energy species wavelength: $\lambda_{G1} = \lambda(E/3)$. The optimisation of the transmission for the Jarrell-Ash consists in setting the grating in the middle of the spectrum, i.e. $\lambda_{G2} = \frac{\lambda(E) + \lambda(E/3)}{2}$ to keep the transmission above 95% up to 140 keV/nucleon.

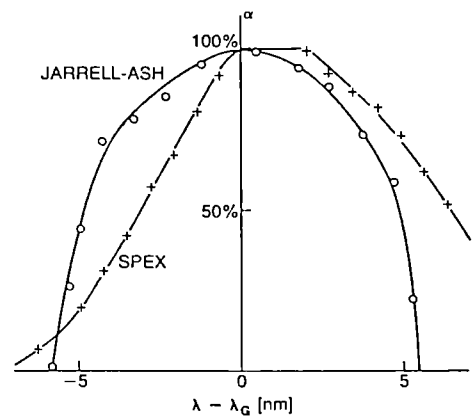

Fig.3 Transmission coefficients (λ_G =Grating wavelength)

2.3 Data acquisition

The monochromator signals are digitised every pulse at a 10 kHz rate. The ADC is triggered at the start of the beam and stays on for 3.2 seconds. Each spectrum scan lasts between 0.1 and 0.3 seconds, which allows up to 30 scans per pulse, and the measurement of species ratios as a function of time during the pulse.

3. DATA ANALYSIS

The processing of the monochromator data requires a dedicated software to reduce 32 kbytes down to four species ratios (including impurities) as a function of time and as a time-average for each monochromator. The Program SPECIES has been implemented for this purpose.

The algorithm of the program consists of two main parts:

a) a pattern recognition routine to identify the Doppler-shifted peaks with a high reliability in noisy operating conditions;

b) a calculation of the time-dependent and time-averaged species ratios.

Each species fraction EPS(S) is defined as the ratio of the corrected integral of the Doppler-shifted peak to the sum of all the corrected integrals.

$$EPS\ (S) = \frac{[\ B(E/S)\ *\ C(E/S)\ /\ \alpha(S)\ ]}{\sum S\ B(E/S) \cdot C(E/S)/\alpha(S)}$$

The first correction $\alpha(S)$ takes into account the transmission function of the apparatus as defined in the previous section.

The second correction coefficient C(E/S) includes the dissociation, recombination and excitation cross-sections producing the neutral atoms. It is defined for each molecular ion species. These coefficients C(E/S) have been computed from measured cross-sections [6,7,8] for the relevant energy range (Fig.4).

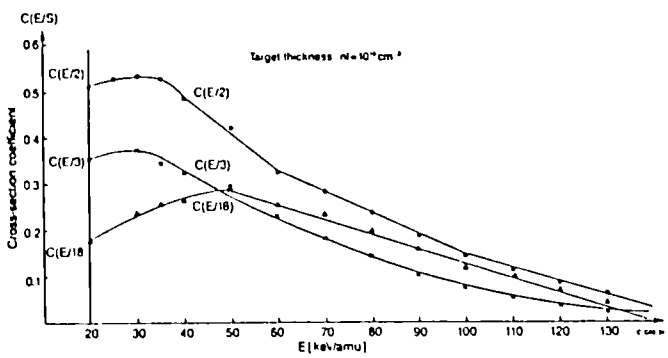

Fig 4 Cross section coefficients vs energy per nucleon (20 to 130 keV/amu)

The dependence of C(E/S) with neutralisation target density is weak above 10^{16} mol/cm^2, which is our normal operating range. Therefore the coefficients are assumed to be independent of target density and dependent only on the energy per nucleon. The species ratios depend on the following parameters:

a) the viewing angle : $\Theta(I)$
b) the grating setting : $\lambda_G(I)$
c) the extraction voltage : V
d) the atomic mass number : N
e) the species number : S

(a) and (b) depend on the monochromator type : I = 1 for the Spex, I = 2 for the Jarrell-Ash. The extraction voltage is averaged over the pulse and is a constant within ± 1%. The mass number N is determined by the selected gas : N = 1 for hydrogen, N = 2 for deuterium. The species number S is an identifier of the peak in each spectrum : S = 1 for the full-energy, S = 2 for the half-energy, S = 3 for the third-energy, S > 9 for the impurities (S = 10 for D_2O^+, S = 18 for H_2O^+).

4. RESULTS AND COMMENTS

4.1 Deuterium species mix as a function of current

The deuterium species mix was evaluated between 14 and 44 Amps from 20 to 40 keV/nucleon at two different pressures for both monochromators. The normal background pressure in the vessel is 7.10^{-5} Torr, and to increase the Balmer emission an additional gas puff is introduced raising the pressure up to 4.10^{-4} Torr during the beam-on time. The comparison of the results at both pressures and between the two monochromators enables a validity check to be carried out. Measurements were made in optimised source operating conditions, i.e. for a minimum beam divergence.

The Spex data are plotted in Fig.5 for the normal background pressure (continuous line) and with additional gas (broken line). The comparison between the two curves shows that the average full-energy species ratio seems higher at the normal pressure by 3 to 4%. This can be explained by a systematic error in the integration procedure: the peak integration is a function of the zero reference calculated by averaging the background noise before each scan. This average is higher at the beginning of the scan and the drop can cause an overestimation of the species ratio derived from the highest peak which is the full-energy peak for these measurements. This error, being inversely

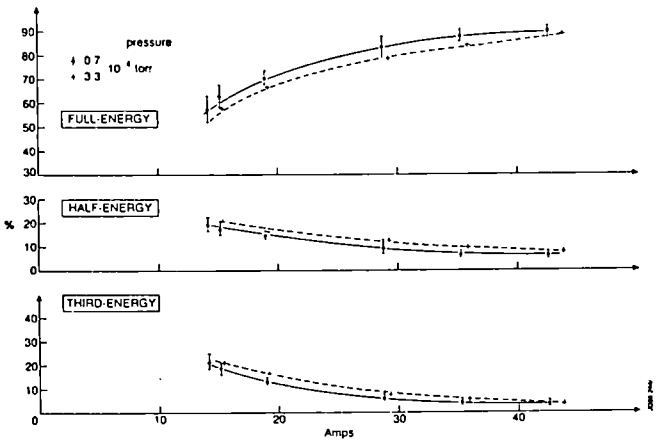

Fig. 5 - Deuterium species ratios vs. beam current at minimum divergence

proportional to the signal-to-noise ratio, is greater at low pressure. The ratios evaluated with additional gas are therefore more reliable and all measurements at normal pressure with the Spex have to be corrected by subtracting 3%. The variation of the species during the pulse represented by the vertical bars is random and is equivalent to an error bar of ± 2 to 3% depending on the signal-to-noise ratio.

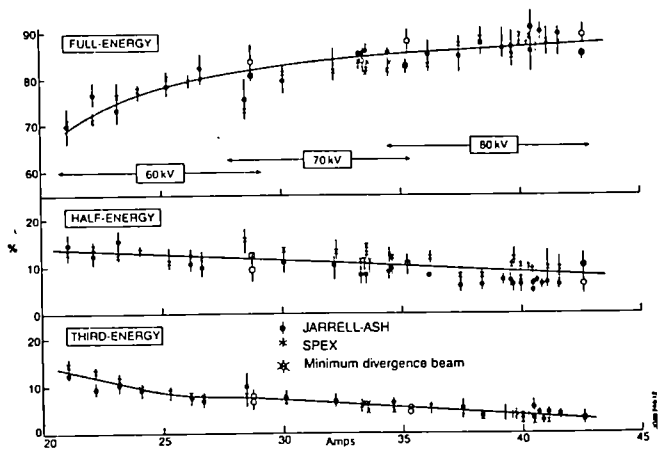

Fig. 6 Deuterium species ratios vs. beam current (for 3 voltage settings)

A more extensive analysis of deuterium shots for variable currents has been carried out at 60, 70 and 80 kV for normal gas pressure for 100 shots with frequent breakdowns during the pulse. Both sets of monochromator data are plotted as a function of beam current on Fig.6 (the dots represent the Spex data, the crosses the Jarrell-Ash).

The full-energy species for the minimum divergence beams (shown as open circles on Fig.6) are higher on average than the species at higher extraction voltage but with the same current. However the variation during the pulse, represented by the error bars, covers the difference and a global trend of increasing full-energy species with current can be seen, independent of the extraction voltage, from 70 to 90%. The half-energy species decreases slowly from 14 to 8% and the third-energy species drops from 14 down to 5% for a current variation of 20 to 44 Amps.

4.2 Hydrogen and deuterium species mix for 80 kV ion sources

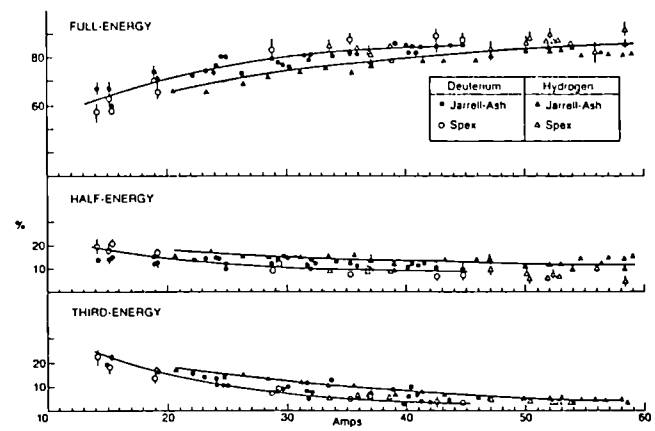

Fig 7 · Species ratios vs extracted current for deuterium and hydrogen operation

A more extensive survey of the species ratios for deuterium and hydrogen operation has recently been made with the 80 kV ion sources. More than 200 shots have been analysed. The energy range is 20 to 80 keV/nucleon and 14 to 60 Amps, and the cross-section coefficients vary by a factor 2 over the energy range. The ratios are plotted as a function of current on Fig.7 for both monochromators at normal background pressure. The deuterium and hydrogen measurements are represented respectively by the circles and triangles for different ion sources. In general both hydrogen and deuterium species follow the same trends with a slightly higher average full-energy fraction in deuterium.

The full-energy ratio increases from 65 to 85% between 20 and 60 Amps for hydrogen. There is no clear evidence of a decrease for the half-energy ratio with current as the whole data set lies between 15 and 10% over the whole range except around 15 Amps where the data is too scarce to be conclusive. The variation at constant current is also about 5% depending on the ion source and the gas type. Between 20 and 40 Amps the H_2^+ ratio is 4 or 5% higher than D_2^+. The D_3^+ ratio is higher than D_2^+ below 20 Amps and decreases down to 4% at 4 Amps. The H_3^+/H_2^+ ratio is on average higher than the D_3^+/D_2^+ one. Impurities are only present at the start-up of ion source conditioning showing water impurities only. A check is made for all pulses by integrating between the unshifted peak and the third-energy peak. The results show that less than 2% impurities are present which is comparable with the fluctuations of the main species ratios.

4.3 Species mix variation during a pulse

Typical examples of species mix measurements throughout a pulse are given for optimised beams and signals for 5 different currents (Fig.8). The ratios remain constant within a 1 to 3% margin. The fluctuations of ratios do not show any pattern through the pulse and the variations seen can be attributed to random errors.

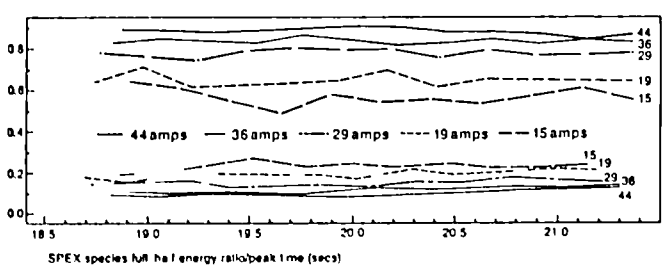

Fig 8 Species ratios vs time variation for minimum divergence deuterium beams

5. CONCLUSION

The Doppler-shift spectroscopy technique is a reliable tool for the species mix measurements in the JET high current neutral beam ion sources. It is limited by the accuracy of the cross-section measurements and the spectrum integration. The accuracy of the integration has been tested and evaluated at ± 2%.

The overall accuracy of the results in a wide range of operating conditions is within ± 3%. The yield of full-energy particles is above 80%: 85% for 80 kV ion sources, between 50 and 60 Amps when the source is operated with hydrogen, and between 40 and 45 Amps when operated in deuterium. The 160 kV ion source data analysed so far with hydrogen show the same trend and 84% H^+ is measured for 120 kV 34 Amps beams and 74% for 80 kV 18 Amps.

The fractional energy particles represent about 10% and 5% at high currents for the half- and third-energy respectively.

REFERENCES

1. A R Martin, Internal Report, Culham M W B L, JDC Meeting, 1985.

2. D Stork, R S Hemsworth, Proc. of the 8th Symp. on Eng. Problems of Fusion Research, San Francisco, 1979, p 1024.

3. J F Bonnal et al, Phys. Letters (1979) p 65.

4. C Burrell et al, Rev. Sci. Instr. (1980) p 1451.

5. T S Green et al, Proc. 10th Int. Conf. on Plasma Physics & Contr. Fus. Res. (London) 1984.

6. I D Williams et al, J. Phys. B Lett., Atom. Mol. Phys. 15 (1982) 1377.

7. I D Williams et al, J. Phys. B Lett., Atom. Mol. Phys. 16 (1983) 2765.

8. R S Hemsworth, JET Internal Report (1985).

DESIGN OF THE PROTECTION CROWBAR FOR THE LHCD KLYSTRONS IN JET

C CHRISTODOULOPOULOS, D CROSS, H HRABAL*, E BERTOLINI, R CLAESEN, W WEIGAND*

JET Joint Undertaking, Abingdon, OXON OX14 3EA, UK
* SIEMENS, D-8520 Erlangen 2, Germany

The JET Lower Hybrid Current Drive Generator (LHCD) will consist of 24 Klystrons. The system is expected to be fully operational in 1990. It will be composed of six modules of four klystrons each and of two klystrons for the testing of the LHCD component. Two klystron modules will be ready for operation with the JET machine in early 1989. In order to protect the klystrons in case of arcing or overvoltage, crowbars near the klystrons are foreseen. For this purpose ignitrons as opposed to thyristors were chosen. The design of the crowbar for the LHCD takes into account the past experience obtained from operation of the Neutral Beam protection crowbars and follows a different approach for the ignitron triggering and the anode/cathode temperature control.

1. INTRODUCTION

The protection crowbar for the LHCD system shall consist of seven identical units to be used for the six klystron modules of the JET machine and the Test Bed. The first two units will be fully commissioned by the end of 1988

Each crowbar unit will use ignitrons as main switching element. The purpose will be protection of the klystrons against damage if either an arc occurs in a klystron, or an overvoltage is applied to the klystron cathode. The crowbar unit will also provide accurate klystron beam current measurements.

2. SYSTEM DESIGN REQUIREMENTS

The overall system shown in fig 1 in a simplified form, illustrates the Crowbar Klystron Protection Unit (CKPU), which is remotely fed from the High Voltage Thyristor Star Point Controlled Supply with its associated filter components, and the four klystrons with their associated resistors.

The CKPU is to provide accurate klystron beam current measurement 20A ± 1% and to protect the klystron against damage if an arc occurs in any of the four klystron loads.

Damage can occur, under an arc situation, if the energy dissipated in the klystron load

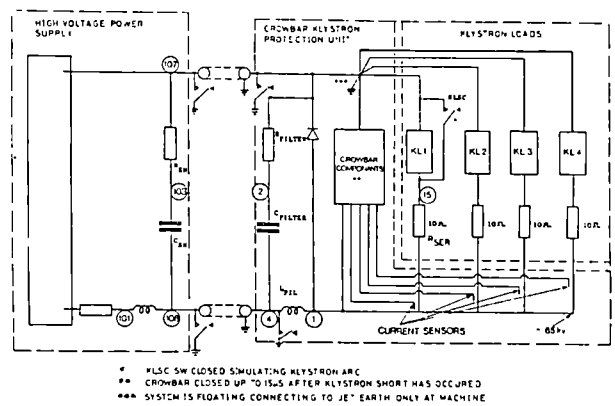

* KLSC SW CLOSED SIMULATING KLYSTRON ARC
** CROWBAR CLOSED UP TO 15μS AFTER KLYSTRON SHORT HAS OCCURED
*** SYSTEM IS FLOATING CONNECTING TO JET EARTH ONLY AT MACHINE

Fig.1. CIRCUITRY RELATED TO THE ASSOCIATED HV POWER SUPPLY SYSTEM

exceeds 30 Joules. The Crowbar is to both sense this overload condition and to protect the klystron by immediately, within 50μs [5], diverting the current from the klystron to the Crowbar, to subsequently discharge the associated High Voltage Power Supply Capacitors and conduct fault current until the thyristors of the HVPS are blocked or the breaker trips.

The CKPU is to self crowbar if the input voltage exceeds -70kV to -80kV, manually adjustable.

Safety earthing switches are to be incorporated within tne Crowbar Cabinet as well as filter components to correctly match to the HVPS supply cables.

3. SYSTEM DESCRIPTION

Refer to fig 2 throughout this section.

3.1 Main Crowbar Stack

The main crowbar stack consists of three D-size ignitrons type NL1489 arranged in series.

The NL1489 ignitron is the coaxial version of the NL1488 and it has the same electrical characteristics, including a conditioned maximum hold-off voltage of 50kV, a capability of 100AS per pulse and peak current of 90,000A.

The coaxial configuration of the Ignitron Crowbar System results in the current flow via

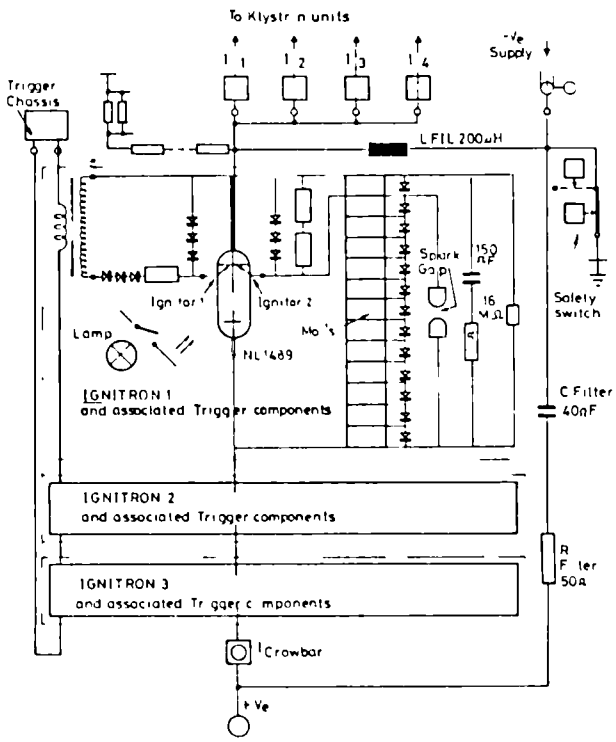

Fig 2 IGNITRON CROWBAR

the arc from anode to cathode, with a return current up the wall of the envelope to the cathode terminal. This has the effect of neutralising the magnetic field, which would otherwise tend to deflect the arc towards the envelope walls at higher peak currents and longer conduction times (more than one millisecond), resulting in erosion of the metal surfaces and subsequent deposition of evaporated metal onto the internal tube structure including the igniter. Eventually the erosive action would lead to severe ignitor wetting, a condition that is the principal mechanism of the ignitron end of life failure (i.e. the inability to trigger the device into conduction).

In the JET LHCD application during a crowbar the peak current will be 3000A with a maximum conduction time up to 14 milliseconds when the HVPS thyristor controller is blocked, or 100 milliseconds if the controller fails to block and the 33kV breaker is tripped.

3.2. Triggering system

The type NL1489 ignitron has two ignitors. Both are used for triggering the ignitron each with a different method.

3.2.1. Separate Excitation

The ignitron is triggered into conduction by discharging a capacitor through the ignitor via transformers. The triggering system for the LHCD crowbar is different from that of the PINI protection system crowbar [3], in that each ignitor at every ignitron is connected to the secondary of a separate pulse transformer, each transformer primary being fed by the same constant current.

Each transformer consists of two ring-core elements made of Permax F arranged into an "8" shape. The primary winding is an HVDC cable, running through the holes of the "8" in four turns for all three stages. The secondary winding surrounds both the cores of the "8" and one end is attached at the ignitron cathode level. The primaries are supplied by a trigger unit installed at ground level.

The trigger unit consists of a 2kV, 3μF capacitive device, which will be switched to the primaries of the pulse transformers via a fast

turn-on thyristor type No Bst RG3 H 200t.

The trigger transformer ratio utilised is 3:1 providing 2000V to the ignitor and an associated ignitor current of 150 to 200A. Trigger pulses of between 2 to 4μs duration will be transmitted to the ignitrons, which is suitable for this application of up to 10,000 shots.

3.2.2. Anode firing

A high energy MOV stack consisting of 13 resistors type S10V E 801-KV252 will be provided across each stage in order to limit the voltage across an ignitron which has not fired and also to provide current with associated energy to the second ignitor of the ignitron thus supplying an additional trigger capability. Back-up spark gaps will be triggered by overvoltage, adjustable over 25kV, so protecting the MOV's in the case of a non-firing ignitron, and will also feed energy into the second ignitor.

The use of spark gaps depends on the presence of a voltage greater than the nominal 25kV across one stage, and as such it is not useful for the klystron arcing condition, which will result in 19kV appearing across the stack at the maximum operational HVPS voltage of 65kV.

3.3. R C Units.

An RC matching unit consisting of a resistor of 50Ω in series with a capacitor of 40nF will be installed in the crowbar cubicle in order to minimise switching voltage transients, which are due to the 200 meters of HVDC coaxial cable. An inductor of 200μH will limit the rate of current rise in the klystron.

In parallel with each crowbar stage RC units are used, which consist of 150nF capacitors, with 10Ω resistors in series. Their main purpose is to enforce ionisation of mercury immediately after firing, operating similarly to a holding anode, so that mis-synchronisation of the three ignitrons can be overcome.

3.4. Cathode and anode temperature control

One of the most troublesome aspects of the use of ignitrons is their tendency to self-fire (breakdown) at voltages below their rated value. Self fire is dominated by three factors:

i) The temperature of the mercury pool,
ii) Mercury droplets in high field regions within the tube,
iii) The presence of foreign gases in the tube.

3.4.1 Cathode temperature control

The ignitron is a device designed to operate at the lefthand side of the Paschen curve, where the breakdown voltage decreases rapidly with increasing Hg vapour pressure. The Hg pressure in turn increases rapidly with increasing temperature (pressure increase from 0.0049mmHg to 0.04471mmHg from 10°C to 36°C). Voltage hold-off capability is almost halved for an increase of 10°C above 30°C.

On the other hand the anode delay time and the ionisation process, which is vapour pressure dependent, will be increased when the cathode temperature decreases.

For the LHCD application, the total firing time is not critical, whereas self-fire is considered important, resulting in a need to keep the cathode temperature constant at 15°C via water cooling. The water cooling plant consists of the compressor, pumps, water storage tank, an ion exchanger loop and a water distribution for 6 crowbar units. A standby system will be provided for a fast changeover in the case of system failure. The system is envisaged to operate day and night in order to keep the ignitron cathodes controlled at the correct temperature.

3.4.2 Anode Temperature Control

In order to inhibit formation of mercury droplets in the high field region a temperature differential of more than 30 degrees will be established between anode and cathode. The anode will be heated by infrared lamps to approximately 50°C.

3.5 Crowbar DC Current Sensing

In order to prevent the possibility of a high leakage current being established in the

Crowbar, which would result in high internal dissipation, a dc current detector will trip the HVPS and alarm the system.

3.6 Maintenance Procedures

The crowbar will be checked daily before klystron operation, at a voltage below 11kV and also the ignitrons will be replaced at regular intervals, defined by the manufacturer and JET operating conditions.

3.7. Mechanical layout

Each crowbar will be installed in a metallic dustproof enclosure with the following dimensions: width: 1550mm, depth: 800mm, height: 2038mm.

The main components of the crowbar are arranged in three stages, which will be supported on four isolating thread rods made of cycloaliphatic epoxy resin. This material has high arc withstand capability and high glow resistance, but a self-igniting temperature of just above 430°C. An alternative under consideration is to use ceramic material despite its breakability.

The crowbar components on the three stages are arranged as closely as possible together in order to get at least 200mm air distance to the earthed parts of the enclosure. The cables and the cooling water pipes will be ducted through the bottom via special tight glands. The side panels will be welded onto the frame. The rear side will be made of panels, which are screwed onto the frame, whereas the front will have two locatable panel doors. Rubber profile door and panel seals will be used to keep the cubicle airtight, which serves three purposes:

i) to stop mercury vapour escaping and contaminating other equipment in the case of fire,

ii) to cause oxygen starvation if a fire starts,

iii) to help control the temperature.

As already mentioned in 3.4 the losses of the ignitrons are carried away by the water cooling system.

4. THYRISTOR CROWBAR STUDY AND TESTS

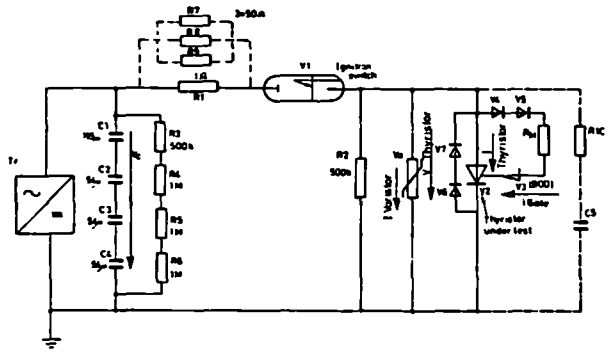

Fig.3 THYRISTOR TEST SYSTEM

The supplier of the crowbar has carried out tests with thyristors, as an alternative to ignitrons, to assess their capability for crowbar operation:

i) dv/dt up to 6kV/μs in forward direction,

ii) di/dt up to 400A/μs,

iii) 10000 pulse capability.

The thyristor, type No SIEMENS Bst RG3 H 200t was chosen because of its high current switching capability and associated high voltage rating of 3,000V. This thyristor also has a non-repetitive impulse current rating of 15kA which is well above the expected minimum crowbar current of 3kA. Three thyristors of this type were randomly selected to be subjected to current pulses of 3kA peak, di/dt pulses of 1000A/μs and dv/dt voltage pulses of 12kV/μs. One thyristor was submitted to 10,000 pulses, one to 2000 pulses and the last one to 1000. All tests were performed successfully, at an ambient temperature of 25°C and at a pulse rate of 1 per minute, which approximates to the maximum crowbar duty ratio.

Based on the fact that the maximum continuous DC voltage in a forward direction should be smaller than 60% of the repetitive reverse voltage (U_{RRM}), a total of 42 thyristors in series is required for a maximum withstand voltage of 75kV. As a single thyristor

could be reliably triggered with an anode cathode potential below 50V, no technical reasons should prevent a complete Thyristor Crowbar Stack being successfully triggered below 2kV, thus providing safe klystron arc protection.

Simulation showed that a klystron arc could still be limited to a safe level using inductors, allowing thyristors with lower di/dt capabilties to be used.[5]

5. OPERATIONAL EXPERIENCE WITH THE JET NEUTRAL BEAM CROWBAR

This crowbar protects the neutral injector beam source. It is located inside the Grid 1 protection system cabinet. When an overcurrent occurs in the grid, which can not be blocked by the series tetrode, the crowbar is fired short circuiting the output of the HVDC power supply that feeds Grid 1. The stack consists of five ignitrons in series with cascade triggering [3].

Many problems have been encountered during operations. False triggering, which has been reduced by improved circuit design and extra filtering, or self firing of the ignitrons has caused a lot of early terminations of neutral beam pulses as shown in fig 4.

Although improved conditioning and maintenance procedures have somehow reduced the number of ignitron self breakdowns [4], this problem has not been resolved. Ignitron breakdown occurs to units at random and at various times, particularly at the beginning and towards the end of operations.

Temperature measurements have shown that in the afternoon the ambient temperature reaches 28-30°C, whereas the temperature in the protection system is at least two degrees higher than the ambient. The ignitron cathodes are not cooled and the anodes are heated by forced hot air supplied through caramic supports from the blower and heater situated below the stack. The temperature of the air blown into the anode of the bottom ignitron at one protection cabinet was found to be 37°C. At the end of JET operation the heater is switched off, which could result in an inadequate temperature

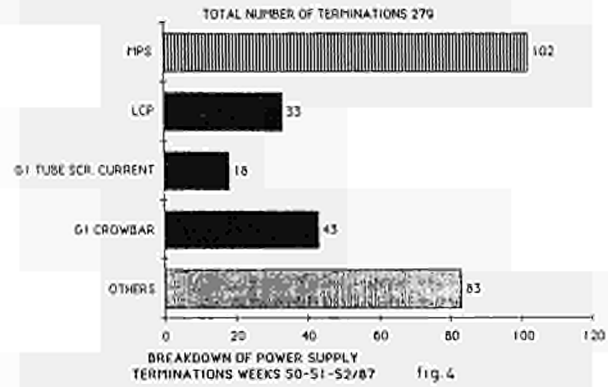

fig.4

differential between anode and cathode at the beginning of the following JET session and could cause self-firing of the crowbar especially when the input voltage is over 100kV.

6. CONCLUSIONS

The decision to utilise ignitrons for the protection of the klystron was based primarily on their lower initial cost and that their known problems had been addressed with this design, whereas potential problems associated with a Thyristor Crowbar were not known when the decision had to be made.

REFERENCES

1. J A Dobbing et al, Design of JET lower hybrid current drive generator and operation of high power test bed, in: 15 Soft, in print.

2. J A Carwardine et al, Early operating experience with the JET neutral injector power supplies, reliability and improvements, in: Proceedings of 12 Symposium on Fusion Engineering, Monterey, Oct 1987.

3. United States Patent 4,232,351, High voltage crowbar circuit with cascade triggered series ignitrons.

4. D B Cummings, Pulsed power ignitron switches, Lawrence Livermore National Laboratory, October 1984.

5. D Cross, Discussion of the design of an SCR crowbar system: for lower hybrid arc protection, JET Ref DAC1/apc/G, 15.6.87.

THE JET REMOTELY CONTROLLED WELDING SYSTEM

A GALETSAS, M WYKES

JET Joint Undertaking, Abingdon, Oxfordshire, OX14 3EA, England

A comprehensive Remote Welding System for use during the remote maintenance of JET has been specified, designed, procured and tested. The system comprises various weld tools, weld current power source, supply for tool actuators, weld gases and cooling water, a command and control interconnection system and the operator Man-Machine Interface (MMI). The welding tools which include orbital, bore, lip and tack welders some with AVC, wire feed or weave have previously been reported elsewhere. Due to the radiation environment at the workpiece all of the weld power and service supply packs are located up to 50 metres from the tool. Standard welding power packs are not usually required to generate and control welding arcs over such long distances and the device used at JET was selected only after a rigorous test programme. The command and control of the power pack from the remote control room is achieved with a standard serial link. This has been successfully implemented in the face of severe interference problems from the h.f. arc starting and weld pulses. The techniques used to overcome these problems are discussed in the paper. The control room MMI has been designed to provide the operator with real time feedback of critical parameters such as weld current and voltage, tool position and speed and wire feed speed. All control commands normally available at the power pack are available at the control room workstation. In addition the gas and cooling water flows/pressures are monitored, displayed and software interlocked for safety. The MMI also provides TV monitors for tools with weld pool viewing incorporated. This paper describes the system and its development. Its performance under remote conditions is also assessed with full scale mock-up tests.

1. INTRODUCTION

During the tritium operation phase of the JET machine, high energy neutrons will activate the machine structure to an extent which inhibits man access to it.

All maintenance, including welding tasks, will then be performed remotely. For this reason an integrated Remote Maintenance System (RMS) has been designed and it is under implementation (1).

The RMS comprises robotic arms and vehicles, servomanipulators, special end-effectors, and viewing systems. All above equipment are controlled and monitored from the Remote Handling Control Room (RHCR).

The JET Welding System (JWS) is part of the RMS and was developed in order to provide remote welding inside and outside of the JET machine.

2. OVERALL REMOTE WELDING SCENARIO

The JWS functional requirements were as follows:

- remote welding is required inside and outside the JET machine.
- the welding tasks are completely predefined.
- the JWS should have a local operating mode for the "hands-on" period of JET maintenance and welding program development.

In order to fulfil the above requirements the following design principles were adopted.

- A number of special automatic welding tools were developed according to the predefined welding tasks (2).
- A standard welding source and auxiliary equipment were modified in order to drive all welding tools remotely. One welding source is used for in-vessel welding and an

identical one for ex-vessel welding.

- The general pattern transporter, end-effector, tool was followed. Thus as it is shown in Fig. 1, the welding tools will be handled by servomanipulators mounted on the two main remote handling transporters, the articulated boom for in-vessel maintenance and the TARM for ex-vessel maintenance. All welding tools are stored in a tool box which is part of the transporter within the servo-manipulator reach. Each welding tool has a short flying lead containing all necessary weld tool services (weld current, instrument control and monitoring signals, video signals, gas, water, etc). To use a welding tool it is retrieved from the tool box by the servomanipulator and plugged into a standard RH connector on the forehead of the manipulator. All required wires and service pipes are routed from this connector through the transporter structure to the appropriate welding source or auxiliary equipment which are situated at least 50 m away in a shielded area.
- All welding sources and their auxiliary equipment are integrated into the RMS so that control and monitoring of welding is done via any RHWS.

3. THE JET WELDING SYSTEM

The JWS consists of all automatic welding tools, two welding sources (WS) and their auxiliary equipment. These include, gas distribution system, chillers, hydraulic systems and TV viewing.

The welding source is a standard programmable TIG welding source which was modified in order to fulfil the JET remote welding requirements.

The main modifications were as follows:

- a serial link (RS232) and communication software was provided for interfacing to the RMS.

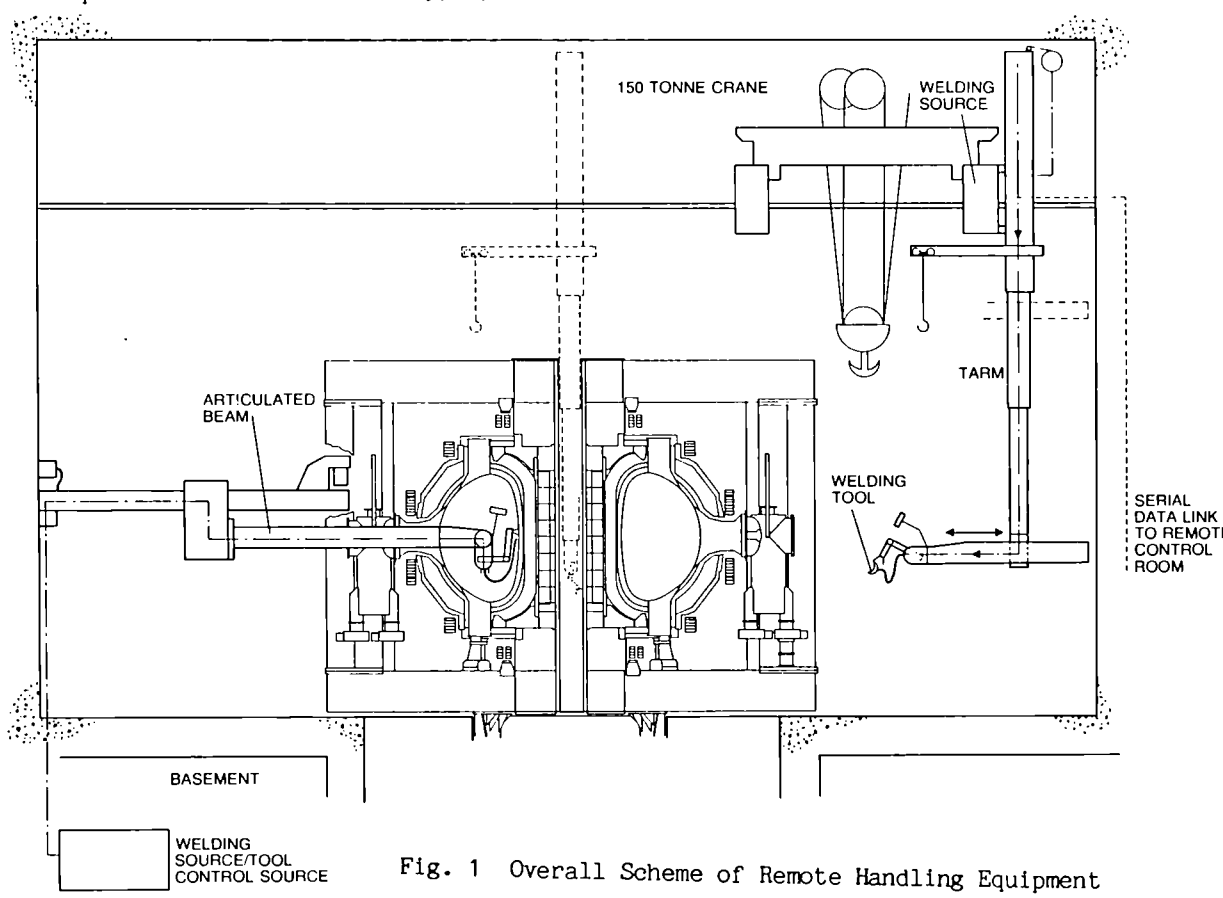

Fig. 1 Overall Scheme of Remote Handling Equipment

- remote control and monitoring of the auxiliary equipment was provided.
- software was developed in order to provide a user friendly Man-Machine Interface (MMI) on any RHWS.

The WS used was chosen because it provided reliable high frequency (50 KHz to 2 MHz) arc start over the long cable which exists between the WS and the welding tool.

3.1. Overview of welding source local operation

The welding source is a microcomputer-based (Intel 8085) welding source which is controlled locally via a standard control panel.

There are five operating modes as follows:

- STANDBY: this mode is entered on power-up.
- PROGRAMMING: this is the main operating mode which allows editing, transfer, loading and storing of welding programs.
- WELDING: during this mode execution of the required welding program occurs. In addition editing of the welding program could be achieved during the actual welding.
- WELDING SIMULATION: this mode is exactly the same as the welding mode, except that the welding current is switched off.
- MANUAL: during this mode, the electrode position and shielding gases could be controlled manually.

All auxiliary equipment (shielding gases etc) are controlled manually.

3.2. Welding source remote operation

For remote operation development work was done in two main areas:

- remote control of auxiliary equipment including TV viewing.
- integration into the RMS, including the development of a new MMI.

The welding source auxiliary equipment comprises, the gas distribution system for air and shielding gases, chiller, hydraulic system and TV viewing which is part of the Remote Handling CCTV system (1). Motorised control valves and transducers were fitted and interfaced into the RMS either directly through the welding source or indirectly through a CAMAC interface (Fig. 2). This is because some auxiliary equipment could be shared with the cutting tools. Thus the WS input/output ports were increased and new CAMAC interfaces were designed.

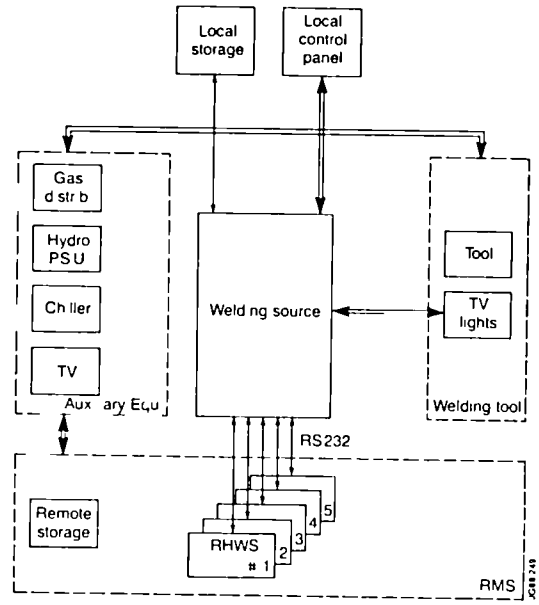

Fig. 2 The JET Welding System

Special attention was given in providing filtering for the new ports because of the strong electro-magnetic interference which is produced during H.F arc start. Also a robot deactivation output was provided for switching off all transporter actuators during the arc start period.

Because of the use of prototype welding tools and their remote requirements, some changes and additions in the welding source servoloops were necessary.

For example, the JET lip welding trolley, required a resolver feedback instead of the tacho feedback which is used by the other tools. Also it required the control of a clamp within the welding program for providing a spot welding sequence before the continuous weld.

In addition to hardware changes, software changes were made in order to accommodate the afore mentioned additional functions and also to provide safety interlocks.

The second main area of development work was the integration of the welding sources into the RMS (1). The RMS consists of the Remote Handling Control Room (RHCR) and its workstations (RHWS), the local controllers of the various RH equipment and the interconnecting local area networks.

It was required to integrate the two welding sources in such a way as to allow control and monitoring from any RHWS, including the additional TV cameras for weld pool viewing.

Graphical displays of all main welding parameters is used for welding process monitoring and control under remote operation instead of the direct weld pool viewing which is used in the local mode operation. However, TV feedback is also provided as a complementary aid.

Because the graphical displays are the main monitoring and, their real-time operation must be guaranteed. Thus 1 sec minimum display time update rate was specified. The same delay was specified for the response to operator inputs. This is because the operator can perform welding parameter adjustment while welding to optimise the welding quality.

The above response times were achieved by using a dedicated serial serial link (RS232) between the WS and the controlling RHWS. A unit selector allows for automatic switching of the serial links between RH workstations and the two WS. For less time critical functions the CAMAC serial highway and Ethernet LAN were used.

The CAMAC was used for controlling some auxiliary units and the Ethernet for the TV camera switching.

The serial links are implemented on optical fibre because of the long distances involved and to avoid the effects of electromagnetic interference which is produced by the WS.

Communication software was developed in order to receive/send commands and data from/to RHWS.

The last area of development in the JWS integration was the design of a new MMI. This MMI was based on the standard JET RHWS hardware (Fig. 3).

The RHWS (1) was designed at JET and is a general purpose workstation allowing the control of any RH equipment.

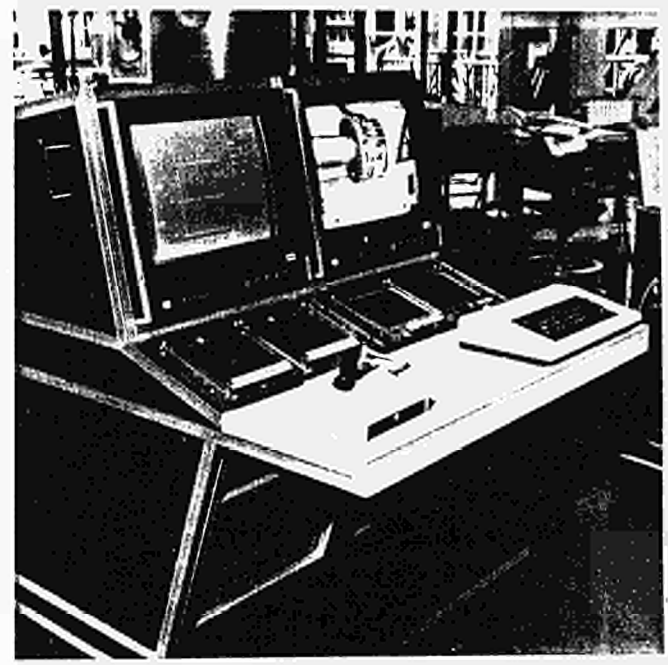

Fig. 3 Remote Handling Workstation (RHWS)

The RHWS is a software configurable workstation, and the software guides the operator through touch panel menus.

The new MMI was designed to fulfil the following requirements.

- The RHWS operation should, as much as possible, resemble the operation and functions of the standard welding source local control panel. Thus operator training will be minimised.
- The RHWS should provide additional remote functions as follows:
  - graphic displays of main weld parameters in real time (1 sec). These are the weld current, voltage, travel speed and wire

feed. Simultaneous display of programmed and measured values with automatic alarm initiation when value out of range during welding (Fig. 3).

- display of TV pictures of the weld pool and general welding environment.
- storage of weld programs in remote computer.
- user friendly operation with the use of touch panel menus and diagnostic messages.

Both in-vessel and ex-vessel welding sources are identical and are integrated into the RMS as described above resulting in a fully remote welding system for the JET machine.

4. WELDING SYSTEM PERFORMANCE EVALUATION

An extensive program of mock-up tests was performed to prove the reliable operation of the welding source under a variety of operating conditions.

For this purpose different welding tools were connected through the RH welding umbilical through which all the required tool services are routed, Fig. 4. The welding source was connected to the RHWS through a serial optical link.

Each function was tested successfully with all available tools.

It was demonstrated that the (1 sec) response time of the new MMI (Fig. 3) was adequate for the production of high quality TIG welds. It was possible also to create a remote library of welding programs which could be downloaded to WS for use.

The error messages were found useful for identification of any problem since this is particularly difficult under remote conditions.

Adjustment of welding parameters during welding was achieved successfully. However as an operating procedure this must be avoided, since in case of a wrong adjustment it might lead to situations from which it is difficult to recover under remote conditions.

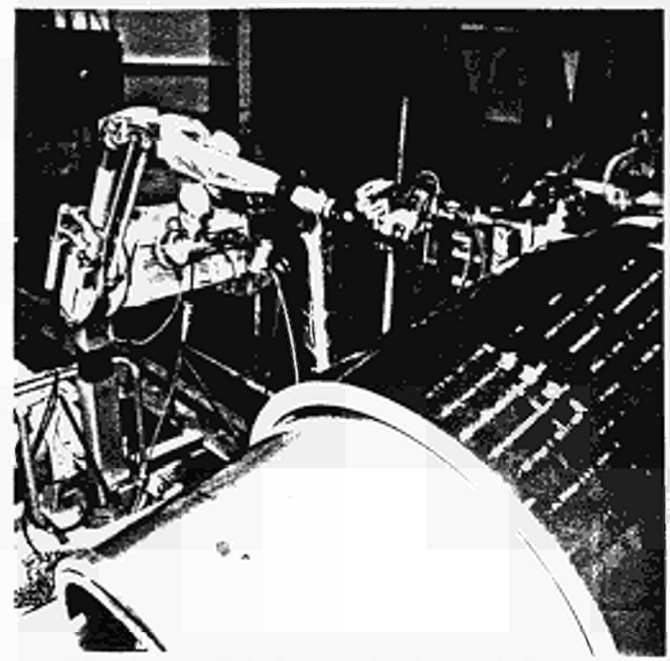

Fig. 4 Welding tool in position

6. CONCLUSIONS

In this paper the design and integration of the JET Remote Welding System (JWS) has been described.

A proven welding source was used as a basic building block. It was then modified for remote operation.

A series of prototype welding tools were designed and interfaced with the welding source. The welding source and its auxiliary equipment were integrated into the RMS thus allowing for remote welding inside and outside the JET machine.

The performance of the JWS has been tested through mock-up tests.

REFERENCES

1. A. Galetsas et al, "An Integrated Control System for Remote Handling Equipment at JET". Proc. IEEE 12th Symposium on Fusion Engineering, Oct 1987, California, USA.
2. S. Mills et al, "A Practical Experience of Using Special Remote Handling Tools on JET". Proc. IEEE 12th Symposium on Fusion Engineering, Oct 1987, California, USA.

32 MW ICRH PLANT OPERATION EXPERIENCE ON JET

G BOSIA, M SCHMID, J Farthing, S Knowlton, A Sibley, T Wade, E Negro

JET Joint Undertaking, Abingdon, Oxfordshire, OX14 3EA, England

The present status of the JET ICRF power plant, and some recent additions are described, with particular emphasis on new phase and frequency regulation systems. Aspects of the computer control are mentioned and some of the best results regarding RF generator output power are given.

1. INTRODUCTION

The JET ICRF system has been presented before [1] and [2]. The upgrade described in [2] has been completed on 6 ICRF units, which now have a nominal output power of 4 MW each. These units are equipped with 2 Thomson TH525 tetrodes, while the remaining 2 units, capable of 3 MW, are equipped with Eimac 8973 tubes. At present the nominal output power capability of the entire plant is therefore 30 MW, for 20 seconds pulses every 10 minutes, over a frequency range of 23 to 57 MHz (8 channels).

Each unit delivers its power to a single antenna through 2 outputs (see Figure 1), which are therefore strongly coupled to each other. Phasing between the 2 outputs for monopole or dipole mode on an antenna has been controlled by electronic means and a new phase regulation system enabling global phase control between antennas has been introduced (see para 5) for ICRF current drive experiments.

The increased complexity of the Plant operation has emphasised the requirement for a real time, automatic impedance matching system. Also, the automatic re-adjustment of the match conditions is often needed during the RF pulse, in order to follow antenna impedance variations caused by RF heating.

The problem of controlling and matching 8 generators has been tackled with automatic hardware controls and with database oriented control software.

2. REMOTE PLANT CONTROL AND COMPUTER ASSISTED MATCHING

The following elements directly influence matching of each generator to its antenna:

- Frequency Channel and Frequency
- Phase (up/down/global) and Power Balance
- Stubtuner (up/down)
- Trombone Phase Shifter (up/down)
- Prematching Stub (up/down), if fitted

Each frequency change involves adjusting these 12 parameters for every generator. In additon, changing the frequency channel automatically adjusts 24 generator internal tuning elements.

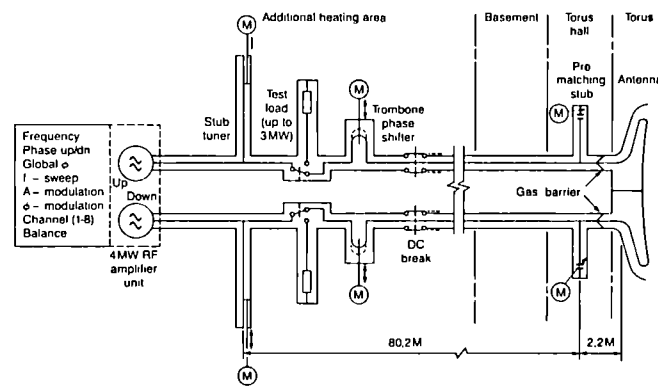

FIGURE 1
ICRF Unit and Matching Elements

The ICRF plant operation into a plasma is always controlled remotely, via CODAS (JET Control and Data Acquisition System), from the Central Machine Control Room, where one Terminal and 2 Graphic Consoles (for mimic dia-

grams) equipped with Touch Panel Controls are dedicated to ICRF heating.

Two RF operators control the plant. The interaction between them, the plant and some software modules is indicated in Figure 2.

Each ICRF Unit can be selected for LOCAL or REMOTE operation (handshake required), IN or OUT of PLANT operation and IN or OUT of GAP (General Acquisition Program). The JET Pulse Control Program will only interact with units which are selected "IN GAP", and ignore the others, even if they are in REMOTE.

The operator can direct commands to be sent to individual units only or to all units which are selected for "PLANT".

3. SOFTWARE TOOLS

Increasingly powerful software was developed, in order to cope with the operational need of the JET experiment to change quickly from one frequency to another. Refer to Figure 2 for the following definitions of software modules.

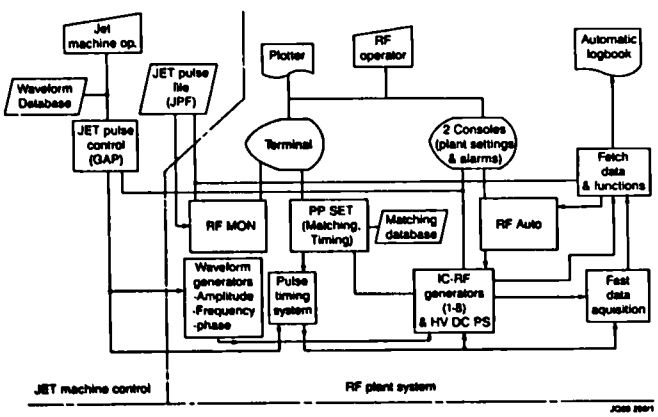

FIGURE 2
ICRF Plant Remote and Semiautomatic Operation

PPSET (Level 1 Pulse Schedule Editor), can perform the following functions, for individual generators or for the entire PLANT:

- store the present ICRF unit matching element settings in the MATCHING DATABASE, under a given pulse-name
- download settings from the MATCHING DATABASE to the ICRF unit matching elements
- re-adjust the ICRF unit timing system with reference to the JET pulse timing, automatically also adjusting the FAST DATA ACQUISITION timing (length and sampling rate) to the power waveform selected.
- edit the MATCHING DATABASE

The matching database contains the data for various plasma conditions and heating scenarios. It also contains some 48 vacuum matches, which were obtained in local, short pulse operation and which are used as starting values for plasma operation on previously unexplored frequencies.

RFMON is the program which permits the RF operator to manually match the antennas to the generators, by analysing raw data and functions of the raw data (ie coupled power, reflection coefficient etc) from the JET Pulse File (JPF). Functions are calculated by a program module called FETCH and some important ones are automatically logged and printed.

RF AUTO is a program module which performs automatic matching; it calculates, from a previous pulse with a frequency sweep, the optimum matching frequency, trombone and stub settings. Consistency checks are made which abort any automatic action on a particular RF unit if the results are inconclusive, and operator intervention is asked for. The program is being tested at present and it is hoped that it will free the operator from routine matching changes and enable him to concentrate on difficult cases, where computer interpretation of the data fails.

3.1. RF pulsing under JET control

The JET machine operator initiates a JET pulse. The waveforms, selected from a database, are downloaded to the RF generators by GAP (General Acquisition Program), as are

the various timer settings. Later on during the JET pulse, a sequence of timing signals triggers various sequence controls, waveform generators and data acquisition modules. The RF data are stored locally and collected after the pulse by FETCH, which archives them in the JET Pulse File (JPF).

All the alarm signals are monitored and can be displayed at the console in real time.

4. AUTOMATIC VSWR CONTROL

The matching technique used in JET is described in [3]. Automatic VSWR control devices [4] have been operated on the Plant in the past.

A conceptually new system has been implemented and operated in 1988, with good performances, in a wide range of operating conditions. The principle of operation of the device is described in [5], and the relevant results are summarised here.

Use is made of the properties of the vectorial quantity:

$$\bar{\sigma} = \frac{\bar{b}_1}{\bar{b}_2} \qquad (1)$$

where $\bar{b}1$ and $\bar{b}2$ are the 2 waves reflected at the stub junction (Figure 3). The modulus and phase of both waves can be measured by means of directional couplers located at each side of the stub base.

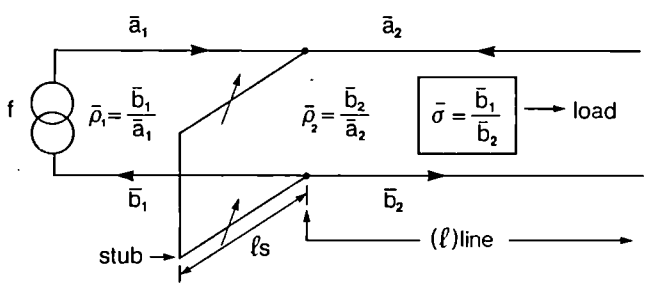

FIGURE 3
Symbol Definitions

It can be shown that:

$$\bar{\sigma} = \frac{\rho}{\cos\theta} \cdot \left\{ e^{j(\phi+\theta)} + j\left(\frac{\sin}{\rho}\right)\theta \right\} \qquad (2)$$

where ρ is the modulus of the load reflection coefficient; $\phi = \phi_1 - 2\beta l$ is the phase of the reflection measured at the stub junction:

$$\theta = tg^{-1}\ (\tfrac{1}{2}\ tg\ \beta l_s) \approx \pi/2 - 2\beta l_s;$$

$\beta = (2\pi f/c)$ and l_s and l are the stub length and line length (Figure 3) respectively. The (measured) real and imaginary parts of $\bar{\sigma}$ are plotted in Figure 4 (curves a and b) together with the modulus of the reflection coefficient at the generator output (curve c).

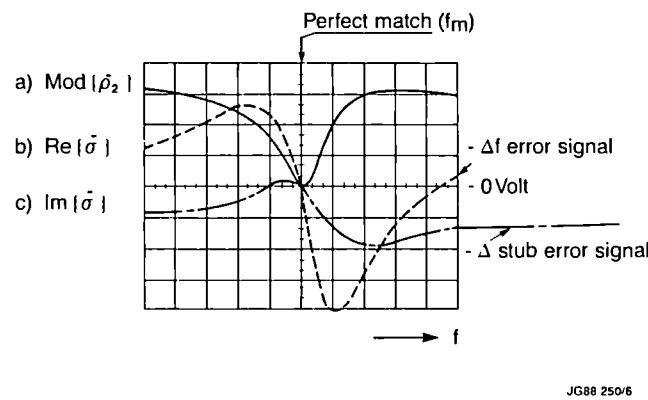

FIGURE 4
Error Signals for Matching Control

The perfect match conditions are of course $Re\{\bar{\sigma}\} = 0$ and $Im\{\bar{\sigma}\} = 0$. The perfect match can be reached from any initial condition, by imposing first:

$$Re\{\bar{\sigma}\} = \left(\frac{\rho}{\cos\theta}\right) \cos(\phi + \theta) = 0 \qquad (3)$$

by means of a feedback loop acting on the operating frequency (or ϕ). ϕ varies rapidly with f, since the stub is placed far from the antenna.

The quantity $Re\{\bar{\sigma}\}$ constitutes an ideal feedback signal, as it symmetrically crosses zero at the frequency of minimum reflection

(Figure 4) for any stub length.

When (3) is true, the perfect match condition reduces to:

$$\rho - \sin\theta = 0 \qquad (4)$$

which can be fulfilled by an automatic loop acting on the stub length (or θ). Only the frequency loop is operated in real time, as the stubs can be moved only at a relatively low speed (5 mm/s).

Figure 5 shows how the servo can reduce the load VSWR from S > 10 to S < 1.5, in 2 consecutive plasma shots and otherwise identical conditions.

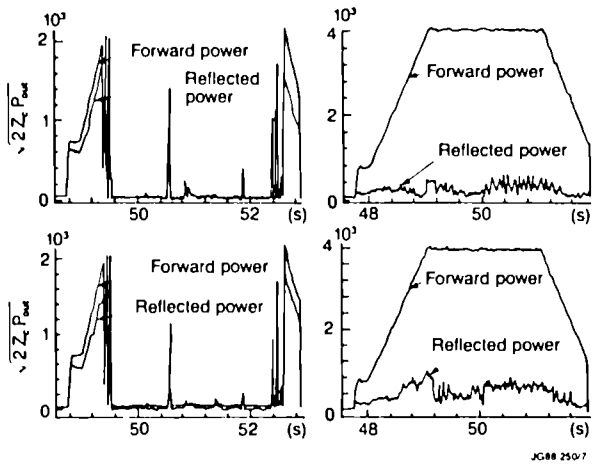

FIGURE 5
Reduction of VSWR by Automatic Control

In Figure 5a (automatic matching off), the generators are prevented from reaching full power by a protective power trip, due to excessive reflected power. In Figure 5b (automatic matching on), the reflected power is reduced and kept low throughout the pulse, despite strong coupling between the 2 antenna halves.

5. INTEGRATED PHASE CONTROL SYSTEM

The ICRH Plant Phase Control System has been re-designed to provide independent phase regulation to each of the 16 RF-plant outputs.

The adopted control technique [6] is shown in Figure 6. It employs coherent frequency translation to produce, from the input RF reference (fc) and with the help of a Phase-Lock-Loop, locked to an IF Phase Reference (fi), an output frequency ($f_{out} = f_c \pm f_i$) which can be phase modulated.

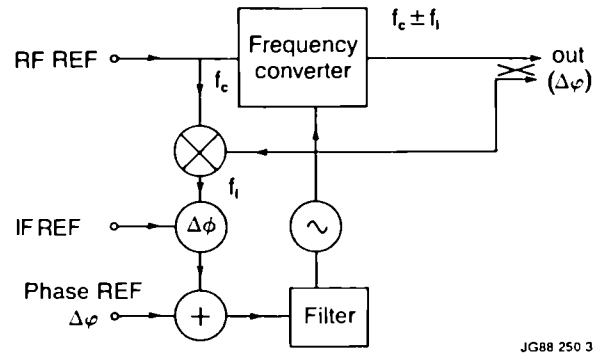

FIGURE 6
Block diagram of one 360° phase shift cell

The phase control cell shown in Figure 6 allows a compact construction. It features a very wide phase dynamic range, (> 360°) and a phase control accuracy independent of the operating RF frequency, since the phase control is performed at the IF frequency (fi = 125 kHz). Precision, linear phase detection is used by means of digital techniques.

In a JET RF unit, 2 complementary frequency translations are performed by locking 2 cells to the same RF and IF references and by connecting them in series, as shown in Figure 7. The output frequency is then the same as the one of the phase reference.

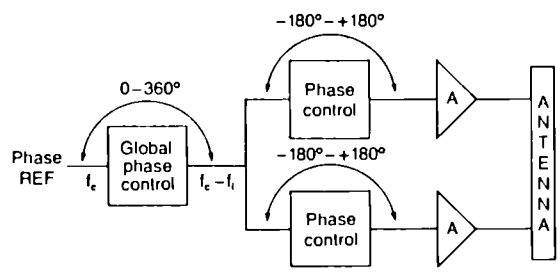

FIGURE 7
Layout of phase control on one RF unit

The system in Figure 7 allows independent phasing of each antenna (2 transmitters) as well as independent phasing of each antenna element. All phases can be unambiguously adjusted over 360 degree with an accuracy of better than 1 %.

Some current drive scenarios require a differential phase modulation between antennae. In Figure 8, the response of one of the loops to a 360° step modulation is shown. The settling time (to 5 %) is 250 μs.

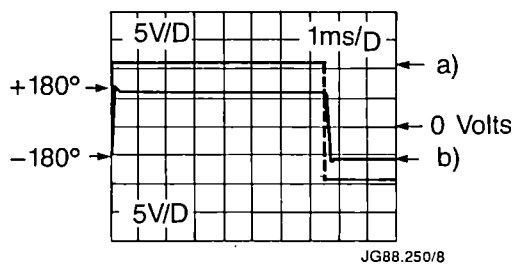

FIGURE 8
Dynamic response of a phase control cell (curve b) to a 360° step excitation (curve a)

When the RF power is turned off, each control cell switches automatically to an auxiliary Phase-Lock-Loop, which memorises the output phase before the transition and maintains it until the power is re-applied. This prevents losses of lock and/or long acquisition times when the RF power is rapidly on-off modulated, for example by protective actions.

6. BEST RESULTS ACHIEVED ON PLASMA AND TESTLOAD

The maximum voltage on transmission lines and antennas which is routinely achieved is approximately 32 kV. With water cooled antenna-screens 20 second pulses at 6 MW total coupled power have been performed.

The highest power coupled to a plasma so far is 17 MW (2 second flat-top), which corresponds to 18.8 MW total generator power (pulse 13544, with uncooled antenna-screens). The power is usually limited by the reflected power (load fluctuations), the line voltage or some not yet fully understood problems in the stability of the various feedback loops of the generators.

On testload (ie stable load conditions) the full nominal capability of the system can be achieved fairly easily and pulses in excess of 28 MW have been performed with pulse lengths up to 20 seconds.

ACKNOWLEDGEMENTS

The authors wish to thank Miss V Shaw (Typing) and the people from the Culham/JET Joint Public Relation Section (Diagrams) for their assistance in preparing this paper.

REFERENCES

1. T.J. Wade, 13th Symposium on Fusion Technology, (Varese, 1984) pp. 727-732.

2. R. Anderson, J. Plancoulaine, M. Schmid, 14th Symposium on Fusion Technology, (Avignon, 1986) pp. 339-345.

3. J. Jacquinot, JDN/J/84.5.

4. G. Bosia et al, Proc. of IV 4th Int. Symp. on Heating in Tor Plasma, I, 445 (1984).

5. G. Bosia, JDN in preparation.

6. G. Bosia, JDN/J/86.X.

EXHAUST DETRITIATION SYSTEM FOR JET

A H DOMBRA, M E P WYKES, J L HEMMERICH, R HAANGE, A C BELL

JET Joint Undertaking, Abingdon, Oxfordshire, OX14 3EA, England

If the torus or other tritium containment is breached for maintenance or accidentally, the Exhaust Detritiation System (EDS) prevents the escape of tritium to the Torus Hall, and elsewhere, by maintaining the breached system at slightly sub-atmospheric pressure. The exhaust gas from the breached system is detritiated and discharged through the stack. The system includes catalytic recombiners for the oxidation of tritiated compounds, and molecular sieve driers for the recovery of water vapour. Provision for internal recirculation of the gas allows a fast start-up of torus detritiation operations (within two minutes) and processing of feed gas at a variable rate. An isotopic swamping technique is used, as required, to displace HTO from molecular sieve during the drier regeneration cycle. All major operations are controlled by a programmable control system.

1. INTRODUCTION

The EDS concept of preventing the escape of tritium from the primary containment presents several advantages over the conventional air detritiation method: the volume of JET Torus Hall is 28000m³, for which the detritiation system would be ten times larger, increasing the water collection rate. In addition, the Torus Hall would be contaminated with tritium.

The EDS concept, however, must meet high reliability and fast start-up requirements: the probability of sequence failure for the maximum credible release of tritium from a breached torus (Table 1) is designed to be less than 10^{-4}. The minimum EDS detritiation factor is 1000, and normally 5000.

Commissioning of the EDS is scheduled to start by mid 1990. The selected EDS supplier is Neue Technologien GmbH (NTG) in Gelnhausen, Germany.

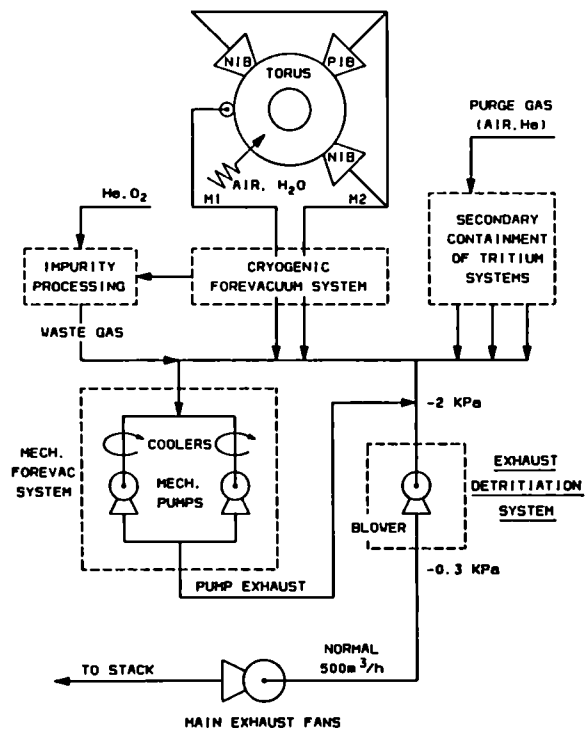

FIGURE 1
Main Exhaust Detritiation Routes

2. EXHAUST DETRITIATION ROUTES

As shown in Figure 1, the EDS provides a suction pressure of 2kPa to draw an exhaust flow, up to 500m³/h, from the torus and other tritium systems[1]. At a lower gas-source pressure, the exhaust may be delivered to the EDS by the Mechanical Forevacuum System.

2.1 Maintenance torus exhaust detritiation

During the torus maintenance periods, the EDS will maintain an air velocity of approximately 1m/s in the maintenance openings to prevent the escape of tritium and radioactive particulate. The concentration of tritium in the torus exhaust is estimated to average 1 GBq/m³, and

higher if maintenance is forced without a prior glow discharge cleaning.

3. AN ANALYSIS OF TORUS VACUUM BREACH

Estimates for the worst-case air inleakage incident[2], summarised in Table 1, postulate that the following are credible events:

1) instantaneous shattering of a 100 mm - diameter vacuum window assembly, causing a choked-flow influx of air until torus and ambient pressures equalize.
2) rapid defrosting of cryopanels connected to the torus at full tritium load; the air cooling effect of the panels is neglected.

A fraction of air in the torus effluxes through the breach as it starts to expand due to heating by the First Wall.

TABLE 1
Estimates for worst-case torus air inleakage

First Wall Conditions	
Temperature	constant 573K
Heat transfer area	220m²
Heat transfer coefficient	5Wm⁻²K⁻¹
Conditions at End of Air Influx	
Air influx time	125s
Air temperature	495K
Mass of air in torus	197kg
Fraction of hydrogen in air	1.5%
Airborne tritium in torus	30gT
Fraction of tritium in methane	4%
Conditions During Air Efflux	
Maximum efflux rate	487m³/h (STP)
Fraction of air expelled	13.6%
Quantity of tritium expelled	4.1gT

Analysis of the postulated events[2] is based on closed solutions of the differential equations representing the First Law of Thermodynamics applied to ingress of air into an idealized evacuated chamber. The thermodynamic processes associated with the ingress of air are illustrated in Fig. 2 for the limiting case of no heat transfer from the First Wall:
Step 1-2, represents an isentropic expansion from ambient to choked flow conditions,
Step 2-3, subsequent free expansion to vessel pressure, and
Step 3-4, compression to the final atmospheric pressure by subsequent influx of air.

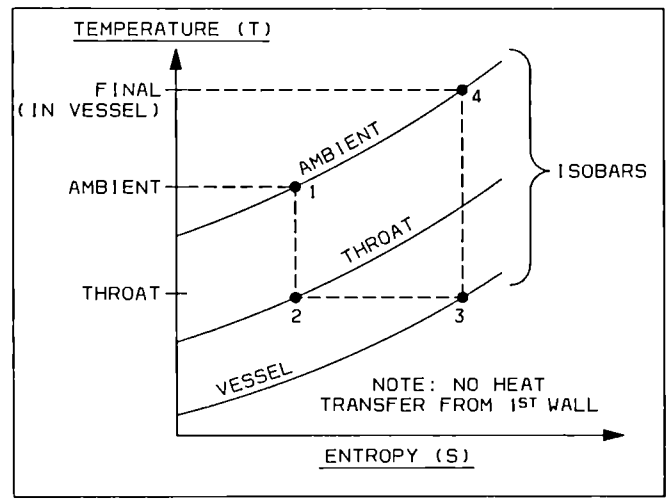

FIGURE 2
Temperature/Entropy diagram for ingress of air into an evacuated vessel

The analysis shows that the lowest air temperature at the end of the influx period (with no heat transfer from the First Wall) is given by the product of ambient air temperature and the isentropic index ($\gamma = 1.4$). The heat transfer from the First Wall increases air temperature above this value.

Table 1 sets two major EDS parameters:
Start up time of operation = 2min
EDS air flow = 500m³/h.

4. RECOMBINER UNIT

As shown in Fig. 3, the gas entering the EDS flows through the following components of the recombiner unit before it enters the driers:

1) a chilled water cooler for control of maximum humidity: this cooler reduces the gas temperature to 6°C and condenses excess moisture.
2) a plate-fin heat exchanger which increases

the gas temperature to 450°C, in two steps.

3) an in-line heater to increase the temperature to the final 500°C. Normal power consumption is 10kW, maximum 45kW.
4) the first recombiner for the oxidation of hydrogen at 150°C to prevent ignition and permeation of tritium at subsequent gas temperature of 500°C.
5) the second recombiner to oxidize methane and the remaining traces of hydrogen at 500°C.
6) a humidifier/cooler for control of minimum humidity: this unit increases gas humidity to a dew point of -21°C to maintain the detritiation factor above 1000 if the inlet gas is very dry.

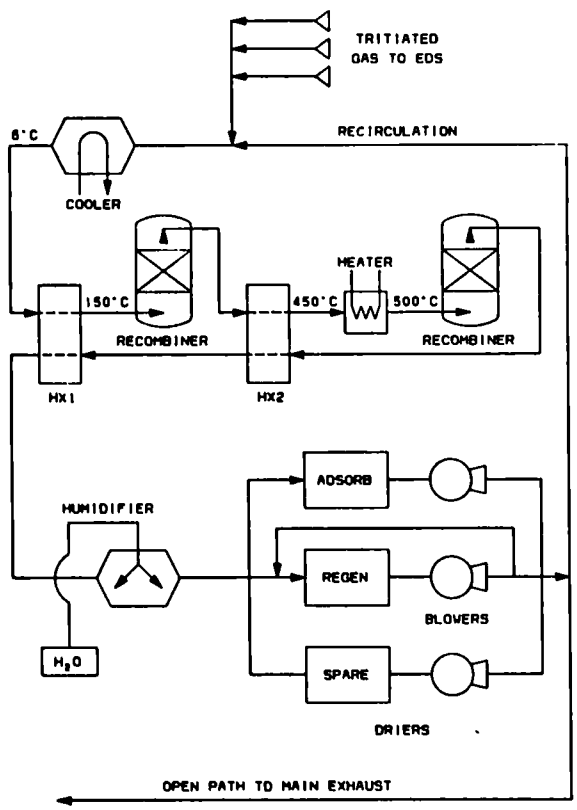

FIGURE 3
Main components of EDS recombiner unit

4.1 Gas recirculation feature

The flow through the recombiner and one of the drier units is always nearly constant 500m³/h, facilitating temperature control. As gas feeds from various sources are generally small, most of the drier flow is recirculated internally. The drier inlet dew point is -21°C, controlled by the humidifier, and the adsorption cycle time is 16 hours. This long cycle meets the two-fold requirements of maintaining the system in a ready-to-start state for torus operations, and processing waste gas from various sources. In addition, the detritiation factor for the feed gas is increased by the ratio of recirculation to feed gas rates.

TABLE 2
Main recombiner parameters

	Unit 1	Unit 2
Operating temperature	150°C	500°C
Catalyst	Pt-Pd/AlO_2	Pd/AlO_2
Catalyst bed - volume	80L	120L
- depth	0.2m	0.2m
- diameter	0.7m	0.87m
Normal pressure drop	200Pa	550Pa
Sp. heat capacity	400kJ/°C	600kJ/°C
Oxidation factor	Approximately 10^6 for hydrogen, 5000 for methane	

5. MOLECULAR SIEVE DRIERS

Figure 4 is a simplified diagram of the drier system. All three drier columns are identical. As each column operates independently, one column is on standby for reliability, instead of duplicating blowers or heaters which increases complexity[3].

5.1 Operating features

1) A change of the operating state is initiated by opening and closing interlocked valves. To rotate a drier column from adsorption to regeneration, the heater circuit valve is opened and the two outer isolation valves are closed, as shown in Figure 4. The closure of heater contacts starts the heating cycle, and lifting of the contacts starts the cooling cycle. The blower is running continuously during all operations.
2) to eliminate flow control valves, the EDS flow rates are preset with appropriate flow

orifices in the main recirculation, drier heater and blower recirculation lines. The selected blower is essentially a constant volume unit when operated at constant speed.

3) The building exhaust fans maintain a subatmospheric pressure of 0.3kPa at the EDS outlet to prevent the escape of tritium to the containment building.

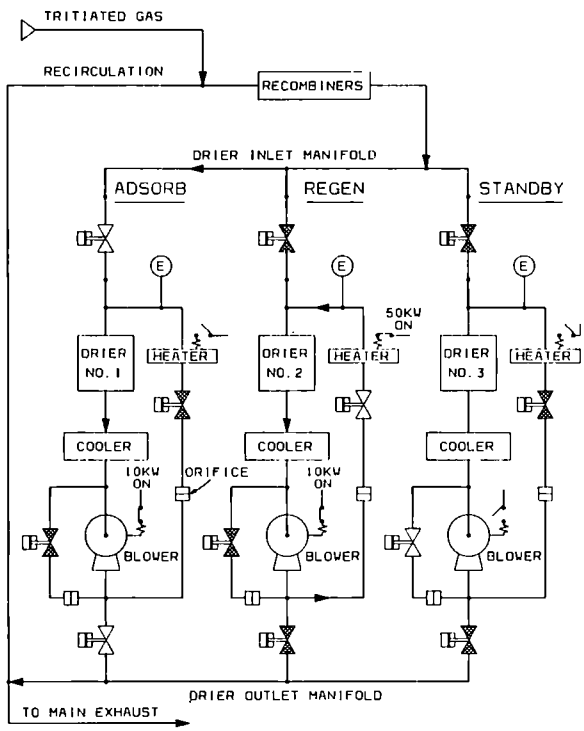

FIGURE 4
Molecular sieve drier system

TABLE 3
Main drier parameters

Weight of molecular sieve type 5A = 350kg
Bed height = 1.2m, diameter = 0.8m
Superficial adsorption velocity = 0.3m/s
Humidity reduction factor:
at inlet dew point 6°C = 8000
at inlet dew point -21°C = 1000

6. PROCESS CONTROL

All major EDS operations will be controlled by Siemens S5-135U Programmable Logic Controller (PLC). This PLC will interface with a central system for coordination of all tritium reprocessing operations, and to an existing higher level computer system (JET CODAS). Some supporting operations will be performed manually via the PLC operators console, or locally. Interlocks and trips provide mainly an independent protection against overheating or overpressure, and will be hardwired.

6.1 Auto rotation of drier columns

This is a high priority requirement for long-term operations: it assists to regenerate driers consistantly at programmed conditions, increase the adsorption capacity, and reduce operator errors.

The desired parameter for the termination of the adsorption cycle is water loading on the bed to about 80% of breakthrough capacity. This control parameter, however, depends on reliable dew point measurements which tend to present difficulties at field conditions. For this reason, the flow chart in Figure 5 calls for operator decision for the termination of the cycle before breakthrough, following review of other pertinent data.

Detection of breakthrough by the rate of change of outlet humidity[3] initiates an automatic termination of the cycle as shown in Figure 5. The controlling parameter for the termination of heating and cooling cycles is drier outlet temperature.

7. ISOTOPIC SWAMPING FEATURE

The current designs for air detritiation generally replace molecular sieve with a fresh charge following exposure to a high concentration of tritium. This method would present difficulties at JET as the EDS processes feed from various sources at different concentrations, and would require a frequent bed replacement.

The selected method for the EDS uses an isotopic swamping technique to displace HTO from

molecular sieve with H_2O vapour. This technique was successfully demonstrated on industrial scale[4] and showed good agreement with the proposed model[3] for displacement of tritium by the isotopic exchange process. Estimates for the EDS based on this model show optimum conditions for the addition of water vapour to the regeneration line (point E in Figure 4) at a rate of 33kg/h, following regeneration of the bed to 290°C. The addition of 80kg of water vapour for 2.5 hours is estimated to reduce the concentration of tritium in the residual water by a factor of 170.

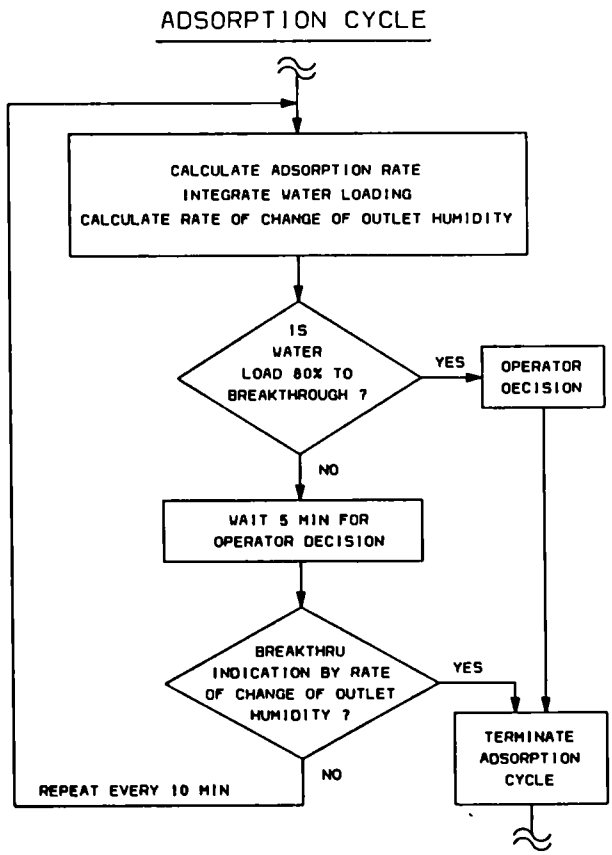

FIGURE 5
Simplified sequence for termination of drier adsorption cycle.

If required, the addition of water vapour will be repeated at the end of the cooling cycle to form a tritium-free saturated section at the drier inlet, which is estimated to increase the detritiation factor during the adsorption cycle by a factor of 40.

8. FUTURE PROSPECTS

Potential advantages of the EDS design concept, if experience is satisfactory, are as follows:

Concept	Potential Advantages
1. EDS versus building air detritiation	- prevent tritium escape and contamination of building.
2. Multi-feed gas processing	- single system.
3. Two recombiners in series	- permeation and ignition control.
4. Presetting of flow rates	- eliminate flow controllers.
5. Hot recirculation	- fast start up.
6. Subatmospheric EDS pressure	- leakage control.
7. Detritiation of MS with H_2O vapour	- eliminate disposal of contaminated MS.
8. In situ isotopic swamping as required	- higher detritiation factor.

REFERENCES

1. J.L. Hemmerich, et al, The JET Active Gas Handling System - Progress Report, this Symposium.

2. M.E.P. Wykes, Safety Analysis of Torus Vacuum Breach, JET-P(88)37, 1988.

3. A.H. Dombra, W.E. Bishop and N.E. Howden, Air Detritiation Systems for Fusion Facilities Based on CANDU Developments, Proceedings 14th SOFT, 1511, 1986.

4. A.E. Everett, A.H. Dombra and R.E. Johnson, Isotopic Exchange in Air Detritiation Dryers, Proceedings Tritium Technology in Fission, Fusion and Isotopic Applications, Toronto, May 1-6, 1988.

DESIGN OF JET LOWER HYBRID CURRENT DRIVE GENERATOR AND OPERATION OF HIGH POWER TEST BED

J A Dobbing, G Bosia, M Brandon, M Gammelin, C Gormezano, J Jacquinot, G Jessop, M Lennholm, M Pain, A Sibley, T Wade

JET Joint Undertaking, Abingdon, Oxfordshire, OX14 3EA, England

The JET Lower Hybrid Current Drive (LHCD) generator consists of 24 klystrons each rated for 650 KW operating at 3.7 GHz, giving a nominal generator power of 15.6 MW for 10 seconds or 12 MW for 20 seconds. This power will be transmitted through 24 waveguides to a phased array launcher on one of the main ports of the JET machine.

In addition, two klystrons are currently being operated on a high power test bed to establish reliable operation of the generators components and test high power microwave components prior to their installation.

1. INTRODUCTION

The JET klystron generator will feed a phased array of 384 waveguides[1] with 10 - 12 MW at 3.7 GHz. This frequency is close to the Lower Hybrid resonant frequency of the plasma. The power will be phased in such a way as to drive 1 - 2.5 MA of current in the plasma. This non-inductively driven current is expected to broaden the plasma current profile and improve the energy confinement of the JET machine.

2. SYSTEM DESIGN

The 24 klystrons which make up the generator are split into modules. Each module consists of 4 klystrons which are fed from a common High Voltage Power Supply (HVPS) and cooled by a common demineralised water system which transfers the heat to the JET site water network. Each module has its own protection and control system which allows the klystrons to be operated locally; independently of the JET machine. In this mode the klystrons are connected to test loads via waveguide switches.

The major components of a klystron module are shown in Figure 1. The HVPS is situated out-of-doors approximately 200 m from the klystrons. The rectified high voltage is transmitted on a co-axial cable terminated in a RC matching network and ignitron protection crowbar.

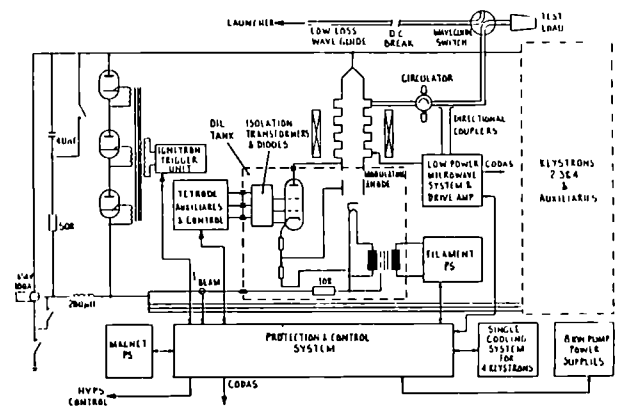

FIGURE 1

Module of 4 Klystrons Feed from Common HVPS

The four klystrons are mounted in oil tanks which also house fault limiting resistors, filament isolation transformers and tetrodes to regulate the modulating anode voltages. These tetrodes are operated through high frequency isolation transformers; the outputs of which are rectified. This allows all the control electronics to be outside the oil tank and at ground potential. Each klystron also has individual filament, magnet and ion pump power supplies to operate it, as well as an RF drive

amplifier and low power microwave system to provide amplitude and phase control of the RF. Each klystron is protected against reflected power by a high power circulator which is situated between the klystron and a waveguide switch. This switch can be turned to a test load or to deliver power to the launcher on the JET machine.

Demineralised cooling water is provided to cool each part of the klystron, test load, waveguide switch, circulator and parts of the waveguide. One cooling system is provided for each module.

A protection and control system co-ordinates all these various elements and provides the interface to the JET machine control system, CODAS, as shown in Figure 2.

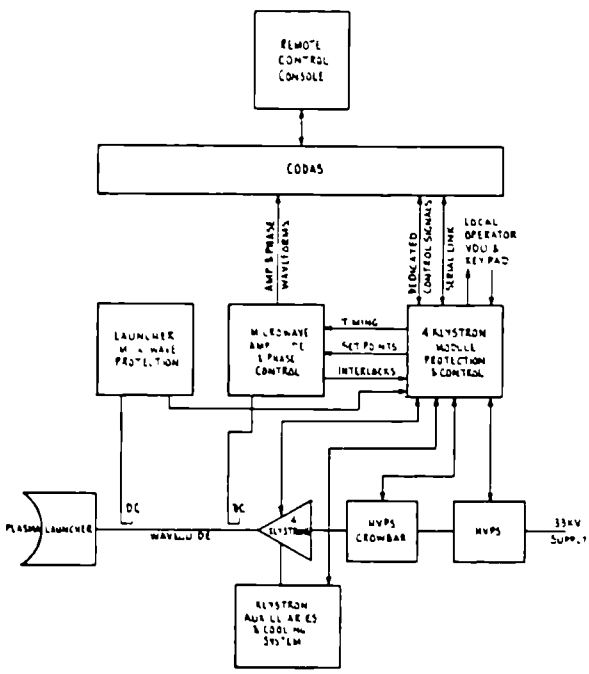

FIGURE 2

JET LHCD Control and Monitoring

Figure 3 shows the timing diagram for a pulse. The HVPS is first ramped to -65 kV over 0.5 seconds. The electron beam current is then established by ramping up the modulating anode voltage in 100 ms.

The continuous power rating of the collector is limited to 1.2 MW while the electron beam power associated with 650 kW is 1.6 MW. The beam current is therefore limited to 18A when no RF is being produced. RF output is established in two stages. First an initial low power level during which the electron beam is brought to full power, the RF phase is locked and checks are made on the reflected power and RF amplitude control loop. Then the output is allowed to rise expodentially to its final set value. This can be a pre-progammed time dependent waveform.

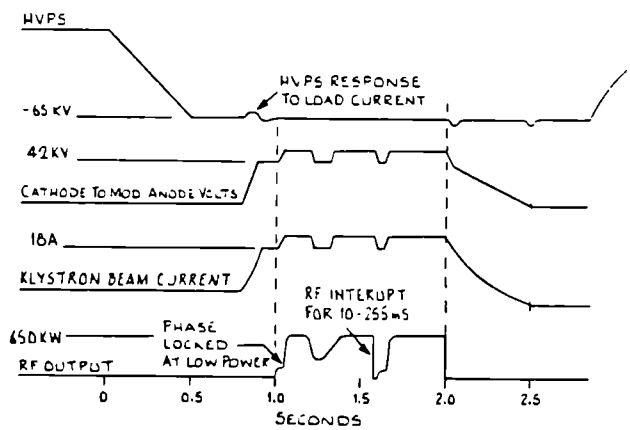

FIGURE 3

Timing Diagram for Klystron Power Supplies

During the pulse a limiting circuit can operate to control the power reflected by the launcher. This circuit will reduce the output power of the klystron to maintain 56 kW reflected power which is the maximum allowed by the circulator. When the collector power exceeds 1.2 MW the collector power limit circuit is activated to reduce the electron beam current to 18A. The position of the launcher is controlled dynamically so that it can be adjusted to improve its matching to the plasma and hence

reduce the reflected power. When this happens the limiting circuits allow the RF and beam power to return to their set values.

Additional protection circuits will detect arcs in the launcher vacuum. When these are activated the RF drive is interrupted for a pre-programmed time of 10 - 255 ms. The RF is then re-applied as before. Up to 255 trip and re-application sequences are allowed in one pulse. During the time that RF is removed the beam current is also reduced.

At the end of the pulse the beam current is rapidly reduced to 18A and then ramped down slowly over 500 ms to minimise sudden transients on the HVPS and also the 33 kV a.c. distribution network.

3. SYSTEM COMPONENTS

3.1. The Klystron

The klystron is TH2103A provided by Thomson-CSF (France). It was originally rated at 500 kW/20 s. However, after extensive testing of seven tubes, the power rating was increased to 650 kW/10 s: the limiting factor being interception of the electron beam at the lips of the output cavity. This additional power rating is also at the expense of a reduced operating VSWR which necessitates the use of a circulator to protect the klystron. As already mentioned, the collector is also unable to withstand the full electron beam at the higher power level requiring additional protection and control circuits.

Other performance parameters are:-

Operating frequency	3.7 GHz
1 dB bandwidth	±3 MHz
Efficiency	40%
Gain	50 dB

3.2. High Voltage Power Supply

The High Voltage Power Supply is voltage stabilised by a.c. thyristor controllers and feeds four klystrons. This gives a power rating of 8 MVA which is close to the limit of what can be achieved using currently available thyristors without resorting to parallel thyristor bridges. The main parameters are:-

Maximum d.c. voltage -65 kV

Maximum current 100A (25A per klystron)

Voltage stability ±1% (±3% at turn on transient)

3.3. HVPS Crowbar[2]

The HVPS crowbar is formed by three ignitrons in series. The anodes of the ignitrons are heated by lamps while the cathodes are maintained at 15°C by a temperature controlled water circuit. The crowbar and its trigger circuit is designed to limit the energy in a spark in the klystron to 30 J.

The main parameters of the crowbar are:-

Voltage withstand test	85 kV
Peak current	3000A
Turn on time	13 μs

3.4. Modulating Anode

The modulating anode voltage of the klystron is controlled by a tetrode. This is operated through high frequency transformers (20 kHz). The tetrode, load resistors and isolation transformers are situated in the same oil tank as the klystrons. This gives a compact design, with no exposed high voltage and the electronics at ground potential.

3.5. Magnet Power Supply

The klystron magnet is made up of three separate sets of coils. These are energised at up to 35A, 70 V by three switch mode transistor regulators operating at 20 kHz. The regulators for two magnets are fed from a common d.c. supply. The magnet currents are tuned for each klystron during factory tests. After this it is not necessary to change them during operation even if the output power level is altered.

3.6. Filament Power Supply

The klystron filament is fed at 9 V a.c. via an isolation transformer. This is fed by a single phase current controlled thyristor regu-

lator'. The current is ramped up and down at 60 seconds to avoid shock heating of the filament.

3.7. Cooling System

Each module of four klystrons has a common demineralised cooling system. This has a high flow, low pressure circuit to cool the collector, test loads, waveguide switches and waveguide around the klystrons and a low flow, high pressure circuit to cool the klystron windows, magnet and klystron cavities. Each cooling system has a 3000 litre surge tank to store the heat produced during the pulse and reduce the flow required in the site water network. The total flow in each demineralised water circuit is 3000 litre min.

3.8. High Power Microwave Components

The following high power microwave components are associated with the klystron generator:-

1) Standard WG 284 water cooled copper waveguide
2) Four port circulator
   - input VSWR 1.1
   - continuous reflected power 56 kW
   - insertion loss 0.15 dB
   - transmitted power 650 kW
3) Waveguide switch
   - insertion loss 0.0025 dB
   - VSWR 1.05
   - isolation 80 dB
4) Water cooled Test load
   - power rating 650 kW
   - VSWR 1.1
5) D.C. Break used to provide d.c. isolation between klystrons and JET machine: isolation voltage 2 kV.
6) Low loss optimised 35 metre waveguides for power transmission to JET machine. These waveguides are 77.20 x 38.60 mm in cross section which is 5 % below the dimensions at which alternative modes could propagate. The total loss allowed in the waveguides is 0.50 dB which are filled with 1 bar (gauge) SF6 to improve voltage hold off capability. Particular attention has been paid to the design of flanges and their gaskets in order to minimise losses and the risk of breakdown.

3.9. Low Power Microwave System

The low power microwave system provides amplitude and phase control of the klystron output. A phase reference is distributed to each module from a central control rack. This is then used to control the phase at the klystron output. The changes in the length of the waveguide and launcher are measured by shifting the operating frequency of each klystron in turn for 10 ms every 500 ms. This shifted frequency is detected on adjacent waveguides due to cross coupling at the launcher mouth and can be used to calculate changes in relative length of the different transmission paths.

3.10. Klystron Protection and Control

Local control of each module is provided by a protection and control system. This can be divided into two parts; a programmable logic controller (PLC) which handles slow interlocks and interfaces to CODAS and the local operator, and a fast interlock system in the form of a state machine.

The state machine states and transitions are shown in Figure 4. The initial state is known as "warm up" when the klystron filaments are turned on, water pump started and circuit breakers closed. The next state "high voltage enable" is triggered by the operator to apply high voltage to the klystron. When the pulse is triggered the "electron beam on" state is entered for 250 ms to ramp up the electron beam. This is followed by the "RF interrupt" state which has no effect as no RF has yet been applied. RF is first applied at low power in the RFL state and allowed to rise to the set value in the RFH state. If an arc is detected

in the launcher a transition to the "RF interrupt" state is triggered to remove the RF drive for a preset time followed by the RFL and RFH transitions.

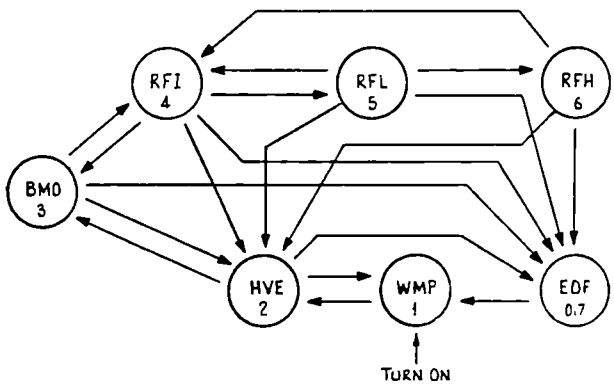

WMP — WARM UP
HVE — HIGH VOLTAGE ENABLE
BMO — ELECTRON BEAM ON
RFI — RF INTERUPT
RFL — RF ON AT LOW POWER (TO ESTABLISH PHASE LOCK)
RFH — RF ON AT HIGH POWER
EOF — EMERGENCY OFF (CROWBAR FIRED)

FIGURE 4
Klysron Fast Controller State Machine

In the event of a serious fault such as voltage breakdown in the klystron the HVPS crowbar is fired by a transition to an "Emergency off" state.

As well as its other functions, the PLC has been programmed to automatically adjust the klystron operating parameters to the required RF power setting and automatically condition the klystrons by continuously pulsing at progressively higher power levels.

4. TEST BED OPERATION

The first klystron in the test bed achieved its initial rated output of 500 kW for 20 seconds in July 1988. Some further development work on the control electronics is required before an endurance test is done of 1000 pulses at 650 kW for 10 seconds. Both test bed klystrons have been operated at this level during factory tests for a few pulses.

The power output from the klystron is monitored by performing calorimetry on the test loads and klystron collector. This uses an integral method to calculate the total heat transferred to the water system. The calculated power balance in the klystron is as follows:-

Test Load	510 kW
Collector	869 kW
Lower body (estimate from factory test)	9.5 kW
Upper body (estimate from factory test)	9.9 kW
Waveguide to test load and switch	5.0 kW
Total	1403 kW
Electrical power input from HVPS	1340 kW
Error	63 kW

This error is 4.7 % of electrical power.

5. CONCLUSIONS

Operation of the test bed will enable high power microwave components to be tested prior to their installation on the JET machine. It will also allow the control system and auxiliary power supplies to be refined to permit klystron operation at 650 kW for 10 seconds. Eight klystrons will start operation with JET after the next major machine shutdown which ends in March 1989.

ACKNOWLEDGEMENTS

The authors would like to thank the Tore Supra team for allowing JET to use their high power test bed and for their help in operation and interpretation of results.

REFERENCES

1. A. S. Kaye, Design of JET Lower Hybrid Launcher, these proceedings.

2. C. Christodoulopolos, Design of the Protection Crowbar for the LHCD Klystrons in JET, these proceedings.

THE JET ICRF ANTENNAE SCREEN: EXPERIENCE WITH THE ACTIVELY COOLED NICKEL SCREEN AND DESIGN OF A NEW BERYLLIUM SCREEN

C I WALKER, H Brinkschulte, M Bures, N Dragomelo, J P Coad, A S Kaye, S Knowlton, J Plancoulaine

JET Joint Undertaking, Abingdon, Oxfordshire, OX14 3EA, UK

The technological performance of the water cooled Nickel screens is described. The benefits of Beryllium as a screen material in terms of plasma radiation, mechanical reliability and thermal suitability are quantified. Design features of the new Beryllium screens are described.

1. INTRODUCTION

Water cooled Nickel electrostatic screens[1] were installed in the A_1 ICRH antennae in JET in 1987. These screens were heavily carbonised by glow discharge in methane[2] before installation. The antennae have operated for over one year. Over this period 1500 RF pulses up to 18 MW total power, up to 4 MW per screen and up to 20 seconds per pulse have been applied. Nickel levels have increased in the plasma but remain a modest contribution to the energy balance. Subsequently, in-situ carbonisation and mechanical cleaning of the surrounding tiles have been used to control the nickel.

The antennae and screens have performed well in terms of RF transmission, withstanding high RF voltages and local heating. Damage to the screens has mainly been due to thermal stresses leading to weld failure and leaking of some screens. Remote Handling equipment has been used to remove screens which have been repaired successfully.

There are plans to replace the Nickel screens. The replacement screens will use solid Beryllium elements; the low Z of Beryllium is anticipated to substantially reduce the metal radiation despite the higher sputtering rates. In addition, the higher conductivity of Beryllium, together with the use of an open structure, reduces the RF losses sufficiently to enable cooling by conduction to the screen sides, thus avoiding the many tube-manifold welds of the present screens. The design of the Beryllium screens, which remains compatible with the A_1 antennae, incorporates assemblies with flexible thermal couplings bolted to a water cooled Inconel frame.

2. NICKEL SCREEN EXPERIENCE

Since operations restarted in 1987 the full set of 8 RF antennae have been available for use and have accumulated 1500 RF pulses until recent failure of one VTL. RF plasma heating results have been reported[3] previously and the value of the screen element alignment with the tokamak field has been demonstrated[4].

There have been no limitations on the peak RF power of the antenna attributable to the screens. A maximum voltage of 40 kV has been attained on all antennae.

A maximum total of RF power of 18 MW in 2 second pulses has been coupled to the plasma. Normal operation is with 2.5 MW per antenna, limited by the generator. This has been increased to a peak of 4 MW per antenna. Pulse lengths of up to 20 seconds have been performed, with a maximum energy of 30 MJ each on 2 antennae.

The screen is a source of metal impurities in the plasma. The effect of pre-carbonisation was evident from the very low initial nickel level in the plasma. This effect decreased

within 50 pulses and in-situ carbonisation was performed. The migration of the screen nickel has been quantified as 5 x 10^{19} atoms/MW per screen. The effect of radiation of this nickel on the plasma energy balance is still negligible. It had been demonstrated on the A_0 antennae that the source of the nickel is the front, plasma facing, surface of the screen[5].

Heat removal from the screens has been adequate. The series connection of the Antennae screens' water cooling with the belt limiter has governed the availability and flow rate of cooling water. The flow rate has to be limited to 4 li/s to avoid resonances in critical bellows; this is half of the design value but no serious consequences have been observed.

Slight arc damage has been seen on one screen. This is a modified screen, with the last element unconnected to the cooling water circuit. The arcing may be due to the poorer electrical connection of this component to the screen by virtue of its Nimonic flexible coupling. Although slight, this damage would have serious consequences if it had penetrated a water channel. No fine bored hole damage, seen in the A_0 antennae, has been observed on these A_1 screens.

Side protection tile erosion is evident. The 'footprint' of the plasma can be clearly seen on the side protection tiles, where they were effectively acting as the first plasma limiter for significant periods of operation. A few tiles along the centre line of the torus have been destroyed by some unidentified process.

The End Contacts (Figure 1), provided to block fringing fields, have suffered severe erosion from melting or arcing.

On Antenna Octant 7 the end contacts have been removed with no apparent effect on the performance of the antenna.

Operation without antenna and limiter cooling and operation of the draining and refilling

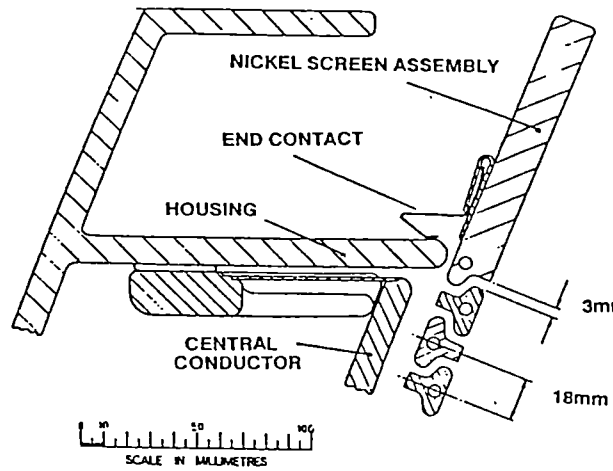

FIGURE 1
Vertical section through nickel screen and antenna

system with the torus hot (up to 350°C) have resulted in thermal stresses much greater than anticipated resulting in 2 small leaks developing near the end element; these screens were replaced. Recently a larger leak appeared in one antenna but operation continued with all antennae hot, during which further leaks have occurred. Operation is now continuing without water cooling with restricted pulse length (typically 5 seconds).

An effective method of removing and replacing a screen has been developed, using the Remote Handling tools and lifting equipment designed for the tritium phase of JET operation. The removed screens have also proved repairable although modest activation (Ni to Co^{56} and Co^{58} transformation giving 35 μSv/hr contact activity) causes some procedural difficulties.

3. THE NEW BERYLLIUM SCREENS

A new Beryllium screen has been designed and is now under manufacture. It has 2 aims:

i. Improved reliability

This is required for the tritium phase of JET operation. The 160 welded joints connect-

ing elements to side manifolds can be avoided by end cooling of solid elements. A secondary benefit is the reduction in cooling water tritiation.

ii. Reduction in plasma radiation

Even accounting for the increased sputtering of Beryllium surfaced screen elements, radiation from the core of the plasma will be less than 1/10 of that seen with nickel. Power radiated from the plasma edge will be reduced by a factor of 1/5 with Beryllium; this is expected to favour H-mode operation and to avoid termination of the H-mode due to radiation collapse. With the present antennae this termination during RF heating corresponds to a steep increase in nickel radiation. Beryllium has been shown to be an effective oxygen getter. The ISX B Beryllium limiter experiments resulted in a reduction of oxygen levels and a corresponding increase in density limit of x2. The density limit of JET plasmas are expected to increase to over 10^{20} m^{-3}, a crucial level to reach conditions of high thermal fusion yield.

4. CHOICE OF MATERIAL FOR END COOLED ELEMENTS

Central to the design of the screen is the operational temperature of the screen elements. This affects both the strength of the screen elements themselves and the temperature and strength of the central conductor of the antenna. The safe working temperature of the Central Conductor is 600°C for which the screen must operate at < 500°C for the present duty cycle to be maintained.

The screen temperature is governed by the geometry of the elements and their spacing, and the element material. The more open structure of screens, demonstrated in ASDEX and JT60, has been chosen (Figure 3), although this allows a clear line of sight to the central conductor. The RF losses are thus reduced by a factor of 3. The total RF loss in a screen with

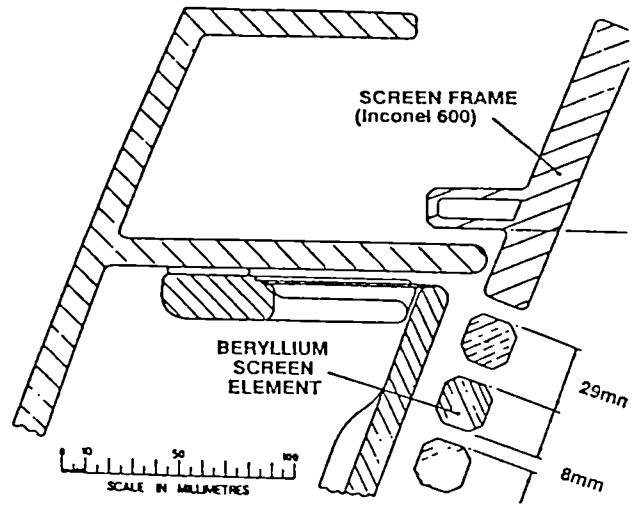

FIGURE 2
Vertical section through Beryllium screen and antenna

alternative materials is given Table 1.

These losses are not uniformly distributed on the screen. In the centre of the screen temperatures are a factor of 2 higher than the mean screen temperature.

The radiant energy exchange between screen and torus is complicated by the sensitivity to torus temperature distribution, operating scenario, and imprecisely known component emissivities.

During the 20 second pulse only conduction through the section of the element is significant. The effectiveness of conduction along the length of the element is indicated by the thermal diffusion time constant of the half length. Local temperature peaks along an individual element are smoothed out in a time typically a quarter of this.

The equilibrium temperature drop along the element for conduction alone is proportional to the time averaged incident power and inversely proportional to the thermal conductivity.

The flexible connection drops the temperature a further 50°C to the water cooled sides of the screen.

The limiting stress in the element is due to

the transient force arising, during a disruption, from a change in vertical flux through the horizontal loop formed by the screen and housing. The resistance of this loop is dominated by the Inconel housing, therefore the magnitude of the limiting stress is only weakly dependent on element material. The radial inward force is 1.5 kN per element with a corresponding maximum stress of 75 MN/mm^2.

Additional thermal stresses appear due to the rapid, non-uniform heating of the elements.

Table 1 lists the maximum operating temperature, T_{max}, for this stress level and other parameters, for a range of potential element materials.

TABLE 1
Comparison of element materials

Material	T_{max} °C	δT_{RF} K	δT_o K	τ_{diff} Min	T_{PEAK} °C	τ_p Min	Z
Beryllium	550	113	430	33	580	13	4
Molybdenum	1200	363	610	27	660	15	42
Nickel	700	359	(1340)	64	(1580)	30	28
Titanium	600	(1162)	-	210	-	-	22
Copper Zirconium	400	155	152	15	290	7	29-40
Stainless Steel	700	615	-	196	-	200	24-26
Graphite	1500	(5400)	(5200)	19	-	-	6

Notes:
T_{max} : Maximum allowable temperature for material, on strength grounds
δT_{RF} : Temperature rise per pulse due to RF losses
δT_o : Time average temperature difference along hottest element for conduction cooling at maximum duty cycle
τ_{diff}: Thermal diffusion time constant over half length of element
T_{PEAK}: Peak temperature on screen at maximum duty cycle
τ_p : Minimum interval between pulses at maximum RF voltage and pulse length
Z : Proton number

Temperatures shown in brackets will be substantially modified by radiation cooling

Titanium, stainless steel, graphite: all materials of high temperature capability but with low electrical conductivity, cannot be used for end-cooled elements. Radiation cooling cannot be used because of the central conductor temperature limits.

Nickel cannot be used because of its excessive temperature except at a much reduced duty cycle.

Copper Zirconium, with its highest operating temperature of the high conductivity copper alloys, has good electrical, thermal and mechanical properties. Copper, however, is generally regarded as highly damaging to the purity of the plasma, due to its high sputtering coefficient (twice nickel) and its high atomic weight.

Molybdenum could be used. The effect of local high temperatures could be avoided with 20 mins duty cycle. Its use as a first wall material, notably JT60 where it was coated with Titanium Carbide, has not proved to be satisfactory.

Beryllium can be seen to somewhat exceed the peak working temperature. This can be avoided with an increase in pulse interval from 10 to 13 minutes, or be reducing the voltage to 44 kV.

It can be seen that Beryllium is a valid choice of material for end cooled screen elements, happily coinciding with favourable plasma effects described in Section 3.

5. DESIGN DETAILS OF BERYLLIUM SCREEN

Beryllium screens have been designed to be used on the existing antennae with the existing protection tiles and to remain compatible with the JET Belt limiter.

The Beryllium screen comprises 50 Beryllium elements mounted in a frame assembly. One of the advantages of this construction method is that the vacuum tight construction can be manufactured and fully tested, by thermal cycling, before Beryllium components are assembled, with its health restrictions.

The Beryllium Elements were made from plates of hot pressed block. One e.d.m. cut (wire eroded under water) providing both a front and a back surface. The advantage of an eroded surface in Beryllium is that it is rela-

tively stress free and no subsequent machining is required. The other surfaces of the element are shaped by multi-pass milling. Sharp edges are radiused with abrasive tools and by the final chemical etch.

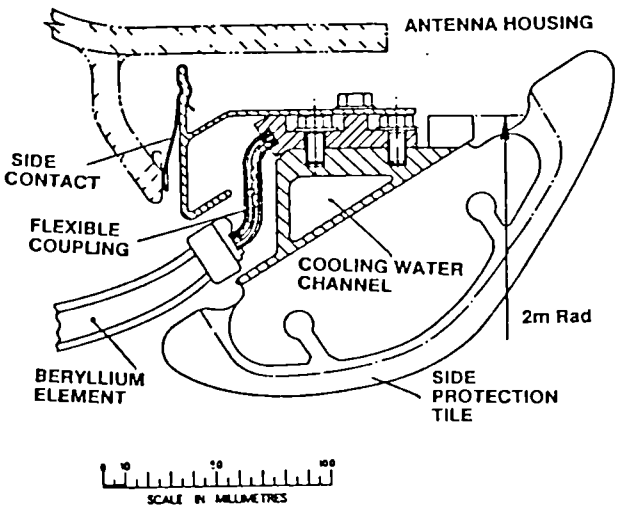

FIGURE 3
Horizontal cross section of Beryllium screen

The Flexible Coupling attached to each end of an element (Figure 3) is designed to allow thermal expansion of the element by up to 6 mm while maintaining a good thermal path between the element and the screen frame side. It must also withstand the forces induced during plasma disruptions while allowing the element to better resist this force by remaining effectively simply supported at its ends. It comprises a stack of Copper, Copper Zirconium and Nimonic strips e-beam welded into solid blocks of Copper.

The flexible coupling is attached to the Beryllium element by means of a shrunk Nimonic sleeve, while to the screen frame it is bolted over a pure silver interface.

The Screen Frame assembly requires no particular electrical properties and consequently its material (Inconel 600) and its all-welded construction have been chosen for mechanical strength, water and high temperature compatibility. The water flow connection between the two sides has been embedded away from the plasma surface of the screen.

The side contacts, linking the screen RF currents to the antenna housing with the highest DC resistance, as used on the nickel screens, have been retained (Figure 3). The end contacts have been abandoned in favour of a simple labyrinth (Figure 2).

6. CONCLUSION

Valuable results have been obtained to date with the JET ICRF Antennae. Even with present uncooled operation of nickel screen a vigorous RF heating campaign has been successful.

With the new screen design the full potential of the ICRH programme can be realised.

ACKNOWLEDGEMENTS

The authors would like to acknowledge the technicians of the Antenna Systems Group of the RF Division for their invaluable contribution in the ICRF programme to date and in the development of the Beryllium screens.

REFERENCES

1. C.I. Walker et al, 14th SOFT, Avignon.
2. J.P. Coad et al, E-MRC Meeting, Strasbourg, June 1987.
3. J. Jacquinot et al, 15th EPS Conference, Dubrovnik, May 1988.
4. M. Bures et al, 15th EPS Conference, Dubrovnik, May 1988.
5. K. Behringer et al, 13th European Conference on Controlled Fusion, Schliersee, 1986.

ANALYSIS OF VERTICAL INSTABILITY IN THE JET EXPERIMENT

R.Albanese [1],E. Bertolini [2],S. Bobbio [3],R. Martone [1],G. Miano [3],P. Noll[2].

[1] Istituto di Ingegneria Elettronica, Università di Salerno, Italy.[2] JET Joint Undertaking, England.[3] Dipartimento Elettrico per l'Energia, Università di Napoli, Italy.

This paper describes the electromagnetic analysis of vertical instability tests performed in JET. These and related mechanical studies are aimed at establishing safe operating limits.

1. INTRODUCTION

In the JET experiment and in other Tokamaks with elongated plasma shape, the vertical plasma position must be stabilized by active feedback control.[1] If the stabilization fails, a vertical instability occurs, followed by a disruption. This causes large forces at the vessel.

This paper describes the electromagnetic analysis of vertical instability tests performed in JET. These and related mechanical studies are aimed at establishing safe operating limits.

One can distinguish three phases of the vertical disruption. Initially, the vertical displacement grows exponentially at constant plasma current: the plasma force balance is provided by magnetic fields from induced toroidal currents in the vessel and in the stabilization coil. In the second phase the plasma comes in contact with the wall at top or bottom, and the plasma motion and the toroidal vessel currents decrease to zero. The current in the stabilizing coil is insufficient to warrant plasma equilibrium; therefore, additional forces must be present. Several mechanisms can be considered to explain the origin of the additional balancing force. Eventually, the plasma disrupts when the q-value at the plasma boundary has decreased to values below two, due to the forced reduction of the plasma size. During the current quench, the plasma moves radially inwards, causing also large radial forces at the vessel.

2. VERTICAL DISRUPTION

Without active stabilization, the JET plasma is vertically unstable due to the destabilizing effects of the iron magnetic circuit and of the quadrupolar component of the equilibrium magnetic field required to produce an elongated plasma shape. Any small radial field perturbance would initiate an esponentially growing vertical motion. The growth rate depends on the effective field index and on the decay time of eddy currents in the stabilization coil, in the vessel and other passive structures around the plasma.

Due to the presence of belt limiters at about ±1 m above and below the equational plane, the vertical motion leads to a reduction of the plasma size, in particular after the plasma becomes in contact with the vessel walls at top or bottom. Consequently, the q-value at the plasma boundary decreases and a hard disruption (current quench) occurs when q becomes smaller than about two.

The vertical force at the vessel caused by the vertical instability is essentially proportional to the vertical plasma displacement and the square of the plasma current. Cases with large initial q-value are therefore particularly severe because the displacement can become large before the current quench starts. Large initial q-values are present in configurations with one or two x-points (magnetic limiter), for example.

Parametric studies of the vertical instability have been performed at low current level by disabling the feedback stabilization at some time during the current flat top[1]. After strengthening of the vessel supports, further tests were carried out with currents up to 3.5 MA, in order to obtain a reasonable estimate of forces and of their effects at very large current (6 - 7 MA).

An example of a test at 3.5 MA and toroidal field B_T=1.8T is shown in fig.1 and fig.2. Fig.1 presents the evolution of currents and of the difference of the toroidal field measured at top and bottom inside the vessel. Fig.2 shows geometrical parameters. Flux plots shortly before

and during an early phase of the instability are given in Fig.3.

We can distinguish 3 phases. In the first phase (t=50.00 to 50.04 sec) the vertical position (Z_p in Fig.2), the radial field coil current and the induced differential current in the vessel (I_R and I_{Vdiff} in Fig.1) increase rapidly at a growth rate $\gamma \approx 160\ s^{-1}$, while the plasma current and the radial position remain constant. The plasma is detached from the vessel walls, but its size is decreasing due to the interaction with the belt limiter (Fig.3). This causes a decrease of the q-value and a flattening of the current profile, implied by the decrease of the normalized internal inductance l_i (Fig.2).

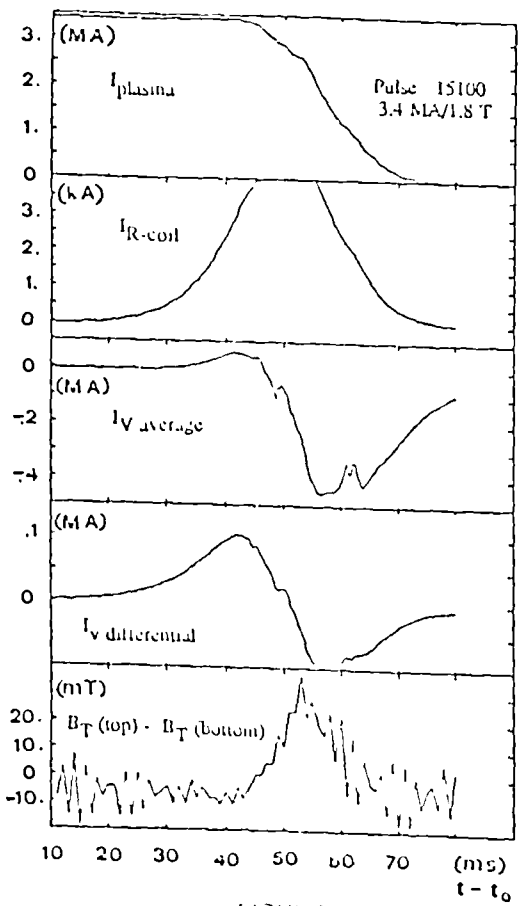

FIGURE 1
Plasma current I_p, radial field coil current I_R, average vessel current I_{Vav}, differential vessel toroidal current I_{Vdiff} and difference of toroidal field top bottom δB_T in pulse 15100, after disabling stabilization at t_0 = 50.0 sec (10 sec after the start of I_p).

This phase can be understood on the basis of electromagnetic and MHD consistent models[2,3] which take into account only the forces arising from toroidal currents. The destabilizing force acting on the plasma is essentially balanced by the stabilizing forces from the radial field coil and the differential vessel current induced by the plasma motion.

The second phase (t=50.04 to 50.05 sec) begins when the plasma comes in contact with the vessel. The plasma continues to move vertically but its speed decreases to zero. The plasma minor radius is consequently further reduced, giving rise to an increase of the plasma external inductance and some associated decrease of the plasma current. The q-value at the boundary has already reached a critical value of about two at the beginning of the second phase so that part of the current decrease may be due to disruptive behavior.

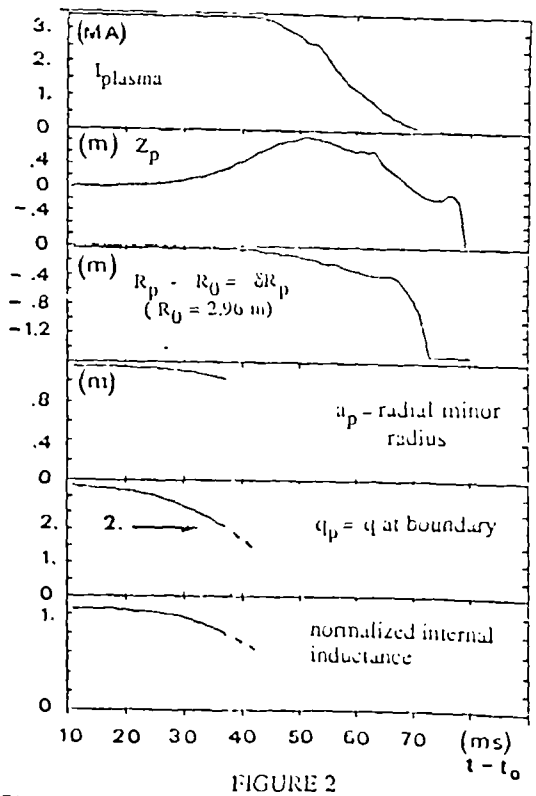

FIGURE 2
Plasma current I_p and geometrical parameters of pulse 15100 after disabling stabilization at = 50.0 sec. Z_p and δR_p are the vertical and radial displacements of the current centroid. Processing of a_p, q_b and l_i stops at 50.038 s.

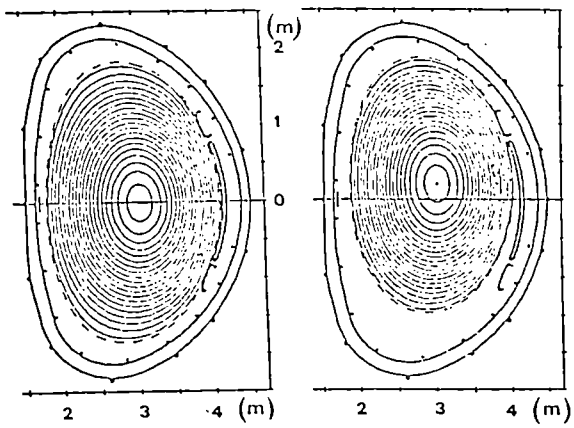

t = 49 s	t = 50.034 s
q_b = 3.027	q_b = 2.324
I_p = 3.4 MA	I_p = 3.4 MA
l_i = 0.978	l_i = 0.843

FIGURE 3
Flux plots of pulse 15100 before and 34 ms after disabling vertical stabilization at t = 50 s.

In other pulses with larger initial q-value, q=2 is reached in the course of phase 2. The differential vessel current decreases to zero, due to the small eddy current decay time $T_V \approx 3$ms, the radial field coil current reaches a maximum due to flux conservation (time constant ≈ 1 sec). Thus, during this phase of the instability, two phenomena occur:

(i) the destabilizing force acting on the plasma reaches its highest value (≈3.7 MN)

(ii) the stabilizing force due to toroidal vessel currents is practically absent, while that of the radial field coil is still present (≈1.5 MN) but insufficient to ensure a balance of forces at the plasma.

Therefore, there must be an additional repelling force between the plasma and the vessel.

In the last phase (t >50.05 sec), the plasma current decreases rapidly to zero, inducing a net vessel current ≈ 0.4 MA (Fig.1) and also a differential vessel current, due to the displaced plasma position. The differential current is actually destabilizing, while the radial field coil current is still stabilizing. The plasma moves radially inwards and vertically downwards, sliding along the inner part of the vessel. Also during this phase, the toroidal currents do not balance the destabilizing force on the plasma.

The force acting on the plasma and the vessel have been estimated from simplified simulations with the PROTEUS finite element code[2] and a new analytic code[3], whereby the initial PF circuit currents and the measured current and position of the current centroid of the plasma were taken as input parameters and the circuit voltages were kept constant and equal zero. The computed current in the radial field coil and loop voltages at certain locations at the vessel agree within about 10% with measured values. This indicates that the effect of screening by eddy currents in the mechanical shell is of minor importance in JET, as was previously estimated analytically. It has also been concluded from analytical models and from computations with the SPARK code[4] and the CARIDDI code[5] that for the JET geometry, the saddle currents in the rigid sectors of the vessel contribute relatively little to the eddy current field derived on the basis of an axisymmetric vessel model, at least in cases where the disruption time is significantly larger than the decay time of toroidal eddy currents (3 ms).

The vessel and plasma vertical forces have also been estimated from a simplified interpretation of measurements as applied previously[1].

Results for pulse 15100 are shown in Fig.4 and Fig.5. Fig.4 indicates that an additional force must be present which is a significant fraction of the basic destabilizing force, in particular during the phases 2 and 3 of the instability. Notice that, in Fig.4, the presence of an additional force even in the first phase of the instability is due to the very crude plasma model (filamentary plasma) utilized in the numerical simulation.There are substantial differences between simulation and simplified evaluation, which may be due to the crudeness of the model used, but the existence of force due to other effects than toroidal current is evident. Fig.5 shows that the vertical force at the vessel is dominated by the additional force, the forces due to toroidal currents being small, in particular around t=50.05 sec, where the plasma displacement has served a maximum.

Several mechanisms can be considered to explain the origin of an additional repelling force between the vessel and the plasma. As suggested by P. Thomas[6], a radial

electric field vxB is induced in the plasma due to its vertical motion. When the plasma becomes in contact with the conducting vacuum vessel, a poloidal current can be driven in the plasma, having a return path in the vessel. A poloidal current circulating in the plasma and the vessel may also be caused by a temperature gradient along the part of the vessel which is in contact with the plasma, as considered by P. Habour[7], but none of these mechanisms seems to be fully convincing. In JET, there is some measurements of the difference of the toroidal magnetic field at top and bottom inside the vessel, as shown in the Fig.1 (bottom trace). The corresponding stabilizing force on the plasma is $2\pi R_c w\ B_T\ B_T/\mu_o$, were w is the radial width of the current loop and B_T is the measured toroidal field difference. An estimate for a plausible value w 1.5 m, with B^T=2.1T at the pick up coil position RC 2.5 m, is shown Fig.4. This force is smaller than the estimated additional force.

These attempts to measure poloidal currents are very inaccurate and may be obscured by local field perturbations. This lead us to envisage a different mechanism to explain the origin of the additional repelling force between the plasma and the vessel (or, at least, a significant part of it).

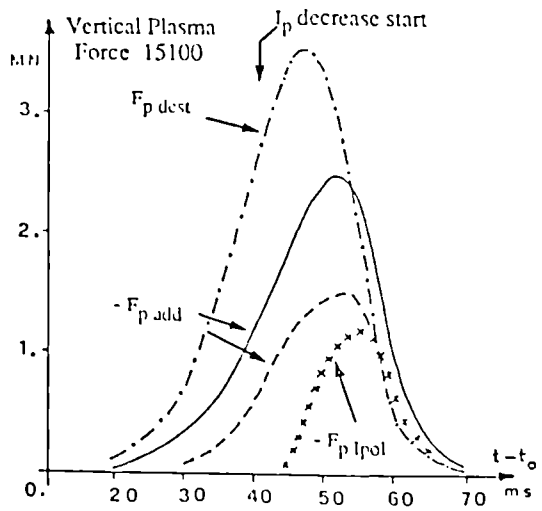

FIGURE 4

Destabilizing force and additional force at the plasma obtained from a simulation with the PROTEUS code (solid line and -----) and from a simplified evaluation of measurements (broken line). Also given is an estimate of a force on the plasma due to poloidal currents across the plasma (xxx).

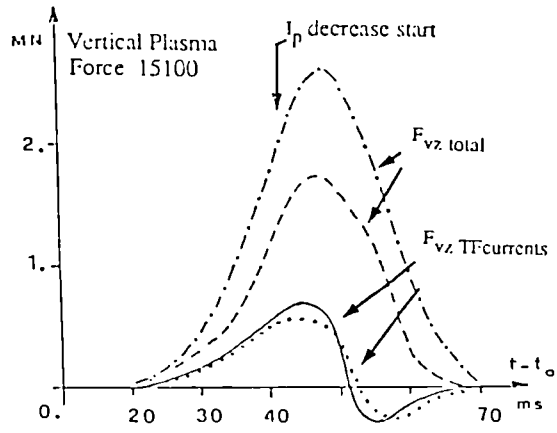

FIGURE 5

Vertical forces at the vessel for pulse 15100 (3.4 MA/1.8T) obtained from a simulation with the PROTEUS code (-·-·- and ———) and from a simplified evaluation of measurements (---- and ·····).

These attempts to measure poloidal currents are very inaccurate and may be obscured by local field perturbations. This lead us to envisage a different mechanism to explain the origin of the additional repelling force between the plasma and the vessel (or, at least, a significant part of it).

3. MAGNETOMECHANICAL INTERACTION MODEL

During the second phase of the vertical instability, the plasma current is only slightly reduced and plasma confinement is still efficient despite the fact that part of the plasma boundary is in contact with the wall. It is considered that the plasma behaves like a balloon squeezed by the net destabilizing force against the vessel. A simplified configuration is shown in Fig.6.

The plasma pressure is constant on magnetic flux surfaces and in the plasma region. In the region A-A' the plasma is bounded by the wall. The net force balance of the plasma can be achieved in two ways. If the plasma pressure is substantial along AA', then this pressure is directly supported by the walls. If the plasma pressure is small, then poloidal currents flow in the plasma which close in a plasma surface current along AA'. The surface current is pushed against the wall by the toroidal field.

With conducting walls, part of this current can be shared by the walls, depending on the relative resistances of the wall and of the plasma surface current.

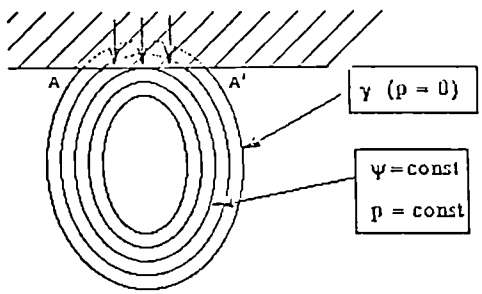

FIGURE 6
Plasma, supported partly by a wall due to kinetic pressure at the region AA' of the boundary γ, partly by poloidal surface currents forced along AA'.

This model is consistent with static equilibrium. A simple slab model can be considered for illustration. Fig.7 slows the current and pressure profiles when a plasma slab of width $2a_0$ is pushed against a wall at $x=a_0$ by an external field B_{ext}, which resembles the residual destabilizing radial field in the torus. Among the possible dynamics, two limiting cases have been considered: frozen current $I(x)=\int_0^x J(x)dx'$ and frozen flux $\psi(x)=\int_0^x B(x')dx'$. The profiles shown in Fig.7 are for frozen current.

The solution at frozen current implies that the force is transmitted to the wall via the kinetic pressure. Conversely, the solution at frozen flux requires the presence of a surface current, with p=0 at the plasma wall interface.

4. CONCLUSIONS

The lack of decisive experimental data does not allow to determine the phenomena occurring during the second phase of a vertical instability: probably, several different mechanisms act together to determine the additional balancing force at the plasma. The magnetomechanical interaction model proposed in this note does not rely on the presence of conducting walls and the presence of a vertical motion of the plasma; it appears therefore suitable to explain the observed slowing down of the vertical speed before thecurrent quench.

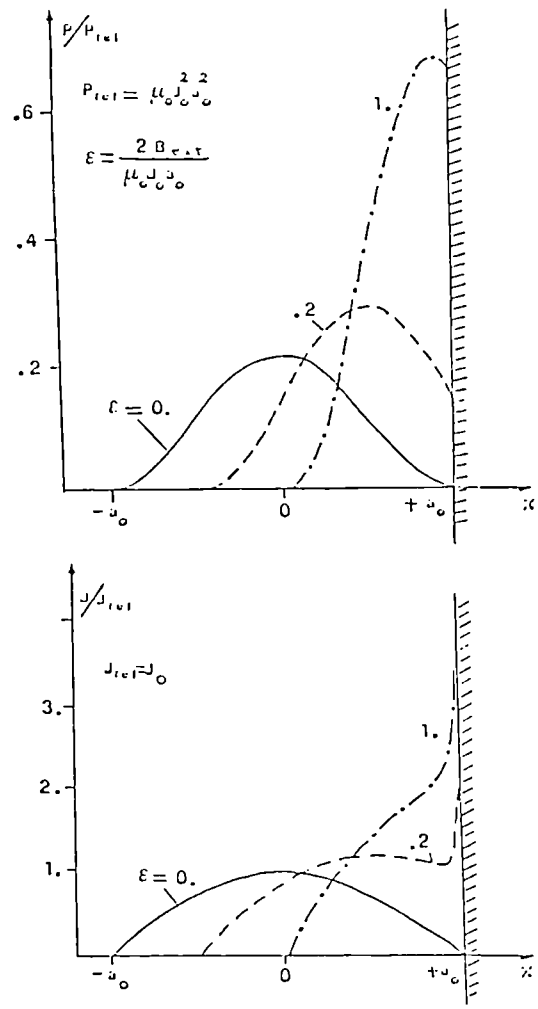

FIGURE 7
Current and pressure profiles of a plasma slab for different values of an external field pushing the plasma against a wall at $x = a_0$. The current is assumed to be frozen.

ACKNOWLEDGEMENTS

The authors wish to thank Dr. M. Garribba for his work concerning the implementation and application of the PROTEUS Code in JET.

REFERENCES

1 a) E. Bertolini, P.L. Mondino, P. Noll, Fusion Technology, vol.11 p.71 (1987).

b)P. Noll et al, Proceedings of the 11th Symposium on Fusion Engineering, Nov. 18-22, 1985, Austin, Texas, Vol.1, pp.33-40.

2 a) R. Albanese, J. Blum, O. de Barbieri, "Numerical Studies of the Next European Torus via the PROTEUS Code", Proc. of the 12th Conference on the Numerical Simulation of Plasmas, San Fransisco1987.

b) R. Albanese et al, "Preliminary Analysis of Vertical Instability and Disruption Effects for JET 7MA Configuration", Report NET/87/TE/075-R-01, 8.10.1987.

3 S. Bobbio, R. Martone, G. Miano, "Analysis of vertical instabilities in JET", work performed partly under a JET Consultancy Assignment.

4 a) DW Weissenburger, the SPARK Code Version One, Report PPPL-2040, Princeton, October 1983.

b) DW Weissenburger, work performed as part of a task agreement with PPPL, JET contract JG6/0158.

5 a) R. Albanese and G. Rubinacci, IEEE Trans. on Magnetics vol.24 n.1 (1988).

b)R. Albanese and G. Rubinacci, "Electromagnetic analysis of shot 1947 in JET, Report NET/IN/87-05, 18.2.87.

6 P. Thomas, JET, private communication

7 P. Harbour, "Current Flow Parallel to the Field in a Scrape-Off Layer", Paper presented at the Workshop on plasma edge theory in fusion devices, Angustusburg, G.D.R., 26-30 April 1988 (JET preprin JET-P(88)24).

JET Results and the Prospects for Fusion

P H Rebut, P P Lallia

ABSTRACT

Recent experiments on JET with increased additional power have resulted in plasma parameters close to those of a thermonuclear reactor. Electron and ion temperature significantly in excess of 10keV have been simultaneously achieved at a plasma density of $2\times10^{19}m^{-3}$; transiently, during an H-mode the fusion product $(\hat{n}_i\hat{T}_i\tau_E)$ has reached $3\times10^{19}m^{-3}$.keV.s at temperatures exceeding 5keV; and plasma current up to 7MA (for 2s) have been achieved. However, degradation of confinement with increased power is observed in all regimes.

The major heat and particle transport phenomena observed in Tokamaks can be interpreted as resulting from a magnetic turbulence, in some respects analogous to the turbulence existing in fluids when the fluid velocity exceeds a certain threshold value. This interpretation has led to local transport and global scaling laws giving satisfactory agreement with experimental results. Accordingly, the fusion product would scale as $I^2B_t R^4$ for a fixed Troyon factor. Reaching ignition would require a plasma current close to 30MA at a moderate field value of 4.5T.

To fully tackle the problems of a controlled burning plasma for at least days in semi-continuous operation, the plasma of the next step tokamak should be similar in size and performance to an energy producing reactor. The scientific and technical aims of such a machine should be to study a burning plasma, to test wall technology, to provide a test-bed for breeding blankets and above all to demonstrate the potential and viability of fusion as an energy source.

The main characteristics of the design of a thermonuclear furnace dedicated to these objectives are presented. Basically the plasma parameters are scaled up from JET by a linear factor of 2.5. Magnets, either superconducting or of copper, should be able to operate continuously. The present design uses watercooled copper magnets to benefit from proven technology and consists of 20 identical sectors. Each incorporates a toroidal field coil, mechanical structure and a part of the vacuum vessel wall as one integrated unit. A single-null divertor configuration ensures helium exhaust and possibly benefits from an H-mode to reach the ignition domain. The X-point position relative to the dump plates would be swept to limit the wall loading to $2MW/m^2$. By changing the operating density, the thermonuclear power could be varied from 0.5 to 4GW(th), according to requirements on power loading and tritium consumption.

I INTRODUCTION

JET is now about mid-way through its experimental programme and its achievements can be usefully compared to the Project objectives, which are:

1. The scaling of plasma behaviour as parameters approach the reactor range;
2. The plasma-wall interaction in these conditions:
3. The study of plasma heating;
4. The study of α-particle production, confinement and consequent plasma heating.

At this stage, the first three aspects have been extensively addressed and a general pattern of the plasma behaviour has emerged. Consequently, it is possible to draw some conclusions relating to the requirements and parameters of a next device.

The present paper is structured as follows. Section II summarizes the major results obtained on JET with their direct implications for a future thermonuclear reactor. In particular, a distinction is made between the achievements which can safely be regarded as steady-state (i.e. fully reactor relevant), and those corresponding to a more transient state of the plasma. Section III briefly describes a possible interpretation of the transport phenomena prevailing in a tokamak and its corresponding scaling. The performance of several 'next-step' devices are also calculated using a simplified 1-D transport code. General considerations governing the choice of a "next step tokamak" are presented in section IV. In section V, a specific "thermonuclear furnace", JIT, is proposed as a desirable step towards a prototype demonstration fusion reactor.

II MAJOR JET RESULTS AND CONSEQUENCES FOR A REACTOR

II.1 Achievements

The technical features of JET and the latest experimental results have been detailed elsewhere [1,2]. A number of major enhancements were carried out during the 1987 shut-down and are listed in Table 1. Fig.1 shows the status inside the vacuum vessel at the beginning of the 1988 operational period (which is due to end in September). New features have extended the operational domain and, in particular, have permitted the following technical and scientific achievements.

1. In quasi steady-state:

- plasma current, I_p, of 7MA has been obtained for 2s;
- JET has operated routinely with I_p above 5MA and a current of 6MA has been maintained for 7s;
- ion and electron temperatures T_i and T_e, in excess of 5keV have been sustained for over 20s at a plasma current of 3MA (see Fig.2);
- additional power up to 24MW has been delivered to a 5MA plasma producing a total energy stored of 8.8MJ (see Fig.3);
- both electron and ion temperatures simultaneously in excess of 10keV for 2s were observed at a plasma density of $2\times10^{19}m^{-3}$ (see Fig.4).

2. In a transient situation (where density, temperature or internal inductance were still varying)

- routine operation with a magnetic separatrix at I_p=4.5MA. H-mode plasmas were regularly observed during neutral beam heating. A record H-mode at 5MA has been obtained. Transiently, during an H-mode, the fusion product $(\hat{n}_i\cdot\hat{T}_i\cdot\tau_E)$ has reached $3\times10^{20}m^{-3}.keV.s$ at temperatures exceeding 5keV (see Fig.5);
- the total plasma energy content has exceeded 10MJ during an H-mode;
- the maximum neutron yield has reached $9\times10^{15}n/s$ produced by deuterium-deuterium fusion reactions during an H-mode at 4.5MA; the plasma was heated by 12MW of deuterium beams at an energy of 80keV;
- high peaked density plasmas were obtained by using pellet injection ($n_{eo}>10^{20}m^{-3}$). Consecutive on-axis ICRF heating of such target plasmas produced transiently peak electron pressures in excess of 1 bar.
- "monster" sawteeth are seen with ICRH (minority heating) during which q_o, the safety factor at the centre, decrease below 1 (0.8) (see Fig.3).

Consequences for a Reactor

Plasmas of thermonuclear quality have been produced in JET and no adverse effects have been observed when both electron and ion temperatures reached thermonuclear reactor values. However, the record values of neutron yield, pressure and total energy have been obtained while the plasma was in a non-steady-state situation. It seems wise to extrapolate the performance of a future machine by starting from discharges already obtained and truly stationary. Transient improvements may prove to be useful to overcome the ignition pass but should not be relied upon when working quasi-continuously at full fusion power required routinely in a reactor.

II.2 Energy Confinement and the Fusion Product

Degradation of energy confinement with additional power is now a well known phenomenon. Recent experiments on JET have extended such observations to higher input power. Fig.6 shows the measured energy confinement time as a function of total power in JET for limiter and L-mode discharges. In this data, the time derivative of the plasma energy content does not exceed 10% of the input power. At high power, the improvement with increased current is obvious but a detailed examination of an individual scan shows a more complex pattern. The gain due to the current saturates in JET when the safety factor at the plasma boundary q_a decreases below 4, since flattening of the pressure profile results from sawtooth relaxations.

Here the safety factor q_a is defined by the current,

$$\text{i.e. } q_a = \frac{2\pi abB_t}{\mu_o I_p R}. \qquad (1)$$

The notation q_ψ is used when q is defined by the magnetic flux.

For the same input power but with a magnetic separatrix limiting the plasma - the so called X-point operation - the confinement of the plasma can bifurcate to a higher value, the H-mode. Fig.7 shows the energy confinement time for JET H-mode discharges. As previously,

the time derivative of the plasma energy content is small for these data, but the density is still rising while the temperature is decreasing. No significant difference was observed between single null and double null discharges. While at low power, τ_E can exceed 1s (i.e. comparable to the ohmic confinement time). It can also show a degradation with power at least as severe as in the L-mode. Similarly, confinement increases with I_p.

Consequences for a Reactor

The degradation of confinement time with the input power is considered a major threat to the success of future tokamak reactor. The difficulty to improve the fusion parameter $(\hat{n}_i \cdot \hat{T}_i \cdot \tau_E)$ (and so the ignition margin of a given machine) by the only virtue of additional power is illustrated in Fig.8. The major gains observed in JET result either from temporary changes in the confinement or from increasing the magnetic field and/or the current. If the scaling laws best describing the energy confinement in JIT continue to apply [2], then a reactor must be very close to ignition without any additional heating power. This means that the required temperatures must be obtained in those conditions; the dependence of radiation and fusion cross-sections imposes in practice an average temperature above 7keV. In addition, density and temperature have not a symmetric effect on confinement: it is easier to get a better energy confinement at high density than at high temperature.

II.3 Particle Transport

Particle and impurity transport in JET have been studied under different operating conditions [3,4]. In most cases, particle confinement, like energy confinement, is anomalous. JET results point strongly towards a common explanation for heat and particle transport. For instance, multi-pellet injection produces peaked high density profiles but flat and low temperature profiles occur in the ohmic regime. Increasing the central electron temperature by on-axis ICRF heating degrades the energy confinement and results mostly in a collapse of the central density (i.e. of the particle confinement). In cases where the collapse is delayed, energy confinement in the plasma centre is also better than in usual additionally heated discharges. The particle confinement time is 5-10 times larger than the energy confinement time.

The anomaly in the particle transport prevents impurity accumulation in the discharge centre. Combined with wall-carbonization, this has kept a low metallic impurity content in JET ($\approx 10^{-4} n_e$) and Z_{eff}=2 has been achieved with large additional power. But for most of the discharges the steady state mean value of Z_{eff} ranges between 2 and 4 with a radial profile which tends to peak on axis. Radiation losses in the plasma core are marginal, as long as the dominant impurities are of low atomic number. Under conditions of improved energy confinement, such as H-modes or peak density profiles, impurities are also better confined. Especially in the latter case, the medium- and low-Z impurities seem to accumulate near the plasma axis, showing neo-classical behaviour. This results in an increased deuterium dilution in the plasma centre and increased central radiation losses.

The scrape-off layer of the JET plasma have been studied under various conditions [5,6]. In limiter discharges, the plasma edge temperature ranges from 25 to 100eV, increasing with the input power and decreasing with density. The scrape-off thickness is typically 1cm; this quantity is invariant under most conditions, except that it increases during ICRF heating. In X-point operation, all atoms and molecules recycling from the divertor near the separatrix are ionised locally.

Consequences for a Reactor

The observation that the particle confinement time is several times the energy confinement time has consequences for the reactivity of the core of the plasma: it will result in a relatively high concentration of impurities and helium. For high Z impurities, the radiation losses may prevent attainment of the required temperature. For low Z impurities, in addition to helium produced by nuclear reactions, dilution of reacting ions will reduce the α-particle power.

The small scrape-off layer thickness results in a high power load on any material in contact with the plasma. This prevents the use of pump-limiters in a reactor in favour of an open divertor to take the plasma exhaust, and will require sweeping the separatrix over the divertor plates to reduce the mean peak thermal load.

II.4 Plasma-Wall Interaction

A variety of materials have been used for wall protection and high heat flux components [7]. JET initially operated with metallic walls, but the inner surface of the vessel (≈200m²) is now more than 50% covered with fine grain and carbon fibre reinforced graphite tiles. The remaining area is carbonised by performing glow discharges with some methane content. The wall temperature is maintained at ≈300°C. If previously conditioned by running discharges in helium, the carbon wall has proved to be a very efficient pump for deuterium during plasma discharges [8]. A variety of models have been proposed but experimental evidence from JET supports the explanation involving co-deposition of hydrogen and carbon in the form of saturated H-C films. It is indeed observed that more than 10-30% of the deuterium introduced into the vessel remains in the form of a deposited layer of hydrocarbons.

The dominant impurities in JET plasmas are carbon and oxygen. Their total amount is controlled mainly by the interaction of the plasma at the limiter. During a discharge, erosion of the limiter material is observed at the point of contact with the plasma and redeposited slightly further outside, as shown in Fig.9. Major plasma disruptions are most efficient in transporting materials from the first wall to the limiter. The ICRF antennae are separated from the plasma by a Faraday shield made of pure nickel. When the ICRF power is turned on metal is released from the screen and can also contaminate the limiters. In absolute terms, the nickel increase is low, especially if the screen has been previously carbonised, but it

is planned to use beryllium in the future to take full advantage of this low Z material.

The increase in additional power and therefore of the heat load in JET has necessitated an increase in the material area in contact with the plasma. Belt limiters are now in use, whose power handling capabilities exceed 40MW for 10s (see Fig.1). For X-point operation, eight graphite poloidal rings were installed to protect the top and the bottom of the vacuum vessel. Water cooled dump plates will be installed during the next shutdown to increase the 40MJ-2s present power handling limitation. Protection tiles have been broken during X-point operation and Fig.10 shows the state of a graphite tile found in the vessel. Needless to say, the falling tile triggered a major plasma disruption. Carbon fibre reinforced graphite has been used in areas where impact of runaway electrons or neutral beams could occur, as these can withstand 30MWm^{-2} for a few seconds.

Consequences for a Reactor

The use of low Z material for the plasma facing components seems still to be the best option. Graphite, as used up to now on JET, behaves generally well but problem areas have been identified such as its role as an impurity source, its high chemical reactivity with hydrogen and its high retention of hydrogen leading to problems with density control and with tritium inventory. Combined use of beryllium carbide and of carbon fibre reinforced graphite is a sensible proposal but this is clearly an area where further research is required.
In order to avoid fragile cooling systems in the immediate proximity of the plasma, the heat load at the divertor plates should be limited to 2MWm^{-2}. To spread the power over a large area and together ease the accuracy required in the shaping of the tiles, the best way seems to sweep the X-point radially.

II.5 Operational Limits

The maximum thermal and mechanical stresses in a tokamak are experienced during plasma major disruptions. The plasma thermal energy is dumped on the limiter and about 50% of the poloidal magnetic energy is dissipated in the vessel walls. The time-scale ranges from 100μs for thermal dump to tens of milliseconds for the dissipation of eddy currents. In addition, runaway electrons are produced in the decaying plasma and can deposit their energy on very small spots (up to 500MJm^{-2}). When the elongation becomes too large (χ1.8), a vertical instability can develop followed by a disruption. In this case, with high currents, vertical forces acting on the vacuum vessel have been measured up to 350tonnes.

Major disruptions occur when the power radiated by the periphery of the plasma, around the q_ψ=2 surface, exceeds the input power in this area or when q_ψ=2 at the plasma boundary. Therefore, they occur preferentially when attempting to increase the plasma density above a limit, which depends on the input power and on the cleanliness of the plasma (see Fig.11) or when attempting to work at a too low q_a value. These can also occur accidentally when a piece of wall material falls into the plasma or subsequent to the crash of "monster" sawteeth where the released energy induces important outgassing from the wall.

Internal disruptions (or sawteeth) present another limitation in performance which can be achieved in JET. The increased volume inside the q_ψ=1 surface is the most likely reason for confinement saturation observed in JET when $q_a < 4$. Fig.12 shows the saturation of the incremental confinement time τ_{inc}(= 8W/8P) when I_p/B(MA/T) exceeds unity in JET (i.e. when $q_a \leq 4$).

So far, JET performance has not been limited by β values that are too high. In experiments performed at 1.4T, and with 10MW ICRF power, the dimensionless factor $g = a.B.\beta/I_p$ has not exceeded 1.6 (i.e. 60% of the Troyon limit).

Consequences for a Reactor
The ignition domain of a reactor must be large enough to avoid operational limits experienced in present days tokamaks. A major disruption at full current cannot be completely excluded and the machine must be able to support the resulting stresses, but repetitive disruptions must be avoided. This means that the required performance should be achieved at $q_a \geq 2.5$ with a reserve in β and with a low enough heat load on the wall. On the other hand, it can reasonably be expected that the ohmic density limit will be overcome in the presence of strong α-particle heating.

Large internal disruptions must also be avoided to ensure a smooth burn of the plasma. By contrast with the present situation, monster sawteeth could be deleterious in a reactor. This depends upon the steady-state current profile, but operating at a medium value of q_a may be necessary. The size of an ignition device must ensure that the central temperature is large enough even in these conditions to sustain production of fusion power.

II.6 Neutron Yield

Maximum neutron yields approaching 10^{16}n/s^{-1} have been observed in JET. Maximum values of Q_{DD} on JET are ≈4x10^{-4}. In a similar 50% deuterium-tritium plasma, the maximum corresponding ratio Q_{DT} would be in excess of 0.1. It must be noted that in these conditions, about half of the neutrons result from reactions between the injected beams at 70/80keV and the target plasma. The other half are produced by true thermonuclear reactions. At low electron density with neutral beam injection, the ion temperature, T_i, significantly exceeds the electron temperature, T_e. Only a combination of NB and ICRF has produced simultaneous high T_i and T_e.

Neutron fluxes in JET have already been sufficient to induce a non-negligible radio-activity of the inner components of the vacuum vessel. When tritium is introduced in JET in 1991, the total value of the ratio Q_{DT} is expected to exceed 0.5. This corresponds to a total nuclear power of about 15MW, taking also into account the beam-plasma reactions. Already, in a D-T plasma, at the achieved temperatures, the percentage of high energy α-particles will be similar to those of a plasma at ignition; it may then be possible to observe the effects of those α-particles in the plasma behaviour and to compare with energetic minority ions created by ICRF.

Consequences for a Reactor

Peak Q_{DD} values achieved in present tokamaks are in an operation mode which is not relevant to an energy producing reactor. These so called "hot-ion" modes cannot be extrapolated towards ignition where the ion temperature should be close to, but lower than, the electron temperature. In a driven system, where the ion temperature could be higher, the recirculating power needed to decouple the ions from the electrons would be prohibitive (see Fig.8).

III HEAT TRANSPORT AND SCALING

The heat and particle transport observed in JET, as well as in other tokamaks, clearly shows anomalous behaviour: the various observed scalings also depend on operating mode. This behaviour has analogies with the appearance of turbulence in fluids. To predict an ignition experiment or a reactor, it is necessary to obtain a plasma description in terms of physics parameters fitting present experiments and allowing calculation of the various temperature and density profiles. This means that the thermal conductivities and the particle diffusion coefficients must be expressed in terms of plasma physics parameters with their proper dimensions. Without even defining local transport, most of the scaling law proposed do not fulfil dimensional constraints.

JET results show a coherence between the anomalous heat conduction of ions and electron and anomalous particle transport. Accordingly, the hypothesis has been made that the anomaly in tokamaks is mainly due to a single phenomenon linked to the topology of the magnetic field. If so, the plasma phenomena of chmically heated plasma, L-mode, H-mode, supershot, etc., must be simulated by the same expressions. It was concluded that a critical temperature model fulfilled these conditions.

In this model, when a critical temperature gradient (which depends on local plasma parameters) is exceeded, anomalous transport develops

$$(\nabla T_e)_c = 5.5\ \left(\frac{\eta j B_t^2}{n^2 T_e}\right)^{1/4} \frac{1}{q} \qquad (2)$$

and

$$\chi_{an} = 0.6 \left| \frac{\nabla T_e}{T_e} + \frac{2\nabla n}{n} \right| \left| \frac{T_e}{T_i}\left(\frac{q}{2}\right)^{1/4} \frac{R}{r} \right| \left| \frac{q^2}{\nabla q B_t R^{1/2}} \right| \qquad (3)$$

where χ is in $m^2 s^{-1}$, T in keV, n in $10^{19} m^{-3}$, B_t in T, lengths are in m, and ηj in V/m; T_e and n_e are the electron temperature and density, T_i the ion temperature, η the plasma resistivity, j the current density, B_t the toroidal magnetic field, and F_e the electron heat flux.

$$\text{If, } |\nabla T| \geq (\nabla T_c), \text{ and } \nabla q > 0$$

$$F_e = \chi_{an}\, n\, |\nabla T_e - (\nabla T_e)_c| \qquad (4)$$

In addition, the ions behave in a similar way:

$$\chi_{ian} \sim \chi_{an}$$

$$\text{with } F_i = \chi_{ian} \left| 1 - \frac{(\nabla T_e)_c}{\nabla T_e} \right| n_i \nabla T_i \qquad (5)$$

These formulae are still subject to some doubt about β_p dependance as the data are not precise enough. (for instance, a dependence on $\beta_p^{1/4}$ could be added): the dependence on geometrical factors such as $k_i.(r/R)$, $(\nabla n/n)$ and $(\nabla T_e/T_e)$ is also difficult to determine as the range of variation is relatively small.

The topology of the magnetic field enters through the shear $(\nabla q/q^2)$. Sawteeth have to be taken into account when q reaches unity in the centre.

The behaviour of the heat flow across the plasma can be compared with the flow of water inside a pipe. A transition occurs at a critical value of the pressure when the turbulent flow sets in at the critical Reynolds number (see Fig.13). Eq.(4) describe a similar behaviour for the heat flow in a tokamak when the transition to anomalous transport occurs above a critical temperature gradient.

This specific model gives a general scaling of the following form for the asymptotic behaviour (at high power).

$$\tau_E \propto \beta^{-\alpha} I_p a R^{1/4} \qquad (6)$$

$$(n\tau_E) \propto q_T^{(1-\alpha)} \left(q_a \frac{R}{a}\right)^{\alpha} I_p^3 B_t R^{1/4} \qquad (7)$$

where q_T is the Troyon factor and α reflects the uncertainty in the β_p dependence. Eq.(3) corresponds to $\alpha = 0$.

Global scalings are useful but only knowledge of radial profiles allow a proper evaluation of plasma performence. Using Eq.(2-4) in a 1-D transport code, good simulations not only of JET results but also of other tokamaks have been achieved [9,10].

The main predictions for JET are given in Table III, where only the thermal component of the α-particle production is taken into account. This model has been also used to predict the size of an ignition device and its conditions of operation. It appears that to ignite within a sensible ignition domain, a tokamak with plasma current capability of 30MA and with a toroidal field of 4-5T is required, i.e. the parameters chosen for JIT. Calculations have also been undertaken for various next-step proposals: Ignitor, NET II and ITER. The dimensions and parameters used are given in Table II.

In these simulations, radiation and dilution caused by impurities were taken into account. The hypothesis is that only low Z impurities ($Z \sim 7$) are present, giving 30% radiation of the total heating power (which include the losses due to recycling particles and charge exchange at the edge), in addition to the Bremsstrahlung which is consistently calculated across the plasma.

Sawtooth behaviour inside the $q = 1$ region plays an important role for the ion and electron central temperature. When sawteeth are fully effective, the electron and ion temperature and the current density are flattened inside the $q = 1$ region (see Figs.14, 17(b)). In "monster" sawteeth cases, the temperature of electrons and ions are allowed to develop and the safety factor value is imposed at the centre (see Figs.15, 16, 17(a)). The density profile is not calculated but taken as given by experiment. Generally, this is a relatively flat profile $(\propto [1-(\frac{r}{a})^2]^{1/4}$ or even flatter in H-mode cases.

Improved confinement, mainly due to a peaked density profile, seems unrealistic in a semi-continuous reactor where there are no particle sources to maintain it.

In this model, increased H-mode confinement is due to pedestals developing in regions of very high shear near the separatrix, but the main core of the plasma behaves as an L-mode (see Fig.16). At high power, gains from the H-mode might disappear as the relative influence of the separatrix weakens. Taking into account impurity behaviour, a stationary H-mode has not yet been found experimentally, which precludes considering its enhanced confinement for a reactor. When ELMs are present, operations closer to steady state have been observed, but are generally associated with a partial loss of confinement. Nevertheless, in a transient way an improved confinement regime (H-mode, monster sawteeth) could be useful to ease the transition to an ignited plasma.

Predictions for proposed future experiments are given in Tables IV and V. In those tables, the factor g does not include the pressure generated by the α-particles and brackets indicated that the additional power has been switched off when the α-particle power has reached sufficient level. No bootstrap current has been included.

One conclusion of the simulation is that it is extremely difficult to vary the electron temperature (and consequently the ion temperature) in a tokamak, without involving heating power larger than the α-particle heating. In other terms, ignition could almost be reached without additional heating; only a modest level would be required in a machine like JIT (25-50MW). The increase in thermonuclear power is realised by increasing the density at almost constant temperature (see Fig.17).
The cases labelled "ohmic and α with monsters" in Table IV and V, can be used to compare the predicted ohmic performances of the various machines. Compact high field machines generally suffer at high densities from an insufficient temperature giving rise to a high level of bremsstrahlung and to a low reactivity, even if the confinement appears good (see Fig.15). In general, except in JIT, sawteeth are able to destroy ignition at low q. NET II should behave almost as JIT and therefore has a larger ignition margin than ITER, if technology development is sufficient to permit the parameters in Table II to be reached (see Fig.17).

This code also predicts that, with monster sawteeth or with an H-mode pedestal at relatively low density, JIT could reach ignition without additional heating.

IV POSSIBLE NEXT STEP TOWARDS A DEMONSTRATION REACTOR (DEMO)

IV.1 Reactor Studies

Reactor studies show that the thickness of the blanket and shielding inside the coils, e_b, should exceed 1m (i.e. 1.5-2m). To use the magnetic field efficiently, the plasma radius, a, should be greater than $2(e_b+e_c/3)$, where e_c is the toroidal coil thickness; this gives as a minimum size of a=3m [11]. With a toroidal field of 4-5T, and an elongation of 2, the plasma current capability of such a machine should be over 30MA. Such a reactor should be able to ignite in the L-mode without problems of confinement. It can be seen that too high confinement might even have a negative impact on the impurity level and on the exhaust of the helium produced; the rate of diffusion of helium towards the wall and of fuel towards the centre needs to be fast enough to maintain the plasma reactivity. Already a particle diffusion coefficient 5 times lower than the heat diffusivity, as it is observed on JET, will affect the power output of the reactor.

IV.2 Questions Relating to First Wall and the Plasma

Before a power reactor can be built, the following problems involving the plasma and the first wall still need to be solved:

1. plasma wall interactions: fuelling, exhaust and level of impurities;

2. concept of the first wall with the high heat transfer elements, erosion of the limiter and divertor plates, and retention of tritium within the first wall;

3. necessity of maintaining smooth operations free of disruptions, giant sawteeth, collapse of H-modes, etc.

IV.3 Next-Step Device

A next-step device could be aimed at producing a full reactor plasma reactor and at demonstrating that solutions for the first wall and smooth plasma operations could be found. Such a plasma will require a very long burn (~30 mins) and a high duty cycle (semi-continuous operation). Such requirements mean that it will also be possible to test the concept of different blankets for DEMO. This specific choice allows a large ignition domain depending on q and on plasma density: the power produced could vary in the range 500-4000MW. The best way to reach ignition appears to start with a plasma at a relatively low density with a moderate current of 25MA and to increase the density and plasma current when ignition is reached to produce a power level of several GW (similar to that of a reactor). This should demonstrate the potential of fusion as an energy source. Such a device is referred to as a "thermonuclear furnace" and a possible choice of parameters (JIT) is given in Table VI.

IV.4 Semi-Continuous versus Continuous Operation

One of the questions which has an overall impact on the choice of solution and on the very concept of a reactor is that of the necessity of continuous operation, which seems almost incompatible with the concept of ignition.

In a reactor, the central temperatures should reach 25keV or more and therefore the voltage per turn will be extremely low (~0.05V or less). Flux consumption of 100V.s during the flat-top will ensure a burn time of more than 30 mins which could even exceed 1 hour in the presence of bootstrap currents near the beta limit. A high duty cycle could be obtained by reversing the plasma current when the transformer has reached saturation.

Continuous operation of a tokamak is more complex in terms of physics and equipment. High energy neutral beams or radio-frequency techniques are required to drive the current. However, the efficiency of non-inductive current drive is quite low compared to the use of a transformer and the gain in the duty cycle may not be significant. In addition to the cost and the complexity of equipment

needed for current drive, the recirculating energy would also increase the overall cost of electricity produced by an amount which could become a dominant factor and condemn such a concept.

On the other hand, semi-continuous operation requires a moderate intermediate thermal storage or a set of tokamak-reactors working together. The main advantage of continuous operation is to reduce the thermal fatigue of components inside the reactor but as long as the burn time is longer than 1 hour this may not be important.

In conclusion, semi-continuous operation with long burn for a next-step device seems to be a proper solution taking into account the complexity of non-inductive current drive and its doubtful relevance for a reactor.

IV.5 Tritium Consumption

The consumption of tritium is proportional to the energy produced 5.5g/GW$_t$h; it is also proportional to the product of the fluence and the surface area of the walls. If a certain fluence is required for testing blanket elements of a given dimension, and if parallel testing of different blankets can be done, the consumption of tritium will be equivalent for various machines. If parallel testing cannot be done, the consumption of tritium will be proportional to the surface area which may not vary more than a factor 2 between different concepts of next-step device.

To maintain simplicity and considering the duty cycle and tritium consumption in the next machine, a breeding blanket seems an unnecessary complication for an apparatus which is unlikely to test any blanket material at high neutron fluence. For the next step, although some test modules of breeding blankets could be introduced, only neutron shielding has to be provided.

IV.6 Conclusions on a Next-Step Device

In conclusion, the next generation of tokamaks must demonstrate that an ignited and burning plasma at high power with semi-continuous operation can be realised.

The aims of such an experiment could be:

- to study the ignition domain;
- to test wall technology;
- to test some breeding blanket modules for DEMO;
- to demonstrate the potential of fusion as an energy source.

From JET results, such a machine can be defined, but it requires a large ignition domain to operate safely with minimum scientific risks. In the same spirit, technical risk for the apparatus must be kept low and the simplicity of the concept must be paramount.

V DESCRIPTION OF THE THERMONUCLEAR FURNACE

V.1 Introduction

The main design characteristics of a thermonuclear furnace (JIT) to meet these objectives are presented, of which the main priorites are simplicity and sturdiness of concept. Basically, the plasma parameters are scaled up from JET by a linear factor of 2.5 and several elements of the JET concept are maintained.

To minimize technical risk, size of the coils, shielding and overall cost, water cooled copper magnets are proposed but superconducting magnets could be envisaged, if advantages compensated for the extra complexity. Low current density is used in the water-cooled copper coils to allow continuous operation. A large flux swing (≳400V.s) would also provide the necessary drive to maintain the flat-top currents for periods up to one hour.

A general view of the apparatus is given in Figs.18 and 19. It should be noted that the magnetic circuit is also used as a radiation shield around the machine.

V.2 Vacuum Vessel, Toroidal Coil, Mechanical Structure

The device concept is based on a highly integrated and modular construction where all the elements would be manufactured on-site, as transport of components of this size would not be possible.

The machine basically consists of 20 sectors supported radially by a cylinder formed by the ohmic transformer. Each of these sectors integrates the toroidal coil, the vacuum vessel and the mechanical structure (see Fig.20). These different sectors are assembled together by welding flexible lips. The torque induced by the vertical field is taken in shear by the light structure which encloses the toroidal coil. This structure around the toroidal coil is sufficiently thin to allow the plasma current to penetrate through the torus. An insulated mechanical element on the external part of the coil directly transmits the shear forces.

The coils are made of a single pancake of water cooled copper corrugated in order to transmit the shear forces while the insulation remains purely in compression (see Fig.21). This feature would allow the use of a purely inorganic insulator for insulation of the coil inner turns, making it possible to withstand high radiation levels. At 4.5T toroidal fields, the power dissipated in the coil would be 1.3GW and the stresses in the copper or in the vacuum vessel structure remain at an acceptable level.

V.3 Poloidal System

The magnetic configuration contains a single null X-point (see Fig.22), where the X-point is located in the lower position to allow the foundations to take the extra forces resulting from the presence of the separatrix giving more access at the top of the machine. This position also decreases the risk of broken tiles falling into the plasma. The presence of the X-point would allow transient H-mode operation during the transition to ignition, but its main purpose is to provide pumping of the plasma at relatively high pressure.

The position of the poloidal coils is similar to that in JET. The coils are Bitter type and made by sectors of thick copper plates (3-4cm) welded together (see Fig.23). Water flowing through holes perpendicular to the plates provides essential cooling. The insulation is not bounded and the whole could be immersed in water. These coils are supported by a magnetic circuit which also provides

radiation shielding. The magnetic circuit is conceived as a massive metallic building. This concept allows the use of ordinary concrete for the foundations and the other elements of the external building.

The total flux swing of the ohmic transformer is 420V.s and the maximum resistive consumption is ~350MW. The flux needed to establish the magnetic configuration at 30MA is 270V.s leaving 150V.s for resistive dissipation during the start-up phase and flat-top. Table IV shows that the loop voltage during flat-top could be as low as 0.04V.

V.4 Internal Shielding and First Wall

The shielding is made of several elements which could be dissassembled remotely without dismantling the main apparatus (see Fig.24(a) and (b)). Each of these elements is made of a single box structure filled with pebbles of metal directly cooled by water (see Fig.21). One of the main problems in maintaining shielding efficiency is the presence of gaps to allow remote handling and thermal expansion of the different elements. These gaps reduce the shielding locally and could permit a high neutron flux to reach the coils. The overall layout includes a series of thicker elements which could easily be replaced by reactor relevant breeding-blanket test modules (see Fig.24) without any modifications of the initial shielding and of the plasma parameters.

The first wall itself is formed by the surface of the shielding box facing the plasma with only local protection by carbon tiles which radiate energy received at a temperature ~1500°K. These tiles would serve as a protection against disruptions from runaways and would mainly cover the inner wall and top and bottom of the machine.

A continuous deposition of beryllium could ensure that the first wall seen by the plasma is of beryllium or its carbide. This would help to limit sputtering and outgassing of the tiles. This design does not present major problems at a load of 2MW/m² for the fusion power produced. The main parameters of the first wall are given in the Table VII.

V.5 Divertor

The divertor presents the main technical challenge in the design of inner wall components. This challenge can be reduced to a managable level if the region of high power deposition is expanded over a larger area. This can be achieved by moving the X-point vertically or horizontally using the existing coil set or preferably by using a set of internal saddle coils. Alternatively, the movement could be achieved by oscillating divertor components horizontally. The main advantages of this scheme would be:

- no need to position the divertor components with mm accuracy (as required in JET) and a feed-back technique could be used;
- in spite of high local thermal loads, the average load remains small;
- heat transfer to the cooling medium corresponds to the average load;
- lifetime increases by reducing the ratio of peak load to average load:
- to compensate for erosion, material (beryllium, hydrocarbons) could be injected;
- deposited and redeposited layers are burned off before they can flake and before large amounts of tritium could accumulate.

For the movement, the limiting factor is the sweep frequency which should be low enough to allow a relatively simple set of additional coils in the vacuum vessel, but on the other hand, should be high enough to minimize thermal stresses in the divertor material.

Fig.25 shows a cross-section through the divertor region, in which the divertor plates extend above and below the X-point. These receive only a moderate average power level of 1.3MWm⁻² from radiation and conduction. The X-point can be moved horizontally by local saddle coils. The target tiles intersect the magnetic flux surfaces at a small angle of incidence and therefore a small radial displacement of the X-point allows a distribution of the power load over the whole divertor surface.

The material proposed for the divertor plates is 40mm thick carbon fibre graphite. It is brazed in 10x10mm² surface area blocks to water cooled copper plates of 10mm thickness. The average heat flux (conduction plus nuclear heating) is ~1.8MWm⁻² which could be removed without having to resort to two phase cooling. In the proposed design, peak surface loads during the sweeping of the X-point would be about a factor of five higher than the average load (~10MWm⁻²). For the calculation of thermal response, the high thermal conductivity of the fibre graphite was not taken into account as it degrades at low neutron doses (~10²⁰cm⁻²) to that of fine grain graphite [12]. For a sweep frequency of 1Hz, surface thermal stresses would be about 25MPa in compression (limit 100MPa) and the peak temperature would be ~1400K. The material thickness is mainly limited by the average load and the resulting front temperatures.

It is proposed to continuously cover the graphite divertor with a thin layer of beryllium to take advantage of the good properties of both materials. A beryllium carbide layer would be formed [13] at temperatures above 700K. It is envisaged that such a scheme will be confirmed in JET.

The lifetime of the divertor plates would be determined by the erosion due to particle impact. A detailed modelling of the plasma edge and the divertor region is required to assess particle fluxes and energies. This is presently not yet available. Therefore, a worst case assessment is made. The energy (~300eV) and the temperature (~750K) of the maximum sputtering yield is taken for the sputtering of carbon by deuterium. When smaller than unity, the self sputtering of the divertor plates is one of the mechanisms which determines the redeposition rate [7].

Neglecting any increase in lifetime of up to a factor 3-10 due to lower particle energy, possible suppression of chemical activity and redeposition, the lifetime should be at least two months of continuous operation at a level of 2.5GW of thermonuclear power. The pumping is carried out by cryopumps with charcoal.

V.6 Auxiliaries and Buildings

1. Additional Heating

As has been seen in the simulation, JIT could reach ignition with ohmic heating alone during monster sawteeth or in the H-mode

regime. Nevertheless, it would be prudent to consider a moderate level of additional heating of ~50MW, which could be ion cyclotron heating (analogous to that in JET). This power would only be used in a transient way (with increased efficiency to that in JET): the power density is lower and the coupling would be improved as more room would be available for the antennae. The radio frequency antennae would be an integral part of the shielding and vacuum vessel in the outer regions. This choice also ensures that the centre of the plasma could be heated.

2. Tritium Plant

Little study has been done on the tritium plant but a modest upgrade of the JET tritium plant should be sufficient to feed the machine. The pumping is done using cryogenic techniques for hydrogen isotopes as well as for helium. Extra elements for the detritiation of the cooling water might be necessary. As a full breeding blanket is not envisaged, there is no corresponding plant.

3. Building - Cooling Plant

The first concept of the building to house such an experiment is shown in Fig.19. This building includes all the facilities for remote handling, maintenance and dismantling.

The cooling power for such an installation must have a peak capability of 6GW, but a much lower average requirement. The method of achieving such cooling depends strongly on siting. The preferred solution would be to take cold water from a lake or sea. The hot water produced during the peak operations could be stored temporarily.

V.7 Cost and Time-Schedule

An approximate cost for such an experiment has been derived from data collected at JET. The cost of the main components is shown in Table VIII, which does not include the test blanket modules. This brings the total construction cost to a value close to 2000MioEcu (1988) without contingencies. Including contingencies and overall cost; 2500MioEcu seems realistic.

Up to 400 professionals over a period of 8 years might be necessary to construct such a device.

VI SUMMARY AND CONCLUSIONS

In conclusion, JET has proved to be a highly successful European collaborative Project. The Project is now midway through its experimental phase, during which its achievements have been significant and has placed it as the major experiment in world fusion research. It is now well set to demonstrate substantial α-heating in a thermonuclear plasma.

The main conclusions are:

1. Plasmas of a thermonuclear grade have been obtained in JET but a large step is still required to reach ignition.

2. JET data shows that a tokamak with a plasma current capability around 30MA is required to produce ignition of a D-T plasma in a practical domain. With lower values of current, the risk of not achieving ignition is large, if sawteeth, impurity radiation, dilution etc., are taken into account.

3. In an optimized reactor, the size would be defined by the blanket and this leads to a tokamak with a current capability greater than 30MA.

4. Confinement would no longer be the dominant problem. However, major uncertainties are in the areas of plasma-wall interaction, fuelling, exhaust and impurity control.

5. Technical considerations of stress level, wall loading and economy result in a concept of a "Thermonuclear Furnace" producing a thermal output of several GW in semi-continuous mode.

6. This device is aimed at demonstrating the potential of a Tokamak Reactor and to test wall technologies and breeding blankets.

7. For such a device, priority must be given to the simplicity and reduction of technical and scientific risks.

If a European programme is to continue, it is important to build on JET achievements and retain and utilize the skills and expertise of its staff as well as their dedication to demonstrating controlled fusion power. To meet these objectives a next step must be conceived which clearly establishes the potential of fusion as a major source of power. Such a device must give a high priority to simplicity of design with minimal technical and scientific risks. It is a Thermonuclear Furnace of several GW. JIT is such a device which seems compatible with the technical and financial capabilities of Europe and would prove that fusion is potentially a major source of future world energy.

VII ACKNOWLEDGEMENTS

The scientific and technical achievements of JET result directly from the dedication of the JET Team [2]. We also wish to thank Drs. K.J. Dietz, B.E. Keen, B. Keegan, E. Lazzaro, T. Molyneux and L. Sonnerup for their help in preparing this paper and calculating some elements of JIT.

REFERENCES

[1] Rebut, P.H., et al, Fusion Technology, 11, pp13-281 (1987);

[2] Gibson, A. and the JET Team, "Plasma Performance in JET: Achievements and Projections", 15th European Conference on Controlled Fusion and Plasma Heating (Dubrovnik, Yugoslavia, 1988) to be published in Journal of Plasma Physics and Controlled Fusion;

[3] Gondhalekar, A. et al, "Simultaneous Measurements of Electron and Particle Transport in JET"; 15th European Conference on Controlled Fusion and Plasma Heating (Dubrovnik, Yugoslavia, 1988), Europhysics Conference Abstracts, Vol.12B, p151;

[4] Behringer, K., et al, "Impurity Transport in JET during H-mode, Monster Sawteeth and after Pellet Injection"; 15th European Conference on Controlled Fusion and Plasma Heating (Dubrovnik, Yugoslavia, 1988), Europhysics Conference Abstracts, Vol.12B, p338;

[5] Tagle, J.A., et al, "The Effect of Edge Temperature on Impurity Production under a Range of Operating Conditions in JET"; 14th European Conference on Controlled Fusion and Plasma Physics (Madrid, Spain, 1987), Europhysics Conference Abstracts, Vol.11D, p662;

[6] Kock, L., et al, Role of the Scrape-off Layer in X-Point Discharges in JET; 15th European Conference on Controlled Fusion and Plasma Heating (Dubrovnik, Yugoslavia, 1988), Europhysics Conference Abstracts, Vol.12B, p655;

[7] Rebut, P.H., Diêtz, K.J. and Lallia, P.P., "Experience with Wall Materials in JET and Implications for the Future"; 8th International Conference on Plasma Surface Interactions in Controlled Fusion Devices (Jülich, F.R.G., 1988), to be published in J. Nucl. Mater. (see JET Report JET-P(88)21);

[8] Cohen, S.A. and the JET Team, "Particle Balance and Wall Pumping in Tokamaks", Controlled Fusion and Plasma Physics, 29, 1205 (1987);

[9] Rebut, P.H., Lallia, P.P. and Watkins, M.L., "Analysis on JET Results and Impact for the Future", 12th IAEA Conference on Plasma Physics and Controlled Nuclear Fusion Research, Nice, France, 1988) to be published;

[10] Taroni, A., et al, "Global Power Balance and Local Heat Transport in JET", 12th IAEA Conference on Plasma Physics and Controlled Nuclear Fusion Research (Nice, France, 1988) to be published;

[11] Reynolds, P. and Worraker, W.J., Study of the Reactor Relevance of the NET Design Concept, Culham Laboratory Report; CLM-R278 (1967);

[12] Kelly, B.T., "Physics of Graphite", Applied Science Publishers, London and New Jersey, 1981;

[13] Nich, T.G., et al, Scripta Metallurgica, 20 (1986) 87;

TABLES

Table I
Major enhancements to JET carried out in 1987

Extensive improvements to the main poloidal circuit to give: improved X-point operation improved control of current rise phase increased volt-second capability	Second NBI box *(first injection, into JET May 1988)* Cryo pellet injection system *(single pellet using Garching gun; multiple pellet using ORNL gun, in collaboration with US–DOE)*
New dual belt limiter system *(carbon tiles on a water cooled base)* plus, carbon tiles on all exposed surfaces *(specially shaped at X-point target)*	Improved vessel mechanical restraints for disruption protection
Eight ICRF antennae between the belts *(water cooled carbidised nickel Faraday screens; carbon side tiles)*	Increased diagnostic capability, especially: Time of flight laser scatter system **(LIDAR)** to measure $T_e(r)$; $n_e(r)$ Faraday rotation polarimeter to measure $B_\theta(r)$

Table II

Main parameters of various devices simulated with the 'critical temperature' code

	R	a	k	B_t	Add.Power	I_p
	m	m		T	MW	MA
JET	3	1.2	1.7	3.4	40	7
ITER	5.8	2	2.2	5.1	100	20
JIT	7.5	3	2	4.5	50	30
Ignitor	1 16	0.43	1.8	14	10	12
NET II	6	2.2	2.2	5.4	50	27

Table III
Predictions for JET; 'critical temperature' simulations

Device	I_p (MA)	n_{e0} ($10^{19}m^{-3}$)	Z_{eff}	P_{add} (MW)	T_{i0} (keV)	$\bar{T}_e$ (keV)	P_α (MW)	g	P_{OH} (MW)	Regime
JET	7	7.5	2	0	3.5	2.6	0.014	0.24	5.6	ohmic q = 1
	7	7.5	2	40	12	5.2	2.2	1.22	3	monster L-mode q = 0.8
	7	7.5	2	40	5.6	3.7	0.5	0.86	3.2	L-mode q = 1
	6	7.5	2	20	11	5.2	2	1.6	1.4	H-mode + monster q = 0.8: Pedestal T_e = 1.5keV
	7	4	2	20*	25	5.8	2.5	0.94	2.1	Hot ion L-mode monster q = 0.8

*NBI heating; 80% of the power coupled to ions.

J CR 88 158 4

Table IV
Predictions for JIT using 'critical temperature' simulations

Device	I_p (MA)	n_{e0} ($10^{19}m^{-3}$)	Z_{eff}	P_{add} (MW)	T_{i0} (keV)	$\bar{T}_e$ (keV)	P_α (MW)	g	P_{OH} (MW)	Regime
JIT	30	5	2	0	5.6	3.9	0	0.25	18	ohmic without α (q = 1 sawteeth)
	30	5	2	0	25	11	90**	0.77	5.5	ohmic + α monster q = 0.8 **Ignited**
	20	10	2	(50)*	29	15	511	3	0.75	L-mode Sawteeth (q = 1) **Ignited**
	20	10	3	50	10	5	51	1	5.9	L-mode Sawteeth (q = 1)
	20	10	3	(50)*	32	12	262	2.3	20	L-mode Monster **Ignited**

* Brackets indicate that P_{add} has been switched off when P_α was large enough.
** P_α still rising.

Table V

Predictions for different experiments;
using 'critical temperature' simulations

Device	I_p (MA)	n_{e0} ($10^{19}m^{-3}$)	Z_{eff}	P_{add} (MW)	T_{i0} (keV)	$\bar{T}_e$ (keV)	P_α (MW)	g	P_{OH} (MW)	Regime
ITER	20	15	2	100	18	11.7	300	2.1	1.9	L-mode Q = 15 q = 1
	20	15	2	(100)*	30	13.2	380	2.4	2.2	L-mode monster q = 0.8 **Ignited**
	20	5	2	0	9.8	4.5	4.5	0.27	9.8	Ohmic + α monster,q = 0.8 Q = 2.3
NETII**	27	5	2	0	13	6.3	13.3	0.3	11	Ohmic + α monster Q = 6
Ignitor	12	100	2	10	9.2	4.4	11.6	0.7	25	Monster Q = 1.7
	12	100	2	0	8.2	4	8.3	0.62	27	Ohmic + α Monster Q = 1.5

* Brackets indicate that P_{add} has been switched off when P_α was large enough.

**At 27MA NETII ignites with 50MW of additional power.

J CR88 158 2

Table VI

Main Parameters of a Thermonuclear Furnace (JIT)

Plasma minor radius (horizontal)	(m)	3
Plasma minor radius (vertical)	(m)	6
Plasma major radius	(m)	7.5
Plasma aspect ratio		2–2.5
Flat top pulse length	(s)	1000-4000
Toroidal field (plasma centre)	(T)	4.5
Plasma current	(MA)	30
Volt seconds	(Vs)	425
Additional heating	(MW)	50
Fusion power	(MW)	500–4000

P CR88 46 1A

Table VII

JIT: Loads on Wall Components at 3 GW(th)

Surfaces		
Wall	(m^2)	1660
Divertor (swept)	(m^2)	190
Wall loads		
Nuclear heating (graphite)	($MW m^{-3}$)	12
Radiation	($MW m^{-2}$)	0.2
Neutron flux	($MW m^{-2}$)	1.5
Divertor loads (when swept)		
50% radiation on 300 m^2	($MW m^{-2}$)	1
50% conduction on 200 m^2	($MW m^{-2}$)	1.5
Nuclear heating (graphite)	($MW m^{-3}$)	12

J CR 88 1583

Table VIII

JIT: Cost Estimate

Machine			
	Poloidal coils	165	
	Toroidal coils	261	
	Vacuum vessel	64	
	Shielding, First wall	100	
	Mag. circuit	60	
		650	MECU
Auxilliaries			
	Building	200	
	Heat Exchanger	150	
	Tritium Pumping	70	
	Remote Handling	50	
	Power supply	150	
	Additional heating	180	
	Control	150	
		950	MECU
	Machine	650	
	Auxilliaries	950	
	Personnel	200	
	Total	2000	MECU
	Contingencies 20%	400	MECU

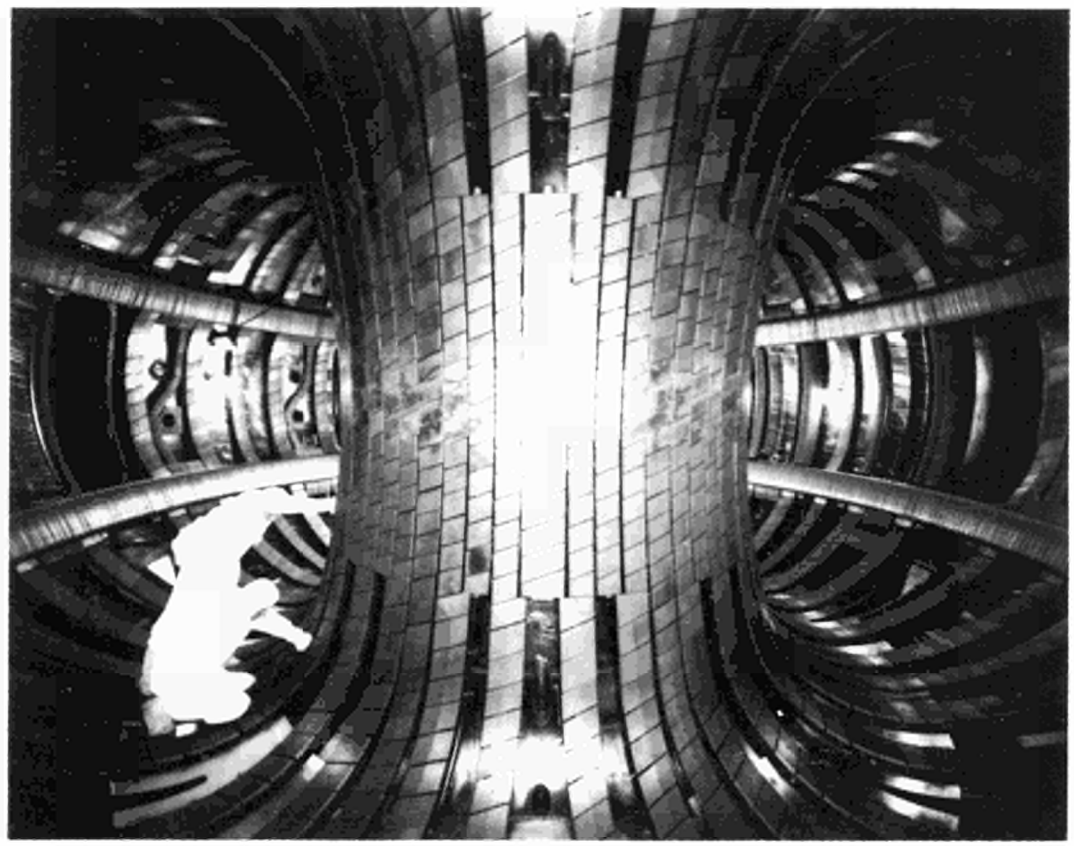

Fig. 1 Status inside the JET vacuum vessel after the 1987/88 shutdown. A large fraction of the vessel was covered with carbon tiles and the metal surfaces were blackened by carbonization. The inner wall protection tiles, the bottom tiles on which the separatrix lies, the belt limiter, the antennae and their protection frames are shown.

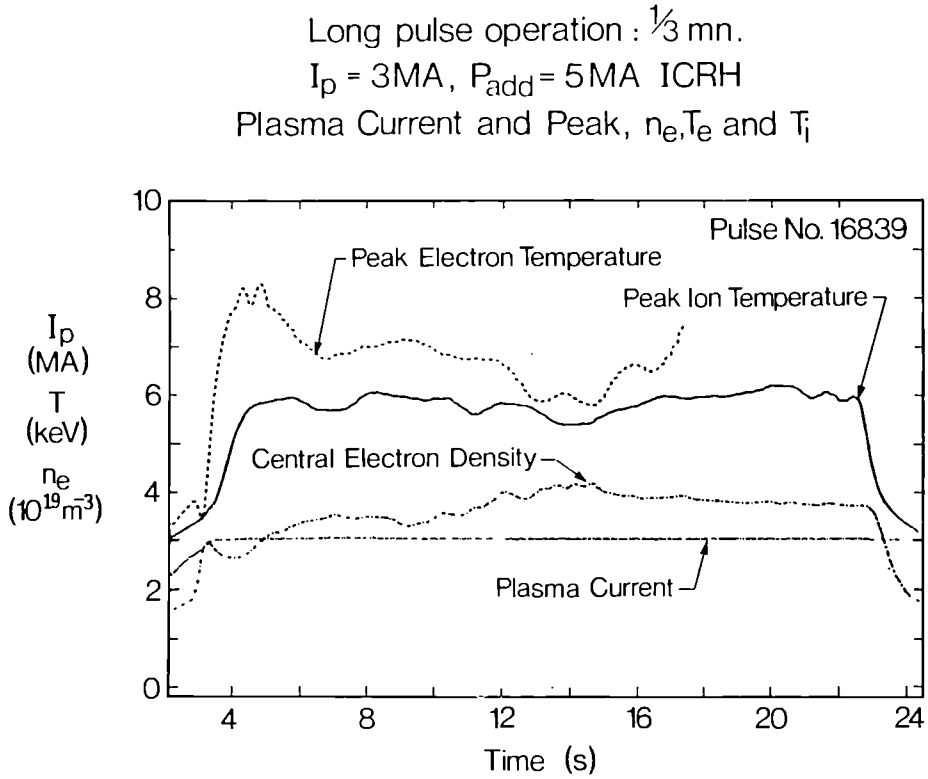

Fig. 2 Quasi-stationary plasma of duration exceeding 30s at temperatures in excess of 5 keV. The 3 MA plasma was heated by 5 MW ICRF power.

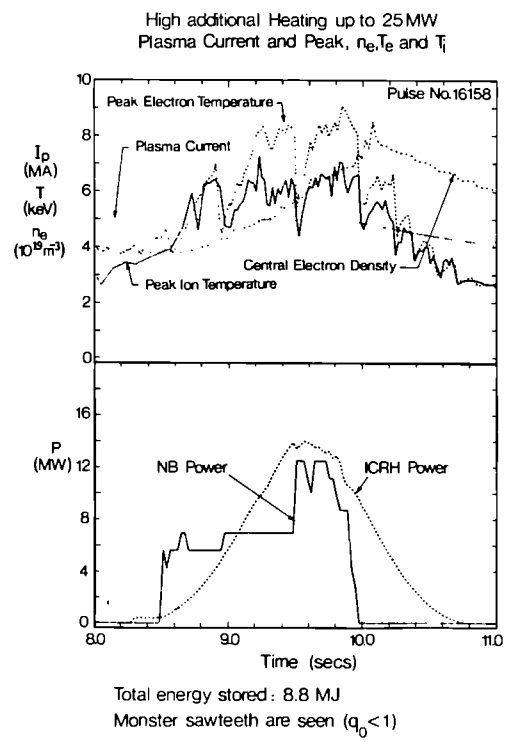

Fig. 3 Evolution of a 5 MA plasma when heated with additional power reaching 25 MW, as shown in the lower figure. The toroidal field is 3.2 T and the stored energy is 8 MJ. The presence of giant sawteeth during the heating is clearly seen.

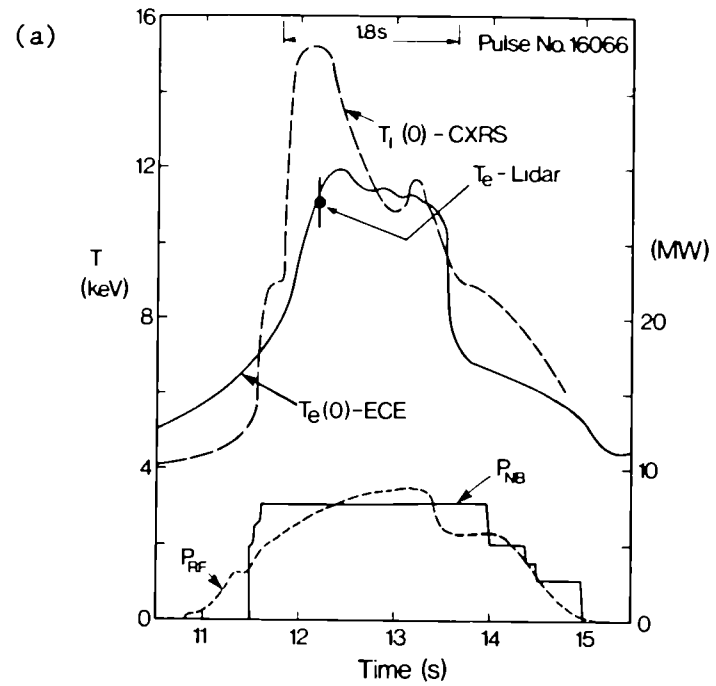

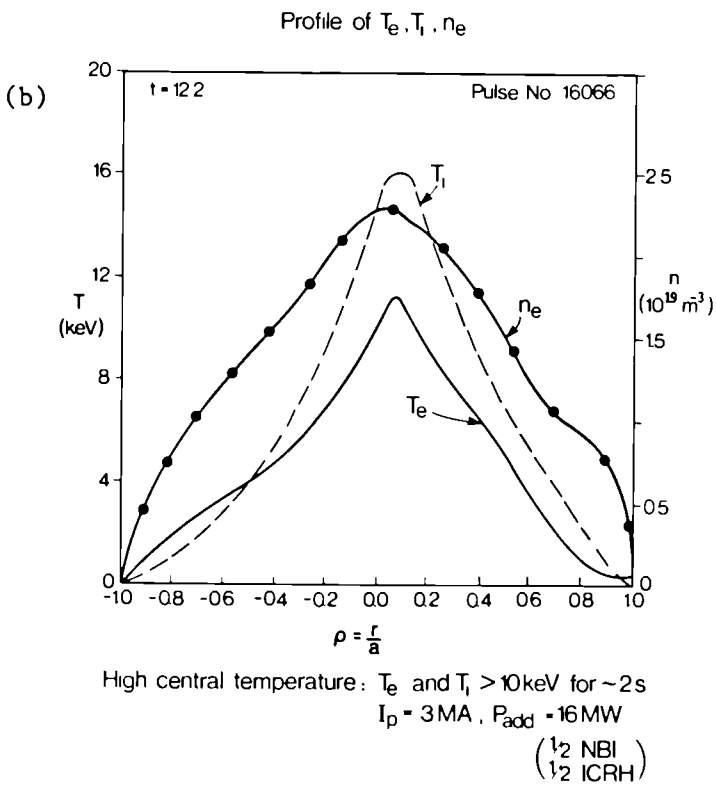

Fig. 4 (a) Peak electron and ion temperatures as a function of time during RF and NB heating; (b) Density and electron and ion temperature profiles at 12.2s for the same pulse No. 16066, which was a double-null X-point plasma at $I_p = 3$MA, $B_0 = 3.2$T.

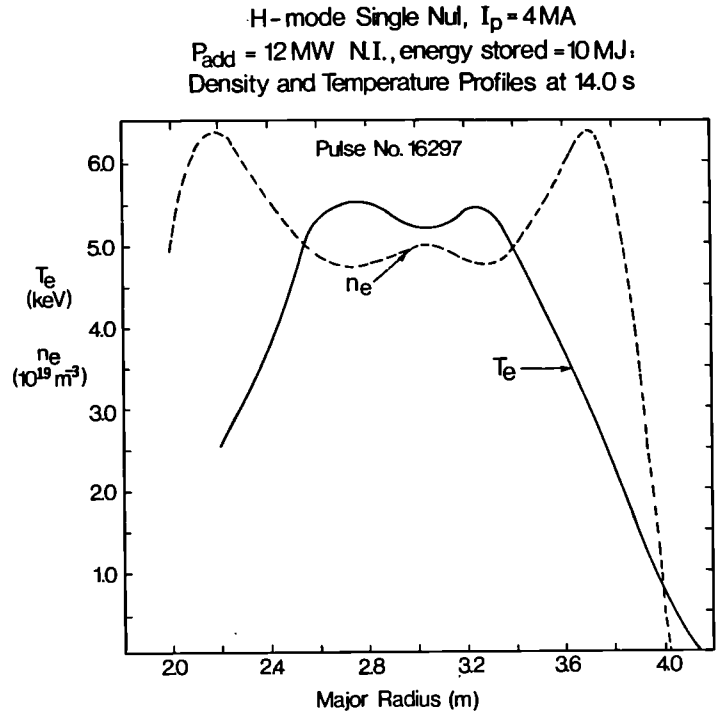

Fig. 5 Density and temperature profiles for a 4MA H-mode plasma with a confinement time reaching 1s. The fusion product ($n_D\ T_i\ \tau_E$) reached 3.4×10^{20}m^{-3}keVs. It should be noted that the density profile is hollow and that a temperature pedestal is not apparent (may be due to poor radial resolution (~10cm)).

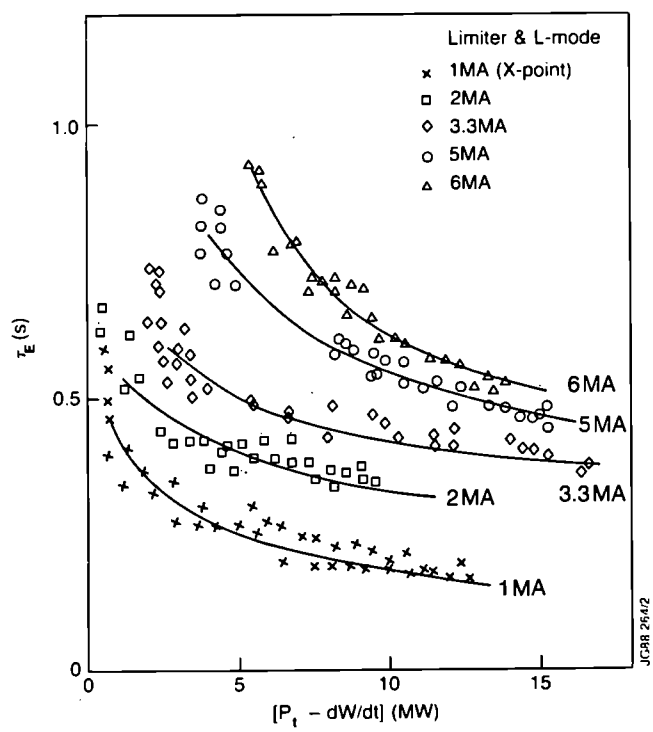

Fig. 6 L-mode confinement time, τ_E, data versus input power, showing degradation with power. The strong degradation of confinement time and the beneficial effect of plasma current is clearly seen.

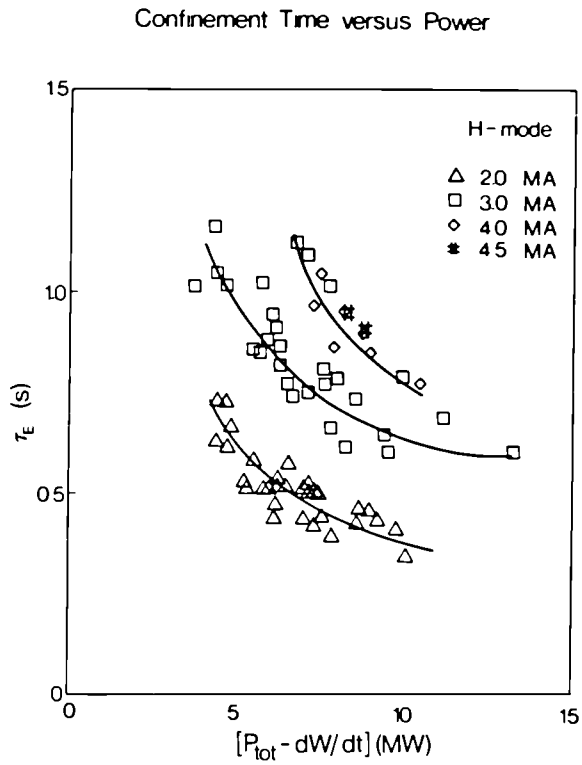

Fig. 7 H-mode confinement time, τ_E, data versus input power showing clear degradation with power. However, confinement is improved by a factor 2 to 3 over the corresponding L-mode case.

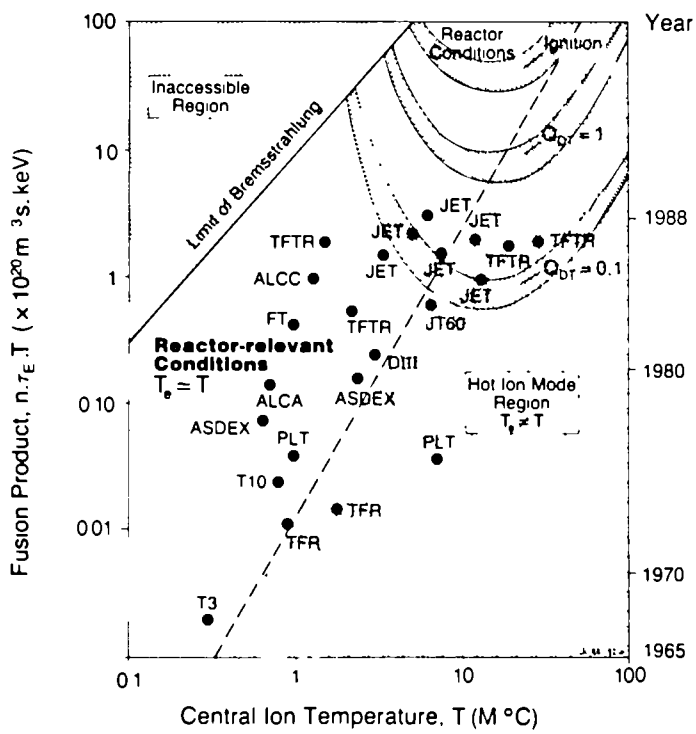

Fig. 8 Fusion parameter as a function of central ion temperature for various fusion devices. The mode of operation relevant for a reactor is where the electron and ion temperatures are nearly equal at values between 15 and 50 keV. The high density/low temperature region is forbidden due to radiation losses.

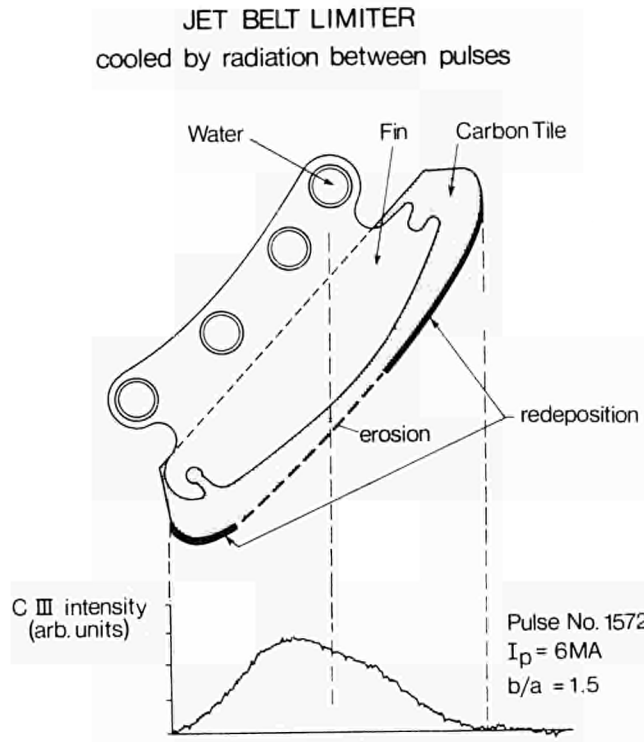

Fig. 9 Cross-section of the belt limiter with radiating tiles on water cooled fins. The carbon intensity is shown together with erosion and redeposition zones.

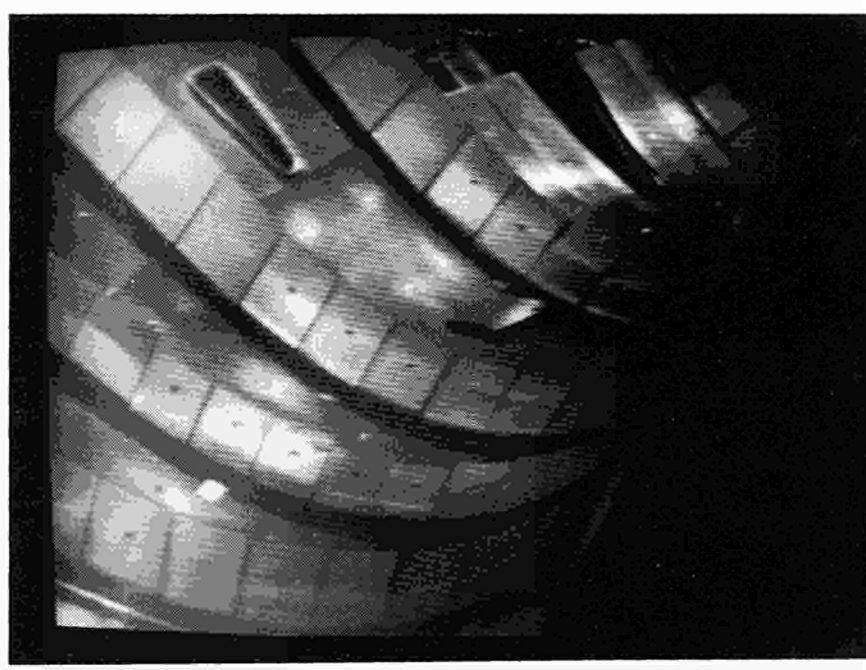

Fig. 10 Picture of the bottom of the JET vacuum vessel taken with a remote handling viewing system. A graphite tile which failed during X-point operation is shown.

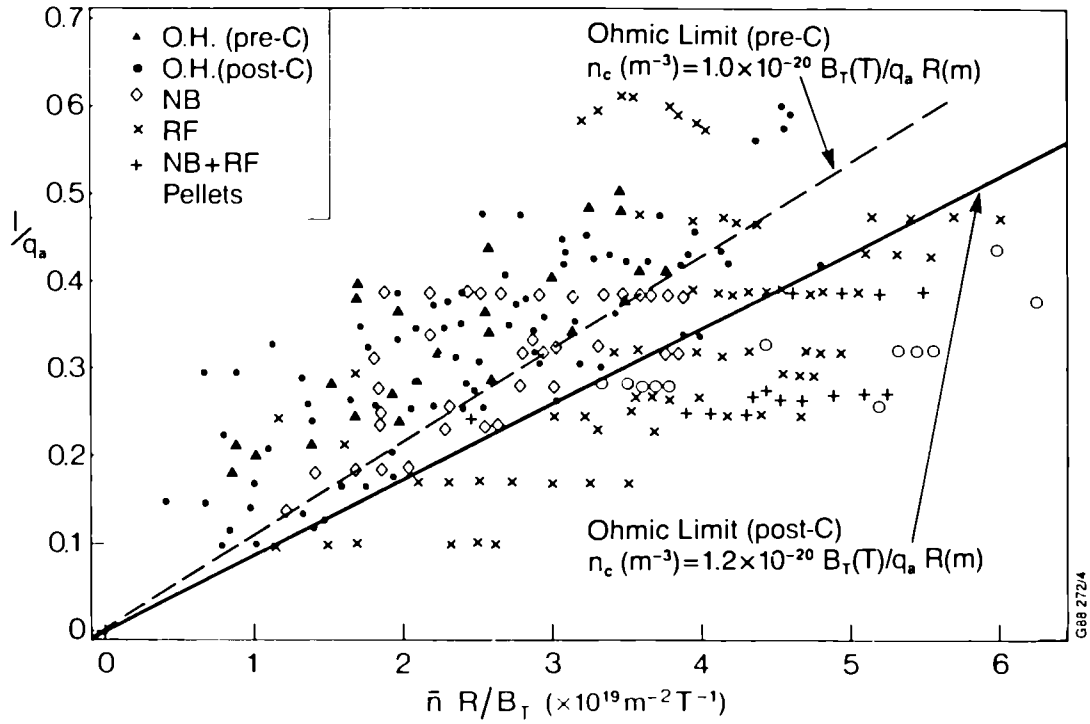

Fig. 11 Shows the Hugill diagram for the density limit. The limits for ohmic discharge without carbonisation, and with carbonisation (low Z) are indicated. Pellets and additional heating allow a higher density to be reached before a disruption occurs.

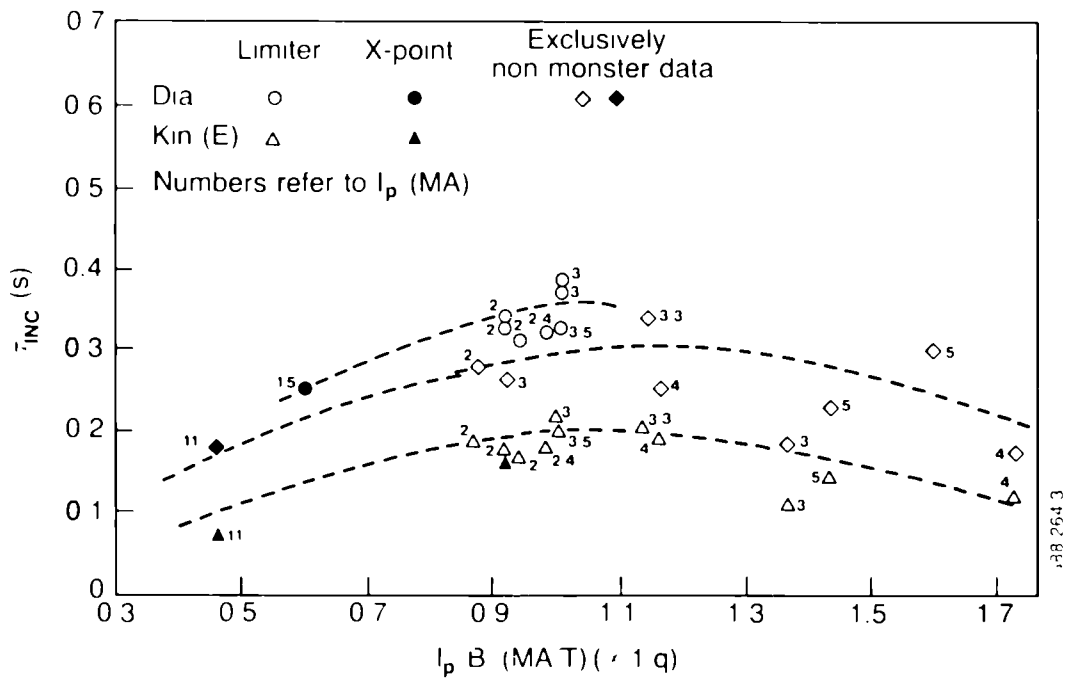

Fig. 12 Incremental confinement time, τ_{inc} ($= \partial W' \partial P$) as a function of (I_p B) ($\propto 1$ q). The effect of the saw teeth on confinement can be seen where the maximum incremental confinement time is reached for a value of $q \sim 4$ (I_p $b \sim 1$).

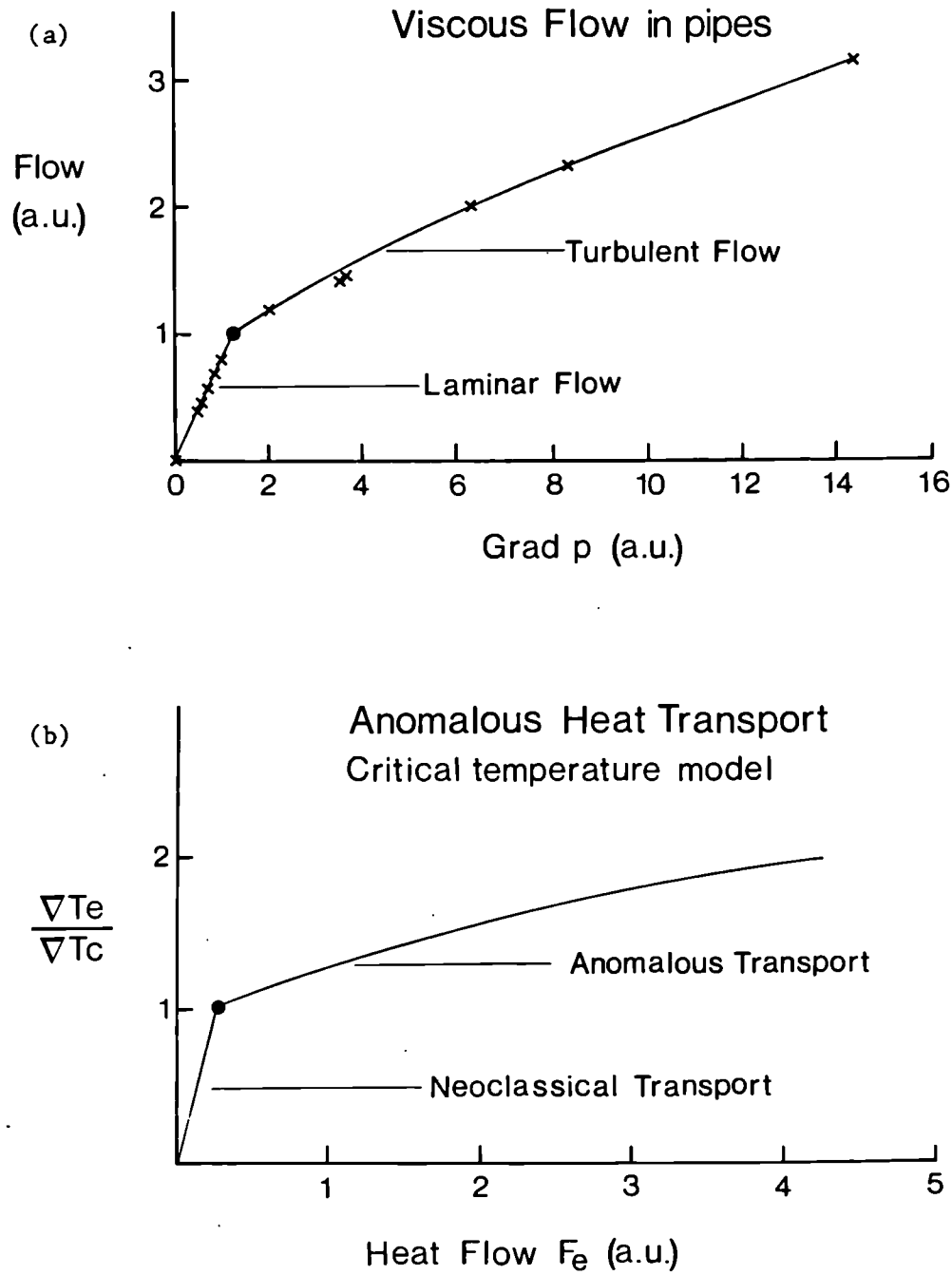

Fig. 13 (a) The experimental relationship governing the flow of a liquid through a long pipe is shown. When the Reynolds number R reaches the critical value R_c, extra resistance is added to the flow which increases with the value of the Reynolds number (curvature of the curve in the turbulent flow regime); (b) For given temperature, density, magnetic field etc., the dependence of the heat flow with electron temperature gradient in the critical temperature model shows the same behaviour: when ∇T *reaches* ∇T_c anomalous transport appears which increases the heat flow. This anomalous transport also varies non-linearly with the ratio ($\nabla T_e / \nabla T_c$).

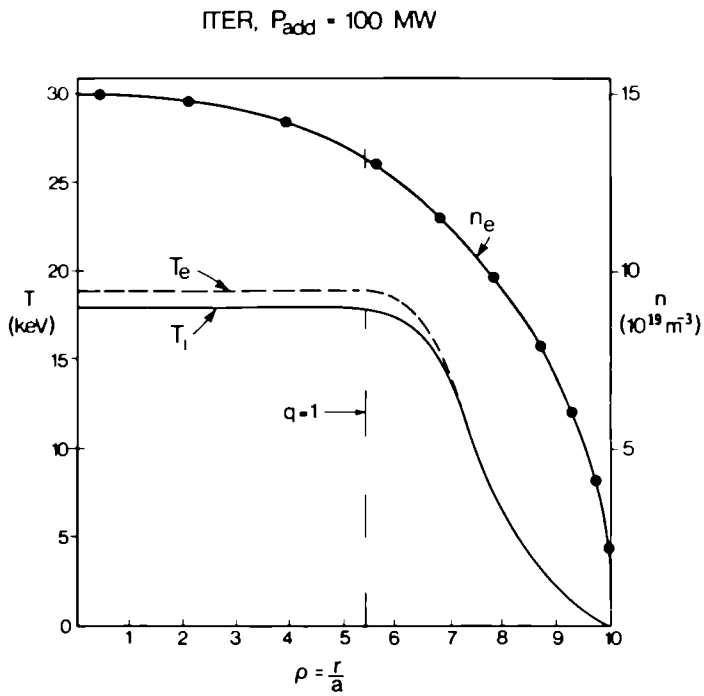

Fig. 14 Critical temperature model simulation of ITER with 300MW of additional power. Ignition is not reached mainly due to the effect of sawteeth. The temperature has been flattened inside the $q=1$ region.

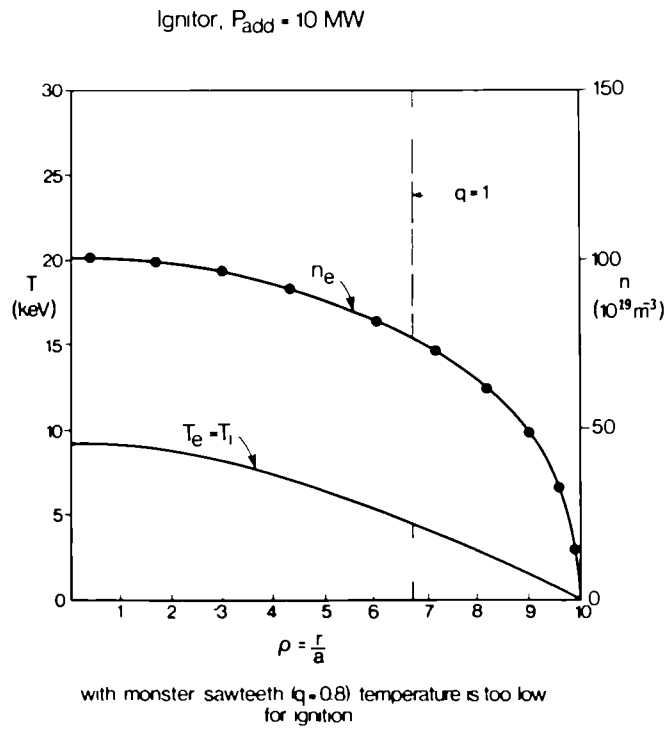

Fig. 15 Critical temperature model simulation of IGNITOR, with additional power of 10MW. The temperature has been allowed to peak inside the $q=1$, simulating a monster sawtooth with q on axis of 0.8. Ignition is not reached as the mean temperature is too low; Bremsstrahlung and impurity radiation play an important role ($Z_{eff}=2$).

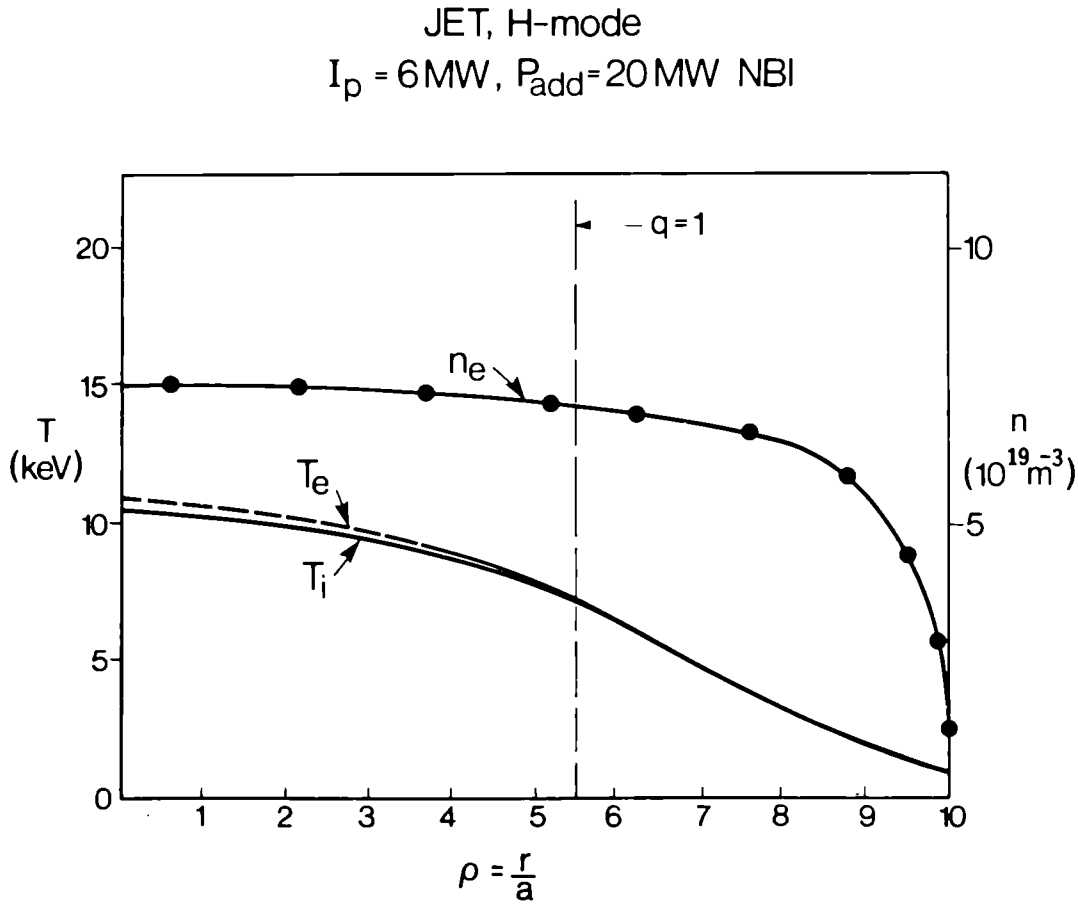

Fig. 16 JET H-modes are fully simulated if the experimental density profile is taken with a pedestal of 1–2keV at the separatrix. The simulation is made for an H-mode at 6MA with 20MW of neutral beam power.

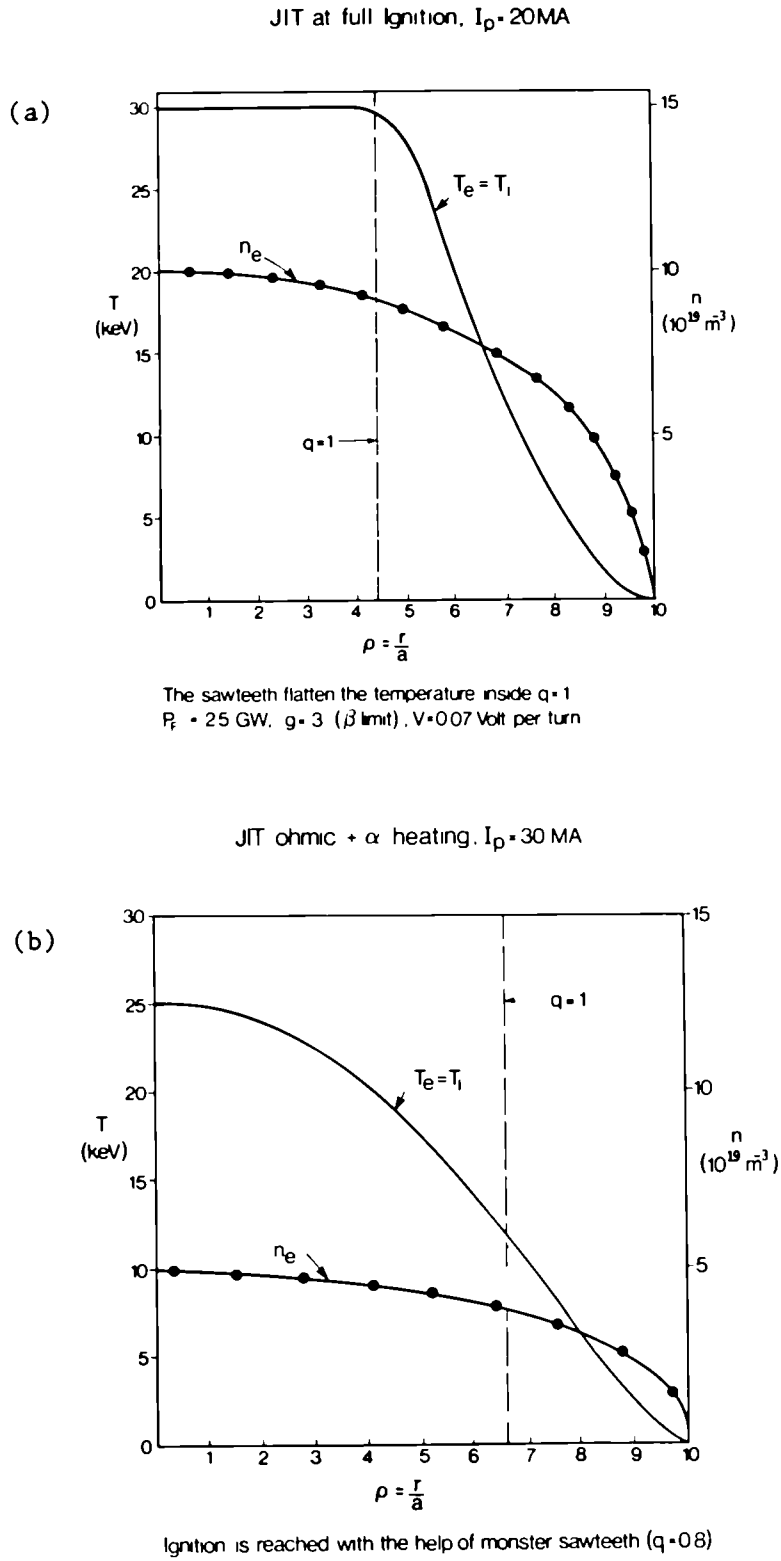

Fig. 17 (a) Critical temperature simulation of JIT. Full ignition is obtained on JIT even with complete flattening of the temperature inside the $q=1$ region at 20MA. The β limit ($g=3.6$) is almost reached; (b) At 30MA with a monster sawtooth, ignition is obtained without additional heating at a lower density.

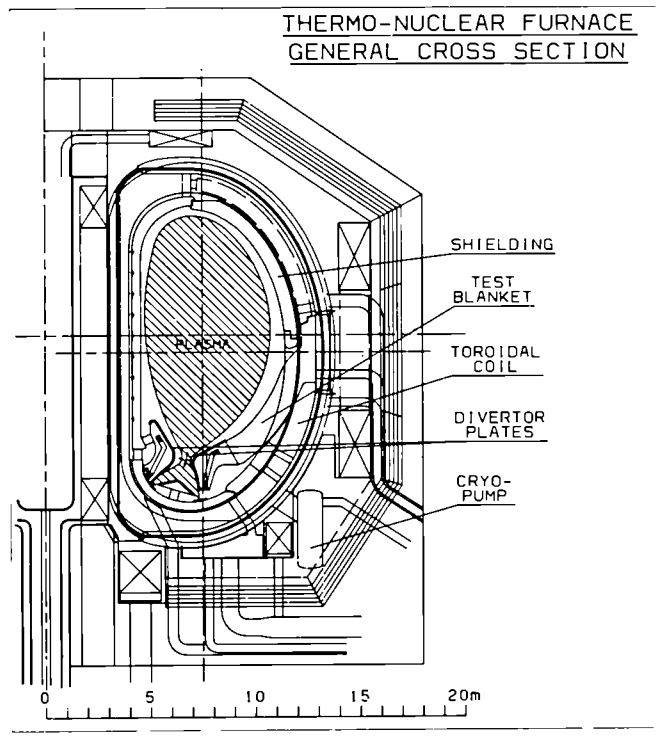

Fig. 18 Cross-section of a thermonuclear furnace (JIT) with a plasma capability of 30MA.

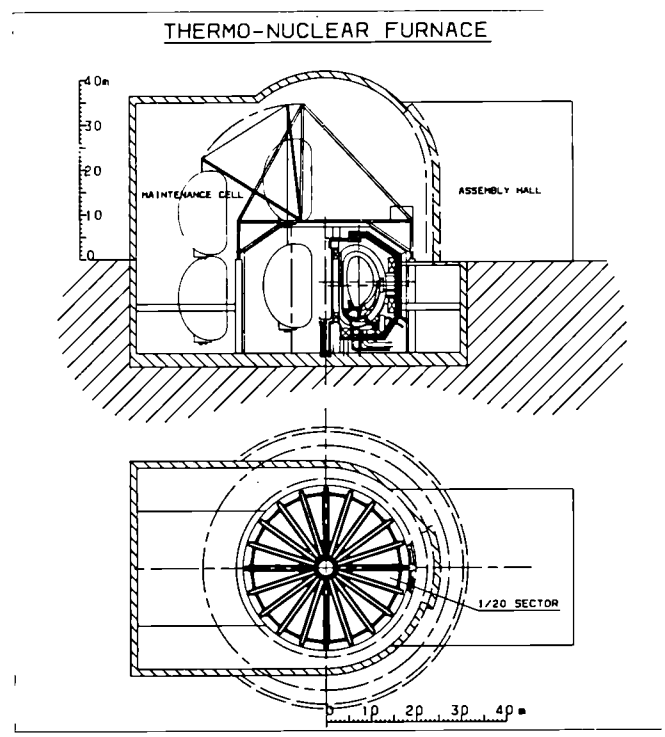

Fig. 19 Overall view of the thermonuclear furnace and the main building including the remote handling facilities and the external shielding.

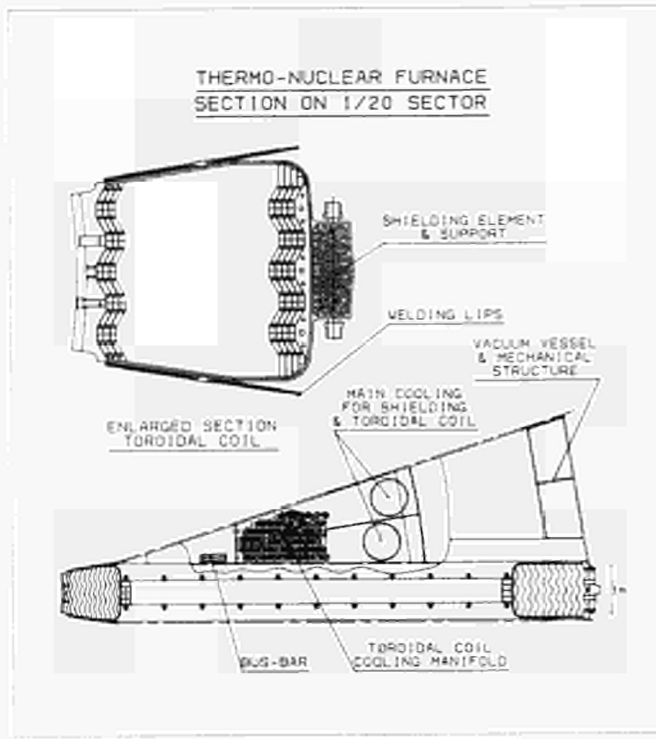

Fig. 20 Section of a sector of JIT conceived as an integrated element including the toroidal coil, the vacuum vessel, and the mechanical structure. Toroidal field coils are shown.

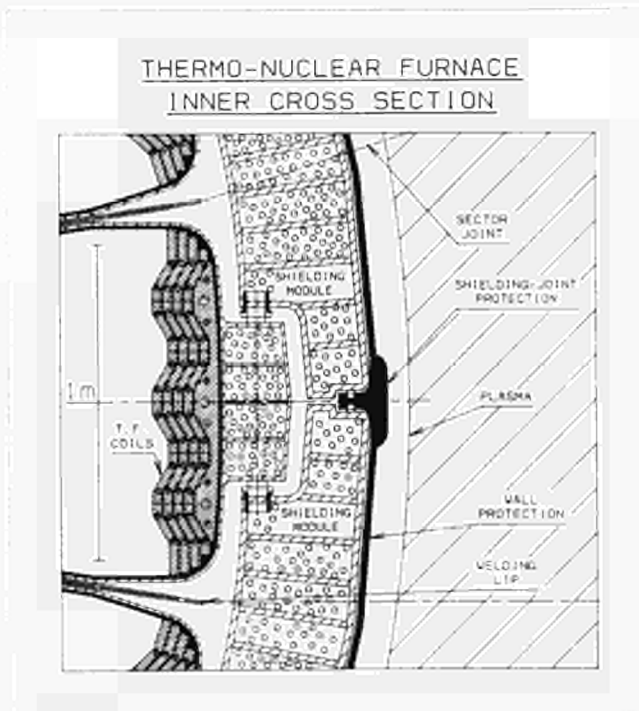

Fig. 21 The concept of the inner wall blanket supported by toroidal field coils and protected by carbon tiles.

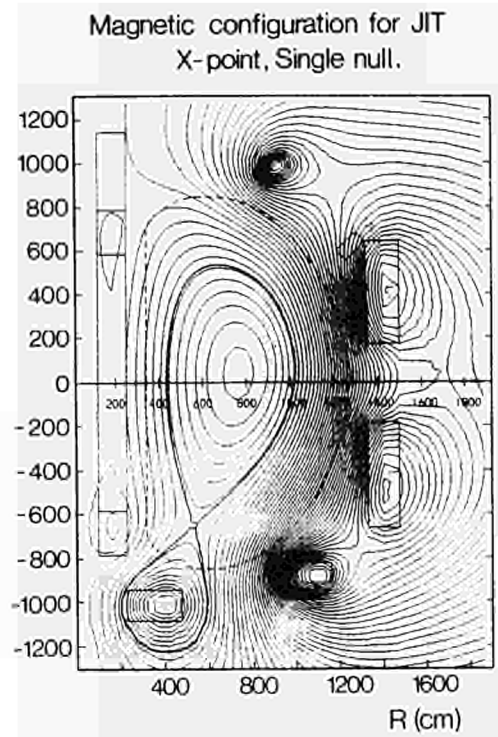

Fig. 22 Typical magnetic configuration calculated for JIT with a single X-point.

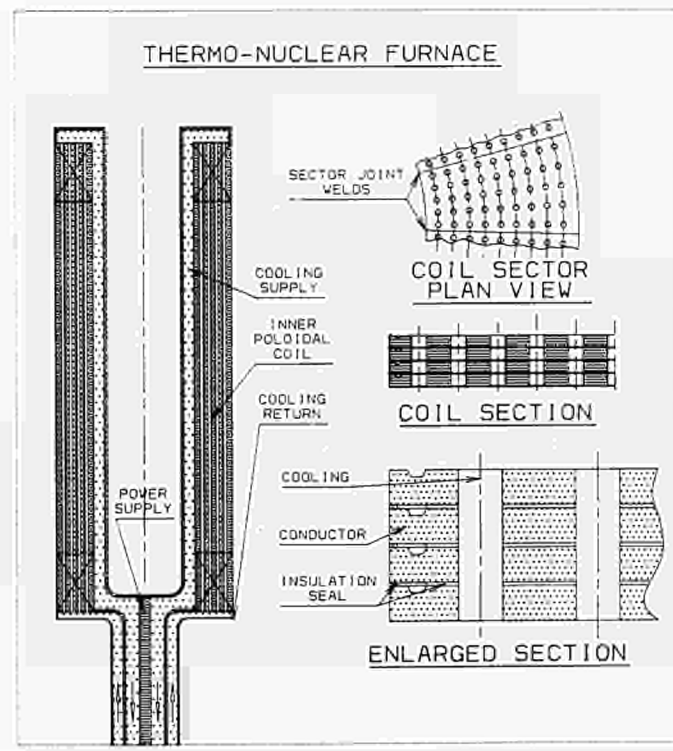

Fig. 23 The internal poloidal field coil, conceived as a Bitter coil with detail of the cooling and insulation.

(a)

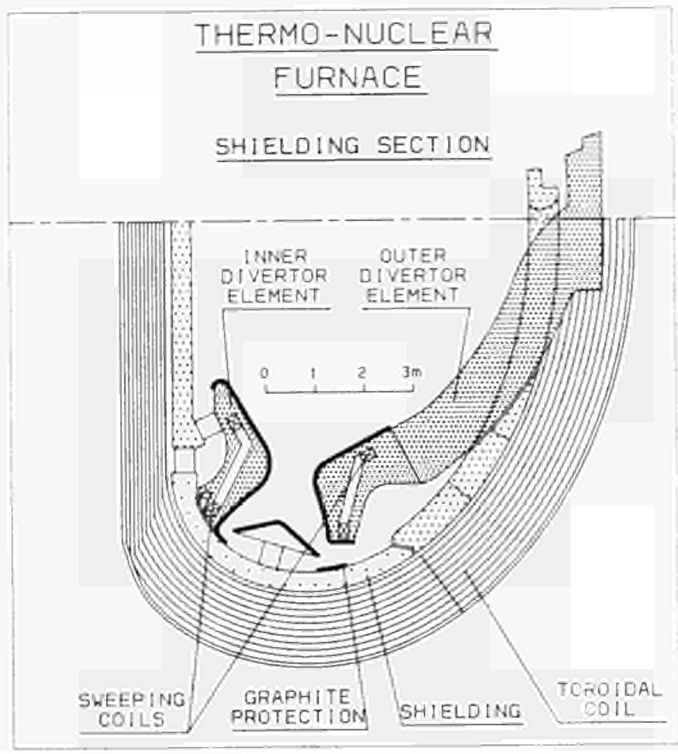

(b)

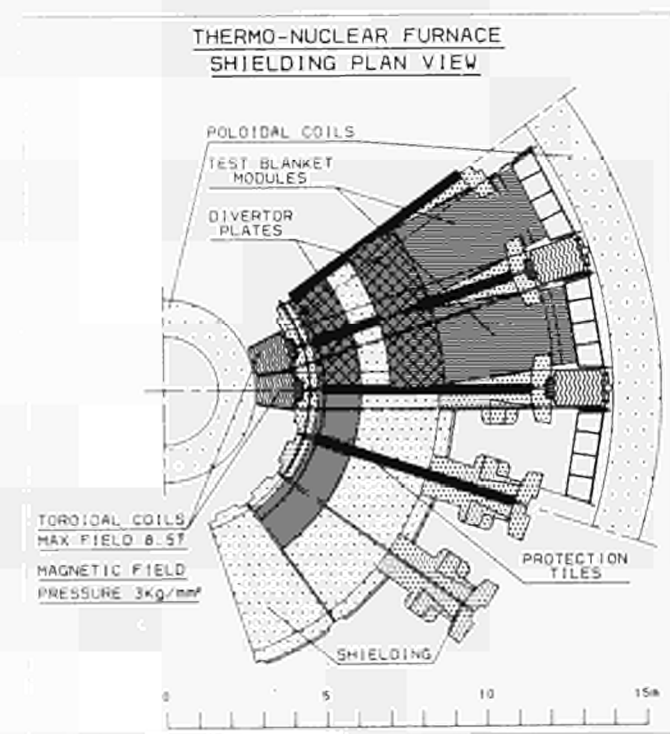

Fig. 24 (a) Sectional and (b) plan view of internal layout of JIT shielding, divertor element and test blanket which can be dismantled remotely through the main ports.

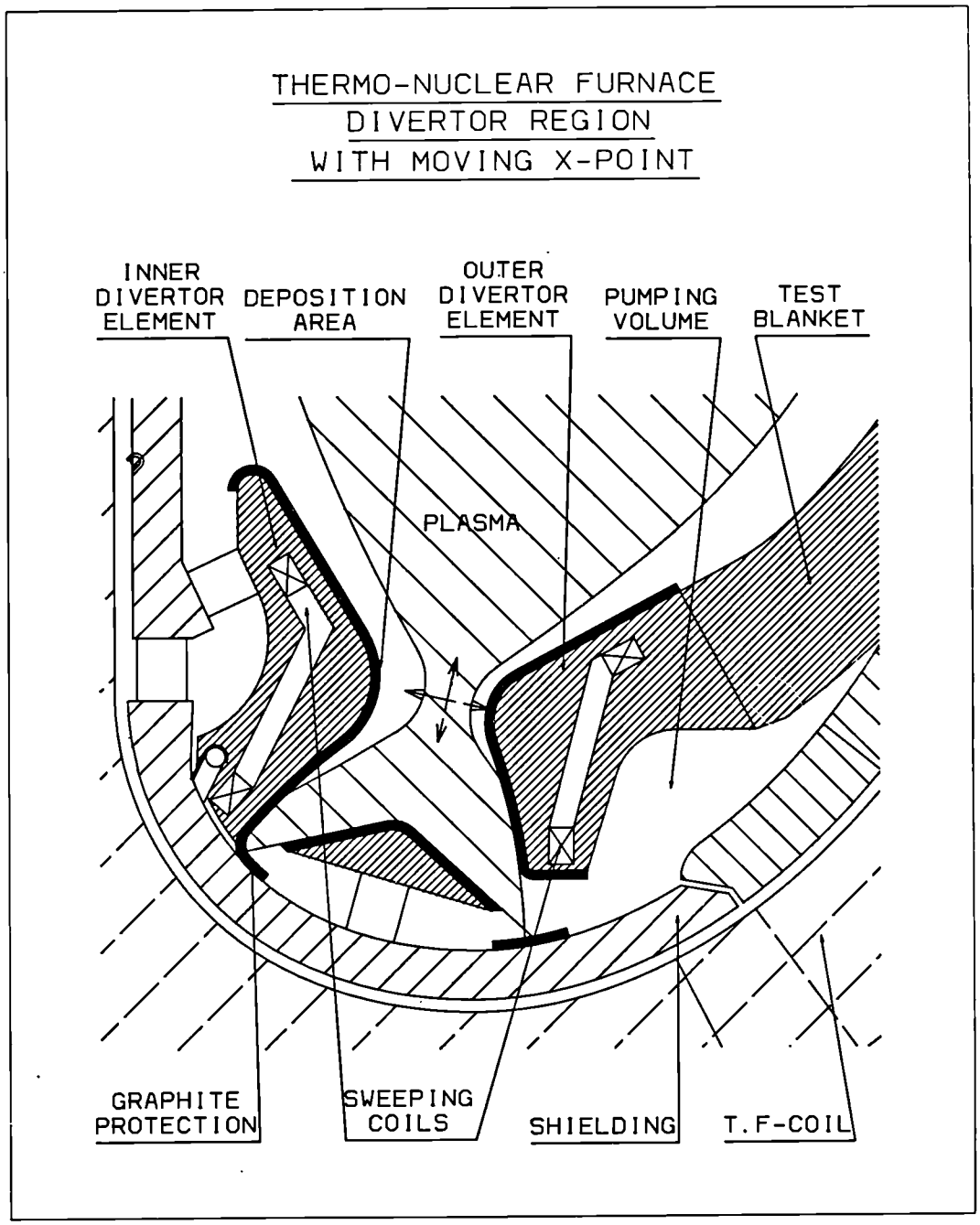

Fig. 25 Divertor region of JIT showing a set of saddle coils which allow sweeping of the thermal load on the divertor plates covered with graphite. Pumping is carried out through a slot at the base of the divertor.

Preparation for D-T Operation at JET

A C Bell, C Caldwell-Nichols, J Campbell, P Chuilon,
C Gordon, G Newbert, M Wykes

Abstract

D-T operation of JET is currently programmed for mid-1991 onwards. An active gas handling plant to extract hydrogen isotopes from the torus exhausts and provide individual isotope feeds is being constructed. Although Torus Systems, additional heating systems and diagnostics have been designed for the tritium operation, their designs are presently subject to a detailed review. Some of the systems in direct contact with tritium will require modifications to improve their reliability and these modifications are being designed. Approval from safety and regulatory authorities is necessary to start operation with tritium, and to satisfy these requirements, analysis is being carried out of routine and accident conditions, waste arisings and compatibility of systems with tritium operation. It is concluded that in parallel with the continuing successful experimental programme of Jet in the D-D phase, the review of all aspects of the JET design and operation for the D-T phase is proceeding satisfactorily and no insurmountable problems are foreseen. The complete JET cycle will have a negligible environmental impact and the measures taken will ensure that radiation doses to workers are low.

1. INTRODUCTION

The Joint European Torus (JET) situated at Abingdon UK is a major experiment to investigate the conditions for thermonuclear fusion in magnetically confined plasma. The main parameters of the JET machine and the recent plasma performance have already been described [1,2]. A major aim of the JET experiment is the study of alpha particle production, confinement and plasma heating. To achieve this a planned programme of enhancement of the JET machine and its ancillaries is being undertaken, leading to the capability of plasma operation with tritium from mid 1991 onwards. The major addition is the Active Gas Handling System (AGHS) whose main function is the extraction and separation of hydrogen isotopes from the torus exhaust so that tritium and deuterium can be recycled [3]. This is planned to be in operation in 1990 so that ample experience can be accumulated prior to operation of JET on a closed cycle with tritium. The major milestones in the programme, including the extensive work of modification for additional heating, disruption control and impurity control amongst other things are shown in Figure 1.

The main features implemented and preparations for D-T operation of JET have been discussed in previous papers [4,5]. This paper follows on in describing the progress being made towards D-T operation of JET, particularly those aspects related to safety approval.

2. TRITIUM COMPATIBILITY OF JET SYSTEM

As one of the ultimate objectives of the JET experiment was the study of alpha particle heating, the majority of JET systems were designed from the outset for D-T operations. These have been described previously [4,5] and include:

i. The massive biological shielding which is designed to reduce the radiation dose due to operation to staff in the control room to well within the JET radiation exposure target, and at the site boundary to less than normal fluctuation in the background dose levels.

ii. The facilities for carrying out remote maintenance on critical components in the torus hall where dose rates prohibit access to the vacuum vessel and make normal hands-on maintenance impossible [6].

iii. The double-walled vacuum vessel and the associated gas baking loop which permits operation at elevated temperature whilst minimising the permeation of tritium to the environment. The gas baking loop which circulates helium through to vacuum vessel interspace to maintain the temperature at ∿ 300°C will allow tritium permeating through the inner wall to be ultimately collected as oxide on a zeolite bed which can be regenerated periodically. Installation of the loop blower in a gas tight housing to minimise tritium losses through the shaft seals has been completed.

However as JET is an experimental device, progressive modifications have been made since commissioning and it is essential to carry out a review to confirm that safety, operability and maintainability are not prejudiced in the tritium phase.

A tritium compatibility analysis is therefore being carried out on all JET systems proposed to be used during the D-T phase. There are four issues to be addressed for each system:

i. Will it operate satisfactorily in the D-T phase?

ii. Can it be maintained or removed remotely?

iii. Are the routine tritium releases resulting from the operation of the system acceptable?

iv. In the event of failure of the system, are operator and public radiation doses acceptable?

In addition to completely new systems such as the AGHS and Lower Hybrid Current Drive, and systems requiring major modification, for example the ventilation system, cooling circuits and overpressure protection, systems basically unchanged need to be considered. In this latter category are the diagnostics of which there are about 55 on JET at present (Fig.2). About 15 non-active phase diagnostics which were not intended for use in the D-T phase will be removed, mainly because they would not survive the neutron dose. The remainder have been assessed for compatibility and a number have required modification such as:

i. Replacing turbopumps with regenerable getter pumps and, where appropriate, replacing rotary backing pumps with sealed ones.

ii. Interspaces evacuated and monitored.

iii. Additional containments.

Some modifications may not be cost effective and the relevant diagnostics will be removed. The KH2 X-ray Pulse Height Spectrometer design provides an example of aspects which require to to be considered. It is currently pumped on the torus side by a turbomolecular pump and one proposal is to replace this with an ion pump (Fig.3). An alternative scheme would be to pump the beamline via the torus. Tritium permeation through the bellows has been assessed and conservatively estimated to be acceptable at 0.06 Tbq/a. Other aspects examined include the method of control of the beryllium window bypass to minimise the tritium contamination of the components outside the torus hall. The In Vessel Inspection System (IVIS)[12] is an example of a system which has been reviewed and is now fully tritium compatible, incorporating ion getter pumps.

However from the availability point of view and from the need to lower the potential for release of activity to the environment, the main modification required to ensure that many of the diagnostics are compatible with tritium operation is to design the quartz windows, of which there are over fifty on the machine, against catastrophic failure. Experience of JET operation so far has shown that a window, which operates up to the vessel wall temperature, may crack as a result of thermal shock if cold water from a leak of one of the internal cooling circuits impinges on it. Although all of the window failures experienced have either been seal failures or, following water leaks [8], cracks, the possibility of complete disintegration of a window which has the potential for release of tritium to the torus hall [15] and would lead to extensive outage, cannot be ruled out. The use of double windows in vulnerable positions is now being considered as a way of minimising this possibility.

Economic factors and the environmental issues associated with discharge of large quantities of tritium have obliged JET to adopt a closed cycle system for extracting hydrogen isotopes from the torus exhaust gases and separating the tritium for re-injection into the JET machine. This plant is designed to the highest standards of tritium containment to minimise operator and public dose and will be housed in a building separate from the main torus building. The major components of the plant have been designed and procurement is underway. As it is designed specially to handle bulk quantities of tritium, tritium comptability is inherent in the design. This includes secondary containment with leak detection on all major systems and provision for reduction of maintenance release by baking and evacuation.

It is described in the accompanying paper [9].

The AGHS also includes a tritium clean-up system, referred to as the Exhaust Detritiation System (EDS), to provide an air flow through the torus during maintenance intervention within the vessel and to detritiate the exhausted air [7].

Other examples of where tritium compatibility analysis has led to design modifications are :

a. The LHCD main double bellows [10]. The initial assessment showed unacceptable tritium permeation to the atmosphere of around 60 TBq/a. This figure was based on clean metal permeation through both bellows at 400°C, as the usual mitigating effect of oxidised surfaces could not be claimed for a bellows constantly cycled during plasma operation. The option of pumping the interspace was rejected due to the excessive pumping speed required to maintain the interspace at the 10^{-4} mbar required to reduce tritium permeation to the atmosphere to an acceptable level of 2 TBq/a. It is now proposed to maintain the outer bellows at ∿ 200°C.

b. Modifications are being made to the cooling water circuits and the protection circuits; particularly to the Neutral Injection System, to minimise the quantity of water entering the main tritium systems if there is an internal leak and thus reduce the quantity of tritiated water to be handled. Different physical methods of leak detection may need to be employed to provide diversity and to enable the conflicting requirements of rapid shut-down and avoidance of spurious trips can be met. For example, box pressure, N_2 boil-off rate and expansion tank level can each give an indication of a Neutral Injection leak. An important consideration is also the ability to separate the highly tritiated arisings during water leak incidents in which cryppumps defrost from the water containing low levels of tritium contamination in the poloidal and toroidal field cooling circuits.

c. The vessel overpressure protection currently consists of a 50 mbar differential rupture disc relieving into the torus hall. This means that a large cryospill or water leak could result in a release of tritium to the torus hall. Such a release of tritium to the environment is unacceptable for a single system failure and further protection is required. This can be achieved by making the first line of defence against over-pressurisation of the vacuum vessel pressure operated valves discharging into the AGHS manifold lines, the rupture disc being retained as the ultimate protection for the vacuum vessel in the remote event of the relief valves failing to operate. As the AGHS has facilities for collection of elemental tritium and tritiated water, releases to the environment are minimised. A variety of circumstances needed to be covered, including H_2 deflagration in the pellet injector box, variations in AGHS suction pressure, the operation of the isolation valve, and tha current concept is shown in Figure 4.

d. Various planned enhancements will be made to the Torus Hall, Access/Hot Cell and basement ventilation plants, to allow air to be extracted from the torus hall at about 1 air change per day. A filtration system for radioactive particulates will be included and the recirculating system will maintain a constant humidity of 7°C dew point (Figure 5).

The system will also need to take into account pressure relief for the fire extinguishing system.

3. SAFETY APPROVAL

The use of radioactive materials in the UK is constrained by Government legislation which controls the licensing of plants, the exposure of employees, the disposal of waste and transport. The main statutes which JET is subject to are listed below:

3.1.1 Radioactive Substances Act 1960

The main impact of the Act on JET is that all routine discharges of tritium or activated substances to the environment for disposal as waste must be approved in advance by Her Majesty's Inspectorate of Pollution (HMIP). JET is required to make a submission to HMIP showing that "Best Practicable Means" have been used in minimising the environmental impact and showing that in all cases, radiation doses to the most exposed members of the public are within the targets recommended by the National Radiological Protection Board (NRPB) [11]. JET will have no difficulty in meeting these targets so the emphasis is on demonstrating that the various options have been considered and that where necessary any particular engineering solutions are justified using cost benefit analysis (CBA). For example the AGHS stack height is 25 m above ground level. CBA, based on a cost of £3000 per man-Sv, was used to show that from dose considerations, a higher stack was not required.

3.1.2 Ionising Radiation Reg's. 1985 (IRR's)

The legislation is concerned with limiting radiation doses to employees and the compliance is monitored by the Health and Safety Executive. JET occupational dose targets are considerably below the legislative limit of 50 mSv for annual committed dose to exposed workers. The legislation requires a contingency plan to be submitted to the HSE if quantities of radioactive material exceed certain limits. The quantity of tritium to be used at JET (90 g) is less than this limit (540 g) but a contingency plan will be produced nevertheless.

The accounting requirements of the IRR's will be met by the arrangements, using periodic PVT measurements which are needed for process monitoring.

3.1.3. Transport Regulations

UK legislation is based on the IAEA Code of Practice for safe tranaport of radioactive materials. It is not JET's intention to develop special transport containers for either tritium or waste as the timescale for approval, particularly in the case of type 'B' containers is of the order of two years.

3.1.4. Nuclear Installations Regulations

Under the 1965 Nuclear Installations Act, nuclear sites in the UK are required to be licensed by the Nuclear Installations Inspectorate (NII). At present, however, UKAEA sites are exempt from licensing and a semi-independent internal unit of the UKAEA, the Safety and Reliability Directorate (SRD) is responsible for ensuring that the same standards are applied to UKAEA sites as if they were licensed. Under the JET Host Agreement, the UKAEA ensures that JET applies similar standards and JET is required to satisfy SRD that the design of the plant, its construction and commissioning, and its operating procedures are acceptably safe. When satisfied, SRD will endorse the issue of an Authority to Operate (ATO) for the plant.

3.2. Design Targets

The overriding consideration for radioactive plants is that ALARP (As Low As Reasonably Practicable) principles should be followed to limit routine and accidental releases. Generally this means that the best up-to-date technology should be employed and that where several options are available, they should be examined to determine which gives the lowest public/ worker risk. In cases of doubt, cost benefit analysis should be used to eliminate solutions of disproportionste cost.

As part of the Quality Assurance (QA) procedures, JET Technical Control Documents require systems to be classified from the point of view of radiation, remote handling, quality and tritium. This allows design and analysis effort to be concentrated efficiently where it is required. For example the criteria for tritium classification listed below are used to determine which systems require detailed safety analysis or need to be taken into account in waste handling.

There are four classes defined as follows:

CLASS 1 - Systems with a high potential for accidental/routine release or exposure of personnel when the effects of the secondary containment or any other barriers are neglected.

CLASS 2 - Systems with a low potential for routine/accidental release and exposure of personnel, - or -

Systems necessary to prevent/limit release or exposure for Class 1 systems under fault conditions.

CLASS 3 - Systems which will generate tritisted operational or decommissioning wastes.

CLASS 4 - Systems with no potential for tritium release/exposure or generation of waste.

3.2.1 Routine Releases and Exposure

The UK NRPB considers that radiation doses of 50 μSv are "of no concern". This value has been chosen as the design target for routine releases. Assessments have been carried out of the annual public doses through various pathways which are as follows:

Direct radiation from torus: < 5 μSv (at site boundary)

Gaseous releases:

Activated air < 5 μSv (inhalation/direct radiation)

Tritium < 5 μSv (inhalation and ingestion)

Liquid Discharges (to Thames):

Tritium << 1 μSv (drinking water for hypothetical critical group)

The occupational dose limits set by JET policy are 5 mSv/a for radiation workers and 1 mSv/a for non-radiation workers. For routine releases and radiation from the torus, the annual dose to the most exposed person on-site would be:

Direct radiation < 50 μSv

Activated Air < 20 μSv

Tritium < 10 μSv

which is clearly well within the above targets. However, the majority of

occupational exposure will arise during maintenance operations and the use of protective clothing, and other dose control measures will be used to limit exposure of individuals in accordance with these limits.

3.2.2. Accidental Releases

A basic JET design philosophy is that no single failure of any system should result in exposure of workers or members of the population to greater than the annual dose limit. To comply with this, the containment philosophy employed in the AGHS is that all the main tritium process lines are doubly contained apart from certain exceptions eg. those which are of thickwalled, all-welded construction and which operate at room temperature and sub-atmospheric pressure such that the permeation losses are low (<0.04 $TBqa^{-1}$) and the probability of a significant release is low [9]. Secondary containments are generally of stainless steel and, where possible evacuated or filled with helium. Leak detection is provided and overpressure protection (eg rupture discs) on systems with a high inventory discharges into evacuated buffer tanks, each capable of holding the complete AGHS inventory.

3.3. Safety Analysis

The above considerations, as well as those of conventional hazards, were analysed qualitatively in the AGHS Preliminary Safety Analysis Report (PSAR) and this was endorsed by SRD before the final plant design was started. A comparable PSAR is in the course of being produced for the torus systems.

For the second phase of the safety analysis, a Design Safety Review is carried out on each of the AGHS subsystems. This includes Failure Mode and Effects Analysis (FMEA) of all components or component groups. For those components which, in the event of failure of a protection system, have the potential for significant tritium release, a Probabilistic Safety Analysis (PSA) is carried out and an event tree produced quantifying the probability magnitude of releases for each initiating event (Figure 6). One major problem, of course, in the application of PSA to new systems is the paucity of reliability data relevant to fusion and cryogenic plant. Generic fission reactor data modified where necessary have been used in the Fault Tree Analysis used to derive the initiating event frequencies (Figure 7). For analysis of torus systems a study has been carried out of the failures during the D-D phase to provide more appropriate data.

Before proceeding to procurement, a Design Safety Review has been carried out in each subsystem of the AGHS and endorsement of SRD obtained.

The design target for each identifiable accident sequence is that the product of frequency and magnitude of release to the environment should be less than 10 Ci a^{-1}. This target is considerably more restrictive than the guidelines laid down for nuclear chemical plant by the UK NII. These are concerned with public dose/frequency for discrete fault sequences and when related to the JET site give the release limits shown in Figure 8 with JET design guidelines for comparison.

The analysis of one of these subsystems (Figure 9) shows that the design targets are met.

Specific torus systems identified through the PSAR as having a high risk of release will be subject to a Design Safety Review.

The final safety submissions before approval for operation is given takes two forms:

i. Final Safety Analysis Report (FSAR)

This takes account amongst other things, of system interactions, modifications following the reviews, procedure for control of operation and QA interfaces.

ii. Commissioning report

This is required to show that safety-related systems are performing as intended.

Approximately one year has been allowed for commissioning, initially with H/D and possibly small amounts of tritium in the AGHS before the D-T phase starts in 1991.

4. RADIOLOGICAL PROTECTION INSTRUMENTATION

Gamma and neutron monitoring instrumentation has been installed in the JET torus building from the start of operations. Enhancement for the D-T phase requires the addition of tritium working area monitoring and measurement of stack discharges of tritium and activated gases.

For the AGHS building and torus building working area, ionisation chambers with a sensitivity of better than 1/10 DAC HTO will be installed. In addition to local alarms, the instruments will be connected to a central CODAS computer to record data and enable trends in chronic levels to be monitored. Discriminating HT/HTO monitors have been ruled out because of the extra complexity, low probability of purely elemental releases and the risk to individuals if protection measures were based on a single instrument reading. During maintenance operations, sampling methods may be used to establish the true level of HTO.

For monitoring of the torus hall air, the instruments are to be installed in the ventilation ducts outside the biological shielding. Activated air measurement and compensation of tritium monitors will be provided.

To demonstrate compliance with discharge limits all discharge stacks will be equipped with a catalyst and silica gel samplers for HT and HTO. Consideration is being given to the need to collect tritiated methane.

A programme of environmental sampling is being carried out. Around 20 tritium sampling points will be installed around the JET site boundary before the D-T phase to establish baseline levels before D-T operation starts and provide data throughout the D-T phase.

5. WASTE HANDLING

Studies have been carried out on the waste arisings at JET and the options for transport, treatment and disposal. The options are constrained by four factors:

i. There is no intermediate level waste disposal facility at present in the UK.

ii. There is only one low level waste repository which, in addition to overall annual limits, imposes a limit of < 12GBq/te on the tritium content.

iii. Discharges of aqueous waste to the Thames may be severely restricted.

iv. When the JET experimental programme is complete, the UKAEA will take over the responsibility for JET and its decommissioning.

Anticipated waste arisings have been categorised as:

i. Process wastes (solid)

These will be mainly absorber beds (molecular sieve, uranium beds, zeolite) containing tritium and/or activated corrosion products. Tests are underway at present to determine if the number of uranium beds produced as waste from the AGHS can be reduced by using a regenerable iron bed for cracking of water in the impurity processing loop [9].

ii. Component waste (solid)

Components which are activated, contaminated and/or tritiated will be removed from the machine and AGHS during maintenance.

iii. Housekeeping wastes.

These will consist of clothing, swabs etc.

iv. Low level tritiated water

During D-T operation, the use of water in situations where it may become tritiated will be minimised; however minor leakages from cooling circuits,

air conditioning condensate and tritiated water collected from the exhaust detritiation system cannot be avoided.

Higher concentrations of tritium may arise from accident situations. Comparable concentrations could also be collected in the EDS driers if they are operated following a major vacuum leak (Ref. 7).

A current strategy for dealing with JET waste taking account of these restrictions and the main types of arisings and wastes is currently being defined.

6. MAINTENANCE

The JET machine was designed from the outset in such a way that essential maintenance and replacement of components in the D-T phase could be carried out remotely. Components are classified according to the need for remote handling and this is periodically reviewed in the light of experience. Progress on development of remote handling is dealt with elsewhere (Ref. 6).

One important aspect of torus maintenance is reduction in tritium emission from in vessel components. Glow discharge cleaning will be carried out to reduce tritium emissions from an estimated 4 TBq/h to negligible levels. The AGHS has been designed to separate this evolved tritium.

In the AGHS, remote maintenance is not necessary but the systems have been designed to facilitate maintenance. For example, where possible, bake-out heaters have been provided so that tritium outgassing can be carried out before opening of containment; extra manual valves are provided to minimise the effects of tritium outgassing of long pipes; containment closures may be replaced by glove-port modules.

7. CONCLUSIONS

In parallel with the continuing successful experimental programme of JET in the D-D phase, the review of all aspects of JET design and operation for the D-T phase is proceeding satisfactorily and no insurmountable problems are foreseen.

In addition a design for the AGHS capable of satisfying the UK safety requirements has evolved and procurement has now started. The complete JET cycle will have a negligible environmental impact and the measures taken will ensure that worker doses are low.

ACKNOWLEDGMENTS

The author wishes to acknowledge the work carried out by the JET team and in particular members of Fusion Technology Division which is summarised in this paper.

REFERENCES

1. E. Bertolini et al., Proc. 12th Symposium in Fusion Engineering, Monterey 1987.
2. A. Gibson et al - Proc 15th European Conf. on Controlled Fusion and Plasma Heating, Dubrovnik 1988.
3. R. Haange et al., Proc. 3rd Topical Meeting on Tritium Technology in Fission, Fusion and Isotope Application - Toronto 1988
4. M. Huguet et al., Proc. 7th Topical Meeting on the Technology of Fusion Energy, Reno 1986
5. Dean et al., Proc. 14th Symposium on Fusion Technology, Avignon 1986
6. T. Raimondi, Proc. 15th Symposium in Fusion Technology - Utrecht 1988
7. A. Dombra et al., Proc. 15th Symposium in Fusion Technology - Utrecht 1988
8. B. Green et al., Proc. 15th Symposium on Fusion Technology - Utrecht 1988
9. J.L. Hemmerich et al., Proc 15th Symposium on Fusion Technology - Utrecht 1988
10. A. Kaye et al - Proc 15th Symposium on Fusion Technology - Utrecht 1988
11. UK National Radiological Protection Board - GS9, November 1987.
12. T. Businaro, Proc. 15th Symposium in Fusion Technology, Utrecht 1988
13. M. Wykes, Safety Analysis of Torus Vacuum Breach, JET P(88)37, 1988.

FIG 1

JET PROGRAMME

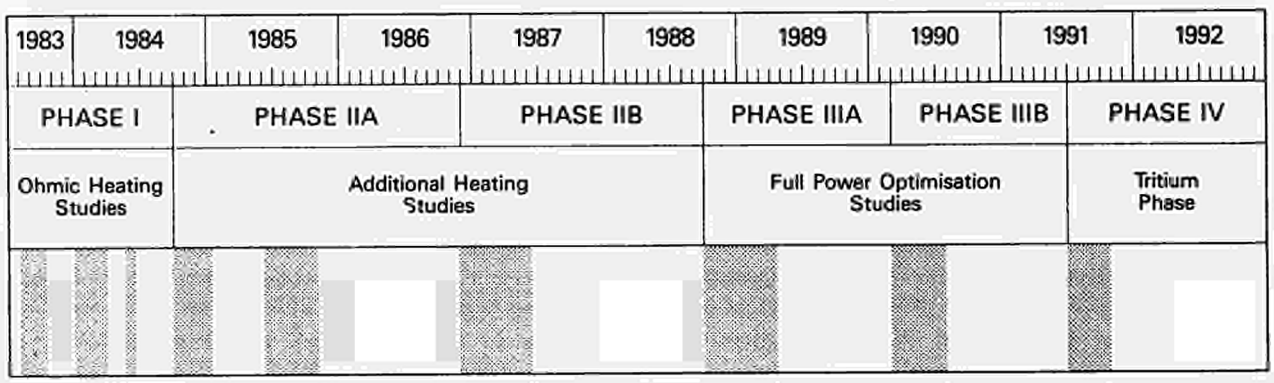

Ohmic Systems	5MA	Vessel restraints and improved volt-seconds for 7MA operation			
Separatrix		Additional P1 Coils	Cooled separatrix dump plates		
Limiters	Eight carbon mid-plane limiters	Carbon belt limiters	Beryllium belt limiters		
Pellets	Single pellet injector	ORNL multiple pellet injector ($1.5\,km\,s^{-1}$)	Prototype high speed pellet injector ($>3\,km\,s^{-1}$)	(Multiple high speed pellet injector)*	
Pump limiters				Adjustable pump limiter	
NBI	First NBI line (80kV)	Second NBI line (2×80kV)	One line modified to 140kV	Second line modified to 140kV	
ICRH	Three A_0 antennae	Eight A_1 antennae			
LHCD			Prototype system	Full system	
Disruption control			Saddle coils		
Tritium and Remote handling				Tritium plant and main RH modifications	Final modifications

*To proceed if successful development takes place outside JET

CR86.2 (rev 24/2/88) - Ro 1540, H1.P CR86.2

Location of J.E.T. Diagnostic Systems

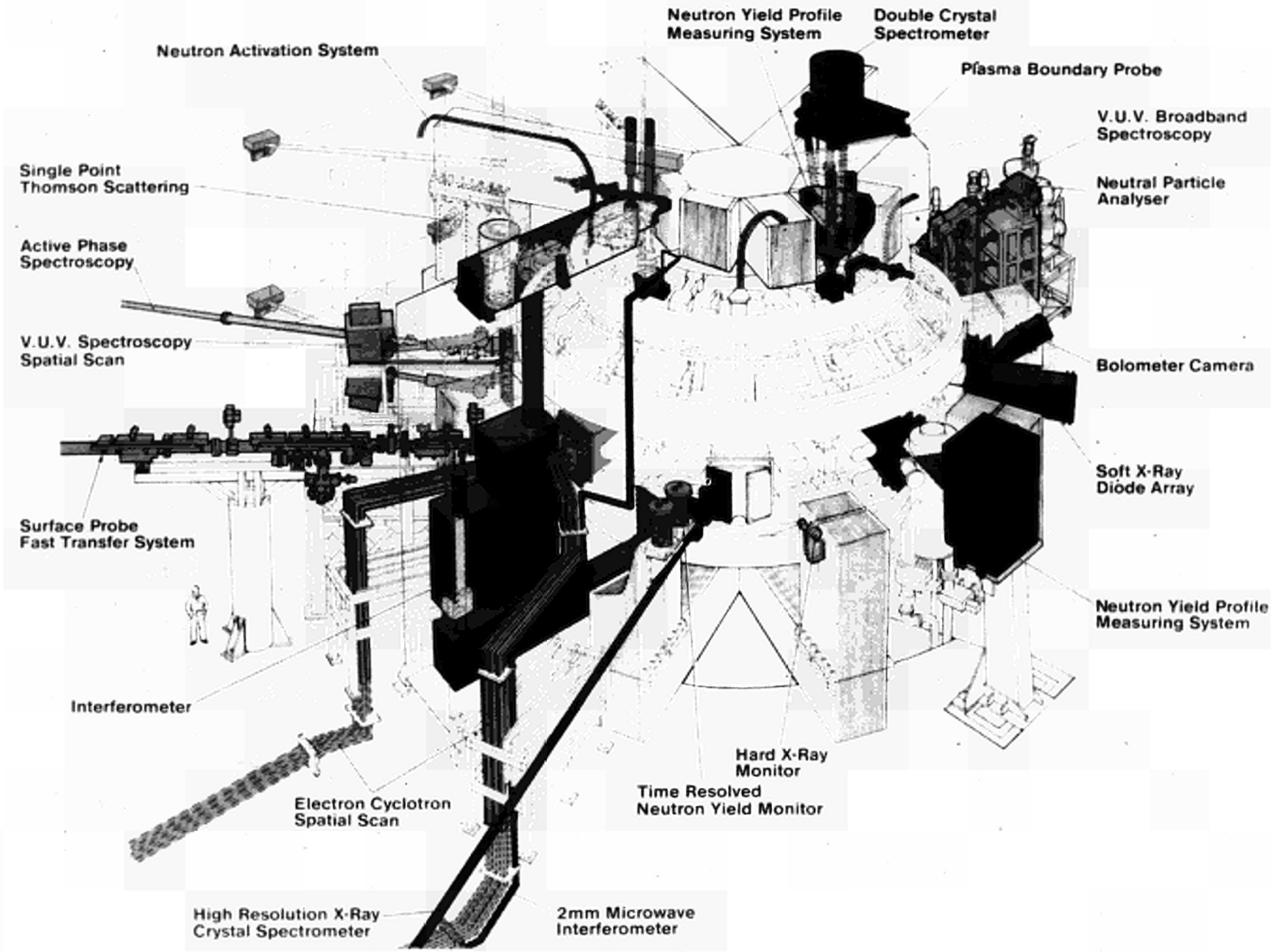

FIG 2

FIG 3 Diagnostic pumping

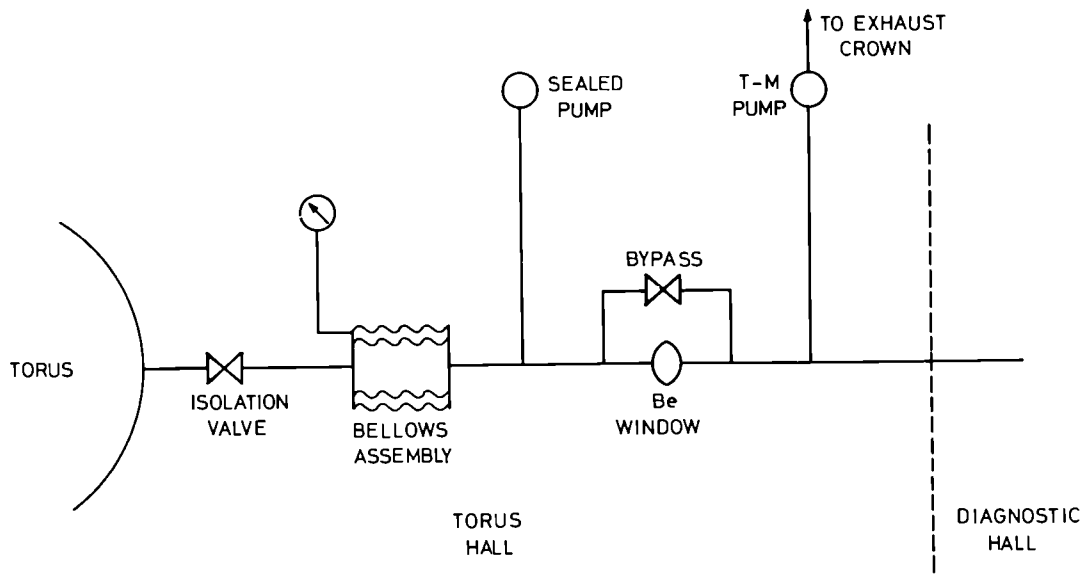

FIG 4 Torus overpressure relief through AGHS

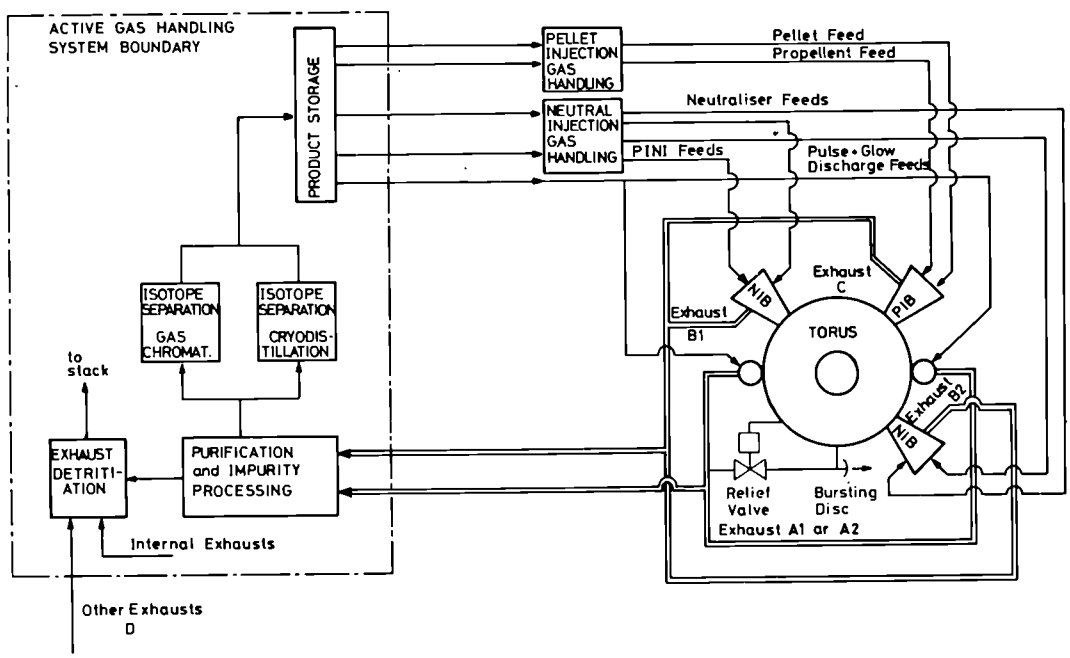

FIG 5 Proposed ventilation system

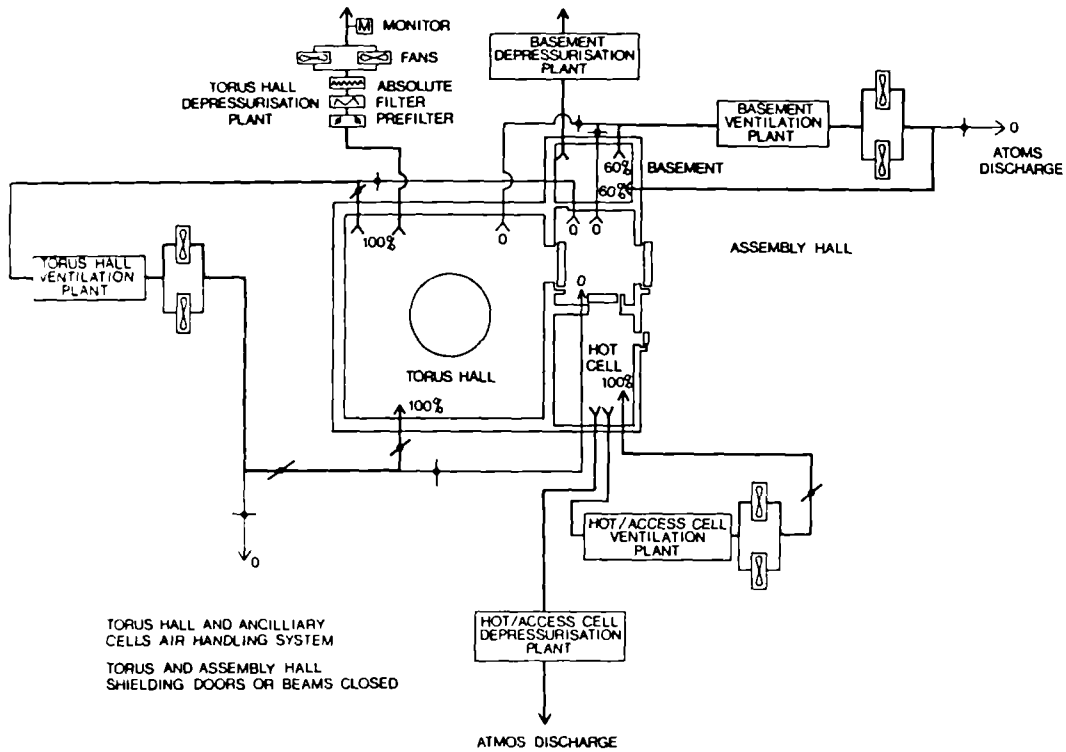

FIG 6 Typical event tree analysis

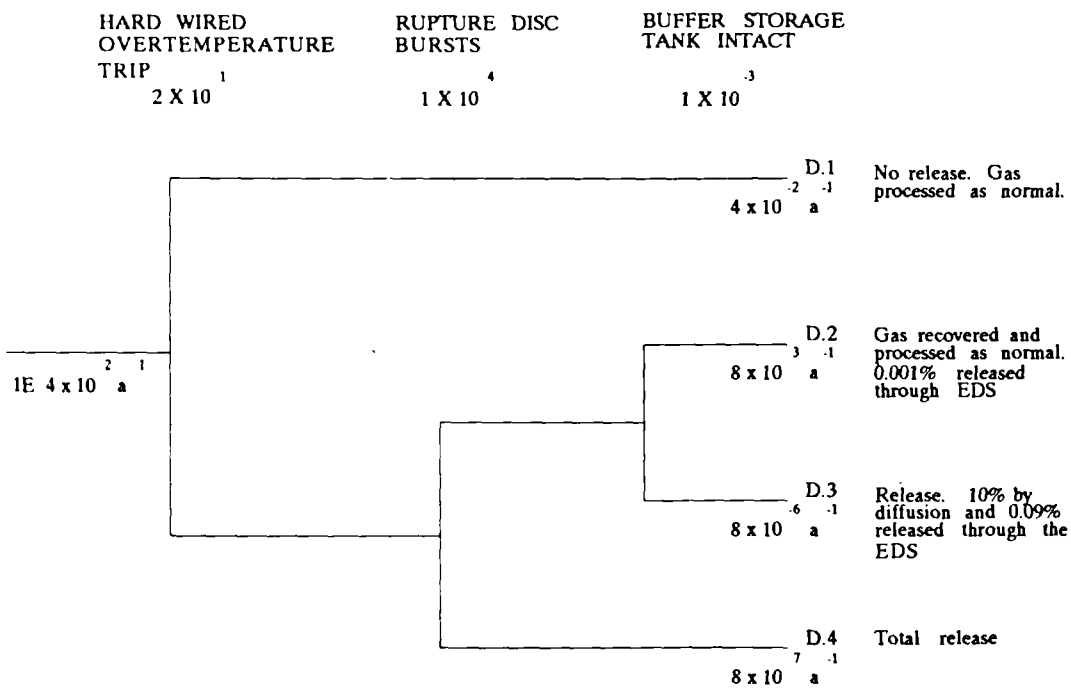

FIG 7 Typical fault tree used to derive initiating event frequency

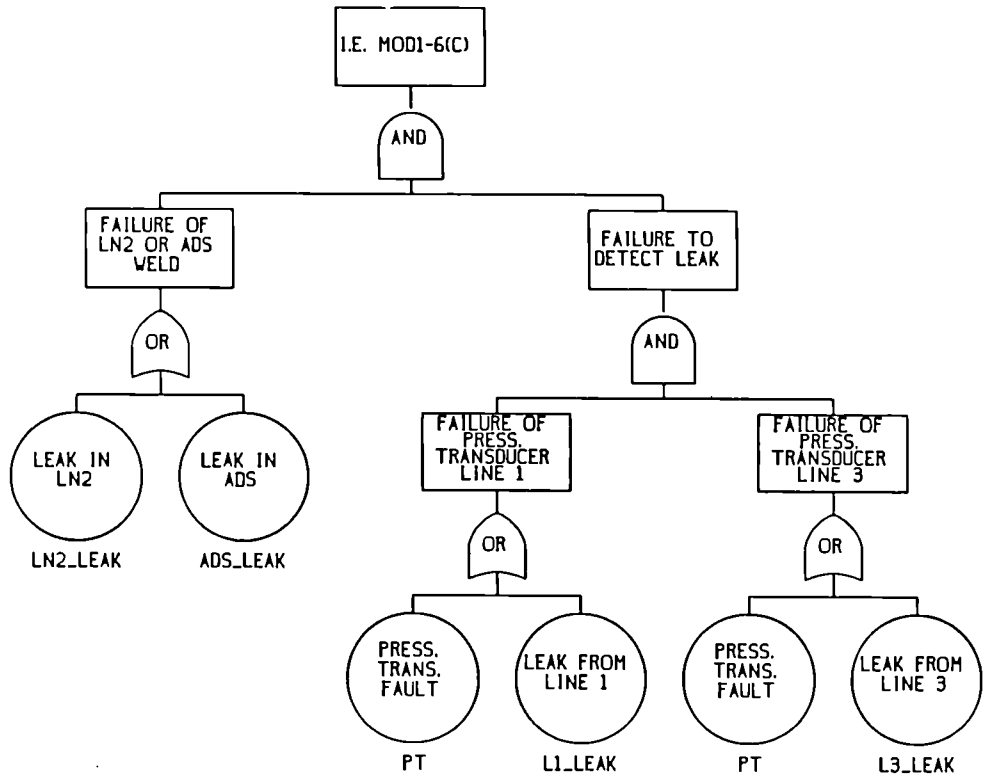

FIG 8 Tritium release target

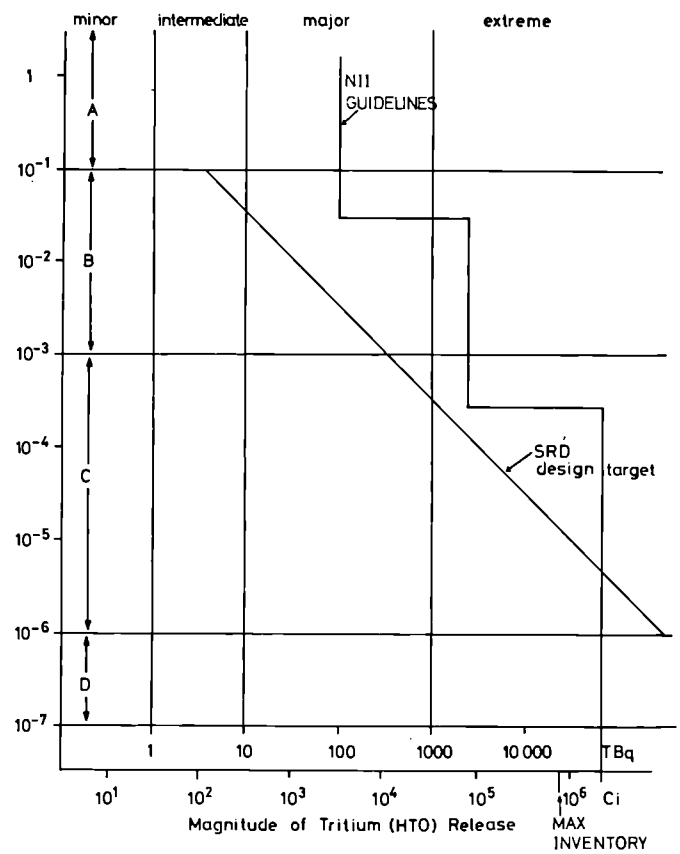

FIG 9

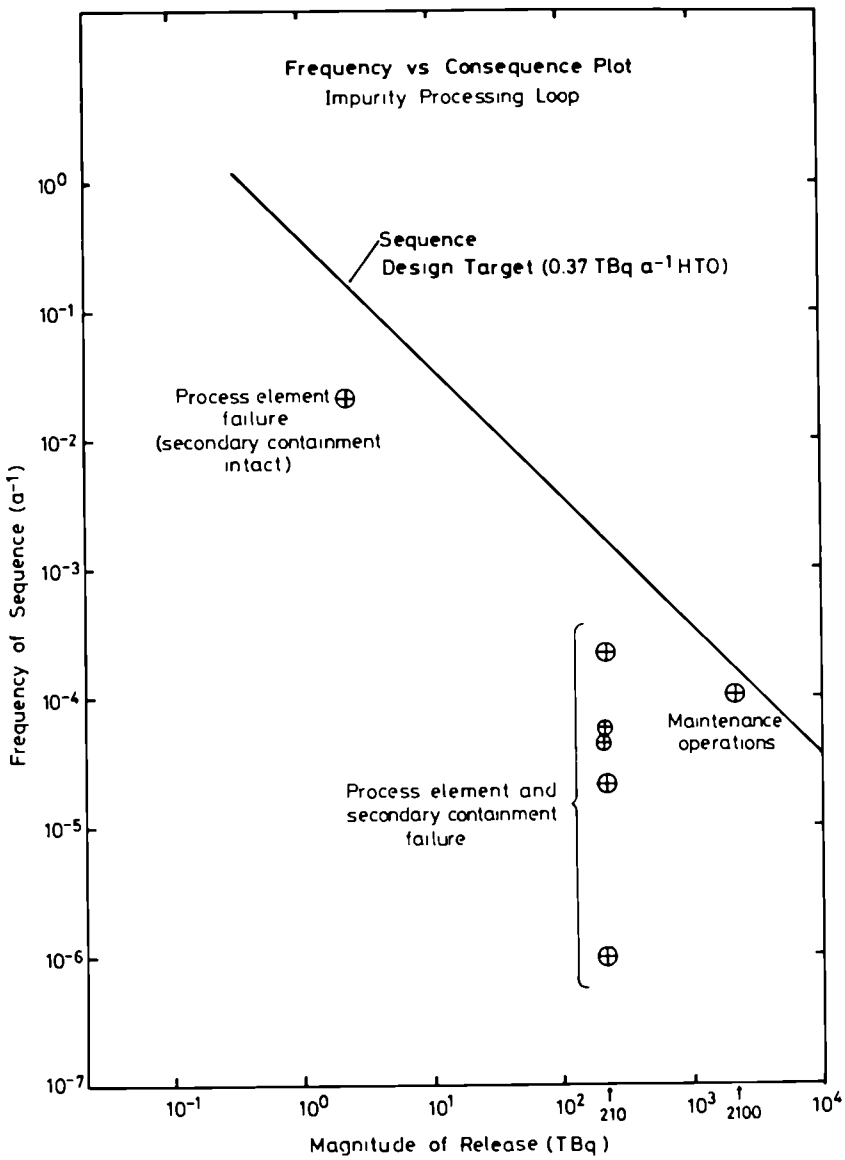
Frequency vs Consequence Plot
Impurity Processing Loop
Sequence
Design Target (0.37 TBq a⁻¹ HTO)
Process element failure (secondary containment intact)
Maintenance operations
Process element and secondary containment failure
Frequency of Sequence (a⁻¹)
Magnitude of Release (TBq)
10⁰
10⁻¹
10⁻²
10⁻³
10⁻⁴
10⁻⁵
10⁻⁶
10⁻⁷
10⁻¹
10⁰
10¹
10²
210
10³
2100
10⁴

The JET Active Gas Handling System Progress Report

J L Hemmerich, A Dombra, J Gowman, E Groskopfs, R Haange
A Konstantellos, E Küssel, R Lässer, P Milverton, K Walker, K Walter

The JET Active Gas Handling System is designed to process mixtures of hydrogen isotopes, helium and impurities during the operation of the JET tokamak with deuterium/tritium plasmas.

The main subsystems of this plant are now designed and contracts for manufacture have been placed or are being placed for:

- cryogenic forevacuum system (CF)
- mechanical forevacuum system (MF)
- exhaust detritiation system (ED)
- impurity processing loop (IP)
- intermediate and product storage (IS, PS)
- cryodistillation isotope separation (CD)
- gaschromatographic isotope separation (GC)

Elements of crucial importance for plant operation have been built as prototypes and test results are reported:

- CF : Accumulation panel pumping speed and impurity separation in cryotransfer pump.
- IP, IS, PS : Uranium beds for hydrogen storage and recovery of tritium from tritiated water; iron bed for water decomposition (regenerable).
- CD : A novel recirculation pump for hydrogen isotope mixtures utilising the surface tension of liquid hydrogen in a porous wall.
- GC : A new method to diagnose the arrival of an isotopic transition inside the column packing on the basis of difference in reaction enthalpies of the various isotopes, leading to characteristic temperature changes.
- General components : valves, valve actuators and all-metal, tritium compatible upstream and downstream pressure regulators.

1. INTRODUCTION

The JET Active Gas Handling System (AGHS) will receive, purify and separate exhaust protium, deuterium and tritium as well as helium and impurities from the JET tokamak and its associated systems (Neutral Beam Heating, Pellet Injection Fuelling) and will supply pure hydrogen isotopes for the operation of the torus and its subsystems.

The basic configuration of the AGHS is shown in Fig 1; its overall function has been described by Hemmerich and Haange [1,2]. Also, the function of major subsystems are described elsewhere:

- Cryogenic forevacuum, by Küssel [3]
- Impurity processing, by Hemmerich [4]
- Gaschromatographic isotope separation, by Botter [5]
- Exhaust detritiation, by Dombra [6]

In this paper we will concentrate on the results of an experimental programme, which is running parallel to the design and procurement of the AGHS, intended to test the performance of crucial plant components on full-scale prototypes.

2. COMPONENT TESTS

2.1. Cryogenic forevacuum

The cryogenic forevacuum system [3] is designed to pump gas mixtures of hydrogen isotopes Q_2 (Q standing for H/D/T, with Q_2 representing all six molecular species) with helium (^4He from the D-T fusion reaction and ^3He added to the plasma for RF minority heating) and impurities resulting from plasma-wall interaction (mainly hydrocarbons C_nQ_{2n+2} and water Q_2O). The pumping and separation of these mixtures is done in two stages. An accumulation panel (ACP) pumps all condensable gases by cryocondensation and the helium isotopes by cryosorption on activated charcoal. During defrosting, helium is released first and pumped through a

precooled cryocondensation element, the cryotransfer pump (CTP) into a buffer tank in the impurity processing loop. The CTP then condenses the subsequently released Q_2/impurity mixture. The performance of the ACP has been tested and found satisfactory earlier [3]. The function of the CTP in separating Q_2 from impurities was recently tested. The CTP is shown schematically in Fig 2.

The Q_2/impurity mixture is pumped on a central cryocondensation surface, cooled with LHe to 4K. After transfer of a complete batch from the ACP, the CTP is isolated and warmed by electrical heating; the Q_2/impurity mixture is boiling at constant temperature (~ 25K), controlled by an upstream pressure regulator on the pump outlet keeping the pressure in the pump constant at ~ 1 bar. The boiled-off Q_2, containing some of the impurities, is forced through an annular gap containing fine wire screen at ~ 25K; this large cold surface area permits the recondensing of any impurities from the gas stream, all impurity vapour pressures at 30K being in the order of 10^{-10} mbar or lower. For test purposes, nitrogen was selected to represent impurities, the vapour pressure of N_2 at 30K being substantially higher than that of the next most volatile impurity CH_4. A mixture of 100ℓ (STP) D_2 with 15ℓ (STP) N_2 was condensed, the D_2 subsequently boiled off; nearing the end of the D_2 inventory as indicated by a sharp pressure rise of the D_2 vapour pressure thermometer coupled to the boiler heater, an evacuated and baked sample flask (1ℓ) was filled to a pressure of 1.5 bar. A quantitative analysis by gaschromatography was performed at Harwell Laboratory (UKAEA) and found D_2 with 5 ppm O_2 and 23 ppm N_2. As our mixture originally had not contained oxygen, this result indicates most likely a very small in-leakage of air either into the sample flask prior to filling or in the sampling equipment during measurement.

In any case, this result shows that impurity separation from Q_2 in the CTP is fully adequate, as the use of uranium beds for transfer to isotope separation will eliminate trace impurities to sub-ppm levels.

2.2 Uranium beds for Q_2 storage and transfer

Uranium beds are to be used in the impurity processing loop for decomposition of tritiated water and Q_2 storage [4], in the intermediate storage system for transfer pumping from CF and IP to isotope separation and after isotope separation for tritium and deuterium product storage.

To meet all requirements of these various applications, the bed capacity has to be high (in our case 18-20 moles of U 238) and the heat transfer to the uranium powder in supplying or removing reaction heat very good. For this reason, we selected a design with a large surface area heat transfer structure, shown in Fig 3.

A central tube contains electrical heaters, vacuum furnace brazed in copper sleeves, and a concentric tube gas cooling device. On its outside, it carries nickel fins transferring the heat flow from the core to the powder. Tubular sinter filters (Inconel, 20 μ pore size inlet bottom and 5 μm pore size outlet top) prevent uranium dust from entering adjacent process pipework. Fig 4 shows a completed bed prior to filling: the uranium is loaded in the form of solid metal platelets between the fins, subsequently the primary containment tube is slid over the internal structure and welded vacuum-tight. The bed is then fitted into a secondary containment, leak tested to 10^{-10} mbℓ s^{-1} and pressure tested to 40 bar with helium gas. Subsequently, the uranium is hydrided with D_2, the first hydriding run shown in Fig 5 required some heating to start the reaction, causing the solid U-metal to diminute into UD_3 powder. Subsequent hydriding runs led to further diminution and activation, eventually (with full cooling gas flow on) to the uptake of the full capacity (27 moles of D_2 in 18 moles of U) within ~ 15 minutes as shown in Fig 6. The distribution of the uranium powder inside the structure after dehydriding at 600°C was checked by radiography, Fig 7, showing clearly the heat transfer fins with the powder in between and the outlet filter tube.

Equilibrium pressure measurements for two compositions $UD_{3.00}$ and $UD_{2.00}$ are shown in Fig 8. The very good agreement between these data and measurements by Wicke and Otto [7] demonstrates the efficiency of the heat transfer structure showing that the temperature gradient between the copper core (location of thermocouple) and the uranium deuteride powder is negligibly small.

Based on these results, we have decided to use identical beds for Q_2 scrubbing from helium carrier gas, storage and transfer pumping of Q_2, and T_2 and D_2 product storage in several AGHS subsystems.

2.3 Uranium and iron beds for water decomposition.

The basic concept of the impurity processing loop [4] consists of catalytic oxidation of all impurities to Q_2O, collection of Q_2O in a 16DK cold trap and subsequent decomposition of Q_2O on a suitable hot metal powder (U, Fe).

Initial tests using the U-bed of Fig 4 by transferring steam into dehydrided powder at ~ 200°C showed that the reaction $6\ H_2O + 7U \rightarrow 3\ UD_2 + 4UH_3$ leads to 100% reaction of the steam with U-powder, with full recovery of hydrogen from UH_3 by subsequent heating to 450°C.

The disadvantage of this method is the consumption of uranium and subsequent disposal of reaction beds as active solid waste. We therefore investigated another process, ie reaction of steam with iron at 500°C, which can be regenerated by pure hydrogen at 600°C. The experimental setup is shown in Fig 9:

A water evaporator is connected with a chemical reaction bed (identical to the U-bed of Fig 4) filled with iron powder, followed by a molecular sieve drier and a uranium bed. Each element was placed on an electronic balance, permitting quantitative measurement of chemical reactions by weight. Steam passes from the evaporator through the iron bed, partially reacting to iron oxide and hydrogen; non-reacted steam is collected in the drier, the hydrogen formed in the iron bed is collected in the uranium bed. In a test run with a total of 6 moles of H_2O in the evaporator, 80% of the steam was reacted in the iron bed, 20% was collected in the drier. Hydrogen was quantitatively recovered from the U-bed by heating.

This first experiment has shown the viability of the iron-steam process in reducing the uranium consumption by a factor of 5. Further experiments to optimise process performance are in preparation.

2.4. Transpiration pump

Separation of all six Q_2 species into pure H_2, D_2, T_2 by means of cryodistillation requires a multicolumn system interconnected with sidestreams recirculating through catalytic equilibrators in order to react the unwanted species HD, HT, DT into the pure species. Mechanical pumps used usually as recirculators for driving these streams are prone to fail due to metal fatigue in continuous operation. We therefore decided to use the physical and thermodynamic properties of the hydrogen isotopes at low temperatures to design a recirculation pump without moving parts, shown schematically in Fig 10.

Liquid hydrogen (from the sump of a distillation column reboiler or from a dedicated feed condenser) is supplied to the outside of a fine-pore sinter filter. Liquid hydrogen wets all substances and is soaked into the

pores by surface tension. A heater evaporates liquid on the inner surface of the sinter filter. This device can deliver cold gas streams against a pressure difference up to a limit

$$\Delta p = \frac{4\gamma}{d} \ [kPa]$$

where γ is the surface tension in dyn cm^{-1} (eg $\gamma \sim 2.0$ dyn cm^{-1} for liquid D_2 at 27K according to Souers [8]) and d is the effective pore size in µm.

We have verified this effect with liquid D_2 for pore sizes between 0.8 µm ceramics and 8 µm nickal sinter filters, obtaining pressure differences of ~ 10 kPa (for 0.8 µm) and ~ 1 kPa (for 8 µm) in agreement with above relation.

Flow rates produced by this device follow the relation

$$\dot{q} = \frac{N}{h}$$

h being the heat of evaporation and N the heater power, meaning that the gas leaves the device actually at the boiling temperature of the surrounding liquid.

Further experiments to modify and optimise the pore size of commercially available metal sinter filters by means of chemical metal deposition are in progress.

2.5. Gaschromatograph diagnostic

One of the two JET AGHS isotope separation systems is based on elusion chromatography on a Pd coated Al_2O_3 packing, using the strong isotopic effects in the PdQ system as described by Botter [5].

Usually, arrival of an isotopic front is indicated by instrumentation on the column exit (ionisation chamber, catharometer) and the fractions are then "cut" to their respective receivers. These signals obtained at the column exit must be acted on immediately and may be occasionally difficult to validate against background noise. We found an additional diagnostic signal obtainable from the separation process itself: arrival of the first isotope (tritium) displacing helium gas is accompanied by a large temperature rise in the packing (formation enthalpy of PdT) of about 20°C, subsequent isotopic transitions by smaller rises of ~ 1.5°C. Using the signal of two differential thermometers embedded in the packing at a distance of ~ 6 cm near the column exit, we can prevalidate signals from column exit diagnostics. Fig 11 shows signals of a test run on helium-D_2-H_2, the differential temperature signal preceding the catharometer signal by ~ 40 seconds.

2.6. General components

2.6.1 Valves

The basic decision to place all critical (high and cryogenic temperature) process elements into all-metal double containments built to UHV standards [1,2] made it particularly difficult to accommodate an unavoidably large number of process valves. Usually, such valves would be built with double bellows stem feedthrough (monitored interspace) and mounted on a container lid with the actuator in ambient atmosphere. In our case, this would have led to very large containment lids and a vast number of interspace monitoring connections (approximately 500 for the whole plant). We have overcome this problem by designing all-metal UHV compatible valve actuators which can be fitted on commercially available valves. Figs 12a and 12b show an example of such an actuator on a Nupro ¼" all-metal valve both in spring open and spring closed version. It should be noted, that both versions are assembled from identical basic parts, the only difference being in some minor assembly hardware and springs of different spring constants.

These actuators, consisting only of springs and bellows, are not subject to friction forces (unlike standard pneumatic piston drives), hence valve position indicators can be mounted outside the containment in the form of high/low pressure switches connected to the pneumatic supply line after the solenoid pilot valve.

Cycling tests on valves have shown deterioration of leak tightness across valve seats on all-metal (Stellite stem tip) valves after several 100 to 2000 cycles; valves with VESPEL stem tips have survived more than 50000 cycles with no measurable leak across the valve seat. We have therefore decided to use VESPEL stem tips on most AGHS process valves.

2.6.2. Pressure regulators

Several AGHS subsystems (CF, GC, PS) use upstream and downstream mechanical pressure regulators to simplify system control : with the exception of the cryodistillation system, no other subsystem employs feedback controlled valves for flow - respectively pressure control. Figs 13a and 13b show our design of all-metal, bakeable and fully tritium compatible pressure regulators, the main body being identical in design except for a few small hardware pieces to obtain the desired configuration. The operating pressure is set by applying a reference pressure (usually helium gas) on the reference side of the control membrane. Tests have shown good control performance: pressure variation on the controlled side ≤ 1 mbar for pressure variations on the opposite side of 1 bar in a flow rate range of 0 to 10l min^{-1}, and a residual leak rate of < 1 x 10^{-1} $mbls^{-1}$ in the closed position for ΔP ~ 1 bar. This performance covers all AGHS applications.

3. CONCLUSIONS

These examples show that the design of a complex tritium handling plant not only requires a good basic concept, but can also greatly benefit from a parallel development programme providing well considered and tested technical solutions for specific problems.

4. STATE OF THE AGHS

- the construction of the plant building started in May 1988
- procurement contracts have been placed for CD, CF, ED, MF, IP
- procurement contracts for most of the other components will be placed by end 1988, early 1989
- final layout/design is in progress on H_2 product storage, analytical equipment and subsystem interconnections
- the control system based on individual subsystem PLC's is in the hardware definition stage.

It is foreseen to complete the main plant assembly by the end of 1989 and start with plant commissioning in 1990, gaining experience with actual tokamak operation during the JET final D_2 operation phase.

Gradual introduction of tritium in the AGHS is planned for 1990, starting operation of JET with DT plasmas mid-1991.

REFERENCES

[1] JL Hemmerich, A Dombra, C Gordon, J Gowman, E Groskopfs, R Haange, M Huguet, A Konstantellos, E Küssel, M Tschudin, K Walter. "The JET Active Gas Handling System: Concept and Status". Proc. 12th Symposium on Fusion Engineering Oct. 12-16 1987, Monterey, California IEEE Catalogue No.87 CH 2507-2, p.1235.

[2] R Haange, JL Hemmerich, AC Bell, C Caldwell-Nichols, A Dombra, C Gordon, J Gowman, E Groskopfs, A Konstantellos, E Küssel, M Tschudin, K Walter."General Overview of Active Gas Handling System at JET". Proc. 3rd Topical Meeting on Tritium Technology in Fisaion, Fusion and Isotopic Applications, May 1-6 1988, in print.

[3] E Küssel, J Gowman, JL Hemmerich, K Walter. "The Cryogenic Forevacuum System for the JET Active Gas Handling Plant" Proc. 3rd Topical Meeting on Tritium Technology in Fission, Fusion and Isotopic Applications, May 1-6 1988, in print.

[4] JL Hemmerich, A Dombra, C Gordon, E Groskopfs, A Konstantellos. "The Impurity Processing Loop for the JET Active Gas Handling Plant" Proc. 3rd Topical Meeting on Tritium Technology in Fission, Fusion and Isotopic Applications, May 1-6, 1988, in print.

[5] F Botter, S Tistchenko, R Lässer, J Gowman, D Léger, JL Hemmerich. "The Gas Chromatography Isotope Separation System for the JET Active Gas Handling Plant" Proc. 3rd Topical Meeting on Tritium Technology in Fission, Fusion and Isotopic Applications, May 1-6 1988, in print.

[6] AH Dombra, JL Hemmerich, AC Bell, R Haange, MEP Wykes. "Exhaust Detritiation System for JET". This conference.

[7] E Wicke and K Otto: "Über das System Uran-Wasserstoff und die Kinetik der Uranhydridbildung" 2. Phys Chem. 31 (1962), 222.

[8] P Clark Souers "Hydrogen Properties for Fusion Energy" University of California Press, Berkeley, Ca, (1986), p.64.

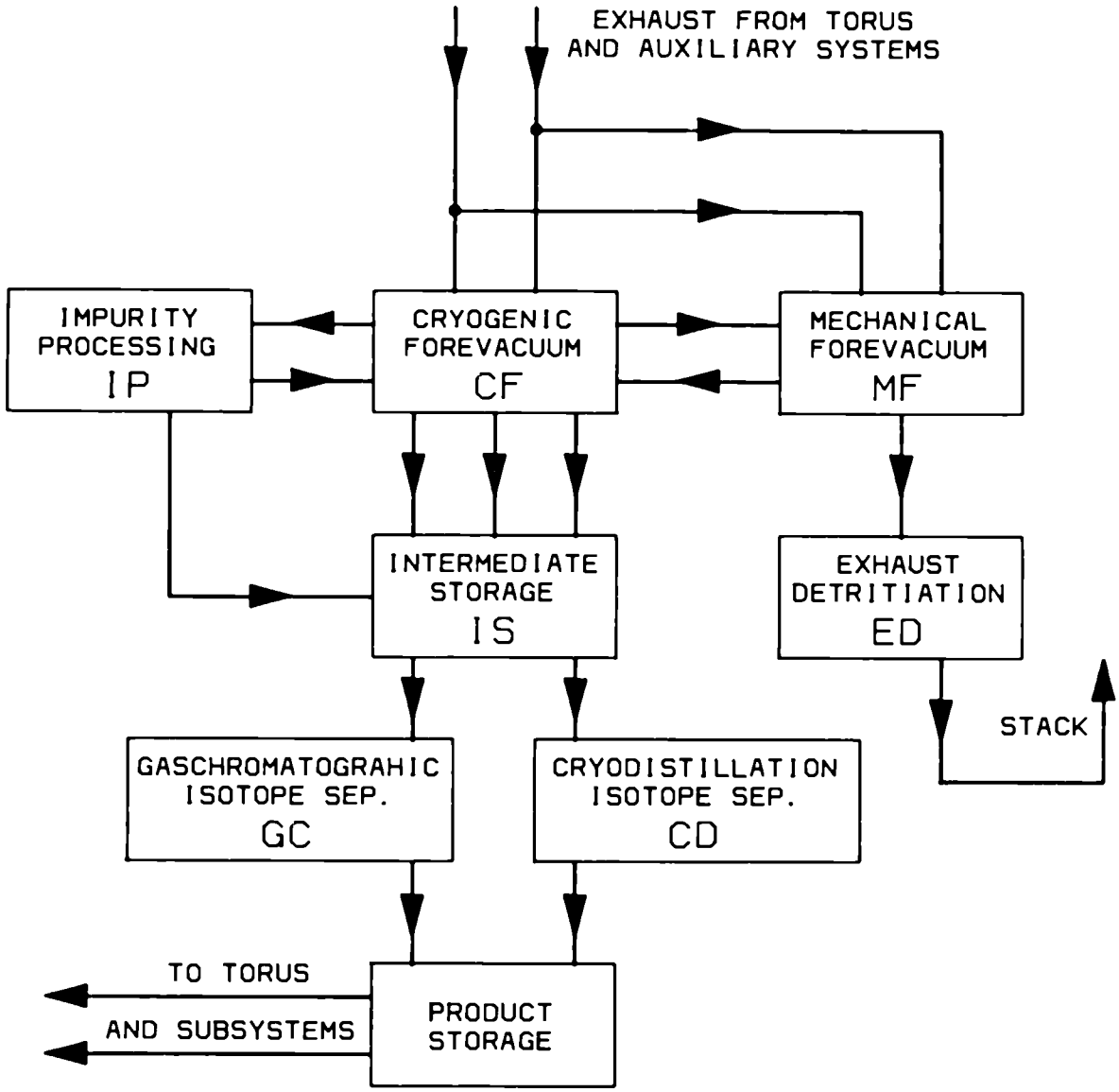

Fig. 1 JET active gas handling system block diagram.

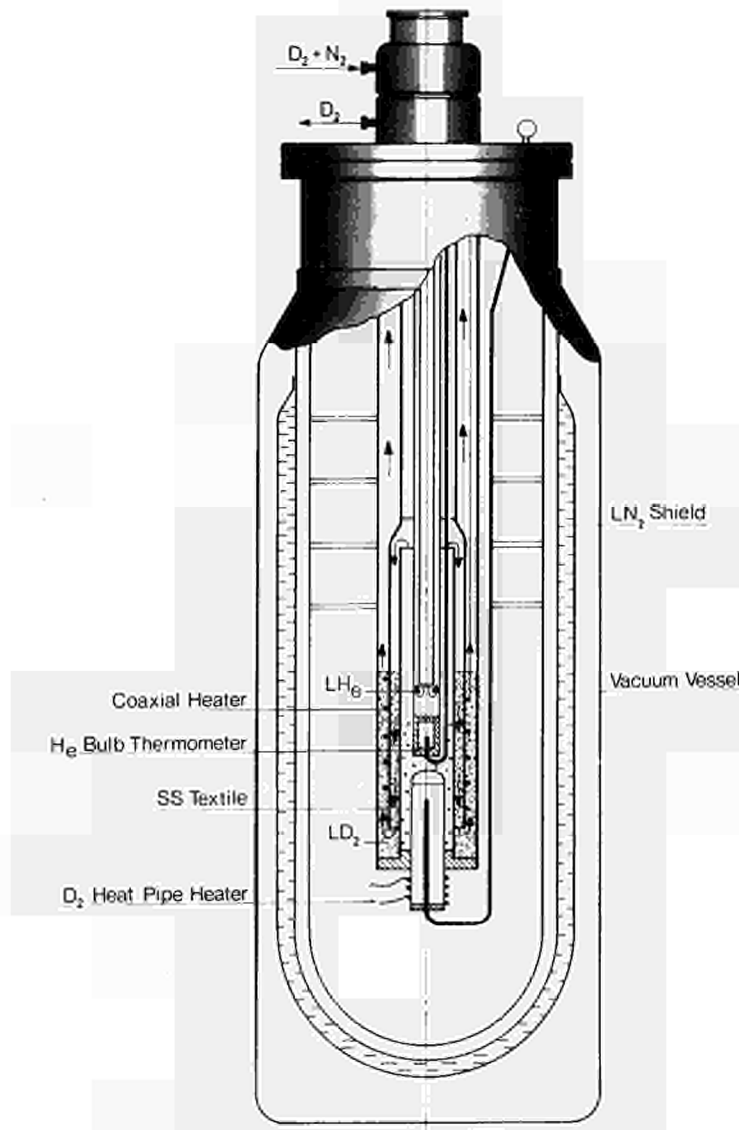

Fig. 2 Cryo-transfer pump (CTP) schematic.

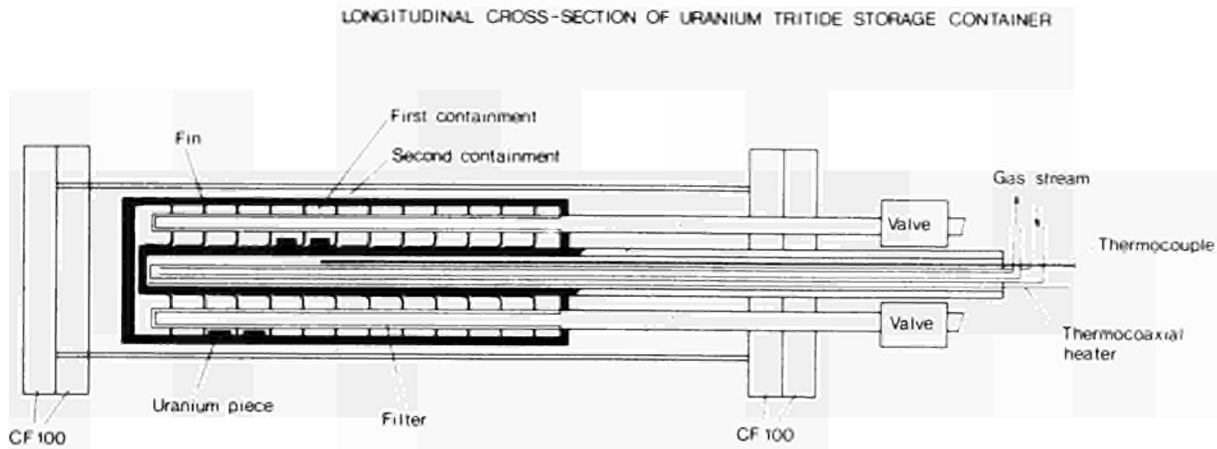

Fig. 3 Uranium bed schematic.

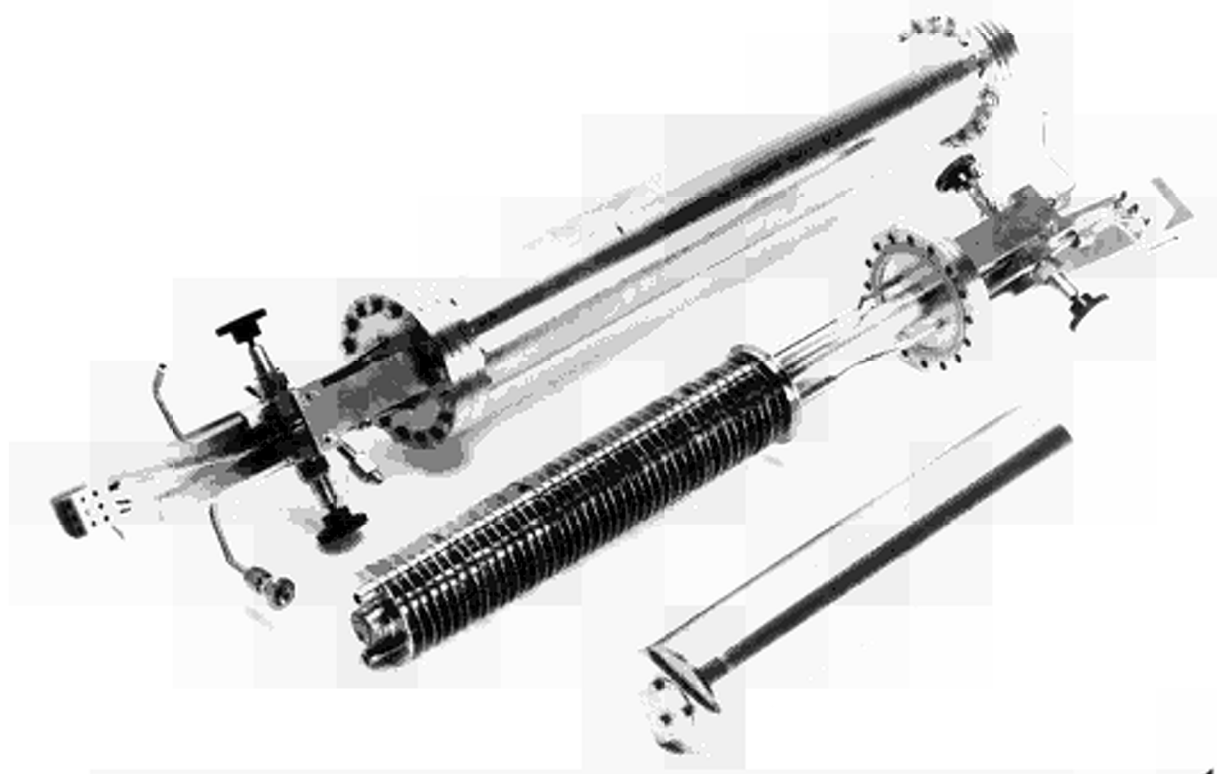

Fig. 4 Uranium bed; bottom: primary container; centre: heat transfer structure; top: bed fully assembled in secondary containment.

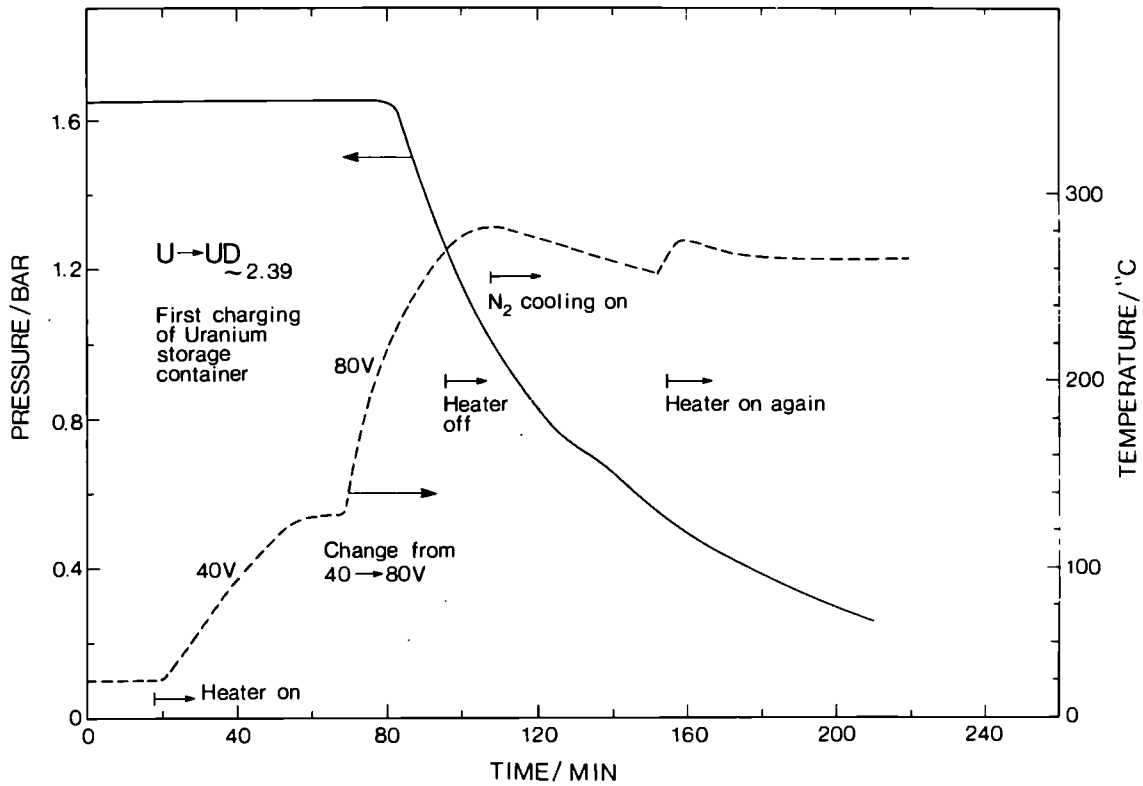

Fig. 5 First hydriding run of U-bed.

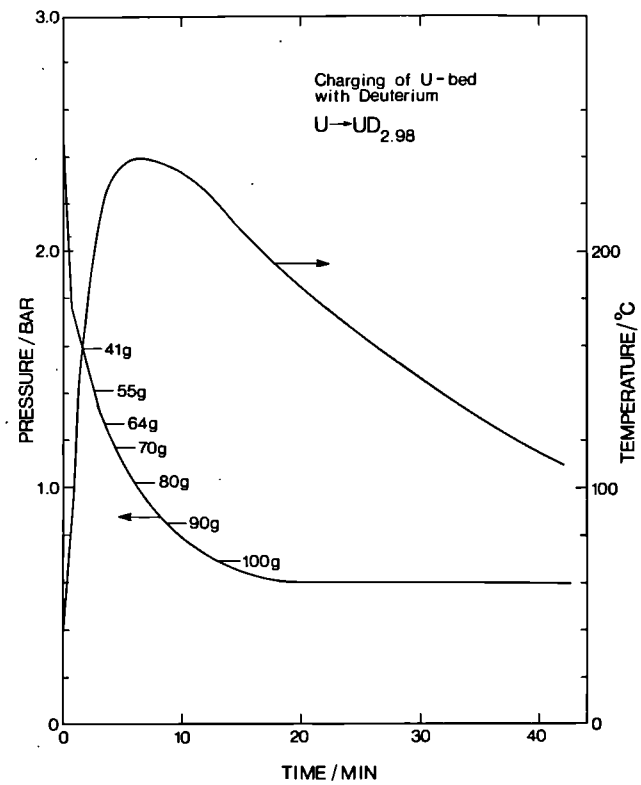

Fig. 6 Deuterium uptake of fully activated U-bed with internal gas cooling.

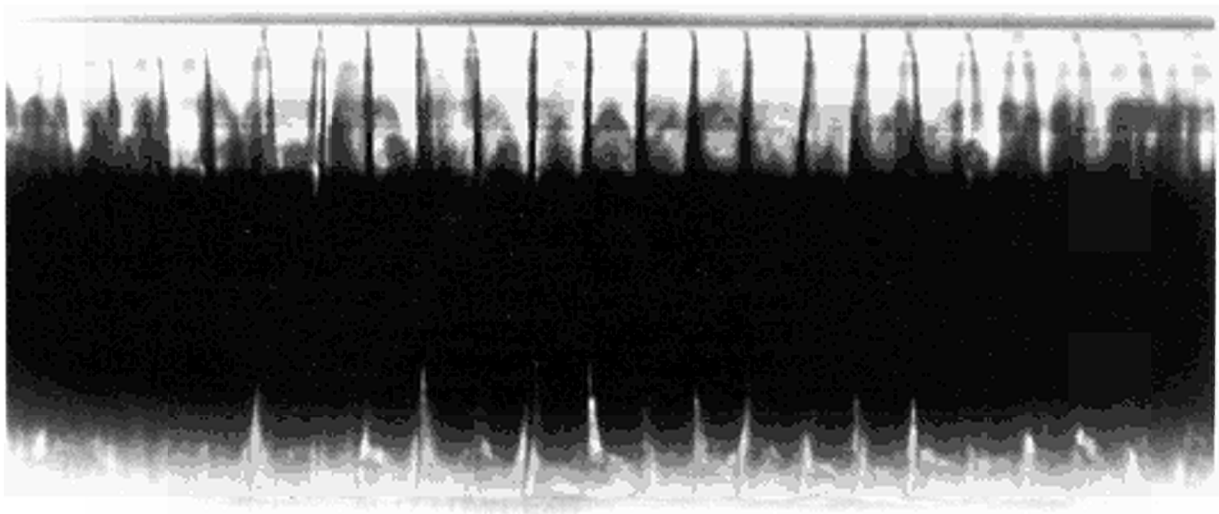

Fig. 7 Radiograph of fully activated U-bed after de-hydriding at 600°C.

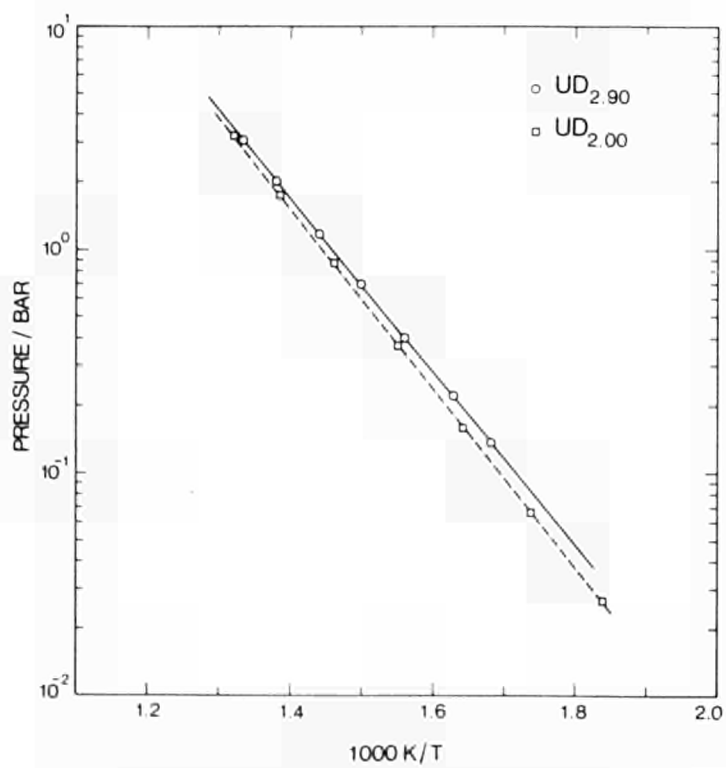

Fig. 8 Equilibrium pressure vs. temperature for the compositions $UD_{2.90}$ and $UD_{2.00}$.

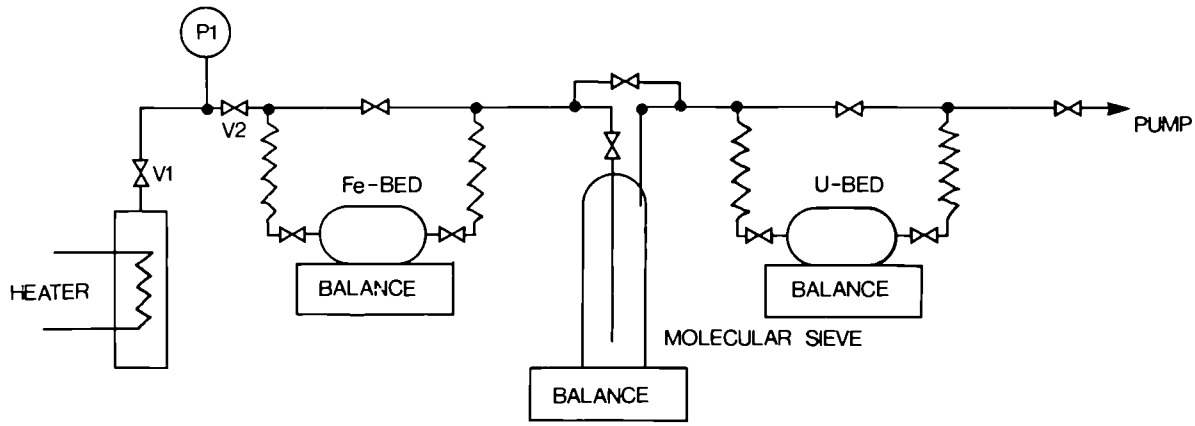

Fig. 9 Water decomposition on iron bed, test set-up.

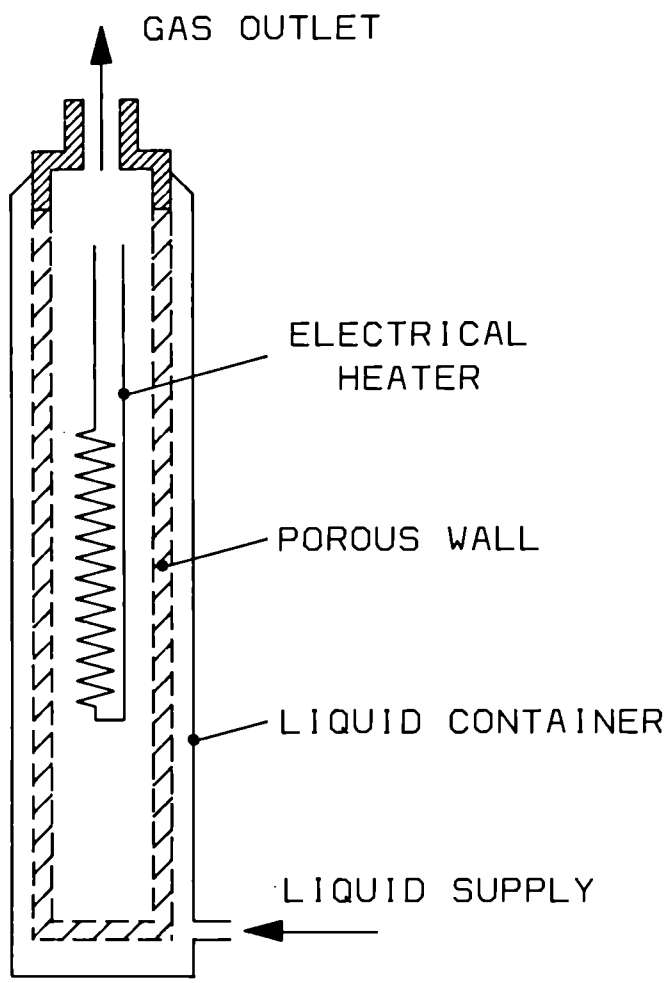

Fig. 10 Transpiration pump schematic.

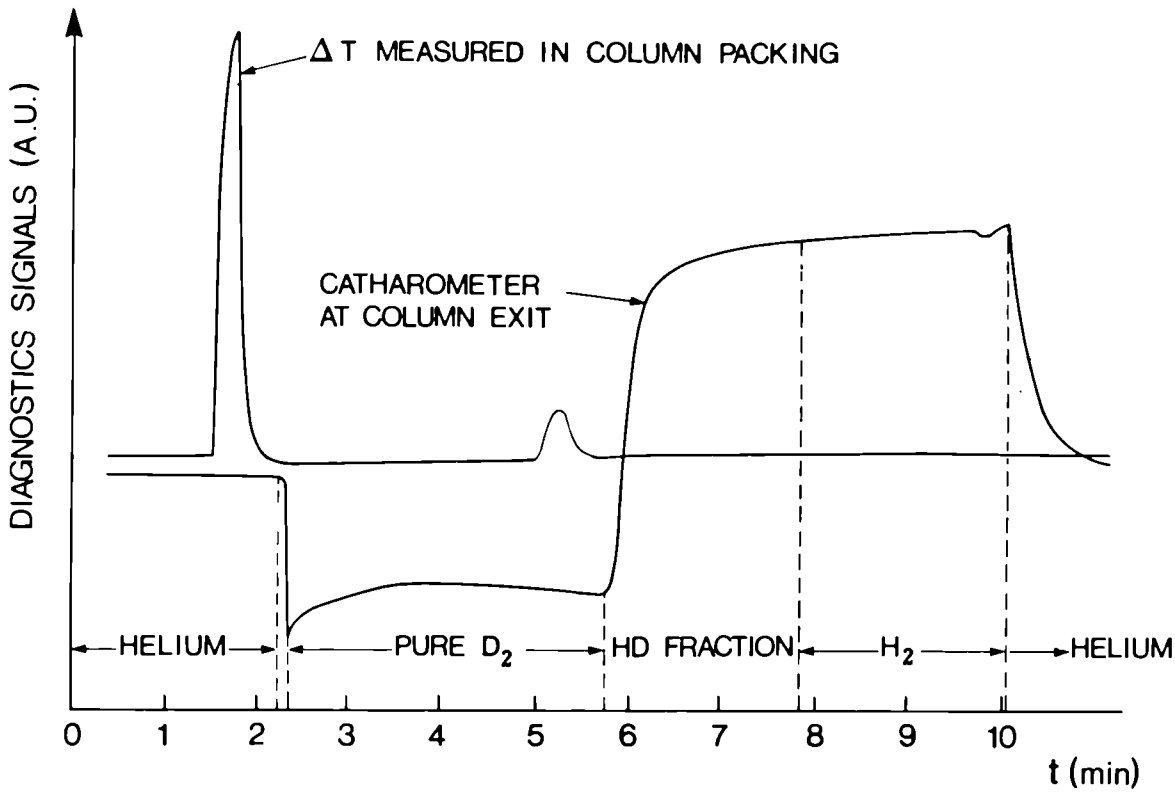

Fig. 11 Differential temperature measured in column packing and catharometer signal at the outlet of a separation column.

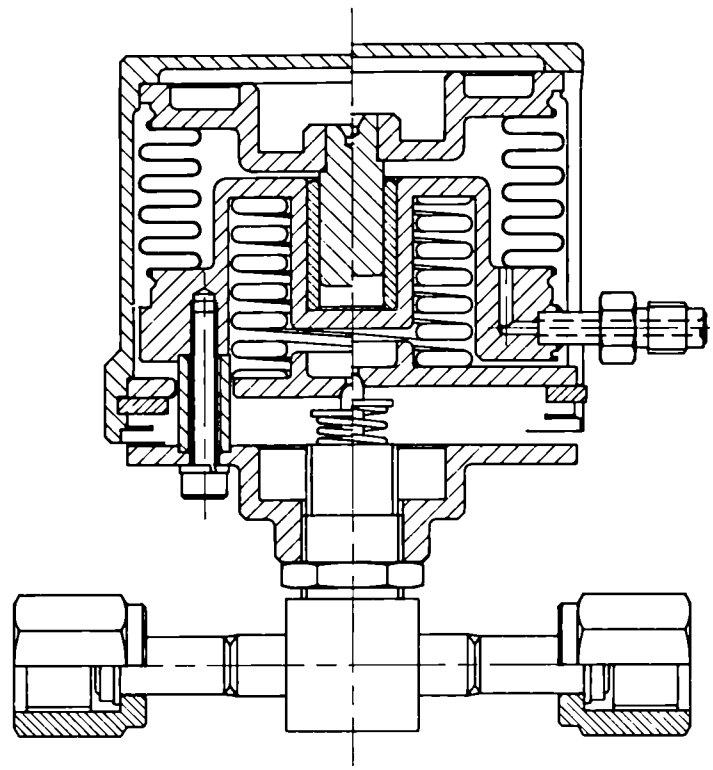

SIZE 4 NUPRO WITH SPRING CLOSED ACTUATOR

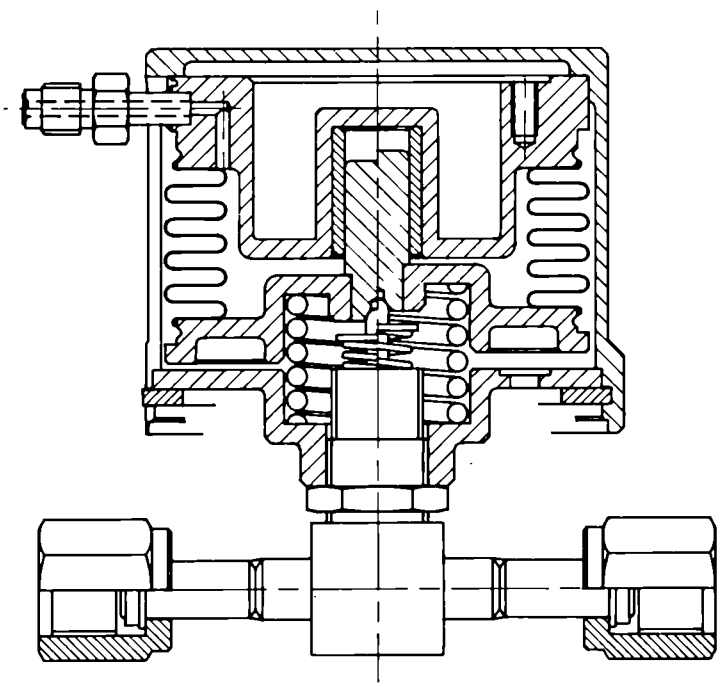

SIZE 4 NUPRO WITH SPRING OPENED ACTUATOR

Fig. 12a/b Spring closed and spring open actuator for ¼'' Nupro valves.

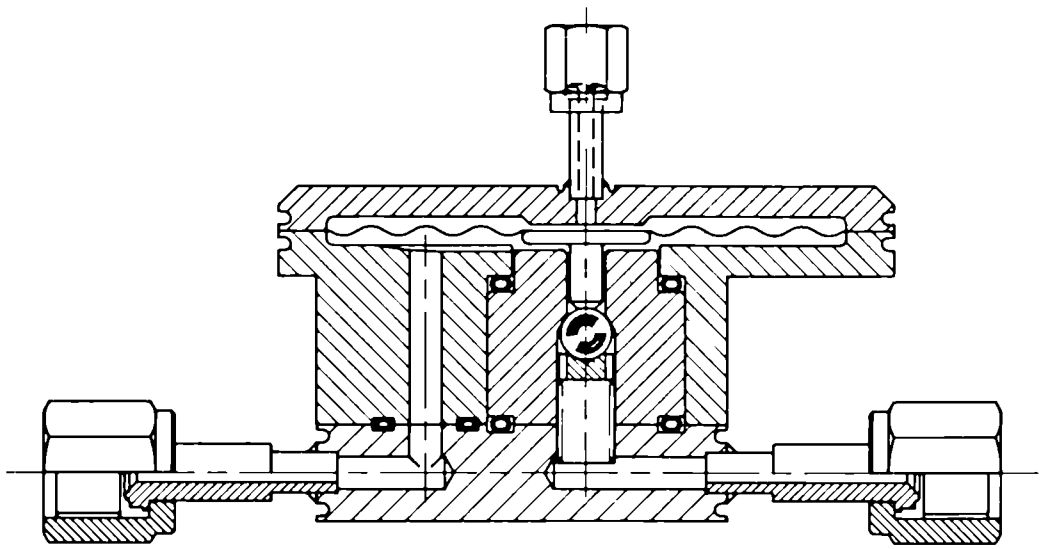

DOWNSTREAM PRESSURE REGULATOR

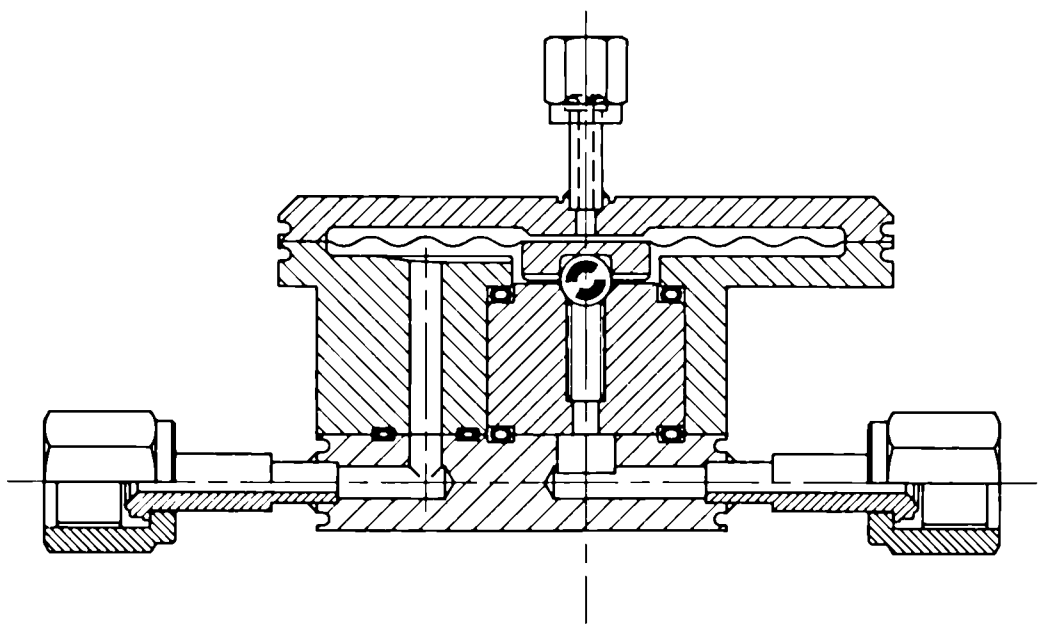

UPSTREAM PRESSURE REGULATOR

Fig. 13a b Upstream and downstream pressure regulators in all-metal, tritium compatible design.

The JET Experience with Remote Handling Equipment and Future Prospects

T Raimondi

ABSTRACT

The commissioning and testing of numerous pieces of equipment are now in progress at JET. Two microprocessor controlled force feedback MASCOT IV servomanipulators have shown comparable characteristics to those of the previous analogue types. Teach and repeat software permits precision welding and repetitive operations in a robotics mode. Other computer aids are planned to improve the man-machine interface: tool-weight compensation, constraints along preferred lines or planes, automatic tracking of the TV cameras. The in-vessel transporter, provided with 5 vertical hinges, a pan-tilt-roll extension and special purpose end effectors, has been used under direct visual control to install 32 toroidal limiters and 8 radio frequency antennae. Tests of remote installation in teach and repeat were done, using the JET spare octant as a mock-up, achieving repeatability of better than 5mm. A considerable number of special remote handling tools were used inside the vessel hands-on to align, cut and weld diagnostics ports and water pipes. The cutting and welding trolleys were used hands-on, on a total of 250m of lip joints. The ex-vessel transporter, a crane-mounted vertical telescope, 17m high with a 10m horizontal arm, is being manufactured. It will be equipped with manipulator and TV systems and controlled via joystick or keyboard or in teach and repeat. Image processing for collision avoidance is being studied. A low level transporter was used for turbo-pump replacement and is now being equipped with remote control. Mock-up work has started on the replacement of the Neutral Injector sources. Bench tests on flanges, heating jackets and connectors are being done to identify refinements needed. The in-vessel inspection system has been used at high temperature in vacuum.

1. INTRODUCTION

The JET remote handling equipment (Fig.1) will be operator controlled from the remote handling control room, which is now near completion [1], [2], [13]. The principal remote handling devices to substitute manual intervention are:

Mascot force-reflecting servomanipulators (Fig.2) which can either position automatic tools developed for particular tasks or use compatible conventional tools. The servomanipulators are positioned where desired by the large transporters - the articulated boom for work inside the vessel, and the crane-mounted articulated arm (TARM) for work on the outside.

A low-level transporter (ROLLT) and turret truck complete the positioning requirements.

For moving heavy components the Mascot is replaced by one of a series of special-purpose end effectors.

Essential for successful remote interventions is the provision of clear viewing of the work area. To this end a system of telecameras are mounted on the manipulator, on articulated arms branching from the boom and TARM and in fixed positions in the Torus Hall to guide the operators who will work using monitors in the control room. They will also be aided by a graphics workstation depicting on line the movements of the boom and TARM in and around the vessel [14]. The In-Vessel Inspection system has been upgraded to perform inspections at 300°C to avoid waiting for the vessel to cool.

2. SERVOMANIPULATORS

2.1 Feasibility trials

A Mascot 3 servomanipulator built in 1970 was acquired from ENEA and modified to suit JET configurations. This was used to try out various operations, e.g spot welding, handling of vacuum flanges, carbon tiles and electrical connectors, to check that they could be done remotely. In all of these tests the value of force-reflection to the operator was apparent. The operator has, as nearly as possible, the tactile sensation of actually doing

the job. This is what Jean Vertut [3] referred to as "telepresence". The manipulator has to be as "transparent" as possible, allowing the operator to concentrate his attention on the task rather than on the manipulator.
This "transparency" depends on the excellence of the servosystem in each joint. Ideally the force and position imposed by the operator on the Master unit would be equal to that imposed by the Slave on the object handled. Consider the block diagram of a mechanical quadrupole representing the bilateral servo connecting two corresponding joints with force ratio 1 (Fig.3). The input force and position T1,θ1 are close, both statically and dynamically, to the output quantities exerted by the slave if 1) the inertias of Master actuator J1 and Slave actuator J2 are negligible, 2) the stiffness of the servo Kc is high, 3) the friction Ca1 and Ca2 in the Master and Slave mechanisms is low and 4) damping Kv is adequate to avoid oscillatory response.

If the servosystem is good it is possible to do operations requiring considerable dexterity. The rather brittle carbon tiles lining the vessel are mounted on dovetail rails with a spring arrangement to prevent damage due to vibrations. This makes it difficult to slide them on and off the rails. When this operation was tried with the manipulator a rudimentary tool was used consisting of a rod clamped to the sides of the tile. Gripping the ends of the rod with the two arms of the manipulator and applying a rocking motion with controlled forces, it was possible to remove the tiles without damaging them.

Another example of a case where fast response of the servosystem allows the operator to act instinctively by trial and error is inserting a pin into a hole. This applies to all operations involving insertion of connectors, doing up bolts or engaging spigots or dowels. Prompt force feedback can make it possible to do operations where viewing is impaired. For example a wrench can be located onto a flange bolt head partially hidden behind a pipe because the operator can feel where it is. Initially difficulties were experienced with the LEMO connectors, particularly the larger sizes, where the weight of the cable dragging on the connector and the tight clearances made connection difficult even by hand. It was found sufficient to chamfer the male connector to resolve the problem.

Confiding in the dexterity of the manipulator, conventional types of connections are used rather than embarking on special designs of automatic devices, which would have been costly and of dubious reliability. An example are the standard bolted vacuum flanges which were proven reliable and reasonably easy to handle (Fig.4). Bench tests have shown that the heating jackets, of very simple and inexpensive design, can be handled using the manipulator. It also proved possible to change Cefilac seals, an operation envisaged in the hot cell.

Trials were also done using the manipulator in different attitudes as problems of geometry and restricted access will not always permit the manipulator to work upright. For example, during insertion through the entrance port the Mascot has to be turned side on and in this attitude remove the tiles that have been added at the top and bottom of the port to prevent damage from the neutral beams. When a tile is lifted off, the operator feels this as a sideways force. However, with a little training he soon gets used to this. The weight compensation system being studied at present should help. It is important that the camera should be in approximately the same attitude with respect to the slave grippers as the operator tends to become disorientated. Operating with the slave upside-down to handle a Lemo connector underneath a simulated junction box also proved satisfactory.

Mascot 3 is still used for bench tests and trials could serve as an emergency backup. It has very good dexterity characteristics but its analogue control system puts it into the antiques class nowadays.

2.2 Mascot IV servomanipulator

Two Mascot IV servomanipulators are on site and a third slave unit has been ordered. This latter one has motors with class H insulation so that it can work for longer periods at full load. The new manipulators, which are slightly smaller in size than Mascot III have the same mechanical characteristics but the control system is microprocessor based, with transmission of signals on a serial link. For operations outside the vessel this is essential due to the considerable length and limited cross section of the connecting cables carried by the crane bridge. Digital control lends itself to the introduction of more sophisticated robotics algorithms:

- Teach and repeat. This is useful for repetitive operations or where viewing is impaired, e.g repair welding. To limit the amount of memory required, parabolic extrapolation, which corresponds to a constant acceleration, is used. Teach and repeat is also used for the transporter which positions the manipulator in the work area and for the TV camera motions. It will result in a great saving of time in getting the manipulator and TV camera into position in the work area.
- Tool-weight compensation. This is particularly important when the slave has to work in a different attitude from that of the master. It also alleviates operator fatigue while allowing good sensitivity. The torques at the various joints, proportional to the angular displacement in a particular configuration of the slave, give, at steady state, information on the weight of the tool. By trigonometric calculations it is possible to compute on line the balancing torques needed at the various joints to compensate the weight in any configuration.
- Constraint of the trajectory on given planes or lines. This is useful, particularly where viewing is not good, to keep a tool on the line or plane of motion. Operations such as sawing, screwing and aligning connectors can be greatly facilitated by this technique. The operator will retain force feedback and freedom of motion in all directions except the one perpendicular to the constraining plane or line. If he deviates from this, he will feel a force opposing him, the stiffer the servo the more sharply the force increases.

The teach and repeat facility has been incorporated in the Mascot software and commissioned. Tests have been done teaching and repeating at various speeds, with the master holding a ball point pen to draw irregularly shaped lines and repeat them. Repeatability is estimated at 0.2mm in ranges of motion where backlash is recovered by gravity. This is sufficient for repair welding with the aid of arc voltage control. The trajectory can be improved in successive trials and then repeated. The precision of the trajectory taught depends on the steadiness of the operator's hand. A better alternative which we intend to pursue is teaching the trajectory as a series of points and repeating with an interpolation algorithm.

The tool-weight compensation and trajectory constraint facilities are at present being developed. Further software which is intended to be developed and incorporated in the Mascot control system is automatic tracking of the telecamera mounted on the Mascot slave. At present orienting the camera takes up too much of the time for any given operation. The camera axis could be kept approximately pointing at the slave grippers by an appropriate transformation which gives the three coordinates (pan, tilt and roll) of the camera in function of the coordinates of the centre of the grippers.

Some other enhancements are also envisaged. In the present system the only signals transmitted from Master to Slave and vice versa are the relevant joint positions (Fig.3). To compensate the damping Kv of the actuators which the operator perceives as a viscous drag, velocity feed-forward signals

obtained by digital derivation of the angular positions are used. This produces some granularity. Transmitting the tacho generator signals should make this disappear. Additionally these will be differentiated to give acceleration feed forward signals useful to reduce the inertia reflected to the operator.

3. IN-VESSEL TRANSPORTER

3.1 Articulated Boom

In its final version the boom [8] consists of five segments articulating on the horizontal plane with a reach of 10m from the first hinge (18m from the support trolley). The terminal segment can also be tilted to position the end effector close to the top or bottom of the vessel. Any part of the vessel is accessible from one port (Fig.5).

Care was taken in the choice of materials to optimize strength versus weight. The first two segments are in stainless steel and the others in aluminium alloy. These are all closed box structures to resist torsion. The boom extension is an aluminium/magnesium casting, strengthened by hot isostatic pressing. It had to be an open structure to accommodate the tool box and was optimised with finite element calculations. The load capacity of the boom is 350kg at full reach, and is being upgraded to 440kg.

Hydraulic fluids were excluded by the high vacuum requirements so all the motors are electric. The actuators are on the joints and there is space above them for the cabling to be routed between the top and bottom hinges. The actuators consist of Harmonic Drive gearboxes, directly coupled to Inland DC torque motors, incorporating a DC tachogenerator. This solution offers the desired compactness for the high torque required (5000Nm), fast response and negligible backlash. This in turn permits installation directly on the joint of a resolver, coupled to a 16 bit R/D convertor, which gives the required repeatability. The main shortcoming of the installed Harmonic Drive gear is a certain degree of elasticity. Stiffer actuators are being developed.

The rotation of each of the main joints and the translation of the support trolley are controlled with a servoloop configuration as in Fig.6. The position error, calculated via software, is applied as an input signal to hardwired velocity servos controlling the motors with PWM pulse width modulation) amplifiers. The torque T developed by each gearbox depends on the angular difference Δ between its input and output shafts and is a function of its elasticity, backlash and efficiency in both direct and backdriven modes. The single joint servoloops are reciprocally coupled through the system dynamics which virtually corresponds to the inertia matrix of the five segments.

A dynamic model was set up, validated and used to optimize the parameters.

The control system [5] is microprocessor based and provides the following functions:

- Closed loop control of all joints and open loop control of adjustment jacks and various end effector motors.
- Control of the boom from either the Remote Handling Workstation or a local handbox.
- Safety interlocks to prevent joint runaway or servo errors.

There are three modes of operation:

a) Direct mode - one or two joints can be selected and moved in rate control from a joystick or position controlled from a keyboard.

b) Resolved motion - either in "tool" coordinate frame located on a preselected segment or "world" coordinate frame in fixed position.

c) Teach - repeat, which allows previously taught sequences to be automatically repeated.

The control system is interfaced to a graphics workstation which offers a powerful visual aid, showing in real time the position of the boom relative to the environment, and also offers a facility for off-line teaching.

3.2 Use of boom

During the 1987 shutdown 32 belt limiter sectors and 8 RF antennae were installed using a handbox under visual control inside the vessel. This year in May two faulty antennae were replaced.

3.2.1 Belt limiter installation

The limiters consist of two belts circling the vacuum vessel, each is composed of interchangeable sectors weighing 80kg. Each sector is basically a set of fins welded onto a cooling water pipe, with graphite or beryllium tiles mounted in the fin interspaces [11].

The installation sequence is as follows:

The limiter sector is offered up to the articulated boom by the turret truck approximately 6m above the floor. It is picked up by the boom end effector, consisting of a "shield" provided with 4 hooks.

A sequence of movements of the hinges then brings the boom from the starting configuration through the port and up to the requested position of the limiter in proximity of the wall (Fig.7).

With a tilt motion combined with a radial adjustment the limiter then follows a trajectory virtually tangent to the vessel with a precision of 5mm, so that its cooling pipe can be positioned behind the adjacent sector, as shown in Fig.8, which refers to an upper segment. Its upper fixing plate engages the top hook fixed to the vessel. For the last belt limiter sector, which closes the belt ring, the positioning precision needed in plan view is in the order of 2mm. The support plate is lifted above the lower spring operated pivoting latch fixed on the vessel and then lowered onto the hook. The boom end effector is then disengaged from the limiter by lowering it slightly so that its hooks can slip out of the engagement holes in the support plate.

3.2.2 Antennae installation

Each antenna [12] consists of two parts:

- The antenna "housing" weighing approximately 300kg is installed on the wall by inserting the two coaxial feedthroughs used as guiding dowels in the corresponding holes in the vacuum vessel wall (Fig.9). Once positioned, the antenna housing is secured by a bayonet engagement manoeuvred outside the VV.
- The electrostatic "screen", weighing approximately 200kg is positioned on guiding pins previously installed on the housing and fastened to this using the servomanipulator.

Up to now these operations have been done positioning the boom under visual control and fixing the components hands on. The cutting and welding of the pipes was done using the RH tools developed for the purpose [6].

A number of handling problems came to light. It was difficult to keep the water pipes accurately aligned for butt welding because the space is too restricted to accommodate strong clamps and the orbital welder. The answer could be a spigot weld configuration to relax alignment requirements and/or initial tack welding before orbital welding. Features are needed to ensure that the screen is accurately homed onto the housing so that the side bolts engage easily.

A load indicator is needed on the boom to ensure that it is not withdrawn before the load has been deposited. The end effector is at present being modified to take a larger load in view of the Low Hybrid antenna and give finer vertical and tilt control, at the same time getting rid of one of the actuators.

3.2.3 Mockup trial

In April 1988, full-scale mockup tests were done using the spare octant and simulated port to install a belt limiter sector, antenna housing and antenna screen. These tests showed that TV viewing of the fixing points of

these components is virtually impossible and so joystick control is not feasible in remote conditions. A trial was done of installing a limiter sector using teach and repeat. This was successful, the precision of the trajectory being within 5mm as required. The whole operation took approximately one hour. When it comes to operation on the actual machine, however, the file taught on the mockup may not be quite correct because of vessel movements. It is intended to develop software which will allow application of a translation of coordinates to correct the taught file at certain visual checkpoints in proximity of the fixing points. The boom support rail will have to be aligned with the entrance port for each new intervention.

It was found difficult to guarantee that the hooks on the shield were totally disengaged from the limiter before retracting the shield. Tiles could be damaged by the shield catching on the limiter and causing the boom to jerk. Actuated hooks have been developed to replace the present ones.

The control system of the boom has been refined and it is now possible to teach in resolved motion and repeat with several joints at a time. This overcomes the difficulties encountered in inserting the boom through the port with the narrow gaps available (approximately 10mm). The time required for full insertion of the boom into the vessel is about half an hour. By rewriting part of the software, originally in BASIC, into FORTH it is expected to reduce to 15 minutes. It is planned to investigate techniques of hybrid position/ force control, using force transducers already installed on the joints. The aim is to improve the dynamic response and to improve stiffness or compliance depending on the operation to be done.

4. EX-VESSEL TRANSPORTERS

The telescopic arm, at present being manufactured and due for delivery in early 1989, is the main transporter for access to areas on the outside of the vacuum vessel. It will be suspended from the crab of the main 150 tonne crane, which was used for the installation of the machine. Auxiliary transporters are the Low-level Transporter and the Turret Truck.

4.1 Main 150 tonne crane

The crane was specified with the fine controls that would be required during remote operations. This turned out to be a bonus during the assembly phase. Positioning the 130 tonne octants with tolerances of about 1mm was no problem. A trial of inserting one octant with TV viewing was successful. Minimum incremental displacement of the load were of the order of 0.2mm in the vertical direction and 1mm horizontally, with negligible swinging effects. All the crane motors are thyristor controlled. The load is continuously monitored by means of load cells. Given the elasticity of the ropes and the low controllable speeds, vertical contact loading can be kept below 300kg. The rotation of the 150 tonne ramshorn hook is motorized. This hook will be replaced by a shackle for remote engagement to lifting eyes.

Position sensors will be installed to transmit the position of the hook to the operator console. This will eventually permit teach-and-repeat control. For emergency retrieval of the crane its motors will be switched to a backup battery via radio.

A fault analysis drawing from operational experience is being done in order to eliminate electronic malfunctions and to make some modifications to increase the reliability of the reeling system.

To lift large, delicate structures such as the outer poloidal field coils a four-rope system with hydraulic load equalizers is used. This system will also be used to raise to its location under the crab the structure supporting the telescopic articulated remote mast (TARM) (Fig.10).

4.2 Crane-mounted telescopic articulated remote mast

Fig.11 shows schematically the TARM motions. Fig.12 shows the operating configurations required to enable the Mascot to reach positions not only above, below and down the central core of the torus, but also halfway across inside the vacuum vessel in order to work in conjunction with the articulated boom during installation of heavy components.

A 250kg jib crane (K) is positioned on the moving vertical telescope so as to be able to lift very long diagnostic equipment out of the top of the machine. A 6 tonne jib crane (J) with motorized hook will carry out most lifting operations in conjunction with the Mascot.

The vertical mast can be coupled directly to the Mascot for access down the middle of the machine or the horizontal telescope may be attached with a purpose designed remote attachment system. A limited (+10°, -15°) tilt action (A1) allows for deflection compensation and also allows the Mascot to reach 0.9m below the floor level for basement maintenance.

In order to minimise cable requirements and for ease of commissioning, the service modules are all attached to the TARM. These include power supplies and local controllers for the drive units, signal conditioning for sensors and TV cameras, Mascot slave controller, water supplies for tools, air supply for tools and air make-up for gaiters.

The microprocessor based control system will have similar features to that of the boom with single joint closed loop servocontrol, teach-and-repeat and resolved motion. Here also control will be from the Remote Handling work station, from a portable handbox, or from the Graphics work station.

A study to test the feasibility of an obstacle avoidance system, using image processing equipment on loan from Euratom, Ispra, is in progress. To avoid complicating the equipment with additional hardware, it is intended to use existing TV cameras, adopting image analysis techniques. For transversal motions a known pattern is altered by any object impinging onto the field of viewing. For longitudinal motions in the direction of the boom a TV camera mounted at the front detects objects coming into focus by sensing the high-frequency content of the video signal.

4.3 Auxiliary transporters

The Low Level Transporter (ROLLT) was specified and procured for operations involving components on the lower half of the vessel which are not accessible to the overhead crane. It is a modified fork-lift truck equipped with an attachment and end effector capable of precisely controlled movements. It will be used in conjunction with a manipulator supported by TARM. In the 1987 shutdown it was used to install seven turbopumps and two VAT valves. It is now being upgraded to remote operation from the RH control room.

The Turret Truck, which is used to lift end effectors and components up to the boom, will also be equipped to carry a third slave unit for four-handed operations in association with TARM, and for work in the hot cell.

5. SPECIAL TOOLS

For operations in areas where access is difficult, or which require high precision or large forces, special tools are being developed. These will be positioned by the manipulator. Efforts were made during the design phase of the machine to standardize and simplify components so that the number and complexity of such tools could be kept to a minimum.

A significant example is the cutting and welding trolley, designed to cut and reweld, if necessary, any of the large vacuum joints [7]. Tools have also been developed for cutting and welding of the 91mm diameter circular sapphire windows for diagnostics.

Recent additions to the in-vessel equipment - the belt limiters and the ICRF antennae - have complicated the remote handling scenario. One of the main difficulties is the cutting and welding of the cooling water piping on the vessel wall. Here the working envelope is very restricted and a series of compact tools to align, weld and cut mating pipes has been developed [8]. These special tools were successfully used hands-on during 1987 (see par.

3.2.2). Problems anticipated in remote conditions are associated with misalignments and irregularities in mating surfaces. Mockup tests, which have now begun, will show the measure of these difficulties.

6. IN-VESSEL INSPECTION

Periodic inspections of the interior of the vacuum vessel have to be done to check for damage due to plasma disruptions. A system [9] was developed to scan the vessel using four TV probes through small apertures in the top of the vessel without breaking the vacuum. A great effort of miniaturization was required to compress the optics and electronics into the small diameter available.

Another problem was to provide sufficient illumination, particularly since the vessel has been carbonized. The initial solution was to use high-energy flashlight and digital framegrabbers. The image obtained of the inner part of the vessel remained hazy because direct light impinging on the viewing glass is scattered inside it. A study is planned on the feasibility of using prisms suspended in the vessel. Recently it has been possible to make a considerable improvement. Some more penetrations were made available to provide continuous lighting. Four vacuum-tight assemblies of silica light guides are illuminated by small powerful purpose-designed projectors sited above the penetrations.

Another drawback with the original system was that the vessel had to be cooled down to below 50°C to do an inspection. After feasibility tests, high temperature probes to be used at 300°C were designed and manufactured [10].

7. CONCLUSION

Much of the principal remote handling equipment is now on site. The task ahead is to get all the equipment together into a working system. This is a task which is just as demanding as the design and development of the equipment. It is easy to underestimate the time and effort required for commissioning complex digitally controlled equipment and correcting the software. Another area of activity not to be overlooked in planning resources is the wiring, the design and preparation of which must go hand in hand with the design of mechanical parts.

A very important programme of trials on partial mockups will alert to possible shortcomings in the equipment and show what further tools are required for the various operations, and also whether any other components have to be modified before the D-T phase.

ACKNOWLEDGEMENTS

Thanks are extended to all the members of the remote handling groups, whose work forms the basis of this paper.

REFERENCES

1. J. Dean et al, "Preparation fo D-T Phase Operation in JET", Proc. 14th SOFT, Avignon, September 1986.
2. A. Galetsas et al, "An integrated control system for remote handling at JET", Proc. 12th SOFE, Monterey, October 1987.
3. Jean Vertut and Philippe Coiffet, "Teleoperation and Robotics" (Robot Technology Vol. 3A), p.45.
4. L.P.D.F. Jones et al, "Design and Operation of the JET Articulated Boom", Proc. 11th Symposium on Fusion Engineering, Austin, 1985.
5. L. Galbiati et al, "Control and Operation of JET Articulated Boom", Proc. 12th SOFE, Monterey, October 1987.
6. M. Wykes, "Remote Handling Tools for JET", Proc. 14th SOFT, Avignon, September 1986.
7. P. Presle et al, "Automatic welding and cutting of JRT standard joint configuration", Proc. of this symposium.
8. S.F. Mills et al, "A Practical Experience of Using Remote Handling Tools on JET", Proc. 12th SOFE, Monterey, October 1987.
9. T. Raimondi, R. Cusack, L. Galbiati, "The JET In-Vessel Inspection System, Proc. 14th SOFT, Avignon, September 1986.
10. T. Businaro et al, "The JET high temperature in-vessel inspection system", Proc. of this symposium.
11. G. Celentano et al, "The JET Belt Limiter", Proc. 14th SOFT, Avignon, September 1986.
12. A. Kaye et al, "Engineering design and preliminary performances of the JET IRCF System", Proc. 11th SOFE, Austin, 1985.
13. A. Rolfe, "Operational aspects of the JET Remote Handling System", Proc. International Symposium on Fusion Nuclear Technology, Tokyo, 1988
14. U. Kühnapfel et al (KfK), "Graphics Support for JET Boom Control", International Topical meeting on Remote Systems and Robotics in Hostile Environments, A.N.S., Pasco, USA, 1987.

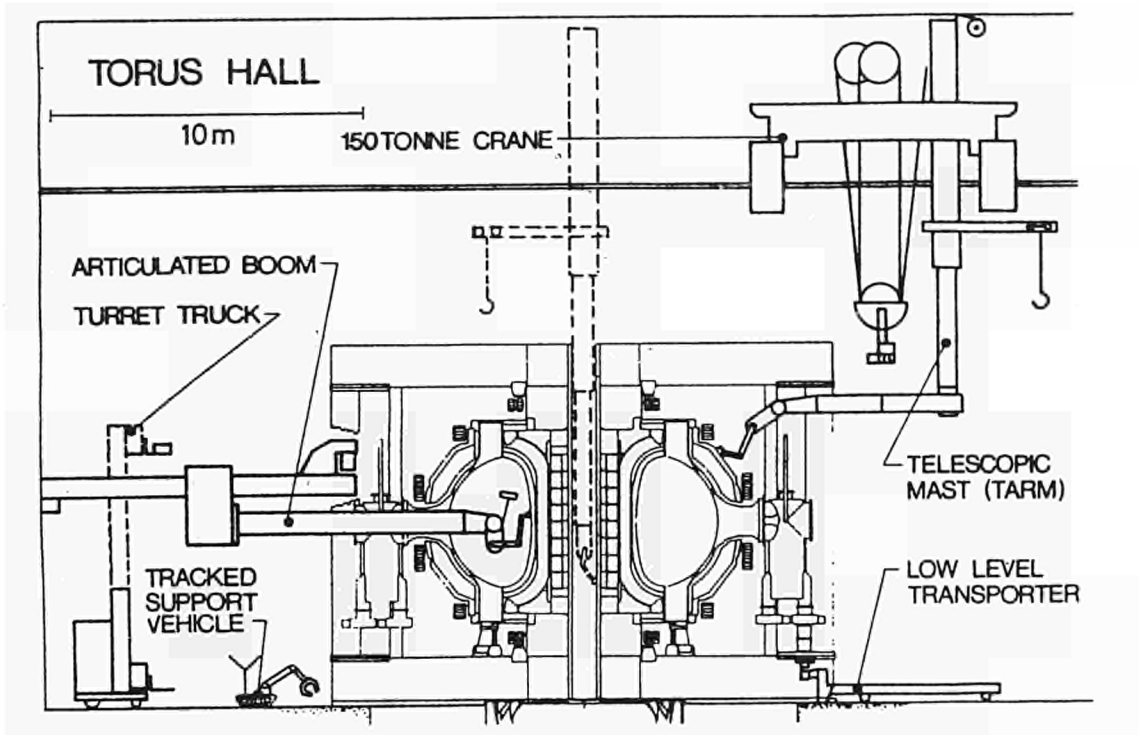

Fig. 1 Remote handling layout.

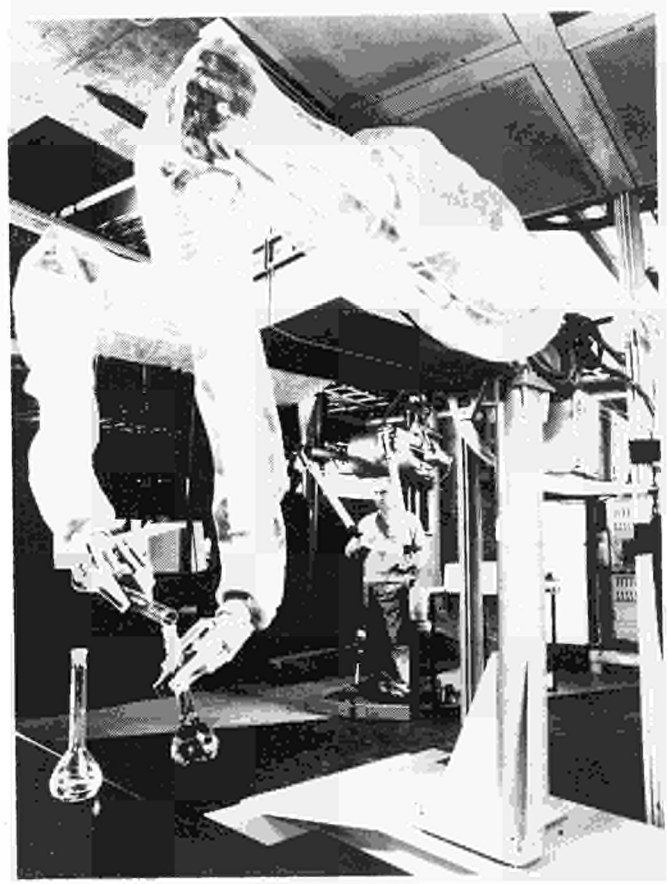

Fig. 2 Mascot IV.

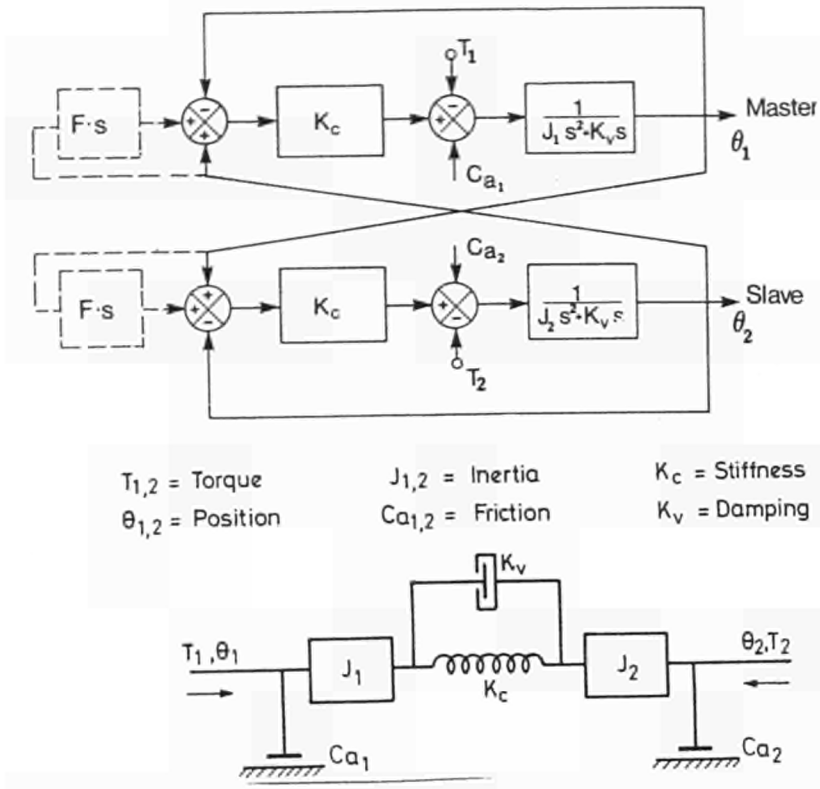

Fig. 3 Mechanical equivalent schematic for one degree of freedom.

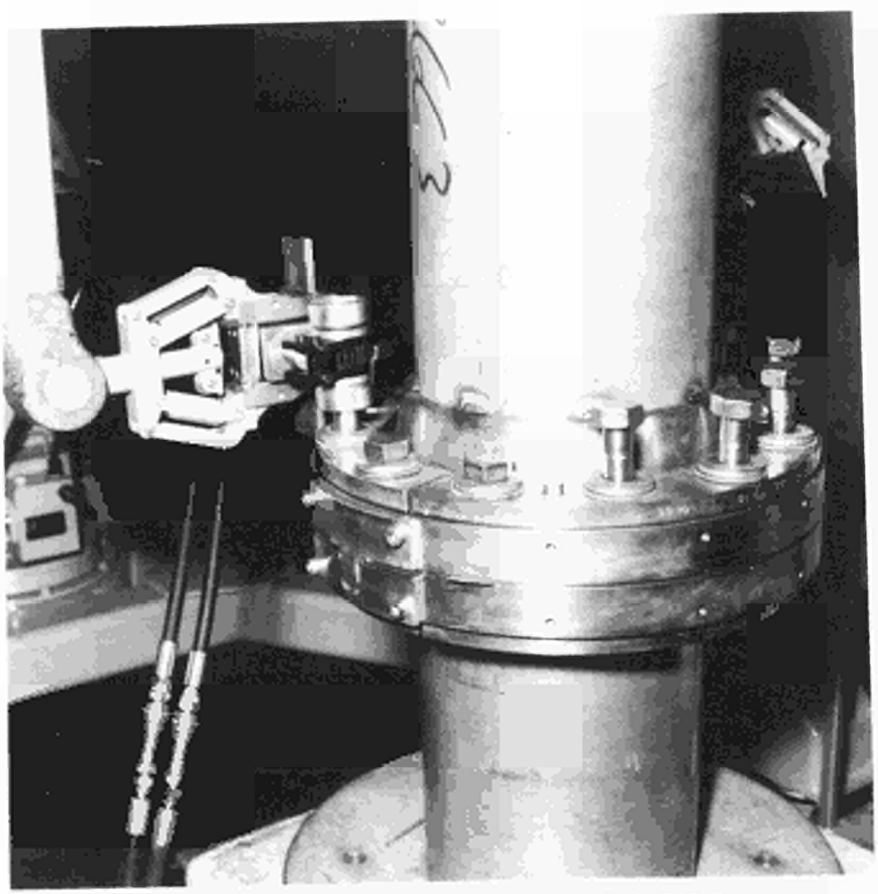

Fig. 4 Mascot III using hydraulic wrench to bolt RH flange.

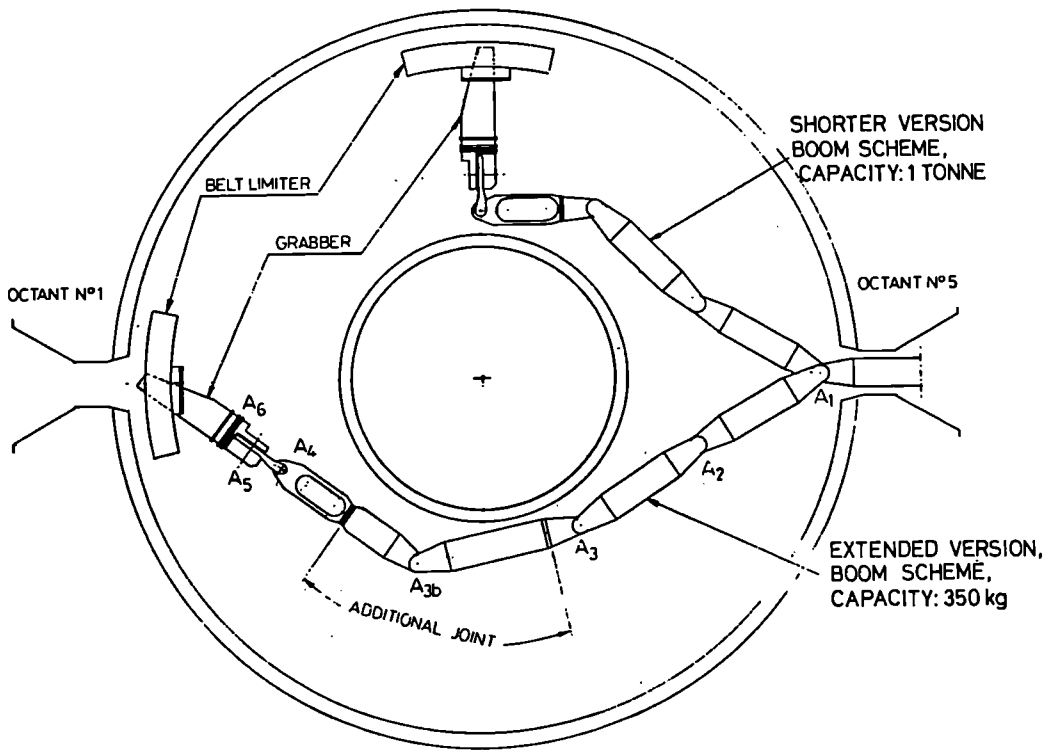

Fig. 5 Configuration of articulated boom in shorter and extended versions.

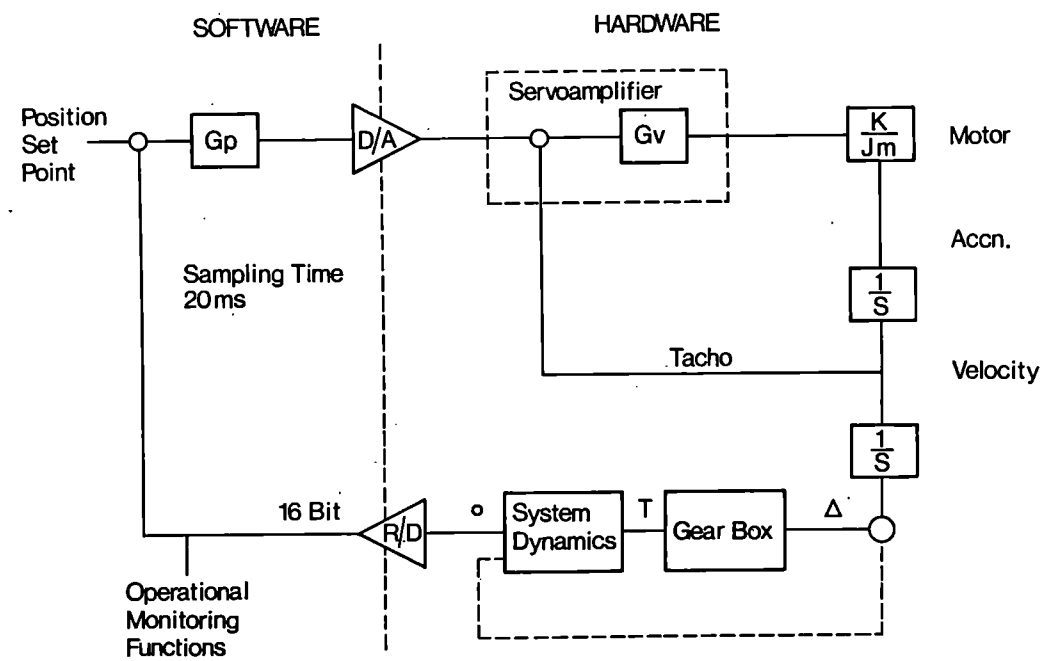

Fig. 6 Servoloop of articulated boom joint.

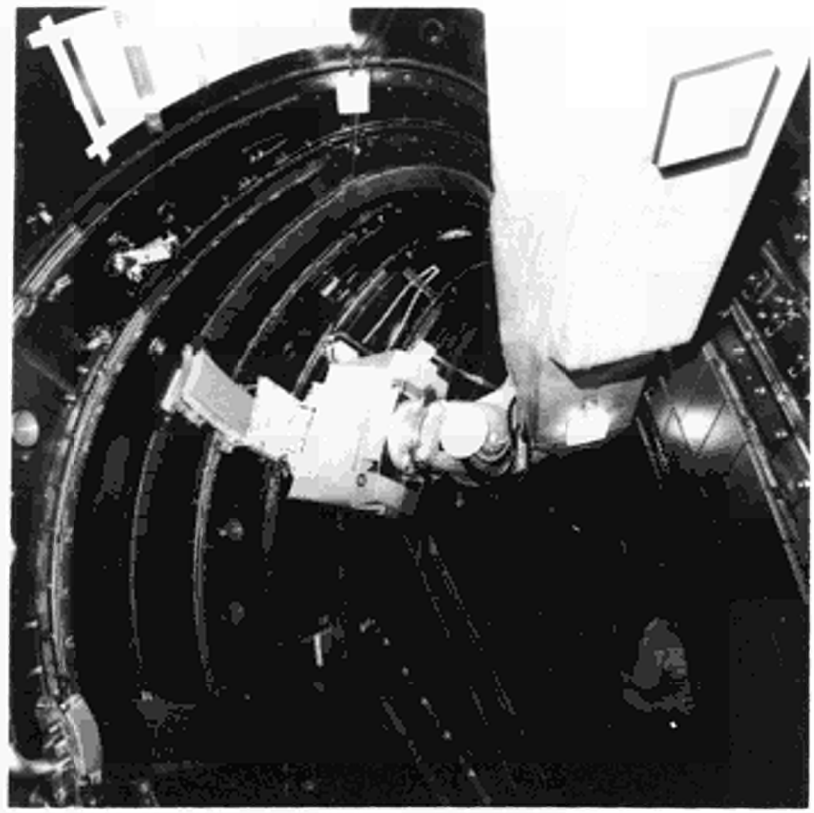

Fig. 7 Boom positioning limiter.

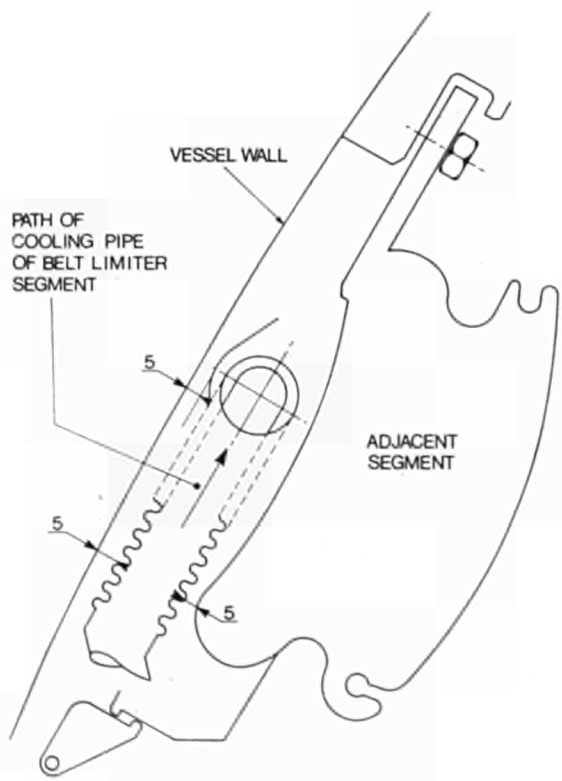

Fig. 8 Limiter installation.

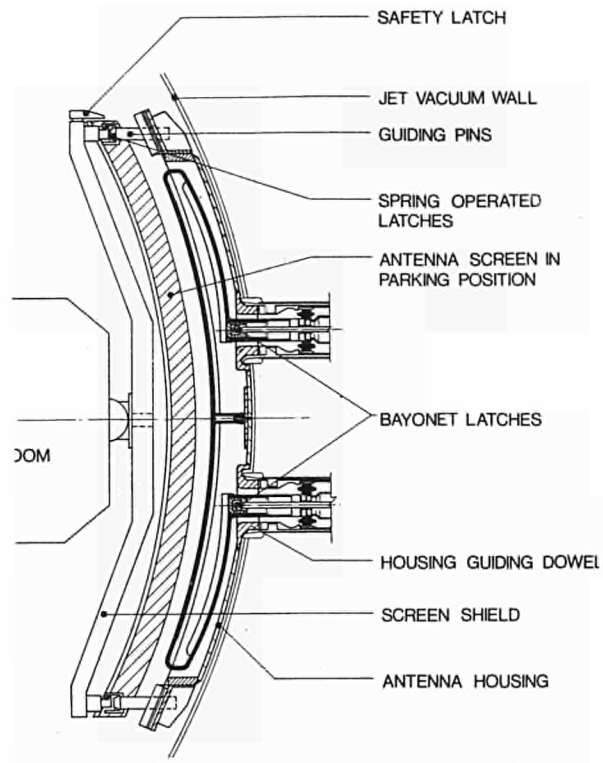

Fig. 9 Schematic of antenna screen handling.

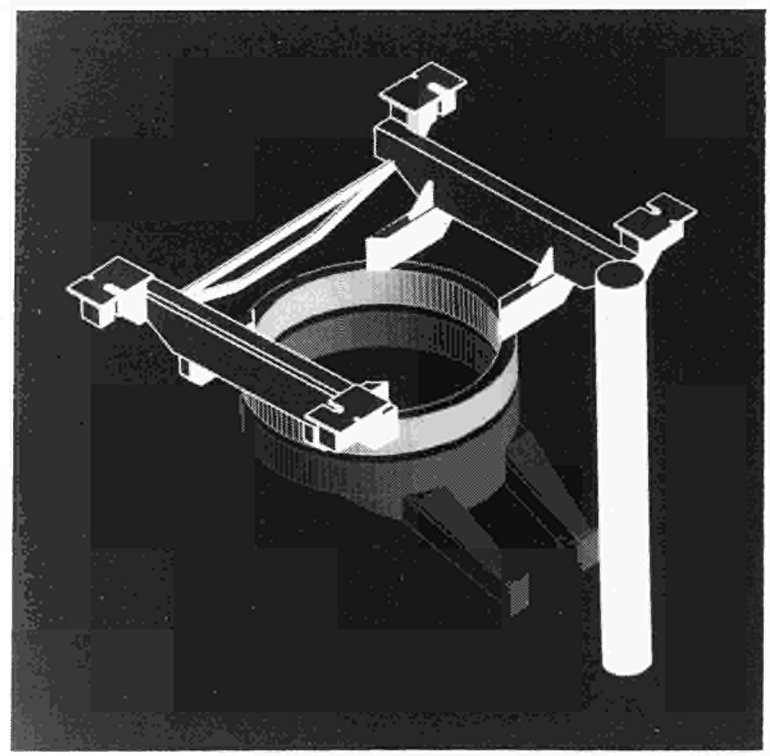

Fig. 10 CAD model of TARM.

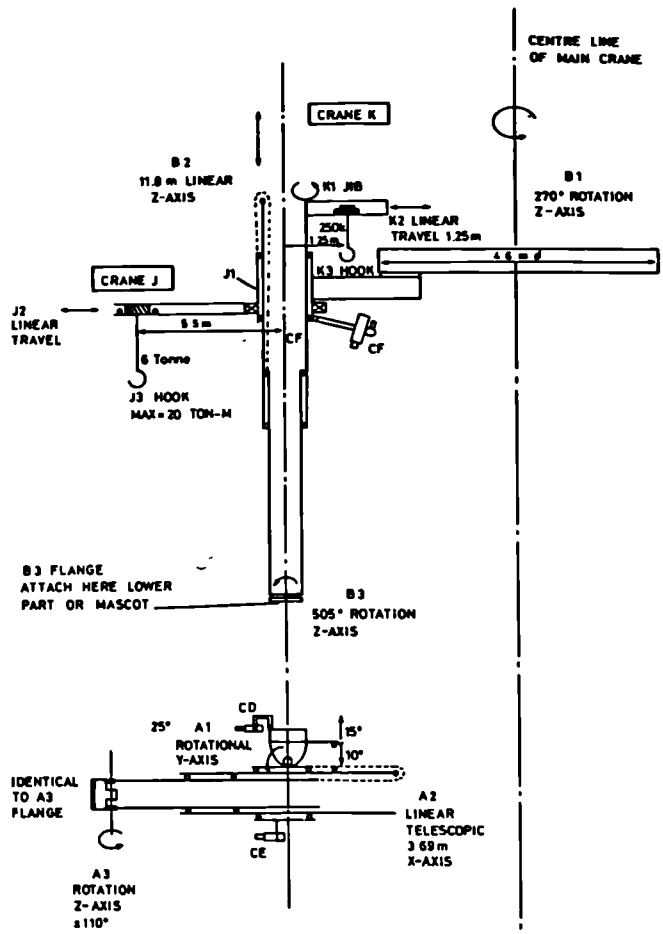

Fig. 11 Schematic of TARM movements.

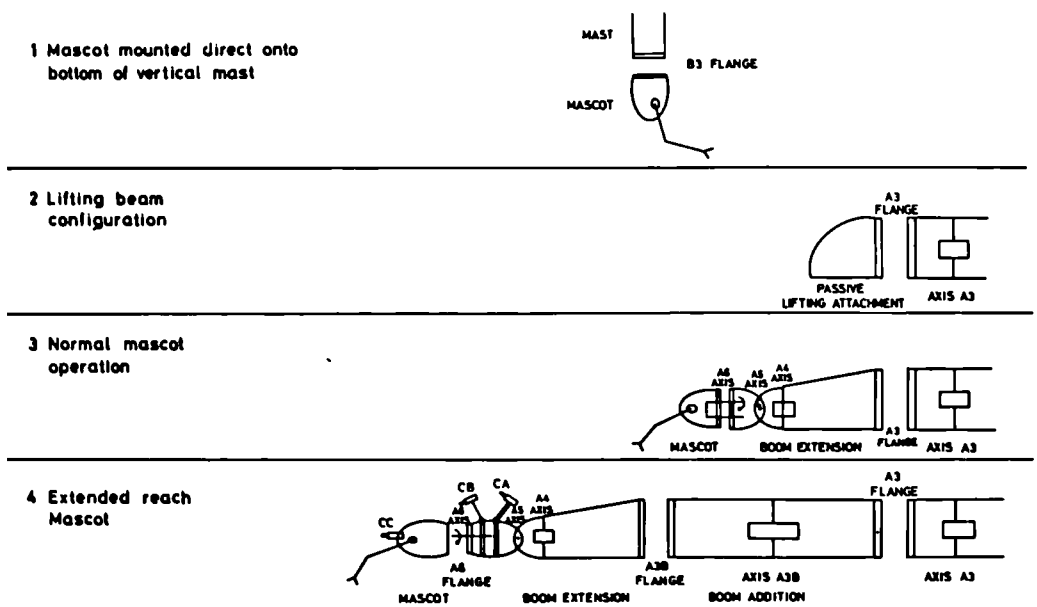

Fig. 12 Operating configurations of TARM.

Contributed papers presented at 12th International Conference on Plasma Physics and Controlled Nuclear Fusion Research (Nice, France, 12th-19th October 1988)

Many Authors

	Title	Presenter	No.
1.	Latest JET Results and Future Prospects (IAEA-CN-50/A-1-3)	R.J. Bickerton (JET Team)	A467
2.	The JET H-Mode at High Current and Power Levels (IAEA-CN-50/A-III-2)	M. Keilhacker (JET Team)	A490
3.	Heating of Peaked Density Profiles Produced by Pellet Injection in JET (IAEA-CN-50/A-IV-1)	G.L. Schmidt (JET Team)	A511
4.	High Temperature Experiments and Fusion Product Measurements in JET (IAEA-CN-50/A-4-4)	P.R. Thomas et al	A532
5.	Experimental and Theoretical Studies of Ion Cyclotron Heating on JET (IAEA-CN-50/E-II-3)	D.F.H. Start et al	A543
6.	The Plasma Boundary in JET (IAEA-CN-50/A-VII-12.2)	L. de Kock et al	A555
7.	Sawtooth Activity and Current Density Profiles in JET (IAEA-CN-50/A-7-2)	D.J. Campbell et al	A567
8.	Global Power Balance and Local Heat Transport in JET (IAEA-CN-50/A-7-1)	A. Taroni et al	A577
9.	Theory of Sawtooth Stabilisation in the Presence of Energetic Ions (IAEA-CN-50/D-4-6)	F. Pegoraro et al	A588

Latest JET Results and Future Prospects

The JET Team*
(presented by R.J.Bickerton)
JET Joint Undertaking, Abingdon, Oxon, OX14 3EA, U.K.

Abstract

Following technical modifications to the machine the plasma current in JET has been increased to 7MA for limiter-bounded plasmas and to 5MA for single-null, magnetic separatrix operation. Additional heating power has been raised to 20MW of neutral beam injection and 18MW of ion cyclotron resonance heating. The maximum total plasma energy content has exceeded 10MJ. Ion temperatures up to 23keV, central densities up to $1.8\times10^{20}m^{-3}$ and energy confinement times up to 1.2s are achieved in different discharges. Simultaneous ion and electron temperatures greater than 10keV have been achieved, showing no deleterious effects on confinement. Plasma temperatures exceeding 5keV have been maintained for 20s in a 3MA discharge heated by ion cyclotron resonance heating (ICRH). The level of carbon and oxygen impurities is a major problem with the ratio between deuterium and electron densities in the range 0.15-0.80 depending on conditions. Several features of α-particle physics have been studied, notably by the RF heating of minority ions to mean energies of order 1MeV. The fast particles slow down and heat the plasma in broad agreement with expectation. Plasma conditions in deuterium plasmas corresponding to an equivalent D-T) thermonuclear $Q\approx0.1$ and total $Q\simeq0.25$ (including non-thermal reactions) have been reached. Exploiting the full high current, high power capability of the equipment is expected to increase these figures to ~0.3 and 0.6, respectively. Still further increases can be expected when various changes and additions are implemented. These are designed to control profiles of density and current and at the same time reduce the impurity content. Extrapolating the JET confinement data to a reactor-scale plasma shows that there should not be a problem with energy confinement but rather with disruptions and the control of particles and impurities. Experiments on both these aspects are planned including fuelling by high-speed pellets and feedback stabilisation of the instabilities which precede disruptions.

1. Introduction

The Joint European Torus (JET) is a large tokamak[1,2] designed to study:
(a) the scaling of plasma behaviour as parameters approach the reactor range,
(b) the plasma wall interaction in these conditions,
(c) plasma heating and
(d) α-particle production, confinement and consequent plasma heating.

The JET tokamak started operation in June 1983 and has since been progressively

*see Appendix I

CR 88 156

upgraded and developed. This paper concentrates on the results of the last two years, indicates further planned changes and discusses the resulting future prospects.

2. Machine Performance

Following the 1986 IAEA Conference[3], substantial modifications and additions were made to JET. These included:

(a) Installation of two water-cooled toroidal belt limiters above and below the mid-plane.

(b) Installation of eight ion cyclotron resonance heating antennae[4], symmetrically placed around the torus on the low-field side between the upper and lower belt limiters. Each antenna is fed by an RF amplifier in the frequency range 23 - 57 MHz with 3 - 4 MW for nominal pulse lengths up to 20 s.

(c) Installation of a second neutral injector box oriented in the same direction as the first, equipped with eight ion sources and designed to inject a power of 10 MW, 80 kV, deuterium (total of two boxes ~ 20 MW).

(d) Improvements to the poloidal field system permitting more flexible operation. This gives the capability to use the available volt-seconds fully and to produce single null configurations at higher currents.

(e) Improved vacuum vessel restraints to allow safe operation at higher currents in elongated plasmas.

(f) Many diagnostic improvements, most notably the time-of-flight short laser pulse, Thomson scattering system giving radially resolved measurements of electron temperature and density (LIDAR) together with modifications to the multi-channel interferometer to permit measurements of Faraday rotation angle and hence the calculation of the poloidal field distribution.

(g) Installation of a multi-pellet injector[5,6] capable of injecting deuterium pellets of 2.7, 4 or 6 mm in diameter at speeds in the range 1 - 1.5 km/s. The injector was supplied and is operated as part of a collaborative programme with US-DOE.

(h) Installation of 32 poloidal rings of carbon tiles as X-point energy dumps.

All these technical elements have been brought into successful operation although not without difficulty. Some water-cooled parts inside the beam boxes and antennae in the main torus have developed leaks as a result of thermal cycling, beam loading or disruption forces. The problems have been dealt with by changes in design.

The JET rated performance and achievements are shown in Table I. The most striking features are the operation at 7 MA, about 45 % higher than the design value and the flexibility of the apparatus which has permitted high current operation with magnetic separatrix-bounded plasmas, not foreseen in the original design.

Table I
JET Parameters

Parameter	Design Values	Achieved Values
Plasma major radius (R_0)	2.96m	2.5–3.4m
Plasma minor radius horizontal (a)	1.25m	0.8–1.2m
Plasma minor radius vertical (b)	2.1 m	0.8–2.1m
Toroidal field strength at R_0	3.45T	3.45T
Plasma Current:		
Limiter mode	4.8MA	7.0MA
Single null X-point	Not foreseen	5MA
Neutral beam (NB) power (80kV, D)	20MW	21MW
Ion Cylotron Resonance Heating (ICRH) power to Plasma	15MW	18MW

3. Operating Limits and Disruptions

The conventional operating diagram in $1/q_c$ versus $\bar{n}_e R/B_t$ space is shown in Fig. 1. Here $1/q_c$ is normalised plasma current defined as $(1/q_c) = \pi RI/5AB_t$ where R is the plasma major radius (m), I the plasma current (MA), A the cross-sectional area of the plasma (m^2) and B_t the toroidal field strength (T) at the major radius R. Fig. 1(a) shows the flat-top parameters of non-disrupting discharges with ohmic heating only. Discharges fuelled by gas-puffing show a density limit given by $\bar{n} < 12B/Rq_c \times 10^{19}\,m^{-3}$, while densities more than 2 times higher can be obtained with pellet fuelling. Fig. 1(b) shows the results with additional heating where similar densities can be obtained without pellets both with RF and neutral beam heating. The density limit disruptions are consistent with a rise in the radiated power in the outer regions to close to 100% of the input, and a resulting narrowing of the current channel leading to MHD instability.

The disruption process then proceeds in stages, a precursor period with externally detected growing $m=2$, $n=1$ magnetic oscillations at ~500Hz. When the amplitude reaches $\sim 10^{-3}$T the mode locks and continues to grow. This is followed by an energy quench in which the major part of the plasma energy is lost in ~1ms. Finally there is a current decay phase in which the plasma current falls to zero in a time which can be as short as 5ms. The poloidal field energy is converted into radiation and runaway electrons (e.g. ~5MJ or >25MeV electrons for a 5MA disruption). Fig. 2 shows the maximum rate of current

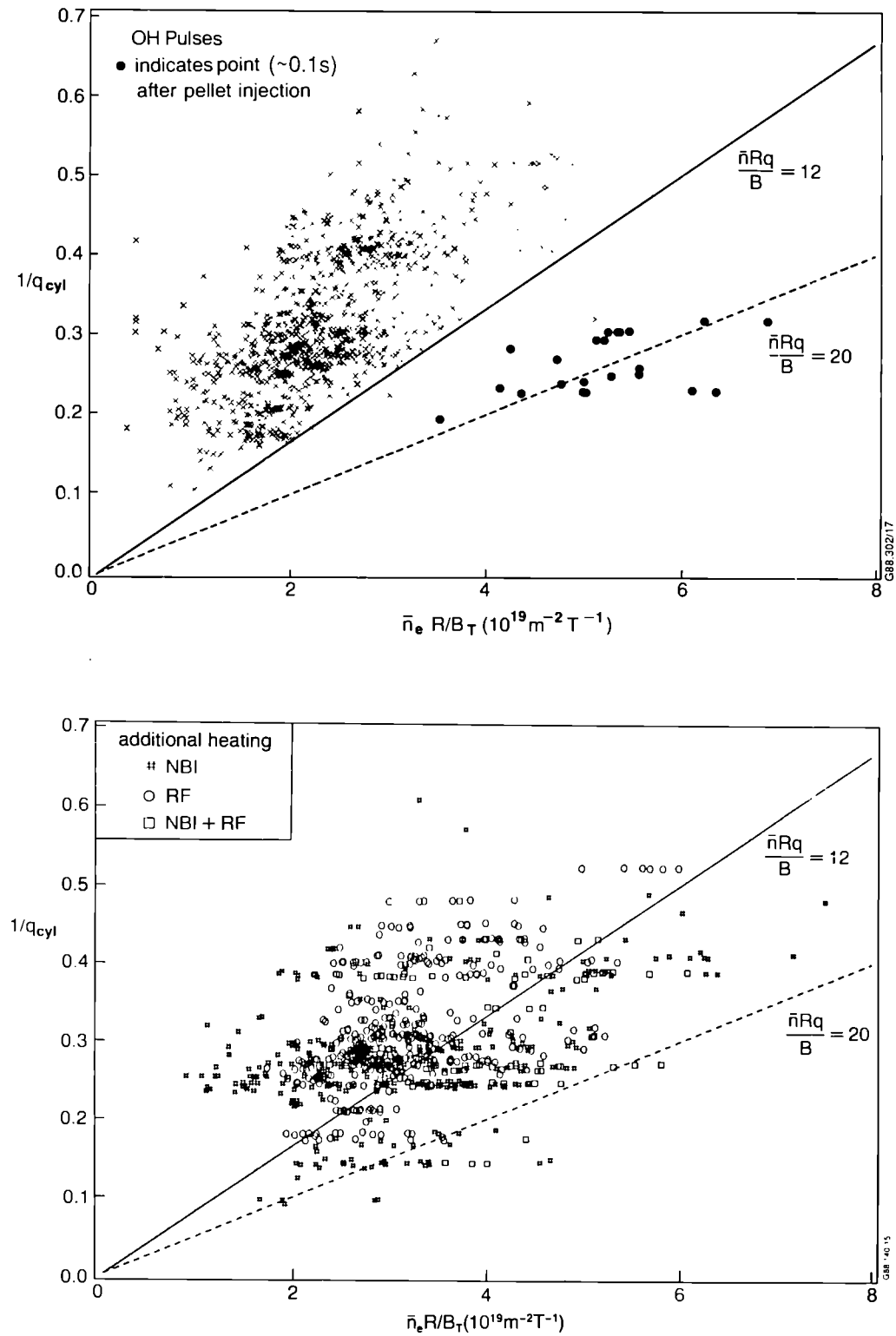

Fig. 1 Normalised plasma current, $1/q_c$ versus normalised density, $\bar{n}R/B_t$ for non-disrupting discharges (a) with ohmic heating, (b) with additional heating.

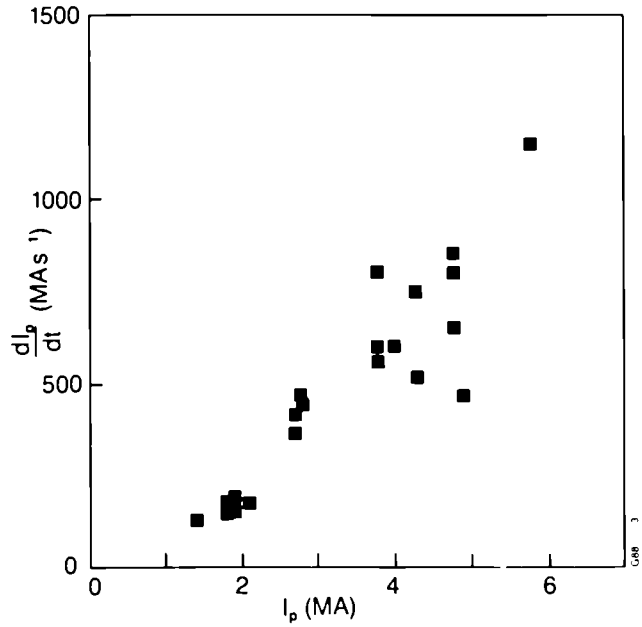

Fig. 2 Maximum dI/dt versus I for current quench phase of disruptions.

collapse versus current in JET. The eddy currents induced in the torus by the rapid current collapse lead to large forces on the vessel of order 20t/m^2. The vacuum vessel mounting has been considerably strengthened to reduce the resulting displacements. Further measures to stiffen the torus by welding toroidal rings on to the inner wall are planned for the next shutdown.

Apart from density limit disruptions the operating diagram also shows disruptions whenever the field line q at the boundary, q_ψ, approaches 2. These low q disruptions are simpler in that there is no long sequence of precursor behaviour. Instead, there is rapid growth of MHD instability followed by an energy quench and current decay similar to the final phases of density limit disruption.

The JET experience so far is that the energy quench and runaway electron production have not caused significant damage to the torus interior. However the impulsive forces on the vessel, on internal and external components, have been the cause of vacuum and water leaks.

It is clear that disruptions are a major problem for future tokamaks since they are planned to operate at much higher currents in essentially steady state. Experiments on the feedback stabilisation of the initial small amplitude magnetic oscillations will be carried out in a later phase of the JET programme.

4. Discharge Types

4.1 Operating Variables

Discharges have been operated with different boundary conditions, heating scenarios, particle fuelling and pumping arrangements. Fig. 3 shows the poloidal flux plots for three cases: (a) with a limiter-bounded plasma; (b) and (c) with

single and double-null magnetic configurations. The fuelling variations include using gas-puffing at the boundary, injecting pellets or neutral injection to provide central fuelling. The particle pumping at the boundary can be varied by using different surfaces in the vacuum vessel and by conditioning those surfaces (eg. by helium discharges before the main pulse operation). The heating scenarios are variations and combinations of neutral beam (NB) and ion-cyclotron resonance heating (ICRH). The neutral beams have been operated entirely in co-injection mode with deuterium at 70-80kV. ICRH has been used with H or ^{3}He minority in D or ^{4}He plasmas. This heats the minority ions to energies in the range 100keV - 1MeV, above the critical energy, so that ultimately the RF power goes to the electrons. The deposition zone has typically a half-width of 30cm. The radial profiles of n, T_e and T_i for various discharges are obtained from the LIDAR Thomson scattering system and charge exchange recombination spectroscopy. q-profiles are deduced by magnetic analysis of external signals, which is inaccurate in the centre except for the 7MA, monster sawtooth and H-mode cases where Faraday rotation and X-ray data have been combined with magnetic analysis.

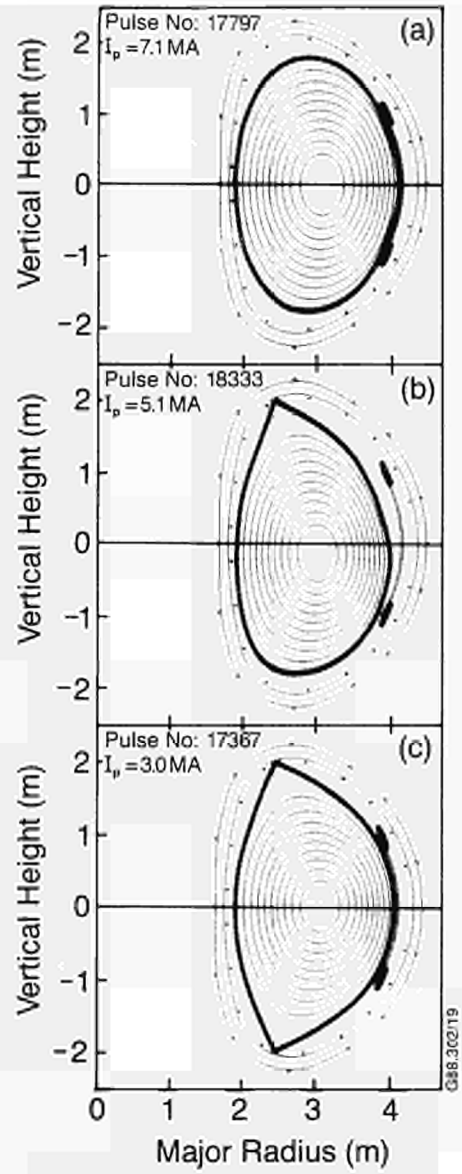

Fig. 3 Poloidal flux contours for (a) 7MA limiter-bounded plasmas, (b) 5.1MA single null magnetic separatrix and (c) 3MA double null separatrix.

4.2 Ohmic Discharges

The radial profiles for a 7MA ohmic discharge are shown in Fig. 4. This particular discharge had a short flat-top time of 2s and was operated cautiously with moderate density to avoid disruption. Since q_ψ is low at 2.8, there is a large central volume inside the $q=1$ surface where the profiles of both density and temperature are flat. The central q value is $0.8+0.1$ and the discharge is sawtoothing. To economise on volt-seconds and hence reach 7MA, it was neccessary to use a helium prefill for the initial breakdown phase. For this reason, the Z_{eff} was

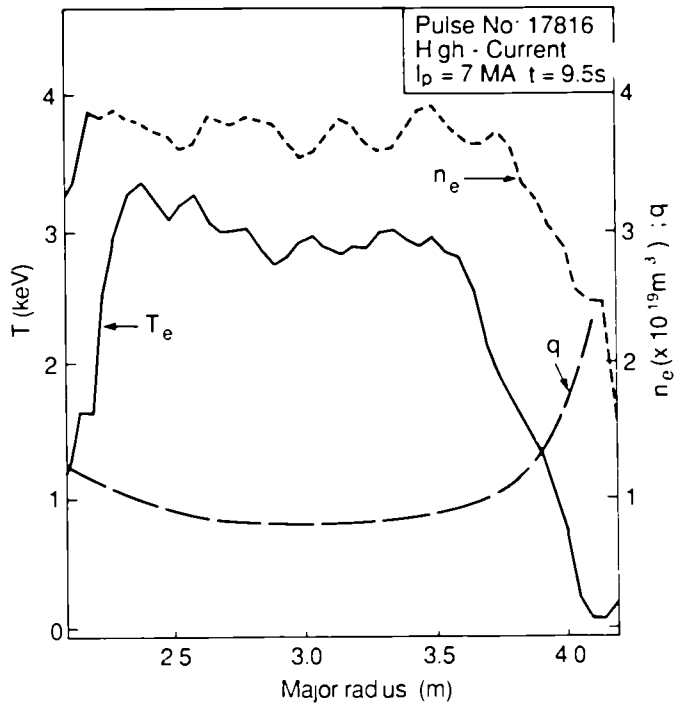

Fig. 4 Radial profiles of electron temperature, electron density and safety factor in a 7MA plasma. From Faraday rotation measurements $q(0)=0.8\pm0.1$. $B=3.1$T, $P_{tot}=8.5$MW, $Z_{eff}=3.7$, $\tau_E=0.6$s.

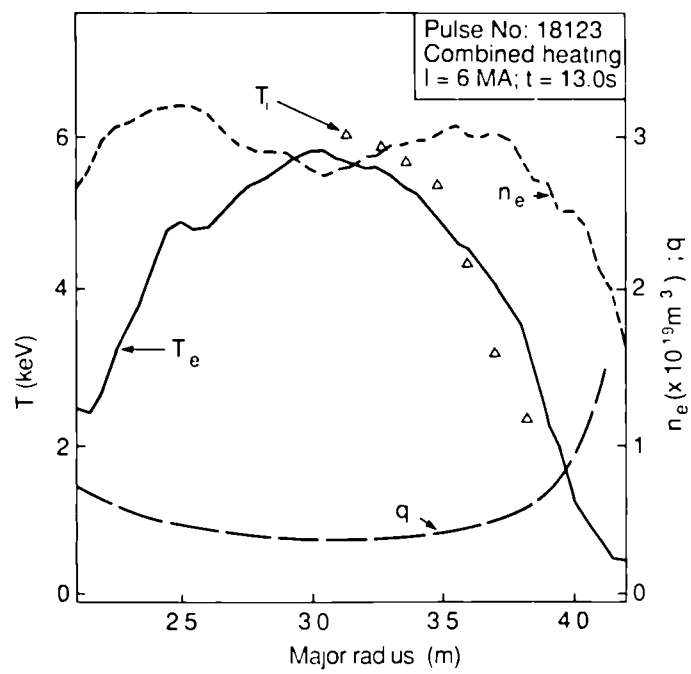

Fig. 5 Radial profiles of electron and ion temperatures, electron density and safety factor in a 6MA discharge with 24MW of heating power. $B-3.1$T, $P_{Rf}-6$MW, $P_{NB}=13$MW, $Z_{eff}=4.8$, $\tau_E=0.33$s.

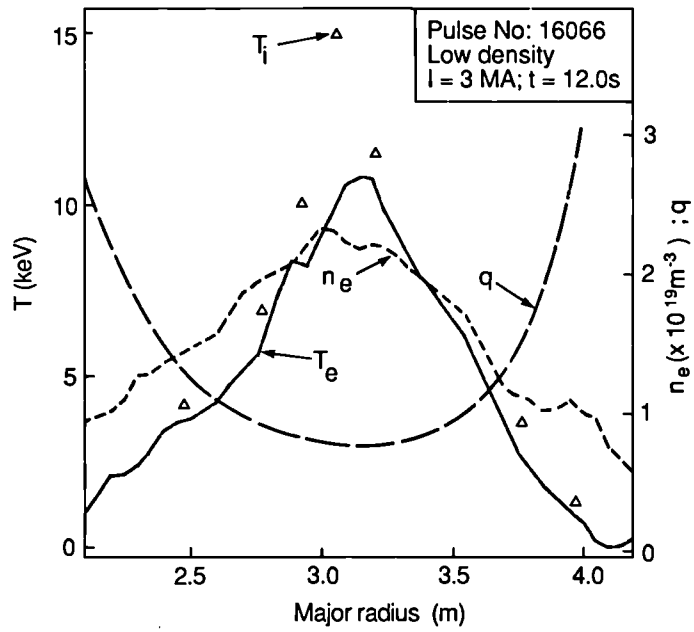

Fig. 6 Radial profiles of electron and ion temperatures, electron density and safety factor in a 3 MA, low density discharge with $B=3.1$ T, $P_{RF}=8$ MW, $P_{NB}=8$ MW, $P_{TOT}=16.5$ MW, $Z_{eff}=5.2$, $\tau_E=0.4$ s.

relatively high and the neutron yield low for the conditions of density and temperature.

4.3 High Current, High Power Discharges

Fig. 5 shows the radial profiles for a 6 MA, limiter-bounded high power discharge. Again, at this high current, there is a large radial zone in which the deduced value of q is less than unity and the gradients in electron temperature and density are low. With the electron temperature at ~ 5 keV, the neutral beams with energy per nucleon of 40 keV give their energy primarily to the ions. However, because of the high density the two temperatures are closely coupled by collisional equipartition.

4.4 High Temperature Discharges

Fig. 6 shows the profiles for a 3 MA discharge in which special measures were taken to keep the density low and hence to achieve high temperatures. There is a relatively small core where $q<1$, and correspondingly both temperatures and density are relatively peaked. Both ion and electron temperatures exceed 10 keV in the centre. The neutron rate is high with the major contribution from beam-plasma reactions. At these temperatures directly relevant to reactor conditions, the energy confinement time is 0.4 s, in agreement with the usual JET scalings and shows no signs of further degradation.

4.5 Monster Sawtooth Discharges

Fig. 7 shows the profiles during a so-called 'monster' sawtooth produced by localised, central minority ion cyclotron resonance heating of moderate q_ψ (~ 4) discharges. Such sawteeth have now been produced with duration up to 3.2s. Magnetic measurements of Faraday rotation[7] show that during the period $q(0)$ is progressively reduced to $\sim 0.8+0.1$. This is consistent with resistive diffusion calculations assuming neo-classical resistivity and the measured central electron temperature. The stabilising mechanism against $m=1$, $n=1$ MHD instabilities is still uncertain although there is the possibility[8] that an essential role is played by the fast minority particles. These 'monster' sawtooth discharges show the increase in reactivity coming from the profile peaking. However they are terminated by a crash in which $\sim 30\%$ of the plasma energy is lost in a few milliseconds. They can be seen as evidence of what could be achieved in steady state with external control of the current distribution in the plasma.

4.6 Pellet-Fuelled Discharges

Fig. 8 shows the profiles for a discharge in which pellets are injected during the current rise phase to produce a highly peaked density distribution[6]. With ohmic heating alone, this decays slowly on a time scale of 2–3 s. Central ion cyclotron resonance minority heating increases the central electron and ion temperatures to ~ 10keV, while $\hat{n}/\langle n\rangle$ and $\hat{n}$ then decay to 2 and $6\times10^{19}\mathrm{m}^{-3}$, respectively, in 1.5 s. Note that there are very steep pressure gradients in the core, and a very high pressure on the axis.

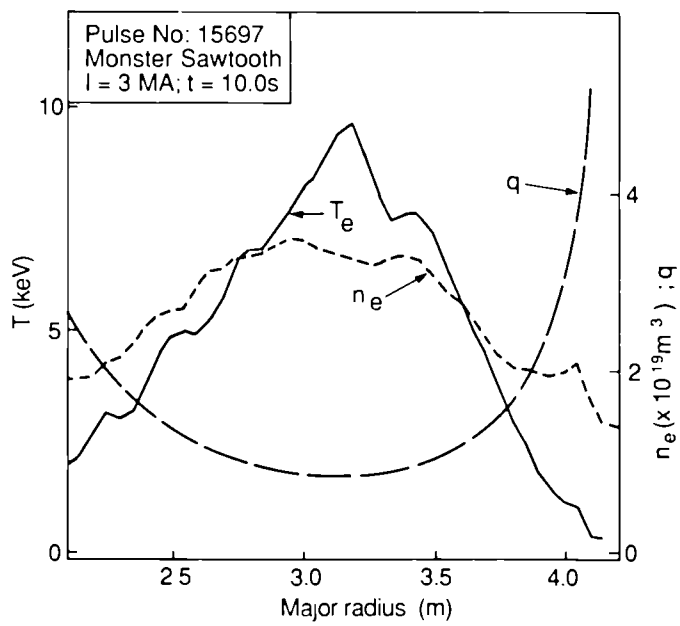

Fig. 7 Radial profiles of electron temperature, electron density and safety factor in a 3MA plasma during a long 'monster' sawtooth. From Faraday rotation measurements $q(0)=0.8\pm0.1$. $B-3.1$T, $P_{RF}-7$MW, $P_{NB}=6.5$MW, $P_{TOT}=14$MW, $Z_{eff}=3.9$, $\tau_E=0.38$s.

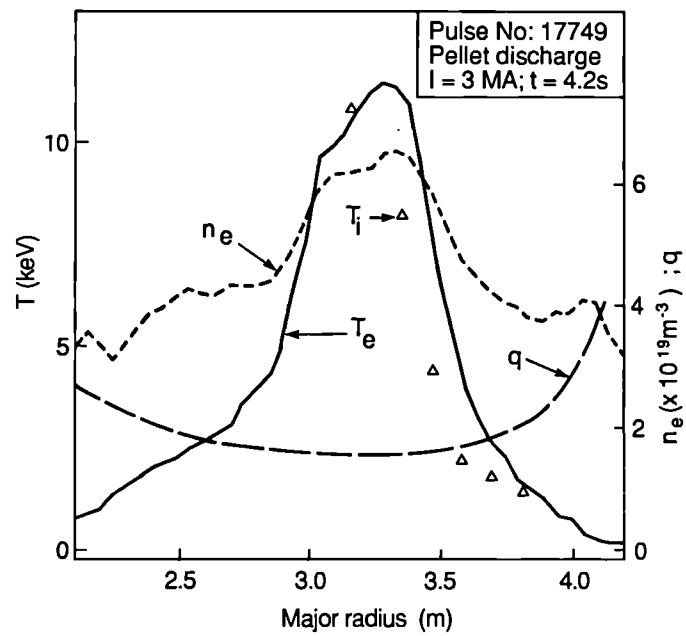

Fig. 8 Radial profiles of electron and ion temperatures, electron density and safety factor in a 3MA, pellet-injected discharge with $B=3.1$T, $P_{RF}=13$MW, $P_{NB}=5$MW, $P_{TOT}=19$MW, $Z_{eff}=2.0$, $\tau_E=0.26$s.

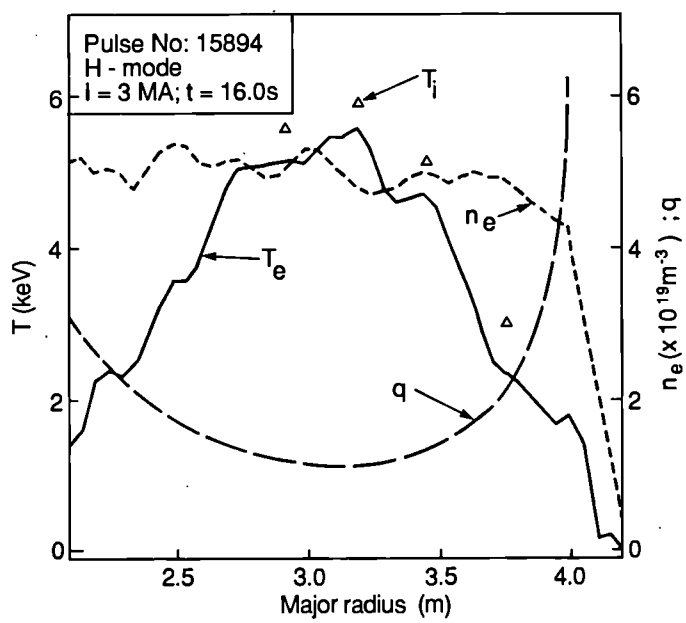

Fig. 9 Radial profiles of electron and ion temperatures, electron density and safety factor in a 3MA, H-mode plasma. Faraday rotation measurements yield $q(0)=0.8+0.1$ and the discharge is sawtoothing. $B=3.1$T, $P_{NB}=7.5$MW, $P_{TOT}=8$MW, $Z_{eff}=3.3$, $\tau_E=1.1$s.

4.7 H-mode Discharges

Fig. 9 shows the profiles during the H-phase of a 3 MA discharge with 7 MW of neutral beam injection. Striking features are the near-flat density profile and the high electron temperature near the separatrix boundary. The confinement time is high as is the density. These H-modes[9] are characterised by increasing density and radiated fraction during the H-phase which is then terminated when the radiated fraction approaches unity. So far, attempts to couple RF power and maintain H-modes have failed. Switching on the RF during a beam created H-mode caused a rapid termination of the mode due to increased radiation. It is clear that the high confinement of energy also extends to bulk ions and impurities and so brings its own problems.

5. Impurities

The main impurities are oxygen and carbon, with concentrations of 1–10%. In addition, there is nickel with concentrations $10^{-5}-10^{-4}$, higher values corresponding to RF heating from the nickel antennae. Fig. 10 shows Z_{eff} versus $\bar{n}$ for a representative set of data. Clearly, there is an overall trend to lower Z_{eff} as the density is raised.

Impurity accumulation is seen in some H-modes[9]. Accumulation is also seen in peaked density profile, pellet produced discharges. Curiously, accumulation is not seen in monster sawtooth cases despite the absence of sawteeth. Normal limiter bounded discharges with sawteeth do not show accumulation.

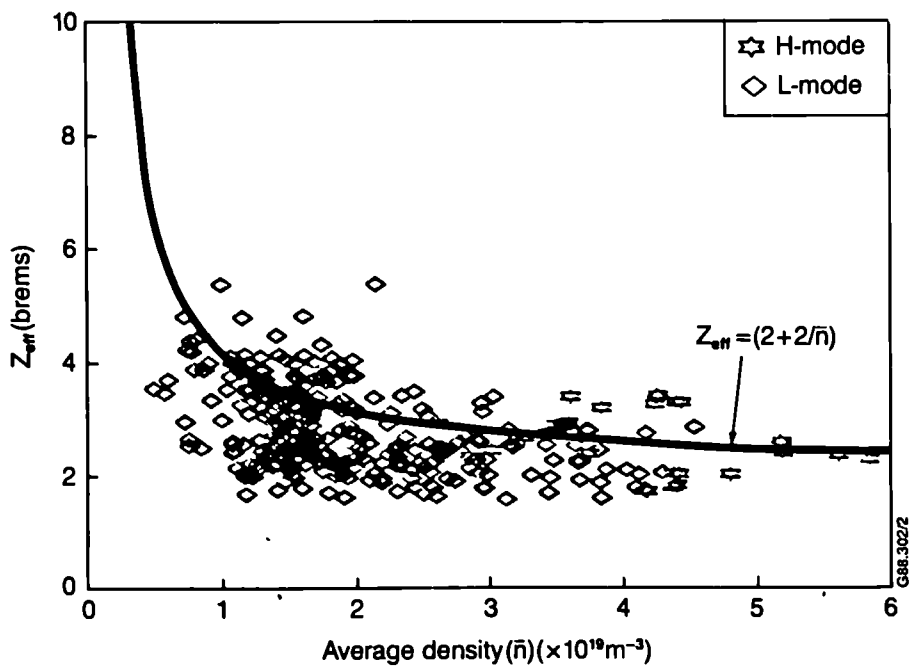

Fig. 10 Effective ion charge Z_{eff} versus average density for JET discharges. H-modes are identified separately. Line is the function $Z_{eff}=2+2/\bar{n}_{19}$ used later in predicting performance.

Radiation profiles are generally hollow so that radiation does not play any significant role in the energy balance in the plasma interior. The primary effect of impurities is to deplete the density of hydrogen isotopes in the core. The ratio of deuteron density to electron density is reduced by the presence of impurity ions with charge Z_i by, $n_D/n_e=(Z_i-Z_{eff})/(Z_i-1)$. With $Z_i=7$, intermediate between carbon and oxygen, and with Z_{eff} between 2 and 6, n_D/n_e is in the range 0.8–0.15.

This range of values is confirmed by neutron yield measurements. The highest values of n_D/n_e are for pellet-fuelled cases, intermediate are H-modes and lowest are low density, high temperature limiter discharges.

6. Bootstrap Current

A significant bootstrap current driven by the pressure gradient[10, 20] is seen most clearly in H-mode discharges. Fig. 11 shows the time-dependence of the surface voltage which transiently reverses sign. The calculated voltages with and without

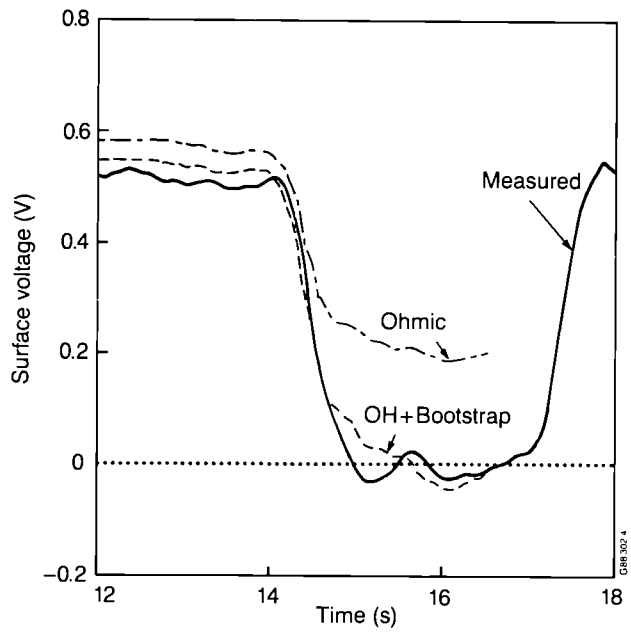

Fig. 11 Surface voltage versus time. Calculated voltage is shown for bootstrap and no bootstrap current. Bootstrap current is 850 kA. Total current is 3 MA. Discharge is in H-mode phase.

the bootstrap current are shown. Only the case including the effect gives sign reversal and agreement with the experiment. The TRANSP code is used which solves the time dependent resistive diffusion equations incorporating the full neo-classical expression[11] for the bootstrap current density as well as beam driven contributions (small here). In this case, 850 kA is bootstrap driven out of a total current of 3 MA.

We can expect bootstrap currents of 1–2 MA in 5 MA discharges with the plasma energy content in the range 15–30 MJ.

7. Alpha-Particle Physics

Some aspects of α-particle physics have been studied. Measurements on triton burn-up[19] show that the 1 MeV tritons produced in the D-D reaction slow down classically on the plasma electrons at the theoretical rate, within 20% experimental error. Other aspects of α-particle physics are simulated in ion cyclotron resonance heating of ^{3}He minority in deuterium plasmas. In these experiments[12], up to 60 kW of fusion power in charged particles is produced and monitored by γ-rays from a low branching ratio nuclear reaction. The energy content in fast ions, as monitored by the difference between diamagnetic loop and magnetic equilibrium measurements, exceeds 1 MJ. The fast particle parameters are displayed in Table II and compared with the expected α-particle numbers for a $Q=1$ experiment on JET and for an ignited ITER type plasma.

Table II
Fast or α-Particle Parameters

Parameter	Achieved in JET	Expected Values	
		JET $Q=1$	Ignited ITER
$(n_{fast}/n_e)_0$	$1-3\times10^{-2}$	10^{-3}	7×10^{-3}
$(\beta_{fast})_0$	1%	0.6%	2%
v_f/v_A	1–2	2	2.8
$\bar{\epsilon}_{fast}$ (MeV)	1	2	2
$p_\perp/p_\parallel$	10–50	1	1
P_f/P_{Loss}	0.8	0.17	1
(ρ_θ/a)	0.2 (3 MA)	0.3 (5 MA)	0.07 (20 MA)

In this table v_f is the mean velocity of fast ions, v_A the Alfven speed, $\bar{\epsilon}$ the mean energy of fast ions, P_f the power input from fast particles to the plasma, $p_\perp$ and $p_\parallel$ the perpendicular and parallel fast particle pressures, ρ_θ the fast particle gyro radius in the poloidal field at the plasma boundary. Fig. 12 shows the calculated ^{3}He distribution function at various radii in a particular discharge. Also shown is the expected α-particle distribution function in a 10 keV plasma. Evidently the two distributions are very similar. Note that more than 30% of the fast particles inside the half-radius of the experiment are super-Alfvenic. The major difference is the high anisotropy of the fast ^{3}He distribution compared with the isotropy expected for α-particles. The anisotropic case would be expected to be more unstable to collective modes so that the classical behaviour observed can be expected to carry over to the α-particle case. The confinement behaviour of these discharges heated by fast particles is if anything slightly better than the

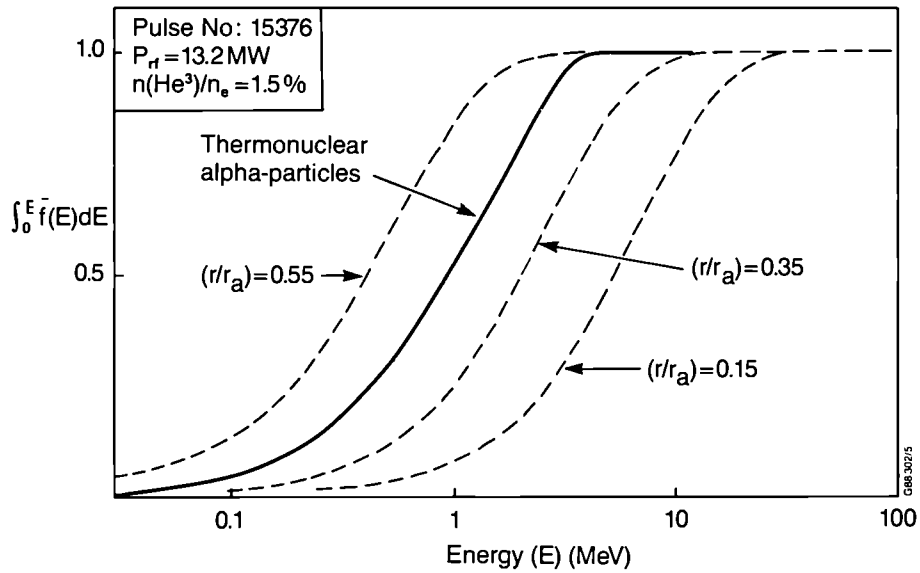

Fig. 12 Energy distribution function of heated (minority) ^{3}He ions at various plasma radii. For comparison the α-particle distribution function for a 10keV plasma is shown.

normal L-mode scaling. There is clear evidence that sawteeth crashes cause the fast particle population to be transferred to the zone outside the inversion radius. Averaging over sawteeth, this serves to flatten the power deposition profile. Of course, thermal instabilities arising from the density and temperature dependence of α-particle production are not simulated in these experiments. However; modes

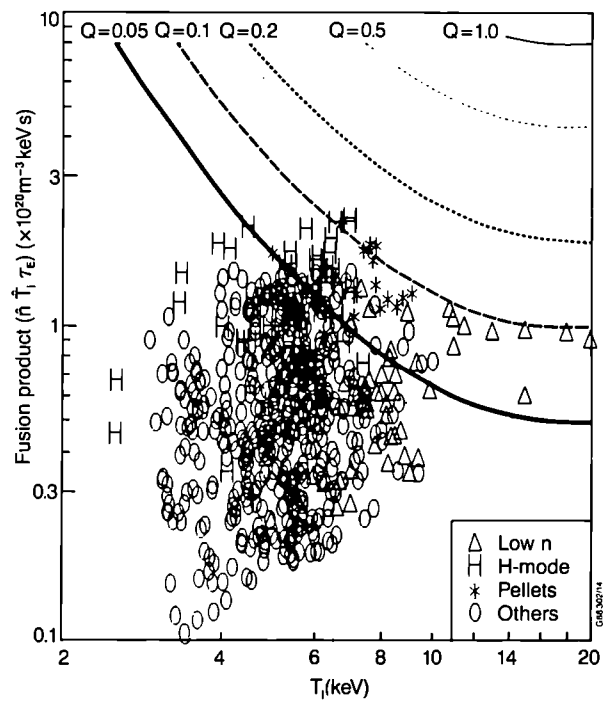

Fig. 13 Experimental values of $\hat{n}_D$ $\hat{T}_i$ τ_E versus $\hat{T}_i$. Curves show the equivalent thermonuclear Q for a 50:50 deuterium plasma. They are calculated assuming $T_e = T_i$ and radial profiles similar to the experimental ones (ratio central to average pressure of 3).

of this type will not be seen in $Q=1$ deuterium-tritium experiments either, since there the α-power is only 17% of the total.

8. Fusion Product and Q

The experimental values of the fusion product ($\hat{n}_D\ \hat{T}_i\ \tau_E$) are plotted versus T_i in Figure 13. Also shown are the contours of constant thermonuclear Q, Q_{th} calculated on the basis of a D-T mixture with the same hydrogen isotype density and with density and temperature profiles typical of JET experiments (pressure ratio $p/\langle p\rangle=3$). It is assumed that $T_e=T_i$ at all radii. Correcting for impurities by taking only the deuteron density overestimates Q_{th} because the energy content of the electrons associated with the impurities is not included in the losses. However for $Z_{eff}<3$, the maximum error is 30%. From the figure it is clear that conditions close to $Q_{th}=0.1$ have been achieved.

Fig. 14 shows the directly measured values of Q_{DD} versus mean density. Here the highest values which are at low density are due to beam-plasma interactions. Scaling these to the planned deuterium beam energy (140keV), accounting for cross-section and yield changes, the equivalent Q_{tot} for a 50:50 D-T plasma is 0.25.

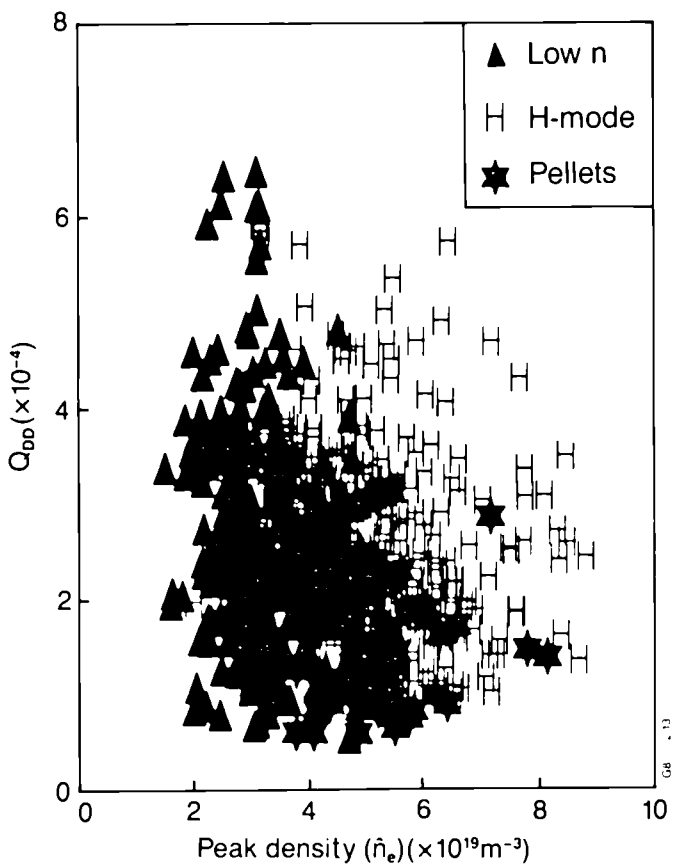

Fig. 14 Measured Q_{DD} versus mean density.

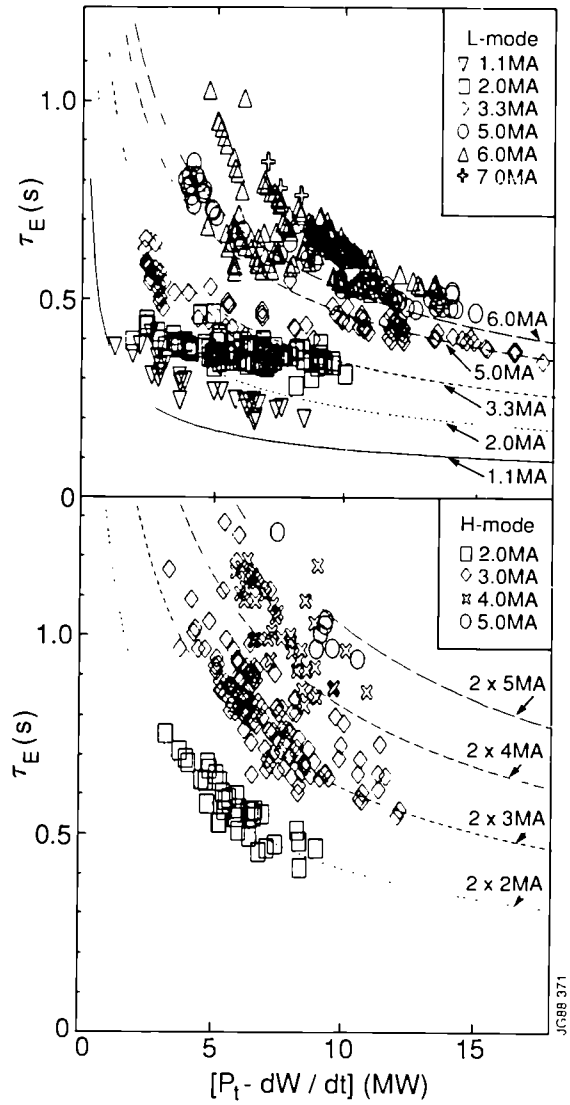

Fig. 15 Global energy confinement time, τ_E, versus input power for the L-mode (curves are Goldston scaling for different currents) and H-mode (curves are 2× Goldston scaling) cases.

9. Confinement and Transport

The global confinement times, defined as $\tau_E = W/(P - \mathrm{d}W/\mathrm{d}t)$, are shown in Fig. 15 as a function of input power for both the L-mode and H-mode case. These results can be equally well represented by the Goldston power law[13]:

$$\tau_E(\mathrm{G}) = 3.7\times10^{-2}\, IR^{1.75} a^{0.37} K^{1/2} \mathrm{P}^{-1/2}$$

or by an offset-linear law derived by Rebut and Lallia[14],

$$\tau_E\,(R-L) = 3.7\times10^{-2}\, M^{1/2}\, T^{1/2}\, n^{3/4}\, B^{1/2}\, L^{11/4}\, Z^{1/4}\, P^{-1} + 1.7\times10^{-2}\, M^{1/2}\, IL^{3/2}\, Z^{-1/2}$$

where M is the atomic mass, $L^3 = Ra^2K$, K = elongation, n = density ($10^{19}\,\mathrm{m}^3$), $Z = Z_{eff}$, and other units are MA, T, m, MW, and s. Fig. 16 and 17 show the JET

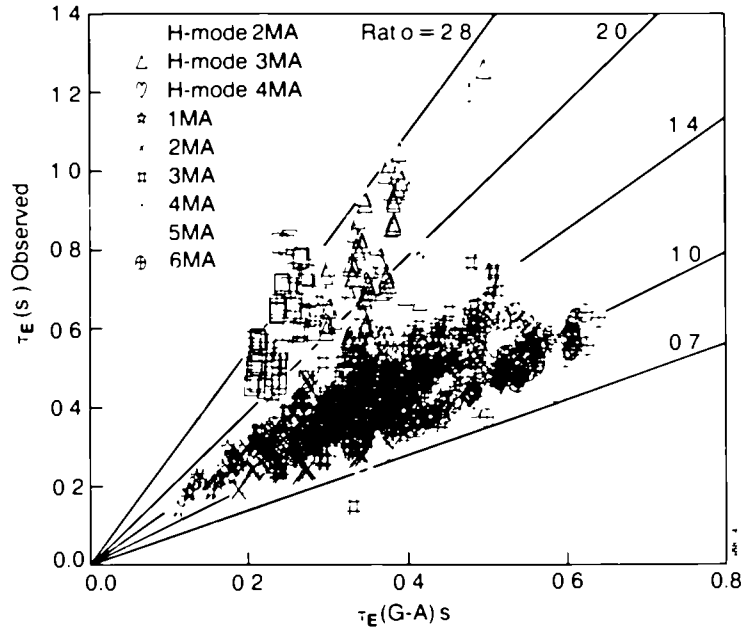

Fig. 16 Comparison between the experimental values of global energy confinement time, τ_E and the predictions of Goldston (84) scaling[13].

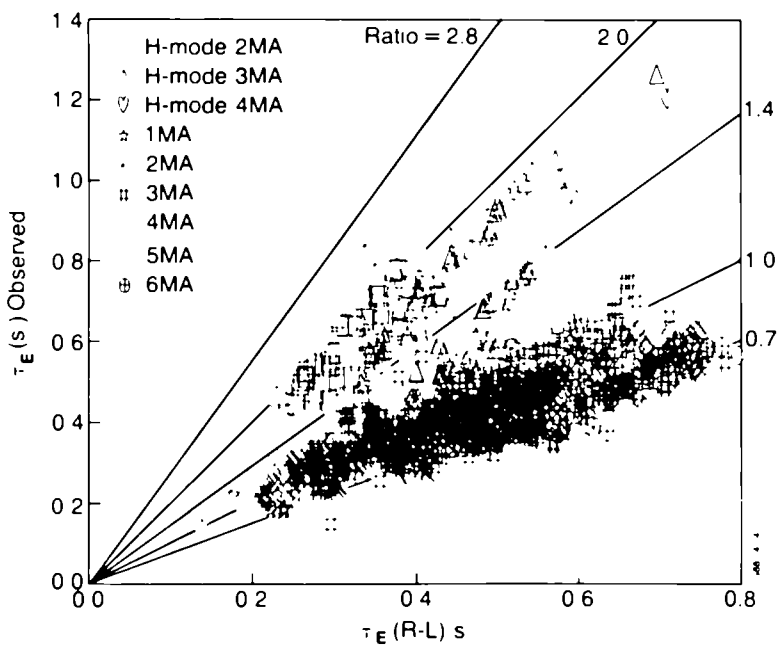

Fig. 17 Comparison between the experimental values of global energy confinement time, τ_E and the predictions of the Rebut-Lallia (88) scaling law[14].

data plotted against these laws. H-modes are clearly improved with respect to Goldston by ~ 2 and to Rebut-Lallia by slightly less.

It seems unlikely that it will be possible to separate these two forms on JET. At high power the ratio of the two confinement times for $Z = M = 2$ is:

$$\tau_E(G)\ /\tau_E(R-L) = 2.2\ (R/a)^{1.25} a^{-0.12}\ P^{-1/2}$$

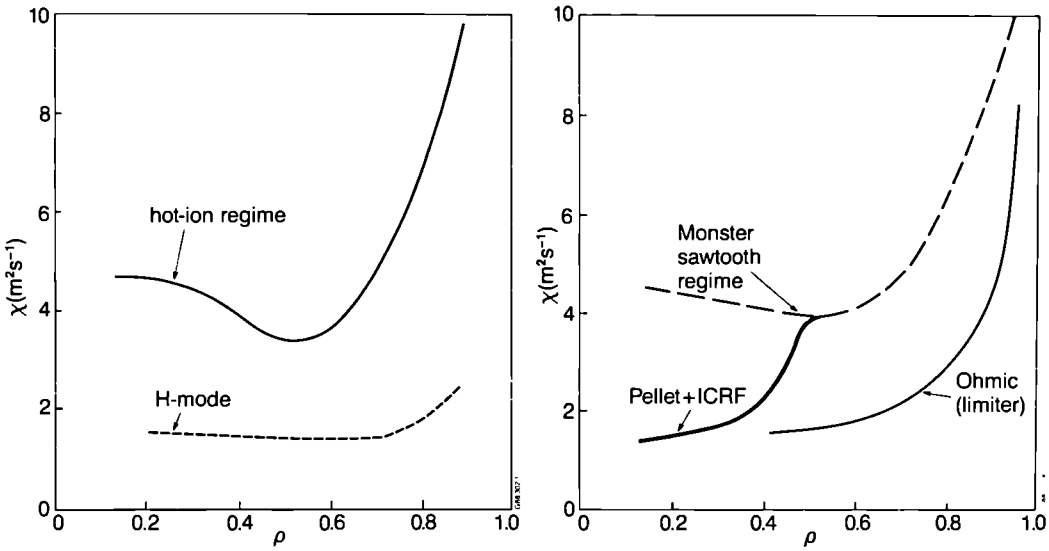

Fig. 18 The single-fluid, thermal conductivity χ versus normalised radius for various types of discharge.

For JET dimensions, $\tau_E(G)$ and $\tau_E(R-L)$ are equal for $P=45$MW. Above 45MW, the offset linear law becomes more optimistic, below this power the combination of the offset and the incremental part is difficult to distinguish from the power law.

Looking ahead to a reactor, note that degradation of the $P^{-1/2}$ type will have to be forced if it does not occur naturally. Only in this way can a reactor be ignited at low power and then moved to its final high power operating point[15].

Local transport analysis[16] of extensive JET data has shown in broad terms that the electron and ion thermal conductivities, χ_e and χ_i, are approximately equal while the particle diffusion coefficient D is typically ($\chi_e/5$). Samples of local analysis are shown in Fig. 17 for different discharge types. The power flow q by conduction is computed taking into account heating profiles, convection and radiation. Then, treating the plasma as a single fluid, the thermal conductivity χ is given by $\chi = q/n(\mathrm{d}T/\mathrm{d}r)$. The results in Fig. 18 are for discharges with $I=3$MA and $3.2<B<3.5$T. Low values of χ are seen in the interior of ohmic, pellet-injected and H-mode discharges. The power deposition profiles highlight the remarkable pellet case, where χ is very low in the core despite strong central power deposition. These results taken together are not simply correlated with variations of η_e, η_i ($=\mathrm{d}lnT/\mathrm{d}ln.n$). Critical temperature gradient (or equivalently heat-pinch) or critical pressure gradient models give a tolerable representation of both steady-state and transient profiles of temperature for most cases. However for the heated pellet case, an ad hoc reduction of χ is required to fit the data[16].

10. Future Prospects

For central ion temperatures >10 keV and moderate profiles ($\gamma_p = p/\langle p \rangle \sim 3$), the ratio, F, of α-particle power to the losses is given by:

$$F = 2 \times 10^{-22}\, \hat{n}\, \hat{T}\, \tau_E$$

corresponding to an energy content W(MJ) in the plasma

$$W = \frac{2.4\, VF}{\gamma_p\, \tau_E}$$

where V is the plasma volume. For low values of F, $\tau_E = W/P$ where P is the input power so that $W = (2.4\, VFP/\gamma_p)^{1/2}$ or in terms of thermonuclear Q_{th},

$$W = \left[\frac{2.4\, V\, Q_{th}\, P}{\gamma_p (5 + Q_{th})}\right]^{1/2}$$

For JET with a plasma volume of 140 m^3 and $\gamma_p = 3$

$$W = 10.6 \left[\frac{Q_{th}\, P}{5 + Q_{th}}\right]^{1/2}$$

This relation is shown in Fig. 19 for $Q_{th} = 0.3$, 0.5 and 1.0. The right-hand ordinate shows the mean density scale corresponding to $\bar{T} = 7$ keV. If for a given plasma energy, the density is higher than the figure given, then the central temperature

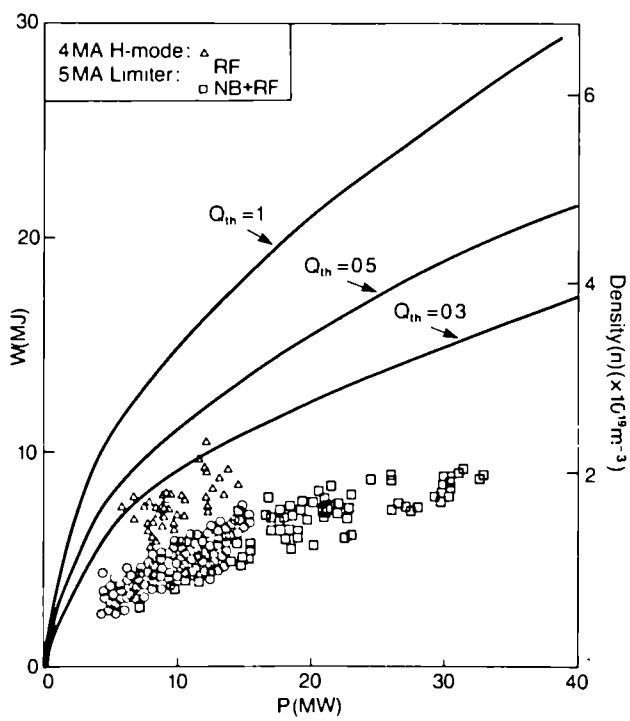

Fig. 19 Plasma energy content versus total power input. Curves are for constant thermonuclear Q assuming an average ion temperature greater than 7 keV. Density must be less than the critical value on the right hand ordinate for this to be the case.

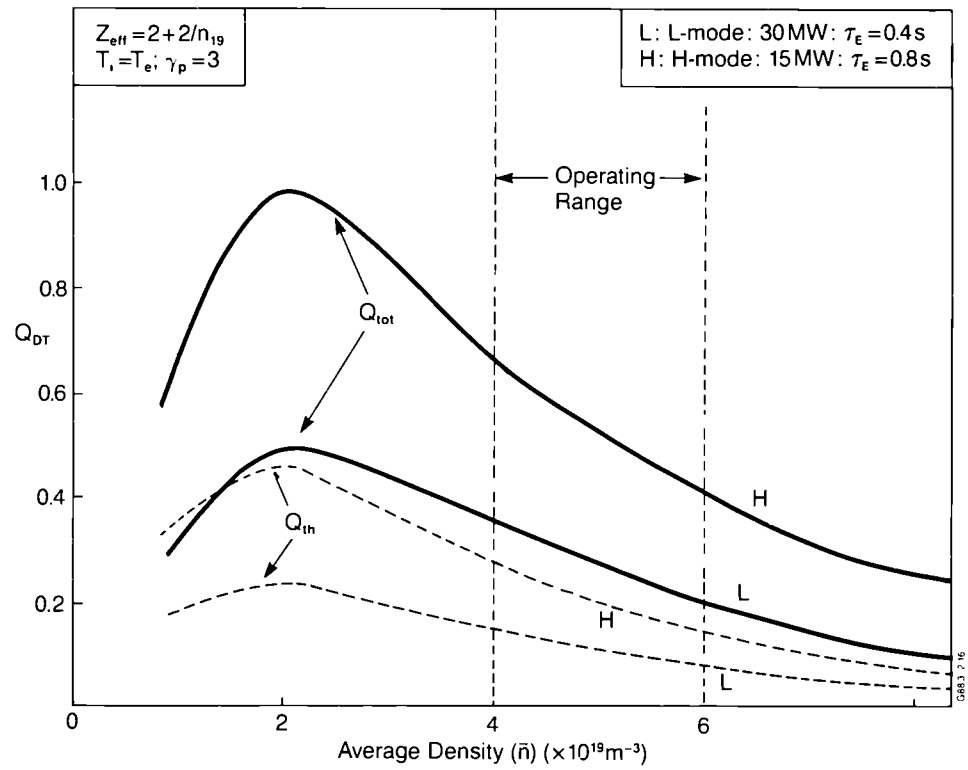

Fig. 20 Predicted thermonuclear and total Q values for H and L-mode cases with 15MW of 140kV beams supplemented in the L-mode case by 15MW of RF. The present operating density range under these conditions is marked.

will be too low, which invalidates the relation used between F and the fusion parameter. The present experimental data for W versus P is also shown on the figure. At first sight, the H-modes have the highest potential but the density is too high for optimum results.

A further assessment including beam-plasma reactions is shown in Fig. 20. Here, it is assumed that $Z_{eff}=(2+2/\bar{n}_{19})$, which is an approximate representation of Fig. 10. The beams are taken to be the 140kV, 15MW deuterium, planned for the D-T phase. Assuming a realistic minimum average density of 5×10^{19}m^{-3} at high current and high power shows a total Q ranging from 0.3–0.6, as τ_E varies from 0.4–0.8s (range of L and H-mode predictions). The corresponding α-power would be of the order 2MW.

A number of technical improvements and additions to the apparatus are in hand which should enable higher performance to be reached. These are:

(a) stiffening of the vacuum vessel to permit routine operation at the highest current level;

(b) improved RF launching antennae with beryllium screens; this should increase reliability and facilitate coupling of RF power to H-modes;

(c) 10MW, 3.7GHz lower hybrid current drive system to control the current density profile;

(d) two pump-limiter modules to improve density control;
(e) single, and subsequently, multiple high speed pellet injectors (~ 4–6 km/s) to enable central fuelling of higher temperature plasmas;
(f) the replacement of carbon tiles on belt limiters and antennae protection by beryllium together with beryllium evaporators. This should reduce the oxygen content and substitute a lower Z element for carbon;
(g) water cooled X-point dump plates with carbon fibre material facing the plasma;
(h) saddle coils are being prepared to go inside the vacuum vessel for feedback control of the precursor instabilities which lead to disruptions;
(i) upgrading of neutral beam energy to 140 kV, deuterium and eventually one of the two beam boxes to 160 kV, tritium;
(j) tritium and remote-handling equipment is under intensive preparation for the deuterium tritium phase.

11. Summary and Conclusions

In summary, the main results achieved on JET have been:

1. JET has operated with 7 MA in limiter mode and 5 MA with a single X-point configuration;
2. Central ion temperatures of 23 keV, central electron temperatures of 12 keV, central electron densities of $1.8 \times 10^{20}\,m^{-3}$ and confinement times of 1.2 s have been obtained in different discharges.
3. Both electron and ion temperatures have simultaneously exceeded 10 keV during several confinement times. Most encouraging is that no further confinement degradation is observed in these conditions directly relevant to reactor operations.
4. Plasma temperatures exceeding 5 keV have been maintained for 20 s during ICRH heating of 3 MA discharges.
5. Plasmas with an equivalent thermonuclear Q of 0.1 and equivalent total Q (including non-thermal reactions) of 0.25 have been achieved.
6. The high current capability combined with the full rated heating power has not yet been exploited. Technical difficulties with water cooled elements and with disruption forces are progressively being overcome.
7. Some aspects of α-particle physics have now been simulated notably in RF heating experiments with a ^3He minority in the plasma. The behaviour is as expected.
8. Extrapolating from present results, taking into account the operating limits on density and impurities a total Q approaching 0.6 is predicted for D-T operation corresponding to an α-power of 2 MW.
9. Technical changes and additions to the apparatus now under preparation

will give greater control of density and current profiles, reduce the impurity content and perhaps reduce the severity of disruptions. These should lead to significant improvements over the base-level performance predictions given above.

In conclusion, extrapolation of JET confinement data using either Goldston or offset-linear scaling suggests that energy confinement itself will not be a problem in reactor-scaled devices such as PCSR[17] operating at the 20MA level. Much more problematic are questions of fuelling, pumping and maintenance of a long burn plasma. JET is the machine with plasma parameters and geometry closest to those required. Therefore, it offers the possibility of developing the technical means and the experience in the delicate balance required between energy and particle (including impurities) confinement.

12. References

[1] Bertolini, E, Huguet, M. et al. Proc. 12th Symposium on Fusion Engineering (Monterey, USA) 1987, (also JET Report P(87)52).

[2] Gibson A. and the JET Team, EPS Conference on Controlled Fusion and Plasma Heating, (Dubrovnik, Yugoslavia, to be published in Plasma Physics and Controlled Fusion, 1988).

[3] Rebut P-H. and the JET Team, Nuclear Fusion Supplement, Plasma Physics and Controlled Fusion Research, Vol. 1, p.31, (Kyoto, Japan) 1987.

[4] Start D F H. et al, Paper IAEA-CN-50/E-11-3, this conference.

[5] Kupschus P. et al, 15th EPS Conference on Controlled Fusion and Plasma Heating, Europhysics Conference Abstracts 12B, 143.

[6] Schmidt G. and the JET Team, Paper IAEA-CN-50/A-1V-1, this conference.

[7] O'Rourke J. et al, 15th EPS Conference on Controlled Fusion and Plasma Heating, (Dubrovnik, Yugoslavia) 1987. Europhysics Conference Abstracts Vol 12B, Part 1, p.155.

[8] Pegoraro F. et al, Paper IAEA-CN-50/D-1V-6, this conference.

[9] Keilhacker M. and the JET Team, Paper, IAEA-CN-50/A-III-2 this conference.

[10] Hawryluk R.J. et al, Nuclear Fusion Supplement, Plasma Physics and Controlled Fusion Research, Vol 1, p51, (Kyoto, Japan), 1987.

[11] Hirshman S.P. and Sigmar D.J., Nuclear Fusion, **21**, 1079, (1981).

[12] Thomas P. et al., Paper IAEA-CN-50/A-IV-4.1, this conference.

[13] Goldston R.J. Plasma Physics and Controlled Fusion, **26**, 87, (1984).

[14] Rebut P-H, Lallia P., Watkins M.L. Paper IAEA-CN-50/D-4-1.

[15] Roberts K.V. Invited Paper, 9th EPS Conference on Plasma Physics and Controlled Fusion, Oxford, 1979.

[16] Taroni A. et al, Paper IAEA-CN-50/A-VII-1, this conference.

[17] Spears W. NET Report EUR-FU/X11-80/86/67, (1986).

[18] Behringer K. et al, 15th EPS Conference on Controlled Fusion and Plasma Heating (Dubrovnik, Yugoslavia, (1988). Europlasma Conference Abstracts. Vol 12B. p.338.

[19] Batistoni P. et al, 15th EPS Conference on Controlled Fusion and Plasma Heating (Dubrovnik, Yugoslavia, 1988). Europlasma Conference Abstracts, Vol 12B. p.135.

[20] Challis C.D. et al, submitted to Nuclear Fusion, (1988).

APPENDIX I

THE JET TEAM

JET Joint Undertaking, Abingdon, Oxon, OX14 3EA, UK

J.M. Adams[1], H. Altmann, G. Appruzzese, W. Bailey, P. Ballantyne, B. Balet, D.V. Bartlett, L.R. Baylor[23], K. Behringer[13], A.C. Bell, P. Bertoldi, E. Bertolini, L.G. Betello, V. Bhatnagar, R.J. Bickerton, A.J. Bickley, J. Bizarro[21], S. Bliman[16], T. Bonicelli, S.J. Booth, G. Bosia, M. Botman, D. Boyd[30], H. Brelen, H. Brinkschulte, M. Brusati, T. Budd, M. Bures, T. Businaro[4], P. Butcher, H. Buttgereit, C. Caldwell-Nichols, D.J. Campbell, P. Card, J. Carwardine, G. Celentano, P. Chabert[16], C.D. Challis, A. Cheetham, J. Christiansen, C. Christodoulopoulos, P. Chuilon, R. Claesen, S. Clement[29], J.P. Coad, P. Colestock[6], S. Conroy[12], M. Cooke, S. Cooper, J.G. Cordey, W. Core, G. Corrigan, S. Corti, A.E. Costley, G. Cottrell, M. Cox[7], P. Cripwell[12], D. Cross, H. de Blank[15], H. de Esch, J. de Haas[15], L. de Kock, E. Deksnis, G.B. Denne, G. Deschamps, G. Devillers, K.J. Dietz, J. Dobbing, A. Dombra, N. Dolgetta, S.E. Dorling, P.G. Doyle, D.F. Düchs, H. Duquenoy, A. Edwards, J. Ehrenberg[13], T. Elevant[11], W. Engelhardt, S.K. Erents[7], L.G. Eriksson[5], M. Evrard[2], H. Fajemirokun[12], H. Falter, J. Farthing, D. Flory, M. Forrest[7], C. Froger, K. Fullard, M. Gadeberg, A. Galetsas, M. Galley, R. Galvao[8], M. Garribba, R. Giannella, A. Gibson, R.D. Gill, A. Gondhalekar, G. Gorini, C. Gormezano, N.A. Gottardi, C. Gowers, B.J. Green, F.S. Griph, W.K. Guo[26], R. Haange, G. Hammett[6], W. Han[9], H.E. Han-Gonge[26], C.J. Hancock, P.J. Harbour, N.C. Hawkes[7], P. Haynes[7], J. Heikkinen[3], T. Hellsten, J.L. Hemmerich, R. Hemsworth, F.B. Herzog, R.F. Herzog, J. Hoekzema, R. Hope, W.A. Houlberg[23], J. How, M. Huart, T.P. Hughes[31], M. Hugon, M. Huguet, M. Irving, J. Jacquinot, O.N. Jarvis, F. Jensen, T.C. Jernigan[23], E. Joffrin, E.M. Jones, L.P.D.F. Jones, T.T.C. Jones, J. Källne, O. Kardaun[13], A. Kaye, B.E. Keen, M. Keilhacker, G.J. Kelly, A. Khare[14], S. Knowlton, A. Konstantellos, M. Kovanen[20], P. Kupschus, P. Lallia, R. Lanza, R. Lasser, J.R. Last, L. Lauro-Taroni, K. Lawson[7], E. Lazzaro, M. Lennholm, B. Liley[25], X. Litaudon, P. Lomas, M. Lorentz-Gottardi[2], C. Lowry, G. Maddison[7], G. Magyar, M. Malacarne, W. Mandl[13], V. Marchese, J. Mart, P. Massmann, G. McCracken[7], J. Mendonca, P. Meriguet, P. Micozzi[4], S.F. Mills, P. Millward, S.L. Milora[23], A. Moissonnier, F. Mompean, P.L. Mondino, P. Morgan, G. Murphy, G. Newbert, M. Newman, P. Nielsen, P. Noll, W. Obert, D. O'Brien, J. O'Rourke, M.G. Pacco-Düchs, M. Pain, S. Papastergiou, D. Pasini[19], A. Peacock, N. Peacock[7], D. Pearson[12], F. Pegoraro, F. Petree, M. Pick, S. Pitcher[7], J. Plancoulaine, J-P. Poffé, F. Porcelli, R. Prentice, T. Raimondi, C. Raymond, P-H. Rebut, J. Removille, F. Rimini, D. Robinson[7], A. Rolfe, R. Romain, R.T. Ross, L. Rossi, R. Rushton, P. Rutter, H.C. Sack, G. Sadler, G. Saibene, N. Salmon[12], H. Salzmann[13], A. Santagiustina, R. Sartori, D. Schissel[24], P.H. Schild, M. Schmid, G. Schmidt[6], R.L. Shaw, K. Schimizu[17], A. Sibley, R. Simonini, J. Sips[15], P. Smeulders, J. Snipes, S. Sommers, L. Sonnerup, K. Sonnenberg, G. Sonnozaro, W. Stacey[28], M. Stamp, P. Stangeby[18], D.F. Start, C.A. Steed, D. Stork, P.E. Stott, T.E. Stringer, D. Stubberfield, D. Summers, H. Summers[19], J. Tagle[29], H. Tamnen, A. Tanga, A. Taroni, C. Tebaldi[22], A. Tesini, P.R. Thomas, E. Thompson, K. Thomsen, J.M. Todd, P. Trevalion, B. Tubbing, F. Tibone, E. Usselmann, A. Vannucci, H. van der Beken, M. von Hellermann, T. Wade, C. Walker, M. Walravens, K. Walter, Z. Wang[27], D. Ward, M.L. Watkins, H. Weisen[10], J. Wesson, D.H. Wheeler, J. Wilks, U. Willen[11], D. Wilson, T. Winkel, S. Wolfe, D. Wong, C. Woodward, M. Wykes, I.D. Young, L. Zannelli, D. Zasche[13]

PERMANENT ADDRESS

1 UKAEA, Harwell, Didcot, Oxon, UK
2 EURATOM Association, LPP ERM KMS, B 1040 Brussels, Belgium
3 Technical Research Centre of Finland, Helsinki, Finland
4 ENEA CENTRO Di Frascati, I 00044 Frascati, Roma, Italy
5 Chalmers University of Technology, Goteborg, Sweden
6 Princeton Plasma Physics Laboratory, New Jersey, USA
7 UKAEA Culham Laboratory, Abingdon, Oxfordshire, UK
8 Plasma Physics Laboratory, Space Research Institute, Sao Jose dos Campos, Brazil
9 Institute of Mathematics, University of Oxford, UK
10 CRPP EPFL, 21 Avenue des Bains, CH 1007 Lausanne, Switzerland
11 Swedish Energy Research Commission, S 10072 Stockholm, Sweden
12 Imperial College of Science and Technology, University of London, UK
13 Max Planck Institut fur Plasmaphysik, D 8046 Garching bei Munchen, FRG
14 Institute for Plasma Research, Gandhinagar Bhat Gujrat, India
15 FOM Instituut voor Plasmafysica, 3430 Be Nieuwegein, The Netherlands
16 Commissariat a L'Energie Atomique, F-92260 Fontenay-aux-Roses, France
17 JAERI, Tokai Research Establishment, Tokai-Mura, Naka-Gun, Japan
18 Institute for Aerospace Studies, University of Toronto, Downsview, Ontario, Canada
19 University of Strathclyde, 107 Rottenrow, Glasgow, G4 0NG, UK.
20 Nuclear Engineering Laboratory, Lapeenranta University, Finland
21 JNICT, Lisboa, Portugal.
22 Department of Mathematics, Univeristy of Bologna, Italy
23 Oak Ridge National Laboratory, Oak Ridge, Tenn., USA.
24 G A Technologies, San Diego, California, USA
25 University of Waikato, Hamilton, New Zealand.
26 IPP, Academia Sinica, P R China.
27 Southwestern Institute of Physics, Leshan, Sechuan, P R China
28 University of Georgia, Atlanta, USA
29 Centro de Investigaciones Energeticas Medioambientales y Techalogicas, Spain
30 University of Maryland, College Park, Marvland, USA
31 University of Essex, Colchester, UK

J CR 88 49 1A rev 30/11 88

The JET H-Mode at High Current and Power Levels

The JET Team*
(presented by M. Keilhacker.)
JET Joint Undertaking, Abingdon, Oxon, OX14 3EA, UK

Abstract

H-mode operation in JET single-null X-point configuration has been extended to plasma currents of 5 MA, toroidal fields of 3.4 T and neutral beam powers of 20 MW (80 keV deuterium injection). Characteristic of JET H-mode discharges is the absence or very low level of ELM activity resulting in a continuous rise in plasma density and a concomitant increase in bulk plasma radiation which finally terminates the H-phase (longest H-phase so far, 4 s). The global energy confinement time, τ_E, of these H-mode discharges is a factor of 2-3 larger than in comparable limiter discharges. The confinement increases roughly linearly with plasma current (provided $q_{95} \gtrsim 3$) and to a lesser extent with toroidal magnetic field but decreases with increasing neutral beam heating power (roughly $\propto P^{-0.7}$). Part of this degradation with power can be attributed to poor beam penetration at the higher densities concomitant with improved particle confinement and the higher power levels. Local transport analysis using time-dependent codes indicates that in the H-mode the total heat transport coefficient, χ_{eff}, in the plasma interior ($r/a \leq 0.8$) is comparable to that deduced in the ohmic phase ($\chi_{eff} \sim 1\,m^2s^{-1}$). The main contribution to the enhanced confinement characteristic of H-modes, however, comes from the plasma edge as manifested by the steep temperature and density gradients (pedestals) observed in this region. With 12 MW of neutral beam heating $\tau_E \sim 1$ s and favourable values of the fusion product $n_D T_i \tau_E \sim 2.5 \times 10^{20} m^{-3}$ keVs have been achieved. On the basis of these results and assuming proper density and impurity control can be achieved, fusion amplification factors close to unity are predicted for tritium operation in JET.

1. Introduction

As is well-known, the H-mode observed in plasmas bounded by a separatrix in closed[1,2,] or open[3,4,5] divertor geometry allows a factor of 2-3 better confinement than in comparable limiter discharges. First H-mode results in JET at plasma currents of up to 3 MA and with neutral beam injection (NBI) heating up to 10 MW were presented in 1986[5]. Since then, using differential currents in the main equilibrium coils has allowed H-mode operation in the single null X-point configuration to be extended to plasma currents of 5 MA, full toroidal fields of 3.4 T and neutral beam powers of 20 MW. With the global energy confinement time, τ_E, increasing roughly linearly with current (provided the safety factor at the 95% flux surface, $q_{95} \gtrsim 3$) τ_E values in the range 0.8-1 s and stored

*see Appendix I

CR88.172

plasma energies of more than 10MJ have been achieved with 12MW of additional heating. H-modes have also been obtained in the double null configuration with currents up to 3MA (technical limit $\lesssim$4MA).

The present discussion of JET H-mode plasmas is restricted to NBI heating (80keV deuterium injection) of deuterium plasmas in a single null X-point configuration. Following a brief discussion of the operational limits for achieving H-modes (section 2) the paper addresses the characteristic features of these plasmas (section 3). Section 4 is devoted to their energy confinement while section 5 addresses particle control and future prospects for H-mode operation.

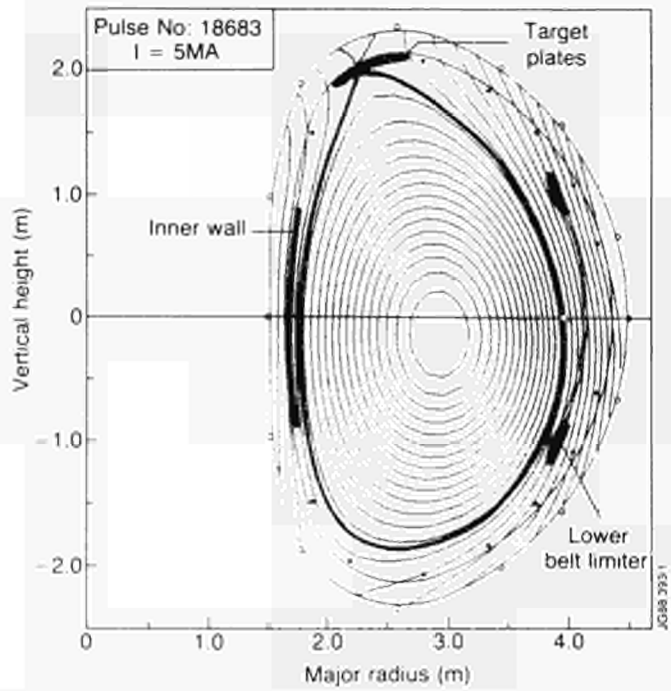

Fig. 1 Poloidal flux contours for a 5MA single null X-point discharge.

2. Operational Limits for H-mode

Fig. 1 shows poloidal flux contours for a 5MA single null X-point discharge together with a schematic view of the vacuum vessel, the upper and lower toroidal belt limiters and the target plates at the top and bottom of the vessel. To achieve an H-mode, minimum separations of the separatrix from the inner wall, δ_{IW}, and from the lower belt limiter, δ_{BL}, are required. The precise clearances required depend on vessel conditioning, plasma parameters and, in particular, on the heating power used. Typical values are

$$\delta_{BL} \gtrsim 0.05\,\text{m} \quad \delta_{IW} \gtrsim 0.05\text{-}0.08\,\text{m}.$$

The separation of the X-point position from the target plates was, for most experiments, in the range of a few centimetres, but it can be reduced practically to zero.

The most stringent requirement for achieving an H-mode is a certain level of heating power. In JET, this threshold power, P_{thr}, increases with toroidal magnetic field, B_T, as shown in Fig. 2 for 3 MA single null X-point discharges. Typical values with NBI are

$$P_{thr} = 5\,\text{MW} \qquad \text{for } B_T = 2.0\text{-}2.4\,\text{T}$$
$$P_{thr} = 8\text{-}12\,\text{MW} \qquad \text{for } B_T = 3.0\text{-}3.4\,\text{T}.$$

A low density limit is set for H-modes by the appearance of locked modes. The edge plasma density at the start of NBI has to be $\geq 1.2\times10^{19}\,\text{m}^{-3}$ (see also discussion in section 3.3).

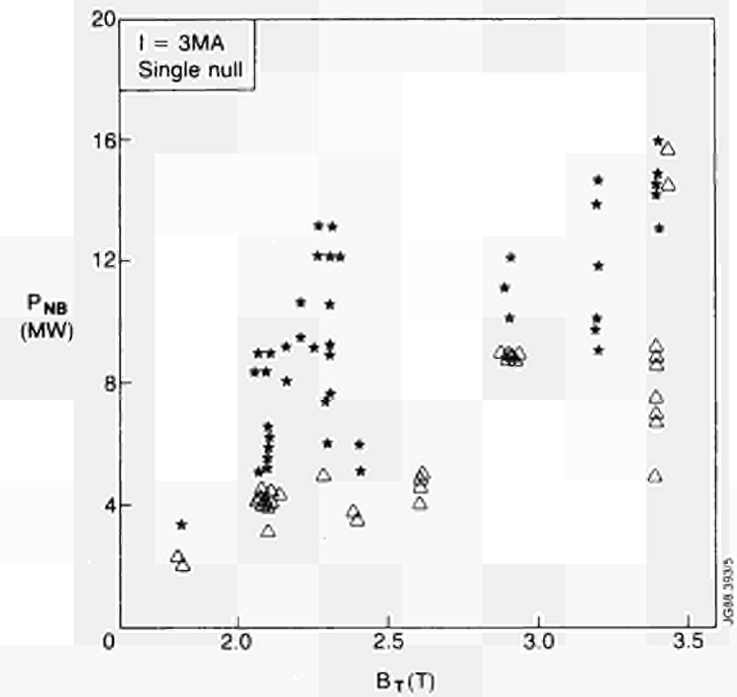

Fig. 2 H-mode threshold power as a function of toroidal magnetic field is determined by distinguishing H-mode (*) and L-mode (Δ) discharges at 3 MA, single null X-point.

3. H-mode Characteristics

3.1 Time evolution of H-mode discharges

The characteristic time evolution of various plasma parameters for JET H-mode discharges is shown in Fig. 3 for a 3 MA discharge (#15894). Characteristic of most JET H-modes is the absence or very low level of ELM activity throughout the whole H-mode phase. This results in a continuous rise in plasma density and a concomitant increase in bulk plasma radiation which finally terminates the H-mode (longest H-phase ~4s) when the bulk radiation reaches about 60% of the input power. The increase in the total energy content of the plasma, W,

during the H-phase results largely from the plasma density increase, while the central electron temperature, T_{eo}, is roughly constant or even decreasing slightly with time.

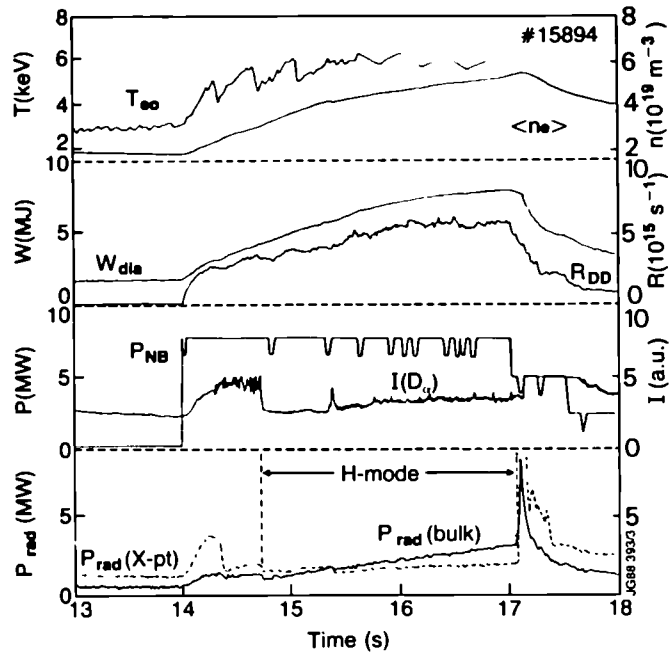

Fig. 3 Time evolution of electron temperature on axis T_{eo}, volume-averaged electron density $\langle n_e \rangle$, total plasma energy W_{dia}, total reaction rate R_{DD}, neutral beam power P_{NB}, D_α intensity $I(D_\alpha)$, bulk radiation P_{RAD} (bulk) and X-point radiation P_{RAD} (X-pt) for a 3 MA H-mode discharge ($B_T = 3.1$ T).

The level of ELM activity depends on the separation of the plasma boundary (separatrix) from the lower limiter and the inner wall. Provoking ELMs can be used to control the rise in plasma density (as is seen for time $t = 15.35$ s in Fig. 3) which can be kept approximately constant throughout the NBI pulse. This occurs, however, at the expense of simultaneously reducing the energy confinement time (see discussion in section 5).

3.2 Evolution of plasma profiles

Typical radial profiles of n_e, T_e, T_i, Z_{eff}, P_{RAD} and j during the H-mode phase are shown in Fig. 4 for discharge #15894. Fig. 4a shows radial profiles of electron density $n_e(r)$ and temperature $T_e(r)$ at $t = 16.0$ s (1.25 s into the H-phase), as measured by the LIDAR-Thomson scattering system[6]. The most characteristic feature of these profiles are the very steep temperature and density gradients at the plasma edge (giving rise to so-called pedestals) which form at the L→H transition. Flat or even slightly hollow density profiles are a common feature of both JET limiter (particularly at low values of q_{cyl}) and X-point discharges[7]

employing NBI heating. In the case of an H-mode the density increases continuously, the profile shape changing little. The electron temperature profile is also broad and changes little with time. Fig. 4a also displays the central ion temperature profile as determined from charge-exchange spectroscopy[8] on the CVI (8→7) line. Within the accuracy of the measurements the two temperatures are equal.

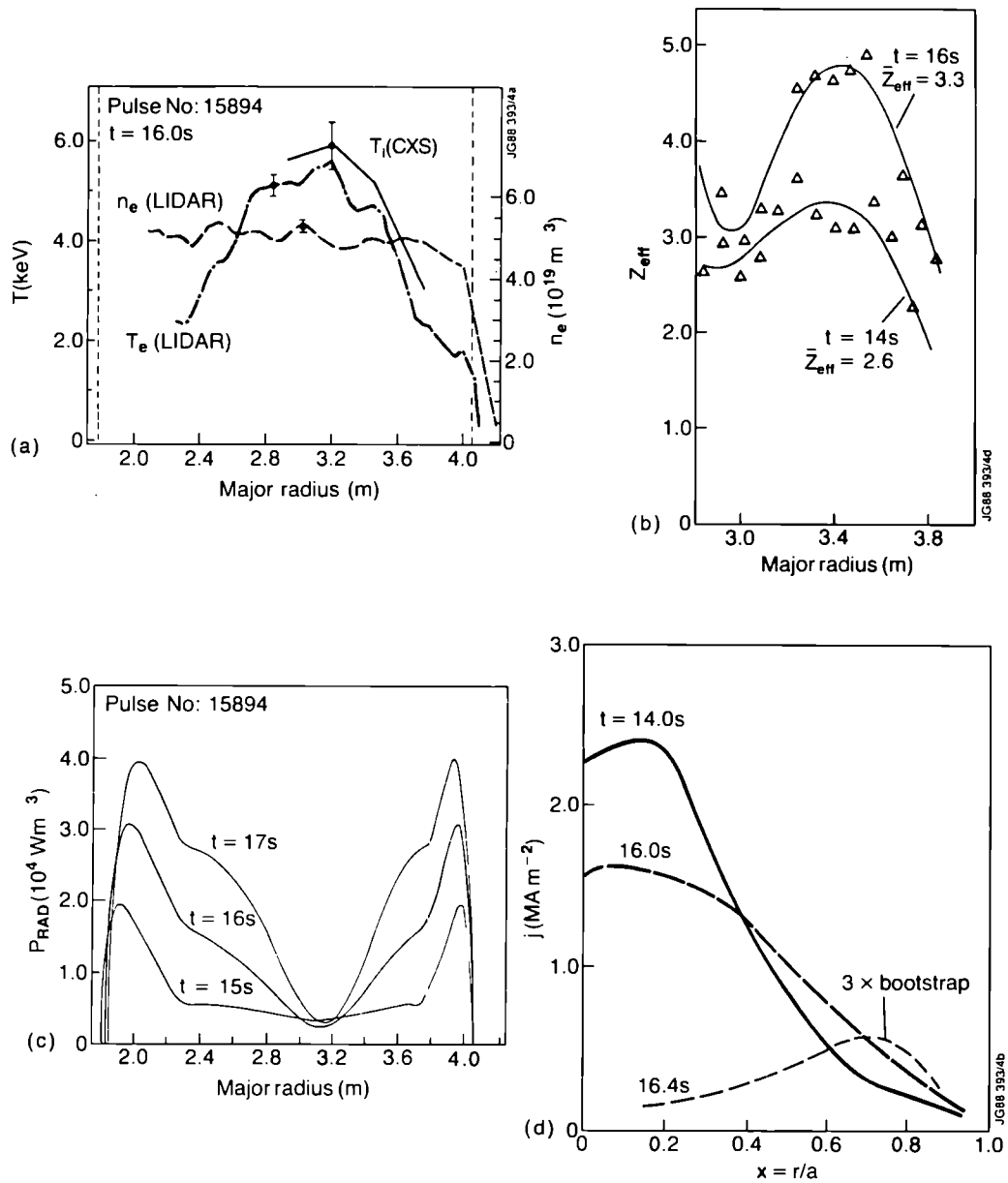

Fig. 4 Radial profiles of (a) electron density, n_e, electron temperature, T_e, and ion temperature, T_i; (b) Z_{eff}; (c) bulk plasma radiation, P_{RAD} (bulk), and (d) current density during the H-phase of the discharge shown in Fig. 3. The dashed lines in Fig. 4a indicate the radius of the 95% flux surface.

Fig. 4b displays radial profiles of Z_{eff} determined from chord measurements of the visible bremsstrahlung emission at 523.5 nm using a 15-telescope array[9] together with $n_e(r)$ and $T_e(r)$ profiles from the LIDAR diagnostic. During the limiter phase that precedes the X-point phase (not shown in Fig. 4b) the profile $Z_{eff}(r)$ is peaked on axis, with an average value $\bar{Z}_{eff}$ of ~ 2.5. Following the formation of the X-point, $Z_{eff}(r)$ becomes hollow on axis (profile at $t=14.0$ s) without much change in $\bar{Z}_{eff}$. The second profile pertains to the H-phase at $t=16.0$ s. $Z_{eff}(r)$ remains hollow, but $\bar{Z}_{eff}$ has increased to ~ 3.3, due to the improvement in impurity and particle confinement.

The evolution of the radiated power profile is shown in Fig. 4c for $t=15.0$, 16.0 and 17.0 s. Again the profiles are hollow throughout the H-phase but tend to fill in somewhat with time. Most of this radiation is emitted by light impurities, the major contribution coming from oxygen. The observed profiles of radiated power and Z_{eff} indicate hollow profiles of the light impurity densities[10]. This is substantiated by charge-exchange spectroscopy measurements. Typical concentrations on axis are 1-3% of the electron density for O and for C and $10^{-5}-10^{-4}$ for Ni. The deuterium density is typically $\sim 0.6 n_e$ due to dilution by (light) impurities.

Fig. 4d shows the evolution of the current profile determined from the multichannel FIR polarimeter[11]. During the H-phase the current density at the plasma periphery rises markedly. This is expected since (a) the resistivity is reduced in the edge region due to the increased edge electron temperature and (b) a large bootstrap current[12] develops due to the increased edge pressure gradient. A concomitant decrease of the central current density is also observed, although experimental uncertainties preclude any definitive conclusion being drawn.

To determine the bootstrap current, a magnetic field diffusion analysis has been completed using the TRANSP code[13]. It is found that the bootstrap current contributes 0.8 MA to the total current of 3 MA and most of the change in the current profile (see Fig. 4d) comes from the development of the bootstrap current rather than changes in the plasma resistivity. The existence of the bootstrap current in 'supershots'[14] and H-modes[15] has important consequences for future high temperature tokamaks. The most beneficial effect is that it reduces the volt-second consumption required to maintain a given current. The broad profile of the bootstrap current may also stabilise the $m/n=1/1$ sawtooth oscillation.

3.3 Edge plasma

The plasma edge parameters play a decisive role in the transition to an H-mode and in the resulting improved confinement properties of the plasma. The simultaneous measurement of n_e and T_e-profiles at the plasma edge using the LIDAR diagnostic allows a critical assessment. Fig. 5 shows a plot of T_{edge} versus n_{edge} for 3 MA single null X-point discharges ($B_T=2.2$ T). T_{edge} and n_{edge} are the tem-

peratures and densities taken at the surface determined by equilibrium analysis to enclose 95% of the total magnetic flux enclosed by the separatrix. The measurements are at various times during OH, L and H-phases determined by the timing and frequency of the laser pulse (0.5 Hz). The domain of edge parameters for an H-mode displays a well-defined lower density limit of $\sim 2\times10^{19}\mathrm{m}^{-3}$ (increasing to $\sim 3\times10^{19}\mathrm{m}^{-3}$ at $B_T=3.0-3.5\,\mathrm{T}$) and a minimum edge temperature of $\sim 0.5\,\mathrm{keV}$.

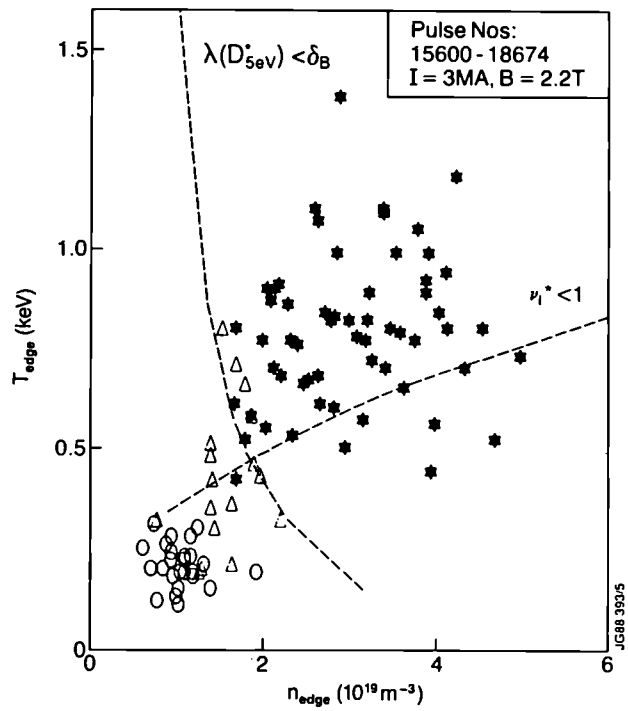

Fig. 5 Edge temperature T_{edge} ($x=0.95$) versus edge density n_{edge} ($x=0.95$) for OH (O), L- (Δ) and H-mode (*) discharges ($I=3\,\mathrm{MA}$, $B_T=2.2\,\mathrm{T}$).

These boundaries may be interpreted in terms of the collisionality of the edge plasma and the requirement to limit edge cooling by ionisation of neutral particles re-entering the plasma from the wall (see also discussion in section 3.5). The former condition, namely that the ion neoclassical collisionality parameter $\nu_i^* < 1$, is plotted in Fig. 5, and shows that H-modes correspond to low collisionality in the plasma edge. The latter condition requires that the ionisation mean-free path of incoming neutrals, $\lambda_{ion}^{(0)}$, be small compared to the thickness of the edge layer, δ_B. The boundary $\lambda_{ion}^{(0)} = \delta_B$ is also plotted in Fig. 5, where δ_B is taken as the width of an ion banana orbit and $\lambda_{ion}^{(0)}$ is evaluated for 5 eV deuterium atoms.

3.4 Stability of edge plasma to ballooning modes

The reconstructed H-phase equilibrium for pulse #15894 has been examined for its stability to ideal MHD ballooning modes. The ideal ballooning equa-

tion has been solved (to leading order in a large aspect ratio expansion) treating the pressure gradient parameter α as an eigenvalue to give the marginally stable value of α on each flux surface. Across the bulk of the plasma the results show two marginally stable α values, corresponding to the usual first and second regions of stability, separated by an unstable zone. Previous studies using model equilibria[16] have shown that close to a separatrix there exists a critical value of the surface averaged current density Λ above which the first and second regions coalesce. A similar result is found for this JET equilibrium, and furthermore the critical Λ in this case is consistent with the experimental Λ close to the separatrix. A preliminary comparison of experimental values of α (determined from the LIDAR diagnostic) with the stability results suggests that across the bulk of the plasma the pressure gradients lie in the first stable region and are about a factor 2 below the first stability boundary. Near to the separatrix, the experimental α rises sharply (electron pressure gradient $\sim 150\,\mathrm{kPa/m}$) to values near the first stability boundary. These preliminary results suggest that the pressure gradients are lower than would be required by the bifurcation model of Bishop[17]. Nevertheless they indicate that the edge pressure gradients in the H-mode are sufficiently steep that ideal ballooning stability becomes relevant. Furthermore the current density parameter Λ is found to be consistent with the critical value needed for coalescence.

3.5 Divertor plasma

The plasma in the vicinity of the X-point target plates (divertor plasma) has been investigated with an array of eight Langmuir probes mounted in the target plates (see inset in Fig. 6), with a reciprocating Langmuir probe (at $R = 3.25\,\mathrm{m}$), and with a 2-dimensional view of the radiation from the divertor region.

Fig. 6 shows profiles of density, temperature and ion saturation current in front of the target plates for a 4.6 MA discharge (OH and H-phase with $P_{NBI} = 14\,\mathrm{MW}$). Although a single-null discharge, the inner divertor plasma is colder and denser than the outer. More power is carried to the outer divertor, suggesting that the main source of power flow into the scrape-off layer is in the vicinity of the outer mid-plane, ie, closer to the outer divertor target. The unequal temperatures lead to thermo-electric currents in the scrape-off layer[18]. Current densities $\leq 10^5\,\mathrm{Am}^{-2}$ have been measured during the H-phase (see Fig. 6) corresponding to more than 10% of the mean current density in the discharge. The scrape-off layer current flows from outer to inner divertor and returns through the target plates, thus flowing in the same direction as the plasma current.

The power estimated to be carried by plasma to the target plates increases from 0.8 MW in the ohmic phase to 1.9 MW at the end of the H-phase. For most of the discharge, i.e. L and H-phases, this is about 15% of $(P_{total} - \mathrm{d}W_{dia}/\mathrm{d}t)$ but about 25% during the ohmic phase.

Profiles with the reciprocating probe in the scrape-off layer agree reasonably

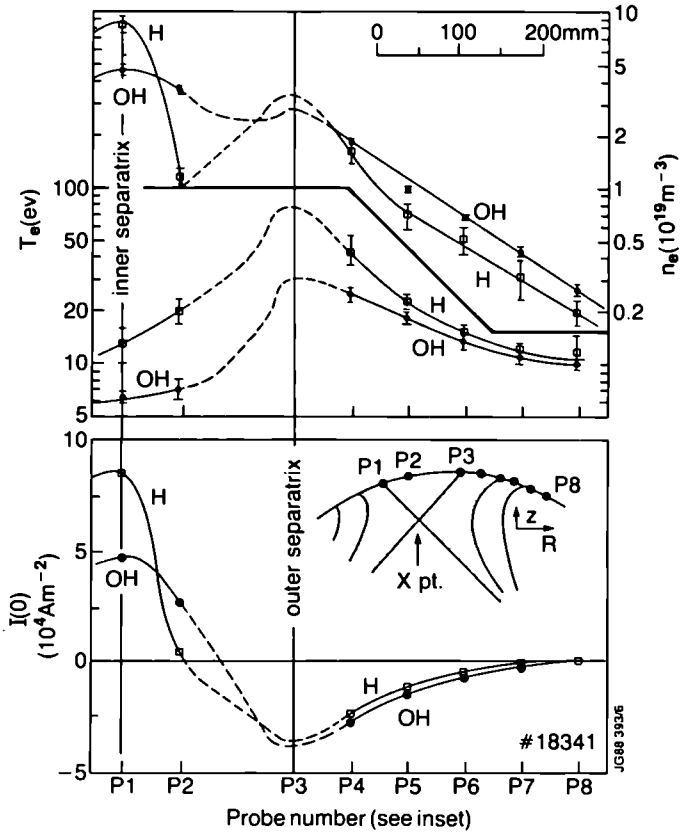

Fig. 6 Profiles of density, temperature and ion saturation current in front of the target plates, measured with Langmuir probes mounted in these plates.

well with those at the divertor target. Preliminary results for two or three pulses show that the radial electric field, just inside the separatrix, $E_r = -(\mathrm{d}V_{plasma})/\mathrm{d}r$ is negative in the ohmic phase and about $+5\,\mathrm{kVm}^{-1}$ with H-mode. This result, if substantiated, would agree with the prediction of Itoh and Itoh[19].

The collisionality of the divertor plasma may have a bearing on whether an H-mode can be achieved. Two aspects of collisionality are considered: Coulomb collisions with electrons, and ionisation of neutral particles in the divertor plasma.

For Coulomb collisions, the Coulomb mean free path, λ_{ee}, is compared with the distance $L_\parallel$ in the divertor measured along a field line from the target to the X-point. With the X-point typically 0.10 m from the target and a pitch angle of the field lines of $\sim 1°$, $L_\parallel \approx 6\,\mathrm{m}$. Fig. 7 shows probe measurements of T_e plotted against n_e on a logarithmic scale. The straight line represents $\lambda_{ee} = 6\,\mathrm{m}$: plasmas with parameters above (below) this line are collisionless (collisional). The parameters for the probes P1 to P8 are shown for OH and H phases. The inner scrape-off layer is cold enough to be highly collisional. The outer scrape-off layer is collisional during the ohmic phase and marginally collisional during the H phase. Discharges at lower currents tend to be slightly less collisional and vice-versa.

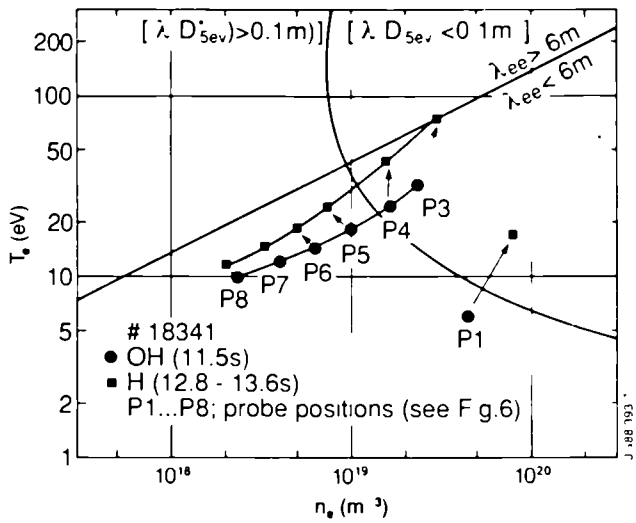

Fig. 7 Collisionality of the plasma in the vicinity of the X-point target plates.

The ionisation of neutrals in the divertor plasma fan is assessed by comparing the ionisation mean free path of neutrals, $\lambda_{ion}^{(0)}$, with the dimensions of the divertor plasma which is typically O.1 m. Fig. 7 shows a curve corresponding to $\lambda_{ion}^{(0)}$ for 5 eV deuterium atoms, typical of dissociation energies. During the H-phase the majority of 5 eV atoms would be ionised in the divertor plasma but some of those from further out in the divertor scrape-off layer might escape. Thus during the H-phase the plasma is highly recycling in the divertor, especially near the separatrix.

These results suggest that flows in the scrape-off layer have a low Mach number, or are nearly stagnant, near the separatrix but are stronger and towards the divertor further away from the separatrix. As discussed in ref. [20,21] flow reversal occurs near the separatrix and plasma also leaves the divertor. This outflow from the divertor, which is stronger during the H-phase, might correspond to an influx of deuterium into the bulk plasma. This would lead to a density increase, as observed in JET and other tokamaks during the H-phase. Additional impurity flow from the divertor could ensue.

4. Energy Confinement

4.1. Scaling of global energy confinement

The dependence of global energy confinement on plasma current and heating power is discussed for ELM-free H-modes in single null X-point configurations. Fig. 8 shows the plasma energy W from diamagnetic measurements (Fig. 8a) and global energy confinement time $\tau_E = W/(P_{tot} - \mathrm{d}W/\mathrm{d}t)$ (Fig. 8b) as a function of the total net input power $(P_{tot} - \mathrm{d}W/\mathrm{d}t)$ for plasma currents of 2, 3, 4 and 5 MA. The limited amount of data at the highest current of 5 MA were obtained

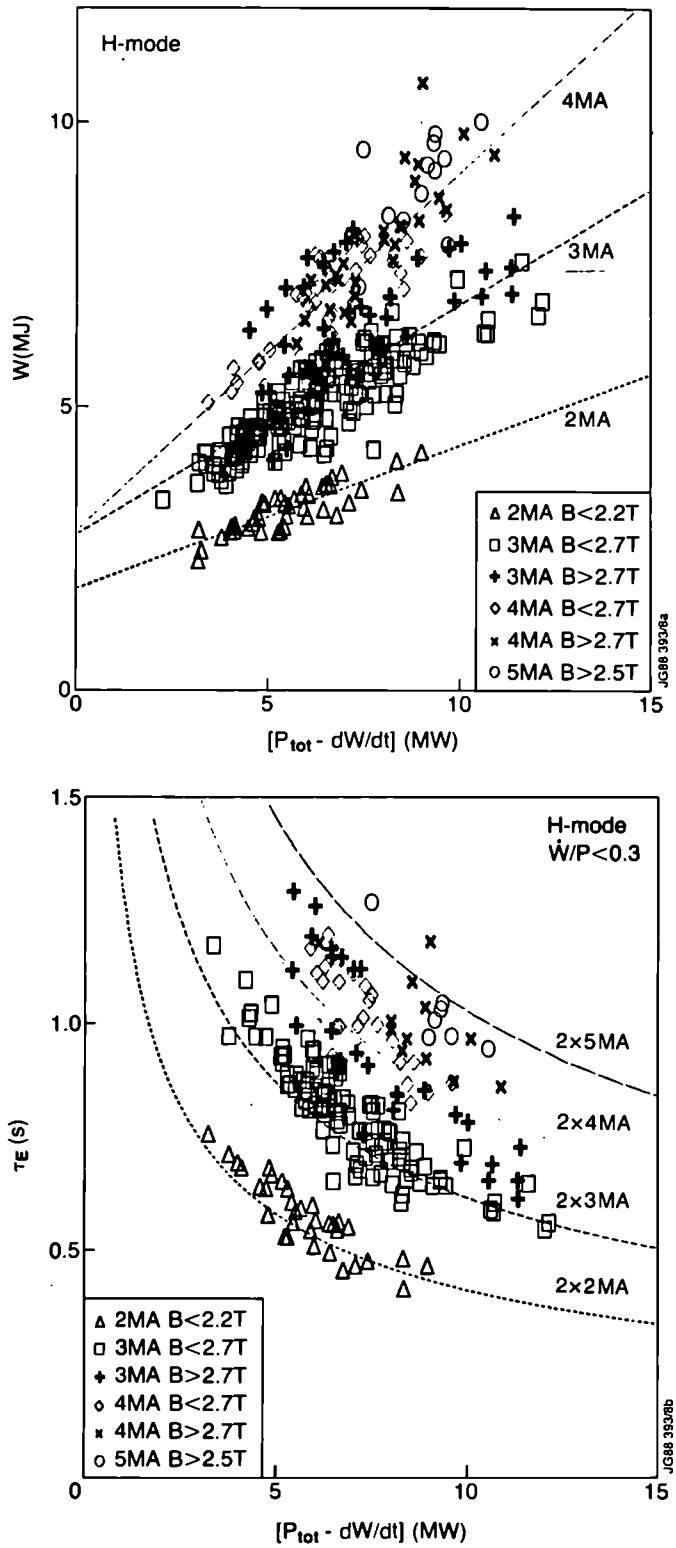

Fig. 8 (a) Plasma energy and (b) global energy confinement time in ELM-free H-mode plasmas versus total net input power for currents of 2, 3, 4 and 5 MA. The dashed lines correspond at each current to (a) off-set linear fits to the data and (b) twice Goldston scaling.

during the last week of operation and the discharges were probably not fully optimised. In all experiments the power range in which ELM-free H-modes could be obtained was limited to $P_{tot} = (P_{NB} + P_{OH}) \lesssim 14\,\mathrm{MW}$ (see section 5).

The data shown in Fig. 8 exhibit two main trends: a roughly linear increase of W and τ_E with plasma current and a degradation of confinement with heating power. Part of this degradation with power can be attributed to increased impurity radiation and poor beam penetration at the higher densities concomitant with higher neutral beam powers. The data at 3 MA and 4 MA which span a sufficiently wide range in toroidal field B_T to allow separation according to lower ($2.1\,\mathrm{T} \leq B_T < 2.7$) and higher ($2.7\,\mathrm{T} \leq B_T \leq 3.4\,\mathrm{T}$) values indicate that the energy confinement is higher at higher B_T. A comparison of L- and H-mode confinement as described, for example, by Goldston scaling[22], shows an improvement in τ_E by at least a factor of 2, and even greater at higher B_T.

Fig. 9 is a plot of the confinement quality factor τ_E/I versus q_{95} for various toroidal fields (for heating powers in the range $8\,\mathrm{MW} \leq (P_{tot} - \mathrm{d}W/\mathrm{d}t) \leq 10\,\mathrm{MW}$). The decrease in confinement for $q_{95} \gtrsim 3$ is probably caused by a reduction in the confinement volume as the sawtooth inversion radius moves outwards.

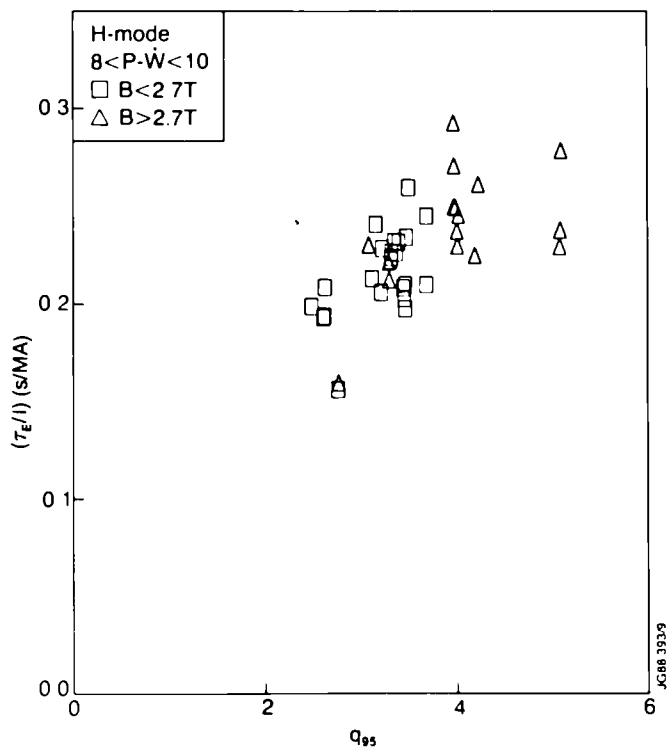

Fig. 9 Confinement quality factor τ_E / I versus safety factor at the 95% flux surface ($8\,\mathrm{MW} \leq (P_{tot} - \mathrm{d}W\ \mathrm{d}t) \leq 10\,\mathrm{MW}$).

To obtain more detailed scaling information a regression analysis of these data has been performed (taking one observation per shot, at times close to when W is maximal and $0 \leq \dot{W}/P < 0.3$; 102 shots in total). The analysis gives the following confinement scaling for JET ELM-free H-mode plasmas:

$$\tau_E(s) = (.63 \pm .015) I^{.76 \pm .08} B_T^{.48 \pm .08} \langle n_e \rangle^{.18 \pm .09} P^{-.69 \pm .05},$$

where $\langle n_e \rangle$ is the volume-averaged electron density and $P = (P_{tot} - \mathrm{d}W/\mathrm{d}t)$. It should be pointed out, however, that at constant $q_{cyl} \sim B_T/I$ the confinement time scales with current as $\tau_E \sim I^{1.2 \pm 0.1}$. The constant is fitted at $I = 3\,\mathrm{MA}$, $B = 2.5\,\mathrm{T}$, $\langle n_e \rangle = 4 \times 10^{19}\,\mathrm{m}^{-3}$ and $P = 10\,\mathrm{MW}$. It was assumed in this analysis that the variables W_{dia}, I, B, $\langle n_e \rangle$ and P have been measured with constant relative (random) errors of 10%, 1%, 1%, 5% and 5% respectively. Fig. 10 shows the observed versus fitted energy confinement times. In deriving such scaling laws it has to be kept in mind, of course, that the plasma confinement depends also on hidden parameters, such as vessel conditioning, which are difficult to assess.

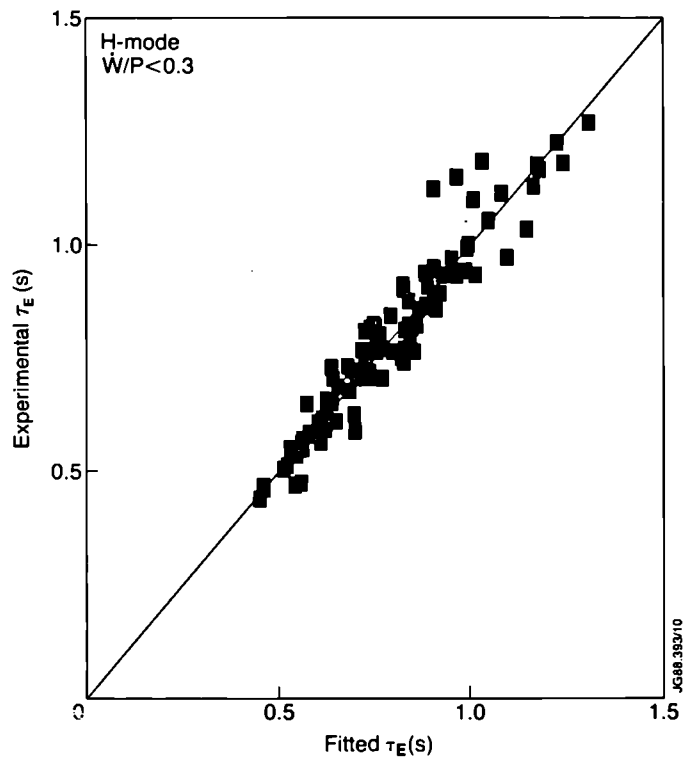

Fig. 10 Experimental versus fitted energy confinement times from an ordinary least squares fit.

As indicated in Fig. 8a, the data can also be described by an offset linear scaling law of the form

$$W = W_0 + P\,\tau_{inc}$$

where τ_{inc} represents the confinement time of the plasma at high heating powers. The present data set of H-mode discharges would suggest that τ_{inc} increases roughly linearly with current at a rate of ~ 0.14s/MA.

The steep temperature and density gradients at the plasma edge (pedestals) characteristic of H-phase suggest the separation of the edge and central confinement properties. To this end the kinetic energy of the plasma has been split into the contributions from the edge pedestal

$$W_p = 3\left(\int_{V_p}^{V} n_e\, kT_e\, dV + n_{e,p} kT_{e,p} V_p\right)$$

and from the plasma core $W_c = W - W_p$, where V_p is the plasma volume inside a certain radius r_p, chosen to be $0.95a$.

Fig. 11 shows the result of this analysis for 3MA H-mode discharges.Wwhen plotted against $(P_{tot} - \mathrm{d}W/\mathrm{d}t)$, $W_c = W - W_p$, like W, *is of offset linear form, indicating degradation with input power. The pedestal energy* $W_p(0.95)$, however, shows no offset indicating little or no degradation with heating power. Thus, H-mode confinement (at least up to 12MW heating powers) may be considered in terms of a power independent contribution from the plasma edge and a power dependent contribution (degraded, L-mode like confinement) from the plasma core.

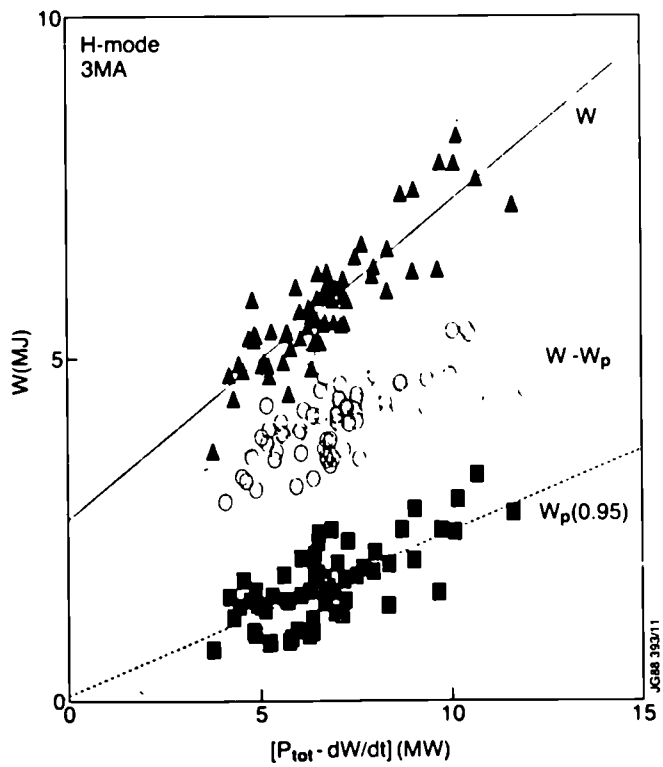

Fig. 11 Plasma energy in pedestal, W_p, and plasma core, $W_c = W - W_p$, respectively, versus total net input power for 3MA H-mode discharges ($B_T \leq 2.7$T).

4.2. Local transport analysis

The time dependent energy balance code, TRANSP[13] has been used to determine the total heat flux through surfaces in the interior of the plasma during the OH-, L- and H-phases of a number of JET pulses. The input comprises the magnetic flux surface geometry, temporal variation of the electron density profile (Abel inverted FIR Interferometer data, checked against LIDAR data when available), electron temperature profile (ECE, checked against LIDAR data when available), radiated power profile (Abel inverted bolometer data), the plasma current, loop voltage, Z_{eff} (visible bremsstrahlung, checked against neutron yield

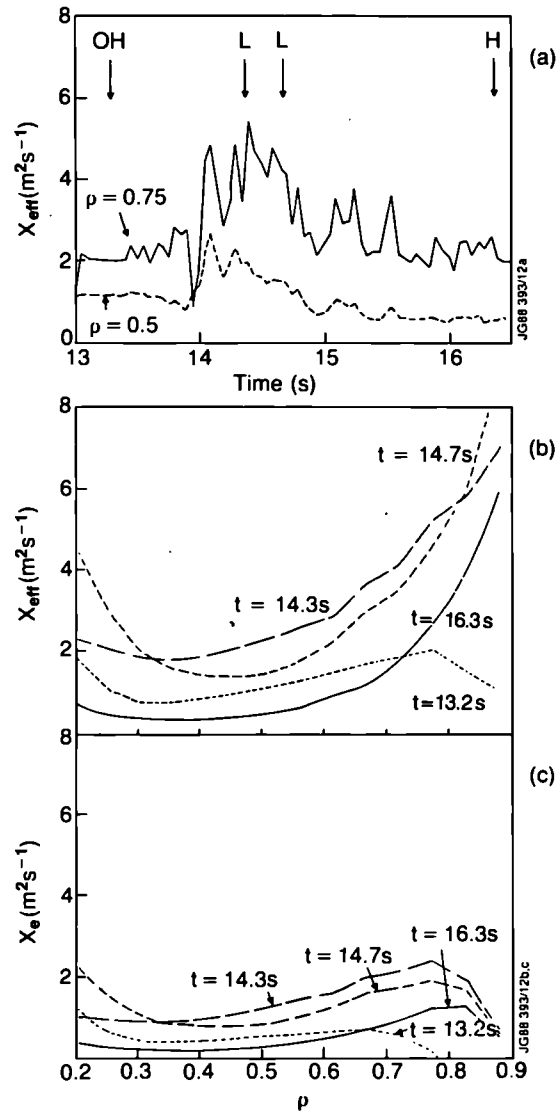

Fig. 12 TRANSP results for (a) the temporal variation of the effective, power balance heat diffusivity, χ_{eff} (b) the spatial profiles of χ_{eff} and the spatial profiles of the electron heat diffusivity, χ_e (assumed equal to χ_i) for JET pulse #15894.

estimates of the deuterium to electron density ratio) and edge particle confinement time (D_α monitors). Neutral beam heating and neutron yields are calculated by Monte Carlo methods.

The ion temperature profile is calculated, for example, by assuming an ion thermal diffusivity proportional to the electron thermal diffusivity. With $\chi_i = \chi_e$ (i.e. strongly anomalous ion transport) good agreement is obtained with the diamagnetic measurement of the total stored energy, with the total neutron yield and, when available, with measured ion temperature profiles from Charge Exchange Spectroscopy. Since the electron and ion temperatures are well coupled to within the experimental uncertainties it is not possible to determine χ_i/χ_e better than to within a factor 2. Accordingly, the transport losses are first represented in terms of the effective, power balance, $\chi_{eff} = Q/n_e \nabla kT_e S$, defined as the ratio of total heat flux (including the effects of energy equipartition and convection) across a surface of area, S, to $n_e \nabla kT_e S$.

Typical results are illustrated by the analysis of JET Pulse #15894. The temporal variation of χ_{eff} at radial positions $\rho = 0.5$ and 0.75 is shown in Fig. 12a. As the neutral beam heating phase begins, χ_{eff} increases above its ohmic value, and then decreases continuously to a level close to its ohmic value at the transition to the H-phase. χ_{eff} is maintained close to this level during the H-phase (see also discussion in Ref[23]).

The spatial profiles of χ_{eff} at selected times throughout the discharge are shown in Fig. 12b. Again it is seen that χ_{eff} is similar in the transport dominated region ($0.3 < \rho < 0.8$) in both OH- and H-phases. In the outer region χ_{eff} is larger in the H-phase, but part of this increase can be attributed to the large losses related to particle recycling and convection. While there is a large uncertainty on these losses, they have been separated out to give χ_e (or χ_i for this model) which is found to decrease in the edge (Fig. 12c) where the shear is high.

The values of χ_{eff} can be compared with χ determined from heat pulse propagation studies. The ECE polychromator system has been used to monitor at various radial positions the delay in the arrival of the peak and the amplitude of the perturbation following the collapse of the sawteeth. This gives values for $\chi_{HPP} \sim 3 \pm 0.6 \mathrm{m^2 s^{-1}}$ in all phases of X-point operation.

5. Particle Control and Future prospects for H-Mode Operation

As a result of the good energy confinement properties of the ELM-free H-mode discharges, favorable values of the fusion product ($n_{Do}\, T_{io}\, \tau_E$) of up to $2.5 \times 10^{20} \mathrm{m^{-3}}$ keVs (Fig. 13) have been achieved. However, the particle confinement improves similarly (impurity injection experiments indicate that impurity confinement times improve by at least a factor three) making density control difficult. Beam penetration is also affected, radiation losses increase and finally terminate the H-phase. At the highest NBI power available (14-20 MW) strong

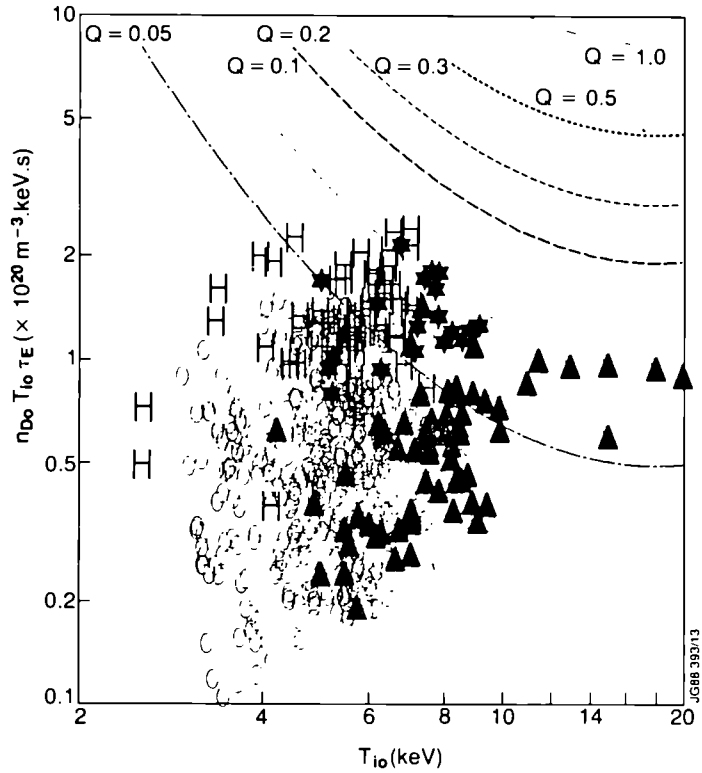

Fig. 13 Experimental values of the fusion product $n_{D0}\ T_{i0}\ \tau_E$ versus central ion temperature for different modes of JET operation: H-mode (H), pellet injection (*), low density hot ion mode (▲) and others (o). Curves show the equivalent thermonuclear Q for a 50:50 D:T plasma. They are calculated assuming $Z_{eff}=1$, $T_e=T_i$ and radial profiles similar to the experimental ones (ratio central to average pressure of 3).

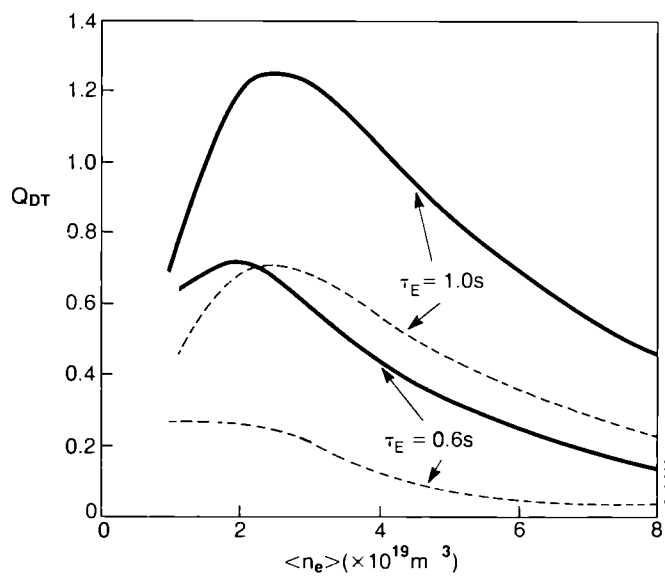

Fig. 14 Fusion amplification factor versus volume-averaged electron density at fixed values of τ_E for 140 kV deuterium injection at a total power of 15 MW and a 50:50 D–T plasma with $Z_{eff}=2+2\times10^{19}/\langle n_e\rangle$. The dotted lines are the thermal contribution.

radiation occurs from a well-defined region near the X-point, and a thermal collapse, reminiscent of a plasma approaching the density limit, results and leads to only very ELMy-H-modes with inferior confinement.

The effect of high density and Z_{eff} on the projected values of the fusion amplification factor, Q_{DT}, for JET H-modes with 15MW of 140kV deuterium NBI can be seen in Fig. 14. It is clear that for τ_E in the range 0.6-1s and volume-averaged electron densities, $\langle n_e \rangle \sim 5 \times 10^{19} m^{-3}$ the projected performance is significantly below the optimum which would occur at lower density and correspondingly higher temperature. It is clearly beneficial to increase τ_E (provided the density does not increase faster) but it is essential to control the plasma density and to improve plasma purity and central heating.

So far, the plasma density has been controlled only by the provocation of sufficient ELM-activity by reducing the separation between the plasma and the inner wall and/or the outer belt limiter. As shown in Fig. 15 this allows the density, $\langle n_e \rangle$, total plasma radiation, P_{rad}, and concentration of metal impurities in the plasma centre (as exemplified by the intensity of a Nixxvi line) to be kept approximately constant for 1 or 2 seconds, but at the expense of a considerable reduction in the energy confinement time, τ_E.

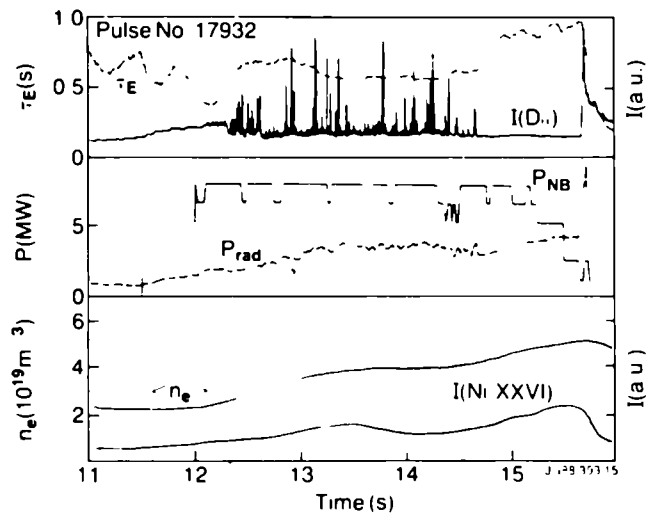

Fig. 15 Time evolution of D_α intensity $I(D_\alpha)$, energy confinement time τ_E, neutral beam power P_{NB}, total plasma radiation P_{RAD}, volume-averaged plasma density $\langle n_e \rangle$ and intensity of Nixxvi line for a 3MA H-mode discharge with ELMs which keep the density (and radiation) approximately constant (until an ELM-free H-mode develops at $t = 14.7$s).

Attempts to improve central heating by using ICRH have, so far, been unsuccessful. In the double null configuration up to 8MW ICRH (hydrogen minority heating at 33.5MHz, monopole phasing of the antennae) has been coupled to the plasma both alone and in combination with a similar level of NBI. A strong increase in radiation resulting from enhanced impurity influxes (mainly nickel, possibly also oxygen) has allowed only short, or very ELMy, H-modes with con-

finement times close to those typical of L-mode plasmas. To overcome these difficulties it is planned to replace the present nickel antenna screens by beryllium screens in the summer of 1989. The introduction of beryllium as a limiter material will also reduce radiation and, possibly, Z_{eff}.

In the first half of 1989 one NBI box will be upgraded to 140 kV/D (the second NBI box will subsequently be upgraded to 140 kV/D or 160 kV/T). This will give better penetration and will inject fewer particles.

To maximise the prospects for JET, however, it may remain necessary to exercise active particle control. First, sweeping the X-point position to help reduce the particle and impurity influxes will be examined. Ultimately, however, it may be necessary to consider pumping in the vicinity of the X-point where the particle flows are most concentrated.

References

[1] Wagner, F., et al., *'Regime of improved confinement and high beta in neutral-beam-heated divertor discharges of the ASDEX tokamak'*, Phys. Rev. Lett., **49** (1982) 1408.

[2] Kaye, S.M., et al., *'Attainment of high confinement in neutral beam heated divertor discharges in the PDX tokamak'*, J. Nucl. Mat., **121** (1984) 115.

[3] Luxon, J., et al., *'Initial results from the DIII-D tokamak'*, Plasma Phys. and Contr. Nucl. Fus. Res. **1** (1987) 159.

[4] Odajima, K., et al., *'Confinement studies of additionally heated plasma in the JFT-2M tokamak'*, Plasma Phys. and Contr. Nucl. Fus. Res. (Proc. 11th Int. Conf., Kyoto, 1986), **1** (1987) 151.

[5] Tanga, A., et al., *'Experimental studies in JET with magnetic separatrix'*, Plasma Phys. and Contr. Nucl. Fus. Res. (Proc. 11th Int. Conf., Kyoto, 1986), **1** (1987) 65.

[6] Salzmann, H.M., et al., (Invited paper at the APS Topical Conference on Plasma Diagnostics, Napa Valley, Calif, USA), (1988).

[7] Smeulders, P., et al., *'Hollow profiles and high-β effects during H-mode in JET'*, JET Internal Report JET-IR(88)11, JET Joint Undertaking, (1988).

[8] Boileau, A., et al., *'The deduction of low-Z ion temperature and densities in the JET tokamak using charge exchange recombination spectroscopy'*, JET Preprint JET-P(87)44, JET Joint Undertaking, (1987). To be published in Plasma Phys.

[9] Morgan, P.D., *'The evolution of $Z_{eff}(r)$ profiles in JET plasmas'*, (Proc. 15th Europ. Conf. on Contr. Fus. and Plasma Heating, Dubrovnik), **12B** (I) (1988) 139.

[10] Behringer, K., et al., *'Impurity transport in JET during H-mode, monster sawteeth, and after pellet injection'*, (Proc. 15th Europ. Conf. on Contr. Fus. and Plasma Heating, Dubrovnik), **12B** (I) (1988) 338.

[11] O'Rourke, J., et al., *'Polarimetric measurements of the q-profile'*, (Proc. 15th Europ. Conf. on Contr. Fus. and Plasma Heating, Dubrovnik), **12B** (I) (1988) 155.

[12] Bickerton, R.J., Connor, J.W., Taylor, J.B., *'Diffusion driven plasma currents and bootstrap tokamak'*, Nat. Phys. Sc., **229** (1971) 110.

[13] Goldston, R.J., et al., *'New techniques for calculating heat and particle source rates due to neutral beam injection in axisymmetric tokamaks'*, J. Comput. Phys., **43** (1981) 61.

[14] Zarnstorff, M.C., et al., *'Non-ohmic currents in TFTR'*. Phys. Rev. Lett., **60** (1988) 1306.

[15] Challis, C., et al., *'Non inductively driven currents in JET'*, JET Preprint JET-P(88)38, JET Joint Undertaking, (1988). To be published in Nucl. Fus.

[16] Bishop, C.M., *'Stability of localised MHD modes in divertor tokamaks: a picture of the H-mode'*. Nucl. Fus., **26** (1986) 1063.

[17] Bishop, C.M., *'Bifurcated temperature profiles and the H-mode'*, Nucl. Fus., **27** (1986) 1765.

[18] Harbour, P.J., Workshop on Plasma Edge Theory in Fusion Devices, Augustusburg, GDR, 26 – 30 April 1988. To be published in 'Contributions to Plasma Physics', (Akademie-Verlag, Berlin, GDR).

[19] Itoh, S.I. and Itoh, K., *'Model of H/L transition in tokamak'*, Phys. Rev. Lett., **60** (1988) 2276.

[20] Harbour, P.J., et al., (8th Int. Conf. on Plasma Surface Interactions in Contr. Fus. Devices, 2 – 6 May 1988, Jülich, FRG). To be published in J. Nucl. Mat.

[21] de Kock, L., et al., *'The plasma boundary in JET'*, Paper IAEA-CN-50/A-VII-12/2. This conference.

[22] Goldston, R.J., *'Energy confinement scaling in tokamaks: some implications of recent experiments with ohmic and strong auxiliary heating'*, Plasma Phys. and Contr. Fus., **26** (1984) 87.

[23] Keilhacker, M., et al., *'Studies of energy transport in JET H-modes'*, (Proc. 15th Europ. Conf. Fus. and Plasma Heating, Dubrovnik), **12B (I)** (1988) 231.

APPENDIX I

THE JET TEAM

JET Joint Undertaking, Abingdon, Oxon, OX14 3EA, UK

J.M. Adams[1], H. Altmann, G. Appruzzese, W. Bailey, P. Ballantyne, B. Balet, D.V. Bartlett, L.R. Baylor[23], K. Behringer[13], A.C. Bell, P. Bertoldi, E. Bertolini, L.G. Betello, V. Bhatnagar, R.J. Bickerton, A.J. Bickley, J. Bizarro[21], S. Bliman[16], T. Bonicelli, S.J. Booth, G. Bosia, M. Botman, D. Boyd[30], H. Brelen, H. Brinkschulte, M. Brusati, T. Budd, M. Bures, T. Businaro[4], P. Butcher, H. Buttgereit, C. Caldwell-Nichols, D.J. Campbell, P. Card, J. Carwardine, G. Celentano, P. Chabert[16], C.D. Challis, A. Cheetham, J. Christiansen, C. Christodoulopoulos, P. Chuilon, R. Claesen, S. Clement[29], J.P. Coad, P. Colestock[6], S. Conroy[12], M. Cooke, S. Cooper, J.G. Cordey, W. Core, G. Corrigan, S. Corti, A.E. Costley, G. Cottrell, M. Cox[7], P. Cripwell[12], D. Cross, H. de Blank[15], H. de Esch, J. de Haas[15], L. de Kock, E. Deksnis, G.B. Denne, G. Deschamps, G. Devillers, K.J. Dietz, J. Dobbing, A. Dombra, N. Dolgetta, S.E. Dorling, P.G. Doyle, D.F. Düchs, H. Duquenoy, A. Edwards, J. Ehrenberg[13], T. Elevant[11], W. Engelhardt, S.K. Erents[7], L.G. Eriksson[5], M. Evrard[2], H. Fajemirokun[12], H. Falter, J. Farthing, D. Flory, M. Forrest[7], C. Froger, K. Fullard, M. Gadeberg, A. Galetsas, M. Galley, R. Galvao[8], M. Garribba, R. Giannella, A. Gibson, R.D. Gill, A. Gondhalekar, G. Gorini, C. Gormezano, N.A. Gottardi, C. Gowers, B.J. Green, F.S. Griph, W.K. Guo[26], R. Haange, G. Hammett[6], W. Han[9], H.E. Han-Gonge[26], C.J. Hancock, P.J. Harbour, N.C. Hawkes[7], P. Haynes[7], J. Heikkinen[3], T. Hellsten, J.L. Hemmerich, R. Hemsworth, F.B. Herzog, R.F. Herzog, J. Hoekzema, R. Hope, W.A. Houlberg[23], J. How, M. Huart, T.P. Hughes[31], M. Hugon, M. Huguet, M. Irving, J. Jacquinot, O.N. Jarvis, F. Jensen, T.C. Jernigan[23], E. Joffrin, E.M. Jones, L.P.D.F. Jones, T.T.C. Jones, J. Källne, O. Kardaun[13], A. Kaye, B.E. Keen, M. Keilhacker, G.J. Kelly, A. Khare[14], S. Knowlton, A. Konstantellos, M. Kovanen[20], P. Kupschus, P. Lallia, R. Lanza, R. Lässer, J.R. Last, L. Lauro-Taroni, K. Lawson[7], E. Lazzaro, M. Lennholm, B. Liley[25], X. Litaudon, P. Lomas, M. Lorentz-Gottardi[2], C. Lowry, G. Maddison[7], G. Magyar, M. Malacarne, W. Mandl[13], V. Marchese, J. Mart, P. Massmann, G. McCracken[7], J. Mendonca, P. Meriguet, P. Micozzi[4], S.F. Mills, P. Millward, S.L. Milora[23], A. Moissonnier, F. Mompean, P.L. Mondino, P. Morgan, G. Murphy, G. Newbert, M. Newman, P. Nielsen, P. Noll, W. Obert, D. O'Brien, J. O'Rourke, M.G. Pacco-Düchs, M. Pain, S. Papastergiou, D. Pasini[19], A. Peacock, N. Peacock[7], D. Pearson[12], F. Pegoraro, F. Petree, M. Pick, S. Pitcher[7], J. Plancoulaine, J-P. Poffé, F. Porcelli, R. Prentice, T. Raimondi, C. Raymond, P-H. Rebut, J. Removille, F. Rimini, D. Robinson[7], A. Rolfe, R. Romain, R.T. Ross, L. Rossi, R. Rushton, P. Rutter, H.C. Sack, G. Sadler, G. Saibene, N. Salmon[12], H. Salzmann[13], A. Santagiustina, R. Sartori, D. Schissel[24], P.H. Schild, M. Schmid, G. Schmidt[6], R.L. Shaw, K. Schimizu[17], A. Sibley, R. Simonini, J. Sips[15], P. Smeulders, J. Snipes, S. Sommers, L. Sonnerup, K. Sonnenberg, G. Sonnozaro, W. Stacey[28], M. Stamp, P. Stangeby[18], D.F. Start, C.A. Steed, D. Stork, P.E. Stott, T.E. Stringer, D. Stubberfield, D. Summers, H. Summers[19], J. Tagle[29], H. Tamnen, A. Tanga, A. Taroni, C. Tebaldi[22], A. Tesini, P.R. Thomas, E. Thompson, K. Thomsen, J.M. Todd, P. Trevalion, B. Tubbing, F. Tibone, E. Usselmann, A. Vannucci, H. van der Beken, M. von Hellermann, T. Wade, C. Walker, M. Walravens, K. Walter, Z. Wang[27], D. Ward, M.L. Watkins, H. Weisen[10], J. Wesson, D.H. Wheeler, J. Wilks, U. Willen[11], D. Wilson, T. Winkel, S. Wolfe, D. Wong, C. Woodward, M. Wykes, I.D. Young, L. Zannelli, D. Zasche[13]

PERMANENT ADDRESS

1. UKAEA, Harwell, Didcot, Oxon. UK.
2. EUR-EB Association, LPP-ERM/KMS, B-1040 Brussels, Belgium.
3. Technical Research Centre of Finland, Helsinki, Finland.
4. ENEA-CENTRO Di Frascati, I-00044 Frascati, Roma, Italy.
5. Chalmers University of Technology, Goteborg, Sweden.
6. Princeton Plasma Physics Laboratory, New Jersey, USA.
7. UKAEA Culham Laboratory, Abingdon, Oxfordshire, UK.
8. Plasma Physics Laboratory, Space Research Institute, Sao Jose dos Campos, Brazil.
9. Institute of Mathematics, University of Oxford, UK.
10. CRPP/EPFL, 21 Avenue des Bains, CH-1007 Lausanne, Switzerland.
11. Swedish Energy Research Commission, S-10072 Stockholm, Sweden.
12. Imperial College of Science and Technology, University of London, UK.
13. Max Planck Institut fur Plasmaphysik, D-8046 Garching bei Munchen, FRG.
14. Institute for Plasma Research, Gandhinagar Bhat Gujrat, India.
15. FOM Instituut voor Plasmafysica, 3430 Be Nieuwegein, The Netherlands.
16. Commissiariat à L'Énergie Atomique, F-92260 Fontenay-aux-Roses, France.
17. JAERI, Tokai Research Establishment, Tokai-Mura, Naka-Gun, Japan.
18. Institute for Aerospace Studies, University of Toronto, Downsview, Ontario, Canada.
19. University of Strathclyde, 107 Rottenrow, Glasgow, G4 0NG, UK.
20. Nuclear Engineering Laboratory, Lapeenranta University, Finland.
21. JNICT, Lisboa, Portugal.
22. Department of Mathematics, Univeristy of Bologna, Italy.
23. Oak Ridge National Laboratory, Oak Ridge, Tenn., USA.
24. G.A. Technologies, San Diego, California, USA.
25. University of Waikato, Hamilton, New Zealand.
26. IPP, Academia Sinica, P.R.China.
27. Southwestern Institute of Physics, Leshan, Sechuan, P.R.China.
28. University of Georgia, Atlanta, USA.
29. Centro de Investigaciones Energeticas Medioambientales y Techalogicas, Spain.
30. University of Maryland, College Park, Maryland, USA.
31. University of Essex, Colchester, UK.

J CR 88 49 1A (rev 30/11/88)

Heating of Peaked Density Profiles produced by Pellet Injection in JET

by

The JET Team

(Presented by GL Schmidt)

JET Joint Undertaking, Abingdon, Oxon OX14 3EA, UK.

Heating of Peaked Density Profiles produced by Pellet Injection in JET

The JET Team*

(Presented by G L Schmidt)

JET Joint Undertaking, Abingdon, Oxon OX14 3EA, UK.

Abstract

A transient enhancement in performance of JET limiter discharges has been obtained when a peaked density profile formed by pellet injection is heated using either ICRH alone or in combination with NBI. Pellet fueling is applied during the current rise. Heating follows the fueling sequence, and must be localized predominately within the plasma core. Electron density profiles are strongly peaked immediately following the pellet injection sequence, $n_e(0)/\langle n_e \rangle_{vol} \leq 5$, and retain a central peak while decaying during the period of enhancement. At a power level of 19MW (P_{rf}=12.5MW,P_{nb}=5MW and P_{oh}=1.5MW) and central density of $6\times10^{19}m^{-3}$, central ion and electron temperatures of 10.5 and 12keV are obtained in 3MA, 3.1T discharges. Global energy confinement 1.6 times the L-mode level has been obtained. Values of $n_d(0)T_i(0)\tau_E(a)$ in the range from 1 to $2\times10^{20}m^{-3}$-keV-s are achieved. Peak neutron rates can exceed those in similar non-enhanced shots by factors of 3 to 5 and increase strongly with heating power. Central ion and electron pressure can be enhanced by a factor of 2 to 3. Electron pressure can be >1bar with a gradient of 4bar/m. Ballooning stability limits are approached within the plasma core. The period of enhanced performance has extended up to 1.2s into the heating pulse, terminating spontaneously. The longest periods terminate with enhanced fluctuations, and a strong and rapid decrease in central electron and ion temperatures. Although mhd activity can be present during this period, sawtooth activity does not appear.

1. Introduction

The combination of peaked density profiles produced by pellet fueling with strong, central ICRF heating has been proposed as a means to enhance performance of limiter discharges[1,2,3]. Such experiments have begun on JET using a pellet injector system jointly built as part of the JET/USDOE collaboration on pellet fueling. The fueling source is a multi-barrel, multiple pellet, pneumatic launcher developed at Oak Ridge National Laboratory[4]. Initial results were reported previously[4,5,6,7]. Improved performance has been obtained with peaked density profiles in previous ohmic and NBI heated experiments[2,8,9,10,11] and recently with RF heating in divertor configuration [12]. Experiments on TFTR[13] and JET[14], with high auxiliary heating power, have demonstrated improved performance in limiter configurations at high temperatures. In those experiments, neutral beam injection was used both to produce and to heat peaked density profiles. We describe here experiments which demonstrate for the first time improved performance in limiter discharges fueled by pellets and heated by ICRH to ion and electron temperatures >5keV. We describe first how peaked density profiles are generated by pellet injection. Such profiles form the target for RF heating. The period of enhanced performance is then discussed.

* See Appendix I

2. Production of Peaked Profiles

Pellet injecton prior to the heating pulse is used to produce a peaked density profile. Both single and multiple pellet sequences have been used. Pellet fueling occurs during the current ramp phase. Primarily 3MA discharges have been studied. Fueling efficiency in these ohmic scenarios is high ($\Delta n_e/n_{pel} \cong 0.7$) and not strongly dependent on penetration. The remaining mass is likely to be lost in the formation and acceleration process. Strongly peaked profiles have been obtained only by penetration to or beyond the magnetic axis. Such penetration is obtained either by a sequence of 2.7mm pellets alone ($7 \times 10^{20} D^o$ per pellet, 5 to 7 pellets at 2.5Hz) or a combination of fewer 2.7mm and a single 4mm pellet ($2.5 \times 10^{21} D^o$). Peaking factors, $n_e(0)/\langle n_e \rangle_{vol}$, from 2.6 to 5 are obtained with central densities of from 0.8 to 2×10^{20} m^{-3}. Line average density exceeds the 3MA ohmic density limit in JET[7]. Density is limited in pellet cases by the appearance of mhd activity (Quasi Stationary Modes), which leads to rapid loss of particles and can precipitate a plasma disruption [15,16]. In the absence of QSMs, the peaked density profile, once formed, decays slowly with a time constant which can be >2s. Average Z_{eff} immediately after pellet injection can be <1.5. Electron temperature is strongly perturbed decreasing is some cases below 500eV on axis. While total radiated power remains from 40 to 60% of input power, the electron temperature profile can become inverted with central radiated power dominating the local power balance. Recovery of electon temperature occurs on the time scale of the density decay. Some mhd activity can be present during this period, but sawtooth oscillations do not appear. This high density, low temperature, sawtooth free discharge forms the plasma target for auxiliary heating.

3. Heating of Peaked Profiles

3.1 Survey of Results

Following termination of the current ramp and pellet fueling sequence, heating by ICRF alone or in combination with NBI is applied as shown in Fig. 1. Results for both a strong (I) and a weak (II) pellet perturbation are compared. Results in case II are similar to no pellet cases. Fueling is produced by injection of a 4mm pellet at 3s in both cases. In case I, an earlier 2.7mm pellet has been injected at 1.5s to lower the central temperature, and thereby allow penetration to the magnetic axis at 3s. Auxiliary heating begins at 3.2s, and is then maintained at roughly a constant level. A period of enhanced performance is obtained in case I beginning with the onset of heating, and ending with a rapid decrease of central ion and electron temperature at 4.4s.

During the heating pulse, the total electron particle content remains roughly constant in both these cases. For case I, the central electron density decays from

the peak values reached after pellet injection. The decay rate is faster than that observed in the absence of heating but remains in the range 4 to $6x10^{19}m^{-3}s^{-1}$. Initially, central electron temperatures increase at similar rates in both cases although density in the enhanced case is 3x higher. Final electron and ion temperatures are larger in the enhanced case by factors of 1.5 and 2. As shown in Figs. 1c and 2, neutron levels reflect these enhancements in core parameters, increasing strongly with RF power and exceeding no pellet results by factors of 3 to 5. On a 1s timescale, impurity ion profiles develop which are markedly more peaked than n_e within the plasma core. Such behaviour is expected from neoclassical transport[17,18]. Outside the core, the usual broad n_i profiles are observed. The ratio $n_i(0)/n_i(a/2) \cong 2$. As a result, central Z_{eff} is some 30% higher and n_d/n_e somewhat lower than the average value. Depending on the mix of heating power applied and the resulting range of O, C and Ni levels obtained, central Z_{eff} after 1s varies from 2.5 to 4 and n_d/n_e from 0.75 to 0.5. The core power balance is little affected by radiated power losses. In the best cases, the period of enhancement terminates as shown with an abrupt loss of central temperature, density and accumulation. Sawtooth oscillations do not appear prior to, or during, the times of interest.

Enhanced core temperatures are obtained only in cases where a strong perturbation of the density and electron temperature is produced, and for which the RF resonance was located within the plasma core. The effect is not dependent on a particular $k_{||}$ spectrum, and has been obtained using either monopole ($k_{||} = 0$) or dipole ($k_{||}=7m^{-1}$) antenna phasing. The enhancement is obtained with H or He^3 minority heating, indicating the effect is not associated simply with a non-maxwellian tail produced by second harmonic heating of the backround deuterium. Neutron emission is predominantly thermal in origin. Enhanced temperatures and neutron yield are not obtained when the resonance location (resonance half width 0.3m) is shifted 0.5m from the magnetic axis, to the region outside the plasma core. Similarly the enhancement in central electron and ion heating is diminished as the neutral beam heating power is increased. At high density in JET, power deposition profiles for 40keV/nucleon beam heating are not strongly peaked within the plasma core.

Fig. 3 shows density and temperature profiles after pellet injection and near the termination of the enhanced period for a pellet and no-pellet pulse. Within a central region of approximately 0.7m diameter, the profiles differ both in magnitude and scale length. In the pellet case, although the central value of the electron density decays from 1.35 to $0.6x10^{20}m^{-3}$ during the first 1s of the heating pulse, the gradient scale length of the core density perturbation has only increased from 0.5 to 0.6m. The gradient scale length of the temperature profile, both for ions and electrons, is more than 2x smaller in the pellet case than in the no-pellet case. The electron temperature profile differs markedly from a triangular shape.

the peak values reached after pellet injection. The decay rate is faster than that observed in the absence of heating but remains in the range from 4 to $6 \times 10^{19} m^{-3} s^{-1}$. Initially, central electron temperatures increase at similar rates in both cases although density in the enhanced case is 3x higher. Final electron and ion temperatures are larger in the enhanced case by factors of 1.5 and 2. As shown in Figs. 1c and 2, neutron levels reflect these enhancements in core parameters, increasing strongly with RF power and exceeding no pellet results by factors of 3 to 5. On a 1s timescale, impurity ion profiles develop which are markedly more peaked than n_e within the plasma core. Such behaviour is expected from neoclassical transport[17,18]. Outside the core, the usual broad n_i profiles are observed. The ratio $n_i(0)/n_i(a/2) \cong 2$. As a result, central Z_{eff} is some 30% higher and n_d/n_e somewhat lower than the average value. Depending on the mix of heating power applied and the resulting range of O, C and Ni levels obtained, central Z_{eff} after 1s varies from 2.5 to 4 and n_d/n_e from 0.75 to 0.5. The core power balance is little affected by radiated power losses. In the best cases, the period of enhancement terminates as shown with an abrupt loss of central temperature, density and accumulation. Sawtooth oscillations do not appear prior to, or during, the times of interest.

Enhanced core temperatures are obtained only in cases where a strong perturbation of the density and electron temperature is produced, and for which the RF resonance was located within the plasma core. The effect is not dependent on a particular $k_{\parallel}$ spectrum, and has been obtained using either monopole ($k_{\parallel} = 0$) or dipole ($k_{\parallel}=7 m^{-1}$) antenna phasing. The enhancement is obtained with H or He^3 minority heating, indicating the effect is not associated simply with a non-maxwellian tail produced by second harmonic heating of the backround deuterium. Neutron emission is predominantly thermal in origin. Enhanced temperatures and neutron yield are not obtained when the resonance location (resonance half width 0.3m) is shifted 0.5m from the magnetic axis, to the region outside the plasma core. Similarly the enhancement in central electron and ion heating is diminished as the neutral beam heating power is increased. At high density in JET, power deposition profiles for 40keV/nucleon beam heating are not strongly peaked within the plasma core.

Fig. 3 shows density and temperature profiles after pellet injection and near the termination of the enhanced period for a pellet and no-pellet pulse. Within a central region of approximately 0.7m diameter, the profiles differ both in magnitude and scale length. In the pellet case, although the central value of the electron density decays from 1.35 to $0.6 \times 10^{20} m^{-3}$ during the first 1s of the heating pulse, the gradient scale length of the core density perturbation has only increased from 0.5 to 0.6m. The gradient scale length of the temperature profile, both for ions and electrons, is more than 2x smaller in the pellet case than in the no-pellet case. The electron temperature profile differs markedly from a triangular shape.

The concurrence of higher density and temperature within this core plasma implies enhanced central electron pressure and pressure gradients as illustrated in Fig. 4. The ideal mhd ballooning stability of the equilibria corresponding to these profiles has been determined using the code HBT[19], assuming a magnetic geometry taken from the equilibrium identification code IDENTC and a radial profile of the total pressure as given by the electron pressure. The magnitude of the pressure is normalized by the Shafranov β (mhd). The ratio of mhd to diamagnetic β indicates the fast ion contribution to the total pressure is small. However, the influence of the fast ion pressure and its gradient within the plasma core may affect plasma stability locally[20]. This effect has not been included in the present calculations. Results of stability calculations are shown in Fig. 5 assuming the q profile to be monotonic. For fixed q(a) the radial variation of the pressure gradient with shear and the first stability boundary vary with q(0). Two values of q(0) are shown in the range of the measured value 1.2 (Fig. 8). The discharge has reached the first stability boundary within the plasma core (r/a=0.3). Although the maximum β obtained is only 40% of the critical Troyon value for optimized profiles, the value of $\varepsilon\beta_p$ is 1.1 to 1.2 times the maximum value for ballooning stability corresponding to the experimental profiles. Should q(0) reach 1.5 the discharge would be marginally stable. The further increase in q(0), which can be attained with multiple pellet injection sequences (Fig.8), and the potential improvement in the stability boundary associated with such a change remains to be exploited as a means to obtain stable operation at higher pressure and low shear.

Although some pellet discharges may approach the stability boundary, the level of incoherent magnetic fluctuations measured externally is approximately the same as is generally observed during auxiliary heating. Low-level, coherent, mhd oscillations and electron temperature relaxations are observed during the period of enhanced performance both on and off-axis; but no specific correlation has yet been established between the level of these fluctuations and loss of enhanced performance. Bursts of mhd activity during the heating can diminish neutron yield. In cases of longest duration, the period of enhanced performance is terminated by an abrupt collapse of the central electron temperature (Fig. 1). Analysis of soft X-ray and ECE measurements shows that the collapse does not follow the JET sawtooth behaviour[21]. A complex radial temperature redistribution occurs with the temperature profile often exhibiting two inversion radii. Up to 100μs preceeding the collapse, no growing m=n=1 core displacement is detected. Successor oscillations are often present with a variety of m,n numbers. The dominant mode is usually m=3,n=2 centered about r=0.25m while edge magnetic measurements show a spectrum of modes with $n \leq 8$. The mode numbers of the successor oscillations, their spectral extent and the fact that sawteeth do not appear throughout the period of heating all indicate that q(0)>1 during this period.

3.2 Energy Confinement

The pellet fueling sequence perturbs several plasma parameters likely to affect both heating and thermal energy transport, but the mechanism responsible for the enhanced performance is not yet established.

The combined change in ion density and temperature profiles alters the discharge η_i parameter [$d\ln(T_i)/d\ln(n_i)$]. Assuming electron and ion temperature profiles are similar, the η_e parameter shown in Fig. 7 reflects η_i during periods early in the enhancement phase when dilution effects are small. Following pellet injection, η_e is first strongly reduced within the plasma core by the formation of a peaked density and broad temperature profile. During the subsequent period of heating and density decay, the radial variation in η_e reflects the evolving shape of the density and temperature profiles. Within the plasma core ($r/a<0.4$), a residual ∇n_e is maintained in the region of maximum ∇T_e. Ultimately the core η values approach and exceed the nominal critical η parameter (1 to 2). The evolution of η within the plasma core is subject to significant uncertainty, however, the behavior shown illustrates the clear tendency of the pellet discharge to low central η_i values during the early period of the enhanced phase.

The current profile is altered by the perturbation of T_e resulting from pellet injection and the subsequent heating. The evolution of q(0) obtained from Faraday rotation measurements is shown in Fig. 8 for a multiple 2.7mm and a 4mm pellet sequence. In these cases, the error in q(0) is estimated to be ±25%. Current diffusion calculations are in general agreement with these measurements. The calculations take the measured value of q(0) at t=1s, assume neoclassical resistivity including a bootstrap current, and vary the resistivity through the Z_{eff} term to match the measured surface voltage. In both sequences, q(0) is greater than 1 during the heating pulse, more strongly in the 2.7mm sequence, due to the extended duration of the temperature purturbation. During the heating following the 4mm sequence, q(0) rises slightly and the q profile broadens markedly. In no-pellet pulses, however, Faraday rotation measurements indicate that a similar effect may also occur. For pellet fuelled discharges, current diffusion calculations attribute this evolution to a substantial bootstrap effect ($I_{bootstrap}/I_{plasma}\cong 0.2$), which in combination with the pellet perturbation can ultimately create a region of negative shear within the plasma core. Such a profile is potentially unstable and could be responsible for the abrupt termination of enhanced performance phase.

Finally, density perturbations may cause variations in minority concentration. Such a variation can change the direct heating of the ions and electrons altering the power balance terms for each species. Detailed modeling of the ion and electron power balance is not complete. However, single fluid modelling of the plasma indicates that thermal transport within the plasma core can be reduced by a factor of 2 to 3 during the enhanced period[22]. This can be seen directly from

the terms shown in Table 1, if comparable power deposition profiles are assumed. This improvement is only weakly reflected in the global energy confinement (+20%) when pellet and no-pellet discharges are compared, probably due to a larger fast ion population in the no pellet shot. However, global confinement is enhanced significantly with respect to L-mode[23]. At an input power of 8 to 10MW, global energy confinement is approximately 450ms. This value is 1.6 times the L-mode level. A further transient improvement is seen during the initial heating phase when the profile is most strongly peaked, but a dW/dt term comparable to more than half the input power is present.

3.3 Particle Confinement

In the absence of heating, the peaked electron density profile formed by pellet injection decays slowly retaining its peaked character for an extended period. Outside the plasma core a region of weak gradient is formed similar to no-pellet cases. This feature has been observed in past experiments [2]. In ohmic discharges, it has been modeled using a neoclassical pinch combined with a diffusion coefficient increasing with radius[2,24]. In modeling present experiments[25], a simple fixed form for that radial variation is assumed. As shown in Fig. 8, the diffusion coefficient incorporates a transition from a low central value to a higher edge value at r=0.45m. With the onset of heating, decay of the density profile becomes more rapid. A similar radial variation in the diffusion coefficient is sufficient to model this change, when a 20% increase in the edge value is included. Again the neoclassical pinch is assumed. However, a wide variation in decay rates is observed when a range of heated pulses is modeled. In some cases this simplified model cannot reproduce the increased decay rate. A significant increase in core diffusion is required, suggesting that another mechanism may be triggered which can further accelerate the central electron density decay.

During the ohmic phase, impurity transport both of nickel (high Z) and carbon (low Z) within this weakly anomolous central region is found to be consistent with neoclassical transport[17]. During the heating phase, impurity transport can remain consistent with neoclassical theory within the plasma core until the termination of the enhanced period. In this phase, impurity transport may reflect the appearance of an ion temperature driving term[17].

4. Summary

A transient enhanced performance mode has been obtained in JET limiter discharges using pellet injection fueling in combination with central RF heating. The occurence of the enhanced period follows strong perturbations in density and temperature profiles which, in the plasma core, lead to a reduction in the η parameter and a change in the q(r) profile. Thermal transport within the plasma core (r<0.5m) is improved by roughly a factor of 2 for both ions and electrons. This improvement occurs in the presence of strong local heating and strong ion and

electron temperature gradients. Central pressure and total neutron emission are increased. Neutron emission is predominantly thermal in origin. Ballooning stability limits are approached within this region. The enhancement is not related to a particular $k_{\parallel}$ spectrum or minority species but does require a resonance location within the plasma core. Decay of the density profile during the heating pulse is more rapid than observed in ohmic discharges, but in the best cases can be modeled using the neoclassical pinch and a diffusion coefficient similar to that obtained for the low temperature ohmic case. Impurity transport is consistent with neoclassical theory within the core and leads to moderate deuterium dilution. The enhanced phase is terminated after 0.75 to 1.2s of heating, often with a rapid loss of central pressure. This event is not a sawtooth. In general, sawtooth oscillations do not appear during the period of enhancement.

5. Acknowledgement

The experimental programme and data evaluation are conducted under a collaboration agreement between the JET Joint Undertaking and the US Department of Energy (USDOE).

6. References

[1] Furth,H.P.(1986) Plasma Physics and Contr. Fus. **28** (94) 1305.
[2] Schmidt, G.L. et. al. (1986) Proc. 11th Int.Conf.Plasma Phys. and Contr. Fus. Res. (Kyoto, Japan), Vol.I, pp171-178.
[3] The JET Team (1986) Proc. 11th Int.Conf.Plasma Phys. and Contr. Fus. Res. (Kyoto, Japan) . Vol.I, pp31-49.
[4] Milora,S.L. et al. (1988) Proc. 15th Eur.Conf. on Contr.Fus. and Plasma Heating (Dubrovnik,Yugoslavia), Vol.I, p147.
[5] Kupschus,P. et al. (1988) Proc. 15th Eur.Conf. on Contr.Fus. and Plasma Heating (Dubrovnik,Yugoslavia.), Vol.I, p143.
[6] Jacquinot,J. et. al. (1988) Plasma Phys and Contr. Fus., **30** (11) 1467.
[7] Gibson, A. et al. (1988) Plasma Phys and Contr. Fus., **30** (11) 1375.
[8] Greenwald, M. et. al. (1984) Phys.Rev.Lett. **53** (4) 352.
[9] Sengoku,S. et. al. (1985) Nucl.Fus.**25** (10) 1475.
[10] Kaufmann,M. et.al. (1988) Nucl.Fus.**28** (5) 827.
[11] Soldner F.X. et.al. (1988) Phys.Rev.Lett. **61** (9) 1105.
[12] Noterdame,J. et al. (1988) E-II-2, this conference.
[13] Strachan, J.D.et al.(1987) Phys.Rev.Lett. **58** (10) 1004.
[14] Thomas, P.R. et al. (1988) A-IV-4, this conference.
[15] Tubbing, B et al. (1988) APS Plasma Phys. Div. Meeting, Hollywood, Fla., USA.
[16] Snipes,J.A., et.al. (1988) Nucl.Fus.**28** 1085.
[17] Behringer et al. (1988) IAEA Pellet Workshop, (Gut Ising,FRG)
[18]GreenwaldM.,et al.,(1986) Proc.11th Int.Conf.Plasma Phys. and Contr. Fus. Res. (Kyoto, Japan) IAEA-CN-47/A-III-1.

[19] Goedbloed,et al., (1984) Proc. 10th Int.Conf.Plasma Phys. and Contr. Fus.Res. (London) Vol.II, p165.
[20] Rosenbluth, M.N. et al.(1983) Phys.Rev.Lett. **51** (21)1967.
[21] Edwards, A (1986) Phys.Rev.Lett. **57**(2) 210.
[22] Taroni, A. et al. (1988) A-VII-1, this conference.
[23] Goldston R.J., Plasma Phys. Contr. Fus. **26** (1984) 87.
[24] Hulse et al. (1988) IAEA Pellet Workshop, (Gut Ising, FRG).
[25] Baylor et al. (1988) IAEA Pellet Workshop, (Gut Ising, FRG).

Table I

Pulse Nos: 17749 / 17747

4.2s/3.5m	Pellet	No-Pellet
P_{tot}(MW)	19	17.5
n_e(x10^{19}m-3)	5.5	3.4
$n_d \cong 0.7 n_e$	-	2.4
$n_d \cong 0.5 n_e$	2.8	-
∇T_i(keVm^{-1})	26	10
∇T_e(keVm^{-1})	35	6.8
$n_d \nabla T_i$	55	24
$n_e \nabla T_e$	192	23

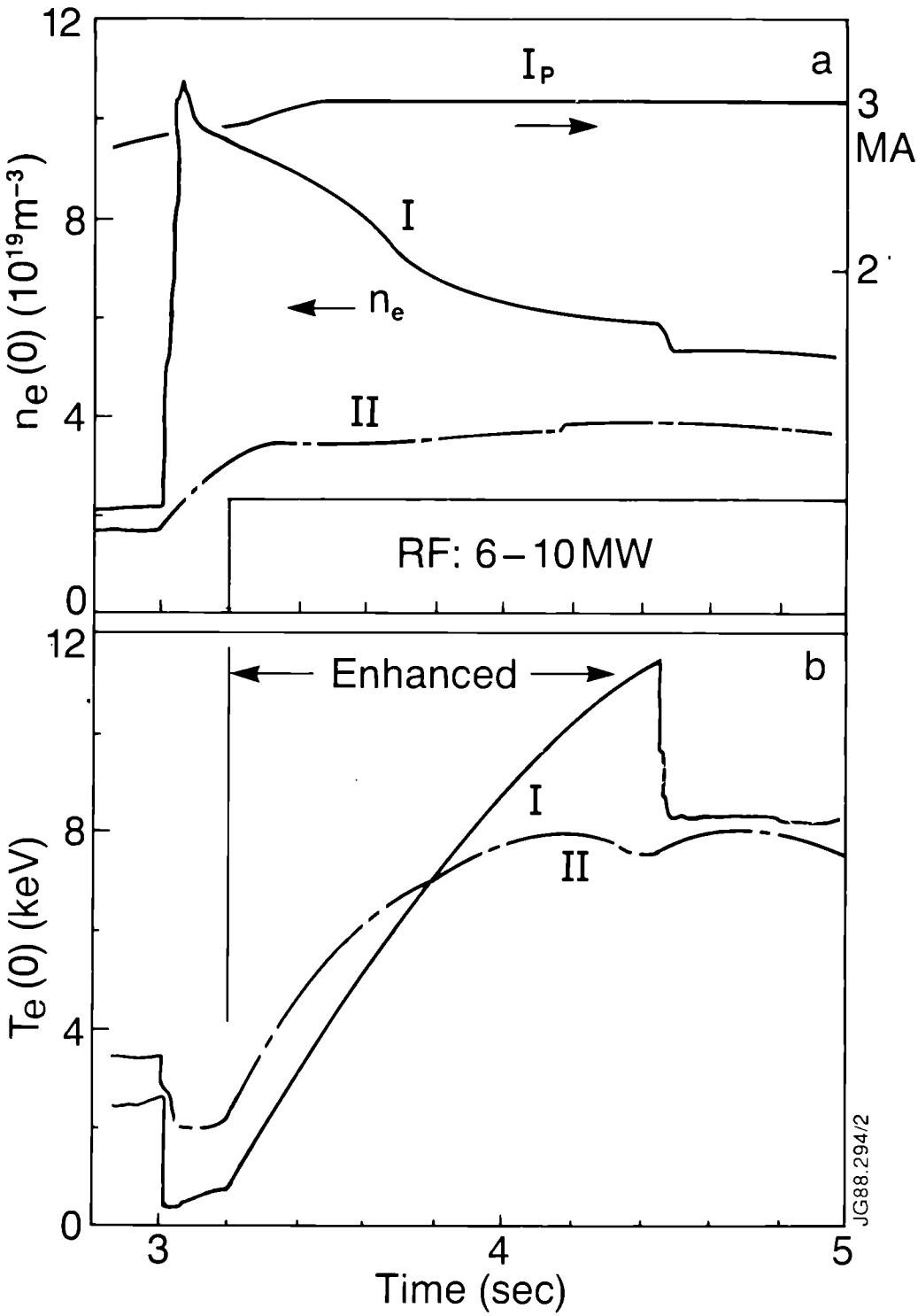

Figure 1: Discharge Overview- Strong(I) Pulse No.16211 and weak(II) PulseNo.16206 pellet perturbations: (a)plasma current, central density, and RF heating power; (b)central electron temperature (second harmonic ECE);

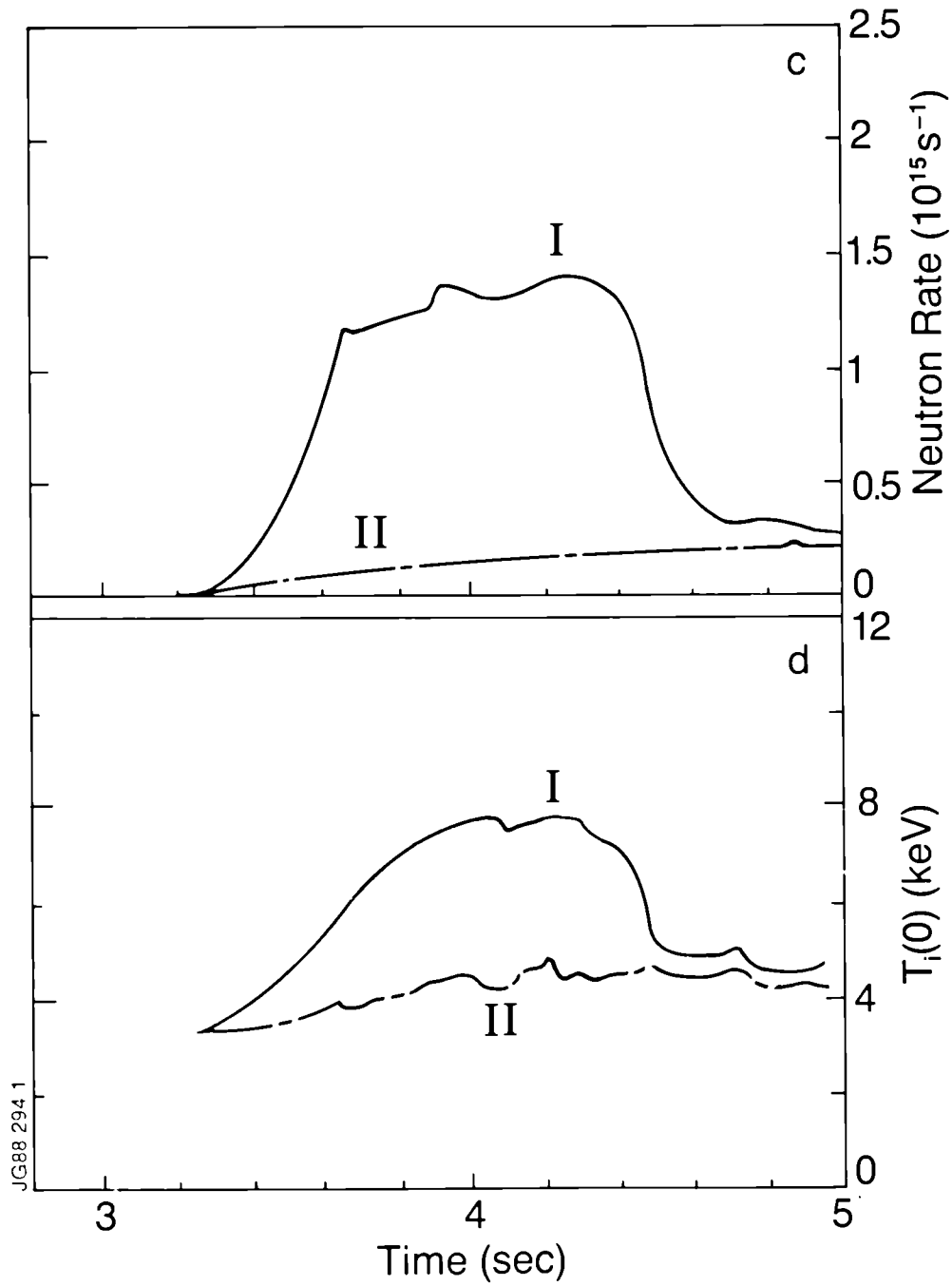

Figure 1: (c)neutron rate; (d)central ion temperature (Doppler broadening He-like Ni).

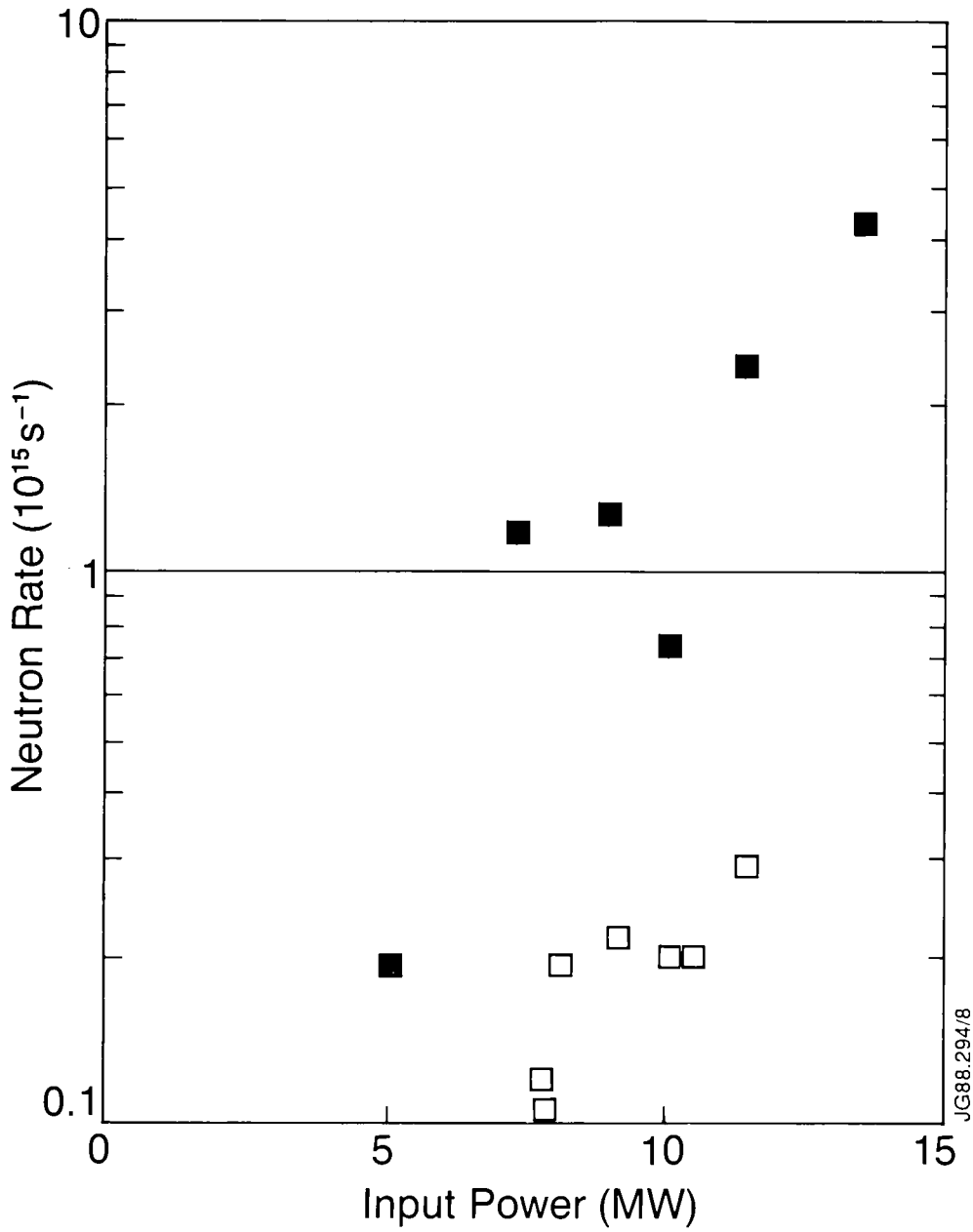

Figure 2: Neutron Rate as function of input power for RF heating only. Solid squares-enhanced phase. Open squares-later phase (t>4.4s).

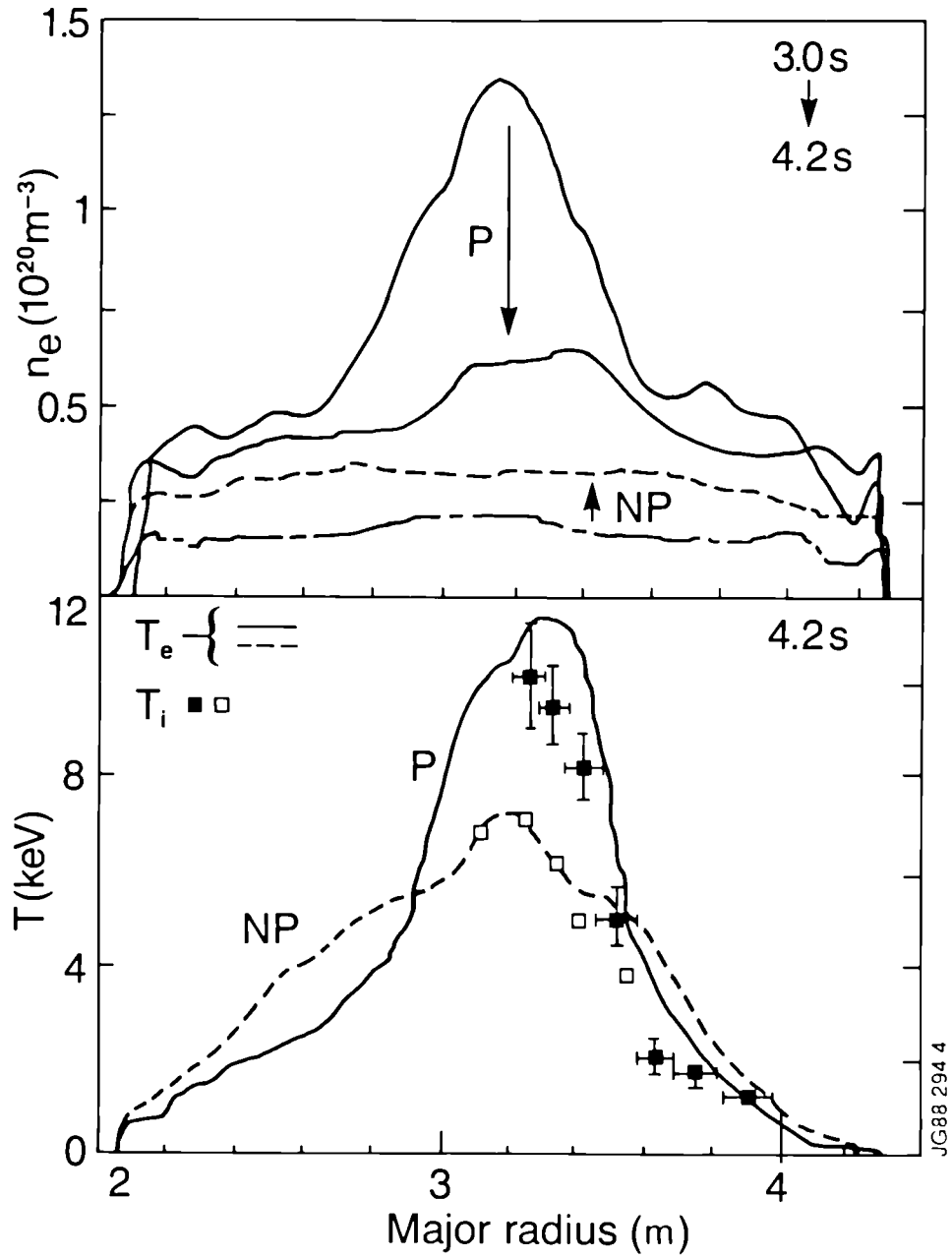

Figure 3: Profiles of electron density at 3.0 and 4.2s and electron temperature (Thomson Scattering) and ion temperature (Charge Exchange Spectroscopy) at 4.2s for pellet (P) and no pellet (NP) cases. Timing of fueling and heating as in Fig. 1. Heating power, (P): RF-12.5MW, NBI-5MW; (NP): RF-11.5MW, NB-5MW (Pulse Nos:17749/17747). Solid squares - pellet case ion temperature, open squares - no pellet case ion temperature.

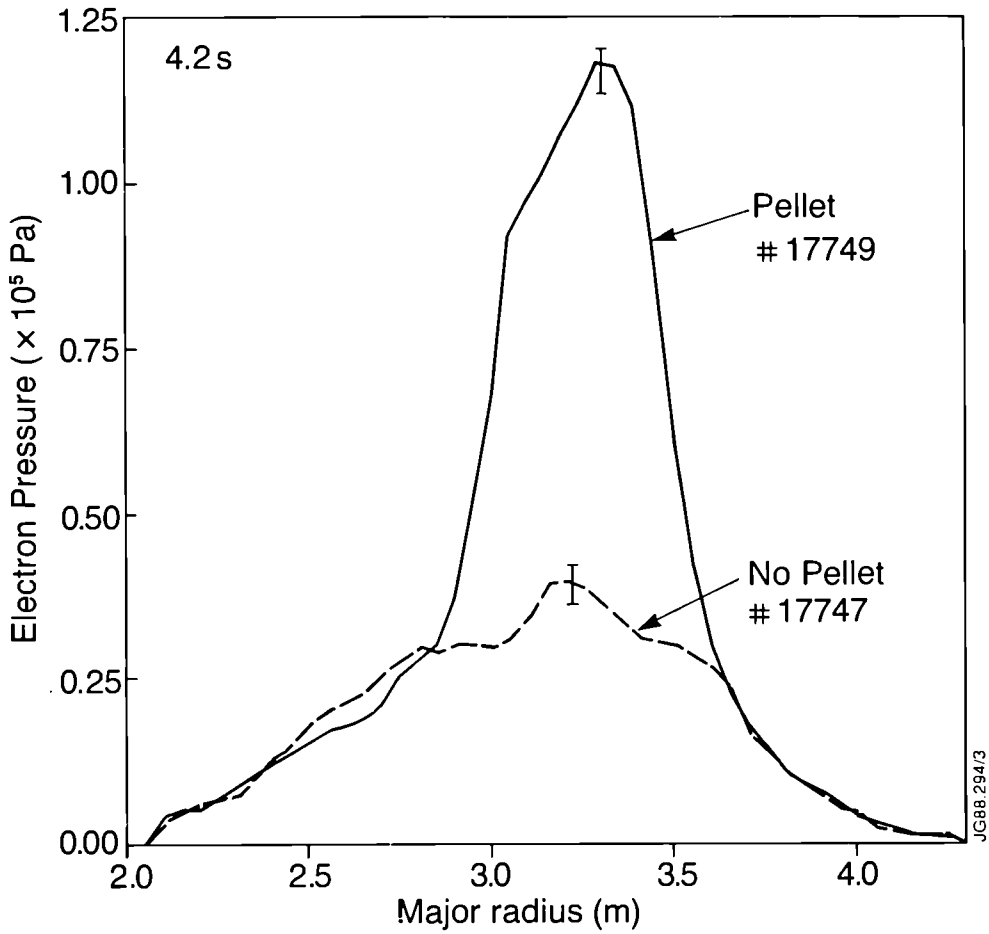

Figure 4: Profiles of electron pressure (Thomson Scattering) for pellet (P) and no-pellet (NP) cases in Fig. 3.

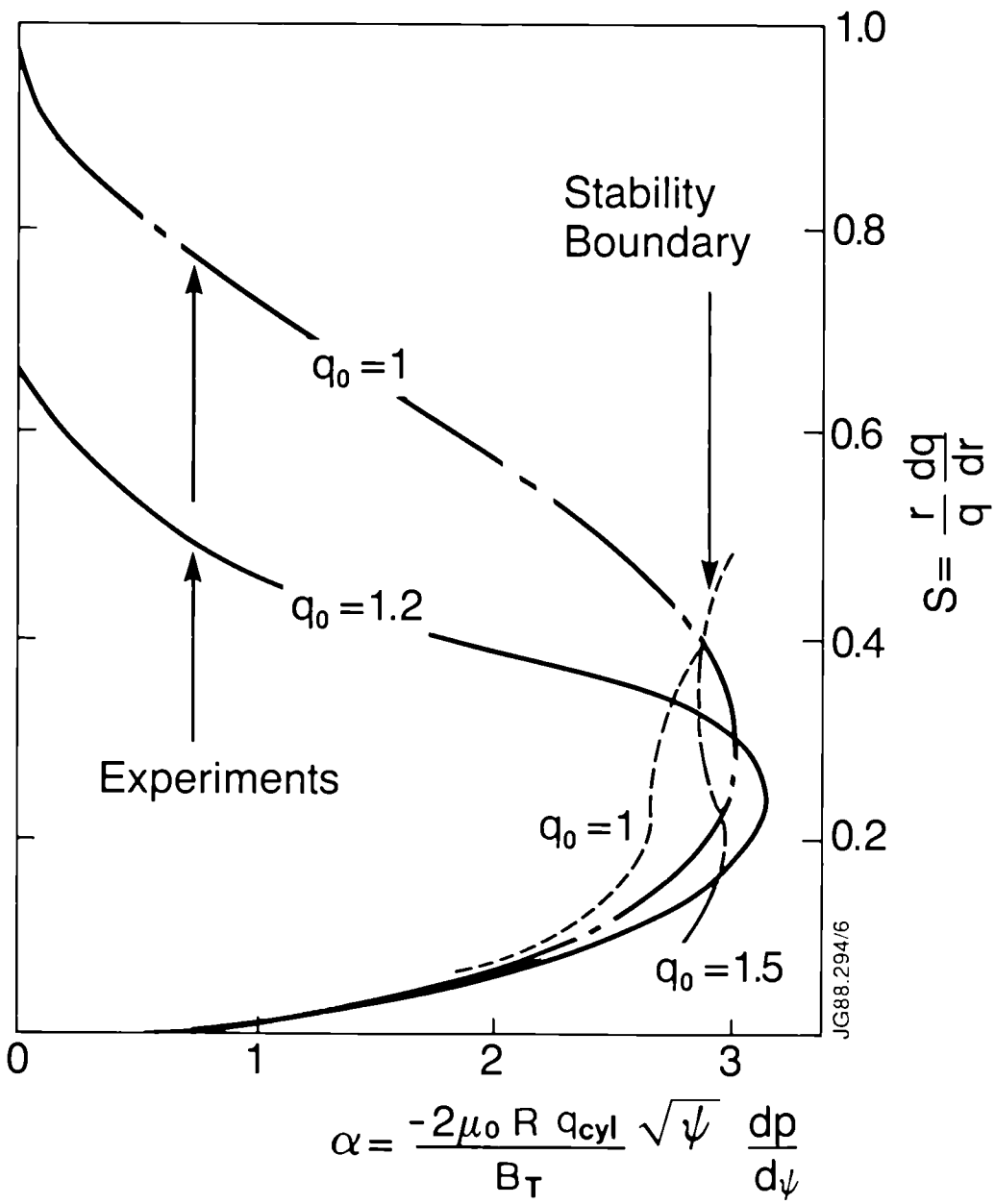

Figure 5: Stability diagram for pellet case similar to Fig. 4. The s-a values of the discharge (experimental) are shown assuming a central q value of 1 and 1.2. The stability boundaries shown are obtained by perturbation of the measured pressure profile assuming a central q value of 1 and 1.5. Values of s-a above or to the left of the boundary are stable.

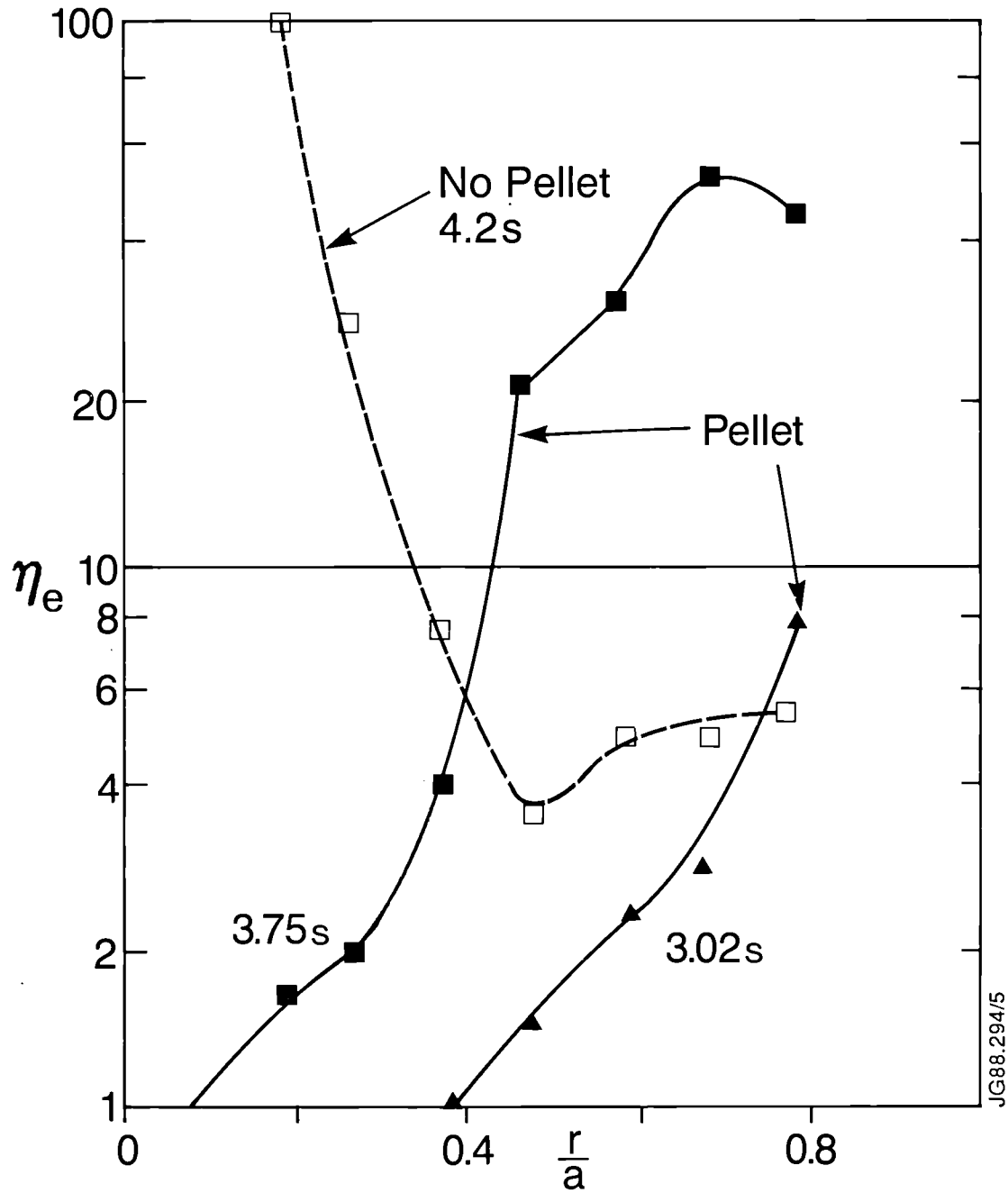

Figure 6: η_{ca}s a function of minor radius following pellet injection at 3s (Pulse No:16235) and 3.75s (Pulse No.17749 - solid points), and at 4.2s during a no-pellet pulse (Pulse No:17747 -open pts).

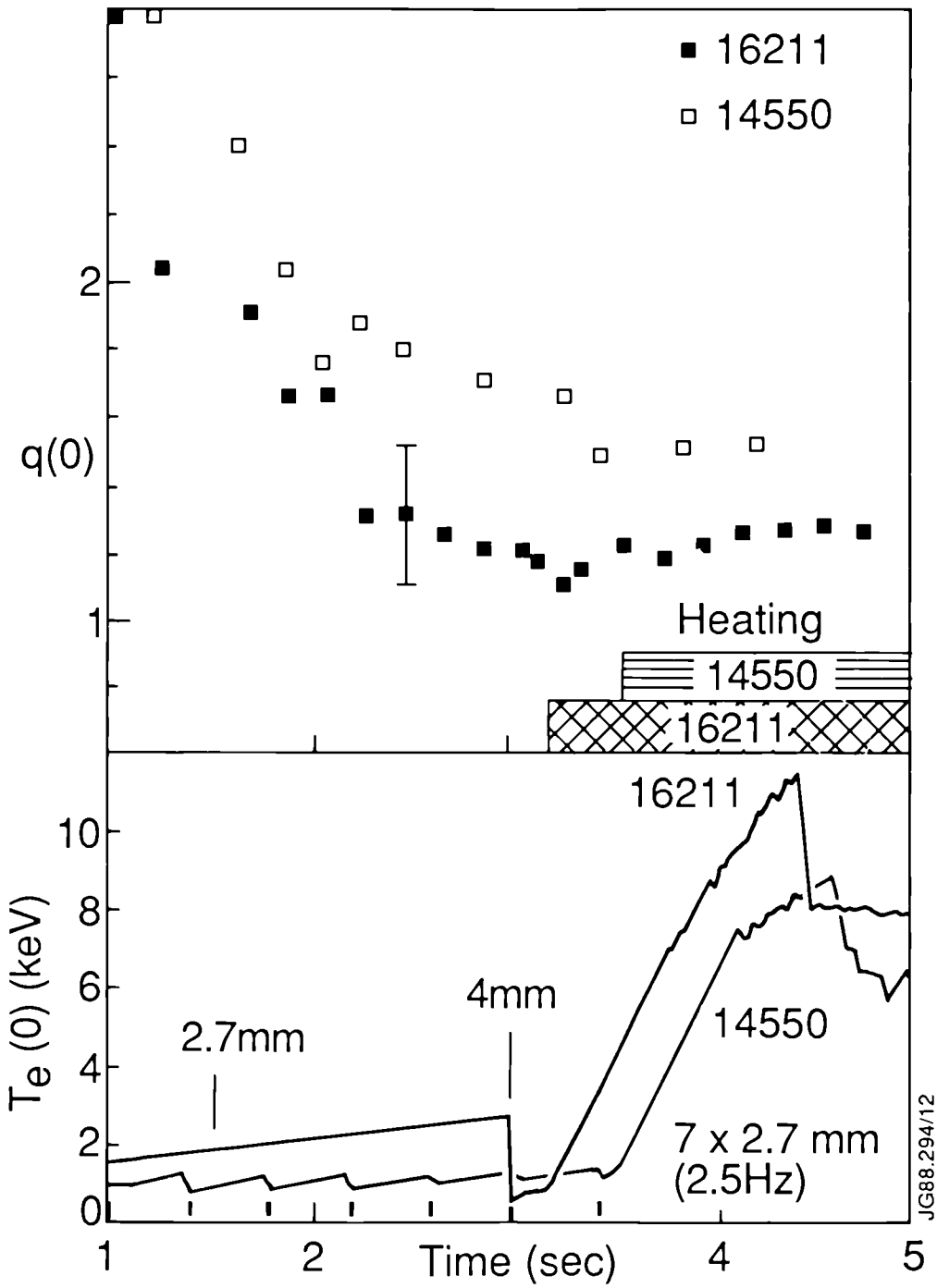

Figure 7: Evolution of q(0) from Faraday rotation measurements and $T_e(0)$, 2.7 and 4mm pellet sequences.

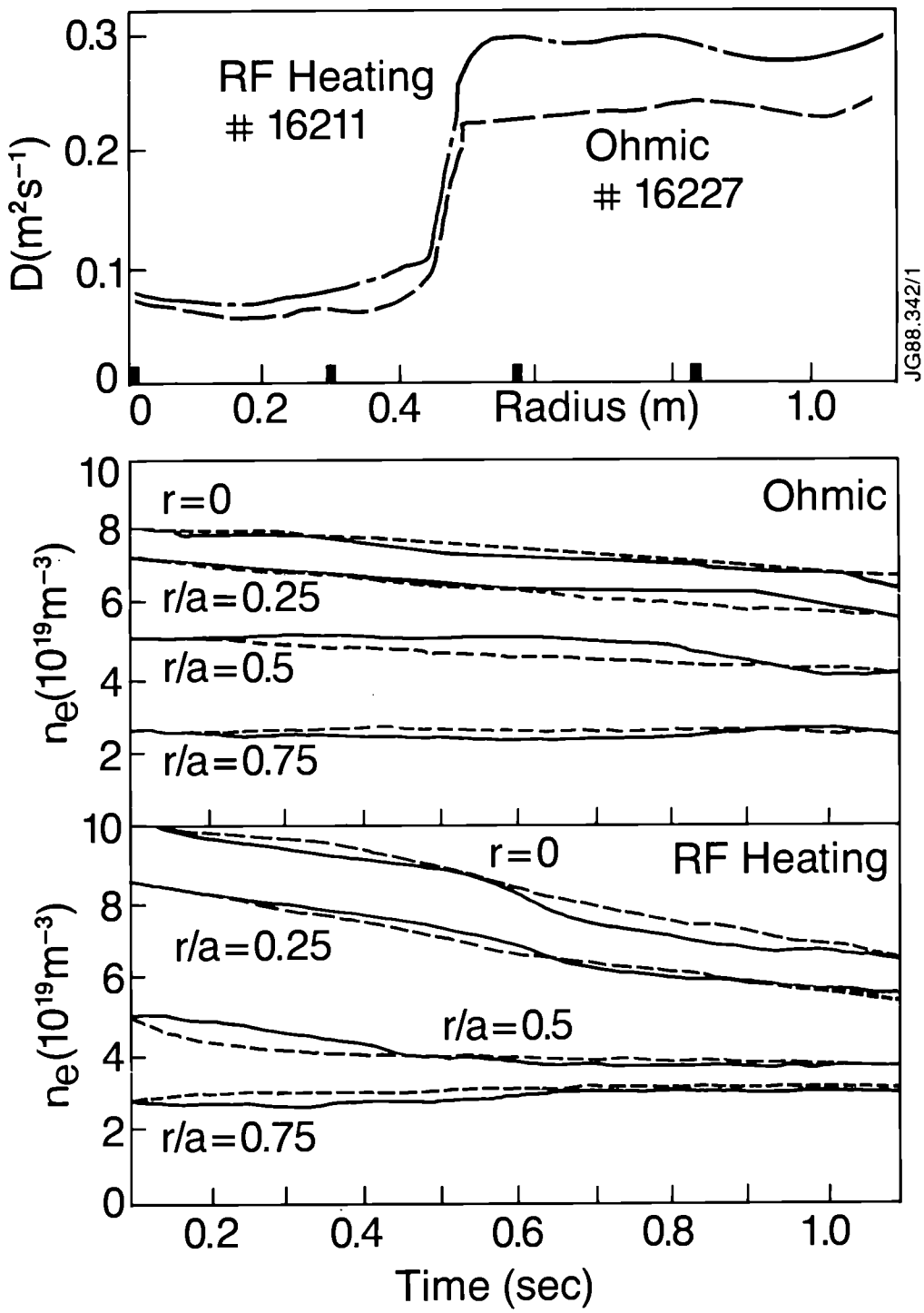

Figure 8: Particle diffusion coefficient for ohmic and heated cases. Evolution of density profile, measured (solid curves) and calculated (dashed curves), at four radii in ohmic and heated cases.

APPENDIX I

THE JET TEAM

JET Joint Undertaking, Abingdon, Oxon, OX14 3EA, UK

J.M. Adams[1], H. Altmann, G. Appruzzese, W. Bailey, P. Ballantyne, B. Balet, D.V. Bartlett, L.R. Baylor[23], K. Behringer[13], A.C. Bell, P. Bertoldi, E. Bertolini, L.G. Betello, V. Bhatnagar, R.J. Bickerton, A.J. Bickley, J. Bizarro[21], S. Bliman[16], T. Bonicelli, S.J. Booth, G. Bosia, M. Botman, D. Boyd[30], H. Brelen, H. Brinkschulte, M. Brusati, T. Budd, M. Bures, T. Businaro[4], P. Butcher, H. Buttgereit, C. Caldwell-Nichols, D.J. Campbell, P. Card, J. Carwardine, G. Celentano, P. Chabert[16], C.D. Challis, A. Cheetham, J. Christiansen, C. Christodoulopoulos, P. Chuilon, R. Claesen, S. Clement[29], J.P. Coad, P. Colestock[6], S. Conroy[12], M. Cooke, S. Cooper, J.G. Cordey, W. Core, G. Corrigan, S. Corti, A.E. Costley, G. Cottrell, M. Cox[7], P. Cripwell[12], D. Cross, H. de Blank[15], H. de Esch, J. de Haas[15], L. de Kock, E. Deksnis, G.B. Denne, G. Deschamps, G. Devillers, K.J. Dietz, J. Dobbing, A. Dombra, N. Dolgetta, S.E. Dorling, P.G. Doyle, D.F. Duchs, H. Duquenoy, A. Edwards, J. Ehrenberg[13], T. Elevant[11], W. Engelhardt, S.K. Erents[7], L.G. Eriksson[5], M. Evrard[2], H. Fajemirokun[12], H. Falter, J. Farthing, D. Flory, M. Forrest[7], C. Froger, K. Fullard, M. Gadeberg, A. Galetsas, M. Galley, R. Galvao[8], M. Garribba, R. Giannella, A. Gibson, R.D. Gill, A. Gondhalekar, G. Gorini, C. Gormezano, N.A. Gottardi, C. Gowers, B.J. Green, F.S. Griph, W.K. Guo[26], R. Haange, G. Hammett[6], W. Han[9], H.E. Han-Gonge[26], C.J. Hancock, P.J. Harbour, N.C. Hawkes[7], P. Haynes[7], J. Heikkinen[3], T. Hellsten, J.L. Hemmerich, R. Hemsworth, F.B. Herzog, R.F. Herzog, J. Hoekzema, R. Hope, W.A. Houlberg[23], J. How, M. Huart, T.P. Hughes[31], M. Hugon, M. Huguet, M. Irving, J. Jacquinot, O.N. Jarvis, F. Jensen, T.C. Jernigan[23], E. Joffrin, E.M. Jones, L.P.D.F. Jones, T.T.C. Jones, J. Kallne, O. Kardaun[13], A. Kaye, B.E. Keen, M. Keilhacker, G.J. Kelly, A. Khare[14], S. Knowlton, A. Konstantellos, M. Kovanen[20], P. Kupschus, P. Lallia, R. Lanza, R. Lasser, J.R. Last, L. Lauro-Taroni, K. Lawson[7], E. Lazzaro, M. Lennholm, B. Liley[25], X. Litaudon, P. Lomas, M. Lorentz-Gottardi[2], C. Lowry, G. Maddison[7], G. Magyar, M. Malacarne, W. Mandl[13], V. Marchese, J. Mart, P. Massmann, G. McCracken[7], J. Mendonca, P. Meriguet, P. Micozzi[4], S.F. Mills, P. Millward, S.L. Milora[23], A. Moissonnier, F. Mompean, P.L. Mondino, P. Morgan, G. Murphy, G. Newbert, M. Newman, P. Nielsen, P. Noll, W. Obert, D. O'Brien, J. O'Rourke, M.G. Pacco-Duchs, M. Pain, S. Papastergiou, D. Pasini[19], A. Peacock, N. Peacock[7], D. Pearson[12], F. Pegoraro, F. Petree, M. Pick, S. Pitcher[7], J. Plancoulaine, J-P. Poffé, F. Porcelli, R. Prentice, T. Raimondi, C. Raymond, P-H. Rebut, J. Removille, F. Rimini, D. Robinson[7], A. Rolfe, R. Romain, R.T. Ross, L. Rossi, R. Rushton, P. Rutter, H.C. Sack, G. Sadler, G. Saibene, N. Salmon[12], H. Salzmann[13], A. Santagiustina, R. Sartori, D. Schissel[24], P.H. Schild, M. Schmid, G. Schmidt[6], R.L. Shaw, K. Schimizu[17], A. Sibley, R. Simonini, J. Sips[15], P. Smeulders, J. Snipes, S. Sommers, L. Sonnerup, K. Sonnenberg, G. Sonnozaro, W. Stacey[28], M. Stamp, P. Stangeby[18], D.F. Start, C.A. Steed, D. Stork, P.E. Stott, T.E. Stringer, D. Stubberfield, D. Summers, H. Summers[19], J. Tagle[29], H. Tamnen, A. Tanga, A. Taroni, C. Tebaldi[22], A. Tesini, P.R. Thomas, E. Thompson, K. Thomsen, J.M. Todd, P. Trevalion, B. Tubbing, F. Tibone, E. Usselmann, A. Vannucci, H. van der Beken, M. von Hellermann, T. Wade, C. Walker, M. Walravens, K. Walter, Z. Wang[27], D. Ward, M.L. Watkins, H. Weisen[10], J. Wesson, D.H. Wheeler, J. Wilks, U. Willen[11], D. Wilson, T. Winkel, S. Wolfe, D. Wong, C. Woodward, M. Wykes, I.D. Young, L. Zannelli, D. Zasche[13]

PERMANENT ADDRESS

1 UKAEA, Harwell, Didcot, Oxon, UK
2 EURATOM Association, LPP ERM KMS, B 1040 Brussels, Belgium
3 Technical Research Centre of Finland, Helsinki, Finland
4 ENEA CENTRO Di Frascati, I 00044 Frascati, Roma, Italy
5 Chalmers University of Technology, Goteborg, Sweden
6 Princeton Plasma Physics Laboratory, New Jersey, USA
7 UKAEA Culham Laboratory, Abingdon, Oxfordshire, UK
8 Plasma Physics Laboratory, Space Research Institute, Sao Jose dos Campos, Brazil
9 Institute of Mathematics, University of Oxford, UK
10 CRPP EPFL, 21 Avenue des Bains, CH-1007 Lausanne, Switzerland
11 Swedish Energy Research Commission, S 100 72 Stockholm Sweden
12 Imperial College of Science and Technology, University of London, UK
13 Max Planck Institut fur Plasmaphysik, D-8046 Garching bei Munchen, FRG
14 Institute for Plasma Research, Gandhinagar Bhat Gujrat, India
15 FOM Instituut voor Plasmafysica, 3430 Be Nieuwegein, The Netherlands
16 Commissariat a L'Energie Atomique, F 92260 Fontenay-aux-Roses, France.
17 JAERI, Tokai Research Establishment, Tokai-Mura, Naka Gun, Japan
18 Institute for Aerospace Studies, University of Toronto, Downsview, Ontario, Canada
19 University of Strathclyde, 107 Rottenrow, Glasgow, G4 0NG, UK
20 Nuclear Engineering Laboratory, Lapeenranta University, Finland
21 JNICT Lisboa, Portugal
22 Department of Mathematics, Universisty of Bologna, Italy
23 Oak Ridge National Laboratory, Oak Ridge, Tenn., USA
24 GA Technologies, San Diego, California, USA
25 University of Waikato, Hamilton, New Zealand
26 IPP Academia Sinica, P.R. China
27 Southwestern Institute of Physics, Leshan, Sechuan, P.R. China
28 University of Georgia, Atlanta, USA.
29 Centro de Investigaciones Energeticas Medioambientales y Techaologicas, Spain
30 University of Maryland, College Park, Marsland, USA
31 University of Essex Colchester, UK

J CR 88 19 1A rev 30/11 88

INTERNATIONAL ATOMIC ENERGY AGENCY

TWELFTH INTERNATIONAL CONFERENCE ON PLASMA PHYSICS AND CONTROLLED NUCLEAR FUSION RESEARCH

Nice, France, 12-19 October 1988

IAEA-CN-50/A-4-4

High Temperature Experiments and Fusion Product Measurements in JET

by

The JET Team
(Presented by PR Thomas)

JET Joint Undertaking, Abingdon, Oxon, OX14 3EA, UK

ABSTRACT

High temperature plasmas ($T_i \leq 23$keV and $T_e \leq 12$keV) have been obtained in JET using NBI and ICRH. The low target densities required for these experiments were produced by using graphite surfaces to pump the plasma. Low density helium pulses were employed to deplete the graphite of deuterium, thereby enhancing the pumping effect. The trapping and slowing down rates for the ICRH minority ions and d-d tritons were were close to the classical values. Although the ICRH minority ions carried as much as one third of the total energy content, the thermal plasma energy confinement was unaffected by their presence. The high temperature plasmas had the same plasma energy confinement as high density, low temperature plasmas and the heating rates of hot electron and hot ion discharges were similar. These results show that the prospects are good for α-particle heating and high temperature operation in thermonuclear plasmas.

1. INTRODUCTION

This paper reports some results obtained with low collisionality, high temperature JET plasmas and the associated fusion product diagnostic measurements. Non-thermal ions arising from neutral beam injection (NBI) or ion cyclotron resonance heating (ICRH) have long slowing down times and so contribute significantly to the fusion yield and the total energy content. At high RF power densities ICRH minority ions provide a good simulation of α-particles in a thermonuclear plasma.

The NBI system has been used to inject 80keV deuterons at powers of up to 21MW. With the central electron temperature, $T_e(0)$, in the range 5-12keV, the NBI power is transferred to the thermal ions. Up to 18MW of ICRH have been launched in the plasma. When tuned to a minority fundamental resonance, ICRH couples mainly to high energy ion tails (mean energy$\approx$0.1-1MeV), which slow down on the electrons. A small proportion of the RF power is transferred directly to the electrons [1] by Landau damping, mode conversion or TTMP. Bulk ion heating and tail formation have been observed with second harmonic ICRH.

NBI has been used to obtain hot ion plasmas with a central ion temperatures, $T_i(0)$, up to 23keV and $T_e(0) \approx$ 8keV at a central electron density, $n_e(0)$, $\approx 2\times10^{19}$ m^{-3}. Hot electron plasmas with $T_e(0)$ up to 12keV and $T_i(0) \approx$ 7keV have been obtained with ICRH at $n_e(0) \approx 3.5\times10^{19}$ m^{-3}. Similarly high T_e and T_i have been obtained simultaneously by using ICRH and NBI together.

2. FUSION PRODUCT MEASUREMENTS

Comprehensive measurements have been made of neutron rates and spectra. The neutron yield has been absolutely calibrated in situ using radio-isotope sources and a pulsed neutron tube to an estimated accuracy of 10%. The neutron energy spectra have been used to separate the sources of neutron emission so that the central deuteron density could be determined.

14MeV neutron emission has been measured by foil activation and silicon diode counters. This latter technique utilises ^{28}Si (n,α) and (n,p) reactions whose cross-sections have effective thresholds at around 6MeV. Good discrimination against γ's and 2.5MeV neutrons is obtained by only accepting large amplitude pulses.

Plasma γ-ray spectrum measurements have provided valuable information about the fast ion distribution in ICRH plasmas. The γ-ray spectra indicate the presence in ICRH plasmas of fast ions with energies higher than 7.5MeV. The details of these measurements and their interpretation are presented elsewhere [2].

3. HIGH TEMPERATURE OPERATION

The low densities required for high temperature operation require that the plasma be pumped both before and during additional heating. Two methods have been used to accomplish this: either the plasma is started on the main limiters and then moved onto the graphite protection tiles on the small major radius side of the vacuum vessel or an X-point configuration [3] is formed. In both cases the graphite surfaces act as a particle sink and the plasma is pumped. Low density helium conditioning plasmas [4] are used to deplete the graphite of deuterium and so increase the pumping action.

Figure 1 illustrates the main features of a typical high temperature plasma (JET pulse 16066) between 10 and 16 seconds after breakdown. The X-point was formed at 8 seconds and $n_e(0)$ fell to a very low level ($0.8\times10^{19}m^{-3}$) before the heating was applied.

The ICRH heats the electrons, so reducing the electron/ion coupling, and provokes a "monster" sawtooth [5]. Both these effects promote ion heating by the NBI. Following the last sawtooth crash before the monster, $T_i(0)$ rises rapidly to 14keV and the neutron emission peaks. The electron and ion temperature profiles, at the time of the maximum $T_i(0)$, are shown in Fig.1(c) and are seen to be highly peaked.

Shortly after the maximum $T_i(0)$ the density begins to rise more rapidly, whereupon both the ion temperature and the neutron emission fall. The electron density profile changes from being peaked to being hollow at this time and carbon line radiation increases. At the monster sawtooth crash the plasma temperatures collapse and show no signs of recovery in spite of an associated fall in density.

4. NEUTRON EMISSION

Similar plasma conditions to those of Fig. 1 had been obtained at the same power level with ^{3}He minority ICRH a few pulses previously. Tuning to hydrogen minority doubled the neutron rate. Whilst the increased neutron emission could be due to the formation of a high energy deuteron tail by $2\omega_{cd}$ ICRH, only 12% of the neutrons can be identified beyond 2.8MeV (which

corresponds to the NBI energy) in the liquid scintillator spectrum.

During the first second of ICRH the γ-spectrum was dominated by $^{12}C(p,p')^{12}C^{*}$ (threshold 4.8MeV). Only in the last second, when the neutron rate had fallen, did $^{12}C(d,p)^{13}C^{*}$ (threshold 0.36MeV) take over. Thus the increased emission cannot be due to high energy deuterons. A possible explanation for the extra neutrons is the effective reduction of the NBI slowing down rate by the RF fields.

The neutron emission of other high temperature pulses can be accounted for by the beam-beam, beam-thermal and thermal-thermal deuteron reactions. Of these, the beam-thermal interactions are the most important and account, typically, for 60% of the neutrons. The beam-beam neutrons are only significant during the low density period of the heating pulse and provide ≈10-50% of the maximum emission.

The interpretation of the neutron yield measurements requires that the deuteron concentration in the high temperature plasmas is rather low, with $n_d/n_e \approx 0.25\text{-}0.45$ being typical. Analysis of other diagnostics such as visible Bremsstrahlung, neutron spectra, triton burn-up and charge exchange recombination radiation give similar values.

5. FAST PARTICLES IN PLASMAS

The energy confinement of ICRH minority ions and the burn-up of tritons produced by d-d fusion reactions test much of the important physics of α-particle heating in thermonuclear plasmas. Not only are the Larmor radii of these ions similar to those of d-t α's but also, in the case of the ICRH fast ions, n_{fast}/n_e ($\approx 10^{-2}$) , β_{fast} (≈1%) and v_{fast}/v_{Alfven} (>1) are in the appropriate range. However, d-t α's have an isotropic $1/v^3$ distribution whereas the ICRH minority ions have a quasi-Maxwellian anisotropic ($v_\perp/v_\parallel \approx 30$) distribution. The anisotropy of the ICRH distribution might be expected to provide rigorous tests for the appearance of loss-cone instabilities, fishbones and stochastic diffusion.

The energy density contained in fast minority particles should be $\tau_s P_{rf}/2$, where P_{rf} is the absorbed power density and τ_s the minority slowing-down time on the electrons. The perpendicular energy contained in the minority particles can be obtained from the diamagnetic loop and equilibrium magnetic fields. The correlation with $\tau_s(0)P_{ICRH}/2$ is satisfactory, as shown in Fig. 2(a). The factor 3-5 between the axes can be accounted for by profile effects, the RF coupling efficiency, finite minority poloidal Larmor radii and, possibly, anomalous losses.

If the ICRH deposition profile calculated with a ray tracing code [6] is combined with profiles of temperature and density, then it is found that RF coupling efficiencies of 0.5 for hydrogen and 0.65 for helium minority are required for the

Stix distribution function [1] to match the experimental data on minority energy and fusion yield [2]. The results of a self-consistent wave propogation and Fokker-Planck code are compared with data in Fig. 2(b). To improve the match with some data points, where τ_s can be as much as 1 second, an additional ad-hoc energy loss with a characteristic time of 0.5 seconds has been added. The absorbtion is calculated to occur mainly on the minority in these plasmas. The extra loss term can be associated with the rather low coupling efficiencies required in the Stix calculation. Neoclassical effects have been neglected in calculation of the minority distribution functions. So these should be assessed before it is assumed that the extra losses are anomalous.

The 14MeV neutron emission from a deuterium plasma provides direct measurements of the slowing down and trapping of d-d tritons (1MeV). Figure 3 shows the temporal evolution of the 2.5MeV and 14MeV neutron emission from a plasma with 2.5MW of NBI and 12.5MW of ICRH. The minority ion energy content was approximately 1MJ compared with 4MJ in the thermal plasma. The delay due to the slowing down of the tritons on the plasma electrons from 1MeV to the peak of the d-t cross-section at 240keV can be seen clearly.

The results of a calculation of the 14MeV emission based on the measurements of plasma temperature and density are also shown in Fig. 3. The slowing down time must be systematically reduced by 15% in order to obtain agreement with the 14MeV measurements from most plasmas. This systematic rescaling of τ_s is within the experimental error, which is typically 20%. The rate of triton burn-up is generally in good agreement with the classical calculation which implies that the trapping is close to 100% in JET plasmas with currents of 3MA or more.

6. ENERGY CONFINEMENT AT HIGH TEMPERATURES

The data from a set of 3MA, 2.8-3.4T discharges has been sorted into $\Delta\Delta$ high T_e ($9<T_e<11$keV, $4<T_i<9$keV), $\square\square$ high T_i ($9<T_i<14$keV, $6<T_e<9$keV), $\Diamond\Diamond$ high T_i and T_e ($T_i, T_e>9$keV) and $\odot\odot$ high density ($n_e>3.5\times10^{19}$m^{-3} and $T_e<6$keV) groups. Figure 4(a) shows the diamagnetic energy content against heating power for these pulses. The diamagnetic energy content shows a considerable spread, with the high density plasmas having the lowest energy contents.

The plasma energy content, determined from magnetic measurements assuming that all fast ions are perpendicular, is plotted against heating power in Fig. 4(b). The spread is now rather small and the different groups are interspersed with no apparent trend in either temperatures or density. The spread in the diamagnetic energy must be predominantly due to fast ions.

The plasma energy confinement is apparently insensitive to overall temperature (or density) variations of a factor of two. The heating rates for the electrons and ions are very similar ($T_{e/i}(0) \approx 2\text{-}3\times10^{19}P_{e/i}(MW)/n_e(0)$ keV). 1-D transport simulations [7] of these plasmas require that the ion and

electron thermal conductivities be approximately equal in order tc satisfactorily reproduce the data. However, at the time of writing, the local transport analysis of the hot electron and hot ion plasmas has not been completed.

By pushing the plasma to a smaller minor radius on the inside wall, plasmas which are similar to the TFTR "supershots" [4] have been produced. Figure 5 shows the temperature and density profiles in one of these pulses (JET pulse 16981). The characteristic narrow electron density and broad temperature profiles can be seen. This pulse has been identified in Fig. 4. The global energy confinement is very similar to other high temperature JET pulses in spite of the different plasma dimensions.

7. CONCLUSIONS

High temperature,low collisionality plasmas have been produced in JET by high power NBI and ICRH. The low plasma densities required for operation im this regime are achieved by using the graphite wall tiles as a plasma pump.

The trapping and slowing down of fast ICRH minority ions and d-d tritons are close to classical expectations. There are some signs of additional losses when the slowing down time is of order one second but this has yet to be fully investigated. Neoclassical losses, in particular, should be assessed. MHD instabilities have been observed to eject fast particles from the plasma core in JET [8]. However the prospects for usable α-particle heating in future tokamak experiments are good.

The plasma energy content is insensitive to the temperature of either the electrons or the ions. The presence of fast ion populations with up to 50% of the plasma energy does not affect the plasma energy confinement. Thus the high temperatures and fast ion heating required in a thermonuclear plasma do not cause any deleterious effects beyond the usual confinement degradation with additional heating.

The fusion performance of the JET high temperature plasmas would be greatly enhanced if the plasma deuteron content were to be increased and the next stage of the experimental development of these discharges will be dedicated to this end.

8. REFERENCES

[1] STIX, T.H, Nuclear Fusion 15(1975)737.
[2] START, D.F.H. et al., paper E-2-3 this conference.
[3] TANGA, A. et al., Proceedings of 11th IAEA Conference on Plasma Physics and Controlled Nuclear Fusion Research, Vol.1, p65, Kyoto, 1986.
[4] STRACHAN, J.D. et al., Phys. Rev. Lett. 58(1987)p1004.
[5] CAMPBELL, D.J. et al., Phys. Rev. Lett. 60(1988)p2148.
[6] BHATNAGAR, V.P. et al., Nuclear Fusion 24(1984)p955.
[7] TARONI, A. et. al., paper A-7-1 this conference.
[8] CAMPBELL, D.J. et. al., paper A-7-2 this conference.

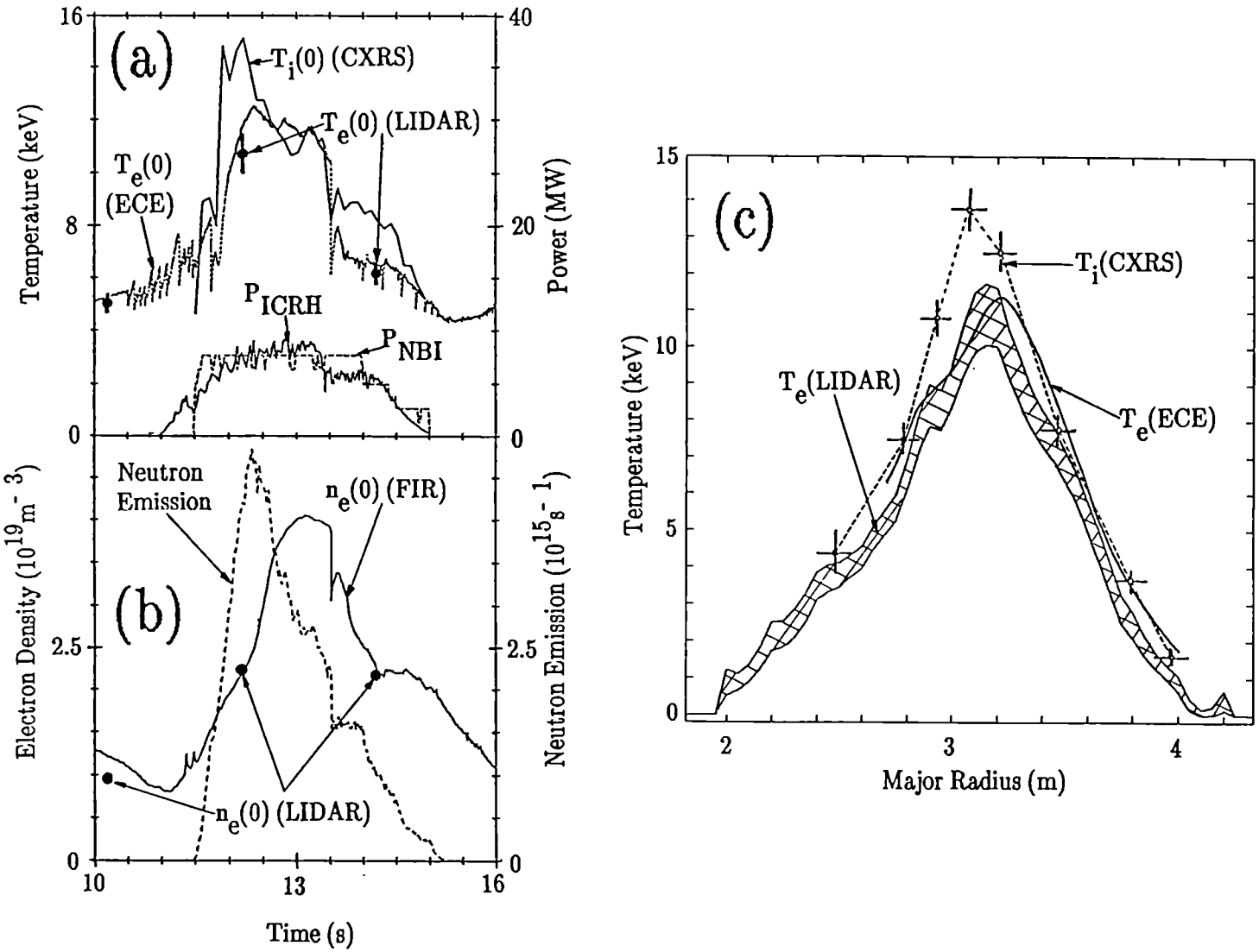

Fig. 1 Data for JET pulse 16066, (a) central temperatures and additional heating powers against time, (b) the central electron density and neutron emission rate against time, (c) the electron and ion temperature profiles. CXRS denotes charge exchange recombination spectroscopy, ECE electron cyclotron emission and LIDAR the time resolved Thomson scattering.

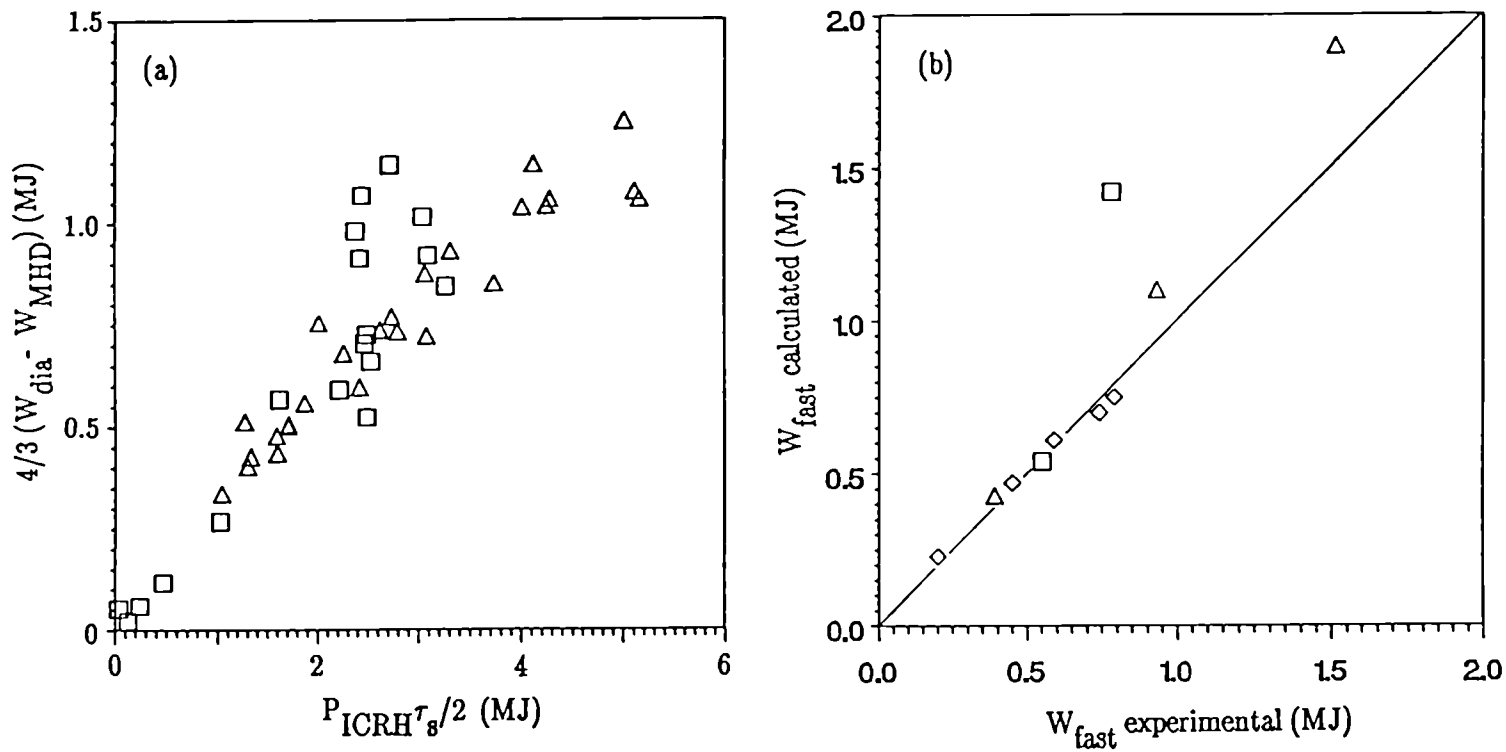

Fig. 2 (a) The measured perpendicular component of fast ion energy against $\tau_s(0)P_{ICRH}/2$ for △ △ hydrogen minority and □ □ helium minority plasmas. (b) The fast ion energy calculated with a Fokker-Planck code against the experimental value for △ △ (h)^{3}He, □ □ (h)^{4}He and ◇ ◇ (^{3}He)d plasmas.

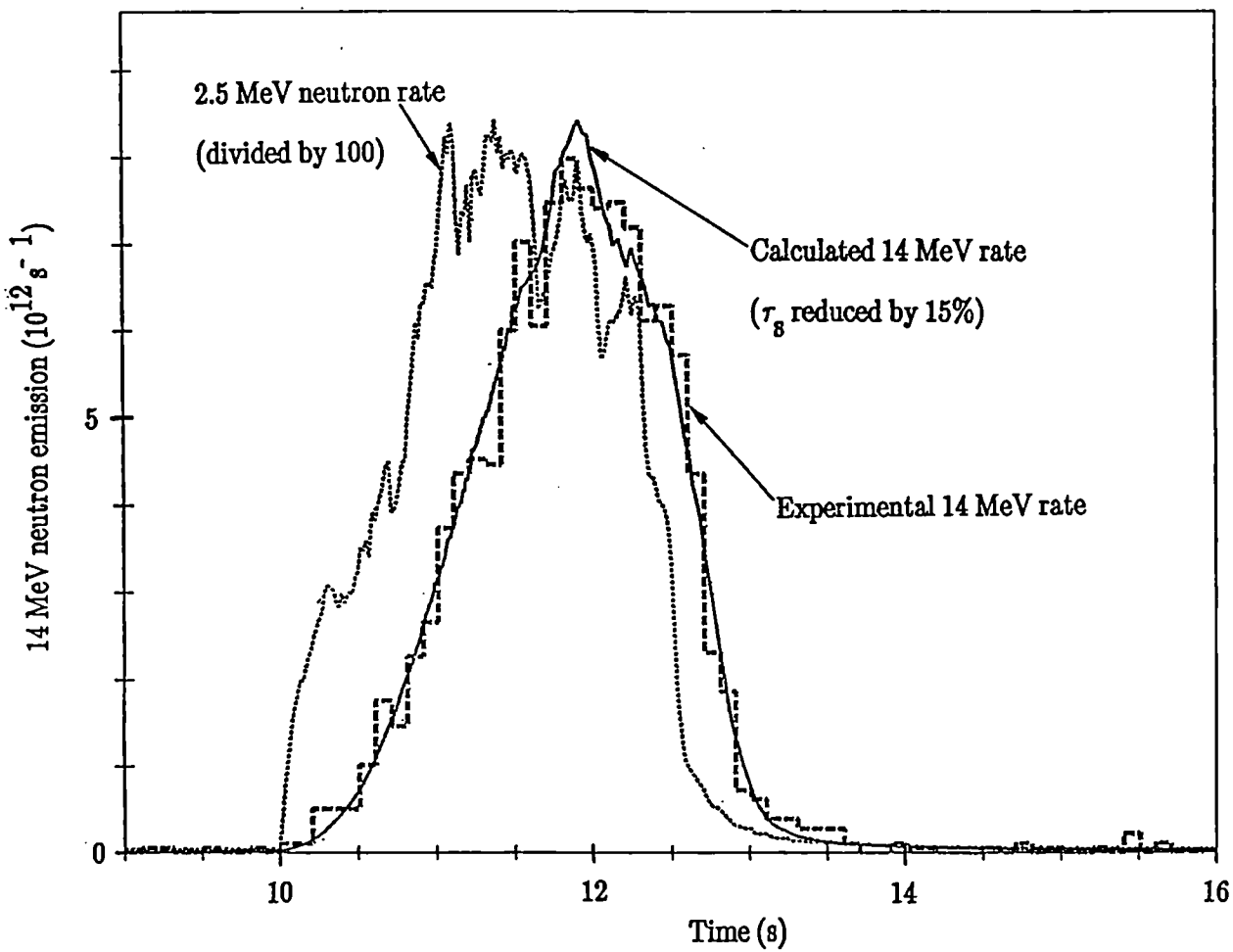

Fig. 3 The 2.5MeV neutron emission rate ....., the experimental 14MeV neutron emission ----- and the calculated 14MeV emission ——— against time for a 3MA/2.9T plasma with 12.5MW ICRH and 2.5MW NBI.

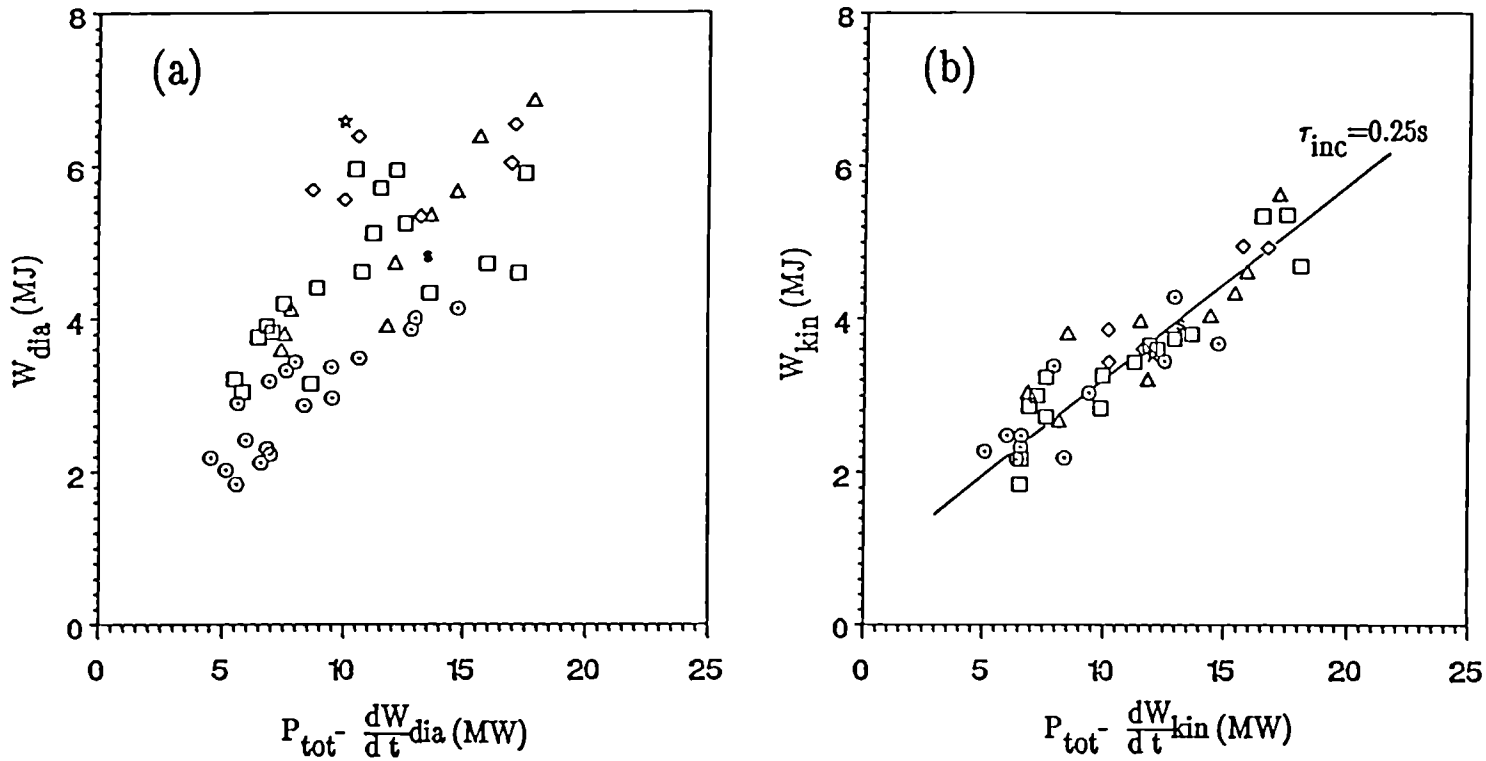

Diamagnetic energy content against heating power and (b) / content against heating power for a set of 3MA/2.8-3.4T △ T_e>9keV, □ □ T_i>9keV, ◇ ◇ T_e and T_i>9keV, ⊙ ⊙ n_e>3.5×10^{19} m^{-3} ☆ ☆ pulse 16066 (Fig.1) and S S pulse 16981 (Fig.5).

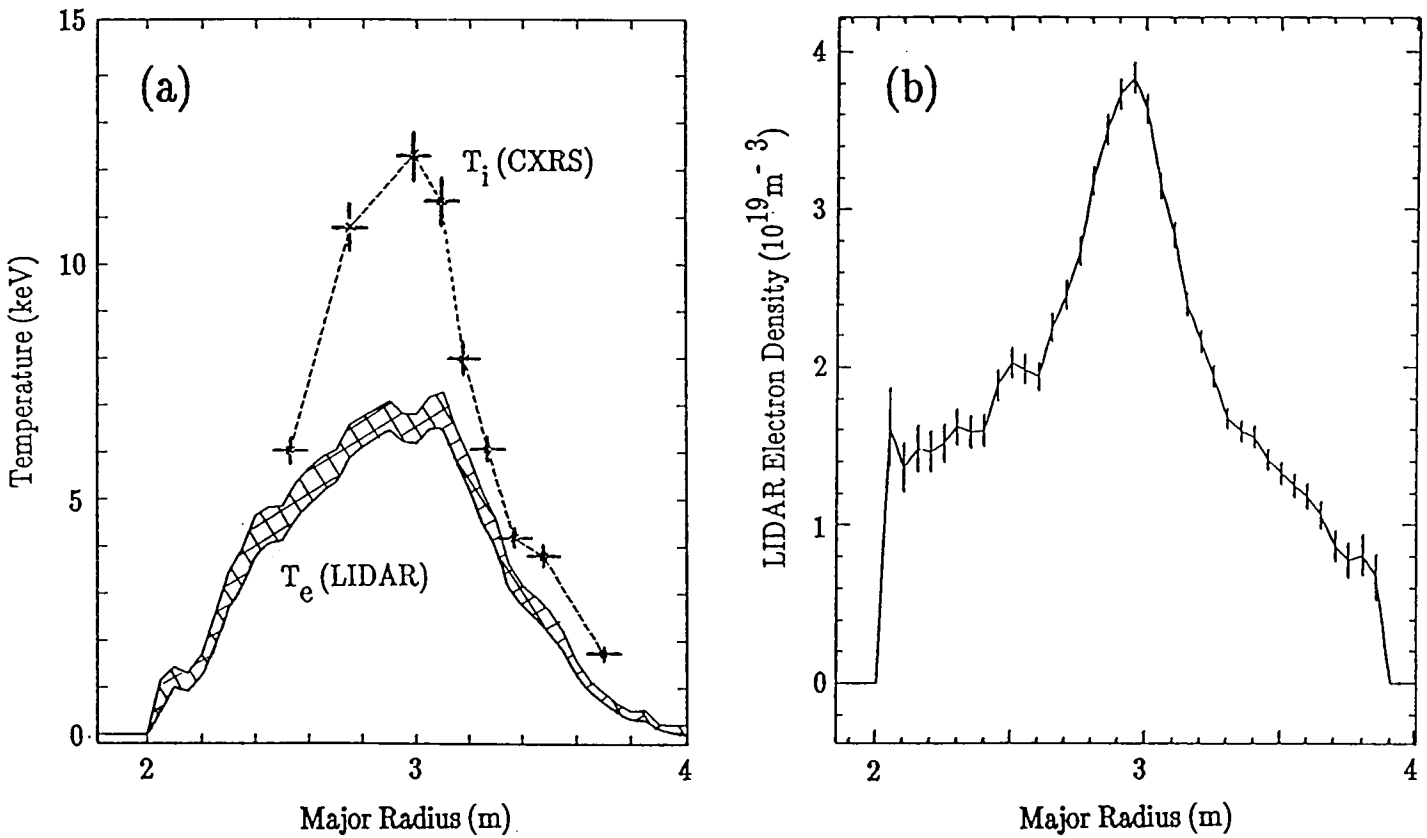

Fig. 5 (a) Electron and ion temperature profiles and (b) the electron density profile for the "supershot", JET pulse 16981.

EXPERIMENTAL AND THEORETICAL STUDIES OF ION CYCLOTRON HEATING ON JET

D F H Start, V P Bhatnagar, D A Boyd[1], M Bures, D J Campbell
J P Christiansen, P L Colestock[2], J G Cordey, W Core
G A Cottrell, L G Eriksson[3], M P Evrard[4], T Hellsten,
J Jacquinot, O N Jarvis, S Kissel, S Knowlton[5], H Lean[6],
P J Lomas, C Lowry, A L McCarthy[7], P Nielsen, J O'Rourke,
G Sadler, A Tanga, P R Thomas, K Thomsen, B Tubbing,
P van Belle and J Wesson

JET Joint Undertaking, Abingdon, Oxon, OX14 3EA, UK

[1] University of Maryland, College Park, Maryland, USA
[2] Princeton Plasma Physics Laboratory, New Jersey, USA
[3] Chalmers University, Gothenberg, Sweden
[4] LPP-ERM/KMS, EUR-EB Association, 1040 Brussels, Belgium
[5] Massachusetts Inst of Technology, Cambridge, Mass 02139, USA
[6] Culham Laboratory, Abingdon, Oxon, OX14 3DB, UK
[7] Flinders University, Bedford Park, 5042 South Australia

EXPERIMENTAL AND THEORETICAL STUDIES OF ION CYCLOTRON HEATING ON JET

ABSTRACT

Minority ICRF experiments are described which exploit the special features of highly localised heating and fast ion production. Power modulation during sawtooth stabilised periods has provided power deposition profiles, direct electron heating fractions and electron thermal diffusion coefficients inside the q = 1 surface. He^3-D fusion reaction experiments with energetic He^3 minority ions have produced 60kW of fusion power (Q ~ 0.5 %). These results agree well with both a Stix model and a combined global wave/Fokker Planck model. On-axis ICRH during the current rise of high current discharges ($I_p \geq 5MA$) has achieved central electron temperatures and D-D reaction rates up to twice as high as those obtained with heating in the current flat top. The first JET H-modes with substantial combined RF and neutral beam injection heating have been produced in a double null X-point configuration.

1. INTRODUCTION

Ion Cyclotron Resonance Heating (ICRH) on JET has reached a coupled power level of 18MW in limiter discharges. Such heating has achieved central electron and ion temperatures of 11.5keV and 8keV respectively, with H or He^3 minority heating of pellet fuelled plasmas in which the peaked density profile was sustained for 1.2 sec. During this time the electron thermal transport was approximately halved [1,2]. A plasma energy content of 7MJ has been attained with 13MW of RF power in a 5MA limiter discharge and about 0.7MJ of this energy resides in the H minority ions [2]. These energetic ions are presently thought to be a possible stabilising agent responsible for 'Monster' sawteeth [3,4]. Sawtooth-free periods have been produced by ICRH for up to 3 secs in deuterium and helium plasmas with either H or He^3 minority ions and occur for safety factors $q_{cyl} \geq 3.3$ [5]. At $q_{cyl} \sim 3.3$, optimum values of the incremental confinement time are found in RF heated limiter discharges. This effect is consistent with on-axis power deposition and a thermal diffusivity, χ_e, which decreases with increasing plasma current but increases as the size of the q = 1 surface increases [6]. Most recently combined RF + NBI (neutral beam injection) experiments have obtained D-D reaction rates up to 2.2×10^{16} s^{-1} in low density, inner wall plasmas [7]. In all the above experiments, the localised on-axis RF power deposition and the energetic minority ions play a key role. These aspects are also central to three of the studies presented in this paper, namely: RF power deposition and heat transport measurements using power modulation during sawtooth-free periods; He^3-D fusion experiments with He^3 minority energies in the MeV range; and improved heating of 5MA discharges by ICRH in the plasma current rise phase. The final section describes recent results of RF heating of double-null X-point plasmas.

2. MODULATION EXPERIMENTS DURING MONSTER SAWTEETH

Sawtooth-free periods enable power deposition profiles and electron transport to be studied inside the q = 1 surface without the complications caused by internal disruptions either locking to the modulation [8] or redistributing fast ions [9]. Experiments have been carried out with (H)He^3 and (He^3)D minority heating schemes and an example of the latter is described here. The deuterium limiter discharge parameters were as follows: plasma current, I_p = 2MA, central toroidal field, B_T= 3.4T, elongation, b/a = 1.5, central electron density, $n_e(0) = 4.2 \times 10^{19}$ m^{-3}, He^3 concentration, $n_{He^3} = 3 \times 10^{18}$ m^{-3} and effective ionic charge state, Z_{eff} = 1.9. The ICRH was applied with monopole phasing at a frequency of 32MHz to give on-axis heating. The power was square wave modulated at 4Hz between 6MW and 9MW. The response in the central electron temperature, $T_e(0)$ during the 1.5s sawtooth-free period was a triangular modulation with an amplitude of 0.25keV about a steady value of 7.7keV. The electron temperature profile was measured by a 12 channel ECE polychromator and the amplitude (Fig. 1a) and phase (Fig. 1b) of the 4Hz component $\tilde{T}_e$ was extracted by Fourier analysis. The amplitude is peaked in the plasma centre and is almost gaussian in shape with a maximum of 200eV and an e-folding width of 0.3m. The phase lag with respect to the RF power is close to 90° on axis and increases with increasing minor radius.

These results have been modelled by solving the heat diffusion equation for electrons in cylindrical geometry. The source term consisted of direct electron heating (by TTMP, electron Landau damping and mode conversion) and indirect heating by collisions with the minority ions. For simplicity, each component was assumed to be gaussian in profile with a width, W. The direct heating power density (50kW m^{-3} on axis) was obtained from the changes in $(\partial T_e/\partial t)$ at the RF switch-up (and switch-down) times so that the only free parameters in the model were W and χ_e.

The results of the calculations are shown in Figs. 1a and 1b for pairs of values of χ_e and W which fit both the amplitude and phase data. Values of χ_e less than $1.4 m^2 s^{-1}$ and greater than $2.8 m^2 s^{-1}$ lead, respectively, to too large and too small values of the peak $\tilde{T}_e$ amplitude. The observed modulated waveforms are also well reproduced when the exact power waveform is used as shown by the 'box-car' averaged signals in Fig. 2. The acceptable range of χ_e values depends on our assumption that all the coupled power appears as central heating. A check on this is given by the modulation on the Shafranov ($\tilde{E}_{mhd}$) and diamagnetic ($\tilde{E}_{dia}$) energy measurements. The total energy $\tilde{E}_{tot}$ is given by:

$$\tilde{E}_{tot} = \frac{2}{3} \tilde{E}_{mhd} + \frac{1}{3} \tilde{E}_{dia} \qquad (1)$$

and, for $\omega\tau_E >> 1$ (τ_E is the energy confinement time and ω is the modulation frequency), the power is determined from

$\tilde{P}_{tot} = \omega \tilde{E}_{tot}$. In the present case $\tilde{P}_{tot}$ is found to be 75% of the coupled RF power which, when taken into account, reduces the model values of $\tilde{T}_e$ by 15 - 20% and improves the fit for $\chi_e = 1.4 m^2 s^{-1}$ and $W = 0.19m$. However, such a low value of χ_e disagrees somewhat with a transport analysis fit to the steady temperature which favours $\chi_e \sim 3 m^2 s^{-1}$. The values of W (Fig. 1a) are somewhat less than that (0.2m) predicted by self-consistent global wave and Fokker Planck calculations [10]. This code also gives a central direct heating power density (TTMP + ELD) of 30kW m^{-3} compared with 50kW m^{-3} observed. The difference could be made up by mode conversion which is estimated at about 15% of P_{tot} but as yet its profile cannot be predicted.

3. He^3 - D FUSION YIELD MEASUREMENTS

The fusion reaction $He^3 + D \rightarrow He^4$ (3.6MeV) + p (14.7MeV) has been studied using (He^3)D minority ICRH in limiter plasmas with the following parameters: $2.5 < I_p(MA) < 4.5$, $3.1 < B_T(T) < 3.4$, $3 \times 10^{19}\ m^{-3} < n_e(0) < 6 \times 10^{19}\ m^{-3}$ and $1\% < n_{He^3}/n_e < 4\%$. RF power levels up to 15MW were coupled at a frequency of 32MHz and with the He^3 fundamental cyclotron resonance within 0.1m of the magnetic axis. The reaction rate was measured by detecting the weak γ-ray branch from the 16.6Mev level in Li^5 using NaI and BGO scintillators [9]. An example of the γ-ray spectra is given in Fig. 3a. The count rate is a rapidly increasing function of the RF power as shown in Fig. 3b, where the maximum value corresponds to 2×10^{16} reactions per second, a fusion power of 60kW and a Q ($= P_{fus}/P_{RF}$) value of 0.5%.

The results have been compared with both a Stix model [11] and the more sophisticated, combined wave absorption and Fokker-Planck calculation [10], In the Stix model the reaction rate R inside a flux surface of minor radius r is given by:

$$R = 2 \times 10^{15} \int_o^r (A/Z^2 \ln\lambda)(n_D/n_e)\, P_d T_e^{3/2} < \sigma v > / T_t \, r dr \qquad (2)$$

in which A and Z are the atomic mass number and charge of the minority ions, n_D is the deuterium density, P_d is the RF power density, $< \sigma v >$ is the rate coefficient averaged over the distribution functions and T_t is the He^3 tail temperature. The reaction rate was calculated using the observed profiles of T_e and n_e and a gaussian power density profile with a width of 0.2m consistent with the modulation experiments and power deposition calculations. Typical radial profiles of P_d, T_t and dR/dr (the reaction rate for each flux surface) are shown in Fig. 4a. Note that the maximum contribution to the reaction rate is 0.26m off axis where the tail temperature is ~ 0.5MeV. In the centre, T_t is 5MeV and a large fraction of the He^3 ions have energies beyond that at which the cross-section peaks. The reduction of the slope of the fusion yield curve at high RF power (Fig. 3b) is due to this overheating of the minority ions so that an improvement may be gained by tailoring P_d using several RF frequencies, for example.

The observed and predicted reaction rates are compared in Fig. 4b. In the calculations, the fraction of the coupled RF power absorbed by the He^3 minority ions was taken to be 65% which was found to best reproduce the observed fast ion energy content and is in reasonable agreement with the modulation experiments ($P_{tot} \sim 0.75\ P_{coupled}$) when direct electron heating is taken into account. A dilution factor $n_D/n_e = 0.3$ was found to give the best simulation of the observed yields. The global wave/Fokker Planck calculations also reproduce the data well and require slightly higher dilution factors, $n_D/n_e \sim 0.45$. These values are within the range $0.25 < n_D/n_e < 0.5$ obtained from D-D thermal reaction rate measurements and are consistent with $n_D/n_e \sim 0.3$ obtained from TRANSP modelling of D-D beam-plasma fusion rates [6]. Similar values have also been deduced from measurements of Z_{eff} profiles.

4. RF HEATING DURING CURRENT RISE PHASE

The objective of applying central ICRH during the rise of the discharge current was to heat the plasma before the onset of sawtooth activity, particularly for high plasma currents $I_p \geq 5MA$, where Monster sawteeth are difficult to produce. By virtue of the raised electron temperature, the ICRH also slows the current penetration to the plasma core thereby delaying the onset of sawteeth. Fig. 5a shows how the first sawtooth crash occurs progressively later in time as $T_e(0)$ and the RF power are increased. In this case, (H)D minority heating (dipole phasing) was used at 48MHz and $B_T = 3.1T$. At 43s the plasma current was 3MA and reached its steady value of 5MA at 47.2s. The saturation of the current penetration is shown by the polarimetric measurement of the central safety factor q(0). The first sawtooth crash occurs when q(0) is close to unity but note that the reduction in $T_e(0)$ is large (2 - 3keV) implying that $q(0) \approx 1$ over a substantial part of the plasma core. This is supported by T_e profile measurements which show the inversion radius to be ~ 40cm compared with ~ 15cm for the ohmic discharges at the first sawtooth crash. In this respect, the crash is characteristic of Monster sawteeth, and indeed a Monster sawtooth has been seen following normal sawteeth during the current rise of a 6MA discharge. Thus both current profile effects and the stabilisation mechanism responsible for Monster sawteeth are apparently involved in enhancing these discharges.

The improvements gained from this method of operation are a large increase (a factor ~ 2 in the best case) in $T_e(0)$ as shown in Fig. 5b, an increase in $T_i(0)$ by 10 - 20%, a similar improvement in the incremental confinement time and almost a factor of 2 gain in neutron yield from D-D reactions for RF power levels in excess of 13MW.

5. X-POINT DISCHARGES WITH ICRH

The double-null X-point geometry in JET provides a good match between the curvature of the antennae and the last closed flux surface and allows RF power to be coupled at plasma-limiter separations greater than the minimum of 3cm required for H-mode

formation. With this configuration H-modes have been obtained in 3MA discharges using combind NBI and central (H)D minority ICRH at power levels in the region of 8MW and 6MW respectively. Comparisons with beam-only H-modes show that the rate of rise of the radiation is greater (typically by a factor of two) with combined heating and this has the effect of shortening the H-mode, since the H-L transition occurs when $P_{rad} \approx P_{tot}$. Also, the confinement time in the combined heating case is reduced by typically 30%. With RF heating alone, the D_α light indicates short periods (~ 0.5s) of reduced deuterium recycling characteristic of H-mode formation. Following such periods the radiation decreases substantially and dn_e/dt changes sign indicating a sudden reduction in particle confinement. Both effects are seen after the H-L transition in beam heated plasmas. However, in the RF only case, the 'pedestal' edge electron temperature of 0.3keV is less than the H-L transition temperature (~ 0.5keV) and the energy confinement of 0.3s is symptomatic of an L-mode. So far, only a few attempts have been made to study H-modes with ICRF or combined heating and as yet the reason for the poorer H-modes is not completely understood. If impurities are the cause, then the new beryllium antenna screens could be greatly beneficial.

6. SUMMARY

The spatial extent of the ICRF power deposition and the ratio of direct to indirect electron heating have been obtained from modulation experiments and agree reasonably well with global wave calculations. Values of χ_e have also been deduced and are somewhat smaller than those given by transport analysis of the steady state. The acceleration of minority ions by ICRF to high energies has been utilised to produce 60kW of fusion power by the He^3-D reaction which agrees with theoretical expectations. On-axis heating during the current rise phase has substantially improved the performance of high current discharges. The best use of the ICRH peaked deposition so far has been to reheat the peaked density profiles produced by pellets [1,2] which benefit from good central confinement and yield one of the highest $n_D \tau_E T_i(0)$ values obtained so far in JET.

7. ACKNOWLEDGEMENTS

We wish to acknowledge the assistance of all our colleagues in the JET team. Particular thanks go to the tokamak operating team and to the members of the diagnostic groups contributing to these measurements.

8. REFERENCES

[1] SCHMIDT, G.L. et al, "Heating of peaked profiles produced by pellet injection", paper A-4-1 this conference.

[2] JACQUINOT, J. et al, "High power ion cyclotron heating in JET", Plasma Physics and Controlled Fusion, to be published.

[3] COPPI, B., HASTIE, R.J., MIGLIOLO, S., PEGORARO, F., PORCELLI, F., "Suppression of internal plasma oscillations by trapped high energy nuclei", Phys. Lett. A to be published.

[4] WHITE, R.B. RUTHERFORD P.H., COLESTOCK, P. and BUSSAC, M.N., "Sawtooth stabilisation by energetic trapped particles", Phys. Rev. Lett. 60(1988).

[5] CAMPBELL D.J. et al, "Sawtooth activity and current density profiles in JET", paper A-7-2, this conference.

[6] BHATNAGAR, V.P. et al, "Effect of sawteeth and safety factor q on confinement during ICRF heating on JET", Controlled Fusion and Plasma Heating (Proc. 15th European Conf. Dubrovnik 1988), Europhysics Conference Abstracts, Vol. 12B, p 358, 1988.

[7] THOMAS, P.R. et al, "High temperature and high neutron yield experiments in JET", paper A-4-4, this conference.

[8] GAMBIER, D.J. et al, "ICRF power deposition profile and determination of χ_e by modulation experiments in JET", submitted to Nuclear Fusion.

[9] SADLER, G., JARVIS. O.N., VAN BELLE, P. and ADAMS, J.M., "Diagnosing RF-driven high energy minority tails with γ-ray and neutron spectroscopy", Controlled Fusion and Plasma Heating (Proc. 15th European Conf. Dubrovnik 1986), Europhysics Conference Abstracts, Vol. 2B, p. 131, 1986.

[10] ERIKSSON, L.G. et al, "Calculations of power deposition and velocity distributions during ICRH, a comparison with experimental results", submitted to Nuclear Fusion.

[11] STIX, T.H., "Fast wave heating of a two-component plasma", Nuclear Fusion 15(1975)737.

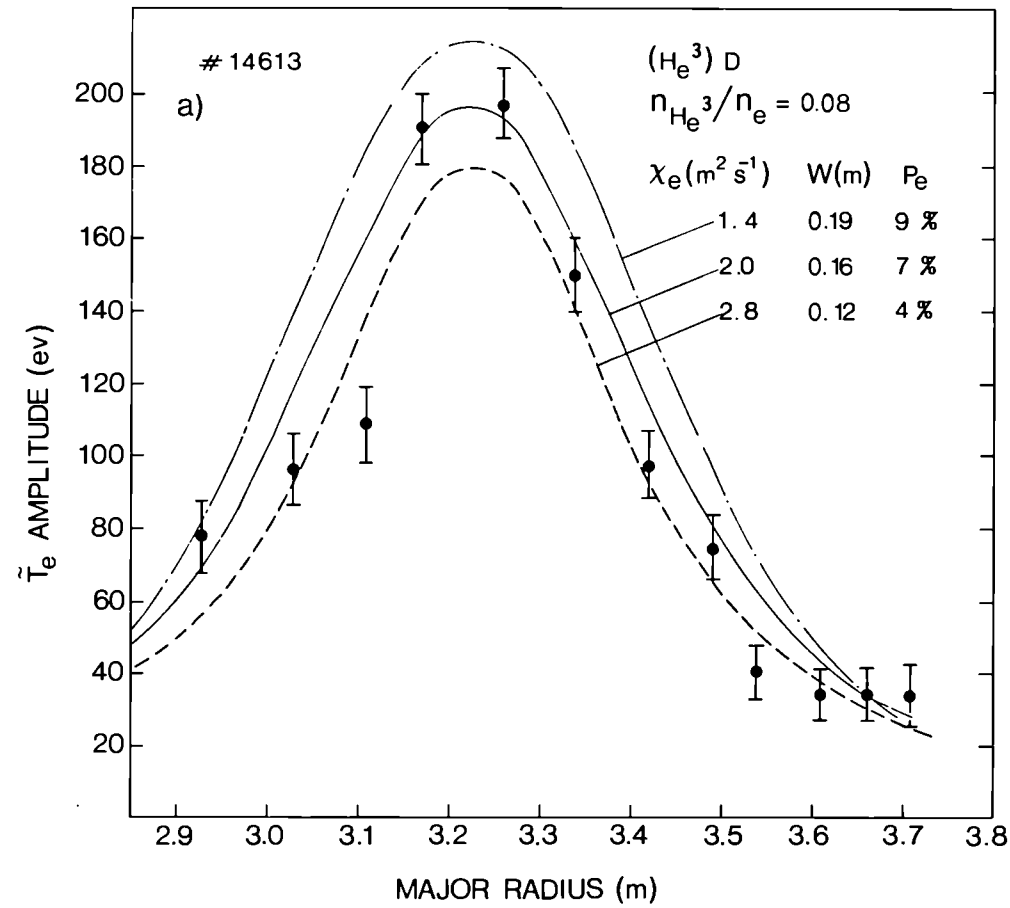

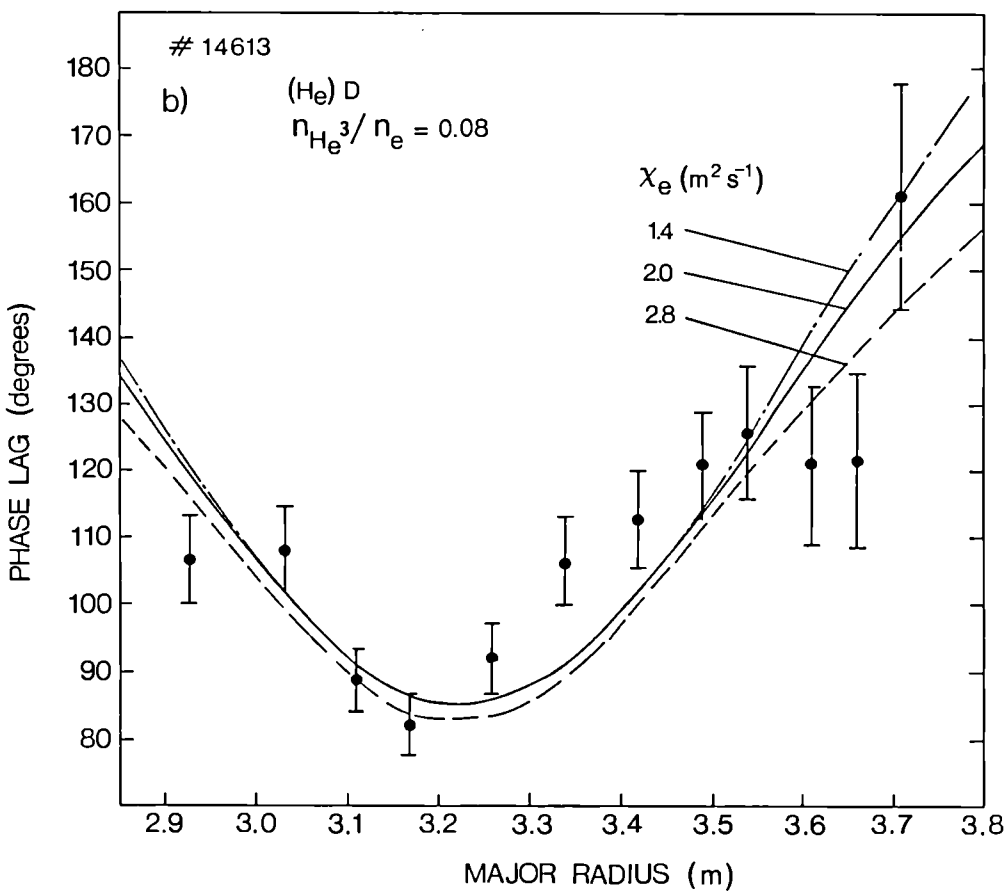

Fig. 1 Amplitude (a) and phase (b) of the electron temperature response to ICRF power modulation

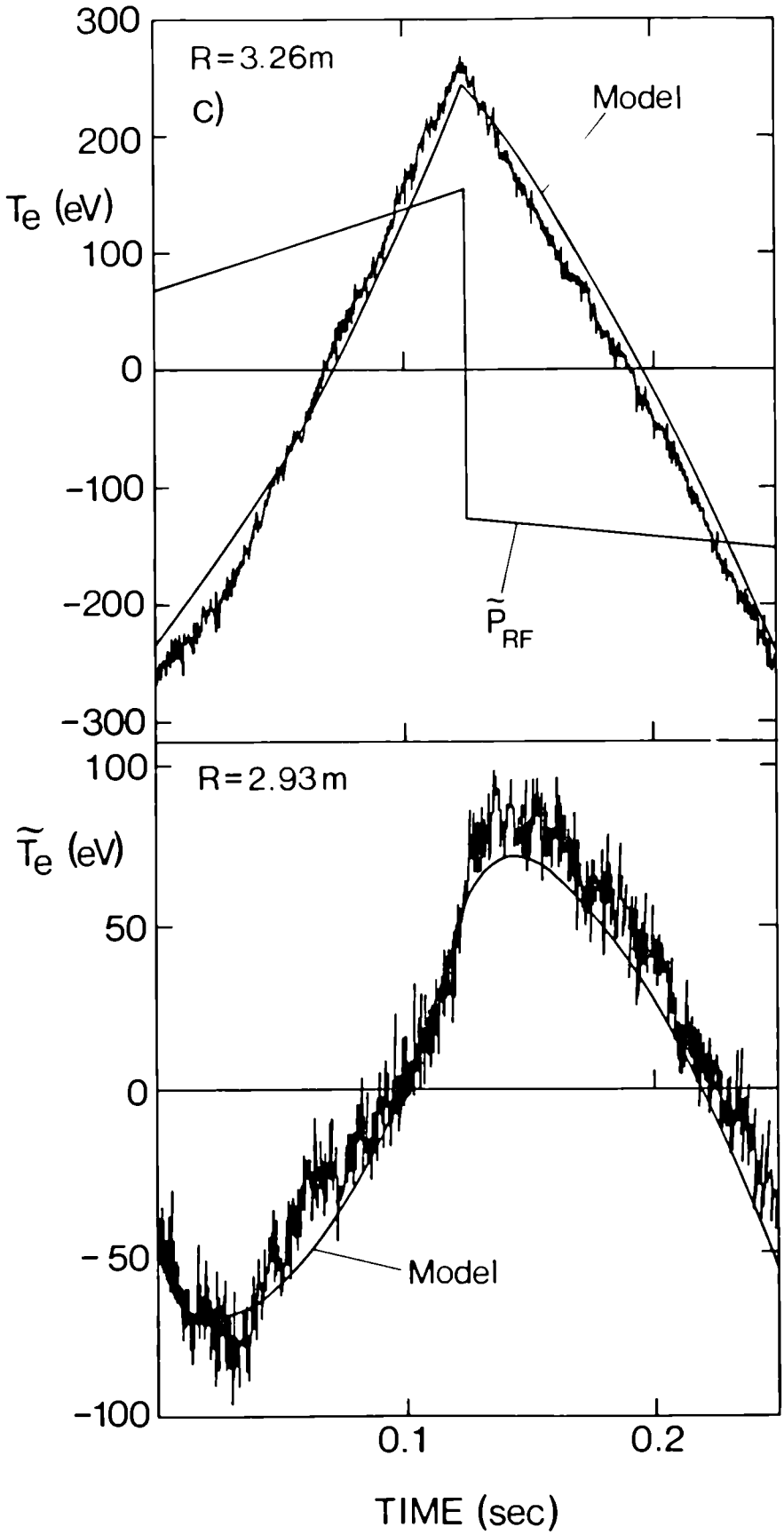

Fig. 2 Comparison of 'box-car' averaged signals at R = 2.93m and R = 3.26m with model calculations

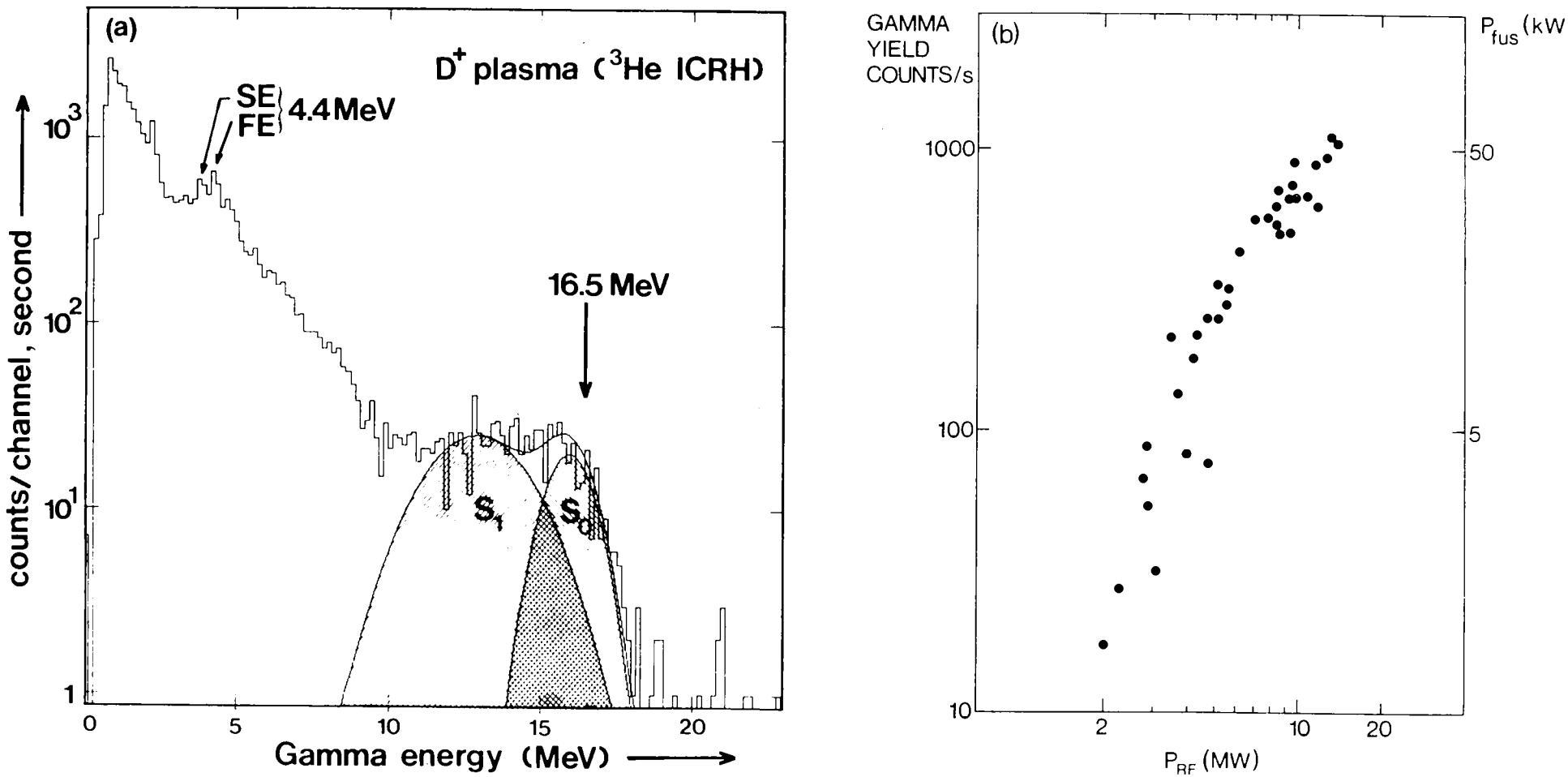

Fig. 3 a) Gamma-rays from the decay of the 16.66MeV state of Li^5 to the ground (S_o) and first (S_1) excited states, b) Fusion power and γ-ray intensity versus RF power

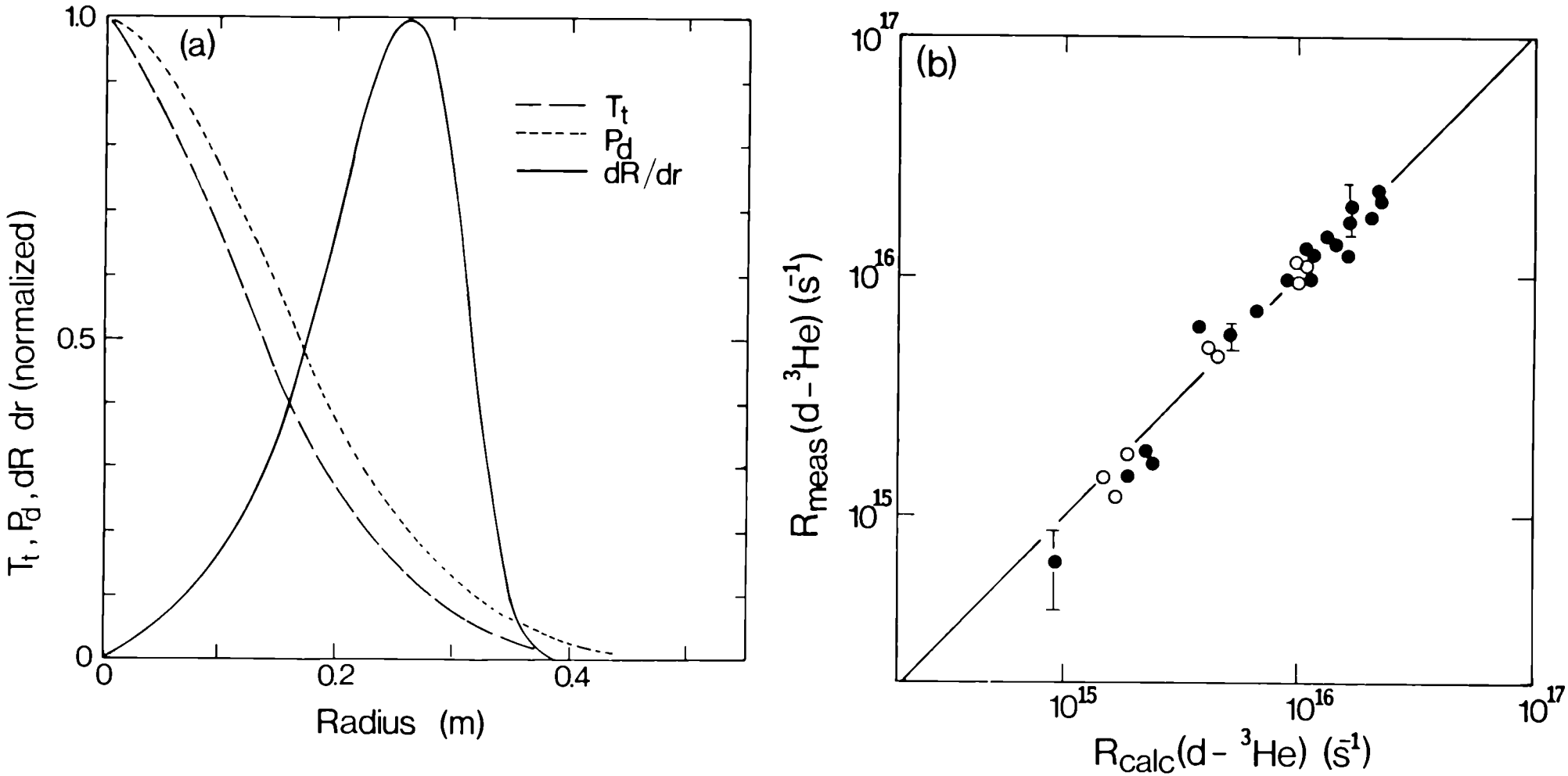

Fig. 4 a) Model profiles of power density, He^3 tail temperature and fusion yield, normalised to on-axis values, b) Comparison of measured and calculated reaction rates

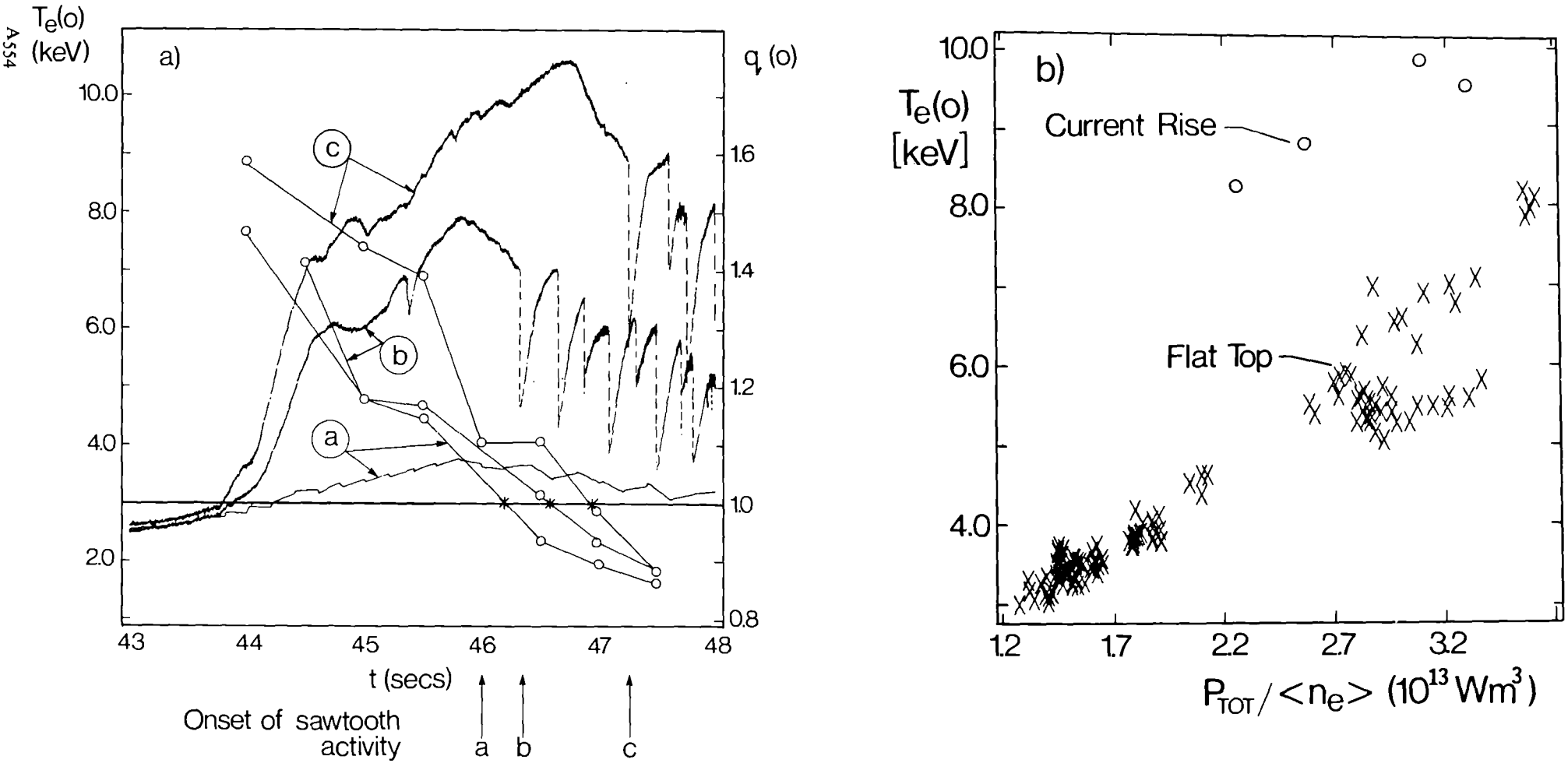

Fig. 5 a) Central electron temperature and safety factor, q(0), during ICRH in the current rise phase. Curves (a), (b) and (c) are for RF power levels of zero, 4.3MW and 11MW respectively, b) Comparison of $T_e(0)$ values obtained during the current rise and flat top phases

A-VII-12.2

THE PLASMA BOUNDARY IN JET

L de Kock, P E Stott, S Clement[1], S K Erents[2], P J Harbour, M Laux[3], G M McCracken[2], C S Pitcher[2], M F Stamp, P C Stangeby[4], D D R Summers and A J Tagle

JET Joint Undertaking, Abingdon, Oxon OX14 3EA, UK

[1] Association CIEMAT-Euratom, Madrid, Spain
[2] UKAEA Culham Laboratory, Abingdon, Oxon, UK
[3] Central Institute of Electron Physics, Academy of Sciences, Berlin, GDR
[4] Institute for Aerospace Studies, Universtiy of Toronto, Canada

THE PLASMA BOUNDARY IN JET

ABSTRACT

The parameters of the scrape-off layer in JET are presented for the case of the new belt limiters and compared with the earlier case of 8 discrete limiters. The scaling with the main plasma parameters is found to be similar and fits a model that correctly describes the dependence on the mean plasma density but shows a discrepancy with the input power.

The carbon influx relative to the deuterium influx, derived from spectroscopic measurements, is compared with the influx calculated from the measured SOL parameters using the physical sputtering plus carbon self-sputtering and the charged particle flux on the belt limiter. Both ratios show a decreasing trend with increasing density, although a discrepancy at low density remains.

The SOL in neutral beam heated discharges, although not steady state, shows a behaviour comparable with that in OH limiter discharges. However in discharges with radio-frequency heating the SOL parameters are instantaneously affected by the r.f. power and its behaviour depends on wall conditions.

Some typical measurements of the SOL parameters in divertor plasmas are given showing that in the outer divertor the plasma is hotter than in the inner one (with correspondingly lower and higher density respectively). Power flow to the outer divertor is higher than to the inner one and the temperature difference indicates that net currents must flow in the SOL.

1. INTRODUCTION

Edge conditions are important in tokamaks as they determine; impurity production by sputtering at the limiter, the ability of the scrape-off layer to screen impurities from the core of the discharge and the establishment of the H mode of enhanced confinement in discharges with a magnetic separatrix. Experimental measurements have been made with Langmuir probes and other diagnostics. Empirical scalings of the scrape-off layer parameters in terms of the main discharge parameters have been established and compared with models of the scrape-off layer. In this paper we review our understanding of Ohmic and additionally heated discharges in limiter and divertor configurations.

2. EXPERIMENTAL RESULTS

(a) Edge Parameters Measured by Means of Langmuir Probes

During the past year JET has operated in limiter and divertor configurations. The limiters are two carbon belts, located on the outboard side of the discharge, approximately ± 1 m from the mid plane. The divertor operation has been mainly single null with the power deposited on carbon tiles at the top of the

vessel. Profiles of scrape-off layer parameters have been measured with a reciprocating Langmuir probe located at the top of the vessel, roughly mid-way between the divertor target tiles and the upper belt limiter. Additional data have been obtained with fixed probes mounted in belt limiters, ICRH antennas and divertor target tiles, and also with a variety of other diagnostics including infrared cameras, spectroscopy, microwave reflectometry and a high resolution ECE system.

Measurements at different toroidal and poloidal positions indicate that these observations are representative of the SOL. A extensive data base of scrape-off layer parameters was established with fixed probes during previous years of operation of JET when there were 8 discrete carbon limiters on the torus mid plane [1]. Measurements with the reciprocating probe in the new belt limiter configuration (the points in Fig. 1) are consistent with the discrete limiter data base (the lines in Fig. 1). In the discrete limiter case the density at the last closed flux surface $n_e(a)$ scales as $\langle n_e \rangle I_p$ and the temperature $T_e(a)$ as $I_p^2/\langle n_e \rangle^2$ [2]. Care has been taken to make these measurements when particle and energy balance have reached steady state. The e-folding length of SOL density at the outer midplane λ_n is usually in the range of 10 mm and the scaling with I_p appears to be $\lambda_n \alpha I_p^{-1}$ rather than $\lambda_n \alpha I_p^{-1/2}$ which might be expected due to constant $D_\perp$, plasma q and connection length effects.

During NB heating in limiter discharges the central density increases and a steady state cannot be obtained. Two competing processes take place in the SOL. The higher power conducted to the SOL causes the edge temperature initially to rise, delayed by the slowing down time of the fast particles, while later the edge temperature decreases when the density rise due to beam fuelling reaches the edge [3]. There is little change in SOL thicknesses. With RF heating the SOL parameters react nearly instantaneously to the applied power indicating a direct power deposition. Edge temperature and density both increase. Scrape-off lengths frequently increase but λ_n is not affected for a very well conditioned vessel (low impurity influx; low gas release) [4]. In these cases the discharge usually reaches a steady state. Mixed heating schemes show a mixture of these effects and can only be used for approximate studies of operational conditions and limitations.

In the divertor configuration, profiles along a poloidal contour obtained from fixed Langmuir probes in the target tiles are shown in figure 2 for a 4.5 MA discharge for both OH and H-modes. The inner and outer separatrix positions are indicated. The inner divertor plasma is colder and denser than the outer; more power is carried to the outer.

Detailed measurements of radial profiles have been made with the reciprocating probe. Figure 3 shows profiles obtained in the Ohmic and Ohmic + ICRH phase of a 3 MA; 3.4 T discharge (taken from two similar discharges). The change in slope in the density SOL is interpreted as indicating that the probe has

crossed the LCFS. Figure 4 shows a similar case for a 3 MA; 2.1 T diverted discharge in H-mode conditions (ie. with NBI). Scrape-off lengths from this probe can only be compared to those obtained with the fixed probes in the target tiles by taking the magnetic configuration ie. compression of magnetic flux surfaces, into account [5]. The ratio of the saturation current on ion and electron side is shown to range from 0.3 to 3. It is less than unity near the outer separatrix but further out it exceeds unity.

(b) Spectroscopic studies of impurity influxes

The main impurities in JET are carbon and oxygen. Some nickel is introduced from the antenna screens during RF heating.

The SOL parameters have been used to calculate the carbon influxes using physical sputtering yields [6] and including carbon self sputtering. The influxes have been integrated over the SOL. The results are presented here as the ratio of sputtered carbon flux Γ_C to the deuterium flux Γ_D incident on the belt limiter (Fig. 5).

For the spectroscopic measurements of influxes, plasma light emitted from areas in front of limiters or wall is collected by telescopes and transmitted by means of a quartz optical fibre (100 m) to spectrometers or detectors equipped with narrow band interference filters. Using atomic constants the influx can be derived from the spectroscopic line intensities and the measured density and temperature profiles. The telescopes observe only a small part of the interaction area. Usually simultaneous measurements of hydrogen, impurities and continuum (for Z_{eff}) are taken [7].

The ratio of carbon to deuterium influx is also obtained experimentally from spectroscopy (Fig. 5). In steady state the local recycling must be close to R=1 and the deuterium influx must be equal to the flux onto the surface. The data refer to a series of discharges where density flat tops at various values were obtained after pellet injection. Both calculated and spectroscopic results show a decreasing trend with $\langle n_e \rangle$.

Oxygen influxes often behave erratically and are only partially understood. Comparison of the behaviour of D_2 and He-discharges indicates that chemical processes involving oxygen are important [8].

Metal impurities, such as nickel, originating from the inconel wall or from the nickel Faraday screen of the RF antennas during the application of RF power are due to localised effects and are not easily explained by the overall SOL parameters. However the removal of metals from the limiters is consistent with the limiter sputtering model [10].

3. INTERPRETATION AND DISCUSSION

The experimental scalings of $T_e(a)$ and $n_e(a)$ as a function of I_p and $\langle n_e \rangle$, are shown in figures 1A, 1B. The indication that JET

has a relatively uniform SOL, has stimulated an effort to model the SOL behaviour from basic principles. The experimental scaling $n_e(a) \alpha I_p \langle n_e \rangle$ may be approximated by $n_e(a) \alpha \langle n_e \rangle^2$ and this relation can be modelled by simple particle diffusion [11,12,13]. The power to the SOL, P_L, ie. the difference between input power and the radiation losses was then taken as a variable. The carbon impurity influx was calculated using the physical sputtering model for carbon [6]. Radiation losses were derived from central carbon concentrations obtained by the analytical transport model of Engelhardt [11].

Assuming simple parallel transport without impurity production we obtain: $T_e(a) \alpha P_L^{2/3}/\langle n_e \rangle^{4/3}$. Including physical sputtering and radiation in a self consistent way yields $T_e(a) \alpha P_L^{0.6}/\bar{n}_e^{1.7}$ [14]. For the comparison of the experiment with the model we note that the loop voltage $V_\ell \approx 1$ V and is approximately constant so that $I_p \alpha P$. Since the radiated power is 40-60% of the input power we obtain for the experimental scaling $T_e(a) \alpha P^2 \langle n_e \rangle^{-2}$. We note that the density scaling agrees well, but that the scaling with power shows a discrepancy. However, the strong dependence on density shows that this is the main controlling factor in the decrease of the temperature and thus sputtering (due to the fall in yield at lower impact energies). The discrepancy with power dependence is due to the change of the SOL thickness with current and more careful examination and further refinement is required for understanding.

Transport of particles and energy described by $D_\perp$ and $\chi_\perp$ can in principle be derived from λ_n and λ_T. λ_n is approximately constant over several orders of magnitude in the SOL profile indicating that $D_\perp \alpha T_e^{1/2}$ (locally). Values of $D_\perp \sim 0.5$ to 4 m^2/s have been deduced [14,15].

Experimental and calculated results for the relative carbon influxes (Fig. 5) are similar. At low density the spectroscopic results show a higher relative carbon influx. Most of this discrepancy is due to the difference between the charged ion flux onto the limiter and that inferred from Dα measurements. The decrease in the relative carbon influx with increasing $\langle n_e \rangle$ is also reflected in the behaviour of the central concentration of carbon which falls with increasing $\langle n_e \rangle$ and increases with I_p [8]. The apparent agreement is maybe fortuitous because there are indications that the sputtering yield under high ion fluxes [9] is higher than the values used in the sputtering model and the sputtering of carbon by oxygen has been ignored.

The data for divertor discharges, which show the outer separatrix hotter than the inner one suggest that a net thermo-electric current must flow in the SOL [16]. This current has been observed ($I \lesssim 10^5$ A/m²) [17,18]. The high ratio of the ion saturation current on opposite sides of the probe (Fig. 4) indicates a flow towards the divertor in the outer region of the SOL and the low ratio implies a reverse flow closer to the separatrix, consistent with high recycling conditions there.

It is sometimes argued that the local recycling in the divertor enables the main plasma to be screened from impurities, but this flow out of a divertor will tend to degrade this screening effect.

4. CONCLUSION

Although many uncertainties remain, it appears that the main mechanisms describing the SOL parameters in relation to the main plasma parameters can be identified and have been modelled analytically with a fair degree of success. In limiter discharges the impurity influx of carbon has been calculated from a sputtering model using measured SOL parameters. It is in good agreement with spectroscopic measurements at higher densities, but shows a deviation at the low densities. The equivalent impurity influx calculation in diverted discharges is not yet possible. The non steady state of the additionally heated discharges makes them less accessible to accurate modelling. However, the trends can be recognised by taking the observed density rise and the increased power conducted to the SOL and referring to the experimental scaling of the limiter discharges. To obtain the lowest possible carbon impurity concentration in JET, discharges have to be operated at the highest possible density at any given level of input power.

REFERENCES

[1] ERENTS, S.K., TAGLE, J.A., McCRACKEN, G.M., STANGEBY, P.C., DE KOCK, L., Nucl. Fusion 26 (1986) 1591-1603.

[2] TAGLE, J.A., ERENTS, S.K., McCRACKEN, G.M., PITTS, R.A., STANGEBY, P.C., LOWRY, C.G., STAMP, M.F., 14th European Conf. on Controlled Fusion and Plasma Physics. Europhysics Conf. Abstracts, Vol 11D, part II, 662.

[3] ERENTS, S.K., TAGLE, J.A., McCRACKEN, G.M., ibid, part II, 740.

[4] TAGLE, J.A., et al, 8th Int. Conf. on Plasma Surface Interactions, 1988, to be published in J. Nucl. Mat.

[5] ERENTS, S.K., et al, ibid.

[6] BOHDANSKY, J., Data Compendium for Plasma-Surface Interactions, Nucl. Fusion Special Supplement 1984 (1984) 61.

[7] STAMP, M.F., BEHRINGER, K.H., FORREST, M.J., MORGAN, P.D., SUMMERS, H.P., 8th Int. Conf. on Plasma Surface Interactions 1988 to be published in J. Nucl. Mat.

[8] BEHRINGER, K., DENNE, B., FORREST, M.J., MORGAN, P.D., STAMP, M.F., ibid.

[9] GOEBEL, D.M., et al. Nucl. Fusion 28 (1988) 1041.

[10] McCRACKEN, G.M., GOODALL, D.H.J., STANGEBY, P.C., COAD, J.P., ROTH, J., 8th Int. Conf. on Plasma Surface Interactions, 1988, to be published in J. Nucl. Mat.

[11] ENGELHARDT, W., et al, J. Nucl. Mat. 111 & 112 (1982) 337.

[12] ALEXANDER, K.F., et al, Nucl. Fusion 26 (1986) 1575.

[13] STANGEBY, P.C., et al, J. Nucl. Mat. 145-147 (1987) 105.

[14] ERENTS, S.K., TAGLE, J.A., McCRACKEN, G.M., STANGEBY, P.C., KOCK DE, L., Nucl. Fusion 28 (1988) 1209.

[15] STANGEBY, P.C., TAGLE, J.A., ERENTS, S.K., LOWRY, C., J. Plasma Physics and Controlled Fusion, in press.
[16] HARBOUR, P.J., Workshop on Plasma Edge Theory in Fusion Devices, Augustusburg, GDR, 1988, to be published in Contributions to Plasma Physics (Akademie-Verlag, Berlin, GDR).
[17] HARBOUR, P.J., et al, 8th Int. Conf. on Plasma Surface Interactions, 1988, to be published in J. Nucl Mat.
[18] KEILHACKER, M., et al, paper AIII-2, this conference.

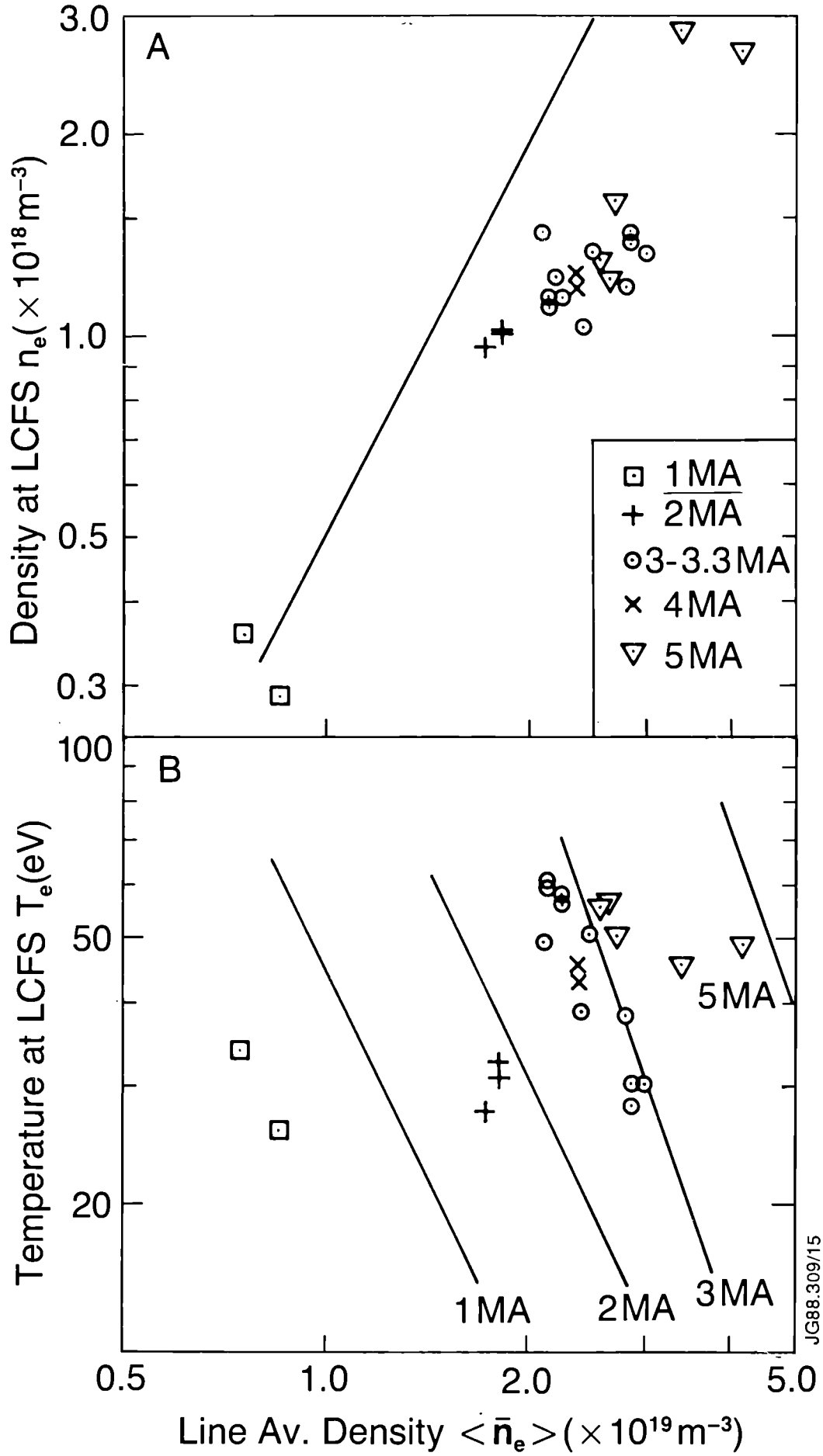

Fig. 1A: The edge density $n_e(a)$ as a function of $\langle n_e \rangle$. The 8 limiter case is shown as drawn lines (from [2]) and the belt limiter case as discrete data points.

B: The edge temperature $T_e(a)$ as a function of $\langle n_e \rangle$ with I_p as parameter.

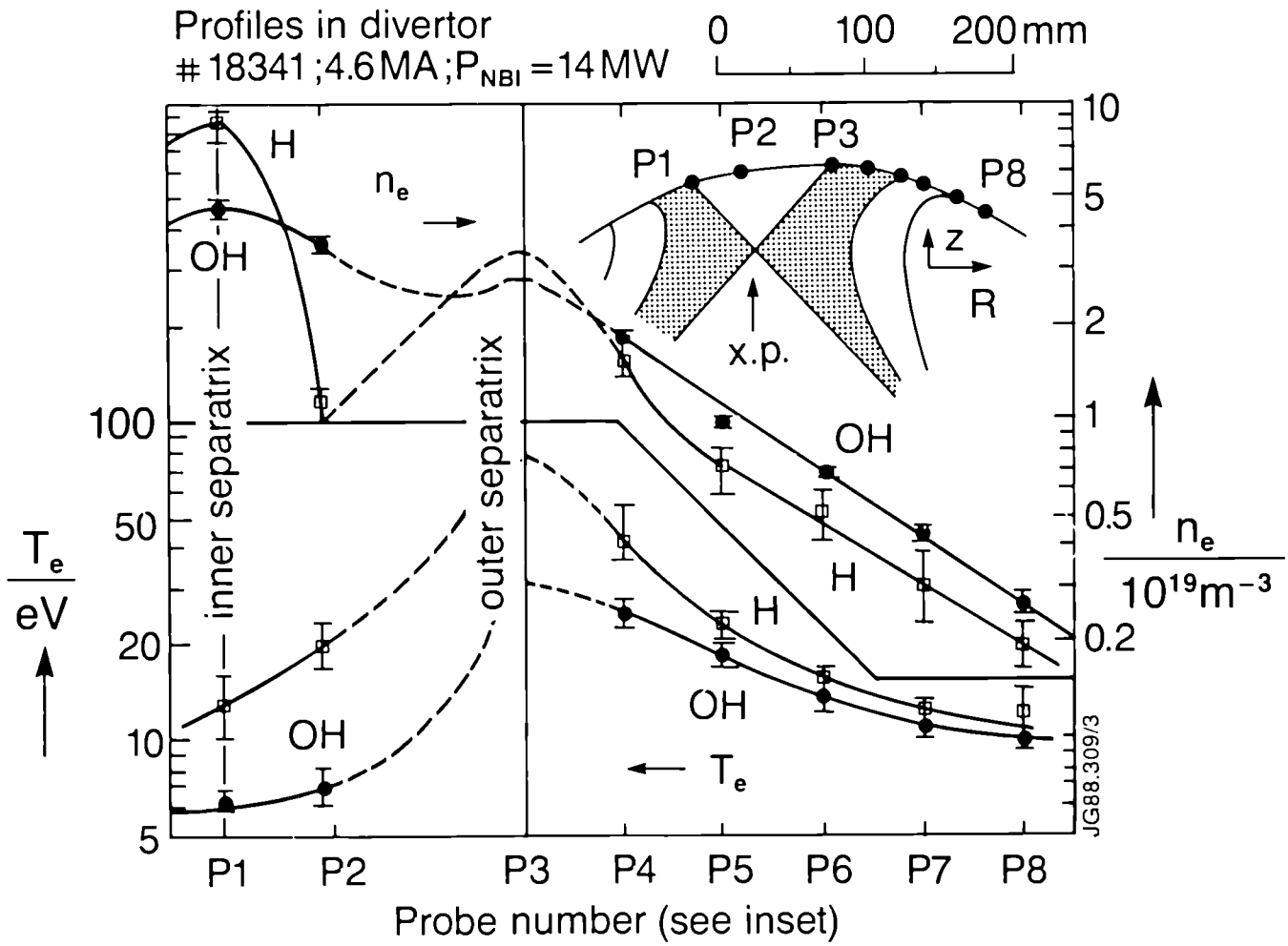

Fig. 2: Profiles of n_e and T_e along the poloidal contour of the divertor target plates. Both the Ohmic and the H mode phase are shown. Discharge parameters I_p = 4.6 MA; B_T = 2.7 T, P_{NB} = 14 MW.

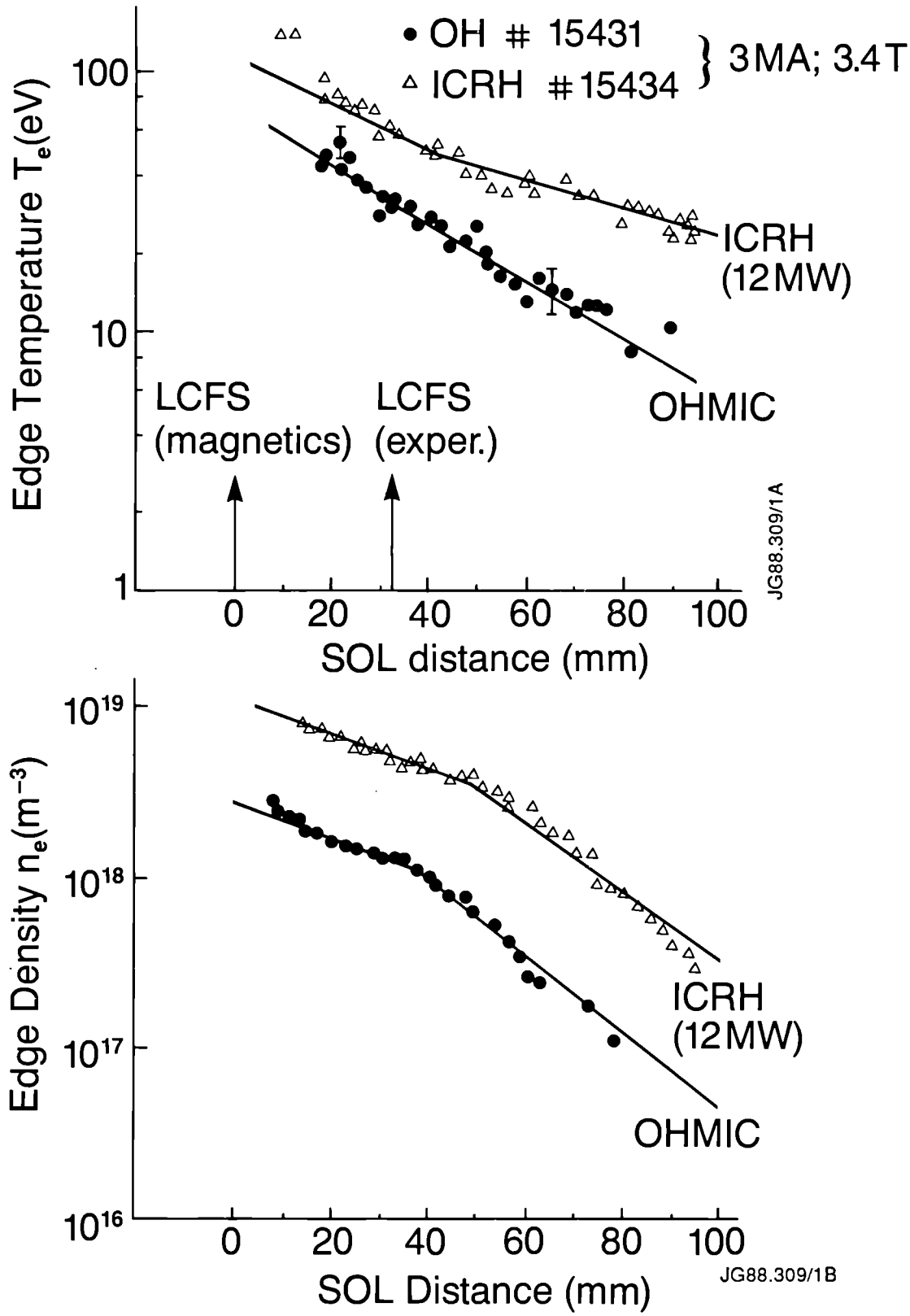

Fig. 3: Reciprocating probe measurements of $n_e(r)$ and $T_e(r)$ in one Ohmic and one Ohmic + ICRH discharge of I_p = 3 MA; B_T = 3.4 T, P_{ICRH}= 12 MW.

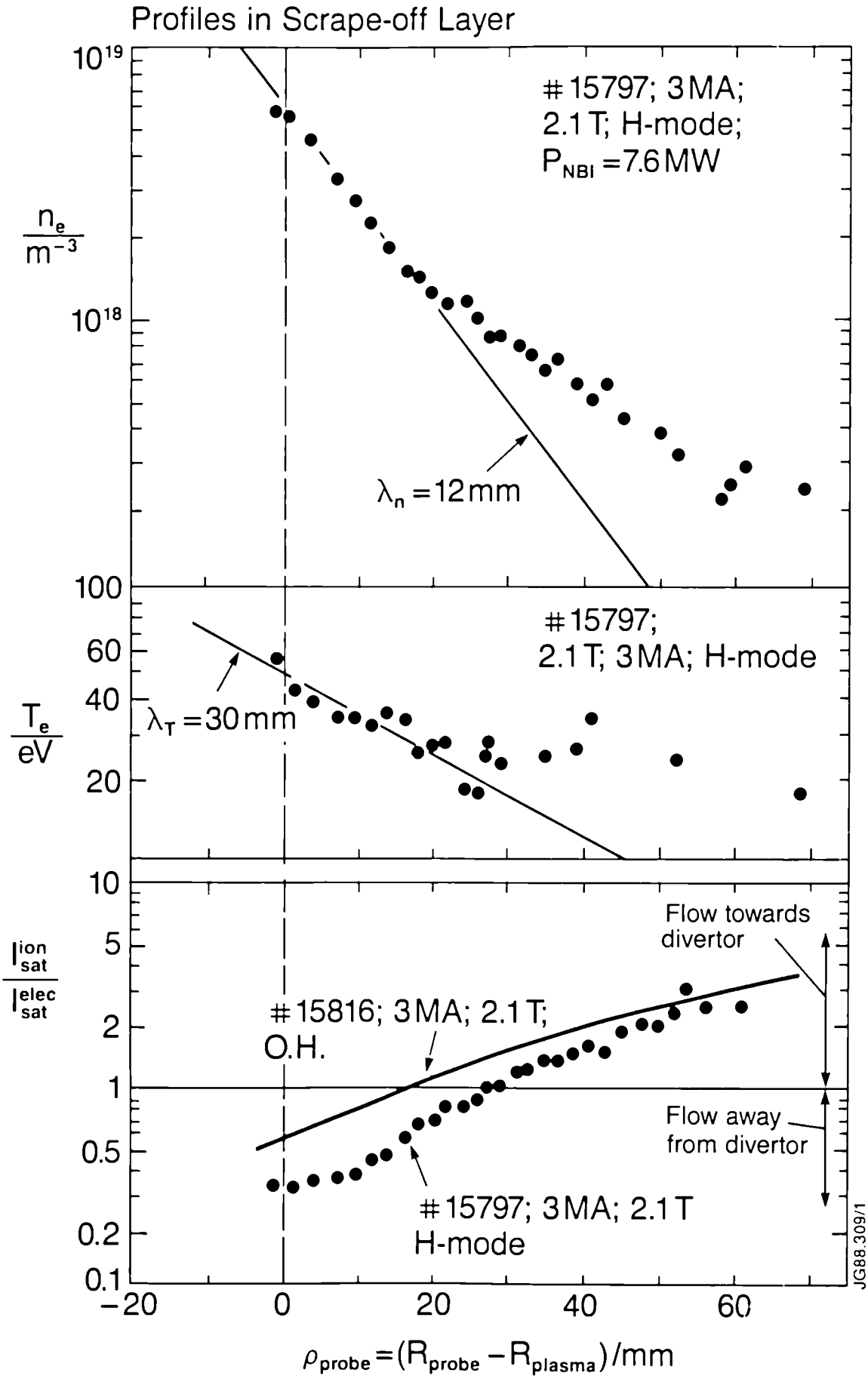

Fig. 4: Reciprocating probe measurements of $n_e(r)$; $T_e(r)$ and $I^{ion}_{sat}/I^{elec}_{sat}$ in a I_p = 3 MA; B_T = 2.1 T diverted discharge in the H-mode phase. P_{NB} = 7.6 MW.

A565

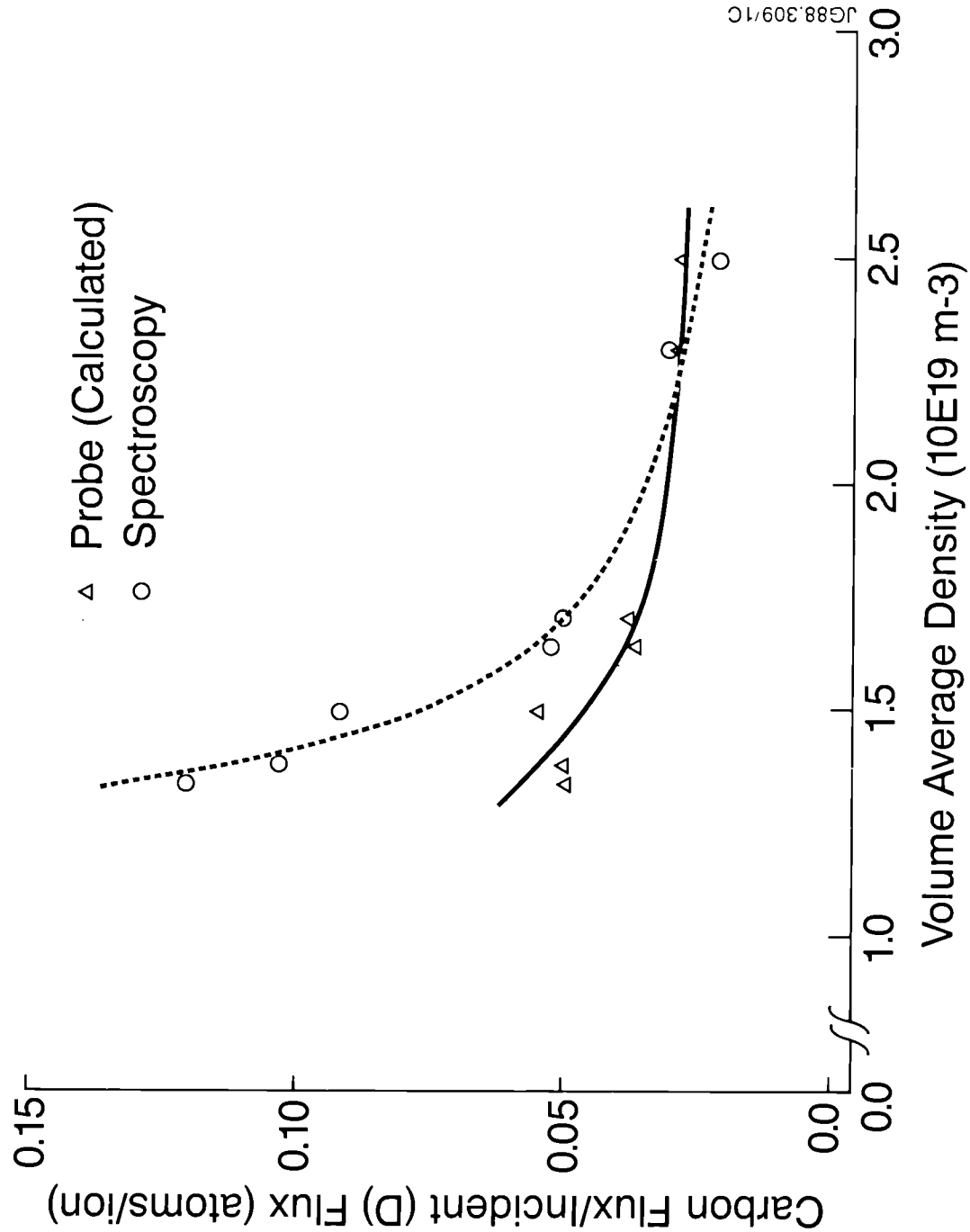

Fig. 5: Ratios of Γ_C/Γ_D from calculations using the measured edge parameters and known sputtering data and from spectroscopic measurements using low ionisation states of carbon + D_α as a function of $\langle n_e \rangle$ in a 3 MA, q = 3.5 limiter discharge. (# 17274 - 17281). Lines are added as guidance.

INTERNATIONAL ATOMIC ENERGY AGENCY

TWELFTH INTERNATIONAL CONFERENCE ON PLASMA PHYSICS AND CONTROLLED NUCLEAR FUSION RESEARCH

Nice, France, 12-19 October 1988

IAEA-CN-50/A-7-2

Sawtooth Activity and Current Density Profiles in JET

by

DJ Campbell, JG Cordey, AW Edwards, RD Gill, E Lazzaro, G Magyar, AL McCarthy[1], J O'Rourke, F Pegoraro, F Porcelli, P Smeulders, DFH Start, P Stubberfield, JA Wesson, E Westerhof[2], D Zasche[3]

JET Joint Undertaking, Abingdon, Oxon, OX14 3EA, UK

[1] Flinders University, Bedford Park, 5042 South Australia
[2]FOM Instituut voor Plasmafysica, Rijnhuizen, The Netherlands
[3]Max-Planck-Institut für Plasmaphysik, D-8046 Garching, FRG

SAWTOOTH ACTIVITY AND CURRENT DENSITY PROFILES IN JET

Abstract

Extensive investigations of sawtooth activity in JET have led to a major revision of our understanding of sawteeth and to further theoretical developments. In addition, experiments with powerful auxiliary heating have revealed a new plasma regime in which sawteeth are stabilized and quiescent plasmas are achieved for periods of over 3s. Measurements of current density profiles using a far–infrared multichannel polarimeter show that the central safety factor q_0 may be below unity in normal sawtoothing plasmas and may reach values as low as 0.6–0.8 during the stable periods. Analysis of pellet ablation and of density perturbations at rational q surfaces ('snakes') yields further information on the evolution of the q–profile during sawteeth. These results have significant implications for theories of the sawtooth instability and for explanations of the sawtooth stabilization.

1. Introduction

In many tokamak plasmas, the sawtooth instability plays a primary role in determining heating and confinement in the plasma centre. In the near–ignition regime, now being explored by large tokamak experiments, sawteeth may cause a substantial reduction of the fusion reactivity and a spatial redistribution of fusion products. Considerable attention is, therefore, focussed on the understanding of the instability mechanism and the investigation of possible stabilization techniques.

Previous studies on JET [1,2] have shown that there are considerable discrepancies between conventional models of the instability and experimental observations. In addition, measurements of the central value of the safety factor q_0 in TEXTOR [3] and observations of the 'snake' in JET [4] suggest that the instability does not involve complete reconnection of the plasma centre. More detailed investigations of sawtooth activity in JET, which are discussed here, together with an analysis of the current and safety factor profiles, confirm the need for a careful reappraisal of sawtooth theory.

2. Sawtooth Activity

Sawtooth activity in JET exhibits considerable complexity, with the sawtooth rise phase often interrupted by one or more subordinate relaxations and substantial associated mhd activity. In addition, during some high–power additional heating experiments (with ICRH and/or NBI), bursts of activity resembling 'fishbones' [5] are observed. Figure 1 shows a sawtooth cycle from a JET plasma with additional heating ($I_p = 5$ MA, $B_\varphi = 3.15$ T, $P_{RF} = 2$ MW). Four major commonly

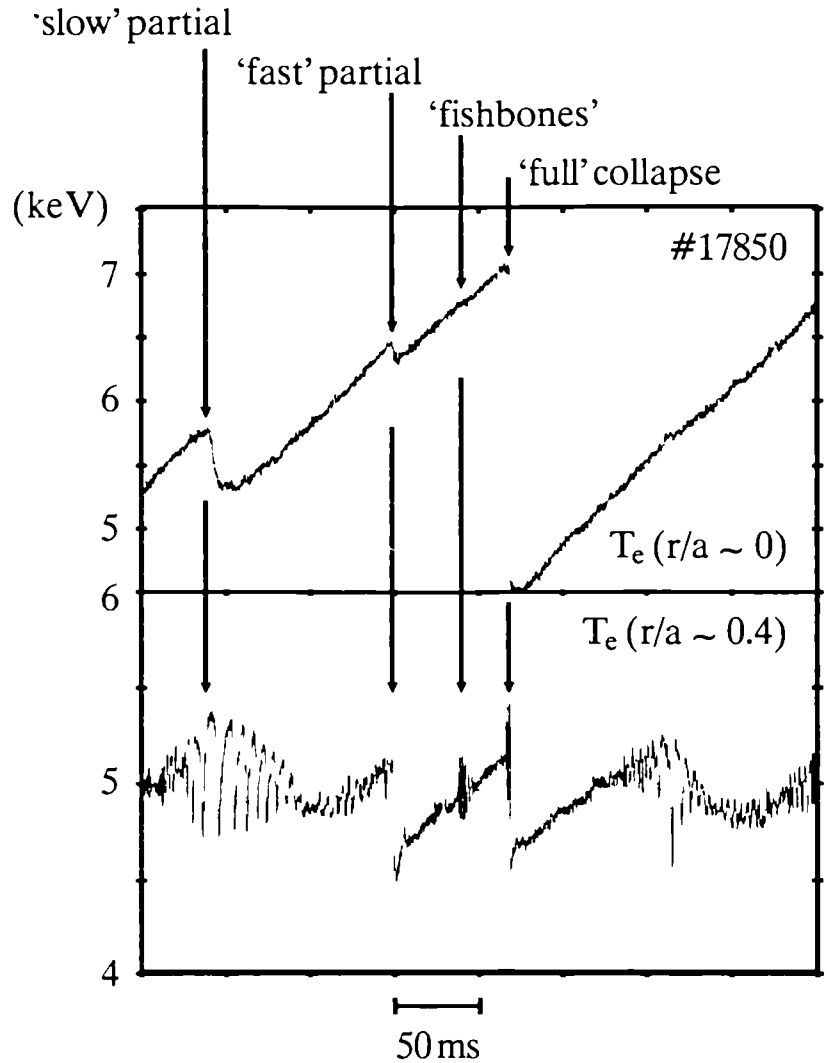

***Figure** 1: Behaviour of the electron temperature at two radii during a sawtooth cycle in a JET discharge with auxiliary heating. Major commonly observed phenomena are indicated.*

observed phenomena are illustrated : a full sawtooth collapse, a 'slow' partial collapse, a 'fast' partial collapse, and 'fishbone–like' bursts.

Detailed studies of the sawtooth collapse [6] have shown that it occurs in two main phases: the sudden appearance of a rapidly growing m=n=1 displacement of the plasma core is followed by a rapid redistribution of energy, resulting in a flattening of the central temperature profile on a timescale of 100μs. This picture of the collapse, obtained by soft X–ray tomography, is supported by reconstructions of successor oscillations using ECE measurements (the former employs measurements from two perpendicular cameras, the latter exploits the plasma rotation to reconstruct two–dimensional images from measurements along a single line of sight through the plasma). Figure 2 compares reconstructions of successor oscillations of the same collapse by the two techniques. Although the ECE reconstructions have lower time resolution, they are in agreement with the soft X–ray results. More detailed analysis confirms the conclusion [1,2] that the collapse resembles a broad convective flow rather than a resistive reconnection in a narrow layer.

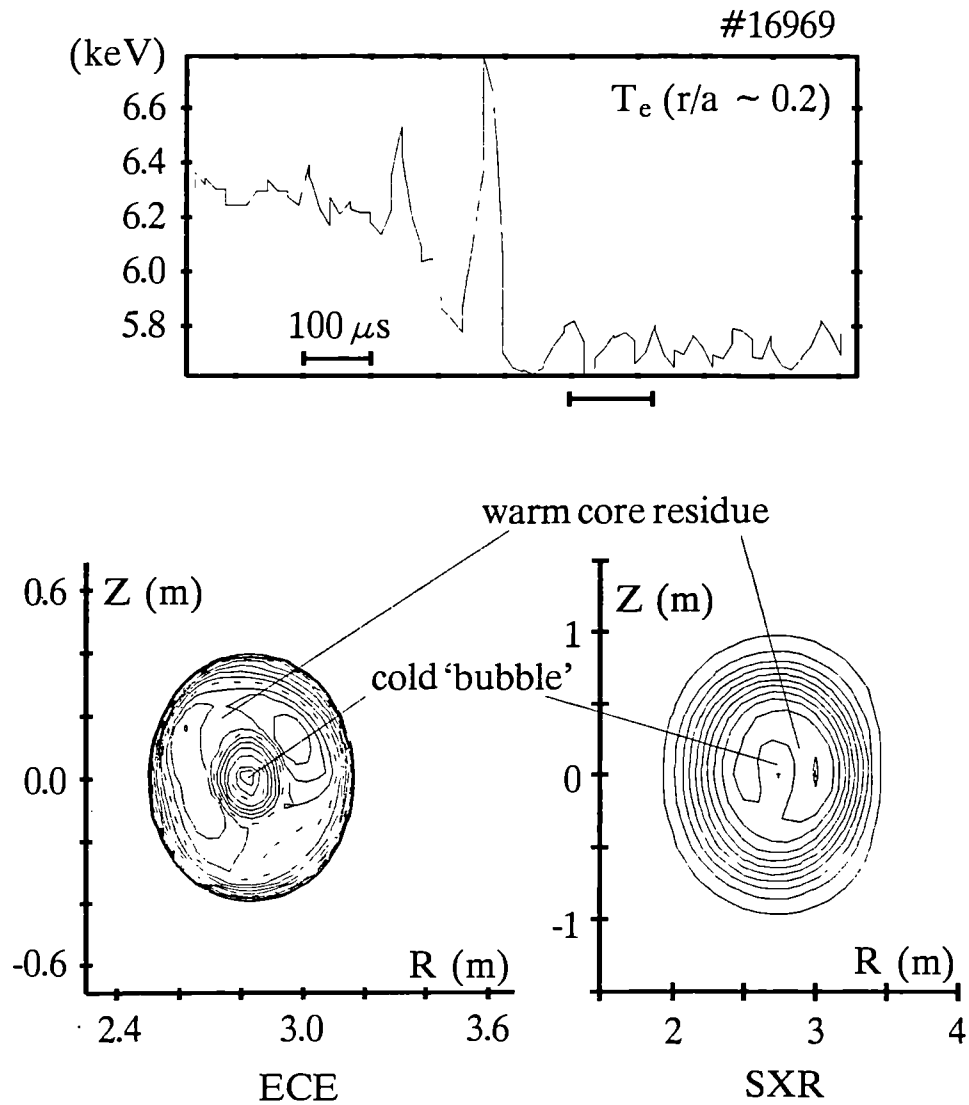

Figure 2: *Reconstructions of successor oscillations after a full sawtooth collapse using electron cyclotron emission (ECE) and soft X–ray tomography (SXR). The bar on the time axis indicates the interval over which ECE measurements are used to reconstruct the contour plot. The SXR contour plot is a 'snapshot' at one instant during this period.*

Certain subordinate relaxations ('fast' partial sawteeth) share some aspects of the full sawtooth collapse: they occur on a rapid timescale and are accompanied by large successor oscillations. However, there are important differences. Whereas the full collapse leads to a convective flow of the hot plasma centre and the formation of a cold bubble in the plasma core, soft X–ray tomography and fast ECE temperature measurements reveal that these subordinate relaxations generate a m=n=1 helical structure which resembles the conventional picture of a magnetic island [7]. This structure evolves to form a poloidally symmetric flattened region around the sawtooth inversion radius, rather than engulfing the plasma core as in the classic theory of the sawtooth instability. ECE reconstructions of the successor oscillations of such a collapse are shown in Fig 3.

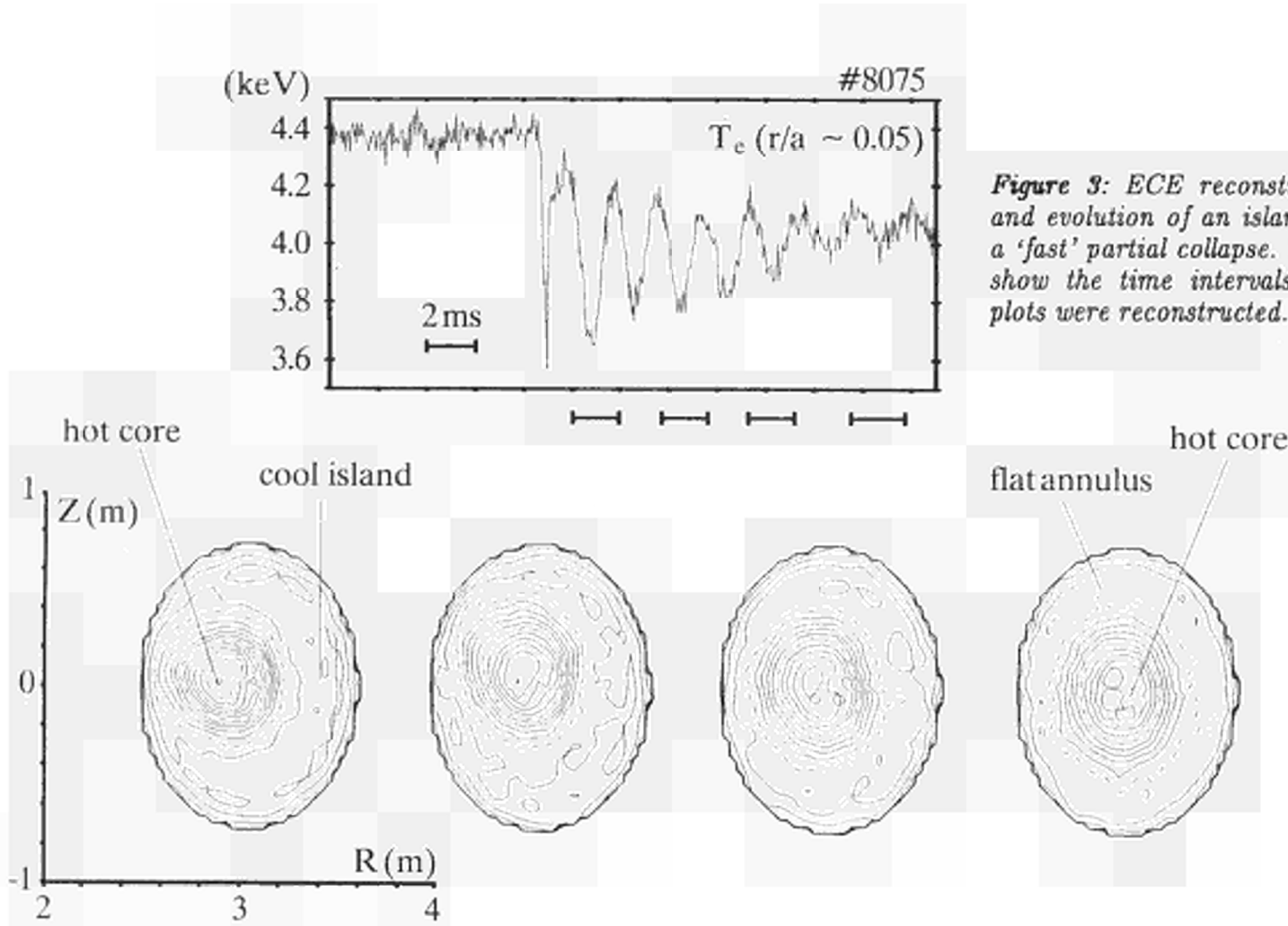

Figure 3: *ECE reconstructions of the formation and evolution of an island–like structure following a 'fast' partial collapse. The bars on the time–axis show the time intervals over which the contour plots were reconstructed.*

3. Sawtooth Stabilization

During auxiliary heating experiments, sawtooth activity usually dominates the evolution of the plasma core, limiting central plasma parameters and modulating the central electron temperature by up to 50% ($T_e(max)/T_e(min)$ - 2). However, under certain conditions, the plasma undergoes a transition to a regime in which sawteeth are suppressed [8]. This has been observed in limiter plasmas with currents of up to 5 MA during periods of ICRF or ICRF + NBI heating, and recently it has also been obtained in 3 MA H–mode plasmas with NBI heating. In the former case, the quiescent period has been extended to 3.2s (~7 energy replacement times), as shown in Fig 4 (I_p = 3 MA, B_φ = 3.15 T). The benefits of the regime include a small increase in energy confinement, by up to 20%, but it appears that the major advantage of sawtooth stabilization in near–ignition plasmas will be an increase in the fusion power product due to peaking of the density and temperature profiles. This may be further enhanced by the reactions of non–thermal particles accelerated by RF fields.

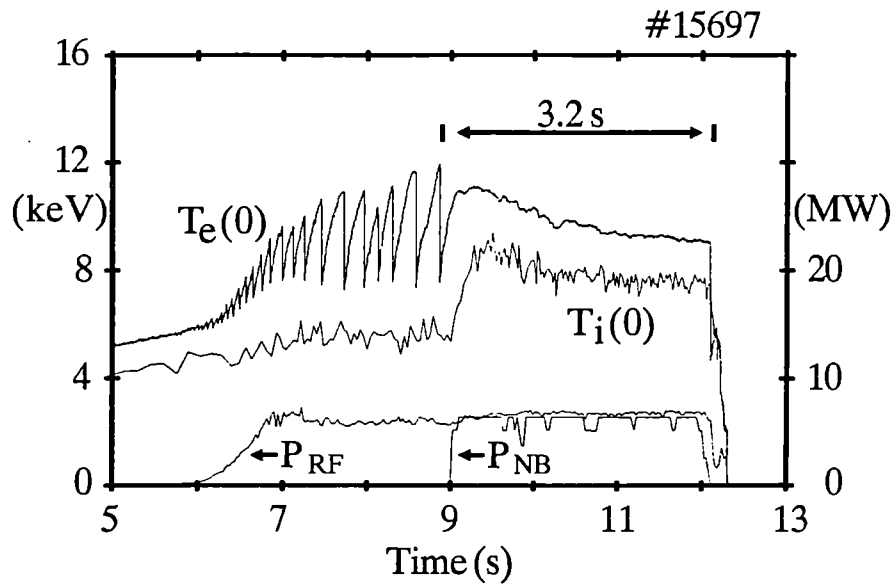

Figure 4: Behaviour of the central electron and ion temperatures during the longest period of sawtooth stabilization observed.

The stable regime is terminated by a normal m=n=1 instability, but the collapse has an inversion radius which may be up to 50% larger than for normal sawteeth. During the stable period, Faraday rotation measurements of the q–profile (see below) indicate that q_0 falls substantially below unity. Thus, stabilization is probably not due to non–inductive currents raising q above 1, but may be caused by the fast particles accelerated by the RF fields or injected by neutral beams [9].

4. Measurement of Current and Safety Factor Profiles

Recently, measurements of the current density profile have been obtained using a six–channel polarimeter to determine the Faraday rotation of

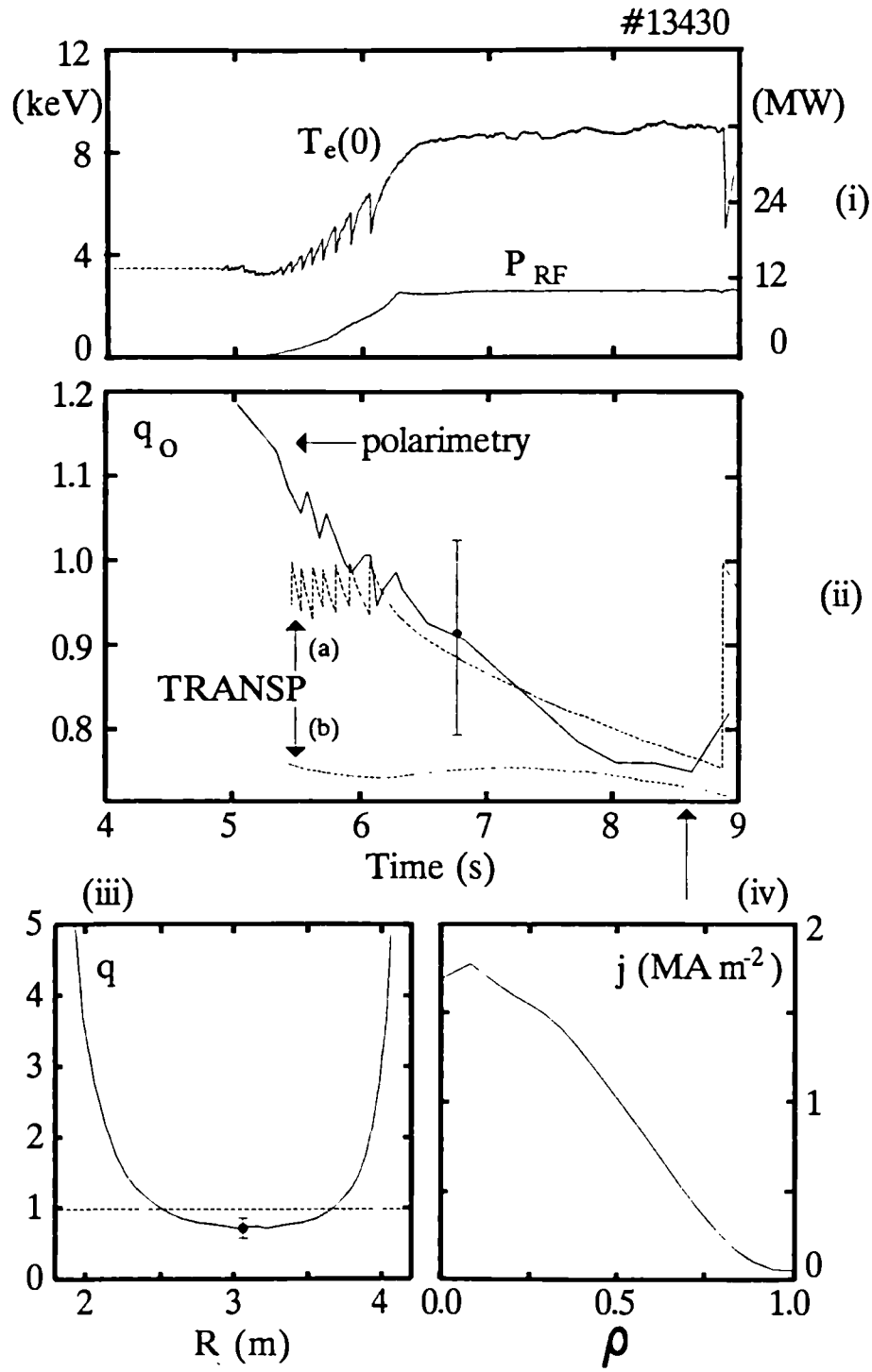

Figure 5: *(i) Behaviour of the central electron temperature during a period of sawtooth stabilization. (ii) Evolution of the central value of the safety factor q_0 as deduced from Faraday rotation measurements (polarimetry), and calculations of the resistive diffusion of current (TRANSP) under two different assumptions (see text). Safety factor (iii) and current density profiles (iv), derived from Faraday rotation measurements, are shown just before the termination of the stable period (arrowed).*

far–infrared (195 μm) radiation [10]. It is found that during normal sawteeth, in both ohmic and additionally heated plasmas, q_0 attains values ~ 0.8 (± 15%). Furthermore, measurements of the q–profile during stable periods show that q_0 may reach values as low as 0.6 [10]. These results are supported, within experimental uncertainties, by calculations of the resistive diffusion of the current (using TRANSP [11]) and by equilibrium analysis of external magnetic measurements (using IDENTC). Figure 5a shows the evolution of q_0 during a period of sawtooth stabilization (I_p = 3.3 MA, B_φ = 2.7 T, P_{RF} = 10 MW), as determined by polarimetry and by TRANSP. Two cases are shown for the latter method. The first (a) assumes that q_0 is reset to 1 after each sawtooth collapse and the second (b) does not. Nevertheless, q_0 attains approximately the same value in both cases. Current density and q–profiles ~300 ms before the collapse terminating the stable period are also shown. Note that the error bar in the polarimetry analysis includes some systematic effects (due, for example, to misalignment relative to the toroidal field and to plasma birefringence) whose magnitude has been estimated but not yet directly measured.

Experiments with injected pellets have revealed that a very localized density perturbation with m=n=1 topology (the 'snake') can persist for periods of up to 2s following pellet injection [4]. The geometry of the structure indicates that it is located at the q=1 surface, which, at the time of the sawtooth collapse, appears to lie very close to the sawtooth inversion radius. In addition, the location of the perturbation undergoes a substantial shift in minor radius ($\Delta r/r$ ~ 30%) during a sawtooth period, from which it is inferred that the position of the q=1 surface undergoes a similar shift. This suggests, in contrast to the Faraday rotation measurements, the existence of a very flat region in the central q–profile (since resistive diffusion can change q in the plasma centre by only a few percent during the sawtooth ramp phase). On this basis, a parabolic q–profile would yield a value for q_0 of 0.97.

Analysis of pellet ablation measurements [12] leads to a similar result. During pellet injection, a substantial fall in H_α and soft X–ray emission is observed as the pellet crosses the q=1 surface . This fall can be explained if it is assumed that on rational q surfaces the reservoir of electrons capable of interacting with and ablating the pellet is much lower than on non–rational q surfaces. This requires that the q=1 surface lies in a region of small shear and, in fact, leads to an estimate of the shear in the vicinity of the q=1 surface. The method yields $(dq/dr)_{q=1} = 5\times10^{-2}$ m^{-1} which, for a parabolic profile, implies q_0 ~ 0.99.

5. Discussion

In spite of substantial agreement between some of our observations of the sawtooth collapse and the predictions of the quasi–interchange model [2], several aspects of the JET results are not explicable in terms of any existing theory. In particular, it is found that the rate of increase of the instability growth rate is much too rapid. In addition, the mechanism for the rapid redistribution of energy which accompanies the collapse is not understood, although this may involve higher order ideal modes or small–scale turbulence.

The q–profile is a key parameter, and we have investigated its behaviour by a number of different techniques. Faraday rotation measurements show that q_0 is most probably below 1 in normal sawtoothing discharges, but, at present, experimental errors do not allow the possibility that $q_0 \simeq 1$ to be excluded. While observations of pellet–induced perturbations suggest values of q_0 close to unity, these measurements are consistent with a q–profile having a region of low shear in the vicinity of the q=1 surface and a central value of q below 1. No direct comparison of these techniques under identical conditions has been possible to date, so an analysis of the consistency of the various methods must await further experiments. In addition, more detailed resistive diffusion calculations will allow the limits imposed by experimental uncertainties to be more fully explored.

The observation that a q=1 surface exists throughout the sawtooth cycle conflicts with the assumption that $|1 - q_0| \sim 10^{-2}$, with q everywhere above 1, underlying the explanation of the sawtooth collapse in JET as a quasi–interchange mode. In addition, significant new problems are raised by the observation that sawteeth may be stabilized with q_0 well below unity. Complete understanding of this phenomenon requires an adequate model of the sawtooth instability. A re–evaluation of resistive theory including diamagnetic and trapped particle effects is, therefore, underway [13]. A central aspect of this analysis is that the sawtooth collapse leads to relaxation of the shear at the q=1 surface rather than a reconnection to q=1 in the plasma centre.

6. Acknowledgements

It is a pleasure to acknowledge contributions to this work and many helpful discussions with our colleagues in the JET Project. In addition, we wish to acknowledge R Goldston and D McCune of PPPL for the use of TRANSP and C Best for supervising its installation at JET.

7. References

[1] Campbell, D.J. et al, "Sawteeth and disruptions in JET", Plasma Physics and Controlled Nuclear Fusion Research 1986 (Proc. 11th Int. Conf. Kyoto, 1986) Vol. 1, IAEA, Vienna (1987) 433.
[2] Wesson, J.A., Kirby, P., Nave, M.F., "Sawtooth oscillations", ibid Vol. 2, 3.
[3] Soltwisch, H., Stodiek, W., Manickam, J., Schlüter, J., "Current density profiles in the TEXTOR tokamak", ibid Vol. 1, 263.
[4] Weller, A., et al, Persistent density perturbations at rational–q surfaces following pellet injection in the Joint European Torus, Phys. Rev. Lett. **59** (1987) 2303.
[5] McGuire, K. et al, Study of high beta magnetohydrodynamic modes and fast ion losses in PDX, Phys. Rev. Lett. **50** (1983) 891 .
[6] Edwards, A.W., et al, Rapid collapse of a plasma sawtooth oscillation in the JET tokamak, Phys. Rev. Lett. **57** (1986) 210.
[7] Westerhof, E. and Smeulders, P., to be published
[8] Campbell, D.J. et al, Stabilization of sawteeth with additional heating in the JET tokamak, Phys. Rev. Lett. **60** (1988) 2148.

[9] Pegoraro, F., Porcelli, F., Coppi, B., Detragiache, P., Migliuolo, S. "Theory of sawtooth stabilisation in the presence of energetic ions", Paper IAEA–CN–50/D–4–6 this conference.
[10] O'Rourke, J., et al, "Polarimetric measurements of the q–profile", Controlled Fusion and Plasma Heating (Proc. 15th Euro. Conf. Dubrovnik, 1988) Vol. 12B(I), Europhysics Conference Abstracts (1988) 155.
[11] Goldston, R.J., et al, New techniques for calculating heat and particle source rates due to neutral beam injection in axisymmetric tokamaks, J. Comput. Phys. **43** (1981) 61.
[12] Gill, R.D., Edwards, A.W. and Weller, A., Determination of the shear on the q=1 surface of the JET tokamak, to be published.
[13] Gill, R.D., et al, "The sawtooth in JET", ibid [10] Vol. 12B(I), 350.

INTERNATIONAL ATOMIC ENERGY AGENCY

TWELFTH INTERNATIONAL CONFERENCE ON PLASMA PHYSICS AND CONTROLLED NUCLEAR FUSION RESEARCH

Nice, France, 12-19 October 1988

IAEA-CN-50/A-7-1

GLOBAL POWER BALANCE AND LOCAL HEAT TRANSPORT IN JET

A. Taroni, B. Balet, G. Betello, V.P. Bhatnagar, J.P. Christiansen, J.G. Cordey, G. Corrigan, S. Corti, D.F. Düchs, R. Galvão*, G. Gorini, N. Gottardi, M. von Hellerman, W. Han, J. Jacquinot, O. Kardaun+, P.P. Lallia, L. Lauro-Taroni, P.J. Lomas, D. Muir, P.H. Rebut, C. Sack, G. Schmidt°, P. Smeulders, D.F.H. Start, T.E. Stringer, P.R. Thomas, K. Thomsen, F. Tibone, M.L. Watkins, H. Weisen

JET Joint Undertaking, Abingdon, Oxon., OX14 3EA, UK.

*Inst. de Pesquisas Espaciais and University of São Paulo, Brazil.
+IPP, Garching, F.R.G.
°PPPL, Princeton, New Jersey, USA.

GLOBAL POWER BALANCE AND LOCAL HEAT TRANSPORT IN JET

A. Taroni, B. Balet, G. Betello, V.P. Bhatnagar, J.P. Christiansen, J.G. Cordey, G. Corrigan, S. Corti, D.F. Düchs, R. Galvão*, G. Gorini, N. Gottardi, M. von Hellerman, W. Han, J. Jacquinot, O. Kardaun+, P.P. Lallia, L. Lauro-Taroni, P.J. Lomas, D. Muir, P.H. Rebut, C. Sack, G. Schmidt°, P. Smeulders, D.F.H. Start, T.E. Stringer, P.R. Thomas, K. Thomsen, F. Tibone, M.L. Watkins, H. Weisen

JET Joint Undertaking, Abingdon, Oxon., OX14 3EA, UK.

*Inst. de Pesquisas Espaciais and University of São Paulo, Brazil.
+IPP, Garching, F.R.G.
°PPPL, Princeton, New Jersey, USA.

GLOBAL POWER BALANCE AND LOCAL HEAT TRANSPORT IN JET

ABSTRACT

Global energy confinement analysis shows that both off-set linear and power law dependences of energy content versus input power can represent JET data. Results of the analysis are presented for the bulk and for selected subsets of data. Studies of local energy fluxes with both interpretive and predictive transport codes show that local transport models implying profile resilience, and in particular a "critical gradient" model, lead to satisfactory description of JET results in most regimes. The limitations of these, as well as of other plasma transport models used to simulate JET discharges, are pointed out.

1. INTRODUCTION

Several lines are followed at JET to study the crucial issue of energy confinement. Global energy confinement studies are carried out on data collected in the JET transport data base. This data base contains information for most JET discharges, referring to a wide range of operating conditions [1]. Analysis based on the bulk of the collected data, and on selected data corresponding to similar operating conditions have been carried out. Results are given in Section 2.

A deeper understanding of the mechanisms of energy confinement is sought by means of local transport analysis using interpretive transport codes (ITC). These studies are performed at various levels of generality and complexity, with different codes. We report in Section 3 results of a study of the local heat flux $q = q_e + q_i$ for ICRF heated discharges with long sawtooth-free periods ("monster" sawteeth). In the same Section we shall report on the analysis of local electron and ion heat fluxes q_e and q_i for a wide range of plasma regimes.

Predictive transport codes (PTC) have been extensively used at JET to test models for q_e and q_i. Two kinds of PTC have been developed and used: simplified 1-D steady state and complete, time-dependent 1½-D (i.e. transport equations coupled to the mhd equilibrium equation). The steady state approach allows quick checks of models on a wide range of discharges. More demanding tests in time-dependent situations are carried out with complete PTC's for a subset of representative discharges. Results of simulations with PTC are reported in Section 4.

2. ANALYSIS OF GLOBAL ENERGY CONFINEMENT

JET has extended the parameter range for confinement scaling studies further than other devices in many directions [1-5], yet important questions remain open. The first is whether the dependence of plasma energy content W on total power input P_{tot} is better approximated by a power law:

$$W = g\,(P_{tot} - \frac{dW}{dt})^{\alpha}, \quad \alpha \approx 0.5 \tag{1}$$

or by an offset linear law:

$$W = W^0 + \tau_{inc}(P_{tot} - \frac{dW}{dt}). \tag{2}$$

Here g, W^0 and the incremental confinement time τ_{inc} are assumed to be represented by power laws of relevant global plasma quantities such as plasma current I_p, toroidal magnetic field B_T, line (volume) average density $\bar{n}$ ($\langle n \rangle$), major radius R, minor radius a, plasma elongation K = b/a, etc.

Both assumptions (1) and (2) lead to scaling laws for W, or for the energy replacement time $\tau_E = W/(P_{tot} - dW/dt)$, with a similar goodness of fit to the available data. The best scaling laws represent the bulk of the experimental values of τ_E or W with a rather large "dispersion" ($\gtrsim \pm 30\%$). This is mainly due to the effect of various mechanisms that, in addition to local thermal transport, contribute to the determination of τ_E (e.g. sawtooth activity at low ($\lesssim 3$) boundary values of the safety factor q_ψ, different power deposition and radiation profiles etc.). These mechanisms play a different role in different operating conditions.

Among the scaling laws derived in the form (1), the Goldston scaling [6] is in reasonable agreement with JET L-mode data (Fig. 1a). An exception is provided by small bore plasmas [5]. JET H-mode data can be well represented by assuming $\tau_E = 2\tau_E$ (Goldston) [3]. However, no clear dependence on the atomic mass of the main plasma ions is apparent from the analysis of JET global data.

The Rebut-Lallia scaling [7] is of type (2) and represents both ohmic and L-mode discharges. Figure 1b has been obtained with this scaling.

It must be noticed that the scaling with the geometrical parameters, which is different in the Goldston and Rebut-Lallia laws, remains an open question and that the dependence of τ_{inc} on plasma current is being revised (see below).

An improvement in this kind of study is achieved by carrying out the global energy confinement analysis of selected subsets of discharges, referring to similar operating conditions. As an example, the scaling law (2) has recently been investigated for a set of ICRH power scans in the 1-5 MA current range [8], accounting for heating efficiency [9] and the effect of sawteeth.

For a series of "monster" sawtooth discharges, it is found that τ_{inc} increases less than linearly with current ($\tau_{inc} \sim I_p^{1/2}$), while it saturates or even decreases for $I_p > 3.5$ MA, when sawtooth stabilisation is not obtained and sawtooth activity plays a role on a wide region.

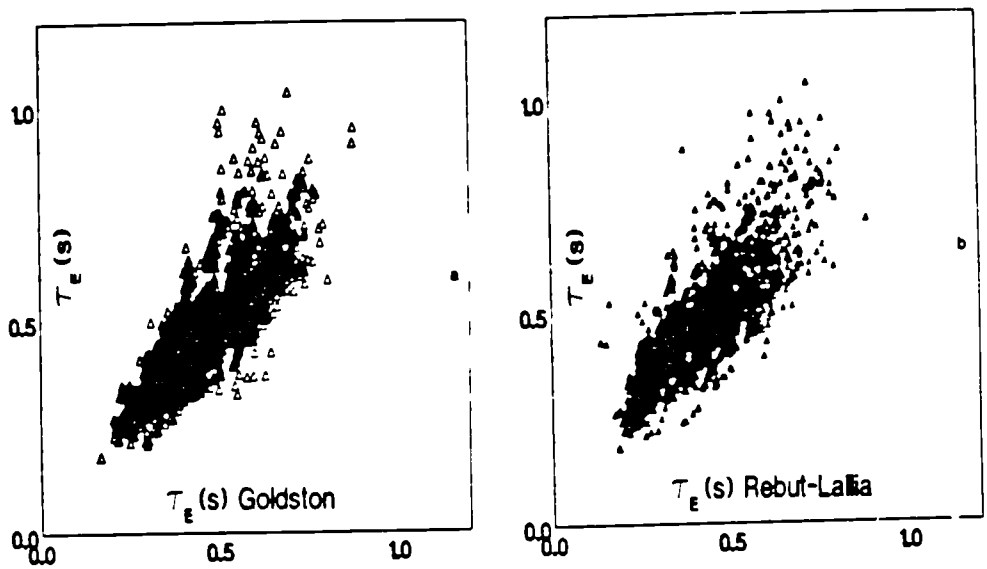

Fig. 1: Observed confinement time τ_E^{ex} versus the one predicted, by the Goldston scaling (Fig. 1a) and the Rebut-Lallia scaling (Fig. 1b). Data refer to the bulk of 1988 discharges with $P_{tot} \geq 1.1\ P_{OH}$, excluding H-modes.

3. LOCAL ENERGY TRANSPORT ANALYSIS BY MEANS OF INTERPRETIVE TRANSPORT CODES

Analysis of Total Heat Flux

Plasma energy transport has been studied for a series of 110-ICRF heated discharges with "monsters" by means of an ITC evaluating the total energy flux through electron and ion channels. Power scans at $I_p = B_T = 2, 2.5, 3, 3.5$ (MA,T) have been considered. For each scan the ICRH power varies from 2 to 14 MW. Data from these discharges have been selected at times during sawtooth-free periods subject to the criterion $0 < \frac{dW}{dt}/P_{tot} < 0.4$. The total local heat flux q is modelled at various radii, x = 1/2, 2/3, 3/4, x being a normalised radial coordinate, by assuming [9,10]:

$$q = - n \chi \langle \nabla T_e \rangle - q_p. \qquad (3)$$

Here q_p represents a non-diffusive "heat pinch"; χ is a "total" heat diffusivity and $\langle \nabla T_e \rangle$ is the flux surface average of ∇T_e. The data derived for the study of (3) show less scatter than the NBI data used in [10]. Figures 2a and 2b are plots of q versus $n\langle \nabla T_e \rangle$. Only data for 2 and 3.5MA pulses are shown: Figure 2a corresponds to local values at the half-radius and yields $\chi = 2 m^2/sec$ without any appreciable dependence upon current. Figure 2b showing 3/4 radius data reveals, on the other hand, a current dependence $\chi = 7.5/I(MA)\ m^2/sec$. This result is confirmed by non-linear

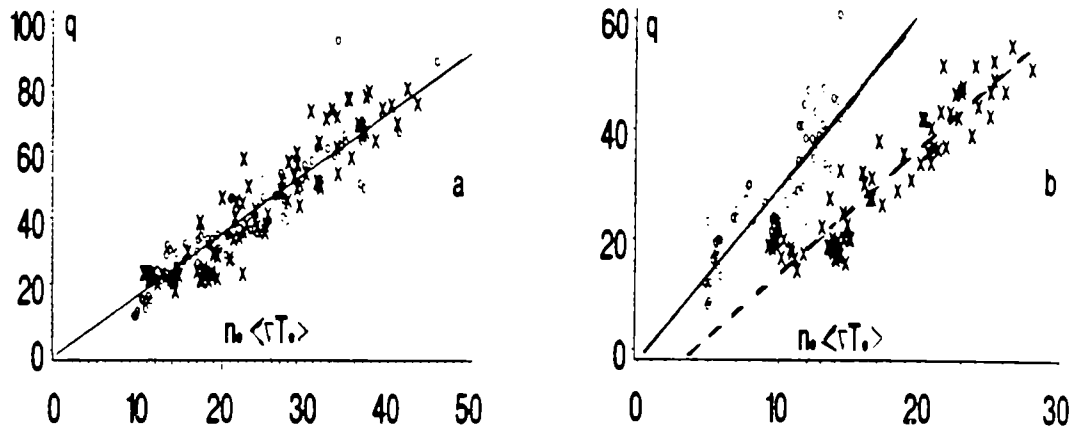

Fig. 2: Total heat flux q (KW/m^2) versus $n_e\langle\nabla T_e\rangle$ (KJ/m^4) for "monster" cases at 2MA (open circles) and 3.5MA (crosses). Figure 2a refers to x = ½, Fig. 2b to x = 3/4.

regression analysis and is consistent with the result on τ_{inc} for ICRF discharges mentioned at the end of Section 2. Further analysis is required to relate it to local theoretical expressions of electron and ion thermal fluxes.

Separate Electron and Ion Energy Balances

Analyses of this type have been carried out with the JICS and TRANSP codes, which may separate q_e and q_i either by modelling q_i or by using the available experimental T_i profiles [11]. JICS may also evaluate local q_e and q_i predicted by several theoretical and empirical models for comparison with the "measured" heat fluxes.

A wide range of plasma regimes is being studied: sawtoothing L-mode discharges with ICRH, NBI and combined heating; discharges with ICRH off-axis heating; discharges with "monster" sawteeth; H-mode cases; experiments at I_p= 3MA with pellet injection.

One general result is that energy transport is anomalous, and with a similar spatial dependence for both electron and ions. This result is confirmed by the time-dependent TRANSP code runs for H-mode and hot-ion mode discharges [3,5]. In these cases values of χ_i as high as $2\chi_e$ have been found.

Another result is that in the "monster" sawtooth regime no significant improvement of the central energy confinement is observed.

Interesting is the analysis of discharges with pellet injection where a novel, transient JET plasma regime is observed when strong additional heating is applied towards the end of the current rise [4]. Strongly peaked sawtooth-free profiles of T_e and T_i are established, with T_{eo} and T_{io} higher than in comparable "monster" cases. Temperature peaking correlates with density peaking. A sharp variation of ∇T_e, ∇T_i (when available) and ∇n_e is observed at a radius $x_p \simeq 0.5$ (Fig. 3).

Transport analysis shows that the local energy confinement improves for $x < x_p$ (leading to a 20-30% improvement in the global

value of τ_E): both electron and ion thermal conductivity are reduced by a factor 2-3 for $x < x_p$.

It is tempting to relate the observed regime to the suppression of the so-called η_i-mode, as a consequence of density peaking. The value of η_i is uncertain but, in cases where T_i profiles have been measured, they are similar to those of T_e; thus the evaluation of η_e is likely to be a reliable estimate of η_i, under reasonable assumptions on the profile of n_i. All estimates of η_e and η_i show that they reach very low values (< 0.5) just after pellet injection, increasing gradually in time to values in excess of 3 in the region $x < x_p$ before the end of the good confinement phase (Fig. 3). This may indicate that η_i exceeds the predicted threshold limit η_{ic} without noticeable change in energy transport, or that η_{ic} is larger than 1.5, a value usually assumed. Notice that $\eta_e >> 3$ for $x > x_p$ in these experiments and through almost the entire plasma cross-section for most JET discharges without pellets.

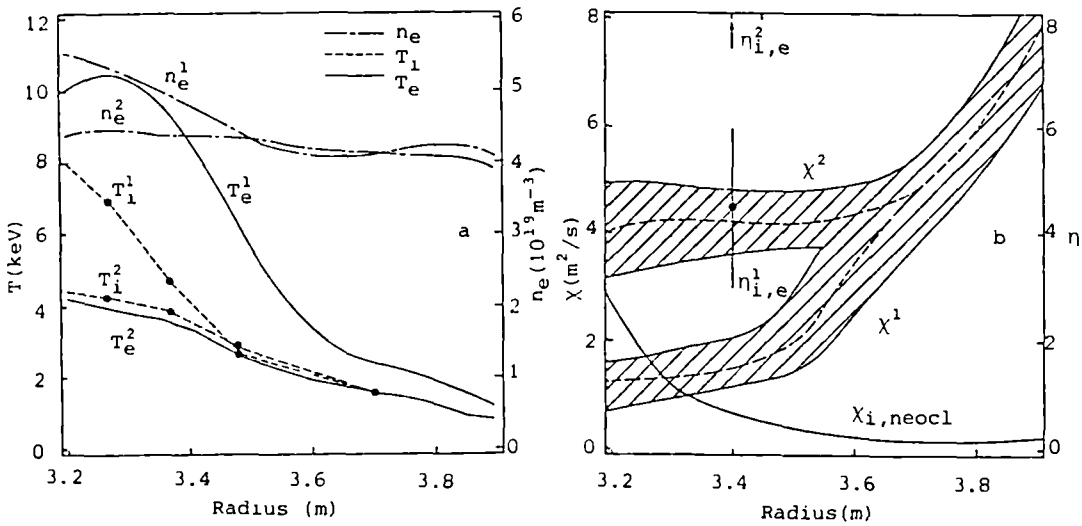

Fig. 3: a) Experimental profiles of T_e, T_i and n_e for a pellet shot (17279). Superscript 1 refers to the phase of enhanced confinement (t_1= 44.6), superscript 2 to the following "normal" phase (t_2= 45). T_e^1 is from ECE, n_e^1 from Abel inversion of interferometer data; T_e^2 and n_e^2 are from Lidar (not available for phase 1); T_i^1 and T_i^2 from charge exchange spectroscopy. b) "Experimental" thermal conductivity $\chi = \chi_e + (n_i \nabla T_i / n_e \nabla T_e)\chi_i$ and values of η_e and η_i at R = 3.4, t = t_1 and t_2. Similar values of η_e and η_i are obtained from Lidar data during phase 1 of other discharges. The neo-classical (Chang-Hinton) value of χ_i at t_1 is given for comparison.

Other observations yet to be explained are: the strong reduction of electron energy transport; the fact that sufficiently vigorous central heating is required to produce the increase in ∇T_e and ∇T_i,

not observed so far with NBI alone; the mhd events at the end of the enhanced confinement phase; the correlation, observed so far, with the evolution of the current density profile [4].

Comparison of "Experimental" and Theoretical Heat Fluxes

A number of models for local energy transport available in the literature (see [7,12] and the references quoted in [13]) has been compared with experimentally determined heat fluxes, in a series of ohmic, sawtoothing L-mode and "monster" discharges.

Local agreement within a factor of 2 between modelled and measured heat flux is accepted as fairly good, keeping in mind the uncertainties in "experimental" fluxes and the strong non-linearity (e.g. local dependence of χ_e on ∇T_e) of most theoretical models.

Our results indicate that in the region outside $q_\psi \simeq 1$, where meaningful comparisons are possible, the resistive mhd model (PT model) [12] and the Rebut-Lallia (RL) model [7] predict energy fluxes in fair agreement with the observed ones. For the RL model, the discrepancy increases when ∇T_e approaches the local critical gradient $\nabla_c T$ (typically, near the plasma edge), suggesting that the transition to low transport below $\nabla_c T$ might have to be smooth rather than sudden. In the same region, pure drift wave models fail to reproduce radial dependence and magnitude of the measured fluxes [13,14]. The microinstability-profile consistency model of Tang [13,15], rescaled by a factor 2 is in agreement with JET data.

4. SIMULATION OF JET RESULTS WITH PREDICTIVE TRANSPORT CODES

We shall present results obtained with the two transport models proposed at JET with reference to results from other models. The RL model [7,12] produces confinement degradation when ∇T_e exceeds a critical gradient. In the PT model [12,16] confinement degradation is due to the non-linear dependence of the heat fluxes on the pressure gradient. In both models $\chi_i \simeq \chi_e$ is assumed.

Uncertainties (± 40%) remain in the values of the numerical constant in the expressions of χ_e [7,12], determined empirically and kept fixed for all simulations. Notice that the corresponding variations of the values of χ_e, χ_i and τ_E are lower ($\simeq$ ± 20%), as a result of the non-linear dependence of the models on gradients of the temperature profiles.

Results of Computer Simulations

Satisfactory results with both models have been obtained when simulating ohmic discharges, L-mode discharges, "monster" sawteeth and ICRH off-axis heating cases. They produce resilient T_e profiles in agreement with experiments, without needing ad hoc modifications, as is the case for models based on drift wave microinstabilities. The time evolution of global quantities and temperature profiles following any modification of the input power is computed correctly by these models. On the other hand, the "profile consistency" (PC) model in [14] causes a delayed plasma response especially when power is suddenly switched off. Such a

delay is due to the dependence $\chi_e \propto \int_0^x P_{net,e}\, x\, dx$ in the PC model, $P_{net,e}$ being the net power input profile to the electrons. It is expected that other PC-related models involving a similar dependence of χ_e (and possibly χ_i) on the power deposition [15], will exhibit similar shortcomings, while being satisfactory for quasi-steady-state conditions.

The main uncertainties with both RL and PT models refer to the plasma core, and show up when attempting to simulate the central temperature evolution during sawteeth, including "monsters". It is difficult, however, to establish whether these uncertainties reflect an intrinsic deficiency of the models or are related to an inadequate evaluation of quantities such as local shear, non-thermal component of Vp, local power deposition. Similar problems appear with most theoretical transport models [13].

As a more demanding test for the models, we performed complete simulations of H-mode discharges at I = 2,3 and 4 MA, starting from the ohmic phase. Notice that JET H-modes are non-stationary. The time evolution of n_e has been input from the experimental data base, while the formation of an edge thermal barrier during the H-mode has been simulated by transiently increasing the boundary temperatures T_{ea}, in agreement with a systematic trend in measurements (a possible model of the edge thermal barrier consistent with the RL model is given in [17]). The adopted models determine the time evolution of the bulk plasma. In these cases (Fig. 4) the critical gradient model seems to perform better than the PT one.

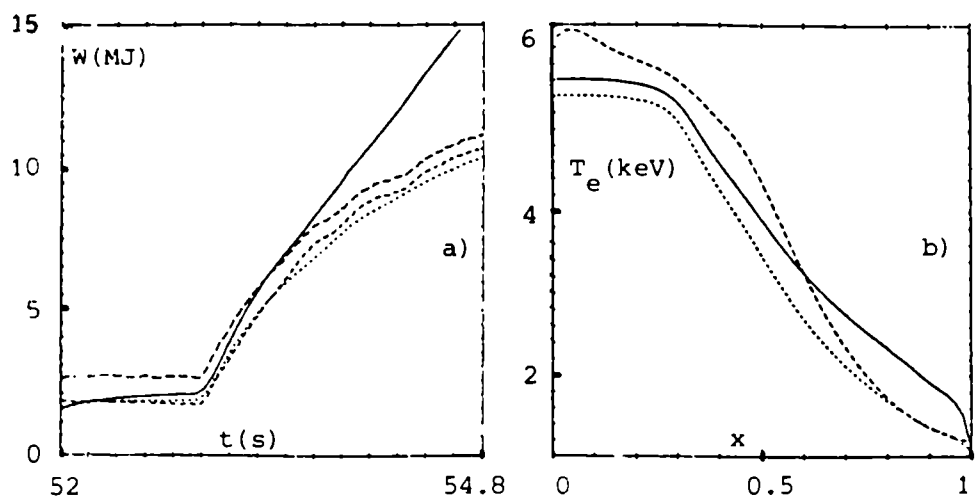

Fig. 4: Results of the simulation of an H-mode discharge at 4MA. Fig. 4a: time evolution of energy content from models (PT ——, RL ...) and measurements (magnetic ---, diamagnetic – –); Fig. 4b: T_e profiles at the beginning of the H-mode, t = 53.5 (PT ——, RL ..., ECE, – – –).

The equivalent thermal conductivity of the RL model in the plasma bulk is, during the H-mode, close to its ohmic value. The

somewhat high values of T_{io} obtained with $\chi_i \approx \chi_e$ may indicate that $\chi_i > \chi_e$, consistent with TRANSP analysis [3]. The model predicts degradation with increasing power, as experimentally observed, by the same mechanism as in the L-mode.

No improved confinement in the core region, when density and temperature profiles are peaked in the first phase of ICRF heating following pellet injection, is predicted by RL and PT models in their present formulation. An ad hoc reduction of χ_e and χ_i by a factor ≈ 2.5 in the region $x < x_p$ is required for reasonably good simulations, in agreement with JICS analysis.

PTC simulations show, consistently with ITC results, that the assumption $\chi_i = \alpha \chi_e$ with $\alpha \approx 1$ [18], does allow a proper simulation of the relevant quantities, e.g. total energy content W, T_{io} and the available T_i profiles. This remains true (with reduced χ_e) even for the pellet experiments with good central confinement. The uncertainty on α is large ($\alpha \approx 0.5$-2). The good performance of models with $\chi_i = \alpha \chi_e$ should simply be considered as a statement that χ_i is anomalous, with a radial dependence similar to that of χ_e (possibly introducing the same kind of profile resilience) and different from the neoclassical one.

6. CONCLUSIONS

Global energy confinement analysis shows that scaling laws such as the Rebut-Lallia or the Goldston one allow a fair representation of JET L-mode results: the question of the dependence of W on P_{tot} remains open. H-mode data roughly fit a "2 x L-mode" scaling.

The analysis of ICRH discharges shows an incremental confinement time saturating at the highest currents in JET ($I_p \gtrsim 5$MA) as an effect of sawtooth activity, and increasing less than linearly with current in the absence of sawteeth. Local analysis is consistent with these results.

Existing transport models fail to reproduce all plasma regimes found in JET. However, models that imply profile resilience and assume $\chi_i \approx \chi_e$ perform better than others. In particular the "critical gradient" model, although it needs to be improved or completed with other mechanisms in the plasma core, (as shown by the unpredicted temporary improvement of confinement in pellet injection cases followed by ICRF), leads to a satisfactory simulation of most JET regimes and can be considered a useful basis for prediction of tokamak performance.

ACKNOWLEDGEMENTS: We thank A. Galway, B. Keegan, E. Springmann and P. Stubberfield for their assistance in the updating and use of the various transport codes. R. Granetz, H. Hamnén, K. Lackner and G.P. Maddison are acknowledged for useful discussions.

REFERENCES

[1] Bickerton, R.J. et al., this conference.
[2] Rebut, P.H. et al., this conference.
[3] Keilhacker, M. et al., this conference.

[4] Schmidt, G. et al., this conference.
[5] Thomas, P. et al., this conference.
[6] Goldston, R., Plas. Phys. and Controlled Fusion, 26 (1984)87.
[7] Lallia, P.P., Rebut, P.H., Watkins. M.L., JET-P(88)05 and 2nd European Fusion Theory Meeting, Varenna, Italy, December 1987
[8] Bhatnagar, V.P. et al., Proc. XV EPS Conference on Controlled. Fusion and Plasma Physics, Dubrovnik, 1988, Vol. I, p. 358.
[9] Callen, J.C. et al., Nucl. Fusion 27 (1987) 1857.
[10] Christiansen, J.P. et al., Nucl. Fusion 28 (1988) 817.
[11] Corti, S. et al., Proc. XV EPS Conference on Controlled Fusion and Plasma Physics, Dubrovnik, 1988, Vol. I, p. 127.
[12] Thomas, P. et al., Proc. XV EPS Conference on Controlled Fusion and Plasma Physics, Dubrovnik, 1988, Vol. I, p. 115.
[13] Ross, D.W. et al., Report DOE/ET-53193 (1987) Washington, USA.
[14] Düchs, D.F. et al., Plasma Physics and Controlled Nuclear Fusion Research, (IAEA, Kyoto), Vol. I, p. 325, 1986.
[15] Tang, W.M., Nucl. Fusion 26 (1986) 1605.
[16] Thomas, P., JET-P(87)17.
[17] Rebut, P.H., Watkins, M.L., Lallia, P.P., Proc. XV EPS Conference on Controlled Fusion and Plasma Physics, Dubrovnik 1988, Vol. I, p. 247.
[18] Taroni, A. et al., Proc. XIV EPS Conference on Controlled Fusion and Plasma Physics, Madrid, 1987, Vol. I, p. 173.

INTERNATIONAL ATOMIC ENERGY AGENCY

TWELFTH INTERNATIONAL CONFERENCE ON PLASMA PHYSICS AND CONTROLLED NUCLEAR FUSION RESEARCH

Nice, France, 12-19 October 1988

IAEA-CN-50/D-4-6

THEORY OF SAWTOOTH STABILISATION IN THE PRESENCE OF ENERGETIC IONS

F. Pegoraro and F. Porcelli

JET Joint Undertaking, Abingdon, Oxon., OX14 3EA, UK

B. Coppi, P. Detragiache and S. Migliuolo

Massachusetts Institute of Technology, Cambridge, MA 02139, USA

THEORY OF SAWTOOTH STABILISATION IN THE PRESENCE OF ENERGETIC IONS

ABSTRACT

Energetic particles affect the stability of internal kink modes and can lead to plasma regimes where both sawtooth and fishbone oscillations are suppressed. This effect was recognised soon after the JET experiment achieved sawtooth free periods which we attributed to the energetic, mostly trapped, ions produced by intense additional heating. The isotropic fusion reaction products in an igniting plasma will have a similar effect, leading to an increase of the allowed values of β_p with the rate of fusion heating.

1. INTRODUCTION

In JET experiments with ICRH and/or NBI heating, sawtooth oscillations have been suppressed for periods up to several seconds [1]. In these regimes poloidal betas β_p often in excess of the ideal mhd threshold β_p^{mhd} for the excitation of internal kink modes have been attained, while the q parameter at the magnetic axis, q(o), has been measured to be significantly below unity. In [2] this improved stability has been attributed to the presence of energetic ions with magnetically trapped orbits and mean energies such that their bounce averaged ∇B + curvature drift frequency $\bar{\omega}_{Dh}$ exceeds the bulk ion diamagnetic frequency ω_{di}. The stability threshold increases for moderate energetic ion poloidal betas β_{ph} up to a limiting value as high as three to four times β_p^{mhd}. The corresponding ratio between the energy content of the energetic and of the bulk ions within the q = 1 surface is in the range of 1/20 to 1/3. The stability criterion is more favourable for energetic ion pressure profiles which are well peaked within the q = 1 surface, as is typical of the minority ions accelerated by ion cyclotron heating on axis.

These results extend to the isotropic fusion products in an igniting plasma. Although an efficiency factor of order $\epsilon_o^{1/2}$ is lost (the trapped to circulating particle ratio), where $\epsilon_o = r_o/R_o$ with $q(r_o) = 1$, β_{ph} can now be as large as $\beta_p/2$, so that values of β_p in excess of β_p^{mhd} can be attained without exciting global mhd instabilities affecting the igniting part of the plasma columns. For a D-T plasma the largest stable value of β_p that can be reached is given approximately by

$$\beta_{p,max} = 0.5 \frac{[n/10^{15}cm^{-3}]^{1/4}}{(9r_o/R_o)(r_o/50cm)^{1/2}\ (B/10T)} [1 + \frac{(\beta_p^{mhd})^2}{2\beta_{p,max}^2}] \quad (1)$$

Accordingly, ignition experiments could be designed with smaller poloidal fields, or alternatively B_p could be reduced after ignition conditions are reached. Under certain circumstances, fishbone oscillations with frequency $\omega \sim \omega_{di}$ [3] can be excited for values of β_{ph} just below the stabilisation threshold. However, if $\omega_{di} << \bar{\omega}_{Dh}$, the induced resonant scattering would affect only the slowed-down ions, leaving the energy balance practically unaltered. The excitation of fishbone oscillations with $\omega \sim \bar{\omega}_{Dh}$ [4] is found to require values of β_{ph} which are too high to be of interest for the currently proposed ignition scenarios.

Finally, resistive internal kink modes are predicted to be stable, provided $\omega_{di}/\omega_A >> \epsilon_\eta^{1/3}$, where $\omega_A = v_A/\sqrt{3}\ R_o$ is the Alfvén frequency and $\epsilon_\eta = \eta c^2/(4\pi\ r_o^2\ \omega_A)$ is the inverse magnetic Reynolds' number.

2. DISPERSION RELATION

In the high β_p regimes of interest, neglecting at first resistivity, m = 1 modes are described by the dispersion relation [3]

$$[\omega(\omega - \omega_{di})]^{1/2} = i[\lambda_H + \lambda_K(\omega)]\omega_A. \quad (2)$$

Here λ_H, which is proportional to the negative of the mhd energy functional δW, is the standard driving term arising from the bulk plasma, $\lambda_K(\omega)$ is the energetic particle contribution, $\omega_{di} = [-c(dp_i/dr)/en\ B\ r)]_{r_o}$ and r is the mean radius. We adopt the simplified model $\lambda_H = (3\pi/2)\epsilon_o^2[\beta_p^2 - (\beta_p^{mhd})^2]$, where $\beta_p = [8\pi/B_p^2(r_o)]$ $[\langle p\rangle_{r_o} - p(r_o)]$. The threshold $\beta_p^{mhd} \sim 0.1 \div 0.3$ depends on the pressure and q profiles and on magnetic shaping. For $\lambda_K(\omega)$ we have [3]

$$\lambda_K(\omega) = \frac{-2\pi i}{B_{po}^2\ s_o} \int_o^{r_o} dr r^2 \int_{-\pi}^{+\pi} d\theta\ [\underline{e}_{||} \times \underline{\kappa} \cdot \nabla(\tilde{\underline{p}}_{\perp} + \tilde{\underline{p}}_{||})] \quad (3)$$

where $s_o = r_o\ q'(r_o)$, $\underline{e}_{||} = \underline{B}/B$, $\underline{\kappa} = (\underline{e}_{||} \cdot \nabla)\underline{e}_{||}$ and $\tilde{\underline{p}}_{\perp}$ and $\tilde{\underline{p}}_{||}$ are the (normalised) perturbed components of the pressure tensor of the energetic ions obtained from Vlasov equation.

3. STABILITY DOMAIN IN ICRH HEATED PLASMAS

The functional $\lambda_K(\omega)$ depends on the spatial and velocity distribution of the energetic ions. In Fig. 1a we show Re $\lambda_K(\omega)$ and Im $\lambda_K(\omega)$ for ICRH heated minority ions assuming typical JET parameters. The dependence of the distribution function f_m on the energy ϵ and on the pitch angle Λ is modelled as a sum of an isotropic component $f_{mc} = n_c(m_i/\pi\,\epsilon_c)^{3/2}\exp(-2\epsilon/\epsilon_c)$, describing the ions in the range of the critical energy ϵ_c, and of a tail component $f_{mt} = 1.6G\,(p_\parallel/\epsilon_t)\,(m_i/2\epsilon_t)^{1/2}\,(\epsilon_o^{1/2}/\Delta)\,(\epsilon/\epsilon_t)^{1/2}\exp\{-[1 + (\Lambda - \Lambda_o)^2/\Delta^2](\epsilon/\epsilon_t)\}$, describing anisotropic ions, accelerated to energies of order $\epsilon_t >> \epsilon_c$. In the limit $\Delta << r/R_o$, the perpendicular pressure $P_\parallel = 3n_t\epsilon_t/2$, $G = (r/r_o)^{1/2}$ and f_m reduces to the single pitch angle distribution of Ref. [2]. The parameter β_{ph} is defined as $\beta_{ph} = -[8\pi/B_p^2(r_o)]\int_o^1 dx\, x^{3/2}\, d(Gp_\parallel)/dx$, with $x = r/r_o$. Re $\lambda_K(\omega)$ changes sign for $\omega/\bar{\omega}_{Dh} = 3$, with $\bar{\omega}_{Dh}$ evaluated at $r = r_o$ for deeply trapped ions with $\epsilon = \epsilon_t$, showing that the non resonant response of the energetic ions is negative, and thus stabilising, for modes with frequency below their characteristic dynamical frequency. For $\omega << \bar{\omega}_{Dh}$, Re $\lambda_K(\omega)$ consists of a linear term [2] plus a constant Re $\lambda_K(o)$ proportional to [q(o) - 1] [5]. The isotropic component contributes appreciably only to Im $\lambda_K(\omega)$ at low frequencies.

For $\lambda_K \equiv 0$, Eq. (1) gives a pair of modes, one unstable and the other stable, which become purely oscillatory for $\lambda_H < \omega_{di}/2\omega_A)$, i.e. for $\beta_p^2 < \beta_p^{*mhd^2} = \beta_p^{mhd^2} + \omega_{di}/(3\pi\,\epsilon_o^2\,\omega_A)$ (FLR stabilisation of the bulk ions) with frequencies approaching asymptotically zero and ω_{di}. The lower frequency mode, which turns out to be destabilised by the resistivity, is associated with the branch leading to the crash phase of sawtooth oscillations. The higher frequency mode is at first destabilised by the energetic ions. The dashed line in Fig. 1b corresponds to the marginal stability condition when only Re $\lambda_K(\omega)$ is included in (1) and separates the domain (above) where almost purely growing internal modes occur, from the domain (below) where the mode is destabilised by resonant interaction with the energetic ions represented by Im λ_K (fishbone oscillations [3]). The dashed line is interrupted at larger β_{ph} where Im $\lambda_K \sim$ Re λ_K. As β_{ph} is increased, the high frequency mode is stabilised by the non-resonant response of the energetic ions until, for $\beta_{ph} = 2.5(s_o/\epsilon_o)\bar{\omega}_{Dh}/\omega_A$, it reverts to instability with frequency in the range of $\bar{\omega}_{Dh}$. The stable domain lies below the solid line defined by λ_H + Re $\lambda_K = 0$. At small β_{ph}, the stability threshold can be expressed as

$$\beta_p^2 = (\beta_p^{mhd})^2 + 0.3 \frac{\beta_{ph}}{s_o \epsilon_o} \left[\frac{\omega_{di}}{\bar{\omega}_{Dh}} + C(1 - q(o))\right] \qquad (4)$$

where C depends sensitively on the profiles of q and of the energetic ion pressure. For the parameters of Fig. 1, C = 2.2.

Electron resistivity affects the stability of the modes in the low frequency range, $\omega \lesssim \omega_{di}$. Its effect can be included in (2) through the simple collisional model used in Ref. [3]. At small β_{ph} a region appears, shaded in Fig. 1b for the relevant resistivity parameter $\Omega \equiv \omega_{di}/(\omega_A\, s_o^{2/3}\, \epsilon_\eta^{1/3})$ equal to 4.5, where both fishbones and resistive kink modes are unstable. The latter modes would extend to higher values of β_{ph} and destabilise the domain at small values of β_p. However, for $\Omega > 2$, the growth rate in this region is small and easily overcome by the effect of the bulk ion viscosity [6] which also reduces the extent of the shaded region. For $\Omega \lesssim 2$ on the other hand, the full domain below the solid line becomes resistively unstable. This may represent a difficulty in the case of JET, as the values of Ω we estimate can, at best, satisfy the stability criterion against resistive kinks marginally. It is therefore desirable to extend the analysis taking full account of kinetic effects in the appropriate collisionality regime.

4. STABILITY IN AN IGNITED PLASMA

The response λ_K of the fusion alpha particles in a D-T plasma is shown in Fig. 2a. We have taken $f_\alpha = (3/4\pi)(m/2)(p_\alpha/\epsilon_\alpha)(\epsilon_c^{3/2} + \epsilon^{3/2})^{-1}\, \Theta(\epsilon_\alpha - \epsilon)$, where $\epsilon_\alpha = 3.5$Mev, $\Theta(\epsilon_\alpha - \epsilon)$ gives the energy cut off; $\beta_{p\alpha} = -\,[8\pi/B_p^2(r_o)] \int_0^1 dx\, x^{3/2}\, dp_\alpha/dx$ and $\bar{\omega}_{D\alpha}$ is evaluated for deeply trapped alphas, at the mean energy $\epsilon_\alpha/\ell n[1 + (\epsilon_\alpha/\epsilon_c)^{3/2}]$. Re λ_K is stabilising for $\omega/\bar{\omega}_{D\alpha} \lesssim 2$ and is dominated at small ω by a constant negative term. This amounts to an effective reduction of λ_H, independent of ω for $\omega \ll \omega_{D\alpha}$, which makes the stability threshold largely independent on ω_{di} in contrast to the anisotropic case. The stability domain is shown in Fig. 2b. The loss of the efficiency factor $\epsilon_o^{1/2}$ is apparent by comparing the horizontal scales of Figs. 1b and 2b. The values of $\beta_{p\alpha}$ in the shaded area are unrealistically large. The ratio $\beta_{p\alpha}/\beta_p$ depends on the central temperature (times a profile factor) and, typically, $\beta_{p\alpha}/\beta_p \lesssim 0.5$ for $T \lesssim 25$keV. The stable range of β_p increases with $\beta_{p\alpha}$ up to the value

$$\beta_{p,max}^2 \simeq (\beta_p^{mhd})^2 + 0.2 \frac{\bar{\omega}_{D\alpha}}{\epsilon_o^2\, \omega_A} \left(1 - 1.5 \frac{\omega_{di}}{\bar{\omega}_{D\alpha}}\right) \qquad (5)$$

If a plasma approaches ignition conditions with $\beta_p^{*mhd} > \beta_p > \beta_p^{mhd}$, in entering the stable domain, it must pass a transient phase, corresponding to the region between the dashed and the solid lines in Fig. 2b, where fishbone oscillations in the ω_{di} frequency range are excited. The crossing of this region should not affect the ignition energy balance significantly [7] since the resonantly scattered α-particles have already deposited most of their energy. Finally, resistive effects can be disregarded as large values of $\omega_{di}/(\epsilon_\eta^{1/3}\ \omega_A) \propto T^{3/2}$ are expected.

ACKNOWLEDGEMENTS

The collaboration of R.J. Hastie in the initial analysis of the sawtooth suppression mechanism is gratefully acknowledged. Three of us (B.C., P.D. and S.M.) have been sponsored in part by the U.S. Department of Energy.

REFERENCES

[1] Campbell, D.J. et al., Phys. Rev. Lett. 60 (1988) 2148.

[2] Coppi, B., Hastie, R.J., Migliuolo, S., Pegoraro, F., Porcelli, F., Phys. Letts. A. in press.

[3] Coppi, B., Porcelli, F., Phys. Rev. Lett. 57 (1986) 2272 and Coppi, B., Migliuolo, S., Porcelli, F., Phys. Fluids 31 (1988) 1630.

[4] Chen., L., White, R.B., Rosenbluth, M.N., Phys. Rev. Lett. 52 (1984) 1122.

[5] Chen, L., Hastie, R.J., Bull. Amer. Phys. Soc. 30 (1985) 1422.

[6] Porcelli, F., Migliuolo, S., Phys. Fluids 29 (1986) 1741.

[7] Coppi, B., Porcelli, F., Fusion Tech. 13 (1988) 447.

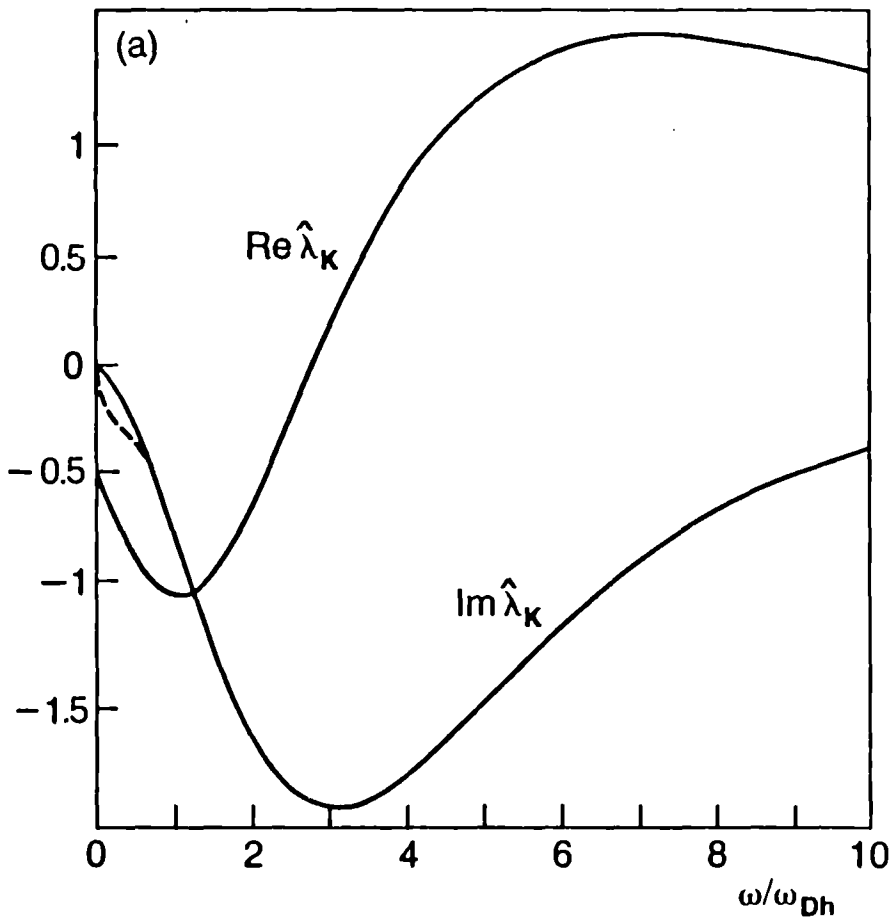

Fig. 1a

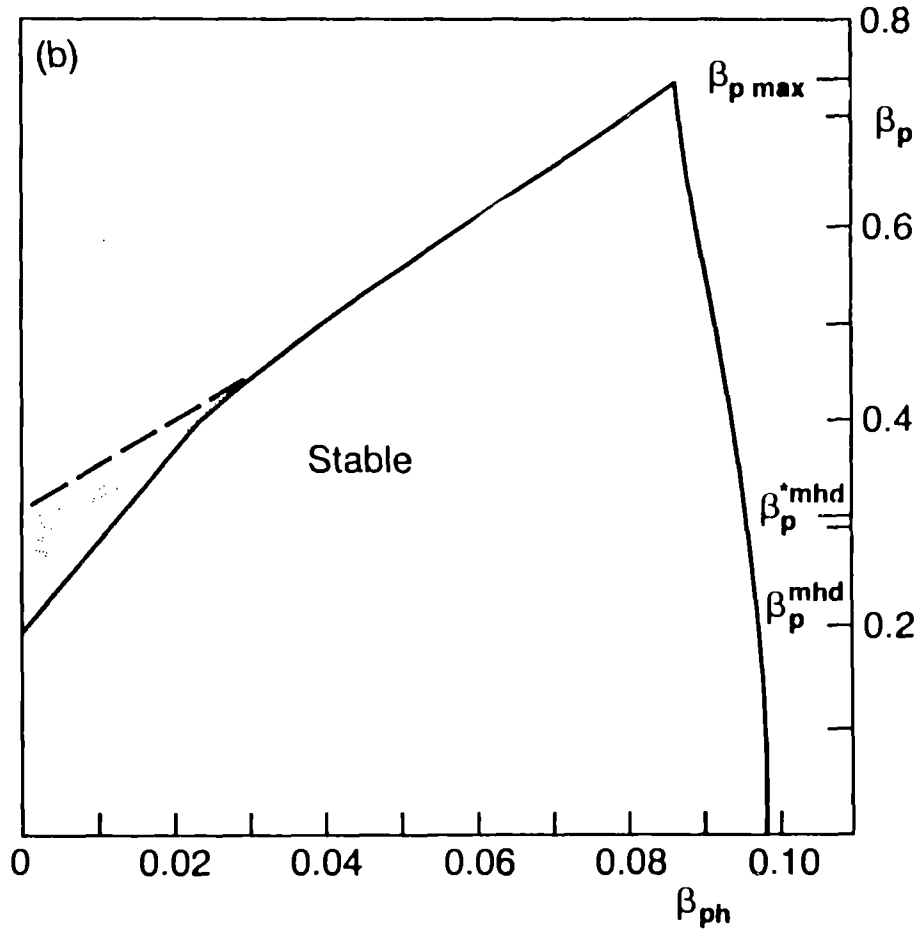

Fig. 1b

Real and imaginary parts of $\hat{\lambda}_K = s_o\ \lambda_K/\epsilon_o\ \beta_{ph}$, as a function of $\omega/\bar{\omega}_{Dh}$, for the ICRH anisotropic distribution f_m (defined in the text). The dotted line includes the low frequency contribution to Im λ_K from the isotropic portion f_{mi}. The parameters are as follows: ϵ_t = 500keV, ϵ_c = 100keV, Λ_o = 1 corresponding to the reflection angle $\theta_o = \pm \pi/2$, $\Delta = 0.1$, $n_t/n_c = 0.8$, the pressure scale length is r_{ph} = 20cm and, locally, $q = 0.7 + 0.3\ (r/r_o)^2$

Corresponding stability domain in the β_p - β_{ph} plane, for $\bar{\omega}_{Dh}/\omega_A = 4.5\times10^{-2}$, $\epsilon_o = 0.13$, $\beta_p^{mhd} = 0.2$, $\omega_{di}/\omega_A = 9\times10^{-3}$. The region between the shaded and the solid curves corresponds to fishbones with $\omega \sim \omega_{di}$. The region to the right of the stable domain corresponds to fishbones with $\omega \sim \omega_{Dh}$. In the shaded area both fishbones and resistive kinks are unstable ($\Omega = 4.5$).

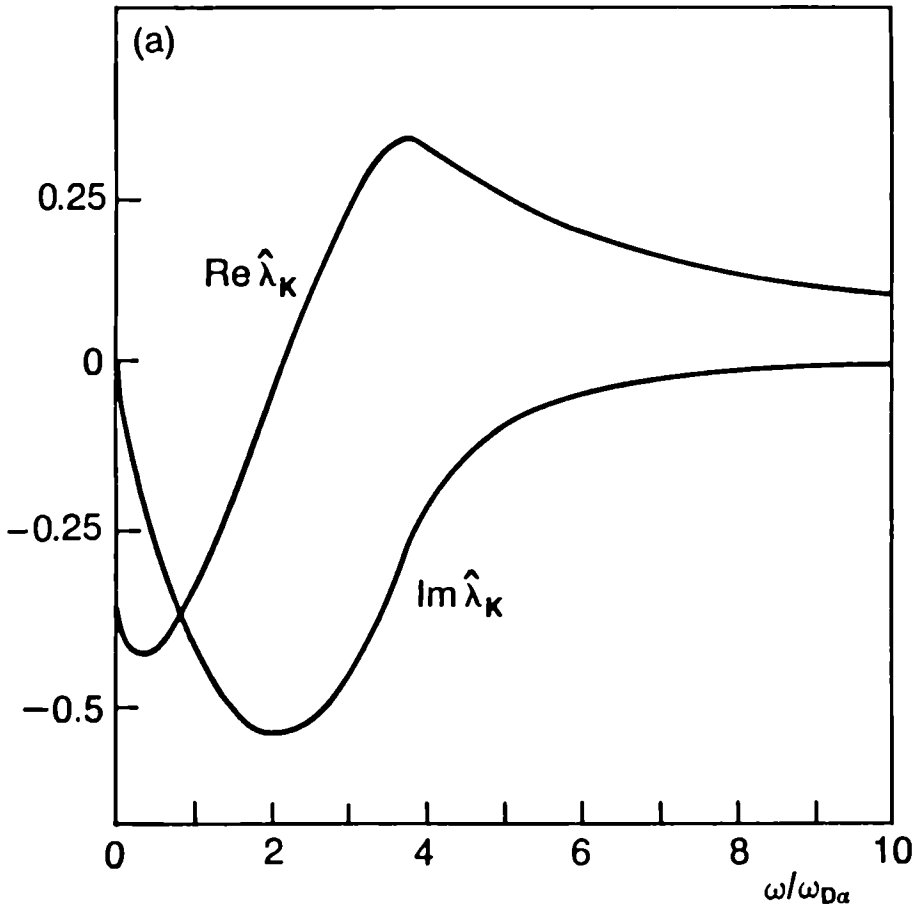

Fig. 2a

Real and imaginary part of $\hat{\lambda}_K$ for α-particles for $\epsilon_c/\epsilon_\alpha = 9\times10^{-2}$ and $r_{p\alpha}/r_o = 1.3$.

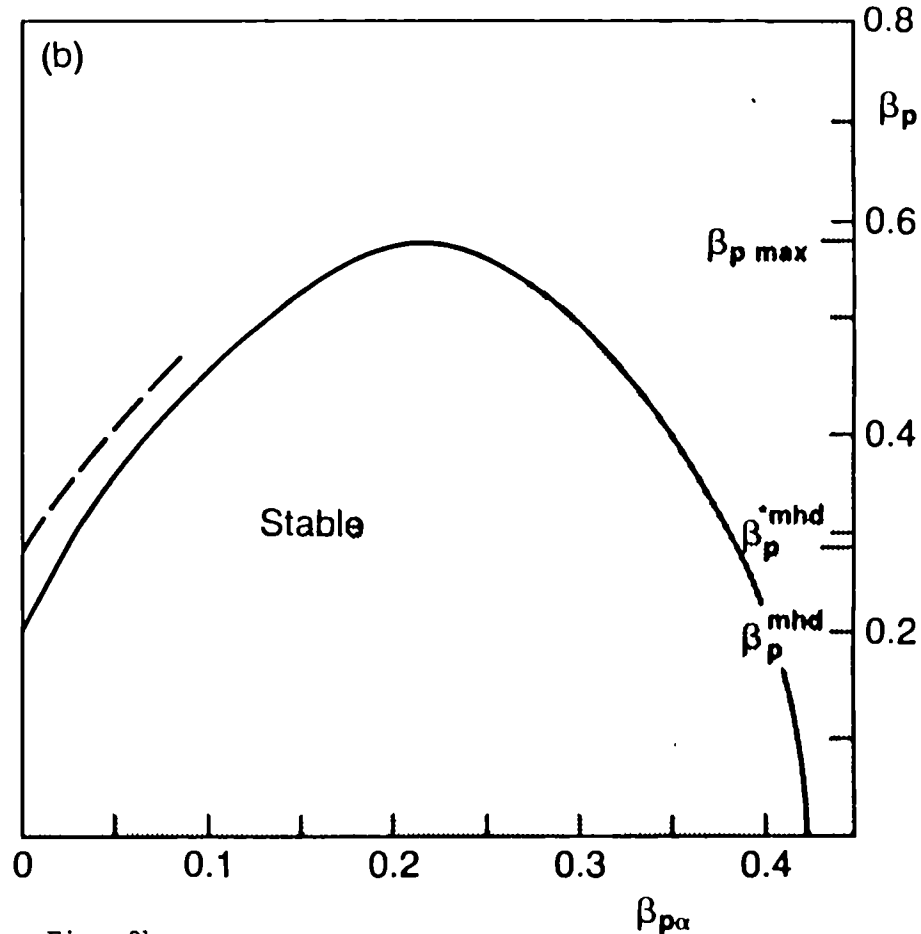

Fig. 2b

Corresponding stability domain in the β_p, $\beta_{p\alpha}$ plane for $\bar{\omega}_{D\alpha}/\omega_A = 2.3\times10^{-2}$, $s_o = 0.5$, $\epsilon_o = 1/9$, $\beta_p^{mhd} = 0.2$, $\omega_{di}/\omega_A = 5\times10^{-3}$.

THE CRITICAL TEMPERATURE GRADIENT MODEL OF PLASMA TRANSPORT: APPLICATIONS TO JET AND FUTURE TOKAMAKS

P. H. Rebut, P. P. Lallia and M. L. Watkins
JET Joint Undertaking, Abingdon, Oxon. OX14 3EA, UK.

Abstract

The diversity and complexity of behaviour in tokamak plasmas place strong constraints on any model attempting a description in terms of a single underlying phenomenon. Assuming that turbulence in the magnetic topology is the underlying phenomenon, specific expressions for electron and ion heat flux are derived from heuristic and dimensional arguments. When used in plasma transport codes, rather satisfactory simulations of experimental results are achieved in different sized tokamaks in various regimes of operation. Predictions are given for the expected performance of JET at full planned power and implications for next step tokamaks are indicated.

1. INTRODUCTION

The complex behaviour in tokamak plasmas that has to be described by any model for heat and particle transport is well illustrated by observations on JET[1]. In particular:

- in ohmic discharges the electron energy transport is anomalously high in comparison with the expectations of neoclassical theory, and shows a different dependence on the plasma parameters;
- the energy transport is even higher with additional heating, and shows yet another dependence on plasma parameters;
- this degradation of energy confinement occurs for either ion heating (NBI) or electron heating (ICRF); none-the-less, ion temperature profiles can be changed more easily ("supershots" and High T_i modes) than electron temperature profiles (High T_e modes);
- the energy confinement improves in H-modes, but exhibits in JET the same degradation with increasing additional input power as L-modes;
- outside the $q = 1$ region the electron temperature profile is resilient to changes in the input power, while the density profile can be changed more readily;
- inside the $q = 1$ region, a variety of phenomena occur, including "monster sawteeth";
- the peaked density profiles obtained with pellet injection relax faster when additional heating is applied;
- the diffusivity deduced from heat pulse propagation is insensitive to the input power, in contrast to that obtained from global confinement analysis.

This diversity of behaviour places strong constraints on any model, particularly if it is based on a single underlying phenomenon. In the "critical electron temperature gradient" model of plasma transport[2], anomalous transport is determined by one such single phenomenon, namely turbulence in the magnetic field topology, which occurs above a certain threshold. An analogy is explored between turbulent fluid and anomalous plasma transport (Section 2). The characteristics of the particular form of magnetic turbulence are described (Section 3) and the transport laws for electron and ion heat flux and the corresponding global scaling law are formulated in non-dimensional terms (Section 4). Using specific forms for the heat flux, simulations of various different sized tokamaks in various plasma regimes allow the role of each element in the model to be identified.The main uncertainty in the heat flux model is with regard to the dependence on the plasma pressure, β. Considering the relatively small extrapolation from present results, the model has been used to predict the eventual performance of JET (Section 6). Implications for the choice of parameters for the next step tokamak are also indicated.

2. ANOMALOUS TRANSPORT IN FLUIDS

In fluid mechanics it is well known that the dimensionless Reynolds number, R, can be constructed from the physics quantities entering the Navier-Stokes equation and that turbulence develops when R exceeds a critical value, R_c. Experimental data show that the laws governing the flow change when the pressure gradient, i.e. the driving force, is such that $R > R_c$ (see Fig.1a).

Such a change in the radial heat and particle flows is also observed in a tokamak. It is tempting therefore to suppose that this is the result of underlying turbulence. A tokamak is an open thermodynamic system in which heat flow could influence its stability. To conform with thermodynamics the driving force for the heat transport in steady state should be the temperature gradient. The role of the Reynolds number in fluid mechanics should be played by the ratio, $\nabla kT/(\nabla kT)_c$, where $(\nabla kT)_c$ is a threshold value above which turbulence develops and the heat transport is enhanced. This behaviour is illustrated in Fig.1b. With ohmic heating alone the temperature gradient should limit itself to a value close to, but above, the onset of turbulence. In the presence of powerful additional heating the confinement properties should be entirely controlled by the anomalous thermal transport.

General features common to all turbulent phenomena should be expected, such as a non-linearity between the flow and the driving force and delays in the onset and propagation of the turbulence.

3. MAGNETIC TURBULENCE

Explaining the anomalous transport in tokamaks by the presence of turbulence is widely accepted. More controversial is the nature of this turbulence. But it is certainly not unreasonable to assume that magnetic confinement is affected by magnetic turbulence [3]. In particular, macroscopic changes in the magnetic topology seems to be responsible for the total loss of confinement observed during major plasma disruptions. An attractive hypothesis is that a single basis, namely the magnetic topology, underlies the various phenomena observed in a tokamak, at least where atomic physics does not play a role. Tokamak physics would then be dominated by tearing and micro-tearing modes [4-9]. The topology would consist not only of well-nested magnetic surfaces but also of small magnetic islands surrounded by chaotic field lines connecting radially hot and cold regions [10]. In the fully relaxed state of the Reversed Field Pinch, all field lines would be chaotic [11].

Chains of islands develop where the safety factor, q, is rational: chaos occurs when the islands overlap radially, i.e. when the overlaping parameter, γ, exceeds a critical value. γ depends on a perturbation of the plasma current. If, as assumed, the critical value of γ corresponds to a critical value of the temperature gradient, then it should be the electron temperature gradient.

The expression given below for the critical electron temperature gradient can be written as the power balance between the directed flow of electrons around the islands and the resistive dissipation of the current perturbation.

The topology is strongly dependent upon the shear of the field lines, ∇q:

- for moderate shear, the field lines may cross many chains of islands and the chaotic volume forms a continuum. To sustain the topology a deficit of current should flow in the islands when $\nabla q > 0$. Self sustainment implies that electrons and ions experience the to

pology differently, i.e. that the characteristic size of the islands be larger than the poloidal Larmor radius of the electrons. The largest possible islands will dominate the transport phenomena. The particle guiding centre trajectories have the same behaviour as the field lines except for a translation arising from the ambipolar radial electric field [10]. The maximum size of the island, λ, could then be:

$$\lambda \approx 2\pi R E_o / (r V_i B \nabla i) \quad \text{where} \quad E_o = (kT_e/e) [(\nabla n_e / n_e) + (\nabla kT_e / 2kT_e)] \quad (1)$$

V_i is the ion thermal velocity, B is the toroidal magnetic field and i is the rotational transform.

- for high shear, as near a magnetic separatrix, the islands are too small and cannot be self-sustained.

- for low shear, as near the plasma axis, only rather large islands can exist and the hypothesis of a continuum might not be justified.

Above the critical electron temperature gradient the effective heat transport should depend on flows both along and across the field lines.

4. DIMENSIONAL ANALYSIS

As in fluid mechanics, laws of similarity are to be expected for plasmas [12,13]. In the absence of relativistic effects and assuming classical resistivity, the dominant physical processes in a tokamak plasma are described not only by the structural parameters representing the plasma pressure, $\beta = nkT / (B_p^2 / 2\mu_o)$, resistivity, $\Delta = \eta J / (B_p V_{th})$ and the diamagnetic thermal drift, $\Omega = (\nabla kT / eB_p V_{th})^2$, but also by the power flow, $\Phi = P / (3\pi^2 r R n kT V_{th})$ [2]. Above a threshold of turbulence, the general form of the power balance can be written as, $\Phi = G(\Omega, \Delta, \beta) . g (\Omega / \Omega_c) + \Phi_{neo}$,where Φ_{neo} represents neoclassical losses and for ohmic heating specifically, $\Omega = \Omega_c (\Delta, \beta)$. Inspection of ohmic, L-mode and H-mode JET data suggests the following forms:

$$\Omega_{ec} = \Delta_e / \beta_e \qquad \Phi_e = \Omega_i^{1/2} \Delta_e^{1/2} (1 - (\Omega_{ec}/\Omega_e)^{1/2}) \qquad (2)$$

The subscripts refer to the species, electrons or ions. It should be noted that numerical coefficients are close to unity. However, the dependence on β_e, is also close to unity. It is therefore the least certain and a dimensionless equation of the type, $\Phi_e = \Omega_i^{1/2} \Delta_e^{1/2} \beta_e^{1/2} (1 - (\Omega_{ec}/\Omega_e)^{1/2})$ cannot be excluded.

A law similar to Eq. (2) is proposed for the ion heat transport, namely:

$$\Phi_i = \Omega_i^{1/2} \Delta_i^{1/2} (1 - (\Omega_{ec}/\Omega_e)^{1/2}) \qquad (3)$$

A global scaling law for the total stored electron energy that is consistent with these expressions is given approximately by:

$$W_e = 2.6\times10^{-2} n_e^{3/4} Z_{eff}^{1/4} B^{1/2} I^{1/2} (Rab)^{11/12} + 1.2\times10^{-2} I (Rab)^{1/2} P_{tot} / Z_{eff}^{1/2}$$

where W_e(MJ), $n_e(10^{19}m^{-3})$, B(T), I(MA), P_{tot}(MW), R,a,b(m). The numerical coefficients have been obtained by a fit to JET ohmic and L-mode data but may contain further shape parameters (such as q, a/R, b/a, and even Z_{eff}) yet to be identified.

This scaling law should be used only as a general guide for prediction. Transport code simulations should be used, since heating, radiation and impurity profiles, for example, can affect performance.

The simulations reported below use the following specific forms of Eq. (2) for the local electron heat flux. This includes the maximum size, λ, of the islands (Eq. (1)):

$$F_e = n_e \chi_{an,e} \nabla kT_e [1 - (\nabla kT_e)_c/(\nabla kT_e)] H [|\nabla kT_e| - |\nabla kT_e|_c] H [\nabla q] + F_{e,neo}$$

$$\chi_{an,e} = 0.15 [(\nabla kT_e/kT_e) + (2\nabla n_e/n_e)] (T_e/T_i)^{1/2} (R/r) (q^2/\nabla q B R^{1/2}) c^2 (\mu_o m_i)^{1/2}$$

$$(\nabla kT_e)_c = 0.06[\eta J B^3 / n_e (kT_e)^{1/2}]^{1/2} (1/q) (e^2 / \mu_o m_e^{1/2})^{1/2}$$

and H is the Heaviside step function.

The specific form of Eq. (3) used for the ion heat flux is also dependent on the departure of the electron temperature gradient from its critical value:

$$F_i = n_i \chi_{an,i} \nabla kT_i [1 - (\nabla kT_e)_c/(\nabla kT_e)] H [|\nabla kT_e| - |\nabla kT_e|_c] H [\nabla q] + F_{i,neo}$$

$$\text{with} \quad \chi_{an,i} = \chi_{an,e} Z_i (T_e/T_i)^{1/2}$$

While there are strong indications that the particle transport is similarly anomalous above the same threshold of turbulence and exhibits many features of energy transport, thereby pointing towards a common explanation, no model is yet proposed and experimental density profiles are used.

5. SIMULATION OF TOKAMAK EXPERIMENTS

Following the earlier work of [14], a number of tokamak transport codes of different complexity have used the above model [15-17]. Inside experimental errors this model has given a rather satisfactory description of several tokamaks, ranging from WEGA ($R = 0.7$m, $a = 0.15$m, $I = 0.05$MA) to JET ($R = 3$m, $(ab)^{1/2} = 1.6$m, $I = 5$MA), and in various plasma regimes. In particular, the results indicate that:

- $(\nabla kT_e)_c$ defines largely the temperature profile in ohmic plasmas (Fig. 2) and leads to confinement which is considerably worse than neoclassical and with a different dependence on plasma parameters. The scaling of confinement time with plasma density is in accord with the results of JET and other tokamaks, but is different from the neoalcator (linear) scaling often associated with ohmic plasmas. A dependence of Z_{eff} on n_e might reconcile this.

- at higher power levels, and especially with large amounts of additional heating, the confinement is dominated increasingly by χ_{an}, which exhibits yet a different dependence on plasma parameters. χ_{an} determines the incremental confinement time, the heat pulse propagation speed, the resilience of the electron temperature profile to changes (Fig. 2) and the degradation of confinement with increased additional heating power. When applying this model to fast perturbations such as heat pulse propagation, the unperturbed values of χ_{an} should be used: it takes time to change the topology.

- near the separatrix in an X-point configuration, the heat diffusivities are reduced by the locally high magnetic shear, and neoclassical transport should be recovered ultimately. Under such conditions it has been shown [16] that a spontaneous change in the electron temperature can occur. This has been identified with the pedestals observed to develop within $\sim$ 0.05-0.1m of the JET separatrix when a transition from the L- to H- mode occurs. Simulating the H-mode has been achieved by using the above model in the plasma interior and either imposing the observed temperature pedestals at the plasma boundary [16] or reducing the edge particle fluxes (Fig. 2) [18]. χ_{an} is reduced during the H-mode in the plasma interior, where the gradients are smaller. In accordance with experiment, H-mode confinement exhibits the same degradation with power as L-mode confinement. At high powers the overall gain in confinement from the H-mode will be determined largely by the pedestals in temperature and density established near the separatrix.

- when ion and electron temperatures are weakly coupled, there are differences depending on which species has the higher temperature: it is easier to achieve high ion temperatures since the ion heat flux depends linearly on ∇kT_i, the electron heat flux depends quadratically on ∇kT_e and $\chi_{an,i} = \chi_{an,e} Z_i (T_e/T_i)^{1/2}$. Simulations of the "monster sawtooth" regime in JET [19] (High T_e) and the "supershot" regime in TFTR [20] (High T_i) are shown in Fig. 3. The main plasma parameters are in Table I. The shape of the profiles might be improved further by including a radial variation of Z_{eff} or by changing the dependence of χ_{an} on the aspect ratio.

Further considerations are important in determining the electron and ion temperatures within the $q = 1$ region:

- the "sawtooth" collapse has to be imposed;

- sometimes when pellets are injected during the current rise, the central temperature gradient is about twice that predicted with this model and a q profile which increases monotonically with radius. This suggests the experimental q profile is inverted [21], and the anomalous transport is strongly reduced;

- the model fails in describing T-10 observations with 2MW of ECRH power deposited on axis, although the ohmic results are well predicted [22]. The model gives too high a diffusivity, but its applicability is questionable since for axial values of $T_e = 10$keV and $T_i = 0.5$keV the estimated size of the islands, λ, is much larger than the poloidal Larmor radius of the ions.

6. IMPLICATIONS FOR JET AND FUTURE TOKAMAKS

Plasma behaviour in tokamaks is interpreted in terms of turbulence in the magnetic topology. Above a critical value of the electron temperature gradient the confinement is degraded. Specific expressions for the threshold and for the diffusivities have been derived heuristically. These allow simulation of various different sized tokamaks in various plasma regimes, including ohmic heating, L-mode, H-mode, "monster sawteeth" and "supershots". The main uncertainty in the heat flux model is with regard to the dependence on β.

Considering the relatively small extrapolation from present results, the model has been used to predict the eventual performance of JET. The alpha particle power to be expected from thermal fusion reactions is given in Table II. Including beam-plasma contributions a total fusion amplification factor, Q_{DT}, between 0.5 and 1 is to be expected.

Although the present model is incomplete with respect to a model for particle and impurity transport, it has implications in the choice of the parameters for the next step tokamak, such as ITER, NET and IGNITOR, being considered on the road towards a fusion reactor. For high power, the confinement time, $\tau_E \propto \beta^{-\alpha} I a R^{1/2}$, for both L - and H - modes. α reflects the uncertainty in the model ($\alpha = 0$ for Eqs. (2,3)) on β. The ignition product for such plasmas at the Troyon β-limit is:

$$n T \tau_E = (q R / a)^{\alpha} I^2 B R^{1/2}$$

This stresses the importance of the current capability of the tokamak. To ensure a large ignition domain the ignition product should be larger than in JET by a factor of about 50 . Considering the thickness of a neutron blanket, a plasma with minor radius $\sim$3m would occupy approximately one-half of the volume enclosed by the magnets. With an elongation of 2, the necessary improvement on JET could be achieved with a toroidal field of 4.5T and a plasma current of 30MA. Simulations indicate that the maximum fusion power in such a "thermonuclear furnace" would be near 4GW [23].

REFERENCES

[1] Bickerton, R.J. and the JET Team, This Conference, Paper IAEA-CN-50/A-I-3 (1988)

[2] Rebut, P.H. and Brusati, M., Plasma Physics and Controlled Fusion **28**, 113 (1986)

[3] Stix, T.H., Nuclear Fus. **18**, 3 (1978)

[4] Furth, H.P., et al, Phys. of Fluids **6**, 459 (1963)

[5] Hazeltine, R.D., et al, Phys. of Fluids **18**, 1778 (1975)

[6] Rechester, A.B. and Rosenbluth, M.N., Phys.Rev.Letters **40**, 38 (1978)

[7] Samain, A., Plasma Physics and Controlled Fusion **26(5)**, 731 (1984)

[8] Rebut, P.H. and Hugon, M., in Plasma Physics and Controlled Fusion Research (Proc. 10th Int. Conf., London, 1984) **2**, 197 (1984)

[9] Kadomtsev, B.B., Comments Plasma Phys. Controlled Fusion **9**, 227 (1985)

[10] Rebut, P.H., et al, in Plasma Physics and Controlled Fusion Research (Proc. 11th Int. Conf., Kyoto, 1986) **2**, 187 (1987)

[11] Taylor, J.B., Phys.Rev.Letters **33**, 19 (1974)

[12] Kadomtsev, B.B., Sov. J. Plasma Phys. **14**, 295 (1975)

[13] Connor, J.W. and Taylor, J.B., Nuclear Fus. **17**, 1047 (1977)

[14] Rebut, P.H., et al, Proc. 14th Eur. Conf. on Cont. Fusion and Plasma Physics, Madrid, 1987, **11D(I)**, EPS, 172 (1987)

[15] Lallia, P.P., Rebut, P.H. and Watkins, M.L., JET Preprint JET-P(88)05 (1988)

[16] Rebut, P.H., et al, Proc. 15th Eur. Conf. on Cont. Fusion and Plasma Heating, Dubrovnik, 1988, **12B(I)**, EPS, 247 (1988)

[17] Taroni, A., et al, This Conference, Paper IAEA-CN-50/A-VII-I (1988)

[18] Cohen, S.A., et al, Plasma Physics and Controlled Fusion, **29**, 1205 (1987)

[19] Campbell, D.J. and the JET Team, This Conference, Paper IAEA-CN-50/A-VII-2 (1988)

[20] Hawryluck, R.J., et al, in Plasma Physics and Controlled Fusion Research (Proc. 11th Int. Conf., Kyoto, 1986) **1**, 51 (1987)

[21] Schmidt, G.L. and the JET Team, This Conference, Paper IAEA-CN-50/A-IV-1 (1988)

[22] Razumora, K., Private Communication (1988)

[23] Rebut, P.H., This Conference, Post Deadline Paper IAEA-CN-50/I-I-1 (1988)

Table I

Parameter	**JET** No:12898	**TFTR** Ref [20]
B(T)	2.45	4.7
I_p(MA)	2.5	0.9
R(m)	2.90	2.50
a(m)	1.15	0.82
b/a	1.5	1.0
n($10^{19}m^{-3}$)	3.0	3.0
P_{add}(MW)	10.6(ICRH)	12.5(NB)

Table II

Predictions for JET; 'critical temperature' simulations

Device	I_p	n_{eo}	Z_{eff}	P_{add}	T_{io}	$\bar{T}_e$	P_α	g*	P_{OH}	Regime
	MA	$10^{19}m^{-3}$		MW	keV	keV	MW		MW	
JET	7	7.5	2	0	3.5	2.6	0.014	0.24	5.6	ohmic q=1
	7	7.5	2	40	12	5.2	2.2	1.22	3	monster L-mode q=0.8
	7	7.5	2	40	5.6	3.7	0.5	0.86	3.2	L-mode q=1
	6	7.5	2	20	11	5.2	2	1.6	1.4	H-mode+ monster q=0.8 Pedestal T_e 1.5 keV
	7	4	2	20	25	5.8	2.5	0.94	2.1	hot ion L mode monster q=0.8

* $g = \beta(\%)\, a(m)\, B(T) / I(MA)$

A6o3

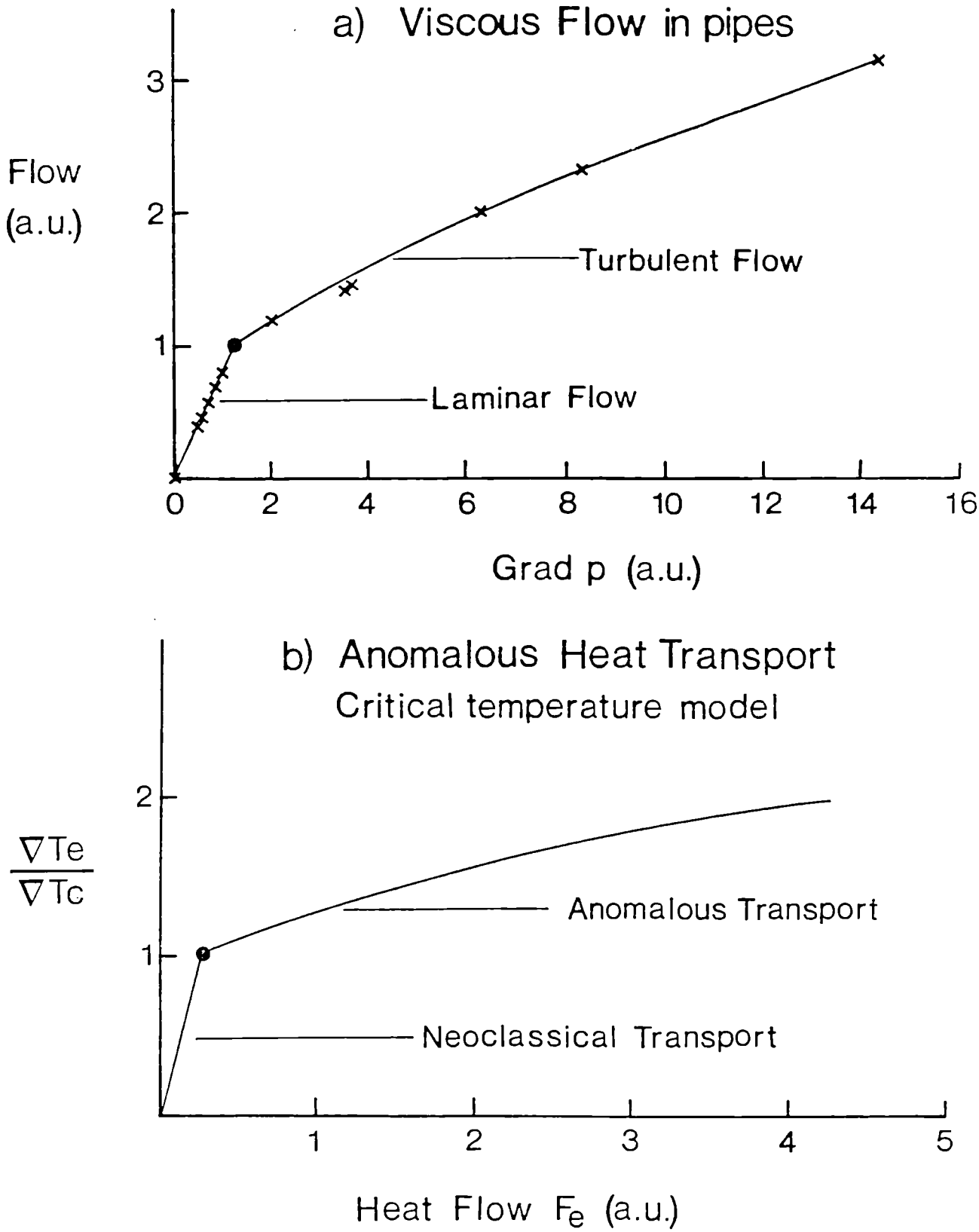

Fig.1: (a) The experimental relationship governing the flow of a liquid through a long pipe is shown. When the Reynolds number, R, reaches the critical value, R_c, extra resistance is added to the flow which increases with the value of R (curvature of the curve in the turbulent flow regime); (b) For given temperature, density, magnetic field, etc., the dependence of the heat flow with electron temperature gradient in the critical temperature gradient model shows the same behaviour: when ∇kT reaches $(\nabla kT)_c$ anomalous transport appears which increases the heat flow. This anomalous transport also varies non-linearly with the ratio $(\nabla kT_e)/(\nabla kT_e)_c$.

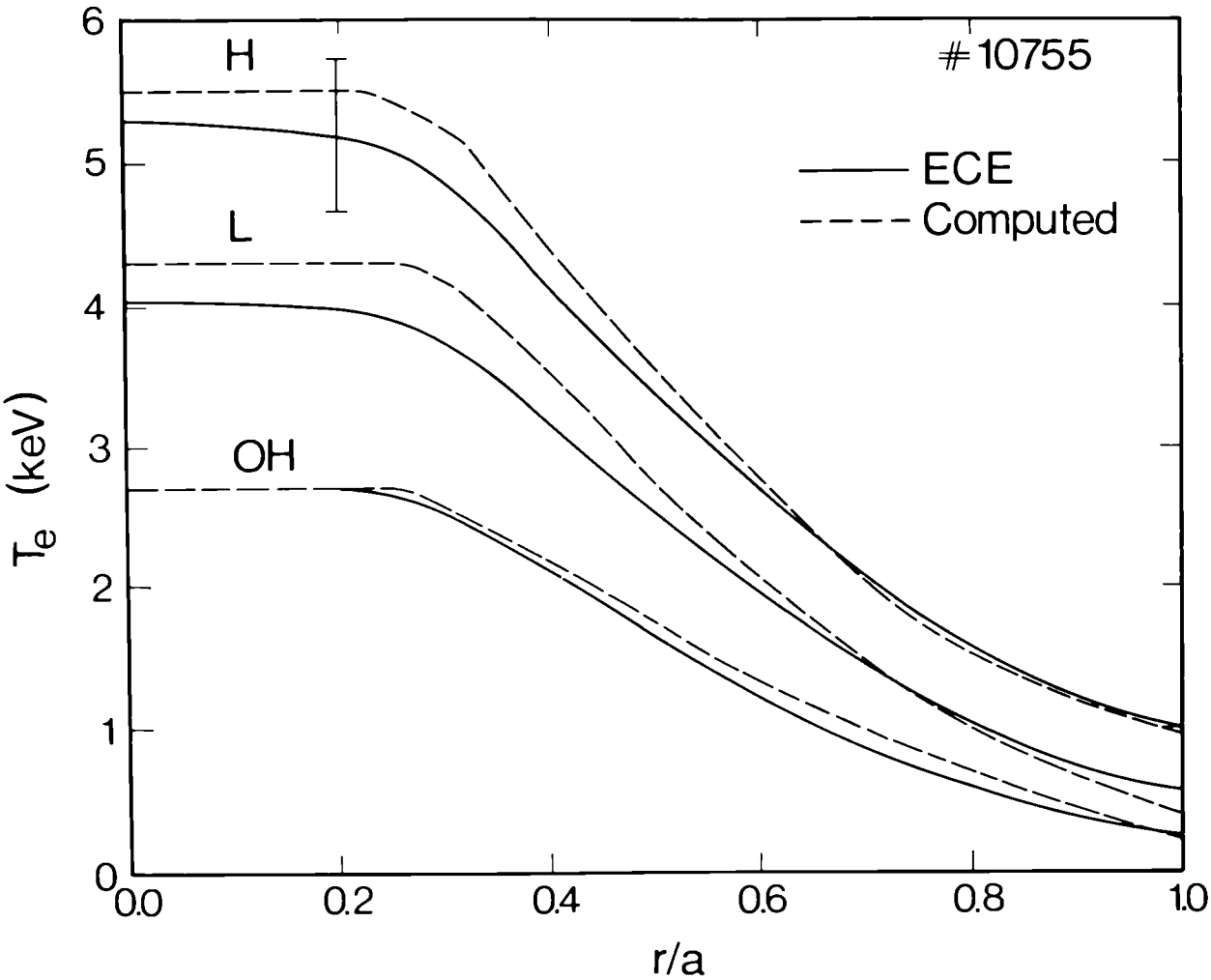

Fig. 2: Experimental (—) and computed (----) electron temperature profiles at times 10.5s (OH), 11.7s (L-mode, P~4MW) and 12.7s (H-mode, P~8MW) during JET Pulse 10755.

Fig. 3(a)

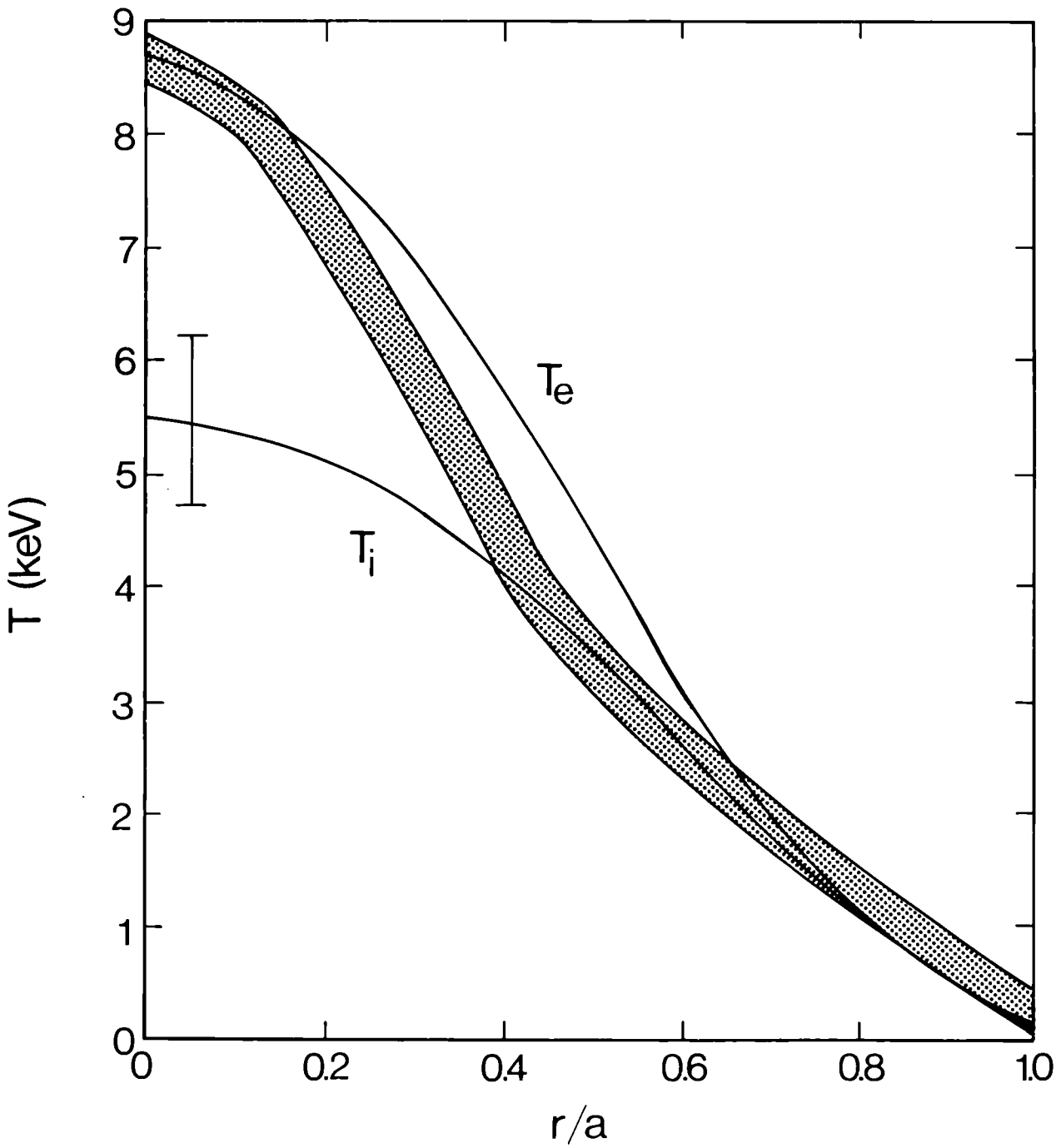

Fig. 3: Experimental (▒▒▒ , ⧫) and computed (—) temperature profiles for (a) JET "Monster sawtooth" and (b) TFTR "Supershot".

Fig.3(b)

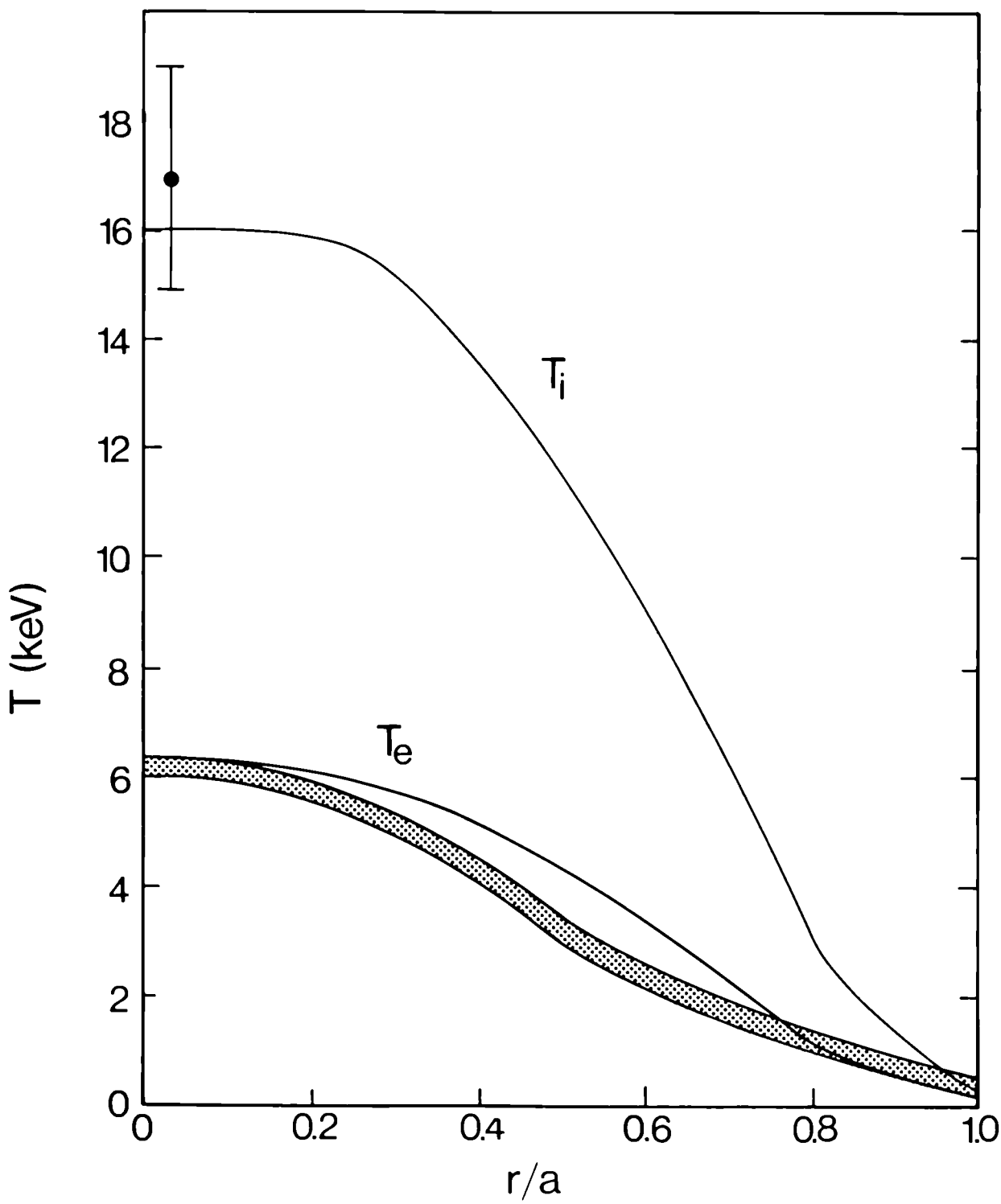

A607

IAEA-CN-50/I-2-2

MEASUREMENTS OF CORRELATIONS BETWEEN THERMAL AND PARTICLE TRANSPORT IN JET

A D Cheetham, A Gondhalekar, J C M de Haas*, O N Jarvis,
P D Morgan, J O'Rourke, G Sadler, and M L Watkins

JET Joint Undertaking, Abingdon, OX14 3EA, UK
*FOM Instituut voor Plasmafysica "Rijnhuizen", The Netherlands.

MEASUREMENTS OF CORRELATIONS BETWEEN THERMAL AND PARTICLE TRANSPORT IN JET

Abstract

Radial thermal and particle diffusivities have been measured using transient methods yielding χ and D simultaneously in the plasma interior at $0.5 \lesssim r/a \lesssim 0.7$. $\chi_e = 2.9 \pm 0.4$ m²/s and $D_e = 0.4 \pm 0.1$ m²/s have been measured in OH plasmas, giving $\chi_e/D_e = 7.2 \pm 3$. NBI heated H-mode plasmas are indistinguishable from OH plasmas in respect of χ_e, D_e and χ_e/D_e in the region specified. The ion thermal diffusivity has also been been measured in H-mode plasmas, giving $1 < \chi_i (m^2/s) < 3$, simultaneously with $\chi_e = 3 \pm 0.5$ m²/s, thus $0.3 < \chi_i/\chi_e < 1$. The large value of χ_e/D_e would suggest that micro-magnetic stochasticity, rather than $\underline{\tilde{E}} \times \underline{B}$ convection, may be the key mechanism in anomalous thermal transport.

1. INTRODUCTION

An important objective in tokamak research is to find suitable descriptions for the measured radial thermal and particle fluxes, and to identify underlying mechanisms of transport. Many models for transport in tokamaks have been developed which make specific predictions for correlations between thermal and particle transport [1,2,3]. Correlations amongst the transport coefficients arise due to mutual interference between the simultaneously occurring processes in the system, which is described by some form of Onsager relations. In order to exclude some of the contending models, accurate measurements of the correlations are required. To reduce uncertainties arising from shot-to-shot and spatial variations it is necessary to determine these coefficients simultaneously in the same spatial region of the plasma. Static experiments involving steady-state analysis for determination of correlations between the coefficients are likely to be inconclusive and transient methods which do not strongly perturb the plasma are needed.

We present simultaneous measurements of radial thermal and particle transport coefficients using a method that satisfies the above requirements, namely, the analysis of the inward propagation of temperature and density perturbations produced when a small pellet is injected into the plasma. The results are compared with those obtained by analysis of electron temperature and density pulses propagating outwards following sawtooth collapse, and time dependent transport analysis applied to non-stationary plasmas. In this paper the pellet injection method is extended to H-mode plasmas, and to measurement of χ_i simultaneously with χ_e and D_e. The paper incorporates results from earlier publications [4,5] where details of the applied methods are given. Other transient methods to measure electron density and thermal transport, by modulating the sources, have also been used in JET [6, 7,8]. However, these methods cannot be applied simultaneously.

In the following we contrast thermal and particle transport behaviour in Ohmically heated (OH) deuterium plasmas in the outer-limiter configuration in the parameter range I_ϕ=3MA, $2.8 \lesssim B_\phi(T) \lesssim 3.4$, $T_e(0) \approx 3$keV, $T_i(0) \approx 1.5$keV and $1.5 \lesssim \bar{n}_e(10^{19}m^{-3}) \lesssim 2.7$ [5], with that in NBI heated H-mode deuterium plasmas limited by a magnetic separatrix formed during single-null X-point operation, in the parameter range I_ϕ=3MA, $B_\phi \approx 3$T, $T_i(0) \approx T_e(0) \approx 5$keV, $\bar{n}_e \approx 5 \times 10^{19} m^{-3}$, with ≈8MW of NBI heating. Table I summarizes the measurements.

2. DETERMINATION OF χ_e, D_e AND χ_i BY PELLET INJECTION

Local thermal and particle diffusivities are determined by analysis of propagation of temperature and density perturbations caused by a small pellet injected in the horizontal mid-plane, penetrating to a radius r_p such that $r_p/a \approx 0.7$, where a is the minor radius. The propagation is analysed in the region $r_c < r < r_p$, where r_c is the sawtooth inversion radius.

2.1 Electron thermal diffusivity, χ_e, is determined by comparing the measured evolution of the electron temperature profile at $r_c < r < r_p$ with a simulation. The evolution of $T_e(r)$ is governed by the continuity equation

$$dW_e(r)/dt = -\mathrm{div}\, Q_e(r) + S(r), \quad W_e(r) = (3/2) n_e(r)\, T_e(r) \qquad -1-$$

Q_e and $S(r)$ are the thermal flux and source. Two models for Q_e, suggested by steady-state power balance analysis[9], are tested:

(a) Diffusive model with a constant thermal pinch in which $Q_e = -n_e \chi_e \nabla T_e + Q_p$. We assume that $\chi_e(r) = \chi_o[1+\alpha(r/a)^\beta]$ and the thermal pinch Q_p are independent of local plasma parameters but have arbitrary spatial profiles. Because the applied perturbation is small $Q_p(r)$ and $S(r)$ are assumed to remain stationary during T_e profile evolution, allowing them to be combined into an effective source, $S_{eff}(r)$, so that eq.1 becomes

$$dW_e/dt = \mathrm{div}\{n_e \chi_e \nabla T_e\} + S_{eff}, \quad S_{eff} = -\mathrm{div} Q_p + S \qquad -2a-$$

(b) Non-linear model for χ_e in which $Q_e = -n_e \chi_e \nabla T_e$ where $\chi_e(r) = \chi_{oo}\{|\nabla T_e|/(T_o/a)\}^\delta + \chi_o\{1+\alpha(r/a)^\beta\}$, (T_o/a) is a normalizing parameter. The first term with χ_{oo} dominates everywhere except near the plasma center where it is zero, and in the edge region where global power balance requires that $\chi_e(r)$ increase sharply. The second term with χ_o adjusts these two end regions and is negligible elsewhere. Thus in the measurement region, the non-linear χ_e is emphasized. This idealized non-linear χ_e model does not admit any thermal pinch. A non-linear χ_e model has also been proposed for modelling of TFTR electron temperature profiles [10]. Eq.1 then becomes

$$dW_e/dt = \mathrm{div}[(n_e \chi_{oo}\{|\nabla T_e|/(T_o/a)\}^\delta + n_e \chi_o\{1+\alpha(r/a)^\beta\})\nabla T_e] + S \qquad -2b-$$

After pellet injection, evolution of $T_e(r)$ takes place initially in the presence of strong temperature gradients. Thus this method will be a sensitive test of the ∇T_e dependence of χ_e.

The initial conditions for solving eq.2a and 2b, the temperature and density profiles instantly after pellet injection, are determined from measurements of $T_e(r)$, $n_e(r)$, pellet mass, ablation rate and penetration depth. Fig. 1 shows $T_e(r)$ and $n_e(r)$ immediately before and after pellet injection. During evolution of $T_e(r)$ the perturbed density profile is assumed to be stationary. This is justified a posteriori because the density perturbation travels much more slowly than the temperature perturbation, as will become clear in the following.

Fig.2 shows a representative comparison between the measured and modelled $T_e(r,t)$ at four radii for a H-mode plasma, applying diffusive model with thermal pinch, eq.2a. Assuming $\chi_e(r)$, $S_{eff}(r)$ is calculated for the equilibrium pre-pellet plasma and maintained stationary thereafter. The modelled evolution of T_e is found to be sensitive only to the local value of χ_e. We have assumed $\chi_e(r)=\chi_o[1+\alpha(r/a)^\beta]$, where α and β are such that $\chi_e(r)$ is nearly constant in the measurement region and increases sharply at the plasma edge. Such a form for $\chi_e(r)$ is suggested by power balance considerations. χ_o is iterated until agreement with the measured T_e is obtained. Fig. 2 shows the close agreement obtained between the measured and modelled T_e profile evolution using this diffusive model with thermal pinch and $\chi_e=3\pm0.5$ m²/s for the H-mode plasma. Application of the same model to the OH case has yielded $\chi_e=2.8\pm0.3$ m²/s [5], table I.

The non-linear χ_e model has been applied similarly, employing eq.2b. Assuming δ and χ_{oo}, $S(r)$ is calculated for the equilibrium pre-pellet plasma and maintained stationary thereafter. χ_{oo} is iterated until a good match between measured and modelled $T_e(r,t)$ is found. The procedure is applied to the OH case [5] to test the admissibility of the non-linear χ_e model. Fig.3 shows such a comparison for three values of δ. The modelled T_e evolution can be understood as follows. Immediately after pellet injection ∇T_e is largest, and therefore χ_e, closest to the pellet penetration radius. This causes a fast initial drop in T_e in the measurement region. As ∇T_e and χ_e decrease the rate of change of T_e decreases. As δ is reduced, the initial $\dot{T}_e$ becomes smaller, giving better match with measurement. The best overall match always requires $\chi_e \approx 3$m²/s in the measurement region. In order to obtain as good a match as in fig.2, the non-linearity must be very weak, $0 \leq \delta << 1$, thus reducing the problem to that of eq.2a. Such analysis has been repeated for the H-mode data. The outcome is similar, but less firm. This is because the change induced in ∇T_e is smaller than in the previous OH case, and also the measurements are situated further away from the location of greatest change in ∇T_e, thus reducing

the measurable effect. On this basis, the non-linear χ_e model may be excluded. Similar conclusions have been reached for NBI [9] and ICRF [11] heated JET plasmas, using steady state power analysis.

2.2 Electron particle diffusivity, D_e, is determined by comparing the temporal evolution of $n_e(r)$ with a simulation using a diffusive model including sources [5],

$$dn_e(r)/dt = -\text{div}\ \Gamma_e(r) + S_e(r) \qquad -3-$$

$\Gamma_e = -D_e \nabla n_e + \Gamma_p(r)$, S_e is the electron source, and $\Gamma_p(r) = n_e(r)V_p(r)$ a convective (pinch) particle flux. The diffusion coefficient is taken as $D_e(r) = D_o[1+\alpha(r/a)^\beta]$, giving a minimum in the core and a sharp increase at the plasma edge. This form for $D_e(r)$ is justified by our previous measurements of density profile dynamics in JET [6,7], where details of determining the source $S_e(r)$ are also given. D_o is iterated until a good match between the modelled and measured $n_e(r,t)$ is achieved. For the OH plasma $D_e = 0.4 \pm 0.1$ m²/s, and the corresponding $V(r) \approx -V_o(r/a)^4$, with $V_o \approx 1$m/s, giving $\Gamma_p = -(2 \pm 0.7).10^{18}/m^2.s$. For the H-mode plasma $D_e = 0.3$-0.6 m²/s, the large uncertainty arising due to uncertainties in determining the particle source.

2.3 Ion thermal diffusivity, χ_i, is determined by analyzing propagation of an ion temperature perturbation using a transport equation analogous to eq.2a. Since the ion temperature cannot at present be measured with the required spatial and temporal resolution, we have employed propagation of perturbations of thermonuclear neutron emission, as evidenced by a multi-chord neutron camera [12], viewing a poloidal cross-section of the plasma from above, to deduce χ_i. In OH plasmas T_i is not high enough to give sufficient neutron flux to the camera for high quality neutron emission profile analysis. Therefore the NBI heated H-mode plasmas have been analyzed for the χ_i determination. Fig.4 shows temporal evolution of line-integrated neutron emission in five chords viewing the outside half of the plasma cross-section. The pellet is injected at t=54.8s, which instantaneously reduces T_i for $r \geq r_p$. Fig.4 shows that the neutron emission on the chords passing through the cold plasma (#19) also instantaneously drops, whereas the neutron emission on the chords viewing the plasma further inside drops more slowly. The geometry of the cords is explained in [11]. In fig.4 we observe a neutron emissivity perturbation due to an ion temperature 'cold' front travelling diffusively into the plasma. We have modelled this process as follows. The equilibrium (pre-pellet) deuteron density profile, $n_i(r)$, is constructed from the measured profiles $n_e(r)$ and $Z_{eff}(r)$. The pre-pellet deuteron temperature profile, $T_i(r)$, is assumed to be Gaussian with the measured peak value $T_i(0)$. The width of the Gaussian is adjusted to match the thermonuclear part of the measured neutron yield, taking into account the proportion of beam-plasma and thermonuclear neutron yield, which is deduced from a model calculation of the neutral beam dynamics within the TRANSP code [13]. The model calculation also gives spatial neutron emissivity profiles for neutrons from each of the two reactions.

After pellet injection the beam-plasma neutron emissivity profile is assumed to remain unchanged, which is reasonable since the pellet produces only a small perturbation of the plasma parameters, and the NBI power remains constant. The observed perturbations in the total neutron yield are attributed to perturbations of ion temperature and its consequences for the thermonuclear neutrons. The initial condition for solving the diffusion equation for χ_i, analogous to eq.2a, is the deuteron density and temperature profiles immediately after pellet injection. $n_i(r,t=0)$ is deduced as before from pellet deposition, and $T_i(r,t=0)$ is derived by assuming adiabatic response of the ion temperature. The temporal evolution of $T_i(r)$, the corresponding thermonuclear neutron emissivity, and the total line-integrated neutron emission observed in each cord of the neutron camera are calculated. The perturbed $n_i(r)$ is assumed to be stationary during evolution of $T_i(r)$. The value of χ_i in the measurement region is iterated until a match is obtained with the observed temporal evolution of the emission, fig. 5. This procedure yields $1<\chi_i(m^2/s)<3$, simultaneously with $\chi_e=3\pm0.5 m^2/s$, giving $0.3<\chi_i/\chi_e<1$ for the H-mode plasmas. Errors in measurements of neutron yield, emissivity profile, $T_i(0)$, and $n_i(r)$ are taken into account in determining the band of admissible χ_i.

3. CONCLUSIONS

Table I summarizes the observations. Modelling of inward propagation of electron temperature perturbation following pellet injection seems to exclude the non-linear χ_e model in favour of the diffusive with constant heat pinch description of thermal fluxes in JET. Simultaneous direct measurements of radial thermal and particle diffusivities yield $\chi_e=2.9\pm0.4$ m²/s and $D_e=0.4\pm0.2$ m/²s, giving $\chi_e/D_e=7.2\pm3$ at $0.5\leq r/a\leq0.7$ in the OH plasma. The H-mode plasma, with ≈8MW of NBI heating, is indistinguishable from the OH plasma in respect of χ_e, D_e, and χ_e/D_e. The ion thermal diffusivity has also been determined in the specified region for the H-mode plasma, giving $1<\chi_i(m^2/s)<3$, thus $0.3<\chi_i/\chi_e<1$. An aim of our future work is to incorporate impurity transport into this scheme.

The large value of χ_e/D_e would suggest that micro-magnetic stochasticity [2], rather than $\tilde{\underline{E}} \times \underline{B}$ convection [3], may be the principal mechanism in the observed anomalous radial thermal transport in JET. The above observation is contrary to that reported from other experiments [14,15], where thermal and particle diffusivities of equal magnitude are deduced and $\tilde{\underline{E}}\times\underline{B}$ transport inferred. The critical temperature gradient model of anomalous transport [16,17], which invokes magnetic stochasticity, has been used to interpret energy transport in JET. The large value of χ_e/D_e seems to be consistent with the model expectations. The similarity of OH limiter plasmas and NBI heated H-mode plasmas in respect of electron thermal and particle transport behaviour in the plasma interior suggests that the same underlying mechanism of anomalous transport is operative in the two cases, although they are quite different in respect of magnetic configuration, temperature range, and density profile shape. The intrinsically better particle (vs thermal) confinement witnessed here, which will similarly affect recycled impurities and helium ash, may pose the more severe barrier in future reactor oriented tokamak experiments.

Table I: Some Elements of the Radial Transport Matrix

	OH limiter plasma [5]			
	$\chi_e(m^2/s)$	$D_e(m^2/s)$	$-\Gamma_D$ $(10^{18}/m^2s)$	$\rho = r/a$
a	2.8±0.3	0.4±0.1	2±0.7	$0.5 \leq \rho \leq 0.6$
b	2.9±0.4	0.4±0.2	-	$0.6 \leq \rho \leq 0.8$
c	-	$0.4^{+0.2}_{-0.1}$	$1.4^{+5}_{-0.5}$	$\rho \approx 0.67$
	NBI heated H-mode plasma			
	$\chi_e(m^2/s)$	$D_e(m^2/s)$	$\chi_i(m^2/s)$	$\rho = r/a$
a	3±0.5	0.3-0.6	1-3	$0.4 \leq \rho \leq 0.6$
b	3±0.6	-	-	$0.5 \leq \rho \leq 0.7$
c	2(d)	0.2-0.3 0.3-0.4	-	$\rho \approx 0.5$ $\rho \approx 0.67$

where
(a) Perturbations of n_e and T_e by pellet injection [5].
(b) Sawtooth density and heat pulse propagation [18,19].
(c) Time dependent transport analysis, 'flux-gradient' method [5]. Inferred χ is for a single fluid plasma.
(d) I_ϕ=2MA, B_ϕ=2T, different from that for the other data.

ACKNOWLEDGEMENTS

The authors are grateful to J Fessey and D Garton for computational support, to J M Adams, M von Hellermann, D Muir, P D Larsen and N Watkins for providing and validating data, and to J D Callen and R Galvao for valuable discussions.

REFERENCES

[1] Callen, J.D., Physics models used to describe plasma confinement and heating. JET Report JET-IR(87)07, JET Joint Undertaking, (1987).
[2] Callen, J.D., Physical Review Letters 39(1977)1540.
[3] Lee, G.S. and Diamond, P.H., Phys. Fluids 29(1986)3291.
[4] Gondhalekar, A., et al., 15th Euro. Conf. on Controlled Fusion and Plasma Physics, Dubrovnik, 1988. Europhys. Cont. Abstracts, Vol.12b, part I, p.151.
[5] Gondhalekar, A., et al., to be published in Plasma Physics and Controlled Fusion, 1988.
[6] Gondhalekar, A., et al., Bull. Am. Phys. Soc. 30(1985)1525 and JET Report JET-P(85)31.
[7] Cheetham, A.D., et al., 13th Euro. Conf. on Controlled Fusion and Plasma Physics, Schliersee, 1986. Europhys. Conf. Abstracts Vol.10c, part I, p.240.
[8] Start, D.F.H., et al., 12th IAEA Conf. on Plasma Physics and Controlled Nuclear Fusion Research, Nice, France, 1988. Paper IAEA-CN-50/E-2-3.
[9] Callen, J.D., et al., Nuclear Fusion 27 (1987) 1857.
[10] Boyd, D.A., et al., 11th IAEA Conf. on Plasma Physics and Controlled Nuclear Fusion Research, Kyoto 1986. Proceedings, 1(1987)387.
[11] Christiansen, J.P., JET Joint Undertaking, private communication.
[12] Adams, J.M., et al., 14th Euro. Conf. on Controlled Fusion and Plasma Physics, Madrid 1987. Europhys. Conf. Abstracts Vol. 11d, part III, p.1224.
[13] Goldston, R.J., et al., J. Comput. Physics 43(1981)61.
[14] Kim, S.K., et al., 15th Euro. Conf. on Controlled Fusion and Plasma Physics, Dubrovnik 1988. Europhys. Conf. Abstracts Vol.12b, part I, p.187.
[15] Efthimion, P.C., et al., 12th IAEA Conf. on Plasma Physics and Controlled Nuclear Fusion Research, Nice, 1988. Paper IAEA-CN-50/A-V-4.
[16] Rebut, P.H., et al., 11th IAEA Conf. on Plasma Physics and Controlled Nuclear Fusion Research, Kyoto 1986. Proceedings, 2(1987)187.
[17] Rebut, P.H., et al., 12th IAEA Conf. on Plasma Physics and Controlled Nuclear Fusion Research, Nice, 1988. Paper IAEA-CN-50/D-4-1.
[18] Hubbard, A., et al., 13th Euro. Conf. on Controlled Fusion and Plasma Physics, Schliersee, 1986. Europhys. Conf. Abstracts Vol.10C, part I, p.232.
[19] Tubbing, B.J.D., et al., Nuclear Fusion 27(1987)1843, and Lopes-Cardozo, N.J., et al., Nuclear Fusion 28(1988)1173.

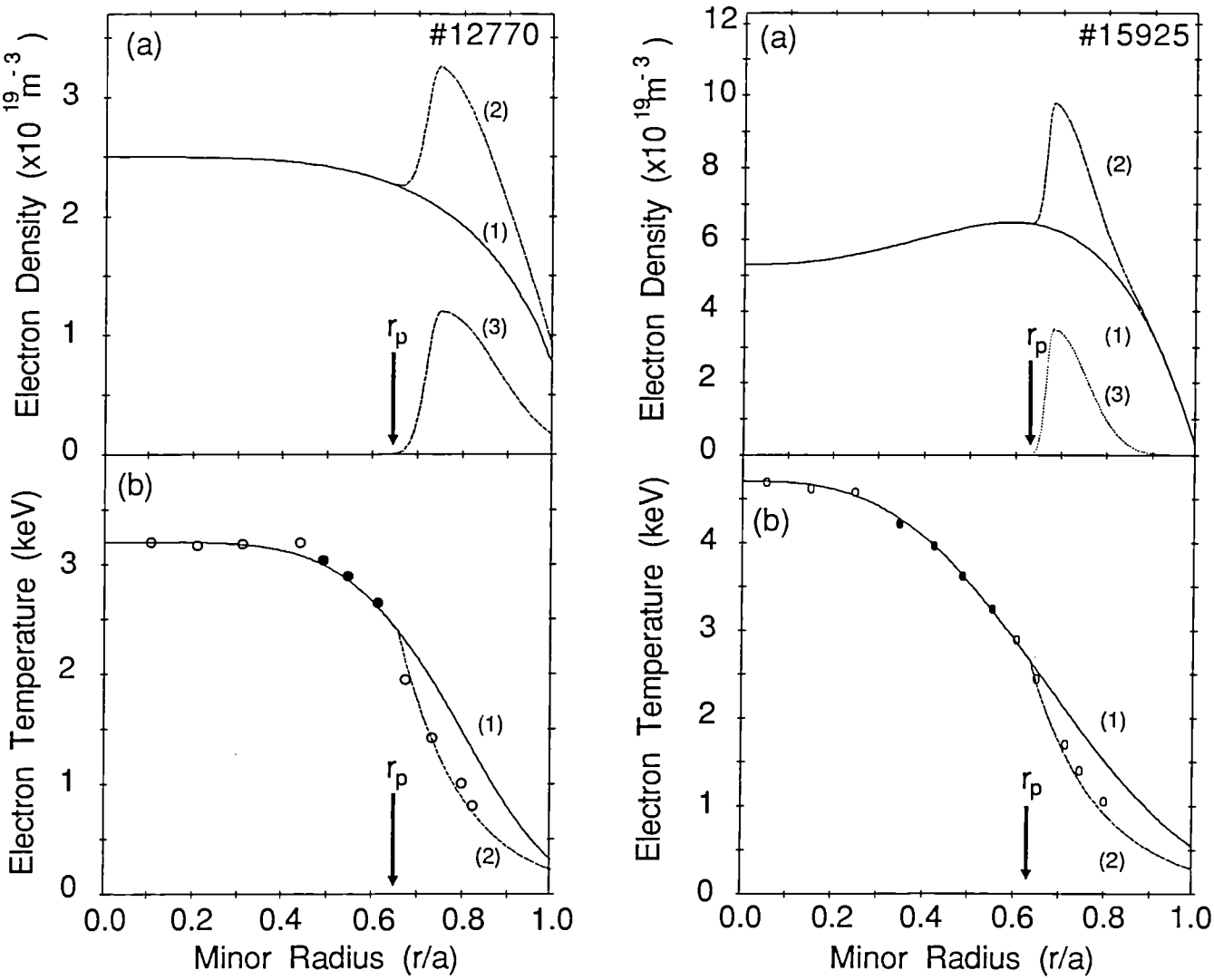

Fig.1 Radial electron temperature and density profiles for the OH (#12770) and NBI heated H-mode (#15925) plasmas.

(a) Pre-pellet equilibrium electron density profile (1), the calculated pellet deposition profile (3), and the total post-pellet density profile (2).

(b) Pre-pellet equilibrium electron temperature profile (1), and post-pellet T_e profile (2). The circles denote the measurements. The solid circles denote the points for which comparisons of measurement and modelling of temperature evolution are made.

The profiles (a2) and (b2) are the initial conditions for the transport calculation.

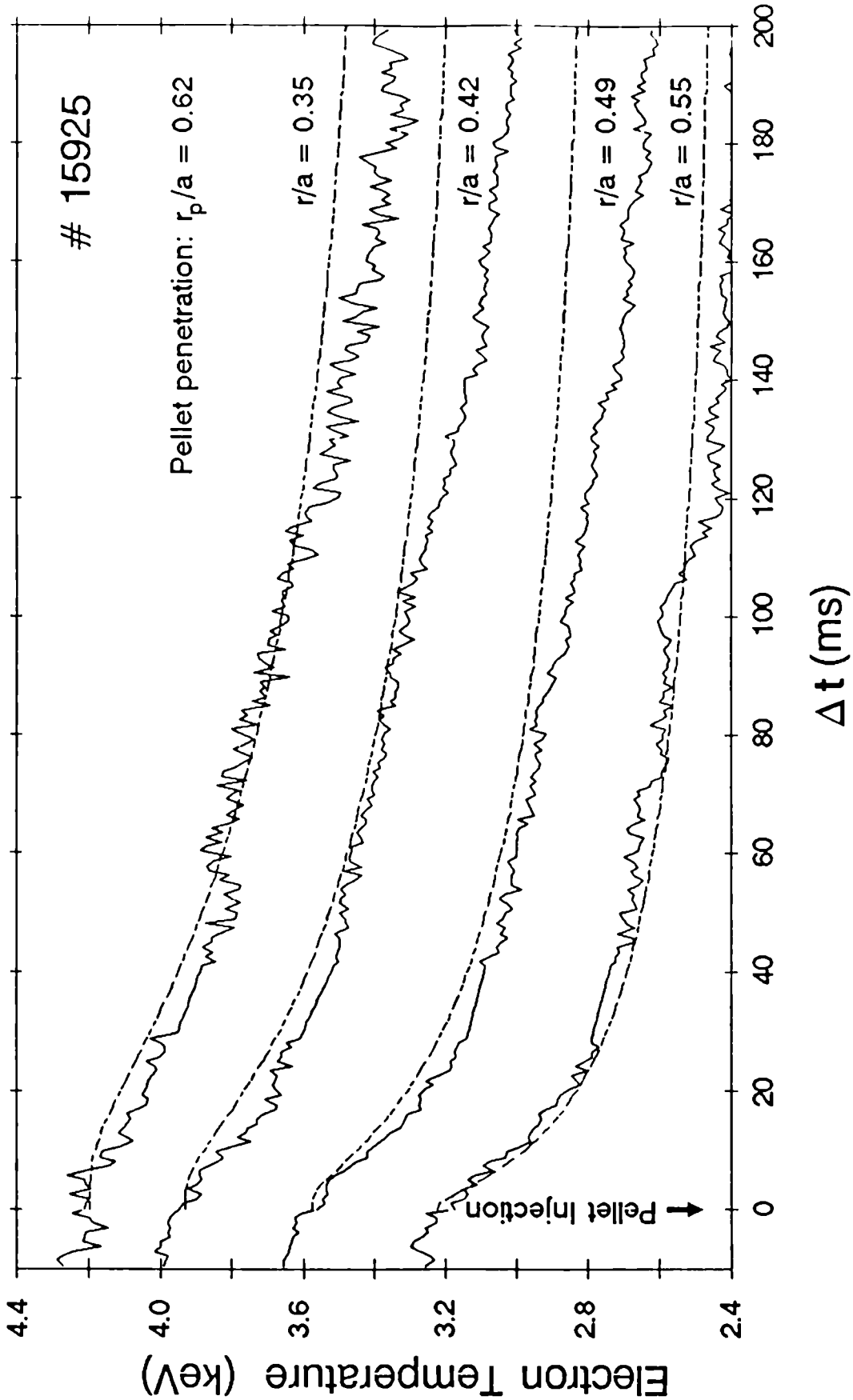

Fig.2 Temporal evolution of the electron temperature at four radii after injection of a pellet into the H-mode plasma (#15925). The full line is the measured electron temperature using ECE, and the dashed line is the modelled evolution using the diffusive model with thermal pinch.

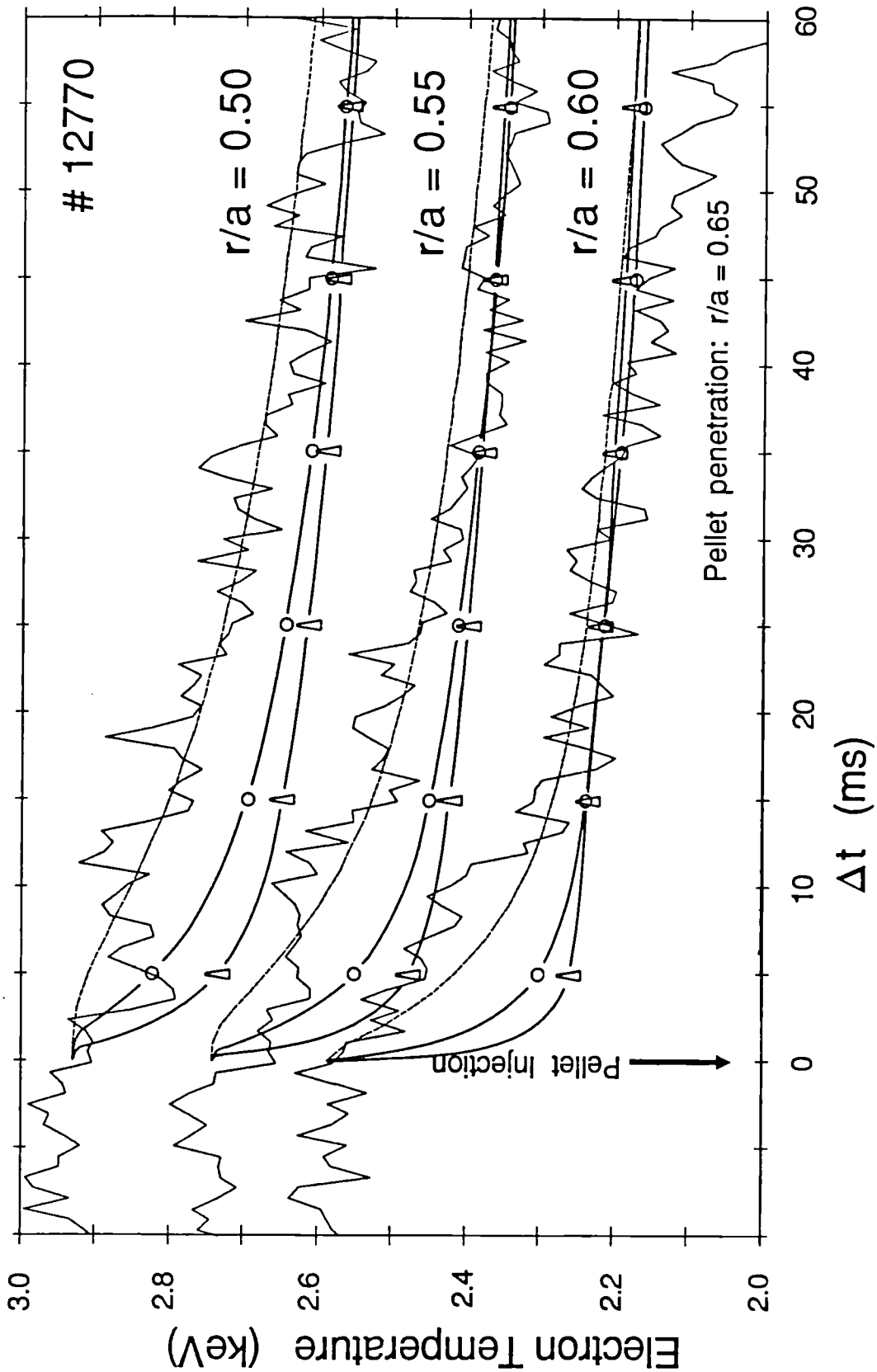

Fig.3 Temporal evolution of the electron temperature at three different radii after injection of a pellet into the OH plasma (#12770). The full line (—) is the measured electron temperature using ECE. The modelled temperature evolution using the non-linear χ_e model with δ=0 (---), δ=0.5 (-o-) and δ=1 (-Δ-) are also shown.

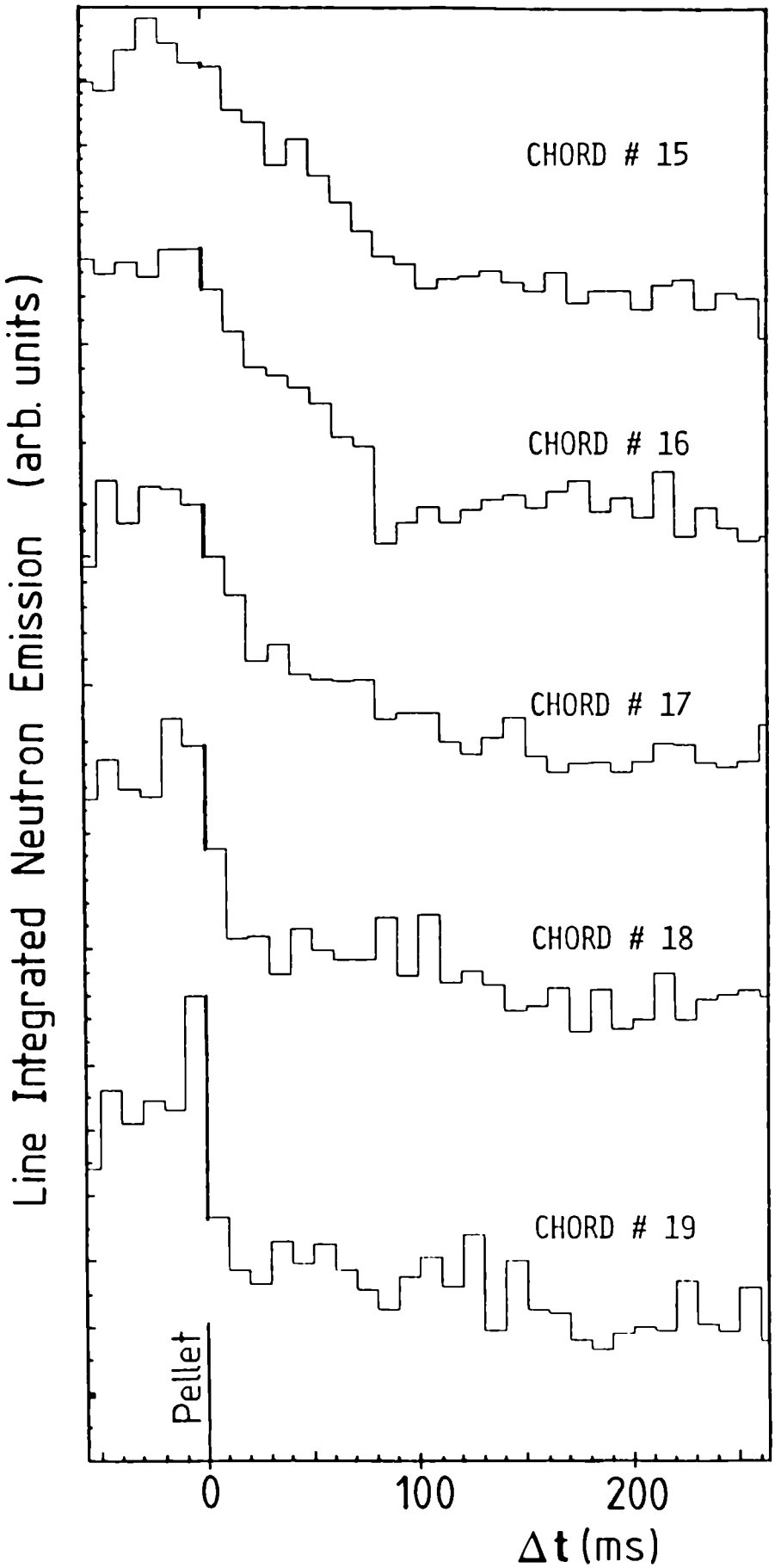

Fig.4 Evolution of line integrated neutron emission after pellet injection along chords with major radius between 3.78m (chord 19) and 3.02m (chord 15).

A619

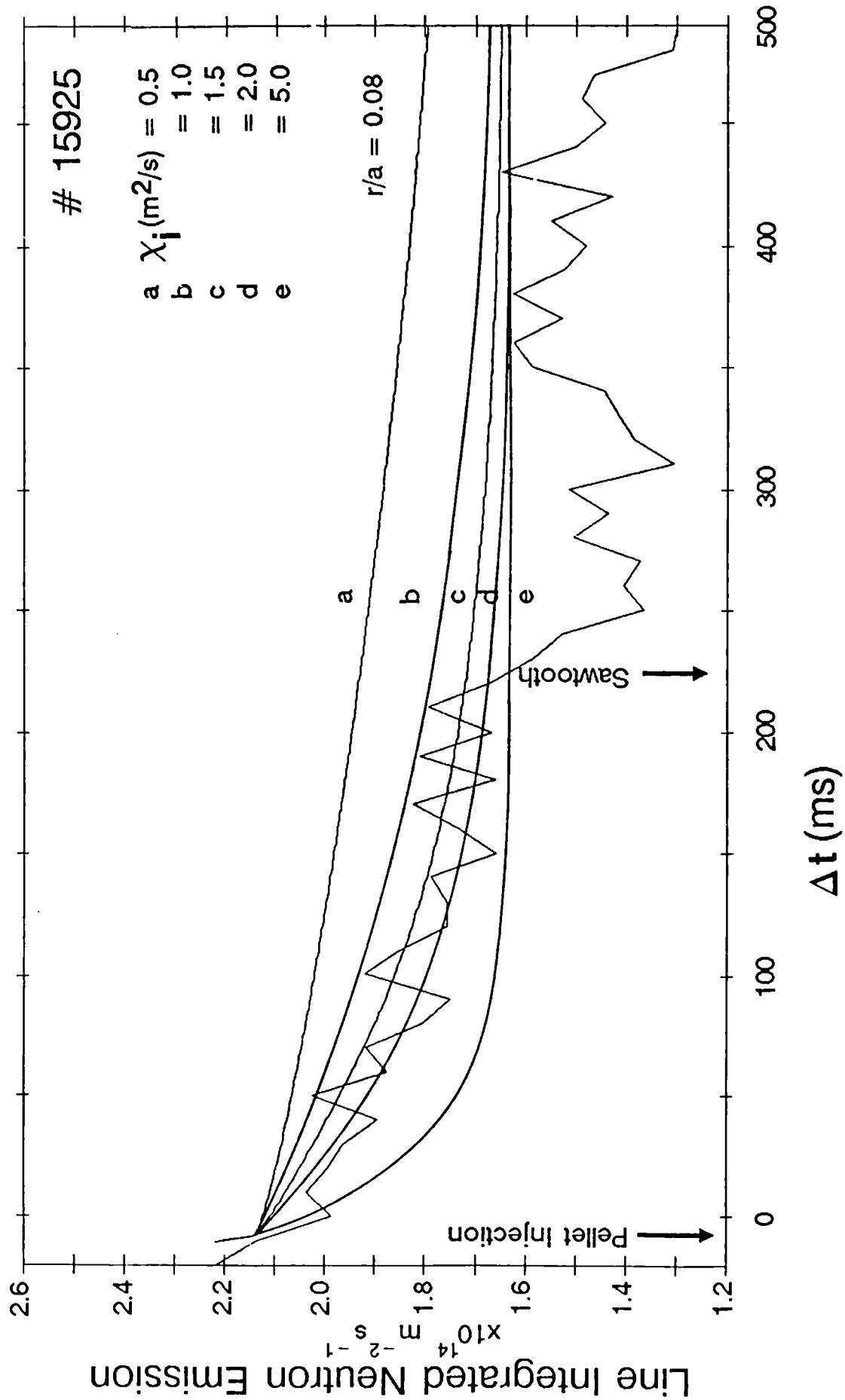

Fig.5 Comparison of modelled and measured temporal evolution of the line integrated neutron emission for different values of the assumed χ_i.

Implications of Fusion Results for a Reactor: A Proposed Next Step Device—JIT

P.H. Rebut

JET Joint Undertaking, Abingdon, Oxon, OX14 3EA, U.K.

Abstract

Simulations with a 'critical-temperature' model have been made of proposed future devices (NET, ITER, JIT, etc.). These show that only machines with a current capability of ~30MA have a sufficient ignition domain to cope with more realistic operating conditions (i.e. taking into account sawteeth effects, impurity dilution and semi-continuous operation). The importance of dilution and Bremsstrahlung radiation are clearly demonstrated; a mean temperature >7 keV is required for ignition. This prevents higher field, lower current devices from reaching ignition. Transient operations with monster sawteeth or H-mode allow such devices (>30MA) to reach ignition at lower density without additional heating.

To investigate the problems of a controlled burning plasma for days in semi-continuous operation, the plasma of the next-step tokamak should be similar in size and performance to an energy producing reactor. The scientific and technical aims of such a machine should be to study burning plasma, test wall technology, provide a test-bed for breeding blankets and most importantly to demonstrate the potential and viability of fusion as an energy source.

The main design characteristics of a Thermonuclear Furnace—JIT—dedicated to these objectives are presented. Basically, the plasma parameters are scaled up from JET by a factor of 2.5. Watercooled copper magnets are used to benefit from proven technology. A single-null divertor configuration ensures helium exhaust and possibly benefits from an H-mode to reach the ignition domain. The X-point position relative to the dump plates would be swept to limit wall loading. By changing operating density, the thermonuclear power could be varied from 0.5 to 4 GW(th), according to power loading and tritium consumption.

1. Introduction

The behaviour of JET thermonuclear grade plasmas, especially relating to energy confinement, allows conclusions to be drawn for conditions in a future reactor.

A critical temperature model permits good simulation of most JET results [1,2,3]. Such a tool has been used to study the ignition of different proposed machines and to define possible parameters for a next step device. Such a device could be conceived as a thermonuclear furnace producing a power reactor plasma, but without a full blanket and superconducting coils.

CR 88 144

2. Consequences of JET Results

Latest JET results[3] lead to the following conclusions:

Energy Confinement: L- and H-mode plasmas both exhibit confinement degradation with power. Confinement times are 2-3 times higher for the H-mode, but the H-mode is transient as the density is still increasing. Confinement times increase with plasma current but degrade at low q as a consequence of sawteeth; the optimum q is 3-4. Anomalous heat transport is similar for ions and electrons.

Generally, the fusion product is insensitive to additional heating power: ignition is a property of the device.

Particle Confinement: Knowledge of particle confinement is needed to define the acceptable level of impurities and the level of fuelling and pumping required by a reactor.

Energy transport and particle transport in JET are linked with $D \sim 1/5\chi_i$. When χ_i becomes close to neoclassical transport, accumulation of impurities is seen.

Impurities: The impurity content is controlled mainly by interactions with the plasma at the limiter, but materials of the first wall could be transported onto the limiter by the plasma at disruptions.

Graphite is employed in JET as the first wall and behaves generally well. However, problem areas have been identified with: its role as an impurity source; high chemical reactivity with hydrogen; problems with density control; and hydrogen (tritium) retention.

At high power, impurity dilution of deuterium becomes serious; without refuelling, the dilution factor, $d = n_D/n_e$, is less than 0.5; with neutral beam injection, d is ~ 0.5; and with pellets, d close to unity was reached.

Density Limit and Disruptions: The limit in density is due to disruptions, which seemed to be linked to edge radiation ($\sim 100\%$ of the total power in the $q \gtrsim 2$ region). The density limit improved with high heating power, cleaner plasmas and peaked plasma profiles (high density in the centre and low on the edge). Disruptions were preceded by locked modes ($m=2$, $n=1$).

Low q Operation: At low q, disruptions could occur at $q_\psi = 2$ ($q_\psi = 3$) or following a giant sawtooth crash. Confinement times also decreased at low q. A β limit has not yet been reached on JET, but its effect has been seen in other devices.

3. Simulation of Ignition with 'Critical Temperature' Model

Generally the critical temperature model successfully describes most JET results in terms of energy transport. Density and impurity profiles must be known as

particle transport has not yet been included. In this model, anomalous transport occurs above a critical temperature gradient[4].

This specific model gives a general scaling, for asymptotic behaviour (at high power), of the form:

$$\tau_E \propto I_p a R^{1/2}$$

$$(\hat{n}\hat{T}\tau_E) \propto g I_p^2 B_t R^{1/2}$$

where g is the Troyon factor and reflects the uncertainty in the β dependence. Using a 1-D transport code, good simulations have been achieved not only of JET results but also of other tokamaks.

This model has been used to predict the size of an ignition device and its conditions of operation. To ignite within a practical ignition domain, a tokamak with plasma current capability of ~30MA and a toroidal field of 4-5T is required, (i.e. the parameters chosen for JIT). Calculations have also been undertaken for various next-step proposals: Ignitor, NET II and ITER (with dimensions and parameters as shown in Table I).

Table I
Main parameters of major fusion devices

	R (m)	a (m)	k	B_t (T)	Add. Power (MW)	I_p (MA)
JET	3	1.2	1.7	3.4	40	7
ITER	5.8	2	2.2	5.1	100	20
JIT	7.5	3	2	4.5	50	30
IGNITOR	1.16	0.43	1.8	14	10	12
NET II	6	2.2	2.2	5.4	50	27

In these simulations, radiation and dilution caused by impurities were taken into account. The hypothesis is that only low Z impurities ($Z \sim 7$) are present, giving a further 30% radiation of the total heating power near the edge, in addition to Bremsstrahlung radiation.

Sawtooth behaviour inside the $q = 1$ region plays an important role on the central ion and electron temperatures. When sawteeth are fully effective, the electron and ion temperatures and the current density are flattened inside the $q = 1$ region (see Fig.1). In 'monster' sawtooth cases, the temperature of electrons and ions are allowed to develop and the safety factor value is imposed at the centre (see Fig.2). The density profile is not calculated but taken as given by experiment. Generally, this is a relatively flat profile ($\propto [1-(r/a)^2]^{1/2}$) or even flatter in H-mode cases.

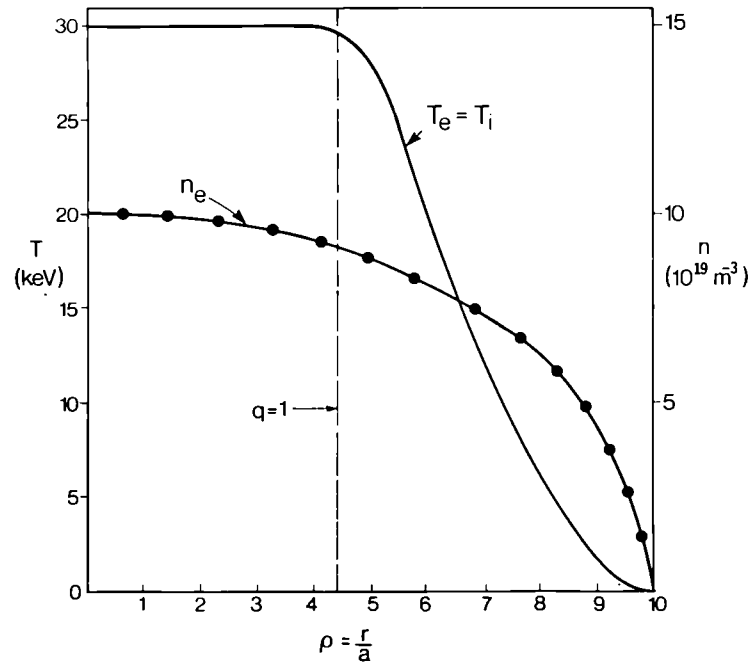

Fig. 1 Critical temperature simulation of JIT. Full ignition is obtained on JIT even with complete flattening of the temperature inside the $q = 1$ region at 20MA. The β limit ($g = 3.6$) is almost reached.

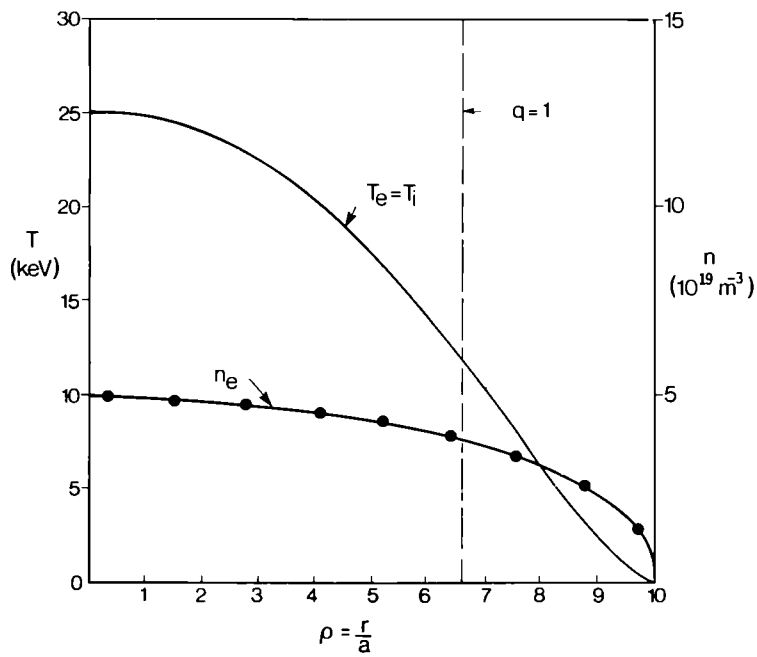

Fig. 2 Critical temperature simulation of JIT at 30MA with a monster sawtooth. Ignition is obtained without additional heating at a lower density.

Improved confinement due to peaked density profiles, seems unrealistic in a semi-continuous reactor where there are no central particle sources to maintain it. In this model, increased H-mode confinement is due to pedestals developing in regions of very high shear near the separatrix, but the main core of the plasma behaves as an L-mode (see Fig.3). Stationary H-mode operation has not yet been found experimentally which precludes considering its enhanced confinement for semi-continuous operation. Nevertheless, a transiently improved confinement (H-mode, monster sawtooth) could be useful in facilitating the transition to an ignited plasma.

Predictions for proposed future experiments are given in Tables II and III.

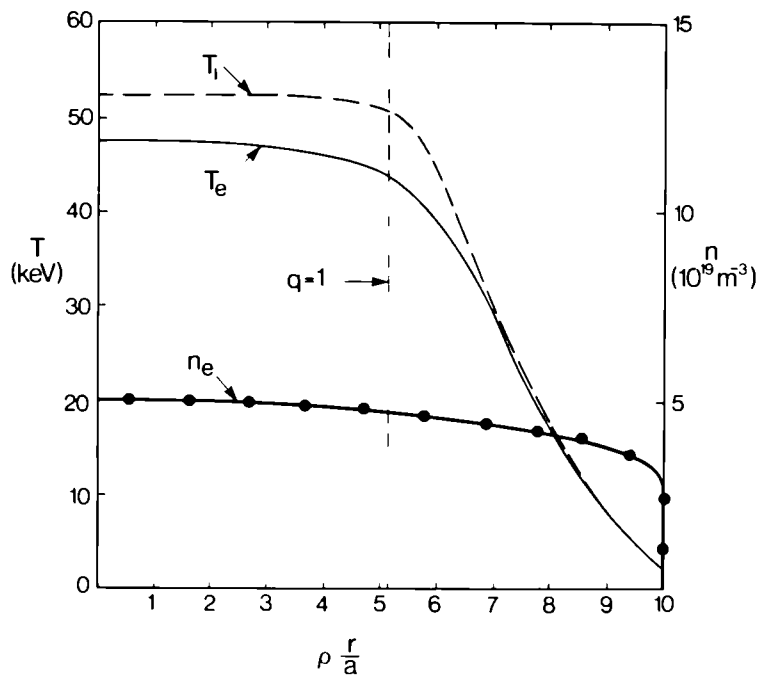

Fig. 3 H-mode simulation of JIT at 25 MA. The effect of the separatrix is taken into account by a pedestal in temperature and a flat density profile. Ignition is obtained without additional heating.

In these tables, the factor g does not include the pressure generated by the α-particles and brackets indicate that the additional power has been switched off when the α-particle power has reached sufficient level. No bootstrap current has been included.

One conclusion from the simulations is that it is extremely difficult to vary the electron temperature (and consequently the ion temperature) in a tokamak, without introducing heating power larger than the α-particle heating. In other terms, ignition could almost be reached without additional heating; only a modest level would be required in a machine like JIT (25-50MW). The increase

Table II
Predictions for JIT using critical temperature model

Device	I_p (MA)	n_{e0} $10^{19}m^{-3}$	Z_{eff}	P_{add} (MW)	$\hat{T}_i$ (keV)	$\bar{T}_e$ (keV)	P_α (MW)	g	P_{OH} (MW)	Regime
JIT	30	5	2	0	5.6	3.9	0	0.25	18	ohmic without α (q = 1 sawteeth)
	30	5	2	0	25	11	90**	0.77	5.5	ohmic + α monster q = 0.8 **Ignited**
	20	10	2	(50)*	29	15	511	3	0.75	L-mode Sawteeth (q = 1) **Ignited**
	25	5	2	0	52	28	270	2.6	0.55	H-mode (2keV) Sawteeth (q = 1)
	20	10	3	50	10	5	51	1	5.9	L-mode Sawteeth (q = 1)
	20	10	3	(50)*	32	12	262	2.3	20	L-mode Monster **Ignited**

* Brackets indicate that P_{add} has been switched off when P_α was large enough.
** P_α still rising.

Table III
Predictions for ITER, NET II and Ignitor
using critical temperature model

Device	I_p (MA)	n_{e0} $10^{19}m^{-3}$	Z_{eff}	P_{add} (MW)	$\hat{T}_i$ (keV)	$\bar{T}_e$ (keV)	P_α (MW)	g	P_{OH} (MW)	Regime
ITER	20	15	2	100	18	11.7	300	2.1	1.9	L-mode Q = 15 q = 1
	20	15	2	(100)*	30	13.2	380	2.4	2.2	L-mode monster q = 0.8 **Ignited**
	20	5	2	0	9.8	4.5	4.5	0.27	9.8	Ohmic + α monster, q = 0.8 Q = 2.3
NETII	27	5	2	0	13	6.3	13.3	0.3	11	Ohmic + α monster Q = 6
Ignitor	12	100	2	10	9.2	4.4	11.6	0.7	25	Monster Q = 1.7
	12	100	2	0	8.2	4	8.3	0.62	27	Ohmic + α Monster Q = 1.5

*Brackets indicate that P_{add} has been switched off when P_α was large enough.

in thermonuclear power is realised by increasing the density at almost constant temperature (see Table II).

High field machines generally suffer at high densities from an insufficient temperature giving rise to a high level of Bremsstrahlung radiation and to a low reactivity, even if the confinement appears good. In general, except in JIT, sawteeth are able to destroy ignition at low q. NET II should behave in a similar

fashion to JIT, if technology development is sufficient to permit the parameters in Table I to be reached.

This code also predicts that, with monster sawteeth or with an H-mode pedestal at relatively low density, JIT could reach ignition without additional heating.

3.1 Impurities

The effect of impurities is relatively dramatic: they dilute the reacting plasma and increase Bremsstrahlung radiation. Ignition is marginal in JIT: (a) with carbon type impurities $Z=7$ at $Z_{eff}=3$ where the dilution factor $d=(n_D+n_T)/n_e \sim 2/3$; or (b) with beryllium impurities, at $Z_{eff}=2.5$ and $d=0.5$. These results have to be compared to JET results at high power, where it is extremely difficult to get $d>0.5$ without particle injection of deuterium beams or pellets.

In the ignition domain, α-particle heating imposes $T_e \gtrsim T_i$ and Bremsstrahlung and fusion cross-sections require $\bar{T}>7\,\text{keV}$. Line radiation requires low Z impurities but dilution becomes a problem. In a reactor, fuelling, exhaust, pumping and impurity level depend on particle transport; a particle confinement, which is too good, could be a major threat to a reactor: $D \sim 1/5\chi_i$ is already a limit.

The β value should not limit the achievement of ignition due to the limitation of additional heating, but it might limit the maximum power produced.

A reactor should be semi-continuous and must be based on a quasi-stationary mode of operation. There is also the necessity of maintaining smooth operations free of disruptions, giant sawteeth, collapse of H-modes, etc. ($q \sim 3$). As no stationary regime has been found, 'Monsters' and H-mode could be used to reach ignition.

Extrapolation to a reactor must be made from experimental results: geometry (aspect ratio, shape) and values of B_0, Z_{eff}, etc. In order to meet these conditions, a device with a plasma capability of 30 MA is required with a sufficiently large domain of ignition to be able to cope with the operating conditions. JIT is such a device.

4. Definition of the Next Step

4.1 Reactor Studies

Reactor studies show that the thickness of the blanket and shielding inside the coils, e_b, should exceed 1 m (i.e. 1.5-2 m). To use the magnetic field efficiently, the plasma radius, a, should be greater than $2(e_b+e_c/3)$, where e_c is the toroidal coil thickness; this gives as a minimum size, $a=3\,\text{m}$. With a toroidal field of 4-5 T, and an elongation of 2, the plasma current capability of such a machine should be over 30 MA[5]. Such a reactor should be able to ignite in the L-mode without problems of confinement. To define the pumping, fuelling and exhaust

specifications, a better knowledge of particle transport and of phenomena controlling plasma wall interactions is required.

4.2 Next-Step Device

A next-step device should be aimed at producing a full reactor plasma and at demonstrating that solutions for the first wall and smooth plasma operations can be found. Such a plasma will require a very long burn (~ 30 minutes) and a high duty cycle (semi-continuous operation). It should also be possible to test different blanket concepts for DEMO. This specific choice allows a large ignition domain depending on q and plasma density: the power produced could vary in the range 500-4000MW. The optimum way to reach ignition appears to start with a plasma at a relatively low density with a moderate current of 25MA and to increase the density and plasma current when ignition is reached to produce a power level of several GW (similar to that of a reactor).

This should demonstrate the potential of fusion as an energy source. Such a device is referred to as a 'Thermonuclear Furnace' and a possible choice of parameters (JIT) is given in Table IV.

Table IV
Main parameters of a Thermonuclear Furnace (JIT)

Plasma minor radius (horizontal)	3m
Plasma minor radius (vertical)	6m
Plasma major radius	7.5m
Plasma aspect ratio	2-2.5
Flat top pulse length	1000-4000s
Toroidal field (plasma centre)	4.5T
Plasma current	30MA
Volt seconds	425Vs
Additional heating	50MW
Fusion power	500-4000MW

4.3 Semi-Continuous versus Continuous Operation

One of the questions which has an overall impact on the choice of solution and on the very concept of a reactor is that of the necessity of continuous operation, which does not seem compatible with the concept of ignition.

In a reactor at temperatures required for ignition and in the presence of bootstrap currents, the voltage per turn should be extremely low (~ 0.05V or less). Flux consumption of 100V.s during the flat-top will ensure a burn time of more than 30 minutes which could even exceed 1 hour in the presence of

bootstrap currents. A high duty cycle could be obtained by reversing the plasma current when the transformer has reached saturation.

Continuous operation of a tokamak is more complex in terms of physics and equipment. High energy neutral beams or radio-frequency techniques are required to drive the current. However, the efficiency of non-inductive current drive is quite low compared to the use of a transformer and the gain in duty cycle might not be significant. In addition to cost and complexity of equipment needed for current drive, the recirculating energy would also increase the overall cost of electricity produced by an amount which could become a dominant factor and condemn such a concept.

On the other hand, semi-continuous operation requires a moderate intermediate thermal storage or a set of tokamak-reactors working together. The main advantage of continuous operation is to reduce the thermal fatigue of components inside the reactor, but as long as the burn time is longer than one hour, this may not be important.

To maintain simplicity and considering the duty cycle and tritium consumption in the next machine, a breeding blanket seems an unnecessary complication for an apparatus which is unlikely to test any blanket material at high neutron fluence. For the next step, although some test modules of breeding blankets could be introduced, only neutron shielding must be provided.

4.4 Conclusions on a Next-Step Device

In conclusion, the next generation of tokamaks must demonstrate that an ignited and burning plasma at high power with semi-continuous operation can be realised.

The aims of such an experiment should be:

(a) to study the ignition domain;
(b) to test wall technology;
(c) to test some breeding blanket modules for DEMO;
(d) to demonstrate the potential of fusion as an energy source.

5. A Specific Concept: JIT

The main design characteristics of a thermonuclear furnace (JIT) to meet these objectives are presented, of which the main priorities are simplicity and sturdiness of concept[6, 7]. Basically, the plasma parameters are scaled up from JET by a linear factor of 2.5 and several elements of the JET concept are maintained.

To minimize technical risk, size of the coils, shielding and overall cost, water cooled copper magnets are proposed but superconducting magnets could be envisaged, if certain advantages compensated for the extra complexity. Low current density is used in the water-cooled copper coils to allow continuous operation. It must be noted that a superconducting version would almost be

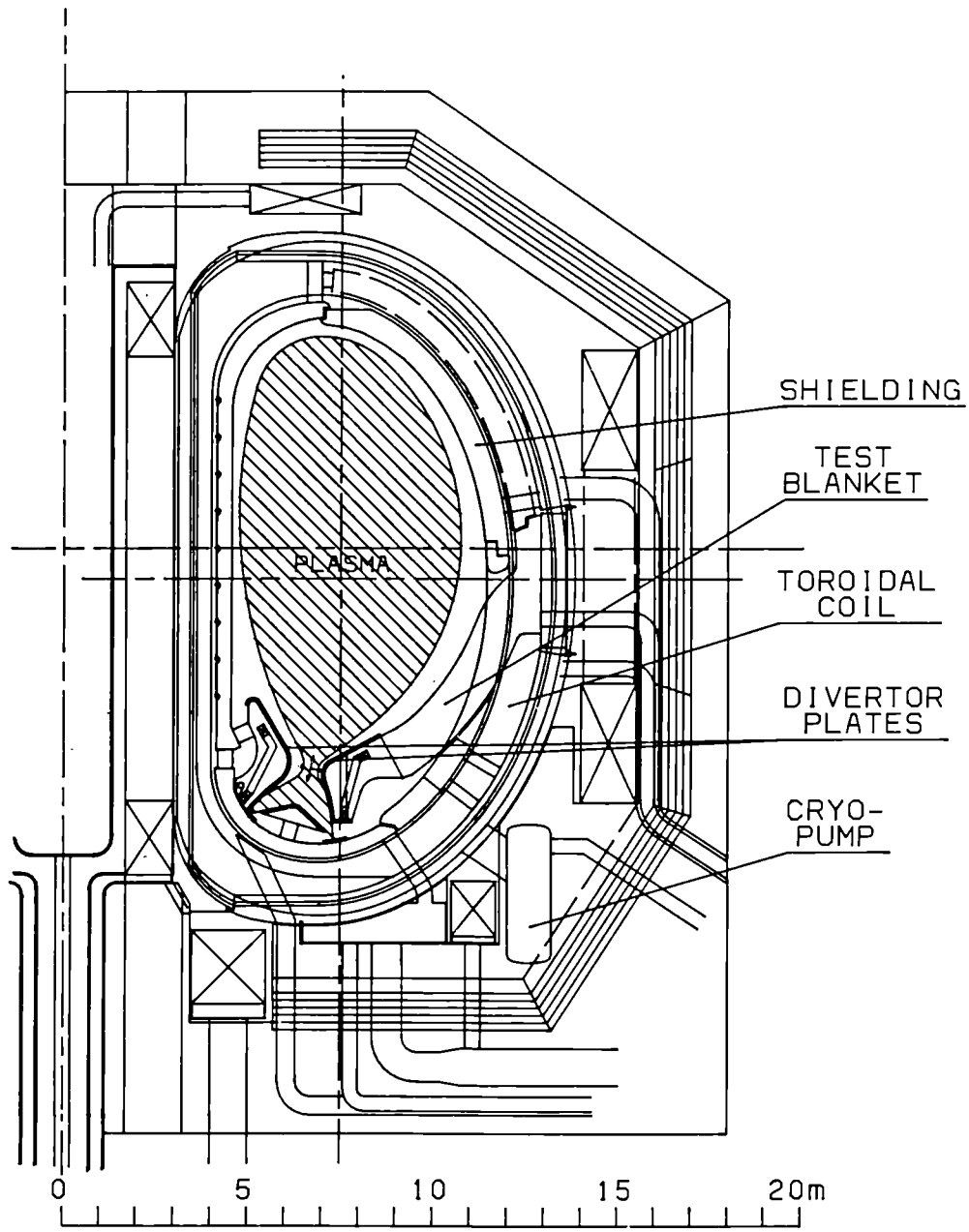

Fig. 4 Cross-section of a thermonuclear furnace (JIT) with a plasma capability of 30MA.

a demonstration reactor if equipped with blankets. A large flux swing (~ 400 Vs) would also provide the necessary drive to maintain the flat-top currents for periods up to one hour.

A general view of the apparatus is given in Fig. 4. It should be noted that the magnetic circuit is also used as a radiation shield around the machine.

5.1 Vacuum Vessel, Toroidal Coil and Mechanical Structure

The device concept is based on a highly integrated and modular construction, where all the elements would be manufactured on-site, as transport of such sized components would not be possible.

The machine basically consists of 20 sectors supported radially by a cylinder formed by the ohmic transformer. Each of these sectors integrates the toroidal coil, the vacuum vessel and the mechanical structure (see Fig. 5). These different sectors are assembled together by welding flexible lips. The torque induced by the vertical field is taken in shear by the light structure which encloses the toroidal coil. The coils are made of single pancakes of water cooled copper corrugated to transmit the shear forces, while the insulation remains purely in compression.

5.2 Poloidal System

The magnetic configuration contains a single-null X-point where the X-point is located in the lower position to allow the foundations to take the extra forces

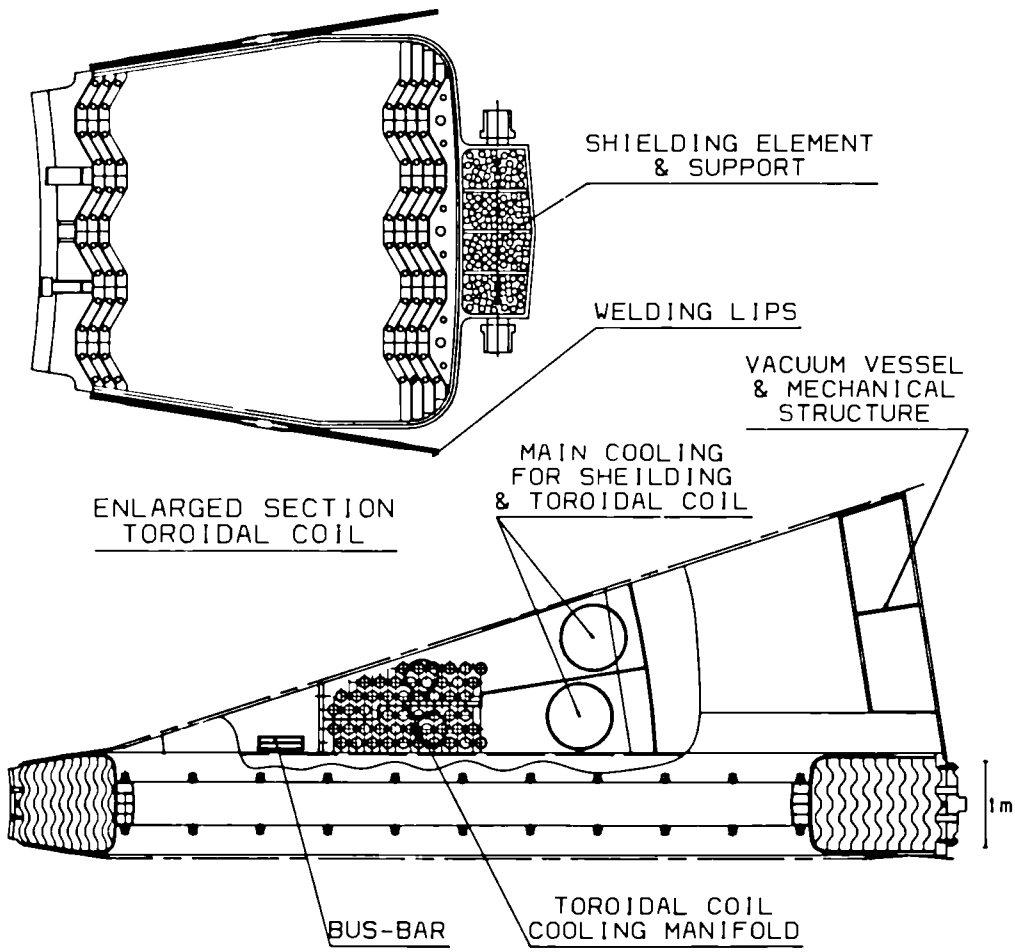

Fig. 5 Section of a sector of JIT conceived as an integrated element including toroidal coil, vacuum vessel and mechanical structure. Toroidal field coils are shown.

resulting from the presence of the separatrix and gives more access at the top of the machine. This position also decreases the risk of broken tiles falling into the plasma. The presence of the X-point would allow transient H-mode operation during the transition to ignition, but its main purpose is to provide plasma pumping at relatively high pressure.

5.3 Internal Shielding and First Wall

The shielding is made of several elements which could be dissassembled remotely, without dismantling the main apparatus. Each of these elements is made of a single box structure filled with pebbles of metal directly cooled by water. One of the main problems in maintaining shielding efficiency is the presence of gaps to allow remote handling and thermal expansion of the different elements. These gaps reduce the shielding locally and could induce a high neutron flux in the coils. The overall layout includes a series of thicker elements which could easily be replaced by reactor relevant breeding-blanket test modules (see Fig.6) without

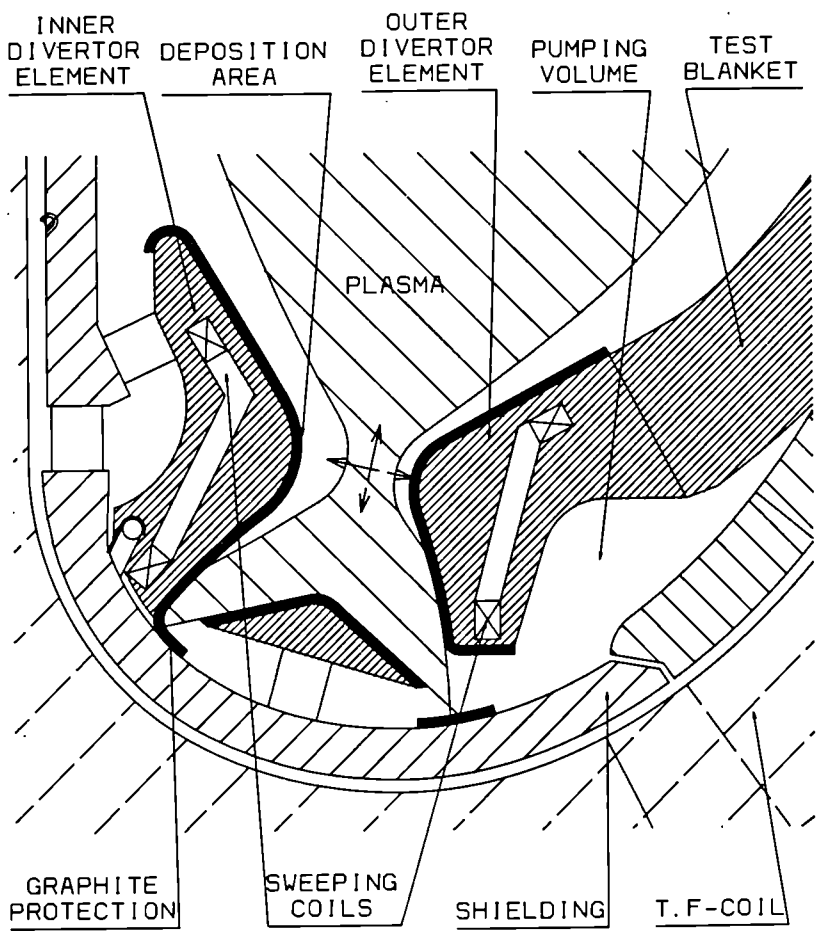

Fig. 6 Divertor region of JIT showing a set of saddle coils which allow sweeping of the thermal load on the divertor plates covered with graphite. Pumping is carried out through a slot at the base of the divertor.

any modifications of the initial shielding and of the plasma parameters.

The first wall itself is formed by the surface of the shielding box facing the plasma with only local protection by carbon tiles which radiate energy received at a temperature ~ 1500°K. A continuous deposition of beryllium could ensure that the first wall seen by the plasma is of beryllium or its carbide to limit sputtering and outgassing of the tiles.

5.4 Divertor

The divertor presents the main technical challenge in the design of inner wall components. This challenge can be reduced to a manageable level if the region of high power deposition is expanded over a larger area. This can be achieved by moving the X-point vertically or horizontally using a set of internal saddle coils.

5.5 Cost

The cost of such a device is estimated at approximately 2.4 Bn ECU over a period of 8 years.

6. Conclusions

JET data shows that a tokamak with a plasma current capability around 30MA is required to produce ignition of a D-T plasma in a practical domain. With lower values of current, the risk of not achieving ignition is large, if sawteeth, impurity radiation, dilution etc., are taken into account.

In a reactor, the size would be defined by the blanket and this leads to a tokamak with a current capability greater than 30MA, when optimized. Confinement would no longer be the dominant problem. However, uncertainties remain in the areas of plasma-wall interaction, fuelling, exhaust and impurity control.

Technical considerations of stress level, wall loading and economy result in a design of a 'Thermonuclear Furnace' producing a thermal output of several GW in semi-continuous mode. This device is aimed at demonstrating the potential of a Tokamak Reactor and to test wall technologies and breeding blankets. For such a device, priority must be given to simplicity and reduction of technical and scientific risks.

If a fusion programme is to continue, it is important to build on JET achievements. To meet these objectives a next-step device must be conceived which clearly establishes the potential of fusion as a major source of power. Such a device must give a high priority to simplicity of design with minimial technical and scientific risks. A Thermonuclear Furnace of several GW—JIT is such a device—which seems compatible with present technical and financial capabilities. It could prove that fusion is potentially a major source of future world energy.

7. Acknowledgements

The scientific and technical achievements of JET result directly from the dedication of the JET Team[2]. The simulations presented would not have been possible without the dedicated efforts of Dr. P.P. Lallia. I would also like to thank Drs K.J.Dietz, B.E.Keen, B.Keegan, E.Lazzaro, T.Molyneux and L.Sonnerup for their help in preparing this paper and calculating some elements of JIT.

8. References

[1] Rebut, P.H., et al, Fusion Technology, 11, pp13-281 (1987).

[2] Gibson, A. and the JET Team, *'Plasma Performance in JET: Achievements and Projections'*, 15th European Conference on Controlled Fusion and Plasma Heating (Dubrovnik, Yugoslavia, 1988) to be published in Journal of Plasma Physics and Controlled Fusion.

[3] Bickerton, R.J. and the JET Team, *'Latest JET Results and Future Prospects'*, Proceedings of the 12th IAEA Conference on Plasma Physics and Controlled Nuclear Fusion Research (Nice, France, 1988), to be published.

[4] Rebut, P.H., Lallia, P.P. and Watkins, M.L., *'Analysis on JET Results and Impact for the Future'*, 12th IAEA Conference on Plasma Physics and Controlled Nuclear Fusion Research (Nice, France, 1988), to be published.

[5] Reynolds, P. and Worraker, W.J., *'Study of the Reactor Relevance of the NET Design Concept'*, Culham Laboratory Report; CLM-R278 (1987).

[6] Rebut, P.H., Dietz, K.J. and Lallia, P.P., *'Experience with Wall Materials in JET and Implications for the Future';* 8th International Conference on Plasma Surface Interactions in Controlled Fusion Devices (Jülich, F.R.G., 1988), to be published in J. Nucl. Mater. (see JET Report: JET – P(88)21).

[7] Rebut, P.H. and Lallia, P.P., *'JET Results and the Prospects for Fusion'*. Proceedings of the 15th Symposium on Fusion Technology (SOFT) (Utrecht, the Netherlands, 1988), to be published in J. Fus. Tech.

Papers presented at 8th Tropical Meeting on Technology of Fusion Salt Lake City, Utah, 10th-13th October 1988

JET Authors

	Title	Author	No.
1.	JET Progress Towards D-T Operation	JET Team (M. Huguet)	A636
2.	Forces on the JET Vacuum Vessel during Disruptions and Consequent Operational Limits	P. Noll et al	A650
3.	Upgrading the JET Magnet System for 7MA Plasma	J.R. Last et al	A658

JET PROGRESS TOWARDS D-T OPERATION

M. HUGUET, E. BERTOLINI AND THE JET TEAM

JET JOINT UNDERTAKING,
Abingdon
Oxfordshire OX14 3EA, U.K.

ABSTRACT

JET PROGRESS TOWARDS D-T OPERATION, M. Huguet and E. Bertolini --- Upgrading of the JET experiment has allowed operation at plasma currents up to 7MA with material limiter and 5MA in the X-point mode. Key experimental results include record values of the fusion parameter $\hat{n}_i x \tau_E \hat{x} T_i$ = $2.5 \times 10^{20} m^{-3}.s.keV$. Future machine enhancements include cooled target plates for high power X-point operation, beryllium as a first wall material and a 12MW Lower Hybrid Current Drive system in order to achieve peaked plasma profiles. The plant which will reprocess the tritiated exhaust gasses from the torus and torus systems is described as well as work progress in safety analysis and waste handling. Recent developments in the area of remote handling are briefly reviewed.

INTRODUCTION

JET is the central and largest experiment of the Fusion Programme of the European Community. JET was established with the aim of extending the plasma parameters to values close to those required in a fusion reactor and to operate with deuterium-tritium (D-T) mixtures for the study of the production and confinement of α particles and their heating effect on the plasma. JET operation started in June 1983 and the basic machine reached its full design rated values of toroidal field and plasma current in 1985. The physics results established JET as a world leading fusion machine but confirmed one of the key problems of fusion research today, ie., the degradation of the energy confinement with increasing heating power [1]. Although disturbing, this result was of major importance and triggered a comprehensive reappraisal of the JET experimental programme. The new JET development plan was presented first in 1986 and includes a number of measures designed to circumvent the problems of confinement degradation. Since JET results showed that energy confinement improved at higher plasma currents, a major feature of the new plan is the requirement to operate at plasma currents up to 7MA, ie., well above the design values. This new requirement initiated the so called "7MA Study", a comprehensive engineering reassessment of the thermomechanical behaviour of the machine components and its power supplies [2].

This paper presents the main results of the "7MA study", the progress achieved so far in the implementation of the new development plan and a summary of the key physics results. It shows that many of the fundamental questions which remain to be solved for JET are also relevant for the next generation of machines and to a significant extent also for future fusion reactors. It is therefore expected that the JET results in the years to come will continue to play a most prominent role in the orientation of the world programme. Moreover, with the date for the introduction of tritium into JET getting closer, the preparation for the D-T phase has intensified. The paper describes the achievements and future plans in the areas of remote maintenance and tritium handling which will make of JET a unique test bed for D-T fusion experiments.

MAIN RESULTS OF THE 7MA STUDY

It can be seen from Table I that the objectives of the 7MA Study were very ambitious since they called for a new operation regime (X-point) and for a considerable extension of machine design parameters. The values shown in Table I for the plasma current and flat top duration are the target values which were selected, following a very preliminary engineering analysis, as being the likely upper limits of what can be safely achieved in JET. The requirements in terms of current, pulse duration, and flux swing for the toroidal and poloidal field systems are also shown in the table. Problems to be expected were both mechanical and thermal due to the increase in current and flat top duration. It is a

Table I. bjectives of the 7MA Study

Parameter	Original Design values	Objectives of the 7MA Study
Plasma current (limiter configuration) (MA)	4.8	7
Plasma current (X point configuration) (MA)	Not foreseen	6
Plasma current flat top at 4.8MA(s)	10	-
at 7MA (s)	Not foreseen	10
Plasma elongation b/a	1.67	~ 2
Toroidal field (Tesla)	3.45	3.45
Toroidal field flat top duration (s)	12	17
Primary winding current (kA)	40	60*
Primary winding flux swing (Wb)	34	42

(Note* 60kA in the 6 central c ils only)

remarkable result that due to the inherent flexibility of the JET design, these new conditions have been found possible at the expense of only minor modifications to the apparatus and subsystems.

Forces acting on the Vacuum Vessel

A major task of the 7MA study was to characterise better the forces acting on the vacuum vessel during radial disruptions and vertical instabilities. These forces can indeed reach dangerous levels when the events are initiated at currents in excess of 5 6MA.

During radial disruptions, the sudden change of the poloidal field configuration induces eddy currents which flow in the vacuum vessel in the toroidal direction. These eddy currents interact with the poloidal field to give forces which are distributed mostly at the outboard part of the vessel. These forces produce a large resultant centripetal force but they do not give rise to unacceptable stress in the vessel structure.

JET plasmas have a poloidal β (β_{pol}) below unity and exhibit paramagnetic behaviour. During a disruption, the change in paramagnetic toroidal field flux induces eddy currents which flow in the vessel in the poloidal direction. These currents interact with the toroidal field to give forces which are distributed mainly at the inboard part of the vessel. These forces result in large radial deflections (10mm at 6MA) at the inboard wall of the vessel and they also initiate large amplitude radial oscillations (6mm at 6MA) of the vertical ports. When the disruption occurs at a plasma current in excess of 6MA, the yield limit of the material (Inconel 600) is exceeded over a significant area at the base of the ports and structural failure would be expected after only a few hundred to a few thousand disruptions.

Vertical instabilities have long been known to be a major hazard for the structural integrity of the vacuum vessel [3]. In vertical instabilities, the pattern of eddy currents in the vessel is still not fully understood. The forces acting on the vessel have been calculated by means of an equilibrium code [4] and also from more simple force balance considerations [3]. The phenomenon has also been investigated experimentally. The vertical resultant force has been measured by means of an array of strain gauges attached to the vessel supports. The forces have also been inferred indirectly from the dynamic displacements observed at vessel ports. Although there are still discrepancies between calculated and measured values, it is clear that the vertical force would reach an amplitude of 6000 to 10,000 kN for the envisaged plasma scenarios at currents of 6 to 7MA [5]

As an outcome of this study, the following remedies were proposed and adopted:

a) The inboard part of the vessel will be reinforced by toroidal Inconel rings welded inside the vessel [6]. These rings will decrease the radial deflection of the vessel wall and virtually eliminate the radial oscillations of the vertical ports during plasma disruptions.

b) The vertical forces acting during vertical instabilities are already contained by inertial brakes [2]. These brakes will be complemented by hydraulic dampers linking the vertical ports to the mechanical structure in order to slow d wn the radial displacement of the ports due to the rocking motion of the vessel.

c) Experimental and theoretical investigations agree that the vertical forces acting on the vessel during an instability is a complex function of the plasma current, of the currents in the various poloidal field coils which control the plasma elongation, and of the safety factor q. A formula has been established in a semi-empirical way to express the so called F parameter which appears to be proportional to the vertical force acting on the vessel [5].

$$F = I_p (I_p + 14 N_s I_s + 300 I_D) (MA)^2$$

where

I_p = plasma current (MA)
I_s = shaping current (MA)
I_D = current difference between the centre and end coils of the primary coil (MA)
N_s = the number of turns in the shaping circuit

Table II summarises the results of the study.

Table II. Summary of forces acting on the vacuum vessel during radial disruptions cr vertical instabilities (all forces in kN)

	Radial force	Vertical force
Radial disruption at 7MA. (Disruption time = 10ms)		
Force due to toroidal currents	12,600	0
Force due to poloidal currents	6,800	0
Vertical instability at 6MA	(see note)	6,000 - 10,000
Atmospheric pressure	6,000	0
Total	25,400	6,000-10,000

Note: There is no radial force during the initial vertical displacement of the plasma. However, when the q = 2 surface of the plasma intersects the wall of the vacuum vessel, a disruption occurs. This gives rise to radial forces which are not symmetrical with respect to the equatorial plane of the machine.

Safe operation has been achieved by the administrative control of the F-parameter below 75(MA)² during the 1988 experimental campaign. The measures a) and b) described above should allow operation with F-values in excess of 100(MA)² which is required for X-point configurations at plasma currents up to 6MA.

Toroidal Field Coils

Table I shows that no attempt has been made to increase the value of the toroidal field. This decision is based on the following considerations = The peak tensile stress in the copper brazed joints of the coils is of the order of 100MPa and fatigue life data indicates that the stress level could in principle be increased. Fatigue life assessments are however of a statistical nature and must be considered cautiously. There is indeed a possibility that a few brazed joints, out of a total of 1536 joints in the coils, are weaker than expected due to undetected internal defects. A joint failure would produce initially an internal cooling water leak which would degrade the electrical insulation and ultimately lead to an electrical fault. In the present conditions, the replacement of a toroidal field coil would represent a major disruption to the JET experimental programme. During the D-T phase, such an event would probably terminate the JET programme. For these reasons, operation at a field above the design value of 3.45T is not being considered for the time being. Operation at 4T may however be attempted towards the very end of JET operation if the benefit versus risk analysis of such operation justifies it.

The requirement to extend the flat top capability of the toroidal field magnet has been achieved by using cooling water chilled down to 7-10°C. Interlocks prevent operation if the water temperature falls below the dew point temperature in the torus hall. The flat top duration has been increased from 12 to 17 seconds at 3.5T.

Operation at higher plasma current increases stresses on the toroidal field coils due to the higher poloidal field crossing the coils. The most critical areas are the upper and lower portions of the D-shape of the coils in the vicinity of the transition between the straight and curved parts. In these areas the coil are supported against azimuthal forces by the inner cylinder and the collar tooth. Extensive analytical work revealed a fairly high level of shear stress and an experimental confirmation of the strength of the coils was therefore necessary. The prototype coil was subjected to, and survived without failure, a severe run of mechanically applied cycled loads. Results summarised in Table III show that operation at high plasma current is possible. Details are available in [7].

Primary Coil

A reduction by a factor 2 to 2.5 of the stray fields which are detrimental at plasma breakdown, was obtained by adding 2 subcoils to the coil stack, thus bringing the number of subcoils to 10[8]. In order to increase the flux swing from 28Wb to 42Wb, the primary

Table III. Toroidal field coils stresses at high plasma current

Parameter	Original Design value	Most severe values expected during operation at high plasma current	Value achieved during test of prototype
Force at collar tooth (kN)	500	700 (7MA limiter)	1,250
Shear stress between turns or pancakes (MPa)	10	16 (7MA limiter)	28
Number of cycles	∿20,000 at full rated values	∿ 5,000	10,000

current in the six central subcoils was increased from 40 to 60kA. From a purely mechanical point of view, this was found to be possible because the toroidal field coils exert an inward pressure which balances the increased outward pressure. The thermomechanical analysis of the coil however identified severe thermal stress due to temperature gradients [7]. For this reason, a new cooling loop was designed and installed. The cooling water is circulated in a closed loop and the water temperature is brought down slowly and in a controlled way after a pulse, so that temperature gradients due to incoming cold water are avoided. With these modifications the primary coil now has the current and flux capability shown in Table I.

Magnetic configuration

A major advance was made in 1987 when new single-null configurations were investigated with a view to minimising the lateral forces acting on the toroidal field coils. It was found that those forces could be significantly reduced if the outer poloidal field coils for the vertical equilibrium field (coil no. 4) were made to contribute to the up-down assymmetry of the configuration. A current imbalance between the upper and lower coils no. 4, together with the contributions of coils nos. 1, 2 and 3, produces a more favourable pattern of the poloidal field crossing the toroidal field coils. Such a single null configuration, as shown on figure 1, will allow X-point operation in the single null mode up to a plasma current of 6MA.

Conclusion

The main conclusion from the 7MA study is that the electromagnetic system, ie., coils and power supplies, would allow operation at plasma currents in excess of 7MA in the limiter mode and X-point mode of operation. The main limitation seems to come from the mechanical problems associated with the forces acting on the vacuum vessel during the vertical instabilities. This will set a limit to the plasma current in the X-point mode in the region of 6MA.

STATUS OF SYSTEMS DURING THE 1988 EXPERIMENTAL CAMPAIGN AND PROGRESS IN THE IMPLEMENTATION OF THE NEW DEVELOPMENT PLAN.

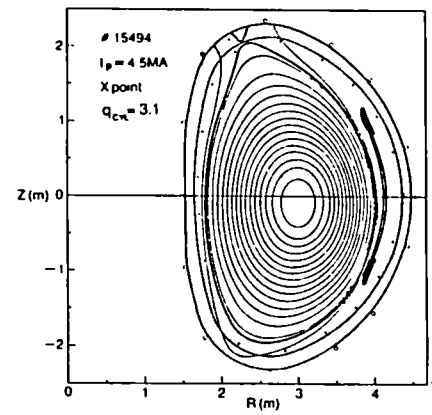

Fig 1: Magnetic flux surfaces for a single null discharge with I_p = 4.5MA. The shaded area represents the vacuum vessel. The cross-sections of the toroidal belt limiters and ICRH antennae are also shown.

First wall components and first wall operating condition

The basic elements of the present first wall configuration were installed during a shutdown early in 1987. Some further improvements were also implemented during short maintenance periods in 1988.

The inboard wall of the vacuum vessel is completely covered with graphite tiles. These tiles have been carefully realigned in order to achieve a more uniform power distribution, and allow operation scenarios with the plasma leaning against the inboard wall. This mode of operation is important since it provides a very effective wall pumping effect. The energy which can be deposited on the inboard wall tiles has been limited so far to 40MJ per pulse. The tiles near the equatorial plane receive a high heat flux during disruptions and have been replaced by carbon fibre reinforced (CFR) graphite [9]. Such CFR tiles sustain the heat load well during disruptions or runaway impacts and provide also an effective wall protection against neutral beam shine-through. Tests have shown that power loads up to 3kW/cm² can be sustained for typically 4 seconds.

The outboard portion of the wall is protected by 40 graphite tile rings in the poloidal direction. For X-point operation, wall protection tiles in the vicinity of the X-points have been specially shaped and carefully aligned to allow a total energy deposition up to 50MJ per pulse.

In the limiter configuration, the plasma normally leans against the two outboard toroidal belts of the belt limiter. This limiter, with a power handling capacity of 40MW for 10 seconds, is made up of graphite tiles mounted on a water cooled radiation structure [10]. There are also eight ICRH (ion cyclotron resonance heating) antennae with water cooled electrostatic screens and lateral graphite protections of a design similar to that of the belt limiter.

In 1988, the vessel and in-vessel components were normally maintained at a constant temperature of 300°C during operation except for the water cooled belt limiter and antennae screens and protections. The presence of water cooled components inside the vessel made recovery from disruptions extremely time consuming. The problem was attributed to the release of hydrogen trapped on the water cooled components. Glow discharge cleaning in helium as experimented in Textor appears to detrap hydrogen and in addition seems efficient in removing impurities like oxygen [11]. Helium glow allows removal of oxygen in the form of carbon oxides and also enhances the pumping capability of the wall. The latter phenomenon was used to reach high ion temperatures at low densities in the so-called hot ion mode. Major sources of high Z impurities were found to be the antenna screens which released nickel into the plasma. Glow discharge with a mixture of deuterium and methane (carbonisation) can cover the walls and the screens with a hard carbide layer, which temporarily suppresses metal contamination. Carbonisation was used successfully several times in 1988 although it renders density control and recovery from disruptions more difficult.

Electromagnetic systems

The new poloidal field power supply circuit is shown on Figure 2. This circuit has been subject to major alterations in 1987 and 1988 in order to meet the requirements of upgraded operation. New systems listed below have considerably enhanced the capability of the circuit and increased the flexibility of operation.

The PFX power supply [12] is connected to the 6 central sub-coils of the primary winding and performs the following functions:

- Active control of stray fields at breakdown.
- Enhancement of the flux swing up to 42Wb by supplying 60kA to the 6 central sub coils.
- Establishment of X-point configurations by promoting leakage flux in the area of the X-point.

The switching network [13] controls the derivative of the plasma current during the early phase of the discharge and thereby allows an optimisation of the flux swing consumption and plasma current profile.

The vertical field amplifier [7] has been split into 2 units in order to allow, by means of a mid point connection, imbalanced currents between the upper and lower coil no.4. This has permitted X-point operation up to 5MA.

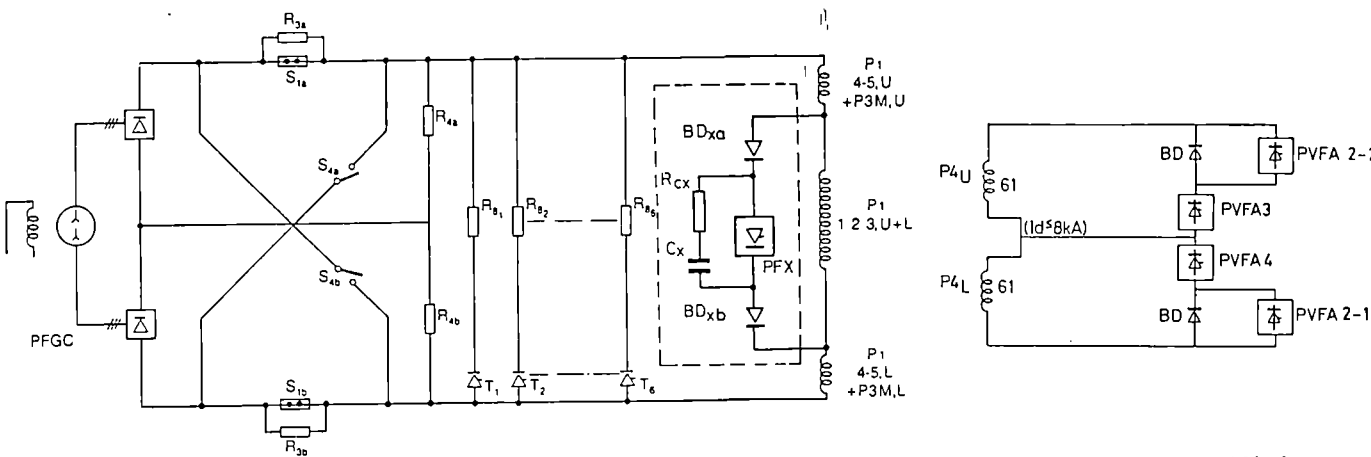

Fig 2: Simplified schematic of the poloidal field circuit power supplies. New additions include:
(a) the switching network (Thyristor switches T_1 to T_6 and resistors R_{61} to R_{66}),
(b) the PFX power supply with associated filters and protective diodes,
(c) the vertical field circuit PVFA 3 and 4 with temporary booster (PVFA 2-1 and 2-2) and mid-point connection for X-point operation.

Fuelling and heating systems

Under a JET-US DOE Collaboration, pellet fuelled discharges, using an Oak Ridge National Laboratory pellet launcher, have c ntributed significantly to physics results in 1988. The injector can deliver 2.6, 4 and 6mm pellets at a velocity of 1-1.5km/s and with a repetition rate between 5 and 1Hz [14].

The neutral beam injection system includes two boxes each with 8 x 80kV, 60A injectors. Due to a combination of power supplies problems and beam line components failures, in particular water leaks inside the vacuum enclosure, it is only towards the end of the operating period which is reported here that the injected power reached 21.6MW exceeding the design value of 20MW. Work is underway to convert the injectors for operation up to 160kV as required for tritium beam injection.

An upgrade of the ICRH generators was initiated in 1988 by replacing the 1.5MW tetrodes with new 2MW tetrodes, thus allowing the antenna to be supplied with 4MW power during 10 seconds. With 5 generators out of 8 being upgraded the JET ICRH system has been able to couple 18MW of heating power to the plasma.

BRIEF REVIEW OF THE EXPERIMENTAL RESULTS OBTAINED IN 1988

Although many new systems were brought into operation in 1988 and required some commissioning time, the 1988 experimental campaign was extremely rich in achievements made indeed possible by these new systems. The main operational achievements are summarised as follows:

- Plasma current up to 7MA.
- Routine operation with plasma current up to 6MA.
- Routine X point operation at plasma current up to 5MA.
- Routine H mode operation at plasma current up to 4.5MA.
- Long plasma current pulse durations including:
  . 10s flat top at 5MA.
  . 6s flat top at 6MA.
- Quasi steady state conditions at 3MA with 6MW of RF heating power for 20 seconds and T_e and T_i both above 5keV.
- High power heating pulse with a duration in excess of 6s.
- Total power delivered to the plasma in excess of 34MW.

The plasma parameters achieved include [15]:

Production and heating of highly peaked density profiles with $\hat{n}_e$ greater than $10^{20}m^{-3}$ with pellet injection.

- Peaked temperature profiles with sawteeth relaxations stabilised ("monster sawteeth") for more than 3 seconds.
- Electron and ion temperatures simultaneoulsy above 10keV during a discharge.
- Total thermal energy content greater than 10MJ.
- A fusion parameter $\hat{n}_i \times \tau_E \times \hat{T}_i = 2.5 \times 10^{20}\ m^{-3}.s.keV$. (H mode operation).
- An equivalent Q_{DT} in the region of 0.3

$$(Q = \frac{\text{Fusion power}}{\text{Total heating power}})$$

These new results are very encouraging and confirm JET in its prominent position in fusion research.

The following observations can be made about the results.

i) The degradation of the energy confinement time τ_E with input power remains the main cause for the limitation of JET performance. Figures 3 and 4 illustrate this effect for L and H mode operations. It should be noted that in the range of parameters explored so far the H mode confinement time is approximately a factor 2 better than the L mode confinement time at the same heating power and plasma current. The degradation with input power is however at least as severe for H mode as for L mode. It is also important to observe that the scaling of τ_E with the plasma current confirms the need for and fully justifies the JET policy for high current operation.

ii) The peakedness of the density and the temperature profiles plays a major role in the achievement of a high Q. The peaked density profiles after pellet injection ($\hat{n}_e/\langle n_e\rangle \sim 3$) and the peaked temperature profiles during "monster sawteeth" ($\hat{T}_e/\langle T_e\rangle \sim 2.5$) seem to open up exciting possibilities. It will be necessary however to sustain the peakedness for longer times than achieved so far. It will also be necessary to assess whether peaked density profiles will also entail peaked impurity profiles.

iii) The results achieved with H mode, pellet injection and stabilised sawteeth are of a transient nature. It has not been established whether such results can be extrapolated to the quasi steady state conditions required in a fusion reactor. L mode results on the contrary are steady

state and can confidently be extrapolated to reactor conditions. In the L mode, the best value of the fusion parameter is of the order of 1 x 10^{20} m^{-3}.s.keV.

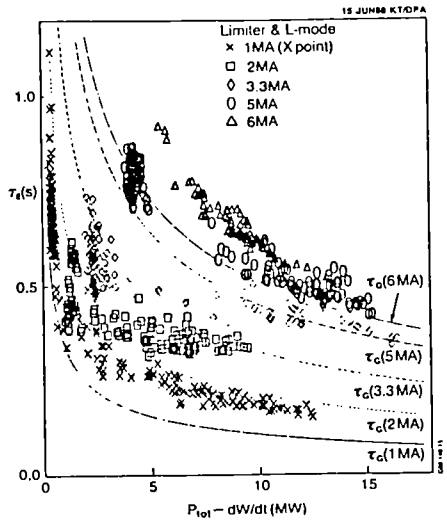

Fig 3: Measured energy confinement τ_E time as a function of total power flow for JET limiter and L mode discharges. $\tau = [W/(P - \frac{dW}{dt})]$ where

W = Total plasma energy
P = Total power input

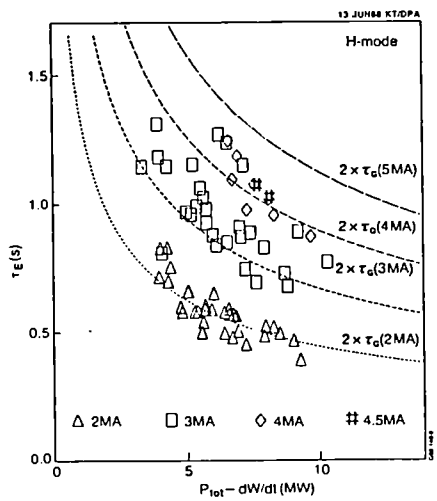

Fig 4: Measured energy confinement time as a function of total power flow for JET H mode discharges.

SOME FUNDAMENTAL QUESTIONS FOR THE DEVELOPMENT OF FUSION ENERGY = HOW CAN JET CONTRIBUTE TO THE ANSWERS?

There are a number of fundamental questions which will determine the JET level of performance during the D-T phase, and will also strongly affect the designs of the next generation of machines.

Can the plasma purity be improved?

A low effective charge (Z_{eff}) is essential to reduce radiation losses and the fuel dilution effect. At present, with 50% graphite coverage of the walls, the contribution from the metal walls to Z_{eff} is negligible. Nickel contamination from the antenna screens is however serious and can be reduced, but only temporarily, by carbonisation. After carbonisation, Z_{eff} is typically 2 and is due mostly to carbon (up to 5%) and oxygen ($\sim$0.5%) contamination. Z_{eff} values close to unity have been achieved after pellet injection but it is not clear whether this can be maintained in quasi steady state conditions.

In most JET discharges, the fuel dilution (defined as the ratio of the deuterium density to electronic density) is below 0.5. Values closer to 1 have been achieved but in transient conditions only with pellet fuelled discharges.

For future machines it is important to know what values of Z_{eff} and dilution factor can be reliably achieved and maintained. Operation at low Z_{eff} and without oxygen contamination may prove beneficial as is suggested by the interesting Textor results with boron [16].

For these reasons JET plans to experiment with a low Z beryllium first wall [17]. The tiles of the belt limiter and antenna protections will be replaced by beryllium tiles and the water cooled nickel screens of the antennae will be exchanged for conduction cooled beryllium screens. The rest of the vessel walls and graphite protections will be covered by a 5-10μm thick beryllium layer. Beryllium evaporators are being tested for this purpose. Beryllium use in JET may start in 1989.

It is expected that operation with beryllium should reduce radiation losses at the plasma edge and consequently reduce the occurrence of disruptions. It is not easy to predict whether the fuel dilution will be increased or reduced with beryllium compared with carbon. This will be a most interesting and crucial result of the planned beryllium experiments.

What is the relevance of H mode operation for future machines?

The best values of the fusion parameter $\hat{n}_i \times \tau \times \hat{T}_i$ achieved so far on JET were obtained in H mode operation [18]. This raises important questions regarding the relevance of H mode operation for future machines.

First, will H mode confinement at high heating power, including α particle heating, continue to surpass L mode confinement by a factor 2?

Second, in view of the very long particle confinement times and the resulting impurity and α particle accumulation effects, can H mode confinement be maintained for quasi stationary conditions?

With up to 40MW of additional heating power, JET should answer the first question relatively unambiguously, provided we learn how to couple some ICRF power into H mode discharges. The D-T phase should also give some indication on the effect of α particle heating on H mode confinement.

With the capability to sustain X point configurations for up to 10 seconds, JET should also provide information on the second question. JET should also be able to experiment with impurity flushing scenarios involving a sequence of alternate H and L modes.

To meet the requirements of high power X point discharges, water cooled dump plates will be installed in 1990 at the top and bottom of the vessel. These dump plates will carry graphite tiles attached onto a water cooled structure. They will be able to sustain full power, ie., 40MW, and full duration, ie., 10 seconds, discharges in the double null configuration. In the single null configuration, the pulse duration may have to be reduced to a value smaller than 10 seconds, depending on the amount of power radiated to the walls.

Can peaked profiles be maintained in order to enhance the reactivity?

JET has already had some success in sustaining additionally heated peaked density profiles for several seconds [19]. This was made possible by an early injection of pellets during the current rise and before the onset of sawtooth relaxations. These techniques will of course have to be perfected but in any case, will also require higher pellet velocities for deep fuelling of hot dense plasmas. JET, in collaboration with CEA (France) are developing a two stage pneumatic gun able to deliver pellets at velocities in the range of 5km s. So far plastic pellets have already been accelerated up to velocities in excess of 4km s. A prototype single shot gun is expected to be available in 1989 and a repetitive system should be developed in 1990 [20]. If this technology can be extrapolated to velocities in the range of 10km s, it may prove an effective fuelling method for the next generation of machines.

The stabilisation of sawtooth relaxation ("monster sawtooth") has been observed in JET with both ICRF and neutral beam heating and allows peaked temperature profiles to be maintained for several seconds. The JET Lower Hybrid Current Drive (LHCD) system should flatten the current profile, increase the central value of the safety factor q, and therefore promote stabilisation of sawteeth. The prototype LHCD system will provide a power of 2MW and will be available in 1989. The full system should be able to drive up to 2MA currents in the outer region of the plasma by means of 24 klystrons (3.7GHz) each capable of delivering 500kW for up to 20 seconds [21] [22].

Can plasma disruptions be controlled?

Disruptions pose a serious threat for JET and for any future tokamak. They are detrimental to nearly every component of the machine due to: heat loads on first wall components, mechanical loads on first wall, vacuum vessel and toroidal field coils; voltage spikes on insulators and coils. Therefore to learn how to avoid them or at least how to mitigate their effects.

The JET scheme to control disruptions is to produce, by means of a set of internal saddle coils, a magnetic perturbation which will oppose the m=2, n=1 mode associated with the disruption phenomenon. These coils would be supplied by feedback amplifiers with a capability of a few kA and a frequency response variable from 0 to 10 kHz.

What will be the effect of α-particles on the plasma?

With an expected α particles power in the range of 3 to 6MW [15], the heating effect in the JET plasma core should be significant. The long JET pulse duration should also allow a meaningful study of α-particle accumulation in the centre of the discharge. Another important contribution of JET will be the study of the effect of α-particles on confinement. It is indeed important to note that in JET, the density of α-particles relative to the plasma density should be similar to that expected in an ignited plasma. This should allow the study of key confinement issues such as the stabilisation of sawteeth by the fast α-particles.

OVERVIEW OF PREPARATION FOR OPERATION WITH TRITIUM

Apart from the construction of tritium handling facilities and the development of remote maintenance techniques, there are many other tasks which have to be completed before tritium operation can start. The main tasks are listed below:

- Engineering review of all systems which are in contact, or may be contaminated with tritium in order to check their

compatibility with D-T operation conditions.
- Installation of a radiological protection instrumentation system.
- Procurement of tritium and transportation arrangements.
- Construction of facilities and development of procedures for the handling of active wastes.
- Submission of safety reports to the safety authorities.

These various activities require a large coordinated effort in order to meet the tight JET schedule which as shown on Table IV calls for a start of tritium operation during the second half of 1991. In particular the engineering work and the preparation of safety reports must progress in parallel, and this calls for a very close working relationship between the designers and the safety engineers. At JET the tritium work has been split between two groups within Fusion Technology Division: one group is responsible for the design and construction of the plant and the other group deals with all safety matters. This organisation provides a framework for a close collaboration between the two groups while ensuring that the safety analysis are carried out independantly from the pressure of engineering requirements.

RECENT DEVELOPMENTS IN THE AREA OF REMOTE MAINTENANCE

The JET remote handling scheme has been described elsewhere [23,24]. The overall system includes large transporters for work inside the vacuum vessel and on the outer surface of the machine, end effectors and special tools for specific operations, and a viewing system. All systems are controlled from a dedicated remote handling control room. In this paper only the most important recent developments are briefly reviewed.

The articulated boom for work inside the vessel has been used on several occasions and is now fully computer controlled. Teach and repeat motion and resolved motion of the tip of the boom have been successfully commissioned and new software packages for obstacles avoidance are being experimented. The Telescopic Articulated Remote Mast (TARM) for work on the outside of the machine is fully designed and construction has started. Installation at JET and tests are planned to start by mid-1989.

A major progress was the upgrade of the In Vessel Inspection System (IVIS) to allow viewing at a vessel temperature up to 300°C. The 4 inspection probes have now been fitted with water cooled jackets and radiation shields which maintain the cameras at a temperature of 30°C. The illumination of the inside of the vessel has also been greatly improved by means of 7 quartz light pipes which can be inserted inside the vessel by means of bellows. The light sources outside the vacuum vessel can be easily replaced if required [25].

A programme of scale 1 mock up tests has been initiated. The effort has concentrated so far on "in-vessel" operations using the articulated boom. The spare vacuum vessel octant and spare components of the belt limiter and RF antennae are being used for this work. In order to simulate the viewing conditions of "in vessel" work, the spare vessel octant is enclosed in a black box and lighting is provided by the actual "in vessel" light pipes and flash lights. Mock-up tests have also started to

Table IV. Time schedule for tritium related work

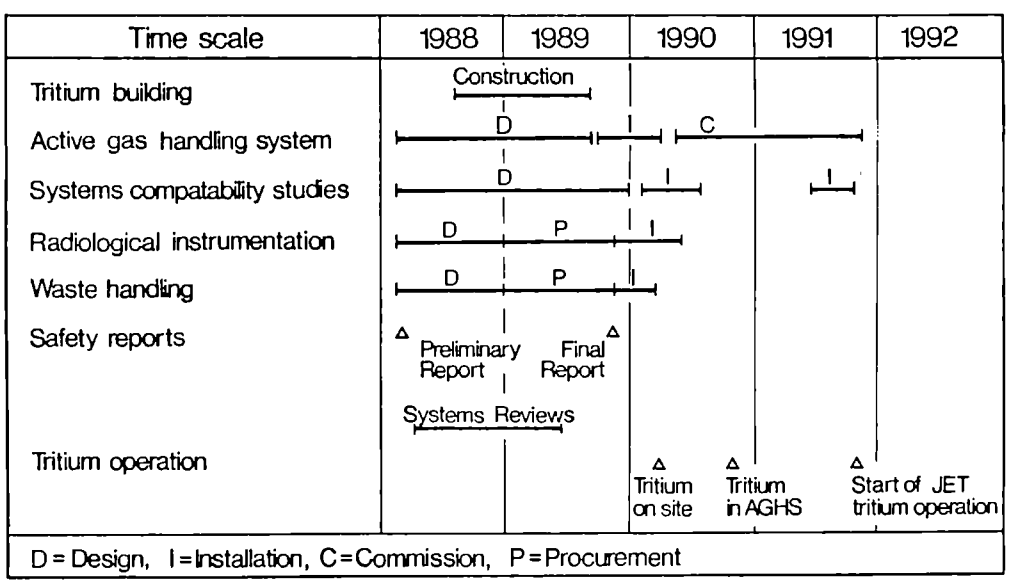

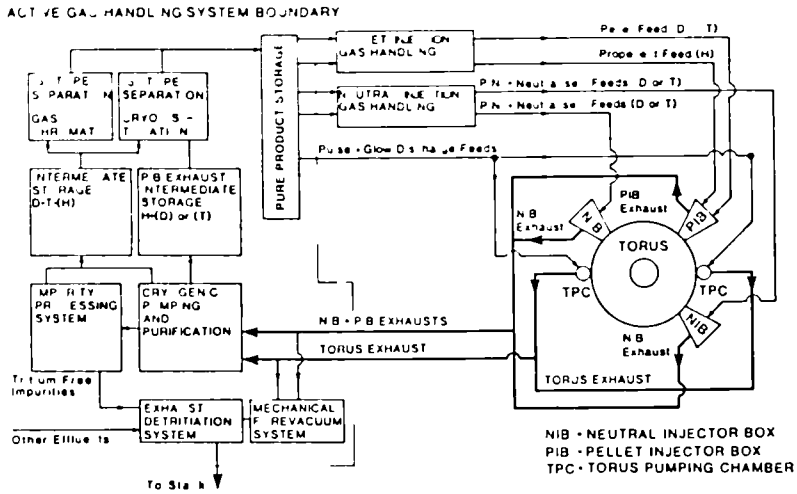

Fig 5: Schematic of the JET active gas handling system

rehearse the replacement of neutral beam ion sources (PINI).

THE JET ACTIVE GAS HANDLING PLANT: A PROTOTYPE FUSION FUEL RECYCLING LOOP

The JET tritium handling facility is called the "Active Gas Handling System" (AGHS) and will recycle the exhaust gases from the torus and torus systems. It will receive all gases from the torus, neutral injectors and pellet injectors, purify these gases from impurities, separate the hydrogen isotopes and store them for reuse. In addition the plant will include an impurity processing system for the extraction and recovery of tritium from impurities such as methane. The plant will also include an exhaust detritiation system, the main function of which will be to allow maintenance work inside the vessel. To this end, an inward air flow will be maintained through the torus opening in order to reduce back diffusion of tritium to the Torus Hall. The plant will be located in a dedicated building. A schematic diagram of the main feeds, exhausts and main systems of the AGHS is shown on Figure 5. The details of the design of the plant have been described elsewhere [26].

The JET AGHS will be the first fusion fuel recycling loop to operate on a fusion machine. Its operation will therefore represent a major milestone in the advance of fusion technology. Furthermore, many design features of the plant point to the future and make it quite relevant for the next generation of machines.

a) For each system the double containment is provided by bakeable vacuum vessels rather than glove boxes. This leads to an open, industrial like, plant configuration which is well suited to large scale installations. The vacuum vessel containment principle also reduces the need for large air detritiations system, and the bakeability of systems facilitates decontamination procedures before maintenance work.

b) Static cryogenic systems have been selected whenever possible rather than systems using mechanical pumps or chemical beds. The pumping and purification functions are entirely performed by cryogenic pumps. The isotope separation is provided by cryogenic distillation columns. The long term reliability, waste free operation and low maintenance requirements of these cryogenic systems make them strong candidates for future fusion applications.

c) The generation of active wastes has been minimised by the impurity processing system. The present design relies on hot uranium beds to crack water molecules and some uranium wastes are therefore generated. Development is however underway to minimise further the production of wastes. Regenerable hot iron beds have already been tested to crack water molecules. Alternatively, hot graphite beds may crack impurity molecules directly.

d) The JET AGHS design is based on a daily throughput of 30g tritium. Such a throughput capability is very close to that required for the next generation of machines.

In conclusion, the JET AGHS plant could be considered as the prototype of the fuel recycling loop of an ignition machine. A fusion reactor will of course require additional and more complex systems for the recovery and processing of tritium from blanket breeding materials.

TRITIUM RELATED WORK

Engineering review and compatibility of systems for tritium operation

Since the early phase of the JET design, considerable attention has been given to making the machine and all associated systems suitable for operation with D-T mixtures. The consequences of this design philosophy in terms of component design, building design and site layout, have been far reaching and have already been described [27]. Prior to the start of operation with tritium, it is nevertheless necessary to carry out a comprehensive appraisal of each system with a view to reassess the design and analyse safety aspects in relation to all operation scenarios and fault conditions. This work which will become an important part of the Safety Analysis report, must identify design modifications and will result in the establishment of operation and maintenance procedures. The systems to be reviewed include those directly connected or related to the torus, ie., the vacuum pumping, the gas baking system, neutral beam systems, radiofrequency heating and current drive systems, and diagnostics. Other systems to be investigated are cryogenic systems, water cooling systems, building ventilation and shielding and fire fighting systems.

From experience in JET, it can be concluded that a breach of the vacuum enclosure is most likely to occur at bellows or vacuum feedthroughs. For this reason, most components use double bellows containment and guard vacuum behind feedthroughs. For diagnostics using optical windows, it is planned to develop double windows, since window failure has occurred several times during JET operation.

It is important to note that this double containment philosophy stems from the requirement to allow operation to continue after the failure of one barrier of the double containment. The double containment is not always necessary from the safety point of view. This is because the Exhaust Detritiation System will be able to maintain an inward flow of air through any vacuum leak on the apparatus, and thereby prevent any significant tritium release to the environment.

The decision to use tritium beams to fuel and heat D-T plasmas has required a full reappraisal of neutral beam systems. A major problem is related to the quantity of tritium which will accumulate on the cryopumps of the neutral injectors. The expected consumption of tritium gas for the ion sources and for the neutralisers is estimated to be of the order of 0.5g for an 8 second long beam pulse. The inventory of tritium after a day of operation with 20 pulses could therefore reach 10g. Faults such as vacuum leaks, internal water leaks or cryogenic fluid internal leaks could set this inventory free in what is essentially a single containment vessel. The safety analysis in progress will result in operation instructions and emergency procedures. In particular the case of a small internal water leak is being investigated in great detail, since it is one of the most probable accidents. It appears that the contamination of water by tritium can be greatly reduced by regenerating the helium cooled panels and thereby evacuating the tritium inventory towards the AGHS, while the water is kept frozen as ice or snow inside the neutral beam injector box.

Radiological instrumentation

A comprehensive radiological monitoring system is already operational at JET for D-D operation. It includes fixed gamma and neutron monitors and a personnel dosimetry system [28]. Further instruments are required for the detection of tritium, radioactive gases such as Ar^{41} and N^{13} resulting from the air activation, and radioactive dust. The devices to be installed will be:

- Fixed monitors in active and non-active areas and exhaust stacks.
- Portable monitors for tritium.
- Monitors for operational and waste fluids (water, helium loop, cryogenic fluids, SF6 gas).
- Environment monitors for tritium in air and liquids.
- Personnel tritium in urine monitoring.

The complete system is expected to be operational by the end of 1990.

Active waste handling

Work on the identification and classification of wastes originating from D-T operation at JET has resulted in the estimates shown on Table V. [29]

Handling of active wastes is intimately related to remote handling since storage and decontamination of remote handling tools will require the same facilities. The existing access cell and hot cell will be used for the decontamination of large components or large remote handling transporters. Large activated components will be stored in the hot cell. Additional facilities are being designed and will extend in the Assembly Hall area as shown on Figure 6. This new installation, planned for 1989, features a new access into the hot cell for fork lift trucks, change rooms, decontamination rooms and active workshops.

Whilst it is expected that solid low level waste will be disposed of to existing sites, the fate of solid intermediate level waste is unclear due to the lack of a disposal facility.

The disposal route for tritiated water specially with a low specific activity is also unclear at present. Solid intermediate level waste and tritiated water may have to be stored or treated on site.

Table V: Estimated active wastes production during the JET D-T phase assuming a total neutron production of 10^{23} in 2 years.

Type of Waste	Category or tritium content	Volume (m^3)
Components	ILW(a)	1.2
Components	LLW(b)	200(c)
Housekeeping (solid wastes)	LLW	small
Routine water arisings	<3Ci/m^3	170 m^3
Accidental water arisings	highly tritiated	5-10
Water arising from decontamination procedures	low tritium content	100

(a) ILW Intermediate level waste >12 GBq/tonne.
(b) LLW Low level waste <12GBq/tonne.
(c) Assumes replacement of neutral beam central column.

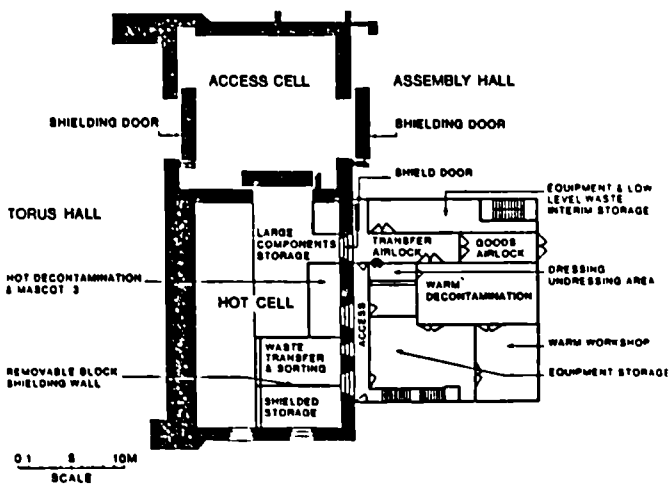

Fig 6: The proposed JET active handling facilities

Safety studies

JET safety work is based on design guidelines for personnel and general public radiation exposure. The target limits set by JET management for JET personnel exposure are 5mSv/year for radiation workers (10% of the ICRP limit) and 1mSv/year for all other staff (20% of the ICRP limit). The JET target dose at the JET site boundary should be less than 50μSv/year. Doses due to wastes or effluents should be minimised according to the general "As Low As Reasonably Practicable" (ALARP) principle. In addition, the design target for accidental releases is such that the product of frequency and release for any event should be less than 10Ci/year [30].

The tritium inventory on the JET site should not exceed a total of 90g of which 60g can be mobile gas. This relatively low limit means that no special security precautions are required on the site and there is in principle no formal requirement for strict tritium accountancy and emergency plans.

The Safety reports are submitted to the Safety and Reliability Directorate (SRD) of the United Kingdom Atomic Energy Authority (UKAEA). The Preliminary Safety Analysis Report was submitted early in 1988 and design safety reviews are presently in progress for each sub systems. The Final Safety Analysis Report should be ready in early 1989 and will form a major part of the basis on which the authorisation to operate with tritium should be granted.

Authorisations must also be obtained from Her Majesty's Inspectorate of Pollution (HMIP) who authorises JET to possess tritium and discharge small quantities of radionuclides to the environment. The present estimates predict routine releases of approximately 1000Ci/year of which 60% are due to maintenance work.

The Health and Safety Executives (HSE) will have to be informed about hazards and they will have to approve the measures to control or mitigate hazards such as accidental tritium releases. Calculations have shown that the worst possible accident, ie., the release of 30g of tritium under the most unfavourable weather conditions, would give rise to a maximum individual dose at the site boundary of less than 1mSv. This dose, calculated assuming a total conversion of elemental tritium into HTO, is much lower than the recommended reference level for sheltering (5mSv) or evacuation (100mSv).

In order to structure the safety analysis, ensure that appropriate effort is devoted to systems and provide a common safety approach to all systems, a tritium safety classification has been established.

Table VI. Tritium safety classifications

Class 1	Systems with a high potential for accidental (or routine) release or exposure of personnel when the effects of secondary containment or other barriers are neglected
Class 2	Systems with a low potential for routine (or accidental) release and exposure of personnel, or systems necessary to prevent (or limit) release or exposure for class 1 systems under fault conditions
Class 3	Systems which will generate tritiated wastes
Class 4	Systems with no potential for tritium release or exposure or generation of waste

The tritium classification is also used to specify Quality Assurance requirements for the manufacture of the components of the AGHS.

The methodology of safety analysis depends on the tritium classification. For class 1 systems a probabilistic approach is being followed. This involves the identification of fault initiating events and the building of event trees. The frequencies of initiating events and top events of event trees are then estimated so that the frequency of a particular accident can be plotted against the magnitude of the release. As mentioned earlier, the product of frequency and release should be less than 10Ci/year.

CONCLUSIONS: THE JET D-T PHASE IS A NECESSARY STEP TOWARDS FUSION POWER

The major effort undertaken within the 7MA study to allow operation up to 7MA, and more generally to upgrade JET performance has already paid back with results which confirm JET as the worlds leading fusion experiment. Further enhancements are still expected when beryllium is used as a first wall material and the Lower Hybrid Current Drive system is operational.

On this basis it is reasonable to expect that in D-T operation the total Q should be in the range of 0.5 to 1. The α-particle power should be of the order of 3 to 6 MW and should provide a significant heating of the plasma core. More importantly, perhaps, the density of α-particles relative to the plasma density should be close to that expected in a fusion reactor and will allow the study of the effect of the α-particles on the plasma properties. Therefore it appears that JET will be able to fulfill all its major scientific objectives including the study of production of α-particles and consequent plasma heating and behaviour.

The technological objectives of the JET D-T phase are equally important for the development of fusion research. The problems related to the use of tritium in a fusion device will be confronted and essential experience will be gained. A fusion fuel recycling loop will be operated on a tokamak for the first time. Remote maintenance procedures under real conditions of activation and tritium contamination will be put to the test. These are all vital aspects of fusion research and they must be addressed on JET before the same problems, albeit on a larger scale, are faced on a machine larger than JET. The JET D-T phase appears as an essential and irreplaceable step towards fusion power.

REFERENCES:

[1] P.H. Rebut and the JET Team. JET latest results and future prospects. Proceedings of the 11th Int. Conf. on Plasma Physics and Controlled Nuclear Fusion. Vol 1, p.31-49 Kyoto (Japan). November 1986.

[2] E. Bertolini, M. Huguet and the JET Team. JET Project Technical development dictated by the recent scientific results and prospects for extensive D-T plasma studies in break-even conditions. Proceedings of the 12th Symposium on Fusion Engineering Vol. 2. p.978 Monterey (USA). October 1987

[3] P. Noll et al, Stabilisation of vertical position and control of plasma shape in JET Proceedings of the 11th Symposium on Fusion Engineering, Vol. 1 p.33-40 Austin (USA). November 1985.

[4] R. Albanese et al, Analysis of vertical stability in the JET experiment. Proceeding of the 15th Symposium on Fusion Technology. To be published. Utrecht (The Netherlands) September 1988.

[5] P. Noll et al, Forces on the JET vacuum vessel during plasma disruptions and consequent operational limits. This Conference.

[6] M. Pick et al, Full power operation at JET : consequences for in-vessel components. Proceedings of the 15th Symposium on fusion technology. To be published. Utretcht (The Netherlands) September 1988.

[7] J. Last et al. Upgrading of the JET Magnet system for 7MA plasma. This Conference.

[8] J. Last et al, The JET Magnets : operational experience and plans for upgrade. Proceedings of the 14th Symposium

on Fusion Technology, Vol. II p.1643, Avignon (France) September 1986.

[9] M. Pick et al, Experience with graphite in JET, Proceedings of the 12th Symposium on Fusion Engineering. Vol 1. p.137, Monterey (USA) October 1987.

[10] G. Celentano et al, The JET belt limiter, Proceedings of the 14th Symposium on Fusion Technology, Vol 1. p.581 Avignon (France) September 1986.

[11] K. Dietz, Modification of the JET vacuum vessel as a result of plasma operation. European Vacuum Conference. Salford (UK) April 1986. To be published in Vacuum 1988. Pergamon.

[12] P.L. Mondino et al, The poloidal field system enhancement in JET to produce plasma currents up to 7MA with material limiter and up to 4MA with magnetic separatrix : a report on the electrical study. Proceeding of the 12th Symposium on Fusion Eng. Vol 2. p.819. Monterey (USA) October 1987.

[13] T. Bonnicelli et al, The additional switching network, a new part of the poloidal field system of JET : design and early operation. Proceedings of the 12th Symposium on Fusion Engineering. Vol. 1 p.398. Monterey (USA) October 1987.

[14] P. Kupschus et al. Proceedings of the 12th Symposium on Fusion Eng. Monterey (USA) October 1987. IEEE Vol.2. p.781 83 (1987).

[15] R.J. Bickerton. Latest JET results and future prospects. Proceedings of the 12th Int. Conf. on Plasma Physics and Controlled Nuclear Fusion Research. Nice. France. October 1988. To be published.

[16] J. Winter et al, First results from the boronization of Textor, 8th International Conference on Plasma Surface Interactions. Jülich (Federal Republic of Germany), May 1988. To be published in Journal of Nuclear Materials.

[17] P.H. Rebut et al, Use of Beryllium as a first wall material in JET. JET report. R(85)03.

[18] A. Tanga, The JET H mode. Proceedings of the 15th European Conference on Controlled Fusion and Plasma Heating. To be published. Dubrovnik (Yugoslavia) May 1988.

[19] P. Kupschus et al, Multi pellet injection on JET. Proceedings of the 15th European Conference on Controlled Fusion and Plasma Heating. To be published. Dubrovnik (Yugoslavia) May 1988.

[20] K. Sonnenberg, Prototype of a high speed pellet launcher for JET. Proceedings of the 15th Symposium on Fusion Technology. Utrecht (The Netherlands). September 1988. To be published.

[21] A. Kaye et al, Design of the JET lower hybrid launcher. Proceedings of the 15th Symposium on Fusion Technology. To be published Utrecht (The Netherlands). September 1988.

[22] J.A. Dobbing et al, Design of the JET lower hybrid current drive generator. Proceedings of the 15th Symposium on Fusion Technology. To be published. Utrecht (the Netherlands) September 1988.

[23] T. Raimondi, The JET experience with remote handling equipment and future prospects. Proceedings of the 15th Symposium on Fusion Technology. Utrecht (The Netherlands) September 1988. To be published.

[24] A.C. Rolfe, Operational aspects of the JET remote handling system. Proceedings of the International Symposium on Fusion Nuclear Technology. Tokyo (Japan), April 1988. To be published.

[25] T. Businaro, The JET high temperature in-vessel inspection system. Proceedings of the 15th Symposium on Fusion Technology. To be published. Utrecht (The Netherlands) September 1988.

[26] R. Haange et al, General overview of the Active Gas Handling System at JET, Proceedings of the 3rd Topical meeting on Tritium Technology in Fission, Fusion and Isotopic Applications. May 1-6 1986 Toronto (Canada). To be published.

[27] M. Huguet, E. Bertolini, Main features implemented in the JET facility for D-T operation. Proceedings of the 7th Topical Meeting on Technology of Fusion Energy, Reno (USA) June 1986. Fusion Technology Journal, November 1986, vol. 10. No.3, p.1398-1403.

[28] C. Caldwell-Nichols, JET Joint Undertaking, Abingdon (UK) Private Communication 1988).

[29] S. Booth, JET Joint Undertaking, Abingdon (UK) Private Communication 1988.

[30] A. Bell et al, Preparation for D-T operation at JET. Proceedings of the 15th Symposium of Fusion Technology. To be published. Utrecht (The Netherlands). September 1988.

PNOLL/LW/G

FORCES ON THE JET VACUUM VESSEL DURING DISRUPTIONS AND CONSEQUENT OPERATIONAL LIMITS

P NOLL, L SONNERUP, C FROGER, M HUGUET and J LAST
JET Joint Undertaking, Abingdon,
Oxford, OX14 3EA, United Kingdom
(0235) 464565

ABSTRACT

Disruptions at high current cause large forces and stresses at the JET vessel. Particularly undesirable are vertical disruptions due to possible failure of the vertical stabilisation system. Forces and stresses are being assessed on the basis of magnetic measurements, vessel deflections, strain gauge measurements at vertical supports and by a finite element mechanical analysis. The present operating restrictions may be relaxed after implementation of two support rings at the inner periphery of the vessel which supplement those at the outer periphery and will prevent unacceptable radial deflections.

INTRODUCTION

JET was designed for operations with up/down symmetric plasmas and currents of 5MA. It has been working successfully at that level. From past experience it emerges, however, that it is necessary to operate at higher current and, preferably, with an up/down asymmetric single X-point magnetic limiter configuration in order to obtain substantial α-particle heating in DT plasmas.

The JET machine is being upgraded for this purpose. Most enhancements have already been implemented. Operations with single X-point configurations were performed up to 5MA. Symmetric plasmas were obtained up to 7MA. The operating parameters have been restricted, however, to avoid damage, in particular in the event of disruptions and vertical instabilities. Studies are under way to establish safe operating limits and to relax the present restrictions as far as possible.

In this paper the effects of disruptions and vertical instabilities on the JET vessel are discussed.

THE VESSEL

Some parameters of the vessel are shown in table 1. The vessel has a double wall and 32 bellows sections to reduce the toroidal resistance. Two restraint rings at the outer periphery at ±1m distance from the equatorial plane provide the radial support against atmospheric and magnetic compression. The rings have insulating breaks at the bellows sections. The vertical support is achieved by two short arms between each of the large vertical ports and the adjacent horizontal limbs of the magnetic circuit. There are 2 x 8 evenly distributed vertical ports at top and bottom. Vertically, the ports are rigidly supported. Radially, the port movement is restrained only dynamically by the mass of attached equipment.

Table 1: Vessel parameters

major (reference) radius	R_o	2.96m
vertical semi-axis	b_v	~2.2m
radial semi-axis	a_v	~1.4m
poloidal length	l_{pol}	11.6m
thickness of rigid sectors		~2 x 12mm
thickness of bellows		2 x 1.8mm
bellows material		Inconel 625
rigid sector material		Nicrofer 7216LC
toroidal resistance		~520μΩ
poloidal resistance		~32μΩ

Forces give rise to a vessel deformation, restrained by the supports. The resulting radial movement of the large vertical ports is recorded with displacement transducers. Vertical deformations of the vessel can also be measured at small vertical ports at top and bottom of rigid sectors adjacent to the vertically supported sectors. These measurements are however obscured by bending and oscillations of the loaded small ports.

Some of the vertical support arms are equipped with strain gauges, giving an indication of vertical forces acting on these supports and on the vessel as a whole.

RADIAL DISRUPTIONS

Estimate of vessel forces

Forces are due to induced toroidal and poloidal currents in the vessel. Toroidal currents arise from the current quench and the radial plasma movement, poloidal curents are produced by the change of the plasma diamagnetism.

In the limiting case of a sudden quench of a plasma with circular cross section in a circular conducting torus the radial force due to toroidal eddy currents is, at the outer and inner periphery,

$$F_{R\ out,in} = -\frac{\mu_o I_p^2}{4}\left(\ln\frac{\bar{a}_v}{\bar{a}_p} + \beta + \frac{l_i - 1}{2} \pm \frac{2R_o}{\pi a_v}\right) \quad \ldots(1)$$

where I_p=plasma current, R_o=major radius, $\bar{a}_v = \sqrt{a_v b_v}$=vessel minor radius, $\bar{a}p$ = plasma minor radius, β=poloidal beta, li=normalised internal poloidal field pressure. With R_o=2.96m, $\bar{a}_v$=1.75m one obtains for a plasma of interest for JET:

I_p=7MA, $\bar{a}p$=1.4m, β=0.3, li=1)

F_{Rout}=-24.6MN
F_{Rin}=+8.5MN
F_{Rtotal}=-16.1MN (2)

This force would decrease rapidly in a time of the order of the toroidal eddy current decay time $\tau_{V\,tor}$~4ms: in JET the quench time τd is usually larger than 15ms. The expected forces are therefore substantially smaller than given by (1).

The poloidal vessel current I_V, induced by the change of the plasma diamagnetism, can be found from the equation:

$$\dot{I}_V L_V + I_V R_V A_T/(A_T - A_V) = -\frac{d}{dt}\Delta\Phi \qquad (3)$$

where L_V = 0.68μH → vessel inductance, R_V = 32μΩ → vessel resistance (poloidal), A_V = 9.7m² → vessel cross section area, A_T = 14.8m² → area of toroidal field coils. The correction $A_V/(A_T - A_V)$ arises from the coupling with the close fitting TF coil assembly, due to flux conservation. The current I_V produces a normal pressure ∝ R^{-2} on the vessel. The resulting total radial force is approximately $F_R = I_V B_T(R_o) A_V/R_o$. For a circular plasma shape the diamegnetism is related to the poloidal beta by:

$$\Delta\Phi = (1 - \beta)\,\mu_o I_p^2/8\pi\, B_T(R_p). \qquad (4)$$

For a current quench in a time which is smaller than the effective eddy current decay time $\tau_{V\,pol}$ = 7.4ms the maximum vessel force becomes in this case:

$$F_{R\,lim} = -\frac{\mu_o}{4} I_p^2(1 - \beta) = -10.8\text{MN}, \qquad (5)$$

where the numerical value is for I_p = 7MA, β=0.3, as considered above. The force decreases with the time constant $\tau_{V\,pol}$.

The combined radial forces from (2) and (5) exceed acceptable limits. It is therefore important to consider the reduction due to finite quench time.

A simulation of a radial disruption has been carried out by means PROTEUS[1], a 2D finite element code[2] which describes the evolution of the plasma equilibrium and of the electromagnetic fields. It includes the effects of eddy currents and the magnetic circuit. The circuit voltages are kept constant (=0). In the cases considered the poloidal beta was assumed to drop from 0.30 to 0.06 in 1ms while the plasma current I_p is still constant. The current quench is modelled by a linear decrease of I_p to zero in times τd=5,10 and 20ms. The plasma current density is assumed proportional to $(\psi_b - \psi)$ where ψ_b is the poloidal flux at the plasma boundary. Other initial parameters are: I_p=7MA, $B_{T\,ext}(R_o)$=3.4T, a_p=1.16m, b_p=1.70m, $\Delta\Phi$=-0.56Vs. Some results are shown in table 2 and fig 1. The flux pattern and the forces at different poloidal sections of the vessel, due to toroidal eddy currents, are illustrated in fig 2 for the case τd=10ms and when I_p has decreased to ~1MA.

Table 2: Vessel forces and currents for 7MA disruptions simulated with PROTEUS. β_o=0.3 at t<0, β=0.06 at t≥1ms, start of quench at t=1ms.

Disruption time τd(ms)	5	10	20
Max toroidal current $I_{V tor}$(MA) (time of maximum)	3.47 (5.5ms)	2.33 (9.5ms)	1.37 (15ms)
Max radial force due to toroidal currents $F_{R tor}$(MN)	-16.7 (5.5ms)	-12.6 (7.5ms)	-8.7 (10ms)
Max poloidal current $I_{V pol}$(MA) (time of maximum)	0.60 (5.0ms)	0.47 (8.5ms)	
Max radial force due to poloidal currents $F_{R pol}$(MN)	-8.7 (5.0ms)	-6.8 (8.5ms)	

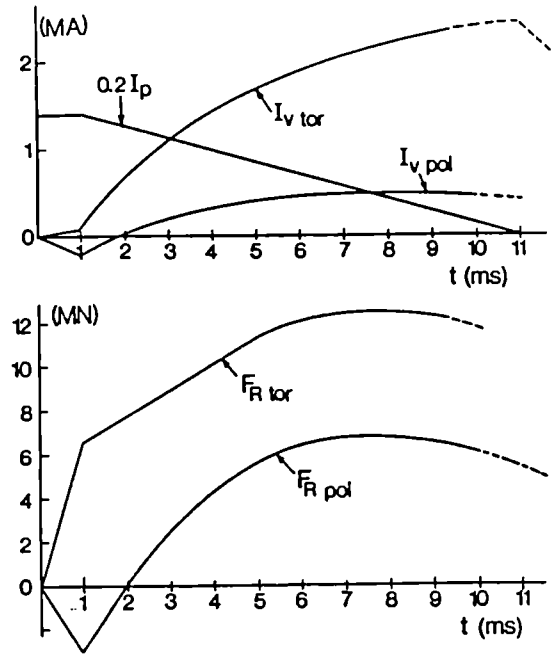

Fig 1: Radial disruption of a 7MA plasma simulated with PROTEUS. (a) Toroidal and poloidal vessel currents, (b) radial vessel forces due to these currents.

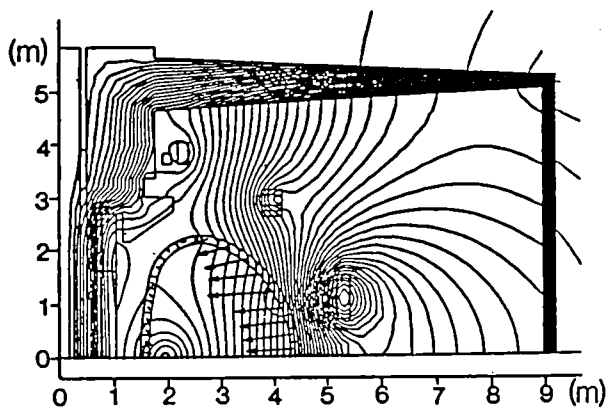

Fig 2: Flux plot and forces due to toroidal currents at vessel segments for a radial 7MA disruption with 10ms quench time, computed with PROTEUS. Time t=9.5ms, I_p=1MA. The configuration is up/down symmetric.

From table 2 one finds that for τd=10ms the total radial force F_R=-20MN is substantially smaller than the rough estimate $F_R(0)$=-27MN from (2) and (3). For more realistic cases τd>15ms one can expect $F_{R\ total} \lesssim$16MN.

Experimental results

Disruptions are unavoidable and one must be prepared for the worst case. An example of a disruption at high current is pulse 18058. Parameters and forces deduced from magnetic measurements are given in table 3, the evolution of some parameters is shown in fig 3. The disruption time τd=15ms is taken from $I_{po}/\dot{I}_p$ when I_p~5MA. The radial inward movement of the plasma centroid is quite small (<.4m) while I_p>2MA. The maximum radial displacement of the vertical vessel ports is ~6mm.

The force due to toroidal currents is deduced from loop voltage and tangential poloidal field measurements along the poloidal vessel perimeter. The evolution of this force could not be followed in detail, but at t=53.058sec (sample time indicated in fig 3) the product $I_p \cdot I_{V\ tor}$ and therefore the force is almost at a maximum. The poloidal current and the related radial force is estimated on the basis of eq(3), assuming $\Delta\Phi = \Delta\Phi_o (I_p/I_{po})^2$ and $I_p = I_{po} \exp((t_o - t)/\tau d)$.

It is considered operating at currents I_p=7MA and B_T=3.4T. If we scale the forces given in table 3, while keeping β_o and τd unchanged, one expects $F_{R\ tor}$=-9.2MN and $F_{R\ pol}$=-5.5MN. These values are similar to values of 10 and 5.6MN, resp., interpolated for τd=15ms from table 2.

Table 3: Parameters and vessel forces deduced from magnetic measurements, for pulse 18058.

Plasma current I_p(MA)	6.15
Toroidal field B_T(T)	3.15
plasma semi-axis a,b(m)	1.17, 1.81
poloidal beta β_o	0.11
diamagnetic flux $\Delta\Phi_o$(Vs)	-0.57
disruption time τd(ms)	-15
toroidal vessel current I_{vtor}(MA) (at t=53.058s)	0.70
poloidal vessel current I_{vpol}(MA) (max at -53.061s)	0.31
radial vessel forces from I_{vtor}:	
outer part $F_{R\ out}$ (MN)	-8.4
inner part $F_{R\ in}$ (MN)	+1.3
total $F_{R\ total}$ (MN)	-7.1
radial force from I_{vpol}: F_{Rpol}(MN)	-4.2

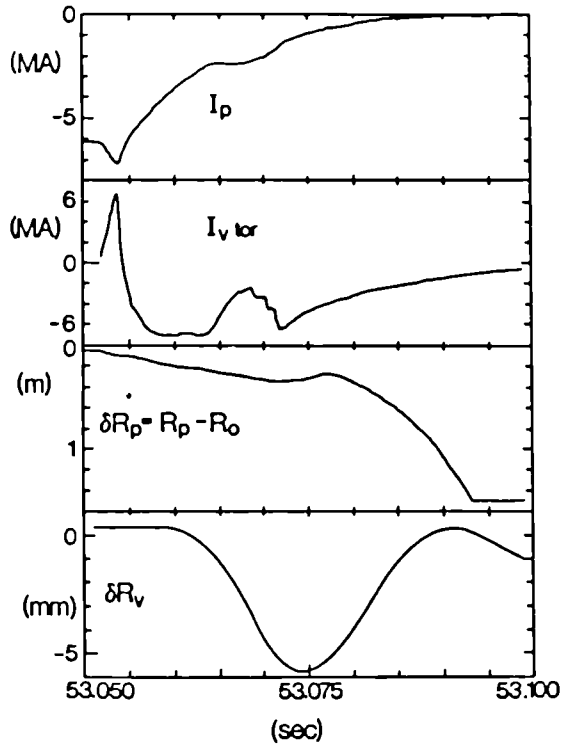

Fig 3: Plasma current I_p, toroidal vessel current I_{vtor}, radial plasma displacement δR_p and radial displacement δR_v of vertical ports during the disruption of pulse 18058

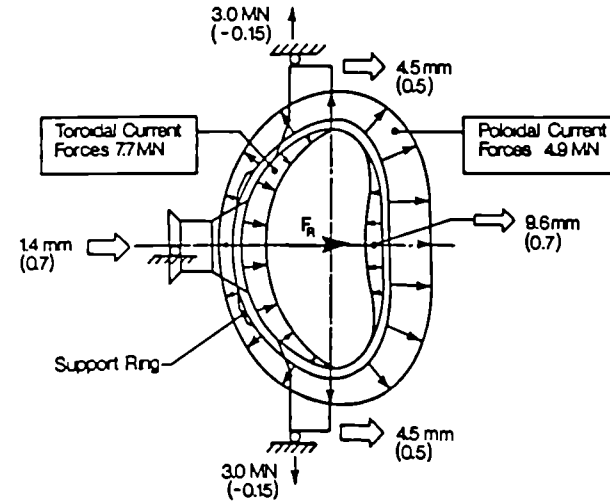

Fig 4: Forces and resulting deflections of the vessel during a radial disruption at 6MA corresponding to pulse 18058. Values in ( ) refer to the case when the inboard vessel wall has been reinforced

Mechanical analysis

Stresses and deflections of the vessel, with its present supports have been assessed by a finite element analysis[3]. Loads according to the 7MA simulation by PROTEUS for disruption time τd=10ms were assumed. For comparison with experiment the loads have been scaled with respect to I_p, β and τd to the parameters of the 6MA disruption in pulse 18058. The scaled forces assumed, F_{Rpol}= -4.9MN, $F_{R\,tor}$=-7.7MN are not much different from values derived from measurements (table 3). The fig 4 shows a sketch of the force distribution and indicates the computed static radial deflections at the inner flexible part of the vessel and at the large vertical ports where the vessel is supported firmly (with pre-compression) in the vertical direction. The deflections are particularly large at the inner part. Small vertical deflections (not shown) occur at top and bottom of adjacent unsupported rigid sectors due to the flexibility of bellows and sectors.

Dynamic radial deflections at the vertical ports are larger than the static ones by a factor 1.4 to 1.7 due to the mass associated directly with the ports (basic 350kg, with additional equipment up to 1000kg) and depending on the duration of the force. The stiffness of the system with respect to radial forces at the ports has been computed and a simplified model was used to obtain the radial dynamic forces and deflections at the ports. For the case of pulse 18058 one expects a radial deflection of about 7mm. This agrees reasonably with the measured amplitude of -6mm shown in fig 3.

Points of high local stress and strain are at the base of the vertical ports. For a disruption time of 15ms, a strain of -0.1% is estimated for a radial deflections of -4.5mm at a port carrying a weight of 1000kg. In pulse 18058 the estimated maximum strain was therefore about 1.4 times higher. Pending an investigation of the low cycle fatigue properties of the vessel material, a strain level of 0.2% (-9mm deflection) for a limited number of cycles is deemed acceptable. This corresponds to a 7MA radial disruption similar to the one in pulse 18058.

VERTICAL INSTABILITY

Expected vertical forces

If the vertical stabilisation system fails the vertical plasma position becomes unstable due to the destabilising effects of the iron circuit and of the quadrupolar component of the equilibrium field required to produce an elongated plasma shape. The plasma moves vertically, governed by the balance of the destabilising force on the plasma,

$$F_{p\,dest} = f I_p^2 Z_p, \qquad (6)$$

and stabilising forces due to currents in the vessel and the radial field coil (R-coil) induced by the plasma movement. The normalised destabilising force f is in the range 0.35 ... 0.60MN/(MA)²m, depending on the magnitude of the applied shaping quadrupolar field.

From a simplified rigid displacement model[3] one expects an initial growth rate:

$$\gamma = \frac{1}{T_v} \cdot \frac{m-k}{1-m} \qquad (7)$$

and a vertical force acting on the vessel

$$F_{zv} = F_{p\,dest} \cdot \frac{(m-k)(1-m)}{(1-k)m} , \qquad (8)$$

where:

T_v=3ms → effective decay time of differential toroidal currents $\pm I_v$ in the upper/lower half of the vessel,

k=0.37 → coupling coefficient between R-coil current I_R and vessel current I_v,

$m = fL_{vv}/L'^2_{vp}$=0.4 ... 0.7 → measure of instability degree

L_{vv}=12μH → vessel inductance for differential current I_v,

L'_{vp}=3.2μH/m → mutual inductance change vessel/plasma for unit displacement Z_p.

For m≤k the growth scales with the R-coil time constant, for m≥1 the plasma position is MHD unstable.

Equilibrium computations for elongated D-shaped plasmas give typically f=0.5MN/(MA)²m and m=0.58. Eq(7) gives γ=170s⁻¹ in accordance with measurements. From eq(8) one finds $F_{zv}=0.24F_{p\,dest}=0.12I_p^2Z_p$(MN). This is only applicable for small displacements, at larger displacements eq(8) underestimates the force F_{zv} due to omission of terms $\propto Z_p^3$. For I_p=7MA and Z_p=1m one expects therefore F_{zv}>6MN, which exceeds substantially the estimated danger level of ~3-4MN for the present status of vessel supports. There are however indications that the forced reduction of the plasma size, after contact with the top or bottom part of the vessel, leads to a disruption when the boundary q-value becomes smaller than about two. This limits the maximum value of $I_p^2(t)Z(t)$, in particular in plasmas with high current which are only possible with relatively small initial q.

Plasmas with single X-point magnetic limiter are more unstable. Typically f=0.55MN/(MA)²m, giving γ=260s⁻¹ and $F_{zv} \geq 0.13 I_p^2 Z_p$ from eq7,8. Displacements Z_p before significant reduction of the current I_p are in general larger than in symmetric plasmas without X-points, vertical vessel forces are therefore relatively large.

Simulations of the vertical instability have been carried out with the PROTEUS code in few cases. For an elongated D-shaped plasma the ratio $F_{zv}/I_p^2Z_p$ was found to be =0.17MN/(MA)²m, which is larger than the corresponding estimate from eq8,6 by a factor 1.4. So far, the computations are however not conclusive because there are significant differences between experiment and prediction concerning growth rates and the orbit of the current centroid.

Experiments

Previously reported vertical instability tests[4] were repeated after modifications of the vessel supports and with higher currents up to 3.5MA. Instabilities are provoked by disabling the feedback stabilisation during the current flat top. Of particular interest are scaled down analog versions of anticipated plasmas with 7MA/3.4T in symmetric limiter configuration and with 6MA/3.2T in single X-point configuration.

The evolution of the vertical instability in a symmetric plasma with elongation ratio b/a=1.6 is illustrated in fig 5. The plasma centroid moves first vertically with an initial growth rate γ=160s⁻¹. The current quench starts when the boundary q-value has decreased to about 2. The vertical displacement increases still further thereafter and reaches a maximum of ~0.85m. During the current quench the plasma moves inwards and returns towards the equatorial plane, following the contour of the vessel.

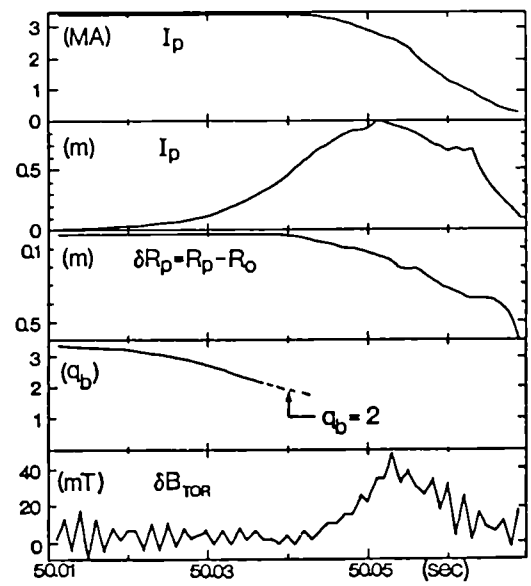

Fig 5: Evolution of pulse 15100 (3.5MA/1.8T) after disabling vertical stabilisation at t=50.00sec (10sec after start). I_p - plasma current, Z_p - vertical position, δR_p - radial displacement, q_b - q at plasma boundary, δB_{tor} - difference of toroidal field at top and bottom.

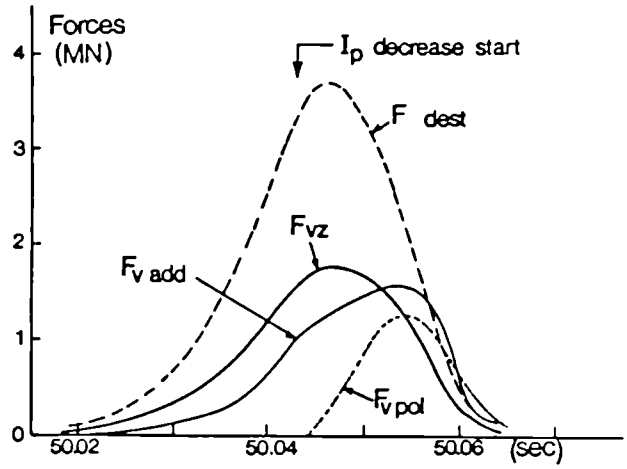

Fig 6: Vertical forces at the plasma and the vessel evaluated from magnetic measurements for pulse 15100 (3.5MA/1.8T)
F_{pdest} - destabilising force at plasma
F_{vz} - total vertical force at vessel
F_{vadd} - additional force at vessel
F_{vpol} - contribution to F_{vadd} estimated from the difference ΔB_{tor} at top and bottom.

The fig 6 shows the vertical forces acting on the plasma and the vessel, evaluated from magnetic measurements in a somewhat simplified way as performed previously[4]. Use is made of the requirement of complete force balance of the plasma. It is found that the destabilising force F_{dest} is not balanced by the stabilising forces from R-coil and differential vessel currents. An additional repelling force $F_{padd}=-F_{vadd}$ must be present between the plasma and the vessel to provide the balance. The flow of poloidal currents across the plasma and returning through the vessel has been considered as a possible mechanism[5]. A rough estimate of the corresponding force $F_{v\,pol}=-2\pi RwB_T\delta B_T/\mu_0$ due to the measured toroidal field difference δB_T (fig 5) is included in fig 6; w=1.5m is the assumed radial width of the poloidal current loop. $F_{v\,pol}$ is zero before the start of the current quench, in contrast to $F_{v\,add}$. So there may be other mechanisms for a repelling force[6]. It should be noted that the ratio $F_{vz}/F_{pdest}=0.5$ is much larger than expected from eq8 for a linear model with toroidal currents only, which gives a ratio 0.24.

The vessel force is also found to be significantly larger than the vertical force at the vessel supports deduced from strain gauge measurements. The latter one has however a longer duration and peaks with about 10ms delay.

Table 4: Results of vertical instability tests for pulses 15100 and 15241

	Unit	15100	15241
Plasma current I_p	MA	3.49	3.46
Toroidal field B_T(2.96m)	T	1.8	1.8
Configuration		D	X-point
Elongation ratio b/a		1.6	1.8
Poloidal beta β		0.1	0.1
Instability growth rate γ	s^{-1}	160	290
Max plasma displacement δZ_p	m	+0.85	-0.95
Current quench time τ_d	ms	-22	-18
Relative destabilising force f	$\frac{MN}{(MA)^2 m}$	0.49	0.57
Max destab. force F_{pdest}	MN	+3.7	-5.2
Max "add'l force" F_{vadd}	MN	+1.54	-2.6
Max vertical vessel force F_{vz}	MN	+1.8	-3.1
Max vessel support force F_{supp}	MN	-1.1	+1.6
F-parameter	$(MA)^2$	32	40
Average of first radial deflection of vertical ports at top and bottom	mm	+1.3	-4.9
	mm	-4.6	+2.8
Instability degree with R-coil open circuit → m		0.57	0.67
R-coil shorted → m-k		0.20	0.30

The table 4 presents a summary of vertical instability tests for the pulses 15100 and 15241, which are analogs of high current limiter and single X-point plasmas. There are unexpected large differences in the relative increase of vertical vessel forces F_{vz}, support forces F_{supp} and mean of top and bottom radial deflection amplitudes of vertical ports between the two pulses, the ratios of these parameters are 1.7, 1.5 and 1.3, resp.. These differences and the differences between vessel and support forces indicate that the evaluation of forces is inaccurate and requires a re-examination.

A direct indication of strong forces are the radial deflections at the vertical ports. For vertical instabilities the first half wave is opposite at top and bottom. For the cases shown the amplitude at the port opposite to the plasma movement exceeds the mean amplitude by a factor 1.6 and 1.3, resp.. At the port on the side of the plasma the second half wave is usually larger than the first one but remains smaller than the deflection at the opposite port.

Net vertical displacements of the unsupported rigid sectors, adjacent to the

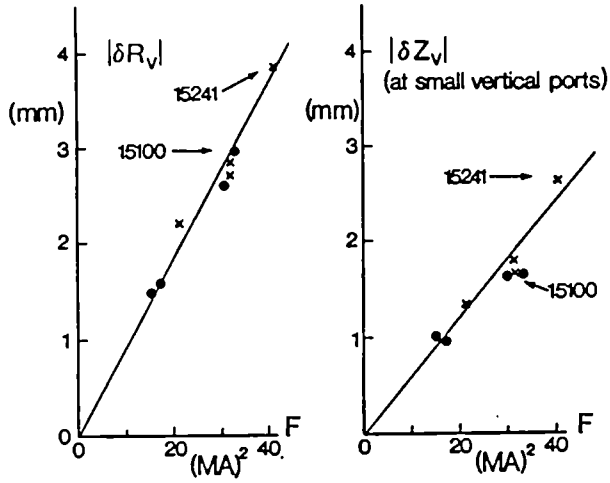

Fig 7: Average amplitudes of radial and vertical displacements at vessel ports of vertical instability tests with symmetric limiter (•) and single X-point plasmas (x) vs "F-parameter".

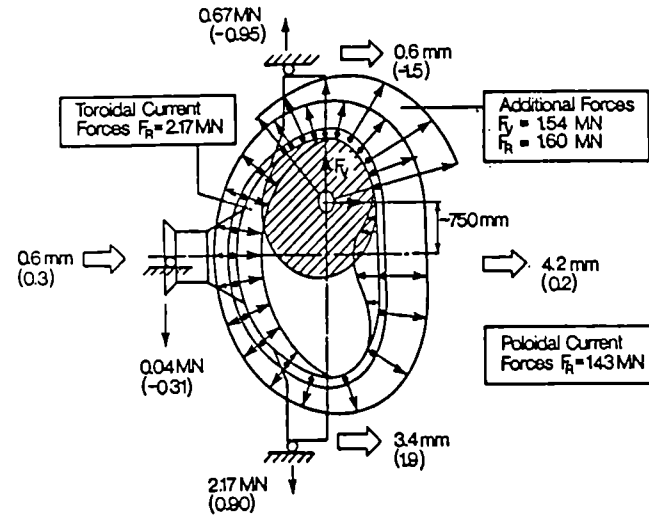

Fig 8: Forces and resulting deflections at the vessel corresponding to the vertical instability in pulse 15100 at 3.5MA. Values in ( ) refer to the case after re-enforcement of the inboard wall.

sectors with vertical supports, are measured at small vertical ports. The fig 7 shows mean radial and vertical vessel port deflections as function of a predeterminable force parameter F for a number of pulses with deliberately provoked vertical instability and with different currents and plasma shapes. The F-parameter is chosen to be proportional to a crude estimate F_{vz}=constI_p^2(m-k) of the vertical vessel force according to eq6,8 (ignoring the factor 1-m):

$$F = I_p(I_p + 14N_{sh}I_{sh} + 300I_d) \quad (MA)^2, \qquad (9)$$

where N_{sh} = preselectable effective turns of the shaping coil assembly, I_{sh} = shaping coil current, I_d = difference current between central and top/bottom sections of the transformer coil. I_{sh} and I_d govern the plasma elongation. The average deflections shown in fig 7 are essentially proportional to F. The maximum radial deflections are on average 1.4 times larger than mean values for pulses with vertical instability.

The F-parameter is used as guideline for operation. With the present vessel support system a limit F=75(MA)² has been accepted for normal operation. A stabilisation failure could give up to ~10mm radial deflection at the large vertical ports and strains of order 0.2% at the base of these ports.

Mechanical analysis

The effects of a vertical instability and subsequent disruption were analysed using loads as estimated for the 3.5MA pulse 15100 (fig 6).

The fig 8 shows the assumed force distribution at time t=50.055sec (when the combined radial and vertical force is maximum) and the static deflections at ports and the inboard side of the vessel. Forces due to global toroidal and poloidal currents arising from the current quench are scaled, with respect to I_p, β and quench times τd, from the simulation by PROTEUS of a 7MA radial disruption (table 2) to pulse 15100 (I_p=3.5MA, β=0.1, τd=20ms). The vertical force is taken from F_{vz} derived from magnetic measurements and assumed to be localised as indicated in fig 8.

The radial deflections are larger at the bottom than on top as found experimentally. The static deflection at top is opposite to the first half wave of the observed oscillation. This may be due to uncertainty of the force distribution and also due to the effect of inertial loads. From a simplified dynamic model one expects an enhancement of deflections by a factor 1.4 to 1.7 for mass loads at the vertical ports between 350 and 1000kg. The corresponding deflections in the range of 4.8 to 5.8mm at the bottom ports are in reasonable accordance with deflections 3.9, 4.8 and 5.0mm (average 4.6mm) measured at three ports (the measurement at the fourth position was faulty).

In a vertical instability of a 7MA D-shaped plasma, with disruption time 20ms, one expects 4 times higher forces and deflections, and the maximum strain at the base of a port loaded with a mass of 1000kg would become of the order 0.4%. This is two times larger than expected in a radial disruption.

VESSEL MODIFICATIONS

With the present system, routine operation at 7MA would be risky. To permit operation at this level some modifications are being prepared: mechanical decoupling of heavy masses from vessel ports, inclusion of two inboard support rings and radial dampers at the large vertical ports.

The mechanical decoupling has been implemented already where possible so that only the basic mass load of 350kg is effective. In these cases the strain at the base of the ports is greatly reduced except for the unlikely event of a fast radial disruption in a time <10ms. The soft X-ray diagnostics at octant 2 (M~1000kg) cannot be decoupled and poses therefore a restriction while it is in use.

The inboard wall will be stiffened by two support rings above and below the equatorial plane. They will be welded across bellows and reduce the resistance of the inner part of the vessel to 1/2. The effects on plasma start-up resulting from larger induced currents are regarded as manageable. The reduction of deflections of vessel ports and of the vessel itself is dramatic ,as can be seen from the values in brackets shown in fig 4 and 8. The contribution of inertial radial forces at the base of ports with heavy mass load will therefore be reduced considerably.

Finally, radial dampers will be implemented at the vertical supports. This measure alone would reduce the effect of mass loads on the strain at the base of the large vertical ports by a factor 2.

SUMMARY

Radial disruptions of 7MA plasmas with 15ms disruption time are expected to produce a radial force of about 16MN on the vessel and local strains of 0.2% at the base of the large vertical ports.

A vertical instability of a 7MA D-shaped plasma will give in addition a vertical force of about 7MN and cause local strains around 0.4%. Similar forces and strains are expected at a lower current of about 6MA when a plasma with single X-point configuration becomes vertically unstable.

Vessel modifications are in preparation to make routine operation possible at these anticipated current levels.

REFERENCES

1. R A ALBANESE et al, "Preliminary Analysis of Vertical Instability and Disruption Effects for JET 7MA Configuration", The NET Team, Report NET/87/TE/075-R-01, 8 October 1987.

2. R A ALBANESE, J BLUM and O DE BARBIERI, "The PROTEUS Code", presented at the Workshop on "Feedback Systems for shape control of non-circular Tokamaks", Lausanne, Switzerland, July 13-17, 1987.

3. L SONNERUP, ,Nuclear Engineering and Design/Fusion, vol 3 (1986) p 235-247, North Holland, Amsterdam.

4. P NOLL et al, Proceedings of the 11th Symposium on Fusion Engineering, Austin 1985, Vol 1 pp 33-40.

5. P THOMAS, JET Joint Undertaking, private communication 1984.

6. R A ALBANESE et al, "Analysis of Vertical Instability in the JET Experiment", paper presented at the 15th Symposium on Fusion Techology, Utrecht, 19-23 September 1988.

UPGRADING THE JET MAGNET SYSTEM FOR 7MA PLASMA

J.R. LAST, E. BERTOLINI, M. HUGUET,
P.L. MONDINO, P. NOLL and L SONNERUP
JET Joint Undertaking, Abingdon, Oxon.,
OX14 3EA, United Kingdom
(0235) 464565

C. BELL and T. MOLYNEAUX
Ove Arup and Partners
London, UK

I. ABSTRACT AND INTRODUCTION

JET was designed for a plasma current of 5 MA and has operated successfully at that level. To enable JET to produce meaningful DT plasmas, it is necessary to upgrade the machine performance.[1] The paper describes the effects on the poloidal and toroidal magnet systems of increasing the plasma current to 7 MA. It has not been necessary to increase the toroidal field but operation at higher plasma current increases the torque loading on the coils. In the case of the poloidal coils an increased flux swing is required so the magnetising current has been increased by 50%. Effects considered include magnetic forces and mechanical and thermal stresses in the coils. Modifications to the coil system and improvements to the power supplies that enable the new performance to be achieved are described. It is concluded that a 7 MA plasma current is feasible.

II DESCRIPTION OF MAGNET SYSTEM

A. Coils

Fig. 1 shows a cross-section through the JET machine in which the toroidal and poloidal magnet systems[2] can be seen.

The toroidal field (TF) system comprises 32 D-shaped coils designed to produce a field of 3.45 T at 2.9 m radius. The coils are conventional water cooled, epoxy glass insulated copper coils. Some important parameters are given in Table 1. The inward forces of the toroidal coils are supported by poloidal coil 1 and the out of plane forces by a shell type mechanical structure and fluted cylinder at the toroidal/poloidal coil interface.

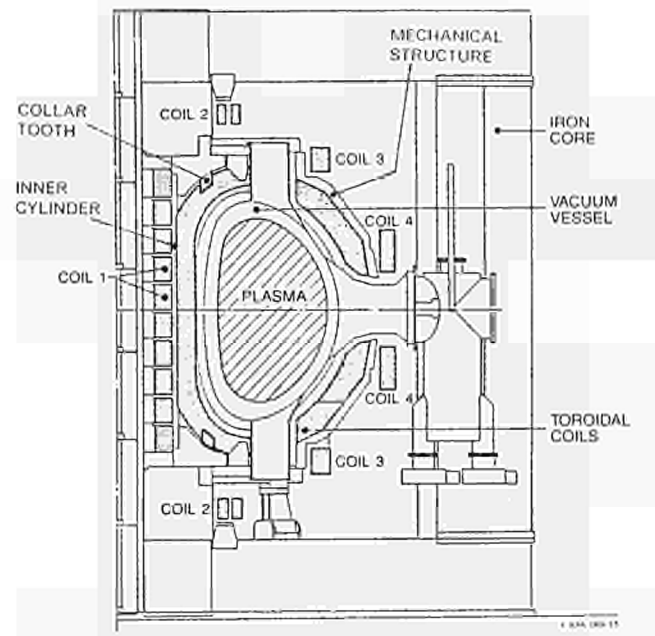

Fig.1 Cross Section through JET Machine

The poloidal coils (P1, P2, P3 and P4 on Fig. 1) are also of water cooled, epoxy glass insulated copper. The inner coil (P1)

Table 1 : Main upgraded parameters of TF and PF coil systems (original parameters bracketed)

TF coils:		PF coils:	P1	P2	P3	P4
number of coils	32	number of coils	10	2	2	2
total weight (tonnes)	380	total weight (tonnes)	100	28	84	158
maximum current (kA)	67 kA	maximum current (kA)	60(40)	40	40	40
effective pulse length (secs)	25(20)	maximum flux swing (Wb)	42(34)			
max. energy per pulse (GJ)	7(5.5)	integral I^2 dt (10^9 A^2sec)	45(30)			32

carries magnetising currents and the flux of this coil passes mainly through the transformer core. Coils P2 and P3 carry shaping and radial field currents and coil P4 carries vertical field currents. S me important parameters are given in Table 1.

B. Power Supplies

The TF coils are fed by a flywheel generator convertor (FGC) in series with static units taking power from the electrical supply grid. The PF coils are fed by a similar FGC via a switching network to give high plasma breakdown voltages. The equilibrium and control coils are fed by static amplifiers.

III OPERATING CONDITIONS OF COILS

Table 2 lists the main forces and thermal effects acting on the coils.

A. General

The operational field of the TF coils (3.45 T at 2.9 m major radius) is sufficient to allow a 7 MA plasma with reasonable stability margins. Although the toroidal field will not be changed, operation at higher plasma current increases stresses on the coils due to higher poloidal field crossing them.

To reach 7 MA plasma current the flux swing of the primary winding has to be increased from its design value of 34 Wb to 42 Wb by increasing the current in the central magnetising coils (P1) from 40 kA to 60 kA. This will more than double the outward force due to the poloidal magnetic field and is made possible because the toroidal coils exert an inward pressure on the poloidal coils, which approximately balances the outwards force.

Plasma equilibrium is maintained by the vertical field coils (P4) and the current in these coils has to increase with the plasma current. However the JET machine was originally designed for high beta and extrapolation of present machine operating condition shows that currents of less 30 kA will be sufficient for 7 MA plasma current compared with the design value of 40 kA.

Plasma shape (elongation and triangularity) is controlled by currents flowing in coils P2 and P3. It is not proposed to increase the current in these coils above the design limit because

- sufficient elongation can easily be achieved
- high triangularity, which would need high shaping currents, also leads to high out of plane forces on the TF coils in the collar tooth region (see section V.)

Table 2 Forces and Thermal Effects Acting on Coils

	TF coils	P1 coils
Magnetic forces	due to toroidal field, forces in plane of coil resulting in tension in coil winding and net inward force (nc)	radially outwards due to axial poloidal field (i)
	due to poloidal field, forces perpendicular to plane of coil resulting in torque on coil stack (i)	vertical due to radial poloidal field (i)
Externally applied forces	none	inward force of TF coils on outer surface (nc) vertical forces due to magnetic circuit and weights (i) torque due to twisting of TF coil structure (i)
Reactions	inward force reacted by inner poloidal coils (nc)	mainly contained within coil structure (i)
	out of plane forces reacted by support structure (i)	external reactions only to take weight (nc)
Thermal effects	temperature rise during pulse 70 deg.C (i)	temperature rise during pulse 50 deg.C (i)
	stresses due to thermal gradients (i)	stresses due to thermal gradients (i)

(nc) no change due to upgrade, (i) increased by upgrade

It can be seen from the above that the main problem areas for increased performance are the toroidal coils and the inner poloidal coils (P1). These are described in more detail in the following paragraphs.

B. Current Waveforms

Fig. 2 shows current waveforms for a 7 MA plasma current pulse. It will be seen that the P1 coil has a relatively complicated waveform, which can be divided into phases as shown. Each phase causes a different loading condition, which has to be analysed. The TF loading scenario is simpler and consists only of in plane loads due to the toroidal field and out of plane loads which follow the plasma current.

IV. MECHANICAL PROPERTIES OF COIL MATERIALS

The main materials used in the JET coil construction are:

copper - in half hard condition

insulation - vacuum impregnated epoxy glass

steel - 13% chromium steel used for P1 support rings

The properties of these materials are given in the following sections.

A. Copper

The copper is in half hard condition (except at brazed joints and electron beam welds) and for TF and P1 coils has 0.1% silver content. Properties are:

Elasticity modulus	120	GPa
0.2% proof stress (minimum)	200	MPa
coefficient of thermal expansion	17.10^{-6}	/deg K

B. Insulation

The insulation is woven glass tape vacuum impregnated with epoxy resin. In the case of the poloidal coils the glass tape is interleaved with Kapton tape to improve the electrical breakdown strength but this has some effect on the mechanical properties. Mechanical properties have been derived from JET tests and from the literature. Values used in the calculations were:

	TF coils	PF coils	
Elasticity modulus (E)	10	10	Gpa
Shear modulus (G)	4	4	GPa

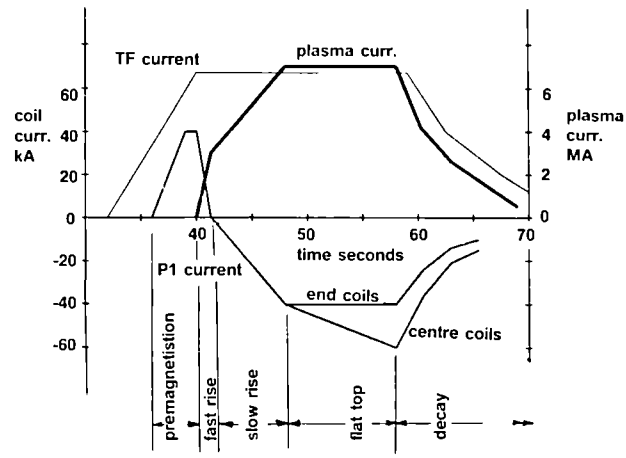

Fig.2 Current Waveforms for 7MA Plasma

Maximum interlaminar tensile stress	20	15	MPa
Maximum compressive stress	80	60	MPa
Maximum interlaminar shear stress	20	15	MPa
Coefficient of thermal expansion	30.10^{-6}	30.10^{-6}	deg K

The allowable shear stress is increased when combined with perpendicular compressive stress and reduced when combined with tensile stress. This behaviour can be modelled by the Mohr Brittle Failure Criterion. Fig. 3 shows graphic representation of a failure envelope a which enables an effective shear stress to be derived from combined stress conditions.

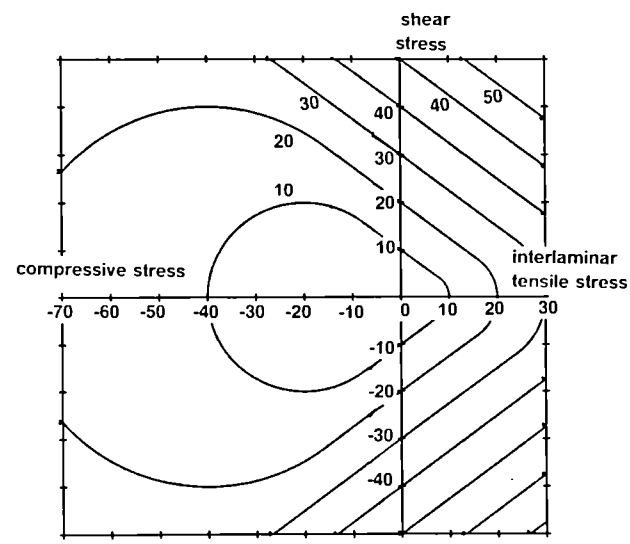

Fig.3 Mohr Brittle Failure Criterion for Epoxy Glass Insulation (contours of effective shear stress)

C. Steel

The steel used for the P1 coil support rings is 13% chromium steel, which has suitable electrical, thermal and mechanical properties for the application. Mechanical properties are:

Elasticity modules (E)	210	GPa
Yield stress	240	GPa
Coefficient of thermal expansion	12.10^{-6}	/deg

V. COIL STRESS ANALYSIS

A. Finite Element Models

Analysis has been made starting with simple models and, when these are understood, proceeding to more complex codes as indicated by the simple ones. Use was also made of global and local models, the global model being used to set boundary conditions for the local models and the results from the local models being used as stress enhancement factors in the global calculation.

The different geometry of the TF and P1 coils led to the use of different types of models. In particular the mainly axisymmetric geometry of the P1 coil allowed a 2D model to be used as a first approach.

For both types of coil the direct stresses in the copper were considered to be acceptable and the main point of concern was the shear stress in the insulation and at the copper insulation interface.

B. TF coil analysis

A simple shear panel model was used to make an overall assessment of stresses and to indicate regions of high stress. To obtain values of peak stress a brick element model was necessary (see Fig. 4). The orthotropic properties of the brick elements were validated using small models detailing the laminated structure of the coil.

The well-known "D" shape of the coils ensures that the toroidal field produces only tension (maximum stress = 100 MPa) in the coil winding together with an inward force of 1800 tonnes. The poloidal field gives out of plane forces resulting in a torque on the coil structure. This torque is restrained by the mechanical structure which has sufficient factors of safety to cope with upgraded performance. Analysis using the simple model showed that the points of concern were shear stresses in the insulation:

- at the collar tooth support (see Fig 1)

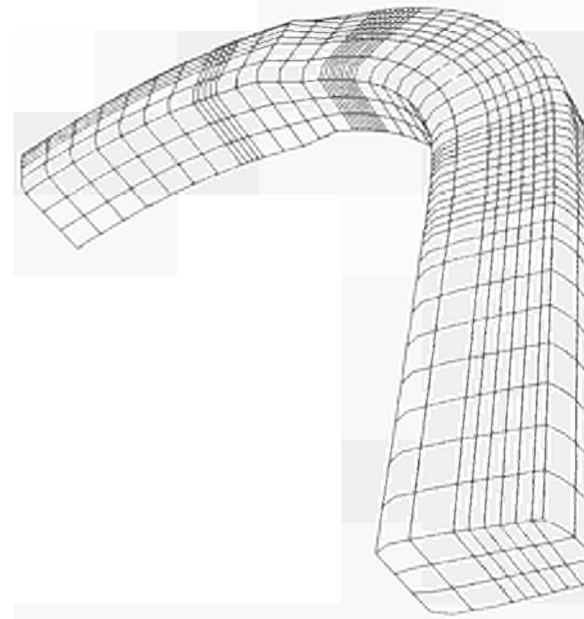

Fig.4 Finite Element Model of Section of Toroidal Coil

- at the end of the straight section where the coil leaves the inner cylinder support.

Many load cases involving different poloidal field configurations have therefore been investigated in detail. Some cases which lead to reasonable stresses are listed in Table 3. Other load cases with, for example, higher elongation or stronger shaping fields can lead to higher stresses. To avoid these high stress conditions a new protection system as described in section VII.A has been implemented.

The same models have been used to analyse the results of the mechanical tests described later. It will be seen that these test results indicate a safety factor of more than 1.5 for shear stress in the insulation.

Table 3 Loading Cases for TF Coils

Plasma curr. MA	Elong -ation	Type	Max. Shear Stress in Insulation Inter-turn MPa	Inter-pancake MPa	Collar Support Force tonnes
7	1.5	limiter	7	6	30
7	1.6	limiter	16	13	70
7	1.6	single X	14	12	63
Prototype coil test			25	28	125

C. P1 Coil Analysis

The P1 coils are subject to operating conditions as described in Table 2, applied in a sequence defined by the current waveforms (section III.B, Fig. 2). It is not obvious what the maximum stress conditions will be for every part of the coil and so stresses have to be calculated throughout the current waveform and subsequent cool down period. To do this efficiently stresses for unit load conditions corresponding to all the possible applied loads and temperatures have been calculated. These unit load stresses were added in the correct proportions to build up stress scenarios as required.

Calculations using a simple 2D axisymmetric model firstly confirmed that hoop stresses due to the poloidal field and toroidal coils were indeed balanced out and secondly showed that thermally induced shear stresses were a major problem. This was because cooling water entered the coil at the top and left at the bottom and therefore, during the cooldown period, the top of the coil was cold while the bottom was still hot. This resulted in large temperature gradients across the coil with associated thermal stresses.

A cooling scheme as described in section VII.B has therefore been implemented in which the temperature difference across the coil is limited to less than 20 deg.C.

In addition to the shear stresses induced by thermal gradients, shear stresses in the coil insulation are also caused by departures from axisymmetry in the winding such as transitions between coil turns and layers. These features have been analysed by detailed 3D global (see Fig. 5) and local models, which show that the shear stresses can be expressed as a linear function of the direct stresses at the location.

For the given scenario (section III.B, Fig. 2) and using the new cooling scheme, a graph of maximum effective shear stress against time is shown in Fig. 6. Consideration of a range of scenarios enabled the diagram shown in Fig. 7 to be constructed, which imposes constraints on machine operation. These constraints have been built into the machine protection systems.

VI. MECHANICAL TESTS

A. Small and Medium Scale Tests

When the JET coils were made, the properties of the copper used was well established. The properties of the insulation were not so well known, especially as the JET insulation incorporated two new (at that time) features:

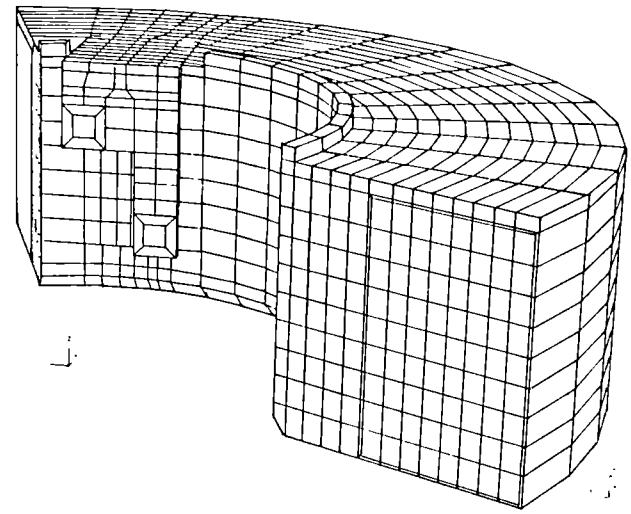

Fig. 5 Finite Element Model of Section of P1 Coil

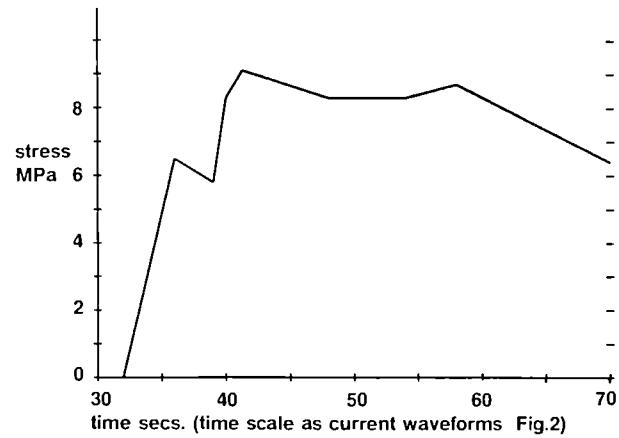

Fig. 6 Maximum Effective Shear Stress versus Time for P1 Coil Insulation

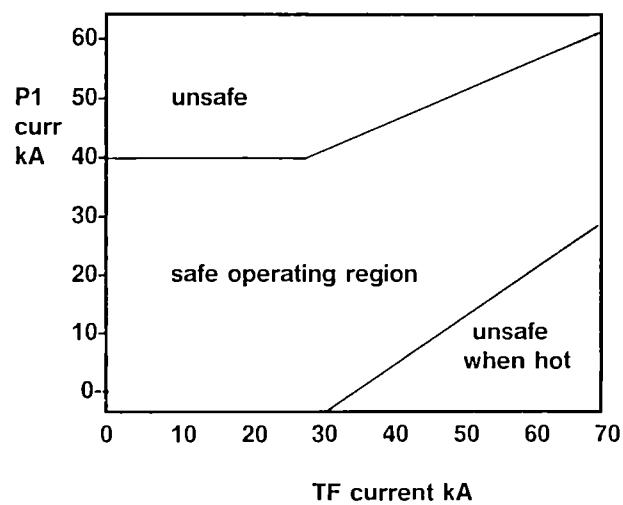

Fig. 7 Safe Operating Region for P1 Coil

- priming of the copper surface with "DZ80" and
- interleaving Kapton tape between the woven glass tapes before impregnation (PF coils only)

Small scale tests were therefore carried out during the JET design and construction phases to establish the basic material properties. Medium scale tests of coil sections were also made during manufacture to validate the process and to test the composite strength of the coil assemblies.

B. Test of Prototype TF Coil

When the stresses in the TF coils for upgraded performance were analysed, it was realised that the critical points were the shear stresses in the collar tooth region and at the transition from straight to curved section of the coil. Stresses in these regions were very high (in some cases higher than the allowable stresses quoted in section IV.B). As a prototype TF coil was available, it was decided to carry out mechanical tests, simulating out of plane loads, on this coil.

Fig. 8 is a diagram of the test arrangement. The loads were applied cyclically by a system of hydraulic jacks at increasing levels up to a maximum of 200 tonnes. The deflections of the coil were measured and periodic electrical interturn tests made in order to detect incipient failure. The test was terminated when the limit of the test rig was reached. No change in mechanical characteristics or damage to the coil was detected. Some results of the test are included in Table 3. Results are given for the highest cyclic load at which 10,000 cycles were made. A total of 100,000 cycles were made at lower loads which nevertheless exceeded the level required for 7 MA operation. It will be seen that the test results exceed the expected stresses by at least 50%. The test was therefore considered satisfactory as a guarantee of safe operation at 7 MA, although less interesting as failure modes were not detected.

VII IMPROVEMENTS TO COIL SYSTEMS

A. TF Coil Protection System

To avoid high stresses as described in section V.B a new protection system has been implemented. This system measures the poloidal flux crossing the TF coil in the collar tooth region and multiplies it by the TF current to give a measure of the out of plane force in this region. If this force exceeds an acceptable level, the machine pulse is terminated. By making a direct measurement of the out of plane forces part of the TF coil protection system, it is not necessary to place limits on the plasma current or other operating parameters.

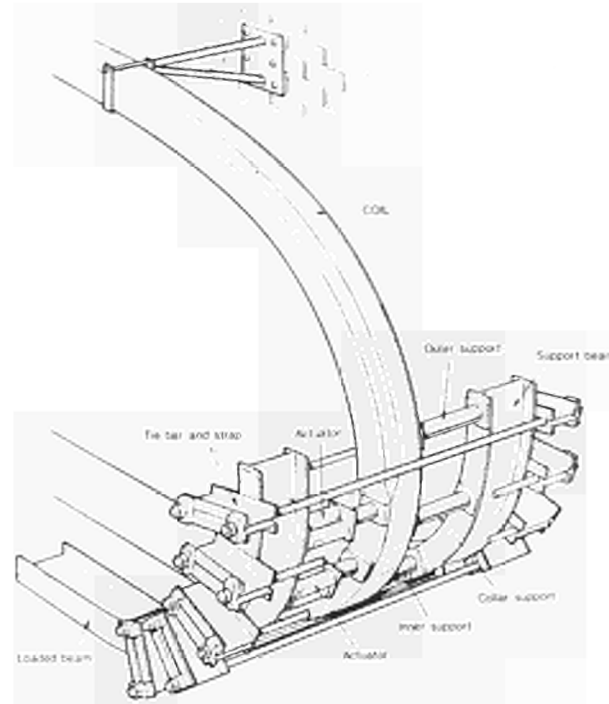

Fig. 8 Arrangement for Mechanical Test of TF Coil

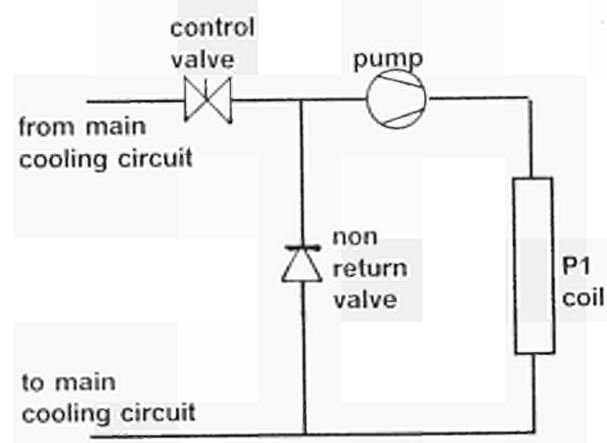

Fig. 9 Recirculating Cooling Water Scheme for P1 Coil

B. P1 Cooling System

To avoid the high thermal stresses described in section V.C. a new cooling scheme was proposed and has been implemented in which the temperature difference across the coil is limited by re-circulating the water rapidly from coil outlet to inlet, as shown in Fig. 9. By this means the temperature difference across the coil can be limited to any desired preset level. With the new cooling scheme it was possible to raise the current heating integral to the value given in Table 1.

VIII POWER SUPPLY UPGRADES

Like the TF coils the TF power supply does not require significant upgrading. The only change is that the pulse has been lengthened from 20 to 25 seconds (at 67 kA). This means that the energy dissipated in a pulse has increased from 5.5 to 7 GJ. The TF generator can supply up to 2.6 GJ so the rest has to come from static power supplies.

The poloidal field supply has evolved considerably since it was first built in 1983. Fig. 10 shows the current version. Recent additions which are relevant to 7 MA plasma operation are:

- current modulation circuit (CMC) controlling current in centre section of P1 coil enabling higher currents and larger flux swing to be achieved
- additional switching network (ASN) connected across P1 coil; thyristor make switches in this network can be closed soon after the circuit breaker is opened to control the rate of plasma current rise
- booster amplifier (PVFB) in vertical field circuit giving sufficient voltage at plasma breakdown to control the vertical field and plasma position correctly
- centre point connection and new controls in vertical field circuit enabling upper and lower P4 coils to have unequal currents - an advantage when setting up single X point plasmas

These changes are described below.

A. Current Modulation Circuit

This circuit enables the current in the centre section of coil P1 to be controlled independently. The main components as shown in Fig. 10 are:

The poloidal X point amplifier (PFX) - a 2.8 kv, 35 kA amplifier identical in construction to the existing vertical field amplifier

the blocking diodes (BDX) to withstand the voltage across P1 coil during the fast rise

the filter (C3 and R13) to protect the amplifier against transient overvoltage when capacitor C is discharged

The PFX amplifier is controlled by an extended version of the Plasma Position and Current Control (PPCC) system. A new protection system has been installed to protect against new fault possibilities introduced by the new circuit.

B. Additional Switching Network (ASN)

The object of the additional switching is to reduce the voltage applied to the P1 coil during early rise of the plasma current. A high voltage is initially required to break down the plasma and this is developed across resistors R3 and R4 when switch S1 is opened. The high voltage, if allowed to decay naturally, would cause too rapid a rise of the plasma current. The voltage is therefore reduced by closing groups of thyristor make switches (TMS) as required (typically 2 groups of 3 switches closed 150 and 230 ms after S1 opens).

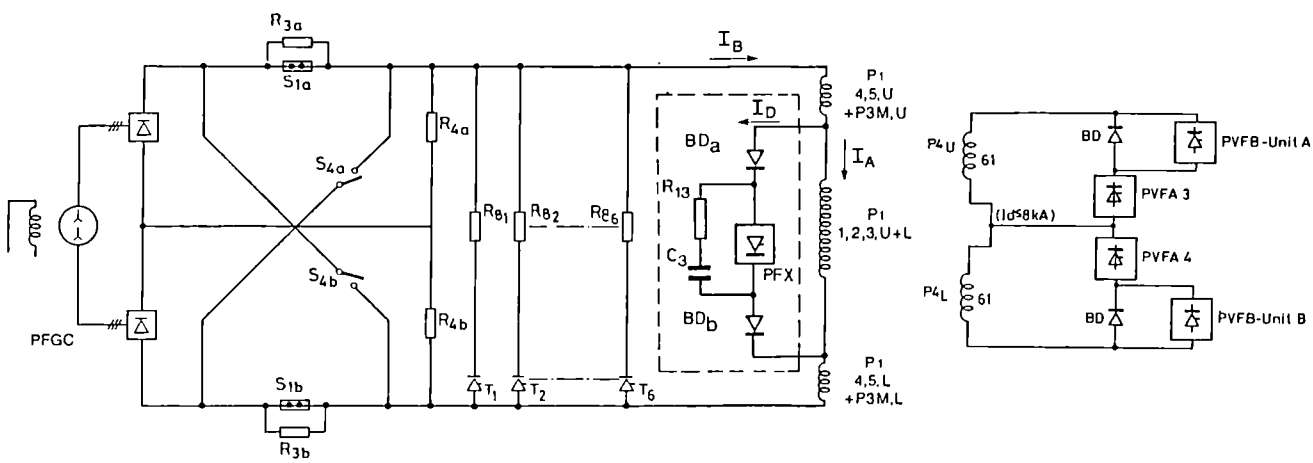

Fig. 10 Poloidal Field Power Supply

C. Booster Amplifier (PVFB)

The booster amplifiers are connected across the blocking diodes of the vertical field amplifier (PVFA). This means that PVFB only has to carry current at the beginning of the fast rise and thereafter the current is carried by the blocking diodes. The output voltage of PVFB is 9 kv at 1 kA falling to 2 kv at 6 kA and it is only expected to carry current for 0.5 s.

D. Unbalanced Operation of Vertical Field Circuit

The connection to the centre point of the P4 coils means that the vertical field amplifier and booster amplifier (PVFA and PVFB) have had to be split into a symmetrical arrangement as shown in Fig. 10. This is possible because of the modular design of the amplifiers,. The control circuits have also been modified so that the amplifiers are fed common and difference voltage corresponding to symmetrical and assymmetrical operation of the coils. The maximum difference current is 8 kA and the maximum difference voltage is set to 240 v.

IX CONCLUSIONS

The studies described above showed that the JET electromagnetic system is capable of producing 7 MA plasma current with a 5 to 10 second flat top time. Most of the upgrades described above have already been implemented and 7 MA plasma pulses have been made.

In fact plasma currents higher than 7 MA may be possible with the same stress levels, as plasma current is not a direct parameter in the limiting stresses on the coil system.

- In the case of TF coils, the limiting factor is the poloidal flux crossing the coil in the collar tooth regions. Thus high plasma currents are acceptable as long as excessive shaping field is not required in this region.

- In the case of the PF coils or, more specifically, the P1 magnetising coil, the limitation is the available flux swing and pulse length. Thus higher plasma currents can be produced at the expense of pulse length or if other methods of minimising flux consumption are found.

In both cases the coil systems are fully protected against damaging operating conditions and are ready for whatever mode of operation may be required.

In future and especially when the coil systems become inaccessible in the tritium phase, development will concentrate on power supplies and protection systems to make best use of the equipment already installed on the torus.

X ACKNOWLEDGEMENTS

Some of the finite element models described were developed by Engineering Analysis Division, Princeton Plasma Physics Laboratory[3]. Modifications to the JET machine and systems were made by members of the JET team.

Thanks are due to all who participated either with helpful discussions or by implementing hardware.

XI REFERENCES

1. E. BERTOLINI, J.R. LAST, P.L. MONDINO, P. NOLL, A. SANTAGUISTINA, "The Development of the JET Electromagnetic System, 14th Symposium of Fusion Technolgy, 1986

2. M. HUGUET, K. DIETZ, J.L. HEMMERICH and J.R. LAST, "The JET Machine: Design, Construction and Operation of the Major Systems", Fusion Technolgy, Vol II, Jan. 1987.

3. Report on JET contract JG6/0158.